

Fracture and Strength of Solids

Part 1

Fracture Mechanics of Materials

DEPT. OF MECHANICAL ENGINEERING 4

20000911 067

Editors:

W. Hwang and K.S. Han

Department of Mechanical Engineering
Pohang University of Science and Technology

DISTRIBUTION STATEMENT A

Approved for Public Release

Distribution Unlimited

ttp TRANS TECH PUBLICATIONS

Key Engineering Materials

ISSN 1013-9826

Specializing in the Field of Basic and Applied Aspects of
Advanced Ceramic Materials and Composites

Editors:

Erian Armanios

Georgia Institute of Technology
School of Aerospace Engineering
Atlanta, GA 30332, USA
Fax +1 (404) 894 9313
e-mail: erian.armanios@aerospace.gatech.edu

Yiu-Wing Mai

The University of Sydney
Centre for Advanced Materials Technology
Sydney NSW 2006, Australia
Fax +61 (2) 351 2290
e-mail: mai@tiny.me.su.oz.au

Golam M. Newaz

Wayne State University
Department of Mechanical Engineering
Detroit, Michigan 48202, USA
Fax +1 (313) 577 8789
e-mail: gnewaz@me1.eng.wayne.edu

Fred H. Wöhlbier

Trans Tech Publications Ltd
Brandrain 6
CH-8707 Zuerich-Uetikon, Switzerland
Fax +41 (1) 922 10 33
e-mail: f.wohlbier@ttp.net

Editorial Advisory Board:

Australia

C.H.J. Davies (Clayton)
B.H. O'Connor (Perth)
L. Ye (Sydney)

Austria

R. Danzer (Leoben)

Canada

Z. Wang (Toronto)

China P.R.

D.L. Jiang (Shanghai)
J.K. Kim (Kowloon)
Z.G. Wang (Shenyang)
A. Xing (Jinan)

Denmark

B.F. Sorensen (Roskilde)

Egypt

M.A. Taha (Cairo)

France

F. Thevenot (Saint-Etienne)
M. Ignat (Saint Martin d'Hères)

Germany

G. Grathwohl (Bremen)
H. Schmidt (Saarbruecken)
H. Schneider (Köln)
G. Tomandl (Freiberg)
W. Weppner (Kiel)

India

D. Chakravorty (Calcutta)
K. Chattopadhyay (Bangalore)
B.V. Radhakrishna Bhat (Hyderabad)
S. Ray (Roorkee)
B.K. Sarkar (Calcutta)
G.S. Upadhyaya (Kanpur)

Ireland

P. McHugh (Galway)

Israel

R. Fischer (Haifa)

Japan

M. Iwasa (Osaka)
H. Hamada (Kyoto)
M. Mitomo (Ibaraki)
O. Nakamura (Osaka)
H. Sekine (Sendai)
K. Uematsu (Nagaoka)

Korea

S. Baik (Pohang)
C.P. Hong (Seoul)
S.H. Hong (Taejon)

Portugal

R.M. Almeida (Lisboa)

Russia

S.M. Barinov (Moscow)

Singapore

C.Y. Yue (Nanyang)

Slovakia

P. Sajgalik (Bratislava)

Spain

L. Esquivias (Cadiz)
A. Ureña-Fernandez (Madrid)

The Netherlands

R. Fordham (Petten)

UK

A. Hendry (Glasgow)
F.L. Riley (Leeds)
R. Taylor (Manchester)

USA

R. Abbaschian (Gainesville)
D.H. Allen (College Station)
I. Dutta (Monterey)
W.W. Gerberich (Minneapolis)
E.J. Lavernia (Irvine)
S. Mall (Wright-Patterson AFB)
R.O. Ritchie (Berkeley)
J.A. Sekhar (Cincinnati)
J.F. Shackelford (Davis)
J.E. Shelby (Alfred)
A. Shukla (Kingston)
W.O. Soboyejo (Columbus)
R. Soleccki (Storrs)
G.J. Weng (New Brunswick)
J.-M. Yang (Los Angeles)

Yugoslavia

D. Uskokovic (Beograd)

Internet:

The table of contents of each volume is freely available on the Internet through Trans Tech Publications' Preview Service (preview@ttp.net) as well as on the World Wide Web at <http://www.ttp.net>.

Subscription Information:

Key Engineering Materials is published in 18 volumes per year. In 2000, volumes 171-188 are scheduled to be published. The subscription rate is US\$ 78.00 per volume or US\$ 1404.00 per year.

ttp Trans Tech Publications Ltd

Brandrain 6 • CH-8707 Uetikon-Zuerich • Switzerland

Fax +41 (1) 922 10 33 • e-mail: ttp@ttp.net

<http://www.ttp.net>

REPORT DOCUMENTATION PAGE					<i>Form Approved</i> OMB No. 0704-0188	
<small>The public reporting burden for this collection of information is estimated to average 1 hour per response, including the time for reviewing instructions, searching existing data sources, gathering and maintaining the data needed, and completing and reviewing the collection of information. Send comments regarding this burden estimate or any other aspect of this collection of information, including suggestions for reducing the burden, to Department of Defense, Washington Headquarters Services, Directorate for Information Operations and Reports (0704-0188), 1215 Jefferson Davis Highway, Suite 1204, Arlington, VA 22202-4302. Respondents should be aware that notwithstanding any other provision of law, no person shall be subject to any penalty for failing to comply with a collection of information if it does not display a currently valid OMB control number.</small> PLEASE DO NOT RETURN YOUR FORM TO THE ABOVE ADDRESS.						
1. REPORT DATE (DD-MM-YYYY) 01-09-2000		2. REPORT TYPE Conference Proceedings			3. DATES COVERED (From - To) 16-18 August 2000	
4. TITLE AND SUBTITLE 4th International Conference on Fracture & Strength of Solids Pohang, Korea, 16-18 Aug 00					5a. CONTRACT NUMBER F6256299M9182	
					5b. GRANT NUMBER 	
					5c. PROGRAM ELEMENT NUMBER 	
6. AUTHOR(S) Conference Committee					5d. PROJECT NUMBER 	
					5e. TASK NUMBER 	
					5f. WORK UNIT NUMBER 	
7. PERFORMING ORGANIZATION NAME(S) AND ADDRESS(ES) Pohang Univ. of Science & Technology Dept of ME, San31 Hyoja-dong Pohang 790-784 Korea (South)					8. PERFORMING ORGANIZATION REPORT NUMBER N/A	
9. SPONSORING/MONITORING AGENCY NAME(S) AND ADDRESS(ES) AOARD UNIT 45002 APO AP 96337-5002					10. SPONSOR/MONITOR'S ACRONYM(S) AOARD	
					11. SPONSOR/MONITOR'S REPORT NUMBER(S) CSP-99-06	
12. DISTRIBUTION/AVAILABILITY STATEMENT Approved for public release; distribution is unlimited.						
13. SUPPLEMENTARY NOTES						
14. ABSTRACT Part 1: Fracture Mechanics of Materials. Includes: Fracture Mechanics; Dynamic Fracture; Computational Mechanics; and Damage Mechanics. (678 Pages) Part II: Behavior of Materials and Structure: Includes: Fracture Physics; Fatigue and Creep; Polymer and Polymer Composites; Metals, MMCs, Ceramics, and CMCs; and Welding. (672 Pages)						
15. SUBJECT TERMS Fracture Mechanics						
16. SECURITY CLASSIFICATION OF:			17. LIMITATION OF ABSTRACT UU	NUMBER OF PAGES 1,350	19a. NAME OF RESPONSIBLE PERSON Thomas D. Kim	
a. REPORT U	b. ABSTRACT U	c. THIS PAGE U			19b. TELEPHONE NUMBER (Include area code) +81-3-5410-4409	

Fracture and Strength
of
Solids
Part 1

Fracture and Strength of Solids

Part 1

Fracture Mechanics of Materials

Editors:

W. Hwang and K.S. Han

Department of Mechanical Engineering
Pohang University of Science and Technology

ttp **TRANS TECH PUBLICATIONS LTD**
Switzerland • Germany • UK • USA

Copyright © 2000 Trans Tech Publications Ltd, Switzerland

ISBN 0-87849-861-3 (2-vol. set)

Volumes 183-187 of
Key Engineering Materials
ISSN 1013-9826

Distributed in the Americas by

Trans Tech Publications Inc
PO Box 699, May Street
Enfield, New Hampshire 03748
USA

Phone: (603) 632-7377
Fax: (603) 632-5611
e-mail: ttp@ttp.net
Web: <http://www.ttp.net>

and worldwide by

Trans Tech Publications Ltd
Brandrain 6
CH-8707 Uetikon-Zuerich
Switzerland

Fax: +41 (1) 922 10 33
e-mail: ttp@ttp.net
Web: <http://www.ttp.net>

Printed in the United Kingdom
by Hobbs the Printers Ltd,
Totton, Hampshire SO40 3WX

The Proceedings of
Fourth International Conference
on
Fracture & Strength of Solids

Pohang, Korea, August 16~18, 2000

Organized by

Far East and Oceanic Fracture Society (FEOFS)
The Korean Institute of Metals and Materials
The Korean Society of Mechanical Engineers
The Korean Society of Precision Engineering

Executive Committee

President : Y.Y. Earmme, Korea Advanced Institute of Sci. &Tech.

Vice-President : W.H. Chen, National Tsinghua University
B. Cotterell, National University of Singapore
K. Kishimoto, Tokyo Institute of Technology
F. Rose, AMRL-AED
W. Yang, Tsinghua University

Directors : M. Kikuchi, Science University of Tokyo
J.K. Lim, Chonbuk National University
C.T. Liu, Institute of Mechanics, Academia Sinica
D. Liu, ASM Assembly Automation Ltd.
Y.J. Liu, Zhengzhou Research Institute
Y.W. Mai, University of Sydney
T. Nishioka, Kobe University of Mercantile Marine
S.H. Teoh, National University of Singapore
T.T. Wu, Hong Kong University of Sci. & Tech.
X.R. Wu, Institute of Aeronautical Materials
T. Yokobori, Teikyo University
T.Y. Zhang, Hong Kong University of Sci. & Tech.

Treasurer : W. Hwang, Pohang University of Sci. & Tech.

Secretary General : K.S. Han, Pohang University of Sci. & Tech.

Organizing Committee

Chairman : K.S. Han, Pohang University of Sci. & Tech.

Secretariat : W. Hwang, Pohang University of Sci. & Tech.

Members : T.J. Kang, Seoul National University
B.S. Kim, Korea Institute of Machinery & Materials
Y.J. Kim, Sungkyunkwan University
K.Y. Lee, Yonsei University
S.B. Lee, Korea Advanced Institute of Sci. & Tech.
O.S. Lee, Inha University
W.I. Lee, Seoul National University
J.K. Lim, Chonbuk National University
H.C. Park, Pohang University of Sci. & Tech.

International Advisory Board

S.N. Atluri	Georgia Institute of Technology
P.T.Y. Chang	Hong Kong University of Sci. & Tech.
W.H. Chen	National Tsinghua University
Y.K. Cheung	University of Hong Kong
C.L. Chow	University of Michigan, Dearborn
B. Cotterell	Nan Yang Technology University
Y.Y. Earmme	Korea Advanced Institute of Sci. & Tech.
J.W. Hutchinson	Harvard University
K.C. Hwang	Tsinghua University
K.S. Kim	Brown University
K.S. Kim	Pohang University of Sci. & Tech.
H. Kobayashi	Tokyo Institute of Technology
Y.W. Mai	University of Sydney
R. McMeeking	University of California, Santa Barbara
C.F. Shih	National University Singapore
P. Tong	Hong Kong University of Sci. & Tech.
J. Xiao	Beijing University of Sci. & Tech.
T. Yokobori	Tekyo University

Sponsors

Far East and Oceanic Fracture Society (FEOFS)
Korea Science and Engineering Foundation
The Korean Federation of Science and Technology Societies
Korea Research Foundation
Air Force Office of Scientific Research
Pohang Iron and Steel Co. (POSCO)
Hyundai Heavy Industry
Safety and Structural Integrity Research Center (SAFE)
Keum Kwang Co.
Pohang University of Science and Technology (POSTECH)

Preface

These proceedings contain papers accepted for presentation at the Fourth International Conference on Fracture and Strength of Solids. The triennial conference is the fourth in the series after the tremendous successes in Singapore (1991), China (1994) and Hong Kong (1997). With the sponsorship of the Far East and Oceanic Fracture Society (FEOFS), the conference is today the premier one concerned with the mechanics and mechanisms of fracture, fatigue and strength of solids.

The FEOFS was founded for the purpose of presenting the latest findings and exchanging ideas with each other in the fields of fracture and strength of materials and have supported the Conference.

The International Conference on Fracture and Strength of Solids has always maintained a high standard as demonstrated by the number of countries/regions from which papers have been submitted and the high quality papers finally selected for inclusion in this volume. This is also a direct reflection of the continuing growth in the pursuance of research and development in this field. The volume covers broad areas of Fracture Mechanics, Computational Mechanics, Dynamic Fracture, Damage Mechanics, Fracture Physics, Fatigue and Creep, Polymer and Polymer Composites, MMCs and CMCs, Welding etc, that is all the areas of Applied Mechanics Parts.

We wish to thank all authors who contributed papers to the conference and all referees for their efforts to review the papers. Thanks are also due to the members of the Executive Committee, Organizing Committee and the International Advisory Committee for their efforts in making the conference a success. We acknowledge the supports by the local and international sponsors, including Far East and Oceanic Fracture Society (FEOFS), Korea Science and Engineering Foundation, The Korean Federation of Science and Technology Societies, Korea Research Foundation, Air Force Office of Scientific Research, Pohang Iron and Steel Co. (POSCO), Hyundai Heavy Industry, Safety and Structural Integrity Research Center (SAFE), Keum Kwang Co., Pohang University of Science and Technology (POSTECH)

Prof. Kyung Seop Han

Chairman of Conference Organizing Committee

Table of Contents

Part 1: Fracture Mechanics of Materials

Conference Information	v
Preface	ix
Fracture Mechanics	
Length-Scale Effects in Nano- and Micro-Mechanics of Solids	
K.-S. Kim and J.A. Hurtado	1
Mechanism-Based Strain Gradient (MSG) Plasticity and the Associated Asymptotic Crack-Tip Fields	
K.-C. Hwang and Y. Huang	9
An Analysis of Fatigue Crack Growth Rate Considering Spatial Variation of Fatigue Crack Growth Resistance	
S.J. Kim	19
Rectangular Array and Zig-Zag Array of Elliptical Holes in Solids under Uniaxial Tension (Formulae of Maximum Stresses and Tensile Stiffnesses)	
H. Igawa	25
Crack Growth in Stainless Steel 304AT 538°C under Fatigue Loading with and without Hold Time	
Y.M. Baik and K.S. Kim	31
An Inverse Fracture Problem of a Shear Specimen with Double Cracks	
Y. Li, Z. Rui and J. Huang	37
Fracture Mechanics Analysis of Cracked Plate Repaired by Composite Patch	
K.H. Chung, W.H. Yang and M.R. Cho	43
Fracture Toughness Test of Small CNS Specimen with an Interface Crack Subjected to Mixed-Mode Loading	
K. Machida	49
Theoretical Investigation of Controllable & Regular Fracture Theory	
A. Zhou, Y. Wei and F. Lang	55
Crack Identification Using Classical Optimization Technique	
M.W. Suh, J.M. Yu and J.H. Lee	61
Study on Strength of Rock Material under Dynamic Triaxial Compressive Loads Based on Sliding Crack Model	
H.B. Li, T.J. Li, J. Zhao, J.G. Gao and J.G. Jiang	67
Kinking out of a Mixed Mode Interface Crack	
T. Ikeda, Y. Komohara, A. Nakamura and N. Miyazaki	73
Global Crack-Line Displacement Fitting Procedure: Edge Cracks	
H.Y. Jiang, Z.L. Li and F.L. Zhan	79

A Stochastic Modeling for Predicting Fatigue Crack Growth under Variable Amplitude Loading	
D.S. Shim and J.K. Kim	85
A Highly Accurate BEM in Fracture Mechanics	
Z.L. Li, F.L. Zhan and S.H. Du	91
Simulation and Experimental Verification of Axial Multi-Crack Propagation and Crack Kinking in Pressurized Fuselage	
A. Shimamoto, T. Oguchi, D.Y. Ju and A.S. Kobayashi	97
Calculation of Stress Intensity Factor Using Weight Function Method for a Patched Crack	
J.H. Kim, K.W. Lee, D.C. Seo and S.B. Lee	103
Interaction of a Horizontal Finite Crack with a Center of Dilatation in Elastic Half-Planes	
K.T. Chau, R.H.C. Wong and R.C.K. Wong	109
Determinations of Stress Intensity Factor in Isotropic and Anisotropic Body by the Photoelastic and Caustics Methods under Various Load Ratios	
A. Shimamoto, J.H. Nam, T. Shimomura and E. Umezaki	115
A Micromechanics Criterion for the Ductile Fracture of a Polycarbonate	
T.J. Wang, K. Kishimoto and M. Notomi	121
Effect of Specimen Thickness and Load History on Crack Growth of 7175-T74 Forging Aluminum Alloy	
J.Z. Liu, X.R. Wu, C.F. Ding and D.X. You	127
Plastic η Factors Based on Load-CMOD Records for SE(B) Toughness Testing Specimens	
Y.-J. Kim	133
Electromagnetic Thermoelastic Solids with an Elliptical Cavity or a Crack under Uniform Heat Flow	
X.L. Liu, X.F. Liu, J.X. Liu and J. Zheng	139
Evaluation of Stress Intensity Factor Using White Light Photoelastic Experiment	
E. Umezaki, K. Kodama and A. Shimamoto	145
Singularity Intensity Factor Calculation in Plates and Shells Based on the Singular Line Mapping Technique in FEMOL	
C. Liu and Y. Xu	151
Collective Evolution Characteristics and Computer Simulation of Voids Near the Crack Tip of Ductile Metal	
H. Yu and Y. Hong	157
The Relationship of SIF between Plate and Plane Fracture Problems and the Effect of the Plate Thickness on SIF	
Y. Xu and C. Liu	163
Fractographic Approach for Fracture Mode	
N. Hattori, S. Nishida and H. Yamamoto	169
Microscopic Deformation at a Crack Tip in a Ferroelectric Material	
W. Yang, F. Fang and T. Zhu	175
The Unified Description of the Three-Dimensional Fields at Notches and Cracks	
W. Guo, T. Chang and Z. Li	181

Buckling and Fracture of Thin Films under Compression	
B. Cotterell and Z. Chen	187
Recent Advances in Three-Dimensional Fracture Mechanics	
W. Guo	193
Static Magnetoelastic Coupling in Soft Ferromagnetic Elastic Solids with Collinear Cracks	
W. Liang, Y. Shen and M. Zhao	199
A Study on Deformation Energy of P/M Copper and Ingot Material	
T. Senthilvelan, A. Venkatraman and K. Raghukandan	205
Fracture Analysis on the Coating Crack Perpendicular to the Interface of Bi-Material	
B. Su and C. Li	211
A Combined Model of Short Crack Closure Accounting for Both Plasticity and Roughness Induced Crack Closures	
X.P. Zhang, C.H. Wang, J.C. Li, Y.-W. Mai and L. Ye	217
Scattering of Plane Compressional Waves by a Spherical Inhomogeneity with a Linear Spring Type Interface	
Z. Zhong and X.B. Yu	223
 Dynamic Fracture	
From Recent Studies on Impact Fracture of Polymers and Polymer Composites	
K. Takahashi	229
Dynamic Stress Intensity Factors of Cylindrical Interface Cracks Subjected to P-Wave	
W.J. Feng and Z.Z. Zou	241
Effects of Impact Loading Rate on the Delamination Behavior of Composite Laminates	
N.S. Choi	247
Shock Adiabatics of Cement Mortar at Intense Dynamical Loading by Taking into Account the Internal Damage	
S. Shih, D. Li and L. Wang	253
A Study on the Impact Failure Mechanism of Aluminum-PMMA Interfacial Crack	
D.K. Shin, J.J. Lee and M.Y. Lyu	259
Experimental Analysis of Dynamic Effects in Brittle Fracture of PMMA	
K. Arakawa, T. Mada and K. Takahashi	265
Impact Damage Behavior and Evaluation of Residual Strength in Plain-Woven Glass/Epoxy Composites	
K.W. Kang and J.K. Kim	271
Measurement of Dynamic Fracture Parameters in the Expansion Process at High Strain Rate	
C.Y. Gao, H.J. Shi, C.L. Liu, C.H. Bai and Z.H. Yao	277

A Study on the Development of the Dynamic Photoelastic Experimental Method for Isotropic/Orthotropic Bimaterials	
J.S. Hawong, D.C. Shin, O.S. Lee, H.J. Lee and J.K. Ha	283
Evaluation of Large Strain in Ductile Polymers under High Speed Loading	
T. Kuboki, T. Mada and K. Takahashi	289
Damages in Woven Polymer Matrix Composites under Impact Loading	
T.W. Kim, H. Park, C. Kim and J.H. Lee	295
Applications of the Shadow Spot Method on the Determination of Dynamic Stress Intensity Factors	
Z. Li and X. Su	301
High Strain-Rate Deformation of Composite Materials Using a Split Hopkinson Bar Technique	
O.S. Lee, J.Y. Lee, G.H. Kim and J.S. Hwang	307
Experimental Studies on Dynamic Fracture Phenomena	
T. Nishioka, T. Fujimoto and K. Sakakura	313
The Fracture Problem of Framed Plate under Explosion Loading	
Y. Li, Y. Wei and Y. Hou	319
Dynamic Mixed Mode Crack Propagation Behavior of Structural Bonded Joints	
O.S. Lee and A.S. Kobayashi	325
Analysis of a Crack in a Functionally Gradient Interface Layer under Static and Dynamic Loading	
Y.S. Wang and D. Gross	331
Fundamental Study of Dynamic Stress Wave Using a Dynamic Photoelastic Method	
T. Kanemitsu and Y. Sawa	337
Using High-Speed Camera to Investigate Failure Waves in K9 Glass	
J. Zhao, C. Sun, Z. Duan, X. Tan, F. Zhao and S. Wen	343
A Study on Dynamic Fracture in Stiffened Cylinder Subjected to a Strong Acoustic Wave	
E. Kim, H.L. Yin, K.S. Kim, C.H. Jo, O.S. Lee and C.W. An	349
 Computational Mechanics	
Static and Mode Analyses of Composite Plates Using Modified 16-Node Solid Elements, and Prediction of Stiffness Errors Resulting from Reduced Integration	
Y.D. Kwon, Y.S. Kim, T.H. Yun and M.H. Cho	355
Shape Optimization of General Structures	
S.Y. Han and J.S. Maeng	361
Simulation of Crack Growth and Creep Fracture by a Multicrack Growth Model	
M. Tanaka	367
Dual-Phase Functionally Graded Composite Materials: Overall and Discrete Analysis Models	
J.R. Cho and D.Y. Ha	373
A Study on Efficiency Improvement of Evolutionary Structural Optimization	
S.Y. Han, T.H. Lee and J.K. Lim	379

Numerical Simulation of Crack Elongation and Reinforcement Effectiveness of the Isolated Rockmass between Shiplocks of Three Gorges Project P. Xu and X.-T. Feng	385
Out-Of-Plane ESPI Simulation for the Harmonic Vibration of a Thin Right-Angled Plate S.S. Jarnng, J.H. Lee, H.G. Ahn and J.C. Park	391
Element Modeling for Vibration Analysis of Plate Y.P. Shi and P. Zeng	397
Hierarchical Models for Laminated Composite Structures Based on p-Extensions J.R. Cho, S.H. Kim and D.Y. Ha	403
Nonlinear Displacement Field in the Vicinity of Notch-Tip in Rubber Toughened PMMA M. Todo, K. Arakawa and K. Takahashi	409
Optimum Design for Fatigue Strength Improvement of Spot-Welded T-Type Bus Window Pillar Member M.H. Kim, D.S. Kim, M.W. Suh and D.H. Bae	415
Dynamic Response Analysis of a Structure under High Over-Load L. Liu and X. Lin	423
Nonlinear Analysis of Thick Composites with Fiber Waviness under Flexural Loading H.-J. Chun and S.W. Lee	427
Fuzzy Mathematical Method for Evaluation of Rock Mechanical Indexes G. Zhang, T. Li and S. Bai	433
Topology Optimization of the Inner Reinforcement for an Automobile Hood Using Modal Design Sensitivity Analysis T.H. Lee, S.Y. Han and J.K. Lim	439
Computational Studies on Dynamic Fracture Phenomena T. Nishioka and T. Fujimoto	445
Nonlinear Dynamic Buckling Analysis of a Grid Structure K.H. Yoon, K.N. Song and Y.S. Lee	451
Dynamic Modeling and Numerical Analysis for Large Scale Chime Group P. Zeng, L. He and G.H. Tang	457
Plastic Analysis of Square Grillage under A Point Load S.C. Lee, K.S. Hong and K.S. Kim	463
Finite Element Analyses of Specific Damping Capacity and Undamped/Damped Forced Motion of Composite Plate Using Modified 16-Node Solid Elements T.H. Yun, Y.D. Kwon, C. Kim and J.G. Park	469
Stress Analysis for New Gasketless Flange and Superseal N.-A. Noda, K.-I. Takeuchi, Y. Takase and M. Nagawa	475
A Study on Stress Wave Propagation in Stiffened Cylinder Subjected to a Strong Acoustic Wave J.H. Choi, K.S. Kim, C.H. Jo, O.S. Lee and C.W. An	481
Element-Free Galerkin Methods for Fracture of Functionally-Graded Materials J. Chen, L. Wu and S. Du	487

A Study on the Shape Design and Contact Characteristic of Wheel-Rail for Rolling Stock	
K.D. Sung, W.H. Yang and M.R. Cho	493
Stress Analysis of Toroidal Hole in an Infinite Body	
T. Matsuo and N.-A. Noda	499
A Parametric Study on the Fracture Mechanics Analysis of Elbow with Surface Crack	
Y.-S. Chang, H.-S. Kim and T.-E. Jin	505
On the Multiple Isoparametric Finite Element Method and Computation of Stress Intensity Factor for Cracks in FGMs	
Z.Z. Zou, S.X. Wu and C.Y. Li	511
The Effect of a Longitudinal Stiffener on the Elastic Shear Buckling of Orthotropic Web Plate	
S.J. Yoon, J.H. Jung and S.K. Cho	517
Interaction among a Row of N Semi-Elliptical Notches and Edge Cracks	
T. Matsuo and N.-A. Noda	523
A Computational Investigation on Metal/Ceramic Joints under Thermal Cyclic Loadings	
M.K. Park and S. Bahk	529
Progressive Failure Analysis of Composite Laminates Using 3-D Finite Element Method	
S.G. Joo and C.S. Hong	535
The Influence of Plastic Deformation on Interface Fracture Behavior	
M. Omiya, K. Kishimoto and T. Shibuya	541
An Analysis of Ironing Limit in Sheet Metal Forming	
J.B. Nam and K.S. Han	547
The Versatility of the Method of K_I, K_{II} Analysis by FEM Based on the Stress Value at a Crack Tip	
H. Nisitani, T. Teranishi, A. Saimoto and K. Fukuyama	553
Detecting Tool Wear in Face Milling with Different Workpiece Materials	
D.W. Cho, W.C. Choi and H.Y. Lee	559
Three Dimensional Finite Element Analysis for Elastic Plastic Crack Propagation in Thin Metallic Plate	
H. Okada, Y. Fukui, N. Kumazawa and T. Fujisaki	565

Damage Mechanics

Study on the Bending Fatigue Damage of the Carbon and the Polypropylene Hybrid Fiber Reinforced Concrete	
Y. Hua, H.B. Qi, Z.Q. Jiang, S.Z. Huang and S.B. Zhang	571
The Effect of Aging Temperatures and Time on Mechanical Properties of CF8M	
J.D. Kwon, J.C. Park, Y.S. Lee, W.H. Lee and Y.W. Park	577
Effect of Temperature on the Damage Behavior of an Adhesively Bonded Butt Joint	
A. Fujinami, K. Osaka, T. Fukuda and M. Imanaka	583

Effect of Yield Strength and Crack Depth on COD-Decrease-Parameter m Q. Li, H. Ni, S. Yang, M. Ma, P. Long and Z. Cui	589
A Study on Intergranular Corrosion of Laser Treated Alloy 600 by DL-EPR Method and Microscopic Examination Y.S. Lim, H.P. Kim, J.S. Kim and H.S. Kwon	595
Damage of FRP Plates Containing Sharp Notches or Blunt Notches H. Hyakutake and T. Yamamoto	601
Radiation Damage of Reactor Pressure Vessel Steels Studied by Nondestructive Methods D.G. Park, T.S. Byun, Y.Y. Song, J.H. Hong and I.S. Kim	607
Reliability Calculation for Piping Containing Circumferential Crack Based on 3-D Elastic-Plastic SFEM L. Huo, B. He and Y. Zhang	613
Optimum Design of Linear Phased Array Transducer for NDE J.-H. Lee and S.-W. Choi	619
A Damage Model for Void Configuration and Failure under Different Constrained Deformation Region in Ductile Matrix M. Kikuchi and M. Geni	625
Modeling of Mechanical Property Degradation by Short-Term Aging at High Temperatures J. Kim and W.I. Lee	631
On Failure Modes and Strength Characterization of Brittle Disordered Materials under Uniaxial Compression and Tension C.A. Tang, P. Lin, H.Y. Liu and Z.Z. Liang	637
Influence of Tool Wear on Hole Damage in Small Diameter Drilling of Printed Wiring Boards - Investigation based on Estimation of Cutting Forces and Internal Damage H. Inoue, T. Hirogaki, E. Aoyama and T. Katayama	643
Damage Tolerance Analysis Software (DATAS) for Crack Growth Life Prediction and Residual Strength Analysis of Aircraft Structures I.S. Putra	649
Prediction of Piping Failure Behavior using Wide-Plate Test N.S. Huh, H.J. Cha, J.B. Choi, Y.J. Kim and C.R. Pyo	655
Vibration Sensing and Impact Location Detection Using Optical Fiber Vibration Sensor Y.C. Yang, W. Hwang, H.C. Park and K.S. Han	661
New Estimates of Effective Moduli of Microcracked Materials X.Q. Feng	667
Realization of Higher-Mode Deformation of Beams Using Shape Memory Alloy Wires and Piezoceramics S.M. Pae, H.J. Lee, H.C. Park and W. Hwang	673
Author Index	xxv
Keyword Index	xxxi

Part 2: Behavior of Materials and Structure

Fracture Physics

Fracture and Strength of Solids Associated with their Textures	
D.N. Lee	679
Overview of Fracture of Piezoelectric Ceramics	
T.-Y. Zhang, R. Fu, M. Zhao and P. Tong	695
Effect of Heat Treatment and Chemical Composition on Caustic Stress Corrosion Cracking of Alloy 600 and Alloy 690	
H.P. Kim, S.S. Hwang, Y.S. Lim, I.H. Kuk and J.S. Kim	707
Nonlinear Evolution Properties of Rock Microfracturing Affected by Environment	
X.-T. Feng, T. Li and M. Seto	713
Case Study on Fracture of Motor Whist Wire	
H. Sakamoto, T. Yamaguchi and M. Mizumoto	719
The Propagation of a Layer-Confined Love Wave in Layered Piezoelectric Structures	
Z.K. Wang, F. Jin, Z. Zong and T.J. Wang	725
Characteristics of Delamination in Graphite/Epoxy Laminates under Static and Impact Loads	
J.S. Kook, I.Y. Yang and T. Adachi	731
An Experimental Observation About Dislocation Nucleation Based On Peierls Concept	
Y.M. Xing, F.L. Dai and W. Yang	737
Effect of Contact Shape on the Cracking Behaviour	
H.-K. Kim and H.-S. Kang	743
Study of Fracture Origin on Low Cycle Fatigue of Spheroidal Graphite Cast Iron Having Various Matrixes	
K. Morino, F. Nishimura and H. Nisitani	749
The Propagation Behavior of Love Waves in a Pre-stressed Piezoelectric Layered Structure	
F. Jin, Z.K. Wang and T.J. Wang	755
The Effect of Nucleation Time on the Growth of a Microvoid in a Viscoelastic Material	
J.K. Chen, Z.P. Huang and S.-L. Bai	761
Effects of Stress Fields around Micro-Surface Defects on the Occurrence of Slip and Micro Cracks	
K.R. Lee and J.B. Kim	767
Studies of Fracture of Piezoelectric Ceramics at HKUST	
T.-Y. Zhang	773

Tensile and Fracture Behaviors of PC/ABS Polymer Alloy M. Notomi, K. Kishimoto, T. Wang and T. Shibuya	779
Influence of Stochastic Mesoscopic Structure on Macroscopic Mechanical Behavior of Brittle Material Y.F. Fu, M.L. Huang and C.A. Tang	785
Fracture and Strength of Notched Thick Composites B.S. Hwang, S.B. Park, B.H. Kim, I.S. Park, H.S. Song and J.K. Lee	791
A Study on the Integrity Evaluation for PWR Vessel by Pressurized Thermal Shock S.G. Jung and T.-E. Jin	797
Crack Healing Behavior and Mechanical Property of Mullite/SiC Composite Ceramics K. Tsuji, K. Ando and S. Sato	803
Multi-Crack Coalescence in Rock-Like Material under Uniaxial and Biaxial Loading P. Lin, R.H.C. Wong, K.T. Chau and C.A. Tang	809
Effects of Temperature and Stacking Sequence on the Mode I Interlaminar Fracture Behavior of Composite Laminates H.S. Kim, W.X. Wang and Y. Takao	815
Effect of Remanent Polarization on Electro-mechanical Fields Near an Elliptic Cavity or a Crack in Piezoelectric Ceramics B. Liu, D.N. Fang and K.C. Hwang	821
Nano-Fractographic Estimation on the Profiles and Dimensions of Fatigue Striation S.J. Choi, H. Ishii and J.D. Kwon	827
Strength of Crack-Healed $\text{Si}_3\text{N}_4/\text{SiC}$ Composite Ceramics M.C. Chu, K. Ando, F. Yao and S. Sato	833
Studies on the New Technique of Rapid Solidification and the Mechanical Behaviors of Microcrystalline Alloys Z. Liu, K. Yang and S.-L. Bai	839
The Effects of Texture on K_{IH} in the Radial Direction in Zr-2.5%Nb Pressure Tube Materials S.S. Kim, S.C. Kwon, K.N. Choo, Y.M. Cheong and Y.S. Kim	845
Influence of Grain Boundary Characteristics on Cavitation Behavior in P/M7475 T. Hirata, S. Tanabe, M. Kohzu and K. Higashi	851
The Effects of Confining Compression on Fracture Coalescence in Rock-like Material R.H.C. Wong, P. Lin, K.T. Chau and C.A. Tang	857
Fracture Toughness Enhancement Due to Stress/Strain-Induced Martensitic Transformations in Solids S.V. Gladkovsky and V.A. Gladkovsky	863
Fracture Behavior of a Crack in Gas Pipeline Considering Constraint Effects D.J. Shim, Y.K. Jang, J.B. Choi and Y.J. Kim	869
Numerical Analysis of Dimple Fracture Process under Different Constraint Conditions M. Kikuchi and A. Takahashi	875

Microstructure of the Carbon and the Polypropylene Hydrid Fiber Reinforced Concrete Acted by Bending and Tensile Stress	
H.B. Qi, Y. Hua, Z.Q. Jiang, S.Z. Huang and S.B. Zhang	881
Acoustic Emission Technique for Pipeline Leak Detection	
M.-R. Lee and J.-H. Lee	887
Fracture Behaviors of GFRP Plates Subjected to Impulsive Loading	
B. Syam, H. Homma and K. Nakazato	893

Fatigue and Creep

Fatigue Strength Decrease of Structural Materials Caused by Atmosphere Corrosion and Aging	
Q.-X. Yang and B.-T. Wang	899
Creep Life and Properties Evaluation by ISM Method and Acoustic Emission for Cr-Mo-V Steels	
S.G. Lee	903
Expanding of the Fatigue Life of Thermal Barrier Coating by Mixing MoSi₂ to Thermal Sprayed Layer	
K. Sonoya and S. Tobe	909
Effects of Pad Material on Fretting Fatigue Behavior in CFRP Laminates	
M.-S. Kim and H.-S. Shin	915
Study on Double Shot Peening and Fatigue Limit of Gear	
K. Ando, K. Matsui and H. Ishigami	921
A Study on Probabilistic Fatigue and Calendar Fatigue Life	
B. Wang and Q. Yang	927
Influence of Microstructures on Fatigue Limit of High Strength Ductile Irons	
J.H. Kim and M.G. Kim	933
Fretting Fatigue Behavior of Structural Steels	
H. Yamamura, Y. Yamada and R. Ebara	939
Fatigue Failure Model for Composite Laminates under Multi-Axial Cyclic Loading	
C.S. Lee, W. Hwang, H.C. Park and K.S. Han	945
A New Method to Deal with the Staircase Fatigue Test	
Q.Z. Fang, S.S. Zhang, M.H. Zhao and Y.J. Liu	951
Fatigue Life Prediction of Spot-Welded Joint by Strain Energy Density Factor using Artificial Neural Network	
I.S. Sohn and D.H. Bae	957
Fatigue Properties of Tungsten Fiber Reinforced Ti-6Al-4V Alloy	
S.Y. Son, S. Nishida, N. Hattori and K. Nakano	963
Failure Analysis of the Fourth Compressor Pans in Aero-Engines	
G. Fu and W. Su	969
Thermal Aging and Low Cycle Fatigue Characteristics of CF8M in a Nuclear Reactor Coolant System	
J.D. Kwon, S.W. Woo, Y.S. Lee, J.C. Park and Y.W. Park	975

Study of Crack Propagation Behavior on Low Cycle Fatigue in Spheroidal Graphite Cast Iron Based on Observation of Surface and Fracture Section	
F. Nishimura, K. Morino and H. Nisitani	981
Cyclic Softening Properties of 30Cr2MoV Steel at Elevated Temperatures	
Z.D. Liu, K. Yang, X.P. Mao, S.-L. Bai and J.Y. An	987
A Study on the Corrosion Fatigue Characteristics of 12Cr Alloy Steel	
S.Y. Cho, C.H. Kim and D.H. Bae	993
Corrosion Fatigue Crack Initiation Life of a Ship Structural Steel in Dilute Sulfuric Acids	
Y. Kobayashi, Y. Tanaka and H. Goto	999
An Analysis of Random Fatigue Strength of K-Type Tubular Joints by Probabilistic Fracture Mechanics Method	
G.H. Nie, R. Shi and R.J. Zhang	1005
Fatigue Life Prediction of Bolted Joints Using Fatigue Modulus	
C.K. Jung and K.S. Han	1011
Study of Crack Propagation Behavior on Low Cycle Fatigue in Squeeze Cast Aluminium Alloy	
K. Morino, F. Nishimura, K. Takahashi, Y.H. Kim and H. Nisitani	1017
Reliability Analysis of Ship Hull Girders Considering the Degradations of Corrosion and Fatigue	
H.-H. Sun, G.-H. Liao and Y. Bai	1023
Fatigue Analysis of Vane Components for Gas Turbine Engine	
J.H. Kim, K.H. Kim, K.K. Joung, K.C. Ham, J.I. Song and S.I. Bae	1029
Fatigue Crack Growth Simulation and Estimation for Rolling Contact	
M. Akama and I. Susuki	1035
The Effect of Tensile Hold Time on the Fatigue Crack Propagation Behavior in STS 316L	
J.W. Im and B.S. Lim	1041
Fatigue Strength of Crack-Healed Ceramics	
K. Ando, M.C. Chu, F. Yao and S. Sato	1047
 Polymer and Polymer Composites	
Fracture Behaviours of Advanced Polymer Composites under Mixed Mode Loading	
K. Kishimoto	1053
Interface Adhesion and Interlaminar Fracture Resistance of Carbon/PEEK Composites influenced by Cooling Rate	
J.K. Kim and S.L. Gao	1063
Nondestructive Evaluation of Degree of Fiber Waviness in Thick Composites	
H.-J. Chun and P.-S. Jang	1069
The Damage Evaluation of Rigid Particle Filled Polymer	
S.-L. Bai, J.K. Chen, Z.P. Huang and Z.D. Liu	1075

Microstructural Morphology of Molded Thin Composites of Thermotropic Liquid Crystalline Polymer and Polyamide 6	
N.S. Choi and K. Takahashi	1081
Optimization of Molding Cure Condition on Al 7075/CFRP Sandwich Composite by the Taguchi Method	
H.K. Yoon, S.H. Lee and W.K. An	1087
An Application of Localized Flexibility Method to Damage Identification in CFRP Laminated Plate	
Y. Aoki and O.I. Byon(Goichi Ben)	1093
Crush Energy Absorbing Characteristics of Graphite/Epoxy Square Tubes	
H.C. Park, Y.H. Choi and K.J. Yoon	1099
Surface Modification of Carbon Fibers by Anodic Oxidation and its Effect on Adhesion	
J.R. Lee, M.H. Kim and S.J. Park	1105
The Bridging Analysis of Dynamic Crack Propagation in Fiber Reinforced PE Pipelines	
Z. Zhuang, S. Qu and Y. Guo	1111
Optimum Stacking Sequence Design of Fiber-Metal Laminates for Using Genetic Algorithm	
H.W. Nam, S.W. Jung, W. Hwang and K.S. Han	1117
A Thermomechanical Analysis of MCM-D Substrate of Polymer and Metal Multilayer	
J.H. Lim, J.S. Kim, K.W. Paik and Y.Y. Earmme	1123
Failure Behavior and Electrical Property of CFRP and CFGFRP	
D.Y. Song, J.B. Park and N. Takeda	1129
Elastic Restraint between the Plate Components of FRP Compression Members	
S.J. Yoon, S.K. Jeong and S.H. Chae	1135
Mixed-Mode Ply Cracking in Multidirectional Continuous Fiber Composite Laminates	
J. Zhang, K.P. Herrmann and X. Zeng	1141
Axial Crush and Energy Absorption Characteristics of Aluminum/GFRP Hybrid Square Tube	
K.H. Kim, K.C. Shin and J.J. Lee	1147
Mechanical Behavior of Carbon/Phenolic Ablative Composites for Nozzle Application	
P.W. Kim, S.H. Hong, Y.C. Kim, B.H. Yeh and Y.G. Won	1153
Fracture Pattern and Lamination Configuration on Flexural Fracture of Multiple Layer CFRP	
M. Kanemitsu and H. Nakayasu	1159
Strength Prediction of Mechanical Joints in Laminated Composite Plates	
K.W. Lee and T.J. Kang	1165
Crystallinity and Mechanical Properties of Glass Fiber Reinforced Thermoplastic Composites by Rapid Press Consolidation Technique	
I.J. Shin, D.Y. Kim and D.J. Lee	1171

Fractography of Damaged Carbon Fiber/Epoxy Composites after Low-Velocity Impact

M.S. Sohn, X.Z. Hu and J.K. Kim 1177

Anisotropic Mechanical Behavior of Three Dimensional Glass Fabric Reinforced Composites

H.S. Lee, S.H. Hong, J.R. Lee and Y.K. Kim 1183

Prediction of Compressive Strength of Stiffened Composite Plate after Impact

C.S. Hong, C.W. Kong and C.G. Kim 1189

Void Nucleation Models and their Implications for the Material Behavior of Rubber-Modified Epoxies

H.-Y. Jeong 1195

On-line Frequency Estimation and Adaptive Vibration Control of Composite Structures with Delaminations

K.-H. Rew, J.-H. Han and I. Lee 1201

Metals, MMCs, Ceramics and CMCs

Strength and Fracture of Cu-Based Filamentary Nanocomposites

S.I. Hong, J.H. Chung and H.S. Kim 1207

Modeling of Thermal Shock Spalling Crack in a Ceramic Slabs

P. He and W.J. Clegg 1213

Analytical Study of Prestrain Effects on Elastic Properties in Shape Memory Alloys

H.G. Kim, H.K. Noh, Y.T. Cho, J.Y. Kim, S.K. Park and D.J. Lee 1219

A Study on the Friction and Wear Characteristics of Brake Pads for Al MMC

Brake Disc

S.J. Kwon and B.C. Goo 1225

On Targets Strength of Ceramic Materials for Impacting Penetration

Y. Sun, J. Ma, Y. Zhou and T. Li 1231

Effects of Heat Treatment on Bending Strength of Aluminum Alloy Matrix

Composites Reinforced Aluminum Borate Whisker

S.C. Huh, H.K. Yoon, K.H. Park and S.P. Lee 1237

Mechanical Properties of Tungsten Fiber Reinforced Ti-6Al-4V Alloy

S. Nishida, K. Hayashi, N. Hattori, K. Nakano, Y. Yanagida and H. Tamasaki 1243

Behavior of Cyclic Fatigue Crack Growth for SiC Ceramics

Y.-H. Huh, K.-J. Yoon, S.-J. Cho and J.H. Song 1249

A Model on the Strengthening and Embrittlement of Devitrified Nanocomposites

H.S. Kim, S.I. Hong and M.-S. Sohn 1255

Contact Damage Analysis of Ceramic/Metal Bilayer Composites with Various Modulus Mismatches

H. Zhao, X. Hu and M.B. Bush 1261

Abrasive Wear Behavior of Hybrid Metal Matrix Composites

J.I. Song, S.I. Bae, K.C. Ham and K.S. Han 1267

Evaluation of Formability Properties of P/M Copper Preforms at Elevated Temperatures

T. Senthilvelan, A. Venkatraman and K. Raghukandan 1273

Effects of Interface and Residual Stress on Mechanical Properties of Ceramic/Metal System

T.W. Kim and S.W. Park 1279

Design and Fabrication of Tooling for P/M Ferrous Gears

A. Venkatraman and T. Senthilvelan 1285

Effects of Sintering Conditions on Mechanical Properties of Mechanically Alloyed Tungsten Heavy Alloys

H.J. Ryu and S.H. Hong 1291

Analysis of Strengthening Mechanism in Hybrid Short Fiber/Particle Reinforced Metal Matrix Composites

S.W. Jung, J.H. Lee, J.B. Nam, H.W. Nam and K.S. Han 1297

Welding

Effects of Welding Process and Crack Orientation on da/dN of Titanium Alloys

Q. Li, H. Ni, S. Yang, Z. Cui, X. Peng and L. Wang 1303

Laser Welding of Ti-Ni Shape Memory Alloy Wire and its Fatigue Properties

Y.S. Kim and J.D. Kim 1309

Investigation on Improving Fatigue Properties of Welded Joints by Ultrasonic Peening Method

L. Huo, D. Wang, Y. Zhang and J. Chen 1315

The Characteristics of Fatigue Strength in Laser Tailored Welded Blanking Sheet Metal

T.Y. Oh, Y.K. Kwon, C.J. Lee and D.S. Kwak 1321

Effect of the Mismatching of J-Integral for Pipe Welded Joint with Circumferential Surface Crack

L.X. Huo, Y.I. Liu, Y.F. Zhang and H.Y. Jing 1327

Validation of Defect Assessment Method for Structures with Weldments

Y.-J. Kim 1333

The Use of Temper Bead Welding for the Repair of Thick Walled Pressure Vessels

R.N. Ibrahim and T. Shehata 1339

Welding Residual Stress Analysis and Fatigue Crack Growth Characteristics of Multi-Pass Welded Pipe Weldment

C.H. Kim, D.H. Bae, S.Y. Cho and B.K. Kim 1345

Author Index 1351

Keyword Index 1357

Length-Scale Effects in Nano- and Micro-Mechanics of Solids

Kyung-Suk Kim and Juan A. Hurtado

Division of Engineering, Brown University, Providence RI 02912, USA

Keywords: Micro-Mechanics, Nanomechanics, Scale Effect, Single-Asperity-Contact Friction, Surface-Roughness Evolution

ABSTRACT

Since many instability mechanisms are length-scale dependent, some interesting length-scale dependent transition behaviors are observed at a small length scale. Two examples are presented for length-scale dependent transitions in stress-driven processes. One is the transition from nano- to micro-mechanisms of interfacial slip in single-asperity adhesive-contact friction. This transition behavior is explained with a dislocation model. The other example is the evolution of the surface roughness of a strained solid caused by chemical etching. The roughening process produces distinct peaks of the frequency-dependent roughening rate on the two-dimensional frequency domain. These peaks are analyzed to be the signature of the stress in the solid near the surface. This analysis provides the principles of surface-roughness evolution spectroscopy (SRES) which can be used as a high-spatial-resolution stress gauge. The Atomic-Force-Microscope-based SRES reveals some other high-frequency peaks than expected by the low-frequency near-equilibrium model. It is believed that the high frequency peaks are caused by length-scale-dependent mechanisms.

1. INTRODUCTION

Recent developments in science have advanced capabilities to fabricate and control material systems on the scale of nanometers, bringing problems of material behavior on the nanometer scale into the domain of engineering. Immediate applications of nanostructures and nano-devices include quantum electronic devices, bio-surgical instruments, micro-electrical sensors, functionally graded materials, and many others with great promise for commercialization. The branch of mechanics research in this emerging field can be termed nano- and micro-mechanics of materials.

The terminology of nanomechanics is embracing many implicit meanings related to the mechanics of physical processes and material behavior at the length scale of nanometers. This length scale is very close to atomic and molecular size scale and thus the mechanics problems in this field are associated with "atomic spatial resolution and transition from quantum to continuum mechanics via atomistics," "richness of underlying electronic degree of freedom for the physical processes in this length scale," "abundant sources of instabilities and localization of motion and deformation" and "non-equilibrium processes and small-number statistics/fluctuations for collective motions of atoms and defects." While the terms nano and micro are often used to indicate length scales, for example, nano-tubes, nano-particles, nano-structures, micro-electronics, micro-gauge and

micro-scope, etc., the term "micromechanics" usually means mechanics of (immediate) underlying mechanisms of physical processes and material behavior at any length scale. Examples include mechanics of dislocation motion, phase transformation, mass and vacancy diffusion, void growth for plasticity and fracture.

In the field of nano- and micro-mechanics of solids we often encounter length-scale effects. Examples include the hardness variation of metals depending on the depth of indentation in nano- and micro-indentation test. While strength of materials at different length scales is actively studied these days with nano- and micro-indentation tests, two other clear examples of scale-dependent deformation characteristics in nano- and micro-mechanics of materials will be described in following sections. One is on scale effects in single-asperity contact friction and the other is about scale effects in the evolution of surface roughness during shallow chemical etching.

2. SCALE EFFECTS IN SINGLE-ASPERITY-CONTACT FRICTION

Amontons [1] presented the empirical friction law that the shear load is proportional to the normal loading in 1699. In 1950, Bowden and Tabor [2] proposed that the shear force required to slide a single-asperity contact of clean surfaces is proportional to the contact area. The proportionality constant, the shear force divided by the area, is the single-asperity friction stress, τ , which has been considered independent of the normal stress on the contact area. The normal load for the friction between two rough surfaces is considered to increase proportionally with the actual area of contact, and thus the Amontons's law holds for sliding processes of many asperity contacts between two clean rough surfaces.

The conjecture of Bowden and Tabor has been verified experimentally by Homola *et al.* [3] in 1990, using a surface force apparatus (SFA) for a single asperity-contact friction between two atomically smooth mica surfaces over the contact-radius range of 40 – 250 μm . More recently, Carpick *et al.* [4] in 1996 and Lantz *et al.* [5] in 1997 have reported that the Bowden and Tabor conjecture holds for contacts of AFM (Atomic Force Microscope) tips over the range of contact radii between 3 and 14 nm. However, the friction stress observed in the SFA experiment was about 1300th of the shear modulus, μ , of the contact-junction material, while the friction stress of the AFM experiment was about 40th of the effective shear modulus of the contact junction. How can we explain the similarity of frictional behavior and the large difference between the friction stresses in distinctively different length scales? A model that provides the answer for this question is described as follows.

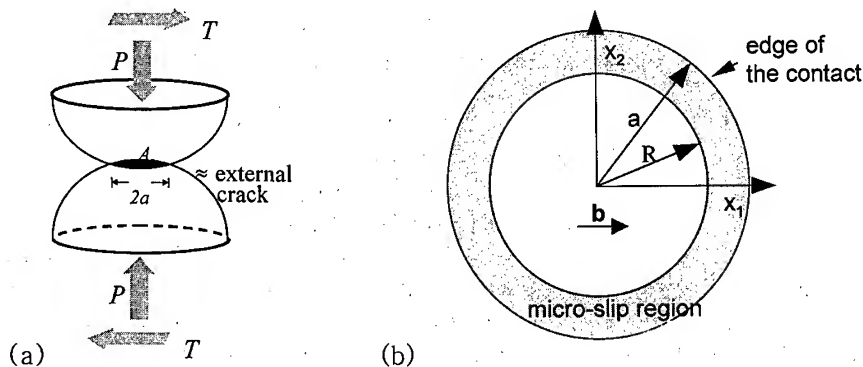


Fig. 1. (a) Schematic of the single-asperity-contact friction. (b) Schematic of the micro-slip process in the contact region prior to total slip.

As two clean surfaces contact, adhesion makes a contact junction which becomes a circular external crack as shown in Fig. 1(a). The external-crack geometry provides stress concentration for the shear loading so that a micro-slip region develops within the contact area prior to total slip as shown in Fig. 1(b). If the micro-slip region sweeps the whole contact region progressively with a local friction behavior of Amontons' type, the entire single-asperity friction would obey the Amontons' law [6]. If it sweeps with a local critical shear stress for slipping, it would have a single friction stress regardless of the contact zone size, providing the Bowden and Tabor behavior of friction for the entire range of length scale [7]. These two models cannot explain the scale effects. However, if the micro-slip region becomes unstable before it sweeps the entire contact area, it will generate a dislocation and the mobile dislocation will constitute the slip process. The unstable dislocation nucleation process near a two dimensional crack geometry has been analyzed by Rice and Thomson [8] and Rice [9]. An important result of these analyses is that there exists a critical dislocation nucleation process zone size, η , that is inversely proportional to the unstable stacking fault energy of the slip plane for a small-scale micro-slip process. Based on the dislocation nucleation criterion of Rice-Thomson type and a model of dislocation stabilization process within the contact zone, the scale effects were explained by Hurtado and Kim [10,11].

As the load T in Fig. 1(a) is increased to a critical level, a circular dislocation loop of Burgers vector b is emitted into the contact region from the edge of the contact. If the contact area is large enough, the dislocation loop will be stabilized by effective Peierls barriers within the contact region, and the next dislocation loop will be nucleated at the edge, piling up the dislocations. As the innermost dislocation becomes unstable and completes the gliding to annihilation, the asperity slips. The condition to steadily sustain the dislocation nucleation at the edge and the instability of the leading dislocation provides the friction stress as a function of the contact radius a and material parameters, η , τ_0 (dislocation core radius) and τ_p (effective Peierls stress) as shown in Fig. 2.

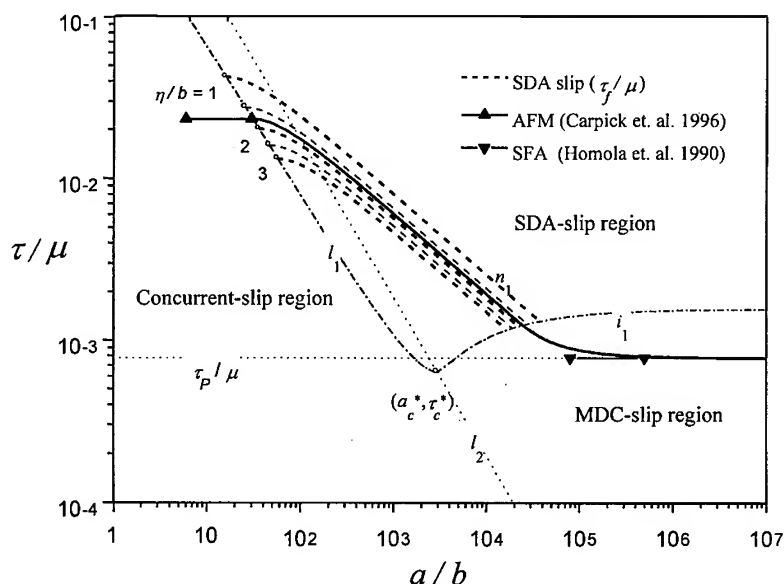


Fig. 2. Friction stress τ as a function of contact radius a . The symbols m , b and τ_p represent the shear modulus of the junction, the Burgers vector and effective Peierls stress of the dislocation.

The analytic predictions are compared, in Fig. 2, with the results of both the AFM and SFA experiments. The dislocation nucleation and instability conditions also generate delineating boundaries (l_1, i_1) on the plane of normalized friction stress versus contact radius. The lines (l_1, i_1) meet at a point (a'_c, τ'_c) and the point moves along l_2 as τ_p varies. On the left side of line l_1 in Fig.2 the contact area is too small to accommodate the nucleation process of the highly curved dislocation to form a distinct core structure before it is emitted from the contact edge. Thus, in this region the asperities slip concurrently without a distinctive dislocation motion. In the region on the right side of l_1 and on the upper side of i_1 , the slip is assisted by a moving dislocation loop; once a dislocation is nucleated at the contact edge, the dislocation is completely unstable until it self-annihilates. This slip mechanism has been named single-dislocation-assisted (SDA) slip. Various SDA slip curves for different η values are shown by dashed lines. A multiple-dislocation-cooperated (MDC) slip mechanism is expected in the region below line i_1 . This analysis predicts that the frictional slip in the AFM experiment is a concurrent slip and the corresponding friction stress is the theoretical strength of the junction. The frictional slip of the SFA experiment is a MDC slip and the friction stress represent the effective Peierl stress of mobile interface dislocations. The slip mechanisms of two friction tests are different due to length-scale effects, although both test results satisfy the Bowden and Tabor postulate in the respective contact-radius range. The theory predicts that transition occurs in slip mechanisms and that the friction stress depends on the contact size between two length-scales of the AFM and SFA tests; the theoretical results await experimental verification.

3. SCALE EFFECTS IN THE EVOLUTION OF SURFACE ROUGHNESS IN SHALLOW CHEMICAL ETCHING

Another interesting example of length-scale effects in nano- and micro-mechanics of solids is the phenomena observed in stress-induced surface roughening. The stress-induced roughening of solid surfaces is considered to be the main cause of failure process in MEMS devices. Stress-induced roughening of solid surfaces, simply termed as "stress roughening," has been extensively studied for stress-induced morphological instability of flat surfaces, which is known as Asaro-Tiller[12] instability or Grinfeld instability[13]; up-to-date references are listed by Kim *et al.* [14].

Surface roughening of long wavelength can be modeled with continuum energetics and kinetics. In the continuum models the tendency of the surface to change the shape of its reference configuration is represented by the total-chemical-potential variation with respect to admissible variation of the surface configuration. As the surface configuration is varied, the (positive) surface energy and the (positive) bulk strain energy, which comprise the chemical potential, change the chemical potential in opposite directions. A positive surface energy tends to flatten the surface, while a positive strain energy is inclined to roughen the surface, lowering the chemical potential. This competition depends on the spatial frequency of the roughness. Two types of major atomic-level mechanisms allow variation of the surface configuration. One type is the addition and removal of atoms on the surface from and to the surroundings of the surface, i.e. the solid bulk or the liquid bulk, if the solid is in contact with a liquid. Chemical etching belongs to this case. The other is the addition and removal of atoms along the surface (or interface) itself. In the latter case a gradient in chemical potential results in diffusive mass transport along the surface. This phenomenon is particularly relevant for processes characterized by high stress, high temperature and small size scales, such as the growth of heteroepitaxial thin films where stresses are of the order of gigapascals, temperatures about 500 °C, and the film thickness is in the submicron scale [15, 16].

The general observation in both cases is that a flat surface under stress is unstable for a

sufficiently large wavelength λ (or small wave number $\omega = 2\pi / \lambda$); there exists a critical wave number ω_{cr} below which roughness grows and above which they decay. Analysis [14] shows, however, that the wave-number dependence of the growth (or decay) rate of the roughness is different for the two cases. In any case, the roughness spectral analysis can be made without ambiguity for shallow amplitude growth.

In the etching experiment, an AFM was used to measure two sets, $h(x,0)$ and $h(x,t)$, of surface roughness before and after etching as shown in Fig. 3 (T.1) and (T.2). The material chosen for the experiment was a structural aluminum alloy, frequently used for computer hard disks. The specimen geometry is depicted in the left inset of Fig.3. It contains an internal hole and an EDM notch. The notch in the specimen was opened by deforming the ligament plastically with the load P as shown in the figure. Then the load P was removed, leaving a high residual stress field in the vicinity of the notch end. The specimen with the residual stress was placed in the AFM, and the region T was etched *in situ*. The etchant employed in this experiment was the Keller reagent, a common aluminum-alloy etchant: HF 48% (2 ml), HCl (3 ml), HNO₃ (5 ml), H₂O (190 ml). We measured the topography with an AFM (PSI AutoProbe CP with Multitask probe head) in contact mode, with a Si₃N₄ tip. Then, the two sets of roughness were fast-Fourier-transformed into, $\hat{h}(\omega,t)$ and $\hat{h}(\omega,0)$, to evaluate the frequency-dependent growth rate, $\ln(\hat{h}(\omega,t) / \hat{h}(\omega,0))$, of the roughness.

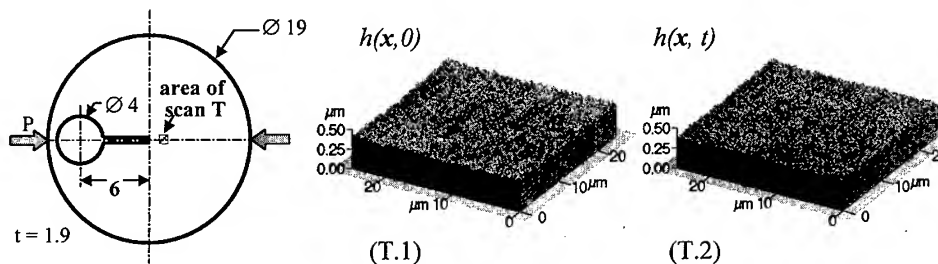


Fig. 3. Specimen geometry of high residual stress for AFM scanning (units in mm), left inset; the squares indicating the areas of scan at T is not in scale. AFM measurements of surface topography before (T.1) and after (T.2) etching for an aluminum specimen with residual stresses at T .

A theoretical prediction of the frequency-dependent growth rate for an isotropic solid is shown in Fig. 4. The distance between the two peaks represents the critical frequency, ω_{cr} , along the notch direction, below which roughness grows and above which they decay. The critical frequency is proportional to square of the principal stress and inversely proportional to the surface energy and the shear modulus of the solid. This theoretical prediction is only applicable for the shallow-etching or low-frequency condition, $\omega \| h \| \ll 1$, where $\| h \|$ is an amplitude norm of the roughness. Details of the theoretical analysis can be found in reference [14].

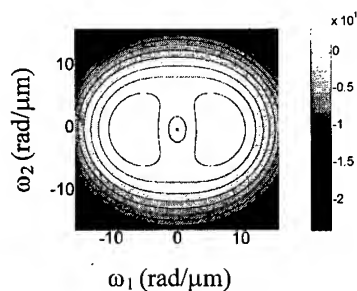


Fig. 4. Frequency-dependent roughness growth rate for an isotropic solid: Theory.

Experimental results are shown in Fig. 5. As shown in Fig. 5(a), the two low frequency peaks are aligned in the notch direction like in Fig. 4, showing that the principal stress in the notch direction is larger than the other one. This result indicates that the notch-tip was plastically deformed and partially unloaded as the external loading was removed. Figure 5(b) shows the high frequency behavior at T . Fig. 5(b) was obtained with a scan size of $10\text{ }\mu\text{m} \times 10\text{ }\mu\text{m}$, while Fig 5(a) was processed with $25\text{ }\mu\text{m} \times 25\text{ }\mu\text{m}$ scan. Many higher frequency peaks are observed other than the low frequency stress peaks. Recently Yu and Suo [17] have investigated the effects of thermally-activated etching processes far from equilibrium, motivated by the observation of Barvosa-Carter et al. [18] that the homoepitaxial growth of the interface roughness at a certain frequency depends on the sign of the applied stress. Yu and Suo [17] have shown that when the kinetic mobility M is thermally activated with an activation strain, two more high frequency peaks can be observed at the frequency range of typically two orders of magnitude higher than that of low frequency peaks. Their analysis is also based on the first order theory; however, the first order approximation may not be safely applied beyond the frequency of $20\text{ rad}/\mu\text{m}$ for the data shown in Fig. 5(b). The negative peaks, dark spots in Fig. 5(b), are most noticeable, which are believed to be caused by length-scale-dependent mechanisms.

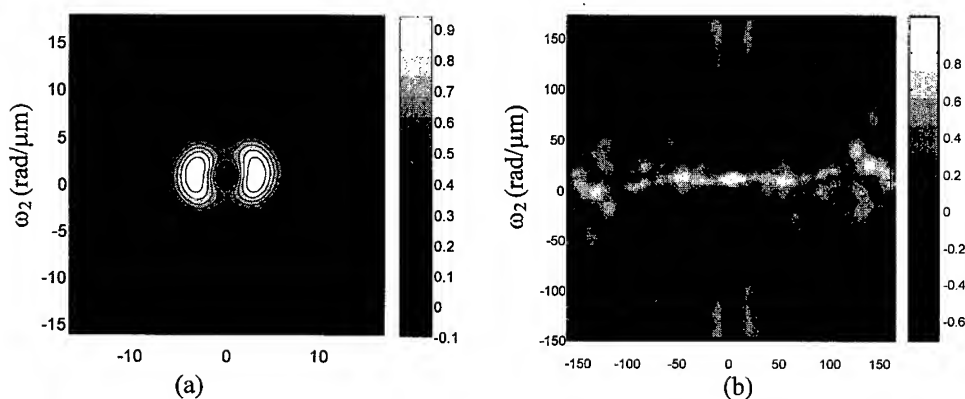


Fig. 5. Experimentally measured values of the function ω_2 , (a) at low frequency range, processed with the roughness data of an area of $25\text{ mm} \times 25\text{ mm}$ and, (b) at high frequency range, with the roughness data of an area of $10\text{ mm} \times 10\text{ mm}$, at the area T

Acknowledgment: This work was supported by the U. S. National Science Foundation Award No. 0070057 and the MRSEC Program of the National Science Foundation Award No. DMR-9632524.

REFERENCE

1. G. Amonton, presentation at the Euroean Academy (1699).
2. F.P. Bowden, D. Tabor, The Friction and Lubrication of Solids, Clarendon, Oxford (1950).
3. A.M. Homola, J.N. Israelachvili, P.M. McGuiggan, M.L. Gee, Wear, **136** (1990) p.65
4. R.W. Carpick, N. Agrait, D.F. Ogletree, M. Salmeron, Langmuir, **12** (1996) p.3334
5. M.A. Lantz, S.J. O'Shea, M.E. Welland, K.L. Johnson, Phys. Rev. B, **55** (1997) p.10776

6. R.D.Mindlin, J. Appl. Mech. **16** (1949) p.259
7. A.R.Savkoor, M. Engng dissertation, Tech. University Delft, The Netherlands (1987)
8. J.R.Rice, R.Thomson, Phil. Mag. **29** (1973) p.73
9. J.R.Rice, J. Mech. Phys. Solids, **40** (1992) p.239
10. J.A.Hurtado, K.-S.Kim, Proc. R. Soc. London. A, **455** (1999) p.3363
11. J.A.Hurtado, K.-S.Kim, Proc. R. Soc. London. A, **455** (1999) p.3385
12. R.J.Asaro, W.A.Tiller, Metall. Trans. **3** (1972) p.1789
13. M.A.Grinfeld, Sov. Phys. Dokl. **31** (1986) p.831
14. K.-S.Kim, J.A.Hurtado, H. Tan, Phys. Rev. Lett. **83** (1999) p.3872
15. H.Gao, J. Mech. Phys. Solids, **39** (1991) p.443
16. L.B.Freund, Int. J. Solids Struct. **32** (1995) p.911
17. H.H.Yu, Z.Suo, J. Appl. Phys. J. Appl. Phys. **87** (2000) p. 1211
18. W.Barvosa-Carter, M.J.Aziz, L.J.Gray, T.Kaplan, Phys. Rev. Lett. **81** (1998) p.1445

Mechanism-based Strain Gradient (MSG) Plasticity and the Associated Asymptotic Crack-Tip Fields

K.-C. Hwang¹ and Y. Huang²

¹Department of Engineering Mechanics, Tsinghua University, Beijing 100084, China P.R.

²Department of Mechanical and Industrial Engineering, University of Illinois,
Urbana IL 61801, USA

Keywords: Crack-Tip Fields, Strain Gradient Plasticity

ABSTRACT

The materials display strong size effect at the micron or sub-micron scale. The classical plasticity theories cannot explain this size dependence because they possess no internal material lengths. Based on the Taylor model in dislocation mechanics, the theory of Mechanism-based Strain Gradient (MSG) plasticity has been derived. It agrees very well with the available micro-scale experiments, such as micro-torsion, micro-bending and micro-indentation hardness experiments. The structure of the asymptotic crack tip fields associated with MSG plasticity is investigated. It is shown that the crack tip field associated with MSG plasticity does not have separable form of solutions. Its implication on the fracture criterion in MSG plasticity is also discussed.

1. INTRODUCTION

Continuum mechanics has enjoyed its tremendous success in many engineering disciplines, in which the length scales involved are typical on the order of, or larger than, millimeters. In recent years, continuum mechanics has been applied to micro-electronics industry, such as the reliability assessment of micro-electronic devices, stress analysis of micro-scale features, and design of micro-electro-mechanical systems (MEMS). One common feature of these applications is that the characteristic length is very small, typically from 0.1 to 10 microns. Accordingly, micro-scale experiments have been developed to measure the mechanical properties at the small scale. For example, micro-indentation and nano-indentation hardness experiments have been developed to determine the elastic modulus and hardness of materials at the micron or sub-micron scale. These experiments, however, have repeatedly shown very strong size-dependence. The measured indentation hardness increases by a factor of two or even three as the depth of indentation decreases

to microns or sub-microns [1-7]. This is very puzzling since the indentation hardness has always been considered as a material property. Some researchers have attributed this increase in hardness to the inaccuracy in experimental measurements, such as the effect of pile-up and sink-in, the indenter tip geometry, the oxidation layer on the surface, or the additional work hardening associated with surface finishing. Significant efforts have been made to account for these effects. The indentation hardness, however, still displays strong dependence on the indentation depth after these factors are accounted for [7].

Other experiments on the micro-scale have also shown strong size dependence. Fleck et al. [8] have observed in micro-torsion of thin copper wires that the scaled shear strength increases by a factor of three as the wire diameter decreases from 170 to 12 microns. Stolken and Evans [9] have found similar strength increase in micro-bending of thin nickel foils as the foil thickness decreases from 50 to 12.5 microns. In particle-reinforced metal-matrix composites, Lloyd [10] have observed substantial increase in work hardening as the particle diameter is reduced from 16 to 7.5 microns at a fixed particle volume fraction of 15%. Classical plasticity theories [11] cannot explain this size-dependence observed at the micron or sub-micron scale because their constitutive models possess no internal material lengths. At the micron scale, however, there are still hundreds of dislocations such that there should be a continuum plasticity theory (but not classical plasticity) that can describe the collective behavior of these dislocations.

Another objective that warrants the development of a micron-level continuum plasticity is to link macroscopic fracture behavior to atomistic fracture processes in ductile materials. This linkage between macroscopic cracking and atomistic fracture will be crucially important in predicting adhesion strength and fracture toughness of multi-layer structures in microelectronic devices [12]. In a remarkable series of experiments, Elssner et al. [13] have measured both the macroscopic fracture toughness and the atomic work of separation of an interface between a single crystal of niobium and a sapphire single crystal. The macroscopic fracture toughness is two to three orders of magnitude higher than the atomic work of separation. This has been attributed to the significant amount of plastic deformation in niobium. According to models based on classical plasticity theories, the maximum stress level around a crack tip is not more than four to five times the yield stress [14]. Elssner et al. [13], however, have observed that the interface crack tip remains atomistically sharp. The stress level needed to produce atomistic decohesion of a lattice or a strong interface is typically on the order of ten times the yield stress, which is significantly larger than the prediction based on classical plasticity theories. In other words, classical plasticity theories cannot explain the atomistically sharp crack tip observed in ductile materials.

Some microscopic understanding of plastic deformation is necessary in order to develop such a continuum plasticity theory intended for micron or sub-micron scale applications. When a material is deformed, dislocations are generated, moved and stored, and the storage causes the material to work harden. Dislocations become stored for one of the two reasons: they accumulate by trapping each other in a random way and are called statistically stored dislocations [15], or they are required for compatible deformation of various parts of the material, which are called the geometrically necessary dislocations and are related to the gradients of plastic shear [15-17].

These considerations have motivated Fleck, Hutchinson and co-workers [8,18,19] to develop phenomenological theory of strain gradient plasticity intended for applications to materials and structures whose dimension controlling plastic deformation falls roughly within a range from a tenth of a micron to ten microns. Strain gradients have been introduced in the constitutive model,

and their work conjugates are the higher order stresses. From a dimensional consideration, several internal material length parameters have been introduced to scale the strain gradient terms and these length parameters are determined to be on the order of microns or sub-microns from fitting the micro-scale experiments of indentation, torsion and bending.

Based on the Taylor hardening relation in dislocation mechanics [20], Nix and Gao [21] have developed a rather simple model that captures the dependence of flow stress σ on the effective gradient η of plastic strains,

$$\sigma = \sigma_{ref} \sqrt{f^2(\varepsilon) + l\eta}, \quad (1)$$

where $\sigma = \sigma_{ref} f(\varepsilon)$ is the uniaxial stress-strain relation, σ_{ref} is a reference stress in uniaxial tension, and l is identified as the internal material length scaling the strain gradient and is given by

$$l = 18 \left(\frac{\mu}{\sigma_{ref}} \right)^2 b. \quad (2)$$

Here μ is the shear modulus and b is the Burgers vector. For typical metallic materials, l is indeed on the order of microns, consistent with the estimate of Fleck and Hutchinson [19] from fitting the micro-scale experiments.

Motivated by the success to estimate the micro-scale flow stress from the dislocation model, Gao, Huang, Nix and Hutchinson [22,23] have derived a three-dimensional theory of Mechanism-based Strain Gradient (MSG) plasticity. The theory is based on a multi-scale, hierarchical framework to link the micro-scale dislocation interactions to the meso-scale continuum plasticity theories. The Taylor model in dislocation mechanics [20] is adopted as a founding principle at the micro-scale, based on which the meso-scale strain gradient plasticity theory is derived. The theory agrees very well with the aforementioned micro-indentation, torsion and bending experiments [24]. It has also been used to study plastic flow localization in order to predict the shear band thickness [25] in terms of the internal material length l .

The theory of Mechanism-based Strain Gradient plasticity is reviewed in the next section, followed by the asymptotic analysis of the crack tip field. Unlike all existing crack tip fields, the asymptotic field associated with MSG plasticity does not have a separable form. Its implication on the fracture criterion is further discussed.

2. MECHANISM-BASED STRAIN GRADIENT PLASTICITY

2.1 Taylor Hardening Model

The Taylor hardening model has been the central pillar of MSG plasticity. It provides a simple mean-field description of the dislocation interaction processes at the micro-scale. The dislocation theory indicates that the Peach-Koehler force due to a pair of dislocations is proportional to the shear modulus μ , Burgers vector b , and is inverse proportional to the distance

L between dislocations, i.e., $\propto \mu b/L$. This sets a critical value for the applied stress to break or untangle the interactive pair of dislocations so that slip can occur even if one of the dislocations is pinned by an obstacle. In the Taylor model this picture is generalized to the interaction of a group of statistically stored dislocations which trap each other in a random way. If the mean dislocation spacing is L , the critical stress required to untangle the interactive dislocations and to induce significant plastic deformation is defined as the Taylor flow stress,

$$\tau = \alpha \mu b / L = \alpha \mu b \sqrt{\rho} = \alpha \mu b \sqrt{\rho_S + \rho_G}, \quad (3)$$

where $\rho = 1/L^2$ is the dislocation density, ρ_S and ρ_G are the densities of statistically stored and geometrically necessary dislocations, respectively, and α is an empirical coefficient on the order of one [26].

2.2 Geometrically Necessary Dislocations and Statistically Stored Dislocations

Geometrically necessary dislocations are dislocations which are necessary to accommodate the geometry of plastic deformation. The density of geometrically necessary dislocations results from the gradients of plastic strain [15-17], and is given by [22]

$$\rho_G = 2\eta/b, \quad (4)$$

where b is the Burgers vector, $\eta = \sqrt{\eta_{ijk}\eta_{ijk}}/2$ is the effective strain gradient, and $\eta_{ijk} = u_{k,ij}$ is the second order gradient of the displacement.

The density of statistically stored dislocations ρ_S can be determined from the uniaxial tension,

$\sigma = \sigma_{ref} f(\varepsilon)$, which involves no geometrically necessary dislocations since the deformation is uniform. For crystalline materials, the tensile flow stress σ is approximately three times the flow stress in shear, τ [20,27-29]. These relations lead to the flow stress in Eq. (1).

2.3 Multi-scale, Hierarchical Framework

Figure 1 shows the multi-scale framework used to construct the theory of MSG plasticity [22,23]. On the micro-scale the scale of analysis is small compared with the length over the strain field varies. The dislocation activities are described by the slip of statistically stored dislocations in a background of geometrically necessary dislocations. The micro-scale flow stress obeys the Taylor hardening relation as exhibited by the strain gradient law, Eq. (1). Stresses and strains are defined in the classical sense at the micro-scale, and the associative rule of plastic flow normality holds if the dislocation slip is governed by the Schmid stress along an appropriate slip system [30,31].

On a higher level, meso-scale analysis, a continuum plasticity theory is constructed to represent the collective behavior of dislocations at the micro-scale. The strain gradients are introduced at the meso-scale as a measure of geometrically necessary dislocations at the micro-scale, and the

higher-order stresses serve as the corresponding stress measures in order to satisfy the essential thermodynamic restrictions. The meso-scale constitutive law of Mechanism-based Strain Gradient plasticity is derived by the equality of virtual work at the two scales. In other words, for given strains and strain gradients at the meso-scale, the strains at the micro-scale (Fig. 1) are obtained from kinematics; the associative flow rule and the strain gradient law, Eq. (1), then give the stresses at the micro-scale; and the equality of virtual work at the two scales then finally lead to the stresses and higher-order stresses at the meso-scale.

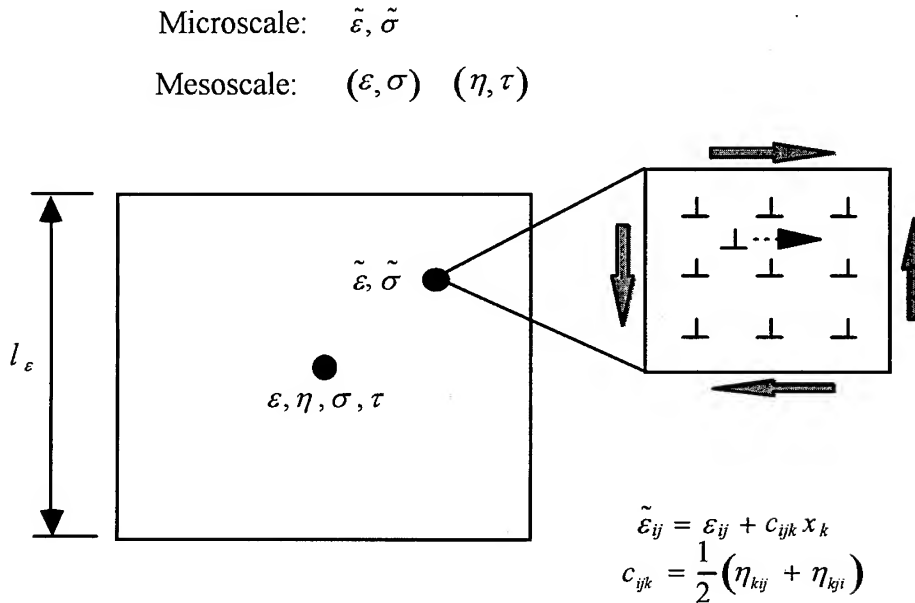


Figure 1. The multi-scale framework for strain gradient plasticity; dislocation interaction is considered on the micro-scale via the Taylor relation. The higher order continuum theory of strain gradient plasticity is established on the meso-scale representative cell; l_ε is the size of the meso-scale representative cell.

2.4 Constitutive Relation in MSG Plasticity

The Taylor hardening model at the micro-scale and the multi-scale, hierarchical framework give the meso-scale constitutive relations of MSG plasticity,

$$\sigma_{ij} = K \varepsilon_{kk} \delta_{ij} + \frac{2\sigma}{3\varepsilon} \varepsilon'_{ij}, \quad (5)$$

$$\tau_{ijk} = l_\varepsilon^2 \left[\frac{K}{6} \eta_{ijk}^H + \frac{\sigma}{\varepsilon} (\Lambda_{ijk} - \Pi_{ijk}) + \frac{\sigma_{ref}^2 f(\varepsilon) f'(\varepsilon)}{\sigma} \Pi_{ijk} \right], \quad (6)$$

where K is the elastic bulk modulus, ε_{kk} and ε'_{ij} are the volume and deviatoric strains,

respectively, $\varepsilon = (2\varepsilon'_{ij}\varepsilon'_{ij}/3)^{1/2}$ is the effective strain, σ is the flow stress in Eq. (1) that has incorporated the strain gradient effects, $\sigma_{ref}f(\varepsilon)$ is obtained from the uniaxial stress-strain relation, η_{ijk}^H is the volumetric part of strain gradients η_{ijk} , and Λ_{ijk} and Π_{ijk} are third-order tensors that depend on the deviatoric parts of strains and strain gradients, as given in [22,23]. The coefficient l_ε scaling the higher-order stresses in Eq. (6) is the meso-scale cell size and is given by $l_\varepsilon = 10\mu b/\sigma_Y$, where μ is the shear modulus, b is the Burgers vector, and σ_Y is the yield stress.

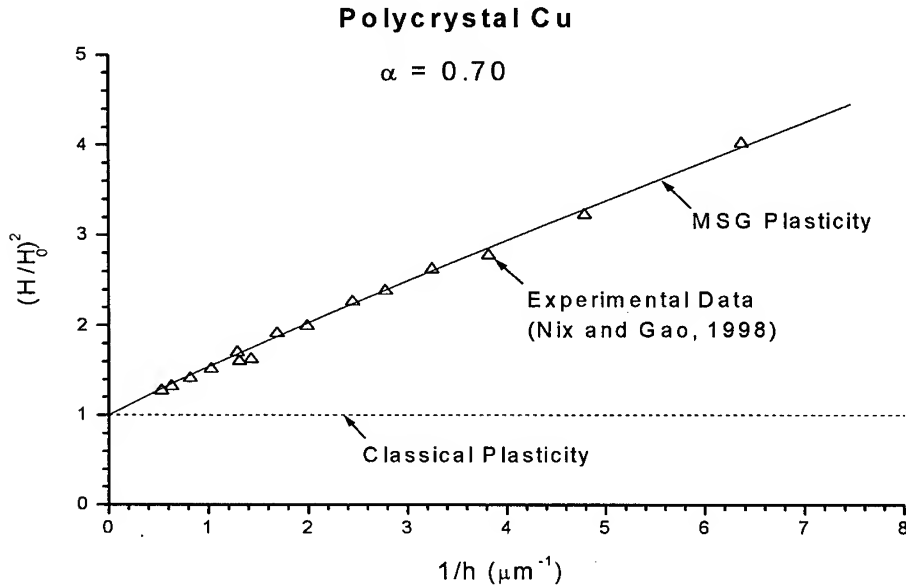


Figure 2. Depth dependence of the hardness of polycrystalline copper; the solid line is the hardness predicted by MSG plasticity; the triangles are experimental data^[7,21], H is the micro-indentation hardness, $H_0 = 834 \text{ MPa}$ is the indentation hardness for large depth of indentation, h is the depth of indentation, the uniaxial stress-strain curve $\sigma = 408\varepsilon^{0.3} \text{ MPa}$, shear modulus $\mu = 45 \text{ GPa}$, and the Burgers vector $b = 0.255 \text{ nm}$.

2.5 Equilibrium Equations and Kinematics Relations

The equilibrium equations in the higher-order continuum theory are give by [19,23]

$$\sigma_{ik,i} + \tau_{ijk,jj} = 0. \quad (7)$$

The kinematics relations give the strains and strain gradients in terms of the displacements u as

$$\varepsilon_{ij} = \frac{1}{2}(u_{i,j} + u_{j,i}), \quad \eta_{ijk} = u_{k,ij} \quad (8)$$

2.6 Experimental Validation

Figure 2 shows the comparison between the MSG plasticity theory and the micro-indentation hardness data [24] for polycrystalline copper. The ordinate is the square of indentation hardness, H , normalized by its counterpart, H_0 , for large depth of indentation (i.e., no strain gradient effects), while the abscissa is the inverse of indentation depth, h^{-1} . It is clearly observed that the numerically predicted hardness based on MSG plasticity agrees very well with the experimental data for a wide range of indentation depth, from one tenth of a micron to several microns. The elastic moduli, Burgers vector, as well as the uniaxial stress-strain curve are known prior to the numerical study such that the only parameter to be determined is the empirical coefficient α in Taylor model. The coefficient is $\alpha = 0.7$ in Fig. 2, which has the correct order of magnitude of one measured from independent experiments [26].

Gao et al. [24] have shown that the MSG plasticity theory also agrees very well with the micro-torsion [8] and micro-bending experiments [9]. The excellent agreements between the MSG plasticity theory and various micro-scale experiments validate it as a micron scale theory which successfully bridges the Taylor dislocation model and continuum plasticity.

3. CRACK TIP FIELDS IN MSG PLASTICITY

Shi et al. [32] have investigated the structure of asymptotic crack tip field associated with the MSG plasticity theory. Following HRR field [33,34] associated with classical plasticity, the crack tip field is tentatively assumed to have a separable form,

$$u_i = r^\lambda \tilde{u}_i(\theta), \quad (9)$$

where (r, θ) are polar coordinates centered at the crack tip, u_i are the displacements, $\tilde{u}_i(\theta)$ are the corresponding angular functions, and λ (>0) is the eigenvalue to be determined. The mode III, mode I and mode II crack tip fields are presented separately in the following.

3.1 Mode III Crack Tip Field

It is straightforward to show that, for the separable field in Eq. (9), the higher-order stresses are more singular than stresses. Keeping the dominating singular terms, the traction-free condition on the crack face can be written as

$$\tilde{r}_3(\theta = \pi) = \tilde{t}_3(\theta = \pi) = 0, \quad (10)$$

where \tilde{r}_3 and \tilde{t}_3 are the angular functions of the higher-order stress and stress tractions, respectively. The anti-symmetry in a mode III problem requires

$$\tilde{u}_3(\theta=0) = \tilde{u}_3''(\theta=0) = 0. \quad (11)$$

If only the most singular terms are kept, the equilibrium equation (7) gives an ordinary differential equation for the angular function $\tilde{u}_3(\theta)$ as

$$\frac{d^4 \tilde{u}_3}{d\theta^4} = \frac{g_1(\tilde{u}_3, \tilde{u}_3', \tilde{u}_3'', \tilde{u}_3''')}{g_2(\tilde{u}_3, \tilde{u}_3', \tilde{u}_3'')}, \quad (12)$$

where the numerator g_1 and the denominator g_2 are functions of the corresponding variables, and very importantly, g_2 vanishes when $\tilde{u}_3 = \tilde{u}_3'' = 0$. It is observed that, at $\theta = 0$, the left hand side of Eq. (12) is zero due to anti-symmetry, while the right hand side would approach infinity because the denominator would vanish. In fact, near $\theta = 0$, \tilde{u}_3 can be expanded in a Taylor series of θ with the odd power only. The left hand side and the denominator of right hand side are both on the order of θ , while the numerator of the right hand side is $g_1[0, \tilde{u}_3'(\theta=0), 0, \tilde{u}_3'''(\theta=0)] + O(\theta^2)$. In order to match the power θ on both sides of Eq. (12) near $\theta = 0$, the only possibility is to make the numerator of the right hand side vanish at $\theta = 0$, i.e.,

$$g_1[0, \tilde{u}_3'(\theta=0), 0, \tilde{u}_3'''(\theta=0)] = 0. \quad (13)$$

This imposes an additional boundary condition on the eigenvalue problem and makes it highly improbable to have solutions. In fact, the numerical shooting method has indeed found no solutions for this eigenvalue problem.

It should be pointed out, however, this extra boundary condition (13) results directly from the assumed separable form (9) in the asymptotic crack tip field. For general displacement field $u_3(r, \theta)$, it can be shown that the coefficient of the highest order derivative with respect to θ in the equilibrium equation, $\partial^4 u_3 / \partial \theta^4$, is not zero. In other words, only when the displacement field u_3 takes the separable form (9), the coefficient of $\partial^4 u_3 / \partial \theta^4$ becomes the denominator g_2 in Eq. (12) and vanishes at $\theta = 0$. Therefore, the asymptotic crack tip field associated with MSG plasticity is non-separable.

3.2 Mode I and Mode II Crack Tip Fields

The separable crack tip fields of (9) have also been investigated for the in-plane deformation, i.e., mode I and mode II asymptotic fields. Even though the ordinary differential equations become much more complicated, they have exactly the same character as the mode III analysis, i.e., the coefficient of the highest order derivative with respect to θ vanishes at $\theta = 0$ and therefore imposes an additional boundary condition. This also makes the eigenvalue problem overly

constrained and solution-less. In fact, the numerical shooting method has indeed found no solutions for the eigenvalue problem. It is once again concluded that the asymptotic crack tip fields associated with MSG plasticity have non-separable solutions only.

It is quite puzzling why there is no separable solution (9) associated with MSG plasticity, contrary to all other existing crack tip fields. This is discussed in the following.

3.3 Implications on the Fracture Criterion

The asymptotic fields only hold within a small distance to the crack tip, typically one tenth of the smallest relevant geometry or material length. In classical plasticity, there is no intrinsic material length such that the dominance zone of the crack tip field is governed by the crack length or plastic zone size. In MSG plasticity, the meso-scale cell size $l_e = 10\mu b/\sigma_Y$ scales the higher-order stresses and becomes the smallest relevant length. The dominance zone of the crack tip field can be estimated as $l_e/10 \sim \mu b/\sigma_Y$. For copper, l_e is around 500 nanometers [35] such that the dominance zone of the crack tip fields associated with MSG plasticity is on the order of 50 nanometers. It is not only outside the intended range of applications for strain gradient plasticity (0.1~10 microns), but also too small for any continuum plasticity theories to be applicable because continuum plasticity represents a statistical average of hundreds of dislocations. For a typical dislocation density of $10^{14} m^{-2}$, a zone of 50 nanometers contains at most one dislocation. Even for an extremely high (and probably unrealistic) local dislocation density of $10^{16} m^{-2}$ near the crack tip, 50 nanometers contains only 5 dislocations. Therefore, even if there had existed a mathematically separable crack tip field as in Eq. (9), the solution would not have a domain of physical validity.

The non-existence of separable solutions also indicates that the crack tip field associated with MSG plasticity is not governed by a single amplitude factor (e.g., J -integral [36]). What is the new fracture criterion in MSG plasticity? Recent efforts in simulation of crack initiation and growth make use of an embedded cohesive zone characterized by a work of separation and a separation strength [37-41]. The cohesive law has the potential to become the fracture criterion that is implicitly built into the continuum analysis. Gao and Klein [42,43] have developed an alternative approach, namely the Virtual-Internal-Bond (VIB) model, to build the fracture criterion into the constitutive model based on the interatomic potentials. If the cohesive zone or VIB model is introduced in MSG plasticity, it is not necessary to establish an explicit fracture criterion.

ACKNOWLEDGMENTS

K.C.H. acknowledges the support from the NSFC and from the Ministry of Education, China. Y.H. acknowledges the support from US NSF under grant #CMS-9896285 and from the NSFC.

REFERENCES

1. W.D.Nix, Metall. Trans. 20A (1989) p.2217.
2. M.S.De Guzman, G.Newbauer, P.Flinn and W.D.Nix, Mater. Res. Soc. Proc. 308 (1993) p.613.
3. N.A.Stelmashenko, M.G.Walls, L.M.Brown and Y.V.Milman, Acta Metall. Mater. 41 (1993) p.2855.
4. M. Atkinson, J. Mater. Res. 10 (1995) p.2908.

5. Q.Ma and D.R.Clarke, *J. Mater. Res.* 10 (1995) p.853.
6. W.J.Poole, M.F.Ashby and N.A.Fleck, *Scripta Metall. Mater.* 34 (1996) p.559.
7. K.W.McElhane, J.J.Vlassak, W.D.Nix, *J. Mater. Res.* 13 (1998), p.1300.
8. N.A.Fleck, G. M.Muller, M.F.Ashby and J.W.Hutchinson, *Acta Metall. Mater.* 42 (1994), p.475.
9. J.S.Stolken and A.G.Evans, *Acta Mater.* 46 (1998) p.5109.
10. D.J. Lloyd, *Int. Mater.Rev.* 39 (1994) p.1.
11. R.Hill, *Mathematical theory of plasticity*, Oxford University Press, Oxford (1950).
12. R.Dauskardt, M.Lane, Q.Ma and N.Krishna, *Eng. Fracture Mech.* 61 (1998) p.141.
13. G.Ellsner, D.Korn and M.Ruehle, *Scripta Metall. Mater.* 31 (1994) p.1037.
14. J.W.Hutchinson, *Advances in Fracture Research*, Pergamon Press, New York (1997) p.1.
15. M.F.Ashby, *Phil. Mag.* 21 (1970) p.399.
16. J.F.Nye, *Acta Metall.* 1 (1953), p.153.
17. A.H.Cottrell, *The mechanical properties of matter*, Wiley, New York (1964) p.277.
18. N.A.Fleck and J.W.Hutchinson, *J. Mech. Phys. Solids* 41 (1993) p.1825.
19. N.A.Fleck and J.W.Hutchinson, *Adv. Appl. Mech.* 33 (1997) p.295.
20. G.I.Taylor, *J. Inst. Metals* 62 (1938) p.307.
21. W.D.Nix and H.Gao, *J. Mech. Phys. Solids* 46 (1998) p.411.
22. H.Gao, Y. Huang, W.D.Nix and J.W.Hutchinson, *J. Mech. Phys. Solids* 47 (1999) p.1239.
23. Y. Huang, H.Gao, W.D.Nix and J.W.Hutchinson, *J. Mech. Phys. Solids* 48 (2000) p.99.
24. H.Gao, Y. Huang and W.D.Nix, *Naturwissenschaften* 86 (1999) p.507.
25. M.X.Shi, Y. Huang and K.C.Hwang, *Plastic flow localization in mechanism-based strain gradient plasticity*, *Int. J. Mech. Sci.* (in the press).
26. W.D.Nix and J.C.Gibeling, *Metals/materials technology series 8313-004*, ASM, Metals Park (1985).
27. J.F.W.Bishop and R.Hill, *Phil. Mag.* 42 (1951) p.414.
28. J.F.W.Bishop and R.Hill, *Phil. Mag.* 42 (1951) p.1298.
29. U.F.Kocks, *Metal Trans.* 1 (1970) p. 1121.
30. J.R.Rice, *J. Appl. Mech.* 34 (1970) p. 728.
31. J.R.Rice, *J. Mech. Phys. Solids* 19 (1971) p. 433.
32. M.X.Shi, Y.Huang, H.Gao and K.C.Hwang, *Non-existence of separable crack tip field in mechanism-based strain gradient plasticity*, *Int. J. Solids Struct.* (in press).
33. J.W.Hutchinson, *J. Mech. Phys. Solids* 16 (1968) p. 13.
34. J.R.Rice and G.F.Rosengren, *J. Mech. Phys. Solids* 16 (1968) p.1.
35. Y.Huang, H.Gao and K.C.Hwang, *Progress in mechanical behavior of materials* (eds. F.Ellyin and J.W.Provan), Fleming Printing Ltd (1999) p.1051.
36. J.R.Rice, *J. Appl. Mech.* 35 (1968) p. 379.
37. A.N.Needleman, *J. Appl. Mech.* 54 (1987) p.525.
38. V.Tvergaard and J.W.Hutchinson, *J. Mech. Phys. Solids* 40 (1992) p.1377.
39. V.Tvergaard and J.W.Hutchinson, *J. Mech. Phys. Solids* 41 (1993) p.1119.
40. X.P.Xu and A.Needleman, *J. Mech. Phys. Solids* 42 (1994) p.1397.
41. G.T.Camacho and M.Ortiz, *Int. J. Solids Struct.* 33 (1996) p.2899.
42. H.Gao and P.Klein, *J. Mech. Phys. Solids* 46 (1998) p. 187.
43. P.Klein and H.Gao, *Eng. Fracture Mech.* 61 (1998) p.21.

An Analysis of Fatigue Crack Growth Rate Considering Spatial Variation of Fatigue Crack Growth Resistance

S.J. Kim

School of Mechanical Engineering, Pukyong National University,
San 100 Yongdang-dong, Nam-gu, Pusan 608-739, Korea

Keywords: Autocorrelation Function, Constant ΔK Fatigue Crack Growth Test, Fatigue Crack Growth Resistance, Spatial Random Process, Weibull Distribution

ABSTRACT

The purpose of the present study is to investigate if it is possible to predict fatigue crack growth rate (FCGR) by using only the fluctuation of the parameter C and discuss the possibility of change of the parameter m in Paris' law. The fluctuation of fatigue crack growth rate is assumed only due to the parameter C . The fatigue crack growth resistance coefficient ($Z=1/C$) of the material to fatigue crack growth was treated as a spatial random process, which varies randomly on the crack path. Constant ΔK FCG test at the various stress intensity levels were performed on CT specimen for SM45C steel. The experimental data were analyzed to determine the autocorrelation function and Weibull distributions of the crack growth resistance. Using the statistical properties, comparison of experimental FCGR and predicted FCGR has been analyzed. And also, the effect of the parameter m of Paris' law due to variation of fatigue crack growth resistance was discussed.

1. INTRODUCTION

Experimental studies on the randomness of FCG have been performed [1-5]. Some deal with the means and variance of material properties and some focus on the characteristics of materials as spatial random processes. There have also been several attempts to construct theoretically a FCG model for the safety evaluation of fatigue critical structures. Such a model assumes FCG as a random process and, therefore, needs to know the stochastic nature of material parameters before any its practical application. For this purpose not only mean and variance of growth rate but also the spatial distribution of resistance are necessary. But, most of the studies for the randomness was on constant amplitude loading. From a statistical point of view, the characterization of the FCG behavior by the traditional constant ΔP test method requires many tests and is therefore time consuming and expensive. An effective and efficient technique for characterizing crack growth behavior is not yet established. The constant ΔK controlled test has the potential for the development of such a method and investigation of the spatial variation of FCGR [6]. The authors [7] already studied the spatial correlation of FCG using the constant ΔK controlled tests.

In the present study, the fatigue crack growth rate (FCGR) was assumed to be given by

$$\frac{da}{dN} = C(\Delta K)^m \quad (1)$$

where, m and C are the material constants, a is the fatigue crack length, N is the number of cycles to load and ΔK is stress intensity factor range. The material constants m and C , hereinafter, called as growth rate exponent and coefficient, respectively, and as a one-dimensional random process model of FCG, only the growth rate coefficient, C , is treated as random variable along the crack path while the growth rate exponent, m , is assumed constant in any point.

This paper will attempt to show the possibility of FCGR prediction if the statistical properties of the parameter $Z=1/C$ are known, and to discuss the effect of the exponent, m of Paris' law.

2. EXPERIMENTAL DETAILS

Carbon steel for machine structural use, SM45C used in the present investigation was available in the form of an original 12-mm-thick hot rolled plate with an identifiable rolling direction. The chemical compositions (wt.%) are; C-0.47, Si-0.16, Mn-0.74, Mo-0.02, P-0.025, S-0.007, Cr-0.03, Al-0.001, Fe-bal. Compact tension specimens (CT) with a LT orientation were prepared as per the various recommendations of ASTM E647-81. In all specimens, the specimen width was held constant at $W=100$ mm. All specimens were cut off the same sheet. The microstructure of the material showed the presence of ferrite and pearlite. In order to align the specimens, circular washers were used to hold the specimens in the midplane of the clevis grips during fatigue crack growth testing. All the specimens were initially pre-cracked to produce a sharp crack front. The fatigue cracking was carried out in an servohydraulic testing machine at room temperature. All tests were carried out in tension-tension under constant ΔK control mode for stress intensity level of 25, 30, 37.5 and 45 $MPa\sqrt{m}$, the stress ratio, 0.2 and the frequency, 10Hz. The ΔK level so adjusted was found to be within $\pm 0.2\%$ of the range, and this was considered satisfactory. The micro computer generates a time series which is used as the input to a multiplying DA-converter. The crack-opening displacement is measured by clip gauge. This signal and the load cell output are simultaneously digitized and take into micro computer. The crack lengths were mainly measured by the compliance method. And also, the crack lengths were measured on both specimen surfaces with the help of a travelling microscope ($\times 100$) by one person.

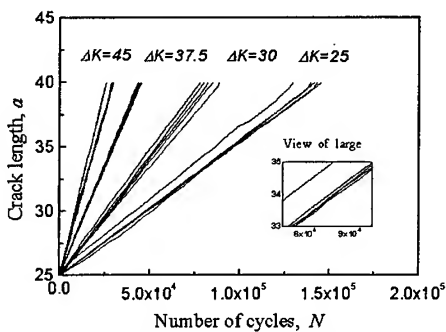
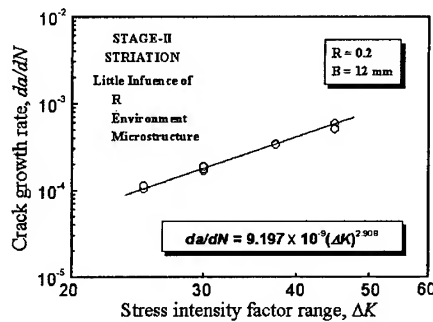
3. PRESENTATION OF EXPERIMENTAL RESULTS

3.1 Fatigue Crack Growth Behavior and the Scatter

Figure 1 provides a diagram of the crack length, a , vs. the number of cycles, N , for each stress intensity level. This figure shows that there is scatter in FCGR data. This scatter seems to be increased for specimen with lower stress intensity level. As shown in this figure, though each relation is approximately linear, the difference of the inclination of each curve for a stress intensity level is seen. It is evident that there is obviously a spatial variation of the local mean value of the growth resistance of material to FCG from specimen to specimen. And, the results show that stress intensity level has apparent influence on the coefficients of variation of the growth resistance. Coefficients of variation of crack growth resistance is decreased by increasing stress intensity level.

Figure 2 shows the form of da/dN versus ΔK plots obtained by constant ΔK control mode. It can be also seen that there is scatter in the data. Applying the Paris equation, value of the growth exponent, m , was obtained as 2.91, and C as 9.197×10^{-9} . It is known that the FCGR for the range

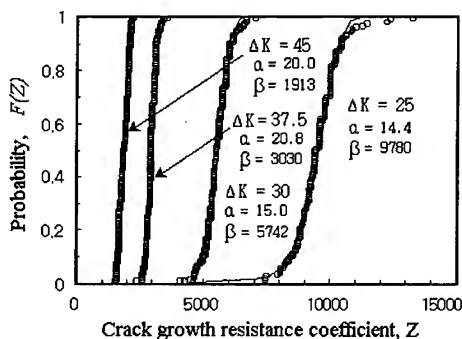
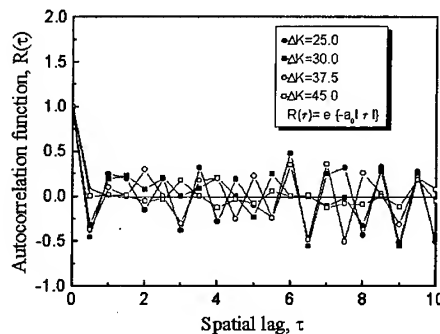
of stress intensity level investigated in this work is associated with striation formation. As shown in these figures, it is evident that the crack growth resistance is dependent on the spatial location within a specimen. It seems to be that m varies from specimen to specimen, and a higher frequency fluctuation is due to C . This problem will, however, not be discussed in the present investigation. In this work, the fluctuation of FCGR is assumed only due to the parameter C .

Figure 1 $a \sim N$ curvesFigure 2 da/dN versus ΔK

3.2 Probability Distribution of the Resistance Coefficient

Since the inverse of $C(x)$ seems better for describing the material property[4,7], $Z(x)=1/C(x)$ is used and called as growth resistance coefficient. The resistance coefficients obtained from the experiments are plotted on Weibull probability paper, as shown in Figure 3. The two-parameter Weibull distribution function is used to fit the data. The parameters α and β are estimated by the direct search of optimization method. The estimated parameters are also shown in the figure. The probability distribution functions of the resistance coefficient obtained from experimental data are two-parameter Weibull distribution and show dependence on the stress intensity factor range. The shape parameter is increased with increasing the stress intensity level, but the scale parameter is decreased.

From all data of $Z(x)$, the ensemble autocorrelation functions for each stress intensity level are shown in Figure 4. It is clear from this figure that the autocorrelation functions are almost independent of the stress intensity level. The rate of decay is very rapid. The exponential function

Figure 3 Probability distributions of $Z(x)$ Figure 4 Autocorrelation functions of $Z(x)$

seems to be a reasonable shape. The function, $\exp(-a_0|\tau|)$, is also shown in this figure with the arbitrarily chosen coefficient. The value of the correlation length is about 0.125 mm. This is well coincide with the result of Itagaki et al[8]. The advantage of this approach is an understanding of the scale of variation for the spatial stochastic process.

3.3 Prediction of Fatigue Crack Growth Rate

As described in the above section, the resistance coefficient shows remarkable spatial variation in the individual specimens. In this section, consider the prediction of FCGR due to spatial variation of growth resistance coefficient. Under constant ΔK control FCG tests, the mean FCGR is proportional to the mean value of $1/Z$. Therefore, The calculated value of FCGR considering spatial variation of growth resistance is written as:

$$\begin{aligned}
 \int_0^\infty \frac{1}{z} f_z(z) dz &= \int_0^\infty \frac{1}{z} \frac{\alpha}{\beta} \left(\frac{z}{\beta} \right)^{\alpha-1} \exp \left\{ - \left(\frac{z}{\beta} \right)^\alpha \right\} dz \\
 &= \int_0^\infty \frac{1}{z} \frac{\alpha}{\beta} \left(\frac{z}{\beta} \right)^{\alpha-1} \exp(-x) \frac{\beta}{\alpha} \left(\frac{\beta}{z} \right)^{\alpha-1} dx \\
 &= \frac{1}{\beta} \int_0^\infty x^{-1/\alpha} \exp(-x) dx \\
 &= \frac{1}{\beta} \Gamma \left(1 - \frac{1}{\alpha} \right)
 \end{aligned} \tag{2}$$

where, Γ is gamma function. This equation is called as the prediction value of FCGR considering spatial variation of growth resistance.

Figure 5 shows the comparison of the experimental values of fatigue crack growth rate and the prediction values using the Eq. (2). As shown in the figure, it is be said that the prediction values describe the experimental value very well. Determining the values of the Weibull parameter for a stress intensity level by using the above results, it is said that the prediction of FCGR of the structures is possible. But, one should be careful when FCGR is estimated by using the statistical properties, because of the scale of the spatial variation according to materials.

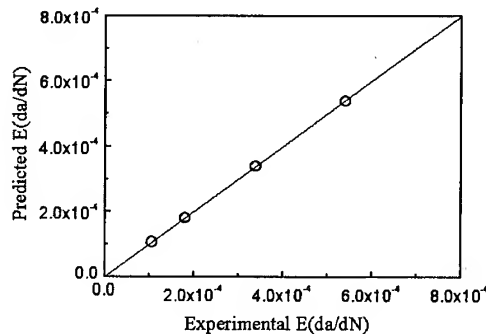


Figure 5 Comparison of experimental $E[da/dN]$ and predicted $E[da/dN]$

3.4 Effect of m for Paris' Law

Suppose that the scale parameter, β is dependent on the size of any region, r , determined by the stress intensity level, ΔK . In this case, if the probability distribution for standard region, r_0 , is 2-parameter Weibull, then the probability distribution for n time region of the standard region, namely ($n \times r_0$) is assumed to follow the distribution of smallest values.

First, the probability that a random variable z_k is less than x can be expressed as:

$$P(z_k \leq x) = 1 - \exp\left\{-\left(\frac{z}{\beta}\right)^\alpha\right\} \quad (3)$$

The probability that all values in a sample of size n of a continuous random variable Z of distribution $F_z(x)$ are larger than x can be expressed as:

$$\begin{aligned} P(\min(Z_1, Z_2, \dots, Z_n) > x) \\ &= P(z_1 > x, z_2 > x, \dots, z_n > x) \\ &= P(z_1 > x)P(z_2 > x) \dots P(z_n > x) \\ &= \exp\left\{-n\left(\frac{z}{\beta}\right)^\alpha\right\} \end{aligned} \quad (4)$$

Therefore, the probability that all values in the sample of size n are less than x is given by:

$$P(\min(z_1, z_2, \dots, z_n) \leq x) = 1 - \exp\left\{-n\left(\frac{z}{\beta}\right)^\alpha\right\} \quad (5)$$

Equation (5) is the probability function of the smallest value in a sample of size n in terms of the initial distribution. The factor of $n(\beta)^{-1/\alpha}$ represents the size effect of the growth resistance.

Therefore, the mean crack growth rate $E(da/dN)$ considering the distribution of smallest values is easily obtained by using the equation (2). That is:

$$E\left(\frac{da}{dN}\right) \propto \frac{n^{1/\alpha}}{\beta} \Gamma\left(1 - \frac{1}{\alpha}\right) \quad (6)$$

from which for $n=1$ the mean crack growth rate is equal to Eq. (2).

If n is especially proportional to power of p (proportional constant, f), the mean fatigue crack growth rate is then expressed as:

$$\begin{aligned} E\left(\frac{da}{dN}\right) &= \frac{n^{1/\alpha}}{\beta} \Gamma\left(1 - \frac{1}{\alpha}\right) (\Delta K)^m \\ &= \frac{(f\Delta K)^{p/\alpha}}{\beta} \Gamma\left(1 - \frac{1}{\alpha}\right) (\Delta K)^m \end{aligned}$$

$$= \frac{f^{p/\alpha}}{\beta} \Gamma\left(1 - \frac{1}{\alpha}\right) (\Delta K)^{m+p/\alpha} \quad (7)$$

This is also proportional to power of $(m+p/a)$ for ΔK .

As shown in the above discussion, there is a possibility that the parameter m can be changed by the spatial variation of the growth resistance within a specimen, even if m is constant condition. Therefore, it is necessary to investigate this fact theoretically and experimentally in the future.

4. CONCLUSIONS

The main results obtained from this investigation are as follows; (1) The scatter of the fatigue crack growth resistance is decreased with an increase in stress intensity factor range. (2) The autocorrelation function of the fatigue crack growth resistance coefficient is almost independent of stress intensity factor range. (3) The probability distribution function of the fatigue crack growth resistance obtained from experimental data is two-parameter Weibull distribution and show dependence on the stress intensity factor range. The shape parameter is increased with increasing the stress intensity level, but the scale parameter is decreased. (4) It is possible to predict fatigue crack growth rate by using only the fluctuation characteristics of Z . (5) There is a possibility that the parameter m in Paris' law is changed by the fluctuation of Z , even if m is in constant condition.

ACKNOWLEDGMENTS

The author wish to thank Dr. H. Itagaki, President of Yokohama National University, for his encouragement in this study. S. H. Yoon and C. H. Jeon, Graduate Student, very gratefully acknowledges the assistance of the experimental work.

REFERENCES

1. D. A. Virkler, B. M. Hillberry and P. K. Goel, *J. of Engrg. Mat. and Tech.*, **101** (1979) p.148
2. H. Ghonem and S. Dore, *Engrg. Fract. Mech.*, **27** (1987) p.1
3. C. Lapetra, J. Mayo and J. Dominguez, *Fat. Fract. Eng. Mat. Struct.*, **19** (1996) p.589
4. K. Ortiz and A. S. Kiremidjian, *Engrg. Fract. Mech.*, **24** (1986) p.657
5. F. Kozin and J. L. Bodganoff, *Engrg. Fract. Mech.*, **14** (1981) p.59
6. Z. Zheng, B. E. Powell, J. Byrne and I. W. Hussey, *Fat. Fract. Eng. Mat. Struct.*, **22** (1999) p.383
7. S. J. Kim, H. Itagaki and T. Ishizuka, *J. Soc. Naval Architects Japan*, **173** (1993) p.327
8. H. Itagaki and M. Shinozuka, *ASTM STP*, **511** (1972) p.168

Rectangular Array and Zig-zag Array of Elliptical Holes in Solids under Uniaxial Tension (Formulae of Maximum Stresses and Tensile Stiffnesses)

H. Igawa

Department of Mechanical Engineering, Kurume Institute of Technology,
2228 Kamitsu-machi, Kurume 830-0052, Japan

Keywords: Crack, Elliptical Holes, Stress Concentration, Stress Intensity Factor, Tensile Stiffness, Tension, Two-Dimensional Elasticity

ABSTRACT

This paper is concerned with a theoretical analysis of a rectangular array and a zig-zag array of elliptical holes in solids under uniaxial tension. Numerical results of the maximum stress represented in dimensionless forms in the whole range of the shapes of the holes including cracks, and the effective Young's modulus of the solids with the holes, are given for various values of the parameters. The analytical values are then fitted to reliable polynomial formulae for convenience of engineering applications.

1. Introduction

In this paper, we consider a rectangular array and a zig-zag array of elliptical holes in solids under uniaxial tension as two-dimensional models of randomly distributed holes in materials.

In the analyses, we choose suitable unit regions, and express Laurent series expansions for the complex potentials in forms satisfying the traction-free conditions along the elliptical hole edges. Then the unknown coefficients in the Laurent series are determined from the boundary conditions at the outer edges of the used unit regions. At this stage, we use a procedure based on element-wise resultant forces and displacements in order to get highly accurate results. Numerical calculations are carried out for various shapes and sizes of the holes, and special arrays of the holes in solids.

2. Theoretical Analysis

In plane problems of elasticity, the Cartesian components of stress, resultant force and displacement are given in terms of two complex potentials $\phi(z)$, $\psi(z)$ as follows:

$$\begin{aligned}\sigma_y + \sigma_x &= 4\phi'(z) \\ \sigma_y - \sigma_x + 2i\tau_{xy} &= 2[\bar{z}\phi''(z) + \psi''(z)]\end{aligned}\quad (1)$$

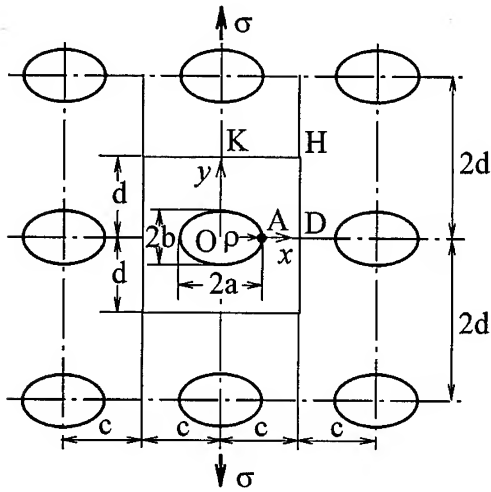


Fig. 1(a) Rectangular array of elliptical holes

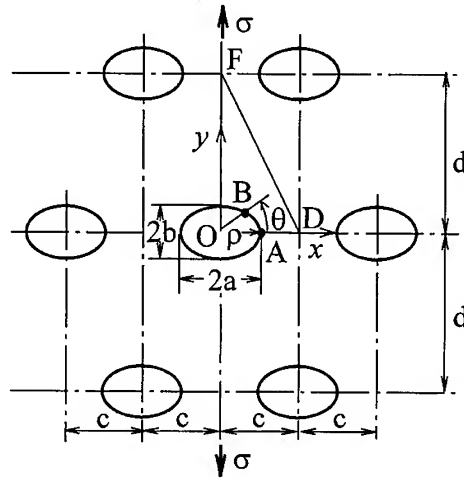


Fig. 1(b) Zig-zag array of elliptical holes

$$P_y + iP_x = -\bar{\varphi}(\bar{z}) - \bar{z}\varphi'(z) - \psi'(z) \quad (2)$$

$$2G(u - iv) = \kappa\bar{\varphi}(\bar{z}) - \bar{z}\varphi'(z) - \psi'(z) \quad (3)$$

where G is the shear modulus and κ is defined by Poisson's ratio ν as

$$\kappa = \begin{cases} \frac{3-\nu}{1+\nu} & \text{(plane stress)} \\ 3-4\nu & \text{(plane strain)} \end{cases} \quad (4)$$

This paper deals with the following two typical distributions of elliptical holes in infinite solids subjected to uniaxial tension:

Problem (a): Rectangular array of elliptical holes (Fig. 1(a))

Problem (b): Zig-zag array of elliptical holes (Fig. 1(b)).

In both the problems, let $2a$ and $2b$ be the major and minor diameters, ρ be the radius of curvature at the end of the major axes of the elliptical holes, and c, d be the spacings in the directions parallel and vertical to the load, respectively, as shown by Figs. 1(a) and 1(b). The x - and y -axes are taken with their origin at the center of one of the elliptical holes, and the solids are subjected to an average tensile stress σ in the y -direction.

We take proper unit regions and express the complex stress potentials in forms satisfying the symmetry conditions of the stress state, as well as the traction-free conditions along the elliptical hole edges. We then determine the unknown coefficients in the stress potentials from the boundary conditions at the outer edges of unit regions.

For the above unit regions, we have chosen the rectangle ODHKO for Problem (a) and the triangle ODFO for Problem (b) shown in Fig. 1(a) and 1(b), noting the symmetry of stress field about both the coordinates' axes.

The complex potentials $\varphi(z)$, $\psi(z)$ must be analytic in the unit regions, and they can be expanded in the following Laurent series:

$$\begin{aligned}\varphi(z) &= \sum_{n=0}^{\infty} (G_{2n} z^{-2n-1} + M_{2n} z^{2n+1}) \\ \psi(z) &= -D_0 \log z + \sum_{n=0}^{\infty} (D_{2n+2} z^{-2n-2} + K_{2n} z^{2n+2}),\end{aligned}\quad (5)$$

where G_{2n} , M_{2n} , D_{2n} , K_{2n} are real coefficients. Eq. 5 also satisfies the conditions of symmetry of the stress state about the x - and y -axes.

Since the elliptical hole is traction-free, some relations must exist among the coefficients of Eq. 5. These relations were given by Isida [1] as follows:

$$\begin{aligned}D_{2n} &= \sum_{p=0}^{\infty} a^{2n+2p+2} (P_{2p}^{2n} K_{2p} + R_{2p}^{2n} M_{2p}) \\ G_{2n} &= - \sum_{p=0}^{\infty} a^{2n+2p+2} (Q_{2p}^{2n} K_{2p} + S_{2p}^{2n} M_{2p})\end{aligned}\quad (6)$$

where P_{2p}^{2n} etc. are constants given by $b/a (= \sqrt{\rho/a})$, the ratio of the shape of the elliptical hole.

Then the unknown coefficients in the Laurent series are determined from the boundary conditions at the outer edges of the rectangular unit region ODHKO in Fig. 1(a) for Problem (a) and the triangular unit region ODFO in Fig. 1(b) for Problem (b). At this stage, we use a procedure based on element-wise resultant forces and displacements [2, 3].

3. Numerical Results and Discussions

3.1. Physical Quantities and Accuracy of Results

Numerical results of the treated problems depend upon the ratio of a , b , c and d , or upon the three dimensionless parameters below:

$$\mu = \frac{c}{d}, \quad \lambda = \frac{a}{c}, \quad \varepsilon = \frac{b}{a} = \sqrt{\frac{\rho}{a}}. \quad (7)$$

In the present problem, we are especially interested in two quantities. One is the distribution of tangential stress along the hole, and other is the effect of holes on the apparent tensile stiffness of the solid. With reference to the latter quantity, the following dimensionless factor C is defined:

$$C = \frac{E^*}{E_0} = \text{tensile stiffness factor}$$

E^* = apparent Young's modulus of solid with elliptical holes

E_0 = Young's modulus of material

$$= \begin{cases} E & \text{(plane stress)} \\ E/(1-\nu^2) & \text{(plane strain)} \end{cases}, \quad (8)$$

where E is Young's modulus of the material measured with thin plate specimens. E^* and E_0 depend on E and ν , but C is independent of them and is common to the plane stress and the plane strain cases.

3.2. Stress Magnification Factors and Their Formulae

In Problem (a), σ_{\max} , the maximum stress around the hole, occurs at point A as shown in Fig. 1(a). In Problem (b), σ_{\max} occurs at point A ($\theta = 0$) in most of the calculated cases of ρ/a and λ , but in some cases of ρ/a and λ , σ_{\max} takes place at some other point B ($\theta \neq 0$) due to interference by the presence of obliquely located holes.

In representing these stresses, we use the following dimensionless factors S_{\max} :

$$S_{\max} = \sigma_{\max} / \sigma_0, \quad \sigma_0 = \sigma(1 + 2\sqrt{a/\rho}), \quad (9)$$

where σ_0 is the maximum stress for a single elliptical hole in a wide plate subjected to tension.

In the case of cracks ($\rho \rightarrow 0$), σ_{\max} diverge towards infinity, but S_{\max} remain finite and are equal to the dimensionless stress intensity factor based on $\sigma\sqrt{\pi a}$, that is

$$(S_{\max})_{\rho \rightarrow 0} = K_I / \sigma\sqrt{\pi a}. \quad (10)$$

The values of S_{\max} for Problem (a) and Problem (b) are plotted with solid curves in Fig. 2(a) and 2(b), respectively. S_{\max} for both the problems increases monotonically as λ increases and diverges towards infinity in extreme cases of λ in which some of adjacent holes touch each other.

Considering the above aspects, we have fitted power series to the analytical values of S_{\max} for both the problems, and the following formulae are obtained:

(a) Square array of elliptical holes for Problem (a) ($\mu=1$)

$$\begin{aligned} S_{\max} = 1 + \frac{\lambda^2}{1-\lambda} [0.2752 - 0.4126\varepsilon + 0.1302\varepsilon^2 - 0.0376\varepsilon^3 \\ + \lambda(-0.2764 + 1.1465\varepsilon - 1.4701\varepsilon^2 + 0.5137\varepsilon^3) \\ + \lambda^2(0.7736 - 2.5802\varepsilon + 6.9170\varepsilon^2 - 2.2693\varepsilon^3) \\ + \lambda^3(-1.0006 + 3.7412\varepsilon - 11.9176\varepsilon^2 + 4.4548\varepsilon^3) \\ + \lambda^4(0.3349 - 2.2530\varepsilon + 7.6266\varepsilon^2 - 3.2603\varepsilon^3)] \end{aligned} \quad (11)$$

(mean error = 0.05 percent)

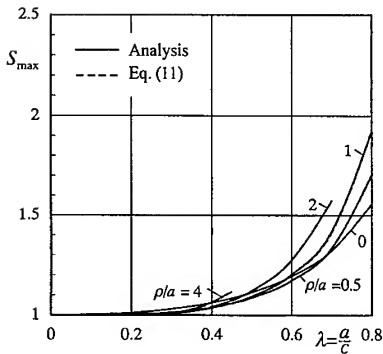


Fig. 2(a) S_{\max} for Problem (a) ($\mu=1$)

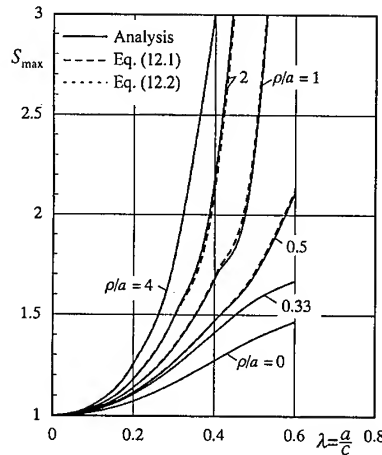


Fig. 2(b) S_{\max} for Problem (b) ($\mu=1$)

(b) Zig-zag array of elliptical holes for Problem (b) ($\mu=1$)

For the range of $\rho/a \leq 1/3$

$$S_{\max} = 1 + \frac{\lambda^2}{1-\lambda} [1.8169 + 1.0436\varepsilon + 0.5876\varepsilon^2 + \lambda(-2.1638 + 1.1838\varepsilon - 6.2676\varepsilon^2) + \lambda^2(3.8925 - 9.3537\varepsilon + 35.7642\varepsilon^2) + \lambda^3(-12.7934 + 3.9338\varepsilon - 56.6534\varepsilon^2) + \lambda^4(10.5138 + 1.9845\varepsilon + 31.5175\varepsilon^2)]$$

(mean error = 0.04 percent) (12.1)

For the range of $\rho/a \geq 1/3$

$$S_{\max} = 1 + \frac{\lambda^2}{1 - \frac{2\varepsilon\lambda}{\sqrt{\varepsilon^2 + 1}}} [1.7170 + 1.3916\varepsilon + 0.2840\varepsilon^2 + \lambda(-1.6954 - 0.0039\varepsilon - 6.7001\varepsilon^2) + \lambda^2(36.2512 - 83.2978\varepsilon + 80.8250\varepsilon^2) + \lambda^3(-138.479 + 306.085\varepsilon - 254.227\varepsilon^2) + \lambda^4(129.517 - 298.641\varepsilon + 246.157\varepsilon^2)]$$

(mean error = 0.6 percent) (12.2)

Values from Eqs. 11-12.2 are plotted in Fig. 2(a), (b) as dotted curves and dashed curves, respectively, showing close agreement with the analytical curves.

3.3. Tensile Stiffnesses and Their Formulae

Tensile stiffness factor C defined by Eq. 8 has been calculated for various values of ρ/a and λ . Results for both the problems are plotted with solid curves in Figs 3(a) and 3(b), respectively. Tensile stiffness factor C decreases with increasing values of ρ/a and λ in both the problems. As compared with both problems, the magnitude of decreasing C for Problem (b) is lower than that for Problem (a).

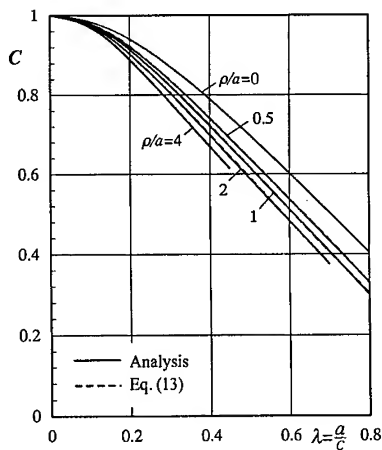


Fig. 3(a) $C = E^* / E_0$ for Problem (a)
($\mu=1$)

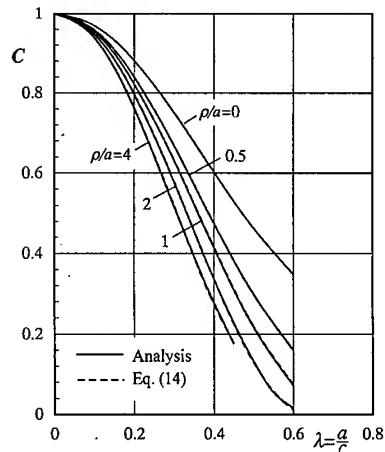


Fig. 3(b) $C = E^* / E_0$ for Problem (b)
($\mu=1$)

We have fitted power series to the analytical values of C for both the problems, and the following formulae are obtained:

(a) Square array of elliptical holes for Problem (a) ($\mu=1$)

$$C = \frac{E^*}{E_0} = 1 + \lambda^2 [-1.5676 - 0.9146\varepsilon + 0.2219\varepsilon^2 - 0.0803\varepsilon^3 \\ + \lambda(-0.0873 + 2.2217\varepsilon - 3.9416\varepsilon^2 + 1.4311\varepsilon^3) \\ + \lambda^2(2.7891 - 7.0999\varepsilon + 20.0590\varepsilon^2 - 6.9753\varepsilon^3) \\ + \lambda^3(-2.7733 + 14.4914\varepsilon - 36.5721\varepsilon^2 + 12.5757\varepsilon^3) \\ + \lambda^4(0.8377 - 9.5030\varepsilon + 21.3973\varepsilon^2 - 7.3065\varepsilon^3)] \\ \text{(mean error} = 0.1 \text{ percent)} \quad (13)$$

(b) Zig-zag array of elliptical holes for Problem (b) ($\mu=1$)

$$C = \frac{E^*}{E_0} = 1 + \lambda^2 [-3.1465 - 1.3896\varepsilon - 0.5452\varepsilon^2 + 0.4750\varepsilon^3 - 0.1201\varepsilon^4 \\ + \lambda(0.1489 - 2.2622\varepsilon + 6.6989\varepsilon^2 - 5.6249\varepsilon^3 + 1.3413\varepsilon^4) \\ + \lambda^2(2.8106 + 8.6220\varepsilon - 16.4720\varepsilon^2 + 12.7023\varepsilon^3 - 2.8505\varepsilon^4) \\ + \lambda^3(5.1229 + 3.7628\varepsilon - 0.6958\varepsilon^2 - 5.1790\varepsilon^3 + 3.1437\varepsilon^4) \\ + \lambda^4(-6.7096 - 10.4973\varepsilon + 8.9222\varepsilon^2 + 4.1250\varepsilon^3 - 4.2437\varepsilon^4)] \\ \text{(mean error} = 0.7 \text{ percent)} \quad (14)$$

Values from Eqs. 13 and 14 are plotted in Fig. 3(a), (b) as dashed curves, respectively, showing close agreement with the analytical curves.

4. Conclusions

- (1) A rectangular array and a zig-zag array of elliptical holes in solids under uniaxial tension were analyzed theoretically. Numerical results were given for a dimensionless stress S_{\max} and a tensile stiffness C .
- (2) In Problem (a), S_{\max} occurred at point A. In Problem (b), S_{\max} occurred at point A ($\theta = 0$) in the most of λ without small and large values of ρ/a , but it took place at some other point B ($\theta \neq 0$) for intermediate values of ρ/a and large values of λ , due to interference by the presence of obliquely located holes.
- (3) The tensile stiffness C decreased with increasing values of ρ/a and λ in both the problems.
- (4) The analytical values of S_{\max} and C were fitted to reliable polynomial formulae for convenience of engineering applications.

REFERENCES

1. M. Isida, Methods of Analysis and Solutions of Crack Problems, Mechanics of Fracture 1 (ed. Sih, G. C.), Noordhoff, (1973) p. 56.
2. M. Isida and H. Igawa, International Journal of Solids and Structure, 27-7 (1991) p. 849.
3. M. Isida and H. Igawa, International Journal of Fracture, 53 (1992) p. 249.

Crack Growth in Stainless Steel 304 at 538°C under Fatigue Loading with and without Hold Time

Y.M. Baik and K.S. Kim

Department of Mechanical Engineering, Pohang University of Science and Technology (POSTECH), San 31 Hyoja-dong, Nam-gu, Pohang 790-784, Korea

Keywords: Crack Growth Rate, Frequency Effects, Hold Time, J-Integral, Stainless Steel 304, Stress Intensity Factor

ABSTRACT

The crack growth behavior in stainless steel 304 is investigated at 538°C in air. The effects of frequency (f), load level (P) and hold time on the crack growth rate are examined. It is shown that fracture mechanics parameters ΔK and ΔJ can correlate crack growth rates reasonably well beyond the regime of small scale yielding for no hold time tests. Depending on the values of $f \times P_{\max}$, three ($f \times P_{\max}$) domains are suggested for characterization of the da/dN - ΔK relation. The crack tends to grow faster at low values of $f \times P_{\max}$ for $\Delta K < 25 \text{ MPa}\sqrt{\text{m}}$. The trend is reversed for $\Delta K > 25 \text{ MPa}\sqrt{\text{m}}$. The SEM fractographs and optical micrographs of fracture surfaces indicate that oxidation plays a significant role on crack growth. The mode of crack propagation is transgranular for loading without hold time, and it becomes intergranular for loading with hold time. The crack growth rate is found to be much higher for loading with hold time.

1. INTRODUCTION

The crack growth behavior in a high temperature component is influenced not only by the mechanical load acting on it, but also by the environmental condition in which it is operating. Mechanical loads could give rise to interaction of fatigue and creep modes of fracture in the high temperature environment. The chemical interaction of the crack tip material with elements in the surrounding often accelerates crack growth. The creep damage and environmentally assisted crack growth are time-dependent and thermally activated processes. Therefore, the frequency of loading and hold time in fatigue cycles influence the crack growth rate. James [1-4] presented a series of papers dealing with fatigue crack growth at elevated temperatures, which covered the effects of frequency [1], hold time [2], environment [3] and stress ratio [4]. Plumtree et al. [5,6] investigated the effects of waveform and hold time. They reported that tensile hold time accelerates crack growth under higher crack driving forces than those of James [2]. The interaction of fatigue, creep, and environment in crack initiation and growth was reviewed by Coffin [7], Pineau [8], Ellison [9] and Michel [10], among others, for a variety of metals including austenitic stainless steels.

The present study is aimed at investigating the combined effects of the applied load level, frequency and hold time to the crack growth behavior in stainless steel 304 at 538°C. The load

level in this study is extended to an elastic-plastic regime. Crack growth parameters to be investigated in this study are the ranges of the stress intensity factor (ΔK) and the J-integral (ΔJ). The dependence of the frequency effect on the magnitudes of ΔK and ΔJ is examined. The effect of hold time on the crack growth rate is also investigated.

2. EXPERIMENTAL PROCEDURES

The material used in this study is stainless steel 304 with chemical composition given in Table 1. The material was acquired in the form of a 15mm-thick plate, which was solution-treated at 1050°C for 24minutes. The compact tension (CT) specimen with width of 50mm and thickness of 12.5mm was used for the test. The specimen was cut in the T-L direction and no side grooves were introduced. All tests in this study were carried out under a load ratio of $R=0.05$ at 538°C in air using an MTS machine. Specimen temperature was achieved by split

Table 1. Chemical Composition of the Test Material (wt. %)

C	Si	Mn	P	S	Ni	Cr	Mo	Cu	Sn	As
0.034	0.62	1.05	0.026	0.003	8.16	18.18	0.097	0.18	0.006	0.002

furnace and controlled to within $\pm 1^\circ\text{C}$. A pre-crack of approximately 2mm in length was introduced at room temperature under fatigue loading of low amplitudes. The crack length was measured using a direct current potential drop (DCPD) system. To examine the effect of hold time, the maximum load was held for time periods of 10 or 30 minutes. The loading and unloading ramps took 0.5 seconds for each. Test conditions were given in Table 2. The fracture surface was examined under a SEM for several specimens to get an insight on the damage mechanism. The fracture surface was examined using an electron probe micro-analyzer (EPMA) for a few specimens to check the degree of oxidation.

Crack growth parameters to be investigated in this study are the range of the stress intensity factor (ΔK) and that of J-integral (ΔJ). The stress intensity factor for a CT specimen is given by [11]:

$$K = \frac{PF(\alpha)}{BW^{3/2}} \quad (1)$$

$$F(\alpha) = \frac{(2 + \alpha)(0.886 + 4.64\alpha - 13.32\alpha^2 + 14.72\alpha^3 - 5.6\alpha^4)}{(1 - \alpha)^{3/2}}$$

where a , W , B are the crack length, specimen width and thickness, respectively, $\alpha = a/W$, and P is the applied load. The ratios of P_{\max}/P_0 , where P_{\max} is the maximum load in a fatigue cycle and P_0 is the limit load [12] at the initial crack length, are in the range of 0.2-0.7 in this study. It is expected that the amount of plasticity developed at the upper end of this load range be well beyond the small-scale yielding regime. Therefore, nonlinear fracture parameters are worth to be explored. The equation for ΔJ under load control can be written as, [13]:

$$\Delta J = \frac{2}{Bb} [\xi A_c + \zeta \Delta P (V_{\max} - V_{\min})] \quad (2)$$

$$\xi = \frac{\eta_c - \eta_r}{2}, \quad \zeta = \frac{\eta_r}{2}$$

where b is the ligament ($W-a$) on the crack plane, $\Delta P = P_{\max} - P_{\min}$, V_{\max} and V_{\min} are the load line displacements (V) at P_{\max} and P_{\min} , respectively, A_c is the complimentary energy defined by the P-V curve, η_c and η_r are the Merkle-Corten constants [14]. The underlying assumption in the above equation is that the compliance of a specimen at a certain crack length can be determined by the loading part of the P-V loop.

3. RESULTS AND DISCUSSION

Crack growth test conditions and results are summarized in Table 2. Simple calculations of the limit load indicated that the final failure of the specimen occurred in all cases due to plastic

Table 2. Summary of fatigue crack growth tests with and without hold time

Specimen	P_{\max} (kN)	Freq. (Hz)	a_i (mm)	a_f (mm)	N_f (cycle)	Specimen	P_{\max} (kN)	Freq. (Hz)	a_i (mm)	a_f (mm)	N_f (cycle)
6f005	6	0.05	22.7	40.4	30262	12f005	12	0.05	22.1	34.2	5398
6f05	6	0.5	22.0	40.9	50775	12f05	12	0.5	22.2	34.0	5843
6f2	6	2	22.4	40.5	54035	12f2	12	2	21.9	31.5	4034
6f5	6	5	22.5	37.2	47426	12f5	12	5	22.4	30.0	3778
6f10	6	10	22.3	37.5	51140	12f10	12	10	22.5	31.4	4201
8f005	8	0.05	22.4	37.3	16814	14f05	14	0.5	23.2	30.5	2106
8f05	8	0.5	22.5	38.2	19733	16f05	16	0.5	22.1	28.7	1454
8f2	8	2	22.9	38.2	19422	Specimen	P_{\max} (kN)	Hold time (minute)	a_i (mm)	a_f (mm)	N_f (cycle)
8f5	8	5	22.2	35.4	16734						
8f10	8	10	22.4	34.8	17156	14h10m	14	10	22.3	30.0	1219
10f005	10	0.05	22.5	35.5	9215	16h10m	16	10	22.7	27.6	348
10f05	10	0.5	22.4	36.2	9891	16h30m	16	30	22.5	27.8	201
10f2	10	2	22.5	32.3	6828	18h10m	18	10	23.0	28.1	241
10f5	10	5	22.1	32.0	7656	18h30m	18	30	22.3	26.7	92
10f10	10	10	22.4	32.0	7052						

collapse. In an attempt to better represent the obtained data for practical applications, the $da/dN-\Delta K$ relation was considered for three frequency-load ($f-P_{\max}$) domains. These domains are shown in Fig. 1. Domains I and II were chosen such that $da/dN-\Delta K$ data points fall mostly within the band of factor 1.5. Most test conditions in this study fall in these domains. In domain I, the $da/dN-\Delta K$ relation can be approximately represented by a single Paris equation for engineering purposes. In domain II, $da/dN-\Delta K$ relation appears to be frequency-independent. Meantime, in domain III the frequency dependence of crack growth rate is prominent. Thus the frequency effect must be explicitly considered. Domain III may be defined as $f \times P_{\max} \leq 2 \text{ kN/s}$, $P_{\max} \leq 8 \text{ kN}$. The boundary between domains I and II may be described by $f \times P_{\max} = 18 \text{ kN/s}$ and $P_{\max} = 13 \text{ kN}$. These boundaries are based on the best engineering judgement within the test data and may be refined by further testing. The variation of $da/dN-\Delta K$ with frequency for $P_{\max} = 6 \text{ kN}$ is shown in Fig. 2. For ΔK less than $25 \text{ MPa}\sqrt{\text{m}}$, higher growth rates are found for 0.05 Hz . This would perhaps result from the embrittlement of the crack tip material due to oxidation. However, the frequency dependence is obscure in the range of $0.5-10 \text{ Hz}$. Figures 3 and 4 represent the crack growth data in domains I and II. The crack tends to grow faster at low values of $f \times P_{\max}$ when ΔK is less than $25 \text{ MPa}\sqrt{\text{m}}$. The trend is reversed when ΔK is greater than $25 \text{ MPa}\sqrt{\text{m}}$. There may be two reasons for this phenomenon. At higher growth rates for $\Delta K > 25 \text{ MPa}\sqrt{\text{m}}$, the crack tip embrittlement is less significant. The higher

degree of oxidation at lower frequencies produces micro-cracks on the fracture surfaces, which disperses the energy for events other than the growth of the main crack [7]. Also, plasticity in the wake of crack growth, the oxides formed on the crack surface and the increased roughness of the crack surface in low frequency tests could result in reduction in effective crack driving force and consequently retardation of crack growth. It is also worth noting that Clavel et al. [15] argues that the unevenness of the fracture surface causes the propensity to deviation of the crack and reduction in the macroscopic crack growth rate.

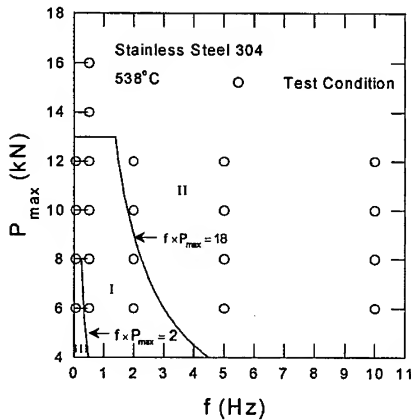


Fig. 1 Three f - P_{\max} domains for characterization of $P_{\max}=6\text{kN}$

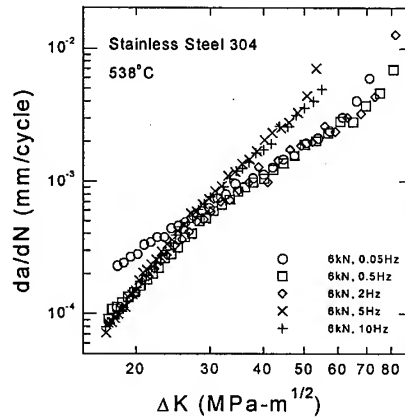


Fig. 2 da/dN - ΔK relation at different frequencies

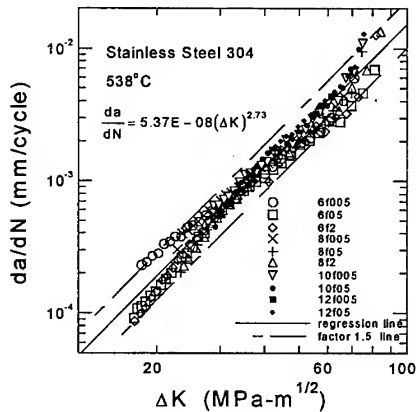


Fig. 3 da/dN - ΔK relation for f - P_{\max} domain I

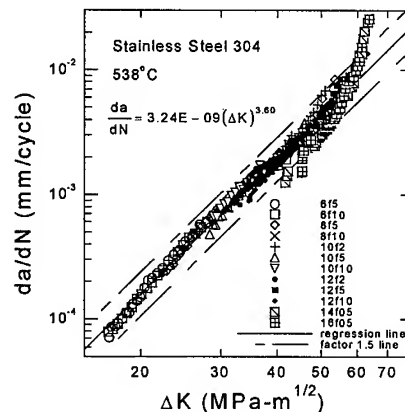
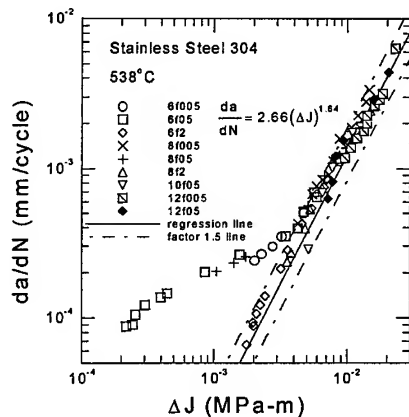
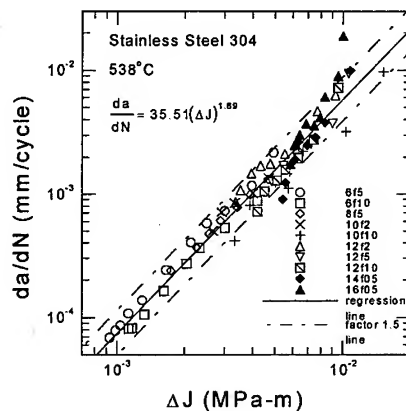


Fig. 4 da/dN - ΔK relation for f - P_{\max} domain II

The da/dN - ΔJ relations were also obtained for domains I and II. The results are shown in Fig. 5 and Fig. 6. The correlation was again good except that there is a branch off from the regression line in Fig. 5. This deviation includes the data from $f=0.05\text{Hz}$, $P=6\text{kN}$ and $f=0.5\text{Hz}$, $P=6, 8\text{kN}$ tests. The phenomenon is thought to be due to the frequency effect.

Fig. 5 da/dN - ΔK relation for f - P_{max} domain IFig. 6 da/dN - ΔK relation for f - P_{max} domain II

The ΔK considered in this study is in the range of 15-80 MPa \sqrt{m} , which is considerably wider than that of James [1] (approximately 12-35 MPa \sqrt{m}). The data obtained for all specimens are shown in Fig. 7 in comparison with James's da/dN - ΔK lines appropriate to the frequency range in this study. The overall trend of no hold time data indicates that da/dN can be related to ΔK by the Paris law. The hold time crack growth rates are found much higher in Fig. 7 than those of no hold time, which is consistent with Plumtree et al. [6] at relatively high load levels.

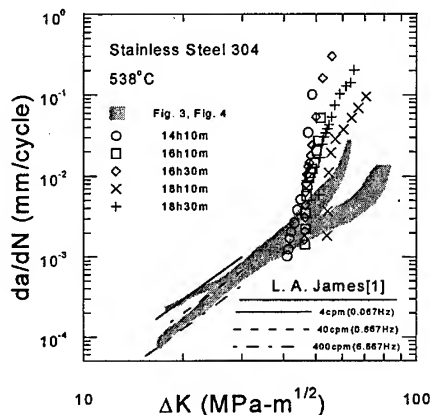
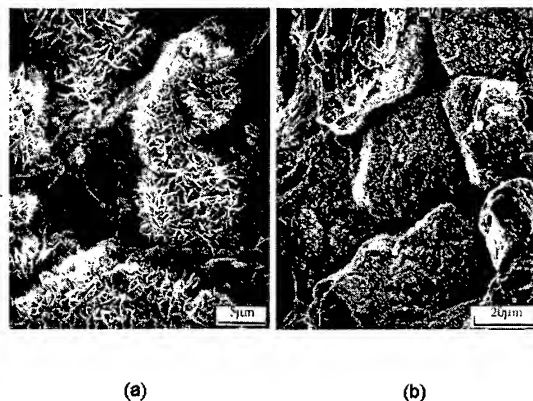
Fig. 7 da/dN - ΔK relation for all test conditions

Fig. 8 SEM fractographs of fracture surfaces: (a) 6kN, 0.05Hz, (b) 18kN, 30min hold time

The fracture surface was examined under a SEM. The crack growth direction in Fig. 8 is downward. Fig. 8(a) shows oxidized fatigue striations on the fracture surface of a specimen tested under $P_{max} = 6\text{kN}$, $f = 0.05\text{Hz}$ with no hold time. This picture was taken in the stage II propagation region approximately 3mm from the initial crack tip. An EPMA analysis for this specimen indicated that the weight percent of oxygen on the surface in the stage I growth region was 8.3%. This was reduced to 4.6% for the $P_{max} = 6\text{kN}$, $f = 5\text{Hz}$ specimen for which test duration was much shorter. In the 18kN, 30 min hold time test, the weight percent of oxygen at a point in the stage I was 9.7%. The oxide was found to be mostly Fe_2O_3 according to an X-ray diffraction analysis. Fig. 8(b) shows intergranular fracture surfaces of the specimen under $P_{max} = 18\text{kN}$, 30 min hold time. The fracture

mode was transgranular in no hold time tests, and it was changed to intergranular in hold time tests. This observation indicates that the acceleration of the crack growth in hold time is associated with the fracture mode change. Similar observations were also made by other researchers [7,10].

4. CONCLUSION

1. The crack growth rate in stainless steel 304 at 538°C with no hold time can be correlated with ΔK for the test conditions used in this study that include a substantial amount of plasticity.
2. Three ($f \cdot P_{\max}$) domains can be considered for approximate characterization of the $da/dN \cdot \Delta K$ relation. The $da/dN \cdot \Delta K$ relation can be approximated by a single Paris equation in each of the two domains where most tests were carried out. In the third domain, where $f \cdot P_{\max}$ is small, the relation is expected to be highly frequency-dependent.
3. The crack tends to grow faster at low values of $f \cdot P_{\max}$ when ΔK is less than $25 \text{ MPa}\sqrt{\text{m}}$. The trend is reversed when ΔK is greater than $25 \text{ MPa}\sqrt{\text{m}}$.
4. ΔJ can also be used as a crack growth parameter. The domains appropriate for ΔK are applicable also to ΔJ with a few exceptions for which the frequency effect is prominent.
5. The fracture mode of fatigue crack growth without hold time is transgranular, and it becomes intergranular when hold time exists.
6. The hold time accelerates crack growth under the loads used in the study.

ACKNOWLEDGEMENT

This study was supported by Korean Ministry of Education through research fund ME96-C-23.

REFERENCE

1. James, L. A., ASTM STP 513, 1972, pp. 218-229.
2. James, L. A., Nuclear Tech., Vol. 16, 1972, pp. 521-530.
3. James, L. A., J. of Eng. Mater. and Tech., Vol. 98, 1976, pp. 235-243.
4. James, L. A., Nuclear Tech., Vol. 14, 1972, pp. 163-170.
5. Guinemer, J. - Y. and Plumtree, A., ASTM STP 765, 1982, pp. 452-465.
6. Plumtree, A. and Tang, N. -Y., Fatigue and Fract. Eng. Mater. Struct, Vol. 12, 1989, pp. 377-386.
7. Coffin, L. F., Creep-Fatigue Environment Interactions, The Metallurgical Society of AIME, 1980, pp. 1-23.
8. Pineau, A., Subcritical Crack Growth Due to Fatigue, Stress Corrosion and Creep, Elsevier Applied Science Publishers, 1984, pp. 483-529.
9. Ellison, E. G., Subcritical Crack Growth Due to Fatigue, Stress Corrosion and Creep, Elsevier Applied Science Publishers, 1984, pp. 531-561.
10. Michel, D. J. and Smith, H. H., Creep-Fatigue Environment Interactions, The Metallurgical Society of AIME, 1980, pp. 165-177.
11. Murakami, Y., Stress Intensity Factors Handbook, Vol. 1, Pergamon Press, 1987.
12. Kumar, V., German, M. D. and Shih, C. F., EPRI NP-1931, EPRI, Palo Alto, Ca., 1981.
13. Sadananda, K. and Shahinian, P., Eng. Fract. Mech., Vol. 11, 1979, pp. 73-86.
14. Merkle, J and Corten, H., J. Press. Vess. Tech., Trans. of ASME, 1974, pp. 286-292.
15. Clavel, M., Levaillant, C. and Pineau, A., Creep-Fatigue Environment Interactions, The Metallurgical Society of AIME, 1980, pp. 24-45.

An Inverse Fracture Problem of a Shear Specimen with Double Cracks

Yutang Li, Zhiyuan Rui and Jianlong Huang

Department of Mechano-Electronic Engineering, Gansu University of Technology,
Lanzhou 730050, China P.R.

Keywords: Boundary Conditions of Displacement, Boundary Conditions of Stress, Double Cracks, Inverse Fracture Problem, Shear, Stress Intensity Factor

ABSTRACT

Fracture is a peculiar phenomenon of solid material. The study of inverse fracture problem is the common needs of crack theory and fracture design. The inverse fracture problems are described first in this paper. Then taking shear specimen with double cracks as example, the boundary conditions of stress and displacement are designed. The actual two level finite element method is used to evaluate the stress intensity factor. Finally, some new useful results are obtained.

1. INTRODUCTION

Fracture is a peculiar phenomenon of solid material. The brittle failures in components are usually caused by flaws or cracks which have been considered as a disaster in traditional viewpoint. The purposes of fracture mechanics are to avoid the emergence and control the propagation of cracks. The history of exploiting the flaw to achieve the fracture is much more remote than the history of fracture mechanics. In fact, making primitive tools using the process of fracture are the one of major starting point of human civilization. Some scientific researchers have paid close attention to inverse fracture problems recently [1-3]. One can turn the disastrous character of crack into profitable effect and apply the low-stress brittle fracture to separate solid materials. This new technique is called "Crack Technique"[7].

Crack technique includes three parts, i.e. the principle of fracture design, the method of fracture design and the fracture equipment. There are several inverse fracture problems in the principle of fracture design, for example, the design of notch's parameters, the regular propagation of crack and the design of boundary conditions.

Crack and its propagation have three forms. Mode I crack is the focal point in fracture mechanics because it is the most common and dangerous. It is followed with interest in fracture design also. Mode II crack must be applied in fracture design when the boundary conditions present some limitation. The fracture problem of shear specimen with double cracks is studied and the boundary conditions of stress and displacement are designed in this paper. The actual two level finite element method is used to evaluate the stress intensity factor. Some new useful results are obtained.

2. INVERSE FRACTURE PROBLEMS

The study of inverse fracture problem is the common needs of crack theory and fracture design. Some inverse fracture problems have been followed with interest at present. Most typical theoretical

problems in fracture design are regarded as inverse problems of fracture mechanics. The inverse fracture problem that maintain close links with fracture design can be so defined: for a given body Ω with a crack whose shape and parameters have been specified (Fig. 1), how should boundary conditions be applied to keep the crack propagation in a given direction and obtain a maximum stress intensity factor in the local region near the crack tip? In fact, there are three inverse fracture forms in the problem: 1) for a given body Ω with crack and stress boundary conditions, design an optimum displacement boundary

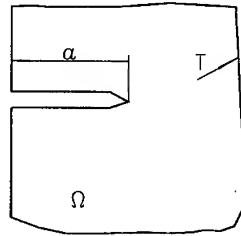


Fig.1. The model of inverse fracture problem

conditions which makes the crack propagation in a given direction and results in a maximum stress intensity factor in the local region near the crack tip. 2) for a given body Ω with crack and displacements boundary conditions, design an optimum stress boundary conditions which does the same as above mentioned. 3) for a given body Ω with crack and partial stress and displacement boundary conditions, design all remainder unknown boundary conditions which does the same as before.

The above problems show the features of fracture design. One can turn the problem into extreme value seeking with the aid of weight function $M(x, a)$ given by fracture mechanics as shown below:

$$K = \int_a^0 \sigma_y^0 M(x, a) dx \quad (1)$$

The σ_y^0 corresponding to the maximum stress intensity factor can be obtained accurately or approximately with the aid of different mathematical methods as long as the weight function $M(x, a)$ is known. The inverse fracture problem, hence, can be solved subsequently. The analytic solution of weight function $M(x, a)$ for finite body is very difficult to be obtained, generally. The stress intensity factor can't be obtained by means of equation (1). The boundary collocation, the boundary integral, and finite element methods have been applied to the inverse elastoplasticity problems [4-6]. The stress intensity factor under one or several boundary conditions can also be obtained by using above methods.

3. THE ACTUAL TWO LEVEL FINITE ELEMENT METHOD AND IT'S FORMULATION

The infinite series formulas defining displacement field in plane crack problem can be written as follows [9]:

$$u_x = \sum_{j=0}^{\infty} \frac{r^{j/2}}{2\mu} \left\{ C_j^R \left[\left(\kappa + \frac{j}{2} + (-1)^j \right) \cos \frac{j}{2} \theta - \frac{j}{2} \cos \left(\frac{j}{2} - 2 \right) \theta \right] \right. \\ \left. + C_j^I \left[\left(\kappa + \frac{j}{2} - (-1)^j \right) \sin \frac{j}{2} \theta - \frac{j}{2} \sin \left(\frac{j}{2} - 2 \right) \theta \right] \right\}$$

$$u_y = \sum_{j=0}^{\infty} \frac{r^{j/2}}{2\mu} \left\{ C_j^R \left[\left(\kappa - \frac{1}{2} - (-1)^j \right) \sin \frac{1}{2} \theta + \frac{1}{2} \sin \left(\frac{1}{2} - 2 \right) \theta \right] - C_j^I \left[\left(\kappa - \frac{1}{2} + (-1)^j \right) \cos \frac{1}{2} \theta + \frac{1}{2} \cos \left(\frac{1}{2} - 2 \right) \theta \right] \right\} \quad (2)$$

where C_j^R and C_j^I are coefficients to be determined after loads and other boundary conditions being imposed. It should be noted that the terms with $j=0$ denote the rigid body translations and the terms with $j=1$ in equation (2) contain a factor which accounts for the singular behavior near the crack tip. Therefore the relationship between stress intensity factor and coefficients C_j becomes

$$K_I - iK_{II} = \sqrt{2\pi} [C_1^R - iC_1^I] \quad (3)$$

In order to study the effect of a crack on the plane elastic problem, an area Ω is taken and divided around the crack tip with an outmost polygon boundary L_1 and, then, a super element for dealing with the singularity is established (Fig. 2). The thickness ratio of the neighboring layer is $c < 1$.

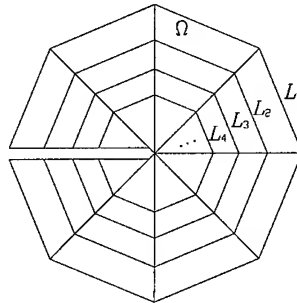


Fig.2. Similar shape element configuration

Equation (2) can be written as following matrix form

$$\{u\} = [T]\{C\} \quad (4)$$

3.1. Transition Formulation of First Layer

Let the nodes on the boundary polygon L_1 be master nodes and those on other inner polygons slave nodes. For solving the problem linking with other elements out of Ω , only the degrees of freedom of slave nodes need to be transformed. The stiffness matrix of first layer after being transformed can be written as follow

$$[K]^f = \begin{bmatrix} K_{mm} & K_{ms} T^f R \\ R^T (T^f)^T K_{sm} & R^T (T^f)^T K_{ss} T^f R \end{bmatrix} \quad (5)$$

where $[T^f]$ is the transition matrix of the boundary polygon L_1 and $[R]$ the relation matrix of the boundary polygon L_2 and boundary polygon L_1 .

3.2. Transition Formulation of Other Layers

All degrees of freedom of inner nodes need to be transformed. The stiffness matrix of inner layers after being transformed can be written as follow

$$K_{ij}^n = c^{(k_i+k_j)(n-1)/2} \begin{bmatrix} (\mathbf{T}_i^f)^T & c^{k_i} (\mathbf{T}_i^f)^T \end{bmatrix} \begin{bmatrix} \mathbf{K}_{11} & \mathbf{K}_{12} \\ \mathbf{K}_{21} & \mathbf{K}_{22} \end{bmatrix} \begin{bmatrix} \mathbf{T}_j^f \\ c^{k_j} \mathbf{T}_j^f \end{bmatrix} \quad (6)$$

It can be found from equation (6) that K_{ij} of different inner layers form geometric progressions. Therefore, we have

$$\sum_{n=2}^{\infty} K_{ij}^n = \frac{R_{ij}}{1-R_{ij}} \begin{bmatrix} (\mathbf{T}_i^f)^T & c^{k_i} (\mathbf{T}_i^f)^T \end{bmatrix} \begin{bmatrix} \mathbf{K}_{11} & \mathbf{K}_{12} \\ \mathbf{K}_{21} & \mathbf{K}_{22} \end{bmatrix} \begin{bmatrix} \mathbf{T}_j^f \\ c^{k_j} \mathbf{T}_j^f \end{bmatrix} \quad (7)$$

where

$$R_{ij} = c^{(k_i+k_j)/2} < 1 \quad \text{for } i, j \geq 1 \quad (8)$$

By using equation (5) and equations (7)~(8), global stiffness matrix for domain Ω can be assembled. Adding the global stiffness to the stiffness matrix of other elements, the general stiffness matrix can be obtained. Solving the equation, the column matrix $\{\mathbf{C}\}$ and stress intensity factor can be obtained directly.

4. DESIGN OF DISPLACEMENT BOUNDARY CONDITIONS

Designing the suitable boundary conditions is one of main tasks in fracture design. The design of boundary conditions means to solve the inverse fracture problem. For the fracture design in engineering, the maximum stress intensity factor in the local region near the crack tip should be gained under the condition of keeping the crack propagation in a given direction. For the finite plane problem, the stress intensity factor can be written as follows [10]

$$K_I = F_1(a/b) \frac{P\sqrt{\pi a/b}}{b^{1/2}B} \quad (9)$$

$$K_{II} = F_2(a/b) \frac{P\sqrt{\pi a/b}}{b^{1/2}B} \quad (10)$$

where $F_1(a/b)$ and $F_2(a/b)$ are dimensionless stress intensity factors. Several forms of displacement boundary conditions are shown in Fig. 3. As shown in Fig. 3, the extended force line of loading P is tangential to the inner boundary of the crack and, in the situations (c) and (d), the fulcrums are located just at outer edge of the cracks. The dimensionless stress intensity factors $F_1(a/b)$ and $F_2(a/b)$ are listed in Tab. 1. It can be found from Tab. 1 that $F_1(a/b)$ is much greater than $F_2(a/b)$ in model (a). For either fixed or simply support problems, the experimental research achievements show that the crack can't propagate along the given direction in the fracture process if either the crack doesn't lie in the symmetry plane of the model or the tensile stress plays a leading role. Therefore, model (a) is not suitable to fracture design. The dimensionless stress intensity factors $F_1(a/b)$ are small in situation (b) and very small in (c) and (d). The dimensionless stress intensity factors $F_2(a/b)$ are nearly identical in all situations. The model (c) and (d) are suitable to fracture design because they can be taken as pure shearing problem and the cracks propagate along the given direction.

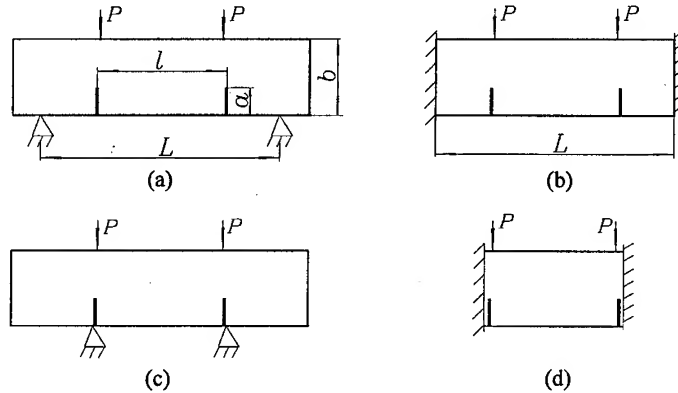


Fig.3. Displacement boundary conditions of a specimen with two cracks

Table 1. Dimensionless stress intensity factors under different displacement boundary conditions
($L/b=4$, $l/L=0.5$)

		a/b						
		0.10	0.20	0.30	0.40	0.50	0.60	0.70
Model (a)	$F_1(a/b)$	2.9197	2.6316	2.2544	1.8146	1.4947	1.0334	0.6123
	$F_2(a/b)$	0.3083	0.2968	0.2935	0.2947	0.2828	0.2676	0.2514
Model (b)	$F_1(a/b)$	0.2912	0.2792	0.2674	0.2557	0.2488	0.2337	0.2252
	$F_2(a/b)$	0.3311	0.3176	0.3060	0.2911	0.2729	0.2589	0.2461
Model (c)	$F_1(a/b)$	0.0912	0.0792	0.0674	0.0557	0.0488	0.0337	0.0252
	$F_2(a/b)$	0.3315	0.3181	0.3069	0.2918	0.2738	0.2606	0.2479
Model (d)	$F_1(a/b)$	0.0905	0.0785	0.0665	0.0551	0.0475	0.0332	0.0248
	$F_2(a/b)$	0.3318	0.3185	0.3075	0.2926	0.2756	0.2644	0.2498

5. DESIGN OF STRESS BOUNDARY CONDITIONS

Several forms of stress boundary conditions for simply support specimen are shown in Fig. 4. The dimensionless stress intensity factors $F_1(a/b)$ and $F_2(a/b)$ are shown in Tab. 2. It can be found from Tab. 2 that the dimensionless stress intensity factors $F_1(a/b)$ is greater than the $F_2(a/b)$ in (a), (b) and (c). Therefore, the propagation of mode I crack plays a leading role and doesn't take place along the given direction in the process of fracture. The dimensionless stress intensity factors $F_2(a/b)$ have little difference in several models. The model (d) can be taken as pure shear because the dimensionless stress intensity factors $F_1(a/b)$ is very small. The crack can propagate along the given direction and the fracture face is regular and smooth. It is a suitable model in fracture design.

6. CONCLUSIONS

The inverse fracture problem can be applied in engineering. According to the practice of fracture engineering, inverse fracture problems can be divided into three kinds. The solution of these inverse fracture problems must meet the needs of fracture engineering. The inverse fracture problem can be solved by actual two level finite element method. The crack can't propagate along the given direction and

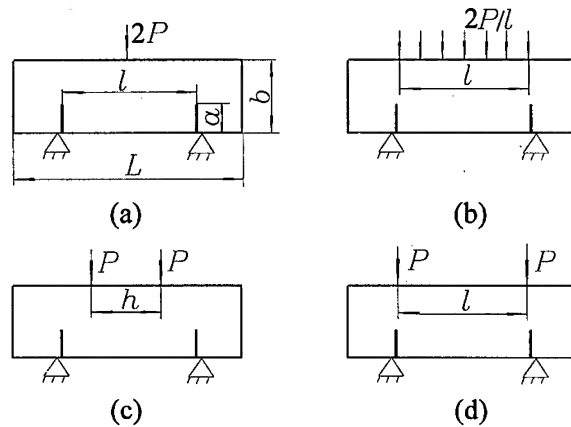


Fig.4. The stress boundary conditions of a specimen with two cracks

Table 2. Dimensionless stress intensity factors under different stress boundary conditions
($L/b=4$, $l/L=0.5$, $h/l=0.5$)

		a/b						
		0.10	0.20	0.30	0.40	0.50	0.60	0.70
Model (a)	$F_1(a/b)$	3.1188	2.9421	2.6541	2.2135	1.7946	1.3326	0.9121
	$F_2(a/b)$	0.3211	0.3047	0.2915	0.2736	0.2603	0.2354	0.2205
Model (b)	$F_1(a/b)$	2.7192	2.4324	2.2231	1.7146	1.3947	1.0234	0.6022
	$F_2(a/b)$	0.3223	0.3068	0.2935	0.2747	0.2628	0.2376	0.2214
Model (c)	$F_1(a/b)$	2.6277	2.3816	2.0515	1.6603	1.3751	0.9559	0.5694
	$F_2(a/b)$	0.3287	0.3124	0.2988	0.2807	0.2649	0.2429	0.2275
Model (d)	$F_1(a/b)$	0.0912	0.0792	0.0674	0.0557	0.0488	0.0337	0.0252
	$F_2(a/b)$	0.3315	0.3181	0.3069	0.2918	0.2738	0.2606	0.2479

the fracture face isn't regular and smooth when the mode I crack plays a leading role for the specimen with double cracks. Pure shear model is the suitable model in fracture engineering.

REFERENCES

1. N.Tada, T.Kitamura and R.Ohtani, *Engng Frac., Mech.*52(1995) p.1015
2. B.J.Zhao, Q.T.Wei and F.Y.Lang, *Int. J. Fracture*, 55(1990) p.R43
3. J.P.Dempsey, R.M.Adamson and S.J.Defranco, *Int. J. Fracture*, 69(1995) p.281
4. A.Maniatty, N.Zabarar and K.Stelo, *J. Engng Mech. Div. ASCE*, 115(1989) p.1302
5. N.Zaaras, V.Morellas and D.Schnur, *Communication in Applied Numerical Methods*, 5(1989) p.547
6. W.Yeih, T.Koya and T.Mura, *J.Appl. Mech.*, 60(1993) p.595~600
7. B.J.Zhao, Q.T.Wei and F.Y.Lang, *Advances in Mechanics*, 18(1988) p. 343(in Chinese)
8. Y.T.li, F.Y.Lang and Q.T.Wei, *Chinese J. Mechanical Engineering*, 29(1993) p.17 (in Chinese)
9. A.Y.T.Leung and R.K.L.Su, *Engng Frac. Mech.*, 51(1995) p.889
10. H.Tada, P.C.Paris and G.R.Irwin, *The stress analysis of cracks handbook*, Del Research Corporation, Hellertwon (1993)

Fracture Mechanics Analysis of Cracked Plate Repaired by Composite Patch

K.H. Chung¹, W.H. Yang² and M.R. Cho³

¹ Graduate School of Mechanical Engineering, SungKyunKwan University,
Chunchun-Dong, Jangan-Ku, Suwon 440-746, Korea

² School of Mechanical Engineering, SungKyunKwan University,
300 Chunchun-Dong, Jangan-Ku, Suwon 440-746, Korea

³ Department of Mechanical Design, Induk Institute of Technology,
Wolgye-Dong, Nowon-Ku, Seoul 139-749, Korea

Keywords: Adhesive, Adhesive Shear Stress, Boundary-Layer Effect, Debonding, Reduction of Stress Intensity Factor

ABSTRACT

The enhancement of service life of damaged or cracked structures is currently major issue to the researchers and engineers. In order to evaluate the life of cracked aging aircraft structures, the repair technique which uses adhesively bonded boron/epoxy composite patched is being widely considered as a cost-effective and reliable method. But, this repair method contains many shortcomings. One of these shortcomings, debonding is major issue. When the adhesive shear stress increases, debonding is caused at the end of patch and plate interface. And this debonding is another defect except crack propagation. In this paper, we assess safety at the cracked Al-plate repaired by Br/Epoxy composite patch. Firstly, the reduction of stress intensity factors near the crack-tip are determined to the effects of various non-dimensional design parameters. Secondly, using the finite element analysis, the distribution of adhesive shear stresses are acquired. Finally, the problem of how to optimize the geometric configurations of the patch has been discussed.

1. INTRODUCTION

The method which had been suggested is not sufficient to restraint the propagation of crack structures. To extend the service life, cracked components must be replaced or repaired. However, replaced method has many shortcomings; inefficiency, difficulty of fabrication, etc., so, the use of bonded composite patch or stiffener on the cracked surface is required.

Baker and Jones[1] studied the repair technique, which uses adhesively bonded Boron/Epoxy composite patches and it is widely considered as a cost effective and reliable method. It is often most economical to employ crack arrestment methods to regain the load carrying capability of the component. Composite material have outstanding strength, stiffness and low specific gravity. The potential use of such composites due to their superior mechanical and thermal properties is well recognized in the aerospace and ship building as well as in other lightweight engineering constructions. A repair method using composite patches to reinforce the damaged or cracked component has been shown to be vary promising due to the high stiffness, high strength, and light weight of the component.

For a successful implementation of this repair technique, however, a thorough understanding of the effect of various design parameters of repair, on the crack-tip stress intensity factors, is necessary. These design parameters included: the size of patch, thickness and material properties of composite patch, and the thickness of adhesive layer. Jone and Callinan [2-3] studied the design aspect of the crack patching using the finite elements method. Chu and Ko[4] proposed using collapsed isoparametric element to preserve the singular stress characteristic at the crack tip. But, this method required large numbers of nodal degree of freedom. To recover this problem,

Denney[5] suggested the finite element alternating method to reduce the analysis time.

In this paper, we studied the fracture mechanics analysis at the crack tip and the behavior of debonding which is caused by adhesive shear stresses. Finally, we will suggest the optimal shape to prevent the propagation of crack and debonding.

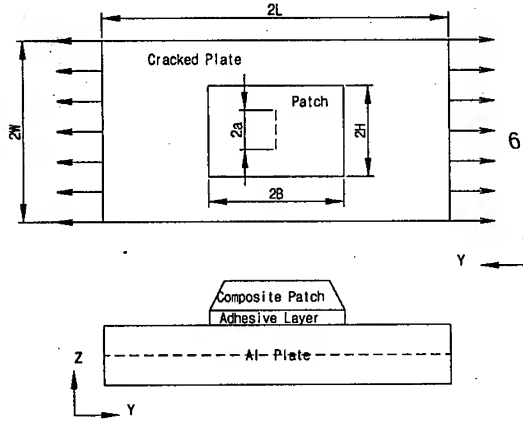


Fig.1 Configuration of bonded repair for cracked plate

2. FRACTURE MECHANICS ANALYSIS

2.1 Analysis of cracked plate repaired by composite patch

Consider a aluminum plate which has center crack repaired by Br/Epoxy composite patch as shown in Fig. 1. Our present analysis is based on the following simplified assumptions.

- (1) There is no bonding. The Al-plate, the Br/Epoxy composite patch and epoxy adhesive layer must remain linear elastic.
- (2) The adhesive layer thickness is relatively thin compare with plate/patch thickness. So it is considered to be a generalized plane stress condition. And the shear stress between plate and patch is treated as a body force.
- (3) The bending effect is ignored.

2.2 Stress Intensity Factor

Firstly, we compare the 2-dimensional finite element solution with the theoretical solution, and then extend to 3-dimensional finite element analysis.

Isida[6] proposed the 2-dimensional S.I.F for the cracked plate.

$$K_I = \sigma \sqrt{(\pi \times a)} \cdot (\alpha, \beta) \quad (1)$$

At the crack tip, calculation of the S.I.F is expressed as :

$$K_I = \frac{2G}{(K+1)} \left(\frac{\pi}{2l} \right)^{1/2} [(4v_{B2} - v_{C2}) - (4v_{B1} - v_{C1})] \quad (2)$$

where, v_B, v_C are y-direction crack opening displacement at the collapsed crack tip elements.

Fig. 2 shows that Ingraffa and Manu[7] proposed the calculation of S.I.F. for the 3-dimensional quarter point finite element analysis:

From Table.1. 2-dimensional S.I.F. corresponding theoretical results and finite element results are shown.

$$K_I = \frac{E}{4(1-\nu^2)} \sqrt{\frac{\pi}{2L_1}} [(2v_B - v_C + 2v_E - v_F - 2v_{B'} + v_{C'} - 2v_{E'} + v_{F'} - v_{D'}) + \frac{1}{2}\eta(-4v_B + v_C + 4v_E - v_F + 4v_{B'} - v_{C'} - 4v_{E'} + v_{F'}) + \frac{1}{2}\eta^2(v_F + v_C - 2v_D - v_{F'} - v_{C'} + 2v_{D'})] \quad (3)$$

Table 1. Comparison of S.I.F. of cracked plate (unit : MPa·mm^{1/2})

crack (2a)	Analytical	F.E.M	Error(%)
10	2.74	2.77	1.08
12	3.00	3.04	1.32
16	3.47	3.51	1.14
20	3.98	3.93	1.52
24	4.26	4.32	1.39
28	4.62	4.68	1.28
30	4.79	4.85	1.24

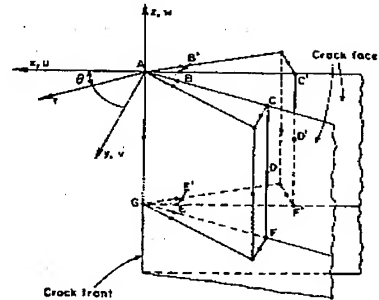


Fig. 2 Arrangement of quarter point element along segment of crack front.

2.3 Reduction of Stress Intensity Factor

For the fracture mechanics safety criteria, we define the reduction of stress intensity factor.

$$K^* = 1 - K_p / K_u \quad (4)$$

where, K_u and K_p are the stress intensity factors for the unpatched and patched cracked plate. From Table 1., the stress intensity factor for the unpatched cracked is 3.93MPa·mm^{1/2} at crack length 2a=20mm.

As K^* increases, the crack propagation decreases respectively. On the other hand, as K^* decreases, the possibility of fracture increases.

2.4 Adhesive Shear Stress

Adhesive shear stress causes the debonding at the patch and plate interface.

The equilibrium equations for a plate and patch are, respectively:

$$\frac{d\sigma_{yy}^s}{dy} = \frac{\tau_{yz}}{h_s}, \quad \frac{d\sigma_{yy}^p}{dy} = -\frac{\tau_{yz}}{h_p} \quad (5)$$

The stress-strain relationships of plate and patch are given by:

$$\varepsilon_{xx}^s = \frac{1}{E_s} (\sigma_{xx}^s - \nu_s \sigma_{yy}^s), \quad \varepsilon_{yy}^s = \frac{1}{E_s} (\sigma_{yy}^s - \nu_s \sigma_{xx}^s) \quad (6)$$

Jones and Callinan[2] proposed the compatibility condition between plate and composite patch;

$$\tau_{yz} = \frac{(\nu^s - \nu^p)}{F}, \quad F = \frac{h_a}{G_a} + \frac{h_s}{4G_s} + \frac{3h_p}{8G_p} \quad (7)$$

Table 2. Material properties for plate, patch and adhesive

	Young's modules (GPa)			Shear modules (GPa)			Poisson's ratio		
	E_1	E_2	E_3	G_{12}	G_{13}	G_{23}	ν_{12}	ν_{13}	ν_{23}
Al-plate	71.02	-	-	-	-	-	0.32	-	-
Pat ch	203.1	8.18	8.18	7.24	7.24	4.94	0.677	0.677	0.035
Adhesive	2.2	-	-	-	-	-	0.32	-	-

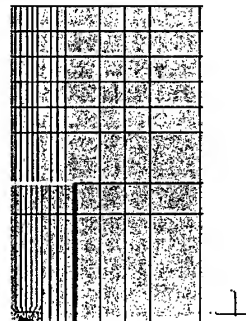


Fig. 3 Finite element modeling

3. FINITE ELEMENT ANALYSIS

The Al-plate with dimensions $240 \times 360 \times 3$ mm contains a central through-crack. The crack is repaired by patching the $[0/90]_s$ boron/epoxy laminate on both sides of the plate. The patch dimensions are 80×160 mm. The thickness of adhesive is 0.2 mm. The material properties and example finite element mesh for a composite patch repair are shown in Table 2 and Fig. 3, respectively. Only the upper half of the patched plate from the middle plane is considered due to geometric symmetry. To solve this problem, ABAQUS v 5.8 is used.

4. RESULTS AND REMARKS

4.1 Effect of Patch Thickness

Fig. 4 and 5 show the stress intensity factors and reduction of stress intensity factors with respect to the thickness of the composite patch. It is seen that the reduction of stress intensity factor increases on the variation of patch thickness. The reductions of stress intensity factors are about 78–90% with the patch thickness increasing.

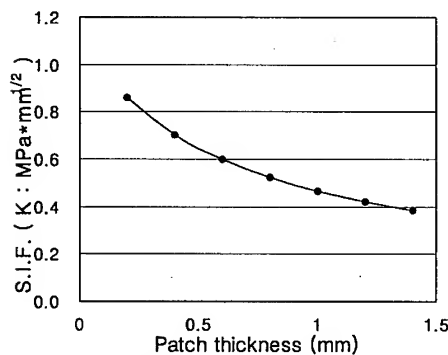


Fig. 4 S.I.F. with respect to patch thickness. ($2a=20$ mm)

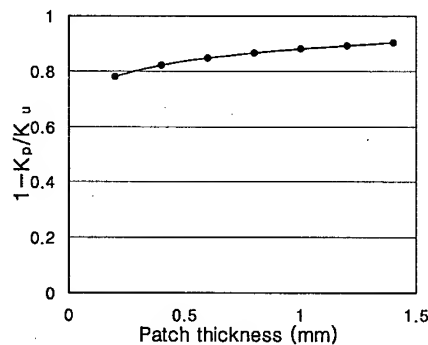


Fig. 5 Reduction of S.I.F. with respect to patch thickness.

4.2 Effect of Patch's Material

Fig. 6 and 7 show the effect of patch material, it is evident that using composite material as patch is more effective than using Al material.

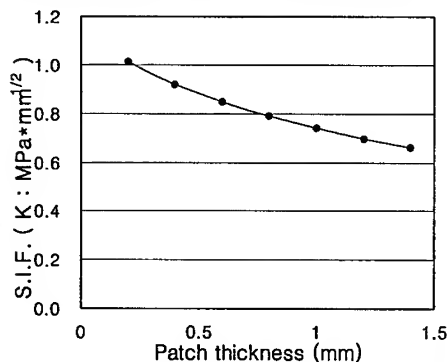


Fig. 6 S.I.F. with respect to Al-patch thickness. ($2a=20$ mm)

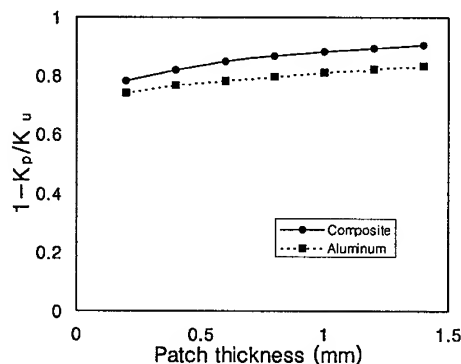


Fig. 7 Reduction of S.I.F. for Al and Br/Ep patch. ($2a=20$ mm)

4.3 Effect of Patch Shape

Fig. 8 and 9 show the stress intensity factors and reduction of stress intensity factors for the two patch type. Overall type is perfectly bonded over the crack. Otherwise, partial type is partially bonded the patch at the crack-tip.

Compared Fig. 8 and 9 with Fig. 4 and 5, stress intensity factors of overall type increases about six times as many as one of partial type, reduction of S.I.F. of overall type increases about two times as many as one of partial type.

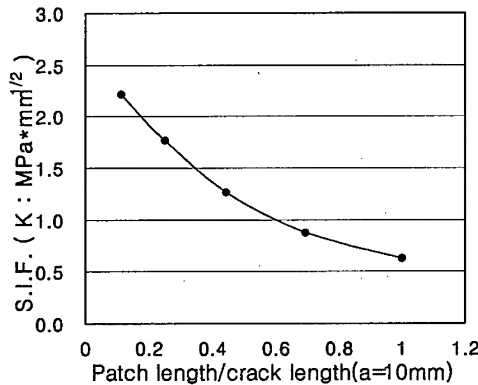


Fig.8 S.I.F. with respect to variable of patch size. (partial type)

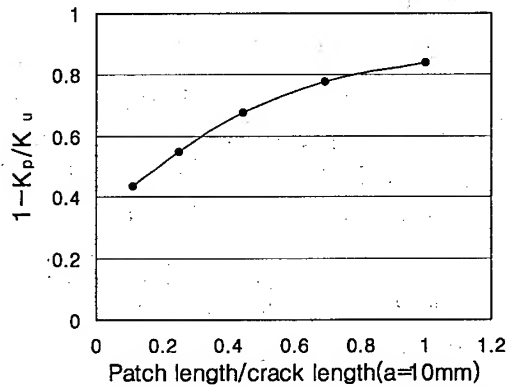


Fig.9 Reductional S.I.F. at the variable patch size.(partial type)

4.4 Distribution of Adhesive Shear Stress

Fig. 10~12 show the adhesive shear stress distribution around the end of patch which is tapered to reduce shear stresses. Generally, adhesive shear stress causes debonding. Adhesive shear stresses are larger at the patch end and thick patch. To reduce adhesive shear stresses, tapered-patch type is suggested. In the paper, tapered degrees are 15° , 30° , 45° , 60° , 75° and 90° . Fig. 10 shows the distribution of shear stresses at the center of the patch. From Fig. 11 it is seen that shear stress is significantly reduced due to tapered patch. From Fig. 12 it is note that tapered patch type prevent the boundary-layer effect [8].

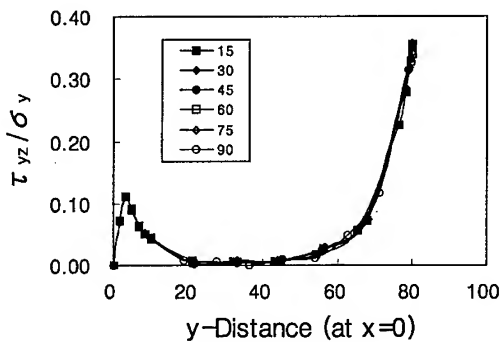


Fig.10 Shear stress distribution to variable of tapered angle. ($2a=20\text{mm}$, $x=0$)

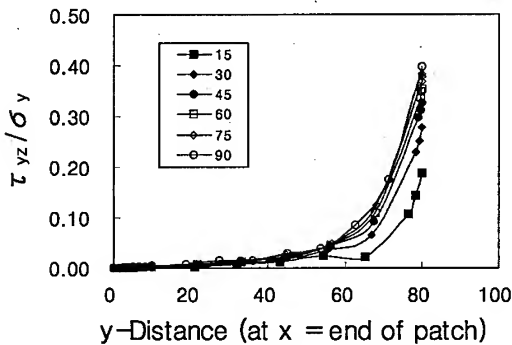


Fig.11 Shear stress distribution to variable of tapered angle. ($2a=20\text{mm}$, $x=\text{patch end}$)

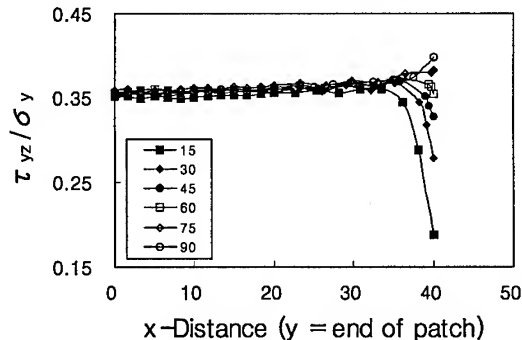


Fig.12 Shear stress distribution with respect to variable of tapered angles. ($2a=20\text{mm}$, $y=\text{patch end}$)

5. CONCLUSIONS

The objective of the study was to analyse the availability crack-repair method and to suggest the optimal patch shape. Using finite element method, we can obtain satisfactory results on the variation of design parameters. The results as following:

1. Reduction of S.I.F is more improved when using the stiffer boron/epoxy patch, whereas the adhesive shear stress at the end of the patch increases more.
2. For the repaired patch, composite material is more effective to prevent the propagation of crack.
3. Reduction of S.I.F of the overall patch type is approximately two time as many as one of partial patch type. If possible, overall type is more effective than partial patch type to restraint cracks growth.
4. Considering both fracture mechanic and debonding, the optimal patch shape is stiffer at the center of the patch and gradually thinner to the end of the patch. But this patch shape is difficult to fabricate, we suggest the tapered patch type.

ACKNOWLEDGEMENTS

The authors are grateful for the support provided by a grant from the Korea Science & Engineering Foundation(KOSEF) and Safety and Structural Integrity Research Center at the Sungkyunkwan University.

REFERENCES

1. A.A.Baker and R.Jones, Dordrecht: Martinus Nijhoff, (1988), Bonded repair of aircraft structures.
2. R. Jones and R.J.Callinan, J. Struct. Mech., 7(1979) p.107-130, Finite element analysis of patched cracks.
3. R. Jones, R.J.Callinan and K.C. Aggarwal, Engng. Frac. Mech., 17(1983) p.37-46, Analysis of bonded repair to damaged fibre composite structures.
4. R.C.Chu and T.C.Ko, Theor. Appl. Frac. Mech., 17(1989) p.93-102, Isoparametric shear spring element applied to crack patching and instability.
5. J.J.Denney, M.S. Thesis. Air Force Inst. Of Tech. (1995), Fatigue response of cracked aluminum panel with partially bonded composite patch.
6. M.Isida, Int. J. Frac., 7(1971) p.301-316, Effect of width and length on stress intensity factors of internally cracked plates under various boundary conditions.
7. A.R.Ingraffa, Int. J. Numer. Meth. Engng., 7(1980) p.1427-1445, Stress intensity factor computation in three dimensions with quarter point element.
8. K.N.Shivakumar and I.S.Raju, Int. J. Frac., 45(1990) p.159-178, Treatment of singularities in three-dimensional cracked bodies.

Fracture Toughness Test of Small CNS Specimen with an Interface Crack Subjected to Mixed-Mode Loading

Kenji Machida

Department of Mechanical Engineering, Science University of Tokyo,
2641 Yamazaki, Noda-shi, Chiba 278-8510, Japan

Keywords: Fracture Toughness, Interface Crack, Mixed Mode, Polynomial Approximation, Stress Intensity Factor, Virtual Crack Extension Method

ABSTRACT

The fracture toughness test was carried out by using small CNS (Compact Normal and Shear) specimens subjected to mixed-mode loading. Small CNS specimens made of 62Sn-38Pb and epoxy resin enable us to carry out the experiment under various kinds of mixed-mode loading. The complex stress-intensity factor associated with an interface crack was evaluated by the virtual crack extension method. K_I and K_{II} values at unstable crack growth were measured under various mixed-mode loading. The energy release rate of interface crack was not constant under various mixed-mode loading. The relationship between K_I and K_{II} values shows the elliptic law.

1. INTRODUCTION

The strength evaluation of the composites, electronic packages, bonded dissimilar materials and adhesive joints have become very important in recent years. Therefore, the strength evaluation and testing method should be established to estimate the strength of interface crack quantitatively. A CNS specimen with an interface crack proposed by Richard et al. [1] was employed. Small CNS specimens made of the 63Sn-37Pb alloy and epoxy resin enable us to carry out the fracture toughness test under various kinds of mixed-mode loading. The energy release rate of interface crack is not constant under the various mixed-mode loading. Then, it is necessary to evaluate the fracture toughness by the components of complex stress intensity factor K . The evaluation of stress intensity factors of the interface crack has been carried out by the finite element analysis. The complex stress intensity factor associated with the elastic interface crack was evaluated by the virtual crack extension method (VCEM) [2-4]. The fracture toughness of interface crack was estimated by using two parameters (K_I , K_{II}). The result of fracture toughness test reveals that the interface is strong to the shear but weak to the delamination.

2. STRESS STATE NEAR AN INTERFACE CRACK-TIP

The stress state along the interface ahead of the crack tip is expressed as follows:

$$(\sigma_{yy} + i\sigma_{xy})_{\theta=0} = K(r/l_k)^{\epsilon} / \sqrt{2\pi r} \quad (1)$$

$$\epsilon = \frac{1}{2\pi} \ln \left[\left(\frac{\kappa_1}{\mu_1} + \frac{1}{\mu_2} \right) / \left(\frac{\kappa_2}{\mu_2} + \frac{1}{\mu_1} \right) \right] \quad (2)$$

$$\kappa_j = \begin{cases} 3 - 4\nu_j & (\text{plane strain}) \\ (3 - \nu_j)/(1 + \nu_j) & (\text{plane stress}) \end{cases} \quad (3)$$

where $(\sigma_{yy} + i\sigma_{xy})$ is the complex stress, K is the complex stress-intensity factor ($K_I + iK_{II}$), r is the distance from the crack tip, l_k is the typical length like a crack length, μ_1 and μ_2 are the shear moduli of materials 1 and 2, ϵ is a bi-material constant, and ν is the Poisson's ratio.

The absolute value and argument are expressed as follows:

$$|\sigma_{yy} + i\sigma_{xy}| = \frac{|K_I + iK_{II}|}{\sqrt{2\pi r}} = \frac{\sqrt{K_I^2 + K_{II}^2}}{\sqrt{2\pi r}} \quad (4)$$

$$\arg(\sigma_{yy} + i\sigma_{xy}) = \arg(K_I + iK_{II}) + \epsilon \ln(r/l_k) = \tan^{-1}(K_{II}/K_I) + \epsilon \ln(r/l_k) \quad (5)$$

When l_k changes to l' , K_I' and K_{II}' are simply evaluated by the following equation.

$$\begin{Bmatrix} K_I' \\ K_{II}' \end{Bmatrix} = \begin{bmatrix} \cos \theta & -\sin \theta \\ \sin \theta & \cos \theta \end{bmatrix} \begin{Bmatrix} K_I \\ K_{II} \end{Bmatrix}, \quad \theta = \epsilon \ln(l'/l_k) \quad (6)$$

First, K_I and K_{II} were calculated by setting $l_k = 2a$ where a is a crack length. K_I and K_{II} values were transformed into the final stress-intensity factors (K_I' and K_{II}') at $l' = 0.01\text{mm}$ considering the compatibility with the stress-intensity factors obtained by the modified crack closure integral [5,6].

3. EXPERIMENT

Figure 1 shows the configuration of compact normal and shear specimen. The loading device is shown in Fig.2. The materials of upper and lower parts of specimen are the 63Sn-37Pb alloy and epoxy resin, respectively. The mechanical properties of two materials are shown in Table 1. A crack was introduced by putting Teflon sheet 0.02mm thick between two pieces. The crack length is 6mm. The specimen was polymerized for 48hours at 120°C, and cooled to the room temperature at the cooling rate of 10°C/h to remove the residual stress. Seven kinds of mixed-mode loading from mode I to mode II were applied to CNS specimens by changing a load application angle. The fracture toughness test was carried out at the tensile speed of 0.5mm/min.

4. MODEL FOR ANALYSIS

Figure 3 shows the model for the 3-D finite element analysis. The half portion of specimen was modeled by the symmetry with respect to the midsection of specimen by using 20 nodes isoparametric elements. Here W is 12mm, H is 20mm, B is 5mm, l_1 is 7.2mm and l_2 is 14.4mm.

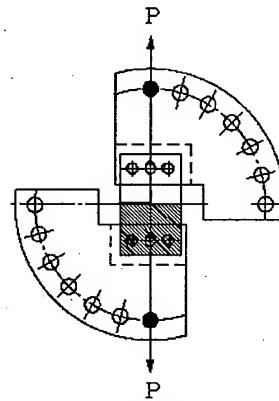


Fig.2 Loading device.

Fig.3 3-D FEM model.

The forces and moments meet the following equilibrium equations.

P_1 , P_2 and P_3 were applied to the centers of each bolt hole in order to make the uniform loading. P is the load applied to the bolt hole on the periphery of loading device shown in Fig.2 and α is the load application angle. The stress-intensity factor was evaluated by the virtual crack extension method. The components of complex stress-intensity factor K were evaluated by the superposition of asymptotic plane-strain solution derived by Sun and Jih [7].

5. RESULTS AND DISCUSSION

The normalized stress-intensity factors (F_I , F_{II}) were evaluated by the following equation from the stress-intensity factors (K_I , K_{II}).

$$F_j = \frac{K_j}{\frac{P}{WB} \sqrt{\pi a}} \quad (j = I, II) \quad (8)$$

Figure 4 shows the distribution of stress-intensity factors along the crack front. Here Z is the distance from the midsection of the specimen. F_I is nearly uniform from the midsection of the specimen to $2Z/B \approx 0.4$ and decreases gradually towards the free surface. F_{II} is nearly uniform along the crack front, but increases slightly near the free surface. F_{II} is not zero even in the case of $\alpha=0$ degree. Therefore the stress state near the interface crack shows the mixed-mode condition under the mode I loading. In the case of $\alpha=90$ degrees, F_I is nearly zero. Consequently the specimen is nearly in the pure mode II condition.

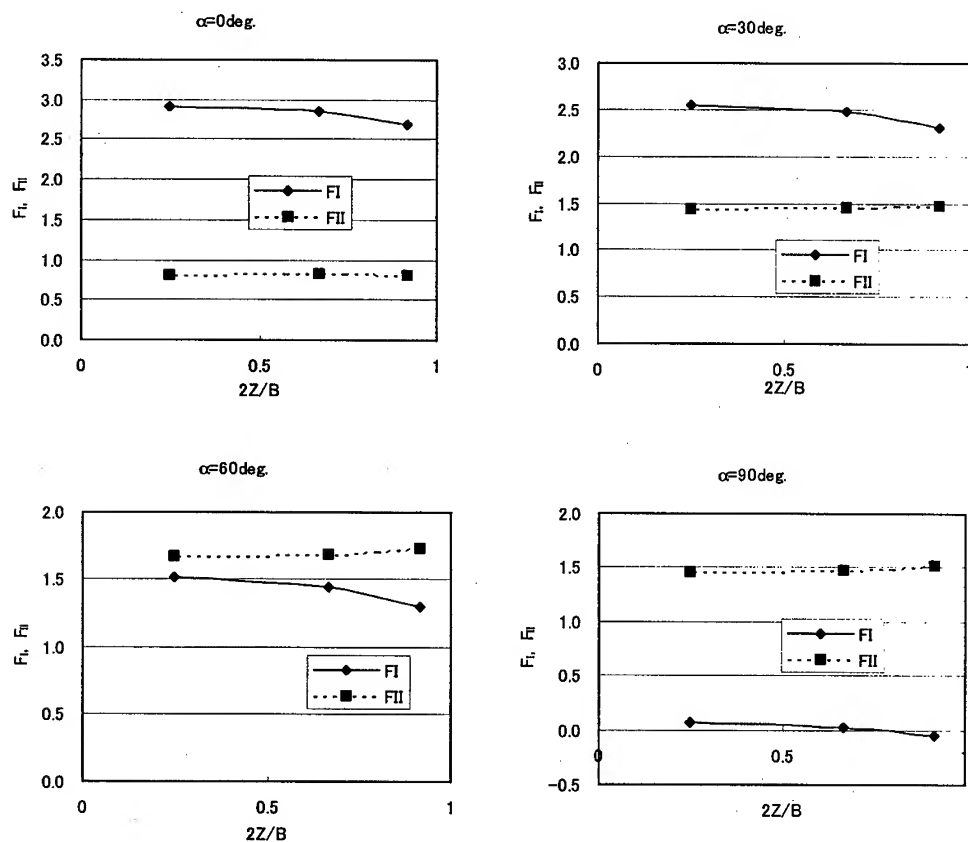


Fig.4 Distribution of stress-intensity factors along the crack front.

Figure 5 shows the variation of stress-intensity factors at the midsection with the load application angle α . As α increases, F_I decreases. On the other hand, F_{II} increases, becomes maximum at about 60 degrees and then decreases gradually. F_{II} at $\alpha=0$ degree is 0.816 and not zero. F_I at $\alpha=90$ degrees is 0.14 and nearly zero. The following stress-intensity factors were evaluated by using F_I and F_{II} values at the midsection of the specimen.

K_I corresponds to the energy release rate and γ denotes the ratio of mixed-mode. Both values are expressed as follows:

$$K_I = \sqrt{K_I^2 + K_{II}^2} \quad (9)$$

$$\gamma = \tan^{-1} \left[\frac{K_{II}}{K_I} \right] \quad (10)$$

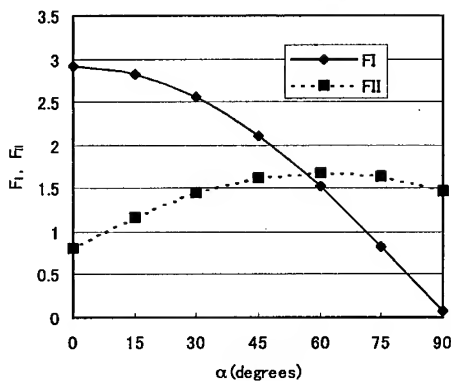


Fig.5 Variation of stress-intensity factors at the midsection with a load application angle.

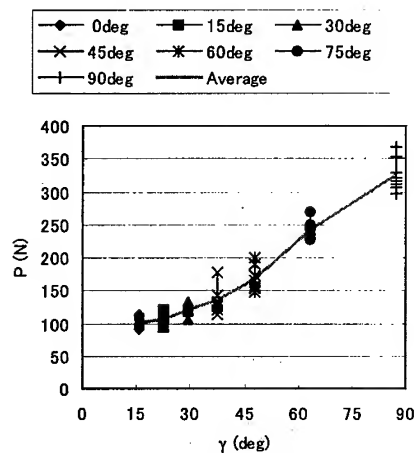
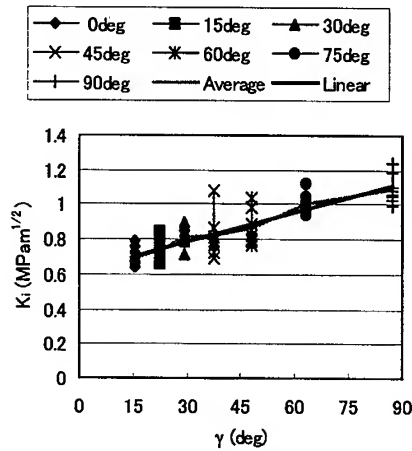
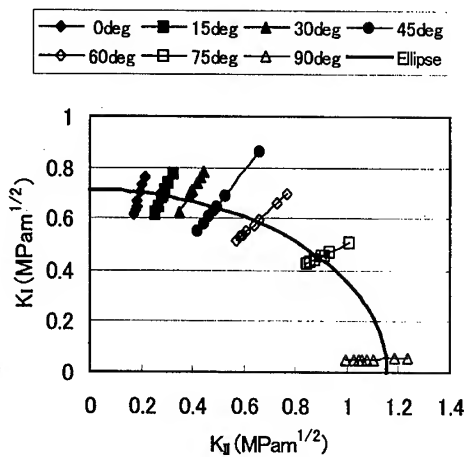


Fig.6 Variation of fracture load with the mixed-mode ratio γ .

Figure 6 shows the variation of fracture load with the mixed-mode ratio γ . An angle in the legend denotes the load application angle α . As γ increases, the fracture load increases gradually up to $\gamma=45$ degrees and then increases rapidly. The fracture load is maximum at $\alpha=90$ degrees. All specimens fractured in the brittle mode.

Figure 7 shows the variation of K_I with the mixed-mode ratio. K_I increases linearly with an increase in the mixed-mode ratio and is not constant. Accordingly, the fracture toughness of interface crack cannot be estimated by the single parameter like the energy release rate. Therefore the mixed-mode criterion using two parameters (K_I , K_{II}) is needed to estimate the fracture toughness of interface crack.

Figure 8 shows the relationship between K_I and K_{II} at the unstable crack growth. An elliptical law holds in those values as follows:

Fig.7 Variation of K_I with mixed-mode ratio.Fig.8 Relationship between K_I and K_{II} .

$$\left(\frac{K_I}{K_{IC}}\right)^2 + \left(\frac{K_{II}}{K_{IIC}}\right)^2 = 1 \quad (11)$$

where K_{IC} ($=0.71\text{MPam}^{1/2}$) and K_{IIC} ($=1.155\text{MPam}^{1/2}$) are the fracture toughness of mode I and mode II, respectively. K_{IIC} is about 1.63 times K_{IC} . Therefore it is considered that the interface is strong to the shear but weak to the delamination.

6. CONCLUSIONS

1. The energy release rate of interface crack at the unstable crack growth varies depending on the mixed-mode ratio.
2. An elliptic law holds in the relation between K_I and K_{II} as follows:

$$\left(\frac{K_I}{K_{IC}}\right)^2 + \left(\frac{K_{II}}{K_{IIC}}\right)^2 = 1$$

3. K_{IIC} is about 1.63 times K_{IC} . Therefore it is considered that the interface is strong to the shear but weak to the delamination.

REFERENCE

1. H.A.Richard and K.Benitz, Int. J. Fract., **22**(1983), p.R55.
2. D.M.Parks, Int. J. Fract., **10**(1974), p.487.
3. K.Machida, Int. Conf. Adv. Tech. Exp. Mech., JSME-MMD(1997), p.249.
4. K.Machida, JSME Int. J., **42**(1999), p.57.
5. K.Machida, Trans. Jpn. Soc. Mech. Eng. (in Japanese), **62**(1996), p.1565.
6. K.Machida, Trans. Jpn. Soc. Mech. Eng. (in Japanese), **63**(1997), p.302.
7. C.T.Sun and C.J.Jih, Eng. Fract. Mech., **28**(1987), p.13.

Theoretical Investigation of Controllable & Regular Fracture Theory

Aixi Zhou*, Yaobing Wei and Fuyuan Lang

Institute of Crack Technique, Gansu University of Technology,
Lanzhou 730050, China P.R.

Keywords: Controllable Fracture, Crack System, Crack Technique, Directional Stability, Fracture Transformation, Generalized Energy Function, Regular Fracture, Stress Cutting

ABSTRACT

Aiming to investigate the controllable fracture procedures and exploit the benefits of cracks, the paper theoretically analyzes the following essential aspects of Controllable and Regular Fracture Theory (CRFT) through both Engineering Control Theory and Fracture Mechanics: (a) The mathematical model of CRFT. In this item, any fracture procedure is regarded as a mathematical transformation named as Fracture Transformation, and a regular fracture procedure can be described as ϵ -Stability. (b) The fundamental analysis models of CRFT are presented after introducing Engineering Control Theory. A fracture procedure is considered as the behavior of the named "Crack System". (c) The conceptual stability of regular fracture procedure is investigated. With the help of Lyapunov's theory of stability in Engineering Control Theory, the stability of crack growth is analyzed. Using a transformation, the ϵ -Stability is proved to have the same meaning of the stability in Lyapunov's theory, and then can be described and analyzed by Lyapunov's stability theory. (d) A sufficient stability criterion of growing crack is established by means of Energy Method.

1. INTRODUCTION

Ordinarily, Fracture Mechanics, in which crack is considered as a disaster and fracture of solids is considered as a kind of loss of stability, deals with the mechanism of fracture, seeks to discover ways to prevent its occurrence and assure the "Safe Design" and "Safe Application" of the practical components or structures. However, as the dialectics of nature shows, the so-called "misfortune" of cracks, could be explored and, where possible, might be exploited so as to be a benefit to human beings. Based on the thought of changing the misfortune into a benefit, combining the "benefit" of crack with Mechanical Manufacturing Engineering, a new technique, which is named as Crack Technique, has been established. Crack Technique[1] is a stress cutting technique using the stress concentration of the artificial cracks under the sensitive stress fields caused by suitable types of loading to separate the continuous faces of the solids

* Corresponding author. Currently pursuing Ph.D. degree at the Dept. of Engineering Science & Mechanics, Virginia Polytechnic Institute and State University, Blacksburg, VA 24061, USA. Email: azhou@vt.edu

quickly and regularly through the growth of crack after initiation. This new prospect for investigation indicates that the crack could be purposely made in advance, controlled to propagate orientationally, and used to perform a task of machine work. The benefit from crack investigation is first related to stock break-off. Conventional methods of stock break-off are metallic cutting (sawing, turning, milling, etc.) and cold or hot shearing. The new technique, called "stress cutting", however, makes use of the singularity of the stress at the sharp end of an artificially cut notch subjected to pre-load to force the notch to be fractured suddenly and propagate quickly with directional stability all the way of the whole stock body. High efficiency and low energy consumption are two unparalleled advantages possessed by stock break-off with crack propagation [1]. In addition to machinework industries, other industries such as military, explosive, building, quarrying, mining and steelworks industries should also recognize and then exploit the benefits of cracks.

This paper investigates the following essential aspects of CRFT: (a) the mathematical model of CRFT; (b) the fundamental analysis models of CRFT; (c) the conceptual Stability of Regular Fracture Procedure; and (d) a sufficient stability criterion of growing crack.

2. MATHEMATICAL MODEL OF CONTROLLABLE & REGULAR FRACTURE

The fracture procedure is considered as a kind of motion of the Crack System, which includes the notches or cracks, boundary conditions, loading, etc., of the solid body. The following two hypotheses for the model were introduced: (1). The described Crack System is considered in Banach Spaces. (2). The solid body is a continuum and meets the axiom of continuity in Continuum Mechanics.

A fracture procedure is regarded as a mathematical transformation. $\Omega_i (i=0,1,2)$ are assumed to be vector space, and $\Omega_i \subset R^3$ where R^3 is the 3-D Banach Spaces. Ω_0 is the whole vector space of the solid body before fracture; Ω_1 and Ω_2 are vector space of the two solid bodies respectively after fracture. Then the fracture procedure

$$\Omega_0 \rightarrow \Omega_1 + \Omega_2 \quad (1)$$

is considered as a kind of mathematical transformation by which the original single and continuous vector space Ω_0 is transformed into two separate parts space Ω_1 and Ω_2 . The detailed definitions of fundamental concepts of a regular fracture procedure follow as:

Assume $\Omega_0, \Omega_1, \Omega_2 \subset R^3$, and $\Omega_1 \cap \Omega_2 = \emptyset$, $\Omega_1 \cup \Omega_2 = \Omega_0$. T is a self-transformation in R^3 . If T transform Ω_0 as: $\Omega_0 \rightarrow \Omega_1 + \Omega_2$. Then T is defined as Fracture Transformation in R^3 .

$\Omega_1, \Omega_2 \subset R^3$, and $\Omega_1 \cap \Omega_2 = \emptyset$. X_0 is a part of the boundary of Ω_1 . $S(X_0, \delta)$ is the neighborhood of X_0 . If for $\forall \delta > 0$ then: $S(X_0, \delta) \cap \Omega_2 \neq \emptyset$. Then Ω_1 and Ω_2 are Contiguous and part Ω_1 and part Ω_2 is defined as Contiguity. All X_0 in Ω_1 (or in Ω_2) are called Contiguity Boundary of Ω_1 and Ω_2 .

$A, B \subset R^3$, and $A \subset B$, $\forall x \in A$. $F_S(x)$ is a mathematical transformation: $F_S: x \rightarrow x'$ [where $x' \in B$, $x' = F_S(x)$]. If for any expected $\varepsilon > 0$, then, $\rho[x, F_S(x)] \leq \varepsilon$, where ρ is the distance between two vectors x and $F_S(x)$ in Banach Space. The above-mentioned $F_S(x)$ is denoted as B_ε . Transformation F_S is defined as ε Limited Boundary Transformation, and the transformation $F_S(x)$ is regarded as a kind of ε Limited Boundary. B_ε is defined as ε Limited Boundary Path of A under the transformation of $F_S(x)$.

$\Omega_0, \Omega_1, \Omega_2 \subset R^3$, Ω_1 and Ω_2 are Contiguous, and C is the contiguity boundary of Ω_1 and Ω_2 . B_ε is the expected ε Limited Boundary Path, and $C \subseteq B_\varepsilon$. If for $\forall \varepsilon > 0$, $\exists T$ (Fracture Transformation) where $C \subseteq B_\varepsilon$ exists all through the whole procedure of the fracture transformation for Ω_1 and Ω_2

2. Then the fracture or transformation procedure T is considered as stable and controllable. The whole procedure T is defined as ϵ Stability. If B_s is Uniform ϵ Limited Boundary Path in the above situation, T is called as Uniform ϵ - Stability. If $C \subseteq B_s$ does not exist through the whole procedure (sometimes $C \subseteq B_s$), then T is defined as ϵ Instability. Fig.1 shows the Uniform ϵ - Stability and Uniform ϵ - Instability, in which crack 1 and crack 2 are stable whereas crack 3 is unstable.

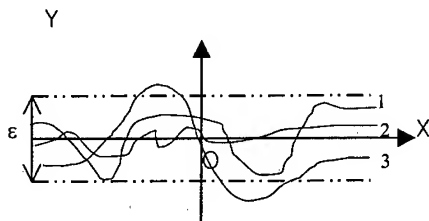


Fig.1 Uniform ϵ - Stability and Uniform ϵ - Instability

For a fracture procedure, which grows stably and regularly for the expected or predicted path, can be described as the following: Consider a solid body Ω_0 , if for an expected ϵ Limited Boundary Path, one can find a Fracture Transformation T which makes: $\Omega_0 \rightarrow \Omega_1 + \Omega_2$, where Ω_1 and Ω_2 are ϵ Congruity. Then the fracture procedure is called ϵ Stability, and the fracture procedure is called as Stable and Regular Fracture Procedure.

3. ANALYSIS MODELS USING ENGINEERING CONTROL THEORY

Consider a solid body with cracks, with the boundary of $S = S_\sigma + S_u + S_c + S_f$, where S_σ is the stress boundary; S_u is the displacement boundary; S_c is the crack or notch boundary, or the crack tip boundary after initiation; S_f is the free boundary. A fracture procedure can be divided into two sub-procedures: (1). In first sub-procedure, the Generalized Loading $X(S, P, T, t)$ is the First-step Input (General Input) and the body's mechanical parameters $Y(\sigma_{ij}, \epsilon_{ij}, u_{ij})$ in Fig.2 describing the mechanical conditions (such as stress, strain and displacement) in S_c and the region around S_c is First-step Output. (2). The mechanical parameters in item (1) act as the Second-step Input, and the crack growth path $P(\Omega_1, \Omega_2)$ in Fig.2 is the Second-step Output (General Output). $X(S, P, T, t)$ is the Generalized Loading (or General Input), which implies the loading may be caused by boundary changing (S); force, moment and pressure (P); Thermal Effects (T) and may be related to time t .

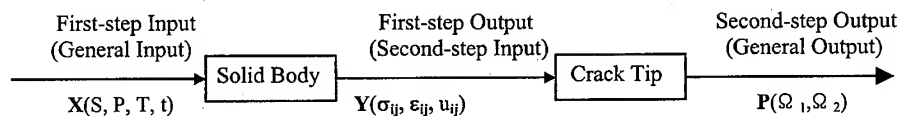


Fig.2 Opened Loop Control of a Crack System

4. STABILITY OF CRACK GROWTH IN CRFT

In the above definitions, and in practical engineering problem of controllable and regular fracture, the expected crack growth path is banded. For example, it is a banded area in 2-dimension (Fig. 1). However, in Lyapunov's description, the stability limitation of a motion is a circle. The above-mentioned difference can be solved by using complex function theory. A banded area can be transformed into a circular region. The banded region as in Fig.1 can be transformed into a unit circle through the following transformation

$$Z_1 = \frac{i - e^{\left(\frac{\varepsilon}{\pi} z_0 + i \frac{\pi}{2}\right)}}{i + e^{\left(\frac{\varepsilon}{\pi} z_0 + i \frac{\pi}{2}\right)}} \quad (2)$$

After the transformation, the stability in crack growth path (ε stability) has the same meanings as in Lyapunov's stability theory in Engineering Control Theory. Then, the stability of a fracture procedure can also be defined using Lyapunov's stability theory in the transformed coordinate system.

Solveing Melin[2] has also studied the directional stability of cracks in his series papers. Melin made the definition of crack's directional stability concentrating on the slope $Y(a)/a$ (where a is the crack length) of the crack. The corresponding definition of directional instability would be that $Y(a)/a$ increases with a or, more precisely, that $[Y(a)/a]/[Y(a_0)/a_0]$ exceeds any predetermined value if a/a_0 is sufficiently large and Y_0/a_0 infinitesimally small. Then the outcome of his stability analysis depends on the ratio between the principle stress σ_x^∞ and σ_y^∞ . The other candidate for the definition of directional instability concentrates on the absolute position of the crack tip as stated in the definition in this paper. However, Melin's definition can not describe the controllable and regular fracture problem in practical engineering application, which is possible in Crack Technique. In addition, Melin investigated the directional stability and instability concentrating only on Fracture Mechanics, no Engineering Control Theory is considered in his research. Other researchers, such as Vladimir V Bolotin[3] who considers Fracture as dynamic instability, have also studied the stability or instability problems in Fracture. However, in this paper, the same work using different analytic tools based on a different approach is studied.

5. CRITERION OF CRACK GROWTH

Several instability criteria of crack growth[4,5,6] are available at the present, which consider the directional stability only on the basis of pure Fracture Mechanics research. This part tries to investigate the stability criterion by Engineering Control Theory.

According to Lyapunov's stability theorem, a Generalized Energy Function is to be found in order to investigate the stability of a control system; the Generalized Energy Function, which is alterable and can be substituted, has to be composed in advance. The following aspects should be considered when choosing the function: (1) It should possess the characteristics of an energy function stipulated in Control Theory. (2) The physical nature of the solid body of the Crack System should be considered. (3) The mechanical parameters of the fracture procedure should be included. (4) The function should generalize as many types and conditions of fracture as possible. For these reasons, the Strain Energy Density Function defined by G.C. Sih is chosen as the Generalized Energy Function. And consider the straight path when $\varepsilon=0$ in ε Limited Boundary as the equilibrium state of the growing crack. Then, the Generalized Energy Function $Z(x)$ is showed as:

$$Z(x) = a_{11}K_I^2 + 2a_{12}K_I K_{II} + a_{22}K_{II}^2 + a_{33}K_{III}^2 \quad (3)$$

where $a_{11}, a_{12}, a_{22}, a_{33}$ are denoted as :

$$a_{11} = \frac{1}{16\pi\mu} (\chi - \cos\theta)(1 + \cos\theta)$$

$$\begin{aligned}
 a_{12} &= \frac{1}{16\pi\mu} \sin \theta [2 \cos \theta - (\chi - 1)] \\
 a_{22} &= \frac{1}{16\pi\mu} [(\chi + 1)(1 - \cos \theta) + (1 + \cos \theta)(3 \cos \theta - 1)] \\
 a_{33} &= \frac{1}{4\pi\mu} \\
 \chi &= \begin{cases} \frac{3-\nu}{1+\nu} & \text{(Plane Stress)} \\ 3-4\nu & \text{(Plane Strain)} \end{cases}
 \end{aligned} \tag{4}$$

where θ is the polar angle, μ and ν are material parameters, K_I, K_{II} , and K_{III} are Stress Intensity Factors. Obviously, $Z(x)$ is a quadratic form type Lyapunov function, and the sign characteristic of $Z(x)$ can be analyzed by its real matrix after represented in matrix form. If the real matrix of $Z(x)$ is larger than zero, then, $Z(x) > 0$.

$$Z(x) = a_{11}K_I^2 + 2a_{12}K_IK_{II} + a_{22}K_{II}^2 + a_{33}K_{III}^2 = [K][P][K]^T \tag{5}$$

$$\text{where } a_{12} = a_{21}, [K] = [K_I \quad K_{II} \quad K_{III}], [P] = \begin{bmatrix} a_{11} & a_{12} & 0 \\ a_{21} & a_{22} & 0 \\ 0 & 0 & a_{33} \end{bmatrix}.$$

Assume λ_i ($i=1,2,3$) are real proper values of matrix $[P]$. According to Matrix Theory, if $\lambda_i > 0$, then $[P] > 0$. Considering $[\lambda_i I - P] = 0$, we have,

$$\begin{aligned}
 \lambda_1 &= a_{33} = \frac{1}{4\pi\mu} > 0 \\
 \lambda_2 &= \frac{1}{16\pi\mu} (\cos^2 \theta - 2 \cos \theta + 2\chi - 1) = \frac{1}{16\pi\mu} [(1 - \cos \theta)^2 + 2(\chi - 1)] \\
 \lambda_3 &= \frac{1}{16\pi\mu} (\cos^2 \theta + 2 \cos \theta + 1) = \frac{1}{16\pi\mu} (1 + \cos \theta)^2
 \end{aligned} \tag{6}$$

For most metal materials, $\nu = 0.3$. Replace ν in equation (4) and (6), we can get that λ_i ($i=1,2,3$) > 0 . Then, the matrix $[P] > 0$, so $Z(x) > 0$. Now, we consider the sign characteristic of $\dot{Z}(x)$,

$$\dot{Z}(x) = 2a_{11}K_I\dot{K}_I + 2a_{12}(K_I\dot{K}_{II} + \dot{K}_IK_{II}) + 2a_{22}K_{II}\dot{K}_{II} + 2a_{33}K_{III}\dot{K}_{III} \tag{7}$$

According to Lyapunov's stability theorem, the following two conditions must be satisfied for a stable system: $Z(x) > 0$ and $\dot{Z}(x) \leq 0$. It has been proved above that $Z(x)$ is a positive definite function for a certain Crack System. If $\dot{Z}(x)$ is semi-negative definite, then the equilibrium state of the growing crack of the Crack System is stable according to Lyapunov's theory. Then, $\dot{Z}(x)$ must satisfy the semi-negative condition if the Crack System is a stable

system. Hence

$$a_{11}K_I\dot{K}_I + a_{12}(K_I\dot{K}_{II} + \dot{K}_IK_{II}) + a_{22}K_{II}\dot{K}_{II} + a_{33}K_{III}\dot{K}_{III} \leq 0 \quad (8)$$

If the Generalized Energy Function of a Crack System satisfies expression (8), then, the system satisfies the Lyapunov's Stability Theorem, and the system is stable. Expression (8), which is called the Stability Criterion of Growing Cracks, is the sufficient condition for a Crack System to be stable.

6. CONCLUSIONS

1. It is necessary and feasible to investigate the directional stability problem of dynamic growing cracks using Lyapunov's Stability Theory. Though fracture of solids is a kind of loss of stability in common Fracture Mechanics research, the growth direction of the growing cracks can be described and analyzed as an engineering stability problem when given certain meanings of the directional stability.

2. It has been theoretically demonstrated that, as shown in expression (8), the directional stability of the growing crack is related to the crack position (polar angle), material parameters, the stress intensity factors, and the ratio of SIFs on the crack tip.

3. $\dot{K}_I, \dot{K}_{II}, \dot{K}_{III}$ are real ratios of SIFs on crack tip. They are different from the ratio of the SIFs in Experimental Fracture Mechanics in which $\dot{K}_I, \dot{K}_{II}, \dot{K}_{III}$ denote the loading ratio, not the real ratio of the SIFs.

4. Expression (8) is a sufficient criterion. Lyapunov's Stability Theorem in control theory is a sufficient condition, not a sufficient and necessary condition. According to Lyapunov's Stability Theorem, if a Crack System does not satisfy expression (8), it can not be stated that the system is not stable.

5. It must be noted, however, that our work, as reported in this paper is just a first-step theoretical investigation. Numerical and experimental investigation and other analysis work should be performed in the future.

REFERENCES

1. Aixi Zhou, Theoretical Investigation and Applicable Analysis of Regular Fracture Theory. Mater's Thesis, Gansu University of Technology, Lanzhou, China. (May, 1999). (In Chinese)
2. Solveing Melin, Growth from A Straight Crack Subject to Arbitrary Remote Loading. Engineering Fracture Mechanics. 46-3(1993) p.511-518.
3. Vladimir V Bolotin, Dynamic Instability in Mechanics of Structures, Applied Mechanics Review. 52-1(1999) R1.
4. A. Shukla, H. Nigam and H. Zervas, Effect of Stress Field Parameters on Dynamic Crack Branching. Engineering Fracture Mechanics. 36-3(1990) p.429-438.
5. K. Ravi-chandar and W.G. Knauss, An Experimental Investigation into Dynamic Fracture: II. Microstructural Aspects. International Journal of Fracture. 26(1984) p65-80.
6. K. Ravi-chandar and W.G. Knauss, An Experimental Investigation into Dynamic Fracture: III. On Steady-state Crack Propagation and Crack Branching. International Journal of Fracture. 26(1984) p65-80.

Crack Identification Using Classical Optimization Technique

M.W. Suh¹, J.M. Yu² and J.H. Lee²

¹ School of Mechanical Engineering, Sungkyunkwan University,
300 Chunchun-dong, Jangan-gu, Suwon 440-746, Korea

² Graduate School of Mechanical Engineering, Sungkyunkwan University,
Chunchun-dong, Jangan-ku, Suwon 440-746, Korea

Keywords: A Beam Structure, Crack Identification, Finite Element Method, Inverse Problem, Optimization Technique, Structure Analysis

ABSTRACT

It has been established that a crack has an important effect on the dynamic behavior of a structure. This effect depends mainly on the location and depth of the crack. To identify the location and depth of a crack in a structure, Nikolakopoulos et al. used the intersection point of the superposed contours that correspond to the eigenfrequency caused by the crack presence. However, the intersecting point of the superposed contours is not only difficult to find but also incorrect to estimate. A method is presented in this paper which uses optimization technique for the location and depth of the crack. The basic idea is to find parameters which use the structural eigenfrequencies on crack depth and location and optimization algorithm. With finite element model of the structure to calculate eigenfrequencies, it is possible to formulate the inverse problem in optimization format. Method of optimization is augmented lagrange multiplier method and search direction method is BFGS variable metric method and one dimensional search method is polynomial interpolation.

1. INTRODUCTION

Techniques to detect cracks and defects hidden in structure and to evaluate their residual life time are very important to assure the structural integrity of operating plants and structures. Many researchers have investigated the potential of system identification to determine the properties of a structure. A state of damage could be detected by a reduction in stiffness. A crack which occurs in a structural element causes some local variations in its stiffness, which affect the dynamics of the whole structure to a considerable degree. An analysis of the changes is tried to identify the crack.

A number of papers have dealt with the problem of crack location and size identification in order to propose efficient and more precise methods. Inagaki et al. [1] used a procedure with eigenfrequency measurements to find the crack size and location. Leung [2] and Anifantis et al. [3] proposed crack identification methods through measurements of the dynamic behavior in bending. Dimarogonas and Massouros [4] investigated the dynamic behavior of a circumferentially cracked shaft in torsion and proposed nomographs for finding the crack depth and location.

Nikolakopoulos et al. [5] presented the dependency of the structural eigenfrequencies on crack depth and location in contour graph form. To identify the location and depth of a crack, they

determined the intersection points of the superposed contours that correspond to the measured eigenfrequency variations caused by the crack presence. However, the intersecting points of the superposed contours are not only difficult to find but also incorrect to evaluate since the procedure mainly depends on men's eye.

To identify the location and depth of a crack in a structure, a method is presented in this paper which uses optimization technique. A beam model constructed by finite element method is used to identify the parameters which are crack location and depth minimizing the difference between the frequencies of the parameter model and the measured frequencies.

2. INVERSE ANALYSIS METHOD

The inverse analysis is generally defined as identifying the parameter set $x^* \in X$ when the measured or reference data $y^* \in Y$ and direct mapping $\psi: X \rightarrow Y$ are known [6]. There are two main strategies for solving inverse problems. One is to solve a set of equations and the other is to directly find the minimum or maximum of a certain function. However, the former is worth noting the following difficulty: the inverse problem can always be defined as an abstract theoretical concept. In general, inverse function is a subset of original input, in fact such a subset could even be empty, so that the usual concept of "function" as a "one-to-one" injection breaks down. Generally, it is reasonable to solve the latter. Out of them, minimizing a least square criterion has been most widely used for identification.

In this approach, optimization techniques are used to find the input by adjusting them until the measured, or reference data match the corresponding data computed from parameter set in the least square fashion, i.e.,

$$\min f(x) \quad (1a)$$

with the cost function

$$f(x) = \sum_{i=1}^m k_i (y_i^* - \Psi_i(x))^2 \quad (1b)$$

where k_i is a weighting factor. Various calculus-based optimization techniques have been intensively used to solve this optimization problem.

3. STRUCTURE ANALYSIS

In the finite element model of the damaged structure, the effect of the crack on the behavior of the structure can be simulated through the introduction of the transfer matrices which are method for finding the stiffness matrix. A planar frame structure can be modeled using two-dimensional beam elements having 3 d.o.f. $(\delta_x, \delta_y, \theta_z)$ per node, that is, with extension and bending, in Fig. 1.

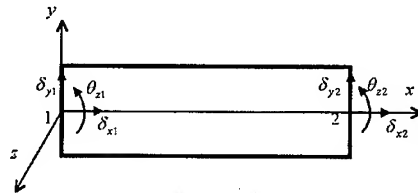


Fig. 1 A beam finite element with extension and bending d.o.f

The corresponding stiffness and consistent mass local matrices [7] are

$$[K_e] = \frac{EI}{L^3} \begin{bmatrix} 12 & 0 & 0 & -12 & 0 & 0 \\ 0 & 12 & 6L & 0 & -12 & 6L \\ 0 & 6L & 4L^2 & 0 & -6L & 2L^2 \\ -12 & 0 & 0 & 12 & 0 & 0 \\ 0 & -12 & -6L & 0 & 12 & -6L \\ 0 & 6L & 2L^2 & 0 & -6L & 4L^2 \end{bmatrix} \quad (2)$$

$$[M_e] = \frac{\rho AL}{420} \begin{bmatrix} 140 & 0 & 0 & 70 & 0 & 0 \\ 0 & 156 & 22L & 0 & 54 & -13L \\ 0 & 22L & 4L^2 & 0 & 13L & -3L^2 \\ 70 & 0 & 0 & 140 & 0 & 0 \\ 0 & 54 & 13L & 0 & 156 & -22L \\ 0 & -13L & -3L^2 & 0 & -22L & 4L^2 \end{bmatrix} \quad (3)$$

where $\beta = A/I_{xx}$, L is the length of element e , A is the cross section area, E and ρ are the modulus of elasticity and mass density, respectively, and I_{xx} is the second moment of inertia about the local z -axis.

From the Euler-Bernoulli theory for the above mentioned degrees of freedom, the transfer matrix [7], which transfers the state variables (displacement, force) from one node to the other node, is

$$[T_e] = \begin{bmatrix} 1 & 0 & 0 & \frac{-L}{AE} & 0 & 0 \\ 0 & 1 & L & 0 & \frac{L^3}{6EI_{xx}} & -\frac{L^2}{6EI_{xx}} \\ 0 & 0 & 1 & 0 & \frac{L^2}{2EI_{xx}} & \frac{L}{EI_{xx}} \\ 0 & 0 & 0 & -1 & 0 & 0 \\ 0 & 0 & 0 & 0 & -1 & 0 \\ 0 & 0 & 0 & 0 & L & -1 \end{bmatrix} \quad (4)$$

A beam finite element of length L_e , containing a crack of depth α at distance L_{ie} from its left end, is depicted in Fig. 2.

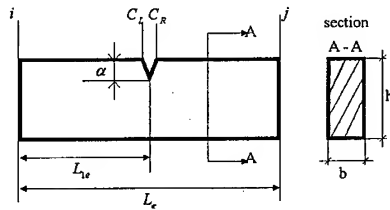


Fig. 2 A cracked beam finite element

The crack introduces a local compliance in the structure. The state vectors at positions i, C_L, C_R and j are

$$\{z_i\} = \{\delta_{xi} \quad \delta_{yi} \quad \theta_{zi} \quad F_{xi} \quad F_{yi} \quad M_{zi}\}^T \quad (5a)$$

$$\{z_L\} = \{\delta_{xL} \quad \delta_{yL} \quad \theta_{zL} \quad F_{xL} \quad F_{yL} \quad M_{zL}\}^T \quad (5b)$$

$$\{z_R\} = \{\delta_{xR} \quad \delta_{yR} \quad \theta_{zR} \quad F_{xR} \quad F_{yR} \quad M_{zR}\}^T \quad (5c)$$

$$\{z_j\} = \{\delta_{xj} \quad \delta_{yj} \quad \theta_{zj} \quad F_{xj} \quad F_{yj} \quad M_{zj}\}^T \quad (5d)$$

If no force is acting between nodes i and j , then it can be derived from simple beam theory, where the four state vectors are related as follows:

$$\{z_L\} = [T_1]\{z_i\} \quad (6a)$$

$$\{z_R\} = [T_C]\{z_L\} \quad (6b)$$

$$\{z_j\} = [T_2]\{z_R\} \quad (6c)$$

where $[T_1]$ and $[T_2]$ are the transfer matrices of the subelements C_L-i and C_R-j , respectively and $[T_C]$ is the point transfer matrix due to the crack. Matrix $[T_C]$, which relates the state vectors on the left and right of the crack, is

$$[T_c] = \begin{bmatrix} 1 & 0 & 0 & c_{11} & 0 & c_{13} \\ 0 & 1 & L & 0 & c_{22} & 0 \\ 0 & 0 & 1 & c_{31} & 0 & c_{33} \\ 0 & 0 & 0 & -1 & 0 & 0 \\ 0 & 0 & 0 & 0 & -1 & 0 \\ 0 & 0 & 0 & 0 & 0 & -1 \end{bmatrix} \quad (7)$$

where subscripts 1, 2 and 3 correspond to tension, shear and bending, respectively. Terms c_{13} and c_{31} , responsible for the coupling of tension and bending[8], are not considered here, whereas the rest are known as follows[9]:

$$c_{11} = \frac{2\Phi_1}{E(1-\nu^2)b} \quad (8a)$$

$$c_{22} = \frac{2k^2\Phi_3}{E(1-\nu^2)b} \quad (8b)$$

$$c_{33} = \frac{72\Phi_2}{E(1-\nu^2)bh^2} \quad (8c)$$

where ν is Poisson's ratio, k is a constant which for rectangular cross sections is known to be 1.5 and Φ_i are functions of the nondimensional crack depth α/h [9]. These functions, which are presented in Fig. 3, are integrals of the empirical formulas used by Tada[10] for computation of stress intensity factors K_I in single edge notch specimens under pure tension, bending and shear.

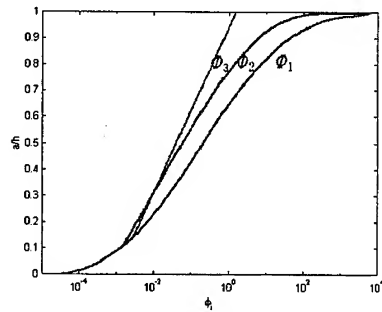


Fig. 3 Φ_i vs α/h for single edge notch specimen under pure tension, bending and shear

From equation(6a-c) the following is obtained:

$$\{z_j\} = [T_c^c] \{z_i\} \quad (9)$$

The transfer matrix $[T_c^c]$ of the cracked element is written in the form

$$[T_c^c] = [T_2][T_c][T_1] = \begin{bmatrix} A_1 & A_2 \\ A_3 & A_4 \end{bmatrix} \quad (10)$$

where $[A_i]$ are 3×3 submatrices. Equation (10) leads to the stiffness matrix of the crack element:

$$[K_c^c] = \begin{bmatrix} -[A_2]^T[A_1] & [A_2]^T \\ [A_3] - [A_4][A_2]^{-1}[A_1] & [A_4][A_2]^{-1} \end{bmatrix} \quad (11)$$

4. PROBLEM DEFINITION

The clamped-free beam of Fig.4 has a length of $L=3m$, rectangular cross section $B \times H = 0.2m \times 0.2m$ and contains a crack of depth α at a distance L_1 from the clamped end. The material properties are $E = 2.07 \times 10^{11} \text{ Nm}^{-2}$, $\nu = 0.3$, and $\rho = 7700 \text{ kgm}^{-3}$. The beam is discretized into 12 two-node finite elements.

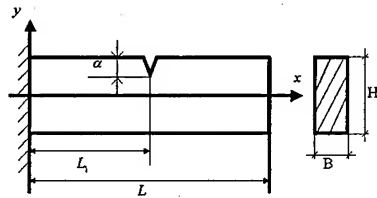


Fig. 4 Model of the cracked clamped-free beam

The equation of motion in matrix form is known to be

$$(-\omega^2[M] + [K])\{x\} = \{0\} \quad (12)$$

where ω is eigenfrequency, x is a displacement vector. The above analysis serves to identify the location and depth of a crack in a plane structure, just by measuring the eigenfrequency variations.

Using the results of the previous section, one can construct crack identification in the format of an optimization problem. The objective function for the optimization to be minimized is defined as follows:

$$\begin{aligned} \min_{\alpha, L_1} F(\alpha, L_1) &= (f_1 - f_1^*)^2 + (f_2 - f_2^*)^2 + (f_3 - f_3^*)^2 \\ 0.01 &\leq \alpha \leq 0.1, 0.1 \leq L_1 \leq 2.9 \end{aligned} \quad (13)$$

where α is the depth of a crack; L_1 is the distance from the clamped end; f_1, f_2, f_3 are the first three eigenfrequencies which are functions of α and L_1 ; and f_1^*, f_2^*, f_3^* are the first three measured, or reference eigenfrequencies.

The main target is to identify the parameters which are crack location and depth minimizing the difference between the frequencies of the parameter model and the measured frequencies.

The method of optimization is the augmented lagrange multiplier method. This method includes the conditions for optimality into the optimization algorithm in order to improve its efficiency and reliability. The method of search direction is Broydon-Fletcher-Goldfarb-Shanno variable metric method and one dimensional search method is polynomial interpolation[11].

5. RESULTS

A cracked clamped-free beam of Fig. 4 is adopted as an example problem, two cases are considered. (I) A crack of depth α of 0.01m exists at L_1 of 0.7m. The first three eigenfrequencies are obtained computationally based on the theory described in chapter 3: $f_1^* = 114.49 \text{ rad/s}$, $f_2^* = 717.27 \text{ rad/s}$, $f_3^* = 2007.49 \text{ rad/s}$. (II) A crack of depth α of 0.03m exists at L_1 of 2.3m. The first three eigenfrequencies are obtained computationally; $f_1^* = 114.65 \text{ rad/s}$, $f_2^* = 713.53 \text{ rad/s}$, $f_3^* = 1977.09 \text{ rad/s}$.

Table 1 Final Analysis Result

	CASE I			CASE II		
	Reference value	Result value	Relative error(%)	Reference value	Result value	Relative error(%)
$\alpha(m)$	0.01	0.0095	-5	0.03	0.0302	0.667
$L_1(m)$	0.7	0.7183	2.61	2.3	2.3109	0.474
$f_1(\text{rad/s})$	114.49	114.52	0.026	114.65	114.65	0
$f_2(\text{rad/s})$	717.27	717.26	-0.001	713.53	713.31	-0.029
$f_3(\text{rad/s})$	2007.49	2007.50	0	1977.09	1977.10	0
Final obj value	-	0.0008	-	-	0.0278	-

The result of table 1 shows that the location and depth of a crack are estimated by the optimization technique within 5% error. Also, the corresponding eigenfrequencies are very close to the reference values within 0.03% error.

6. CONCLUSIONS

A methodology of optimization technique for the crack identification from the eigenfrequencies is proposed based on the fact that a crack has an important effect on the dynamic behavior of a structure. To estimate the crack parameters optimization technique and finite element method are combined into the proposed technique. The finite element method is for the approximation of the eigenfrequencies as the functions of the crack parameters and the optimization technique is for finding crack parameters which minimize the difference from the measured eigenfrequencies.

The effectiveness of this technique is confirmed by example problem. The crack parameters of the clamped-free beam problem are estimated within small error. It can be concluded that good agreements are obtained between the estimated crack depth and location and the reference ones.

The optimization technique can be generalized for general boundary condition and structure to estimate the crack location and depth provided that the reference data are properly prepared.

ACKNOWLEDGEMENTS

The authors are grateful for the support provided by a grant from the Korea Science & Engineering Foundation(KOSEF) and Safety and Structural Integrity Research Center at the Sungkyunkwan University.

REFERENCES

1. T. Inagaki, H. Kanki and K. Shiraki, *J. Mechanical Design*, **104** (1981) p.1-11.
2. P. S. Leung, *Rotordynamics'92. Int. Conf. on Rotating Machine Dynamics*, Italy, Venice(1992) p.59-67.
3. N. Anifantis, P. Rizos and A. D. Dimarogonas, *11th Biennial ASME Conf. on Mechanical Vibration and Noise*, U.S.A., Boston(1987).
4. A. D. Dimarogonas and G. Massouros, *Engng. Fracture Mech.*, **15** (1981) p.439-444.
5. H. G. Nikolakopoulos, D. E. Katsareas and C. A. Papadopoulos, *Computer & Structures*, **64** (1997) p.389-406.
6. S. Kubo, *Inverse Problem*, Baifu-kan, Tokyo(1993).
7. Walter D. Pilkey, *Mech. of structures variational and computational methods*, Walter Wunderlich, CRC Press(1994).
8. G. D. Gounaris and A. D. Dimarogonas, *Computational Structure*, **28** (1988) p.309-313.
9. C. A. Papadopoulos and A. D. Dimarogonas, *J. Vibr. Acoust. Stress Reliab. Design*, **110**(1988) p.1-8.
10. H. Tada, *The Stress Analysis of Cracks Handbook*, Del Research Co. PA(1973).
11. G. N. Vanderplaats, *Numerical optimization techniques for engineering design with applications*, McGraw-Hill international editions(1993).

Study on Strength of Rock Material under Dynamic Triaxial Compressive Loads Based on Sliding Crack Model

H.B. Li¹, T.J. Li¹, J. Zhao², J.G. Gao¹ and J.G. Jiang¹

¹ Institute of Rock & Soil Mechanics, The Chinese Academy of Sciences,
430071 Wuhan, China P.R.

² School of Civil and Structural Engineering, Nanyang Technological University,
Nanyang Avenue, Nanyang 639798, Singapore

Keywords: Dynamic Triaxial Compressive Loads, Rock Material, Sliding Crack Model, Strength

ABSTRACT

Sliding crack model is employed to simulate the strength of rock material under dynamic triaxial compressive loads. Stress intensity factor of crack array considered is estimated by pseudo-traction method. A dynamic crack growth criterion is used in the analysis. The simulated strengths of a granite obtained by the sliding crack model agree with the experimental results.

1. INTRODUCTION

Strength of rock material under dynamic triaxial compressive loads is one of the important parameters in assessing stability of rock cavern under dynamic loads induced from blasting excavation or earthquake. Researches on this topic are mainly through experimental studies [1-2]. Those studies indicate that the compressive strength of rock material generally increases with increasing strain rate and confining pressure.

After 1980s, with the utilisation of scanning electron microscope (SEM) equipment, useful works have been conducted to microscopically investigate failure process of brittle rock material under compression. These works indicated that the dominant failure mechanism of brittle rock materials is the growth and nucleation of the pre-existing microcracks under compression.

Based on those works, various mathematical crack models, such as cylindrical pore model, dislocation pile-up model and sliding crack model, have been introduced in an effort to simulate the failure process and the macroscopic mechanical properties of rock materials under compression. The primary difference of these models is the formation of tensile cracks. For instance, for sliding crack model, the tensile crack is due to the sliding of pre-existing crack, while for the cylindrical pore model, tensile crack is due to stress concentration around pores. Among these models, sliding crack model is widely accepted.

In the present paper, the emphasis is to simulate the strength of rock material under dynamic triaxial compressive loads using sliding crack model. The simulated results for a granite are further compared to the experimental results.

2. SLIDING CRACK MODEL

The sliding crack model, as shown in Figure 1, was first proposed by Brace and Bombolakis [3], as a mechanism to study non-elastic dilation of rock materials under compression (axial compressive stress σ_1 and lateral compressive stress σ_2). It contains an initial crack, at length of $2c$, oriented at an angle θ with respect to σ_1 direction, and a pair of tensile cracks. The tensile cracks are caused by the sliding of initial crack under compressive loads.

In order to model the shear failure of rock material under triaxial compressive loads, an array of sliding cracks, as shown in Fig.1, is presented in the present analysis. In Fig.1, the axis of the sliding crack array lies an angle α to the direction of axial stress. The spacing between two cracks is $2w$.

Similar to the works by [5-7], Fig. 1 can be simplified and decomposed as crack configuration in Fig. 2(a) and (b). In Fig.2 (a), an array of tensile cracks, at length of $2l$, and crack spacing of $2w$, respectively, are loaded at its centre to a pair of splitting forces F . The forces F represent the effect on the tensile crack of the initial crack's sliding. When cohesive stress is neglected, F can be estimated by:

$$F = 2c\tau^* \text{ and } \tau^* = \frac{1}{2}(\sigma_1 - \sigma_2)\sin 2\theta - \frac{1}{2}\mu[\sigma_1 + \sigma_2 - (\sigma_1 - \sigma_2)\cos 2\theta] \quad (1)$$

where μ is the frictional coefficient of crack faces.

In Fig.2 (b), an array of tensile cracks are subjected to axial stress (σ_1) and confining pressure (σ_2).

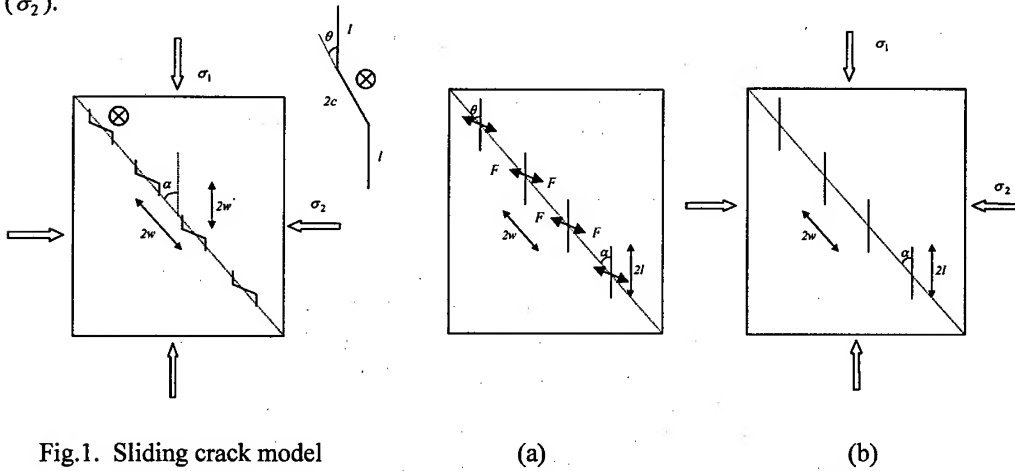


Fig.1. Sliding crack model

(a) (b)
Fig.2. Decomposition of Fig.1.

3. PSEUDO-TRACTION METHOD AND STRESS INTENSITY FACTOR DETERMINATION

Pseudo-traction method is used to calculate the stress intensity factor of crack array in Fig 2(a) and 2(b). The method is first presented by Horri & Nemat-Nasser [7] to study crack interaction.

Consider an elastic solid containing two cracks, as shown in Fig. 3(a). Each crack is loaded at its centre to a pair of normal forces P^1 and P^2 , as well as shear forces Q^1 and Q^2 . By the pseudo-traction method, the original problem in Fig. 3(a) can be decomposed into two subproblems, as shown in Fig. 3(b). In each subproblem, an elastic body contains only one crack. The crack is loaded by P^i and Q^i ($i=1,2$), as well as unknown pseudo tractions σ^{pi} and τ^{pi} ($i=1,2$), which are induced from the near crack.

The pseudo tractions can be expanded into Taylor series as [7,8]:

$$\sigma^{pj} - i\tau^{pj} = \sum_{n=0}^{\infty} (\sigma_n^{pj} - i\tau_n^{pj}) (x^j / l^j)^n \quad (j=1,2) \quad (2)$$

where n is the term of Taylor series, σ_n^{pj} and τ_n^{pj} are n term components of pseudo tractions.

The stress intensity factor of the crack array in Fig. 3(a) can then be calculated as:

$$K_I^j = \sqrt{\pi l^j} \left(\frac{P^j}{\pi l^j} + \sum_{k=0}^{\infty} 2g_k \sigma_{2k}^{pj} \pm \sum_{k=1}^{\infty} 2g_k \sigma_{2k-1}^{pj} \right) \quad (j=1,2) \quad (3)$$

Considering crack array in Fig. 2(a), as pseudo tractions on each crack are symmetric, it is easy to obtain [7,8]:

$$\sigma_{2n-1}^{pk} = \tau_{2n-1}^{pk} = 0, \quad (n=1,2,\dots,N; \quad k=0,\pm 1,\pm 2,\dots,\pm \infty) \quad (4)$$

In addition, as a result of periodicity, the pseudo tractions in each crack are identical. Therefore, if we consider $2M+1$ cracks in Fig. 2(a), $2N$ term approximation of pseudo tractions are given by [7,8]:

$$\begin{aligned} \sigma_{2n}^p &= \sum_{m=0}^N \left\{ \left(2 \sum_{k=1}^M A_{2n2m} \right) \sigma_{2m}^p + \left(2 \sum_{j=1}^M B_{2n2m} \right) \tau_{2m}^p \right\} + \left(2 \sum_{k=1}^M E_{2n} \right) P + \left(2 \sum_{j=1}^M F_{2n} \right) Q \\ \tau_{2n}^p &= \sum_{m=0}^N \left\{ \left(2 \sum_{k=1}^M B_{2n2m} \right) \sigma_{2m}^p + \left(2 \sum_{j=1}^M D_{2n2m} \right) \tau_{2m}^p \right\} + \left(2 \sum_{k=1}^M F_{2n} \right) P + \left(2 \sum_{j=1}^M H_{2n} \right) Q \end{aligned} \quad (5)$$

where, $P = F \sin \theta$ $Q = F \cos \theta$. The definition of, A_{2n2m} B_{2n2m} , etc., can be referenced to [8].

According to Equation (3), the stress intensity factor of crack array in Fig. 2(a) is:

$$K_I^{\text{array}} = \frac{1}{\sqrt{\pi l}} \left(P + \sum_{k=0}^{\infty} 2g_k \sigma_{2k}^p \right) \quad (6)$$

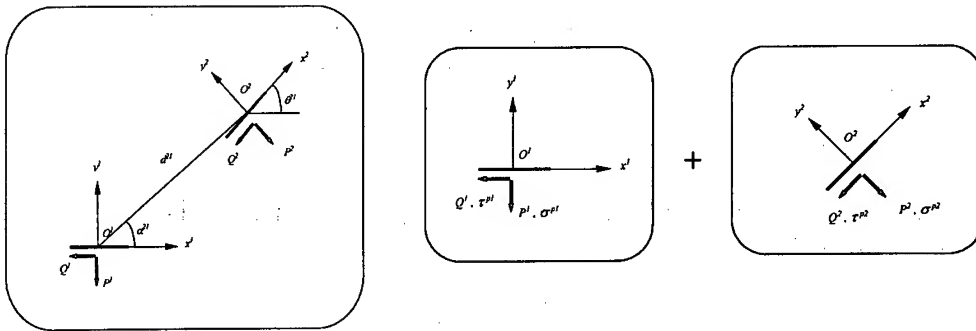


Fig.3. (a): A elastic body containing two cracks; (b): Two subproblems of Fig 3(a)[8]

Similarly, considering the crack array containing $2M+1$ cracks in Fig. 2(b), $2N$ term of pseudo tractions are given by [7,8]:

$$\begin{aligned}\sigma_{2n}^p &= \sum_{m=0}^N \left\{ \left(2 \sum_{k=1}^M A_{2n2m} \right) \sigma_{2m}^p + \left(2 \sum_{j=1}^M B_{2n2m} \right) \tau_{2m}^p \right\} + \left(2 \sum_{k=1}^M A_{2n0} \right) \sigma_2 \\ \tau_{2n}^p &= \sum_{m=0}^N \left\{ \left(2 \sum_{k=1}^M B_{2n2m} \right) \sigma_{2m}^p + \left(2 \sum_{j=1}^M D_{2n2m} \right) \tau_{2m}^p \right\} + \left(2 \sum_{k=1}^M B_{2n0} \right) \sigma_2\end{aligned}\quad (7)$$

The mode I stress intensity factor of crack array in Fig. 2(b) is then given by:

$$K_I^{array} = \sqrt{\pi l} \left(\sigma_2 + \sum_{k=1}^{\infty} 2g_k \sigma_{2k}^p \right) \quad (8)$$

In the present paper, for the simplicity, we only consider 2 ($N=1$) term of pseudo traction, and neglect pseudo traction components containing terms of orders higher than $(l/w)^2$, the stress intensity factor of crack array in Fig. 1 can then be expressed as:

$$K_I^{array} = \frac{1}{\sqrt{\pi(l+l^*)}} \left(\frac{1 - 2 \sum_{k=1}^M A_{00} + 2 \sum_{k=1}^M E_0 + 2 \sum_{k=1}^M F_0 \cotg \theta}{1 - 2 \sum_{k=1}^M A_{00}} \right) P - \frac{1}{1 - 2 \sum_{k=1}^M A_{00}} \sigma_2 \sqrt{\pi l} \quad (9)$$

where $l^* = 0.27c$, which ensure the validity of Equation (9) when the tensile crack length is very small [11].

Further analysis based on sliding crack model indicated that when the angle α is about $20^\circ \sim 30^\circ$, the crack interaction coefficients reach the maximum value. This implies that the failure plane of rock material under triaxial compressive loads will be along this direction. These results agree with the experimental observation reported by Zhao et al [4], where they investigated that the granite rock mostly failed at an angle of $20^\circ \sim 30^\circ$ with respect to the direction of axial stress. Therefore, in the present analysis, we assume $\alpha = 20^\circ$, we further assume $\theta = 45^\circ$ as the work by Kemeny [5], the stress intensity factor of crack array in Fig. 1 is then given by:

$$K_I^{array} = \frac{1}{\sqrt{\pi(l+l^*)}} \left[\frac{1 + 0.84 \left(\frac{l}{w} \right)^2}{1 - 0.56 \left(\frac{l}{w} \right)^2} \right] P - \frac{\sigma_2 \sqrt{\pi l}}{1 - 0.56 \left(\frac{l}{w} \right)^2} \quad (10)$$

4. SIMULATED RESULTS

According to [6], crack growth criterion of crack array in Fig. 1 under dynamic compressive loads can be described as:

$$\frac{v_r - v}{v_r - 0.75v} \frac{1}{\sqrt{\pi(l+l^*)}} \left[\frac{1 + 0.84 \left(\frac{l}{w} \right)^2}{1 - 0.56 \left(\frac{l}{w} \right)^2} \right] P - \frac{v_r - v}{v_r - 0.5v} \frac{\sigma_2 \sqrt{\pi l}}{1 - 0.56 \left(\frac{l}{w} \right)^2} = K_{IC}' \quad (11)$$

where K_{IC}^d is the dynamic toughness for rock material. v is the crack growth velocity, and v_r is the critical crack growth velocity, which is normally regarded as the Rayleigh wave speed in the material.

In Equation (11), note that $v = dl/dt$, the Equation can be integrated using four-order Runge-Kutta method. As a result, the simulated strength of rock material can be determined.

Fig. 4 plots the change of simulated strength of a granite with strain rate ranging from 10^{-4} to 10^0 s^{-1} , under confining pressures of 20, 50 and 80 MPa. It is shown that the simulated strengths generally increase with increasing strain rate and the rising rate decrease with increasing confining pressure. The simulated results are consistent with the experimental results reported by Li et al [10].

The simulated strengths of granite increase with the increasing confining pressures, as shown in Fig. 5. The changing rates of strengths with confining pressure are almost identical at different strain rates. Again, the simulated results obtained from sliding crack model are consistent with experimental results.

5. CONCLUSIONS

Sliding crack model is available to simulated study the strength of rock material under dynamic triaxial compressive loads. The simulated results agree with the experimental results. The model also predicts the shear failure mode and orientation of rock material under triaxial compressive loads. It can be further concluded from crack growth criterion, Equation (11), that the crack growth velocity and the rate dependence of rock material result in the strength's increment of rock material with increasing strain rate. In addition, the impediment of confining pressure on the growth of sliding crack cause the increment of compressive strength with increasing confining pressure.

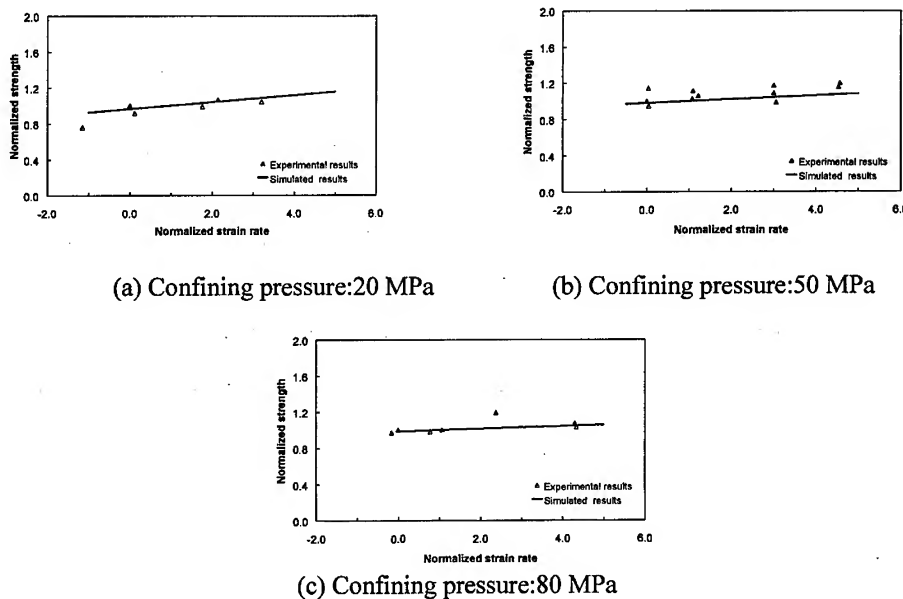


Fig. 4. Change of strength with strain rate under different confining pressures (simulated and experimental results; strain rate is normalised by the minimum strain rate and strength is normalised by the strength at the minimum strain rate)

6. REFERENCES

1. F.A.Donath and L.S.Fruth. Dependence of strain-rate effects on deformation mechanism and rock type. *J. Geol. Soc.*, **79** (1971) 347-371.
2. K. Masuda, H. Mizutani and I.Yamada. Experimental study of strain-rate dependence and pressure dependence of failure properties of granite. *J.Phys.Earth.*, **35** (1987) 37-66.
3. W.F.Brace and E.G.Bombolakis. A note on brittle crack growth in compression. *J. Geophys. Res.*, **68** (1963) 3709-3713.
4. J. Zhao, H.B.Li and Y.H.Zhao. Dynamic strength tests of the Bukit Timah granite. Geotechnical Research Report NTU/GT/98-2, Nanyang Technological University, Singapore, (1998).
5. J.M.Kemeny. A model for non-linear rock deformation under compression due to sub-critical crack growth. *Int. J. Rock. Mech. Min. Sci.*, **28(6)** (1991) 459-467.
6. S. Nemat-Nasser and H. Deng. Strain-rate effect on brittle failure in compression. *Acta Metal Materials.*, **42(3)** (1994) 1013-1024.
7. H. Horii and S. Nemat-Nasser. Elastic fields of interaction inhomogeneties. *Int. J. Solids Structures.*, **21(7)** (1985) 731-745.
8. H. Deng and S. Nemat-Nasser. Microcrack interaction and shear fault failure. *Int. J. Damage Mech.*, **3** (1994) 3-37.
9. H.Horri and S. Nemat-Nasser. Brittle failure in compression: splitting, faulting, and brittle-ductile transition. *Phil. Trans. Royal. Soc. London.*, **319** (1986) 337-374
10. H.B Li, J. Zhao and T.J.Li. Triaxial compression tests of a granite at different strain rates and confining pressures. *Int. J. Rock. Mech. Min. Sci.*, **36(8)** (1999) 1057-1063.

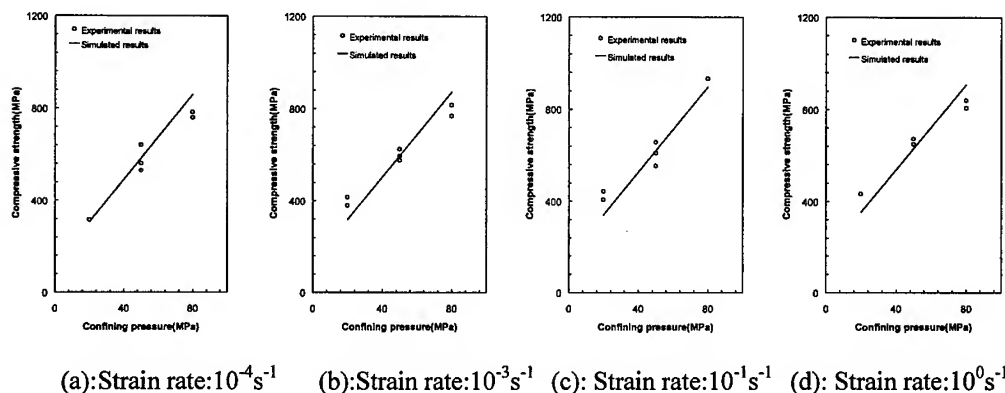


Fig.5. Change of strength with confining pressures under different strain rates (experimental and simulated results)

Kinking out of a Mixed Mode Interface Crack

T. Ikeda¹, Y. Komohara², A. Nakamura³ and N. Miyazaki¹

¹ Department of Material Process Engineering, Kyushu University,
 6-10-1 Hakozaki, Higashi-ku, Fukuoka 812-8581, Japan

² Nippon Mektron, Ltd., 1-12-15 Shiba-Daimon, Minato-ku, Tokyo 105-0012, Japan

³ Yodogawa Steel Works Ltd., Yodoko Build., 4-1-1 Minami Honmachi,
 Cyuo-ku, Osaka 541-0054, Japan

Keywords: Crack Kinking, Fracture Toughness, Interface Crack, Mixed Mode, Residual Stress

ABSTRACT

In this study we focus on the mixed mode fracture toughness and the kink angle of an interface crack. We measure residual stress and perform mixed mode fracture tests for three types of interface crack. Each mixed mode fracture toughness including residual stress is successfully described by stress intensity factors K_I and K_{II} for each interface crack. The kink angle of each interface crack also can be expected by the stress intensity factors using the modified maximum hoop stress criterion.

1. STRESS INTENSITY FACTORS AND CRACK KINKING OF AN INTERFACE CRACK

1.1 Stress Intensity Factors of an Interface Crack

The asymptotic solution of the stress distribution around an interface crack as shown in Fig. 1 was proposed by Erdogan [1]. The stress along the x -axis is shown as

$$(\sigma_{yy} + i\sigma_{xy})_{\theta=0} = \frac{K_I + iK_{II}}{\sqrt{2\pi r}} \left(\frac{r}{l_k}\right)^{\epsilon} \quad (1)$$

$$\alpha = \frac{\mu_1(\kappa_2 + 1) - \mu_2(\kappa_1 + 1)}{\mu_1(\kappa_2 + 1) + \mu_2(\kappa_1 + 1)}, \quad \beta = \frac{\mu_1(\kappa_2 - 1) - \mu_2(\kappa_1 - 1)}{\mu_1(\kappa_2 + 1) + \mu_2(\kappa_1 + 1)} \quad (2)$$

$$\epsilon = (1/2\pi) \ln(1 - \beta/1 + \beta) \quad (3)$$

$$\begin{cases} \kappa_i = 3 - 4\nu_i & (\text{Plane strain}) \\ \kappa_i = (3 - \nu_i) / (1 + \nu_i) & (\text{Plane stress}) \end{cases} \quad (4)$$

where α and β are Dundurs's parameters [2], ϵ is the bimaterial constant, and μ_1, μ_2, ν_1 and ν_2 are shear moduli and Poisson's ratios for respective materials. σ_{yy} and σ_{xy} are stresses, K_I and K_{II} are the stress intensity factors (SIF) for respective mode and i is the complex number ($i^2 = -1$). l is an arbitrary characteristic number. Argument of the stress in Eq. (1) is shown as

$$\arg(\sigma_{yy} + i\sigma_{xy}) = \gamma + \epsilon \ln\left(\frac{r}{l_k}\right) \quad (5)$$

γ is argument of the complex stress intensity factor $K_I + iK_{II}$ which is defined as Fig. 2 and

$$\gamma = \text{sign}(K_{II}) \cos^{-1}\left(\frac{K_I}{K_i}\right) \quad (-\pi < \gamma < \pi), \quad (6)$$

$$\text{sign}(K_{II}) = 1 \quad (K_{II} \geq 0), \quad = -1 \quad (K_{II} < 0), \quad (7)$$

where K_i is $K_i = \sqrt{K_I^2 + K_{II}^2}$. γ is easily transformed for another value of $l_k = l'_k$ [3].

$$\gamma' = \gamma + \epsilon \ln(l_k/l'_k) \quad (8)$$

It is obvious by Eq. (5) that σ_{xy}/σ_{yy} on x -axis corresponds to K_{II}/K_I at $r = l_k$. In other words, K_{II}/K_I characterizes the ratio of shear stress and normal stress, σ_{xy}/σ_{yy} , at $r = l_k$. It is difficult to decide the suitable length of l_k . However, it is obvious that we should use a fixed value for l_k , because a set of K_I and K_{II} cannot express unique stress field around a crack tip for different lengths of l_k . Rice [4] recommended to select the length of l_k to be $1\mu\text{m}$.

1.2 Crack Kinking Angle

He *et al.* [5, 6] proposed the maximum energy release rate criterion for an interface crack between dissimilar materials. They analytically obtained the kinking angle based on this model for an interface crack between dissimilar materials whose Dundurs parameter β in Eq. (2) is zero. The combination of materials whose β is zero is limited to the combination of similar materials. Geubelle and Knauss⁽⁸⁾

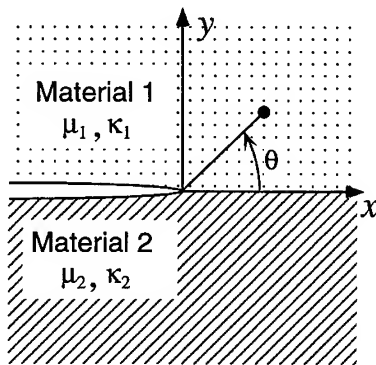


Fig. 1 Coordinates system around an interface crack tip.

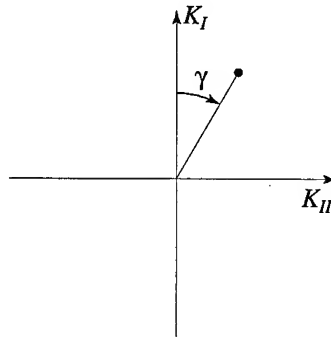


Fig. 2 Definition of γ on the K_I - K_{II} field.

applied the maximum energy release rate criterion to an interface crack between dissimilar materials whose β is not zero using the finite element method. They slightly extended the crack with different kinking angle, and obtained the energy release for each angle. The crack kinking angle expected by this theory depends on the crack extension length.

On the other hand, Yuki and Xu [8] proposed the maximum hoop stress criterion. The distribution of hoop stress $\sigma_{\theta\theta}$ around an interface crack as shown in Fig. 1

$$\sigma_{\theta\theta j} = \frac{\sqrt{K_I^2 + K_{II}^2}}{2\sqrt{2\pi r} \cosh(\epsilon\pi)} [B \cos \psi - C \sin \psi] \quad (j=1, 2) \quad (9)$$

$$\psi = \epsilon \ln(r/l_k) \quad (10)$$

where $\sigma_{\theta\theta j}$ is hoop stress in the area of material j , the functions B and C are given as

$$B(\theta, \epsilon, \gamma) = W_j \left[2 \cos \left(\frac{\theta}{2} + \gamma \right) - (\cos \theta + 2\epsilon \sin \theta) \cos \left(\frac{\theta}{2} - \gamma \right) \right] + \frac{1}{W_j} \cos \left(\frac{3}{2}\theta + \gamma \right) \quad (11)$$

$$C(\theta, \epsilon, \gamma) = W_j \left[2 \sin \left(\frac{\theta}{2} + \gamma \right) + (\cos \theta + 2\epsilon \sin \theta) \sin \left(\frac{\theta}{2} - \gamma \right) \right] + \frac{1}{W_j} \sin \left(\frac{3}{2}\theta + \gamma \right) \quad (12)$$

$$W_1 = e^{-\epsilon(\pi-\theta)}, \quad W_2 = e^{\epsilon(\pi-\theta)} \quad (13)$$

They simplified Eq. (9) by assuming $\Psi=0$ because of the small value of ϵ .

$$\sigma_{\theta\theta j} = \frac{\sqrt{K_I^2 + K_{II}^2}}{2\sqrt{2\pi r} \cosh(\epsilon\pi)} B(\theta, \epsilon, \gamma) \quad (14)$$

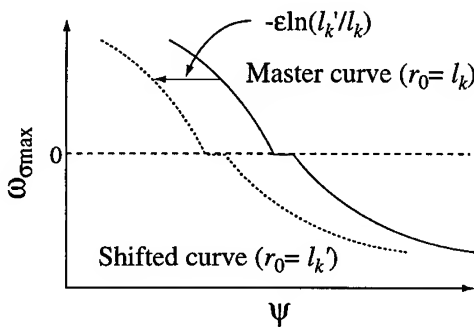


Fig. 3 Shift of the estimated kink angle with the value of r_0 .

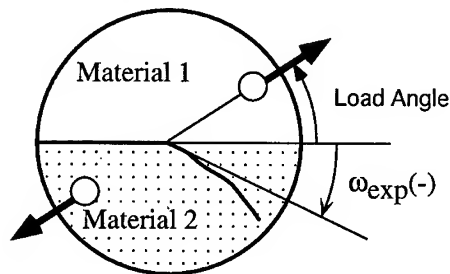


Fig. 4 Round shape mixed mode interface crack specimen and kink angle.
($t=12\text{mm}$ for case 1, 13mm for case 2 and 3).

$\sigma_{\theta\theta}$ takes maximum value if $\partial B / \partial \theta = 0$. However, the value of Ψ in Eq. (10) cannot be ignored even if ε is small, because the absolute value of $\ln(r/l_k)$ increases with decreasing r . For example, if $\varepsilon = -0.033$ and $r/l_k = 0.001$, $\cos\Psi$ and $\sin\Psi$ are equal to 0.974 and 0.228 respectively.

We modified maximum hoop stress criterion proposed by Yuuki and Xu [8]. An interface crack kinks out in the direction of maximum hoop stress at some fixed distance, r_0 , from a crack tip. The direction of maximum hoop stress can be obtained easily if $r_0 = l_k$ because Ψ takes zero at $r = l_k$. According to this theory, the expected crack kinking angle $\omega_{\sigma\max}$ for $r_0 = l_k$ can be illustrated as 'master curve' in Fig. 3. The angle $\omega_{\sigma\max}$ for another r_0 , $r_0 = l'_k$, can be obtained by shifting the master curve by $\Delta\gamma = -\varepsilon \ln(l'_k/l_k)$ according to Eq. (8) as Fig. 3.

2. MIXED MODE FRACTURE TESTS OF INTERFACE CRACKS

Fracture tests were performed using round shapespecimens with mixed mode interface crack as shown in Fig. 4. Two combinations of materials, Aluminum - Epoxy resin A (Combination 1) and Aluminum - Epoxy resin B (Combination 2) were used for these specimens. Material properties of Aluminum, Epoxy resin A and Epoxy resin B are given in Table 1. A semicircular aluminum plate was set in a circular shape cast, then epoxy resin was pored into the cast. The cast was kept at 120°C for 16 hours to cure the resin. The splicing surface of an aluminum plate was roughened by a piece of emery paper beforehand and release agent was applied on a part of the surface for making an interface crack.

Residual stress along a jointed interface is sometimes very great. We evaluated the residual stress by measuring the released strain, $\Delta\varepsilon_r$, of the end notched joint specimen at the delamination. The released strain, $\Delta\varepsilon_r$, was measured by a strain gauge attached to the surface of a specimen as shown in Fig. 5. The relative expansion ratio, $\Delta\beta_{\exp.}$, between material 1 and 2 is expected by the beam theory. The SIF's of a round shape specimen caused by residual stress were calculated from $\Delta\beta_{\exp.}$ by the virtual crack extension method (VCEM) with the finite element method (FEM) which developed in the previous study [9]. They are indicated in Table 2 for Combination 1 and Combination 2.

Mixed mode fracture tests were performed using the round shape specimens as shown in Fig. 4 and a universal testing machine (Shimazu Autograph). The load angles in Fig. 4 were selected as 30 deg., 60 deg., 90 deg., 120deg. and 150 deg. The rate of displacement was 1mm/min for all cases. The fracture load was determined as maximum load because the fracture modes of all specimens were brittle. The actual SIF's at the fracture can be obtained from the fracture load and the relative expansion ratio, $\Delta\beta_{\exp.}$, using the VCEM [9]. The crack kinking angle was measured as the angle of the tangent

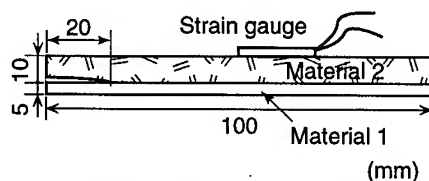


Fig. 5 End notched joint specimen for measuring residual stress.

Table 1 Material constants.

Material	Young's Modulus (GPa)	Poisson's Ratio
Aluminum	73.1	0.32
Resin A	3.35	0.43
Resin B	3.84	0.37

Table 2 Measured released strain and stress intensity factors caused by residual stress ($l_k = 10 \mu\text{m}$).

Case	$\Delta\epsilon_r$ (μstrain)	$\Delta\beta_{\text{exp}}$ (%)	K_I ($\text{MPa}\sqrt{\text{m}}$)	K_{II} ($\text{MPa}\sqrt{\text{m}}$)
Comb. 1	961	-0.105	0.214	-0.450
Comb. 2	381	-0.0421	0.117	-0.176

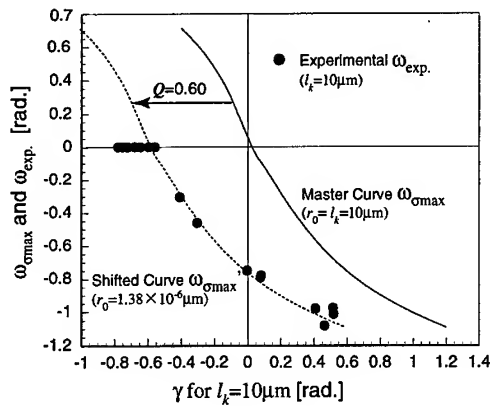


Fig. 6 Angle of crack kinking for Case 1.

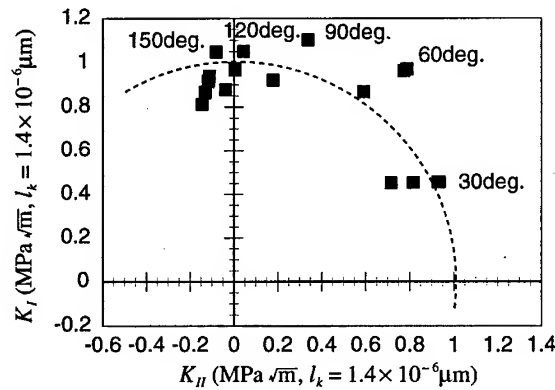
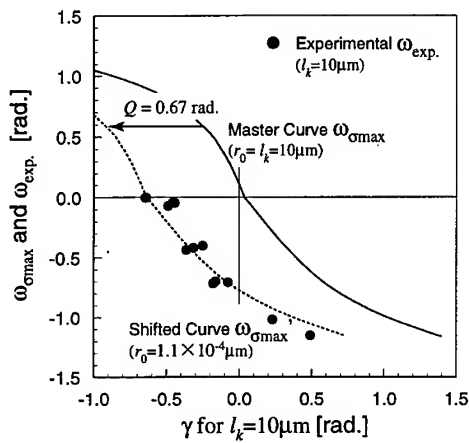
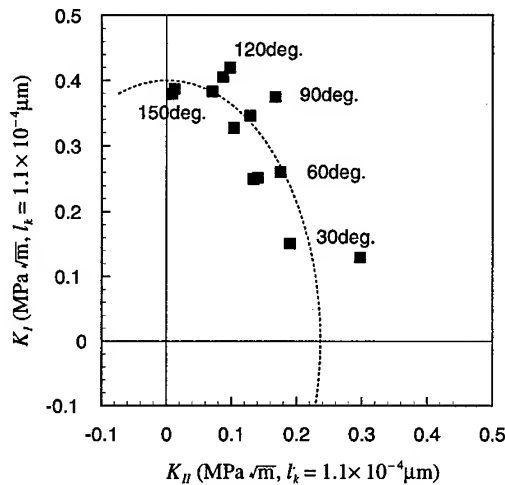
Fig. 8 Mixed mode fracture toughness for Case 1 ($l_k = 1.4 \times 10^{-6} \mu\text{m}$).

Fig. 7 Angle of crack kinking for Case 2.

Fig. 9 Mixed mode fracture toughness for Case 2 ($l_k = 1.1 \times 10^{-4} \mu\text{m}$).

of an extended crack at the initial crack tip in Fig. 4. The crack kinking angles measured on the both sides of a specimen were averaged.

The measured crack kinking angles with the master curves and the shifted curves of expected crack kinking angles for the combination 1 and 2 are shown in Fig. 6 and Fig. 7 respectively. The master curves do not correspond well with the experimental data in both cases. However, each shifted curve fits the experimental data very well. The values of r_0 at which the shifted curves fit the experimental data best are $1.4 \times 10^{-6} \mu\text{m}$ and $1.1 \times 10^{-4} \mu\text{m}$ respectively. These values of r_0 for both combinations seem to be too small as real distances which characterize the crack kinking. We consider that the value of r_0 is a kind of fitting parameter. The mixed mode fracture toughness for both combinations are shown in Fig. 8 and Fig. 9 respectively. The values of l_k are taken as the same as the values of r_0 for the shifted curves in Fig. 6 and Fig. 7 respectively. In these figures, $K_{II} = 0$ corresponds to the crack kinking angle being zero (the crack extended along the interface). The curves of the mixed mode fracture toughness are described by elliptical curves as

$$\left(K_I/K_{IC}\right)^2 + \left(K_{II}/K_{IIC}\right)^2 = 1 \quad (15)$$

where K_{IC} and K_{IIC} are constants for a joint system.

3. CONCLUSION

- (1) The crack kinking angle of an interface crack between dissimilar materials is well described by the modified maximum hoop stress criterion.
- (2) The crack kinking angle fits well with the experimental data if the evaluation distance r_0 is taken as an appropriate value.
- (3) The mixed mode fracture toughness of an interface crack can be described by a elliptical curve if the value of l_k is taken as the value of r_0 which describes the crack kinking angle well.

REFERENCES

- [1] Erdogan, F., ASME J. Appl. Mech., **32** (1965) p. 403.
- [2] Dundurs, J., ASME J. Appl. Mech., **36** (1969) p. 650.
- [3] Wang, J. S. and Suo, Z., Acta Metall. Mater., **38-7** (1990) p. 1279.
- [4] J. R. Rice, Trans. ASME Series E, J. Appl. Mech., **55** (1988) p. 98.
- [5] He, M. Y. and Hutchinson, J. W., ASME J. Appl. Mech., **56** (1989) p. 270.
- [6] He, M. Y., Bartlett, A. *et al.*, J. Am. Ceram. Soc., **74-4** (1991) p. 767.
- [7] Geubelle, P. H. and Knauss, W. G., ASME J. Appl. Mech., **61** (1994) p. 560.
- [8] Yuuki, R. and Xu, J. Q., Eng. Frac. Mech., **41** (1992) p. 635.
- [9] Ikeda, T., Komohara, Y. and Miyazaki, N., Advances in Electronic Packaging, ASME EEP **19-2** (1998) p. 1137.

Global Crack-Line Displacement Fitting Procedure: Edge Cracks

H.Y. Jiang¹, Z.L. Li² and F.L. Zhan²

¹Department of Civil Engineering, Beijing Polytechnic University,
100 Pingleyuan, Chaoyang, Beijing 100022, China P.R.

²Solid Mechanics Research Center, Beijing University of Aeronautics and Astronautics,
37 Xueyuan Road, Haidian, Beijing 100083, China P.R.

Keywords: Edge Cracks, Global Displacement Fitting Procedure, Stress Intensity Factor

ABSTRACT

The Global Crack-line Displacement Fitting Procedure [1] to extract SIFs of internal cracks is extended for edge crack problems in this work. In the procedure, COD data of the edge crack are fully used, the numerical calculation only involves the displacement fields, and the error of the obtained SIF can be estimated from the error information of COD data in themselves. Reliable and well consistent SIFs are obtained for two typical edge crack problems, the accuracy of SIFs is in the same order of accuracy of the COD data.

1. INTRODUCTION

Although 1% to 5% accuracy of stress intensity factor (SIF) obtained by currently most used numerical methods may not be sufficient for some problems such as numerical simulation of fatigue crack growth. More accurate, efficient and reliable technique is needed. Local displacement field procedure is based on the asymptotic analysis of the CODs near a crack tip, the accuracy and consistency are not good[2-4]. It is natural to think that if the SIFs are extracted from the total COD data, the accuracy will be much better. The examples of this kind of method are path independent J -integral method, energy release rate method and self-similar crack expansion method [5]. Cooper et al. [4] compared various methods on a set of about forty basic test problems by using finite element analysis.

Recently, a new global crack-line displacement fitting procedure (GCDFP) to extract SIFs of internal cracks, was proposed by Li and Li [1]. In GCDFP, the total COD fields of an internal crack are expanded into an infinite series of Chebyshev functions of the second kind which have the correct asymptotic displacement behavior near both crack tips of the internal crack, and the SIFs can be expressed by the coefficients of the infinite series. The error of SIF is related to the errors of the coefficients of the series which can be obtained from the error distribution of the COD fields which should be known a priori for a meaningful COD data. By careful error analysis, the truncation number of the series can be determined by using the criterion of the minimum SIF error. The procedure has the following features. (1) Full COD data are used. (2) The numerical calculation only involves displacement fields. (3) The post processing is simple. (4) The procedure can be

easily applied to mixed mode crack problems with arbitrary crack shapes. And (5), the error of the calculated SIF can be estimated from the error information of COD data in themselves. Reliable, consistent and highly accurate SIFs are obtained for various internal crack problems. In this work, the GCDFP to extract internal crack SIFs is extended for edge crack problems.

2. GCDFP FOR A STRAIGHT EDGE CRACK

Let Δv be the COD component in the y direction of a straight edge crack ($0 \leq x \leq a$). In reference [1], the COD components of an internal crack have been expanded into an infinite series of Chebyshev functions of the second kind, which is not suitable for edge crack problems. According to the theory of linear elastic fracture mechanics, near the crack tip we have,

$$\Delta v(x) = HK_I \sqrt{x} + O(x^{3/2}), \quad H = 8(1 - \nu^2) / (E\sqrt{2\pi}), \quad (\text{plain strain}) \quad (1)$$

where K_I is the mode I SIF, E and ν are the Young's modulus and Poisson's ratio, respectively. We express $\Delta v(x)$ as the following infinite series expansions:

$$\Delta v(z) = \Delta v[x(z)] = \sum_{m=1}^{\infty} \alpha_m T_{m-1}(z) \sqrt{1+z} = \sum_{m=1}^{\infty} \alpha_m P_m(z) \quad z = 2x/a - 1, \quad (2)$$

where $T_m(z) = \cos(m \cos^{-1} z)$ is m th-order Chebyshev polynomial of the first kind. Note that each term at the right-hand side of Eq. (2) has the correct square root asymptotic behavior as x goes to zero. Substituting Eq. (2) into Eq. (1) and letting x tends to zero, we obtain

$$K_I = h \sum_{m=1}^{\infty} (-1)^{m-1} \alpha_m, \quad h = E / [4(1 - \nu^2)] \sqrt{\pi/a}. \quad (3)$$

The curve fitting procedure will be used to obtain the coefficients α_m in Eq. (2). In numerical calculation, the right-hand side of Eq. (2) must be truncated. Truncation criterion is the key point of this method. Suppose the infinite series in the right-hand side of Eq. (2) is truncated at $m = M$. A genuinely objective and meaningful fitting procedure should provide the criterion to determine the value of M , the accuracy of α_m , and the consistency of the results. Suppose that we have N calculated values of COD fields: $w_n = \Delta v(z_n)$. Any numerically calculated COD fields are certainly subject to calculation errors, let σ_n be the standard deviation of w_n . For a straight edge crack ($0 \leq x \leq a$), we will use the following approximate expression for σ_n

$$\sigma_n \approx d / \sqrt{x_n/a}, \quad (4)$$

where d can be chosen as the average COD error or the COD error at $x = a$. Now, we fit $w_n(z)$ to

$$W(z; \alpha_1, \alpha_2, \dots, \alpha_M) = \sum_{m=1}^M \alpha_m P_m(z),$$

where $\alpha_m, m = 1, 2, \dots, M$, are the parameters that can be determined by minimizing the following quantity called "chi-square" (e.g., refer to [6])

$$\chi^2 = \sum_{n=1}^N [w_n - W(z; \alpha_1, \alpha_2, \dots, \alpha_M) / \sigma_n]^2$$

The results are

$$\alpha_m = \sum_{k=1}^M D_{mk} \left(\sum_{n=1}^N w_n P_k(z_n) / \sigma_n^2 \right), \quad D_{mk} = 1 / \left(\sum_{n=1}^N P_m(z_n) P_k(z_n) / \sigma_n^2 \right). \quad (5)$$

The standard deviations of the parameters α_m are determined by the following relation:

$$\delta\alpha_m = \sqrt{D_{mm}}. \quad (6)$$

Note that D_{mm} are dependent on z_n , M , N , and σ_n , but independent on w_n . The variance of the curve fitting can be expressed by

$$\sigma_M = \sqrt{\sum_{n=1}^N [w_n - W(z_n; \alpha_1, \alpha_2, \dots, \alpha_M)]^2 / (N - M)}. \quad (7)$$

Now let

$$\sigma = \sqrt{\sum_{n=1}^N [w_n - w^{an}(z_n)]^2 / (N - 1)} \quad (8)$$

denote the average standard deviation of the calculated COD fields, where $w^{an}(z_n)$ is the true value of $\Delta v(z_n)$. If the value of σ_M is bigger than the value of σ , the truncation number M should be increased to decrease the value of σ_M . It seems that the smaller the σ_M is, the better the effect of the curve fitting will be. But this is not true. Since Chebyshev polynomials are complete, σ_M may become very small as M increases for big enough N . When σ_M is much less than σ , the unnecessary surplus terms only reflect the smoothing effect of the errors of the calculation data by the fitting procedure. The additional terms are not only unnecessary, but also will significantly increase the errors of K_I evaluated from Eq. (3). The determination of the truncation number M is the key point in the application of the GCDFP. For a given M , the conservative error estimates of the calculated SIF may be expressed as,

$$\delta K_I \approx h \sum_{m=1}^M |\delta\alpha_m| + h \left| \sum_{m=M+1}^{\infty} (-1)^{m-1} \alpha_m \right|, \quad (9)$$

where $\delta\alpha_m$ are defined by Eq. (6). It is found that the value of $\delta\alpha_m$ varies very slowly with increasing m , but $|\alpha_m|$ decreases rapidly as m increases. As M increases the first term in the right-hand side of Eq. (9) will increase, but the second term in the right-hand side of Eq. (9) will decrease. Thus, the truncation number M may be determined by minimizing δK_I with respect to M . It is very important to note that the values of δK_I are obtained directly from the error distribution of the COD fields. This is just we wanted.

In conclusion, the truncation number M should satisfies two conditions: $\sigma_M < \sigma$ and δK_I is the minimum value with respect to M . Similar discussion will be for mode II case.

3. GCDFP FOR A CURVE EDGE CRACK

Let s denote the arc length of a curve edge crack measured from the tip of the crack. For this mixed mode edge crack problem, COD components can not distinguish between modes I and II. In this case, instead of dealing with COD component, the amplitude square of the COD fields $g(s)$

$$g(s) = \Delta u^2(s) + \Delta v^2(s) = H^2 (K_I^2 + K_{II}^2) s + O(s^2), \quad (10)$$

is expanded into an infinite series of Chebyshev polynomial of the first kind multiplied by s :

$$g(z) = g[s(z)] = \sum_{m=0}^{\infty} \gamma_m T_m(z) (z+1) = \sum_{m=0}^{\infty} \gamma_m Q_m(z), \quad z = 2s/a - 1. \quad (11)$$

The following analysis is similar to that in section 2, for simplicity, only main results will be presented. Let $g(z_n)$, $n = 1, 2, \dots, N$, be the calculated values of $g(z)$ at $z = z_n$, and let σ_n be the standard deviation of $g(z_n)$. Truncating the right-hand side of Eq. (11) at $m = M$ and using curve-fitting procedure, we obtain

$$\gamma_m = \sum_{k=1}^M E_{mk} \left[\sum_{n=1}^N g(z_n) Q_k(z_n) / \sigma_n^2 \right], \quad E_{mk} = 1 / \left(\sum_{n=1}^N Q_m(z_n) Q_k(z_n) / \sigma_n^2 \right). \quad (12)$$

Letting z go to -1 , we obtain from Eq. (10) and Eq. (11)

$$K^2 = K_I^2 + K_{II}^2 = h \sum_{m=0}^{\infty} \gamma_m T_m(-1) = h \sum_{m=0}^{\infty} (-1)^m \gamma_m, \quad h = 2 / (H^2 a). \quad (13)$$

For a given M , the conservative error estimates of K^2 may be expressed as,

$$\delta K^2 \approx h \sum_{m=1}^M |\delta \gamma_m| + h \left| \sum_{m=M+1}^{\infty} (-1)^m \gamma_m \right|. \quad (14)$$

In Eq. (14), $\delta \gamma_m$, the standard deviations of the parameters γ_m , can be determined by

$$\delta \gamma_m = \sqrt{E_{mm}}. \quad (15)$$

The variance of the curve fitting can be expressed by

$$\sigma_M = \sqrt{\sum_{n=1}^N \{g(z_n) - [\sum_{m=1}^M \gamma_m Q_m(z_n)]\}^2 / (N - M)}. \quad (16)$$

Denote the average standard deviations of $g(z_n)$ by σ which is known for a given COD fields. Thus, under the condition $\sigma_M < \sigma$, the truncation number M may be determined by minimizing δK^2 in Eq. (14) with respect to M . For a given M , γ_m can be obtained from Eq. (12), then, K^2 and the error estimate of δK^2 can be obtained from Eqs. (13) and (14), respectively. It is very important to note that the values of δK^2 are obtained directly from the error distribution of $g(z)$. Notice that

$$K_I / K_{II} = \lim_{s \rightarrow 0} [\Delta u_n(s) / \Delta u_t(s)], \quad (17)$$

where Δu_n and Δu_t are the normal and tangential COD component, respectively. The value of right-hand side of Eq. (17) can be obtained from the COD values at crack tip element. K_I and K_{II} can then be calculated from Eq. (13) (truncated at $m = M$) and Eq. (17).

4. NUMERICAL EXPERIMENTS

For all numerical examples, $\nu = 0.3$, COD fields are obtained by BEM. The crack line is discretized with N equal-sized elements.

First, consider a problem of double edge cracks in an infinite long strip under tensile stress p with zero shear traction and zero normal displacement on the side boundaries as shown in Fig. 1. Let ΔK_I denote the difference of calculated K_I and K_I^{an} , where K_I^{an} is the analytical results of K_I which can be found in [7]. The percentage errors of $\delta K_I / K_I$ and $\Delta K_I / K_I$ as a function of element number N are shown in Fig. 2. The truncation number M equals 2 for $N=50$ and 3

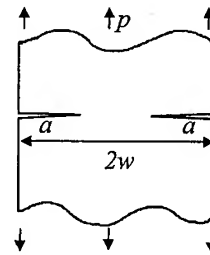


Fig.1. Double edge cracks

for other element numbers. Notice that the value of $\delta K_I / K_I$ is a little larger than that of $\Delta K_I / K_I$, the reason is that $\delta K_I / K_I$ is a conservative estimation of SIFs. Fig. 2 also shows that $\delta K_I / K_I$ are uniformly

convergent as N increases, but the convergence is not consistent for $\Delta K_I/K_I$. The inconsistency of $\Delta K_I/K_I$ takes place when the truncation number M increases from 2 to 3. The $\Delta K_I/K_I$ obtained from the comparison of the numerically estimated SIF with analytical result is not always reliable. Further more, in most practical problems, the analytical results are not available and the accuracy of the numerically extracted SIF results has to be estimated from the COD data. Since $\delta K_I/K_I$ have been obtained from the errors of COD data only, it is of good reason to use it as the estimation of the calculating error. $\delta K_I/K_I$, the relative errors of SIFs, are 2.5% for $N=50$ to 0.5% for $N=250$. Considering that the simplest constant elements are used in BEM, the results very satisfactory. We point out here, the SIF errors are in the same order of the errors of the corresponding COD data that are used to extract SIF.

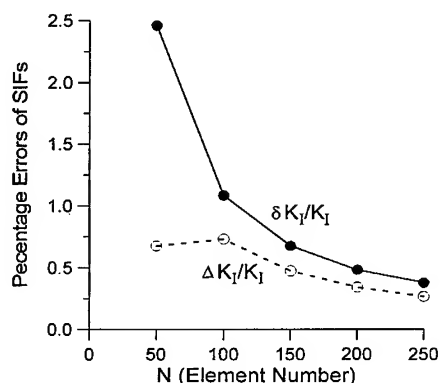


Fig. 2. Errors of SIFs vs N for double edge cracks with $w/a=2$.

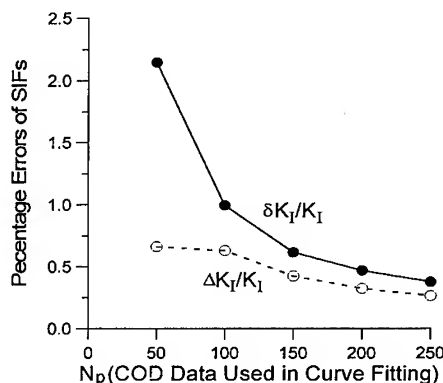


Fig. 3. Errors of SIFs vs N_p for double cracks with $w/a=2$, total COD data $N=250$.

Consider the case when total element number $N = 250$ on a crack, but only part data near the crack tip, $N_p \leq N$, are used in curve fitting. The relation between the calculated SIFs and N_p is shown in Fig. 3. As anticipated, the more the COD data being used, the better the calculated SIF results are obtained. It is very interesting to notice that, although the meaning of the abscissa in Fig. 2 is totally different to that in Fig. 3, the shapes of the curves in the two figures are very similar.

The purpose of the second example is to examine the GCDFFP to extract SIF of a curve edge crack. Consider a circular edge crack of radius R and included angle $\theta = 45^\circ$ in a half plane subjected to a uniform tensile stress p with zero normal displacement and zero shear traction components on the surface of the half plane as shown in Fig. 4. First, the COD fields are obtained by using our newly developed BEM where the displacement and its tangential derivatives are continuous at points between elements, and special crack-tip element includes the second term of the near crack-tip COD field series expansion. With

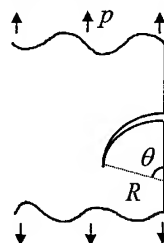


Fig. 4. Arc edge crack.

these measures, the accuracy of the calculated COD fields can be greatly improved. Then we use the GCDFFP to calculate K^2 as a function of truncation number M from Eq. (13). The error δK^2 can also be calculated as a function of truncation number M in curve fitting for the calculated COD data from Eq. (14). The final result of K^2 is the one where δK^2 is the minimum with respect to M . Let

$\Delta K^2 = K^2 - (K^{an})^2$, $G = G^{an}$ where G be the energy release rate. The analytical SIFs of this problem can be found in [8]. The percentage errors of $\delta G/G = \delta K^2 / K^2$ and $\Delta G/G = \Delta K^2 / K^2$ as a function of element number N are shown in Fig. 5. Since $\delta G/G$ are conservative estimations of the relative error of G , the value of $\delta G/G$ is a little larger than that of $\Delta G/G$, and again $\delta G/G$ are uniformly convergent as N increases. With K^2 obtained and using Eq. (17), K_I and K_{II} of this problem can be calculated. The percentage errors of $\Delta K_I/K_I$ and $\Delta K_{II}/K_{II}$ obtained by GCDFP as functions of element number N are shown in Fig. 6. For comparison, the percentage errors of $\Delta K_I/K_I$ and $\Delta K_{II}/K_{II}$ obtained by two point method, where two near crack tip COD data are used to extract SIFs, are also shown in Fig. 6. It is found that the errors are larger for larger N for two point method. The explanation is that as N increases, the average accuracy of the COD fields is better, but since the first two points are more close to the crack tip the accuracy of these two data are worse. The GCDFP does not have this kind of inconsistency. The errors of $\Delta K_I/K_I$ and $\Delta K_{II}/K_{II}$ by GCDFP are about 0.1% for 50 elements as shown in Figs. 6, which are very accurate results.

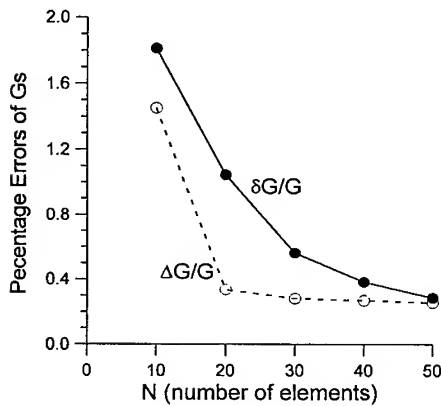


Fig. 5. Percentage errors of G vs N for an arc edge crack ($\theta = 45^\circ$) in a half plane.

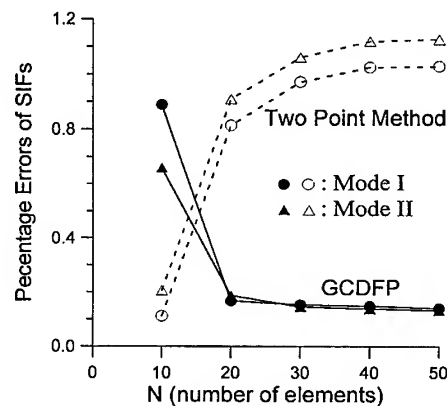


Fig. 6. Percentage errors of SIFs vs N for an arc edge crack ($\theta = 45^\circ$) in a half plane.

ACKNOWLEDGMENTS—The financial support from the Beijing Natural Science Foundation is gratefully acknowledged.

REFERENCES

1. Z. L. Li and Z. J. Li, *Int. J. Fracture*, **99**(2000), P. 259.
2. I. L. Lim, I. W. Johnston and S. K. Choi, *Int. J. Fracture*, **58**(1992)p. 193.
3. H. L. J. Pang, *Engng. Fracture Mech.*, **44**(1993)p. 741.
4. D.B. Cooper, G. Meda and Sinclair, G.B., *Int. J. Fracture* **70**(1995)p. 237
5. Y. L. Xu, *Engng. Fracture Mech.*, **59**(1998)p.165.
6. P. R. Bevington and D. K. Robinson, , *Data Reduction and Error Analysis for the Physical Sciences*, McGraw-Hill, New York (1992).
7. H. Tada, P. C. Paris, and G. R. Irwin, *The stress Analysis of Cracks Handbook* (2nd edition), Paris Productions Incorporated, St. Louis(1985).
8. T.P. Rook and D.J.Cartwright, *Compendium of stress intensity factors*, HMSO, London(1976).

A Stochastic Modeling for Predicting Fatigue Crack Growth under Variable Amplitude Loading

D.S. Shim¹ and J.K. Kim²

¹ Department of Mechanical Design and Production Engineering, Hanyang University,
17 Haengdang-Dong, Sungdong-Gu, Seoul 133-791, Korea

² School of Mechanical Engineering, Hanyang University, 17 Haengdang-Dong,
Sungdong-Gu, Seoul 133-791, Korea

Keywords: Fatigue Crack Growth, Normal Distribution, Random Variable, Retardation Coefficient, Variability, Variable Amplitude Loading

ABSTRACT

In this study, to investigate and to predict the crack growth behavior under variable amplitude loading, crack growth tests are conducted on 7575-T6 aluminum alloy. The loading waveforms are generated by normal random number generator. All waveforms have same average and RMS (root mean square) value, but different standard deviation, which is to vary the maximum load in each wave. The modified Forman's equation is used as crack growth equation. Using the retardation coefficient D defined in the previous study, the load interaction effect is considered. The variability in crack growth process is described by the random variable Z that was obtained from crack growth tests under constant amplitude loading. From these, a statistical model is developed. The curves predicted by the proposed model well describe the crack growth behavior under variable amplitude loading and agree with experimental data. In addition, this model well predicts the variability in crack growth process under variable amplitude loading.

1. INTRODUCTION

Mechanical systems are usually subjected to variable amplitude loading. In this condition, load interaction or sequence effects significantly affect crack growth rates and fatigue lives. Thus, to predict fatigue lives more practically, a model for predicting crack growth under variable amplitude loading is needed.

These models have been studied in the form of characteristic K method [1, 2] or cycle-by-cycle method [3, 4, 5]. Characteristic K method ignores sequence effect and convert variable amplitude loading into equivalent constant amplitude loading using simple statistical parameter. Using root mean square (RMS) stress intensity, Barsom [1] predicted the average crack growth behavior of various bridge steels subjected to variable amplitude random sequence load fluctuations. Hudson [2] employed the Barsom's concept to predict the crack growth under flight simulation loading. This approach is very simple. However, when the loading history is highly uneven, the prediction is difficult because large peaks may delay crack growth and the sequence effects of applied cycles become important.

Cycle-by-cycle methods have been proposed to consider sequence effect. Schijve [3] measured crack closure under flight-simulation loading and predicted crack growth based on a constant crack opening stress level. Johnson [4] presented a phenomenological load interaction model that accounted for crack growth retardation and acceleration by decreasing or increasing the effective stress ratio. Newman [5] developed an analytical crack closure model based on the Dugdale model

[6] that left plastically deformed material along the crack surfaces as the crack advances. These models produce better results than the above-mentioned characteristic K methods, but are difficult to apply and sensitive to stress state.

By the way, it has been reported that crack growth rates have a considerable amount of scatter despite same loading condition. Bogdanoff and Kozin used a discrete state-discrete time Markov process for modeling the uncertainties in crack growth [7, 8]. Yang [9], Lin [10], and Ortiz [11, 12] employed the appropriate crack growth equation based on LEFM that had the scatter parameter to randomize crack growth process. These approaches were applied to crack growth under constant amplitude loading but scarcely variable amplitude loading.

This paper presents a new approach for predicting crack growth behavior and fatigue lives under variable amplitude loading that can consider load sequence effect as well as the variability of crack growth rates.

2. EXPERIMENTAL PROCEDURE

The material used in this experiment was a high strength aluminum alloy 7075-T6. The type of specimen was compact tension (CT) with a width W of 50.8 mm and the thickness B was 9.8 mm. Specimens were machined in the L-T orientation. The loading waveforms are generated by normal random number generator proposed by Box and Muller [13]. Figure 1 shows the constructed waveforms. As shown in Table 1, all waveforms have 10,000 reversals, and same average and RMS value, but different standard deviation, which is to vary the maximum load in each wave.

By applying the same waveform repeatedly, crack growth tests were performed until a preset crack was reached. During the tests, the crack length was monitored continuously by the image analyzer, and test data were automatically recorded in the PC as the crack increased by 0.2 mm.

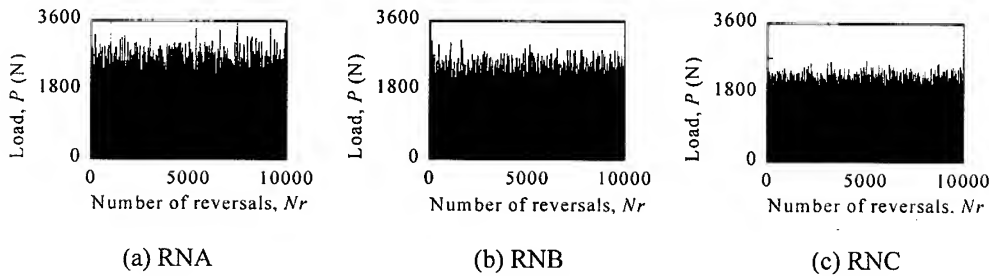


Fig. 1. Wave forms

Table 1. The probabilistic properties of wave forms

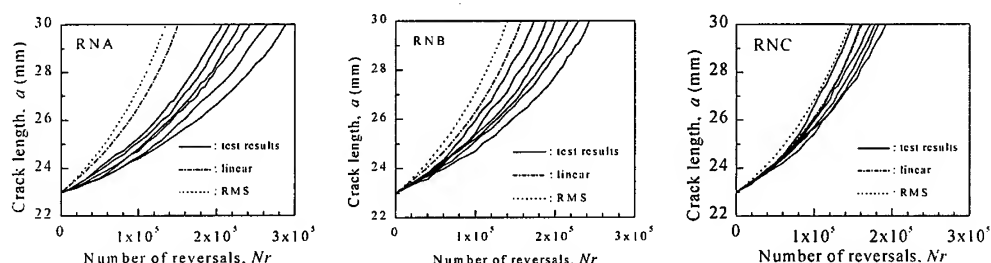
Wave	Average (N)	RMS (N)	Standard deviation (N)	Maximum load (N)
RNA	1797	1865	500	3569
RNB	1799	1843	400	3122
RNC	1807	1824	245	2655

3. RESULTS AND DISCUSSION

3.1. Crack growth behavior

Figures 2 (a), (b) and (c) show $a-N_r$ (a : crack length, N_r : number of reversals) curves under RNA, RNB and RNC, respectively. In each Figure, crack growth curves have much variation despite the same loading condition because the variability due to the uncertainties in crack growth process also exists in variable amplitude loading condition. In addition, dot line and dashed line are the predictions by root mean square value and the Miner's rule, respectively. These lines do not describe the variability and also deviate from experimental data. The difference between experimental data and predictions is the largest in RNA and the smallest in RNC. This implies that

the maximum load in variable amplitude load produces a strong sequence effect as Dominguez [14] reported. Since the higher the overload, the longer the crack growth retardation remains in effect, crack grows slowly in RNA that the maximum load is the highest in three waveforms. Thus, in order to predict crack growth under variable amplitude loading practically, the prediction model is to consider the retardation behavior by overloads as well as the variability in crack growth process.



(a) RNA

(b) RNB

(c) RNC

Fig. 2. $a-N_r$ curves under variable amplitude loading

3. 2. Crack growth retardation model

Well-known retardation models were presented by Elber, Wheeler and Willenborg. These models have some difficulties in applying to crack growth under variable amplitude loading. In the case of Elber's model, measuring the opening stress under variable amplitude loading is very difficult and determining the opening stress level is not clear. The retardation parameter in the Wheeler's model must be newly determined by experiment if load spectrum is changed. The Willenborg's model can not describe the delayed retardation.

In the previous study [15, 16], we proposed a retardation model that can predict the retardation behavior including the delayed retardation. This model is very simple and well describes the macroscopic mechanism of retardation. In this model, the retardation behavior is described by the coefficient D as follows :

$$D = \log(da/dN)_{ca} / \log(da/dN)_{retard} \quad (1)$$

where $(da/dN)_{ca}$ is the crack growth rate under constant load and $(da/dN)_{retard}$ is that after an overload. a is a crack length and N is the number of cycles and equals to $N_r/2$.

Outside the overload affected zone, the retardation does not occur. Retardation coefficient D is, thus, equal to 1 when $a < a_{ol(i)}$ or $a > a_{old(i)}$. $a_{ol(i)}$ is the initial crack length at which an overload $P_{ol(i)}$ is applied. $a_{old(i)}$ is the crack length at which crack growth rate reaches the pre-overload steady-state. Inside the overload affected zone, retardation coefficient $D \leq 1$. The crack growth rate linearly decreases after the overload and reaches its minimum after the crack has grown a distance by $a_{ol\min(i)}$. Then, crack growth rate increases up to the pre-overload steady-state value. According to the retardation behavior, the retardation coefficient D can be formulated as follows :

$$D = \frac{D_{ol\min(i)} - 1}{a_{ol\min(i)} - a_{ol(i)}} (a - a_{ol(i)}) + 1 \quad (a_{ol(i)} \leq a \leq a_{ol\min(i)}) \quad (2a)$$

$$D = D_{ol\min(i)} + (1 - D_{ol\min(i)}) \sqrt{1 - \left(\frac{a_{old(i)} - a}{a_{old(i)} - a_{ol\min(i)}} \right)^2} \quad (a_{ol\min(i)} \leq a \leq a_{old(i)}) \quad (2b)$$

$a_{old(i)}$ is usually written as $a_{ol(i)} + \gamma_{ol(i)}$. $\gamma_{ol(i)}$ is the plastic zone size induced by an overload.

$$\gamma_{ol(i)} = (1/\beta\pi)(K_{ol(i)}/\sigma_{ys})^2 \quad (3)$$

where, $K_{ol(i)}$ is the stress intensity factor by the overload $P_{ol(i)}$, and σ_{ys} is the yield strength. The thickness of specimen used in this experiment is 9.8 mm and plane strain state prevails, β experimentally determined in the previous study equals to 2.5, because the surface of specimen significantly affects the retardation.

Vardar and Yildirim [17] observed that the maximum retardation occurs at $0.24 \times$ plastic zone size ($a_{ol\min(i)} = a_{ol(i)} + 0.24\gamma_{ol(i)}$) for 7075-T6 aluminum alloy. The lowest retardation coefficient $D_{ol\min(i)}$ can be formulated as a function of the overload ratio. [15]

$$D_{ol\min(i)} = 1.0325 - 0.0029(\%OL) \quad (4)$$

$$\%OL = ((P_{ol(i)} - P_{(i)})/P_{(i)}) \times 100 \quad (5)$$

The retardation by an overload $P_{ol(i)}$ continues until $a_{ol(i+1)} + \gamma_{ol(i+1)} > a_{ol} + \gamma_{ol(i)}$.

Figures 3 (a), (b) and (c) show the change of retardation coefficient D in RNA, RNB and RNC, respectively. As shown in these Figures, the retardation coefficient D changes with the load fluctuation. The higher maximum load becomes, the larger crack growth retards and the lower the retardation coefficient D becomes. The retardation coefficient D has the lowest value in RNA that the maximum load is the highest, and is closer to 1 in RNC that the maximum load is the lowest, because $D_{ol\min(i)}$ approximates to 1 as the maximum load is close to the mean load.

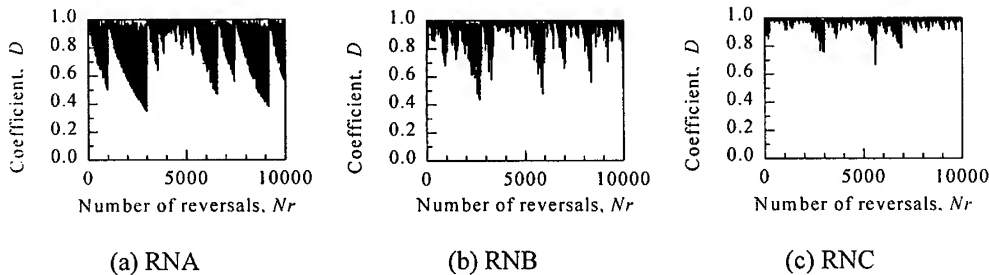


Fig. 3. The changes of retardation coefficient under variable amplitude loading

3.3. Crack growth prediction

Generally, crack growth rates have been formulated from the logarithmic relationship between da/dN and ΔK . Since crack growth behavior exhibits the sigmoidal $da/dN - \Delta K$ relationship and has much dispersion, we modified the Forman's crack growth equation as follows [16]:

$$\frac{da}{dN} = Z \cdot \frac{C(\Delta K - K_o)^m}{(1-R)K_c - \Delta K} \quad (6)$$

where, C and m are the material constants. K_o is an initial stress intensity factor and crack growth does not occur below this value. K_c is the critical stress intensity factor at which the fracture occurs. R is the stress ratio. Z is the random variable describing the variability of crack

growth rates and is calculated from the variance of $\log Z$. $\log Z$ is stationary and a normal random variable with zero mean and the variance of $\log Z$ depends on the thickness of specimen.

$$\sigma^2_{\log Z} = p \cdot B^q \quad (7)$$

where, p and q is the material constants. For aluminum alloy 7075-T6 $p=0.0143$ and $q=-0.792$.

Applying the lognormal model to equation (6), the distribution of retardation cycles can be obtained. The γ percentile of Z can be as follows :

$$\gamma = 1 - \Phi[(\log Z_r - \mu_{\log Z}) / \sigma_{\log Z}] = 1 - \Phi[\log Z_r / \sigma_{\log Z}] \quad (8)$$

where $\sigma_{\log Z}$ is the standard deviation of $\log Z$ and $\mu_{\log Z}$ is the mean of $\log Z$. Φ is the normal distribution function. Inverting equation (8), Z_r are given as follows :

$$Z_r = 10^{\sigma_{\log Z} \cdot \Phi^{-1}[1-\gamma]} \quad (9)$$

Substituting equation (9) into equation (6) and using the definition of D , the distribution of retardation cycles can be obtained.

$$N = \int_{a_0}^{a_f} \left(\frac{1}{Z_r} \cdot \frac{(1-R)K_c - \Delta K}{C(\Delta K - \Delta K_0)^m} \right)^{1/D} da \quad (10)$$

Obtaining Z_r every 5%, $a-N_r$ curves are simulated as shown in Figure 4. The correlation between the simulation and the experimental data (Fig. 2) is quite reasonable. Thus, it can be said that the variability in crack growth under variable amplitude loading can be predicted by the probabilistic characteristics of random variable Z obtained from crack growth test under constant amplitude load, and the retardation behavior can be well described by the coefficient D .

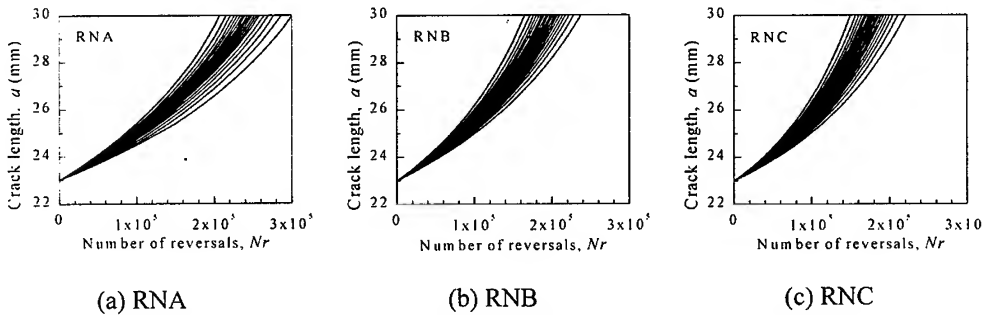


Fig. 4. $a-N_r$ curves simulated by the proposed statistical model

By drawing a horizontal line through the particular crack size in Figure 4, the distribution of fatigue lives can be obtained as shown in Figure 5. The fatigue lives in this study are the reversals when crack reaches to 30 mm. The predicted lines have good agreement with the experimental data in all waveforms. Therefore, it can be concluded that the fatigue lives under variable amplitude loading are well predicted by the proposed model.

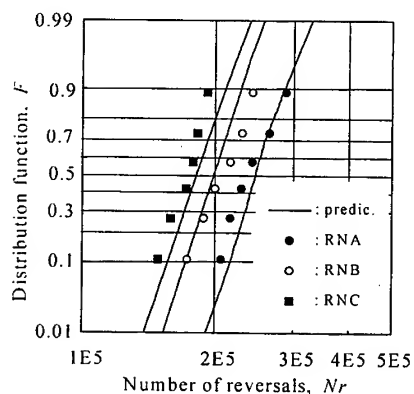


Fig. 5. Distribution of number of reversals predicted by the proposed model

4. CONCLUSIONS

To investigate the crack growth behavior under variable amplitude loading, crack growth tests were conducted on 7575-T6 aluminum alloy. Based on the experimental results, a statistical model was developed to predict crack growth behavior and fatigue life including the variability of crack growth. The curves predicted by the proposed model were compared with the experimental data. From these the following conclusions have been drawn.

(1) Fatigue crack growth behavior under variable amplitude loading is dominantly affected by the maximum load and have much scatter in $a-N_r$ curves despite the same wave form.

(2) Tensile overload forms a large plastic zone and affects the following small amplitude load, which can be well formulated by the retardation

coefficient D that is obtained from the crack growth test under single tensile overload.

(3) By using the probabilistic characteristics of random variable Z obtained from crack growth test under constant amplitude load, the variation of crack growth under variable amplitude loading can be predicted. The predicted results show good agreements with experimental results.

ACKNOWLEDGEMENT

The authors gratefully acknowledge the financial support of Safety and Structural Integrity Research Center (Sung-Kyun-Kwan University) in the Korea Science and Engineering Foundation.

REFERENCES

1. J. M. Barsom, *ASTM STP* 595, (1976) pp. 217~235
2. C. M. Hudson, *ASTM STP* 748, (1981) pp. 41~52
3. J. Schijve, *ASTM STP* 700, (1980) pp. 3~34
4. W. S. Johnson, *ASTM STP* 748, (1981) pp. 85~102
5. J. C. Newman, Jr., *ASTM STP* 748, (1981) pp. 54~84
6. D. S. Dugdale, *Jour. of the Mechanics and Physics of Solids*, Vol. 8, No. 2, (1960) pp. 100~104
7. J. L. Bogdanoff, *Jour. of Applied Mechanics*, Vol. 45, (1978) pp. 246~250.
8. J. L. Bogdanoff and F. Kozin, *Jour. of Applied Mechanics*, Vol. 49, (1982) pp. 37~42.
9. J. N. Yang, et al., *Engineering Fracture Mechanics*, Vol. 18, No. 2, (1983) pp. 257~270.
10. Y. K. Lin and J. N. Yang, *AIAA JOURNAL*, Vol. 23, No. 1, (1985) pp. 117~124.
11. K. Ortiz, et al., A. S., *Engineering Fracture Mechanics*, Vol. 24, No. 5, (1986) pp. 657~675.
12. K. Ortiz, et al., A. S., *Engineering Fracture Mechanics*, Vol. 29, No. 3, (1988) pp. 317~334.
13. G. E. P. Box, and M. E. Muller, *Ann. Math. Stat.*, Vol. 29, (1958) pp. 610~611
14. J. Dominguez, et al., *Engineering Fracture Mechanics*, Vol. 56, No. 1, (1997) pp. 65~76
15. J. K. Kim, and D. S. Shim, *Trans. KSME, A*, Vol. 23, No. 7, (1999) pp. 1164~1172
16. J. K. Kim, and D. S. Shim, *Trans. KSME, A*, Vol. 22, No. 8, (1998) pp. 1523~1532
17. O. Vardar and N. Yildirim, *Int. J. Fatigue*, Vol. 12, (1990) pp. 283~287.

A Highly Accurate BEM in Fracture Mechanics

Z.L. Li, F.L. Zhan and S.H. Du

Solid Mechanics Research Center, Beijing University of Aeronautics and Astronautics,
37 Xueyuan Road, Haidian, Beijing 100083, China P.R.

Keywords: Boundary Element Method, Fracture Mechanics, Single-Node Quadratic Element

ABSTRACT

The continuous conditions of displacements and its tangential derivatives at regular inter-element points are automatically satisfied with single-node quadratic element (SNQE). Special crack-tip SNQE includes the second term of the asymptotic series expansion of the near crack-tip displacement fields. If an inter-element point is a corner point, the multi-valued tractions can be modeled appropriately. For a straight crack under tension, the relative crack opening displacement (COD) error at the center of the crack is only 0.01% for 20 SNQEs. Highly accurate results are also obtained for other numerical tests.

1. INTRODUCTION

More accurate and efficient technique is needed for solving crack problems such as numerical simulation of fatigue crack growth. The boundary integral equation itself is a statement of the exact solution to the problem posed, errors are due to discretization and numerical approximations. If the numerical integration procedure is made sufficiently sophisticated, then errors so introduced can be very small. Much attention has been paid to the smoothness requirements of shape functions. In general BEM, piecewise continuous Lagrangian shape functions are used, which enforce only displacement continuity between elements (C^0 continuity) with no consideration given to the tangential derivative continuity of displacement (C^1 continuity). Various cubic shape functions with C^1 continuity have been proposed [1-3], the accuracy can be improved, however, they are computationally expensive.

A single-node quadratic element (SNQE) is proposed in this work. By using SNQE, the C^1 continuity conditions at regular inter-element points are automatically satisfied. The singular behaviors of displacement and traction fields near a crack-tip are carefully modeled by including the second term of the asymptotic series expansion of the near crack-tip displacement fields. Considering the fact that the continuity order of the displacement fields is higher than that of the traction fields by one, quadratic elements are used for displacement fields but linear element are used for traction fields. Since there is only one node in one SNQE, the programming is greatly simplified. The numerical tests are taken for problems of internal single straight cracks, curve cracks, and edge cracks. Highly accurate results are obtained by using SNQEs. In the test of a

single straight crack subjected to uniform tension in an infinite plane, the relative COD error at the center of the crack is only 0.01% for 20 SNQEs and 0.003% for 100 SNQEs, respectively. Highly accurate results are also obtained for other numerical tests. The consistency is very good for all tests.

2. BOUNDARY INTEGRAL EQUATIONS FOR CRACK ANALYSIS

Let S be the boundary of an elastic body V and n_j the outward normal components of S . The displacement and stress components, $u_i(q)$ and $\sigma_{ij}(q)$, are continuous if q is an inner point of V . Note that in the limiting process when q tends to Q , where Q is a point on S , $u_i(Q)$ is continuous, but $\sigma_{ij}(Q)$ (or displacement gradients) may be or they may not be continuous depending on the boundary conditions at Q . If the boundary is not locally smooth at point Q , the traction at Q will be multi-valued. In the following, Q is called regular if it is locally smooth and $du_i(Q)/dS$ are continuous, otherwise it is called irregular. The examples of irregular boundary points are crack-tips, crack kinks and corners. The displacement boundary integral equations can be expressed by [4]

$$c_{ki}(P)u_i(P) + \oint_S T_{ki}(P, Q)u_i(Q)ds(Q) = \int_S U_{ki}(P, Q)t_i(Q)ds(Q), \quad P \in S, \quad (1)$$

where t_i are traction components, U_{ki} and T_{ki} are displacement and traction fundamental solutions, respectively, \oint stands for the Cauchy principal-value integral, $c_{ki}(P)=0.5\delta_{ki}$ if P is regular. If COD is used as field variable, the following traction boundary integral equations should be used

$$t_i(P) = \oint_S F_{ik}(P, Q) \frac{d\Delta u_k(Q)}{ds(Q)} ds(Q), \quad (2)$$

where Δu_i are the COD components, F_{ik} is the integral kernel with Cauchy singularity [4]

3. SINGLE-NODE QUADRATIC ELEMENT FOR REGULAR BOUNDARY

Suppose that both the geometry and boundary field variables are described by piecewise continuous shape functions, and collocation is always performed with the source point at the boundary element nodes. The conditions of the existence of the Cauchy principal-value integrals require that t_k in Eq.1 or $d\Delta u_k/ds$ in Eq.2 are continuous. With usual Lagrangian quadratic shape functions, the continuity requirements at inter-element points for u_i are satisfied, but they are generally not satisfied for du_k/ds (or $d\Delta u_k/ds$). A single-node quadratic element (SNQE) is proposed in this section. An important advantage of SNQE is that C^1 continuity conditions at regular inter-element points are automatically satisfied. Moreover, various kinds of physical conditions at irregular points such as crack-tips or corners, can be modeled properly. With the use of SNQE, the accuracy of numerical calculations can be highly improved.

Let the surface S be divided into N elements, $x_i^{\beta 1}$, x_i^{β} and $x_i^{\beta 2}$ be the coordinates at the beginning, middle and ending point of the β th element, respectively, and ξ be the natural coordinate, $-1 \leq \xi \leq 1$. The geometry of the β th element is represented as

$$x_i(\xi) = \frac{1}{2}\xi(\xi-1)x_i^{\beta 1} + (1-\xi^2)x_i^{\beta} + \frac{1}{2}\xi(\xi+1)x_i^{\beta 2}, \quad (3)$$

but the displacement fields of the β th element are approximated by

$$u_i(\xi) = \phi_{(1)}(\xi)u_i^{\beta 1} + \phi_{(0)}(\xi)c_i^{\beta} + \phi_{(2)}(\xi)u_i^{\beta 2}, \quad (4)$$

where $u_i^{\beta 1}$ and $u_i^{\beta 2}$ are displacements at $x_i^{\beta 1}$, and $x_i^{\beta 2}$, respectively, while c_i^{β} is introduced as an auxiliary quantity of the β th element. Shape functions $\phi_0(\xi)$ are of the following form:

$$\phi_{(1)}(\xi) = 0.25(\xi - 1)^2; \quad \phi_{(0)}(\xi) = 0.5(1 - \xi^2); \quad \phi_{(2)}(\xi) = 0.25(\xi + 1)^2, \quad (5)$$

If the point between β th and $(\beta-1)$ th element is regular, by using Eq.4 and the continuous conditions of u_i and du_i/ds we obtain

$$u_i^{(\beta-1)2} = u_i^{\beta 1} = a^{\beta} c_i^{\beta-1} + b^{\beta} c_i^{\beta}, \quad (6)$$

$$a^{\beta} = J^{\beta}(-1)/[J^{\beta-1}(1) + J^{\beta}(-1)], \quad b^{\beta} = J^{\beta-1}(-1)/[J^{\beta-1}(1) + J^{\beta}(1)] \quad (7)$$

where $J^m(\xi)$ is the Jacobian $ds/d\xi$ of the m th element. Substitution of Eq.6 into Eq.4 yields

$$u_i(\xi) = f_{(1)}(\xi) c_i^{\beta-1} + f_{(0)}(\xi) c_i^{\beta} + f_{(2)}(\xi) c_i^{\beta+1}, \quad (9)$$

where the shape functions are given by

$$f_{(1)}(\xi) = a^{\beta} \phi_{(1)}(\xi), \quad f_{(0)}(\xi) = b^{\beta} \phi_{(1)}(\xi) + \phi_{(0)}(\xi) + a^{\beta+1} \phi_{(2)}(\xi), \quad f_{(2)}(\xi) = b^{\beta+1} \phi_{(2)}(\xi) \quad (10a,b,c)$$

Since the displacement fields are expressed by parameters c_i^0 , only one node is needed in an element, generally, the mid-point of an element is selected as the node. Since the node is an internal point of the element, the continuity requirements of the Cauchy principal-value integral and the smoothness of the geometry at the collocation point are satisfied.

4. CORNER SNQE

Consider a rectangle corner, C , as shown in Fig. 1. The displacements u_i at C are continuous, but the tractions t_i at C are multi-valued. It is reasonable to assume that the stresses are continuous at C , but stress symmetry may be lost, i.e. σ_{12} and σ_{21} may not be equal. Notice that

$$t_1^m = \sigma_{11}(C), \quad t_2^m = \sigma_{12}(C),$$

$$t_1^{m+1} = \sigma_{21}(C), \quad t_2^{m+1} = \sigma_{22}(C).$$

By using Hooke's law, the following relationships between the normal traction components and the displacement components at C can be established:

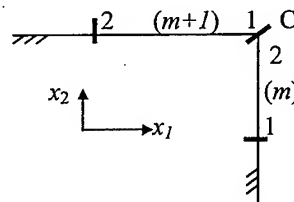


Fig. 1 Corner elements.

$$u_1^{m2} = u_1^{(m+1)1} = c_1^{m+1} - p^{m+1} t_2^{m+1} + q^{m+1} t_1^m, \quad (11)$$

$$u_2^{m2} = u_2^{(m+1)1} = c_2^m - p^m t_1^m + q^m t_2^{m+1}, \quad (12)$$

where

$$p^m = J^m(1)\nu_1/E_1; \quad q^m = J^m(1)/E_1; \quad p^{m+1} = J^{m+1}(-1)\nu_1/E_1; \quad q^{m+1} = J^{m+1}(-1)/E_1, \quad (13a,b,c,d)$$

where $E_1 = E/(1-\nu^2)$, $\nu_1 = \nu/(1-\nu)$, E is Young's modulus, ν is Poisson's ratio of the elastic body.

5. CRACK SNQE

Let the tip of a crack be located at the left end of m th element as shown in Fig. 2, thus $\Delta u_i^{m1} = 0$. Special crack-tip element that correctly represents the asymptotic behavior to the second term of the series expansion of the COD fields can be expressed as

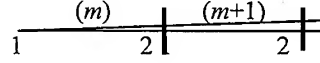


Fig. 2 Crack-tip elements

$$\Delta u_i(\xi) = \Delta c_i^m \sqrt{\xi+1} + \alpha_i(\xi+1)^{3/2}. \quad (14)$$

The continuous conditions of Δu_i and $d(\Delta u_i)/ds$ at the right end of the crack-tip element lead to

$$\Delta u_i^{m2} = \Delta u_i^{(m+1)1} = A^{m+1} \Delta c_i^m + B^{m+1} \Delta c_i^{m+1}, \quad (15)$$

where $A^{m+1} = 2\sqrt{2}J^{m+1}(-1)/[3J^{m+1}(-1) + 4J^m(1)]$; $B^{m+1} = 4J^m(1)/[3J^{m+1}(-1) + 4J^m(1)]$. Thus, in crack-tip element, we have

$$\Delta u_i(\xi) = [\sqrt{\xi+1} + (\frac{1}{2\sqrt{2}}A^{m+1} - \frac{1}{2})(\xi+1)^{3/2}]\Delta c_i^m + \frac{1}{2\sqrt{2}}B^{m+1}(\xi+1)^{3/2}\Delta c_i^{m+1}, \quad (16)$$

and in $(m+1)$ th element (near crack-tip element), we have

$$\Delta u_i(\xi) = A^{m+1}\phi_{(1)}\Delta c_i^m + [B^{m+1}\phi_{(1)} + \phi_{(0)} + a^{m+2}\phi_{(2)}]\Delta c_i^{m+1} + b^{m+2}\phi_{(2)}\Delta c_i^{m+2}. \quad (17)$$

6. NUMERICAL EXPERIMENTS

The following numerical experiments will show the high accuracy by using SNQE for various crack problems. Eq.1 will be used in examples 1 and 2, while Eq.2 will be used in example 3. For all examples, Poisson's ratio $\nu = 0.3$.

Example 1. A straight crack of length $2a$ on the x_1 -axis in an infinite plane under uniform tensile stress σ acting on the crack line. The analytical COD solution of the problem is:

$$\Delta u_2(x_1) = [4(1-\nu^2)/E]\sigma a \sqrt{1-x_1^2/a^2}.$$

The distributions of percentage errors of CODs calculated by BEM with 500 constant elements, 20 SNQEs and 100 SNQEs are shown in Fig. 3. The percentage COD error at the mid-point of the crack is: 0.018% for 500 constant elements; 0.011% for 20 SNQEs and 0.0026% for 100 SNQEs. The percentage COD error at the node

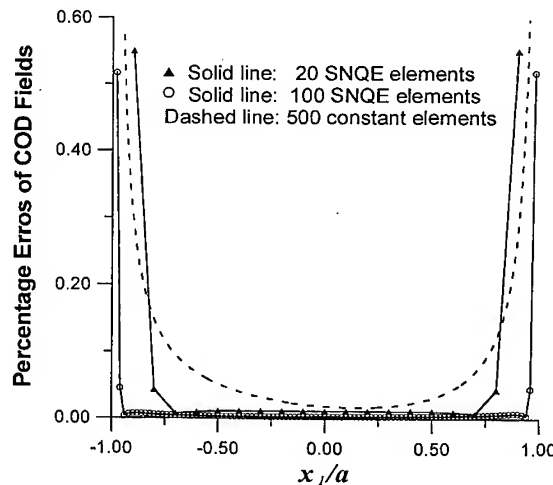


Fig.3. Relative COD errors of a straight crack.

closest to the crack-tip for 100 SNQE ($x_1/a=0.98$) is 0.52%, in contrast, it is 1.65% at the same place ($x_1/a=0.98$) for 500 constant elements. The accuracy by using SNQE is very high. It is also noted that the errors are very smooth except for the two nodes nearest to the crack tips.

Example 2. A circular arc crack with radius R and included angle 2θ in an infinite plane under a remote uniform uniaxial tension σ . The configuration is shown in Fig. 4.

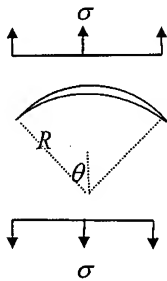


Fig. 4 A circular arc crack under tension

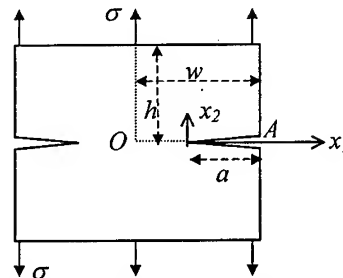


Fig. 5. Double edge cracks under tension

We have not found the analytical expressions of COD fields for this problem, but the analytical stress intensity factors of this problem can be found in [5]. The COD fields of the problem is calculated by BEM with 100 SNQEs, then the stress intensity factors (SIFs) are extracted through global crack-line displacement fitting procedure (GCDFF) developed by Li and Li [6]. All the COD data are used to extract SIFs in GCDFF and the errors of SIFs are in the same order of the average error of COD data. The numerical results of SIFs of the crack problem are shown in Table I for θ varying from 15° to 90° . The highest error of all cases is only 0.1333%.

Table I. Comparison of calculated SIFs using SNQE of arc cracks under remote tensile stress with analytical results.

θ	K_I	Theory K_I	%error	K_{II}	Theory K_{II}	%error
15	0.478638	0.478826	0.0394	0.129422	0.129443	0.0162
30	0.550022	0.550062	0.0072	0.329961	0.330401	0.1333
45	0.457249	0.457370	0.0264	0.511221	0.511246	0.0048
60	0.261771	0.261926	0.0594	0.616975	0.616526	0.0729
75	0.030058	0.030045	0.0435	0.621038	0.621354	0.0520
90	-0.176574	-0.176574	0.0114	0.529678	0.530330	0.1245

Example 3. Double edge cracks in a rectangular plate under tension σ . The crack length is a , the width and height of the plate are $2w$ and $2h$, respectively, the configuration is shown in Fig.5. There are no analytical solutions available for this problem. The approximate closed form solution for $h/w > 3$ was given by Nisitani [7]

$$u_2(x_1) = u_2^M \{1 + (0.407d - 0.959)x + (0.450d - 0.528)x^2 - (0.857d - 0.487)x^3\}^{1/2}, \quad (18)$$

Where $x = a - x_1$; $d = a/w$, u_2^M is the displacement of u_2 at the mouth of the edge crack:

$$u_2^M / a = 2(1 - \nu)(1.458 - 0.308d + 0.985d^2 - 1.869d^3 + 2.009d^4), \quad (19)$$

The accuracy of Eq.19 was claimed by Nisitani [7] to be $\pm 0.3\%$ for $a/w \leq 0.8$. In numerical calculation, by taking the advantage of symmetry only one-fourth of the plate ($h/w = 4$) is used. Eqs.11 and 12 is applied at the corners. There are 60 equally sized SNQE elements on the bottom boundary OA . The distribution of COD ($= 2u_2$) of the edge crack for $a/w = 0.5$ is shown in Fig. 6. It is noted that our numerical results are a little bit different from the results from Eq.18 (the maximum relative difference is about 1%), but the agreement at the mouth of the edge crack is much better. COD ($= 2u_2^M$) at the mouth of the edge crack as a function of a/w is shown in Fig. 7. The relative errors of COD at crack mouth for all $a/w \leq 0.8$ are less than 0.3% compared with the results from Eq.19.

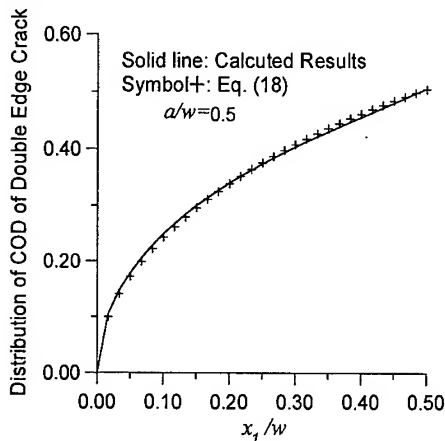


Fig. 6. Distribution of COD on the edge crack for $a/w = 0.5$

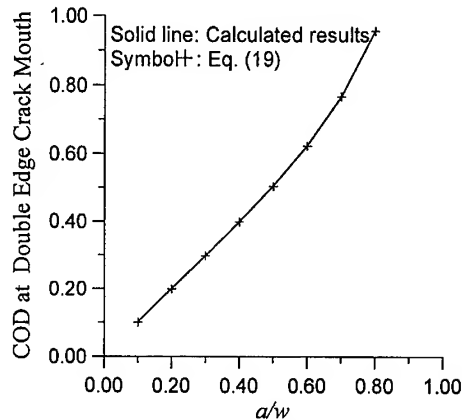


Fig. 7. Edge crack mouth COD as a function of a/w .

Acknowledgments—The financial support from the National Natural Science Foundation of China under grant number 19872011 is gratefully acknowledged.

REFERENCES

1. J.A. Liggett, J.R. Salmon, *Int. Journ. Num. Meth. Engng.* 17(1981) p. 453
2. H.G. Walters, J.C. Ortiz, G.S. Gipson, J.A. Brewer, *Advanced Boundary Element Methods*, Springer-Verlag(1988) p. 459
3. J.O. Watson, *Advanced Boundary Element Methods*, Springer-Verlag(1988) p. 465
4. T.A. Cruse, *Boundary Element Analysis in Computational Fracture Mechanics*, Kluwer Academic Publishers (1988)
5. T.P. Rook and D.J. Cartwright, *Compendium of stress intensity factors*, HMSO, London(1976).
6. Z. L. Li and Z. J. Li, *Int. J. Fracture*, 99(2000) p. 259
7. H. Nisitani, *Trans. Japan Soc. Mech. Engrg.*, 49(1975) p. 2518

Simulation and Experimental Verification of Axial Multi-Crack Propagation and Crack Kinking in Pressurized Fuselage

A. Shimamoto¹, T. Oguchi², D.Y. Ju¹ and A.S. Kobayashi³

¹ Department of Mechanical Engineering, Saitama Institute of Technology,
1690 Fusaiji, Okabe, Saitama 369-0293, Japan

² Graduate School of Engineering, Saitama Institute of Technology,
1690 Fusaiji, Okabe, Saitama 369-0293, Japan

³ Department of Mechanical Engineering, University of Washington,
Seattle WA 98195-2600, USA

Keywords: Combined Stress, Crack Kinking, Finite Element Method, Fracture Mechanics, High Strain Rate, Multiple Cracks

ABSTRACT

Interaction of multiple axial pre-cracks in a pressurized fuselage was investigated using a small-scale model of an idealized fuselage. The strain between multiple cracks under rapidly crack propagation was measured. The recorded crack velocities justified the use of a successive finite element analysis with large shell deformation. The experimental results of a rupturing model fuselage represented the variations in the mixed mode stress intensity factors K_I and K_{II} and the remote stress components σ_{0X} with crack extension. The crack kinking location, kinking angle and the off-axis crack trajectory are predicted by numerical analysis and the validity of the calculated results is discussed in comparison with the experimental data.

1. INTRODUCTION

The tear strap as stiffening plate on aircraft space shuttle fuselage structure has important significance to stop the fatigue crack progress loaded by high-pressure in long time. When the crack growth of a crack tip reaches nearly the tear strap, crack flapping and kinking will occur. The elucidation of this phenomenon in the fuselage structure is important to establish the design criterion considering curvature condition of the crack tip [1-6]. However, to decide an optimum fuselage structure, we have sufficiently to open the behavior on crack growth and curvature in having the multi-cracks for the fuselage structure, and analyze design conditions influenced that stress intensity factor K_I , K_{II} and crack curvature standard, progress direction of each crack. The multi-crack progress of the crack and curvature of the crack by tear strap and the interference between cracks also should be estimated. In this study, the main approach is to consider crack growth and curvature in pressurized fuselage structure with the axial multi-crack by an experimental technology and a numerical analysis method.

2. BASIC THEORY OF CRACK KINKING

The crack kinking criterion predicts a positive θ_c for a negative K_{II} or a negative θ_c for a positive K_{II} . Without K_{II} , however, the Erdogan-Sih [7] criterion predicts a self-similar crack propagation or $\theta_c=0$ and fails to explain the physically observed crack instability where crack kinking takes place in a pure K_I field. The static elastic crack-kinking criterion, incorporates the second order term in the stress field of the crack tip, or its dynamic counterpart predicts such crack kinking and these agrees well with the available experimental data. In the following, a brief account of a mode II extension of this crack kinking theory is given. The mixed mode, elastic crack tip stress field near a crack tip under mode I + II loading is given by

$$\begin{aligned}\sigma_{rr} &= \frac{1}{\sqrt{2\pi r}} \cos \frac{\theta}{2} \left[K_I \left(1 + \sin^2 \frac{\theta}{2}\right) + \frac{3}{2} K_{II} \sin \theta - 2 K_{II} \tan \frac{\theta}{2} \right] + \frac{\sigma_{0x}}{2} (1 + \cos 2\theta) \\ \sigma_{\theta\theta} &= \frac{1}{\sqrt{2\pi r}} \cos \frac{\theta}{2} \left[K_I \cos^2 \frac{\theta}{2} - \frac{3}{2} K_{II} \sin \theta \right] + \frac{\sigma_{0x}}{2} (1 - \cos 2\theta) \\ \tau_{r\theta} &= \frac{1}{2\sqrt{2\pi r}} \cos \frac{\theta}{2} [K_I \sin \theta + K_{II} (3 \cos \theta - 1)] - \frac{\sigma_{0x}}{2} \sin 2\theta\end{aligned}\quad (1)$$

where, σ_{0x} is the second order term and is commonly referred to as the remote stress component.

The maximum circumferential stress criterion is then used to derive a mixed mode crack extension criterion by assuming that fracture will occur when the maximum circumferential stress is equal to the equivalent circumferential stress of a mode I crack. Thus, the mixed mode crack-kinking criterion is given by

$$K_{IC} = K_I \cos^3 \frac{\theta_c}{2} - 3 K_{II} \cos^2 \frac{\theta_c}{2} \sin \frac{\theta_c}{2} + \frac{\sqrt{2\pi c}}{2} \sigma_{0x} (1 - \cos 2\theta_c) \quad (2)$$

Equation (2) which incorporates the second order term into the Erdogan-Sih criterion can be satisfied by a proper combination of non-vanishing K_I, K_{II}, σ_{0x} and θ_c , or $K_I = K_{Ic}$ and $\theta_c = 0$. The latter provide a self-similar crack extension criterion that will be used here. Otherwise, an off-axis crack extension always occurs when Eq. (2) is satisfied. The crack-kinking angle can be obtained by maximizing the crack tip circumferential stress and results in the following transcendental equation:

$$\frac{K_{II}}{K_I} = \frac{-\sin \frac{\theta_c}{2}}{(3 \cos \theta_c - 1)} \left[2 \cos \frac{\theta_c}{2} - \frac{16\sqrt{2\pi}}{3} A \cos \theta_c \right] \quad (3)$$

$$A = \sqrt{r_c} \frac{\sigma_{0x}}{K_I} \quad (4)$$

where, A is related to the critical distance r_c , from the crack tip and is proportional to the nonsingular stress σ_{0x} . For the stress field of a pure mode I at a crack tip, Ramulu[8] et al. have Eq.(3) shown that r_c is a material dependent parameter which must be determined experimentally. Thus, dose not like the crack-kinking criterion represented by Erdogan-Sih [7].

$$K_I \sin \theta_c + K_{II} (3 \cos \theta_c - 1) = 0 \quad (5)$$

The crack kinking angle computed by Eq. (3) incorporates the second order term and represents a mixed-mode extension of the crack kinking criterion of Ramulu[8] et al and Streit[9] et al.

The crack kinking angle θ_c increase with increasing σ_{0x} . Where a negative σ_{0x} tends to stabilize the crack path. After kinking under mixed mode loading, i.e. K_I and K_{II} crack tip loading, the crack could propagate under a pure mode I loading due to the lack of a constraining stringer. By setting $\theta=0$ and $K_{II}=0$ in Eq.(3), the critical distance r_c where the maximum stress deviate from the position of symmetry, can be derived as eq. (6) and eq. (7)

$$r_0 = \frac{9}{128\pi} \left(\frac{K_I}{\sigma_{0x}} \right)^2 < r_c \quad (6)$$

$$\theta_c = \cos^{-1} \frac{1 \pm \sqrt{1 + \frac{1024\pi}{9} \left(\frac{\sigma_{0x}}{K_I} \right)^2}}{\frac{512\pi}{9} \left(\frac{\sigma_{0x}}{K_I} \right)^2} \quad (7)$$

Equation (1) shows that the maximum $\sigma_{\theta\theta}$ in the two parameter crack stress representation does not have to be at $\theta=0$ when $r_0 > r_c$. However, the kinking criterion was triggered only when $r_0 < r_c$.

The crack curving angle, θ_c can be obtained by setting $K_{II}=0$ in Eq.(3). The development of a flap and the constraints due to the presence of a tear strap and a frame most likely will reduce the dominant K_I during the crack curving process and will result in crack arrest. On the other hand, K_I and the possible K_{II} could be elevated by the presence of MSD. The effect of MSD obviously is to promote self-similar crack extension, as seen in the NTSB report (1989), and can be incorporated into this analysis by artificially increasing K_I by a magnification factor which represents the interaction effect between the axial crack and the small crack emanating from an adjacent fastener hole.

3. EXPERIMENTAL METHOD AND TEST MODEL

The test specimen consisted of a pressurized thin 2024-T3 aluminum cylinder of diameter $D=360\text{mm}$, length $L=914\text{mm}$, thickness $t=0.3\text{mm}$ and two riveted and bonded lap or butt joints. This assembly represents the diameter-to-length ratio of a typical passenger plane. And, two sub cracks were made for the main crack and the right and left in stringer vicinity of this test-piece. The crack conducted the sealing by crack board from the back surface. Strain gauges with 8 points were bonded together along the progress direction of the crack. A High-speed camera (FASTCAM ultra UV) is used to present the nonlinear behavior of the crack growth and the progress vicinity of the crack by the photographs.

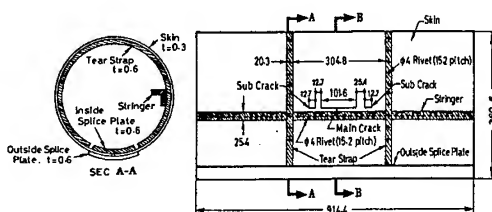


Fig.1 Small-scale fuselage specimen.

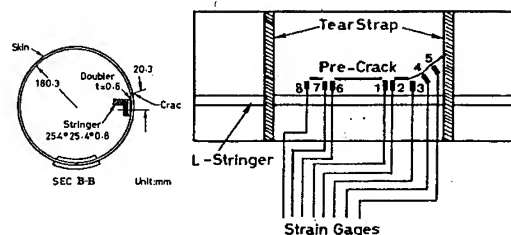


Fig.2 Setup of strain gages.

4. APPROACH OF SIMULATION

To understand the propagating behavior of axial multi-cracks turning propagating along tear strap under high-pressure with axial pre-cracks in a fuselage were investigated using a small-scale model. The strain behavior of multiple crack tips under rapidly crack propagation at high pressure was measured by strain gages. The crack velocities calculated that use of a finite element method for analyzing large deformation and elasto-dynamic behavior of the shell. The simulation results from the crack of the fuselage were calculated the variation stress intensity factors K_I , K_{II} in the mixed mode and the remote stress component σ_{ox} , with cracks extension.

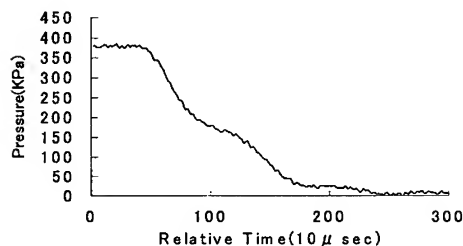


Fig.3 Loading variation in fuselage.

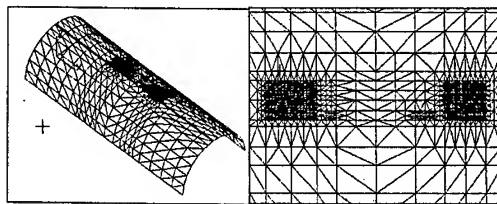


Fig.4 Model of the fuselage.

In order to understand the propagation behavior of multi-cracks along the tear strap and a numerical analysis based on the elasto-dynamic theory considered with large deformation of a shell structure is carried out, and is developed by authors [10]. The crack kinking location, kinking angles and the off-axis crack trajectories were predicted by the numerical analysis, and the validity of the calculated results is compared with the experimental results. It was good agreement between the predicted and measured crack kinking angles and the subsequent self-similar crack extension were demonstrated.

5. RESULTS OF NUMERICAL SIMULATION AND EXPERIMENTS

The measured strains on the strain gage No.1, No.2, No.6 and No.7 where near the crack tip are shown in Fig. 5. Also, shown is the strains obtained by the finite element analysis. As seen from Fig.5 (a)-(d), this low crack velocity justified the use of the static stress field in the crack tip to extract the variation stress intensity factors K_I , K_{II} in the mixed mode and the remote stress components σ_{ox} with crack extension. The calculated strain at the crack tips based on FE analysis also is in good agreement with the experimental data. Table 1 shown the crack kinking angles on some measured points and compared with the experimental data to verify the simulated results by a FE analysis. These results show that the proposed crack kinking criterion is a good prediction.

Table 1 Crack kinking angles

Gage No.	1	2	3	6	7	8
Kinking angle [deg] (Computed)	16.7	29.4	32.6	19.3	17.9	29.6
Kinking angle [deg] (Measured)	19.0	37.5	35.0	14.5	18.5	28

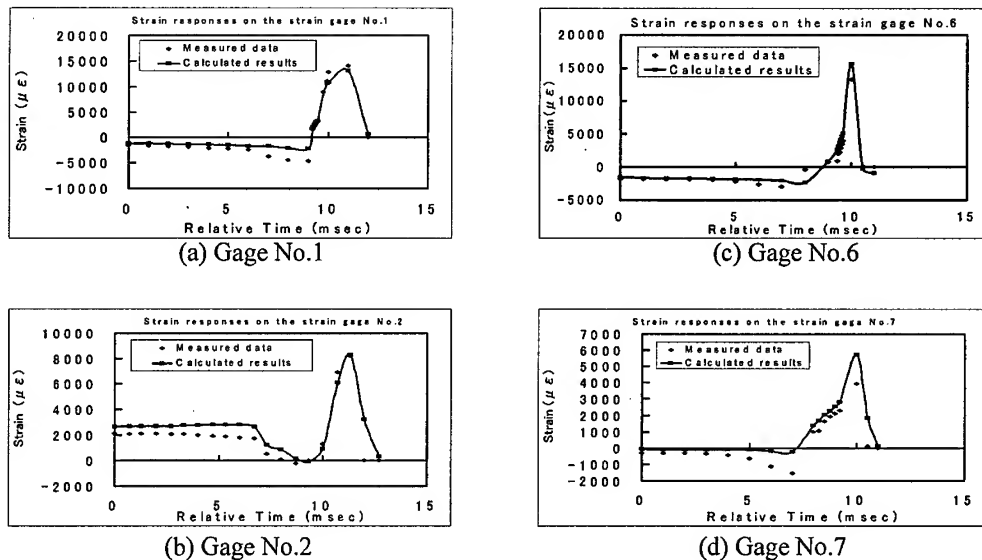


Fig. 5 Strain responses on the strain gages

Table 2 Computed results of K_I and K_{II}

Gage No.	1	3	4	5	6
K_I [Mpa \sqrt{m}]	95.0	126.1	155.0	157.0	92.6
K_{II} [Mpa \sqrt{m}]	-14.7	-68.9	25.2	-22.3	-16.8

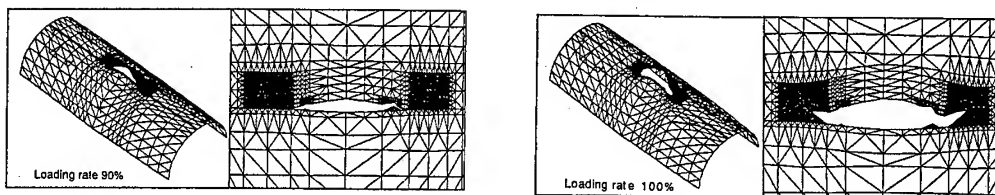


Fig. 6 Deformation of fuselage with variation of loading.

Table 2 denotes predictor the mixed mode stress intensity factors, K_I and K_{II} based on the FE analysis. Because the stress intensity factors K_I in the mixed mode of the main crack tip is larger than the sub-crack, the presented results show the mechanical behavior of crack kinking under a high strain rate. The main crack was propagated towardly to the sub-crack. Figure 6 shows the evolution of cracks kinking based on the FE analysis. The angles of multi-crack tips described by the mode of deformation also can be verified by the experimental data. The fig. 7 shown the crack growth behavior which taken from a high-speed camera. From these photographs, we can know that progress of crack growth is to begin from the main crack, and the results are good agreement with the numerical analysis shown in Fig.5. When the main crack connected with sub-crack of the left side, the crack growth of the longer crack will begins on changed direction of crack kinking to right side of the fuselage. From these results, we verified that the simulation method proposed by authors[10] is effectively.

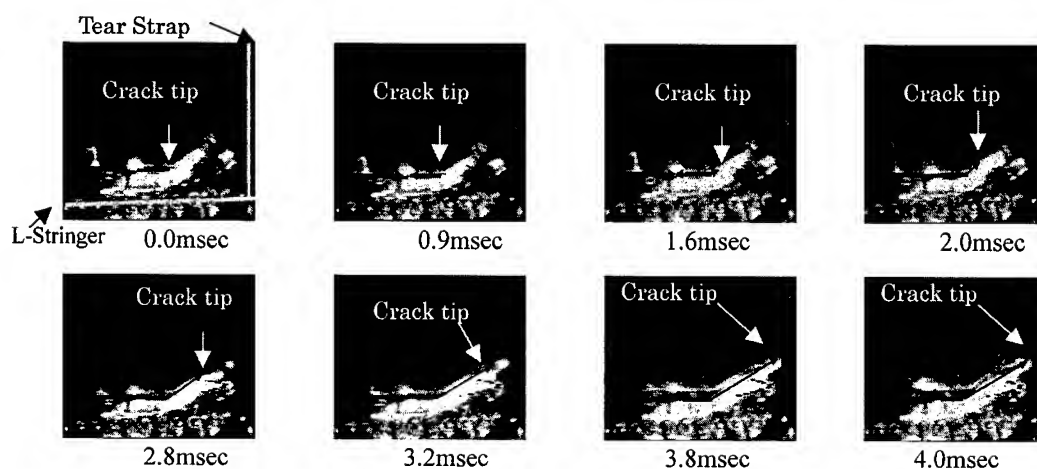


Fig. 7 High Speed Photographs of a rupturing small-scale fuselage

6. CONCLUSION

In this research, we obtain the some useful comments and conclusions as followings:

- (1) the proposed simulation method is effective, in order to axially analyze crack arrest function of tear strap in the pressurization fuselage with the multi-crack.
- (2) in the numerical analysis model, which utilizes the large deformation theory and elastodynamic finite element method, was effectively used to describe the mechanical behavior of crack kinking in the presence of multi-cracks and arrest at a tear strap in the pressurized fuselage.

ACKNOWLEDGEMENT

This work was supported by the High-Tech Research Center of Saitama Institute of Technology.

REFERENCES

1. A.S.Kobayashi, A.F. Emery, W.J. Love, Y.H. Chao and O. Johansen (T.A. Cruse ed.) Fracture Mechanics: Nineteenth Symposium ASTM STP Vol.969 (1988) 441-465 .
2. M. Kosai and Kobayashi A.S. Structural Integrity of Aging Airplanes, Springer-Verlag (1991) 225-239.
3. S. Sampath and D. Broek (S.N. Atluri S. G. Sampath and P. Tong eds.) Structural Integrity of Aging Airplanes, Springer-Verlag (1991) 339-389.
4. M. Fyfel. and V. Sethi, AIAA paper 914086 32nd Structures Structural Dynamics and Materials Conference Baltimore D.(1991).
5. M. Kosai, A.S. Kobayashi and M. Ramulu (S.N. Atluri C.E. Harris A. Hoggard N. Miller and S.G. Sampath eds.) Durability of Metal Aircraft Structures (1992) 443-457 Atlanta Technological Pub.
6. A. Shimamoto M.Kosai and A.S.Kobayashi, J. Eng. Fracture Mech. Vol.47 pp.59-73(1994)
7. F. Erdogan and G.C. Shi, ASME J. Basic Eng. Vol.85(1963) 519-527.
8. M. Ramulu and A.S. Kobayashi Exp. Mech. Vol.23(1983) 1-9.
9. R. Streit and J. Finnie Exp. Mech. Vol.20(1980) 17-23.
10. D.Y. Ju, A. Shimamoto and A.S. Kobayashi, JSME, (A), in press.

Calculation of Stress Intensity Factor Using Weight Function Method for a Patched Crack

J.H. Kim, K.W. Lee, D.C. Seo and S.B. Lee

Department of Mechanical Engineering, KAIST, 373-1 Kusong-Dong,
Yusong-Gu, Taejeon 305-701, Korea

Keywords: Crack Bridging Model, Crack Surface Displacement, Patched Crack, Weight Function Method

ABSTRACT

A center-cracked plate with a patch bonded on one side is treated with a crack-bridging model: assuming continuous distribution of springs acting between crack surfaces. Adopting weight function method, the stress intensity factor for the patched crack within infinite plate is successfully obtained by numerical calculation. When the crack length a is very small, the reduction in stress intensity factor was mainly due to the stress reduction from σ_∞ to σ_0 which was calculated in the case of uncracked plate. As the crack length a increases, the restraint on the relative displacement of the crack faces for a given value σ_0 became increased. The constant relative displacement (or crack surface displacement) did explain the reason for the constant stress intensity factors being independent to the crack length.

1. INTRODUCTION

The use of adhesive bonding as a joining method in aircraft structure is an accepted means of attaining high structural efficiency and improved fatigue life. Especially, the development of high-strength fibers and adhesives has made it possible to repair cracked metallic plates by bonding reinforcing patches to the plate over the crack. However, in order to evaluate the remaining service life of those structure, it is necessary to find damage tolerant criteria and to establish an allowable design stress for limiting the amount of slow fatigue crack growth. The linear elastic fracture mechanics approach has been successfully used to predict crack growth in the reinforced metallic plates [1,2]. Rose [3] showed that for a center-cracked plate bonded to an uncracked reinforcing plate, the stress intensity factor did not increase infinitely with increasing crack length, as it would if there was no reinforcement. He also explained that the reason for this asymptotic behavior was due to the crack-bridging mechanism of the reinforcing patches, such that the applied load could be fully transmitted across the crack with only a finite relative displacement between the crack faces. The reinforcement mechanisms, i.e. crack-bridging mechanism, for cracks in solids or structures can be modeled by a continuous distribution of springs acting between the crack faces [4,5]. These springs may be linear or nonlinear and they may be distributed across the whole or only part of the crack faces. Meanwhile, it is not easy to obtain the stress intensity factor for the through-thickness cracks with or without reinforcing patches, especially in a finite body. However, the weight function method proposed by Bueckner [6] and Rice [7] has proved to be a very useful and versatile method

of calculating stress intensity factors for cracks subjected to non-uniform stress fields such as residual stress or thermal loading. In this study, the stress intensity factor for a center crack with a patch bonded on one side in an infinite plate is calculated by using a weight function.

2. BASIC PROBLEM FORMULATION

The problem being considered is an infinite center-cracked plate, with crack length $2a$ under a remote uniform tensile stress σ_∞ , repaired by a bonded reinforcement as shown in Fig.1(a) and (b). The problem is to determine the stress intensity factor K_r in the repaired plate, as a function of crack length. Subscripts, P , R , A will be used to identify parameters pertaining to the plate, the reinforcing patch or the adhesive layer, respectively. Thus E_P , E_R will denote the Young's modulus of the plate and the reinforcement, G_A the shear modulus of the adhesive, and t_P , t_R , t_A the respective thickness. Here are some assumptions; (i) The plate and the reinforcement are both isotropic and have the same Poisson ratio ($\nu_P = \nu_R = \nu_A$) and all deformations are linearly elastic. (ii) There is no out-of-plane bending due to the one-sided reinforcement and no residual thermal stress induced by bonding. (iii) The reinforced plate ignores any variation across the thickness. For the cross-section configuration shown in Fig.1(b), the redistribution of stress in uncracked plate can be calculated explicitly using the one-dimensional theory of bonded joints. Rose[3] obtained the stress, σ_0 , expressed as $\sigma_0 = \sigma_\infty / (1 + S)$, where $S = E_R t_R / E_P t_P$ represents the stiffness ratio between the plate and the reinforcement. Here $E' = E / (1 - \nu^2)$ is the Young's modulus for plane strain condition, $E' = E$ for plane stress condition.

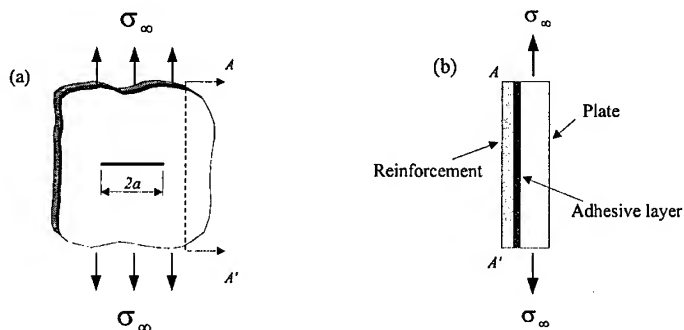


Figure 1. Repair configuration: (a) Patched crack with reinforcement, (b) Cross-section along A-A'

Then it is assumed that distributed linear spring act between the crack faces as shown in Fig.2. The boundary conditions are described by

$$\sigma_{yy} = \sigma_0, \quad \text{as } x^2 + y^2 \rightarrow \infty, \quad (1a)$$

$$\sigma_{yy} = k E_P u_y(x), \quad \text{at } |x| < a, \quad y = 0, \quad (1b)$$

where k is the spring constant. Under plane stress condition, the appropriate value of k can be determined from the stress-displacement relation for the overlap shear joint as shown in Fig.3. Using the 1D theory of joints, Rose[3] obtained the displacement as

$$u_p = \frac{\sigma_0 t_p t_A \beta}{G_A} \quad (2)$$

And he also defined the spring constant as $1/\pi\Lambda$ and calculated using Eq.1b as

$$k = \frac{1}{\pi\Lambda} = \frac{\sigma_0}{E_p u_p} = \frac{G_A}{E_p t_p t_A \beta} \quad (3)$$

And β is denoted as

$$\beta = \sqrt{\frac{G_A}{t_A} \left(\frac{1}{E_p t_p} + \frac{1}{E_R t_R} \right)} = \sqrt{\frac{G_A}{t_p t_A E_p} \left(1 + \frac{1}{S} \right)} \quad (4)$$

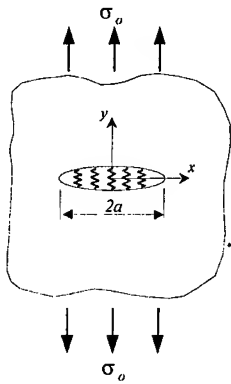


Figure 2. Distributed springs model for a patched crack

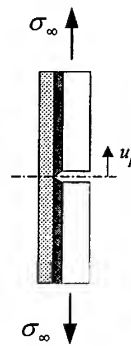


Figure 3. Cross-section for overlap shear joints

3. CALCULATION OF THE STRESS INTENSITY FACTOR AND THE CRACK SURFACE OPENING DISPLACEMENTS USING WEIGHT FUNCTION

The weight function $m(x, a)$ is defined as

$$m(x, a) = \frac{E_p'}{K_{(1)}} \frac{\partial u_{(1)}(x, a)}{\partial a}, \quad (5)$$

where $u_{(1)}(x, a)$ is the crack surface displacement, $K_{(1)}$ is the known stress intensity factor for a loading system (1). Thus, the stress intensity factor and the crack surface displacement for arbitrary stress $\sigma^{(2)}(x)$ is expressed as

$$K_{(2)} = \int_0^a \sigma^{(2)}(x) m(x, a) dx \quad (6)$$

$$u_{(2)}(x, a) = \frac{1}{E_p'} \int_x^a \left[\int_0^x \sigma(x) m(x, a) dx \right] m(x, a) da \quad (7)$$

The crack surface displacement $u_0(x)$ under a remote applied stress $\sigma_0(x)$ and the crack surface displacement $u_s(x)$ due to stresses $\sigma_s(x)$ exerted on distributed springs between the crack surface can be calculated by using the weight function. Thus the resultant crack surface displacement $u_y(x)$ at x is expressed as

$$u_y(x) = u_0(x) - u_s(x) \quad (8a)$$

$$= \frac{1}{E_p'} \int_x^a \left[\int_0^x \sigma_0(x) m(x, a) dx \right] m(x, a) da - \frac{1}{E_p'} \int_x^a \left[\int_0^x \sigma_s(x) m(x, a) dx \right] m(x, a) da. \quad (8b)$$

On the other hand, the crack surface displacement at x_i due to a uniform stress σ_j acting on a segment $2w$ of the crack surface located at x_j as shown in Fig.4 can be expressed as

$$u(x_i, x_j) = \frac{1}{E_p'} \int_{x_i}^a \left[\int_{x_i-w}^{x_i+w} \sigma_j m(x, a) dx \right] m(x_i, a) da. \quad (9)$$

The influence function is defined as $g(x_i, x_j) = u(x_i, x_j)/\sigma_j$ using Eq.9. Thus, the crack surface displacement at x_i for uniform stresses acting on n segments corresponding to distributed spring is simply expressed as

$$u_s(x_i) = \sum_{j=1}^n \sigma_j g(x_i, x_j), \quad (10)$$

where σ_j is given as $E_p' k u_y(x_j)$ defined in Eq.1b. By substituting Eq.10 into Eq.8a, the unknown crack surface displacement $u_y(x_i)$ located at x_i is finally obtained as

$$u_y(x_i) = u_0(x_i) - \sum_{j=1}^n \sigma_j g(x_i, x_j) = u_0(x_i) - \sum_{j=1}^n E_p' k u_y(x_j) g(x_i, x_j). \quad (11)$$

Expressing the influence function $g(x_i, x_j)$ as g_{ij} , the numerical solution for the linear system of Eq.11 can be obtained from the Gauss-Seidel iterative method as proposed by Newman[8]. Thus, the recurrence form is written as

$$u_y(x_i) = \frac{\left[u_0(x_i) - \frac{1}{2} \sum_{j=1}^{i-1} E_p' k u_y^I(x_j) g_{ij} - \sum_{j=i+1}^n E_p' k u_y^{I-1}(x_j) g_{ij} \right]}{k g_{ii} + 1}, \quad (12)$$

where the superscript I is the current iteration number. This process is repeated until the changes in $u_y(x_i)$ are less than the preset tolerance. Using the crack surface displacement obtained from Eq.11, the stress intensity factor $K_r(a)$ for the reinforcement crack is calculated as

$$K_r(a) = \int_0^a \sigma_0(x) m(x, a) dx - \sum_{i=1}^n \int_{x_i-w}^{x_i+w} E_p' k u_y(x_i) m(x, a) dx. \quad (13)$$

The weight function $m(x, a)$ for a center crack in an infinite plate[7] is given as

$$m(x, a) = \sqrt{\frac{a}{\pi}} \frac{1}{\sqrt{a^2 - x^2}}. \quad (14)$$

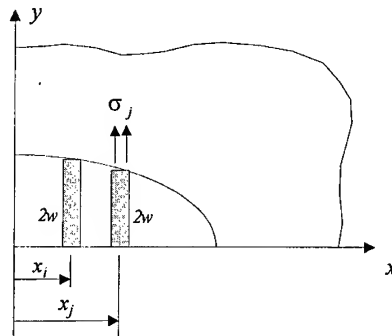


Figure 4. Model for the crack surface displacement at x_i due to a uniform stress σ_j acting on a segment $2w$ of the crack surface located at x_j

4. RESULTS AND DISCUSSION

The width of segment in Eq.9, $2w=0.1\text{mm}$ is used to calculate the stress intensity factor K_r . The dimensions and material properties of the cracked plate, reinforcement and the adhesive layer are summarized in Table 1.

Table 1. Physical dimensions and material properties of a typical repair

Layer	Young's Modulus (GPa)	Poisson's ratio	Thickness (mm)
Plate	70	0.33	3.0
Reinforcement	200	0.33	1.0
Adhesive	0.7*	0.33	0.2

* Adhesive's shear modulus G_A

For a center crack with a patch bonded on one side in an infinite plate as shown in Fig.1(a), Rose[3] obtained the upper bound $K_c = \sigma_0 \sqrt{\pi A}$ and the analytical approximate solution $K_r = \sigma_0 \sqrt{\pi a \Lambda / (a + \Lambda)}$ using physical parameter Λ defined in Eq.3. Figure 5 shows the comparison between the numerical solution obtained from Eq.13 and the analytical solution by Rose[3], and indicates that two solutions are almost same. Upper bound K_c , and $K_o = \sigma_0 \sqrt{\pi a}$ for a center crack subjected to the reduced remote stress σ_o are also shown. When the crack length a is very small, the reduction in stress intensity factor K_r is mainly due to the stress reduction from σ_o .

to σ_0 . As the crack length a increases, the stress intensity factor K_r approaches the constant value K_c . This indicates the increase of the restraint on the relative displacement of the crack faces for a given value σ_0 . Figure 6 represents the crack surface displacement $u_y(x)$ obtained from Eq.11 and the crack surface displacement for a center crack subjected to remote stress σ_0 [7]. The crack surface opening displacement along the crack surface is constant and finite due to the large stress values exerted on the distributed spring elements, and explains that the constraint on the crack surface displacement become increase. Thus, the reason for the constant stress intensity factor being independent on crack length can also be explained.

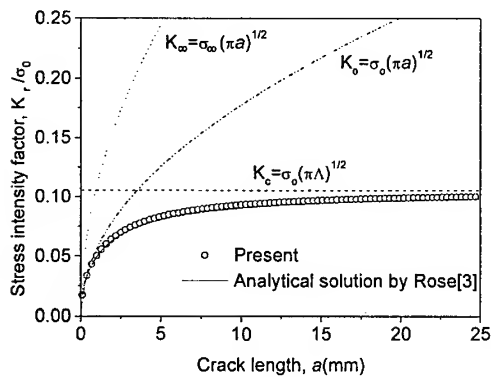


Figure 5. Variation K_r with crack length.

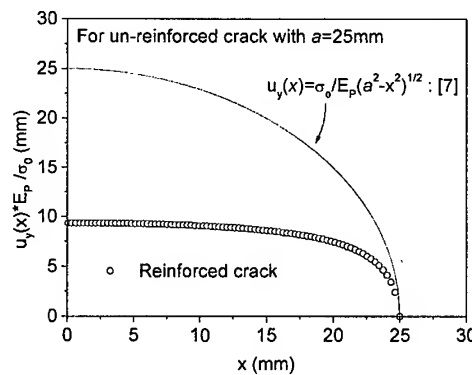


Figure 6. Crack surface displacement $u_y(x)$ with distance from crack mouth.

5. CONCLUSION

For a reinforced center crack subjected to remote uniform stress in an infinite plate, the stress intensity factor was calculated by weight function method, and compared with the analytical approximate solution. The agreement of two solutions showed that the weight function method could be effectively used to obtain the stress intensity factor for the reinforced cracks subjected to non-uniform stress field such as residual stress or thermal loading.

REFERENCE

1. A.A. Baker, *Fatigue Fract. Engng Mater. Struct.*, **16**(7) (1993) p. 753
2. A.T. Zehnder, D.V. Swenson and T.J. Pienkos, *Int. J. Fract.*, **84** (1997) p.307
3. L.R.F. Rose, A.A. Baker and R.Jones, editors, *Bonded Repair of Aircraft Structures*, Martinus Nijhoff Publishers, Dordrecht, The Netherlands (1988) p.77
4. D.B. Marshall, B.N. Cox and A.G. Evans, *Acta Metall.*, **33**(11) (1985) p.2013
5. L.R.F. Rose, *J. Mech. Phys. Solids*, **35**(4) (1987) p.383
6. H.F. Bueckner, and Z. Angew, *Math. Mech.*, **50** (1970) p.529
7. J.R. Rice, *Int. J. Solids Struct.* **8** (1972) p.751
8. J.C. Jr. Newman, *ASTM STP 761* (1982) p.255

Interaction of a Horizontal Finite Crack with a Center of Dilatation in Elastic Half-Planes

K.T. Chau¹, R.H.C. Wong¹ and R.C.K. Wong²

¹ Department of Civil and Structural Engineering, The Hong Kong Polytechnic University, Hung Hom, Kowloon Hong Kong, China P.R.

² Department of Civil Engineering, The University of Calgary, Calgary Alberta, Canada

Keywords: Center of Dilatation, Elastic Half Plane, Horizontal Crack, Stress Intensity Factor

ABSTRACT

This paper summarizes the recent results obtained by Chau and Wong [1] on the interaction of a two-dimensional crack parallel to the free surface of a half-plane subject to the action of an internal center of dilatation. The method of solution follows the principle of superposition. The problem is first decomposed into two auxiliary problems: (I) a half-plane containing a center of dilatation; and (II) a finite crack in half-plane subjected to traction that cancel those induced by the Auxiliary Problem I. The final solution is obtained as the summation of those of the two Auxiliary Problems. Numerical results suggest that as long as the crack is not too close to the free surface of the half-plane, the present solution is accurate enough for practical applications. If the overburden stress due to gravity and the friction on crack surface are neglected, both mode I and II stress intensity factors are induced at the crack tips.

1. INTRODUCTION

Heavy oil and bitumen are major energy resources in Canada, and have become a major focus for the oil and gas industry. The challenge in developing this resource is the difficulty in recovering these highly viscous substances. Steam stimulation is one of the viable thermal recovery methods to extract bitumen from the oil sand ores buried in deep overburden. In this steam-based recovery method, large volumes of steam at high temperatures and pressures (300°C and 10 MPa) are injected into the oil sand formation at depths of 450-500 m through wells in rows of 100 m in spacing (Butler [2]; Boone et al. [3]).

Steam injection produces stress and thermal dilatation of oil sand. Overlain the oil sand formation are low-permeability clay shales forming an impermeable barrier to migration of fluid. Natural horizontal fissures or fractures are commonly found in these shale formations (Wong [4]). These fractures have been formed or subject to large shearing process during glaciation. Therefore, there is no tensile strength or small residual strength remained along these fractures. One of the geomechanics-related problems is if these pre-existing fractures would propagate under steam injection. Interception of these fractures with subsurface well casing could lead to casing impairment or rupture.

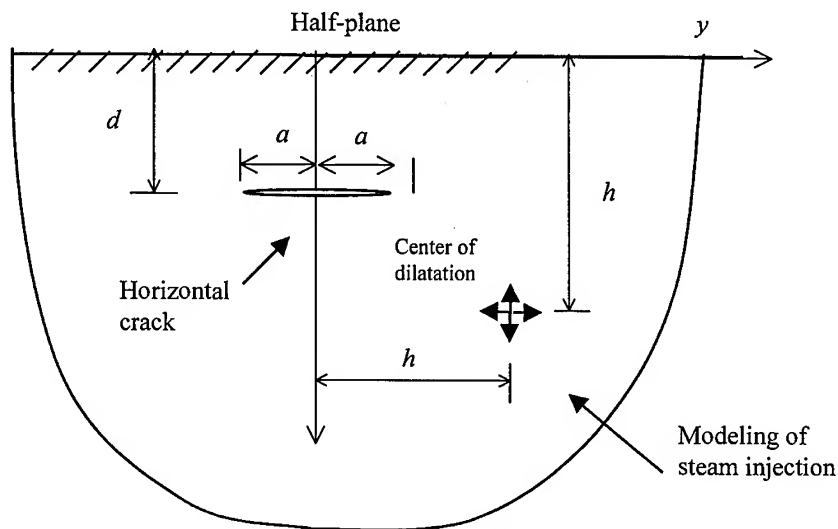


Fig. 1 A sketch for the steam injection into an elastic half-plane is modeled by a center of dilatation located at the point (h_1, h_2) . The depth and size of the crack are d and $2a$.

The main objective of the present paper is to summarize a simple analytical model to analyze and investigate the problem, which is proposed recently by Chau and Wong [1]. The essence of this model is that steam injection to the oil sand formation can be modelled by introducing a center of dilatation in a two-dimensional homogenous isotropic elastic half-plane. More specifically, we will consider the stress intensity factor induced at the tips of a pre-existing horizontal crack, which is parallel to the free surface of the half-plane, by a center of dilatation within the half-plane. Since the steam is capped within the oil sand formation that is far away from the horizontal crack, thermal stress is only induced locally and will not affect the pre-existing horizontal crack far above. Therefore, to simplify our analysis here, the thermal effect induced by the heat source will only be incorporated into the strength of the center of dilatation.

Crack problems in half-planes or half-spaces have received considerable interest because of its possible application in earthquake mechanics (e.g. Rudnicki and Wu [5]; Jeyakumaran and Keer [6]). However, no solution exists for crack problems in half-planes or half-spaces under the action of a center of dilatation. The solutions for the interactions between a plane or 3-D crack under the action of a center of dilatation only exist for an infinite domain (e.g. Weertman and Hack [7-8]; Kachanov and Karapetian [9]; Karapetian and Kachanov [10]; Gross and Wagner [11]).

Therefore, the main objective of the present paper is to summarize our recent solution (Chau and Wong [1]) for the interaction of center of dilatation with 2-D cracks in half-planes. The counterpart solution for 3-D cracks in half-space will be presented in our later publication.

In particular, the problem of a crack parallel to the surface of half-plane under a center of dilatation is first decomposed into two Auxiliary Problems: (I) a half-plane consisting of a center of dilatation; and (II) half-plane with a crack parallel to the free surface and tractions are applied on the crack surface to cancel out the stresses induced on the position of the crack in the

Auxiliary Problem I. The solution of the first problem has been given by Rani et al. [12], while that for the second problem has not been solved. To simplify the problem mathematically, we employ the fundamental solution in an infinite plane, expressed in terms of the Westergaard stress function (e.g. Tada et al. [13]). Mathematically, the present solution is not exact since the fundamental solution on the crack surface that we propose to use does not satisfy the traction free condition on the surface of the half-plane. However, as long as the horizontal crack shown in Fig. 1 is not too close to the surface of the half-plane, the present solution should provide a reasonably good approximation for the problem.

2. MATHEMATICAL FORMULATION

The strategy in solving the problem is that the original problem can be decomposed into two auxiliary problems (I) and (II). The first Auxiliary Problem (I) is the solution of the center of dilatation due to an internal center of dilatation, and the second Auxiliary Problem (II) is an internal crack with surface tractions which cancel those created by the center of dilatation on the line of the crack surface ($z=d$ and $-a < y < a$ in Fig. 2).

2.1 Center of Dilatation in Half-plane

The center of dilatation in a half-plane can be obtained by superimposing two orthogonal force dipoles at a point. Consider a Cartesian coordinate with the origin on the surface of a half-plane as shown in Fig. 2. The appropriate form of the Airy stress function for a center of dilatation located at (h_1, h_2) as shown in Fig. 2 in a linear elastic half-plane can be expressed as (Rani et al. [12]):

$$\varphi = (1-\alpha) \frac{c_0}{\pi} \left[\ln \left(\frac{R_2}{R_1} \right) - \frac{2z(z+h_2)}{R_2^2} \right] \quad (1)$$

where

$$R_1^2 = (y-h_1)^2 + (z-h_2)^2, \quad R_2^2 = (y-h_1)^2 + (z+h_2)^2, \quad \alpha = 1/[2(1-\nu)] \quad (2)$$

and ν is the Poisson's ratio of the half-plane, and c_0 is the strength of the center of dilatation (in unit of force). For elastic materials without body force, the Airy stress function φ satisfies the biharmonic equation. The corresponding stresses can be found as (Chau and Wong [1]):

$$\sigma_{yy} = (1-\alpha) \frac{c_0}{\pi} \left\{ -\frac{1}{R_1^2} - \frac{3}{R_2^2} + \frac{2(z-h_2)^2}{R_1^4} + \frac{6(z+h_2)(3z+h_2)}{R_2^4} - \frac{16z(z+h_2)^3}{R_2^6} \right\} \quad (3)$$

$$\sigma_{yz} = (1-\alpha) \frac{c_0}{\pi} (y-h_1) \left\{ -\frac{2(z-h_2)}{R_1^4} - \frac{2(3z+h_2)}{R_2^4} + \frac{16z(z+h_2)^2}{R_2^6} \right\} \quad (4)$$

$$\sigma_{zz} = (1-\alpha) \frac{c_0}{\pi} \left\{ \frac{1}{R_1^2} - \frac{1}{R_2^2} - \frac{2(z-h_2)^2}{R_1^4} - \frac{2(z+h_2)(5z-h_2)}{R_2^4} + \frac{16z(z+h_2)^3}{R_2^6} \right\} \quad (5)$$

Therefore, the solution for the Auxiliary Problem I is known.

2.2 Fundamental Solution for Point Forces on Finite Crack

As mentioned in the Introduction that the fundamental or point force solution on cracks parallel to the surface of a half-plane is not available in the literature. Therefore, the fundamental solution for point force in an infinite plane will be employed in the present analysis. In particular, for the normal and tangential pairs of point forces (P and Q) on the crack face, the Westergaard stress function can be given by Tada et al. [13]. The corresponding stress intensity factor at crack tip $+a$ and $-a$ are given by (Tada et al. [13]):

$$\begin{Bmatrix} K_I \\ K_{II} \end{Bmatrix}_{\pm a} = \frac{1}{\sqrt{\pi a}} \begin{Bmatrix} P \\ Q \end{Bmatrix} \sqrt{\frac{a \pm b}{a \mp b}} \quad (6)$$

where the upper sign is for the crack tip at $\xi=+a$ while the lower one for the crack tip at $\xi=-a$. The stress intensity factors for tensile and shear modes are denoted by K_I and K_{II} , respectively. Using the principle of superposition, we can replace b , P , Q by ξ , $\sigma_{xx}(\xi, d)d\xi$ and $\sigma_{yz}(\xi, d)d\xi$, respectively, and integrate the point forces from $-a$ to $+a$. The stresses $\sigma_{xx}(\xi, d)$ and $\sigma_{yz}(\xi, d)$ are the corresponding normal and shear stresses induced on the line of the horizontal crack and given in (3-5). More specifically, the stress intensity factors due to the center of dilatation can be approximated using the following integration over the crack face:

$$\begin{Bmatrix} K_I \\ K_{II} \end{Bmatrix}_{\pm a} = \frac{1}{\sqrt{\pi a}} \int_{-a}^{+a} \begin{Bmatrix} -\sigma_{xx}(\xi, d) \\ -\sigma_{yz}(\xi, d) \end{Bmatrix} \sqrt{\frac{a \pm \xi}{a \mp \xi}} d\xi \quad (7)$$

Although the square root term in the integrand of (7) approaches infinity at the tip $+a$ for mode I and at the tip $-a$ for mode II, it is straightforward to verify that the integration exists and converges. Thus, the integration can be done by following a standard procedure using an algorithm of Simpson's rule with error control (e.g. Press et al. [14]) except at the crack tips. In addition, for the mode I cracking, stress intensity factor can only be induced by tensile stress. Thus, we should set compressive normal stress, which is required to cancel out the effect due to the center of dilatation on the crack face, to zero in our integration if both frictional and overburden effects are neglected.

The final stress field in the half-plane can now be obtained by adding the solutions of the two auxiliary problems. However, the only singularity at the crack tips is due to the Auxiliary Problem (II). To increase the computational efficiency of integrating (11), Chau and Wong [1] also proposed an analytical treatment for the integrand at the crack tips. The details will be not be reported here and is referred to Chau and Wong [1].

3. NUMERICAL RESULTS AND DISCUSSION

Figure 2 plots the normalized mode I stress intensity factors $K/(\sigma_0 \sqrt{a})$ at crack tips $+a$ against the normalized horizontal distance h_1/a of the center of dilatation from the z -axis for various values of h_2/a with $d/a=3$, where $\sigma_0 = (1-\alpha)c_0/(\pi a^2)$ is the normalized strength of the center of dilatation (in unit of stress). Numerical results by Chau and Wong [1] showed when the center of dilatation is close to the crack surface, the present solution is accurate. When

the center of dilatation is far above the crack (e.g. $h_2/a=1$), the center of dilatation, as expected, will not induce tensile cracking.

More expensive numerical results can be found in Chau and Wong [1] and due to page limit they will not be given here. In general, Chau and Wong [1] found that as long as the crack is not too close to the free surface of the half-plane (say more than 1.5 times of the crack length), the present solution is accurate enough for practical applications. If the overburden stress and the friction on crack surface are neglected, both mode I and II stress intensity factors (K_I and K_{II}) are induced at the crack tips. The maximum of K_I occurs when the center of dilatation is located behind the crack tips while the maximum of K_{II} occurs when the center of dilatation is located in front of the crack tips. The tensile cracking is likely to be prohibited by the overburden stress (except for extremely strong center of dilatation), while shear cracking remains possible even including the effects of both overburden and friction on the crack surface.

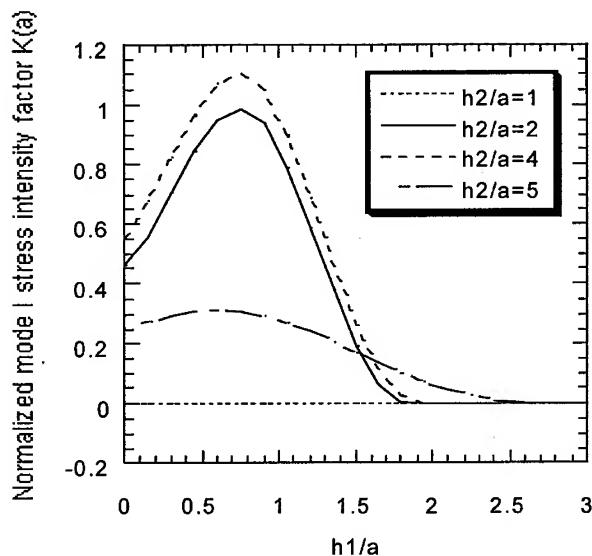


Fig. 2 The normalized mode I stress intensity factors at crack tip $+a$ against the normalized distance h_1/a for various values of h_2/a with $d/a=3$. The effects of overburden and friction on crack surface have been ignored.

4. CONCLUSION

We have summarized an approximate solution proposed recently by Chau and Wong [1] for the stress intensity factor at the crack tips of a finite crack of length $2a$ which is located at a depth of d below and is parallel to the free surface of the half-plane, under the action of an internal center of dilatation. The problem is decomposed into two Auxiliary Problems: (I) a half-plane containing a center of dilatation; and (II) a finite crack in half-plane subjected to

traction that cancel those created by the Auxiliary Problem I. The present solutions should provide a simple method to assess the critical strength of the center of dilatation such that further cracking can be avoided. More recently, the solution for a penny-shaped in an elastic halfspace under the action of 3-D center of dilatation had been obtained. The results were found comparable to those given by Chau and Wong [1] for the 2-D case.

5. ACKNOWLEDGEMENT

This research was done in the summer of 1999 when KTC was on sabbatical leave at the University of Calgary. The visit was made possible by the financial support from both the University of Calgary (through NSERC and Imperial Oil Grants) and the Hong Kong Polytechnic University (through Staff Development fund of the CSE department).

REFERENCES

1. Chau K.T., and R.K.C. Wong, Submitted to Int. J. Numer. Anal. Meth. Geomech. (1999).
2. Butler, R. Thermal Recovery of Oil and Bitumen. Prentice-Hall, New York (1991).
3. Boone, T.J., Gallant, R.J. and Kry, P.R. Exploiting high-rate injection and fracturing to improve areal thermal conformance in cyclic steam stimulation. *SPE #25796*, First presented at the Int. Thermal Operations Sym. held in Bakersfield, CA, Feb. 8-10 (1993).
4. Wong, R.C.K. Canadian Geotechnical Journal, **35** (1998), 206-221.
5. Rudnicki, J.W. and Wu, M. Journal of Geophysical Research, **100** (1995), 22173-22186.
6. Jeyakumaran, M. and Keer, L.M. Bull. Seismol. Soc. Am., **84** (1994), 1903-1915.
7. Weertman, J. and Hack, J.E. Int. J. Fract., **30** (1986), 295-299.
8. Weertman, J. and Hack, J.E. Int. J. Fract., **36** (1988), 27-34.
9. Kachanov, M. and Karapetian, E. Int. J. Solids and Structures, **34** (1997), 4101-4125.
10. Karapetian, E. and Kachanov, M. Int. J. Solids and Structures, **33** (1996), 3951-3967.
11. Gross, D. and Wagner, Ch. Archive Appl. Mech., **62** (1992), 134-145.
12. Rani, S., Singh, S.J., and Garg, N.R. Phys. Earth Planetary Interiors, **65** (1991), 276-282.
13. Tada, H., Paris, P.C., and Irwin, G.R. The Stress Analysis of Crack Handbook. Del Research Corporation, St. Louis, Missouri (1985).
14. Press, W.H., Flannery, B.P., Teukolsky, S.A. and Vetterling, W.T. Numerical Recipes: The Art of Scientific Computing. 2nd ed., Cambridge University Press, New York (1992).

Determinations of Stress Intensity Factor in Isotropic and Anisotropic Body by the Photoelastic and Caustics Methods under Various Load Ratios

A. Shimamoto¹, J.H. Nam¹, T. Shimomura² and E. Umezaki³

¹ Department of Mechanical Engineering, Saitama Institute of Technology,
1690 Fusaiji, Okabe, Saitama 369-0293, Japan

² Graduate School of Engineering, Saitama Institute of Technology,
1690 Fusaiji, Okabe, Saitama 369-0293, Japan

³ Department of Mechanical Engineering, Nippon Institute of Technology,
4-1 Gakuendai, Miyashiro, Saitama 345-8501, Japan

Keywords: Biaxial Load, Biaxiality Ratios, Caustics Method, Fracture Mechanics, Photoelastic Experiment, Stress Intensity Factor

ABSTRACT

In this study, stress intensity factors were investigated and determined by caustics method and photoelastic experiment to clarify the behavior of a crack tip under various biaxiality ratios on the polycarbonate plate with isotropy and anisotropy used as structural components. As result, It was confirmed that only " K_I " affected without receiving the effect by biaxiality ratio, isotropy and anisotropy in case of the crack angle $\Theta = 0^\circ$ under the biaxial loading. It was confirmed that an affects on only K_I in the isotropic polycarbonate plate with crack angle $\Theta = 45^\circ$ under the biaxial load (1:1). However, it is proven that simultaneously affected the mode-I and mode-II in the biaxiality ratio is more than 1:1. Furthermore, The stress intensity factor value K_{II} was extremely to rise from over biaxiality ratios of 3.0 by extrusion direction and biaxiality ratio in case of polycarbonate plate with the anisotropy.

1. INTRODUCTION

The high polymer material makes high-strengthen and high-elasticity to be features and it is used with enlargement and lightening of machinery and structure as structural members such as aircraft, ship, automobile and so on. However, the complicated fracture event has been produced by performance improvement of the machinery and cruel service condition. The stress states of the components are few that are under the uniaxial stress, but it was usually under biaxial or multiaxial stress. Therefore, authors developed a static and dynamic biaxial loading device to clarify the fracture problem in a complicated load and under biaxial stress. [1] (Fig.1)

In this study, stress intensity factor was investigated and determined by caustics method and photoelastic experiment to clarify the behavior of a crack tip under various biaxiality ratios on the polycarbonate plate with isotropy and anisotropy used as structural components.

2. TEST PIECE AND EXPERIMENTAL METHODS

2.1. Test piece

In this study, the test pieces used two kinds of the polycarbonate plate with isotropy (molding) and anisotropy (extrusion molding), and the dimension is shown in Fig.2. Test pieces were 6 mm thickness, length and width 300mm, the fillet s radius 50mm, and using the vertical machining center, the cruciform test piece was produced by drilling and end milling. The crack was processed to the 28mm length using the long end mill of the 0.8mm diameter in addition, 1mm was processed by pushing in razor edge of the 0.08mm thickness in both sides of the crack-tip, and it brought it close to the natural crack. The extrusion direction was set to be Y direction in the polycarbonate plate with the anisotropy and the cracks oriented 0° and 45° to the direction.

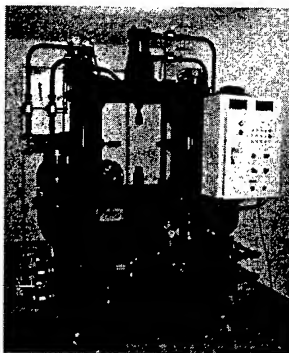


Fig. 1 A photograph of biaxial loading device

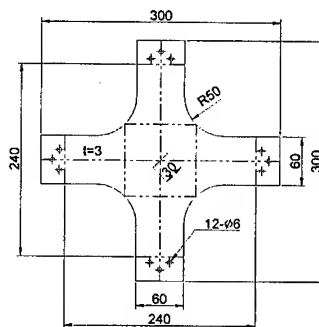


Fig. 2 Dimension of cruciform specimen.
(unit:mm)

2.2. Experimental Method

In this study, used experiment equipments are the biaxial loading device that authors developed (Fig.1) with photoelasticity and caustics equipment. In experiment, tension velocity was constant at 0.1mm/s, and load of Y axis (P_y) was made to be fixed at 490N in case of isotropy, and only the load of the X-axis (P_x) was changed to four stages to 490N~1961N(1:1~1:4) and the extrusion direction was made to be the Y direction in case of anisotropy, and the biaxiality ratio(defined as $\beta = P_x/P_y$) and load of X-axis was taken under the equal condition to the polycarbonate with isotropy and only the load of Y axes was changed to four stages to 1:1~1:4, experiment was carried out. The photoelasticity isochromatic fringe pattern and caustic images of crack tip vicinity under each biaxiality ratio were continuously observed and photographs taken.

3. DETERMINATIONS OF STRESS INTENSITY FACTOR

3.1. Photoelasticity Method

In the determination of stress intensity factor K_I and K_{II} value, a photoelasticity isochromatic fringe pattern and image of caustics in each load point were continuously taken by a camera, input to the computer, and the necessary value was measured. For the calculation of stress intensity factor K_I and K_{II} value from the isochromatic fringe loop, distance R_m and angle θ_m to the most apo-center of the each isochromatic fringe loop around the crack tip as shown in Fig. 3 which were measured, and the case of mode- I was obtained by Irwin's method[2] of eq.1 and K_{II} of mixed-mode were obtained by Smith's method [3] of eq.2a, eq.2b and eq.2c.

$$K_I = \frac{n\sqrt{2\pi r_m}}{\alpha \sin \theta_m} \left(1 + \left(\frac{2}{3 \tan \theta_m}\right)^2\right)^{-0.5} \times \left(1 + \frac{2 \tan(3\theta_m/2)}{3 \tan \theta_m}\right) \quad (1)$$

$$K_I = \frac{n(2\pi r_m)^{1/2}}{\alpha \left\{ (\sin \theta_m + 2A \cos \theta_m)^2 + A^2 \sin^2 \theta_m \right\}^{1/2}} \quad (2a)$$

$$K_{II} = \frac{An(2\pi r_m)^{1/2}}{\alpha \left\{ (\sin \theta_m + 2A \cos \theta_m)^2 + A^2 \sin^2 \theta_m \right\}^{1/2}} \quad (2b)$$

$$A = \frac{K_{II}}{K_I} = \frac{2}{3} \left(\cot 2\theta \pm \sqrt{\cot^2 \theta_m + \frac{3}{4}} \right) \quad (2c)$$

where n is the number of the fringe, t is the thickness of specimen, α is the photoelasticity sensitivity constant, r and θ_m are, respectively, the distance and angle in polar coordinates at point M , shown schematically in Fig. 3. In the calculation of the stress intensity factors, $73.5^\circ < \theta < 134^\circ$ range with small error was measured, and it calculated respectively K_I , K_{II} value. [4]

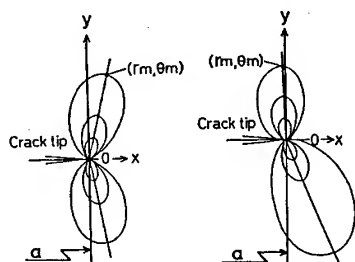


Fig. 3 Geometry of isochromatic fringe roop at the crack tip

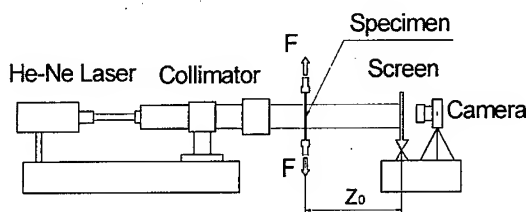


Fig. 4 Schematic of caustics experiment apparatus

3.2 CAUSTICS METHOD

In case of caustics method, experiment was carried out using caustics equipment shown in Fig. 4. The light source was He-Ne Laser (He-Ne Laser LHG-3223), and the specimen under the biaxial tension load was made to penetrate parallel light beam by collimator (Auto Collimator, Nikon-6B), and took photographed of the caustic image from the screen rear. The fundamental shape of caustic curves in mode-I and mode-II are shown in Fig.5. In the calculation of stress intensity factor K_I and K_{II} in a parallel light beam, in case of mode-I was obtained by eq 3 [5,6] and case of mixed mode was obtained by eq 4 and eq 5 [7-8].

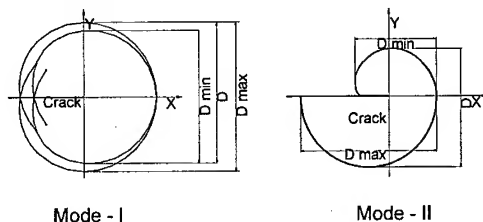


Fig. 5 Schematic of caustic curve of Mode I and Mode II

$$K_I = \frac{1.671}{Z_0 t |C_0|} \times \left(\frac{D_{\min}}{\delta} \right)^{5/2} \quad (3)$$

$$K_I = \frac{1.671}{Z_0 t |C_0|} \times \left(\frac{D_{\min}}{\delta} \right)^{5/2} \times \frac{1}{\sqrt{1 + \mu^2}} \quad (4)$$

$$K_{II} = \frac{1.671}{Z_0 t |C_0|} \times \left(\frac{D_{\min}}{\delta} \right)^{5/2} \times \frac{\mu}{\sqrt{1 + \mu^2}} \quad (5)$$

where, Z_0 is a distance of test piece and screen, t is the specimen thickness, D_{\min} is a smallest diameter of the crack tip caustic on the screen, C_0 is an optical constant, δ and μ are material constants.

4. EXPERIMENTAL RESULTS AND DISCUSSION

The effect under the biaxial stress of the polycarbonate with optically isotropic and anisotropic on the crack tip was investigated. Examples of the isochromatic fringe pattern and caustic image under each biaxiality ratio (β) are shown in Fig. 6.

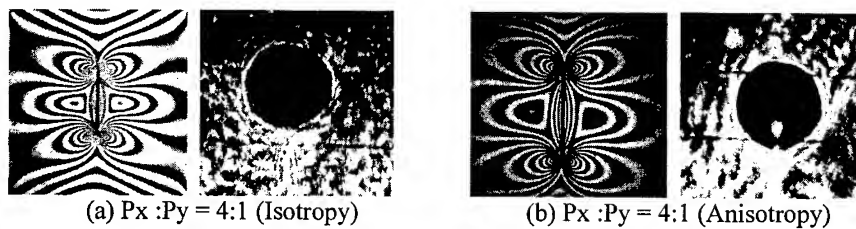


Fig. 6 The isochromatic fringe patterns and the caustic images under biaxiality ratios in the polycarbonate with optically isotropy and anisotropy. ($\theta = 0^\circ$)

It is proven from Fig. 6(a), (b) that is an isochromatic fringe pattern under biaxiality ratios ($\beta = 1 \sim 4$) of polycarbonate plate with optically isotropy and anisotropy are the left-right symmetries for the crack direction and those are almost arising perpendicularly. The caustic image becomes almost a perfect circle. It is proven from these facts, there is only effect of K_I in the crack angle zero ($\theta = 0^\circ$) without also receiving either an effect biaxiality ratio, optically isotropy and anisotropy. It is proven from Fig. 7(a), (b) and Fig. 8(a), (b) the isochromatic fringe patterns and caustic images are having affects on only K_I in the isotropy polycarbonate plate with crack angle 45° under the biaxiality ratio $\beta = 1$. However, the isochromatic fringe loop becomes asymmetric and tilted form, as the biaxiality ratio increases from $\beta = 1$, and the caustic image becomes a volute that collapsed from the perfect circle. That is to say, it is proven that simultaneously, opening type stress intensity factor K_I and in-plane shear type stress intensity factor K_{II} affected. The isochromatic fringe patterns under biaxiality ratio $\beta = 1$ of the anisotropy polycarbonate plate shows almost the tendency in mode- I (K_I). However, a slight collapses on the caustic image from the perfect circle shows the tendency in mixed mode. These facts, it seems to occur for anisotropic properties according to the extrusion direction. It became tilted form in which the photoelasticity fringe loop was similar to isotropy that asymmetric with the increase the load ratio and the caustic image became a shape of volute.

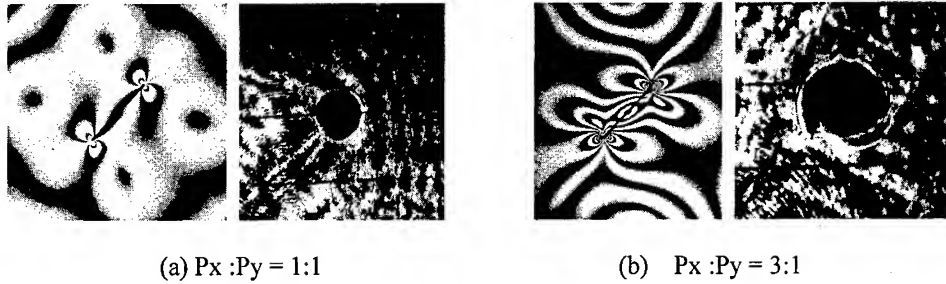


Fig.7 The isochromatic fringe patterns and the caustic images under biaxiality ratios in the polycarbonate with optically isotropy. ($\theta = 45^\circ$)

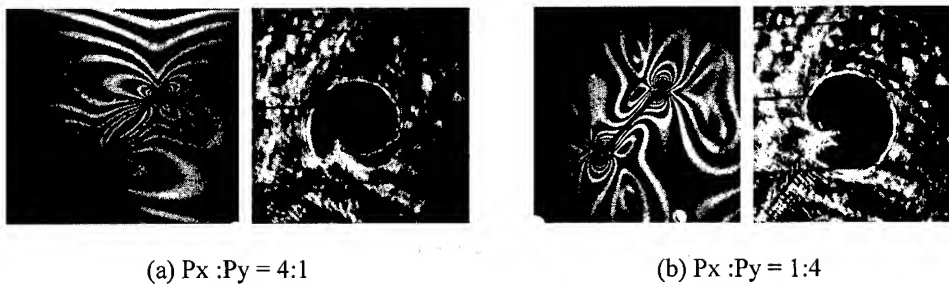


Fig.8 The isochromatic fringe patterns and the caustic images under biaxiality ratios in the polycarbonate with optical anisotropy. ($\theta = 45^\circ$)

4.1. The relationship between stress intensity factors K_I , K_{II} and load ratios.

The relationship between stress intensity factors and biaxiality ratios were calculated by photoelasticity approach and caustics method from the experimental result and the values are shown in Fig. 9 and Fig.10. Fig. 9 shows the relationship between a biaxiality ratio and stress intensity factor K_I with crack oriented zero deg in the polycarbonate plate with isotropy and anisotropy. It was proven that the stress intensity factor K_I of photoelasticity approach and caustics methods are almost agreeing from these facts and the effect by isotropy and anisotropy could be not recognized.

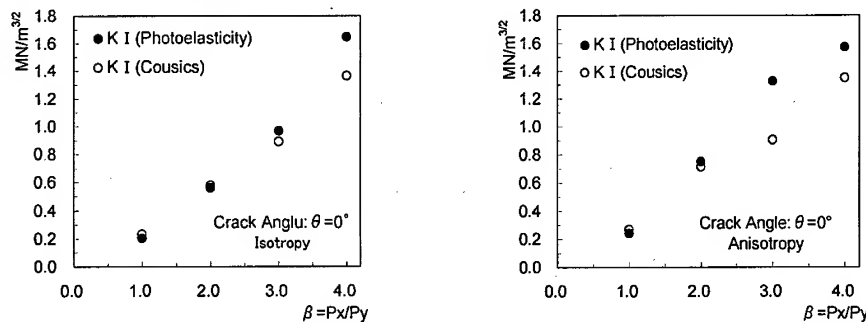
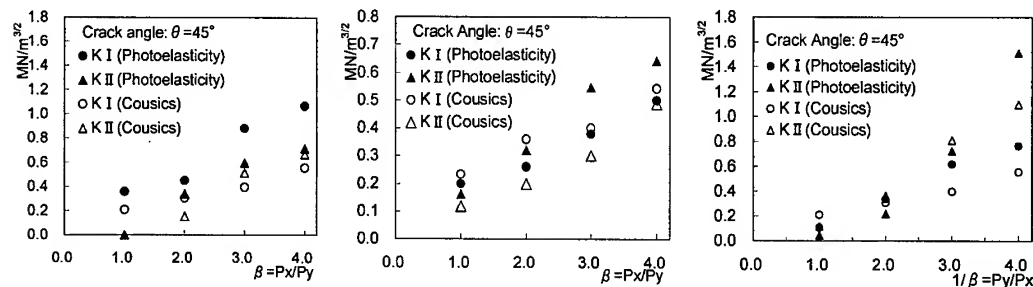


Fig. 9 Comparison of stress intensity factors by photoelasticity approach and caustics method

However, It is proven from Fig. 10(a), (b) and (c) that the biaxiality ratio also increased the stress intensity factor (K_I , K_{II}) at over all range with the increase in case of the crack oriented 45 degrees. Especially, it was proven that an amount of change of the K_{II} value remarkably increased

than the K_I value. And, it was confirmed that the effect according to the extrusion direction was most received, when the biaxiality ratio consists more than $\beta=3$ and $1/\beta=3$ for the relationship between stress intensity factors (K_I , K_{II}) by the extrusion direction and biaxiality ratio of polycarbonate plate with the anisotropy, it was proven from figure 10(b) and (c). Designing a considering extrusion direction and biaxiality ratio is important, when the anisotropic material is used as machinery component to prove from these facts.



(a) Isotropy ($\theta=45^\circ$, P_x/P_y) (b) Anisotropy ($\theta=45^\circ$, P_x/P_y) (c) Anisotropy ($\theta=45^\circ$, P_y/P_x)

Fig. 10 Relationship between a biaxiality ratio and stress intensity factor

5. CONCLUSIONS

In this research, we obtain the knowledge as followings that stress intensity factor K_I , K_{II} was comparison and investigation in the polycarbonate plate with isotropy and anisotropy under biaxial stress by photoelastic experiment and caustics method.

1. It was confirmed that only K_I affected without receiving the effect by biaxiality ratio(β), isotropy and anisotropy in case of the crack angle $\theta=0^\circ$ under the biaxial loading.
2. It was confirmed that an affects on only K_I in the isotropic polycarbonate plate with crack angle $\theta=45^\circ$ under the biaxiality ratio $\beta=1$. However, it is proven that simultaneously affected the mode- I and mode- II in the biaxiality ratio is more than $\beta=1$.
3. The stress intensity factor value K_{II} was extremely to rise from over biaxiality ratios $\beta=3$ and $1/\beta=3$ by extrusion direction and biaxiality ratio in case of polycarbonate plate with the anisotropy.

ACKNOWLEDGEMENT

This work was supported by the High-Tech Research Center of Saitama Institute of Technology.

REFERENCES

1. J. Nam, A. Shimamoto, T. Shimomura, S. Tsukagoshi, Proc. of ATEM'99, Japan, Vol. 1,
2. G. R. Irwin, Proc. of SESA, 16-1 (1958), p93-96. [p.350-355]
3. D. G. Smith and C. W. Smith, Eng. Frac. Mech., 4 (1972), p.357-366.
4. J. M. Etheridge and J. W. Dally, Experimental Mechanics, 17 (1977), p.248-254.
5. P.S. Theocaris and E.Gdoutos, Trans. ASME, Ser. E, 39-1(1972), p.75.
6. K. Shimizu, H. Shimada, T. Sasaki, JSME, (in Japanese) A, 46-411 (1980), p.1196.
7. P.S. Theocaris and E.Gdoutos, Trans. ASME, Ser. E, 39-1(1972), p.91.
8. H. Shimada, K. Shimizu, The Japan Society for Photoelasticity, (in Japanese) No.1 (1979), p.29.

A Micromechanics Criterion for the Ductile Fracture of a Polycarbonate

T. Wang¹, K. Kishimoto² and M. Notomi³

¹ Department of Engineering Mechanics, Xi'an Jiaotong University, Xi'an 710049, China P.R.

² Department of Mechanical and Intelligent Systems Engineering, Tokyo Institute of Technology,
2-12-1 O-okayama, Meguro-ku, Tokyo 152-8552, Japan

³ Department of Mechanical Engineering, Meiji University, 1-1-1 Higashimita,
Tama-ku, Kawasaki-shi, Kanagawa 214-8571, Japan

Keywords: Deformation, Ductile Fracture, Micromechanics, Polycarbonate, Polymer, Stress Triaxiality, Thermoplastics

ABSTRACT

In this paper, experiments and micromechanics analysis are carried out to understand the deformation and fracture behavior of a polycarbonate (PC) under different triaxial stress fields. Effect of triaxial stress constraint on the deformation and fracture behavior of the PC is experimentally investigated. The other purpose of this paper is to discuss the extent to which a micromechanics criterion proposed by the first author can serve as a fracture criterion for ductile polymers. A new ductile fracture parameter is emphasized, which can be employed to evaluate the fracture ductility of polymers. Stress state independence of the parameter for the PC has been experimentally verified.

1. INTRODUCTION

It is well-known that traditional structural metallic materials are being replaced with polymers in a number of critical engineering applications. However, the research into the fracture of polymers is in its infancy compared with the fracture of metals, and much of the necessary theoretical framework is not yet fully developed for polymers [1]. J integral has had success with many ductile polymers, in which the fracture resistance is measured in terms of the critical value of J denoted J_{Ic} [1,2]. Although conventional J integral test can provide a measure of fracture toughness of polymers, it is important to recognize the limitations of such an approach which involves additional problems [1,3]. For example, J may be inadequate. Measurement of J_{Ic} needs rather specialized equipment and techniques. The standards for measuring J_{Ic} and J - R curves in polymers are not yet developed. The size requirements make the application of J integral to measure the toughness of thin polymer films impossible. The validity of utilizing a blunting line to determine the critical value of J integral is questioned for some ductile polymers, etc. So, how to evaluate the fracture property of polymers is

still an open problem and the research of alternative method is urgently required.

As an alternative approach to predicting fracture, damage mechanics are being widely researched and appear promising. Many idealized models involving continuum damage mechanics [4-9] and micromechanics [10-12] have been proposed to assess the behavior of ductile fracture. In what follows, experiments and micromechanical analysis will be carried out to understand the effect of triaxial stress constraint on the deformation and fracture behavior of a polycarbonate (PC). Then, the extent to which a micromechanics criterion for ductile fracture proposed by Wang and Kuang [12] can serve as a criterion for the fracture of ductile polymers will be discussed.

2. EXPERIMENTAL

2.1. Material and Testing

The material considered here is a ductile thermoplastic PC with a molecular weight of 22000. Intensity of triaxial stress constraint is measured by means of stress triaxiality denoted by σ_m/σ_{eq} with σ_m and σ_{eq} being hydrostatic and von Mises equivalent stresses, respectively. In order to vary the stress triaxiality experimentally, tests were performed on the circumferentially blunt-notched bars with six kinds of profile notch radius R ranged from 0.8, 1.2, 2.0, 4.0, 8.0 mm to infinite, as shown in Fig.1. The initial diameter, $D_0=5\text{mm}$, of the minimum cross-section remains unchanged for all the bars. Thus, the maximum value of σ_m/σ_{eq} can be calculated as [11]

$$\frac{\sigma_m}{\sigma_{eq}} = \frac{1}{3} + \ln\left(1 + \frac{D}{4R}\right). \quad (1)$$

Thus, the stress state is defined by the specimen geometry.

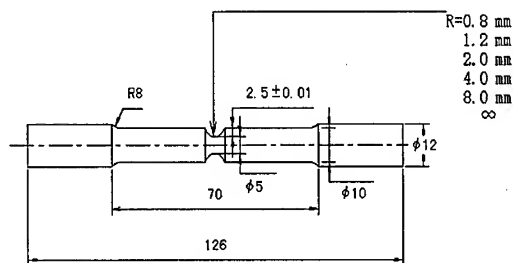


Fig.1. Geometry and dimensions of the notched tensile bars.

The bars were carefully manufactured from 12 mm-thick plates of the PC. A MTS-810 machine was used for the tensile tests at room temperature, approximately 20°C. Two sensors with the requisite sensitivity were used in the experiments. One was used to monitor the continuous variations in the minimum diameter of the notch, another 25-mm extensometer was mounted across the notch to control the axial displacement rate and to measure the axial strain. The crosshead speed is 1mm/min. Stress and strain responses were obtained from the tensile tests of smooth and notched bars, where the average axial stress is the load divided by the original minimum cross-section area, and the axial strain is calculated from the 25-mm extensometer. Thus, the Young's modulus, E , and

yield stress, σ_y , can be calculated from the smooth bar tests. For notched bar tests, the initial slopes of the stress-strain curves and the corresponding yield stresses are defined as pseudo-Young's modulus, E' , and pseudo-yield stress, σ_y' , respectively. The fracture strain ε_c under different stress states were calculated from the variations in the minimum diameter of the notch [11]

$$\varepsilon_c = 2 \ln \left(\frac{D_0}{D_c} \right), \quad (2)$$

where D_c is the critical value of the minimum notch diameter. Most of the data represent average values of three test specimens.

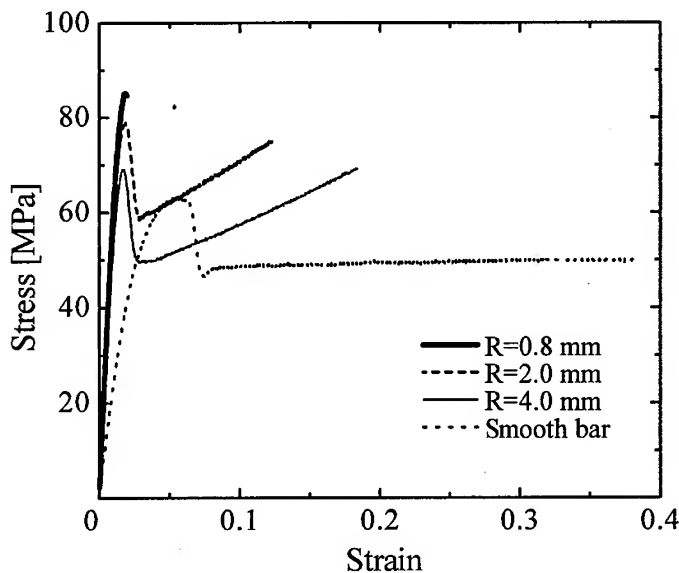


Fig.2. Stress – strain covers for the PC in different triaxial stress fields.

2.2. Experimental Results

Figure 2 shows the average axial stress and strain responses of the PC obtained from a series of tensile tests of smooth and notched bars. It is seen that deformation of the PC behaves very differently in different triaxial stress fields. In the case of smooth bar with low stress triaxiality ($\sigma_m/\sigma_{eq} = 1/3$), the unmodified PC exhibited an initial yield at maximum stress, then accompanied by the formation of a neck, and finally followed by a long propagation process of the neck. This leads to a significant strain softening and a constant stress deformation. At middle level of stress triaxiality ($\sigma_m/\sigma_{eq} = 0.605$ and 0.819 or $R=4\text{mm}$ and 2mm), the PC yields at a maximum stress first, then accompanied by a sharp strain softening, and finally followed by a strain hardening process. In the case of higher triaxial stress constraint ($\sigma_m/\sigma_{eq} = 1.274$ or $R=0.8\text{mm}$), deformation behavior of the PC is similar to a brittle material. Effect of stress triaxiality on Young's and pseudo-Young's modulus

and initial yield and pseudo-yield stresses of the PC are shown in Figures 3 and 4, respectively. It is seen that rigidity of the PC increases with the increase of stress triaxiality. It indicates that triaxial stress constraint has important effect on the deformation behavior of the PC. Figure 5 shows the effect of triaxial stress constraint on the critical fracture strain ϵ_c of the PC. It is clear that the value of ϵ_c decreases with the increase of stress triaxiality. Apparently, tensile stress triaxiality results in the brittle fracture of the PC.

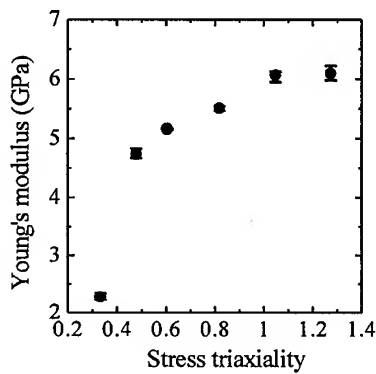


Fig.3. Effect of stress triaxiality on Young's modulus.

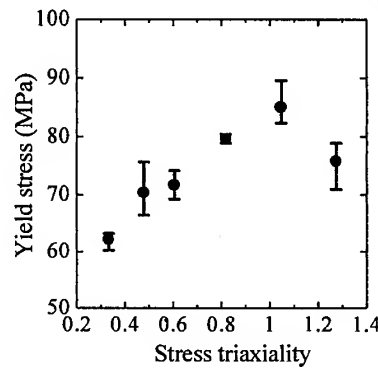


Fig.4. Effect of stress triaxiality on yield stress.

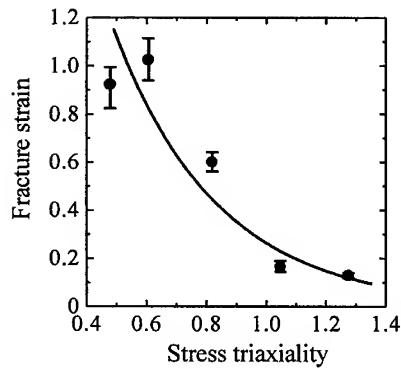


Fig.5. Effect of stress triaxiality on the fracture strain of the PC.

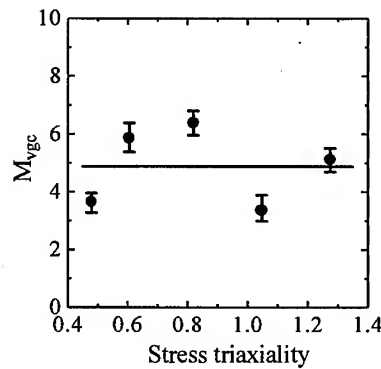


Fig.6. Stress state independence of M_{vgc} .

3. A MICROMECHANICS CRITERION FOR DUCTILE FRACTURE

Based on the well-known Rice-Tracey void growth model [10],

$$\frac{dR}{R} = 0.283 \exp\left(\frac{3}{2} \frac{\sigma_m}{\sigma_{eq}}\right) d\epsilon_{eq}^p, \quad (3)$$

a micromechanics parameter for ductile fracture was proposed, see [11, 12] for more details,

$$V_{gc} = \varepsilon_{eq}^c \exp\left(\frac{3}{2} \frac{\sigma_m}{\sigma_{eq}}\right), \quad (4)$$

where R is the size of voids, ε_{eq}^c is the critical value of equivalent plastic strain ε_{eq} at fracture. The normalized critical void growth ratio R_c/R_0 can be expressed as

$$\frac{R_c}{R_0} = \exp(0.283V_{gc}), \quad (5)$$

with R_0 being the initial void radius. Thus, the criterion for ductile fracture initiation can be expressed as

$$V_g = V_{gc}, \quad (6)$$

where

$$V_g = \exp\left(\frac{3}{2} \frac{\sigma_m}{\sigma_{eq}}\right) \varepsilon_{eq}^p. \quad (7)$$

Equations (4) and (5) are the macroscopic and microscopic forms of the critical void growth parameters, respectively. Unfortunately, experiments of metallic materials have shown that V_{gc} is not always a material constant, but alters with stress state, and the values of R_c/R_0 calculated from eq.(5) are found to be approximately one-half of those obtained from the tests for metals. See [12] for more details. The reason may be attributed to the single void model used to derive eqs (4) and (5), which neglects the interaction of the neighboring voids in the real situation. Considering this, a modified micromechanics parameter was proposed [12], namely

$$M_{vgc} = \varepsilon_{eq}^c \exp\left(\alpha \frac{\sigma_m}{\sigma_{eq}}\right), \quad (8)$$

where α is a constant to reflect the interaction of the neighboring voids. Extensive experiments of metallic materials have shown that M_{vgc} is a material constant independent of stress state, see [12] for more details. Thus, eq.(5) can be modified as

$$\frac{R_c}{R_0} = \exp(0.283M_{vgc}). \quad (9)$$

In what follows, the stress state independence of M_{vgc} for the PC will be verified according to the experimental results of fracture strain as shown in Fig.5, from which one can easily determine the value of M_{vgc} . Variation of M_{vgc} with stress triaxiality is shown in Fig.6. It is readily seen that M_{vgc} is a material constant independent of stress state. So, it is reasonable to use M_{vgc} as a critical parameter of fracture for the PC, and the criterion for ductile fracture initiation of the PC can be expressed as

$$M_{vg} = M_{vgc}, \quad (10)$$

where

$$M_{vg} = \exp\left(\alpha \frac{\sigma_m}{\sigma_{eq}}\right) \epsilon_{eq}^p. \quad (11)$$

4. CONCLUSION

Triaxial stress constraint has important effect on the deformation and fracture behavior of the Polycarbonate (PC). It was shown that fracture strain of the PC decreases with the increase of stress triaxiality. In the case of higher tensile stress triaxiality, the PC behaves like a brittle material, but it is really a very ductile material in the case of low stress triaxiality. In the other words, tensile stress triaxiality results in the brittle fracture of the PC.

The micromechanics criterion for ductile fracture proposed by Wang and Kuang [12] can sever as a fracture criterion for ductile polymer. Experimental results for the PC indicates that the characterizing parameter M_{vgc} is a material constant independent of stress state. We hope M_{vgc} can provide a new parameter for evaluating the fracture ductility of polymers.

ACKNOWLEDGEMENTS

Wang would like to acknowledge the supports by JSPS through a Fellowship Program (March 1997 to March 1999), and by the Science Foundations of China Education Ministry and Xi'an Jiaotong University, Xi'an 710049, China. Thanks are also due to support by Japan Synthetic Rubber Co. Ltd. for providing polymeric materials.

FEFERENCES

1. T.L. Anderson, Fracture Mechanics – fundamentals and applications, CRC Press, Inc., Florida (1995)
2. J.G. Williams, Fracture Mechanics of Polymers, Ellis Horwood Ltd., Chichester (1984)
3. J. Wu and Y.W. Mai, Polymer Engineering and Science, **36** (1996) p. 2275
4. J. Lemaitre, J. Engineering Materials and Technology, ASME Trans., **107** (1985) p. 83
5. T.J. Wang, Engineering Fracture Mechanics, **40** (1991) p. 1075
6. T.J. Wang, Engineering Fracture Mechanics, **42** (1992) p. 177
7. T.J. Wang, Engineering Fracture Mechanics, **42** (1992) p. 185
8. T.J. Wang, Engineering Fracture Mechanics, **48** (1994) p. 213
9. T.J. Wang, Acta Mechanica Sinica, **11** (1995) p. 83
10. J.R. Rice and D.M. Tracey, J. Mech. Phys. Solids, **17** (1969) p. 201
11. J.W. Hancock and A.C. Machenzie, J. Mech. Phys. Solids, **24** (1976) p. 147
12. T.J. Wang and Z.B. Kuang, J. Pressure Vessels and Technology, ASME Trans., **117** (1995) p. 395.

Effect of Specimen Thickness and Load History on Crack Growth of 7175-T74 Forging Aluminum Alloy

J.Z. Liu, X.R. Wu, C.F. Ding and D.X. You

Beijing Institute of Aeronautical Materials, PO Box 81-23, Beijing 100095, China P.R.

Keywords: Fatigue Crack Growth, Load Interaction, Microscopic Mechanism, Selected Load Sequence, Thickness Effect

ABSTRACT

In this paper, large crack growth behavior for different thickness specimens of 7175-T74 forging aluminum alloy was experimentally studied under constant amplitude, several selected sequences and Mini-TWIST flight simulation spectrum loads. Thickness and load history effects on fatigue crack growth were investigated and summarized. Moreover, using some SEM results of fracture surfaces explained possible-microscopic-mechanisms of the specimen thickness and load history effects found in this investigation.

1. INTRODUCTION

For many metallic materials, retardation/acceleration behavior of fatigue crack growth have received much attention under simple selected loading sequences in order to study experimentally and model the behavior that may occur under various complex variable amplitude loads ^[1]. However, there is no similar study on load interaction for 7175-T74 forging aluminum alloy at present. On the other hand, although thickness effect in the process of crack growth has been more and more studied, so far, the study has still been concentrated on constant amplitude, single overload and flight simulation spectrum loads for a few materials ^[1,2]. More study is obviously helpful for understanding of the thickness effect on fatigue crack growth. In the present paper, large crack growth behavior for different thickness specimens of 7175-T74 forging aluminum alloy under constant amplitude and various variable amplitude loads was experimentally studied in order to investigate the thickness and load interaction effects of crack growth for this material. SEM analyses of fracture surfaces for some specimens were also carried out to identify the possible mechanisms being responsible for the observed effects.

2. EXPERIMENT

The material for this investigation was 7175-T74 forging aluminum alloy. All specimens for tensile and crack growth tests were cut from hand forging with length 620mm, width 160mm and thickness 67mm. M(T) specimens for crack growth tests were machined along L-T direction and with length 300mm and width 75mm and two kinds of thickness about 3mm and 10mm. The

specimens for static tensile tests were machined along L direction. The mechanical properties and the chemical composition of the material are given in Table 1 and 2, respectively.

Table 1. Mechanical properties of the material used in this investigation

Elastic Modulus GPa	Yield Strength MPa	Tensile Strength MPa	Elongation δ_5 (%)	Reduction of area (%)
70	502	556	12.3	34.6

Table 2. Chemical composition of the material in this investigation (%)

Zn	Mg	Cu	Cr	Fe	Si	Mn	Ti	Al
5.57	2.45	1.53	0.24	0.13	0.12	<0.05	<0.05	Balanced

Fatigue crack growth tests under constant amplitude loading were performed at two cyclic stress ratios $R=0$ and -1 for two thickness specimens. Six kinds of simple load sequences were selected in crack propagation tests: (1). Periodic overload (OL) blocks: 5 OL cycles after every 50 baseline loads (BLs) with stress ratio $R=0$; (2). Periodic OL blocks: 5 OL cycles after every 100 BLs with $R=0$; (3). Periodic OL-underload (UL) blocks: 5 OL-UL cycles after every 50 BLs with $R=-1$; (4). Periodic OL-UL blocks: 5 OL-UL cycles after every 100 BLs with $R=-1$; (5). Periodic single OL-UL: a single OL-UL cycle after every 39 BLs with $R=0$ and -1 ; (6). Periodic single UL-OL: a single UL-OL cycle after every 39 BLs with $R=0$ and -1 . For the first four sequences, all OL and/or UL ratios are 1.5. For the other sequences, the OL and UL ratios are 1.8. For BL with $R=0$ and -1 , the BL stress levels are 62.5MPa and 35MPa, respectively. Besides the selected load sequences above, Mini-TWIST flight simulation spectrum was also used in crack growth tests for different thickness specimens. For Mini-TWIST spectrum tests, the mean stress level of flight spectrum 50 MPa was selected.

Crack growth tests were conducted under constant stress controlling condition on MTS testing machines. Crack lengths in tests were measured by travelling microscopes with magnification 20 ($\times 20$). For simple selected sequence tests, before the sequences were applied, all specimens were pre-cracked under constant amplitude loading and initial crack lengths were about 10mm.

3. RESULTS AND DISCUSSION

3.1. Thickness effect under constant amplitude loading

Under constant amplitude loading, there are some studies^[3,4] in which an obvious thickness effect in crack growth tests for different thickness specimens was not found. There are also some other studies in which different thickness effects were found. For example, Jack et al^[5] found crack growth rates decrease with specimen thickness increasing, however, Broek et al^[6] found crack growth rates increase with specimen thickness increasing. In this investigation, it is found that crack propagation rates of two different thickness specimens under $R=-1$ and 0 and the same stress intensity factor ranges were almost the same. An obvious thickness effect does not exist for 7175-T74 alloy. It is important to explain these different results for understanding the crack growth behavior better. Some researchers owed the different thickness effects to different plastic zone sizes ahead of crack tip or different crack closure level of different thickness specimens. Also, there are

some researchers who tried to explain the thickness effects by considering the relationships between the transition from flat-to-slant crack growth and stress intensity ranges. In fact, all these factors, the plastic zone sizes, crack closure level and the transition from flat-to-slant crack growth, are connected with constraint behavior near the region ahead of crack tip. Recently, the constraint behavior of center crack plate has been analyzed by Newman^[7] and Wang, et al^[8]. According to their fitting equations for calculating the constraint factor ahead of crack tip, values of the constraint factor for two thickness specimens in crack growth process were computed. It is found that the difference between the corresponding constraint factors of the two thickness specimens is within 6% when crack half-length, a , is not greater than 25mm, and within 20% while $a \leq 30$ mm. The obtained constraint factors and Newman's crack opening stress equations^[9] were used to calculate the crack opening stresses, then, effective-stress-intensity-factor ranges. It was found that the difference between the corresponding effective-stress-intensity-factor ranges of two thickness specimens is less than 1% while $a \leq 25$ mm, and also within 9% while $a \leq 30$ mm. These results can be used to explain why the obvious thickness effect on crack growth was not found in the present tests.

3.2. Thickness effect under various variable amplitude loading

The results of some materials under a single OL or periodic single OL have shown that the retardation effect weakens with the specimen thickness increasing^[2]. In this investigation, from the test results under periodic OL blocks with different BL cycles, the same conclusion is also obtained. However, contrary results were got under periodic single UL-OL at BL $R=0$ and -1 . Figure 1 showed a - N curves of crack propagation under periodic single UL-OL with different BL stress ratios. It can be found that the retardation increases with the specimen thickness increasing. The trend is more obvious at BL $R=-1$ than BL $R=0$. The fact that thickness effect is more obvious at BL $R=-1$ than at BL $R=0$ was also found under periodic single OL-UL sequence. In order to compare and study the thickness effects under periodic OL-UL blocks with different BL cycles (OL and UL ratios are 1.5) and under periodic single OL-UL (OL and UL ratios are 1.8), the a - N curves for different thickness specimens under these load cases are shown together in Fig. 2.

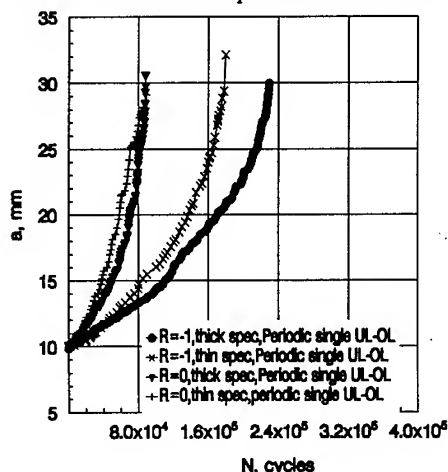


Fig.1 Comparisons of a - N curves of crack growth under periodic single UL-OL with different BL stress ratios

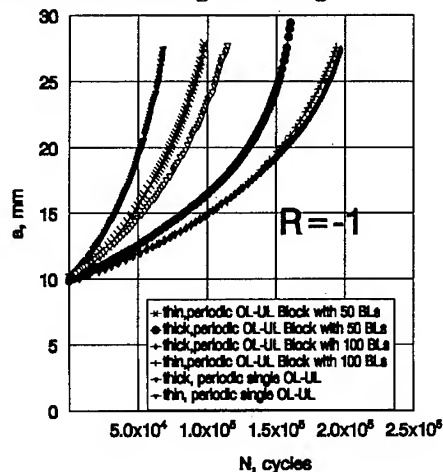


Fig.2. Comparisons of a - N curves of crack between different thickness specimens for various periodic OL-UL sequences at BL $R=-1$

Different thickness effects can be found from the figure. Under periodic OL-UL blocks with BL interval of 50 cycles, the retardation increases with specimen thickness increasing. However, when enlarging the number of BL cycles and all other parameters being kept constant, the thickness effect disappears. Under periodic single OL-UL with OL and UL ratios 1.8, the retardation weakens with specimen thickness increasing on the contrary. The trends above may be relevant to change of crack growth mechanism under BL after high OL and UL ratios were applied (See SEM fractographs shown in the later section). From the present and previous results, it can be found that the thickness effect on crack growth is dependent on not only selected load sequence but also BL interval and stress ratio in the load sequence, and OL and /or UL ratios.

The a-N curves of crack growth for two thickness specimens under Mini-TWIST spectrum loading are given in Fig.3. It can be found from the figure, the thickness effect does not exist while crack length is not bigger than 10mm. After crack length exceeds 10mm, the thinner specimen appeared a marked crack growth retardation and thickness effect becomes obvious. Many results showed that the effect of a given change in a flight-simulation load spectrum on fatigue crack growth is strongly related to that spectrum type and often depends on the design load level, material and spectrum geometry. It has been found that in general, the sensitivity to a given spectrum variation is different in the crack initiation stage (i.e. during crack growth up to some tenths of a millimeter in size) and in the crack propagation stage^[10]. Obviously, It is found from Fig.3 that the sensitivity to the thickness effect under Mini-TWIST spectrum loading is also different in the two different stages of crack growth.

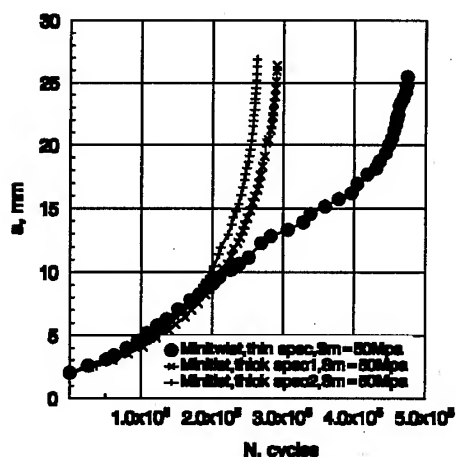


Fig.3 The a-N curves of crack growth for two thickness specimens under Mini-TWIST spectrum loading

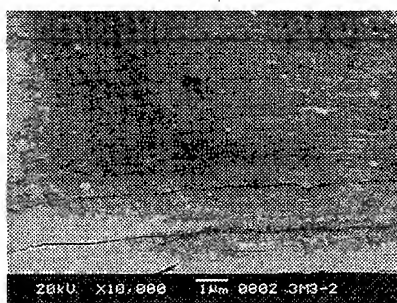


Fig.4 Fractograph showing delayed crack growth retardation for thick specimen under periodic OL-UL blocks with the interval of 50 BL cycles

SEM analyses of fracture surface were carried out in the present investigation in order to get better understanding of the experimental results above. In Fig.4, the fractograph of thick specimen under periodic OL-UL blocks with the interval of 50 BL cycles is given here. From the figure, some wider fatigue striations can be found immediately after the OL block (with very wide striations). The widths of the striations become smaller and uniform after about 5 to 6 cycles away from the

OL. These showed an obvious delayed crack propagation mechanism of post-OL. Fractographs of fracture surfaces of thick and thin specimens under periodic single OL-UL with BL $R=-1$ are shown in Fig.5(a, b), respectively. We can know from the figures that fatigue striations for BL cycles after OL-UL are obviously wider in thick specimen than in thin specimen. This may be the microscopic reason that the crack growth in Fig.2 is found to be faster in thick specimen than in thin specimen for this loading sequence.

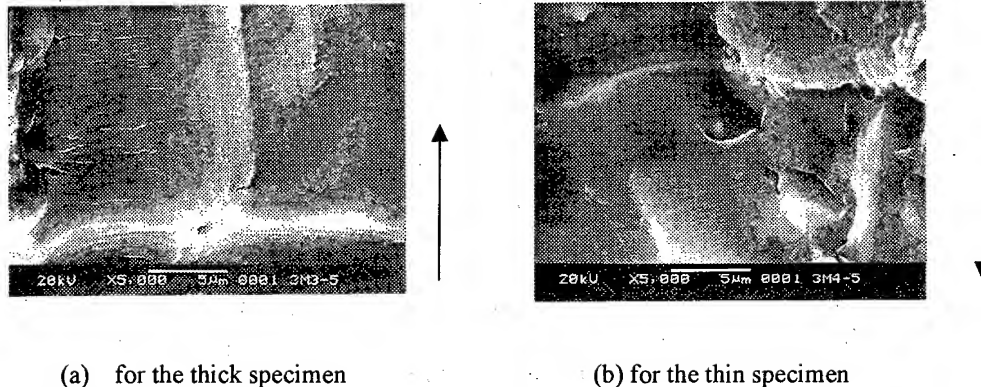


Fig.5 (a,b) Fractographs of fracture surfaces of thick and thin specimens under periodic single OL-UL with BL $R=-1$ (Arrows present the direction of crack propagation)

3.3. Load history effect and thickness influence of load history effect

Crack propagation rates for different load sequences under the same specimen thickness and BL stress ratios were compared with each other. It can be found that under periodic OL block loadings for two thickness specimens and all other parameters being kept constant, the longer the interval of BL, the more severe retardation is produced. This result is same as those from other studies under single periodic OL or periodic OL blocks^[1,11,12]. The difference of the retardation between periodic OL block loadings with different interval of BL cycles was found to be more obvious for thinner specimen. For periodic OL-UL block loadings, an increase in the amount of retardation was found if the OL-UL loadings were applied less frequently. Moreover, for thin specimen the marked increase in the amount of the retardation appeared while for thick specimen the increase is not as obvious as one for the thin specimen. For the simple load histories containing combinations of single OL and UL cycle, an UL applied immediately after an OL reduced the post-OL retardation more significantly than an UL that immediately precedes an OL. Most available test results under the simple load histories containing combinations of OL and UL cycles^[2] got the same conclusion as one above. Contrary to the thickness effect in periodic OL or OL-UL with different intervals of BL cycles, the difference between the amount of retardation for periodic single OL-UL and periodic single UL-OL was found to be more obvious for thick specimen when BL stress ratio is equal to -1. And the difference is almost same between two thickness specimens when BL stress ratio is 0. The results above showed that not only an obvious load history effect on fatigue crack growth for 7174 forging aluminum alloy exists, but also the effect is markedly influenced by specimen thickness.

4. CONCLUSIONS

For 7175-T74 forging aluminum alloy, large fatigue crack propagation behavior was studied experimentally for two different thickness specimens under constant amplitude, several selected simple sequences and Mini-TWIST flight simulation spectrum loadings. The following results were obtained.

- (1). Under constant amplitude loading, no thickness effect on crack growth was found. The reason has been explained by crack closure analyses.
- (2). Under selected simple sequence loadings, the thickness effects on crack growth are dependent on not only selected load sequence but also BL interval and stress ratio in the load sequence, and the OL and /or UL ratios.
- (3). The sensitivity to thickness effect under Mini-TWIST spectrum loading is different in the two different stages of crack growth. In the present investigation, when crack length is less than 10mm the thickness effect is not found. However, an obvious thickness effect can be found when crack length exceeds 10mm.
- (4). Not only an obvious load history effect on fatigue crack growth for the material exists, but also it is markedly influenced by specimen thickness.
- (5). SEM analyses of fracture surfaces for different thickness specimens under different loading conditions are very interesting, which can provide some explanations from microscopic mechanisms for some load history and thickness effects on crack growth.

REFERENCES

1. J.Petit, et al: Fatigue crack growth under variable amplitude loading, Elsevier Applied Science, London (1988)
2. M.Skorupa, Fatigue Fract. Engng Mater. & Struct., **21**(1998) p.987
3. N.E.Forst, et al, Effect of sheet thickness on the rate of growth of fatigue in mild steel, J. of Mech. Engng Sci., **3**(2) (1961)
4. R.W.Hertzberg, et al, Application of electron fractography and fracture mechanics on fatigue propagation, Proceeding Int. Conf. On Fracture, Sendai, Japan (1965)
5. A.R.Jack, et al, Effect of thickness on fatigue crack initiation and propagation in notched mild steel specimens, Acta Metallurgic, **20** (1972)
6. D.Broek, et al, Aircraft Engng, **38** (1966) p.31
7. J.C.Newman, C.A.Bigelow and K.N.Shivakumar, Engng Fract. Mech., **46**(1) (1993) p.1
8. J.Wang, J.X.Gao, W.L.Guo, et al, Theory Applied Fract. Mech., **29**(1) (1998), p.49
9. J.C.Newman, Jr, NASA-TM 104159, Washington D.C., (1992)
10. P.Heuler, et al, Int J Fatigue, **8** (1986) p.225
11. N.A.Fleck, Acta Metall, **33** (1985) p.1339
12. S.Zhang, et al, Fatigue Fract. Engng Mater. & struct., **10** (1987) p.315

Plastic η Factors Based on Load-CMOD Records for SE(B) Toughness Testing Specimens

Yun-Jae Kim

School of Mechanical Engineering, SungKyunKwan University,
 300 Ch'onch'on-dong, Changan-gu, Suwon 440-746, Korea

Keywords: Finite Element Analysis, J-Integral, Limit Analysis, Toughness Testing Standards

ABSTRACT

This paper addresses the accuracy of the experimental J estimation equation based on the load-CMOD curve for SE(B) specimens, proposed by Kirk and Dodds. Systematic investigations, based on 2-D FE analysis with realistic stress strain data for various materials, show that the estimation equation by Kirk and Dodds is not sensitive to the material but shows a large error for very deep cracks such as $a/W=0.7$. Based on slip line field analysis, a slight modification to the J estimation equation by Kirk and Dodds is given, then provides consistent results for all possible crack lengths.

1. INTRODUCTION

Testing shallow cracked single edge cracked bend (SE(B)) specimens, Fig. 1a, is important for investigating the constraint effect on fracture toughness [1]. Investigating several possibilities of J integral estimation for shallow cracked SE(B) specimens [2], Kirk and Dodds [2] have concluded that the use of the load-crack mouth opening displacement (CMOD) records provides the most reliable experimental J estimation. Consequently, they proposed the J estimation equation for SE(B) specimens with a wide range of the crack length:

$$J = \frac{K^2(1-\nu^2)}{E} + \eta_p^{CMOD} \cdot \frac{U_p^{CMOD}}{B_N \cdot (W-a)} \quad (1)$$

In eqn. (1), K is the elastic stress intensity factor; E and ν is Young's modulus and Poisson's ratio; U_p^{CMOD} denotes the plastic component of the area under the load-CMOD curve (Fig. 1b); B_N denotes the net section thickness of the specimen; η_p^{CMOD} is a plastic η factor based on the load-CMOD records, given by:

$$\eta_p^{CMOD} = 3.785 - 3.101 \cdot x + 2.018 \cdot x^2 \quad \text{for } 0.05 \leq x = a/W \leq 0.7 \quad (2)$$

Although such J estimation equation was developed based on extensive finite element (FE) analysis, the use of idealised stress strain curves, such as Ramberg-Osgood materials, could raise some questions on the accuracy of the proposed the plastic η factor solution. Noting that the plastic η factor solutions are dependent on the range of deformation levels taken from the FE analysis, Wang *et al.* [3,4] indeed proposed an expression slightly different from eqn. (2), simply by taking different deformation levels to extract the plastic η factor solutions. It suggests that the use of idealised stress strain curves needs care on choosing a meaningful range of the deformation.

This paper addresses the accuracy of the J estimation equation, eqn. (1), based on 2-D FE analysis. Using several actual material stress strain data, it will be shown that the η_p^{CMOD} solution, eqn. (2), provides acceptable results, except for very deep cracks such as $a/W=0.7$. Accordingly, based on slip line field analysis, a modification to eqn. (2) is given, which then provides consistent results for all crack lengths.

2. FINITE ELEMENT (FE) ANALYSIS

Elastic-plastic FE analyses were performed for plane strain SE(B) specimens, depicted in **Fig. 1a**, using the general purpose ABAQUS FE code [5]. Materials were modelled as isotropic elastic-plastic materials which obey J_2 flow theory, and a small geometry change continuum FE model was employed. Various crack lengths were considered, ranging $a/W=0.1$ to 0.7 . **Figure 2** depicts a typical FE mesh employed in the present investigation. The number of elements and nodes in a typical FE mesh ranges from ~ 500 elements/1600 nodes for deep cracks to ~ 700 elements/2200 nodes for shallow cracks. Reduced integration 8 node elements were used to avoid problems associated with incompressibility.

To investigate accuracy of the J estimation equation, eqn. (1), stress strain curves of several different real materials were chosen, covering a wide range of yield stresses, σ_Y , and ultimate tensile strengths, σ_U (and thus a wide range of hardening capacity). The materials chosen in this work are summarised in Table 1 and the tensile curves are shown in **Fig. 3**. The J integral can be easily extracted from the FE results (in ABAQUS using domain integral approach), as a function of load. Moreover, the FE results provide other relevant information, such as load-line displacement, CMOD.

3. RESULTS

Based on information extracted from the FE analysis, the J integral can be estimated according to the recommended estimation equation, eqn. (1), using K estimated from [7]. The percentage error in J , $E(\%)$, is defined as

$$E(\%) = \left(J^{est} - J^{FE} \right) / J^{FE} \times 100, \quad (3)$$

where the superscripts "est" and "FE" denote the estimate and the FE value of J , respectively.

The resulting values of $E(\%)$ for various values of a/W are shown in **Fig. 4**, as a function of normalised load, P/P_L . Note that P_L denotes the plastic limit load of the SE(B) specimen, which was determined in the present work from separate FE analysis based on elastic, perfectly plastic material. For a given material, the results are presented from $P=0.5P_L$ to $P=P_{max}=0.5(\sigma_Y+\sigma_U)/\sigma_Y P_L$. Such realistic range of P would eliminate any artificial error at unrealistically high deformation levels. The results in **Fig. 4** show that the η_p^{CMOD} solution by Kirk and Dodds, eqn. (2), shows a rather strange behaviour for a deep crack such as $a/W=0.7$. This will be fully discussed in the next section. Excluding the results for $a/W=0.7$, eqn. (2) is generally accurate, although the error increases slightly as a/W decreases. In particular, for $a/W=0.1$, the error increases as P approaches P_L , and then decreases when $P > P_L$. Such tendency is possibly due to a simple linear addition of linear elastic and fully plastic components of J , eqn. (1), and thus neglecting a non-linear contribution in contained yielding, which can be significant for shallow cracks. However, for all crack lengths considered, the J estimation equation, eqns. (1) with (2), is not sensitive to the strain hardening.

4. MODIFICATION TO THE J ESTIMATION EQUATION

It was shown in the previous section that the η_p^{CMOD} solution by Kirk and Dodds gave a significant error for $a/W=0.7$. This can pose a problem when such equation is to be adopted in testing standards, since it does not provide toughness values compatible to existing ones, obtained from load-load line displacement records. **Figure 5** shows the corresponding error $E(\%)$ in J for $a/W=0.5$ and 0.7 , according to the current testing standard [7] based on FE load-load line displacement

records, which shows that the current J estimation equation based on the load-load line displacement record provides satisfactory results for deep cracks.

At this point, it would be worth comparing eqn. (2) with the solution from the slip line field (SLF) analysis. The η_p^{CMOD} solution can be estimated from the SLF analysis, as follows. Firstly, the SLF analysis provides the limit load solution, P_L , which in turn gives the plastic η factor based on experimental load-load line displacement curve, η_p^{VLL} [8]:

$$\eta_p^{VLL} = -\frac{(W-a)}{P_L} \cdot \frac{\partial P_L}{\partial a} \quad (4)$$

The SLF analysis also provides the rotation factor, r_p , from which the η_p^{CMOD} solutions can be obtained

$$\eta_p^{CMOD} = \left[\frac{\eta_p^{VLL}}{a/W + r_p(1-a/W)} \right] \quad (5)$$

Note that the P_L and r_p solutions for SE(B) specimens were given by Wu *et al.* [8,9].

Figure 6 compares the resulting SLF solutions with eqn. (1). The figure also includes the expression proposed by Wang *et al.* [3] for comparison. The difference between the SLF solution and eqn. (2) for shallow cracks ($a/W < 0.3$) can be explained as follows. The assumption of the rigid-plastic material being a basis of the SLF analysis is appropriate only when the plastic strain (deformation) dominates. Since much more plastic deformation is needed for shallow cracked bend specimens, due to plasticity spreading to the back surface, the results from the SLF analysis for shallow cracked SE(B) specimens is likely to be valid only when “unrealistically” large plastic deformation is applied. Such explanation can be indirectly supported by Sumpter [10], who showed that the r_p solutions from the SLF analysis showed the larger discrepancy for the shallower cracks, compared to experimental data. Due to the inaccuracy of the r_p solution, the resulting η_p^{CMOD} solution will not be accurate for shallow cracked bend specimens, see eqn. (5).

In this context, the SLF solution should be accurate for deeply cracked specimens, whereas **Fig. 6** still indicates some difference between the SLF solution and eqn. (2), even for deep cracks ($a/W > 0.5$). Assuming that eqn. (2) is accurate for shallow cracks and that the SLF solution is accurate for deep cracks, the η_p^{CMOD} solution by Kirk and Dodds can be slightly modified, by fitting eqn. (1) and the SLF solution:

$$\eta_p^{CMOD} = 3.724 - 2.244 \left(\frac{a}{W} \right) + 0.408 \cdot \left(\frac{a}{W} \right)^2 \quad (6)$$

As shown in **Fig. 6**, the proposed equation, eqn. (6), differs from that by Kirk and Dodds, eqn. (2), only at $0.5 < a/W < 0.7$, but is almost identical elsewhere. **Figure 7** shows the resulting error in J for two different crack lengths, $a/W = 0.1$ and 0.7 . As expected, eqn. (6) does not change the result for $a/W = 0.1$, but gives significantly improved results for $a/W = 0.7$.

5. CONCLUSION

This paper addresses the accuracy of the experimental J estimation equation based on the load-CMOD curve for SENB specimens, proposed by Kirk and Dodds [2]. Systematic investigations, based on 2-D FE analysis with realistic stress strain data of various materials, show that the solution by Kirk and Dodds is not sensitive to the material but shows a large error for very deep cracks such as $a/W = 0.7$. Based on slip line field analysis, the J estimation equation by Kirk and Dodds is slightly modified, and the resulting J estimation equation then provides consistent results for all crack lengths:

ACKNOWLEDGEMENT

The author wishes to acknowledge Prof. K-H Schwalbe at GKSS Research Centre (Germany) and Prof. Y-J Kim at the Safety and Structural Integrity Research Centre at the Sungkyunkwan University, for their support and valuable comments.

REFERENCES

1. J A Joyce, E M Hackett and C Roe, Constraint Effect in Fracture, ASTM STP 1171, American Society for Testing and Materials, Philadelphia (1993), pp. 239-263
2. M T Kirk and R H Dodds Jr., Journal of Testing and Evaluation Vol. **21**, No. **4** (1993), pp. 228-238
3. Y-Y Wang and J R Gordon, In Shallow Crack Fracture Mechanics, Toughness Test and Applications, M.G. Dawes, Cambridge, U.K (1992)
4. Y-Y Wang, M T Kirk, J R Gordon, P Horner and C Eripret, In Mis-Matching of Interfaces and Welds, K.-H. Schwalbe and M. Koçak, GKSS Publications, Geesthacht, Germany (1997), pp. 281-294
5. ABAQUS Standard/User's Manual, Version 5.7, Hibbit. Karlsson & Sorensen, Inc, Pawtucket, RI, USA (1998)
6. H Tada, P Paris and G Irwin, The Stress Analysis of Cracks Handbook, Paris Production Inc., St. Louis, Missouri (1985)
7. ASTM Standards, E1739-96, Annual Book of ASTM Standards, Section 3, Vol. **03.01**, pp. 957-980
8. S X Wu, Y-W Mai and B Cotterell, International Journal of Fracture, Vol. **45** (1990), pp. 1-18
9. S X Wu, B Cotterell and Y-W Mai, International Journal of Fracture, Vol. **37** (1988), pp. 13-29
10. J D G Sumpter, Fatigue and Fracture of Engineering Materials and Structures, **10** (6) (1987), pp. 479-493

Table 1. Tensile properties of the materials used in the present study: materials with a yield strain.

	High strength (HS)	450 EMZ steel (450)	Carbon steel (CS)
σ_Y (MPa)	800	540	285
σ_U (MPa)	840	656	410

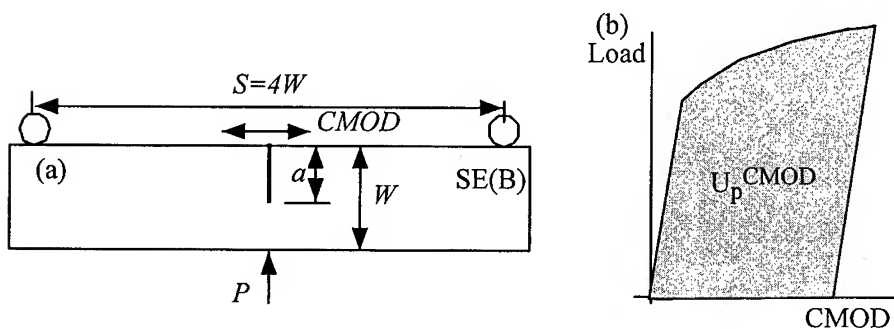


Fig. 1. Relevant dimensions of the SE(B) specimen, and (b) the definition of U_p^{CMOD} .

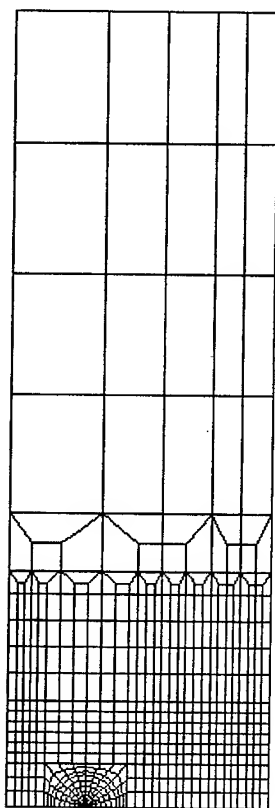


Fig. 2. FE mesh used in the present work, for $a/W=0.3$.

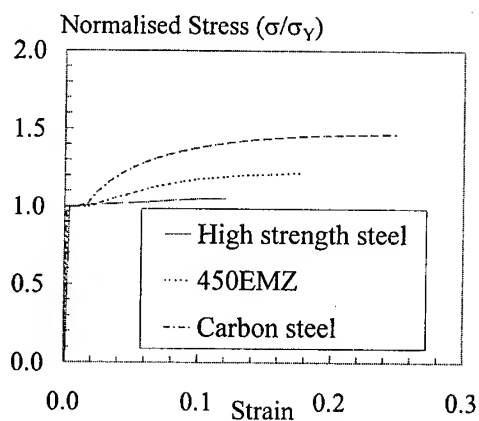
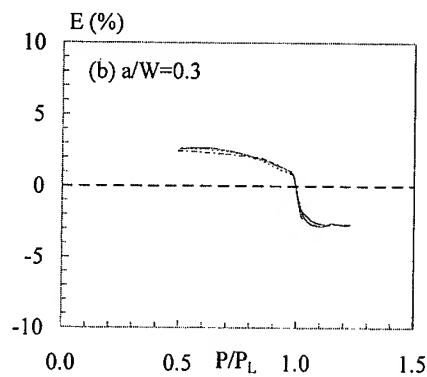
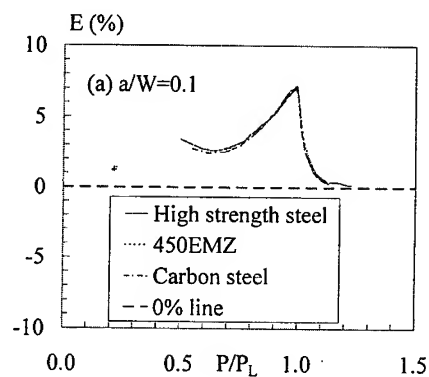


Fig. 3. Tensile properties of the materials used in the present analysis.

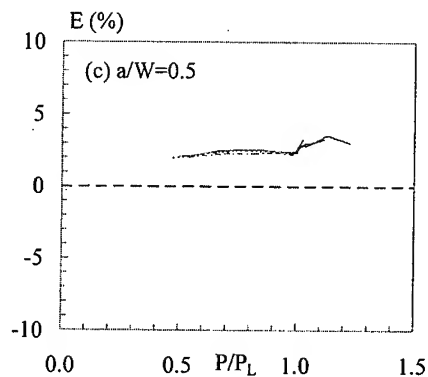


Fig. 4(a-d). The percentage error $E(\%)$ in J , according to Kirk and Dodds [2], eqn. (1).

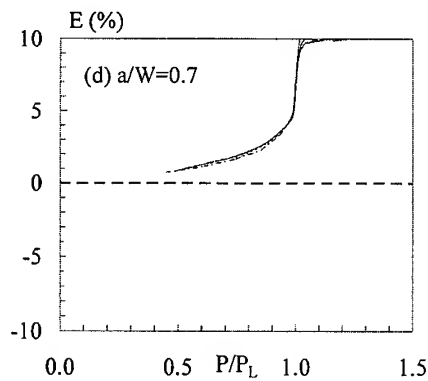
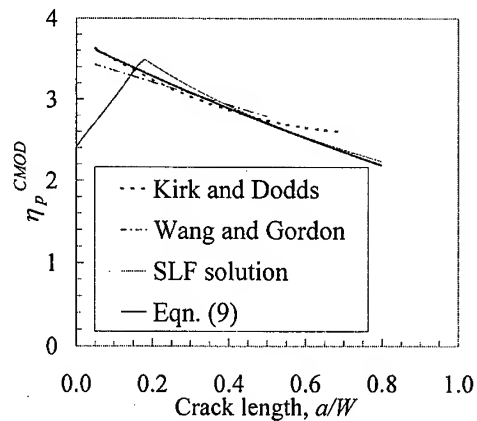
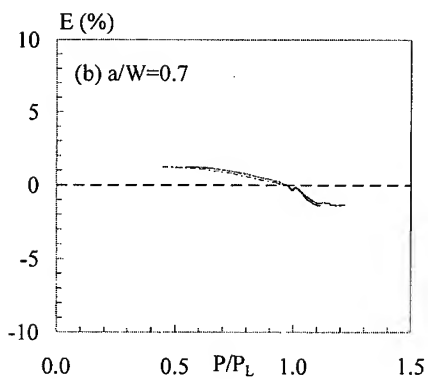
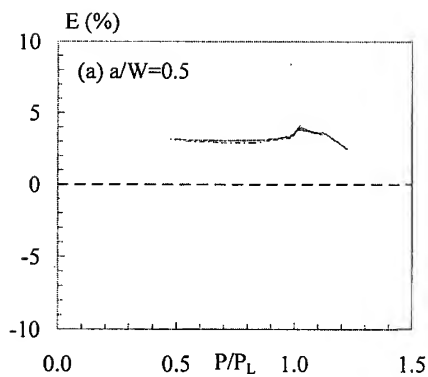
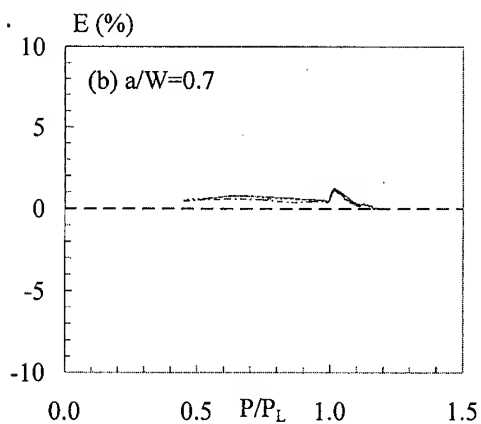
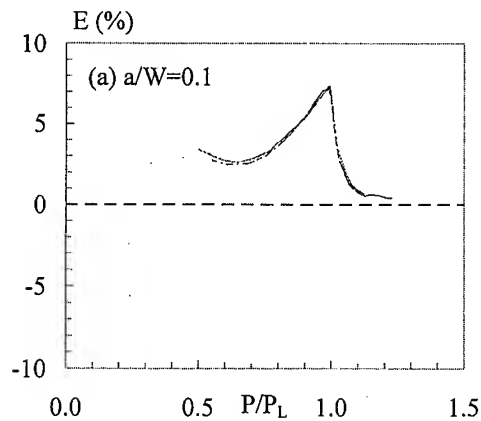


Fig. 4(a-d). cont'd.

Fig. 6. Comparison of the η_p^{CMOD} solutions.Fig. 5(a-b). The percentage error $E(\%)$ in J , according to the ASTM testing standard.Fig. 7(a-b). The resulting percentage error $E(\%)$ in J , according to the proposed η_p^{CMOD} solution, eqn. (6).

Electromagnetic Thermoelastic Solids with an Elliptical Cavity or a Crack under Uniform Heat Flow

X.L. Liu¹, X.F. Liu¹, J.X. Liu² and J. Zheng²

¹ Department of Basic Courses, Shijiazhuang Railway Institute,
Shijiazhuang 050043, China P.R.

² Department of Civil Engineering, Shijiazhuang Railway Institute,
Shijiazhuang 050043, China P.R.

Keywords: Cavity, Coupled Field, Crack, Electromagnetic Thermoelasticity, Intensity Factor

ABSTRACT

The two-dimensional problem of the electromagnetic thermoelastic medium containing an elliptical cavity subjected to a remote uniform heat flow is considered. Using the extended Stroh formalism, and the technique of conformal mapping, the explicit and closed-form expressions for the coupled fields are obtained both inside and outside the cavity. The exact electromagnetic boundary conditions on the cavity surface are adopted in this analysis. When the elliptic cavity degenerates into a slit crack, the corresponding solution and the intensity factors are given explicitly. The effect of the heat flow direction and the dielectric constant and magnetic permeability of air inside the crack on the thermal magneto-electroelastic fields is discussed.

1. INTRODUCTION

The inclusion or cavity problems of materials exhibiting partial or full coupling between multiple fields such as thermoelasticity, piezoelectricity or magneto-electroelasticity, etc., have been a topic of interest to many researchers because of their practical importance in understanding and optimizing the coupled properties of these materials. A considerable amount of work on inclusion or cavity problems in thermoelastic materials and piezoelectric media with or without thermal effects can be found in the literature. Detailed literature survey may be found in the recent papers by Chao and Shen [1] for thermoelasticity and by Meguid and Zhong [2] for piezoelectricity, respectively. In contrast, relatively little work has been done for the inclusion or cavity problems of media possessing simultaneously piezoelectric, piezoelectric and magneto-electric effects, namely, magneto-electroelastic solids. A wide class of materials [3] and the newly emerging composite materials that are made from the piezoelectric media and piezomagnetic media [4-7] do have these mixed properties. Recently, Huang and Kuo [6], Li and Dunn [7], investigated the inclusion problems and the effective behaviors of magneto-electroelastic composite materials. To the best of our knowledge, the cavity or crack problems of magneto-electroelastic solids with thermal effects were not considered before.

Based on the extended Stroh formalism in anisotropic thermoelasticity [8], a simple and compact version of general solutions in the anisotropic electromagnetic thermoelasticity is first presented. Applying this newly derived solution and the method of conformal mapping, the temperature field and the thermal magneto-electroelastic fields in the whole region disturbed by an

elliptical cavity are obtained. The solution for the crack problem is obtained by setting the minor axis of the ellipse approach to zero. The intensity factors are also given in an explicit form.

2. BASIC EQUATIONS FOR ELECTROMAGNETIC THERMOELASTICITY

In a fixed rectangular coordinate system x_i ($i=1,2,3$), the basic equations of the linear magnetoelectroelastic solids with thermal effects can be written in a shorthand notation as

$$h_i = -k_{ij}T_{,j}, \quad h_{i,j} = -k_{ij}T_{,ij} = 0 \quad (1)$$

$$\Sigma_{ij} = E_{ijkl}u_{k,l} - \Pi_{ij}T, \quad \Sigma_{ij,i} = E_{ijkl}u_{k,il} - \Pi_{ij}T_{,i} = 0 \quad (2)$$

in which

$$\begin{aligned} u_K &= \begin{cases} u_k & K=1,2,3 \\ \varphi & K=4 \\ \phi & K=5 \end{cases}, & E_{ijkl} &= \begin{cases} C_{ijkl} & J,K=1,2,3 \\ e_{ijl} & K=4, J=1,2,3 \\ q_{ijl} & K=5, J=1,2,3 \\ e_{ikl} & J=4, K=1,2,3 \\ -\varepsilon_{il} & J=4, K=4 \\ -\alpha_{il} & J=4, K=5 \\ q_{ikl} & J=5, K=1,2,3 \\ -\alpha_{il} & J=5, K=4 \\ -\mu_{il} & J=5, K=5 \end{cases} \\ \Sigma_{ij} &= \begin{cases} \sigma_{ij} & J=1,2,3 \\ D_i & J=4 \\ B_i & J=5 \end{cases}, & \Pi_{ij} &= \begin{cases} \lambda_{ij} & J=1,2,3 \\ p_i & J=4 \\ m_i & J=5 \end{cases} \end{aligned} \quad (3)$$

In Eqs.(1)-(3), a comma denotes partial differentiation and the repeated indices mean summation. k_{ij} , T and h_i are the heat conduction coefficients, temperature change, and heat flux, respectively; u_i , φ and ϕ are the elastic displacements, electric potential and magnetic potential, respectively; σ_{ij} , D_i and B_i are the stress, electrical displacement and magnetic induction, respectively; C_{ijkl} , e_{ikl} , q_{ikl} and α_{il} are the elastic, piezoelectric, piezomagnetic and magnetoelectric constants, respectively; ε_{il} and μ_{il} are the dielectric permittivities and the magnetic permeabilities, respectively; λ_{ij} , p_i and m_i are the thermal stress constants, pyroelectric coefficients and pyromagnetic coefficients, respectively.

For two-dimensional problems, all the field variables are independent of x_3 . Following the solution procedure proposed by Hwu for thermoelasticity [8] and by Lu, *et al.* [9] for thermopiezoelectricity[9], the solutions to Eqs.(1)₂ and (2)₂ are, respectively,

$$T = 2 \operatorname{Re}\{g'(z_i)\}, \quad \mathbf{u} = \{u_k, \varphi, \phi\}^T = 2 \operatorname{Re}\{\mathbf{A}\mathbf{f}(z_\alpha) + \mathbf{c}g(z_i)\} \quad (4)$$

where $\mathbf{A} = [\mathbf{a}_1, \mathbf{a}_2, \mathbf{a}_3, \mathbf{a}_4, \mathbf{a}_5]$, $\mathbf{f}(z_\alpha) = \operatorname{diag}[f(z_1), f(z_2), f(z_3), f(z_4), f(z_5)]$, $z_i = x_1 + \mu_i x_2$, $z_\alpha = x_1 + \mu_\alpha x_2$; $g(z_i)$ and $f(z_\alpha)$ are arbitrary functions to be determined, respectively; Re stand for the real part; the superscript T denotes the transpose; the prime (') denotes the derivative with respect to the associated arguments. z , z_α , \mathbf{A} and \mathbf{c} are constants determined by

$$\begin{cases} k_{22}\mu_i^2 + (k_{12} + k_{21})\mu_i + k_{11} = 0, & [\mathbf{Q} + (\mathbf{R} + \mathbf{R}^T)\mu_\alpha + \mathbf{T}\mu_\alpha^2]\mathbf{a}_\alpha = 0 \\ [\mathbf{Q} + (\mathbf{R} + \mathbf{R}^T)\mu_i + \mathbf{T}\mu_i^2]\mathbf{c} = \Lambda_1 + \mu_i\Lambda_2 \end{cases} \quad (5)$$

where Λ_i are 5×1 vectors, and \mathbf{Q} , \mathbf{R} and \mathbf{T} are 5×5 matrices defined by

$$\Lambda_i = \{\lambda_{i1}, \lambda_{i2}, \lambda_{i3}, p_i, m_i\}^T \quad (i=1, 2), \quad Q_{JK} = E_{1JK1}, R_{JK} = E_{1JK2}, T_{JK} = E_{2JK2} \quad (6)$$

Substituting Eq.(4) into Eqs.(1)₁ and (2)₁, the heat flux components h_i , the stresses, electric displacement and magnetic induction Σ_i can be written as

$$h_i = -2\text{Re}\{(k_{i1} + \mu_i k_{i2})g'(z_i)\} \quad (i=1, 2), \quad \Sigma_1 = \{\sigma_{1j}, D_1, B_1\}^T = -\Phi_{,2}, \Sigma_2 = \{\sigma_{2j}, D_2, B_2\}^T = \Phi_{,1} \quad (7)$$

where Φ is the generalized stress vector given as

$$\Phi = 2\text{Re}\{\mathbf{B}\mathbf{f}(z_a) + \mathbf{d}g(z_i)\} \quad (8)$$

with

$$\mathbf{B} = \mathbf{R}^T \mathbf{A} + \mathbf{T} \mathbf{A} \mathbf{\Gamma} = -(\mathbf{Q} \mathbf{A} + \mathbf{R} \mathbf{A} \mathbf{\Gamma}) \mathbf{\Gamma}^{-1}, \mathbf{d} = (\mathbf{R}^T + \mu_i \mathbf{T}) \mathbf{c} - \Lambda_i = -(\mathbf{Q} + \mu_i \mathbf{R}) \mathbf{c} / \mu_i + \Lambda_i / \mu_i \quad (9)$$

in which $\mathbf{\Gamma} = \text{diag}[\mu_1, \mu_2, \mu_3, \mu_4, \mu_5]$.

Using Eq.(7), the resultant heat flow Θ , the resultant force and the resultant normal components of the electric displacement and the magnetic induction Σ along any curve can be expressed by

$$\Theta = \int h_1 dx_2 - h_2 dx_1 = -2k_i \text{Im}\{g'(z_i)\}, \Sigma = \{t_j, S_D, S_H\}^T = \int \Sigma_1 dx_2 - \Sigma_2 dx_1 = -\Phi \quad (10)$$

where Im denotes imaginary part and $k_i = \sqrt{k_{11}k_{22} - k_{12}^2}$.

3. UNIFORM HEAT FLOW DISTURBED BY AN ELLIPTICAL CAVITY

3.1 Statement of the Problem

Consider an infinite anisotropic electromagnetic thermoelastic medium containing an elliptical cavity subjected to a uniform heat flow h_0 directed at an angle θ with respect to the positive x_1 -axis, as shown in Fig. 1. The regions occupied by the material and the cavity are referred to as Ω and Ω_c , respectively. In addition, the cavity is assumed to be free of forces, charge and electric current along its surface, but to be filled with the homogeneous gas (air or vacuum) of permittivity (ϵ^c) and permeability (μ^c), where superscript c refers to the quantities in the cavity.

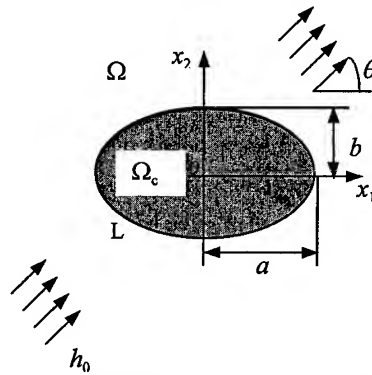


Fig. 1. An elliptical cavity in an infinite solid.

Unlike elastic fields, the electric fields and the magnetic fields can permeate vacuum and can exist inside the cavity of a magnetoelectroelastic material. The electric potential and the magnetic potential in the cavity satisfy the Laplace equation

$$\nabla^2 \varphi^c = 0, \quad \nabla^2 \phi^c = 0 \quad \text{in } \Omega_c, \quad (11)$$

and the constitutive relations are

$$D_i^c = \varepsilon^c E_i^c = -\varepsilon^c \frac{\partial \phi^c}{\partial x_i}, \quad B_i^c = \mu^c H_i^c = -\mu^c \frac{\partial \phi^c}{\partial x_i}, \quad i = 1, 2 \quad \text{in } \Omega_c, \quad (12)$$

The general solutions to Eq.(11) are

$$\phi^c = 2 \operatorname{Re}\{f_1^c(z)\}, \quad \phi^c = 2 \operatorname{Re}\{f_2^c(z)\} \quad (13)$$

With Eqs.(12) and (13), The sums of the normal components of the electric displacement and magnetic induction along an arc may be expressed, respectively, as,

$$S_D^c = -2\varepsilon^c \operatorname{Im}\{f_1^c(z)\}, \quad S_B^c = -2\mu^c \operatorname{Im}\{f_2^c(z)\}. \quad (14)$$

For convenience of the latter derivation, we define

$$\Psi^c = \{\phi^c, \phi^c\}^T = 2 \operatorname{Re}\{f^c(z)\}, \quad S^c = \{S_D^c, S_B^c\}^T = -2\Pi^c \operatorname{Im}\{f^c(z)\} \quad (16)$$

where $f^c(z) = \{f_1^c(z), f_2^c(z)\}^T$ and $\Pi^c = \operatorname{diag}[\varepsilon^c, \mu^c]$.

According to the above description, the boundary conditions of the present problem are

$$\Theta = 0, \quad \mathbf{g}^T \mathbf{u} = \Psi^c, \quad \Phi = -\mathbf{g} S^c \quad \text{along the cavity boundary } L \quad (17)$$

$$h_1 = h_0 \cos \theta, \quad h_2 = h_0 \sin \theta, \quad \Sigma_{ij} = 0 \quad \text{at infinity} \quad (18)$$

where

$$\mathbf{g} = \begin{bmatrix} 0 & 0 & 0 & 1 & 0 \\ 0 & 0 & 0 & 0 & 1 \end{bmatrix}^T. \quad (19)$$

3.2 Solution of the Problem

Introducing the following mapping functions

$$z_\alpha(\zeta_\alpha) = R_{1\alpha}\zeta_\alpha + R_{2\alpha}\zeta_\alpha^{-1}, \quad R_{1\alpha} = (a - ip_\alpha b)/2, \quad R_{2\alpha} = (a + ip_\alpha b)/2 \quad (\alpha = 1-5, t) \quad (20)$$

$$z(\zeta) = R(\zeta + m\zeta^{-1}), \quad R = (a + b)/2, \quad m = (a - b)/(a + b) \quad (21)$$

the general expressions for the fields outside and inside the elliptical cavity can now be written in the mapped plane as following

$$T = 2 \operatorname{Re}\{g'_h(\zeta_t) + g'_p(\zeta_t)\}, \quad \Theta = -2k_t \operatorname{Im}\{g'_h(\zeta_t) + g'_p(\zeta_t)\} \quad \text{in } \Omega \quad (22)$$

$$\mathbf{u} = 2 \operatorname{Re}\{\mathbf{A}f(\zeta_\alpha) + \mathbf{c}g_p(\zeta_t)\}, \quad \Phi = 2 \operatorname{Re}\{\mathbf{B}f(\zeta_\alpha) + \mathbf{d}g_p(\zeta_t)\} \quad \text{in } \Omega \quad (23)$$

$$\Psi^c = 2 \operatorname{Re}\{f^c(\zeta)\}, \quad S^c = -2\Pi^c \operatorname{Im}\{f^c(\zeta)\} \quad \text{in } \Omega_c \quad (24)$$

where $g_h(\zeta_t)$ represents the function associated with the unperturbed temperature field which related to the solution of the homogeneous media, while $g_p(\zeta_t)$ denotes the function corresponding to perturbed temperature field of the material due to the presence of the cavity. $\mathbf{f}(\zeta)$ is the function corresponding to the fields inside the cavity. It should be note that since the complex function $\mathbf{c}g_h(\zeta_t)$ and $\mathbf{d}g_h(\zeta_t)$ associated with the solutions of the homogeneous problem due to a remote

uniform heat flow will not produce stress, electric field and magnetic field, these complex functions can be subtracted from Eq.(23) without difficulty.

Applying the boundary conditions (17) and (18) and after the tedious manipulation, the functions in Eqs.(23) and (24) are obtained as follows

$$g_h(\zeta_i) = \frac{1}{2} g_0 (R_{1i}^2 \zeta_i^2 + R_{2i}^2 \zeta_i^{-2}), \quad g_0 = -\frac{\cos \theta + \bar{\mu}_i \sin \theta}{2k_i^2} k_{22} h_0 \quad (25)$$

$$g_p(\zeta_i) = a_{1p} \ln \zeta_i + a_{2p} \zeta_i^{-2}, \quad a_{1p} = R_{1i} (\bar{g}_0 \bar{R}_{1i} - g_0 R_{2i}), \quad a_{2p} = R_{2i} (\bar{g}_0 \bar{R}_{1i} - g_0 R_{2i})/2 \quad (26)$$

$$f(\zeta_\alpha) = \langle \ln \zeta_\alpha \rangle \Pi + \langle \zeta_\alpha^{-2} \rangle \mathbf{q}, \quad \alpha = 1-5 \quad \text{in } \Omega \quad (27)$$

$$f^c(\zeta) = (\zeta^2 + m^2 \zeta^{-2}) \mathbf{e} \quad \text{in } \Omega_c \quad (28)$$

In the above equations, the overbar stands for the conjugate of a complex number. 5×1 vectors Π and \mathbf{q} , 2×1 vector \mathbf{e} , respectively, are

$$\Pi = 4\mathbf{B}^{-1}\mathbf{L}[\text{Im}(a_{1p}\mathbf{c}) - i\bar{\mathbf{M}}\text{Im}(a_{1p}\mathbf{d})] \quad (29)$$

$$\mathbf{q} = \mathbf{B}^{-1}[ig\Pi^c(\bar{\mathbf{e}} - m^2\mathbf{e}) - a_{2p}\mathbf{d}] \quad (30)$$

$$\mathbf{e} = (m^4\mathbf{W} - \mathbf{V}\mathbf{W}^{-1}\bar{\mathbf{V}})^{-1}(m^2\mathbf{Y} - \mathbf{V}\mathbf{W}^{-1}\bar{\mathbf{Y}}) \quad (31)$$

with

$$\mathbf{W} = \mathbf{I} + \mathbf{g}^T \mathbf{M} \mathbf{g} \Pi^c, \quad \mathbf{V} = \mathbf{I} - \mathbf{g}^T \mathbf{M} \mathbf{g} \Pi^c, \quad \mathbf{Y} = a_{2p} \mathbf{g}^T (\mathbf{c} + i\mathbf{M}\mathbf{d}) \quad (32)$$

in which \mathbf{I} is the 2×2 unit matrix, while \mathbf{L} and \mathbf{M} are

$$\mathbf{L} = -2i\mathbf{B}\mathbf{B}^T, \quad \mathbf{M} = i\mathbf{A}\mathbf{B}^{-1} \quad (33)$$

where \mathbf{L} is the real and nonsingular matrix, and \mathbf{M} is called the impedance matrix and is nonsingular [3]. With the functions given in Eqs.(25)-(28), one can calculate the stresses and the electromagnetic fields without difficulty. In addition, substituting Eq.(28) with Eq.(21) into Eq.(13) and Using Eq.(12), we find that the electromagnetic fields in the cavity are always linear functions of the coordinates.

4. UNIFORM HEAT FLOW DISTURBED BY A SLIT CRACK

When the minor semi-axis b of the ellipse approaches zero, the elliptic cavity reduces to a slit crack of length $2a$. The solutions for the crack problem may be studied accordingly. Since $R_{1i} = R_{2i} = R = a/2$ and $m = 1$ when $b = 0$, Eqs.(29) and (30) can be simplified as

$$\Pi = 2a^2 \mathbf{B}^{-1} \mathbf{L} [i\bar{\mathbf{M}} \text{Re}\{\mathbf{d}\} - \text{Re}\{\mathbf{c}\}] \text{Im}\{g_0\} \quad (34)$$

$$\mathbf{q} = ia^2 \mathbf{B}^{-1} [\mathbf{d} + 2 \text{Im}\{\mathbf{M}\mathbf{d}\} - \text{Re}\{\mathbf{c}\}] \text{Im}\{g_0\} / 4 \quad (35)$$

Eq.(27) together with Eqs.(34) and (35) indicates that $f(\zeta_\alpha)$ is independent of Π^c . This means the coupled fields in the cracked material are not related to Π^c . Noting from Eq.(25)₂ that $\text{Im}\{g_0\} = 0$

when the uniform heat is flowing parallel to thermally insulated crack ($\theta = 0$), we immediately find that the electromagnetic elastic fields are not induced under steady-state condition in terms of Eqs.(7)_{2,3}, (26) and (27) together with Eqs.(34)-(35).

Differentiating the functions $f(\zeta_a)$ and $g_p(\zeta_l)$ with respect to z_a and z_p , respectively, and then considering that $x_2 = 0$, $x_1 > a$, the stresses, electric displacement and magnetic induction near the tips of the crack along the x_1 axis are obtained by

$$\Sigma_2 = \text{Re}\left\{\Pi - 2\zeta^{-2}\mathbf{q} + a_{pl}(1 - \zeta^{-2})\right\} \frac{1}{\sqrt{x_1^2 - a^2}} \quad (36)$$

where $\zeta = (x_1 + \sqrt{x_1^2 - a^2})/a$. From Eq.(36), it can be seen that the stresses, electric displacement and magnetic induction exhibit the traditional square root singularity. The amplitudes of the singular fields can be characterized by the intensity factors $\mathbf{K} = \{K_{II}, K_I, K_{III}, K_D, K_B\}^T$, where K_{II} , K_I and K_{III} are the traditional stress intensity factors, while K_D and K_B are the electric displacement factor and the magnetic induction factor, respectively.

With the usual definition, the intensity factors are given by

$$\mathbf{K} = \lim_{x_1 \rightarrow a} \sqrt{2\pi(x_1 - a)} \Sigma_2 = 2\sqrt{\frac{\pi}{a}} \text{Re}\{\Pi - 2\mathbf{q}\} \quad (37)$$

Eq.(37) with Eqs.(34) and (35) shows that the intensity factors are dependent on the material properties.

5. CONCLUSIONS

The following main conclusions can be drawn:

- (1) The electromagnetic fields inside the cavity vary linearly with the coordinates.
- (2) In a slit crack case, the coupled fields in the materials are independent of the dielectric constant and magnetic permeability of air inside the crack.
- (3) A thermally insulated crack doesn't disturb the uniform heat flow parallel to it. This means that the stresses, electric fields and magnetic fields are not induced in the materials.
- (4) The intensity factors are related to the material properties.

REFERENCES

1. C.K. Chao and M.H. Shen, J. Appl. Mech., **65**(1998) p. 51
2. S.A. Meguid and Z. Zhong Int. J. Solids Struct., **34**(1997) p. 3401
3. V.I. Alshits, A.N. Darinskii and J. Lothe, Wave Motion, **16** (1992) p. 265
4. G. Harshe, J.P. Dougherty and R.E. Newnham, Int. J. Appl. Electromag. Mater., **4**(1993) p. 145
5. C.W. Nan, J. Am. Ceram. Soc. **80**(1997) p. 1333
6. J.H. Huang and W. S. Kuo, J. Appl. Phys. **8**(1997) p. 1378
7. J.Y. Li and M.L. Dunn, J. Intel. Mater. Syst. Struct., **9**(1998) p. 404
8. C. Hwu and W.J. Yen, J. Appl. Mech., **60**(1993)p. 626
9. P. Lu, M. J. Tan and K.M. Liew, Archive Appl. Mech., **68**(1998) p. 719

Evaluation of Stress Intensity Factor Using White Light Photoelastic Experiment

E. Umezaki¹, K. Kodama¹ and A. Shimamoto²

¹ Department of Mechanical Engineering, Nippon Institute of Technology,
4-1 Gakuendai, Miyashiro, Saitama 345-8501, Japan

² Department of Mechanical Engineering, Saitama Institute of Technology,
1690 Fusaiji, Okabe, Saitama 369-0293, Japan

Keywords: Fracture Mechanics, Image Processing, Irwin Method, Isochromatics, Photoelasticity, Stress Intensity Factor, White Light Photoelastic Experiment

ABSTRACT

In this study, a method was proposed for evaluating the stress intensity factor using the isochromatics multiplied and extracted from original isochromatic images which obtained from a white light photoelastic experiment. This method utilizes R, G and B isochromatics, which are captured using a color CCD camera and an image processor in dark- and light-field circular polariscopes. First, for each color, the dark-field intensities are subtracted from the light-field ones so that each point of the resultant image has a positive, zero or negative value. Then, the isochromatics are obtained as a series of points at which the value is zero, which are extracted using an image processing. The fringe orders are assigned to the extracted isochromatics using calibration curves. The stress intensity factor is determined using the Irwin method. This method is applied to an epoxy resin plate with a crack formed at one side under 3-point bending. The result shows that the stress intensity factor is accurately evaluated using the R, G and B isochromatics near the crack tip.

1. INTRODUCTION

The stress intensity factor, K , which expresses the intensity of stress field near the crack tip, is used to investigate initiation and propagation of cracks in many materials. In order to evaluate K , the isochromatic fringes obtained from a photoelastic experiment are often used. When the stress intensity factor is determined, many isochromatics must be used to improve the accuracy of the determination. Few isochromatics appear in a model which is made of low-sensitive photoelastic material. In such case, the isochromatics must be multiplied and extracted.

There are three techniques for extracting linear isochromatics from an isochromatic image

captured using a monochromatic CCD camera: (a) a thinning technique by which the centers of binarized fringes are obtained[1]; (b) a technique for detecting the minimum light intensity points[2],[3], and (c) a technique in which the dark-field light intensity is subtracted from the light-field one[4],[5]. To multiply isochromatics, subtraction of the dark-field light intensity from the light-field one[4]-[8] and the n multiple-angle relations of the sine and cosine functions[5],[7],[8] have been used. Using these techniques, the multiplication and extraction of isochromatics have been markedly improved.

All the above mentioned techniques have been used for one or two monochrome isochromatic images, which are captured separately. Instead of these techniques, a multiplication and extraction technique for a one color isochromatic image, which is captured using a color CCD camera and has information at multiple wavelengths, is considered[9].

In this study, a method was proposed for evaluating the stress intensity factor using the isochromatics multiplied and extracted from original isochromatic images which obtained from a white light photoelastic experiment, and was applied to an epoxy resin plate with a crack formed at one side under 3-point bending.

2. FRINGE MULTIPLICATION AND EXTRACTION METHOD

2.1 White Light Photoelasticity

The light intensities, I_{di} and I_{li} ($i=R, G, B$), emerging from the RGB filters of a color CCD camera in the dark- and light-field circular polariscopes using a white light when the error of the quarter-wave plates, ε is taken into account become[10]

$$I_{d,i} = \frac{1}{\lambda_{i2} - \lambda_{i1}} \int_{\lambda_{i1}}^{\lambda_{i2}} F_{i(\lambda)} I_{0(\lambda)} \sin^2 \pi N_{\lambda} (1 - \cos^2 2\phi \sin^2 \varepsilon) d\lambda + I_{B,i} \quad (1)$$

$$I_{l,i} = \frac{1}{\lambda_{i2} - \lambda_{i1}} \int_{\lambda_{i1}}^{\lambda_{i2}} F_{i(\lambda)} I_{0(\lambda)} [\cos^2 \pi N_{\lambda} (1 - \cos^2 2\phi \sin^2 \varepsilon) + \cos^2 2\phi \sin^2 \varepsilon] d\lambda + I_{B,i} \quad (2)$$

where $I_0(\lambda)$, which is a function of wavelength, λ , is the amplitude of the light emitted from the polarizer, $I_{B,i}$ ($i=R, G, B$) are the background light intensities on the R, G and B images, ϕ is the direction of the principal stress, σ_1 , to a selected reference, N_{λ} ($=\Delta/\lambda$ where Δ is the retardation) is the fringe order at wavelength λ , $F_{i(\lambda)}$ ($i=R, G, B$) are the spectral responses of the RGB filters of the camera, $\varepsilon = (\pi/2)\{(\lambda_0/\lambda)-1\}$ where λ_0 is the matching wavelength of the quarter-wave plates and λ is the generic wavelength, and λ_{i1} and λ_{i2} ($i=R, G, B$) are the lower and upper limits of the spectrum as acquired by the filter i .

2.2 Multiplication and Extraction Method

The subtraction of the light intensities in the dark-field isochromatics image from those in the light-field one, and the extraction of the points with zero values using an image processing technique was used for multiplying and extracting isochromatics [5],[9],[11].

As shown in Fig.1, subtraction of I_{di} (shown by Eq.1) from I_{li} (by Eq.2) yields

$$I_{s,i} = I_{l,i} - I_{d,i}$$

$$= \frac{1}{\lambda_{i2} - \lambda_{i1}} \int_{\lambda_{i1}}^{\lambda_{i2}} F_{i(\lambda)} I_{0(\lambda)} \left[(2 \cos^2 \pi N_{\lambda} - 1)(1 - \cos^2 2\phi \sin^2 \varepsilon) + \cos^2 2\phi \sin^2 \varepsilon \right] d\lambda \quad (3)$$

where $i=R, G, B$.

Equation 3 indicates that the values of N_{λ} at which $I_{s,i}=0$ ($i=R, G, B$) are not $1/4, 3/4, 5/4, \dots$, though those at which $I_{s,i}=0$ when a single wavelength, λ , is used are $1/4, 3/4, 5/4, \dots$ [5]. Here the apparent fringe orders of $N_{if}=(2m-1)/4$ ($i=R, G, B, m=1,2,3,\dots$) are assigned to the points at which $I_{s,i}=0$ ($i=R, G, B$) temporarily.

2.3 Fringe Order Assignment Method

A method for assigning the correct fringe orders to the extracted R, G and B isochromatics to which the apparent fringe orders were assigned as shown in section 2.2 using calibration curves was as follows [11].

First, the light intensities, $I_{d,i}$ and $I_{l,i}$ ($i=R, G, B$), in the dark- and light-field isochromatic images obtained using the RGB filters of a color CCD camera shown in Fig.2 were calculated using Eqs.1 and 2. The value of $I_{0(\lambda)}$ required to calculate $I_{d,i}$ and $I_{l,i}$ ($i=R, G, B$) was taken as 1, and $F_{i(\lambda)}$ ($i=R, G, B$) as the relative spectral responses, T_i , of the RGB filters, respectively. The values of $\lambda_{R1}=530$ and $\lambda_{R2}=700$ nm, $\lambda_{G1}=440$ and $\lambda_{G2}=620$ nm, and $\lambda_{B1}=400$ and $\lambda_{B2}=550$ nm were obtained from Fig.2 as λ_{i1} and λ_{i2} ($i=R, G, B$). Furthermore, $\phi=0^\circ$ was used because, if $\varepsilon \neq 0$, the effect of ϕ on the light intensities is minimal at $\phi=45^\circ$ and maximal at $\phi=0^\circ$ and 90° , although if $\varepsilon=0$, the effect does not occur at any ϕ , as known from Eqs.1 and 2. The values of N_{if} ($i=R, G, B$) were obtained from $N_{\lambda}=N_{\lambda G} \cdot \alpha_{\lambda} / \alpha_{\lambda G}$, where $N_{\lambda G}$ is the fringe order at wavelength $\lambda_G=540$ nm, α_{λ} is the photoelastic sensitivity at wavelength λ , and $\alpha_{\lambda G}$ is the photoelastic sensitivity at wavelength $\lambda_G=540$ nm. The value of α_{λ} was obtained from $\alpha_{\lambda}=0.152-0.000149 \lambda$ (λ in nm), which was determined on the basis of $\alpha_R=0.061$ mm/N, $\alpha_G=0.071$ mm/N and $\alpha_B=0.08$ mm/N measured using the color CCD camera.

Second, the light intensities, I_d and I_b , in the dark- and light-field isochromatic images obtained at a single wavelength of $\lambda_G=540$ nm were calculated from $I_d=\sin^2 \pi N_{\lambda G}$ and $I_l=\cos^2 \pi N_{\lambda G}$. Third, the points at which $I_{s,i}=0$ ($i=R, G, B$) with the apparent fringe orders were extracted. Lastly,

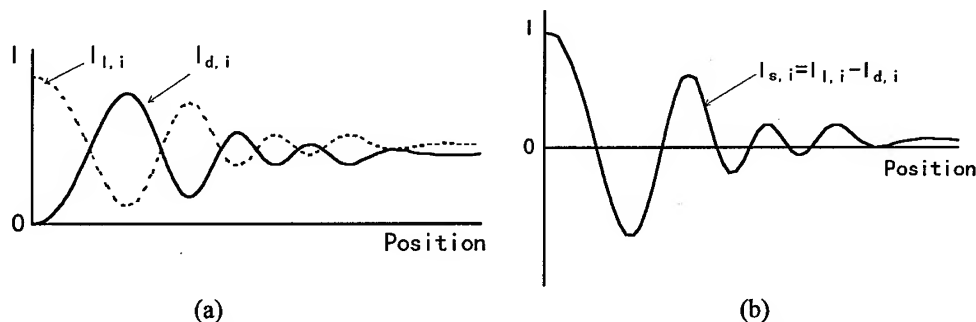


Fig.1 Subtraction of light intensities in dark field image from those in light field one.

the calibration curves were made comparing the positions of isochromatics having the apparent fringe orders with those having the correct fringe orders obtained at a single wavelength of $\lambda_G = 540\text{nm}$ in the range of $N_{\lambda G} = 0$ to 3.

Figure 3 shows the calibration curve for the R filter in the color CCD camera. Using the calibration curve, the apparent fringe orders, $N_{Rf} = 1/4, 3/4, 5/4, \dots$ of isochromatics extracted using the R filter were converted to $N_{\lambda G}$ obtained using $\lambda_G = 540\text{nm}$. The calibration curves for the G and B filters were expressed by $N_{\lambda G} = -0.064 N_{Gf}^2 + 1.0247 N_{Gf} - 0.007$ and $N_{\lambda G} = -0.00002 N_{Bf}^2 + 0.8784 N_{Bf} - 0.0024$.

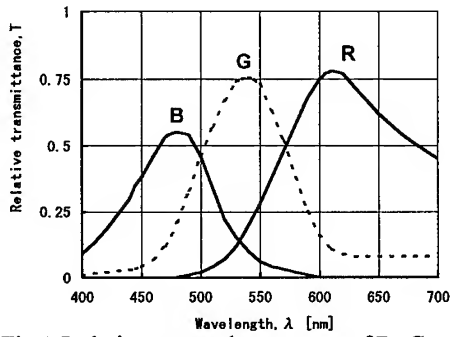


Fig.2 Relative spectral responses of R, G and B filters of color CCD camera.

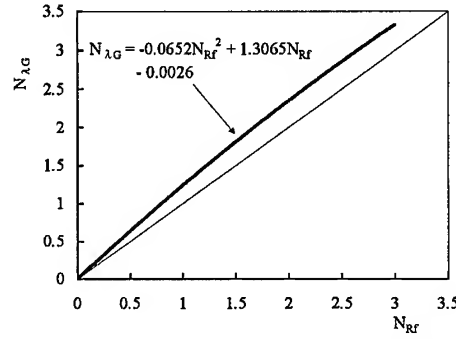


Fig.3 Calibration curve for assigning fringe orders to isochromatics multiplied and extracted using red filter in CCD camera.

3. STRESS INTENSITY FACTOR EVALUATION METHOD

The stress intensity factor, K_I , for mode I loading was evaluated by the Irwin method using the equation[12]

$$K_{I(exp)} = \frac{N_{\lambda} \sqrt{2\pi r_m}}{\alpha_{\lambda} t \sin \theta_m} \left[1 + \left(\frac{2}{3 \tan \theta_m} \right)^2 \right]^{-0.5} \left(1 + \frac{2 \tan(3\theta_m/2)}{3 \tan \theta_m} \right) \quad (4)$$

where r_m is the radius to the furthest point, M , on the fringe loop, and θ_m is the angle of fringe tilt.

4. APPLICATION

The proposed method was used to evaluate the stress intensity factor, K_I , for a crack formed at one side in an epoxy resin plate under 3-point bending as shown in Fig.4. Figure 5 shows a polariscope system for multiplying and extracted isochromatics. Video signals output from a color CCD camera were converted into R, G and B signals using a component transcoder. The R, G and B signals in the dark and light fields were separately input into a monochromatic image processing device, digitized and stored as a 256×256 pixel array in a floppy disk. After R, G and B images were taken in each field, the two images for each color were used to multiply and extract the

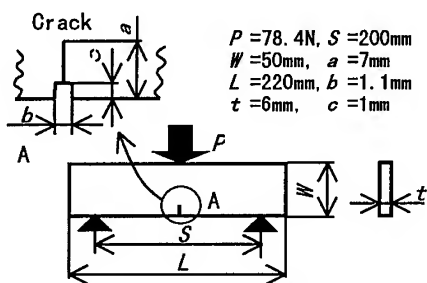


Fig. 4 Beam with crack in one side subjected to 3-point bending.

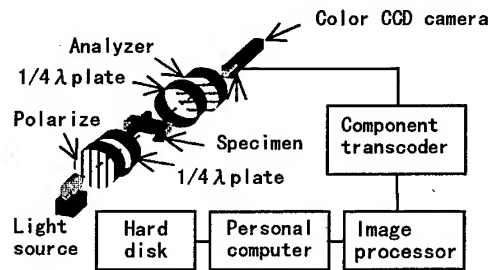
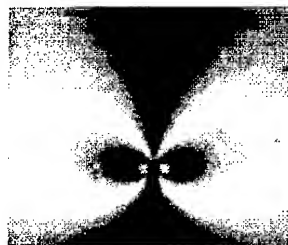
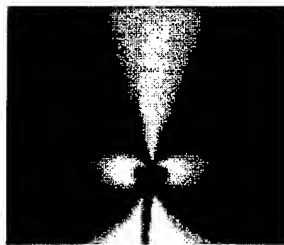


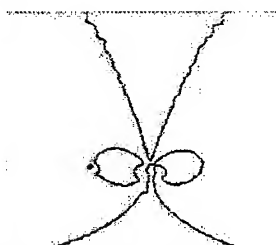
Fig. 5 Experimental setup.



(a) Red



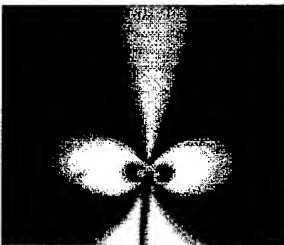
(a) Red



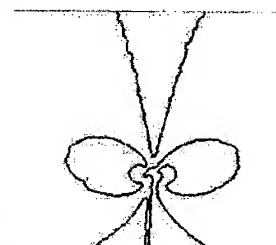
(a) Red



(b) Green



(b) Green



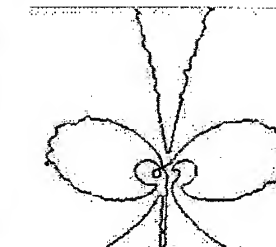
(b) Green



(c) Blue



(c) Blue



(c) Blue

Fig. 6 Isochromatics in the dark field

Fig. 7 Isochromatics in the light field

Fig. 8 Extracted isochromatics

isochromatics using a personal computer. The fringe orders were assigned to the extracted isochromatics using calibration curves.

The values of $\lambda_R=610\text{nm}$, $\lambda_G=540\text{nm}$ and $\lambda_B=480\text{nm}$ was selected as typical wavelengths for the R, G and B filters shown in Fig.2, at which the filters had the maximum relative spectral responses. The values of $\alpha_R=0.061\text{mm/N}$, $\alpha_G=0.071\text{mm/N}$ and $\alpha_B=0.08\text{mm/N}$ were obtained using the R, G and B filters in the polariscope.

Figures 6 and 7 show the R, G and B images in the dark and light fields, respectively. Figure 8 shows the isochromatics extracted from the R, G and B images shown in Figs.6 and 7. The multiplied isochromatics shown in Fig.8 were used to evaluate the stress intensity factor, $K_{I(exp)}$, using Eq.4.

Table 1 shows the comparison between the stress intensity factor, $K_{I(exp)}$, evaluated by the proposed method using the calibration curves and $K_{I(thy)}$ obtained by the theory[13]. The isochromatics with fringe orders 0.25, 0.75 and 1.25 on each color image were used to evaluate $K_{I(exp)}$. The average of the error of $K_{I(exp)}$ was about 3%. The error of $K_{I(exp)}$ evaluated without using the calibration curves was about 7%. Hence the proposed method was effective to evaluate the stress intensity factor accurately.

Table 1. Comparison between $K_{I(exp)}$ evaluated by the proposed method and $K_{I(thy)}$ obtained by the theory.

Image	$K_{I(exp)}$ (N/mm ^{3/2})	$K_{I(thy)}$ (N/mm ^{3/2})	Error (%)	Average error (%)
R	9.74	9.55	2	3.2
G	9.85		3.1	
B	9.99		4.6	

5. CONCLUSIONS

A method was proposed for evaluating the stress intensity factor using the isochromatics multiplied and extracted from original isochromatic images which obtained from a white light photoelastic experiment. The method was applied to an epoxy resin plate with a crack formed at one side under 3-point bending, and its effectiveness was discussed. The results showed that the stress intensity factor was accurately evaluated using the R, G and B isochromatics near the crack tip.

REFERENCES

1. Y. Seguchi, Y. Tomita and M. Watanabe, Exp. Mech., **19**-10 (1979), pp.362-370.
2. E. Umezaki, T. Tamaki and S. Takahashi, Exp. Tech., **13**-12 (1989), pp.22-27.
3. K. Ramesh and B.R. Pramod, Opt. Eng., **31**-7 (1992), pp.1487-1498.
4. B. Han and L. Wang, Exp. Tech., **18**-6 (1994), pp.11-13.
5. Y. Nanka and E. Umezaki, Proc. Intl. Conf. on Material Engineering, Italy (1996), pp.267-274.
6. S. Toh, S.H. Tang and J.D. Hovanement, Exp. Tech., **14**-4 (1990), pp.21-23.
7. X. Liu and Q. Yu, Exp. Tech., **17**-1 (1993), pp.26-29.
8. T.Y. Chen, J. Strain Analysis, **30**-1 (1995), pp.1-7.
9. Y. Nanka, E. Umezaki and H. Watanabe, Proc. of ATEM'97, Japan (1997), pp.435-440.
10. A. Ajovalasit, S. Barone and G. Petrucci, Exp. Mech., **35**-3 (1995), pp.193-200.
11. E. Umezaki, Y. Nanka and A. Shimamoto, Proc. of ATEM'99, Japan (1999), pp.87-92.
12. S. Takahashi and F. Nogata, Science of Machine (in Japanese), **38**-1 (1986), pp.82-86.
13. H. Okamura, Introduction to linear fracture mechanics, Baihukan, Tokyo, (1976), pp.218-219.

Singularity Intensity Factor Calculation in Plates and Shells Based on the Singular Line Mapping Technique in FEMOL

Chuntu Liu and Yongjun Xu

Institute of Mechanics, Chinese Academy of Sciences,
Beijing 100080, China P.R.

Keywords: Finite Element Method of Lines, Reissner Plate, Reissner Shell, Singular Line Mapping, Stress Intensity Factor

ABSTRACT

In this paper, a brief review of the singular line mapping technique in finite element method of lines (FEMOL) for plate and shell crack/notch problems is given. By using the singular line mapping technique, the solution property is changed, the computation is speeded up and the accuracy is improved. The displacement and its derivative can be obtained accurately after an accurate singular line mapping, and the lowest stress intensity factor can be solved from the derivative. Some numerical examples are given to show the general excellent performance.

1. INTRODUCTION

Stress analysis in practical engineering applications inevitably encounters stress singularities caused by sudden changes in geometry, e.g. around re-entrant corners (notches) or, more severely, around crack tips. Their presence causes great difficulty to the numerical solutions that have to be invoked when analytical solutions are not available. A numerical recipe for accurate and efficient computation of stress singularity factors (SIFs) usually consists of two major ingredients, namely a powerful numerical method for general stress analysis and a novel approach to obtaining the desired SIFs which may include special treatment of various singularities. The underlying numerical method employed in this paper is the FEMOL [1-4], which is a newly developed, general-purpose, semi-analytical method. In this method, a partial differential equation defined on an arbitrary domain is semi-discretized, by finite element techniques via energy theorems or variational principles, into a system of ordinary differential equations (ODEs) defined on straight or curved mesh lines. At present, the resulting ODE system is solved directly and efficiently by state-of-the-art ODE solver, e.g. COLSYS [5,6] is exclusively adopted in the present paper. Such solvers have built-in self-adaptivity features such that the accuracy of the ODE solutions satisfies the user pre-specified error tolerances. With the solver used, FEMOL has been proved to be a distinguished numerical method with efficient adaptivity in the mesh line directions automatically built in, so that its inherent semi-analytical characteristics are well preserved. Its power and versatility have been demonstrated by a series of theoretical analysis and computational applications to various linear and nonlinear problems. A general-purposed computer code FEMOL92 [7] that is capable of static and vibrative analysis of various linear elastic structures has been developed. For a more detailed and systematic description of FEMOL, see Ref. [4]. FEMOL could be directly applied to notch/crack

problems [3,4]. The success in establishing 'triangular' elements (Yuan [8]) by degenerating an element end-side to a point allows the use of the optimum radial line meshes, i.e. mesh lines emanate from crack tips. With no special treatment, except for judicious use of radial line meshes with sufficiently high polynomial degree p used in the element displacement shape functions, FEMOL is able to produce remarkably accurate solutions even when very few elements are used [4]. Most of numerical methods, directly or indirectly, make use of the available eigen-solutions when applied to the SIF computation for crack/notch problems so that singularity can be treated in a more efficient, accurate and reliable way. Recently, Xu and Yuan [9] presented an effective implementation of the imbedding method for accurate and reliable computation of complete real or complex eigen-solutions in two dimensional notch/crack singularities with multiple materials, arbitrary opening angles and various surface conditions. The resulting algorithm is robust and may be employed by any numerical methods that make use of singular solutions.

In order to take full advantage of the power of FEMOL and the usefulness of the local singular solutions, the singular mapping technique [10] is utilized in this paper to remove the singularity from the FEMOL solving to the mapping. This nonlinear mapping not only can map an interval to a standard one, but also can change the behavior of the solution function. Combined with the self-adaptivity features, the computation is speeded up and the accuracy is improved, especially, the tolerances can be imposed on the derivatives as the displacement for the singular solutions. The displacement and its derivative can be obtained accurately after an accurate singular line mapping, and from the derivative we can solve the lowest stress intensity factor. Recently, Xu and Yuan [11] use this technique in anti-plane and in-plane problems to solve the SIFs. In the present paper, a brief review of the singular line mapping technique in finite element method of lines (FEMOL) for plate and shell crack/notch problems is given. By using the singular line mapping technique, both the displacement and its derivative can be obtained accurately after an accurate singular line mapping, and from derivative the lowest stress intensity factor can be solved. Some numerical examples are given to show the general excellent performance.

2. SINGULAR MAPPING TECHNIQUE OF FEMOL

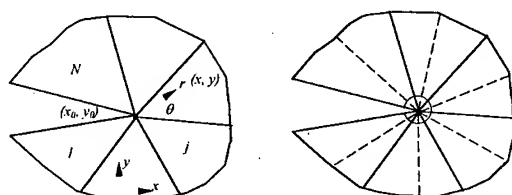
Figure 1 shows a two dimensional singular problem with N different materials around notch/crack tip. The body forces are assumed to be negligible. For convenience sake we omit the different material domain subscript j shown in the Fig. 1(a). In the polar coordinates shown in Fig. 1(a), for the Reissner plate and shell, the general displacement components can be written as the following double series form

$$(i) \begin{cases} u_r^j = \sum_i \sum_n r^{\lambda_i+n} f_n^j(\theta) \\ u_\theta^j = \sum_i \sum_n r^{\lambda_i+n} h_n^j(\theta) \end{cases} \quad (ii) \quad w^j = \sum_i \sum_n r^{\lambda_i+n} c_n^j(\theta), \quad \begin{cases} \psi_r^j = \sum_i \sum_n r^{\lambda_i+n} a_n^j(\theta) \\ \psi_\theta^j = \sum_i \sum_n r^{\lambda_i+n} b_n^j(\theta) \end{cases} \quad (1)$$

part (i) is omitted for the Reissner plate. It shows that the singularity may appear when $n=0$ and in the first two or three terms of i . Here we only take into account of the main part of $n=0$, the Reissner plate and Reissner shell could be divided into two basic parts of anti-plane part and in-plane part. The well-known Williams' displacement $w_0(r, \theta)$ and potential function $\phi_0(r, \theta)$ are

$$(i) \quad w_0(r, \theta) = \sum_{i=0,1,2,3,\dots} \alpha_i r^{\lambda_i} f_i(\theta), \quad (ii) \quad \phi_0(r, \theta) = \sum_{i=0,1,2,3,\dots} \alpha_i r^{\lambda_i+1} F_i(\theta) \quad (2)$$

where both $f_i(\theta)$ and $F_i(\theta)$ are certain normalization eigen-functions corresponding to the eigen-value λ_i , and the well known explicit forms are



(a) Original problem (b) FEMOL mesh with radial lines

Fig. 1 N-material notch problem

$$f_i(\theta) = A_i \cos \lambda_i \theta + B_i \sin \lambda_i \theta, \quad F_i(\theta) = A_i \sin(\lambda_i + 1)\theta + B_i \cos(\lambda_i + 1)\theta + C_i \sin(\lambda_i - 1)\theta + D_i \cos(\lambda_i - 1)\theta \quad (3)$$

where $\{A_i, B_i\}$ and λ_i in $f_i(\theta)$ are real constants, $\{A_i, B_i, C_i, D_i\}$ and λ_i in $F_i(\theta)$ are complex constants. $(u_{r0i}, u_{\theta0i})$ and $(\psi_{r0i}, \psi_{\theta0i})$ can be derived from the stress potential function

$$u_{r0i}, \psi_{r0i} = r^{\lambda_i} \frac{(1 - \nu \lambda_i)(1 + \lambda_i)F_i(\theta) + F_i'(\theta)}{\lambda_i E}, \quad u_{\theta0i}, \psi_{\theta0i} = r^{\lambda_i} \frac{(1 + \lambda_i - (1 - \lambda_i)\lambda_i \nu + 2\lambda_i^2)F_i'(\theta) + F_i(\theta)}{\lambda_i(1 - \lambda_i)E} \quad (4)$$

the corresponding stress components of both anti-plane and plane problem are

$$\begin{cases} \tilde{Q}_{r0i} = G \lambda_i r^{\lambda_i - 1} \alpha_i f_i(\theta) \\ \tilde{Q}_{\theta0i} = G r^{\lambda_i - 1} \alpha_i f_i'(\theta) \end{cases} \quad \begin{cases} \tilde{M}_{r0i} \{\tilde{N}_{r0i}\} = r^{\lambda_i - 1} \alpha_{iM} \{\alpha_{iN}\} [F_i'(\theta) + (\lambda_i + 1)F_i(\theta)] \\ \tilde{M}_{\theta0i} \{\tilde{N}_{\theta0i}\} = r^{\lambda_i - 1} \alpha_{iM} \{\alpha_{iN}\} [\lambda_i(\lambda_i + 1)F_i(\theta)] \\ \tilde{M}_{r\theta0i} \{\tilde{N}_{r\theta0i}\} = r^{\lambda_i - 1} \alpha_{iM} \{\alpha_{iN}\} [-\lambda_i F_i(\theta)] \end{cases}, \quad i = 0, 1, 2, 3, \dots \quad (5)$$

when $r \rightarrow 0$, the stresses will tend to infinity because there are singular terms $r^{\lambda_i - 1}$, the same singularity will exist in the derivative when implement FEMOL. When the following variable substitution is taken, the singularity that in the derivative and the strain or stresses will be removed

$$\rho = r^{\lambda_i} \quad (6)$$

where λ_i is the first eigen-value. The corresponding expansions can be rewritten as

$$w_0 = \sum_{i=0,1,2,3,\dots} \alpha_i \rho^{\frac{\lambda_i}{\lambda_1}} f_i(\theta), \quad \begin{cases} \psi_{r0} \{u_{r0}\} = \sum_{i=0,1,2,3,\dots} \alpha_{iM} \{\alpha_{iN}\} \rho^{\frac{\lambda_i}{\lambda_1}} \frac{(1 - \nu \lambda_i)(1 + \lambda_i)F_i(\theta) + F_i'(\theta)}{\lambda_i E} \\ \psi_{\theta0} \{u_{\theta0}\} = \sum_{i=0,1,2,3,\dots} \alpha_{iM} \{\alpha_{iN}\} \rho^{\frac{\lambda_i}{\lambda_1}} \frac{(1 + \lambda_i - (1 - \lambda_i)\lambda_i \nu + 2\lambda_i^2)F_i'(\theta) + F_i(\theta)}{\lambda_i(1 - \lambda_i)E} \end{cases} \quad (7)$$

solving derivative of variable r is replaced by solving the derivative term of variable ρ , and the singularity is removed. To achieve this ideal situation in FEMOL, we judiciously choose a radial line mesh as shown in Fig. 1b. For the n -th line, the mapping and the inverse mapping relations are

$$\eta = -1 + 2 \left(\frac{r}{L_n} \right)^{\lambda_i}, \quad r = L_n \left(\frac{\eta + 1}{2} \right)^{\frac{1}{\lambda_i}} \quad (8)$$

After singular line mapping, the Williams expansions in formula (7) will be changed as

$$w_0 = \sum_{i=0,1,2,3,\dots} \bar{\alpha}_i (\eta + 1)^{\frac{\lambda_i}{\lambda_1}} f_i(\theta), \quad \begin{cases} \psi_{r0} \{u_{r0}\} = \sum_{i=0,1,2,3,\dots} \bar{\alpha}_{iM} \{\bar{\alpha}_{iN}\} (\eta + 1)^{\frac{\lambda_i}{\lambda_1}} \frac{(1 - \nu \lambda_i)(1 + \lambda_i)F_i(\theta) + F_i'(\theta)}{\lambda_i E} \\ \psi_{\theta0} \{u_{\theta0}\} = \sum_{i=0,1,2,3,\dots} \bar{\alpha}_{iM} \{\bar{\alpha}_{iN}\} (\eta + 1)^{\frac{\lambda_i}{\lambda_1}} \frac{(1 + \lambda_i - (1 - \lambda_i)\lambda_i \nu + 2\lambda_i^2)F_i'(\theta) + F_i(\theta)}{\lambda_i(1 - \lambda_i)E} \end{cases} \quad (9)$$

where $\bar{\lambda}_i = \lambda_i / \lambda_1$, $\bar{\alpha}_i = \alpha_i L_n^{\lambda_i} / 2^{\lambda_i}$

3. COMPUTATION FOR THE LOWEST SIF

For both the anti-plane and the in-plane parts, to seek the SIFs is tantamount to find the corresponding coefficients α_i of the Williams expansions in (2), especially the lowest coefficient α_1 . From the formula (9) we know that, if the coefficients of $\bar{\alpha}_i$ are known, the coefficients α_i are obtained too

$$\alpha_0 = \bar{\alpha}_0, \quad \alpha_1 = 2\bar{\alpha}_1 / L_n^{\lambda_1} \quad (10)$$

From FEMOL solutions, the displacement terms and the derivative can be easily calculated, then we can get the lowest one or two coefficients by using the following way

$$\begin{aligned} \text{(i)} \quad & \bar{\alpha}_{jN} = \lim_{\eta \rightarrow -1} \frac{\partial^j u_{r0}(\eta, \theta)}{\partial \eta^j} / \delta_{1j} \quad \text{or} \quad \bar{\alpha}_{jN} = \lim_{\eta \rightarrow -1} \frac{\partial^j u_{\theta 0}(\eta, \theta)}{\partial \eta^j} / \delta_{2j}, \quad j = 0, 1 \\ \text{(ii)} \quad & \begin{cases} \bar{\alpha}_0 = \lim_{\eta \rightarrow -1} w_0(\eta, \theta) / f_0(\theta), \quad \bar{\alpha}_1 = \lim_{\eta \rightarrow -1} \frac{\partial w_0(\eta, \theta)}{\partial \eta} / f_1(\theta) \\ \bar{\alpha}_{jM} = \lim_{\eta \rightarrow -1} \frac{\partial^j \psi_{r0}(\eta, \theta)}{\partial \eta^j} / \delta_{1j} \quad \text{or} \quad \bar{\alpha}_{jM} = \lim_{\eta \rightarrow -1} \frac{\partial^j \psi_{\theta 0}(\eta, \theta)}{\partial \eta^j} / \delta_{2j}, \quad j = 0, 1 \end{cases} \end{aligned} \quad (11)$$

where, without losing the generality, we use $d^0/d\eta^0$ to indicate the displacement and

$$\begin{aligned} \delta_{10} &= \frac{4D_0 \cos(\theta) - (1-\nu)F_0(\theta)}{E}, \quad \delta_{20} = \frac{-4D_0 \sin(\theta) - (1-\nu)F_0'(\theta)}{E} \\ \delta_{11} &= \frac{(1-\nu\lambda_1)(1+\lambda_1)F_1(\theta) + F_1'(\theta)}{\lambda_1 E}, \quad \delta_{21} = \frac{(1+\lambda_1 - (1-\lambda_1)\lambda_1\nu + 2\lambda_1^2)F_1'(\theta) + F_1''(\theta)}{\lambda_1(1-\lambda_1)E} \end{aligned}$$

It is well known that the coefficients of the r^{λ_1-1} -stress singularity are related to the stress intensity factors, From the relationship between the coefficients and the stresses, the SIFs are generally defined as

$$\text{(i)} \quad \begin{cases} K_I^s = \lim_{r \rightarrow 0} \left(\sqrt{2\pi} r^{\lambda_1-1} \max_{\theta} (N_{\theta 0}(r, \theta)) \right) \\ K_{II}^s = \lim_{r \rightarrow 0} \left(\sqrt{2\pi} r^{\lambda_1-1} \max_{\theta} (N_{r\theta 0}(r, \theta)) \right) \end{cases} \quad \text{(ii)} \quad \begin{cases} K_I^b \approx -\lim_{r \rightarrow 0} \left(\sqrt{2\pi} r^{1-\lambda_1} \max_{\theta} \left(\frac{h}{2} \zeta \tilde{M}_{\theta 0}(r, \theta) \right) \right) \\ K_{II}^b \approx -\lim_{r \rightarrow 0} \left(\sqrt{2\pi} r^{1-\lambda_1} \max_{\theta} \left(\frac{h}{2} \zeta \tilde{M}_{r\theta 0}(r, \theta) \right) \right) \end{cases} \quad (12)$$

where superscript s indicates the membrane stress part, b indicates bending part.

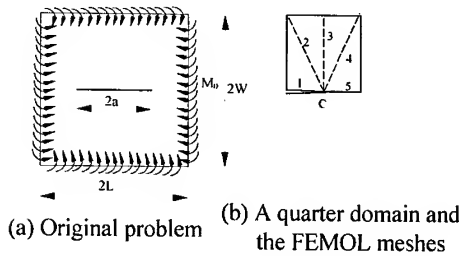


Fig. 2 Reissner plate with a center

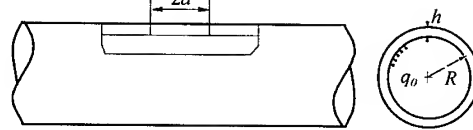


Fig. 3 A pressurized cylindrical shell with a longitudinal crack

4. NUMERICAL EXAMPLES

To assess the performance of the proposed method, some numerical examples are given in this section. The following notations are used

- L_i — i -th line on which the SIFs are calculated
- L_n —the line length
- p —polynomial degree used for element displacements
- TOL —tolerance specified for ODE solutions.

In the following examples, all FEMOL tolerances are taken as $TOL=0.01\%$.

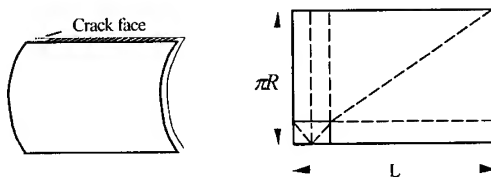
Example 1 Reissner plate with a center crack

In this example, as Fig. 2(a) shows, we consider a Reissner plate problem with a center crack. A quarter body was taken in computing by using the symmetry as Fig. 2(b) shows. The necessary constants are $M_0=1.0$, $E=1.0^7$ and $\nu=0.3$, the length of crack is $2a$ and the thickness of the plate is h , $2L=2W=4a$, with $a=1$. Table 1 gives the derivative $\psi_{\theta,\eta}$ of the vertices and the lowest SIF K_I along the line 3 corresponding to the different thickness.

Table 1 Computed results of derivative and lowest coefficient α_1 , and SIF K_I

(h/a)	p	3	4	5	Ref. [12] (K_I)
0.5	$\psi_{\theta,\eta}$	0.400878e-4	0.374249e-4	0.369290e-4	
	α_1	59.389364	55.444255	54.709682	34.18575
	K_I	37.216765	34.744366	34.284209	
1.0	$\psi_{\theta,\eta}$	0.501775e-5	0.512247e-5	0.513005e-5	
	α_1	7.433703	7.588846	7.600080	9.56300
	K_I	9.316766	9.511198	9.525287	

Example 2 A pressurized cylindrical shell with a longitudinal crack



(a) A quarter domain (b) FEMOL meshes

(b) Fig. 4 A finite length problem

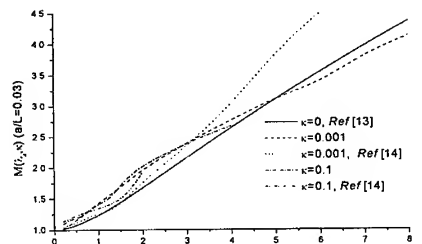


Fig. 5 $M(\lambda_a, \kappa)$ ($a/L=0.03$)

In this example, as Fig. 3 shows, we consider a pressurized cylindrical shell with a longitudinal crack. In most references, the SIF K_I [14] and the bulging factor M are defined as

$$K_I = K_I^b + K_I^s = (K_{mm} + K_{hm}) \frac{q_0 R}{h} \sqrt{\pi a}, \quad M = K_{mm} + K_{hm}$$

the necessary constants are $\lambda_a = \sqrt{12(1-\nu^2)} a / \sqrt{Rh}$, $\kappa = D/Ca^2$, $E=2 \times 10^6$, $\nu=0.3$, $a=1$, $p=2$.

Consider a finite problem as $a/L=0.03$, a quarter body is taken in computing by using the symmetry as Fig. 4(a) shows, the FEMOL meshes as Fig. 4(b) shows. Table 2 gives the computed results of bulging factor and the compare with Ref. [13] and Ref. [14]. Fig. 5 gives the compared curves according to the Table 2.

Table 2 Computed results of the bulging factor ($a/L = 0.03$)

λ_a	κ				
		0	0.001	0.1	
		Ref. [13]	$M(\lambda_a, \kappa)$	Ref. [14]	$M(\lambda_a, \kappa)$
0.2		1.0137	1.012392	1.04	1.088197
0.4		1.0483	1.096604	1.09	1.177397
0.6		1.0985	1.214868	1.14	1.192948
1.0		1.2329	1.426322	1.27	1.434653
1.2		1.3122	1.533991	1.28	1.453101
1.6		1.4866	1.739218	1.47	1.811987
2.0		1.6743	1.974668	1.78	2.043780
3.0		2.1636	2.406444	2.34	2.400734
4.0		2.6469	2.766640	3.01	2.674663
5.0		3.1096	3.127763	3.86	
6.0		3.5459	3.366533	4.49	
7.0		3.9685	3.829041		
8.0		4.3667	4.121953		

5. CONCLUDING REMARKS

To sum up and end up this paper, the following conclusions can be drawn:

- (1) **Generality:** The present algorithm is a general approach and is applicable to any two dimensional singular problems, if only the lowest eigen-value λ_1 is given.
- (2) **Accuracy:** Ref. [4] gives some rules and tips to the ODE solving (COLSYS) that one is 'Do not impose tolerances on derivatives for singular solutions'. These rules have been broken down by the singular mapping technique. The tolerances can be confined on the derivatives and the accuracy is fully controlled by the user with a desired error tolerance specified to the solver. This guarantees that the solutions of singular problem are in the desired accuracy.
- (3) **Efficiency:** By using the technique, FEMOL elements can be constructed with the desired singular behavior built-in. The computation is speeded up and the accuracy is improved.
- (4) **Strongpoint:** In FEMOL, the present singular line mapping is not limited to the crack case. It is applied to notches with any opening angles. The accurate derivatives around the vertices can be computed.
- (5) **Lowest SIF:** SIF can be easily solved from the accurate derivatives along the different lines.

Acknowledgments

This work was supported by the National Natural Science Foundation of China.

REFERENCES

1. Si Yuan, A *Proceedings of 1st National Conference on Analytical and Numerical Combined Methods*, Hunan (1990) p. 132-136 (in Chinese).
2. Si Yuan and Jianling Gao, *Proceedings of International Conference on EPMESC*, Macau, 3 (1990) p. 517-526.
3. Si Yuan, *Chinese Journal of Numerical Mathematics and Applications*, 15, 1 (1993) p. 45-59.
4. Si Yuan, *The Finite Element Method of Lines: Theory and Applications*, Science Press, Beijing, New York (1993).
5. U. Ascher, et al, *ACM Transaction of Mathematical Software*, 7, 2 (1981) p. 209-222.
6. U. Ascher, et al, *ACM Transaction of Mathematical Software*, 7, 2 (1981) p. 223-229.
7. Si Yuan, *Computational Structural Mechanics and Applications*, 10, 1 (1993) p. 118-122 (in Chinese).
8. Si Yuan, *Science in China, Series A*, 23, 5 (1993) p. 552-560 (in Chinese).
9. Yongjun Xu and Si Yuan, *International Journal of Fracture*, Vol. 18, (1996) p. 373-381.
10. Yuan Si, *Computational Mechanics '92*, Proc. Of ICCES, Hong Kong, (1992) p. 47.
11. Xu Yongjun and Yuan Si, *Engineering Mechanics*(Spe. Iss), (1999) p. 85-91 (in Chinese)
12. Yingzhi Li and Chuntu Liu, *ACTA MECHANICA SINICA*, 4 (1983) p. 366-375 (in Chinese)
13. F. Erdogan and J. J. Kibler, *Int. J. of Fracture Mechanics*, 5, 3, (1969) p. 229-237.
14. Chuntu Liu and Xijia Wu, *ACTA MECHANICA SINICA*, 19, 4 (1987) p. 366-375 (in Chinese).

Collective Evolution Characteristics and Computer Simulation of Voids Near the Crack Tip of Ductile Metal

Hualong Yu and Youshi Hong

LNM, Institute of Mechanics, Chinese Academy of Sciences,
Beijing 100080, China P.R.

Keywords: Collective Evolution, Crack Tip, Equilibrium Equation, Voids

ABSTRACT

In this paper, we consider the collective evolution of voids in front of crack tip, which always means high stress/strain gradient existed there. We use the equilibrium equation of void number density to describe the evolution behavior of voids during the process of crack growth. With the assumption and computation, we are able to solve the equilibrium equation and obtain corresponding results, which present similar tendency with experimental measurements.

1. INTRODUCTION

The nucleation, growth and coalescence of voids are the major characteristics of the failure process of ductile materials. The study on this field has received rich achievements. Since Gurson published his paper on stress field near a single void in a matrix, many scientists have been focusing on the behavior of single void or limited number of voids. In recent years, the damages as a whole were paid more and more attention during the process of failure of material. Bai et al^[1] proposed an equilibrium equation of damage number density to describe a mean-field damage. Hong et al^[2] applied this method to describe the property of collective evolution of short cracks during fatigue damage and of overall crack number density. From the experiments on two weld materials, Hong and Zheng^[3] found isolated voids did not coalesce with crack tip and the coalescence of limited voids might not be the critical stage of crack growth. Also the void area fraction increases with increasing value of COD. As the COD reaches its critical value or beyond, the overall void damages tend to a steady distribution. This phenomenon suggests that we could analyze the collective evolution of voids with equilibrium equation of void number density.

2. EQUILIBRIUM EQUATION OF VOID NUMBER DENSITY

In this paper, we consider the static growth of ductile crack. Here we attempt to use the equilibrium equation of damage density. Based on the evolution process of voids, we may develop an equation to express the collective evolution of voids^[4].

$$\int_{\sigma_0}^{\sigma_{\max}} \frac{\partial n}{\partial \xi} d\sigma + \frac{\partial}{\partial r} \left(\int_{\sigma_0}^{\sigma_{\max}} Rn d\sigma \right) = N_g \int_{\sigma_0}^{\sigma_{\max}} n_N d\sigma \quad (1)$$

where n is void number density, σ is local stress, ξ is COD which also means generalized time of crack growth, r represents the radius of voids and R is void growth rate which depends on the dimension of the void and the stress state there. Two characteristic stresses σ_0 and σ_{\max} are local stresses near crack tip when it starts to grow and when it grows steadily. n_N is nucleation rate of voids and N_g is dimensionless coefficient.

The equation above implies that the total number of voids of given size depends on the nucleation and the growth of voids before the applied load reaches the critical value of growth.

3. THEORETICAL ANALYSIS AND SIMULATION

Based on the equilibrium equation, we can get more simple expressions according to the following assumptions. Because the voids are near the crack tip, the stress/strain field there should be under careful consideration for the high stress/strain gradient existed. Though the equation itself does not show materials parameters, the high gradient of stress can be included in the local stress σ in the equation.

First we discuss the condition when the growth process is near the steady state, which means the stress distribution does not depend on time. It can be a small time interval during whole crack growth process that the variation of stress with time can be neglected. From Eq. (1) we have

$$\frac{\partial n}{\partial t} + \frac{\partial(Rn)}{\partial r} = N_g n_N \quad (2)$$

The stress is not explicit in the equation. But it is in fact one of independent variables of n . So the stress gradient is included. Then we use HRR field as stress field^[5]. It gives

$$\sigma(x) = \sigma_w \ln \left(\frac{x_0}{x} \right)^{\frac{1}{m-1}} \quad (3)$$

where x is the distance to the crack tip, x_0 is the dimension of plastic zone of crack tip, m is strain-hardening exponent of material, and σ_w is related to the stress field. From Eq.3 we notice the singularity of stress exists at the point of $x=0$.

The nucleation rate of voids depends on both the void size and local stress state. So we choose the nucleation formula as^[6]

$$n_N = \dot{N} P \left(\frac{r}{r_{\max}} \right) \exp \left(\frac{\sigma - \sigma_0}{\sigma_1} \right) \quad (4)$$

where σ_0 , σ_1 and r_{\max} are material constants, \dot{N} is average void nucleation rate and $P(\dots)$ is a probability distribution function expressing the positive relation between nucleation rates and the dimensions of voids.

The void growth rate should also be given. Here we use the rate based on Gurson Model^[7]. Such that

$$R = \frac{\dot{\epsilon}_0}{2} \left(\frac{3n}{2} d^2 \right)^{1/m} r (r^2 + d^2)^{-1/m} \quad (5)$$

where ε_0 is a material constant and d is the distance between two voids. From above we can get the analytic solution due to the first assumption.

Then we assume that the stress distribution does depend on time. Similar to Eq. (2) Let

$$\frac{\partial \sigma}{\partial t} = \Sigma \quad (6)$$

We have

$$\frac{\partial n}{\partial t} + \frac{\partial(Rn)}{\partial r} + \frac{\partial(\Sigma n)}{\partial \sigma} = N_g n_N \quad (7)$$

We still chose HRR stress field. In order to eliminate the singularity of stress field at the crack tip we design a kind of stress gradient. Here we use Weibull distribution as stress distribution near the crack tip. The general expression of Weibull distribution is

$$Weibull(s, x) = sx^{s-1} \exp(-x^s) \quad \text{for } x > 0 \quad \text{and } s > 0 \quad (8)$$

Then the stress field can be

$$\left[\begin{array}{ll} \sigma(x, t) = \sigma_w(t) \ln \left(\frac{x_0}{x} \right)^{\frac{1}{m-1}} & x > x_1 \\ \frac{\partial \sigma(x, t)}{\partial x} = \sigma_w(t) \frac{\partial Weibull(s, x)}{\partial x} & x \leq x_1 \end{array} \right. \quad (9)$$

where x_1 is a point near the crack tip. The formula for void nucleation rate is the same as the first assumption. Thus the analytic solution can also be made. Here we assume stress near crack tip is positive related to COD which is described by t according to strip yield model^[8]. $\sigma_w(t) = K\sigma_Y t/t_0$, in which t_0 is characteristic time, K is a constant, σ_Y is yield stress when t reaches t_0 and COD reaches critical value..

4. RESULTS AND DISCUSSION

The analytical solutions to the first and second assumption are as the following

$$n(r, x, t) = \frac{1}{R} \int_A^r n_N N_g dr \quad (10)$$

$$n(r, x, t) = \frac{\left\{ 1 - \exp \left[\int_0^t - \left(\frac{\partial R}{\partial r} + \frac{\partial \Sigma}{\partial \sigma} \right) dt \right] \right\} N_g n_N}{\frac{\partial R}{\partial r} + \frac{\partial \Sigma}{\partial \sigma}} \quad (11)$$

And each order moment can be then solved from above. The zero-th order moment:

$$nn(x,t) = \int_0^{r_{\max}} n(r,x,t) dr \quad (12)$$

The second order moment:

$$f(x,t) = \int_0^{r_{\max}} n(r,x,t)r^2 dr \quad (13)$$

Void area fraction

$$\bar{f}(x,t) = \frac{f(x,t)}{\int_0^{r_{\max}} n(r,x,t)d^2 dr} \quad (14)$$

We consider the condition are shown of $\dot{N}=10000$, $K_{IC}=120\text{MPa}\sqrt{\text{m}}$ and $\sigma_Y=450\text{MPa}$. So we can get the numerical results which in Figs. 1-4.

From the results of the first assumption (Figs. 1 and 2) we can see that when the crack growth process is near the steady state, the number of voids and void area fraction are decreasing to steady state away from the crack tip. Also the distribution of void area fraction is converging to a steady distribution. Such distribution does not vary as time increases. It means that the collective evolution of voids reaches a saturation state.

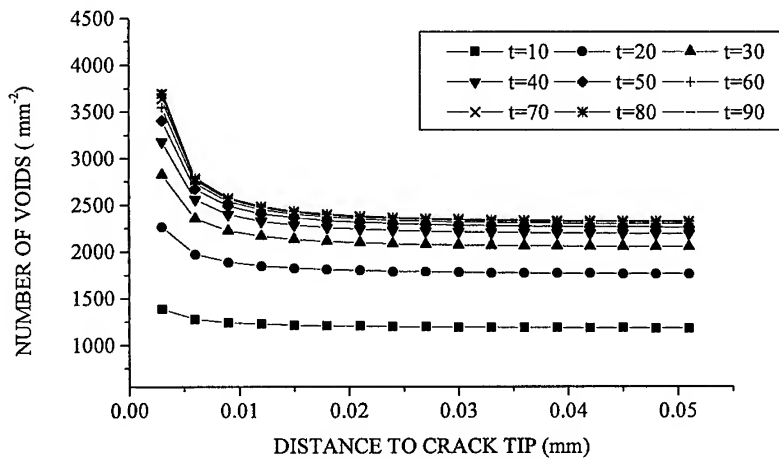


Fig. 1 Relation between number of voids and distance to crack tip.
(t represents time)

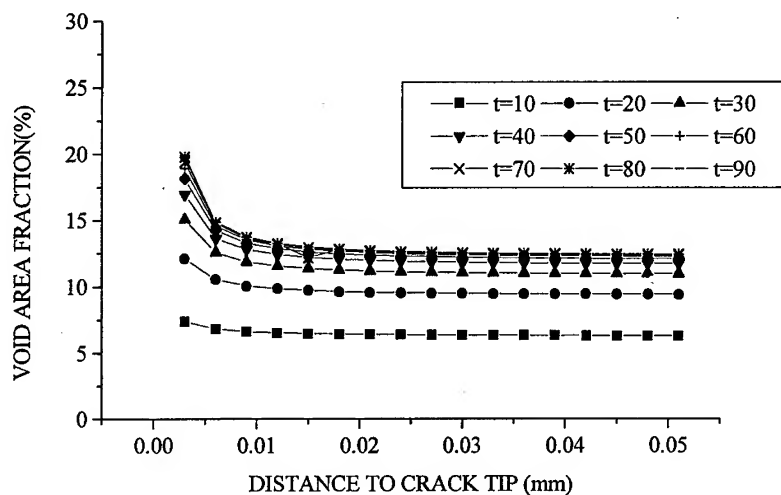


Fig. 2 Relation between void area fraction and distance to crack tip.
(t represents time)

The results of the second assumption (Figs. 3 and 4) also show the similar tendency. Though stress field varies with time, saturate tendency of collective evolution of voids still exists. It should be a critical value for further growth of crack tip.

Comparing two groups of results with the experimental measurements of Hong et al^[3] on two materials (Fig. 5), we can observe a similar tendency. Near the crack tip the number of voids and void area fraction increase. As time goes by, the void fraction distribution increases and tends to a steady one. The critical stage does exist.

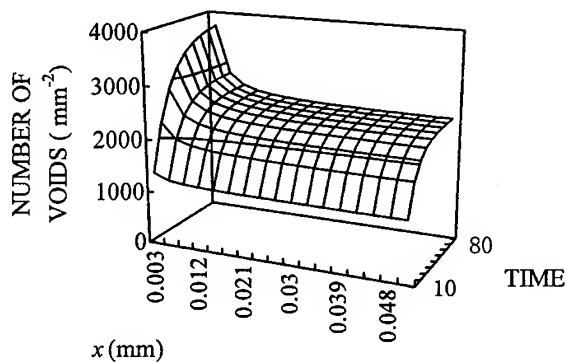


Fig. 3 Relation between number of voids, distance to crack tip x and time.

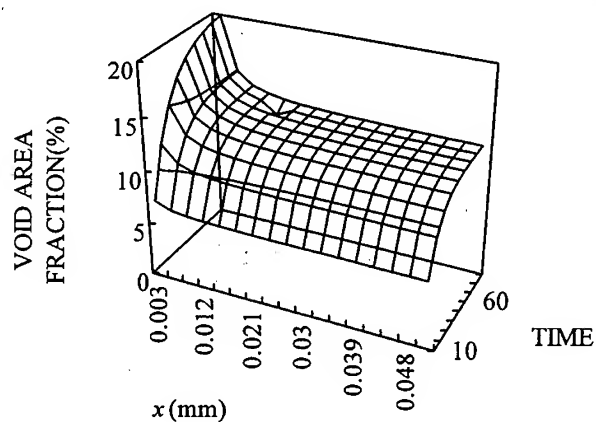


Fig. 4 Relation between void area fraction, distance to crack tip x and time.

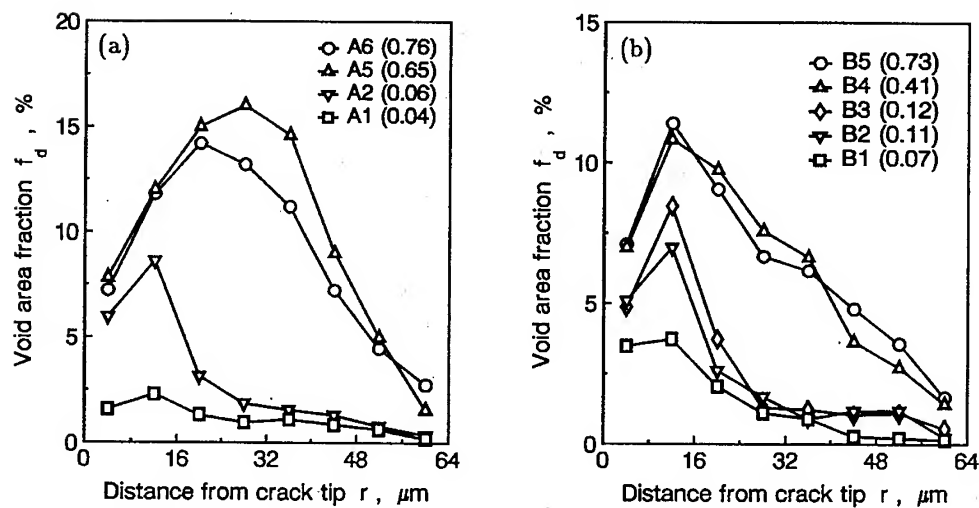


Fig.5. Void area fraction away from crack tip for Material A (a) and B (b).
Number in brackets denotes the value of COD, dimensions in mm.

5. REFERENCES

1. Y. L., Bai, F. J., Ke and M. F., Xia, Acta Mechanica Sinica, Vol. 23, No. 3, (1991) p.290
2. Y. S., Hong and Y., Qiao, N., Liu and X. H. Zheng, Fatigue Fract. Engrg. Mater. Struct., 21 (1998) p. 1317
3. Y. S., Hong and X. H. Zheng, Advances in Fracture Research, ICF9, Vol. 5 (1998) p.2441
4. Y. S., Hong, J. Inner Mongolia Polytechnic University(in Chinese), 16(3) (1997) p.2
5. Y. C., Gao and K. C., Hwang, Francois D. ed. Advances in Fracture Research. Proc.of 5th Int. Conf. on Fracture. (1981) p. 669
6. D. R., Curran, L., Seaman and D. A., Shockey, Phys. Report. 147. 5-6 (1987) p.253
7. A. L., Gurson, J. Engng. Mater. Tech., 99(1977), p.2
8. D. S., Dugdale, J. Mech. Phys. Solids. 8(1960) p. 100

The Relationship of SIF between Plate and Plane Fracture Problems and the Effect of the Plate Thickness on SIF

Yongjun Xu and Chuntu Liu

Institute of Mechanics, Chinese Academy of Sciences,
Beijing 100080, China P.R.

Keywords: Eigenfunction, Eigenvalue, Reissner Plate, Stress Intensity Factor

ABSTRACT

In the present paper, it is shown that the zero series eigenfunctions of Reissner plate cracks/notches fracture problems are analogous to the eigenfunctions of anti-plane and in-plane. The singularity in the double series expression of plate problems only arises in zero series parts. In view of the relationship with eigen-values of anti-plane and in-plane problem, the solution of eigen-values for Reissner plates consists of two parts: anti-plane problem and in-plane problem. As a result the corresponding eigen-values or the corresponding eigen-value solving programs with respect to the anti-plane and in-plane problems can be employed and many aggressive SIF computed methods of plane problems can be employed in the plate. Based on those, the approximate relationship of SIFs between the plate and the plane fracture problems is figured out, and the effect relationship of the plate thickness on SIF is given.

1. INTRODUCTION

Stress analysis in practical engineering applications inevitably encounters stress singularities caused by sudden changes in geometry, e.g. around re-entrant corners (notches) or, more severely, around crack tips. The complete eigenvalue solution and the stress intensity factor (SIF) calculation play an important role in the linear elasticity fracture mechanics (LEFM). Most of numerical methods, directly or indirectly, make use of the available eigen-solutions when applied to the SIF computation for cracks/notches problems so that singularity can be treated in a more efficient, accurate and reliable way. Recently, Xu and Yuan [1] presented an effective implementation of the imbedding method for accurate and reliable computation of complete real or complex eigen-solutions in two dimensional notch/crack singularities with multiple materials, arbitrary opening angles and various surface conditions. This algorithm is robust and may be employed by any numerical methods that make use of singular solutions. The singularity causes great difficulty to the numerical solutions that have to be invoked when analytical solutions are not available. A numerical recipe for accurate and efficient computation of stress singularity factors (SIFs) usually consists of two major ingredients, namely a powerful numerical method for the general stress

analysis and a novel approach to obtaining the desired SIFs which may include special treatment of various singularities. The underlying numerical method employed in this paper is the finite element method of lines (FEMOL) [2-5], which is a newly developed, general-purpose, semi-analytical method. In this method, a partial differential equation defined on an arbitrary domain is semi-discretized, by finite element techniques via energy theorems or variational principles, into a system of ordinary differential equations (ODEs) defined on straight or curved mesh lines. Recently, Xu and Yuan [6] exploited the orthogonal relationship between eigen-functions for anti-plane and in-plane notch problems, and a set of contour integral extraction methods (so called orthogonal integral extraction method) for SIF calculation is developed, which appears to be most powerful and efficient. Xu [7] extended the orthogonal integral extraction method to the general two-dimensional fracture problems. In the present paper, It is shown that the zero series eigenfunctions of Reissner plate cracks/notches fracture problems are analogous to the eigenfunctions of anti-plane and in-plane. The singularity in the double series expression of plate problems only arises in zero series parts. In view of the relationship with eigen-values of anti-plane and in-plane problem, the solution of eigen-values for Reissner plates consists of two parts: anti-plane problem and in-plane problems. As a result, the corresponding eigenvalues or the corresponding eigenvalue solving programs with respect to the anti-plane and in-plane problems can be employed and many aggressive SIF computed methods of plane problems can be employed in the plate problems. Based on those, the approximate relationship of SIFs between the plate and the plane fracture problems is figured out, and the effect relationship of the plate thickness on SIF is given. Two examples are given to show the two approximate relationships.

2. PRELIMINARY CONSIDERATION

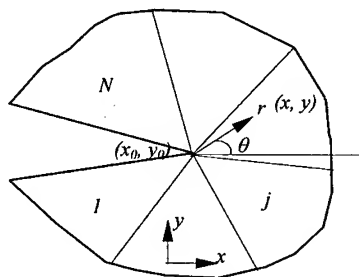


Fig. 1 N-material notch problem

Figure 1 shows a two dimensional singular problem with N different materials around notch/crack tip. The body forces are assumed to be negligible. For convenience sake we omit the different material domain subscript j shown in the Fig. 1. In the polar coordinates shown in Fig. 1, for the Reissner plate, the general displacement components can be written as the following double series form

$$w^j = \sum_i \sum_n r^{\lambda_i + n} c_{ni}^j(\theta), \quad \begin{cases} \psi_r^j = \sum_i \sum_n r^{\lambda_i + n} a_{ni}^j(\theta) \\ \psi_\theta^j = \sum_i \sum_n r^{\lambda_i + n} b_{ni}^j(\theta) \end{cases} \quad (1)$$

It can be showed that the singularity maybe appear when $n=0$ and in the first two or three

terms of i . Here we only take account of the main part of $n=0$, the Reissner plate could be divided into two basic parts of anti-plane part and in-plane part. So the well-known Williams' displacement $w_0(r, \theta)$ and potential function $\phi_0(r, \theta)$ are

$$(i) \quad w_0(r, \theta) = \sum_{i=0,1,2,3,\dots} \alpha_i r^{\lambda_i} f_i(\theta), \quad (ii) \quad \phi_0(r, \theta) = \sum_{i=0,1,2,3,\dots} \alpha_i r^{\lambda_i+1} F_i(\theta) \quad (2)$$

where both $f_i(\theta)$ and $F_i(\theta)$ are certain normalization eigen-functions that corresponding to the eigen-value λ_i , and the well known explicit form is

$$\begin{aligned} f_i(\theta) &= A_i \cos \lambda_i \theta + B_i \sin \lambda_i \theta \\ F_i(\theta) &= A_i \sin(\lambda_i + 1)\theta + B_i \cos(\lambda_i + 1)\theta + C_i \sin(\lambda_i - 1)\theta + D_i \cos(\lambda_i - 1)\theta \end{aligned} \quad (3)$$

where $\{A_i, B_i\}$ and λ_i in $f_i(\theta)$ are real constants, $\{A_i, B_i, C_i, D_i\}$ and λ_i in $F_i(\theta)$ are complex constants. The corresponding displacement $(\psi_{r0i}, \psi_{\theta0i})$ for plane part can be derived from the stress potential function

$$\psi_{r0i} = r^{\lambda_i} \frac{(1 - \nu \lambda_i)(1 + \lambda_i)F_i(\theta) + F_i'(\theta)}{\lambda_i E}, \quad \psi_{\theta0i} = r^{\lambda_i} \frac{(1 + \lambda_i - (1 - \lambda_i)\lambda_i \nu + 2\lambda_i^2)F_i'(\theta) + F_i(\theta)}{\lambda_i(1 - \lambda_i)E} \quad (4)$$

The corresponding stress components of both anti-plane and plane problems are

$$\begin{cases} \tilde{Q}_{r0i} = G\lambda_i r^{\lambda_i-1} \alpha_i f_i(\theta) \\ \tilde{Q}_{\theta0i} = G r^{\lambda_i-1} \alpha_i f_i'(\theta) \end{cases} \quad \begin{cases} \tilde{M}_{r0i} = r^{\lambda_i-1} \alpha_{iM} [F_i'(\theta) + (\lambda_i + 1)F_i(\theta)] \\ \tilde{M}_{\theta0i} = r^{\lambda_i-1} \alpha_{iM} [\lambda_i(\lambda_i + 1)F_i(\theta)] \\ \tilde{M}_{r\theta0i} = r^{\lambda_i-1} \alpha_{iM} [-\lambda_i F_i(\theta)] \end{cases}, \quad i = 0, 1, 2, 3, \dots \quad (5)$$

When $r \rightarrow 0$, the stress in formula (5) will tend to infinity because there are singular terms r^{λ_i-1} in the expansions. Compared the anti-plane part and the in-plane part of Reissner plate problem shown in equations (2-5) with real anti-plane and in-plane problems^[6], the following assimilated relationships can be deduced

$$\begin{aligned} w_0 &\sim w, \quad \tilde{Q}_{r0} \sim \tau_{rz}, \quad \tilde{Q}_{\theta0} \sim \tau_{\theta z} \\ \begin{cases} \psi_{r0} \sim u_r, \quad \psi_{\theta0} \sim u_\theta \\ \tilde{M}_{r0} \sim \sigma_{rr}, \quad \tilde{M}_{\theta0} \sim \sigma_{\theta\theta}, \quad \tilde{M}_{r\theta0} \sim \sigma_{r\theta} \end{cases} \end{aligned} \quad (6)$$

where $\{w, \tau_{rz}, \tau_{\theta z}\}$ and $\{u_r, u_\theta, \sigma_{rr}, \sigma_{\theta\theta}, \sigma_{r\theta}\}$ are the displacements and stresses corresponding to the anti-plane and in-plane problems, respectively.

3. GENERAL DEFINITION OF SINGULARITY INTENSITY FACTORS (SIFs)

For two dimensional fracture problems, the general singularity intensity factors defined as

$$K_{III} = \lim_{r \rightarrow 0} \left(\sqrt{2\pi} r^{1-\lambda} \max_{\theta} (\tau_{r\theta0}(r, \theta)) \right), \quad \begin{cases} K_I = \lim_{r \rightarrow 0} \left(\sqrt{2\pi} r^{1-\lambda} \max_{\theta} (\sigma_{\theta\theta}(r, \theta)) \right) \\ K_{II} = \lim_{r \rightarrow 0} \left(\sqrt{2\pi} r^{1-\lambda} \max_{\theta} (\sigma_{r\theta0}(r, \theta)) \right) \end{cases} \quad (7)$$

For Reissner plate fracture problems, substitute the shears and moments into Eq. (7), the SIFs are generally defined as

$$K_{III} \approx \lim_{r \rightarrow 0} \left(\sqrt{2\pi} r^{1-\lambda} \max_{\theta} \left(\frac{5}{4} (1-\zeta^2) \tilde{Q}_{\theta 0}(r, \theta) \right) \right), \quad \begin{cases} K_I \approx -\lim_{r \rightarrow 0} \left(\sqrt{2\pi} r^{1-\lambda} \max_{\theta} \left(\frac{h}{2} \zeta \tilde{M}_{\theta 0}(r, \theta) \right) \right) \\ K_{II} \approx -\lim_{r \rightarrow 0} \left(\sqrt{2\pi} r^{1-\lambda} \max_{\theta} \left(\frac{h}{2} \zeta \tilde{M}_{r\theta 0}(r, \theta) \right) \right) \end{cases} \quad (8)$$

where $\zeta = 2z/h$, we take the maximum value as $\zeta = 1$, λ is the corresponding eigenvalue.

4. TWO RELATIONSHIPS OF SINGULARITY INTENSITY FACTORS (SIFs)

Firstly, we consider the different between zero order stresses $\{\tilde{M}_0, \tilde{Q}_0\}$ and the real stresses $\{M, Q\}$; secondly, compare the equivalent between the Reissner plate and the plane problems; we consider the same equivalent boundary conditions between the Reissner plate and the plane problems. We have the following approximate relationship with respect to SIFs between the Reissner plate and the plane fracture problems

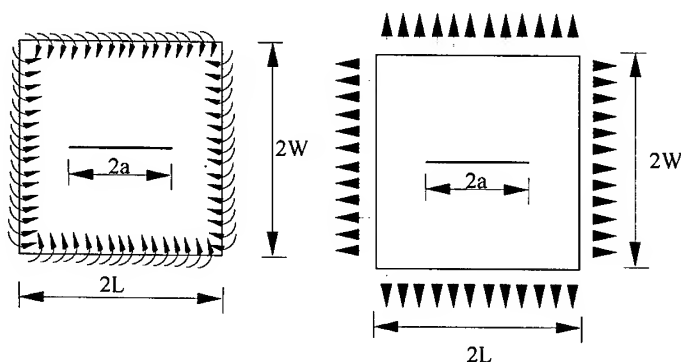
$$K_{III \text{ plate}} \approx \frac{3}{2h} K_{III \text{ anti-plane}}, \quad \begin{cases} K_{I \text{ plate}} \approx \frac{6}{h^2} K_{I \text{ in-plane}} \\ K_{II \text{ plate}} \approx \frac{6}{h^2} K_{II \text{ in-plane}} \end{cases} \quad (9)$$

For the two Reissner plate notch/crack problems, the only different part is the plate thickness (h_1 and h_2). Form Eq. (9), the approximate relationship with respect to SIFs between the different plate thickness can be deduced

$$\frac{K_{III}(h_1)}{K_{III}(h_2)} \approx \frac{h_2}{h_1}, \quad \frac{K_{I,II}(h_1)}{K_{I,II}(h_2)} \approx \left(\frac{h_2}{h_1} \right)^2 \quad (10)$$

5. NUMERICAL EXAMPLES

To assess the performance of the two relationships, a number of numerical examples are given in this section. The following examples are computed by the newly developed method [6-7] namely orthogonal integral extraction method.



(a) Bending plate with a center crack (b) Uniform stretch with a center crack

Fig. 2 Finite plate with a center crack

Example 1 Approximate relationship of SIFs between bending plate and uniform stretch plane

In this example, as Fig. 2 shows, we consider a finite bending plate with a center crack and a finite uniform stretch plane with a center crack. The crack length is $2a$, the plate thickness is h , and the necessary constants are $2L=2W=4a$, $E=2 \times 10^6$, $\nu=0.3$, $a=1$, $h=1$. Table 1 gives a list of the computed results of SIFs K_I and the approximate ratio of the SIFs for bending plate and plane. Where r_0 indicates the integral radius along the crack tips.

Table 1. The computed results of finite plate with a center crack

r_0	Bending	Uniform stretch	$K_{I\text{plate}}/K_{I\text{plane}}$ (Theory ≈ 6)
0.00001	9.728794	2.363948	4.115486
0.0001	9.743342	2.363946	4.121643
0.001	9.784121	2.363943	4.138899
0.01	9.865933	2.363946	4.173502
0.1	9.832484	2.363945	4.159354
0.5	10.099617	2.363951	4.272346

Example 2 Approximate effect on SIFs (K_I) of the different plate thickness

In this example, as Fig. 2(a) shows, we consider a finite bending plate with a center crack. The crack length is $2a$, and the necessary constants are $2L=2W=4a$, $E=2 \times 10^6$, $\nu=0.3$, $a=1$. The three cases of the different thickness are $h_1/a=0.1$, $h_2/a=0.5$ and $h_3/a=1.0$. Table 2 gives a list of the computed results of SIFs K_I , where r_0 indicates the integral radius along the crack tips. Fig. 3 gives out two ratio curves of the different SIFs K_I with respect to the different cases, the approximate values match very well with the theory values.

Table 2. The computed results of K_I for finite bending plate with a center crack

$r_0 \backslash h/a$	0.1	0.5	1.0
0.00001	793.823490	36.101453	9.728794
0.0001	793.800340	38.376926	9.743342
0.001	794.154503	42.004670	9.784121
0.01	800.501913	33.544143	9.865933
0.1	842.029973	35.785873	9.832484
0.5	929.598925	38.401774	10.099617

6. CONCLUDING REMARKS

In this present paper, the Relationship of SIF between plate and plane fracture problems and the effect of the plate thickness on SIFs are discussed. Both of the two approximate relationships are checked by two simply examples. From example 2 we know that the numerical values match very well with the theory values in the second relationship with respect to the different plate thickness. From the two relationships, we can give an approximate estimate for the unsolved problems from

the corresponding solved problems and a check to computed results and some methods based on the well known examples.

Acknowledgments

This work was supported by the National Natural Science Foundation of China.

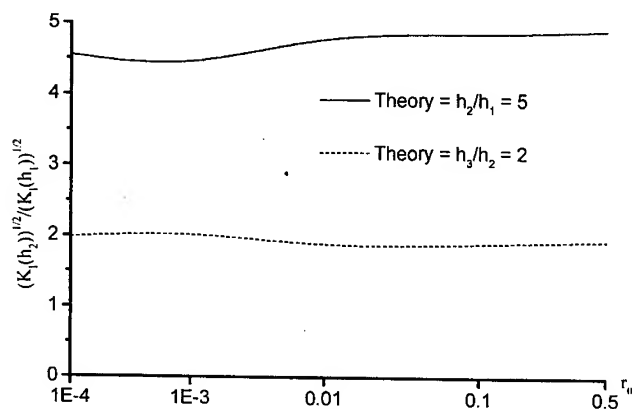


Fig. 3 $\sqrt{\frac{K_I(h_2)}{K_I(h_1)}}$

REFERENCES

1. Yongjun Xu and Si Yuan, *International Journal of Fracture*, Vol. 18, (1996) p. 373-381.
2. Si Yuan, *Proceedings of 1st National Conference on Analytical and Numerical Combined Methods*, Hunan (May, 1990) p. 132-136 (in Chinese).
3. Si Yuan and Jianling Gao, *Proceedings of International Conference on EPMESC*, Macau, 3 (Aug. 1-3, 1990) p. 517-526.
4. Si Yuan, *Chinese Journal of Numerical Mathematics and Applications*, 15, 1 (1993) p. 45-59.
5. Si Yuan, *The Finite Element Method of Lines: Theory and Applications*, Science Press, Beijing, New York (1993).
6. Yongjun Xu, Complete eigenvalue solution and SIF calculation in fracture mechanics based on FEMOL, Ph.D. Thesis. Department of Civil Engineering, Beijing: Tsinghua University, 1996 (in Chinese).
7. Yongjun Xu, SIF calculation in plates, shells and three dimensional problems based on FEMOL, Postdoctoral report. Institute of Mechanics, Beijing: Chinese Academy of Sciences, 1999 (in Chinese).

Fractographic Approach for Fracture Mode

N. Hattori¹, S. Nishida¹ and H. Yamamoto²

¹ Faculty of Science and Engineering, Saga University,
Honjo-machi 1, Saga-shi 840-8502, Japan

² Nippon Steel Corporation, 20-1 Shintomi, Futtsu-shi,
Chiba 293-0011, Japan

Keywords: Crack Initiation, Crack Propagation, Fractography, Fracture, Mode I, Mode II

ABSTRACT

The disk test is performed to examine the characteristics of Mode I or II fracture in the viewpoint of fractography. Test pieces of fracture surface are prepared by the disk test method. In this method, the circular specimen with a central crack is subjected to the concentrated diametrically opposed loads in an inclined direction to the central crack orientation. The main results obtained in this test are as follows; (1) No remarkable difference of the roughness of fracture surfaces between Mode I and II is observed because the Mode II specimen is not necessarily fractured in Mode II after crack propagating. (2) There is remarkable difference on fracture roughness measured in the crack propagation direction and in the perpendicular direction of crack propagation. It is considered that the measurement in the crack propagation direction is more reasonable than that in the perpendicular direction of the crack propagation. (3) As the measurement magnification becomes lower, the measured area increases but the accuracy of measurement decreases. Therefore, it is necessary to determine the optimal measurement magnification.

1. INTRODUCTION

Fractography is one of the effective techniques when the damage cause generated on the site is elucidated [1]. However, a considerable experiences are necessary to give a correct judgement with this technique. Therefore, it is not necessarily easy to use this method. This research has been recently progressed for the sake that one aided with a computer will be required not much experiences to analyze a specified fracture problem[2].

For instance, the damage such as the pitching or spalling often becomes a problem in the machine elements with slip/rolling at the high contact pressure. Afterwards, the damage area becomes the crack initiation point, and machine fails. There are a lot of reports of serious accidents [3]. Then, many researches on this type of crack initiation or propagation mechanism have been reported using fatigue examination of non-contact type or analysis calculated aided with a computer so far [4 - 7]. In this case, the crack initiation and propagation behaviors have been discussed only from the standpoint of dynamic characteristics on typical Mode I and Mode II. Then, it is reported that the resistance of the material to these damages may be fatigue crack growth resistance threshold stress ΔK_{th} of the crack sliding shearing mode[8, 9]. However, the fracture of some machine elements would be generated under the condition of other fracture mode such as Mode I type or the mixture type.

In this study, the test materials which failed under the conditions of Mode I and Mode II are prepared. Then, the difference between the above two kinds of fracture appearance are examined using proper fractographic technique. Consequently, it is examined whether this technique can be

applied as an evaluation method for the fracture analysis.

2. EXPERIMENTAL PROCEDURE

Four kinds of test materials, referred to as AD, HCR, HX(SKH) and DC were used. Table 1 and 2 list their chemical composition and mechanical properties, respectively. In addition, the test specimens for Mode I and II fracture were made by disk test method as shown in Fig. 1 [10, 11]. The preliminary crack installed at the center of the disk is set in fixed angle α (in case of Mode I: $\alpha = 0$ degrees, and Mode II: $\alpha = 27.2$ degrees [11]). Afterwards, the crack is fractured due to the tensile stress generated by applied compressive load.

Table 1. Chemical composition

	mass %									
	C	Si	Mn	Ni	Cr	Mo	V	W	P	S
AD	1.7	0.4	0.5	0.7	1.0	0.3	—	—	0.003	0.007
HCR	2.8	0.5	0.5	—	17.5	1.3	—	—	0.021	0.013
HX(SKH)	2.0	0.5	0.5	—	5.0	6.0	5.0	6.0	0.014	0.018
DC	3.3	1.5	0.6	1.8	—	0.4	—	—	0.060	0.014

Table 2. Mechanical properties

	Tensile strength (MPa)	Hv (-)	Fracture toughness (MPa $\cdot\sqrt{m}$)
AD	608	430	19.3
HCR	853	686	21.9
HX(SKH)	1138	745	26.7
DC	540	372	34.0

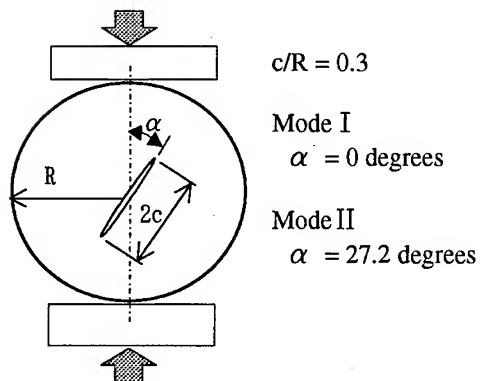


Fig.1. Schematic illustration of experimental procedure.

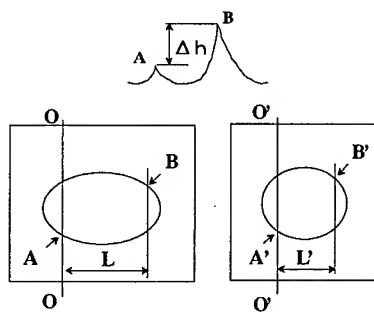


Fig.2. Calculation method on the range of roughness in fracture surface.

Every test specimen is observed with a pair of fractographs using a scanning electronic microscope. In the arbitrary observation area shown in Fig. 2, the difference Δh between the heights of point A and point B is calculated using the following equation.

$$\Delta h = \frac{L}{\tan \theta} - \frac{L'}{\sin \theta} \quad (1)$$

where θ is the tilting angle respected to the O-O axis, and $\theta=10$ degrees was set in this test. The value of Δh is the average value measured at three typical positions in the measurement area under the specified magnification.

3. RESULTS AND DISCUSSIONS

Figures 3 and 4 show the observation result of the fracture surfaces for the crack initiation area and the comparatively steady propagation area of the material AD and the material HCR, respectively. From these figures, it is understood that the value of roughness (Δh) in the crack initiation area is larger than that in the steady propagation area. In addition, although the results of all materials are not shown in these figures, there is remarkably difference on the characteristic of each material in the fracture state. However, it is difficult to analyze quantitatively the real effects of material properties on the value of Δh of the fracture mode. Therefore, it is attempted to evaluate such a qualitative difference with a quantitative value calculated by equation (1).

Table 3. Average range of roughness Δh at the crack initiation area (Unit: μm)

	In the perpendicular direction of crack propagation		In the direction of crack propagation	
	Mode I	Mode II	Mode I	Mode II
AD	30.8	25.6	40.2	20.2
HCR	25.9	22.7	16.4	15.2
HX(SKH)	35.0	34.6	44.8	31.8
DC	20.8	13.8	5.8	19.2

To examine the influence of the fracture mode on the fracture surface state, Table 3 lists the values of roughness (Δh) on the fracture surfaces measured in the perpendicular direction and in the propagation direction at the crack initiation area. The value of Δh measured in the direction of the crack propagation tends to be relatively less than that in the perpendicular direction of the crack propagation. The fracture surface state in the direction of the crack propagation is smooth, and this means that the fracture surface is formed like a continuous state in that direction. On the other hand, the crack in the perpendicular direction of the crack propagation dose not necessarily initiate at one point, then two or more different cracks may propagate, and make some steps at their combining zones. When the influence of the fracture mode on the fracture surface state is investigate, it can be considered that it is more appropriate to take the measured value in the direction of the crack propagation. For the above mentioned reason, the roughness of the fracture surface is examined with the value of Δh measured in the direction of the crack propagation.

Figure 5 shows the effect of the fracture mode on the fracture surface state at the crack initiation area and the steady propagation one. Regardless of the fracture mode, the roughness in steady propagation area is generally less than that at the crack initiation area. Briefly, the fracture surface state at the crack initiation area is comparatively rough. On the other hand, the fracture surface state

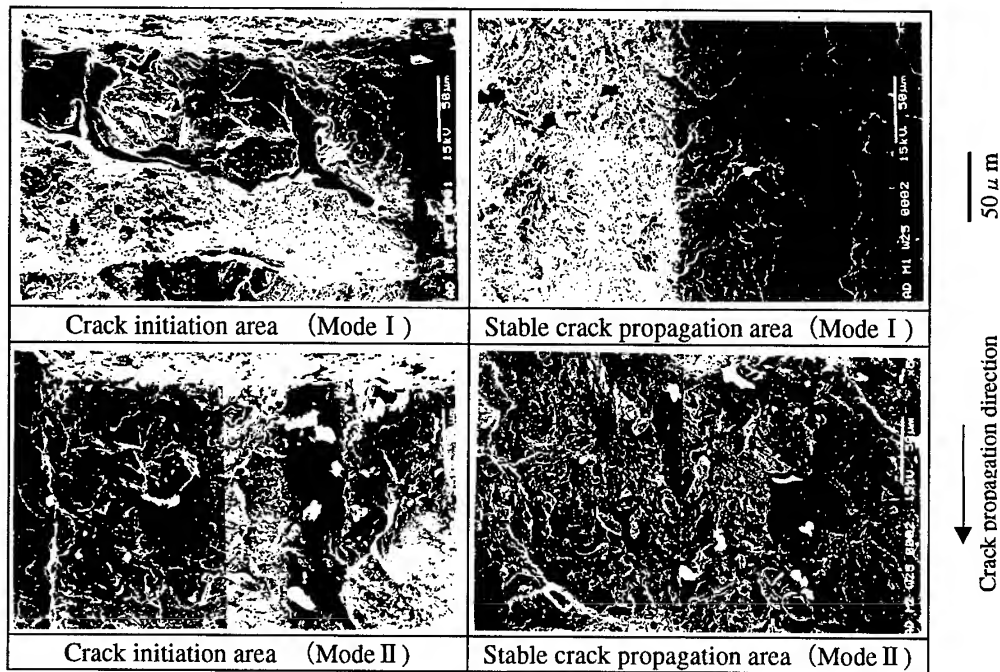


Fig.3. The observation results of specimen's surface for AD.

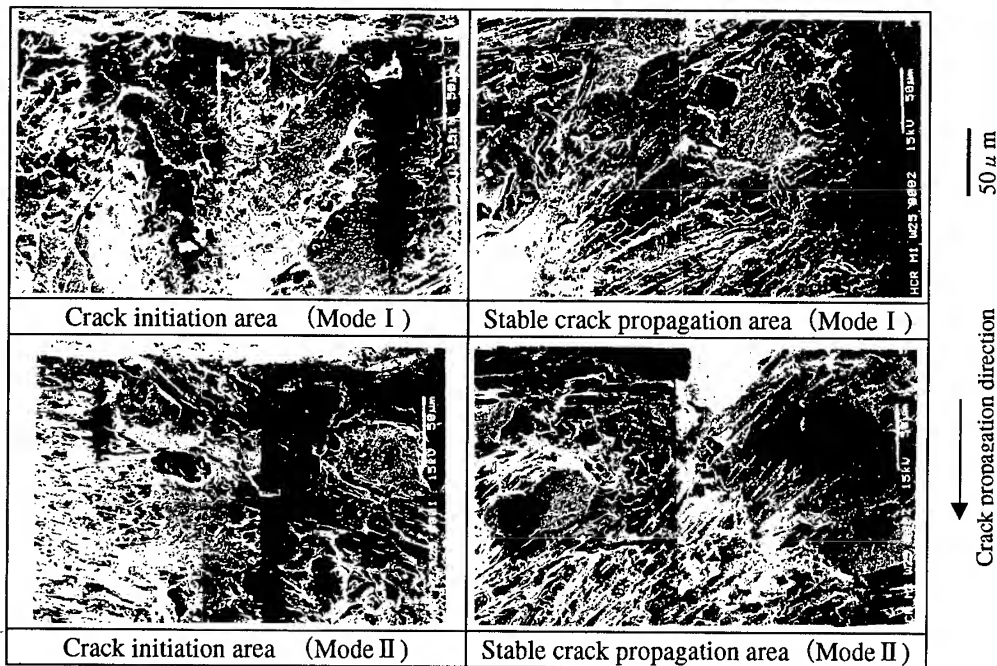


Fig.4. The observation results of specimen's surface for HCR.

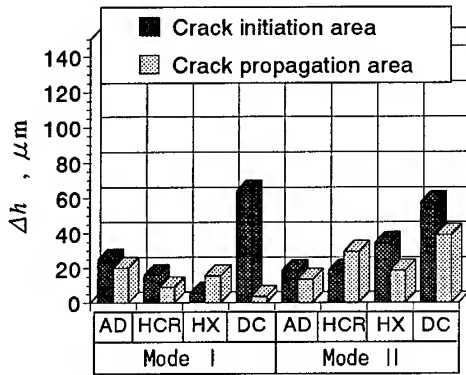


Fig.5. Effect of fracture mode on Δh (Measurement magnification ; $\times 500$).

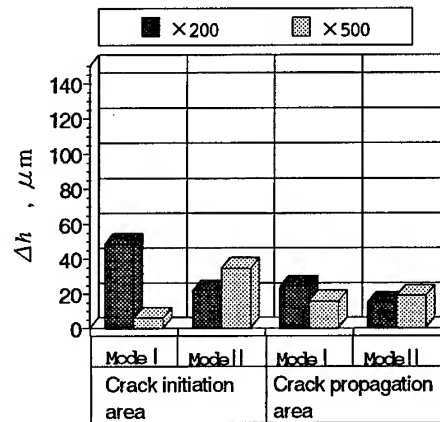


Fig.6. Effect of measurement magnification on Δh about HX.

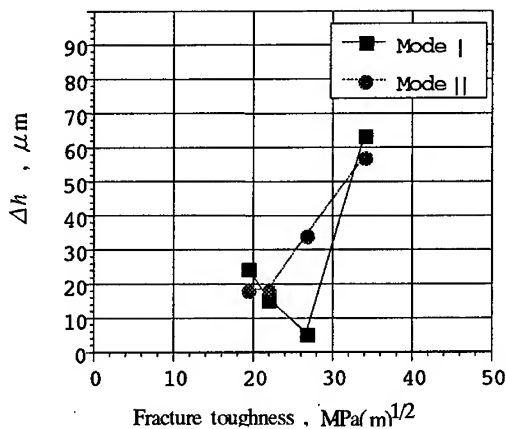


Fig.7. Relation between Δh at crack initiation area and fracture toughness.

in the steady crack propagation area is quite smooth. In addition, there are no remarkable differences on the measured results for the test specimens failed under the conditions of Mode I and Mode II. In the case of test specimens failed under Mode II condition, it is considered that the fracture mode in propagation area is not necessarily in Mode II type, even if the fracture near the crack initiation area is Mode II. The difference of fracture mode do not clearly affect on the roughness of the fracture surface.

Figure 6 shows the effect of the measurement magnification on the roughness in the fracture surface for material HX. Considering the result of other test materials, the Δh measured under the low magnification becomes higher than that measured under the high magnification. That is, the

maximum value of Δh shows the increasing tendency so that the examination area may extend as the measurement magnification decreases. However, the accuracy of the measurement value decreases occasionally when the measurement magnification is lowered too much. In this case, an appropriate evaluation might not be necessarily obtained. Therefore, it is necessary to examine the optimal magnification experimentally.

It is thought that the value of fracture toughness influences in the roughness on the surface of the damaged material. Figure 7 shows the relation between the value of Δh near the crack initiation area and that of fracture toughness. It is difficult to give any clear conclusion from this figure. However, it seems that the value of Δh increases with increasing the value of fracture toughness. Therefore, even if the test specimens fail in the same fracture mode, there is much difference on the values of Δh between a high toughness material and a low toughness one and hence it is difficult to determine the fracture mode only according to the surface roughness without understanding the characteristic of each material when this technique is used.

When the method examined in this study is practically used, the optimal measurement magnification or the influence of mechanical properties for each material on the roughness, etc, should be firstly examined. However, those factors will be easily obtained by some fundamental experiments. Therefore, this method will be effectively used because it is very simple and does not require much experience.

4. CONCLUSIONS

The results obtained in this research are as follows :

- (1) No remarkable difference of the roughness on fracture surfaces between Mode I and II is observed because the Mode II specimen is not necessarily fractured in Mode II after crack propagating.
- (2) Considering the measuring direction of the fracture surface roughness, there is remarkably difference on the value of fracture roughness measured in the crack propagation direction and in the perpendicular direction of crack propagation. It is considered that the measurement in the direction of the crack propagation is more reasonable than in the perpendicular direction of the crack propagation.
- (3) As the measurement magnification becomes lower, the measured area increases but the measurement accuracy decreases. Therefore, it is necessary to determine the optimal measurement magnification.

REFERENCES

1. e.g. H.Kitagawa and R.Koterasawa, Fractography, Baifu-kan Ltd.
2. S.Masuda et al 2, J. JSME (in Japanese), 51-461(1985), p.136
3. e.g. S.Nishida, Failure Analysis in Engineering Application, Butterworth-Heinemann Ltd(1991)
4. A.Otsuka, et al 3, J. JSME (in Japanese), 42-357(1976), p.1313
5. H.Kitagawa, et al 2, J. JSME (in Japanese), 47-424(1981), p.1283
6. A.Otsuka, et al 4, J. JSME (in Japanese), 41-466(1992), p.1136
7. Y.Murakami, J. JSME (in Japanese), 59-558A(1993), p.283
8. M.Kaneta, et al 2, J. JSME (in Japanese), 51-470C(1985), p.2618
9. Y.Murakami, et al 2, J. JSME (in Japanese), 58-556A(1992), p.2313
10. H.Awaji and S.Sato, J. Engineering Materials and Technology, 100(1978), p.175
11. H.Awaji and S.Sato, J. Carbon, 105(1981), p.52

Microscopic Deformation at a Crack Tip in a Ferroelectric Material

W. Yang, F. Fang and T. Zhu

Department of Engineering Mechanics, Tsinghua University,
Beijing 100084, China P.R.

Keywords: Crack, Ferroelectrics, Microscopic Deformation

ABSTRACT

We discuss the microscopic deformation at the crack tip of ferroelectric ceramics by domain switching. Experiment for polycrystal ferroelectrics after out-of-plane poling indicates the crack tip domain switch by the application of a lateral electric field. The theory of crack tip domain switch is presented to explain electric fracture. The analysis is developed for both in-plane and out-of-plane poling. Implication on how to raise the fracture toughness of ferroelectrics will be addressed.

1. INTRODUCTION

Ferroelectric ceramics are featured by large switching strain and low fracture toughness. The incompatible strain during domain switch may cause internal stress as high as hundreds of megapascals, while the fracture toughness assumes a typical value of $1\text{MPa}\sqrt{\text{m}}$. Therefore, fracture may occur from a flaw of a few microns. Fracture toughness anisotropy for poled ferroelectrics was extensively reported in the literatures [1] through Vickers indentation. Park and Sun [2] performed compact tension tests under combined mechanical and electrical loading and found that the apparent fracture toughness varied asymmetrically for poled ferroelectrics under positive and negative electric fields.

The analysis for the fracture of ferroelectrics under electrical and/or mechanical loading becomes a focus point of solid mechanics. Considering the nonlinear effect, Yang and Suo [3] modelled the electrostrictive material and derived the stress intensity factor on the flaws around the electrode edge under electric loading. Lynch *et al* [4] provided a preliminary explanation for the cracking in relaxor ferroelectrics. Gao *et al* [5] proposed a strip saturation model to investigate the effect of electric yielding.

The non-linear effect dominates in the vicinity of internal flaws. The stress and electric fields around the flaw attempt to reorient the domains. Constrained by the un-switched material outside, the stress distribution near the flaw is altered. It is the variation of the stress intensity factor at the crack tip that dictates the apparent fracture of ferroelectrics. Pursuing along this approach, the case of in-plane poling was explored by Yang and Zhu [6]. The present work explores the effect of poling directions to the variation of the stress intensity factor at the crack tip. The theory is used to explain Vickers indentation data for PZT-5 polycrystals and for PLZT single crystals.

2. CRACK TIP DOMAIN SWITCHING

$(\text{Pb}_{0.96}\text{La}_{0.04})(\text{Zr}_{0.40}\text{Ti}_{0.60})_{0.99}\text{O}_3$ (PLZT) ceramics were synthesized by the conventional powder processing technique. The x-ray diffraction pattern reveals that at room temperature, PLZT ceramics adopt a tetragonal perovskite structure with $a = b = 0.4055\text{ nm}$, and $c = 0.4109\text{ nm}$. Consequently, the aspect ratio c/a is 1.013 and the spontaneous strain γ_s is 1.3%. The PLZT ceramic samples were mechanically cut and ground into specimens with the size of $3.5\text{mm} \times 5\text{mm} \times 25\text{mm}$. One $5\text{mm} \times 25\text{mm}$ surface was ground and polished [7]. The two opposing $5\text{mm} \times 25\text{mm}$ surfaces were sprayed with Au electrodes. The samples were then poled under an electric field of

2.3kV/mm at 120°C. After removing the Au electrodes, the polished surface of 5mm×25mm were indented under 5kg load. The two opposing surfaces of 3.5mm×25mm were sprayed with Au electrodes and lateral electric field of $0.6E_c$ ($E_c = 1100\text{V/mm}$) was applied. The poled PLZT ceramics with different lateral electric fields were etched. The etching rates of ferroelectric domains of different orientations are different, so that the "c⁻" domains appear bright, "c⁺" domains appear dark, and the "a" domains appear gray in a SEM micrograph [7]. The zone of domain switch near the crack tip was observed by SEM. It was shown that lamellar 90° domain structure appeared in poled PLZT, illustrating the formation of 90° domain switching near the crack tip, as shown in Fig. 1a. In the grain ahead of the crack tip, 90° domain switching takes place in several strips, and leads to marks of straight 90° domain walls.

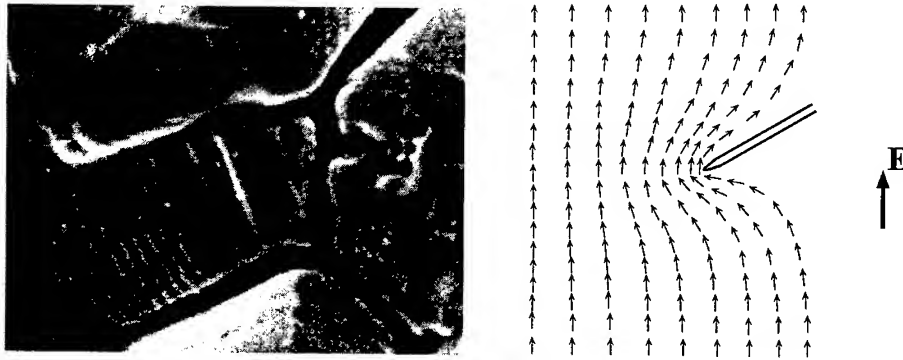


Fig. 1 Poled PZT with $0.6E_c$ lateral electric field
(a) formation of 90° domain switching at the crack tip; (b) field lines around the crack tip.

As shown in Fig. 1b, the indentation crack forms an inclined angle α with the horizontal axis. The applied electric field can be decomposed into a component of $E \sin \alpha$ parallel to the indentation crack and a component of $E \cos \alpha$ normal to it. The electric field concentration near the indentation cracks drives a localized 90° domain switching. The singular part of the crack tip electrical field can be described by [3]

$$\begin{Bmatrix} E_1 \\ E_2 \end{Bmatrix} \approx \frac{K_E}{\sqrt{2\pi r}} \begin{Bmatrix} -\sin(\theta/2) \\ \cos(\theta/2) \end{Bmatrix} \quad (1)$$

We label the in-plane co-ordinates by x_1 (parallel to the crack) and x_2 (normal to the crack), and the out-of-plane co-ordinate by x_3 . Polar co-ordinates r and θ are centered at the crack tip. The intensity of the crack tip electrical field is given by $K_E = E \cos \alpha \sqrt{\pi L}$, where L denotes the half-length of the irreparable crack. The field lines are depicted in Fig. 1b.

3. SMALL SCALE 90° DOMAIN SWITCHING

In the presence of electric and mechanical fields, switch of 90 degrees is activated by the combined mechanical and electrical work, see Hwang *et al* [8]

$$\sigma_{ij}\Delta\varepsilon_{ij} + E_i\Delta P_i \geq 2P_s E_c. \quad (2)$$

In (2), σ_{ij} and $\Delta\varepsilon_{ij}$ are the stress and the switching strain tensor, E_i and ΔP_i are the electric field and the polarization switch vectors, P_s the magnitude of the spontaneous polarization, and E_c the coercive field. The right hand side of (2) describes an energy threshold for polarization switch.

Small scale domain switching consists of a practical configuration. In terms of the electric loading, the recent experimental observation gave merit for the case of crack growth below the coercive field. Under such circumstances, the zone of domain switching is either focused at the crack tip or along the crack wake. For the case of mechanical loading, the presence of a crack necessarily causes the stress concentration. Consequently, the zone of domain switch (as activated by the crack tip stress) is confined near the crack tip [6].

For the case of small scale switching, the geometry can be regarded as a semi-infinite crack in an otherwise infinite medium. The remote stress field is characterized by K_{app} , the applied SIF, and is given by

$$\begin{Bmatrix} \sigma_{11} \\ \sigma_{22} \\ \sigma_{12} \end{Bmatrix} = \frac{K_{app}}{\sqrt{2\pi r}} \cos \frac{\theta}{2} \begin{Bmatrix} 1 - \sin \frac{\theta}{2} \sin \frac{3\theta}{2} \\ 1 + \sin \frac{\theta}{2} \sin \frac{3\theta}{2} \\ \sin \frac{\theta}{2} \cos \frac{3\theta}{2} \end{Bmatrix} \quad (3)$$

Denote K_{app} as the applied stress intensity factor, and $K_{tip} = K_{app} + \Delta K$ as the stress intensity factor that governs the fracture process at the crack tip. Presence of 90° switching zone alters the near tip stress intensity factor by an amount of ΔK . The value of ΔK can be evaluated in the spirit of transformation toughening. For poled ferroelectrics, the toughness variation induced by switching strain can be evaluated along the boundary Γ_s of the switching zone by [6]:

$$\Delta K = \oint_{\Gamma_s} T_i h_i d\Gamma. \quad (4)$$

For an instantaneous elastic isotropic response, the amount of body force layer T_i is given by

$$T_i = 2\mu\Delta\varepsilon_{ij}n_j. \quad (5)$$

In (5), μ denotes the shear modulus, and n_i the outward normal of Γ_s . Volume conservation during domain switch is used in deriving (5). The weight function h_i in (4) denotes the SIF caused by a unit point force along the i -th direction. The expressions of h_1 and h_2 are given below:

$$h_i = \frac{\tilde{h}_i}{(\kappa+1)\sqrt{2\pi r}}, \quad \begin{Bmatrix} \tilde{h}_1 \\ \tilde{h}_2 \end{Bmatrix} = \begin{Bmatrix} (1-\kappa)\cos \frac{\theta}{2} + \sin \theta \sin \frac{3\theta}{2} \\ (1+\kappa)\sin \frac{\theta}{2} - \sin \theta \cos \frac{3\theta}{2} \end{Bmatrix}. \quad (6)$$

For the case of plane strain, $\kappa = 3-4\nu$; and for the case of plane stress, $\kappa = (3-\nu)/(1+\nu)$, where ν denotes the Poisson's ratio.

4. DOMAIN SWITCH WAKE BY A GROWING CRACK

The attention is focused on the case for crack extending in steady state, and domain switch is activated by the stress field. Domain switching wakes are formed by the activation of the crack tip stress field. Yang and Zhu [6] studied the formation of domain switching wakes for the case of in-plane poling. New analysis is presented herein for the case of out-of-plane poling.

4.1. Domain switch wakes in specimens poled in out-of-plane direction

Consider a specimen poled in the out-of-plane direction. Undergone a domain switch of 90 degrees, the out-of-plane poling axis may rotate to an in-plane polarization of any angle ω with the crack. The induced domain switching strain is

$$\Delta \varepsilon_{ij} = \gamma_s \begin{bmatrix} \cos^2 \omega & \sin \omega \cos \omega \\ \sin \omega \cos \omega & \sin^2 \omega \end{bmatrix} \quad (9)$$

where γ_s denotes the spontaneous strain of 90° switching. Substituting (3) and (9) into the left-hand side of (2), one has

$$\sigma_y \Delta \varepsilon_{ij} = \frac{K_{app} \gamma_s}{\sqrt{2\pi r}} \cos \frac{\theta}{2} \left[1 - \sin \frac{\theta}{2} \sin \left(\frac{3\theta}{2} - 2\omega \right) \right]. \quad (10)$$

Polarization switching should proceed in a manner to release the maximum amount of that stress work. The maximization of (10) leads to the following expression of ω ,

$$\omega = \frac{3\theta + \text{sgn}(\theta)\pi}{4}. \quad (11)$$

The above expression implies that all domains along a radial ray from the crack tip have the same polarization switch. The shape of switching zone, denoted by $R(\theta)$, is determined by equating the maximum of the switching work to the energy threshold $2E_c P_s$. The profile is given by:

$$\sqrt{R} = \sqrt{R_0} \cos \frac{\theta}{2} \left(1 + \left| \sin \frac{\theta}{2} \right| \right). \quad (12)$$

The size of the switching zone is scaled by

$$R_0 = \frac{1}{8\pi} \left(\frac{K_{app} \gamma_s}{E_c P_s} \right)^2. \quad (13)$$

As the crack grows, switching wakes form above and below the crack [6]. The height of the switching wake equals to the maximum vertical position of the switching zone. For a specimen poled in the out-of-plane direction, the height of its switching wake is given by $H \approx 1.5735 R_0$.

4.2. Shielding on crack tip stress intensity factors

Yang and Zhu [6] discussed switch toughening under in-plane poling, their expression of the apparent fracture toughness is

$$K_{IC} = K_{intrinsic} / \left(1 - \frac{8\mu\gamma_s^2\Omega}{(\kappa+1)P_sE_c} \right) \quad (14)$$

where $K_{intrinsic}$ denotes the intrinsic fracture toughness for the sample without any domain switching and the dimensionless function Ω depends on the domain orientation. The plane strain calculation [6] indicated that $\Omega = 0.022$ for a polycrystalline specimen poled along the direction parallel to the crack; and $\Omega = 0.044$ for poled along the direction normal to the crack. Both results were derived under the assumption that the domain polarizations are distributed uniformly within a fan between -45 and 45 degrees with respect to the poling axis.

For a specimen poled out-of-plane, the shielding on the stress intensity factor can be computed by tracing various strips of infinitesimal height dy . Omitting the details, one find the value of Ω is

$$\Omega = \frac{1}{16\pi} (2.4077\kappa - 0.0322). \quad (15)$$

5. VERIFICATION BY EXPERIMENTS

5.1. Three-point bending tests

Single-edge-notch-beam (SENB) specimens were cut to $4 \times 2 \times 15$ mm dimension for the three point bending tests. The specimens were divided into three groups with 10 specimens each, and poled along the x (thickness), y (longitudinal), and z (height) directions. The poling is conducted at 130°C under an electric field of 2.5 kV/mm for 0.5 h . After poling, a 0.3 mm notch was cut by a diamond saw for a depth of 1.85 mm . In an ascending order, the average fracture loads are $F_1 = 16.95\text{ N}$, $F_2 = 19.31\text{ N}$, and $F_3 = 22.25\text{ N}$ for the specimens poled along the longitudinal, height and thickness directions. For a SENB specimen, the fracture toughness can be estimated from the fracture load F as: $K_{IC}^{(0)} = 0.94\text{ MPa}\sqrt{\text{m}}$, $K_{IC}^{(h)} = 1.08\text{ MPa}\sqrt{\text{m}}$, $K_{IC}^{(t)} = 1.24\text{ MPa}\sqrt{\text{m}}$.

For polycrystalline PZT-5, the formula (15) would predict an Ω value of 0.079 for the mono-domain case under plane strain condition. The actual domain configuration under an out-of-plane poling, however, is described by distribution of polarization vectors covering a fan of -45 to 45 degrees from x_3 axis. One may still use (14) to estimate the toughening but to scale the Ω value by a factor of $8/\pi^2$. The corrected Ω value is 0.064 , considerably higher than the one for in-plane poling.

An intrinsic fracture toughness of $0.83\text{ MPa}\sqrt{\text{m}}$ is taken and it fits to three sets of experimental data. For the specimen poled in the longitudinal direction, the present analysis predicts a K_{IC} value of $0.939\text{ MPa}\sqrt{\text{m}}$ against the experimental measurement of $0.94\text{ MPa}\sqrt{\text{m}}$. For the specimen poled in the height direction, the present analysis predicts a K_{IC} value of $1.081\text{ MPa}\sqrt{\text{m}}$ against the experimental measurement of $1.08\text{ MPa}\sqrt{\text{m}}$. For the specimen poled in the thickness direction, the present analysis predicts a K_{IC} value of $1.253\text{ MPa}\sqrt{\text{m}}$ against the experimental measurement of $1.24\text{ MPa}\sqrt{\text{m}}$. Thus, the present analysis is supported by the experiments.

5.2 Vickers indents for ferroelectric single crystals

We conduct Vickers indents for ferroelectric single crystals. The single crystal has uniform lattice structure, then leads to uniform poling. The single crystal is free of grain boundaries, then rules out the possibility of pre-existing microcracks. The micrographs of Vickers indents on single crystal PLZT are shown in Fig. 2. The micrograph on the left refers to the case of outward poling.

Domain bands perpendicular to the indenting cracks are formed, and effectively suppress the crack extension. That measurement agrees with the prediction in (14), since Ω assumes a large value of 0.079 for the case of a single crystal.

The micrograph on the right of Fig. 2 refers to the case of upward poling. The theoretical prediction for the apparent fracture toughness is again given by (14), where $\Omega = 0.0056$ for the prediction of K_{\perp} and $\Omega = 0.062$ for the prediction of K_{\parallel} [6]. The micrograph shows that indenting cracks under the same indenting load grow longer under upward poling than the ones under outward poling, in agreement with the theoretical prediction. Moreover, since the predicted value for K_{\perp} is smaller than the one for K_{\parallel} , the indenting cracks tilt toward the direction normal to the poling axis, as would be predicted under the present model.



Fig. 2 Micrographs for Vickers indentation on single crystal PLZT under different polings, (a) outward poling, (b) upward poling.

ACKNOWLEDGEMENTS

The authors would like to express their gratitude for the supports by the National Natural Science Foundation of China.

REFERENCE

1. K.Mehta and A.V.Virkar, J. Am. Ceram. Soc. 73(1990) p.567
2. S.Park and C.T.Sun, J. Am. Ceram. Soc. 78(1995) p.1475
3. W.Yang and Z.Suo, J. Mech. Phys. Solids 42(1994) p.649
4. C.S.Lynch, W.Yang, L.Collier, Z.Suo and R.M.McMeeking, Ferroelectrics, 166(1995) p.11
5. H.Gao, T.Y.Zhang and P.Tong, J. Mech. Phys. Solids 45(1997) p.491
6. W.Yang and T.Zhu, J. Mech. Phys. Solids 46(1998) p.291
7. F.Fang, W.Yang and T.Zhu, Journal of Materials Research 14(1999) p.2940
8. S.C.Hwang, C.S.Lynch and R.M.McMeeking, Acta Metall. Mater. 43(1995) p.2073
9. J.Mencik, Glass Science and Technology, Elsevier publisher, Amsterdam-New York-Tokyo, 172 (1992)

The Unified Description of the Three-dimensional Fields at Notches and Cracks

W. Guo^{1,2}, T. Chang² and Z. Li²

¹ Department of Aeronautical Engineering, Nanjing University of Aeronautics
and Astronautics, Nanjing 210016, China P.R.

² The State Key Laboratory of Mechanical Strength and Engineering,
Xi'an Jiaotong University, Xi'an 710049, China P.R.

Keywords: Crack, Notch, Three-dimensional Fields, Unified Description

ABSTRACT

The relationship of notch fields and crack fields is concerned in this paper. Based on theoretical studies and 3D numerical simulations, some common features of the 3D elastic-plastic notch fields and the crack fields are analyzed and the unified description of the fields is discussed. It is surprising to find that the 3D stress constraints at a circular hole, a notch and a crack can be described uniformly. Fracture of notches is discussed and some interesting topics in this direction are listed to unify fatigue mechanics and fracture mechanics.

1. INTRODUCTION

Both notches and cracks are stress raisers in structures. They have the same importance in strength analysis and safe design. For sharp cracks, the fracture mechanics method of stress-strain analyses has been shown to be effective and successful. However, the stress-strain fields at notches with blunt ends are much more complicated and difficult to deal with. Even for two-dimensional (2D) notch problems, there is no rational description available for the elastic-plastic fields near the notch-root. In the three-dimensional (3D) frame, the additional scale of the finite notch-root radius will introduce several mechanics parameters which are necessary to be considered in stress analyses, such as the ratio of root radius to thickness, root radius to the size of the plastic zone, *etc.* On the other hand, notches and cracks have many common features. Physically, there is no ideally sharp crack. When the depth to root radius ratio and the size of interesting region to the radius ratio become larger, the effect of the notch-root radius become less important and a notch can be treated as a crack. Another typical case is circular holes for which 2D as well as 3D elastic theoretical solutions can be found in the literatures.

As shown by Fig.1, the geometrical variation from a hole to a notch and to a crack is a continuous process so that there is no determined distinction between notches and cracks. In the

figure, ρ is the notch-root radius, a is the notch depth, B is the thickness of a plate.

It is well known that the elastic solution of a 2D crack can be obtained by the solution of a elliptical hole as ρ/a is approaching zero. The Creager and Paris solution [1] and the recent work by Kuang [2] and Lazzarin and Tovo [3] have built a relation between the 2D notch-root and crack-tip elastic stress fields. The elastic solution for a circular hole in a finite thickness plate has been obtained by Chang and Guo [4]. For general notches in finite thickness plates, the in-plane stress distributions are insensitive to the notch radius to thickness ratio ρ/B [5] while the stress concentration factor K_t is a function of ρ/B and changes through the thickness. In elastic-plastic situation, theoretical solutions can only be obtained for 2D circular holes under specific loading conditions [6] and sharp cracks. The 3D fields and the elastic-plastic deformation near general notches which are more interesting in engineering are poorly understood, thus it will be the focus of the following discussions.

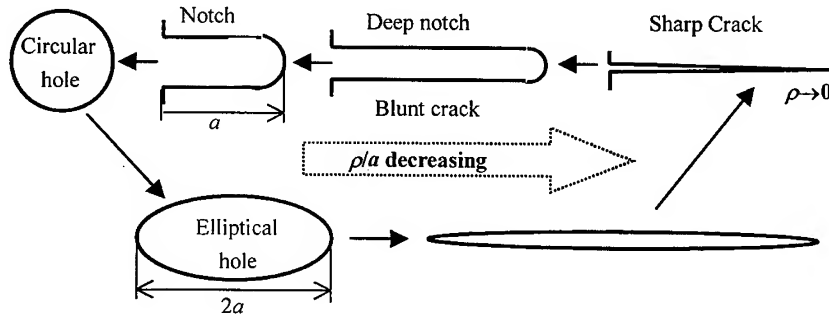


Fig.1. The geometrical relationship between notches and cracks

2. ELASTIC STRESS ANALYSIS

2.1. A Unified Description of Notch and Crack Tip Fields

When the stress solution is formulated for a general notch, the stress function expressed in variable separated form of r and θ ,

$$\varphi = A_0 r^\mu \tilde{\varphi}_0(\theta) + \sum_{k=1}^m A_k r^{\lambda_k} \tilde{\varphi}_k(\theta) \quad (1)$$

should satisfy the governing equation of the problem,

$$\nabla^2 \sigma_y + \frac{1}{1+\nu} \sigma_{kk,jj} = 0. \quad (2)$$

Where the second and higher terms in (1) are the solution for a sharp crack or a sharp V-notch which can be solved easily by the fracture theory, the first term represents the influence of blunt notch-root and $\mu < \lambda_1 < \lambda_2 < \dots$. Once the terms for a sharp crack or V-notch are obtained by solving the standard two-point boundary value problem, the first term can not be solved accurately along the notch boundary, as shown in [3], but μ and $\tilde{\varphi}_0, \tilde{\varphi}_0', \tilde{\varphi}_0'', \tilde{\varphi}_0''', \tilde{\varphi}_0''''$ can be solved accurately on

the line of $\theta=0$ by the boundary conditions at the notch-root and eq.(2) [7]. Thus the stress solution for a deep blunt notch can be written as

$$\sigma_{ij} = A_0 r^{\mu-2} \tilde{\sigma}_{ij}^0 + [\sigma_{ij}]_{sharp} \quad (3)$$

and μ and $\tilde{\sigma}_{ij}^0$ can be determined completely by the solution of the sharp notch. It is important to find that not only the singular term of the sharp notch field, but also the higher term(s) have strong influence on μ and $\tilde{\sigma}_{ij}^0$. Therefore, $\mu-2=-3/2$ as obtained by Creager & Paris for a blunt crack [1] and Hui & Ruina for a small hole at the crack tip [8] is only a specific value under certain in-plane constraint. For example, μ is a function of the T-stress for a blunt crack as shown in Fig.2 where W is the width of the plate.

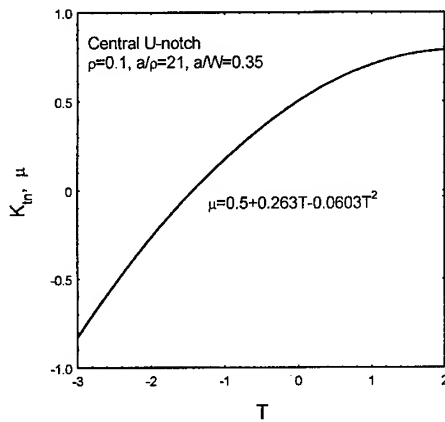


Fig.2 The effect of T-stress on the notch-root stress solution.

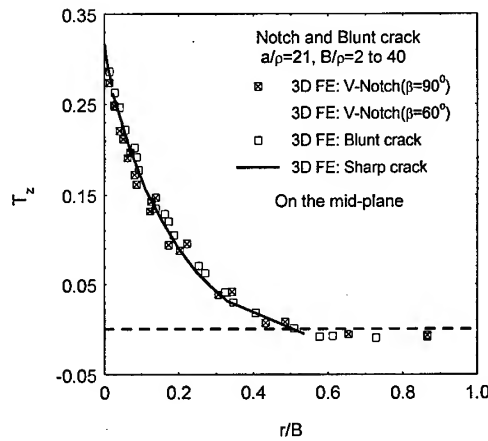


Fig.3 The out-of-plane constraint ahead of cracks and notches in finite thickness plates

2.2. 3D Constraints

3D finite element analyses [5] show that in front of a opening mode notch in finite thickness plate, the distribution of the normalized stress $\sigma_{yy}/\sigma_{yy\max}$ and the in-plane stress ratio $T_x = \sigma_{xx}/\sigma_{yy}$ with r/ρ is nearly independent of the plate thickness and can be predicted well with the corresponding 2D solutions. Therefore, the out-of-plane stresses become an important parameter in describing the 3D notch-root fields. For convenience, the out-of-plane constraint factor $T_z = \sigma_{zz}/(\sigma_{xx} + \sigma_{yy})$ used by Guo [9] for 3D cracks is introduced. For elastic through-thickness cracks, T_z can be expressed approximately by

$$T_z = \sqrt{1 - 1.79\left(\frac{r}{B}\right)^{1/2} + 0.113\left(\frac{r}{B}\right) + 0.631\left(\frac{r}{B}\right)^{3/2}} f(z/B). \quad (4)$$

When the origin of the coordinate r setting at the middle point of the center of the notch root arc and the notch-root, the variation of T_z with r/B in front of a blunt crack, a shallow notch and a hole can collapse to a unified curve, as shown by Fig.3. Therefore, the solution for a circular hole or

for a through-thickness crack can be used to estimate T_z for general notches. It can be seen from the figure that when $B/\rho < 1$, T_z will remain less than $T_{zmax}/4$ and merit less attention in practical application.

3. Elastic-plastic Stress-Strain Fields

The elastic-plastic deformation near notches is much more complicated than elastic one, theoretical solution can only be found for some simple notch geometry and loading configurations. Recently Guo [6] obtained the solution for an equal-biaxial stressed infinite plate with a circular hole. He found that the elastic-plastic solution of the problem can be obtained from the elastic solution by a simple replacement of variable. If the elastic solution of the equivalent strain ahead of the notch is known as

$$\frac{\varepsilon_{eq}}{\varepsilon_{ys}} = f(r), \quad (5)$$

then the corresponding elastic-plastic solution can be obtained as

$$\frac{\varepsilon_{eq}}{\varepsilon_{ys}} = f(r'), \quad r' = r \times \frac{r_{p0}}{r_p} \quad (6)$$

where ε_{ys} is the yield strain of the material, r_{p0} is defined by $f(r_{p0})=1$ and r_p is the size of the plastic zone ahead of the notch. This is the so called Strain-Equivalent-Rule (SER).

Finite element analyses show that the SER can not only be applied to general 2D and 3D notches, but can also be applied to short cracks. Some typical results are given in Figs.4 and 5.

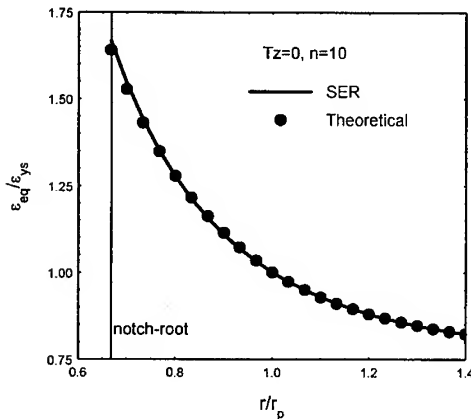


Fig.4. Strain distribution at a circular hole in a plane stress state

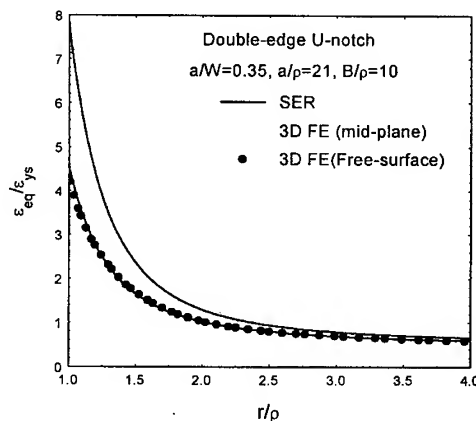


Fig.5. Strain distribution at a deep U-notch in a finite thickness plate.

For long cracks the SER can not hold good, but the plastic zone size is still a useful controlling parameter of the elastic-plastic fields.

4. FRACTURE CRITERIONS FOR NOTCHES AND CRACKS

It is well known that the fracture of a material element is strongly dependent on the 3D stress state. With increasing a/ρ , the stress triaxiality R_σ which is equal to the ratio of the mean stress to the equivalent stress will increase. For a smooth bar R_σ is about 3/4 and for notched bar $R_\sigma=1$ to 2. For sharp cracks R_σ is about 3 on the mid-plane. Figures 6 and 7 give the simulation results by use of 3D finite element and a cell model [10]. It is shown clearly that both the critical fraction of void volume and the V_{GC} are not constant and do not change monotonously with R_σ . For notched bar (R_σ is about 1 to 2), V_{GC} is nearly constant as has been investigated in many experiments. However, in front of a crack V_{GC} may be much higher. For lower R_σ as in a smooth bar V_{GC} is obviously higher than in notched bars as well. Therefore, with proper initial values of the material parameters the 3D cell model simulation can provide us a more complete picture of fracture of notched and cracked bodies.

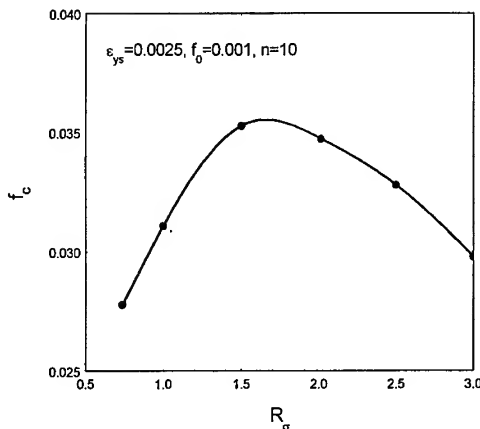


Fig.6. Critical fraction of void volume against stress triaxiality

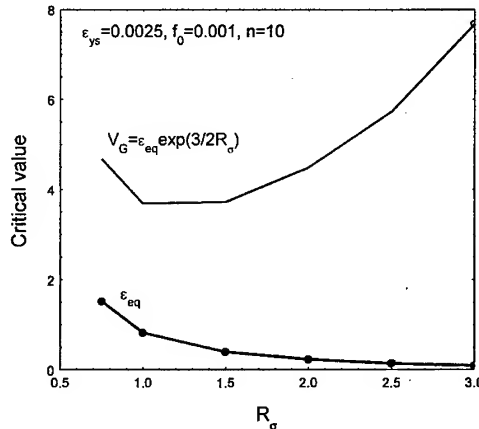


Fig.7. Variation of the critical strain and V_{GC} with stress triaxiality

5. DISCUSSIONS

Rational prediction of the life of structural components has long been the main objective of fatigue mechanics and fracture mechanics. The traditional fatigue mechanics determines the life by stress-strain concentration analysis of notches and mainly concerns the crack initiation life. In contrast, fracture mechanics is based on crack analysis and always provides the life of crack growth. To predict the whole life of a component rationally, confusion of fatigue mechanics and fracture mechanics is necessary. The following topics will be interesting in this direction:

- i) Mechanics behavior in the crack blunting zone in which the fracture process occurs.
- ii) Unified description of 3D elastic-plastic notch fields and crack fields.
- iii) Fatigue damage mechanism of material elements at notches and cracks.
- iv) Unified description of the whole process of crack initiation from material defects or pits

and crack growth.

- v) Whole life prediction based on unified descriptions of notches and cracks.

Acknowledgment: This work is supported by the National Distinguished Young Scientist Fund of China and the Cheung Kong Scholars Programme.

REFERENCES

1. M.Creager and P.C.Paris, Int. J. Fract. Mech., **3**(1967)p.247
2. Z.-B. Kuang, Engng Fract. Mech., **16**(1982)p.19
3. P.Lazzarin and R.Tovo, Int. J. Fract., **78**(1996)p.3
4. T. Chang, W. Guo and Z. Li, Thickness effects for a circular hole in elastic plate. Int. J. Fatigue, (submitted)
5. Z. Li, W. Guo and Z.-B. Kuang, Three dimensional elastic stress fields near notches in finite thick plates, Int. J. Struct. Solids, (In the press)
6. W. Guo, A strain equivalent method for elastic-plastic notch fields, Int. J. Struct. Solids, (in processing)
7. Guo, W., A unified approach for the stress fields in the neighborhood of cracks and notches under constraint, (to be published)
8. C.Y. Hui and A. Ruina, Int. J. Fract., **72**(1995)p.97
9. W. Guo, Engng Fract. Mech., **51**(1995)p.51
10. Z. Li, W. Guo and Z.-B. Kuang, The three-dimension elastoplastic finite element analysis on double-edge U-notch plates, *Acta Mechanica Sinica*. (In the press).

Buckling and Fracture of Thin Films under Compression

B. Cotterell and Z. Chen

Institute of Materials Research & Engineering,
3 Research Link, Singapore 117602, Singapore

Keywords: Buckling, Compliant Substrate, Cracking, Delamination, Thin Film

ABSTRACT

The energy release rate when thin films on compliant substrates delaminate and buckle with or without cracking is shown to be much greater than if the substrate is stiff. For very compliant substrates relative to the film, such as indium tin oxide on polyethylene terephthalate the energy release rate can be more than an order of magnitude greater than the value obtained if the deformation of the substrate is neglected. The mode-mixity is also less on compliant substrates than on stiff ones.

1. INTRODUCTION

This paper was motivated by the Institute of Materials Research and Engineering's interest in flexible organic light emitting displays (OLED) and in particular the mechanical behaviour of conducting transparent oxides such as Indium-Tin oxide (ITO). Experimental studies have been undertaken on ITO deposited on a thin polyethylene terephthalate (PET) substrate, which is commercially available. When the composite film is flexed, the brittle ITO can crack under tension or compression. The steady state tension cracking of a brittle film on a substrate has been adequately studied and will not be discussed here. If the PET film is bent by controlled buckling so that the ITO is in compression, cracks appear in the ITO coating aligned normal to the direction of bending. Since the ITO film is conducting, the critical radius of curvature of the film, and hence the strain, can be determined by monitoring the resistance of the ITO. The cracks are superficially similar to cracks formed when the ITO is under tension. However, closer examination shows that the cracks grow behind delaminated buckles that propagate across the film (see Fig. 1).

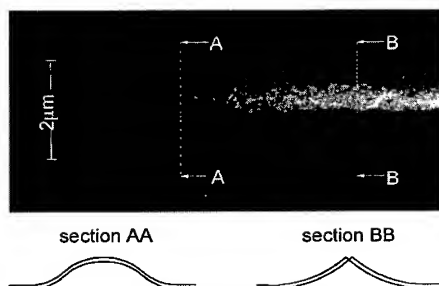


Fig. 1 SEM picture showing tunnelling delamination-buckle-crack

When the existing analysis of compression cracking of thin films [1] was used to analyse the compression cracking of ITO films on PET substrates, it was found that the indicated interfacial toughness was too low to be believed (5 J/m^2). As a result the analysis of thin films under compression is revisited and an analysis for steady state delamination and buckling on compliant substrates is presented.

2. BUCKLING OF FILMS ON COMPLIANT SUBSTRATES

Under uniaxial strain, a delaminated buckle propagates normal to the applied strain with stable straight sides [2]. The analysis follows that of Hutchinson and Suo [3], but deformation in the substrate is taken into account. Provided the ratio of the half width of the delamination, b , to the film thickness is large, the deformation in the substrate due to the relaxation in the buckled film is independent of the delamination width. On buckling the normal axial force in the film relaxes from the applied value, N , to the critical buckling value, N_c , and the substrate relaxes by an axial displacement, u_0 . The bending moment, M_0 , at the edge of the delamination causes a rotation, ϕ . In addition the change in axial force causes a rotation and the bending moment causes an axial displacement. The compliances are defined by

$$\begin{aligned} u_0 &= \frac{(N - N_c)}{\bar{E}} A_{11} + \frac{M_0}{\bar{E}h} A_{12} \\ \phi &= \frac{(N - N_c)}{\bar{E}h} A_{21} + \frac{M_0}{\bar{E}h^2} A_{22} \end{aligned} \quad (1)$$

where \bar{E} is the plane strain elastic modulus. The compliances depend upon the two Dundurs' parameters, α and β [4] and have been calculated by the finite element method. The first Dundurs' parameter, α , is the most important. Results are presented for $\beta=0$ when the stress intensity factors at the tip of the delamination are real and for an infinitely thick substrate are given by

$$\begin{aligned} K_I &= \sqrt{\frac{h}{2}} \left[2\sqrt{3} \frac{M_0}{h^2} \cos \omega - \frac{(N - N_c)}{h} \sin \omega \right] \\ K_{II} &= \sqrt{\frac{h}{2}} \left[2\sqrt{3} \frac{M_0}{h^2} \sin \omega + \frac{(N - N_c)}{h} \cos \omega \right] \end{aligned} \quad (2)$$

where ω is a function of α [3].

2.1. Buckling without cracking

The buckled deflection, w , of the delamination can be written as

$$w = \frac{12M_0}{\bar{E}h^3\lambda^2} \left[1 - \frac{\cos \lambda(b-x)}{\cos \lambda b} \right] \quad (3)$$

where $\lambda^2 = 12N_c / \bar{E}h^3$. The bending moment, M_0 , can be found by equating the rotation given by Eq. 1 to that given by Eq. 3 at $x=0$. The eigen value of λ can then be found from the change in length of the buckled form and the displacement given by Eq. 1. There are multiple eigen values

and the one chosen is that which gives the minimum potential energy with the constraint that $\lambda b < \pi$. The compliance A_{II} has the most effect on buckling. In the limit for a rigid substrate $\lambda b = \pi$.

For steady state tunnelling, the energy released by delamination and buckling is the difference between the energy stored well ahead of the buckle and that well behind it. The average energy release rate can be obtained from this difference. The local energy release rates can be obtained either from the stress intensity factors given in Eq. 2 or by differentiating the average values. For a rigid substrate the energy release rates are only dependent upon the ratio $\varepsilon/\varepsilon_c$ where ε_c is the critical buckling strain for a rigid substrate and is given by

$$\varepsilon_c = \frac{\pi^2}{12} \left(\frac{h}{b} \right)^2 \quad (4)$$

The average and local energy release rates, G_d , normalised by, $G_0 = \bar{E} \varepsilon^2 h / 2$ the energy release rate if all the strain energy in the film were released by the delamination, are plotted against $\sqrt{(\varepsilon/\varepsilon_c)}$, is plotted in Fig. 2. The square root is chosen rather than the ratio $\varepsilon/\varepsilon_c$ because the square root is proportional to the delamination width, b , for a given film thickness and strain.

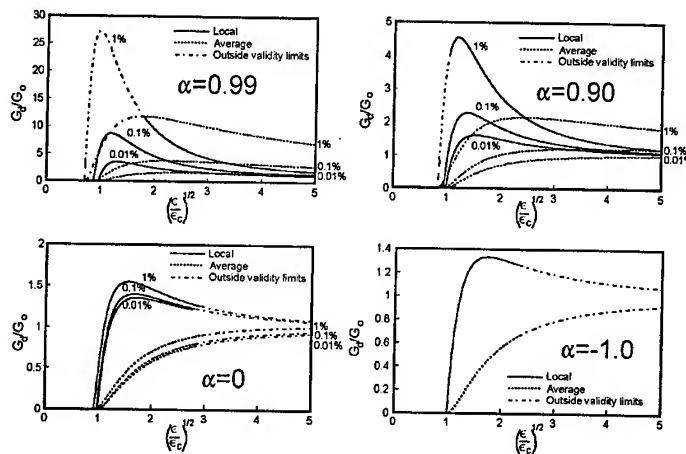


Fig. 2 Average and local energy release rates for delamination and buckling at indicated strains on substrates varying from very compliant ($\alpha=0.99$) to rigid ($\alpha=-1$).

The result for a rigid substrate ($\alpha=-1$) has already been given by Hutchinson and Suo [3]. On compliant substrates, the energy release rate is much greater than that for a rigid substrate. For ITO on a PET substrate $\alpha=0.97$. In addition even the average energy release rate has a maximum value when the substrate is compliant which limits the width of the delamination. There are two limits to the validity of the curves in Fig. 2: one limit arises from the assumption that b/h is large, and another limit arises at large values of b/h when there is compressive contact between the buckled delamination and the substrate [5,6]. The limits of validity are indicated in Fig. 2.

The mode-mixity angle defined by

$$\psi = \tan^{-1}(K_{II}/K_I) \quad (5)$$

has been calculated from Eq. 2 and is shown in Fig. 3. For compliant substrates, the mode-mixity

angle increases relatively slowly with delamination width. And it is suggested that the width, b , of the buckled delamination is limited more by the decrease in energy release rate with b than by the increase in mode-mixity. However, if the substrate is stiff then the Hutchinson and Suo [3] explanation that it is the increase in mode-mixity that limits b is reasonable.

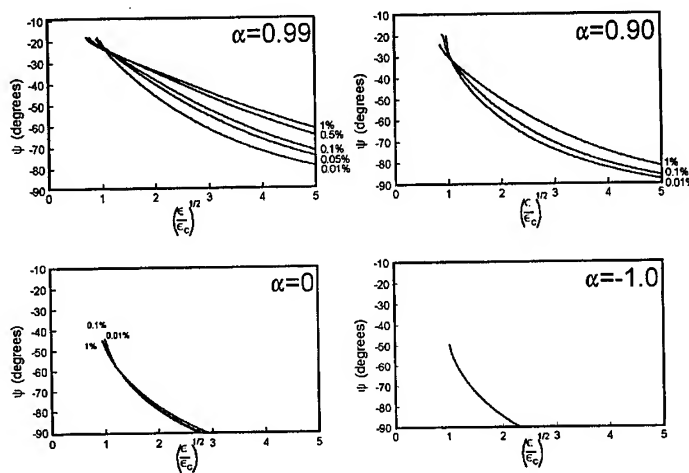


Fig. 3 Mode-mixity for delamination and buckling at indicted strains on substrates varying from very compliant ($\alpha=0.99$) to rigid ($\alpha=-1$).

2.2. Buckling with cracking

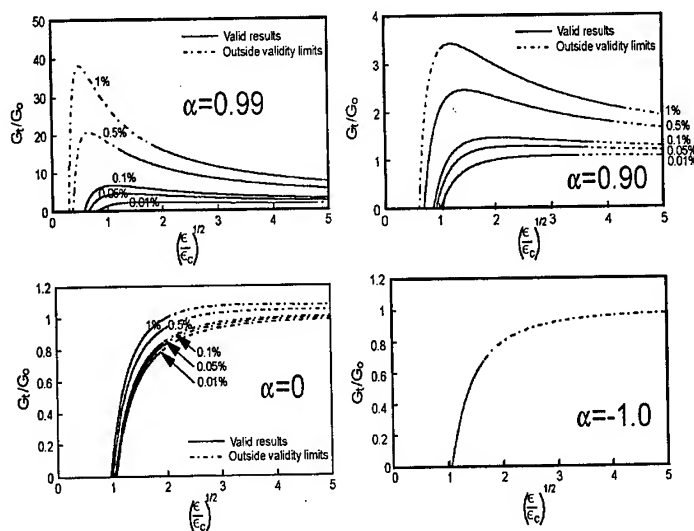


Fig. 4 The total energy release rates for delamination and buckling with cracking at indicted strains on substrates varying from very compliant ($\alpha=0.99$) to rigid ($\alpha=-1$).

The analysis follows closely on the work of Thouless [1] for rigid substrates, but it is assumed when cracking is complete the force acts through the bottom edge of the cracked film rather than at the centre of the film. The displacement of the buckled and cracked film can be written as

$$w = \frac{\phi}{\lambda} \sin \lambda x + (\delta - h/2)(1 - \cos \lambda x) \quad (6)$$

where δ is the deflection of the buckle at the cracked centre. The values of ϕ , δ , and λ can be found as in section 2.2. The average energy release rate, G_t , is a combination of the energy released by delamination, G_d , and the energy released by the cracking of the film, G_c , and is given by

$$G_t = G_d + G_c(h/2b) \quad (7)$$

The total energy release rate, G_t , is shown in Fig. 4; the limits of validity are indicated.

The mode-mixity has also been calculated and is shown in Fig. 5. The mode tends to pure mode II at smaller values of $\sqrt{(\varepsilon/\varepsilon_c)}$ than in the uncracked case, hence the width of the buckled delamination is more restricted

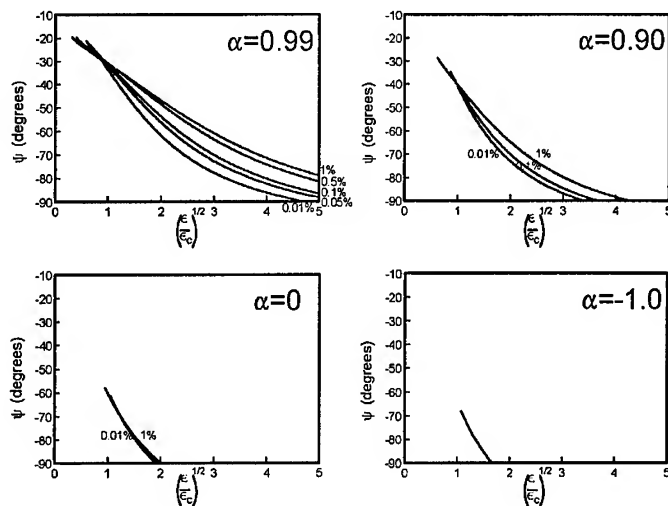


Fig. 5 Mode-mixity for delamination and buckling with cracking at indicted strains on substrates varying from very compliant ($\alpha=0.99$) to rigid ($\alpha=-1$).

3. DISCUSSION AND CONCLUSIONS

When thin films delaminate and buckle from compliant substrates under compressive strain, with or without cracking, the energy released from the substrate can be very much more than the energy stored in the film itself.

The explanation that delaminating and buckling films tunnel without increasing the width of the delamination due to increased mode-mixity is probably correct for films on stiff substrates.

However, the change in mode-mixity with increase in width of the delamination is much less pronounced for films on compliant substrates. However, on compliant substrates, the average energy release rate does exhibit a maximum with increase in width and hence in this case the width of the delamination is also limited because of the decrease in energy release rate.

The analysis of the delamination, buckling and cracking under compression has been used to estimate the interfacial delamination energy for ITO on a PET substrate. The total energy release rate given in Eq. 7 comes largely from the interfacial delamination energy and an estimate of the delamination energy can be obtained even if the film cracking energy is unknown. In this case film-cracking energy, 62 J/m^2 , was obtained from tension tests on the ITO film on a PET substrate. Using the value of $\alpha=0.97$ for ITO on a PET substrate and the measured delamination with, the interfacial delamination energy was estimated to be 35 J/m^2 which is seven times the value obtained if the compliance of the substrate is not taken into account.

REFERENCES

1. M.D. Thouless, J. Amer. Ceram. Soc., **76** (1993) p. 2936.
2. H.M. Jensen, Acta Metall. Mater., **41** (1993) p. 601.
3. J.W. Hutchinson and Z. Suo, Advances in Applied Mechanics, **29** (1991) p. 63.
4. J. Dundars, J. Appl. Mech., **36** (1969) p. 650.
5. M.D. Thouless, J.W. Hutchinson, and E.G. Linger, Acta Metall. Mater., **40** (1992) p. 2639.
6. R.G. Stringfellow and L.B. Freund, Int. J. Solids Struct., **30** (1993) p. 1379.

Recent Advances in Three-Dimensional Fracture Mechanics

W. Guo^{1,2}

¹The State Key Laboratory of Mechanical Strength and Engineering,
Xi'an Jiaotong University, Xi'an 710049, China P.R.

²Department of Aeronautical Engineering, Nanjing University of Aeronautics
and Astronautics, Nanjing 210016, China P.R.

Keywords: Constraints, Fracture Mechanics, J - Q - T_z Theory, Stress-Strain Fields, Thickness Effect, Three-dimensional Cracks

ABSTRACT

Some basic three-dimensional (3D) problems in fracture mechanics are discussed in this paper. Firstly, the interaction between the stress-strain fields and the out-of-plane constraint is analyzed. The weaker singularities of stresses at the crack border in both linear elastic and elastic-plastic materials are shown to be confined to an infinite small zone at the intersection point of the crack front line and the free surface of the cracked body. Therefore, the K -based linear elastic fracture mechanics theory and J -based nonlinear fracture mechanics theory can be extended to 3D cracked bodies. The influence of the out-of-plane constraint factor T_z on the crack tip fields was analyzed and the variations of some important fracture parameters from plane stress to plane strain state are summarized. Then, in consideration the influences of both the in-plane and out-of-plane constraints, a general J - Q - T_z or J - A_2 - T_z theory is proposed and proven to be more effective. Finally, the 3D effect on fracture of engineering materials is outlined.

1. FUNDAMENTAL EQUATIONS

For a 3D isotropic continuum without body force, the stress tensor σ and strain tensor ϵ should satisfy the equilibrium and compatibility equations

$$\sigma_{ij,j} = 0, \quad e_{mkl} e_{nij} \epsilon_{ki,jl} = 0. \quad (1)$$

Where $e_{ijk} = (i-j)(j-k)(k-i)/2$.

In the frame of deformation theory we have

$$\varepsilon_{ij} = \varepsilon_{ij}^e + \varepsilon_{ij}^p = \frac{1 + \nu_{ep}}{E_s} S_{ij} + \frac{1 - \nu_{ep}}{E} \sigma_m \delta_{ij} \quad (2)$$

where E is the Young's module, E_s is secant module, ν_{ep} is the elastic plastic Poisson's ratio

$$\nu_{ep} = \frac{1}{2} - \left(\frac{1}{2} - \nu \right) \frac{E_s}{E} \quad (3)$$

Consider a sheet element in the normal plane of the crack front line at any point P on the line, the in plane strains can be get from (2) and (3) as

$$\begin{aligned} \varepsilon_{rr} &= \frac{1}{E_s} \left[(1 - \nu_{ep} Tz) \sigma_{rr} - \nu_{ep} (1 + Tz) \sigma_{\theta\theta} \right], \\ \varepsilon_{\theta\theta} &= \frac{1}{E_s} \left[(1 - \nu_{ep} Tz) \sigma_{\theta\theta} - \nu_{ep} (1 + Tz) \sigma_{rr} \right], \\ \varepsilon_{r\theta} &= \frac{1}{E_s} (1 + \nu_{r\theta}) \sigma_{r\theta}. \end{aligned} \quad (4)$$

And the out-of-plane strain can be written as

$$\varepsilon_{zz} = \frac{1}{E_s} (Tz - \nu_{ep}) (\sigma_{rr} + \sigma_{\theta\theta}). \quad (5)$$

At the tip of an open mode crack, $(\sigma_{rr} + \sigma_{\theta\theta}) > 0$, $\varepsilon_{zz} \leq 0$ and $\sigma_{zz} \geq 0$, so that

$$0 \leq Tz \leq \nu_{ep} \leq \frac{1}{2}. \quad (6)$$

When the Ramberg-Osgood constitutive relationship is assumed,

$$\nu_{ep} = \frac{1}{2} - \left(\frac{1}{2} - \nu \right) \frac{1}{1 + \alpha (\sigma_e / \sigma_0)^{n-1}}. \quad (7)$$

When the Maxwell stress functions ϕ_{ii} ($i=1,2,3$) are introduced, the stress tensor satisfying the equilibrium equation (1) can be expressed as

$$\sigma_{mn} = e_{mkl} e_{nij} \phi_{ij,kl}. \quad (8)$$

2. CORNER SINGULARITY OF 3D ELASTIC CRACKS

It has been shown by previous work that the near tip stresses can be expressed in form of variable separation for 2D cracks and in the interior of a 3D cracked body:

$$\sigma_{ij} = \sum_{k=1}^{\infty} A_k r^{\lambda_k} f_{ij}^{(k)}(\theta), \quad \lambda_k = \frac{k}{2} - 1. \quad (9)$$

At corner points where the crack front intersected with the free surfaces, weaker singularity was found in spherical coordinate (ρ, φ, ψ) :

$$\sigma_{ij} = A\rho^{-\lambda}\tilde{\sigma}(\varphi, \psi), \quad \lambda < 1/2. \quad (10)$$

So the dominate term of the Maxwell functions for general 3D cracks can be assumed as

$$\phi_{ii} = r^{f_i(z)}\tilde{\phi}_i(\theta, Tz), \quad Tz = Tz(r, \theta, z) \quad (11)$$

Substituting (11) into the compatibility equation (1) and using (6) it can be gotten finally that:

i) When $\frac{\partial Tz}{\partial z} < \infty$, the stress singularity is the same as in (9), or is $r^{-\frac{1}{2}}$.

ii) When $\frac{\partial Tz}{\partial z} \rightarrow \infty$, $r^{-\frac{1}{2}}$ singularity can not be determined. So only in this case a weaker singularity may exist.

For through-cracks in plates with thickness of $2h$ under tension, Tz satisfying the equilibrium and boundary conditions can be expressed as

$$Tz = \nu \left[1 - \left| \frac{z}{h} \right|^{g(r)} \right]^2 F(r/h). \quad (12)$$

Then by means of variational method, it can be found that the only stationary value of the complementary energy is $g(r) \rightarrow \infty$ at the tip of the crack. So that

$$Tz = \nu \left[1 - \left| \frac{z}{h} \right|^{\infty} \right]^2, \quad r \rightarrow 0. \quad (13)$$

or the Tz - z curve tends to a rectangle as $r \rightarrow 0$ (Fig.1). The region in which $\frac{\partial Tz}{\partial z} \rightarrow \infty$ is infinite small, so is the possible weaker singularity region.

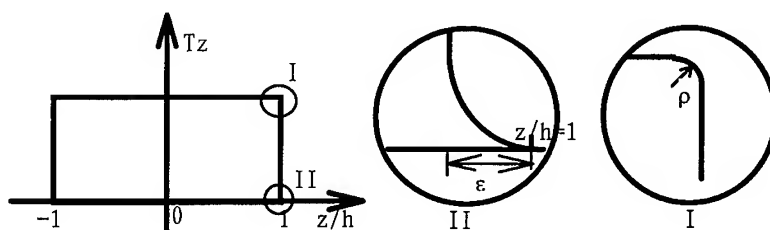


Fig.1 Through thickness variation of Tz ($\varepsilon \rightarrow 0$ & $\rho \rightarrow 0$ as $r \rightarrow 0$)

3. 3D ELASTOPLASTIC CRACK BORDER FIELDS

3.1 Singular Structure of the Fields

Under 3D condition, the dominate term of the crack border stresses can be assumed as

$$\sigma_{ij} = r^{f_{ij}(z)} \tilde{\sigma}_{ij}(\theta, Tz), \quad Tz = Tz(r, \theta, z) \quad (14)$$

By using the basic equations of the problem as well as the properties of Tz , it can be found that:

i) Providing $\frac{\partial Tz}{\partial z} < \infty$, the singularity and angular distribution of stresses and strains are functions of the triaxial stress constraint Tz , that is

$$\sigma_{ij} = Kr^{f-2} \tilde{\sigma}_{ij}(\theta, Tz), \quad \varepsilon_{ij} = \frac{3}{2} \alpha K^n r^{f-2} \tilde{\varepsilon}_{ij}(\theta, Tz), \quad (i, j = 1, 2) \quad (15)$$

and

$$\sigma_{zz} = Tz Kr^{f-2} (\tilde{\sigma}_{xx} + \tilde{\sigma}_{yy}), \quad \varepsilon_{zz} = \left(Tz - \frac{1}{2} \right) K^n r^{n(f-2)} \tilde{\varepsilon}_{zz}(\theta, Tz) \quad (16)$$

The traverse shear stresses and strains are one order lower as $r \rightarrow 0$. In this case the problem can be simplified to a quasi-planar problem with Tz being considered. This makes it possible to solve the problem analytically.

ii) In the case of $\frac{\partial Tz}{\partial z} \rightarrow \infty$, singular structure of the fields can not be settled. It is similar to the corner problem in 3D elastic cracks. Again, this region will be infinite small and not important in application.

3.2 Asymptotic Solution Under Triaxial Stress Constraint

In the case of $\frac{\partial Tz}{\partial z} < \infty$, all of the singular stresses in a 3D cracked body bear relation to only one stress function ϕ_{33} , and it can be get from (14) that

$$\phi_{33} = Kr^{f(z)} \tilde{\phi}(\theta, Tz), \quad (17)$$

where $f(z)$ is a function of Tz .

Substituting (17) into (8), (2) and (1), the governing equation in a strain hardening material can be obtained under given Tz

$$\begin{aligned} & \frac{1+Tz}{3} \left\{ a_1 \left[\tilde{\sigma}_e^{n-1} (f^2 \tilde{\phi} + \tilde{\phi} \tilde{\phi}') \right] - \left[\tilde{\sigma}_e^{n-1} (f^2 \tilde{\phi} + \tilde{\phi} \tilde{\phi}') \right]' \right\} + \left[\tilde{\sigma}_e^{n-1} (f \tilde{\phi} + \tilde{\phi}') \right]' \\ & + a_2 \left(\tilde{\sigma}_e^{n-1} \tilde{\phi}' \right) + n(f-2) \left[\tilde{\sigma}_e^{n-1} (a_3 \tilde{\phi} + \tilde{\phi}') \right] = 0 \end{aligned} \quad (18)$$

where $(\cdot)' = \frac{\partial}{\partial \theta}$, a_i are functions of f and n .

For a stress free mode I crack in homogeneous continuum, the problem can be summarized as a two point boundary problem of (18) with

$$\tilde{\phi}(\pi) = \tilde{\phi}'(\pi) = \tilde{\phi}'''(0) = \tilde{\phi}'(0) = 0. \quad (19)$$

Solution of (18) and (19) shows that both the exponent of singularity f and angular distributions of the fields change with Tz . $(f-2)$ is highest at $Tz=0$ and 0.5 and agrees with 2D HRR solution, but when $0 < Tz < 0.5$, the singularity becomes weaker and Rice's line energy integral J will no longer be path independent. The amplitude coefficient K is related to J by

$$J = \alpha \varepsilon_0 \sigma_0 K^{n+1} r^{(n+1)(f-2)} I(n, Tz). \quad (20)$$

Substituting (20) into (15) leads to

$$\begin{aligned} \sigma_{ij} &= \left[\frac{J}{\alpha \varepsilon_0 \sigma_0 I(n, Tz) r} \right]^{1/(n+1)} \tilde{\sigma}_{ij}(\theta, Tz), \\ \varepsilon_{ij} &= \frac{3}{2} \alpha \left[\frac{J}{\alpha \varepsilon_0 \sigma_0 I(n, Tz) r} \right]^{n/(n+1)} \tilde{\varepsilon}_{ij}(\theta, Tz). \end{aligned} \quad (21)$$

3.3 Distribution of Tz in Front of 3D Cracks

In front of a mode I through-crack in finite thick plate, Tz can be predicted very well by the following expression (where $\xi = r/2h$)

$$Tz = \nu_{cp} \left(1 - 1.218 \xi^{1/2} - 0.359 \xi + 0.361 \xi^{3/2} \right) \left[1 - \left| \frac{z}{h} \right|^{0.94 \xi^{-0.58}} \right]^2 \quad (22)$$

Substituting (22) into (21), 3D stress and strain fields near the tip of a real crack can be predicted.

3.4 Effect of 3D Constraint on Interface Crack Tip Fields

From (22) and (3) it can be seen that Tz will change with materials. Then in the case of crack on the interface of two different materials, crack tip fields may be affected by the change of Tz from one material to another.

Our investigation on the near tip fields of cracks lying on the interface of two strain hardening materials under 3D stress constraints has shown strong effects of Tz on the continuities and singularities of the radial and equivalent stresses.

4. J - A_2 - Tz THEORY

4.1 Out-of-plane and In-plane Constraint of Plane Strain Cracks

In plane strain state, $\epsilon_{zz}=0$. So from (5) and (7) it can be get that

$$Tz = \nu_{ep} = \frac{1}{2} - \left(\frac{1}{2} - \nu \right) \frac{1}{\alpha} \left(\frac{\sigma_0}{\sigma_e} \right)^{n-1} \quad (23)$$

Therefore, the in-plane stress-strain fields are coupled with Tz . This coupling relation is hard to be revealed properly by the asymptotic solutions. Based on the higher order solution which can match the in-plane constraint very well and the above analysis we propose the following J - A_2 - Tz theory

$$\begin{aligned} \sigma_{ij} &= \left[\frac{J}{\alpha \epsilon_0 \sigma_0 I r} \right]^{\frac{n}{n+1}} \tilde{\sigma}_{ij}(\theta) + A_2 \left[r^{\frac{n}{2}} \hat{\sigma}_{ij}(\theta) + A_2 r^{\frac{n}{2}} \bar{\sigma}_{ij}(\theta) \right], \quad (i, j = 1, 2) \\ \sigma_{33} &= Tz(\sigma_{11} + \sigma_{22}), \quad (Tz = \nu_{ep}) \\ \sigma_e &= \left[(1 - Tz + Tz^2)(\sigma_{11}^2 + \sigma_{22}^2) - (1 - 2Tz - 2Tz^2)\sigma_{11}\sigma_{22} + 3\sigma_{12}^2 \right]^{\frac{1}{2}}. \end{aligned} \quad (24)$$

When a J - Q representation is used to replace the J - A_2 solution in (24), a J - Q - Tz theory can be obtained.

4.2 J - A_2 - Tz Theory for General 3D Cracks

For general three-dimensional cracks, the constraints consist of the in-plane constraint as well as the out-of-plane constraint.

i) Out-of-plane constraint

The out-of-plane constraint is defined as the stress constraint out of the plane of the sheet element in consideration. It can be represented by Tz . For general 3D cracks the real distribution of Tz of the cracked body should be used. For through-thick cracks, Tz is given by eq.(22).

ii) In-plane constraint

In-plane constraint is defined as the constraint caused by the boundary conditions of the sheet element. The J - Q representation or higher order solutions can be used to match the in-plane stresses for various in-plane constraints.

Considering both of the in-plane and out-of-plane constraints, a J - A_2 - Tz or J - Q - Tz theory can also be proposed for general 3D crack problems:

- i) In-plane stresses σ_{ij} ($i, j=1, 2$): described by J - A_2 or J - Q theory.
- ii) The equivalent stress σ_e and σ_{zz} : determined by eq.(22) and the last two equations of (24).
- iii) Strain field and other parameters should be calculated on the basis of i) and ii).

Acknowledgment: This work is supported by the National Distinguished Young Scientist Fund of China and the Cheung Kong Scholars Programme. Limited by the space the references are not listed, gratitude is given to the contributors in this field.

Static Magnetoelastic Coupling in Soft Ferromagnetic Elastic Solids with Collinear Cracks

Wei Liang, Yapeng Shen and Minghao Zhao

The State Key Laboratory of Mechanical Structural Strength and Vibration,
Xi'an Jiaotong University, Xi'an 710049, China P.R.

Keywords: Collinear Cracks, Infinite Plate, Magnetoelasticity, Plane Problem, Soft Ferromagnetic Materials

ABSTRACT

By applying the linearized theory of Pao and Yeh [1], the governing equations are derived for determining the magnetoelastic coupling between through cracks in soft ferromagnetic elastic solids and magnetic fields. Using the complex potentials, the explicit solution of coupling fields for the ferromagnetic solid with collinear cracks is derived by employing singular integral equation technique.

1. INTRODUCTION

The general theory of interaction between induced magnetization and reformation was developed on the basis of continuum mechanic and the classical theory of magnetism [2]. In the work [1], the perturbation of magnetic field generated by deformation are assumed to be very small and magnetic quantities are decomposed into two parts. A linear theory for ferromagnetic deformable solids is then developed for small deformation in a quasi-static state [3,4]. By employing Fourier transform, the magnetoelastic crack problems for the case of the magnetic field normal to the crack was analyzed [5,6]. Closed form solution was also obtained [7] for the magnetic field generated by mechanical singularity in a half plane. Complete solution for linear magnetoelastic coupling in half space was found by developing the Papkovitch-Neuber solution of elasticity [8]. As well known, complex potentials is valuable for analyzing crack problems [9]. In this paper, complex potential solution is derived for magnetoelastic field in a ferromagnetic elastic materials. The crack problem in soft ferromagnetic materials is then obtained by solving the singular integral equation problems.

2. THE LINEAR THEORY

For a ferromagnetic deformable material in magnetic field, the deformation is coupling with the magnetic field. The effect of the coupling field on the material can be expressed in terms of the magnetoelastic stress tensor, t_{ij} . The field equation of the magnetoelasticity can be expressed as following for the case $|m_i| \ll |M_j u_{i,j}|$.

$$\begin{aligned} t_{ij,i} + \mu_0 (\overline{M}_i \overline{H}_{j,i} + \overline{M}_i h_{j,i} + m_i \overline{H}_{j,i}) &= 0 \\ e_{ijk} \overline{H}_{k,j} &= 0, \overline{B}_{i,j} = 0, e_{ijk} h_{k,j} = 0, b_{i,i} = 0 \end{aligned} \quad (1)$$

where \overline{H}_i and h_i are respectively the magnetic intensity in the rigid state and perturbed state, The permutation tensor is e_{ijk} , and comma denotes partial derivative with respect to the spatial variable. The linear constitutive relations of an isotropic solid with the magnetostrictive neglected are [6]

$$\begin{aligned} t_{ij} &= \sigma_{ij} + \frac{\mu_0}{\chi} \overline{M}_i \overline{M}_j + \frac{\mu_0}{\chi} (\overline{M}_i m_j + \overline{M}_j m_i) \\ \sigma_{ij} &= \lambda \delta_{ij} u_{k,k} + G(u_{i,j} + u_{j,i}) \\ \overline{M}_i &= \chi \overline{H}_i, \overline{B}_i = \mu_0 (\overline{H}_i + \overline{M}_i) = \mu_0 \mu_r \overline{H}_i \\ m_i &= \chi h_i, b_i = \mu_0 (h_i + m_i) = \mu_0 \mu_r h_i \end{aligned} \quad (2)$$

where u_i is the displacement while σ_{ij} is the Cauchy stress. $\mu_0 = 4\pi \times 10^{-7}$ N/A², $\mu_r = 1 + \chi$ is the relative magnetic permeability and λ and G are Lamé constants.

The continuity conditions on a jump plane of the linear theory are

$$\begin{aligned} e_{ijk} n_j [[\overline{H}_i]] &= 0, n_i [[\overline{B}_i]] = 0, e_{ijk} (n_j [[h_k]] - n_p u_{p,j} [[\overline{H}_i]]) = 0 \\ n_i [[b_i]] - n_p u_{p,i} [[\overline{B}_i]] &= 0, n_i [[t_{ij}]] = \frac{1}{2} \mu_0 n_j [[\overline{M}_n^2]] + \mu_0 n_j [[\overline{M}_n m_n]] \end{aligned} \quad (3)$$

where, $M_n = M_i n_i$, $m_n = m_i n_i$. The unite vector of the boundary is n_i . The symbol $[[\]]$ represents a discontinuity jump.

3. THE COMPLEX POTENTIALS

Consider an infinite soft ferromagnetic elastic solid with a number of collinear through cracks subjected to in-plane magnetic field and mechanical load at infinity (Fig.1). The x-axis of coordinate lying in the line of the cracks. The material are assumed to be homogeneous and isotropic.

From the theory related in the last section, it can be derived that the magnetic field in the materials is in-plane, $\overline{B}_3 = b_3 = 0$. Introducing harmonic magnetic potential function $\xi(x, y)$, and letting

$$h_x = \frac{\partial \xi}{\partial x}, h_y = \frac{\partial \xi}{\partial y} \quad (4)$$

where

$$\nabla^2 \xi = 0 \quad (5)$$

From continuity condition in Eqs.3, one can obtain that the quantities of \overline{H}_1 and \overline{B}_2 are no change between the two side of the jump plane with $n=(0,1,0)$. Thus, from Eqs.1, the solution for

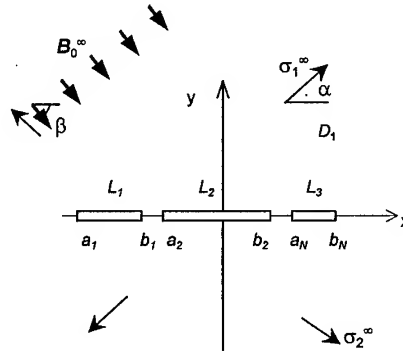


Fig.1 Collinear cracks subject to applied magnetic field and loads

the rigid body sates in the original configuration are obtained as

$$\overline{H}_1 = H_1^\infty, \quad \overline{B}_2 = B_2^\infty \quad (6)$$

Putting Eq.4, Eq.5 and Eq.6 into Eq.1, it yields that

$$\begin{aligned} \frac{\partial \sigma_{xx}}{\partial x} + \frac{\partial \sigma_{xy}}{\partial y} + 2\mu_0 \chi \left(\overline{H}_1 \cdot \frac{\partial^2 \xi}{\partial x^2} + \frac{\overline{B}_2}{\mu_0 \mu_r} \frac{\partial^2 \xi}{\partial x \partial y} \right) &= 0 \\ \frac{\partial \sigma_{xy}}{\partial x} + \frac{\partial \sigma_{yy}}{\partial y} + 2\mu_0 \chi \left(\overline{H}_1 \cdot \frac{\partial^2 \xi}{\partial x \partial y} + \frac{\overline{B}_2}{\mu_0 \mu_r} \frac{\partial^2 \xi}{\partial y^2} \right) &= 0 \end{aligned} \quad (7)$$

The solution of the above can be represented by the stress function,

$$\sigma_{xx} = \frac{\partial^2 \Phi}{\partial y^2} + V, \quad \sigma_{xy} = -\frac{\partial^2 \Phi}{\partial x \partial y}, \quad \sigma_{yy} = \frac{\partial^2 \Phi}{\partial x^2} + V \quad (8)$$

where

$$V = -2\mu_0 \chi \left(\overline{H}_1 \cdot \frac{\partial \xi}{\partial x} + \frac{\overline{B}_2}{\mu_0 \mu_r} \frac{\partial \xi}{\partial y} \right) \quad (9)$$

In Eq.8, the stress σ_{ij} satisfy the equations of compatibility to ensure the existence of single value of displacement. Making use of Eq.2, Eq.5, and Eq.8, the equation of compatibility for the magnetoelastic problem can be represented by the same form as in elasticity

$$\nabla^4 \Phi = 0 \quad (10)$$

Employing the theory of analytic functions, the general solution to Eq.10 and Eq.5 can be represented by

$$\Phi = 2 \operatorname{Re}(\overline{z} \varphi(z) + \zeta(z)), \quad \xi(z) = \operatorname{Re}(\omega(z)) \quad (11)$$

where $z=x+iy$, $\varphi(z), \omega(z), \zeta(z)$ are analytic complex functions.

Similar to Muskhelishvili's complex representation of stress and displacement, the coupling field can be written as

$$\begin{aligned} \sigma_{xx} + \sigma_{yy} &= 2(\varphi'(z) + \overline{\varphi'(z)}) + c_3 \omega(z) + c_3 \overline{\omega'(z)} \\ \sigma_{yy} - \sigma_{xx} + 2i\sigma_{xy} &= 2((\overline{z} - z)\varphi''(z) - \varphi'(z) + \Omega'(z)) \\ 2G(u_x + iu_y) &= \kappa \varphi(z) - (z - \overline{z})\overline{\varphi'(z)} - \overline{\Omega(z)} + \beta c_3 \omega(z) \\ h_x - ih_y &= \omega'(z) \end{aligned} \quad (12)$$

where

$$\begin{aligned} \kappa &= 3 - 4\nu \text{ and } \beta = 2(1 - 2\nu) \text{ for the plane strain,} \\ \kappa &= (3 - \nu)/(1 + \nu), \beta = 2(1 - \nu)/(1 + \nu) \text{ for plane stress;} \\ \Omega(z) &= z\varphi(z) - \zeta'(z), c_3 = C_1 + iC_2 = -\mu_0 \chi \overline{H}_1 + i\chi \overline{B}_2 / \mu_r \end{aligned}$$

Putting Eq.11 and Eq.12 into Eq.3, The boundary conditions on a plane normal to y-axis can be obtained. For the case of the out side is vacuum, it is reduced to

$$\begin{aligned} (1 + \frac{\chi}{2})\omega'(z) - \frac{\chi}{2}\overline{\omega'(z)} - \frac{1}{\mu_0}ic_3\frac{\partial u_y}{\partial x} &= \omega^{*'}(t) \\ \llbracket \sigma_{yy} - i\sigma_{xy} \rrbracket &= \gamma + (C_2(\chi - 2) - iC_1)h_y + iC_2h_x \end{aligned} \quad (13)$$

where $\gamma = (C_2^2(\chi - 2) - iC_1C_2)/(2\mu_0\chi)$, the quantity with a prime of '*' is the quantity in the vacuum side and $\sigma_{yy} - i\sigma_{xy}$ are functions of $\omega(z)$, $\varphi(z)$ and $\Omega(z)$,

$$\sigma_{yy} - i\sigma_{xy} = (z - \bar{z})\overline{\varphi''(z)} + \varphi'(z) + \overline{\Omega'(z)} + c_3\overline{\omega(z)} + c_3\overline{\omega'(z)}$$

4. THE SOLUTION FOR COLLINEAR CRACKS

It can be regarded that the effect of cracks on the stress and magnetic fields far from the crack is neglectable. Then the fields at infinity can be represented by the applied magnetic field and load.

$$\begin{aligned} \overline{H_1} &= H_1^\infty, \overline{B_2} = B_2^\infty, h_x(\infty) = h_y(\infty) = 0 \\ \sigma_{xx}^\infty + \sigma_{yy}^\infty &= 4B, \quad (\sigma_{yy}^\infty - \sigma_{xx}^\infty + 2i\sigma_{xy}^\infty) = 2B' \end{aligned} \quad (14)$$

where H_1^∞ and B_2^∞ denote the magnetic quantities at infinity. σ_{ij}^∞ is the stress in the region where the effect of cracks are neglectable, which represents the resultant of the mechanical loads and the force of magnetic field on the materials in the region.

The cracks are defined by the $L: \{(t,0): a_k \geq t \geq s_k, k=1,2, \dots, N\}$. The complex functions $\varphi(z)$, $\omega(z)$ and $\Omega(z)$ are analytic in the Region D_1 , that is the complex plane except L . On the up faces of the cracks and on the down faces of the cracks, the boundary conditions are respectively

$$\begin{aligned} \kappa\varphi'(t)^+ - \kappa\overline{\varphi'(t)}^- + \Omega'(t)^+ - \overline{\Omega'(t)}^- + C_7\omega'(t)^+ + C_8\overline{\omega'(t)}^- &= c_5\omega^{*'}(t) \\ \varphi'(t)^+ + \overline{\Omega'(t)}^- + C_9\omega'(t)^+ + C_{10}\overline{\omega'(t)}^- &= \gamma \end{aligned} \quad (15)$$

$$\begin{aligned} \kappa\varphi'(t)^- - \kappa\overline{\varphi'(t)}^+ + \Omega'(t)^- - \overline{\Omega'(t)}^+ + C_7\omega'(t)^- + C_8\overline{\omega'(t)}^+ &= c_5\omega^{*'}(t) \\ \varphi'(t)^- + \overline{\Omega'(t)}^+ + C_9\omega'(t)^- + C_{10}\overline{\omega'(t)}^+ &= \gamma \end{aligned} \quad (16)$$

where

$$\begin{aligned} c_5 &= \frac{-4\mu_0G}{c_3}, \quad c_7 = \beta\overline{c_3} + \frac{c_3(\chi+2)}{2}, \quad c_8 = -\beta c_3 - \frac{c_3\chi}{2} \\ c_9 &= \frac{1}{2}(C_1 + iC_2(\chi+1)), \quad c_{10} = \frac{1}{2}(3C_1 - iC_2(\chi-1)) \end{aligned} \quad (17)$$

Combine of Eq.15 and Eq.16 are equivalent to the following equations

$$\begin{aligned} [\kappa\varphi'(t) + \Omega'(t) + C_7\omega'(t)]^+ - [-\kappa\overline{\varphi'(t)} - \overline{\Omega'(t)} + C_8\overline{\omega'(t)}]^+ \\ - [\kappa\varphi'(t) + \Omega'(t) + C_7\omega'(t)]^- - [-\kappa\overline{\varphi'(t)} - \overline{\Omega'(t)} + C_8\overline{\omega'(t)}]^- = 0 \end{aligned}$$

$$\begin{aligned}
& [\kappa\varphi'(t) + \Omega'(t) + C_7\omega'(t)]^+ + [-\kappa\bar{\varphi}'(t) - \bar{\Omega}'(t) + C_8\bar{\omega}'(t)]^+ \\
& + [\kappa\varphi'(t) + \Omega'(t) + C_7\omega'(t)]^- + [-\kappa\bar{\varphi}'(t) - \bar{\Omega}'(t) + C_8\bar{\omega}'(t)]^- = 2c_5\omega^*(t) \\
& [\varphi'(t) + C_9\omega'(t)]^+ - [\bar{\varphi}'(t) + C_{10}\bar{\omega}'(t)]^+ = [\varphi'(t) + C_9\omega'(t)]^- - [\bar{\varphi}'(t) + C_{10}\bar{\omega}'(t)]^- \\
& [\varphi'(t) + C_9\omega'(t)]^+ + [\bar{\varphi}'(t) + C_{10}\bar{\omega}'(t)]^+ + [\varphi'(t) + C_9\omega'(t)]^- + [\bar{\varphi}'(t) + C_{10}\bar{\omega}'(t)]^- = 2\gamma
\end{aligned} \quad (18)$$

The value of the functions at infinity are deduced from Eqs.14. The solution for Eqs.18 can be obtained by using the singular integral equation technique [10].

$$\begin{aligned}
\omega(z) &= c_{11} + c_{12}z^N X(z) + \sum_{k=0}^{N-1} d_{1k}z^k X(z) \\
\varphi(z) &= c_{21} + c_{22}z^N X(z) + \sum_{k=0}^{N-1} d_{2k}z^k X(z) \\
\Omega(z) &= c_{31} + c_{32}z^N X(z) + \sum_{k=0}^{N-1} d_{3k}z^k X(z)
\end{aligned} \quad (19)$$

where, $X(z)$ is the basic solution of the problem. The branch for $\lim_{|z| \rightarrow \infty} z^N X(z) = 1$ is

$$X(z) = \prod_{k=1}^N (z - s_k)^{-1/2} (z - a_k)^{-1/2} \quad (20)$$

the constants are

$$\begin{aligned}
c_{11} &= (-2B(1+\kappa) - \bar{B}' + \frac{1}{2}(-1+\kappa)(-\bar{B}' - B') - B'(-\bar{c}_7 - c_8)/d + \frac{1}{2}c_{14}(\gamma + \bar{\gamma})) \\
c_{12} &= \frac{1}{2}c_{14}(4B + B' + \bar{B}') - \frac{1}{2}c_{14}(\gamma + \bar{\gamma}), \quad c_{14} = (-\bar{c}_7 - c_8)(1+\kappa)/d \\
c_{21} &= -\frac{1}{2}\bar{B}' - c_9c_{11} + \frac{1}{2}\gamma, \quad c_{22} = -\frac{1}{2}(2B + \bar{B}') - c_9c_{12}\gamma \\
c_{31} &= -\frac{1}{2}B' - \bar{c}_{10}c_{11} + \frac{1}{2}\bar{\gamma}, \quad c_{32} = -\frac{1}{2}(2B + B') - \bar{c}_{10}c_{12} - \frac{1}{2}\bar{\gamma} \\
d_{1k} &= c_{14}(q_{2k} + \bar{q}_{2k}) - \frac{1}{2}\gamma d_{0k}, \quad d_{2k} = q_{2k} - c_9d_{1k} - \frac{1}{2}\gamma d_{0k} \\
d_{3k} &= \bar{q}_{2k} - \bar{c}_{10}d_{1k} - \frac{1}{2}\bar{\gamma} d_{0k} \\
d_{0k} &= \sum_{j=1}^{N-k} (-\vartheta_j), \text{ with } \vartheta_m = \begin{cases} s_m, & m=1,2,\dots,N \\ a_m, & m=(N+1),(N+2),\dots,2N \end{cases}
\end{aligned} \quad (21)$$

and q_{2k} are determined by the following algebra equations

$$\sum_{k=1}^{N-1} (\kappa d_{2k} - d_{2k} + \beta \bar{c}_3 d_{3k}) \int_{s_m}^{a_m} z^k X^+(x) dx = 0, \quad \sum_{k=1}^{N-1} d_{3k} \int_{a_m}^{s_m} z^k X^+(x) dx = 0, \quad m=1,2,\dots,N \quad (22)$$

In the above, the single-valued of displacement and magnetic potential function along the closed curve enclosing every crack are used.

Thus, the stress, displacement and perturbation of magnetic field are obtained by substituting Eqs.19 into Eqs.12

$$\sigma_{xx} + \sigma_{yy} = 4\text{Re} \left(c_{21} + \bar{c}_3 c_{11} + (c_{22} + \bar{c}_3 c_{12}) z^N X(z) + \sum_{k=0}^{N-1} d_{2k} + \bar{c}_3 d_{1k} + z^k X(z) \right)$$

$$\begin{aligned}
\sigma_{yy} - \sigma_{xx} + 2i\sigma_{xy} = & 2 \left(-c_{21} + c_{31} - (c_{22} - c_{32})z^N X(z) + \sum_{k=0}^{N-1} d_{1k} z^k X(z) \right. \\
& \left. + (-z + z) \left(c_{22} (Nz^{N-1} X(z) + z^N X'(z)) + \sum_{k=0}^{N-1} d_{2k} (kz^{k-1} X(z) + z^k X'(z)) \right) \right) \\
h_x - ih_y = & \left(c_{11} + c_{12} z^N X(z) + \sum_{k=0}^{N-1} d_{1k} z^k X(z) \right)
\end{aligned} \quad (23)$$

An infinite crack defined the interval $-a < x < a$ is considered as a examples. The stress fields are get by reducing Eq.23. The singular stress near a crack tip can be obtained by letting $r \rightarrow 0$, $z = a + re^{i\theta}$. The result shows that the stress singularity is inversely proportional to the square root of the radius from the crack tip, which is same as the result in [5]. A rectangular crack plate with biaxial tension

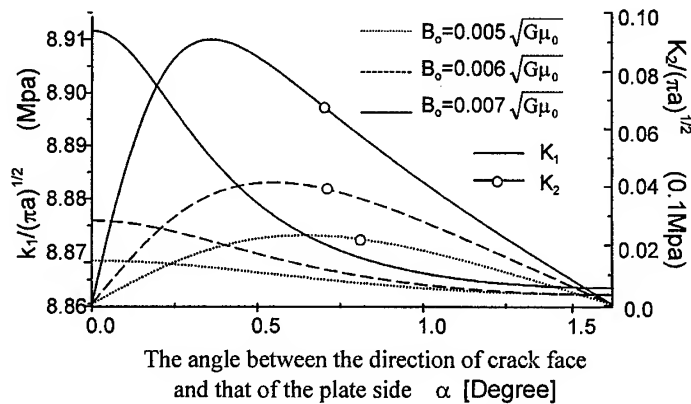


Fig.2 The stress singularity for a magnetoelastic crack problem

$p=8.862\text{MPa}$ to be in magnetic field normal to one side of the plate is considered. The stress singularity are described in Fig.2, which shows magnetic field have effect on the stress field near the crack tip.

REFERENCES

- 1 Y. H. PAO, C. S. YEH, *Int. J. Eng. Sci.*, **11**(1973) p.415
- 2 W. F. Brown Jr.: *Magnetoelastic Interactions*, Springer-Verlag, New York, (1966)
- 3 F. C. Moon, *Magneto Solid Mechanics*, John Wiley & Son Inc., New York, (1984).
- 4 Maugin, G. A., *Continuum Mechanics of electromagnetic solids*, North Holland (1988)
- 5 Y. Shindo, *ASME J. of Applied Mechanics*, **44**(1977) p.47
- 6 Y. Shindo, *Int. J. of Solid & Structures*, **46**(1980) p.537
- 7 C. S. YEH, *ASME J. of Applied Mechanics*, **56**(1989), p.89
- 8 K.F. Hang, M.Z. Wang, *ASME J. of Applied Mechanics* **62**(1995), p.930
- 9 G. C. Sih, *Methods of analysis and solutions of crack problem*, Noordhoff (1973)
- 10 N. I. Muskhelishvili, *Singular Integral Equations*. Wolters-Noorhoff., Groningen Netherlands. (1962)

A Study on Deformation Energy of P/M Copper and Ingot Material

T. Senthilvelan¹, A. Venkatraman¹ and K. Raghukandan²

¹ Department of Mechanical Engineering, Pondicherry Engineering College,
Pondicherry 605 014, India

² Department of Production Engineering, Annamalai University,
Annamalai Nagar 608 002, India

Keywords: Deformation Energy, Ingot Material, P/M Copper, Strain Hardening Exponent

ABSTRACT

Energy crisis is expected to be the major problem in the new millennium. Industries are the major consumers of energy in the form of electrical, mechanical, chemical etc. Especially metal forming industries are energy intensive industries. This paper aims at determining the requirement of deformation energy of P/M copper and ingot material at elevated temperatures in order to make comparative analysis.

1. INTRODUCTION

Powder metallurgy route of manufacturing gains momentum mainly because of material and energy savings due to easier recycling of swarf. The research work [1] indicates that there is 26.5% saving in the cost of manufacture of commutator sleeves by cold forming of sintered iron preforms compared to the extrusion of wrought parts. Kannan [2] has observed 11.5% and 16.5% reduction in cost and deformation energy respectively, when recycling the copper powder to make tubes by Hooker extrusion. In the research work [3], it is indicated that 50% of energy is saved when manufacturing differential pinions through powder metallurgy process instead of wrought material. However not much work has been done so far in the comparison of deformation energy requirement between P/M and ingot material.

2. EXPERIMENTAL DETAILS

In the present investigation P/M copper preforms were prepared at three different density values viz., 7.00, 7.35 and 7.70 g/cc. The above preforms were sintered in endogas atmosphere at 1173 K for 60 minutes. Rings with dimensions in the ratio of 6:3:2 as Outer Diameter : Inner Diameter : Height were prepared to perform the standard ring compression tests. Rings with the above mentioned dimensions were prepared from ingot electrolytic copper also.

The above rings (both P/M and ingot material) were compressed at different temperatures ranging from room temperature to 1073 K in steps of 473 K. During compression, force vs. stroke plots were developed to determine the forming energy requirements. Optical micrographs were taken on the P/M and ingot material, compressed at elevated temperatures to obtain the structural – property correlation.

3 RESULTS AND DISCUSSION

3.1 Effect of Strain Hardening Exponent on Deformation Energy

The force vs. stroke diagrams for P/M copper and ingot copper are shown in Figures 1 and 2.

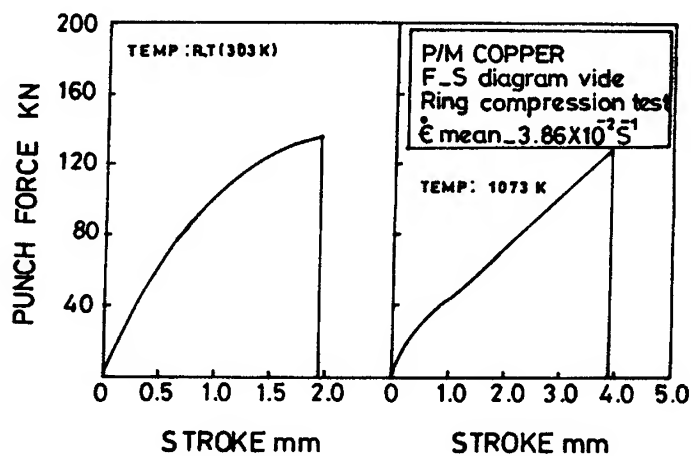


Fig.1 F – S diagram for P/M Copper

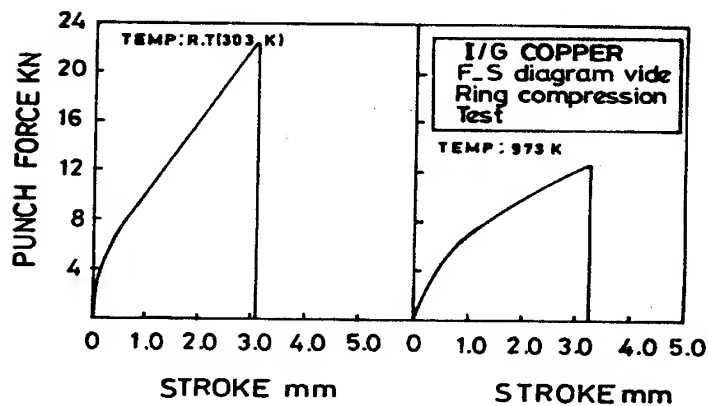
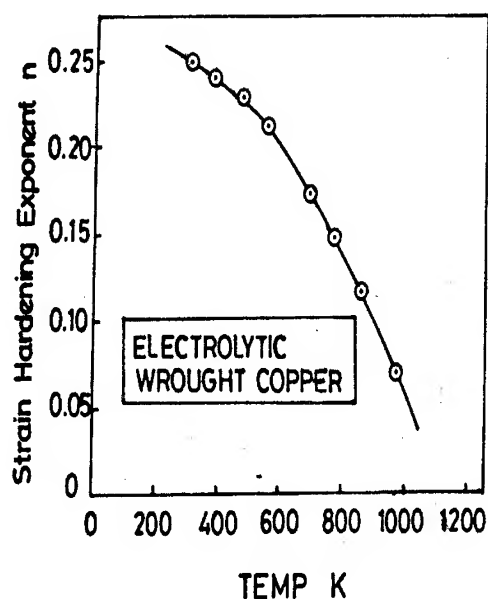
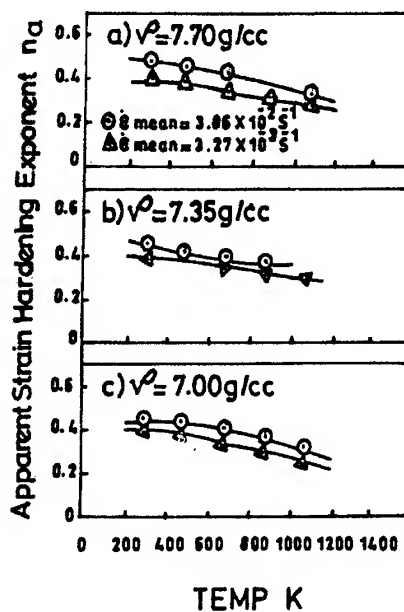


Fig. 2 F – S diagram for Wrought Copper

From the compression test data, strength co-efficient and strain hardening exponent for P/M copper (K_a , n_a) and ingot material (K , n) were calculated. The effect of forming temperature on the strain hardening exponent (n) for ingot material is shown in Fig. 3. Similarly for P/M copper, the effect of forming temperature on n_a is shown in Fig. 4. Generally when deforming ingot materials at very high temperatures, the material do not experience strain hardening and as a result, the value of n approaches zero but in the case of P/M materials n_a does not approach zero as temperature increases since persistent densification takes place [1]. This is evident from the Figures 3 and 4. Even at 1073 K for P/M materials the n_a value is 0.30 whereas in the case of ingot material the value of n at this temperature is not significant (0.05). Similar observation was made in the research work [2]. Higher the value of strain hardening exponent, more is the resistance for deformation and hence energy requirement is more.

Fig.3 Variation of n with TemperatureFig.4 Variation of n_a with Temperature

3.2 Effect of Temperature on Energy Requirements

Energy required for deformation with forming temperatures is shown in Fig.5 for different initial densities of P/M copper preforms and corresponding ingot material. It is seen that sintered preforms consume more energy than ingot material. This can be attributed to the following reasons:

- (i) In the research work [3], it is mentioned that after each working stage, the grain size of P/M material became markedly finer than that of wrought material. If the grain size is smaller, according to Hall-Petch equation, strength is higher which augments the resistance for deformation. This causes more energy requirement during deformation.

(ii) Forming force can be estimated from the Hollomon - Ludwick equation, which is widely used. This equation is,

$$\sigma = K_a \epsilon^{n_a} \quad [1]$$

where

σ = flow stress

ϵ = strain

K_a = strength co-efficient

n_a = strain hardening exponent

Due to pore closure, P/M material strain hardens more than that the wrought material. Hence the strain hardening exponent n_a is higher for P/M copper [4] than the ingot material. This causes more resistance for deformation and demands more force and energy.

From Fig. 5, it is also observed that the difference in the deformation energy requirement between P/M and ingot is more at lower temperatures and it gradually decreases at elevated temperatures. Because at higher temperatures, P/M material undergoes persistent densification and the density approaches to the theoretical value.

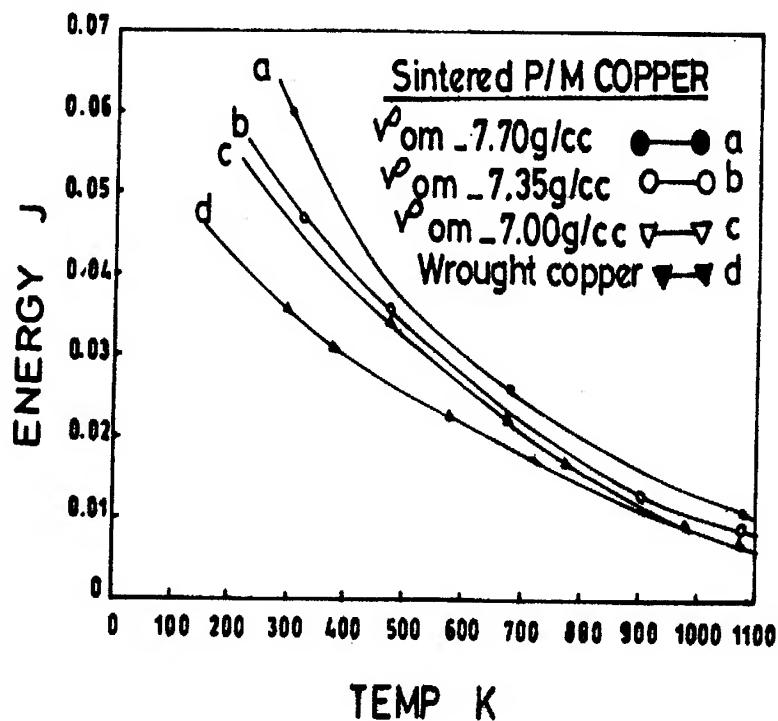
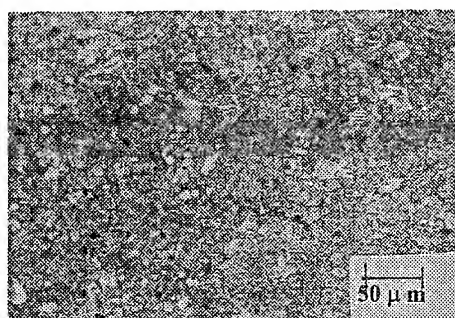
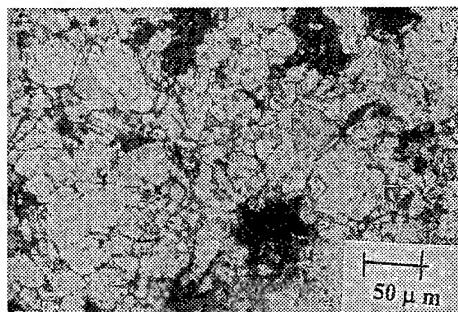
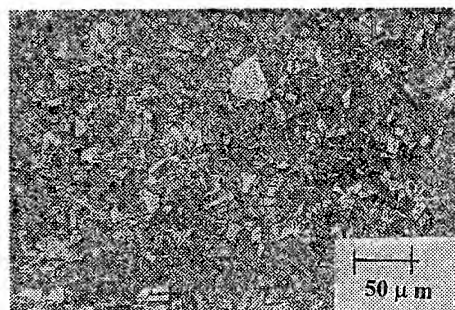
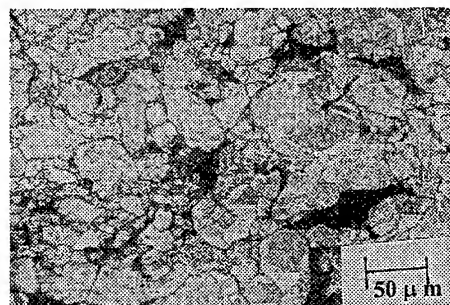
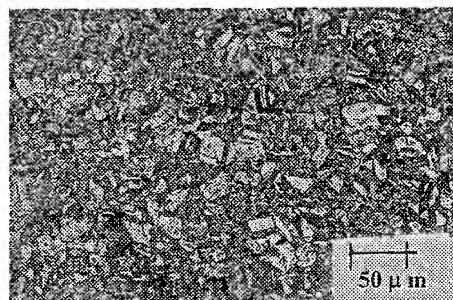
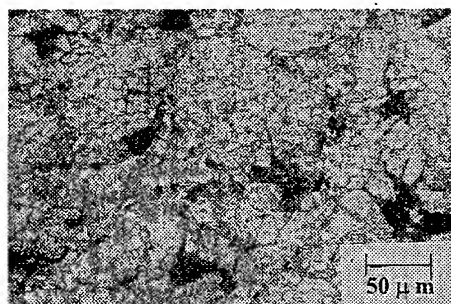
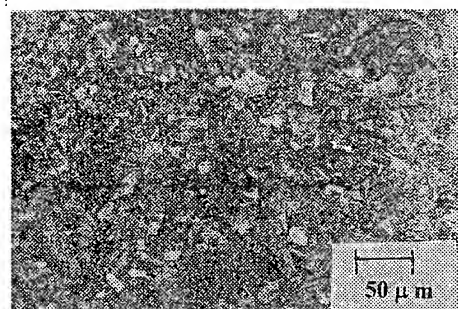
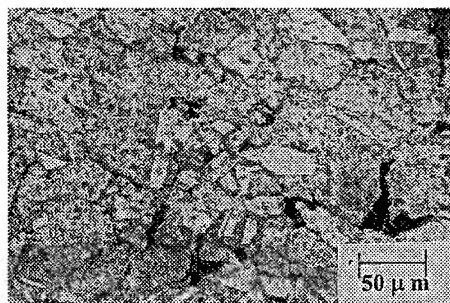


Fig.5 Comparison of Deformation Energy of P/M with Wrought Copper

Fig.6 Micrographs**303 K****303 K****473 K****473 K****673 K****673 K****873 K Ingot Copper****873 K P/M Copper**

3.3 Micrographs

Optical micrographs were taken on all the compressed ring specimens to obtain the structure-property correlation at elevated temperatures. The micrographs are shown in Fig. 6. In the copper ingot, twinning increases as temperature increases. Twinning starts at 473 K and completes at 673 K. Also, recrystallisation starts at 873 K.

In P/M copper, significant reduction in porosity is evident as the temperature increases. This may also consume more energy during deformation. At 873 K grain growth and twinning increase.

4. CONCLUSIONS

The following conclusions are drawn from this investigation:

- (1) Strain hardening exponent (n_a) is higher for P/M copper than the ingot material. Due to this the deformation energy requirement is more for P/M copper than the ingot material.
- (2) Preforms with lower initial density require more energy. This is due to higher value of strain hardening exponent for lower preform density.
- (3) Twinning and pore closure are observed in the micrographs taken on the ring specimens compressed at elevated temperatures.

REFERENCES

1. H.W. Antes, Progress in Powder Metallurgy, 28 (1972) p.5
2. S.D. Elwakil, 15th MTDR Conference, Birmingham, U.K. (1974) p.443
3. P.W. Taubenblatt and G. Goller, Source Book on Powder Metallurgy, ASM, 98 (1970) p.387
4. A. Kumar et.al., Tran. Indian Institute of Metals, 37 (1984) p.569

Fracture Analysis on the Coating Crack Perpendicular to the Interface of Bi-Material

B. Su and Ch. Li

Laboratory of Materials' Properties, Beijing Institute of Aeronautical Materials,
PO Box 81-23, Beijing 100095, China P.R.

Keywords: Coating Crack, Interface of Bi-Material, Stress Intensity Factor

ABSTRACT

The objectives of this paper are to study the fracture properties of a coating structure through analysis on the stress intensity factor of a coating crack perpendicular to the interface between the coating-material and the base-material, and arrested in the base-material. The weight function of the coating crack is given and the coefficients of the weight functions are determined. Using this weight function and the finite element method, the analytical expression of the stress intensity factors for the crack is given, and a good agreement between the calculated stress intensity factors by the weight function method and that by the finite element method is reached. The influences of the materials' properties and the geometrical dimensions on the stress intensity factors are analyzed and discussed.

1. INTRODUCE

In modern composites, such as the fiber strengthen Silicon-Carbide(SiC), coating cracks often appear in fiber layer and strongly influence the properties of the composite[1-2]. In Ref.[3-16], the singularity and the stress intensity factors of the singular stress fields around this kind of cracks were analyzed by different methods and some work has been done to analyze the effects of this kind of cracks on the properties of the fiber strengthening composites in Ref.[17]. But there seems no reports, at least rarely or not systematically, about the stress intensity factor of this kind of the coating crack, especially, about the influence of the geometrical dimensions and the materials' properties on stress intensity factors. So it is very necessary to carry out some researches on this subject.

2. GEOMETRICAL CONFIGURATION OF THE COATING CRACK

The geometrical configuration of the coating crack is shown in Fig. 1. M_1 and M_2 indicate the base material and the coating material, respectively. The crack is perpendicular to the interface of the base-material and the coating-material, the crack length(a) is equal to the coating thickness(t). The other geometrical dimensions are shown in Fig. 1. E_1 , E_2 , ν_1 and ν_2 denote the elastic module and Poisson's ratio of the base-material and the coating-material, respectively. The geometrical configuration is symmetrical and belongs to the pure mode I loading even though material inhomogeneity exists in the coating structure. So only mode I stress intensity factor K_I appears.

3. FINITE ELEMENT METHODS(FEM) FOR THE CALCULATION

The researches on the singularity of this kind of coating cracks have shown that the stress field near the crack-tip of this kind of the crack is still of the $1/\sqrt{r}$ singular property[18-19, 6-8]. So based on the theory of fracture mechanics, the eight node isoparameter element can be used to calculate the stress intensity factor of the coating crack[20, 22-23]. To get real stress intensity factor, the stress components ahead the crack-tip in the range within $r < 10^{-7}$ (mm) were at first calculated by the finite element method, then by the stress method[20, 22-23], the stress intensity factors are calculated. Tab. 1 shows the comparison between the stress intensity factors by this

method and the results in Ref.[21]. The crack is in homogeneous material and is subjected to mode I unit crack surface pressure. It can be seen that the stress intensity factors from both methods agree with each other very well. Further researches on the convergence and the exactness of this finite element method have been carried out in Ref.[18-19, 22-23]. The finite element program package Abaqus in Research Center of Karlsruhe, Germany, were used in the numerical calculations.

Tab. 1 Comparison Of The Stress Intensity Factors From Different Methods

$a/W(W/H_1=1)$	$K_I^{[20]}/\sigma\sqrt{a}$	$K_I/\sigma\sqrt{a}$	$(K_I^{[20]} - K_I)/K_I$
0.2500	2.6591	2.6110	0.01828
0.1750	2.33095	2.32651	0.00190
0.0999	2.10943	2.05105	0.02768
0.09167	2.09124	2.03399	0.02738
0.08571	2.07906	2.01937	0.02871
0.08125	2.07038	2.00492	0.03162
0.07778	2.06389	2.00192	0.03003
0.07599	2.06067	1.98026	0.03902

4. WEIGHT FUNCTION METHOD(WFM)

Based on the general principle of weight function methods[18, 22-23], for this kind of the coating crack under a arbitrary crack surface load ($P = P_x i + P_y j$), the stress intensity factor K_I can be calculated by the following equation:

$$K_I = \int_0^a P \cdot h_I dx \quad (1)$$

Here h_I is the weight function. If only the K_I factor will be calculated, h_I can be expressed as following[22]:

$$h_I = \sqrt{\frac{2}{\pi a}} \sum_{n=0}^{\infty} D_{I,n} \left(1 - \frac{x}{a}\right)^{n-\frac{1}{2}} \quad (2)$$

$D_{I,n}$ are coefficients of the weight function, which can be determined with the help of different conditions. In principle, all the coefficients $D_{I,n}$ can be determined with different conditions[18, 22-23]. However, it has been found that the three terms' weight functions are good enough to meet the needs of this kind of the coating cracks, and the first term's coefficient of the weight function has been analytically derived as following[18, 22-23]:

$$D_{I,0} = 1 \quad (3)$$

So the weight function for this kind of the coating crack can further be expressed as following:

$$h_I = \sqrt{\frac{2}{\pi a}} \left[\frac{1}{\sqrt{(1-x/a)}} + D_{I,1} \sqrt{(1-x/a)} + D_{I,2} (1-x/a)^{\frac{3}{2}} \right] \quad (4)$$

The second term's and the third term's coefficients can be determined in terms of the reference system shown in Fig. 2. In Fig. 2, the coating crack is acted by unit pressure. Based on the theory of the weight function[22-23] and the reference system, the second term's and the third term's coefficients are:

$$D_{I,1} = \frac{4}{5} \sqrt{\frac{\pi}{2}} Y_I - 2 \quad D_{I,2} = \frac{5}{12} \sqrt{\frac{\pi}{2}} Y_I - \frac{5}{3}$$

Here Y_I is geometrical function of the coating crack under the unit pressure. The geometrical functions can be calculated by the finite element method.

5. COMPARISON BETWEEN THE CALCULATED STRESS INTENSITY FACTORS BY WEIGHT FUNCTION METHOD AND FEM

The loads, which act along the crack surface in the coating-material and along the crack surface in the base-material, are different. The two parts of the loads can be respectively seen as constants, which are shown in Fig. 3, because both of the coating thickness t and the crack length a are generally very small[24]. According to the balance principle, there is a relationship between the two parts of the load[24]:

$$\frac{P_1}{P_2} = \frac{E_1}{E_2} \quad (5)$$

Here P_1 and P_2 stand for the two parts of the constant pressure, which act respectively in the coating material and in the base-material. So the pressure acted along the coating crack surface can be expressed as the following vector[22-23]:

$$P(x) = \begin{cases} 0i + P_2j & 0 \leq x \leq t \\ 0i + P_1j & t \leq x \leq a \end{cases} \quad (6)$$

Set the load Equ.(6) and weight function Equ.(4) into Equ.(1), then the stress intensity factor of the coating crack can be expressed as following:

$$K_I = \sqrt{\frac{2a}{\pi}} \left\{ \left[2 + 2 \left(\frac{E_1}{E_2} - 1 \right) \left(1 - \frac{t}{a} \right)^{\frac{1}{2}} \right] + \left[\frac{2}{3} + \frac{2}{3} \left(\frac{E_1}{E_2} - 1 \right) \left(1 - \frac{t}{a} \right)^{\frac{3}{2}} \right] D_{I,1} + \left[\frac{2}{5} + \frac{2}{5} \left(\frac{E_1}{E_2} - 1 \right) \left(1 - \frac{t}{a} \right)^{\frac{5}{2}} \right] D_{I,2} \right\} P_2 \quad (7)$$

By using the Equ.(7), the stress intensity factors K_I for different conditions have been calculated. To be convenient, let P_2 be equal to the unit in the following calculations.

Fig. 4 shows the comparison between the stress intensity factors calculated by the weight function method and by the finite element method for different a/t and different E_1/E_2 . The geometrical dimensions, $(a-t)$, L and H_1 , are constant. From Fig. 4, it can be seen that the calculated stress intensity factors from the two methods agree very well with each others; the stress intensity factors increase with the increase of the value E_1/E_2 for a constant a/t value, i.e., the coating-material plays the role of the strengthen material; and the tendency of the distribution of the calculated K_I factors against the value a/t is also supported by the results in Ref.[25].

The stress intensity factors for different crack length a and different E_1/E_2 are calculated by the weight function method and by the finite element method. The calculated results are shown in the Fig. 5. The geometrical dimensions, t , W and H_1 , are constant. Both of the calculated results by the two methods coincide perfectly with each other. The K_I -factors increase with the increase of the crack length as well as with the increase of the value E_1/E_2 .

Through the comparison between the calculated stress intensity factors for different coating

thickness t by the two methods, the effects of the coating thickness t on the stress intensity factors are shown in Fig. 6. The geometrical dimensions, a , W and H_1 , are constant. The stress intensity factors by the two methods agree very well with each other. From Fig. 6, it can also be seen that the stress intensity factors increase with the increase of the coating thickness if the $E_1/E_2 < 1$. But the factors decrease for the $E_1/E_2 > 1$, which means clearly that the coating-material acts as the role of the strengthen material in a coating structure.

7. INFLUENCE OF THE GEOMETRICAL DIMENSIONS OF THE COATING STRUCTURE AND THE MATERIALS' PROPERTIES E_1/E_2 OF THE COATING STRUCTURE ON THE STRESS INTENSITY FACTORS

Fig. 7 shows the influence of the base material's thickness L on the stress intensity factor. The other geometrical dimensions are $t/H_1 = 0.125$, $a/t = 2$. The material's properties are $E_1/E_2 = 0.69$, $\nu_1/\nu_2 = 1$. From Fig. 7, it can be seen that the geometrical dimension L has larger influence on the stress intensity factor when the L is smaller; this influence seems to disappear if the L is very large.

The effects of the coating structure's height H_1 on the stress intensity factor are shown in Fig. 8. The other geometrical dimensions are $t/W = 0.125$, $a/t = 2$. The material's properties are the same with those about the influence of the base-material's thickness L . From Fig. 8, it can be seen that the smaller the H_1 is, the larger the influence of this dimension on the stress intensity factor is. The stress intensity factors for different E_1/E_2 are shown in Fig. 9. The geometrical dimensions are $a/t = 1.83$, $H_1/W = 1$. The other materials' property is $\nu_1/\nu_2 = 1$. Fig. 9 shows clearly the effect of the value E_1/E_2 on the stress intensity factors. From Fig. 9, it can be seen that the strengthening role of the coating-materials is expressed through the decrease of the stress intensity factors with the increase of the value E_1/E_2 .

8. CONCLUSIONS

8.1 The finite element method and the weight function's method have very successfully been applied to calculate the stress intensity factors of the coating crack under different conditions. The calculated K-factors by the weight function method and the finite element method agree very well with each other.

8.2 The general weight function for the coating crack has been given. The weight function's coefficients and the geometrical functions have been determined, and the influence of the geometrical dimensions and the materials' properties of the coating structure on the geometrical functions and the weight functions have been discussed.

8.3 The stress intensity factors are calculated by the two methods for different conditions. The strengthening role of the coating-materials for the coating structures has been clearly shown by analyzing the different effects of the geometrical dimensions and the materials' properties on the calculated stress intensity factors.

REFERENCE

1. W. S. Johnson, J. M. Larsen and B. N. Cox, Life Prediction Methodology For Titanium Matrix Composites, ASTM Publication Code Number (PCN), 04-012530-33
2. R. Kussmaul, Einfluss Unterschiedlicher Fugeflaechengeometrien Auf Die Eigenspannungen Und Die Festigkeit Von Geloeteten Keramik-Metall-Verbunden, KfK-Bericht 5322, Kernforschungszentrum Karlsruhe, April 1994
3. A. K. Gautesen, The Interface Crack Under Combined Loading: An Eigenvalue Problem For The Gap, Int. J. Fract., Vol. 60, pp. 349-361, 1993
4. J. R. Rice and G. C. Sih, Plane Problems Of Cracks In Dissimilar Media, J. Of App. Mech., Vol. 32, pp. 418-423, 1965
5. N. E. Ashbaugh, On The Opening Of A Finite Crack Normal To An Interface, J. Of App. Mech., Vol. 40, pp. 626-628, 1973
6. O. Tamate and N. Iwasaka, An Arbitrarily Oriented Crack In a Semi-infinite Medium With A

- Surface Layer Under Tension, *Int. J. Solids Struct.*, Vol. 11, pp. 1257-1268, 1975
7. N. E. Ashbaugh, Stress Solution For A Crack At An Arbitrary Angle To An Interface, *Int. J. Fract.*, Vol. 11, pp. 205-219, 1975
 8. C. Actkion, On Stress Singularities And Interface In Linear Elastic Fracture, *Int. J. Fract.*, Vol. 13, pp. 807-820, 1977
 9. F. Delale and F. Erdogan, On The Mechanical Modeling Of The Interface Region In Bonded Half-planes, *J. Of App. Mech.*, Vol. 55, pp. 317-324, 1978
 10. V. M. Gharpuray, J. Dundurs and L. M. Keer, A Crack Terminating At A slipping Interface Between Two Materials, *J. Of App. Mech.*, Vol. 58, pp. 960-963, 1991
 11. M. D. Thouless, A. G. Evans, M. F. Ashby and J. W. Hutchinson, The Edge Cracking And Spalling Of Brittle Plates, *Acta. Metall. Mater.*, Vol. 35, pp. 1333-1341, 1987
 12. J. R. Rice, Z. Suo and J. S. Wang, Mechanics And Thermodynamics Of Brittle Interface Failure In Bimaterial System, Metal-ceramic Interface, Edited By M. Rühle et al, pp. 269-294, Pergamon Press, 1989
 13. D. Bogy, On The Plane Elasto-static Problem Of A Loaded Crack Terminating At A Material Interface, *J. Of App. Mech.*, Vol. 38, pp. 911-918, 1971
 14. F. Erdogan, Fracture Problems In Composite Materials, *Eng. Fract. Mech.*, Vol. 4, pp. 811-840, 1972
 15. T. S. Cook and F. Erdogan, Stress In Bonded Materials With A Crack Perpendicular To The Interface, *Int. J. Engng. Sci.*, Vol. 10, pp. 677-697, 1972
 16. N. E. Ashbaugh, Stresses In Laminated Composites Coating A Broken Layer, *J. Of App. Mech.*, Vol. 40, pp. 533-540, 1973
 17. Yutaka Kagawa, Chitoshi Masuda et al, Effects Of Reaction Layer On Interfacial Shear Properties And Strength Of Fiber In Silicon-Carbide (SiC) Fiber-Reinforced Titanium Alloy Composite, ASTM ASTP 1253, pp. 26-42, 1996
 18. B. Su, et al, Analytical And Numerical Analysis On Fracture Properties Of Coating Crack, submitted to *Material Science & Engineering*, December, 1999
 19. H. G. Hahn, *Bruchmechanik*, B. G. Teubner Stuttgart, 1976
 20. T. Fett and D. Munz, Stress Intensity Factors And Weight Functions For One Dimension Cracks, KFK-Berich 5290, Kernforschungszentrum Karlsruhe, December 1994
 21. B. Su, et al, General Principle Of Two Dimensional Weight Functions In Fracture Mechanics, submitted to *Eng. Fract. Mech.*, November, 1999
 22. B. Su, et al, Weight Functions And Stress Intensity Factors For The Parallel Subinterface Crack In Bi-Material, submitted to *Materials Science & Engineering.*, November, 1999
 23. A. K. Gutesen and J. Dundurs, The Interface Crack Under Combined Loading, *J. Of App. Mech.*, Vol. 55, pp. 580-586, 1988
 24. F. Erdogan and V. Biricikoglu, Two Bonded Half Planes With A Crack Going Through The Interface, *Int. J. Engng. Sci.*, Vol. 11, pp. 745-766, 1973
 25. R. Thomas Watkins and David J. Green, Fracture Behavior of CVD Sic-Coated Graphite: II, Conditions for the Onset of Multiple Cracking, *J. Am. Cera. Soc.*, Vol. 77, pp. 717-720, 1994

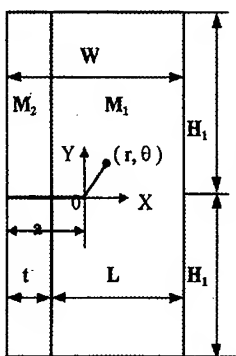


Fig.1 Geometrical configuration

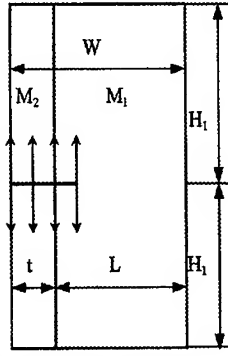


Fig. 2 Reference system

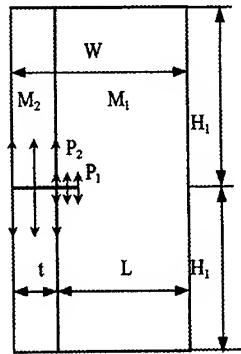


Fig. 3 Coating crack load's system

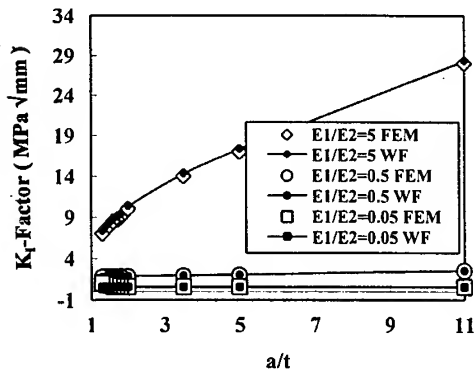


Fig. 4 Stress Intensity factors for different $E1/E2$ with constant ($a-t$), L and $H1$

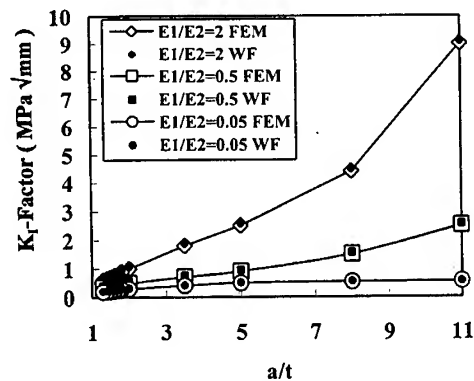


Fig. 5 Stress intensity factors for different $E1/E2$ and different crack length a

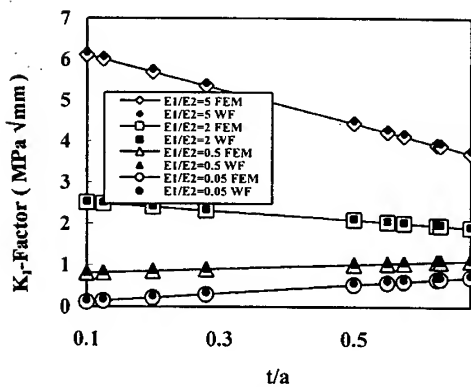


Fig. 6 Stress intensity factor for different $E1/E2$ and different coating thickness t

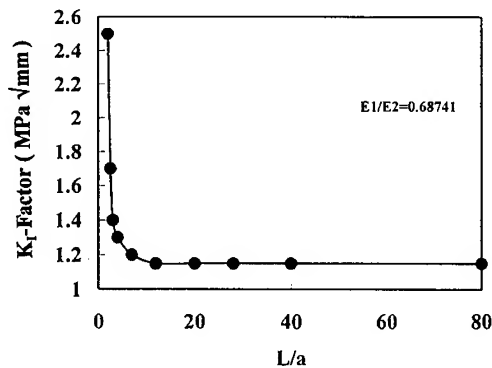


Fig. 7 Stress intensity factor for different based material's thickness L

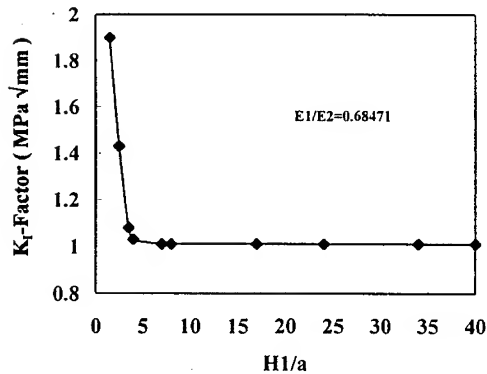


Fig. 8 Stress intensity factor for different coating structure's height $H1$

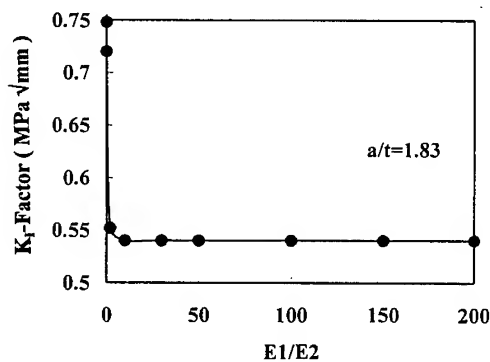


Fig. 9 Stress intensity factor for different $E1/E2$

A Combined Model of Short Crack Closure Accounting for Both Plasticity and Roughness Induced Crack Closures

X.P. Zhang¹, C.H. Wang², J.C. Li³, Y.-W. Mai¹ and L. Ye¹

¹ Centre of Expertise for Damage Mechanics, Department of Mechanical and Mechatronic Engineering, The University of Sydney, Sydney NSW 2006, Australia

² Aeronautical and Maritime Research Laboratory, DSTO, Melbourne 3001, Australia

³ Department of Civil Engineering, University of Technology Sydney, Broadway, Australia

Keywords: Crack Closure, Mechanistic Model, Plasticity, Roughness, Short Crack

ABSTRACT

A new model combining both plasticity-induced and surface roughness-induced crack closures is proposed to describe short fatigue crack growth. The numerical results obtained using this model agree well with the analytical predictions of Budiansky-Hutchinson and are reasonably close to the experimental data.

1. INTRODUCTION

The characterisation of short fatigue crack growth is critical for accurate lifetime prediction of components and structures since anomalously fast crack growth rates are often observed at stress intensity factors well below the threshold where long cracks are generally presumed dormant. As is commonly accepted, crack closure is one of the most important factors resulting in the anomaly of short crack growth and the distinction of growth behaviour from long cracks [1-4]. It is agreed that plasticity-induced closure is the primary mechanism of crack closure arising from the development of residual plastic stretch in the crack-wake. However, it has been recognised, both theoretically and experimentally, that the total crack closure should include both plasticity- and surface roughness-induced closures. This paper is a first attempt to develop a new short fatigue crack growth model including simultaneously both closure mechanisms.

2. A NEW MODEL OF SHORT FATIGUE CRACK CLOSURE

An improved short fatigue crack growth model should include both mechanisms of plasticity- and roughness-induced crack closures. It should not only consider the mix of both crack closures, but should also recover their limiting functions. Due to the existence of the plastic wake and the surface roughness as shown in Fig.1, the onset of crack opening (δ_{op}) or equivalently, the total crack closure, is given by:

$$\delta_{op} = \delta_{op}^p + \delta_{op}^r \cos \theta \quad (1)$$

where δ_{op}^p and δ_{op}^r are equivalent crack surface displacements due to plasticity-induced crack closure and roughness induced-crack closure, respectively. At the crack-tip, the crack-opening displacement can be expressed by Dugdale's model [5] as:

$$\delta = K_I^2 / (E \sigma_y). \quad (2)$$

Thus, the crack opening stress intensity factor, K_{op} , can be obtained from the models of Dugdale and Suresh-Ritchie [6] and Eq.2. That is:

$$\frac{K_{op}}{K_{max}} = \sqrt{\frac{\delta_{op}}{\delta_{max}}} = \sqrt{\frac{\delta_{op}^p + \delta_{op}^r \cos \theta}{\delta_{max}}}. \quad (3)$$

$$\cos \theta = \frac{h}{\sqrt{h^2 + (w/2)^2}} = \frac{1}{\sqrt{1 + (\frac{1}{2h/w})^2}} = \frac{2\gamma}{\sqrt{4\gamma^2 + 1}}. \quad (4)$$

γ is defined as the fracture surface roughness factor, $\gamma = h/w$, where w denotes the mean base width of surface asperities, and h is the average height of asperities.

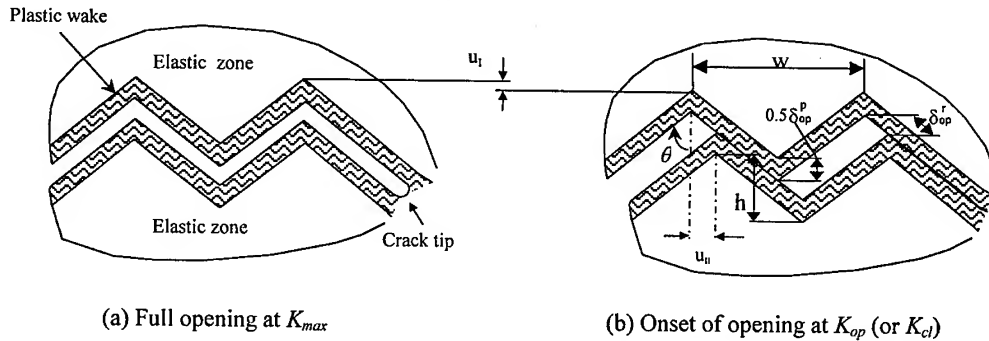


Fig.1. Illustration of a deflected crack at (a) full opening and (b) commencement of opening.

Using Dugdale's model again and substituting Eq.4 into Eq.3, we have

$$K_{op} = \sqrt{(K_{op}^p)^2 + (K_{op}^r)^2 \frac{2\gamma}{\sqrt{4\gamma^2 + 1}}}. \quad (5)$$

K_{op}^p and K_{op}^r can be calculated by modifying Newman's numerical method [7,8] and the Suresh-Ritchie model, respectively. K_{op}^p is dependent on plane strain or plane stress, cyclic stress ratio R and applied to yield stress ratio σ/σ_y . In Suresh-Ritchie's model, K_{op}^r can be estimated by

$$K_{op}^r = K_{max} \sqrt{\frac{2\gamma\chi}{1 + 2\gamma\chi}}. \quad (6)$$

where χ is the ratio of mode II to mode I displacements, i.e. $\chi = u_{II} / u_I$. It does not depend on the state of stress at the crack-tip. That is, plane strain or plane stress. Combining Eq.5 and Eq.6 gives

$$K_{op} = \sqrt{(K_{op}^p)^2 + (K_{max})^2 \frac{4\gamma^2\chi}{(1 + 2\gamma\chi)\sqrt{4\gamma^2 + 1}}}. \quad (7)$$

Clearly, K_{op} for the two limiting cases of pure plasticity-induced crack closure and pure surface roughness-induced crack closure can be recovered easily from Eq.7. Also, in this closure model, the effective stress intensity factor range ratio, or the effective crack driving force, U , is given by:

$$U = \frac{K_{\max} - K_{op}}{K_{\max} - K_{\min}} = \frac{K_{\max} - K_{op}}{(1-R)K_{\max}} = \frac{1 - \sqrt{\left(\frac{K_{op}^p}{K_{\max}}\right)^2 + \frac{4\gamma^2\chi}{(1+2\gamma\chi)\sqrt{4\gamma^2+1}}}}{1-R} \quad \text{or} \quad (8a)$$

$$U = \frac{1 - \sqrt{[1 - (1-R)U^p]^2 + \frac{4\gamma^2\chi}{(1+2\gamma\chi)\sqrt{4\gamma^2+1}}}}{1-R} \quad (8b)$$

where

$$U^p = \left[1 - \sqrt{\left(\frac{K_{op}^p}{K_{\max}}\right)^2} \right] / (1-R) \quad (8c)$$

and is the effective crack driving force arisen from pure plasticity-induced crack closure.

The above combined mechanisms of plasticity and roughness induced crack closures can also be obtained from Budiansky-Hutchinson's small scale yielding model [9] and Suresh-Ritchie's model. Budiansky-Hutchinson presented an analysis to characterise fatigue crack growth with crack closure behaviour using ΔK_{eff} . In light of the B-H results, still referring to Fig.1, the closure stress intensity factor, K_{cl} , is given by

$$\frac{K_{cl}}{K_{\max}} = 1 - \frac{1}{\sqrt{0.54}} \sqrt{1 - \frac{\delta_R}{\delta_{\max}}} \quad (9)$$

where δ_R and δ_{\max} are the total plastic stretch and the maximum crack-tip opening displacement at maximum load. Assuming that the plastic stretch is not coupled to the fracture surface roughness and that it is only a function of stress ratio R [10], the effective plastic stretch is

$$\delta_R = \delta_R^p + \delta_R^r \quad (10)$$

where δ_R^p and δ_R^r are, respectively, the plastic stretch pertaining to plasticity-induced closure and surface roughness contribution. Using the Suresh-Ritchie and Dugdale models, Eq.9 becomes:

$$\frac{K_{cl}}{K_{\max}} = 1 - \frac{1}{\sqrt{0.54}} \sqrt{1 - \frac{2\gamma\chi}{1+2\gamma\chi} - \frac{\delta_R^p}{\delta_{\max}}} \quad (11)$$

which recovers the B-H analytical result for $\chi=0$ (i.e. pure mode I deformation) or $\gamma=0$ (i.e. flat fracture surface). Accordingly, the effective stress intensity factor range ratio, U , is given by

$$U = \frac{K_{\max} - K_{cl}}{(1-R)K_{\max}} = \frac{1}{1-R} \frac{1}{\sqrt{0.54}} \sqrt{1 - \frac{\delta_R}{\delta_{\max}}} \quad (12)$$

In the absence of surface roughness and noting Eqs.10 and 12, we have

$$U^p = \frac{1}{\sqrt{0.54}} \cdot \frac{\sqrt{1 - \frac{\delta_R^p}{\delta_{\max}}}}{1-R} \quad (13)$$

where U^p is the effective stress intensity factor range ratio for pure plasticity-induced closure. The crack closure stress intensity can now be derived from Eqs.11 and 13. That is,

$$K_{cl} = K_{\max} \left\{ 1 - \frac{1}{\sqrt{0.54}} \sqrt{0.54[(1-R)U^p]^2 - \frac{2\gamma\chi}{1+2\gamma\chi}} \right\} \quad (14)$$

Consequently, the effective stress intensity factor range ratio Eq.12 becomes

$$U = \sqrt{\left[U^p \right]^2 - \frac{2\gamma\chi}{1+2\gamma\chi} \frac{1}{0.54(1-R)^2}} \quad (15)$$

It should be noted hereto we consider K_{cl} to be identical to K_{op} , since the difference between them is generally less than the scatter related to the crack closure measurements.

3. DISCUSSION

3.1. Comparisons of Present Model, B-H Analytical Solution and Experimental Data

Crack closures estimated using the present model were compared with the experimental results [11,12] obtained from 10 mm thick specimens of a structural aluminum alloy 2024 in T3 and T6 heat treatment conditions, respectively, in Fig. 2. The numerical predictions under different stress ratio R were carried out in plane strain condition using Eq.7 for $\sigma/\sigma_y=0.15$ and 0.77 and $\gamma=0.5$, $\chi=0.2$ from fracture surface profile measurements [6]. It can be seen that the predictions are reasonably close to the test data at high values of R . Comparisons of crack closure and effective crack driving force under plane stress condition estimated based on Budiansky-Hutchinson's analytic solutions (Eqs.11 and 12) are shown in Figs. 3 and 4, respectively. It is clear that they agree quite well with the predictions from the present model (Eqs.7 and 8).

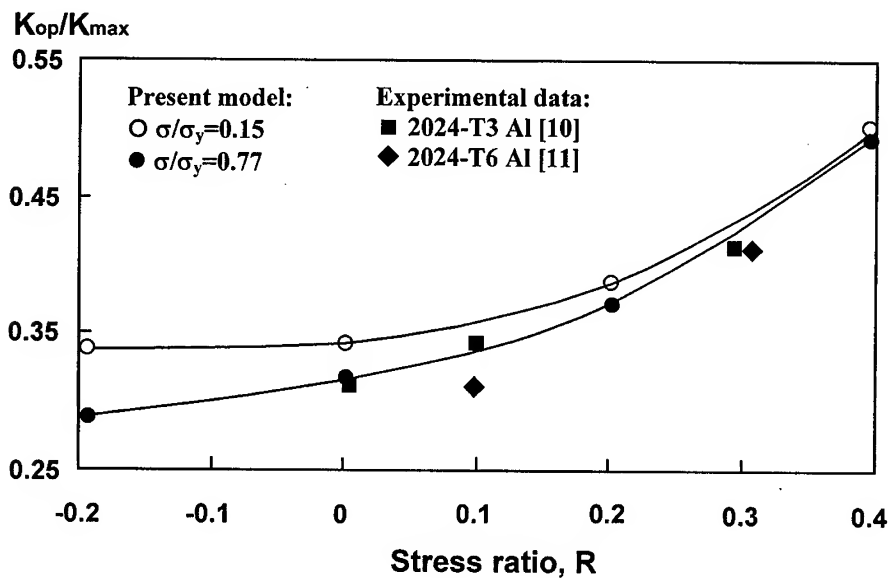


Fig. 2. Comparisons of theoretical predictions and experimental data for plane strain.

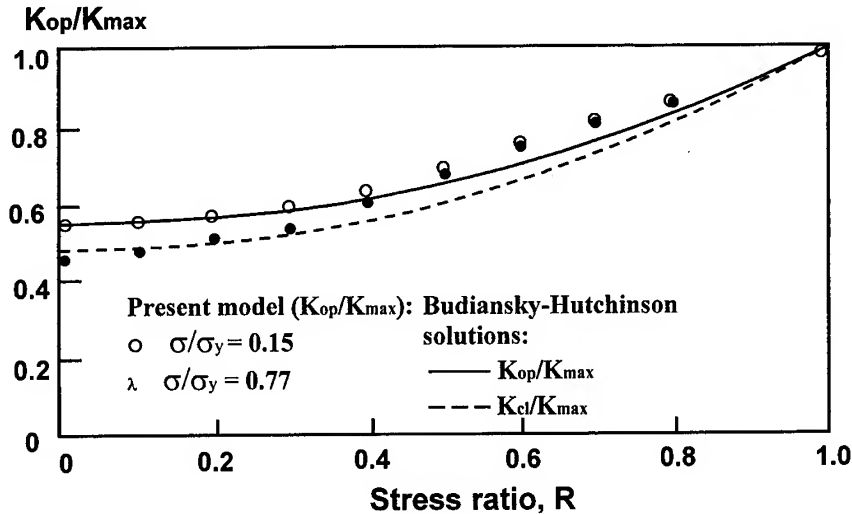


Fig.3. Comparisons of crack closure between current numerical results and analytic solutions based on B-H analyses (both for plane stress condition).

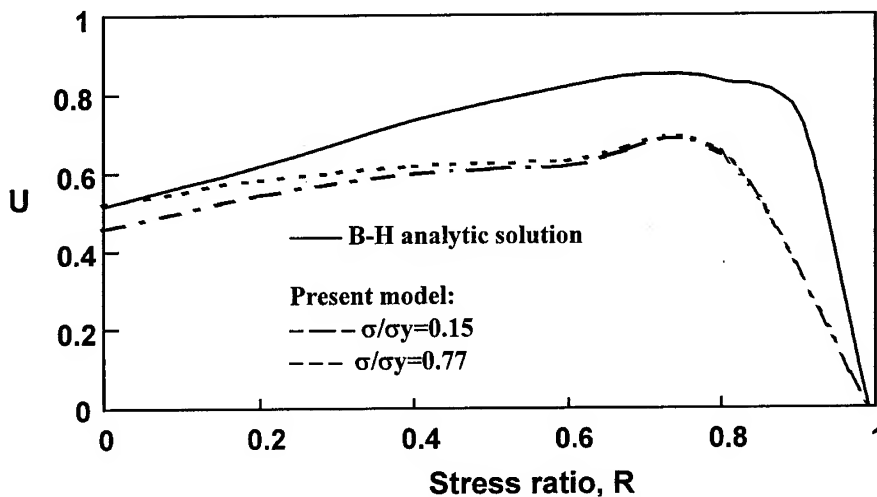


Fig. 4. Comparison of effective crack driving force between numerical results from present model and results from B-H solution.

3.2. Effect of Crack-Tip Shear Sliding on Crack Closure and Crack Driving Force

Roughness induced crack closure is strongly attributed to the crack path deflections caused by the heterogeneous material microstructures and the shear sliding of the crack-tip. This effect is predominant at low R , where the minimum crack-tip opening displacement is significantly smaller than the asperity height of the fracture surface. Fig. 5 shows the influence of crack-tip shear sliding on the plane stress effective crack driving force U calculated from Eq.8 for different intensity of crack surface roughness. Clearly, U decreases with increasing shear sliding χ , since a larger shear sliding gives a stronger engagement of asperities on the fracture surfaces leading to more severe crack closure. In the limit, $\gamma=0$, there is no surface roughness induced crack closure for flat fracture surfaces (except plasticity induced crack closure) at any level of crack-tip shear sliding, χ .

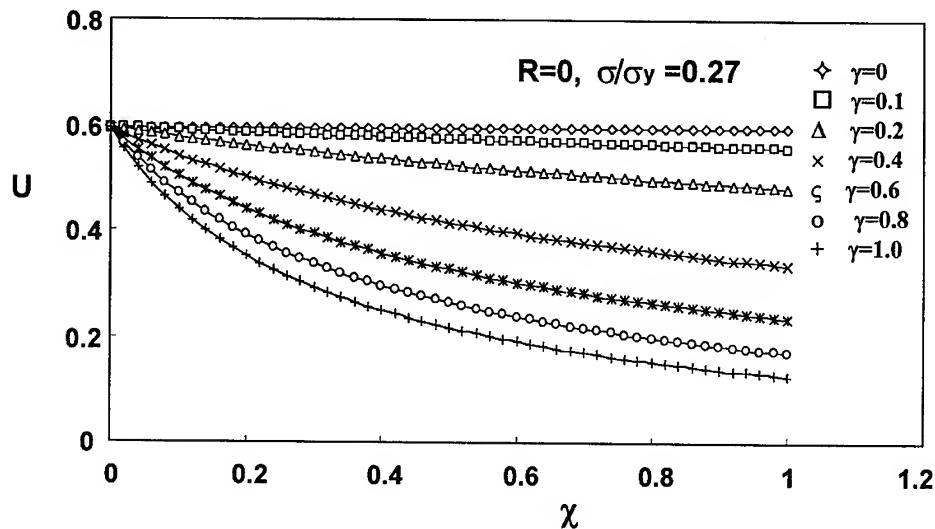


Fig.5. Influence of mode II sliding on crack driving force at short crack length ($a=0.10$ mm) in plane stress condition.

4. CONCLUSIONS

A combined model of short crack closure accounting for both mechanisms of plasticity- and roughness-induced crack closures was developed to characterize crack growth characteristics. The results of crack closure and effective crack driving force estimated by numerical simulation with the present model agreed well with available test data and those analytic solutions obtained by the Budiansky-Hutchinson model. Crack-tip shear sliding also enhanced crack closure and reduced the effective crack driving force. The higher the shear sliding the more was the crack closure.

ACKNOWLEDGMENTS

This work was supported in part by the Airframe and Aero-Engine Division, Aeronautical & Maritime Research Laboratory, Defense Science and Technology Organisation of Australia and in part by an Australian Research Council Large Project Grant awarded to Y-WM, XPZ and CHW.

REFERENCES

1. S. Pearson, *Engineering Fracture Mechanics*, **7** (1975) p. 235
2. K.J. Miller, *Fatigue of Engineering Materials and Structures*, **5** (1982) p. 223
3. K. Tanaka, *JSME International Journal (Bulletin of the JSME)*, **30** (1987) p. 1
4. J.C. Newman, Jr, *Progress in Aerospace Science*, **34** (1998) p. 347
5. D.S. Dugdale, *Journal of the Mechanics and Physics of Solids*, **8** (1960) p. 100
6. S. Suresh, and R.O. Ritchie, *Metallurgical Transactions*, **13A** (1982), p. 1627
7. J.C. Newman, Jr., *ASTM STP 748* (1981) p. 53
8. J.C. Newman, Jr., *AGARD Conference Proceedings*, No.328, Canada (1982) p. 6.1
9. B. Budiansky, and J.W. Hutchinson, *Journal of Applied Mechanics*, **45** (1978) p. 267
10. S.X. Wu, Y.-W. Mai and B. Cotterell, *International Journal of Fracture*, **57** (1992) p. 253
11. C.Y. Kim, and J.H. Song, *Engineering Fracture Mechanics*, **49** (1994) p. 105
12. N.E. Ashbaugh, B. Dattaguru, M. Khobaib, T. Nicholas, R.V. Prakash, T.S. Ramamurthy, B.R. Seshadri, and R. Sunder, *Fatigue & Fracture of Engng. Mater. & Struct.*, **20** (1997) p. 951

Scattering of Plane Compressional Waves by a Spherical Inhomogeneity with a Linear Spring Type Interface

Z. Zhong and X.B. Yu

Solid Mechanics Key Laboratory of MEC, Department of Engineering Mechanics and Technology, Tongji University, Shanghai 200092, China P.R.

Keywords: Imperfect Interface, Interfacial Compliance, Plane Compressional Wave, Scattering, Spherical Inhomogeneity

ABSTRACT

In this paper, we study the scattering of plane compressional waves by a spherical inhomogeneity with an imperfect interface. The interface is modeled by a linear spring assuming that the tangential and normal interfacial displacement jumps are proportional to the associated tractions. By using series expansion method an analytical solution is obtained for the displacement potentials of the reflected and refracted waves as well as the stress fields in the inhomogeneity and the matrix. Results of some special cases are then discussed.

1. INTRODUCTION

Recently there has been more and more interest in the research of imperfect interfaces and their effect on the properties of composite materials. The imperfect interface is a simplified description of the complex interfacial zone between the reinforcement and the matrix in composite materials. It may be a thin layer of another material introduced by design or by chemical interaction of the constituents, or it may be a region containing many small defects such as voids or cracks.

One of the most useful imperfect interface condition is a linear spring type interfacial condition, which assumes a linear relation between interfacial displacement discontinuities and associated traction components. This kind of linear interfacial condition has been employed to investigate the effect of imperfect interfaces on the local stress distribution inside and outside an inhomogeneity in an infinite matrix [1,2], and on the elastic properties of composite materials [3,4]. In order to characterize the interfacial properties by nondestructive means such as ultrasonic techniques, it is needed to study the scattering of elastic waves by inhomogeneities or obstacles in an infinite medium. A large number of contributions concerning the scattering problems of elastic waves have appeared in the literature [5].

In the present paper, we study the scattering of plane compressional waves by a spherical inhomogeneity with a linear spring type interface. By using series expansion method an analytical solution is obtained for the displacement potentials of the reflected and refracted waves as well as

the stress fields in the inhomogeneity and the matrix. Results of some special cases are then discussed.

2. BASIC EQUATIONS

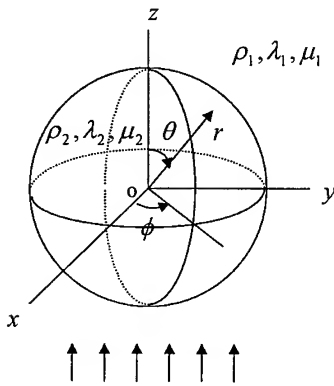


Fig.1. Spherical inhomogeneity

Consider a spherical inhomogeneity of radius a embedded in an infinitely extended elastic matrix. The inhomogeneity has elastic moduli and density $(\lambda_1, \mu_1, \rho_1)$ different from those of the matrix $(\lambda_2, \mu_2, \rho_2)$. Assume a plane compressional wave propagating symmetrically about the z -axis, as depicted in Fig. 1. The displacement component u_ϕ and the stress components $\sigma_{r\phi}, \sigma_{\theta\phi}$ vanish due to axial symmetry. Accordingly, the displacement vector in spherical coordinates (r, θ, ϕ) can be expressed in terms of two displacement potentials Φ and Ψ as

$$\mathbf{u} = \nabla\Phi + \nabla \times (\mathbf{e}_\phi \partial\Psi / \partial\theta) \quad (1)$$

where ∇ is a vector differential operator and \mathbf{e}_ϕ is a unit vector normal to constant ϕ coordinate surface.

These two displacement potentials satisfy the following wave equations:

$$c_1^2 \nabla^2 \Phi = \partial^2 \Phi / \partial t^2 \quad c_2^2 \nabla^2 \Psi = \partial^2 \Psi / \partial t^2 \quad (2)$$

where $c_1 = [(\lambda + 2\mu) / \rho]^{1/2}$, $c_2 = (\mu / \rho)^{1/2}$ are the velocities of compressional waves and shear waves, respectively; λ , μ are Lamé's constants, and ρ the density of the material.

The stress σ is related to the displacement \mathbf{u} by Hooke's law, such that

$$\sigma = \lambda(\nabla \cdot \mathbf{u}) \mathbf{I} + 2\mu(\nabla \mathbf{u} + \mathbf{u} \nabla) \quad (3)$$

where \mathbf{I} denotes the unit tensor.

Assume that the interface between the inhomogeneity and the matrix is imperfectly bonded, which can be modelled by a linear spring, i.e., the interfacial conditions on $r = a$ are given by

$$\sigma_r^M = \sigma_r^I \quad \sigma_{r\theta}^M = \sigma_{r\theta}^I \quad (4)$$

$$u_\theta^M - u_\theta^I = f_1 \sigma_{r\theta}^I \quad u_r^M - u_r^I = f_2 \sigma_r^I \quad (5)$$

where the superscript "M" and "I" are used respectively for the quantities associated with matrix and inhomogeneity. Eq.4 and Eq.5 imply that the interfacial tractions remain continuous, while the tangential and normal interfacial displacement jumps are proportional to the associated traction components. f_1 and f_2 denote the respective compliance in the tangential and normal directions of the interface. It can be seen that f_1 and f_2 characterize the interfacial behavior. For example, the case where $f_1 = 0$ and $f_2 = 0$ corresponds to a perfectly bonded interface, while the case $f_1 \rightarrow \infty$ and $f_2 \rightarrow \infty$ represents a completely debonded interface.

3. SOLUTION

Let the incident plane compressional waves propagating along the positive z direction be described by two potentials

$$\Phi^{(i)} = \Phi_0 e^{i(\alpha_1 z - \omega t)} \quad \Psi^{(i)} = 0 \quad (6)$$

where $\alpha_1 (= 2\pi/L)$ is the wave number of compressional waves in the matrix, L denotes the wavelength, ω is circular frequency, and Φ_0 is a constant. It can be found from Eq.2 that $\alpha_1^2 = \omega^2 \rho_1 / (\lambda_1 + 2\mu_1)$. In spherical coordinates, the potential $\Phi^{(i)}$ can be given by a series expression

$$\Phi^{(i)} = \Phi_0 \sum_{n=0}^{\infty} (2n+1) i^n j_n(\alpha_1 r) P_n(\cos \theta) \quad (7)$$

in which $j_n(x)$ is the spherical Bessel function of first kind, $P_n(x)$ is the Legendre polynomials. In Eq.7 and sequel the time factor $e^{-i\omega t}$ is omitted whenever its occurrence is apparent. Then the displacement and stress due to the incident waves can be determined by substituting Eq.6 and Eq.7 into Eq.1 and Eq.3.

The reflected waves in the matrix can also be written by a series expression

$$\Phi^{(r)} = \sum_{n=0}^{\infty} A_n h_n(\alpha_1 r) P_n(\cos \theta) \quad \Psi^{(r)} = \sum_{n=0}^{\infty} B_n h_n(\beta_1 r) P_n(\cos \theta) \quad (8)$$

where $h_n(x)$ is the spherical Hankel function of first kind. The refracted waves, being confined in the spherical inhomogeneity, are standing waves, which can be represented by

$$\Phi^{(f)} = -\sum_{n=0}^{\infty} C_n j_n(\alpha_2 r) P_n(\cos \theta) \quad \Psi^{(f)} = -\sum_{n=0}^{\infty} D_n j_n(\beta_2 r) P_n(\cos \theta) \quad (9)$$

In Eq.8 and Eq.9

$$\alpha_i^2 = \omega^2 \rho_i / (\lambda_i + 2\mu_i) \quad \beta_i^2 = \omega^2 \rho_i / \mu_i \quad (i = 1, 2) \quad (10)$$

and A_n, B_n, C_n, D_n are coefficients to be determined from the interfacial conditions, Eq.4 and Eq.5.

As a result the resultant waves in the matrix are then determined by the superposition of the incident and reflected waves, i.e., the two potentials can be written as

$$\Phi^M = \Phi^{(i)} + \Phi^{(r)} \quad \Psi^M = \Psi^{(i)} + \Psi^{(r)} \quad (11)$$

Accordingly, displacements and stresses in the matrix are obtained as

$$\begin{aligned}
u_r^M &= \frac{1}{r} \sum_{n=0}^{\infty} [-\Phi_0 \varepsilon_1^n + A_n \varepsilon_{11}^n + B_n \varepsilon_{12}^n] P_n(\cos \theta) \\
u_\theta^M &= \frac{1}{r} \sum_{n=0}^{\infty} [-\Phi_0 \varepsilon_2^n + A_n \varepsilon_{21}^n + B_n \varepsilon_{22}^n] \frac{dP_n(\cos \theta)}{d\theta}
\end{aligned} \tag{12}$$

and

$$\begin{aligned}
\sigma_r^M &= \frac{2\mu_1}{r^2} \sum_{n=0}^{\infty} [-\Phi_0 \varepsilon_3^n + A_n \varepsilon_{31}^n + B_n \varepsilon_{32}^n] P_n(\cos \theta) \\
\sigma_{r\theta}^M &= \frac{2\mu_1}{r^2} \sum_{n=0}^{\infty} [-\Phi_0 \varepsilon_4^n + A_n \varepsilon_{41}^n + B_n \varepsilon_{42}^n] \frac{dP_n(\cos \theta)}{d\theta}
\end{aligned} \tag{13}$$

with

$$\begin{aligned}
\varepsilon_1^n &= -i^n (2n+1) [nj_n(\alpha_1 r) - \alpha_1 r j_{n+1}(\alpha_1 r)] & \varepsilon_2^n &= -i^n (2n+1) j_n(\alpha_1 r) \\
\varepsilon_3^n &= -i^n (2n+1) [(n^2 - n - \beta_1^2 r^2 / 2) j_n(\alpha_1 r) + 2\alpha_1 r j_{n+1}(\alpha_1 r)] \\
\varepsilon_4^n &= i^n (2n+1) [(n-1) j_n(\alpha_1 r) - \alpha_1 r j_{n+1}(\alpha_1 r)] \\
\varepsilon_{11}^n &= n h_n(\alpha_1 r) - \alpha_1 r h_{n+1}(\alpha_1 r) & \varepsilon_{21}^n &= h_n(\alpha_1 r) \\
\varepsilon_{31}^n &= (n^2 - n - \beta_1^2 r^2 / 2) h_n(\alpha_1 r) + 2\alpha_1 r h_{n+1}(\alpha_1 r) \\
\varepsilon_{41}^n &= (n-1) h_n(\alpha_1 r) - \alpha_1 r h_{n+1}(\alpha_1 r) & \varepsilon_{12}^n &= -n(n+1) h_n(\beta_1 r) \\
\varepsilon_{22}^n &= -(n+1) h_n(\beta_1 r) + \beta_1 r h_{n+1}(\beta_1 r) \\
\varepsilon_{32}^n &= -n(n+1) [(n-1) h_n(\beta_1 r) - \beta_1 r h_{n+1}(\beta_1 r)] \\
\varepsilon_{42}^n &= -(n^2 - n - \beta_1^2 r^2 / 2) h_n(\beta_1 r) - \beta_1 r h_{n+1}(\beta_1 r)
\end{aligned}$$

Other stress components can also be easily determined from Eq.3, which we omit here.

Since the refracted waves are the only waves in the inhomogeneity, then the potentials in the inhomogeneity are

$$\Phi^I = \Phi^{(I)} \quad \Psi^I = \Psi^{(I)} \tag{14}$$

And corresponding displacements and stresses in the inhomogeneity can be obtained as

$$\begin{aligned}
u_r^I &= -\frac{1}{r} \sum_{n=0}^{\infty} [C_n \varepsilon_{13}^n + D_n \varepsilon_{14}^n] P_n(\cos \theta) \\
u_\theta^I &= -\frac{1}{r} \sum_{n=0}^{\infty} [C_n \varepsilon_{23}^n + D_n \varepsilon_{24}^n] \frac{dP_n(\cos \theta)}{d\theta}
\end{aligned} \tag{15}$$

and

$$\begin{aligned}
\sigma_r^I &= -\frac{2\mu_2}{r^2} \sum_{n=0}^{\infty} [C_n \varepsilon_{33}^n + D_n \varepsilon_{34}^n] P_n(\cos \theta) \\
\sigma_{r\theta}^I &= -\frac{2\mu_2}{r^2} \sum_{n=0}^{\infty} [C_n \varepsilon_{43}^n + D_n \varepsilon_{44}^n] \frac{dP_n(\cos \theta)}{d\theta}
\end{aligned} \tag{16}$$

with

$$\begin{aligned}
 \varepsilon_{13}^n &= n j_n(\alpha_2 r) - \alpha_2 r j_{n+1}(\alpha_2 r) & \varepsilon_{23}^n &= j_n(\alpha_2 r) \\
 \varepsilon_{33}^n &= (n^2 - n - \beta_1^2 r^2 / 2) j_n(\alpha_2 r) + 2 \alpha_2 r j_{n+1}(\alpha_2 r) \\
 \varepsilon_{43}^n &= (n-1) j_n(\alpha_2 r) - \alpha_2 r j_{n+1}(\alpha_2 r) & \varepsilon_{14}^n &= -n(n+1) j_n(\beta_2 r) \\
 \varepsilon_{24}^n &= -(n+1) j_n(\beta_2 r) + \beta_2 r j_{n+1}(\beta_2 r) \\
 \varepsilon_{34}^n &= -n(n+1) [(n-1) j_n(\beta_2 r) - \beta_2 r j_{n+1}(\beta_2 r)] \\
 \varepsilon_{44}^n &= -(n^2 - n - \beta_1^2 r^2 / 2) j_n(\beta_2 r) - \beta_2 r j_{n+1}(\beta_2 r)
 \end{aligned}$$

Substituting Eq.12, Eq.13, Eq.15 and Eq.16 into the interfacial conditions, Eq.4 and Eq.5 leads to four simultaneous algebraic equations, which can be used to determine the four unknowns A_n, B_n, C_n, D_n . These equations can be written in matrix form

$$\begin{bmatrix} E_{11}^n & E_{12}^n & E_{13}^n + \frac{2\mu_2 f_2}{a} E_{33}^n & E_{14}^n + \frac{2\mu_2 f_2}{a} E_{34}^n \\ E_{21}^n & E_{22}^n & E_{23}^n + \frac{2\mu_2 f_1}{a} E_{43}^n & E_{24}^n + \frac{2\mu_2 f_1}{a} E_{44}^n \\ E_{31}^n & E_{32}^n & p E_{33}^n & p E_{34}^n \\ E_{41}^n & E_{42}^n & p E_{43}^n & p E_{44}^n \end{bmatrix} \begin{bmatrix} A_n \\ B_n \\ C_n \\ D_n \end{bmatrix} = \Phi_0 \begin{bmatrix} E_1^n \\ E_2^n \\ E_3^n \\ E_4^n \end{bmatrix} \quad (17)$$

where $E_{ij}^n = (\varepsilon_{ij}^n)_{r=a}$, $E_i^n = (\varepsilon_i^n)_{r=a}$, $p = \mu_2 / \mu_1$. Once A_n, B_n, C_n, D_n are determined, it is easy to obtain displacements and stresses in the matrix and inhomogeneity from Eq.12, Eq.13, Eq.15 and Eq.16.

4. RESULTS OF SPECIAL CASES

(1) When the interface is perfectly bonded, i.e., $f_1 = f_2 = 0$, Eq.17 reduces to

$$\begin{bmatrix} E_{11}^n & E_{12}^n & E_{13}^n & E_{14}^n \\ E_{21}^n & E_{22}^n & E_{23}^n & E_{24}^n \\ E_{31}^n & E_{32}^n & p E_{33}^n & p E_{34}^n \\ E_{41}^n & E_{42}^n & p E_{43}^n & p E_{44}^n \end{bmatrix} \begin{bmatrix} A_n \\ B_n \\ C_n \\ D_n \end{bmatrix} = \Phi_0 \begin{bmatrix} E_1^n \\ E_2^n \\ E_3^n \\ E_4^n \end{bmatrix} \quad (18)$$

which confirms the result of Pao and Mow [6].

(2) If the inhomogeneity is much harder than the matrix, it may be treated as a perfectly rigid body. Let U_z denote the rigid body translation of the spherical inhomogeneity along the direction of incident waves (z-axis). The interfacial conditions at $r = a$ become

$$\sigma_r^M = \sigma_r^I \quad \sigma_{r\theta}^M = \sigma_{r\theta}^I \quad (19)$$

$$u_\theta^M + U_z \sin \theta = f_1 \sigma_{r\theta}^M \quad u_r^M - U_z \cos \theta = f_2 \sigma_r^M \quad (20)$$

The translation U_z is determined by the following equation of motion

$$\frac{4\pi a^3 \rho_2}{3} \frac{\partial^2 U_z}{\partial t^2} = \oint_S (\sigma_r^M \cos \theta - \sigma_{r\theta}^M \sin \theta) a^2 \sin \theta d\theta d\phi \quad (21)$$

with the integration domain s taken over the spherical surface ($r = a$). Resorting the time factor $e^{-i\omega t}$ and substituting Eq.16 into Eq.21, we have

$$U_z = \frac{\eta}{a} [3i\Phi_0 j_1(\alpha_1 a) + A_1 h_1(\alpha_1 a) - 2B_1 h_1(\beta_1 a)] e^{-i\omega t} \quad (22)$$

where $\eta = \rho_1 / \rho_2$. Substituting (22) into (20) leads to the following equations for the unknowns A_n and B_n :

$$\begin{bmatrix} e_{11}^n & e_{12}^n \\ e_{21}^n & e_{22}^n \end{bmatrix} \begin{bmatrix} A_n \\ B_n \end{bmatrix} = \Phi_0 \begin{bmatrix} e_1^n \\ e_2^n \end{bmatrix} \quad (23)$$

where

$$\left. \begin{aligned} e_{11}^1 &= E_{11}^1 - \eta h_1(\alpha_1 a) - (2\mu_1 f_2 / a) E_{31}^1 & e_{12}^1 &= E_{12}^1 + 2\eta h_1(\beta_1 a) - (2\mu_1 f_2 / a) E_{32}^1 \\ e_{21}^1 &= E_{21}^1 + \eta h_1(\alpha_1 a) - (2\mu_1 f_1 / a) E_{41}^1 & e_{22}^1 &= E_{22}^1 - 2\eta h_1(\beta_1 a) - (2\mu_1 f_1 / a) E_{42}^1 \\ e_1^1 &= E_1^1 + 3i\eta j_1(\alpha_1 a) - (2\mu_1 f_2 / a) E_3^1 & e_2^1 &= E_2^1 - 3i\eta j_1(\alpha_1 a) - (2\mu_1 f_1 / a) E_4^1 \\ e_{11}^n &= E_{11}^n - (2\mu_1 f_2 / a) E_{31}^n & e_{12}^n &= E_{12}^n - (2\mu_1 f_2 / a) E_{32}^n \\ e_{21}^n &= E_{21}^n - (2\mu_1 f_1 / a) E_{41}^n & e_{22}^n &= E_{22}^n - (2\mu_1 f_1 / a) E_{42}^n \\ e_1^n &= E_1^n - (2\mu_1 f_2 / a) E_3^n & e_2^n &= E_2^n - (2\mu_1 f_1 / a) E_4^n \end{aligned} \right\} \quad (n \neq 1)$$

ACKNOWLEDGMENTS

This work has been supported by the National Natural Science Foundation of China, the Teaching and Research Award Fund for Outstanding Young Teachers in High Education Institutions of MOE, P. R. C., Shanghai Education Development Foundation and Shanghai Education Committee.

REFERENCES

1. Z. Hashin, ASME J. Appl. Mech., **58** (1991) p.444
2. Z. Zhong and S.A. Meguid, ASME J. Appl. Mech., **63** (1996) p.877
3. Y. Benveniste, Mech. Mater., **4** (1985) p.197
4. I. Jasiuk, J. Chen and M.F. Thorpe, J. Mech. Phys. Solids, **40** (1992) p.373
5. Y.H. Pao and C.C. Mow, Diffraction of Elastic Waves and Dynamic Stress Concentrations, Crane and Russak, New York (1973)
6. Y.H. Pao and C.C. Mow, J. Appl. Phys., **34** (1963) p. 493

From Recent Studies on Impact Fracture of Polymers and Polymer Composites

K. Takahashi

Research Institute for Applied Mechanics, Kyushu University,
Kasuga-shi, Fukuoka 816-8580, Japan

Keywords: Dynamic Fracture Toughness, High Density Polyethylene, High Impact Polystyrene, Impact Fracture, Interlaminar Fracture Toughness, Optical Extensometer, Polycarbonate, Polymer Composite

ABSTRACT

An optical extensometer has been in-laboratory constructed to precisely measure large displacement or deformation of materials under static as well as dynamic loading. The use of the apparatus has made it possible to elucidate new aspects of dynamic deformation and fracture problems of materials. Some examples are presented from recent research of the author's group on dynamic mechanics in three-point impact bending, rate dependency of mode-I dynamic fracture toughness of PC, annealing effect on fracture energy of HDPE under impact, impact energy characteristics of HIPS under dynamic tensile loading and mode-II dynamic interlaminar fracture toughness of polymer composites.

1. INTRODUCTION

In the application of polymers and polymer composites to structural materials, it is important to correctly understand mechanics and mechanical properties of the materials under dynamic loading [1]. As far as mechanics are concerned, situations should be similar to cases of other materials. Dynamic effects greatly influence on the measurement procedure, particularly on the force measurement, under dynamic loading when the impact velocity becomes higher [2]. The effects come from wave and vibration phenomena generated through impact against a stationary member, a specimen, in the testing system. Well-known Hopkinson bar method is a way to avoid the dynamic effects. However, in the application of this method to soft materials like polymers and polymer composites, we have several problems. The major one is that mechanical impedance mismatches between Hopkinson bars and a specimen material is so great that the measurement sensitivity becomes significantly poor. If we should adopt polymeric materials for the bars to avoid the mismatching problem, then non-linearity of the bar materials becomes a course of measurement error. Soft materials which undergo large nonlinear deformation even under dynamic loading has been required to find a way better for dynamic mechanical characterization other than the bar method.

It is important, therefore, to add a new repertory to our limited number of methods for dynamic mechanical measurements. Beguelin et al. [3,4] proposed a new extensometer to evaluate a large dynamic strain of a tensile specimen on a servo-hydraulic tester. The extensometer made use of

optical fibers as position indicators on a specimen: a set of photo-detectors quantitatively sensed each position, i.e., a change in the distance between each position of the fibers, from whose ends laser light rays had been emitted onto the PSD detectors.

Recently, the present author has constructed a general purpose impact machine [5,6], where the optical fiber extensometer was utilized [6]. And further, coupled with a usual instrumented impact machine, the extensometer has been used in various three-point impact bend tests [7-14]. This paper introduces the in-laboratory constructed optical apparatus and describes some results recently obtained from the dynamic tests.

2. MESURING SYSTEM

A schematic diagram of the PSD sensor is shown in Fig.1. In this case, the displacement y can be obtained from the currents $Y1$ and $Y2$ at the electrodes 1 and 2 using the following relation:

$$\frac{y}{L} = \frac{Y2 - Y1}{Y2 + Y1} \quad (1)$$

The dynamic displacement measuring system using a PSD sensor is shown in Fig.2. In this system, L2+PSD is used as a monolithic component. There is a linear relation between the displacement and the electrical output, and the relation is obtained as a calibration beforehand. One end of the optical fiber is attached to the object using a sticky tape, and the laser light condensed by the lens L1 is introduced into the other end of the fiber. The output of the laser light from the attached end is focused on the PSD sensor through the lens L2. Mechanical effects of the fibers are considered to be negligible because the fibers are very thin, light and flexible. Therefore, this type of measurement can be regarded as a non-contacting measurement although the fibers are stuck to the object.

The result of a dynamic characteristic evaluation of the measuring system using a luminescent semiconductor circuit (LED1,2) indicated that the system possesses a frequency characteristic of 100kHz [6].

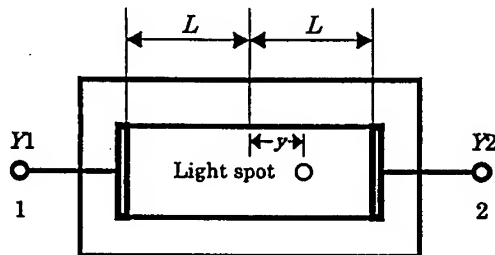


Fig.1 Schematic drawing of a PSD sensor

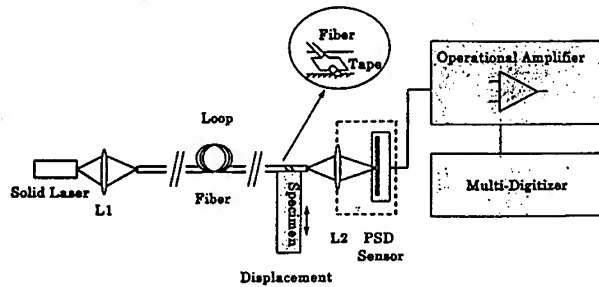


Fig.2 Schematic drawing of the optical displacement meter

3. EXAMPLES OF DYNAMIC DISPLACEMENT MEASUREMENT

3.1 Application to three-point impact bending test for polymers

3.1.1 Waveforms at Charpy impact

Deformation behavior of a Charpy specimen with V-notch under drop weight impact was observed by attaching an optical fiber on the upper surface of the specimen [2]. The impact rate was 2.8m/s that corresponded to a testing rate for a standard Charpy test. The relation between the fiber position during impact and the output of the strain gage attached to the dart is shown in Fig.3. In this figure, the number 1 indicates the initiation of deformation (impact), 2 is the time at which the impact was transmitted to the dart gage, 3 corresponds to the fracture initiation and 4 is the fracture initiation exhibited by the dart gage. 2 and 4 delayed about 20 μ s from 1 and 3, respectively. Fig.3 shows that dynamic effects have significant influences on the dart gage output at this impact rate. The fiber velocity can be obtained at intervals of 10ms by differentiating the displacement signal from the fiber with respect to time, and the velocity varied oscillationally with the central value of 2.8m/s.

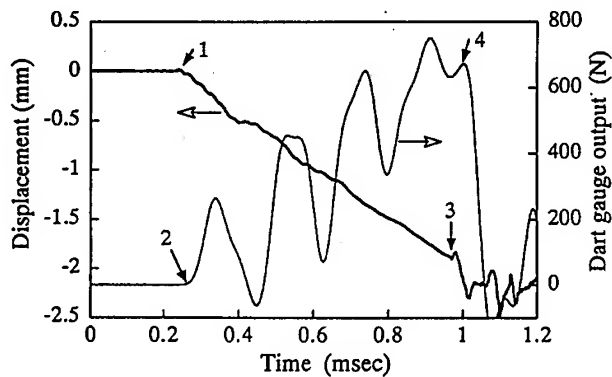


Fig.3 An example of the experimental result obtained by Charpy impact test of PC

3.1.2 Determination of K_{IC} for Polycarbonate as a function of loading velocity

An experimental method for K_{IC} evaluation in which dart gage output is not used is described in the following [7]. A strain gage is attached in the vicinity of the notch-tip of the three-point impact bend specimen shown in Fig.4. Since dynamic effect can be negligible at a low impact rate of 1 m/s, the compliance C_s is evaluated using the load F_d obtained from the dart gage and the displacement δ_s measured by the fiber with the aid of the following relation:

$$C_s = \delta_s / F_d \quad (V_i = 1 \text{ m/s}) \quad (2)$$

It is assumed that the C_s value obtained is approximately equivalent to that at $V_i = 2.8$ – 5.5 m/s. For the higher rates (2.8–5.5 m/s), the F value is calculated using the C_s and values of δ_s measured by the fiber system. On the other hand, a calibration of the crack-tip gage (CTG) is also made at the impact rate of 1 m/s (Fig.5). By assuming that the calibration factor can be used at 2.8–5.5 m/s, the load is estimated by both the compliance method and CTG. Critical stress intensity factor (fracture

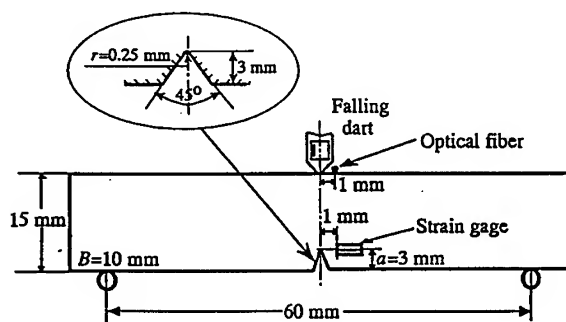


Fig.4 Geometry of Charpy PC specimen with optical fiber and crack-tip strain gage

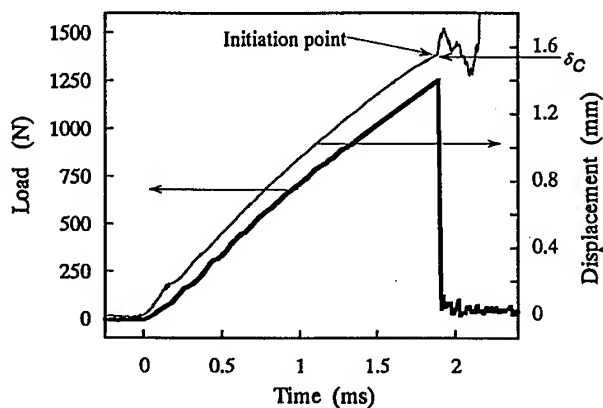


Fig.5 Crack-tip load and deflection versus time for a Charpy PC specimen obtained at 1 m/s

toughness) K_{IC} is then evaluated from the maximum value F_{max} of the load curve obtained using the following formula:

$$K_{IC} = \frac{3}{2} \frac{S}{BW^2} \sqrt{aY(a/W)} F_{max} \quad (3)$$

where S is the span, B the specimen thickness, W the width, a the notch length and $Y(a/W)$ the geometrical factor.

Dependence of K_{IC} of PC specimens with V-notch on impact rate is shown in Fig.6 [7]. K_{IC} values obtained using the load values evaluated by the deflection method with optical fiber, the CTG method and the dart gage method (dart; attached to the drop weight of 2.6 kg) are shown in this figure for comparison. The K_{IC} values obtained by the fiber displacement meter and the CTG slightly decrease as impact rate increases up to 5.5m/s, while the K_{IC} value estimated using the dart gage output increases. The latter is considered to be caused by the error induced by dynamic effect. In the former methods, the modulus and compliance of the material are assumed to be unchangeable. However, in general, the modulus tends to increase and the compliance tends to decrease as impact rate increases. In that case, the downward slope of K_{IC} is reduced. Fracture surface morphology of the specimens substantiates this deduction.

Loading-rate dependence of the impact strength of PC specimens has been investigated [15-18]. Most of the studies exhibited that the strength tends to decrease as loading rate increases, except the study by Beguelin et al [7] indicating that the strength is almost independent of loading rate up to 10m/s.

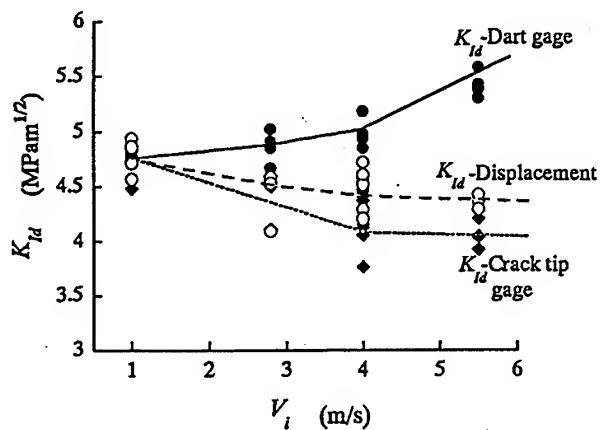


Fig.6 K_{IC} versus impact velocity relations for PC obtained by three different methods

3.1.3 Effect of annealing on impact fracture energy for HDPE

In general, annealing embrittles polymers; therefore, some impact fracture test results showed that brittle-ductile transition temperatures of polymers shifted to higher temperatures. PE's except high density PE (HDPE) exhibit this kind of behavior. On the contrary, the transition temperature of HDPE shifted to lower temperature and its fracture energy increases as a result of annealing [19].

Impact testing results for HDPE obtained using the instrumented impact bending Charpy testing machine with the optical fiber system are shown in Fig.7 [9,20]. It is understood from Fig.7 that the

increase of impact fracture energy described above mainly corresponds to the increase of absorbed energy during the fracture propagation process. On the other hand, annealing hardly influences K_{IC} .

A model to explain the increase of fracture propagation energy due to annealing is shown in Fig.8 [8]. Embrittlement induced by annealing results in extensive microcracking in the vicinity of crack-tip as shown in Fig.8. As a result, surface energy increases due to the increase of total fracture surface.

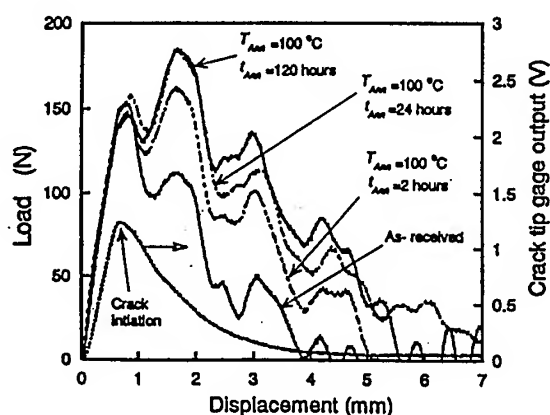


Fig.7 Load-displacement curves of HDPE specimens impacted at 3.8 m/s

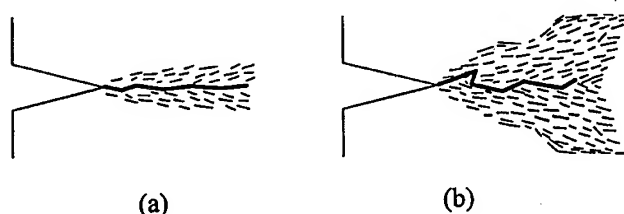


Fig.8 A model to show enlargement of the process zone for an annealed (b) HDPE specimen as compared with as-received (a) specimen

3.2 Application to dynamic tensile loading test for HIPS

Tensile and compressive displacements under high-speed deformation can be measured by using a pair of the displacement meter with two optical fibers as described before [1]. The experimental system is shown in Fig.9. Two types of drop weight impact testing machine (tensile and bending) with piezo load cell were developed [1]. High speed photography was also conducted to assess the reliability of the measurement of elongation using the optical extensometer. Strains evaluated by the two different methods coincide reasonably well [21].

Impact tensile deformation behavior of two kinds of HIPS containing rubber particles with

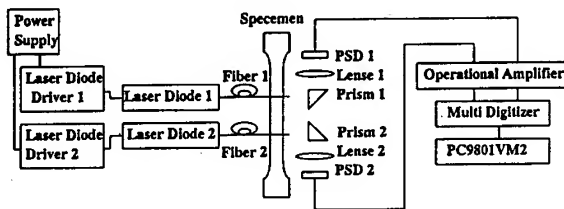


Fig.9 Schematic drawing of the optical extensometer

micron or submicron diameter [10,21]. The material properties are shown in Table 1. Stress-strain curves for 0.45S and 0.84S obtained using the impact tensile testing machine are shown in Figs.10(a) and (b). Fig.10(a) shows a typical viscoelastic deformation behavior in which strain at fracture decreases as tensile rate increases (three quasi-static rates: 0.003, 0.02, 0.15/sec and an impact rate: 18/sec). On the other hand, in Fig.10(b), the elongation at the impact rate (18/sec) is much larger than those at the quasi-static rates, and furthermore the impact response exhibited a large deformation greater than 15%. A craze model to explain the enlargement of 'yield' strain at impact rate is shown in Fig.11 [8]. The 'yield' strain in HIPS is assumed to be mostly induced by the rubber elastic elongation of crazes, which is different from permanent plastic deformation. It is considered that fracture induced from surface defects prevents the material from the large deformation at quasi-static rates. The results shown in Fig.10 suggest that the rubber particle size has a significant influence on the dynamic craze formation. It is noted that it is very difficult to obtain those stress-strain relations shown in Fig.10 by strain gage method because the strain gage stuck on the specimen surface affects the deformation and usually quantitative measurement of such large deformation is very difficult using strain gages.

Table 1 Material data for tested HIPS specimens

Specimen	Composition (wt%)		Weight average molecular weight of PS	Average size of rubber particles (μm)	Morphology of rubber particles
	St	Bd			
0.45s	92	8	239,500	0.45	Salami
0.84s	92	8	225,300	0.84	Salami

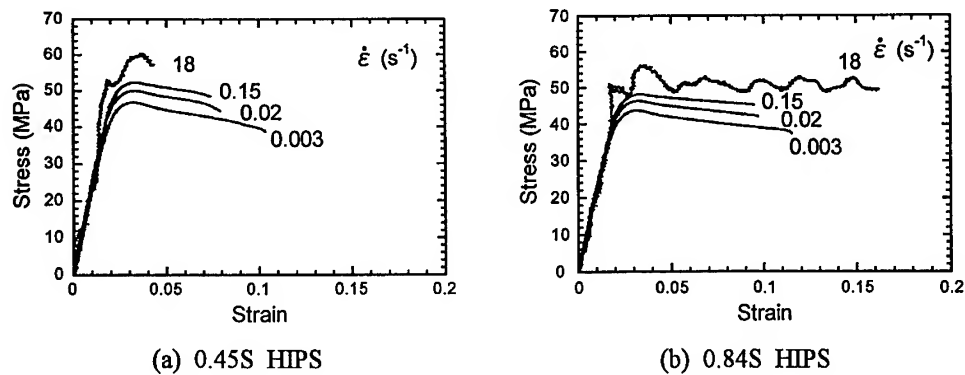


Fig.10 Strain rate dependence of S-S curves for HIPS specimens with different rubber particle size

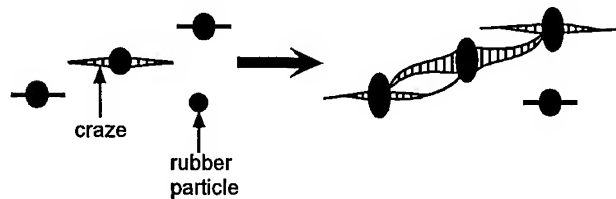


Fig.11 A craze model to explain enlargement of deformation and fracture energy at a high strain rate

3.3 Application to dynamic interlaminar fracture test for polymer matrix composites

The optical displacement meter was used in the measurement of the dynamic mode II interlaminar fracture toughness of carbon/epoxy composite laminates [11,22]. Impact testing system consisting of an instrumented drop weight testing machine and the displacement measuring apparatus is shown in Fig.12. End Notched Flexure (ENF) specimen was used as the mode II interlaminar fracture specimen. Applied load was obtained through the output of the strain gages attached to the loading dart. Load-point displacement was measured by placing an optical fiber on the bottom surface of the specimen as shown in Fig.12. Strain on the specimen surface close to the crack-tip was also recorded to detect the initiation of crack propagation. An example of experimental results obtained from low speed (0.9m/s) impact testing is shown in Fig.13. Several sudden changes caused by the initiation of crack growth are seen on all the data, namely, the load, the displacement and the strain gage signal. Those inflection points took place in the order of the strain gage signal, the displacement and the load. The strain gage signal measured at the closest point to the crack-tip indicated the fastest response to the crack initiation.

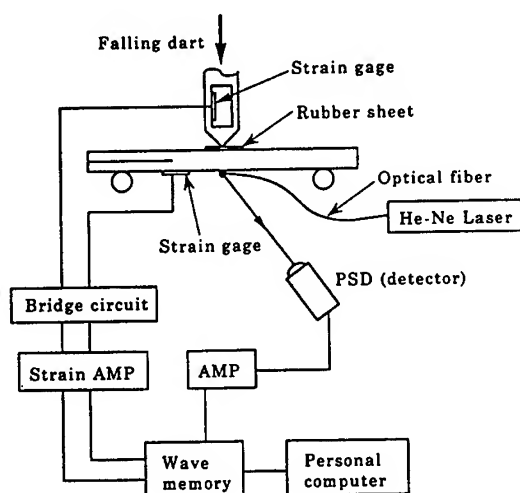


Fig.12 Dynamic mode II interlaminar fracture testing system

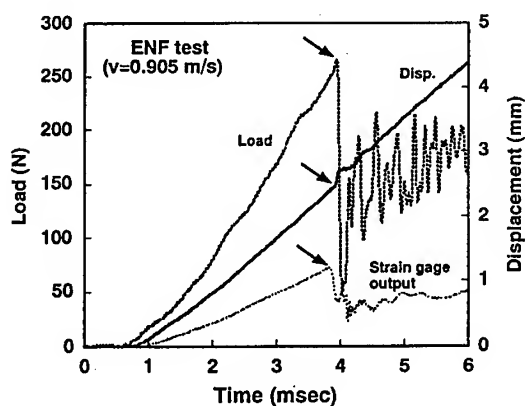


Fig.13 Dynamic load, displacement and surface strain-time curves of T800H/2500

For all the data obtained, those three different inflection points (load, displacement and strain) were evaluated, and the dynamic mode II interlaminar fracture toughness was estimated by evaluating the critical load and the critical displacement on the basis of the following two methods A and B:

(A) The critical load and displacement are estimated at the time of the maximum of the strain gage signal. These critical values are denoted by P_A and δ_A .

(B) The critical load and displacement are obtained at the inflection points of the load and displacement curves, respectively. These values are denoted by P_B and δ_B , respectively.

The mode II interlaminar fracture toughness was then evaluated using the following formula with the aid of those critical values:

Table 2 Static and dynamic mode II interlaminar fracture toughnesses of CFRP laminates

	Static	Dynamic			
	G_{IIC} (J/m ²)	$G_{IIC}(P_c)$ (J/m ²)	$G_{IIC}(\delta_c)$ (J/m ²)	$G_{IIC}(P_B)$ (J/m ²)	$G_{IIC}(\delta_B)$ (J/m ²)
T800H/2500	534	533	467	599	482
T800H/3631	727	612	596	717	615

$$G_{IIC} = \frac{9a_0^2 P_c^2}{16EB^2 h^3} = \frac{36a_0^2 \delta_c^2 E h^3}{(2L^3 + 3a_0^3)^2} \quad (4)$$

where P_c and δ_c are the critical load and the critical displacement, respectively. a_0 is the initial crack length, E the bending modulus, B the specimen width and $2h$ the specimen thickness. G_{IIC} values obtained for two types of carbon/epoxy composites are shown in Table 2. All the dynamic toughnesses obtained by the method A are smaller than the corresponding static toughnesses, while $G_{IIC}(P_B)$ of T800H/2500 is higher than the static toughness. This result implies that the rate-dependence of the interlaminar fracture toughness depends upon how to determine the critical point. This corresponds to a fact that a definite tendency for the rate-dependence on the interlaminar fracture toughness of FRP laminates has not been obtained yet [23]. Also, all the load-based G_{IIC} values are higher than the corresponding displacement-based G_{IIC} values. This is because the critical load values were overestimated due to the effect of oscillation appeared on the load data. These results imply that the accurate detection of crack initiation is one of the critical factors in dynamic interlaminar fracture test. It appears that the proposed method (the method A), in which crack initiation is determined from the strain signal measured on specimen surface and then interlaminar fracture toughness is evaluated on the basis of load-point displacement measured using the optical displacement meter, is a suitable way to evaluate the dynamic interlaminar toughness of FRP laminates accurately.

4. CONCLUSION

An optical system for the quantitative measurement of displacement and elongation under high speed deformation was developed. This system has been applied to impact bending and tensile tests of polymers and polymer matrix composites, and valuable knowledge has been obtained.

ACKNOWLEDGMENT

The author is thankful to Dr. Todo, Dr. Aggag, Dr. Kuboki, and Mr. Mada of RIAM, Kyushu University for their contribution in the works described here. Professor Kausch and Dr. Beguelin of EPFL, Switzerland is much appreciated for their kind help in the construction of the optical extensometer through the International Cooperative Research Project sponsored by Monbusho, Japan. Specimens of HDPE and HIPS were kindly supplied by Dr. Kitao of NKK Co. and Mr. Shinmura of DENKA Co. respectively, for which the author is much indebted.

REFERENCES

1. K. Takahashi and A. F. Yee, (eds.). *Impact Fracture of Polymers -Materials Science and Testing Techniques-* Kyushu University Press (1992)pp.0-500
2. G. Aggag and K. Takahashi, *Polym. Eng. And Sci.*, **36**(17)(1996)2260-2266
3. Ph. Beguelin, M. Barbezat and H. H. Kausch, *J. de Physique III*, **1**(1991)No10
4. Ph. Beguelin, Ph-D Thesis, EPFL(1996)
5. K. Takahashi, T. Mada and Ph. Beguelin, *Transactions of the Japan Soc. Mech. Engineers*, **64**(628)(1998)2975
6. T. Mada and K. Takahashi and Ph. Beguelin, *Transactions of the Japan Soc. Mech. Engineers*, **63**(611)(1997)1431
7. K. Takahashi, G. Aggag and T. Mada, *J. de Physique IV*, **7**(1997)L77
8. K. Takahashi, *Proc. 7th Int.Symp. on Plasticity and Its Current Applications*, (Cancun, Jan. 1999)pp.975-978
9. G. Aggag and K. Takahashi, to appear in *Abstracts of 11th Int. Conf. on Def., Yield and Fracture of Polymers* (Cambridge, April 2000)
10. T. Kuboki and K. Takahashi, *ibid.* and this Proceedings
11. M. Todo, T. Nakamura, T. Mada and K. Takahashi, *Adv. Comp. Mater.*, **7**(3)(1998)285.
12. H. W. Nam, G. A. Aggag, K. Takahashi and K. S. Han, *Comp. Sci. and Tech.*, to appear
13. P. Compston, P.-Y.B. Jar, P. J. Burchill and K. Takahashi, *Comp. Sci. and Tech.*, to appear
14. P. Compston, P.-Y. B. Jar and K. Takahashi, *J. Mater. Sci., Letts.*, to appear
15. G.C. Adams, R.G. Bender, B.A. Crouch and J.G. Williams, *Polym. Eng. Sci.*, **30** (1990) p. 241
16. J.G. Williams, in *Fracture Mechanics of Polymers*, Ellis Harwood, Chichester, (1984) p. 238
17. Ph. Beguelin and H.H. Kausch, *ESIS Publication No.19* (1995) p. 209
18. R. Selden, Ph.D. thesis, Lausanne Institute of Technology (1996)
19. K. Kitao, *Polymer Eng. Sci.*, **37** (1997) p. 777
20. G. Aggag, Ph.D. thesis, Kyushu University (1999)
21. T. Kuboki, Ph.D. thesis, Kyushu University (1999)
22. M. Todo, T. Nakamura, T. Mada and K. Takahashi, *Adv. Comp. Mater.*, **7**, 3 (1998) p. 285
23. M. Tohdoh, S.K. Chaturvedi and R.L. Sierakowski, *Proc. of the 6th Japan-U.S. Conference on Comp. Mater.*, (1992) p. 694

Dynamic Stress Intensity Factors of Cylindrical Interface Cracks Subjected to P-Wave

W.J. Feng and Z.Z. Zou

Department of Basic Courses, Shijiazhuang Railway Institute,
Shijiazhuang 050043, China P.R.

Keywords: Cylindrical Interface Crack, Dynamic Stress Intensity Factor, Elastic Wave Scattering, Singular Integral Equation

ABSTRACT

In this paper, we investigate the scattering of an axially symmetric longitudinal elastic wave by the cylindrical interface cracks between an elastic cylindrical inclusion and its surrounding material. The number and length of the cracks are arbitrary. By using the Fourier transformation and introducing the dislocation density functions, we reduce the problem to a set of singular integral equations of the second type, which is solved numerically for a range of values of the frequencies. The variations of the dynamic stress intensity factors are plotted versus the frequency of the incident wave. Numerical results show that the size of cylinder radius has important influences on the resonance peak.

1. INTRODUCTION

Because of its practical importance in various engineering and seismological applications, the elastic wave scattering by the cylindrical interface cracks between an infinitely long cylinder and its surrounding material has received considerable attention in recent years. And a number of papers concerning the problems have been published [1-3]. The interface cracks under consideration in those papers are all assumed to be infinite in the direction of the cylinder length.

However, the interface cracks are often finite. In this paper, we study the interaction of longitudinal waves with cylindrical interface cracks. By using Fourier transformation and introducing the dislocation density functions, we reduce the problem to a set of singular integral equations of the second type, which can be easily solved numerically to calculate the dynamic stress intensity factors (DSIFs). Numerical results show that resonance peaks occur only at low frequencies, and that the size of cylinder radius has important influence on the resonance peak.

2. STATEMENT OF THE PROBLEM

Consider the problem shown in Fig.1, there are n cylindrical interface cracks between an infinitely long cylinder with radius b and its surrounding material. Use cylindrical coordinates (r, θ, z) , and let the z coordinates of the k th crack tips be a_k and b_k ($k = 1 \sim n$). An incident plane P wave propagating in z -direction with circular frequency ω excites the cracks.

The total field may be divided into the incident field and scattered field. Set $\{u^{(i)}, \sigma^{(i)}\}$

represent the wave field when no cracks exist, and set $\{u^{(s)}, \sigma^{(s)}\}$ represent the scattered field which is the modification to the incident field due to the existence of the cracks. Considering the symmetry of the problem, the potential functions of the scattered field should satisfy the following wave motion equations (for simplicity, superscript (s) and the time factor $\exp(-i\omega t)$ having been all suppressed in this paper)

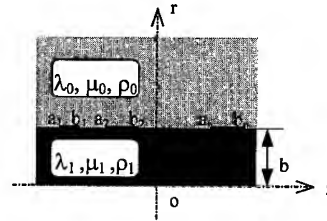


Fig. 1. Mechanic model

$$\begin{cases} \nabla^2 \varphi_j + K_{lj}^2 \varphi_j = 0 \\ \nabla^2 \psi_j - \frac{1}{r^2} \psi_j + K_{Tj}^2 \psi_j = 0 \end{cases} \quad j = 0, 1 \quad (1)$$

where $\nabla^2 = \frac{\partial^2}{\partial r^2} + \frac{1}{r} \frac{\partial}{\partial r} + \frac{\partial^2}{\partial z^2}$, $K_{lj} = \omega / \sqrt{(\lambda_j + 2\mu_j) / \rho_j}$, $K_{Tj} = \omega / \sqrt{\mu_j / \rho_j}$, ρ_j is the mass density, and λ_j and μ_j are Lamé constants. The subscript $j=1$ represents the cylinder, and $j=0$ represents the surrounding material. The continuous interface conditions and stress boundary conditions on the cracks, respectively, can be written as

$$\begin{cases} \sigma_{rr1} = \sigma_{rr0}, & \sigma_{rz1} = \sigma_{rz0} \\ u_{r1} - u_{r0} = D_r, & u_{z1} - u_{z0} = D_z \end{cases} \quad r = b, \quad -\infty < z < +\infty \quad (2)$$

$$\begin{cases} \sigma_{rr1} = -\sigma_{rr1}^{(i)} \\ \sigma_{rz1} = -\sigma_{rz1}^{(i)} \end{cases} \quad r = b, z \in \sum_{k=1}^n (a_k, b_k) \quad (3)$$

where

$$\begin{cases} D_r(z) = \begin{cases} 0 & z \notin \bigcup_{k=1}^n (a_k, b_k) \\ D_{r,l}(z) & z \in (a_l, b_l), \forall l \in \{1, 2, \dots, n\} \end{cases} \\ D_z(z) = \begin{cases} 0 & z \notin \bigcup_{k=1}^n (a_k, b_k) \\ D_{z,l}(z) & z \in (a_l, b_l), \forall l \in \{1, 2, \dots, n\} \end{cases} \end{cases}$$

$$\begin{cases} D_{r,l}(z) = u_{r1}(b, z) - u_{r0}(b, z) \\ D_{z,l}(z) = u_{z1}(b, z) - u_{z0}(b, z) \end{cases} \quad z \in (a_l, b_l), \forall l \in \{1, 2, \dots, n\},$$

$D_{r,l}$ and $D_{z,l}$ are dislocation functions of the l th crack. $\sigma_{rr1}^{(i)}$ and $\sigma_{rz1}^{(i)}$, which are assumed to know, are stress components corresponding to the incident field. In addition, the scattered field must satisfy the radiation condition at infinity.

3. THE DERIVATION AND NUMERICAL SOLUTION OF SINGULAR INTEGRAL EQUATIONS

3.1. Dual Integral Equation Groups of Dislocation Functions

By using the Fourier integral transformation, we can get the scattering potentials in the transformation domain. By employing the defining solution conditions (2), (3) and the radiation condition at infinity, the dual integral equation groups about the unknown functions \overline{D}_r and \overline{D}_z can be obtained as follows

$$\begin{cases} \frac{1}{2\pi} \int_{-\infty}^{+\infty} \frac{P_{11}(\xi) \overline{D}_r(\xi) + P_{12}(\xi) \overline{D}_z(\xi)}{\Delta(\xi)} e^{-i\xi z} d\xi = -\sigma_{rr1}^{(i)}(b, z) \\ \frac{1}{2\pi} \int_{-\infty}^{+\infty} \frac{P_{21}(\xi) \overline{D}_r(\xi) + P_{22}(\xi) \overline{D}_z(\xi)}{\Delta(\xi)} e^{-i\xi z} d\xi = -\sigma_{rz1}^{(i)}(b, z) \end{cases} \quad z \in \bigcup_{k=1}^n (a_k, b_k) \quad (4)$$

$$\begin{cases} \frac{1}{2\pi} \int_{-\infty}^{+\infty} \overline{D}_r e^{-i\xi z} d\xi = 0 \\ \frac{1}{2\pi} \int_{-\infty}^{+\infty} \overline{D}_z e^{-i\xi z} d\xi = 0 \end{cases} \quad z \notin \bigcup_{k=1}^n (a_k, b_k) \quad (5)$$

where \overline{D}_r and \overline{D}_z , respectively, denote the Fourier transformations of D_r and D_z , and Δ , P_{11} , P_{12} , P_{21} and P_{22} , which can be omitted here [4], are known functions of ξ .

3.2. Singular Integral Equations of Dislocation Density Functions

Substituting \overline{D}_r and \overline{D}_z for D_r and D_z and noticing the intrinsic properties of $\Delta(\xi)$, $P_{11}(\xi)$, $P_{12}(\xi)$, $P_{21}(\xi)$ and $P_{22}(\xi)$, we have

$$\begin{cases} \sum_{k=1}^n \left\{ -s_2 \delta_{kl} f_{z,k}(z) + \frac{s_1}{\pi} \int_{a_k}^{b_k} \frac{f_{r,k}(v)}{v-z} dv \right. \\ \quad \left. + \frac{1}{\pi} \int_{a_k}^{b_k} [Q_{11}(v, z) f_{r,k}(v) + Q_{12}(v, z) f_{z,k}(v)] dv \right\} = \sigma_{rr1}^{(i)}(b, z) \\ \sum_{k=1}^n \left\{ s_2 \delta_{kl} f_{r,k}(z) + \frac{s_1}{\pi} \int_{a_k}^{b_k} \frac{f_{z,k}(v)}{v-z} dv \right. \\ \quad \left. + \frac{1}{\pi} \int_{a_k}^{b_k} [Q_{21}(v, z) f_{r,k}(v) + Q_{22}(v, z) f_{z,k}(v)] dv \right\} = \sigma_{rz1}^{(i)}(b, z) \end{cases} \quad z \in \bigcup_{l=1}^n (a_l, b_l) \quad (6)$$

where $f_{r,k}(v) = \frac{dD_{r,k}(v)}{dv}$ and $f_{z,k}(v) = \frac{dD_{z,k}(v)}{dv}$ are called crack dislocation density functions. $Q_{11}(v, z)$, $Q_{12}(v, z)$, $Q_{21}(v, z)$ and $Q_{22}(v, z)$ are known functions, and s_1 and s_2 are two different constants. Limited by the length of this paper, they are all omitted here and can be found in reference [4]. By setting $c_k = \frac{b_k - a_k}{2}$, $d_k = \frac{b_k + a_k}{2}$ and applying the substitutions

$$\begin{aligned}
v &= c_k \eta + d_k, \quad z = c_l \zeta + d_l \\
F_{r,l}(\zeta) &= f_{r,l}(c_l \zeta + d_l), \quad F_{z,l}(\zeta) = f_{z,l}(c_l \zeta + d_l) \\
H_{mi}^{kl}(\eta, \zeta) &= c_k Q_{mi}(c_k \eta + d_k, c_l \zeta + d_l) \quad (m, i = 1, 2) \\
\sigma_{rr,l}(b, \zeta) &= \sigma_{rr}^{(l)}(b, c_l \zeta + d_l), \quad \sigma_{rz,l}(b, \zeta) = \sigma_{rz}^{(l)}(b, c_l \zeta + d_l),
\end{aligned}$$

equations 6 can be further converted to a set of standard singular integral equations

$$\begin{aligned}
&\sum_{k=1}^n \left[\begin{array}{cc} 0 & -s_2 \delta_{kl} \\ s_2 \delta_{kl} & 0 \end{array} \right] \begin{Bmatrix} F_{r,l}(\zeta) \\ F_{z,l}(\zeta) \end{Bmatrix} + \frac{s_1}{\pi} \int_{-1}^1 \begin{bmatrix} 1 & 0 \\ 0 & 1 \end{bmatrix} \begin{Bmatrix} F_{r,k}(\eta) \\ F_{z,k}(\eta) \end{Bmatrix} \frac{c_k}{(c_k \eta - c_l \zeta) + (d_k - d_l)} d\eta \\
&+ \sum_{k=1}^n \frac{1}{\pi} \int_{-1}^1 \begin{bmatrix} H_{11}^{kl}(\eta, \zeta) & H_{12}^{kl}(\eta, \zeta) \\ H_{21}^{kl}(\eta, \zeta) & H_{22}^{kl}(\eta, \zeta) \end{bmatrix} \begin{Bmatrix} F_{r,k}(\eta) \\ F_{z,k}(\eta) \end{Bmatrix} d\eta = \begin{Bmatrix} \sigma_{rr,l}(b, \zeta) \\ \sigma_{rz,l}(b, \zeta) \end{Bmatrix} \quad \forall l \in \{1, 2, \dots, n\}
\end{aligned} \quad (7)$$

Recalling that $F_{r,l}(\zeta)$ and $F_{z,l}(\zeta)$ represent z-derivatives of displacement differences, the single-valued conditions may be expressed as [5]

$$\begin{aligned}
&\int_{-1}^1 F_{r,l}(\zeta) d\zeta = 0 \\
&\int_{-1}^1 F_{z,l}(\zeta) d\zeta = 0 \quad \forall l \in \{1, 2, \dots, n\}
\end{aligned} \quad (8)$$

3.3. Derivation and Numerical Resolution of Cauchy Singular Integral Equations

For simplicity, in this section we take the case of one crack as an example to solve Eqs.7 and 8. By setting $a_1 = -c$, $b_1 = c$ and $\gamma = s_2/s_1$, we can easily have

$$\begin{aligned}
&\begin{bmatrix} 0 & -\gamma \\ \gamma & 0 \end{bmatrix} \begin{Bmatrix} F_{r,1}(\zeta) \\ F_{z,1}(\zeta) \end{Bmatrix} + \frac{1}{\pi} \int_{-1}^1 \frac{1}{\eta - \zeta} \begin{Bmatrix} F_{r,1}(\eta) \\ F_{z,1}(\eta) \end{Bmatrix} d\eta \\
&+ \frac{1}{\pi s_1} \int_{-1}^1 \begin{bmatrix} H_{11}^{11}(\eta, \zeta) & H_{12}^{11}(\eta, \zeta) \\ H_{21}^{11}(\eta, \zeta) & H_{22}^{11}(\eta, \zeta) \end{bmatrix} \begin{Bmatrix} F_{r,1}(\eta) \\ F_{z,1}(\eta) \end{Bmatrix} d\eta = \frac{1}{s_1} \begin{Bmatrix} \sigma_{rr,1}(b, \zeta) \\ \sigma_{rz,1}(b, \zeta) \end{Bmatrix} \quad |\zeta| < 1
\end{aligned} \quad (9)$$

Clearly, the dominant parts of Eqs.9 are coupled. Substituting

$$\begin{Bmatrix} F_{r,1}(\zeta) \\ F_{z,1}(\zeta) \end{Bmatrix} = [R] \begin{Bmatrix} \phi_{r,1}(\zeta) \\ \phi_{z,1}(\zeta) \end{Bmatrix} \quad (10)$$

into (10) and then multiplying the obtained equation by $[R]^{-1}$, we get

$$\begin{aligned}
&\begin{bmatrix} \gamma & 0 \\ 0 & -\gamma \end{bmatrix} \begin{Bmatrix} \phi_{r,1}(\zeta) \\ \phi_{z,1}(\zeta) \end{Bmatrix} + \frac{1}{i\pi} \int_{-1}^1 \frac{1}{\eta - \zeta} \begin{Bmatrix} \phi_{r,1}(\eta) \\ \phi_{z,1}(\eta) \end{Bmatrix} d\eta \\
&+ \frac{1}{i\pi s_1} \int_{-1}^1 [N(\eta, \zeta)] \begin{Bmatrix} \phi_{r,1}(\eta) \\ \phi_{z,1}(\eta) \end{Bmatrix} d\eta = \frac{1}{is_1} [R]^{-1} \begin{Bmatrix} \sigma_{rr,1}(b, \zeta) \\ \sigma_{rz,1}(b, \zeta) \end{Bmatrix}
\end{aligned} \quad (11)$$

where

$$[R] = \begin{bmatrix} 1 & 1 \\ -i & i \end{bmatrix}$$

$$[N(\eta, \varsigma)] = [R]^{-1} \begin{bmatrix} H_{11}^{11}(\eta, \varsigma) & H_{12}^{11}(\eta, \varsigma) \\ H_{21}^{11}(\eta, \varsigma) & H_{22}^{11}(\eta, \varsigma) \end{bmatrix} [R].$$

At the same time, $\phi_{r,1}(\varsigma)$ and $\phi_{z,1}(\varsigma)$ should also satisfy

$$\int_{-1}^1 \begin{Bmatrix} \phi_{r,1}(\varsigma) \\ \phi_{z,1}(\varsigma) \end{Bmatrix} d\varsigma = 0 \quad (12)$$

Equations 11 are two standard Cauchy singular integral equations of the second type. By using the methods described by Erdogan and Gupta [6], the algebraic equations corresponding to Eqs. 11 and 12 are obtained and can be solved numerically. The dynamic stress intensity factors at the crack tips $-c$ and $+c$ can be given as follows [4]

$$\begin{cases} \begin{Bmatrix} K_I(+c) \\ K_{II}(+c) \end{Bmatrix} = -s_1 \sqrt{1-\gamma^2} [R] \begin{Bmatrix} M_r(1) \\ M_z(1) \end{Bmatrix} \\ \begin{Bmatrix} K_I(-c) \\ K_{II}(-c) \end{Bmatrix} = -s_1 \sqrt{1-\gamma^2} [R] \begin{Bmatrix} M_r(-1) \\ M_z(-1) \end{Bmatrix} \end{cases} \quad (13)$$

where $M_r(t) = (1-t)^{-\alpha} (1+t)^{-\beta} \phi_{r,1}(t)$, $M_z(t) = (1-t)^{-\beta} (1+t)^{-\alpha} \phi_{z,1}(t)$. The detailed analysis can be found in reference [4].

4. NUMERICAL RESULTS AND CONCLUSIONS

For a given incident plane P wave, it is quite difficult to obtain the accuracy stress components $\sigma_{rr}^{(i)}(b, z)$ and $\sigma_{rz}^{(i)}(b, z)$. Considering that $\sigma_{rr}^{(i)}(b, z)$ and $\sigma_{rz}^{(i)}(b, z)$ should exist as stress waves, for simplicity, here we directly set $\sigma_{rr}^{(i)}(b, z) = \sigma_0 e^{iK_{L1}z}$ and $\sigma_{rz}^{(i)}(b, z) = 0$ (the DSIFs corresponding to $\sigma_{rr}^{(i)}(b, z) = 0$, $\sigma_{rz}^{(i)}(b, z) = \tau_0 e^{iK_{L1}z}$ can also be calculated similarly). Because of the symmetry, only the DSIFs as $z \rightarrow c^+$ need to be evaluated. As an example, assume that cylinder and surrounding material are glass and epoxy, respectively. The values for material parameters are set to be the same as those given in reference [5].

To verify if the results for $K_{L1}c \rightarrow 0$ approach the corresponding static resolutions, the DSIFs have first been calculated in the case of $\sigma_{rr}^{(i)}(b, z) = \sigma_0$ and $K_{L1}c = 10^{-4}$. Figure 2 shows good agreement between the results of the present study as $K_{L1}c \rightarrow 0$ and the static results of Erdogan and Ozbek [5].

For different b/c , the normalized first and second DSIFs versus $K_{L1}c$ are presented in Fig. 3. As shown in Fig. 3, both the first and second DSIFs have obvious resonant peaks, and there are total

two resonant peaks within the range of the wave number considered. In general, the main peak values of the first DSIF are higher than those of the second DSIF, and the peak values of both K_I and K_{II} vary with b/c .

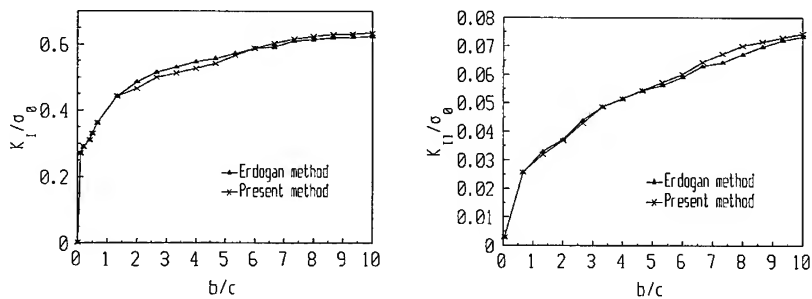


Fig.2. $K_{LI} c=10^{-4}$, comparison with the static results for different b/c

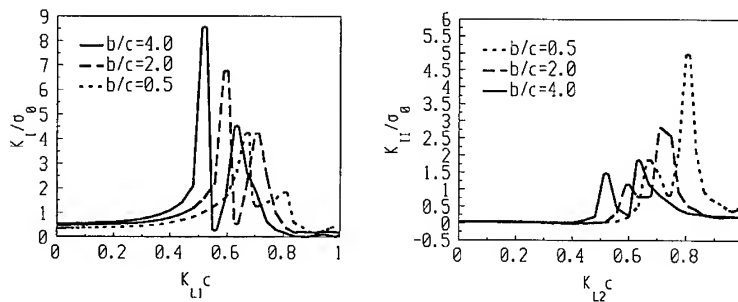


Fig.3. Effect of geometry criterion on dynamic stress intensity factors

REFERENCES

1. V. Z. Parton, and B. A. Kudryavtsev, Mechanics of deformable bodies and constructions (in Russian), Mashinostroyeniye, Moscow (1975) p.379
2. C. Coussy, Wave Motion, **6**(1982) p. 223
3. Y. Yang, and A. Norris, Wave Motion, **15**(1992) p.43
4. W. J. Feng, The scattering of elastic waves by multiple cylindrical interface cracks and the elastic wave identification of two dimensional flaws (in Chinese), Ph. D. dissertation, HIT, 1999
5. F. Erdogan, and T. Ozbek, ASME J. Appl. Mech., **36**(1969) p.865
6. F. Erdogan, and G. D. Gupta, Int. J. Solids Structures, **7**(1971) p.1089

Effects of Impact Loading Rate on the Delamination Behavior of Composite Laminates

N.S. Choi

Department of Mechanical Engineering, Hanyang University,
Ansan-si, Kyunggi-di 425-791, Korea

Keywords: Crack Velocity, Delamination Fracture, Effective Flexural Modulus, Fiber Bridging, Multidirectional Composites, Rate of Test

ABSTRACT

The present study has shown the experimental results for characterization of the mode I delamination fracture of continuous carbon fiber/epoxy multidirectional composites under a wide range of test rates, up to high rate of 11.4 m/s. At the high rates of test ≥ 1.0 m/s, Equation (4) requiring the values of the actual arm displacement and flexural (axial) modulus was better for deduction of G_{IC} . However the maximum value of G_{IC} so obtained was considerably underestimated and needed a compensation of loss. With increasing the rate up to 1.0×10^{-1} m/s, there was little differences in the delamination fracture behavior, whereas with an increase of the rate beyond 1.0 m/s the maximum value of G_{IC} decreased considerably.

1. INTRODUCTION

Fiber composites, based on continuous fibers embedded in a polymeric matrix, are very promising for applications in various mechanical structures where a high stiffness-to-weight ratio and strength-to-weight ratio are required. A limitation of the fiber composites, however, is their poor resistance to delamination. The majority of the works on the delamination fracture of composite materials has been conducted through the application of linear-elastic fracture-mechanics (LEFM), which are concerned with the determination of the interlaminar fracture energy G_c . The interlaminar fracture energy G_{IC} often shows an initial increase with crack length: an increasing resistance effect, i.e. rising "R-curve" is found during the initial propagation of a crack [1-4], which mainly arises from the increasing degree of fiber bridging behind the crack-tip, crack-tip blunting and/or damage zone development around the crack-tip.

As the fiber composites have been increasingly applied in engineering structures, characterization of the interlaminar fracture behavior under high-rate loading has been significant. For unidirectional fiber composites, the extent of decreasing rate in G_{IC} for similar fiber-composites was considerably various from report to report [5-7], which sometimes offered a conflicting finding. Blackman et al. [8] showed that a considerable care must be taken in the experimental aspects when undertaking the tests at high rates of test. They further analysed the dynamic effects on the behavior of G_{IC} being invariably associated with high-rate tests [9]. The above high-rate test studies were all conducted on unidirectional fiber composites.

The purpose of the present study is to characterize the mode I – delamination fracture of continuous carbon fiber / epoxy multidirectional laminates under slow and high rates of test (0.5mm/min – 11.4m/s). Recently, the present authors studied the delamination fracture of the multidirectional laminates under a slow rate of test (0.5mm/min) [10] and showed that the values of G_{IC} at crack initiation were significantly greater than those for the unidirectional laminates. On the basis of the static test results the present study considers (i) the dynamic effects in the double-cantilever beam tests and (ii) rate effects on the behavior of the delamination fracture energy.

2. THEORETICAL CONSIDERATION

2.1 Static analysis

In the standard Mode I double-cantilever beam (DCB) specimen as shown in Fig.1 with an end deflection of δ , a crack length of a and the beam width B , the two arms of the test specimen are loaded by applying symmetrical opening loads. For the static analysis the value of the interlaminar fracture energy G_{IC} is expressed [4] by

$$G_{IC} = \frac{F}{N} \cdot \frac{3P\delta}{2B(a + \chi_1 h)} \quad (1)$$

or, alternatively

$$G_{IC} = \frac{F}{N^2} \cdot \frac{3h^3 \delta^2 E_{11}}{16(a + \chi_1 h)^4} \quad (2)$$

From Equation (1), the value of G_{IC} can be deduced directly by measuring the crack length a and corresponding values of P and δ . Since Equation (2) does not require a direct knowledge of the load, the expression (2) may be used for deducing values of G_{IC} in the high-rate tests. In this case, not only the displacement δ and corresponding crack length a , but also the value of the modulus E_{11} have to be determined.

From the modified beam theory [4], the expression for the compliance C is given by

$$\begin{aligned} C &= \delta/P \\ &= \frac{8N}{Bh^3 E_{11}} \cdot (a + \chi_1 h)^3 \end{aligned} \quad (3)$$

where h is the thickness of one arm of the specimen; E_{11} the axial(flexural) modulus of the laminate arm; χ_1 a correction to the crack length to allow for end-rotation and deflection of the crack tip; F a correction for large displacement and N a correction for the stiffening caused by the metal end-blocks.

2.2 Dynamic effects

For steady-state crack propagation when $\dot{a} > 0$, there is a crack velocity contribution to the kinetic energy term. Therefore

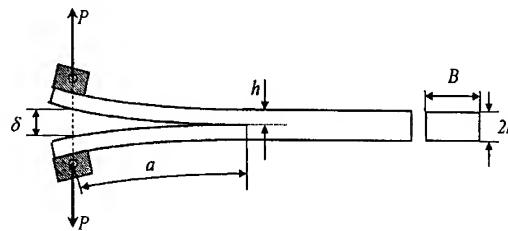


Fig.1 The Mode I double cantilever beam (DCB) composite specimen

$$G_I = \left(\frac{3}{16} \cdot \frac{F}{N^2} \cdot \frac{h^3 E_{II} V^2}{(a + \chi_I h)^4} \right) \cdot t^2 - \frac{111 E_{II} h}{1120} \left(\frac{V}{C} \right)^2 \quad (4)$$

where V is the rate of test; t the loading time; C_0 is the longitudinal wave speed in the composite arms and is given for the plane strain condition. It is to be further mentioned that effects of stress waves propagating in the specimen are not taken into account in Equation (4).

3. EXPERIMENTAL

3.1 Multidirectional composite specimens

The multidirectional fiber composite panels were prepared from 24-ply layups of $(-45^\circ/0^\circ/+45^\circ)_{2S} (+45^\circ/0^\circ/-45^\circ)_{2S}$ utilizing a continuous unidirectional carbon fiber/epoxy prepreg tape ('Fibredux 6376C' supplied by Ciba Geigy plc, UK). A layer of "Teflon" release-film of $12.5\mu\text{m}$ in thickness was inserted onto the $-45^\circ/+45^\circ$ interface at the mid-plane of the laminate lay-up in order to make the initial delamination that acts as a starter crack for the interlaminar fracture testing. The composite panels were cured in an autoclave according to the manufacturer's instructions. The fiber volume fraction and total thickness of the laminate were nominally 65% and 3.4mm, respectively. From the cured panels, the specimens were cut to be nominally 24.5mm wide and 130mm long. One longitudinal edge of the test specimens was coated with a white brittle paint, i.e. type writer correction fluid, to render the crack tip more visible, and was marked with a millimeter scale to aid the measurement of the crack-tip location.

3.2 Mode I interlaminar fracture tests

Slow-rate tests were performed at constant displacement rates of 0.5mm/min (i.e. 0.83×10^{-5} m/s) and 5mm/min (i.e. 0.83×10^{-4} m/s) using a screw-driven tensile-testing machine. The tests were conducted at $23 \pm 2^\circ\text{C}$.

At intermediate and high test rates, i.e. in excess of 1.0×10^{-2} m/s and up to 11.4m/s, a servo-hydraulic testing machine (Instron Model 1343) was used. The DCB specimens were fixed on to the test rig between two titanium shackles. The lower shackle on the stationary side of the specimen was coupled to the piezo-electric load cell (PCB 208A) having a high natural frequency of 70kHz and its short rise-time of $10\mu\text{s}$. Each test was photographed using a high speed camera (Hadland 16mm Photec IV) with a maximum operation speed of 40,000 frames per second. To determine the actual specimen displacement δ and the crack length a at any time during the test, each film negative was projected and greatly enlarged on to a screen, from which precise measurement of the crack length and specimen arm displacement could be made.

To deduce values for G_{IC} via Equation (4), the value of the flexural modulus E_{flex} should be accurately determined. Bend specimens were the multidirectional composite beams about 1.7mm in thickness (h), about 11.5mm in width (b) and 60mm in test span (S), which was the same materials as those in the fracture tests. A small V-shaped striker about

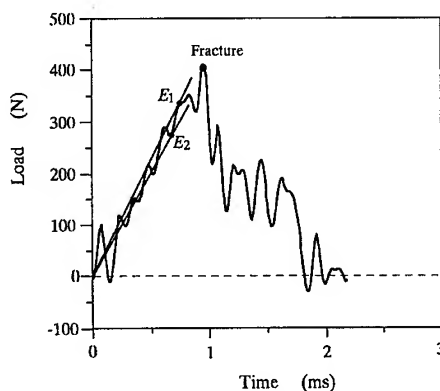


Fig. 2 Three point bending load-time traces of the multidirectional composite tested at a displacement rate of 4.94m/s.

1.5mm in the tip radius and 3.6g in weight was made of a light weight and high strength aluminium alloy to minimize the inertia effect. Except for the 1st cycle formed by an inertia effect, the two consecutive upper and lower peaks in advance of the maximum load in the P - δ curve are adopted to measure the average value of the corresponding slopes (i.e. $(E_1 + E_2) / 2$ in Fig.2), which is used as the measurement method of E_{flex} at test rates $\geq 1.0\text{m/s}$. Figure 3 shows values of E_{flex} for the multidirectional fiber composites measured as described above. As the rate increased to 1m/s , E_{flex} reached 47.4GPa . For the rate beyond 1.0m/s values of E_{flex} were considerably scattered but more enlarged on an average.

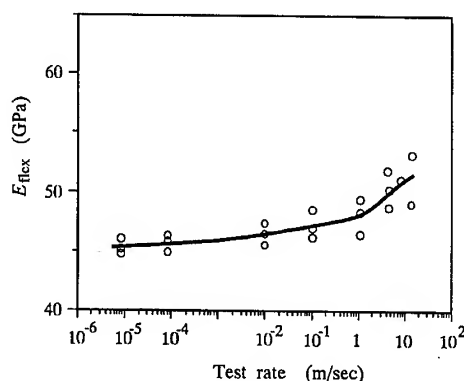


Fig.3 Flexural modulus E_{flex} measured as a function of test rate

4. RESULTS AND DISCUSSION

4.1 Load versus time curves

Load (P) versus time (t) traces of the multidirectional DCB specimens tested at four different loading rates are exhibited in Fig.4. At a test rate of $1.0 \times 10^{-2}\text{m/s}$, the load (Fig.4a) increased initially, showing a linear elastic behavior with an increase of time in advance of the crack initiation and then decreased little by little as the crack began to propagate. During the initial propagation of the crack, fiber bridging might be formed behind the crack tip, hindering the crack propagation and thus resisting considerably the external load. However, Fig.4b shows the dynamic behavior at the increasing test rates. The presence of an increasing number and amplitude of oscillations on the trace arose owing to the dynamic effects. These dynamic effects are likely to occur from several causes: The 1st peak in the trace was greatly influenced by inertia effects. The following multiple

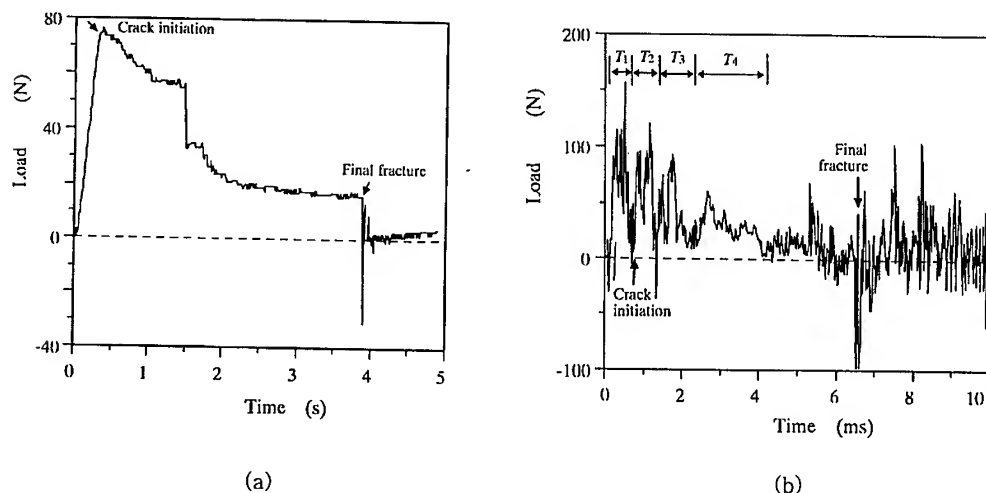


Fig. 4 Typical load(P)-time(t) traces of the DCB multidirectional composite specimens under a specimen arm displacement rate of (a) $1.03 \times 10^{-2}\text{m/s}$ and (b) 5.7m/s .

oscillations were caused by resonant vibration due to "spring-mass effect"[11] of the specimen and loading rigs as well as flexural stress waves propagating in the specimen.

4.2 Interlaminar fracture energy in the slow rate tests

Utilizing Equations (1) and (2), the values of G_{IC} of a specimen tested at a rate of 0.5mm/min may be measured as a function of the propagating crack length a , as shown in Fig.5. The results obtained through Equation (1) [denoted by " $G_{IC}(P\delta)$ "] are straightforward to deduce. In Equation (2) [denoted by " $G_{IC}(\delta^2 E)$ "], however, the axial modulus E_{11} of the composite is required: the values of the flexural modulus independently measured by a three-point bend test (E_{flex}) or the effective flexural modulus ($E_{c/n}$) calculated from the measured compliance in Equation (2). The value of G_{IC} obtained through Equation (1) at the initiation of crack growth was almost the same in value ($\approx 0.46\text{kJ/m}^2$) as that obtained through Equation (2). With an increase of a to about 48mm, a "rising R-curve" was obviously shown: the maximum value of G_{IC} ($G_{IC,max}$) was obtained from the " $G_{IC}(\delta^2 E_{flex})$ ", which was considerably lower by about 13% than that from the " $G_{IC}(P\delta)$ ". This is due to the fact that E_{flex} was considerably lower than $E_{c/n}$, due to the presence of the fiber bridging behind the crack tip. At longer crack lengths, when the crack jumped into the 0° ply, it resulted in an intraply (0°) fracture, which was initially accompanied by a high degree of fiber bridging. The value of G_{IC} eventually decreased to the minimum value ($G_{IC,min}$) of 0.30kJ/m^2 . Because the value of G_{IC} at the crack initiation ($G_{IC,i}$) and the minimum value ($G_{IC,min}$) obtained via Equation (2) were equivalent to those via Equation (1), Equation (4) may be used for the deduction of $G_{IC,i}$ and $G_{IC,min}$. However, the values of $G_{IC,max}$ obtained through Equation (4) could be considerably underestimated as described in Fig.5, and thus had to be compensated for the loss, which may be given by

$$G_{IC,max} = 1.15G_{IC}(\delta^2 E_{flex}) - \frac{111E_{11}h}{1120} \left(\frac{V}{C} \right)^2 \quad (5)$$

4.4 Rate effects on G_{IC}

The values of G_{IC} for the specimen tested at a rate of 5.7m/s are shown in Fig.6, which were obtained via Equation (5) [$G_{IC}(\delta^2 E_{11})$]. In comparison with the corresponding value in the slow rate test (Fig.5), the value of G_{IC} (0.38kJ/m^2) at the crack initiation was a bit lower. In the case of $G_{IC,max}$, the value corrected via Equation (5) was 0.77kJ/m^2 which was also lower. However the minimum value ($\approx 0.30\text{kJ/m}^2$) was almost identical.

For the multidirectional carbon-fiber/epoxy composites, Figure 7 summarizes the values of G_{IC} at crack initiation ($G_{IC,i}$), the maximum values ($G_{IC,max}$) and the minimum values ($G_{IC,min}$) as a function of test rate from $0.83 \times 10^{-5}\text{m/s}$ to 11.4m/s . Firstly, there is no major difference in the values for either $G_{IC,i}$ or $G_{IC,max}$ or $G_{IC,min}$ with increasing rate up to $1.0 \times 10^{-1}\text{m/s}$. Secondly,

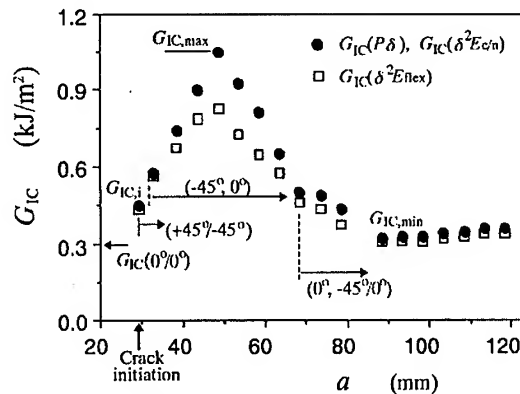


Fig. 5 Values of the Mode I interlaminar fracture energy G_{IC} , obtained by the two data reduction schemes, versus the length a of the propagating crack for the multidirectional laminate.

average values of either $G_{IC,i}$ or $G_{IC,min}$ remained to be constant with an increase of rate until $1.0 \times 10^{-1} \text{ m/s}$, but showed a modest reduction only at rates in excess of 1.0 m/s . Thirdly, the values of $G_{IC,max}$ decreased considerably with an increase of the rate to $\geq 1.0 \text{ m/s}$, but at 11.4 m/s , $G_{IC,max}$ showed a drastic change depending on the initial crack length a_i : at short a_i , values of $G_{IC,max}$ largely increased while at long a_i they decreased equivalent to the value at 5.7 m/s .

5. CONCLUSIONS

The present study has shown the experimental results for characterization of the mode I delamination fracture of continuous carbon fiber/epoxy multidirectional composites under a wide range of test rates, up to high rates of 11.4 m/s . At the slow rates of test $\leq 1.0 \times 10^{-1} \text{ m/s}$ the delamination fracture energy showed a "rising R-curve" due to the large extent of crack jumping and ensuring fiber bridging. In this respect Equation (4) requiring the values of the load and displacement was better for deduction of the interlaminar fracture energy G_{IC} . With increasing rate up to $1.0 \times 10^{-1} \text{ m/s}$, there was little differences in the delamination fracture behaviors. However, with an increase of the rate beyond 1.0 m/s the maximum

values of G_{IC} decreased considerably for long a_i .

ACKNOWLEDGEMENTS: The author would like to express his appreciation to Prof.A.J.Kinloch and Prof.J.G.Williams for helpful discussions.

REFERENCES

1. D.L.Hunston, et al. *Toughened Composites* ed. by N.L.Johnston, ASTM STP 937 (1987) p.74.
2. P.Davies, et al. *Comp. Sci. Tech.*, 39 (1990) p.193.
3. J.J.Ploaha, et al., *J. Reinforced Plastics and Comp.*, 15(1996) p.141.
4. S.Hashemi, A.J.Kinloch and J.G.Williams, *Proc. Royal Soc. London*, A427(1990) p.173.
5. A.J.Smiley and R.B.Pipes, *J. of Composite Materials*, 21(1987)p.670.
6. Ph.Beguelin, M.Barbezat and H.H.Kausch, *Journal de Physique III France*, 1(1991) p.1867.
7. A.A.Aliyu and I.M.Daniel, *ASTM STP876*, edited by W.S.Johnson, Philadelphia (1985) p.336.
8. B.R.K.Blackman, et al, *J. Materials Science*, 30 (1995) p.5885.
9. B.R.K.Blackman, et al, *J. Materials Science*, 30 (1996) p.4451.
10. N.S.Choi, A.J.Kinloch and J.G.Williams, *J. Composite Materials*, 33 (1999)p.73.
11. J.G.Williams, *Fracture Mechanics of Polymers*, Ellis Horwood Ltd, Chichester, UK (1987)p.237.

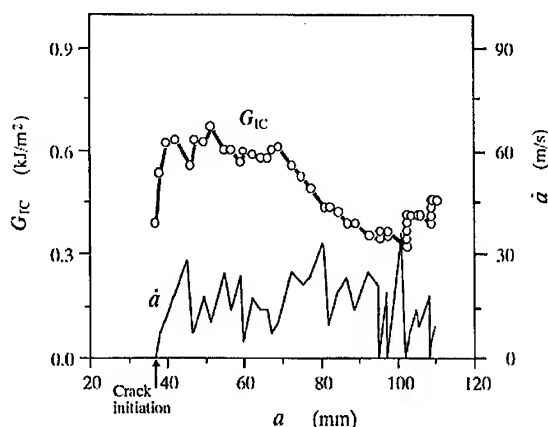


Fig. 6 Typical delamination fracture energy G_I and the corresponding crack velocity \dot{a} versus crack length a for the DCB specimen tested at a displacement rate of 5.7 m/s .

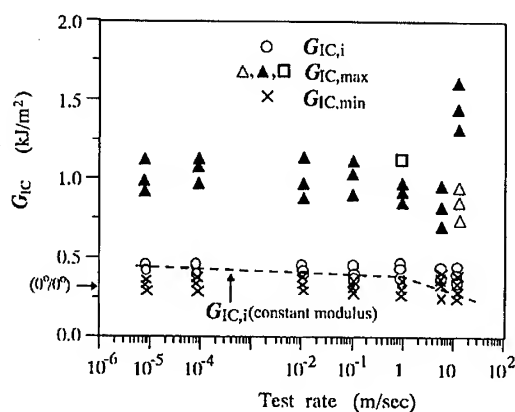


Fig. 7 Values of G_{IC} versus displacement rate for the $(-45^\circ/0^\circ/+45^\circ)_{2s}(+45^\circ/0^\circ/-45^\circ)_{2s}$ multidirectional carbon fiber/epoxy composite specimens.

Shock Adiabatics of Cement Mortar at Intense Dynamical Loading by Taking into Account the Internal Damage

Shaochiu Shih^{1,2}, Dahong Li¹ and Lili Wang^{1,2}

¹ Institute of Fluid Physics, CAEP, PO Box 523, Chengdu 610003, China P.R.

² Mechanics and Material Science Research Center, Ningbo University,
Zhejiang, Ningbo 315211, China P.R.

Keywords: Cement Mortar, Damage, Dynamical Loading, Shock Adiabatics

ABSTRACT

The plate impact experiments at strain rate up to 10^5s^{-1} for the cement mortar were performed by using a one-stage gas gun under the pressure ranged from 1GPa to 5GPa. It was found that the shock velocity D versus particle velocity u for this material can be expressed by a linear relation: $D = 2.29 \times 10^3 + 0.831u$ (m/s). Furthermore, the Hugoniot for the solid cement mortar, as a mixture of cement and sand, was theoretically obtained by virtue of the different shock data for the constituents. Moreover, the effects of the internal damage such as microcracks and voids were taken into consideration, and the corresponding Hugoniot at different levels of damage were calculated. The comparison between the experimental Hugoniot and the theoretical predictions shows a good agreement when and only when the damage effects are taken into account.

1. INTRODUCTION

While the dynamical behavior of concrete since seventies have been studied widely ^[1,2], but its constitutive equation at various strain rates has not been described systematically and appropriately so far. Recently in China, these fields have gained attention increasingly ^[3,4]. But these works were limited within the one dimensional stress state for cement mortar and the one dimensional strain state just for pure cement stone. In this study, the plate impact experiments at strain rate up to 10^5s^{-1} for the cement mortar were performed by using a one-stage gas gun for studying the dynamical behavior of this material at intense dynamical loading.

2. EXPERIMENTAL METHOD

The mix of the cement mortar specimen is listed in Table 1. After casting of the cement mortar in six steel molds, mixing, vibration and first 24 hours mold curing, the cast was pushed out of the molds. Then the specimens were placed in the moisture room for 28 days cure. After this, specimens were further ground on both end surfaces to ensure their smoothness and parallelism. The density of the specimens is 2210Kg/m^3 .

The experiments were performed in a one-stage gas gun with 100 mm inside diameter. The schematic of the experimental apparatus is shown in Fig.1. Both of flyer and target were made of LY12 aluminum alloy. The thickness of flyer and target is 10mm and 5mm respectively. The

diameters of them all are 95 mm. The specimen of cement mortar is composed of seven pieces of test elements with 5mm thickness and 70mm diameter. The four pieces of Manganin piezoresistive pressure gages were used. The one of them is embedded between the aluminum target plate and the first test element. The others were embedded among the followed test element slices. The recorded pulses of voltage can be transformed to the corresponding dynamical stresses through the calibrated formula.

Table 1-Mix of cement mortar specimens

Water cement ratio	0.5
525# Portland cement	10Kg
Sea sand	20Kg
Water	5Kg

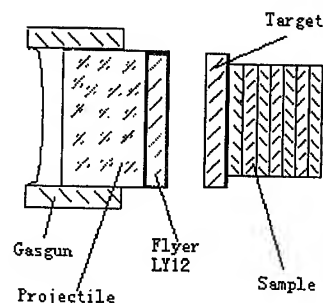


Fig.1 schematic of the experimental apparatus

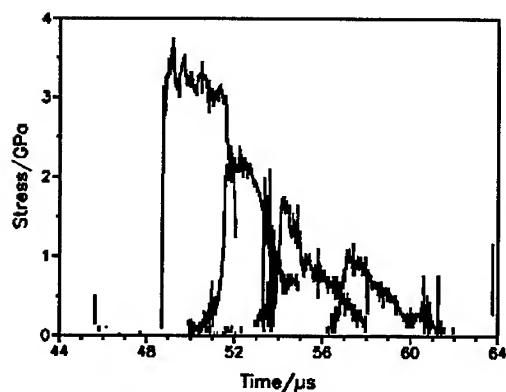


Fig.2 The typical shock stress profiles at different distances of the specimen

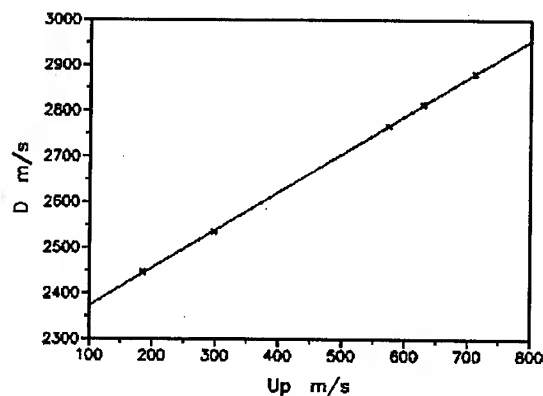


Fig.3 $D-u$ relationship

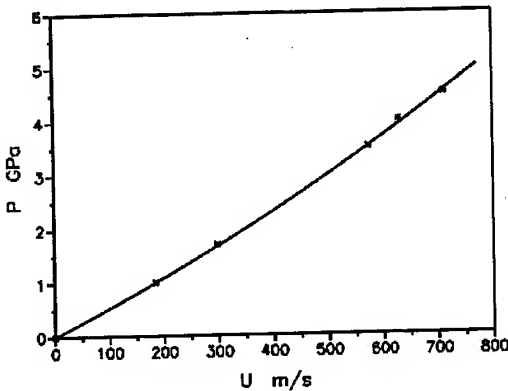
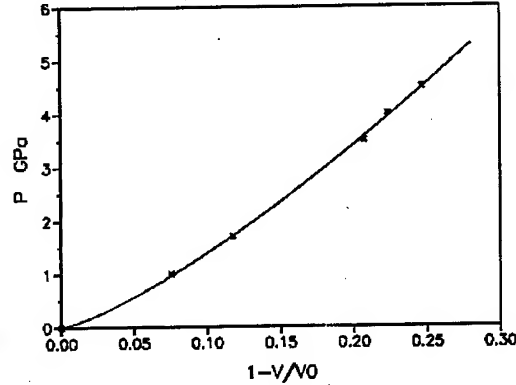
3.EXPERIMENTAL RESULTS AND DISCUSSION

In experiments, the velocities of the flyer plates are 200, 321, 402, 500, 733 m/s respectively. The typical shock stress profiles at different distances of the specimen are shown in Fig.2. According to the different rise points of shock pressure profiles recorded by the Manganin gage in different positions, the velocity of shock front in specimen D can be calculated. Because Manganin gages were embedded in specimen to measure the shock pressure directly in our experiment, the particle velocity u in specimen can be determined from shock pressure P and the velocity of shock front in specimen D . This point is on the 2S-2R curve of reflected wave in standard material LY12 aluminum. The experimental and calculated results are listed in Table 2. The shock velocity in specimen D vs. specimen particle velocity u is shown in Fig.3. The pressure P vs. particle velocity u is shown in Fig.4. The pressure P vs. volume strain $1-V/V_0$ is shown in Fig.5. In Fig.3 it is

demonstrated that for cement mortar the linear relationship between D and u can also be formulated like the most types of materials. According to formula: $D = C_0 + S \cdot u$, the experimental data were fitted and we got: $C_0 = 2.29 \times 10^3 \text{ m/s}$, $S = 0.831$. That is: $D = 2.29 \times 10^3 + 0.831 \cdot u \text{ (m/s)}$

Table 2

Specimen ID No.	Impact Velocity W / m/s	Shock velocity in specimen D / km/s	Specimen par- ticle velocity u / m/s	Shock pressure P / GPa
5	200	2.45	185	1.0
4	321	2.54	298	1.7
7	402	2.77	574	3.5
2	500	2.81	629	4.0
6	733	2.88	711	4.5

Fig.4 $P-u$ relationshipFig.5 $P-1-V/V_0$ relationship

3.1 Equation of state for multi-phase mixtures

For two- phase (or more) mixtures, we have an equilibrium taking place between the pressures in the two phases during the passage of the shock wave. McQueen et al. recommended a rigorous method to obtain the Hugoniot pressure of the mixture by virtue of the different EOS for the constituents (γ_0 and V_0 are different)^[5]. By numerical integrating the equation below, one establishes the 0 °K pressure-volume plot from the Hugoniot for each element:

$$\left(\frac{dP}{dV}\right)_{T_0} + \frac{\gamma_0}{V_0} P_{T_0} = \frac{\gamma_0}{2V_0} \left[P_H + \left(\frac{V_0}{\gamma_0} + V - V_0 \right) \cdot \frac{\{C^2 + 2S[V_0 - S(V_0 - V)]\}}{[V_0 - S(V_0 - V)]^4} \right]$$

One now mix the 0 °K isotherm on a mass fraction basis (mass fraction of i th component is m_i) and obtain the isotherm for the mixture. The γ_0 values are assumed to be unchanged with temperature.

$$\left(\frac{V_0}{\gamma_0}\right)_{\text{mixture}} = \sum m_i \left(\frac{V_0}{\gamma_0}\right)_i$$

With this value one can now convert the $0^\circ K$ isotherm into the shock Hugoniot for the mixture. The inverse differential equation to be solved is

$$\left(\frac{dP}{dV}\right)_H + \frac{P_H}{2V_0/\gamma_0 + V - V_0} = \frac{(2V_0/\gamma_0)(dP/dV)_{0K} + 2P_{0K}}{2V_0/\gamma_0 + V - V_0}$$

Here, we used a much simpler procedure that is based on the interpolation of C_0 and S values in the EOS by mass averaging. Thus,

$$C_0 = \sum m_i C_{0i} \quad S = \sum m_i S_i \quad \rho_0 = \sum m_i \rho_{0i}$$

For the cement mortar, we treated it as a two-phase mixture composed of pure cement and sands. Yang mosong et al. measured the shock Hugoniot of the pure cement ranging from 10~50GPa by means of a plane-wave generator (explosive lens) and optical technology. The linear fitted formula for the measured shock velocity D and the particle velocity u behind the wave front is: $D = 2260 + 1.58 \cdot u$ [6]. Its initial density $\rho_0 = 1942 \text{ Kg/m}^3$, initial volume $V_0 = 5.15 \times 10^{-4} \text{ m}^3/\text{Kg}$. In the other hand, the density of solid sea sands is measured by using the filling water method: 2550 Kg/m^3 , which is close to the density of quartz. The main constituent of sands fully weathered is SiO_2 coincided with the quartz. The linear fitted formula was obtained for shock velocity D and particle velocity u behind the wave front ranging in $P < 30 \text{ GPa}$ for quartz [8]: $D = 916.2 + 1.37 \cdot u$. Its initial density $\rho_0 = 2650 \text{ Kg/m}^3$, initial volume $V_0 = 3.77 \times 10^{-4} \text{ m}^3/\text{Kg}$, used as the calculated parameters for quartz. Thus, the weight fraction of the constituents of the cement mortar, C_0 , S and ρ_0 are shown in Table 3:

Table 3

Constituents	Wt. %	C_0 m/s	S	$\rho_0 \text{ Kg/m}^3$
Sands	57%	916.2	1.37	2650
Pure cement	43%	2260	1.58	1942

By mass averaging: $\rho_0 = \sum m_i \rho_{0i} = 2346 \text{ Kg/m}^3$, $V_0 = 4.26 \times 10^{-4} \text{ m}^3/\text{Kg}$

$$S = \sum m_i S_i = 1.46, \quad C_0 = \sum m_i C_{0i} = 1.49 \times 10^3 \text{ m/s}$$

So the relationship between D and u for the cement mortar as a two-phase mixture predicted by the theoretical analysis is as follows: $D = 1.49 \times 10^3 + 1.46 \cdot u$. That is different from the experimental results: $D = 2.29 \times 10^3 + 0.831 \cdot u$

It should be noticed that the cement mortar is treated as an ideal solid material in above discussion. But in practice, the cracks and voids are induced in the interfaces between aggregates and cement matrix unavoidably. Details of analysis for this is as follows.

3.2 Equation of state for damaged materials

By mass averaging, the theoretical predicted density of cement mortar should be 2346 Kg/m^3 . But the practical measured density is just 2210 Kg/m^3 , which equals about 94% of the theoretical value. It can be estimated that 6% voids were induced because of the mixing of sands. It is easy to understand that as the fine aggregates-sands mixed, the weak interfaces were created between the cement gels and the aggregates. A large amount of micro-cracks exist in the interface. G.Farran in France suggested the concept of "transition zone" in interface in 1972. Soon other models followed. All these models unanimously agreed that in transition zone the porosity is large. Thus, all its density and strength are low.

The three equations for the conservation of mass, momentum, and energy (Rankine-Hugoniot relationships) are simultaneously applied to both the porous material and the solid. The relationship between P and V for the damaged material can be derived:

$$P = \frac{2V - \gamma(V_0 - V)]C^2(V_0 - V)}{[2V - \gamma(V_0 - V)][V_0 - S(V_0 - V)]^2}$$

The above theoretical relationship of $D \sim u$ for cement mortar is:

$$D = 1.49 \times 10^3 + 1.46 \cdot u \quad \rho_0 = 2346 \text{ Kg/m}^3, V_0 = 4.26 \times 10^{-4} \text{ m}^3 / \text{Kg}$$

They are used as the parameters of solid cement mortar. Grüneisen parameter is related to S :

$$S = \frac{\gamma_0}{2} + \frac{1}{3} + \frac{t}{6}, \text{ where } \gamma_0 \text{ is the Grüneisen parameter for zero pressure, } t = 0, 1, 2 \text{ (express three}$$

different Grüneisen parameters $\gamma_s, \gamma_{DM}, \gamma_t$), taking γ_{DM} : $\gamma_0 = 2S - 1 = 1.92$. It is commonly

assumed that: $\frac{\gamma_0}{V_0} = \frac{\gamma}{V} = \text{const}$. Above equation was slightly modified to incorporate the constant

$$\text{ratio } \frac{\gamma_0}{V_0} \text{ and get: } P = \frac{2V - (\gamma_0/V_0)(V_0V - V^2)]C^2(V_0 - V)}{[2V - (\gamma_0/V_0)(V_0V - V^2)][V_0 - S(V_0 - V)]^2}$$

let: $\alpha = \frac{P_{00}}{\rho_0}$. Take: $\alpha = 0.95, 0.85, 0.75$ and 0.65 respectively. From this equation, different curves

for $P \sim V$ can be calculated and drawn, as shown in Fig.6. There the experimental results for cement mortar are marked with star. It can be seen that its corresponding density is about nineties percent. It is much close to the above estimation 94%.

4. CONCLUSIONS

- (1) By using the plate impact experiments at strain rate up to 10^5 s^{-1} for cement mortar, it is found that the shock velocity D versus particle velocity u for this material can be expressed by the linear relation:

$$D = 2.29 \times 10^3 + 0.831 \cdot u \quad (\text{m/s})$$

- (2) By virtue of the different shock data for the constituents, the Hugoniot for the solid cement mortar, as a mixture of cement and sand, was theoretically obtained. Moreover, the effects of the internal damage such as micro-cracks and voids were taken into consideration, and the

corresponding Hugoniot for different levels of damage were calculated. The comparison between the experimental Hugoniot and the theoretical predictions shows a good agreement when and only when the internal damage effects are taken into account.

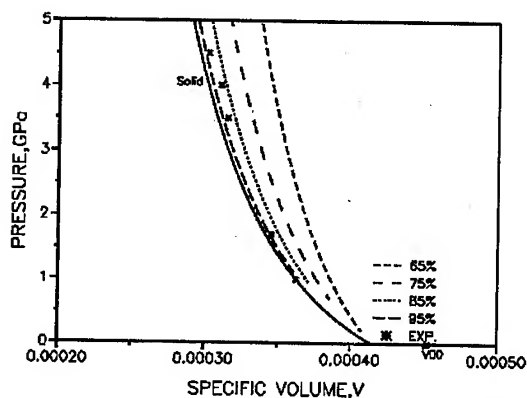


Fig. 6 The comparison of $P \sim V$ curves for different porosities with the experimental results

REFERENCE

1. S.Mindess and S.P.Shah(eds.), Cement-based Composite: Strain Rate Effects on Fracture, Vol.64, Mater.Res.Society;1986
2. Tang Tianxi, Behavior of Concrete under Dynamic Compressive Loading, PhD dissertation, Univ. of Florida, 1990
3. Chen Jiangying, The dynamic behavior of cement mortar, Master Degree dissertation, Zhejiang Univ., 1997
4. Chen Yeqing, Lagrangian analysis method and constitutive relation of cement stone on intense dynamic loading, PhD dissertation, The Railway Science Research Institute, 1994
5. G.McQueen, S.P.Marsh, in: The Equation of State of Solids from Shock Wave Studies, High Velocity Impact Phenomena, ed. R.Kinslow, Academic, New York,1970
6. Yang Mosong, Measures of shock adiabatics of cement stone, restricted material
7. M.A.Meyers, Dynamic Behavior of Materials,John Wiley & Sons,Inc., NewYork, 1994
8. M.B.Reinokoletov, The experimental data of shock compression and adiabatic expansion for condensed materials at high energy density, Institute of Fluid Physics, CAEP, 1997

A Study on the Impact Failure Mechanism of Aluminum-PMMA Interfacial Crack

D.K. Shin¹, J.J. Lee¹ and M.Y. Lyu²

¹Department of Mechanical Engineering, Korea Advanced Institute of Science and Technology,
373-1 Kusong-dong, Yusong-gu, Taejon 305-701, Korea

²Polymeric Materials Research Samyang Central R&D, 63-2 Hwaam-dong,
Yusong-gu, Taejon 305-348, Korea

Keywords: Dynamic Fracture, Energy Release Rate, Interaction Energy Method, Stress Intensity Factor

ABSTRACT

Energy release rate (J integral) and stress intensity factors of bimaterial specimens, under the dynamic loading condition were studied using both numerical and experimental methods. Low velocity impact test was performed with three point bending type of bimaterial specimens composed of aluminum and PMMA [Poly-Methyl Methacrylate]. Experimental results were analyzed by FEM and fracture parameters of interfacial crack were calculated by the programmed post-processor. Domain integral method and interaction energy method were used in the post-processor. Post-processor showed good performance in the decomposition of stress intensity factors with path independency. Phase angle of stress intensity factor varied with time. The relationship between energy release rate and phase angle at the onset of crack propagation showed unsymmetrical graph.

1. INTRODUCTION

Energy release rate (J integral) and stress intensity factors (K) are important fracture parameters not only in the static fracture but also in the dynamic fracture. To analyze the dynamic crack problem, dynamic fracture mechanics have been applied to various research topics such as wave propagation, crack initiation, propagation, arresting, kinking, curving, branching and so on [1].

Recently, reliability assessment of bimaterial under the impact loading becomes very important because bimaterial is widely used in various engineering structures, such as military armor, transportation vehicle, aerospace, electronic package and so on. Researches about the fracture parameters of bimaterial have been performed in various ways since the experimental study of Tippur and Rosakis [2]. However, a few dynamic experimental results with numerical analysis are

found compared with the static results. Therefore, we studied fracture parameters of crack tip, such as energy release rate and stress intensity factors, under the condition of dynamic loading using numerical and experimental method. We confined this study to the low velocity impact and fracture parameters at the onset of cracking. Firstly, we performed experiments using bimaterial specimens under the mixed mode impact loading. Secondly, we analyzed the dynamic problem using FEM. Finally, we calculated elastodynamic J integral and stress intensity factors using domain integral method and interaction energy method with the programmed post processor. The post processor performed calculation using data such as coordinates, displacements, velocities, accelerations and stresses obtained from the commercial FEM package program (ABAQUS). In the interaction energy method, auxiliary fields, formed by the far field pure mode I and mode II loading condition, were used to calculate stress intensity factors.

2. FRACTURE PARAMETERS IN DYNAMIC FRACTURE MECHANICS

According to Atluri [3], the energy release rate under the dynamic loading condition could be written as

$$G \equiv \lim_{r \rightarrow 0} \int_{\Gamma_r} \left[(W + T)n_i - t_i \frac{\partial u_i}{\partial x_1} \right] ds \quad (1)$$

where W , T , Γ_r , r , n , t , u , are strain energy, kinetic energy, integration path, radius of path, normal vector, traction and displacement, respectively.

Lo et al. [4] showed that J based interaction energy of the current field, A, and auxiliary field, B, could be written as

$$J^I = \lim_{r \rightarrow 0} \int_{\Gamma_r} \left\{ \sigma_{ij}^A \varepsilon_{ij}^B n_i - (\sigma_{ij}^A u_{i,1}^B + \sigma_{ij}^B u_{i,1}^A) n_j + \rho \frac{\partial u_i^A}{\partial t} \frac{\partial u_i^B}{\partial t} n_i \right\} d\Gamma \quad (2)$$

When we choose bimaterial stress field (Suo, 1989) as auxiliary field, and consider pure mode I (B_1) and mode II (B_2) such that $K = 1+i0$ and $K = 0+i1$, stress intensity factors could be written as

$$K_1^A = \frac{8 \cosh^2(\pi \varepsilon)}{c_1 + c_2} J^{A, B_1}, \quad K_2^A = \frac{8 \cosh^2(\pi \varepsilon)}{c_1 + c_2} J^{A, B_2} \quad (3)$$

where ε , J^{A, B_1} and J^{A, B_2} are oscillation index, interaction energies of AB_1 and AB_2 , respectively, and

$$c_1 = \frac{1 + \kappa_1}{\mu_1}, \quad c_2 = \frac{1 + \kappa_2}{\mu_2}, \quad \kappa_j = \begin{cases} 3 - 4\nu_j & : \text{plane strain} \\ \frac{3 - \nu_j}{1 + \nu_j} & : \text{plane stress} \end{cases} \quad (4)$$

where μ and ν are shear modulus and Poisson's ratio. Suffix represents the index of material.

Mode mixity is defined as [6]

$$\psi = \tan^{-1} \left(\frac{\text{Im}[Ka^{i\varepsilon}]}{\text{Re}[Ka^{i\varepsilon}]} \right) \quad (5)$$

3. EXPERIMENT

Impact test was performed by using Dynatup 8250 [Instron Co.]. The mass of impactor was 5.41Kg and the impact velocity was 2.17m/sec. The impact load was measured at the mid-position of tup by the load cell and impact velocity was measured by the photo detector. Crack initiation time was measured by conductive grid technique [Dotite, electro-conductive] and signals were stored to the personal computer via digital oscilloscope. Figure 1 shows schematic diagram of the experimental setup.

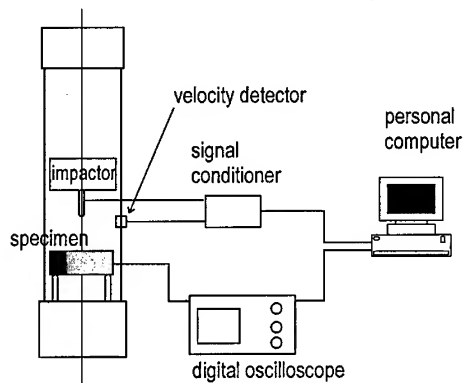


Fig. 1. Schematic diagram of the experimental setup

Aluminum 6061-T6 and PMMA [Poly-Methyl Methacrylate, Hanhwa Co.] that had 130mm height and 7.8mm thickness were bonded by commercial adhesive 'Weld-On 40' [IPS Co.] as shown in Fig. 2. The widths of aluminum were 40, 75, and 110mm and the widths of PMMA were 260, 225, and 190mm. Contact surface of aluminum was treated by sand blaster and PMMA was treated by abrasive sand paper #220. Initial crack with 20, 50 or 80mm was made by Teflon film which was inserted into the interface before the bonding process. Adhesive was cured at room temperature for 48 hours. The thickness of bonding layer was about 90 μ m. These bimaterial specimens have nine different crack tip positions as shown in Fig. 2.

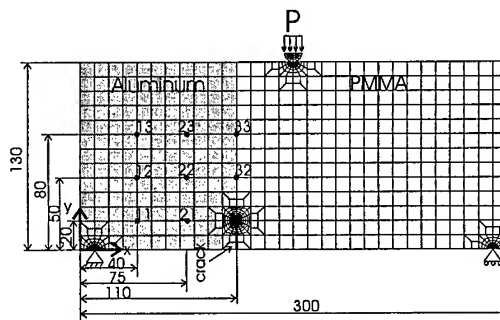


Fig. 2. Crack tip positions, size of specimen and FEM modeling of TIP₃₁

4. FEM ANALYSIS

The dynamic response of interfacial crack tip of bimaterial was analyzed by the use of commercial FEM package program ABAQUS/implicit. Fracture parameters were calculated by the programmed post processors which used data such as coordinates, displacements, velocities, accelerations and stresses obtained from the ABAQUS. Material properties are shown in Table 1. FEM model of TIP_{31} and crack tip positions of bimaterial specimen are shown in Fig.2. Crack tip positions were marked as TIP_{ij} where i was the index of x position and j was the index of y position. Eight node quadratic plane stress elements were used for this model except the crack tip region where degenerated quadratic elements were used. Interface elements, which contact without friction, were used for the crack face. The nearest elements to the crack tip ($r = 0.04\text{mm}$) were excluded in the calculation. We assumed that two points at the base of specimen were simply supported because specimen was supported by two rollers. Load history which was measured in the test was applied to the tup by the pressure load in the FEM analysis. Under the assumption that crack initiates when J reaches critical value, J_{ID} , we determined the calculated J value at the measured crack initiation time to be J_{ID} .

Table 1. Material properties of PMMA and aluminum

Property	PMMA	Aluminum
$E(\text{GPa})$	3.02	80
ν	0.35	0.33
$\rho(\text{kg/m}^3)$	1190	2710

5 EXPERIMENTAL AND NUMERICAL RESULTS

Typical examples of crack propagation paths are shown in Fig. 3. Crack initiates at critical J_{ID} and propagates along the interface some distance. After then, crack kinks to the PMMA and propagates toward the impact position. At the crack tip position of TIP_{11} , only one of five specimens was fractured at the impact energy level (12.7J , $v = 2.17\text{m/sec}$).

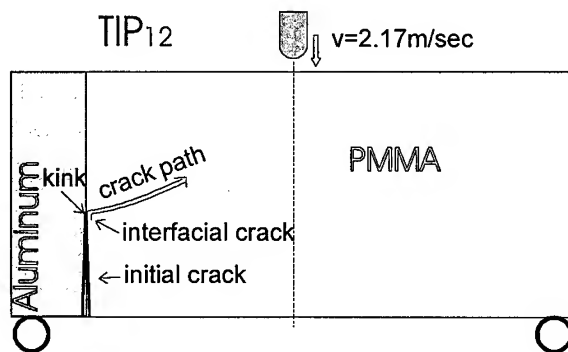


Fig. 3 Schematic diagram showing crack propagation path of bimaterial specimen TIP_{12}

Figure 4 shows the typical variation curve of energy release rate (J) and stress intensity factors with time at the TIP_{12} under the impact load. In this figure, solid line shows the J and K curves before the crack initiation. Cross symbol (x) represents the onset of crack initiation. Dotted line after the symbol (x) shows the case that the crack was not initiated. For all cases of $TIPs$, K_I increased monotonically according to time increase except TIP_{11} . However, K_{II} has (+) value initially, but soon decreases and reaches (-) values. This variation range could be divided into three parts. Those are region 1 ($K_{II} > 0$, increasing), region 2 ($K_{II} > 0$, decreasing), and region 3 ($K_{II} < 0$). In the region 3, K_{II} has (-) value and it is observed that crack tends to propagate along the interface. TIP_{21} , TIP_{31} and TIP_{32} belong to region.

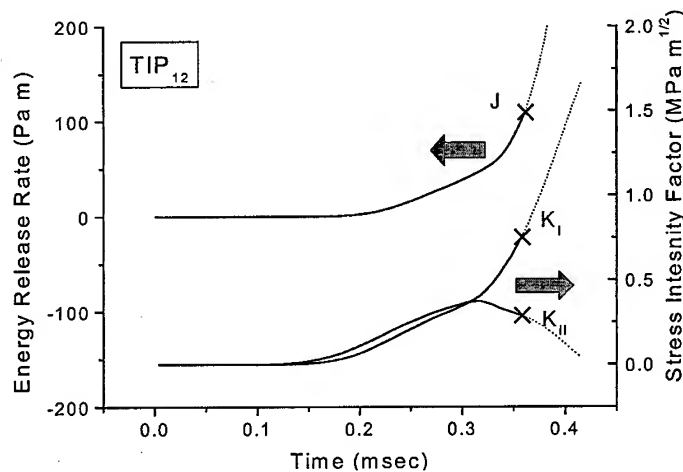


Fig. 4 Variation curves of energy release rate and stress intensity factors with time for the case of TIP_{12}

The relationship between energy release rate, J , and phase angle, ψ , at the crack initiation time are summarized in Fig. 5(a). Phase angle varies from -30° to 60° , and J varies from 150 Pa m to 600 Pa m. This figure shows unsymmetrical concave graph which had maximum at the TIP_{31} and had minimum values about 10° degree except TIP_{11} . One important point is TIP_{11} , that is, only one of five TIP_{11} specimens was fractured in this experiment. It seems that current FEM model is insufficient to simulate for the case of TIP_{11} . The dependency of mode mixity on the energy release rate is also found in this Fig. 5(a) under the dynamic loading condition. To compare the dynamic result with the static result, phase angle of the crack under the static condition at $J = 100$ Pa m is shown in Fig. 5(b). All conditions of FEM model are same as the dynamic conditions except that the external load is applied quasi-statically. Phase angle shows (+) values only on TIP_{12} and TIP_{13} . All phase angles of Fig. 5(b) vary from -25° to 5° and has minimum on TIP_{31} . Therefore, it can be said that estimation of phase angle of the dynamic condition from the static result is not correct.

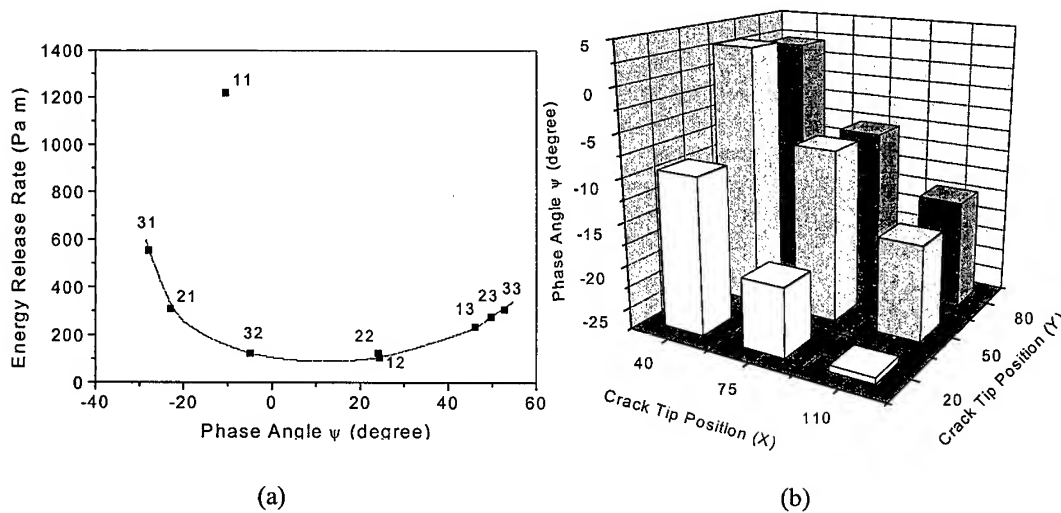


Fig. 5 Energy release and phase angle at the onset of crack initiation under the (a) dynamic condition and (b) static condition

6. CONCLUSION

As a result of this study we obtained following results. Interaction energy method showed good performance in the decomposition of stress intensity factor with path independency. The effect of J was not shown until about 0.2msec and then increased with time until it reach J_{ID} . Phase angle of stress intensity factors varied with time. Both K_I and K_{II} increased at first but K_{II} turned to decrease soon. Under the static condition, phase angle showed $-25^\circ \sim 5^\circ$ degree, however, it expanded to $-30^\circ \sim 60^\circ$ degree under the dynamic condition. Therefore estimation of phase angle of the dynamic condition from the static result was improper. The relationship between energy release rate, J , and phase angle, ψ , at the onset of crack initiation showed unsymmetrical concave graph which had maximum at the TIP_{31} and had minimum values about 10° degree except TIP_{11} . Through this result, mode mixity dependency on the energy release rate was found under the dynamic loading condition, similarly with the static condition.

REFERENCES

1. L.B.Freund, Dynamic fracture mechanics, Cambridge University Press, Cambridge (1990)
2. H.V.Tippur and A.J.Rosakis, Experimental Mechanics, **31** (1991) p.243
3. S.N.Atluri, Computational methods in the mechanics of fracture. Elsevier Science Publishers, Amsterdam (1986)
4. C.Y.Lo, T.Nakamura and A.Kushner, I. J. of Solids and Structures, **31** (1994) p.145
5. Z.Suo, Mechanics of Interface Fracture, Harvard University, Cambridge (1989)
6. J.R.Rice, Journal of Applied Mechanics, **55** (1988) p.98

Experimental Analysis of Dynamic Effects in Brittle Fracture of PMMA

K. Arakawa, T. Mada and K. Takahashi

Research Institute for Applied Mechanics, Kyushu University,
Kasuga-shi, Fukuoka 816-8580, Japan

Keywords: Brittle Polymers, Caustic Method, Crack Velocity, Dynamic Crack Propagation, PMMA, Stress Intensity Factor, Unloading Behavior, Unloading Rate

ABSTRACT

Dynamic fracture behavior of PMMA was studied using the method of caustics. Single-edge-cracked tensile specimens were pin-loaded so that cracks could undergo both the acceleration and deceleration process in one fracture event. The effect of loading position H_1 was examined measuring the stress intensity factor K_{ID} , crack velocity \dot{a} and load P as a function of time t . Unloading rate \dot{P} , time derivative of P , was also evaluated to investigate for a correlation with the time variations of K_{ID} and \dot{a} .

1. INTRODUCTION

To characterize the behavior of dynamic crack propagation in brittle materials, crack velocity \dot{a} has been measured as one of the fracture parameters using different types of specimen geometries and loading conditions, and it has been reported that \dot{a} changed as a crack propagated [1,2]. Stress intensity factor K_{ID} has also been measured using different experimental techniques, and K_{ID} reportedly changed during dynamic fracturing [3-12]. The change in these fracture parameters probably has a close relationship with the geometries and loading conditions of specimens, since they modify the state of stress ahead of a crack front.

The present work studied this problem using the method of caustics [3]. Single-edge-cracked tensile specimens of PMMA were fractured under pin-loading conditions so that cracks underwent acceleration and deceleration stages in a single fracture process. The pin-loading position H_1 was changed to modify the stress distribution ahead of a crack tip. To examine the effect of H_1 , crack velocity \dot{a} and stress intensity factor K_{ID} were measured in the course of crack propagation. Load P applied to the specimens was also evaluated to study the unloading behavior of the specimen. Attention was focussed particularly on the effect of H_1 on the behaviors of \dot{a} , K_{ID} and P . Unloading rate \dot{P} , the time derivative of P , was determined to correlate with the time variations of \dot{a} and K_{ID} .

2. EXPERIMENTAL PROCEDURES

Experiments were performed on single-edge-cracked tensile specimens of PMMA as shown in Fig. 1. The material properties of PMMA are listed in Table 1. A sharp precrack was generated

by momentum-controlled chisel-impact into a pre-machined saw-cut on the specimen edge. The specimens were loaded using U-shaped steel pin fixtures to record caustic patterns at the loading points and to evaluate load history during dynamic fracturing [11].

The specimen dimensions were 5 mm of thickness and 150 mm of width. The height $2H$ was 110 mm or 150 mm; and the loading position H_1 was determined as indicated in Fig. 1, so that H_1 was 30 mm or 50 mm. This was done to examine the effect of loading position on fracture behavior of the specimens. All specimens were tested under a displacement controlled condition, and the load up to the time of fracture initiation was measured using a tensile testing machine. Tests were performed at room temperature and at a constant crosshead rate of 1 mm/min.

Dynamic crack propagations were photographed with a modified Cranz-Schardin camera which provided bifocal photographs [12,13]. One focal distance was selected for specimen-focussed images and another for caustic images. Figure 2 shows examples of high-speed photographs for a fast crack in a PMMA specimen, where series (a) represents the specimen-focussed images and (b) the corresponding caustic patterns. Size of the caustic at a crack tip increased in an early stage of crack propagation and then decreased in the later stage, while caustic size at the loading points decreased as the crack lengthened. This was typical fracture behavior with the specimen geometry and loading method employed.

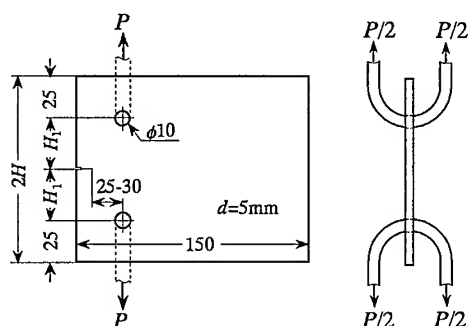


Fig. 1. Specimen geometry and loading method

Table 1. Material properties of PMMA

c^* m ² /N	4.90×10^{-11}
E_d GPa	5.97
c_L m/s	2540
c_s m/s	1415

c^* : stress-optical constant,
 E_d : Young's modulus,
 c_L : longitudinal wave speed,
 c_s : shear wave speed.

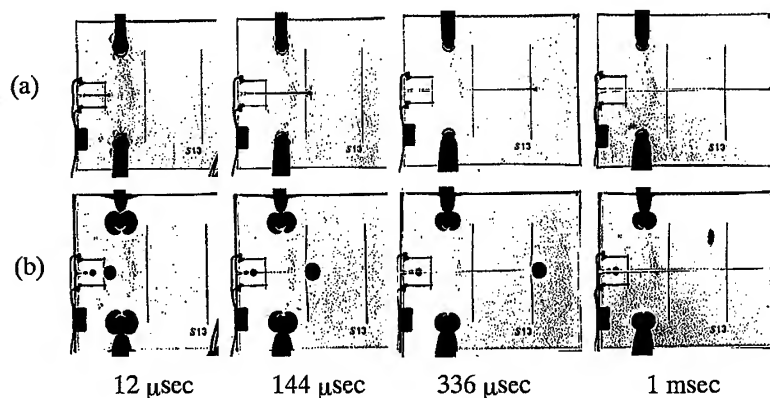


Fig. 2. Example of dynamic crack propagation in a PMMA specimen
 (a) Specimen-focussed images, (b) Caustic patterns

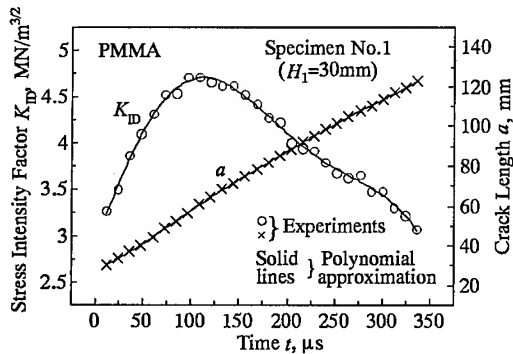


Fig. 3. Stress intensity factor K_{ID} and crack length a for a PMMA specimen as a function of time t ($H_1=30\text{mm}$)

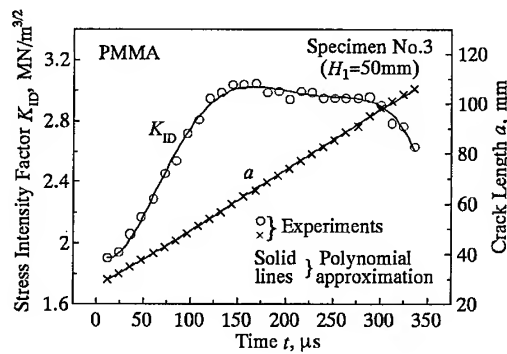


Fig. 4. Stress intensity factor K_{ID} and crack length a for a PMMA specimen as a function of time t ($H_1=50\text{mm}$)

3. EVALUATION OF DYNAMIC FRACTURE PARAMETERS

3.1. Dynamic Stress Intensity Factor K_{ID}

The stress intensity factor K_{ID} was determined using the following equation [3]:

$$K_{ID} = (2\sqrt{2\pi}/3z_0dc^*\eta^{3/2})(\phi/3.17)^{5/2} \quad (1)$$

where ϕ is the caustic diameter at a crack tip, z_0 is the distance between the specimen and the image plane, d is the specimen thickness and η is a convergency factor for incident light rays.

Figures 3 and 4 show variations of K_{ID} and crack length a versus time t . As seen, values of K_{ID} increased in an early stage of crack propagation and then decreased in the later stage. The effect of H_1 can be seen: Figure 3 shows rapidly increasing and decreasing regions of K_{ID} for a relatively small value of $H_1 (=30\text{ mm})$. With increasing H_1 , the slope of K_{ID} gradually decreased, especially in the later stage (Fig. 4). This implies that H_1 was an important factor in changing the behavior of K_{ID} when a crack was propagated dynamically.

3.2. Dynamic Load P

In Figs. 5 and 6, caustic size ω at the loading points of the specimen are plotted as a function of time t , where ω represents the maximum size of caustics perpendicular to the loading axis (see Fig. 2(b)). Load P applied to the specimen during dynamic crack propagation was determined using the following relation [11]

$$P = k(\omega/\omega_{d0} - 1)^n, \quad (2)$$

where k and n are coefficients, and ω_{d0} is the caustic size just after a crack had propagated completely through the width of the specimen (see Fig. 2(b)).

Noticeably larger caustics were obtained at the loading points after the fracture. This can be attributed to plastic or viscoelastic deformations around the loading points [11]. Load P during the dynamic fracturing was determined using the P - ω relationship identified under static conditions (see Fig. 7) and the following assumptions: (i) The static P - ω relationship can be valid up to load P_f at fracture initiation as shown in Fig. 8, where P_f values for the three specimens are indicated by the squares. (ii) The viscosity of the material can be neglected under dynamic conditions. (iii) $\omega = \omega_{d0}$ at $P=0$, as indicated by the open circles, so that the change $P_f \rightarrow \omega_{d0}$ is elastic.

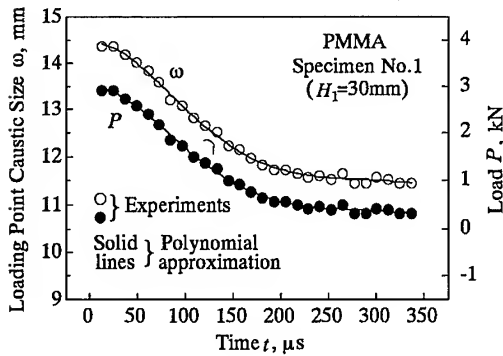


Fig. 5. Loading point caustic size ω and load P for a PMMA specimen as a function of time t ($H_1=30$ mm)

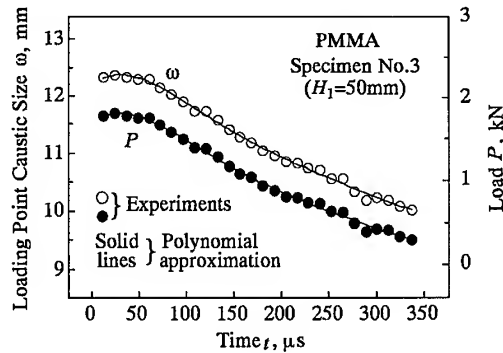


Fig. 6. Loading point caustic size ω and load P for a PMMA specimen as a function of time t ($H_1=50$ mm)

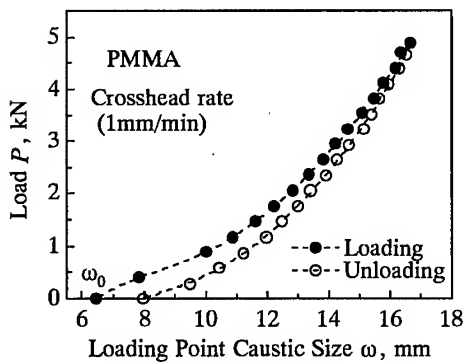


Fig. 7. P - ω relationships for a PMMA specimen under static condition

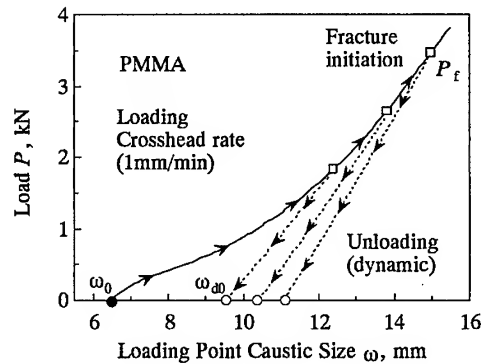


Fig. 8. P - ω relationships for PMMA specimens under static and dynamic conditions

Based on these assumptions, Eq.2 was employed and the coefficient $n=1.04$ obtained from the epoxy specimens which was not strongly dependent on the rate of unloading caused by dynamic crack propagation [11]. The values of k was determined for each specimen using the values of P_f and ω_{d0} . The dynamic P - ω relationships are indicated by the dotted-curves in Fig. 8.

The values of P evaluated by Eq.2 are plotted in Figs. 5 and 6 versus time t . Although P decreased with t , the behavior altered according to H_1 . Values of P for $H_1=30$ mm showed a large decrease in the early stage of fracture and a slight change in the later stage (Fig. 5). As H_1 increased, the slope of P tended to approach a constant except in the initial and final stage of fracture (Fig. 6). This implies that H_1 was also influential in changing the unloading behavior of the specimen.

3.3. Crack Velocity \dot{a} and Unloading Rate \dot{P}

To minimize data scattering in Figs. 3 and 4, the authors employed a numerical computational procedure which was proposed in a previous work [9]. Values of K_{ID} and crack length a were expressed as ninth order polynomial of t based on the least-squares method so that they closely fitted their observed values (see Fig. 3 and 4). Crack velocity \dot{a} was then obtained from

the first time derivative of the fitted curve $a(t)$. This procedure permitted accurate determination of \dot{a} when a crack was accelerated and decelerated in one fracture event.

The unloading behaviors in Figs. 5 and 6 would be related to the change in potential or strain energy of the specimen material, there could be a close relationship with dynamic fracture parameters such as K_{ID} or \dot{a} . To examine such a relation, the values of P were expressed as ninth order polynomial of t , and determined the first time derivative \dot{P} , i.e. the unloading rate of the specimen using the computational procedure stated above.

4. CORRELATIONS AMONG THE DYNAMIC FRACTURE PARAMETERS

Figures 9 and 10 show the correlations among K_{ID} , \dot{a} and \dot{P} as a function of t . It is worth noting that the change in \dot{a} or \dot{P} was qualitatively in accord with the change in values of K_{ID} . However, there existed a slight difference among the values of t giving the maximum \dot{P} , \dot{a} and

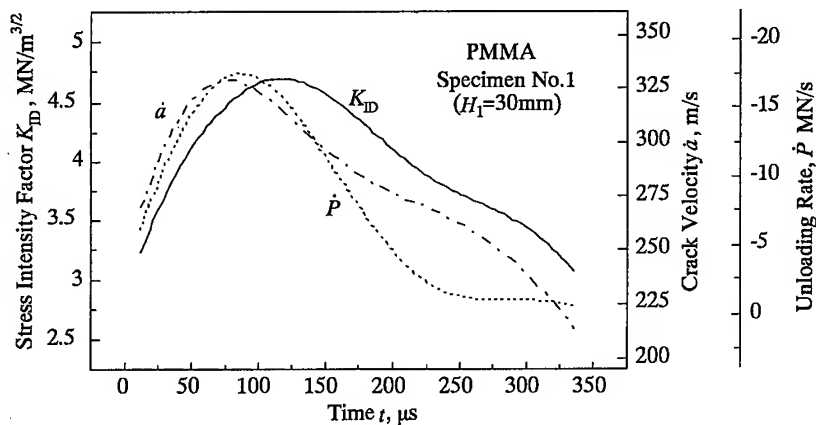


Fig. 9. Time correlations among the stress intensity factor K_{ID} , crack velocity \dot{a} and unloading rate \dot{P} for a PMMA specimen ($H_1=30\text{mm}$)

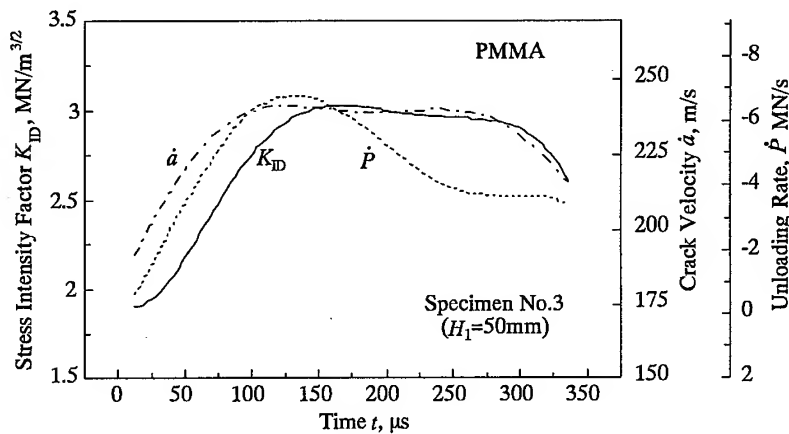


Fig. 10. Time correlations among the stress intensity factor K_{ID} , crack velocity \dot{a} and unloading rate \dot{P} for a PMMA specimen ($H_1=50\text{mm}$).

K_{ID} . The peak value of \dot{P} was reached later than that of \dot{a} , but earlier than that of K_{ID} , so that the order was \dot{a} , \dot{P} and K_{ID} .

To study the physical meaning for this, the procedure described in a previous work [11] was employed: First, the crack tip positions at the maximum \dot{a} and K_{ID} were determined. Second, L_1 and L_2 , the distances between the crack tips and the loading points were measured. Finally, time intervals Δt_1 and Δt_2 were evaluated with L_1/c_L and L_2/c_L , respectively, where c_L is the longitudinal wave speed in PMMA (see Table 1). $\Delta t_1=15.6 \mu\text{sec}$ and $\Delta t_2=17.6 \mu\text{sec}$ were obtained for $H_1=30 \text{ mm}$ (Fig. 9). The values were $\Delta t_1=22.4 \mu\text{sec}$ and $\Delta t_2=24.4 \mu\text{sec}$ for $H_1=50 \text{ mm}$ (Fig.10). It is worth noting that almost the same time intervals are shown between the two peaks \dot{a} and \dot{P} , and \dot{P} and K_{ID} . This suggests that \dot{a} affected the values of \dot{P} , and K_{ID} was influenced by \dot{P} according to the time interval associated with the wave propagation between the crack tip and the loading points. Hence, the loading position of specimens clearly appears to be an important factor in changing the dynamic fracture behavior of the material.

5. CONCLUSIONS

Single-edge-cracked tensile specimens of PMMA were fractured under pin-loading conditions. To study the effect of loading position H_1 , stress intensity factor K_{ID} and crack velocity \dot{a} were measured during dynamic crack propagation which included both crack acceleration and deceleration in one fracture event. Load P applied to the specimen was also measured as a function of time t . Unloading rate $\dot{P}(t)$, time derivative of $P(t)$, was evaluated to correlate with the time variations of $K_{ID}(t)$ and $\dot{a}(t)$, and the following findings were obtained:

- (1) H_1 was an important factor in changing $K_{ID}(t)$, $\dot{a}(t)$, $P(t)$ and $\dot{P}(t)$.
- (2) The change in $\dot{a}(t)$ or $\dot{P}(t)$ was qualitatively in accord with the one in $K_{ID}(t)$, and the maximum $\dot{P}(t)$ existed between $\dot{a}(t)$ and $K_{ID}(t)$.
- (3) The peak value of $\dot{a}(t)$ was attained earlier than that of $K_{ID}(t)$ with respect to time t . The time difference between two peaks tended to increase as H_1 increased.

REFERENCES

1. Anthony, S. R. et al. (1970), *Philosophical Magazine* **22**, 1201-1216.
2. Katsamanis, F., Raftopoulos, D. and Theocaris, P. S. (1977), *Exp. Mech.* **17**, 128-132.
3. Beinert, J. and Kalthoff, J. F. (1981), *Mechanics of Fracture* **7**, (Edited by G. C. Sih), Martinus Nijhoff Publishers, 281-330.
4. Rosakis, A. J., Duffy, J. and Freund, L. B. (1984), *J. of Mech. Phys. of Solids* **32**, 443-460.
5. Ravi-Chandar, K. and Knauss, W. G. (1984), *Int. J. of Frac.* **26**, 141-151.
6. Dally, J. W., Fournery, W. L. and Irwin, G. R. (1985), *Int. J. of Frac.* **27**, 159-168.
7. Kobayashi, A. S., et al. (1986), *Int. J. of Frac.* **30**, 275-285.
8. Shukla, A. and Nigam, H. (1986), *Eng. Frac. Mech.* **25**, 91-102.
9. Takahashi, K. and Arakawa, K. (1987), *Exp. Mech.* **27**, 195-200.
10. Nishioka, T., et al. (1991), *Eng. Frac. Mech.* **39**, 757-767.
11. Arakawa, K., Nagoh, D. and Takahashi, K. (1999), *Int. J. Frac.* **96**, 345-358.
12. Arakawa, K. and Takahashi, K. (1991), *Int. J. Frac.* **48**, 245-259.
13. Takahashi, K. and Mada, T. (1993), *20th International Congress on High-Speed Photography and Photonics* (Edited by J. M. Dewey and R.G. Racca), SPIE 1802, 901-909.

Impact Damage Behavior and Evaluation of Residual Strength in Plain-Woven Glass/Epoxy Composites

K.W. Kang and J.K. Kim

School of Mechanical Engineering, Hanyang University,
17 Haengdang-dong, Seongdong-gu, Seoul 133-791, Korea

Keywords: Critical Impact Energy, Impact Damage, Plain-Woven Glass/Epoxy Composites, Residual Strength, Thickness Effect, Threshold Impact Energy

ABSTRACT

This study is experimentally performed to evaluate the relationship between impact damage and residual strength of plain-woven Glass/Epoxy composites, including the thickness effect. The results indicate that the major impact damage of Glass/Epoxy composites is quite different from that of unidirectional Carbon/Epoxy composites. Among the residual strength prediction models, previously proposed on unidirectional laminates, Avva's and Caprino's models well describe the strength reduction behavior of Glass/Epoxy composites. Also, the threshold and critical impact energy are significantly influenced by the thickness.

1. INTRODUCTION

Since impact-induced damage in composites causes large drops in the load-carrying capacity of a structure, their damage and strength reduction behaviors under impact deserve careful investigation.

The impact damage behaves as a discontinuity when the composites are loaded; therefore, it appears that fracture mechanics concept must be employed when the problem of residual strength is faced. Based on this theoretical basis, several models have been proposed for unidirectional laminates and successfully described the strength reduction behavior due to impact damage[1-3]. The strength reduction behavior seems, however, to be quite different with material characteristics, thus more extensive research is necessary.

It is well known that thickness of unidirectional laminates has greatly influenced on the impact damage and strength reduction behavior. Also the damage resistance of laminates depends greatly on thickness, resulting from the change of damage behavior with thickness[4]. Although these behaviors are dependent on both the thickness and material characteristics, not much effort has been directed to study these topics.

In the present study, experimental investigations are performed to correlate impact damage to residual strength of plain-woven Glass/Epoxy composites with various thickness. The damage behavior of plain-woven composites is identified through non-destructive technique. Subsequently, the strength reduction behavior in plain-woven composites is analyzed and compared to that by residual strength prediction models proposed for unidirectional laminates. Also, the effect of thickness on damage resistance is discussed.

2. RESIDUAL STRENGTH PREDICTION MODELS

To assess the strength of composites after impact, it is generally assumed that the impact damage causes the same strength reduction as a hole or a crack of same size. Based on such an analogy, several models to assess residual strength as a function of impact energy have been developed.

Husman et al[1] considered an orthotropic plate with a narrow slit of length ($2c$) subjected to a tensile stress. To derive the relation of the impact damage to the impact energy, it was assumed that the difference between the unnotched and notched strain energy density (W_s, W_b) was proportional to the absorbed impact energy (E_a) per thickness (B) as follows:

$$W_s - W_b = K\bar{E}_a = KE_a / B \quad (1)$$

where K is the material constant and \bar{E}_a is the absorbed impact energy per thickness. For relating the strain energy density to damage length, it is assumed that the failure of unnotched composites is characterized by a intrinsic damage length (c_0) and hence the critical energy release rates (G_{IC}) of the unnotched and notched can be expressed as follows:

$$G_{IC} = \pi \left\{ 2S_{11} / S_{22} \left[(S_{22} / S_{11})^{1/2} + (2S_{12} + S_{66} / 2S_{11}) \right]^{1/2} \right\}^{1/2} \cdot c_0 W_s \quad (2)$$

$$G_{IC} = \pi \left\{ 2S_{11} / S_{22} \left[(S_{22} / S_{11})^{1/2} + (2S_{12} + S_{66} / 2S_{11}) \right]^{1/2} \right\}^{1/2} \cdot (c + c_0) W_b \quad (3)$$

where S_{ij} are the compliance of orthotropic plate. Combining Eq. (1) – (3) and introducing the strength prediction model by Waddoups et al[5], we obtain the equation that can evaluate the strength reduction due to impact damage as follows:

$$\frac{\sigma_R}{\sigma_0} = \sqrt{\frac{W_s - K\bar{E}_a}{W_s}} \quad (4)$$

where σ_0 and σ_R are the tensile and residual strength, respectively.

Avva et al[2] assumed that the length of impact damage ($2a$) was related to an incident impact energy per unit thickness (\bar{E}_i) by

$$a = k(\bar{E}_i - \bar{E}_b) \quad (5)$$

where k is the constant and \bar{E}_b is the threshold value of \bar{E}_i . Under the assumption that the impact damage was equivalent to the through-the-thickness crack ($2c$), the strength of an infinite plate with a central crack was given by the average stress criterion[6].

$$\frac{\sigma_N^\infty}{\sigma_0} = \sqrt{\frac{c_0}{2c + c_0}} \quad (6)$$

where σ_N^∞ is the notched strength of infinite plate. Combining Eq. (5) and (6), we get the model for residual strength of a plate with impact damage as follows:

$$\frac{\sigma_R}{\sigma_0} = \frac{1}{F_w} \sqrt{\frac{c_0}{2k(\bar{E}_i - \bar{E}_b) + c_0}} \quad (7)$$

where F_w is the finite width correction factor[7].

Caprino[3] showed that for failure of laminates with a notch of length ($2c$), the ratio of cracked to uncracked strength was given by

$$\frac{\sigma_R}{\sigma_0} = \left(\frac{c_0}{c} \right)^m \quad (8)$$

where m is the constant, c_0 is the length of an existing defect in laminates. Later, Caprino considered the residual strength of impact damaged laminates and assumed that strength reduction due to impact damage was equivalent to that of a notch size ($2c$). The impact damage (a) was assumed to be related to the incident impact energy (E_i) as follows:

$$a = kE_i^n \quad (9)$$

where k and n are the constants. Combining Eq. (8) and Eq. (9) leads to

$$\frac{\sigma_R}{\sigma_0} = \left(\frac{E_{th}}{E_i} \right)^m = \left(\frac{E_{th}}{E_i} \right)^\alpha \quad (10)$$

where α is the material constant and E_{th} is the threshold value of E_i .

3. EXPERIMENTS

3.1 Materials and specimen

The materials used in this study were plain-woven Glass/Epoxy composites. The mechanical properties of this material were obtained from unidirectional tensile test, according to ASTM D-3039-93[8], and summarized in Table 1. The specimen was straight-sided type and its dimension was 250×40 mm. The thickness B of Glass/Epoxy composites was 2.3, 3.0, 4.0, 5.0 and 6.6 mm for identifying thickness effect. The specimens were clamped on two opposite edges and left free on the other two edges.

Table 1. Mechanical properties of plain-woven Glass/Epoxy composites

E_{xx} (GPa)	E_{yy} (GPa)	G_{xy} (GPa)	ν_{xy}	σ_0 (MPa)	B (mm)
19.96	19.96	3.1	0.136	247.6	2.3

3.2 Impact and tensile tests

The impact tests were performed using the compressed nitrogen gas gun that allowed the variation of striking velocity from 5 to 200 m/sec. The striking velocity was measured from the time of passage between the laser sensors connected to an electronic timer. The tip radius and mass of projectile were 12.7 mm and 57.2 g, respectively. The damaged specimens were inspected by the 35 mm camera and the scanning acoustic microscope (Sonix HS1000 Hi SPEED™, 75 MHz). The standard 100 kN capacity machine (Shimazu, AG-100KNE) was used for tensile testing with crosshead speed of 1 mm/min.

4. RESULTS AND DISCUSSIONS

4.1 Impact damage behavior

Various failure modes, such as delamination, fiber breakage and matrix crack, can occur during the impact of unidirectional laminates. Among these, the first damage to occur is the interlaminar cracks within plies and it propagates to ply interfaces and the associated stress concentration may then leads to the delamination growth. The delamination is known to occur at the interface between two plies with different fiber orientation. Its shape is usually peanut-shaped with its major axis oriented in the direction of fiber orientation of the lower ply[1], as shown in Fig. 1. It is, however, not clear that plain-woven Glass/Epoxy composites reveal the same damage behavior because the impact damage is significantly sensitive to the material properties.

To identify damage behavior of plain-woven Glass/Epoxy composites, impact test was made at the plate center, with the energy level of 5.0 J. Fig. 2 shows the typical damage states in plain-

woven Glass/Epoxy composites, which were observed by a scanning acoustic microscope (C-scan). Here the damage was captured at the opposite surface against the impact point. The figure shows that the impact damage of plain-woven composites consists of fiber breakage and matrix crack. In particular, the damage shape is slit-shaped with its major transverse impact damage but little longitudinal impact damage. Also, the damage occurs at the opposite surface against the impact point though that of unidirectional laminates occurs inside the laminates. It can be, therefore, said that the major impact damages of plain-woven composites are the fiber breakage and matrix crack occurring on the surface of composites, unlike as the unidirectional laminates.

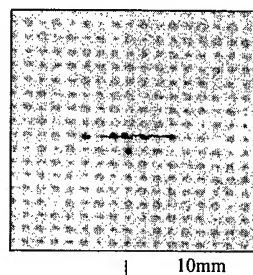
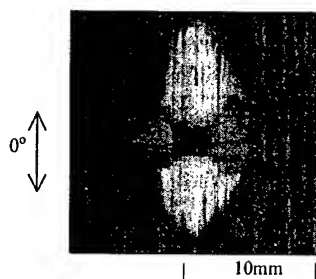


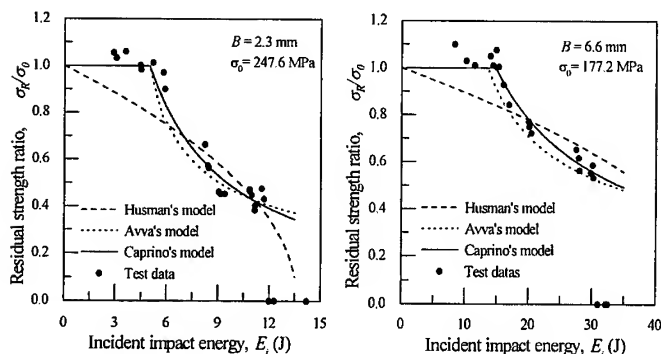
Fig. 1 Impact damages in Carbon/Epoxy [(0/90)₃]_s

Fig. 2 Impact damages in Glass/Epoxy

4.2 Residual strength

Since strength reduction behavior seems to be dependent on material characteristics[1], more research on the strength prediction models that were proposed on unidirectional laminates is necessary. To verify the applicability of these models on plain-woven composites, the residual strengths of thickness $B=2.3$ and 6.6mm specimens are plotted in Fig. 3, together with the results by residual strength prediction models, Eqs. (4), (7) and (10). The parameters in each model were obtained from the least square fitting analysis of experimental data, and are presented in Table 2. This figure indicates that Husman's model cannot predict the threshold impact energy and strength reduction behavior. On the other hand, Avva's and Caprino's models well describe the threshold energy as well as the tendency of strength reduction with impact energy regardless of thickness.

As described previously, each prediction models have simple relationships Eqs. (1), (5) and (8) for the impact energy and the equivalent notch size. These relationships seem to greatly influence on accuracy of the models. To identify this, the transverse damage length $2a_t$ and strain energy density $W_s - W_b$ are plotted as a function of the incident impact energy in Fig. 4. Here the regression lines are obtained by Eqs. (1), (5) and (8). This diagram indicates that Eq. (1) in



(a) $B=2.3\text{mm}$

(b) $B=6.6\text{mm}$

Fig. 3 Residual strength of Glass/Epoxy composites

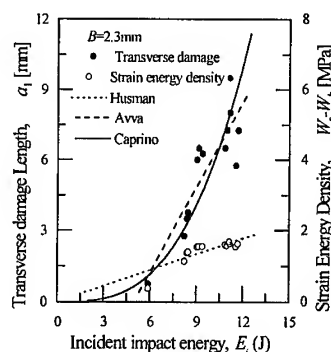


Fig. 4 Damage & strain energy density with energy

Husman's model cannot evaluate the threshold energy E_{th} , which is the minimum impact energy required to cause the reduction of strain energy density. On the other hand, Eqs. (5) and (8) describe reasonably the threshold energy as well as the damage behavior in terms of impact energy. It can be, therefore, stated that the basic assumptions in Avva's and Caprino's models well describe the damage behavior and subsequently the residual strengths predicted by both models agree well with the experimental results.

Table 2. Parameters of residual strength prediction models

B (mm)	Husman's model		Avva's model			Caprino's model	
	$K(\text{MPa mm}^2/\text{J})$	$W_s(\text{MPa})$	$c_0(\text{mm})$	$K(\text{mm}^2/\text{J})$	$\bar{E}_{th}(\text{J/mm})$	α	$E_{th}(\text{J})$
2.3	0.930	1.982	3.299	2.777	2.220	1.070	4.992
3.0	0.488	1.921	3.200	6.472	2.227	1.610	6.121
4.0	0.094	1.224	14.307	2.568	2.630	0.529	12.091
5.0	0.055	1.224	11.625	3.206	3.935	0.947	21.829
6.6	0.098	0.766	10.538	5.376	2.053	0.739	13.845

4.3 Threshold and critical impact energy

The threshold E_{th} and critical impact energy E_c , which are the minimum energies to cause strength reduction and breakage of a specimen, respectively, are the important design factors in damage resistance against foreign object impact[9]. These energies are determined from experimental data and plotted in Fig. 5. From this figure, it is seen that the two increase with thickness, up to a maximum, and then gradually decreased. This trend implies that damage mode may change with thickness.

To identify the damage behavior of plain-woven Glass/Epoxy composites with thickness, the

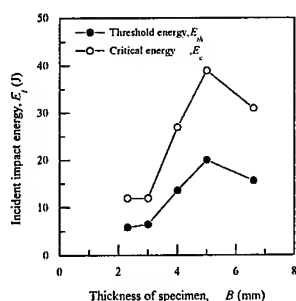
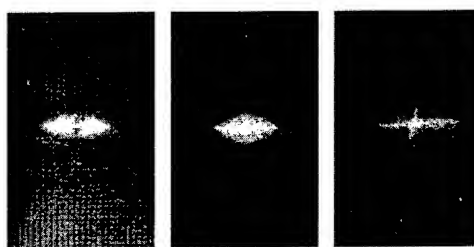
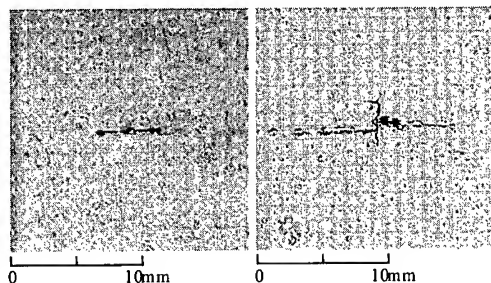
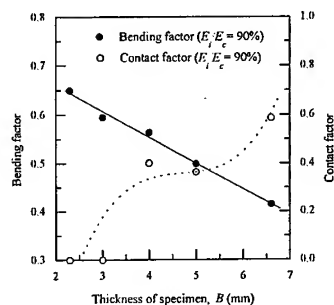


Fig. 5 Threshold & critical impact energy with thickness

Fig. 6 Change of impact damage with thickness ($E_i/E_c=75\%$)Fig. 7 SAM photograph of impact damage ($E_i/E_c=75\%$)Fig. 8 Effect of bending and contact with thickness ($E_i/E_c=90\%$)

damages at identical impact energy ratio E_i/E_c are captured using a 35mm camera and shown in Fig. 6. Also Fig. 7 shows the impact damages in 2.3mm and 6.6mm specimen captured by C-scan. In the case of 2.3mm specimen, the impact damage occurs in transverse direction whereas the longitudinal damage also occurs in the thicker specimen. Consequently, the damage behavior of plain-woven Glass/Epoxy composites is greatly influenced by thickness; the bending stiffness is a dominant factor in thin specimen while the effect of contact stiffness on impact damage gradually increases in thick one[9].

For further understanding the effect of thickness on damage behavior, let us define the bending $(W - 2a_1)/W$ and contact factor $2a_2/D_t$ referred to the effect of bending and contact stiffness on impact damage, respectively. Here the symbols a_1 and a_2 denote the transverse and longitudinal damage length, respectively. Also D_t is the tip radius of the impactor and W denotes the specimen width. Fig. 8 shows the two factors calculated at $E_i/E_c = 0.9$ with thickness. The rising trend of the contact factor contrasts with the bending factor of lowering tendency. The effect of contact on impact damage increases gradually with thickness and reaches a maximum at $B=6.6\text{mm}$ whereas that of bending decreases to reach a minimum at $B=2.3\text{mm}$. The results described above and Fig. 5 suggest that the bending and contact stiffness influence on the damage resistance simultaneously and give the highest damage resistance at $B=5.0\text{mm}$.

5. CONCLUSIONS

In this study, the impact damage and strength reduction behavior of plain-woven Glass/Epoxy composites, including the thickness effect, were experimentally evaluated and its residual strength is compared with the results by residual strength prediction models. The following conclusions have been drawn.

1. The impact damages are mainly fiber breakage and matrix crack in plain-woven Glass/Epoxy composites whereas the dominant damage of unidirectional Carbon/Epoxy composites is delamination, which depends on the stacking sequence.
2. Among several residual strength prediction models proposed on unidirectional laminates, Avva's and Caprino's models well describe the strength reduction behavior of plain-woven Glass/Epoxy composites due to foreign object impact. Also the threshold and critical impact energy increase with thickness, up to a maximum, and then gradually decrease.
3. The threshold and critical impact energy are simultaneously influenced by bending and contact stiffness. The effect of contact increases with thickness, while that of bending decreases.

ACKNOWLEDGEMENTS

The authors gratefully acknowledge the financial support of Safety and Structural Integrity Research Center(Sung-Kyun-Kwan University) in the Korea Science and Engineering Foundation

REFERENCE

1. G.E.Husman, J.M.Whitney and J.C.Halpin, ASTM STP 568(1975) p.92
2. V.S.Avva, J.R.Vala and M.Jeyaseelan, ASTM STP 893(1986) p.196
3. G.Caprio, J. Composite Materials, 18(1984) p.508
4. W.J.Cantwell, Composite Structures, 10(1988) p.247
5. M.E.Waddoups, J.R.Eisenmann and B.E.Kaminski, J. Composite Materials, 5(1971) p.446
6. R.J.Nuismer and J.M.Whitney, ASTM STP 593(1975) p.117
7. S.C.Tan, J. Composite Materials, 21(1987) p.925
8. ASTM D 3039-93 "Standard Test Method for Tensile Properties of Fiber Resin Composite"
9. W.J.Cantwell and J.Morton, Composite Structures, 12(1989) p.39

Measurement of Dynamic Fracture Parameters in the Expansion Process at High Strain Rate

C.Y. Gao¹, H.J. Shi¹, C.L. Liu², C.H. Bai² and Z.H. Yao¹

¹ Department of Engineering Mechanics, Tsinghua University,
Beijing 100084, China P.R.

² Department of Mechanical Engineering, Beijing Institute of Technology,
Beijing 100081, China P.R.

Keywords: Expansion Fracture, Experimental Measurement, Explosive Loading, High Strain Rate, Large Strain

ABSTRACT

A typical cylindrical explosion device is selected as the test object, which is scaled down with the actual Fuel-Air-Explosive device. The behaviors and properties of material at large deformation and high strain rate are referred. An electrical measurement is carried out in an explosion chamber. The dynamic strain history of the expanding shell is measured. The crucial fracture parameters have been obtained. The fundamental principle and specific test method are given, and the results are discussed in detail in the paper. Some data are compared with theoretical solutions and they tally well with each other.

1. INTRODUCTION

The fracture process of metal cylindrical shells under inner explosive loading has been studied for decades. Many observations of rupture's state of shells were published, and some experiential formulae of dynamic fracture criteria were given. The behaviors and properties of materials at large deformation and high strain rate are complex so that the physical mechanism of them is still not very clear today. According to a great deal of tests, micro-damages arise in the dynamic fracture process when the first explosive wave arrives at the shell wall, then rapid growth of micro-cracks appears during the accelerated expansion period. Macroscopic fracture finally results from the very rapid propagation of a number of micro-cracks. In addition, there are a variety of descriptions about the strain-rate sensitive constitution of material, in which parameters must be obtained by meticulous experiment. However, there are not consistent and credible data of sensitivity in existing references, especially for aluminum alloys in common use. The constitutive relations with more

validated data are often selected. Just for this reason, every criterion needs indispensable validation in experiment.

The work of electrical measurement of dynamic fracture parameters in the expansion process at high strain rate is the emphasis in the paper. The time course from shell's initial expansion to final rupture is very short because of the high strain rate. The optical method is generally used in the conventional measurement. A new electrical measurement, however, is designed subtly and implemented in the paper. We have measured the dynamic strain history of the cylindrical shell under interior explosive loading, and have obtained the fracture parameters such as critical strain, expansion rate and rupture moment etc.

2. EXPERIMENT MODEL

Three identical specimens were made for tests. The model is illustrated in Fig.1. The shell's material is aluminum alloy that is most commonly used in the Fuel-Air-Explosive device. The linking way between endplates and shell is fastening. The four tension bars are used to restrict the endplates from breaking off. The height of the shell H is 80 mm, the thickness of the shell δ is 0.3 mm, the diameter of the cylinder D is 65.6 mm, the diameter of the central explosive tube d is 6 mm, and the thickness of the endplate h is 4 mm. There are not grooves on the surface of shell. In fact, the cracks simultaneously extend from the outside and inside of the shell for the thin shell, and extend along surface grooves if notches have been prefabricated. The shape and thickness of the shell are vital factors to the structural dynamic response.

The type of the explosive used is 8701, the TNT equivalent of which is 153% [1]. The loading density is 1.72 g/cm^3 . The loading way is squashing. The diameter of the explosive column must satisfy the following limit [2]

$$D_c < D < D_L \quad (1)$$

Here D_c is called critical diameter that ensures the steady detonation velocity, D_L is maximum

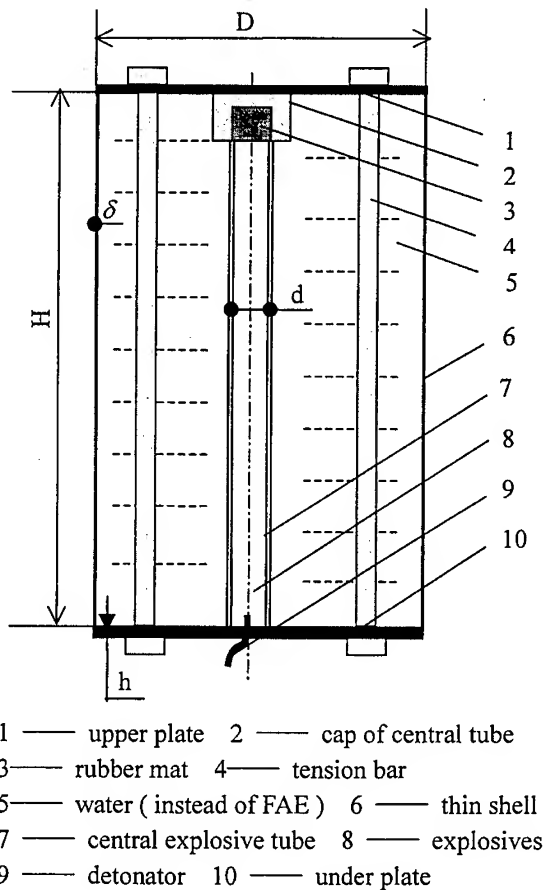


Fig.1. Sketch map of experiment model

diameter at which the detonation velocity will not go up with the diameter increasing. The factors influencing the boundary values include loading density, granularity, shell's constraining conditions and so on.

3. EXPERIMENT PRINCIPLE

In the measurement, resistance coils are wound on the surface of the cylindrical shell and linked in a potential allotting circuit. Thus coils will stretch together with the shell's expanding. A high-frequency recording apparatus can record the voltage increment in resistance coils. The history of peripheral strain can be obtained and other fracture parameters can be calculated subsequently from it.

There are three circuits applied on the upper, middle and under surfaces of shell, respectively. The coil in each one has several loops to avoid the random effect of shell's rupture. The conversion procedures from directly measured values to needed parameters are given as follows:

a). Thread of copper alloy is used as resistance coils which are insulated and permit $\pm 5\%$ resistance error. The resistivity of resistance coils is constant. Its formula is

$$\rho = R \frac{S}{L} \quad (2)$$

where, R is resistance, S is cross section, L is length. In our measurement, the cross section is $0.125 \times 10^{-6} m^2$ and the resistivity $\rho = 6.91 \times 10^{-6} \Omega \cdot m$. Now the resistance is known for a segment of coils with any length.

b). Set that r is initial radius, r' is real-time radius, Δr is the altered quantity of radius. n is the loop of coils. Then the alteration of length ΔL is

$$\Delta L = n \times (2\pi r' - 2\pi r) = 2n\pi \Delta r \quad (3)$$

And peripheral strain ε_θ is

$$\varepsilon_\theta = \frac{\Delta r}{r} = \frac{\Delta L}{2n\pi r} = \frac{\Delta L}{L} \quad (4)$$

c). When the length of coils changes there is the volume unvarying principle

$$V = L \cdot S = L' \cdot S' \quad (5)$$

Here V is coil's volume, L' and S' are respectively altered length and cross section. So

$$R' = \rho \frac{L'}{S'} = R \left(\frac{L'}{L} \right)^2 \quad (6)$$

Substitute Eq.6 into the following

$$\Delta R = R' - R = R \left[\left(\frac{L'}{L} \right)^2 - 1 \right] \quad (7)$$

Set

$$L' = L + \Delta L \quad (8)$$

The following equation can be obtained

$$\frac{\Delta L}{L} = \sqrt{1 + \frac{\Delta R}{R}} - 1 \quad (9)$$

d). Now we will give the relationship of the parameters in circuit (e.g. resistance and voltage). The experiment principle is shown in Fig.2.

U_0 is the voltage of the isobaric power supply. R_a is the voltage allotting resistance. Set initial values as $U_0 = 6V$, $R_a = 100\Omega$. The initial value of R_a should be greater while U_0 should be less so that the display of voltage increment in coils is obvious and convenient to record. Because the resistance of coils will change during the expanding process, the coils are comparative to an

alterable resistance in circuit. Set that ΔU and ΔR respectively stand for voltage increment and resistance increment in coils. It is known that

$$\Delta U = U' - U = \left(\frac{R'}{R' + R_a} - \frac{R}{R + R_a} \right) U_0 \quad (10)$$

$$\Delta R = R' - R \quad (11)$$

R' is the real-time resistance of coils, and R has been given in the first step. By substituting Eq.11 into Eq.10

$$\Delta R = \frac{(R + R_a)^2 \Delta U}{R_a U_0 - (R + R_a) \Delta U} \quad (12)$$

It shows that ΔR not only results in ΔU but also can be expressed by ΔU explicitly.

e). Assemble Eqs.4, 9, 12, we can finally establish the corresponding function relation of peripheral expanding strain ε_θ and directly measured parameter ΔU as follows

$$\varepsilon_\theta(t) = f(\Delta U(t)) \quad (13)$$

The quantitative relational expression is illustrated as the plotted graph in Fig.3. From the visual description it is obvious that their relation is approximately linear.

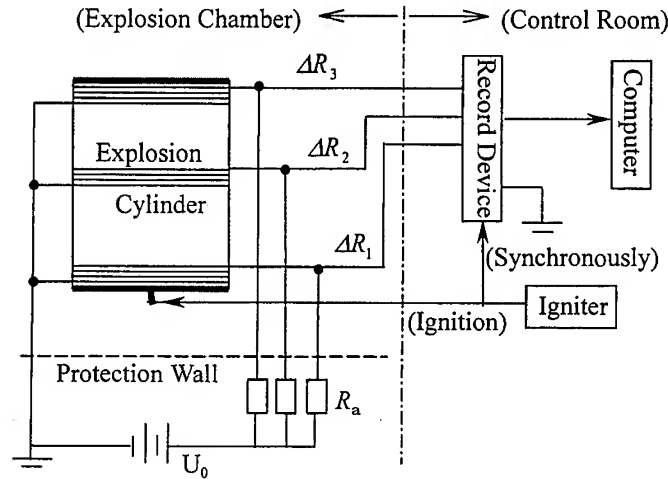


Fig.2. Sketch map of experiment principle

4. RESULT AND DISCUSSION

Three circuits are arranged in different locations of the shell. There are three routes of signal in one experiment. The time range is set at thirty microseconds on the base of theoretically evaluated rupture moment. The voltage range is set at 500 milli-volts. Once rupture happens in the shell, resistance coils will disconnect simultaneously, and the circuits become open. The input voltages of the recording instrument will be equal to power supply's voltage, which is far greater than the selected measurement range. Then there appears an abrupt leap in each curve for the case. The leap just means open circuit.

The relations of the peripheral strain to time are shown in Fig.4~Fig.6. They are individually listed below.

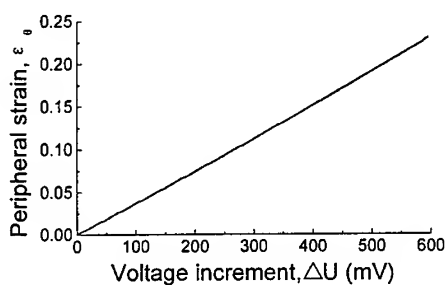


Fig.3. Relation of peripheral strain to voltage increment

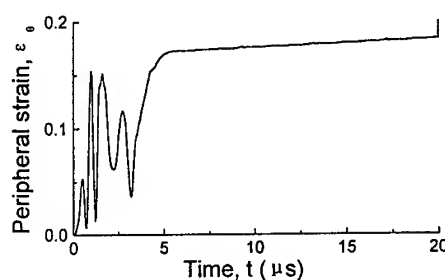


Fig.4. Plot of peripheral strain against time for the upper shell

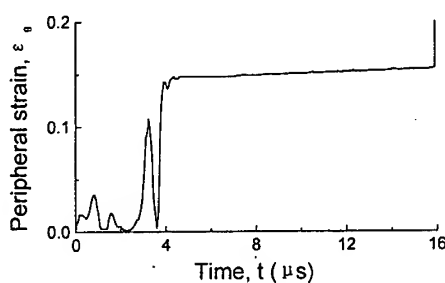


Fig.5. Plot of peripheral strain to time for the middle shell

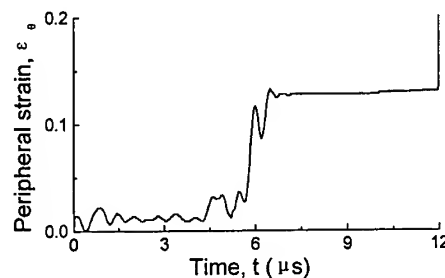


Fig.6. Plot of peripheral strain to time for the under shell

There are several experimental conclusions in the light of our elementary analysis:

1). Frequent anomalous vibration of the measured signal appears in every circuit. This phenomenon proves our theoretical prediction that stress waves in cylinder will have a great reflective and refractive effect on the inner surface of shell during the expanding process. It is found that the first stress wave is very considerable relative to the late waves, and the amplitude of vibration decreases from the shell's upper location to the shell's under location.

2). There exists temporal lag between three circuit signals. The spreading velocity of detonation

wave along central tube can be calculated from the time delay. That is namely the explosive velocity important in explosive test. It is obtained formerly only by the estimation of the explosive's characteristic parameters. In our test it is about 10000 *m/s* or so.

3). The disconnecting voltage and disconnecting moment both are different in each circuit. They decrease from the upper circuit to the under circuit. In the curves the critical strains and rupture moments of different locations are unlike with one another for it. Although the maximal expansion presents at the upper location, rupture first emerges at the under location where the expansion extent is minimum. This is really noticeable.

4). In all curves the peripheral strain's values increase quickly at the beginning and very slowly at the later. It indicates that the cylindrical shell expands with an accelerative rate during the initial period and with a constant rate during the succedent period. This fact testifies that our proposed theoretical assumption [3] about the shell's expansion under inner explosive loading is rational.

The reason that distinct differences exist among above curves is that the endplate's constraint brings about end effect to the side circuits. Moreover, ignition at the upper end results in the unsymmetrical loading. We have gotten the modified theoretical form by considering the end effect into the fracture criterion [3], and its results cope well with the test results. For example, we compared fracture parameters of the middle circuit with theoretical ones. The average critical strain in test is 0.160, while modified theoretical solution is 0.166. The error is 3.75 %. The rupture moment in test is 16 microseconds, theoretical solution is 17 microseconds. The error is 6.25 %. The comparison proves that the modified theoretical fracture criterion is generally consistent with the actual case of the expanding process at high strain rate.

5. CONCLUSION

One type of specific experiment model is introduced originally, then the experiment apparatus and experiment principle are presented in the paper. The experiment results and their discussion are listed. Altogether, the following conclusions can be known: i). The transformation from the measured parameter to the objective fracture parameters has been established successfully. ii). We have determined the peripheral strain's history from the arriving of the first explosive wave at the shell's inner wall to shell's entire bursting, and obtained some vital fracture parameters. The rupture moment provides the beneficial data for us to study the comparability of FAE devices. iii). Stress waves in a cylinder will give birth to a great reflective and refractive effect on the inner surface of shell during the expanding process. The fact explains the frequent damped vibration of expansion velocity in numerical simulation.

REFERENCE

1. Y.B. Song, Explosion Effect and Explosive Loading Design, Defence Industry Press, Beijing (1987)
2. S.R. Yun, Calculation Method of Explosion Mechanics, Beijing Institute of Technology Press, Beijing (1995)
3. C.Y. Gao, H.J. Shi, et al. Tsinghua Science and Technology, 5(1), (2000) p.15-19

A Study on the Development of the Dynamic Photoelastic Experimental Method for Isotropic/Orthotropic Bimaterials

J.S. Hawong¹, D.C. Shin¹, O.S. Lee², H.J. Lee¹ and J.K. Ha³

¹ Department of Mechanical Engineering, Yeungnam University,
214-1 Dae-dong, Kyungsan, Kyongbuk 712-749, Korea

² Division of Mechanical, Aerospace and Automation Engineering,
Inha University, 253 Younghyun-dong, Nam-ku, Incheon 402-751, Korea

³ School of Automobile, Kimchun Science College, 480 Samrak-dong,
Kimchun, Kyongbuk 740-200, Korea

Keywords: Crack Propagating Velocity, Dynamic Isochromatics, Dynamic Loading Device, Dynamic Photoelastic Experimental Method, Dynamic Photoelastic Hybrid Method, Dynamic Stress Component, Isotropic/Orthotropic Bimaterials, Lower Edge Crack, Upper Edge Crack

ABSTRACT

Using the dynamic photoelastic experiment, to analyze stress distribution of isotropic/orthotropic bimaterial which the interfacial crack is propagated with constant velocity along the interface. The dynamic photoelastic experimental device, the dynamic physical properties, the dynamic photoelastic experimental model material for isotropic/orthotropic bimaterial, the dynamic stress component and stress analyzing method etc. are needed. In this research, the requirements of the dynamic photoelastic experimental method for isotropic/orthotropic bimaterials are studied.

Edge crack should be located along the interface of the acute angle side of softer material in order that the interfacial crack is propagated along the interface of bimaterial with arbitrary slanted angle of crack. In this paper, the dynamic photoelastic experimental hybrid method for bimaterial under dynamic load is introduced.

1. INTRODUCTION

Most machine structures in the industrial fields are under the dynamic load. Bimaterial have been variously used in the industrial fields recently, because the bimaterial have a lot of merits which homogeneous materials cannot contain. In most bimaterial, the interface is very weak. Therefore most people are studying the debonding and delamination problem of bimaterial. In the bimaterial, many researches on the interfacial crack of isotropic/isotropic or orthotropic /orthotropic bimaterial have been doing when interfacial crack is propagated with constant velocity[1], but in the isotropic/orthotropic bimaterial, any researchers have not been done. Therefore, the main purposes of this research are to develop the requirements of the dynamic photoelastic experiment for the

stress analysis of the isotropic/orthotropic bimaterial when the interfacial crack is propagated with constant velocity along the interface of bimaterial with arbitrary slanted angle of crack.

2. STRESS COMPONENTS OF A PROPAGATING CRACK ALONG THE INTERFACE OF ISOTROPIC/ORTHOTROPIC BIMATERIALS AND DYNAMIC PHOTOELASTIC HYBRID METHOD

The near-field stresses of a propagating crack along the interface of isotropic/orthotropic bimaterial materials are given by eq. (1) [2]

$$\begin{aligned}\sigma_{11k} &= \sum_{n=1}^{\infty} \operatorname{Re} \left[\lambda_n \left(E_{1k} M_{1kn} z_{1k}^{\lambda_n-1} + \bar{E}_{1k} M_{2kn} \bar{z}_{1k}^{\lambda_n-1} + E_{2k} M_{3kn} z_{2k}^{\lambda_n-1} + \bar{E}_{2k} M_{4kn} \bar{z}_{2k}^{\lambda_n-1} \right) \beta_n \right] \\ \sigma_{22k} &= \sum_{n=1}^{\infty} \operatorname{Re} \left[\lambda_n \left(F_{1k} M_{1kn} z_{1k}^{\lambda_n-1} + \bar{F}_{1k} M_{2kn} \bar{z}_{1k}^{\lambda_n-1} + F_{2k} M_{3kn} z_{2k}^{\lambda_n-1} + \bar{F}_{2k} M_{4kn} \bar{z}_{2k}^{\lambda_n-1} \right) \beta_n \right] \quad (1) \\ \sigma_{12k} &= \sum_{n=1}^{\infty} \operatorname{Re} \left[\lambda_n \left(G_{1k} M_{1kn} z_{1k}^{\lambda_n-1} + \bar{G}_{1k} M_{2kn} \bar{z}_{1k}^{\lambda_n-1} + G_{2k} M_{3kn} z_{2k}^{\lambda_n-1} + \bar{G}_{2k} M_{4kn} \bar{z}_{2k}^{\lambda_n-1} \right) \beta_n \right]\end{aligned}$$

where

$$\begin{aligned}E_{1k} &= \mu_{1k}^2 & E_{2k} &= \mu_{2k}^2 + a_2 R (\mu_{2k}^2 - \mu_{1k}^2) & F_{1k} &= -\mu_{1k}^2 & F_{2k} &= -[\mu_{1k}^2 + a_1 R (\mu_{2k}^2 - \mu_{1k}^2)] \\ G_{1k} &= -(1 - (a_1 - a_2)R)\mu_{1k} & G_{2k} &= -(1 - (a_1 - a_2)R)\mu_{2k}\end{aligned}$$

where $a_6 = 2(a_1 - a_2)$, $\underline{a} = a_{ij}$ is defined in the plane stress and $\underline{a} = b_{ij}$ is defined in the plane strain. μ_k are the root of characteristic equations and subscript $k(=1,2)$ mean material. λ_n is n -th eigenvalue. M_{mn} ($m=1,2,3,4$) are the complex coefficients determined by material properties and crack propagating velocity and known quantities. z_{ik} are the functions of the locations from the crack-tip. Therefore, the unknown variables in eqs. (1) are only the complex coefficient β_n 's.

Substituting eq. (1) into dynamic stress-optic law, eq. (2), gives eq. (3).

$$D = \left(\frac{f_{od} N_f}{t} \right)^2 = (\sigma_{11} - \sigma_{22})^2 + 4\sigma_{12}^2 \quad (2)$$

$$\begin{aligned}D &= \left\{ \sum_{n=1}^{\infty} \operatorname{Re} \left[\lambda_n \left(2E_{11} z_1^{\lambda_n-1} + 2\bar{E}_{11} M_{21n} \bar{z}_1^{\lambda_n-1} + (E_{21} - F_{21}) M_{31n} z_2^{\lambda_n-1} + (\bar{E}_{21} - \bar{F}_{21}) M_{41n} \bar{z}_2^{\lambda_n-1} \right) \beta_n \right] \right\}^2 \\ &+ 4 \left\{ \sum_{n=1}^{\infty} \operatorname{Re} \left[\lambda_n \left(G_{11} z_1^{\lambda_n-1} + \bar{G}_{11} M_{21n} \bar{z}_1^{\lambda_n-1} + G_{21} M_{31n} z_2^{\lambda_n-1} + \bar{G}_{21} M_{41n} \bar{z}_2^{\lambda_n-1} \right) \beta_n \right] \right\}^2 \quad (3)\end{aligned}$$

where f_{od} is dynamic stress fringe value, N_f the dynamic fringe order, t the thickness of specimen. Therefore, eq. (3) is function of only β_n . Applying the non-linear least square method of dynamic photoelastic experiment to the eq. (3), we can obtain β_n . Substituting β_n into eq. (1), stress components are obtained.

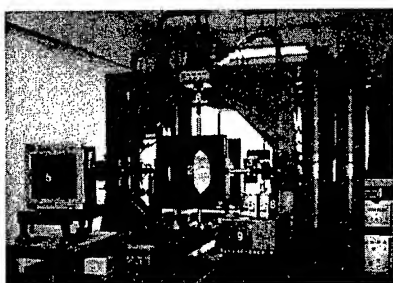
We can separate stress components from the only isochromatic data. Therefore, this method is called "the dynamic photoelastic experimental hybrid method for bimaterial".

3. DYNAMIC PHOTOELASTIC EXPERIMENTAL DEVICE AND SPECIMEN

Fig. 1 shows the dynamic photoelastic experimental device. Controlling the oil valve, the loading device has the function which the biaxial or uniaxial dynamic and static load can be applied. The maximum strain rate of the device is 31.637 s^{-1} , that is within the resonance of machine or structure. Dynamic photoelastic experimental device is composed of dynamic biaxial loading device and Cranz-Schardin pattern camera system. Spark time of Cranz-Schardin pattern camera system is controlled from $1 \mu\text{s}$ to $9999 \mu\text{s}$.

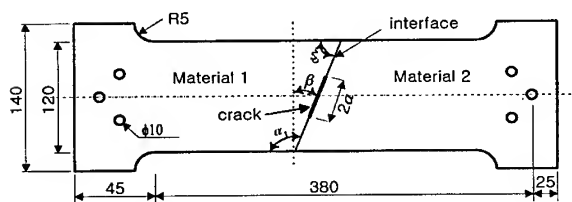
Specimens for isotropic material and orthotropic material are respectively made from the epoxy resin plate(material 1) and carbon fiber epoxy composite plate(material 2), the crack is molded from the teflon-molding method[2]. Specimen dimension is shown in Fig. 2.

In the bimetals manufactured by adhesive method, the residual stresses are not originated. Therefore we should make the photoelastic experimental specimen for the bimaterial using the adhesive method. Thickness of adhesive is less than $50 \mu\text{m}$. To strengthen bonding force, surface roughness is produced on the bonding surface by using files and #200 sandpaper. After finishing the manufacturing, surfaces of two materials should be washed by distilled water.



1. Dynamic biaxial loading frame
2. Field lens & Polarizer & Quarter wave plate
3. Multi-spark light source
4. Multi-spark control box
5. Multi-camera
6. Load-cell
7. Accumulator
8. Dynamic amplifier
9. Oscilloscope

Fig. 1 Dynamic photoelastic experimental device



β : the slanted angle of crack, $\alpha_1(\alpha_2)$: the acute(obtuse) angle of softer material

Material 1: Epoxy resin(softer material), Material2: Al 6061 or Ca. F. E. C.(stiffer material)

Fig.2 Dimension of the bimaterial specimen

4. EXPERIMENTAL RESULTS AND DISCUSSIONS

Fig. 3 and fig. 4 respectively show dynamic isochromatics of epoxy resin /Ca. F. E. C. bimaterial

with central crack when β is 0° and 45° respectively. As shown in Fig. 4, the black point (point A: the lower crack tip of central crack) in the lower portion of the central crack is moved in the epoxy resin region. The upper crack tip of central crack is propagated along the interface.

Fig. 5 shows the dynamic isochromatics of epoxy resin/aluminum bimaterial with lower edge crack when β is 45° . In the epoxy resin/aluminum bimaterial, when the initial crack is located at the acute region of softer material in the bimaterial, crack is propagated along the interface.

Fig. 6 and fig. 7 respectively show dynamic isochromatics of epoxy resin/Ca. F. E. C. bimaterial with lower edge crack when β is 0° and 45° respectively. As shown in Fig. 6 and fig. 7, crack is propagated along the interface of bimaterial when the initial edge crack is located at the acute angle region of softer material.

Fig. 8 indicates the dynamic isochromatics of epoxy/aluminum bimaterial with upper edge crack. As shown in Fig. 8, crack is propagated along the interface by a little, and then crack is deviated into the softer material from the interface when the edge crack is located at the obtuse angle region of softer material.

Fig. 9 and fig. 10 respectively show the dynamic isochromatics of epoxy resin /Ca. F. E. C. bimaterial with upper edge crack when β is 30° and 45° respectively. As shown in Fig. 9 and fig. 10, crack is propagated along the interface when the initial crack is located at the obtuse angle region of softer material. As shown in Fig. 8, fig. 9 and fig. 10, when the stiffer material is aluminum, crack is more or less propagated along the interface and deviated into the softer material from the interface. When the stiffer material is carbon fiber epoxy composite and the slanted angle of crack is less than

1 μ sec26 μ sec

Fig. 3 Dynamic isochromatics of epoxy/Ca.F.E.C. bimaterial($\beta=0^\circ$, central crack)

3 μ sec32 μ sec

Fig. 4 Dynamic isochromatics of epoxy/Ca.F.E.C. bimaterial($\beta=45^\circ$, central crack)

9 μ sec46 μ sec

Fig. 5 Dynamic isochromatics of epoxy/Al 6061 bimaterial($\beta=45^\circ$, lower edge crack)

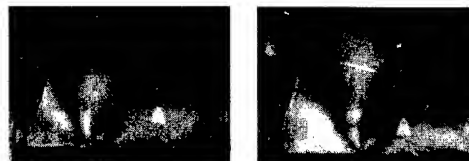
2 μ sec29 μ sec

Fig. 6 Dynamic isochromatics of epoxy/Ca.F.E.C. bimaterial($\beta=0^\circ$, edge crack)

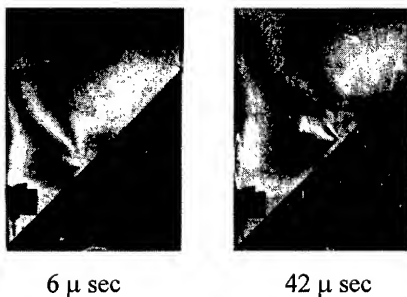


Fig. 7 Dynamic isochromatics of epoxy/Ca.F.E.C. bimaterial($\beta=45^\circ$, lower edge crack)

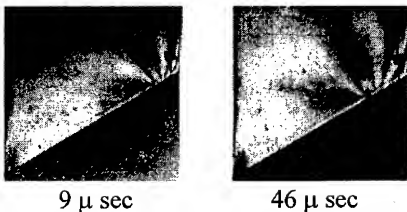


Fig. 9 Dynamic isochromatics of epoxy/Ca.F.E.C. bimaterial($\beta=30^\circ$, upper edge crack)

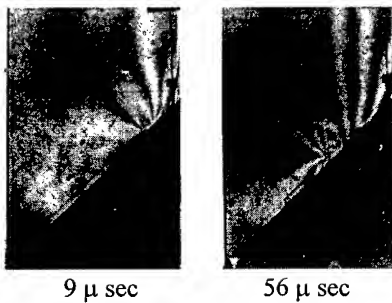


Fig. 10 Dynamic isochromatics of epoxy/Ca.F.E.C. bimaterial($\beta=45^\circ$, upper edge crack)

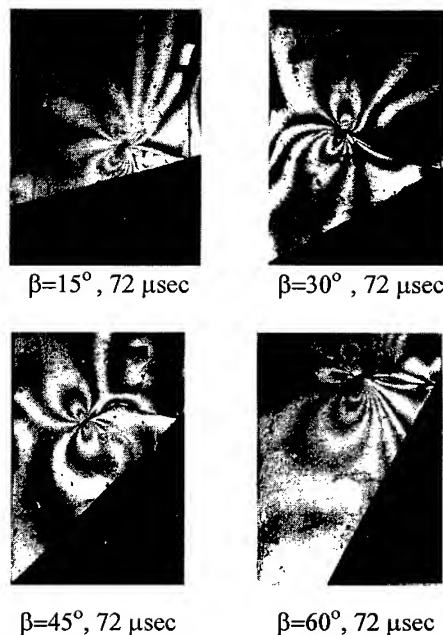


Fig. 8 Dynamic isochromatics of epoxy/Al 6061 bimaterial(upper edge crack)

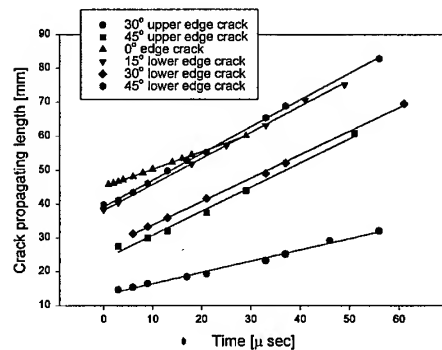


Fig. 11 Variations of crack propagating length with propagating time(epoxy/Ca.F.E.C.)

30° , the initial crack in the obtuse angle of softer material is propagated along the interface, but when the stiffer material is carbon fiber epoxy composite, the microcracks are originated and very small when the slanted angle of crack is 30° , and they are more originated largely and main crack is deviated from the interface of bimaterial when the slanted angle of crack is 45° . These situations are produced due to the difference of adhesive force between epoxy resin and aluminum and between epoxy resin and carbon fiber epoxy composite.

Fig. 11 shows the variations of crack propagating length of epoxy resin/Ca. F. E. C. bimaterial with time. The crack propagating velocities are almost constant about 37.4 %~89.4 % of rayleigh wave velocity of epoxy resin.

Until now, the stress components and displacement component in the vicinity of interfacial crack tip are derived when the crack propagating velocity is only constant and crack is only propagated along the interface. Therefore, to use them, the initial crack should be located at the acute angle region of softer material when bimaterial is epoxy resin/aluminum, that is, the bonding force is weak, the initial crack can be made at the acute angle region or at the obtuse angle region of softer material when bimaterial is epoxy resin/ Ca. F. E. C.. But isochromatic fringe orders are produced more in the obtuse angle region than in the acute angle region of the softer material.

5. CONCLUSION

1. When interfacial crack is propagated with constant velocity along the interface of isotropic/orthotropic bimaterials, the dynamic photoelastic experimental hybrid method for is suggested.
2. When edge crack is located along the interface of the acute angle side of softer material in the bimaterial, interfacial edge crack is propagated with constant velocity along the interface of bimaterial with arbitrary stiffer material.
3. When edge crack is located along the interface of the obtuse angle side of softer material in the bimaterial composed of epoxy and Ca. F. E. C., when the slanted angle of crack is less than or equal to 30° , the interfacial edge crack is propagated with constant velocity along the interface of bimaterial. When the slanted angle of crack is greater than 30° , the interfacial edge crack is propagated with constant velocity more or less along the interface of bimaterial with arbitrary stiffer material and deviated into the softer material from the interfacial crack.
4. The crack propagating velocities of epoxy resin/Ca. F. E. C. bimaterials are almost constant and about 37.7 %~89.4 % of rayleigh wave velocity of epoxy resin.
5. When the dynamic photoelastic experiment for bimaterial is done, edge crack should be located along the interface of the acute angle side of the softer material in the bimaterial.

ACKNOWLEDGEMENT

These authors wish to acknowledge the financial support of Korean Research Foundation made in the program year of 1997.

REFERENCE

1. M. A., Aminpour and K. A., Holsapple, Engineering Fracture Mech., **36(1)** (1990) pp. 93-103
2. J. S., Hawong, D. C., Shin, K. R., Kim, and H. J., Lee, APCFS'99, China, Xi'an (1999)

Evaluation of Large Strain in Ductile Polymers under High Speed Loading

T. Kuboki, T. Mada and K. Takahashi

Research Institute for Applied Mechanics, Kyushu University,
6-1 Kasuga-koen, Kasuga-city, Fukuoka 816-8580, Japan

Keywords: Ductile Polymer, High Impact Polystyrene, High-Speed Loading, High-Speed Photography, Large Strain, Optical-Fiber Extensometer, Strain Gauges

ABSTRACT

Dynamic performance of an in-laboratory constructed optical-fiber extensometer was examined under actual impact testing conditions for ductile specimens of high impact polystyrene (HIPS) using two well-known methods; strain gauge measurement and high-speed photography. Impact tests were carried out at a strain rate of 19 s^{-1} . Strains determined by the three methods were compared. It has been shown that the dynamic strain of HIPS evaluated by the optical extensometer is in a good agreement with the one by the strain gauge in an elastic region and that beyond the elastic limit the latter exhibits much smaller values and breakdowns halfway. High-speed photography provided strains in a good agreement with those by the optical extensometry up to a strain of around 13 % when fracture took place. High-speed photography also revealed that during impact there was little torsional rotation of the specimen which could have caused significant errors in the optical measurement. It is concluded that the optical-fiber extensometer can accurately measure large deformation under high-speed loading and that it can be an apparatus to calibrate performance of strain gauge measurements on soft materials like polymers.

1. INTRODUCTION

Mechanical properties of polymers strongly depend on time and temperature influenced by their viscoelasticity. As for the structural materials under high-rate loadings, it is important to know mechanical properties such as Young's modulus, strength, toughness, strain at fracture and fracture energy under dynamic situations. However, this is not easy because of a technical difficulty involved particularly in large dynamic deformation measurement. Use of strain gauge is a typical method for strain measurement of a material under impact loading. However, in most polymers, fracture initiates at an edge of gauge adhered on the specimen surface even if its strain at fracture is smaller because the gauge edges become stress-concentrated sites. Therefore, strain at fracture is mostly underestimated. When polymers are ductile and undergo large deformation under impact loading, problems are much significant with the strain gauge measurement. Deformation can go up to a region where the gauge can not operate any more. For this reason, use of non-contact devices is preferable for large strain measurement of polymers under not only static but also dynamic loading.

Recently Beguelin et al. [1] have developed an optical extensometer for quasi-non-contact measurement of deformation, where a distance between optical fibers slightly bonded on a specimen surface is monitored by a position sensing detector (PSD). The features of this extensometer are as follows: (1) effect of bonded fibers on mechanical properties of a material can be ignored because they are thin and light. Fracture does not occur at bonding points, (2) the extensometer can be used for large strain measurement under dynamic load. Frequency characteristics of the extensometer were explored by Mada et al. [2] utilizing the simulated optical source movement and it predicts that the electronic response is as high as 100 kHz. However, its actual feasibility has never been studied for evaluation of large strain under impact loading.

In this paper, dynamic characteristics of the optical extensometer were examined on actual ductile polymer specimens using different methods; strain gauge measurement and high-speed photography. Effect of the fiber bonding on a specimen as well as the rotating movement of a specimen during dynamic loading was also explored.

2. OPTICAL-FIBER EXTENSOMETER

2.1. Tensile Impact Tests

An in-laboratory constructed optical-fiber extensometer [2, 3] and a tensile impact apparatus [3] were used in the present study. Rubber-toughened polystyrene HIPS was employed as a specimen material. HIPS pellets were injection-molded to form dumbbell type specimens, as shown in Fig. 1.

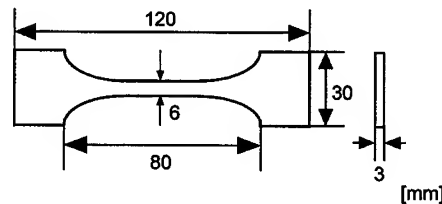


Fig.1. Specimen geometry.

Fig. 2 shows a schematic diagram of a falling weight type impact tensile test machine [3]. A falling striker, 10 kg in mass, impacts on a lower crosshead (the shaded portions in the Figure). The impacted lower crosshead applies a tensile load on a specimen at a high speed corresponding to the preset height of the mass. A piezo-electric load cell connected to an upper crosshead measures impact load. A rubber sheet of 8 mm thickness is placed on the impacted surface of the lower crosshead to reduce vibration noises.

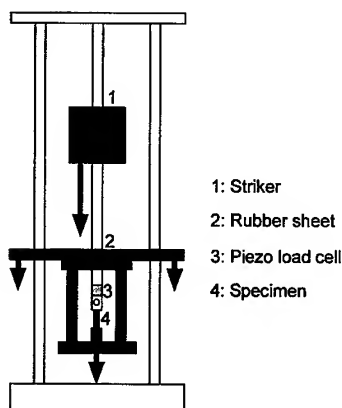


Fig.2. Impact tensile test machine.

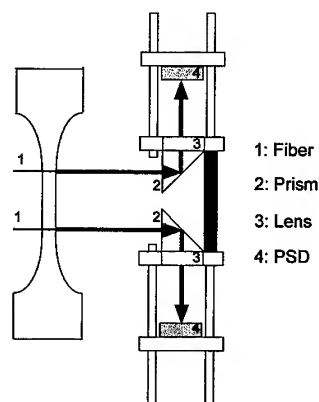


Fig.3. Optical-fiber extensometer.

2.2. Optical-Fiber Extensometer

A schematic diagram of an optical-fiber extensometer is shown in Fig. 3. Two fibers of diameter $250\text{ }\mu\text{m}$ are put on a gauged portion of a specimen with a thin adhesive tape. Laser light emitted from the end of fiber passes through a prism and is focused on each of PSDs. Details of the extensometer can be seen in Refs. 2 and 3. The distance between two fibers in advance of loading is 25 mm .

2.3. Strain Measurement

Dynamic performance of the optical as well as load measurement for a HIPS specimen is shown in Fig. 4. The strain rate is 19 s^{-1} . Displacements of the two fibers and load from the piezo-electric load cell are given as a function of time. It is noted that time derivative of the upper fiber displacement, i.e., velocity, greatly decreases around at the yielding point. In contrast, the velocity of the lower fiber exhibits only a small change. This is rational because plastic deformation is produced mostly in the gauge portion between the upper and lower fiber. Elongation is obtained by subtracting upper fiber displacement from lower fiber displacement. The four signals exhibit sudden changes around at $t = 4\text{ ms}$, when fracture occurred.

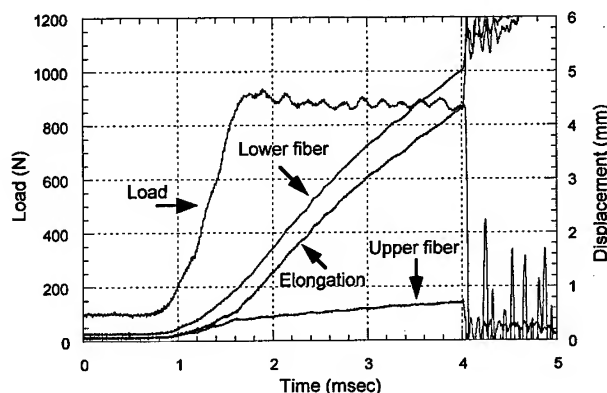


Fig. 4. Simultaneous measurements of displacements of the fibers and load under a strain rate of 19 s^{-1} .

Fig. 5 shows a stress-strain curve derived from the result in Fig. 4. Mechanical properties of the material can be well estimated from this curve. Young's modulus, strength, strain at fracture and fracture energy are 2.3 GPa , 50 MPa , 0.17 and 3.6 J , respectively. The elastic limit is at a strain of 0.025 . Stress thereafter is almost constant.

3. COMPARISON WITH STRAIN GAUGE MEASUREMENT

Two optical fibers and a strain gauge of 5 mm in length are put on a HIPS specimen for simultaneous comparison of the strain measurement. A strain gauge amplifier used in this experiment has a frequency response of 200 kHz . According to a catalogue, the strain gauge is capable of measuring a strain up to 15% under static loading. Fig. 6 shows strains obtained from the two methods together with the piezo output as a function of time. The strain rate is 19 s^{-1} . Strain evaluated by the extensometer is in a good agreement in an elastic region with the one by the

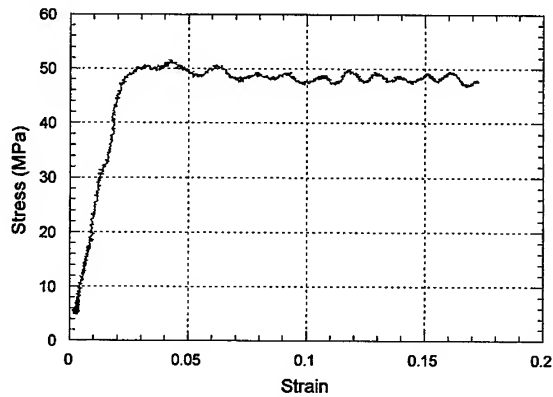


Fig. 5. Stress-strain curve obtained from the results in Fig. 4.

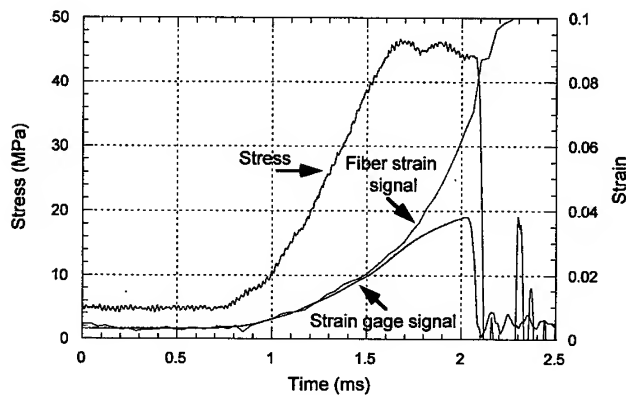


Fig. 6. Comparison of strain measurements using the optical-fiber extensometer and strain gauge.

strain gauge. However, the difference becomes larger as deformation proceeds from the elastic limit due to lower estimation in the strain gauge measurement. This is considered mainly because an adhesive used to bond the strain gauge onto a specimen surface has a modulus higher than that of the specimen, which should put restraint upon specimen deformation underneath the gauge. It is noted therefore that this quasi-non-contact optical extensometer can be a calibration device to check performance of a strain gauge on polymeric materials if its performance is confirmed by high-speed photography.

4. COMPARISON WITH MEASUREMENT BY HIGH-SPEED PHOTOGRAPHY

4.1. High-Speed Photography

For the above-mentioned reason, high-speed photography was carried out using a Cranz-Shardin type high-speed camera [4]. The camera is equipped with 30 spark gaps (see Fig. 7 (a)). Light rays from each gap are focused on a corresponding lens (see Fig. 7 (b)). An optical setup is

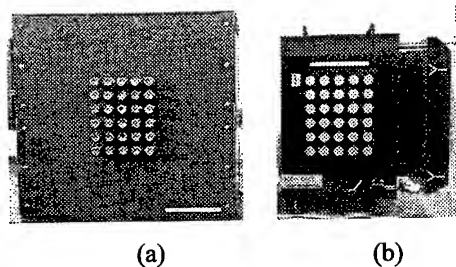


Fig. 7. Cranz-Shardin type high-speed camera: (a) Spark gaps, and (b) Lens box.

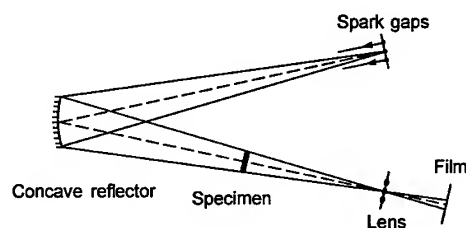


Fig. 8. Optical setup for high-speed photography.

shown in Fig. 8. A series of 30 frames can be taken through photography with an exposure time of 450 ns (half width) for each spark. The time interval between adjacent frames is 80 μ s in this study.

4.2. Simultaneous Measurement

High-speed photography was carried out together with the strain measurement by the optical-fiber extensometer. Fig. 9 shows selected photographs from successive 30 ones for a HIPS specimen loaded under a strain rate of 19 s^{-1} . Fibers on the specimen are visible. It is noted that there is little torsional rotation of the fibers during the impact and that fibers are fixed on the

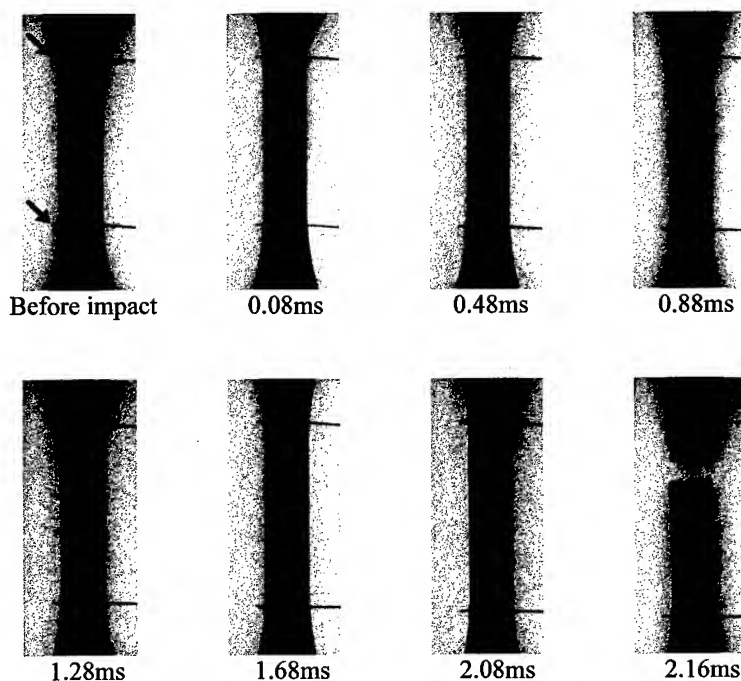


Fig. 9. High-speed photographs of a HIPS specimen under strain rate of 19 s^{-1} (The arrows indicate ends of fibers where laser lights were emitted to PSD detectors).

specimen firmly. Strains are obtained by measuring the distance between the fibers on the photographs. Fig. 10 shows results of strain measurements by the two methods. They agree quite well with each other. The maximum strain of around 13 % is obtained from the extensometer and high-speed photography with a time to fracture of about 2.05 ms. Periodic noises on the strain signal from the extensometer are due to sparks of the camera and these can be a good time base in the comparison of deformation measurements.

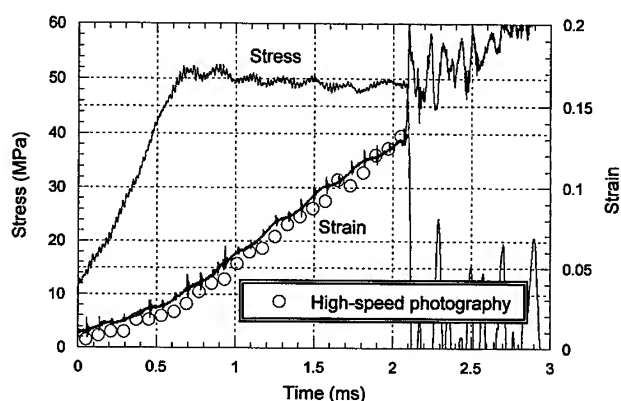


Fig. 10. Comparison of strain measurements using the optical-fiber extensometer and high-speed photography (The open circles represent strains measured by high-speed photography).

5. CONCLUSIONS

Actual reliability of the optical-fiber extensometer was examined for HIPS tensile specimens under high-speed loading by comparing its performance with those of strain gauge measurement and high-speed photography. Results indicate that the extensometer functions satisfactory for measurement of large deformation under high-speed loading and that it can be used for calibration of strain gauge measurement on soft materials like polymers.

ACKNOWLEDGEMENT

The authors are indebted to Dr. Ph. Beguelin and Professor Kausch's laboratory at EPFL for providing technical information of the optical extensometer.

REFERENCES

1. Ph. Beguelin, M. Barbezat and H.H. Kausch, *J. Physique III*, **1** (1991) p. 1867
2. T. Mada, K. Takahashi, Ph. Beguelin and G. Aggag, *Transactions of the Japan Society of Mechanical Engineers*, **63 A** (1997) p. 1431 (in Japanese)
3. K. Takahashi, T. Mada and Ph. Beguelin, *Transactions of the Japan Society of Mechanical Engineers*, **64 A** (1998) p. 2975 (in Japanese)
4. K. Takahashi and T. Mada, *Reports of Research Institute for Applied Mechanics, Kyushu University*, **28** (1980) p. 21

Damages in Woven Polymer Matrix Composites under Impact Loading

T.W. Kim¹, H. Park², C. Kim¹ and J.H. Lee³

¹ School of Mechanical Engineering, Kook-Min University, Seoul, Korea

² HK-Electronics, Seoul, Korea

³ Department of Mechanics, Korea Polytechnic University, Korea

Keywords: Damage, Glass Fiber, Low-Velocity Impact, Polymer Matrix Composites PMC

ABSTRACT

Material damages after a low-velocity impact on a woven glass-fiber/epoxy PMC (polymer matrix composite) were investigated. The initial development, and the extent of induced material damages were measured after a variety of drop-weight impacts. The retained post-impact residual mechanical properties were evaluated. The mechanical properties were found to decrease gradually with the successive number of impacts. The ultrasonic flaw scanner results were analyzed with the measured mechanical properties. The material property degradation appeared to be initiated mostly by brittle matrix cracking followed by crack propagation.

1. INTRODUCTION

PMC (Polymer matrix composites) have many advantages over monolithic metal or polymers such as high specific strength, high specific stiffness and resistance to corrosion and fatigue [1,2]. PMC have been applied to many mechanical and automotive components including bumpers, autobody frames, and car-seats, requiring more sturdiness and lower weight than ever.

Common types of reinforcement in PMC include unidirectional, angle ply, or woven fabric fibers in polymer matrix materials. The PMCs, unlike soft metals showing local plastic deformations at the surface, tend to dissipate impact energy by inducing material internal damages when impacted. The types of damage [2] include delamination, matrix cracking, fiber/matrix debonding, and/or fiber fracture. The impact damages usually occur within a short period of time, and the combined material damages are difficult to distinguish.

In order to accomplish light-weight structure and components, materials need to be used minimally, and thus the dimensions of the material become smaller and thinner. As the strength of the PMCs becomes an important property to possess, the retained property of the composite after low-velocity impact [3,4,5] needs to be known thoroughly in order to provide safety and reliability for the use of the material. Especially, the impact on the composites is prone to be repetitive in nature before complete repair [6] and replacement can take place.

Therefore, the present study investigates the mechanical properties retained after single and/or multiple impact loading on the composites selected. The retained elastic moduli of the composites were measured by the 4-point bending method. The data were analyzed as a function of impact

energy and impact times. Through observations of impact history and property change, the type of material damages were determined.

2. EXPERIMENTAL PROCEDURE

The Dynatup-impact testing machine was used in the present study, and is schematically shown in Fig. 1. The impactor was hemispherical with a diameter of 12.7mm. The set-up was composed of a stop block to avoid secondary impact, a fixture to hold the specimen by hydraulic pressure, and a guided post. The energy can be adjusted either by a change of drop-height or a change of drop-weight. The change of height was chosen in the present study. The impact force versus deflection curves during impact were obtained with piezoelectric sensor attached at the impactor tip, and the signal was sent to a PC, and processed with software provided by the Dynatup.

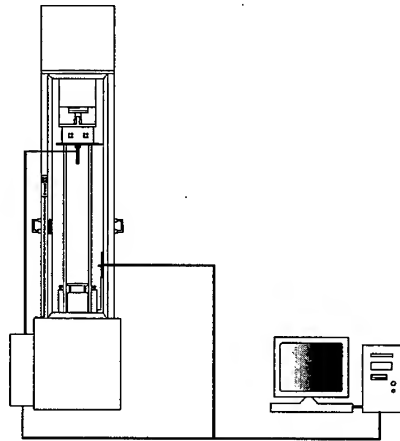


Fig. 1. Schematic of experimental setup for the drop-weight impact test

Figure 2. shows the schematic of the ultrasonic A and C-scan test to explore the internal damages of the composites after impact. The set up includes (1) a scanner with transducer, (2) a motion control drive module, (3) a motion-controlling PC to guide transducer's direction and velocity, (4) data acquisition and analysis PC.

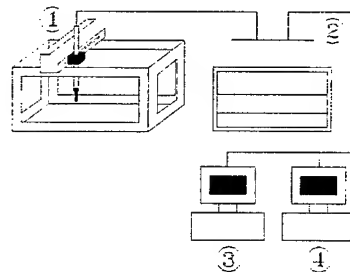


Fig. 2. Schematic of ultrasonic material damage scanner

The fiber/matrix system used in the present study was a glass fiber woven/epoxy matrix supplied by the Korea-fiber company. The composite was sectioned to be 100 *100 mm for each impact test. The preliminary impact test indicated the composite was perforated after more than 32 impact times under 6.5 joule. In order to provide comparisons among damages, three different levels of impact energy was predetermined to be 3.2, 5, and 6.5 joules. The composites were then impact damaged sequentially.

In order to avoid any parasitic edge damage induced during sectioning, only a 50*50 mm area was examined under the ultrasonic tester. The averaged data with at least 3 times of measurement were taken as the final data.

The ultrasonic A-scan provided an attenuation ratio for the impacted composites, reflecting the degree of internal damages with impact. The ultrasonic C-scan measured the impact damaged areas, and they were examined as compared with that for the virgin specimen. The retained moduli, indicating the stiffness change, were measured by the 4-point bending method under the crosshead speed of 1.5mm/min. The bending fixture was made based on ASTM D790~792, and the inner and outer span for the bending method were 25 and 76mm, respectively.

3. RESULTS AND DISCUSSION

3.1 Impact History

Figure 3 shows the force versus time curve under 3 different levels of impact energies(3.2, 5 and 6.5 Joules) under single impact. The higher impact force for 6.5J can be seen as compared to that for 3.2J. The curve obtained after the impact of 6.5J shows a conspicuous variation at the peak load, which is unseen for curves for 3.2J, which is considered to be an indication of substantial material damage such as brittle matrix cracking and/or delamination during impact.

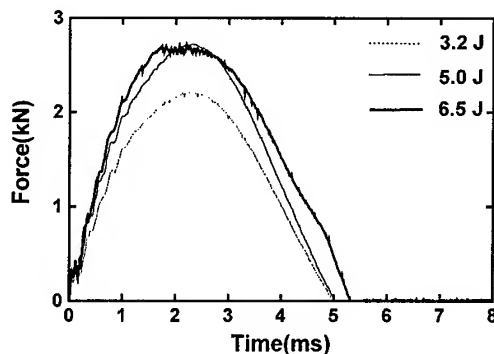


Fig. 3. Force and time curves under different impact energy level

Fig. 4 shows the force and time curves under 2 different impact levels up to 30 impacts. No prominent change among the curves can be seen for the impact energy of 3.2 Joule, illustrating the presence of an impact fatigue threshold. The accumulated impact damages under 3.2 Joule can be considered to be minimal based on the measurements. As the level of impact energy increased from 3.2 to 6.5 Joule, the curves showed discrepancies with the successive number of impacts. In addition, the initial slope of the time versus force curves tends to be decreased, which can be considered as the progressive accumulation of material damages. The repetition of higher impact

energies also showed a larger reduction of the slope representing a larger accumulation of material damages.

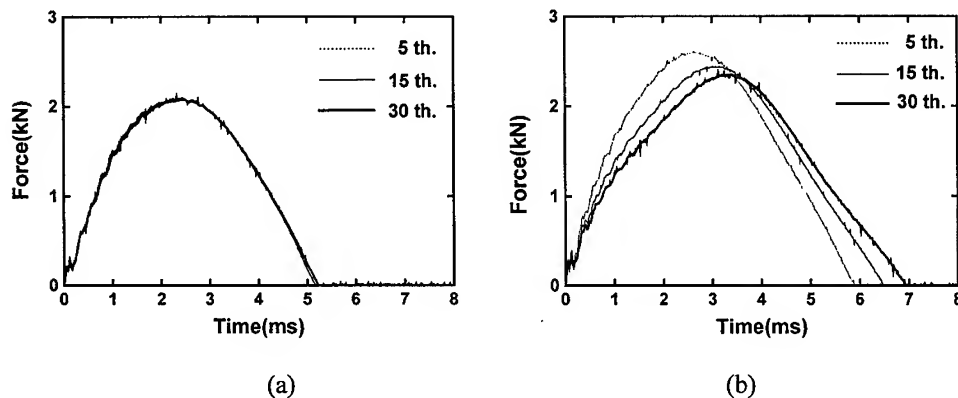


Fig. 4. Force and time curves under repetitive impacts under
(a) 3.2 J, (b) 6.5Joules

3.2 Evaluation of Material damage by ultrasonic Test

Figure 5 shows the attenuation change of the ultrasonic A-scan result under different levels of impact on the composites. The extent of cracking can be regarded with the increase of the attenuation ratio on the composites. The composites showed an almost linear increase of attenuation with the increase of impact energy. The increase of the attenuation ratio suggest that the density of the impact-induced brittle matrix-cracking tends to increase with the increase of impact energy levels.

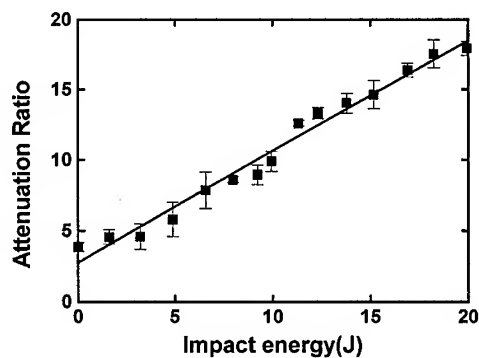


Fig. 5. Variation of attenuation ratio with increasing impact energy level

Figure 6 shows a typical ultrasonic C-scan image measured for the composite after a single or multiple impacts. The internal circular core represents the damaged area as compared with the surrounding undamaged matrix area[7,8]. The circular damaged shape remained to be almost

circular with multiple impacts, with the proportional increase of the contact area.

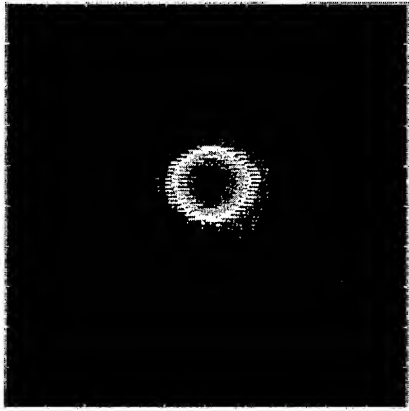


Fig. 6. Typical ultrasonic C-scan image showing internal material damage

3.3 Retained Mechanical Property

Figure 7 shows the change of the flexure modulus of composite materials, as compared with the baseline for the undamaged sample, after a single impact. The decrease of the flexural modulus with an increase of the impact energy indicates the increase of internal material damage with impacts. The modulus reduction of the composite impacted decreased gradually with the increase of impact energy. The change of reduction was smaller at lower impact energy levels, suggesting the impact fatigue threshold. The modulus of the composite after 6.5J decreased from 27.5GPa down to 25GPa, which corresponded to nearly 10% from that of a virgin. The damage is considered to be severe matrix cracking and/or delamination[9] of the laminates.

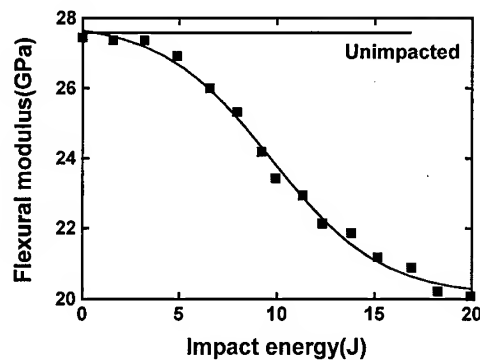


Fig. 7. Change of the flexural modulus with the change of impact energy

4. CONCLUSIONS

The following conclusions were drawn based on the impact tests on woven glass fiber/epoxy composites up to 30 times of multiple impact loading. The damages reflected by the retained

modulus for composites impacted under 3.2 Joule were negligible up to 30 times, indicating the presence of an impact fatigue threshold. As the level of impact is increased, the extent of the damage also increased and accumulated. The damages appeared to have been initiated by brittle matrix cracking followed by the increase of matrix crack density within the composite laminates.

REFERENCE

1. D. Hull and T.W. Clyne, *An Introduction to Composite Materials*, Cambridge (1996)
2. R. Laramée, *Materials Selection and Design*, ASM International (1997) p.648
3. B.Sankar, and C.T. Sun, *AIAA J.*, 23 (1962) p.1962
4. Y.S.Kwon, and B. Sankar, *J. Comp. Tech. and Res.* (1993) p.101
5. J. Roll, W.D. Bascom, J.C. Weidner, and W.J. Murri, *J. Mater. Sci.*, 21 (1986) p.2667
6. W.J. Cantwell, P. Daview, and H.H. Kausch, *SAMPE J.* (1991) p.30
7. H. Kaczmarek, *J.Comp. Mater.*, 29 (1995) p.59
8. P. Walkden, *Materials Evaluation*, 47 (1989) p.1000
9. H.Wang and T. Vu-Khanh, *J. Comp. Mater.*, 29 (1995) p.156

Applications of the Shadow Spot Method on the Determination of Dynamic Stress Intensity Factors

Zheng Li and Xianji Su

Department of Mechanics and Engineering Science, Peking University,
Beijing 100871, China P.R.

Keywords: Cement Block, Dynamic Fracture Toughness, Dynamic Stress Intensity Factor, Shadow Spot Method, Y4 Steel

ABSTRACT

The shadow spots, which are obtained by using the optical method of caustics to experimentally determine dynamic stress intensity factors, are usually interpreted on the basis of an elastic model. In this paper, an attempt is made to consider the effect of crack-tip plastic field about the elastic-plastic materials, and dynamic fracture toughness of Y4 steel is measured by means of the reflective caustics using typical three point bending specimens. This method also is applied to determine the dynamic fracture toughness of cement blocks with some mix designs.

1. INTRODUCTION

The shadow spot method has been a powerful tool to experimentally determine dynamic fracture properties of materials, since expanded by Kalthoff and his colleagues [1] to the dynamic fracture process in 1976. Commonly the application of this method for measuring the intensity of stress fields around crack tip is underlying the field of linear elastic fracture mechanics. For cracks in ductile steels, elastic relations need to include the plastic effect near crack tip field.

The plastic analysis about the elastic-plastic stress strain field around the crack-tip is complicated, because the elastic-plastic qualities of ductile materials are quite different. Theocaris [2] first introduces the corn region concept, in which the effect of the non-linear elastic or plastic zone surrounding the crack tip is included, and he solves the elastic-plastic fracture problems by this concept [3].

In this paper, by means of the reflective type of dynamic caustics, an attempt is made to evaluate the dynamic fracture toughness of high strength Y4 steel and some reinforced cement blocks. For a propagating crack, the experimental results show that the stress intensity factor and crack tip speed undergo abrupt changes during the growth process. Furthermore, the dynamic fracture toughness can be determined. If the heat processes of Y4 steel have a little difference, the material behaviors investigated by the shadow spot method will differ in the dynamic fracture toughness. To the reinforced cement blocks, we compare and analyze the influence of dynamic fracture toughness about the different mix designs under impact loading.

2. STRESS INTENSITY FACTOR DETERMINED BY DYNAMIC CAUSTICS

Consider a group of parallel light rays incident on the reflective surface of a pre-cracked opaque plate under tensile stress, due to the stress concentration at crack tip the thickness of the

specimen is reduced, they are deflected outwards when they are reflected from the deformed surface. As a consequence, on a reference screen positioned parallel to the specimen surface and with a distance z_0 , a relatively dark region (the shadow spot) is observed which is bordered a bright curve (called caustic curve). According to geometrical optics, the position of image point on the screen will depend on the slope of the reflecting surface at corresponding point. The mapping relation is not invertible for those points lying on the caustic curve, and the Jacobian determinant of the transformation must vanish at the points that map into the caustic curve. The locus of these points on the object plane is defined as initial curve in which mapping onto the reference plane is caustic curve.

For a mode I crack in static state, we can obtain that the initial curve is a circle with the radius r_0 around the crack tip, and can determine the stress intensity factor by the maximum diameter of the caustic curve.

For a stationary crack subjected to a dynamic loading, the stress distribution near crack tip field is the same as for a statically loaded crack, but the stress intensity factor becomes a function of time. For a propagating crack the near-field stress distribution differs from that stationary one due to inertia effects. However, Freund [4] has given the solution in this case with an instantaneous crack velocity, and SIF evaluation formula for mode I crack becomes

$$K_I^d(t) = \frac{2\sqrt{2\pi}F}{3dz_0|C_f|} \left[\frac{3}{10 \sin \frac{2\pi}{5}} \right]^{5/2} (D(t))^{5/2} \quad (1)$$

where d is the specimen thickness; C_f is the optical constant in reflective case; and D is the maximum diameter of the caustic curve. Eq.1 for a propagating crack is the same as that for a stationary crack except for a correct factor $F(v)$. This factor F as a function of crack velocity v can be accounted, and the result demonstrates that the factor F is less than 1, but for practically relevant crack velocities it is nearly equal to 1.

The size of shadow spot is not only concerned in varying the external load, the optical and mechanical parameters of the experimental arrangement and the specimen, but also in varying the radius of the initial curve r_0 . Theocaris and Petron [3] indicate that the stress intensity factor measured by the shadow spot will be constant, when the initial curve position at a certain region on the plate surface, so it is accurate. If the initial curve is outside (or inside) this region, the value of SIF calculated by the caustic curve is larger (or smaller) than the accurate one.

For elastic-plastic material, if the influences of the local plasticity and non-linear elasticity stress statement are considered, this is usually achieved by settling the optical arrangement for satisfying the initial curve outside the plastically deformed region. Rosakis and Freund [5] find that the error introduced through the neglect of plasticity effects in the analysis of caustic curve data will be small, as long as the distance r_0 is more than about twice the plastic zone size.

If we assume that the crack propagating onset at time τ with a constant velocity v , there will be a group of stress wave spreading abroad instantly from crack tip during fracture process. Consider the dynamic properties of crack propagation, dynamic K control field at time t^* will be established within the region around the crack tip with radius r [6], as follow

$$r \ll (t^* - \tau)(C_s - v) \equiv \xi \quad (2)$$

where C_s is the shear wave velocity of material.

3. EXPERIMENTS

The specimens used in this investigation are of the single edge crack configuration commonly known as the three-point bending beam of high intensity Y4 steel. The heat treatment of Y4-1 steel is performed by an oil quench at 1100°C and a temper to 630°C +610°C, each step for 2 hours; and Y4-2 steel is treated similarly except for the oil quench at 1150°C and the temper to 650°C +630°C. The material behaviors determined experimentally under the same as impact loading for fracture are shown in Table 1. The final specimens of size 200×40×6mm with initial notches of 8mm are struck by a hammer of 15kg at a height of 1m. An Al film of 0.03mm thickness is glued onto the specimen surface by a mirror transferring method for increasing the reflective index. In these experiments, we separately employed fifteen specimens for measuring the dynamic fracture toughness of Y4 steel under the same as drop weight loading.

Table 1 Dynamic material constants of Y4 steel

Material	Elastic Modulus E_d (GPa)	Poisson's Ratio ν_d	Optical Constant C_f ($\times 10^{-10} \text{ m}^2/\text{N}$)	Shear Wave Velocity C_s (m/s)
Y4-1	244.4	0.342	-0.0140	3434
Y4-2	244.6	0.347	-0.0142	3424

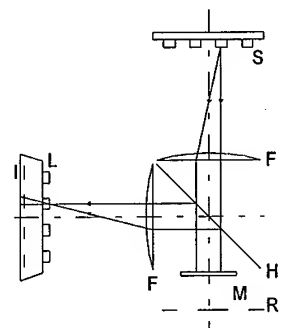
In these experiments, the optical arrangement shown in Fig.1 is used in the dynamic method of shadow spot in reflective case for reducing the oblique angles of light rays. In order to photo the shadow spots clearly, the 16 sparks of Cranz-Shardin type camera are modified to point sources. Otherwise, the lenses of optical field and camera are also instead by longer focus length ones, so that the distance z_0 between the specimen and the reference plane can be changed in a large region. Here the distance z_0 is set 700mm.

The application of the shadow spot method for determining dynamic fracture properties of Y4 steel has been performed. The typical shadow spot patterns of Y4 steel recorded during dynamic fracture process are shown in Fig. 2 and 3. From these shadow spot patterns, the dynamic stress intensity factor and the position of crack tip can be plotted as functions of time t in Fig. 4. The time τ of crack onset measured from the $a(t)$ curve in Fig. 4 is 47~58 μs for Y4-1

steel and 67~85 μs for Y4-2 steel. After the crack has become unstable, the crack velocity steadily increases up to a rather high value of 760~780m/s for Y4-1 steel and 740~800m/s for Y4-2 steel. The critical stress intensity factor at the onset of crack propagation, i.e. the dynamic fracture toughness K_{ID} , is about 18.6~21.7MPa·m^{1/2} for Y4-1 steel and 31.0~40.9MPa·m^{1/2} for Y4-2 steel.

In addition, we also utilize the dynamic shadow spot method to determine the dynamic fracture toughness of cement blocks with some mix designs utilized in oil industry for improving mechanics behaviors. The mix designs and dynamic properties of reinforced cement blocks under impact loading are measured and shown in Table 2.

Similarly, the cement block is machined into the three point bending beam of the single edge crack with a mirror surface, and is performed the dynamic caustic test underlying a drop loading.



S: light source; F: field lens;
M: model; H: half mirror;
L: camera lens; I: image
R: reference plane;

Fig. 1 Optical arrangement

The optical system is arranged to set the distance z_0 of 600mm. From the shadow spot patterns recorded by the high-speed camera during the dynamic fracture process, $K_I^d(t)$ and $a(t)$ curves can be calculated by Eq.1 and plotted in Fig. 5 (for 3# material). The dynamic fracture toughness K_{ID} obtained on an average of fifteen specimens for each material is shown in Table 2.

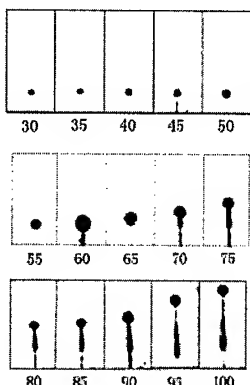


Fig. 2 A series of shadow spot photos of Y4-1 steel (t:μs)

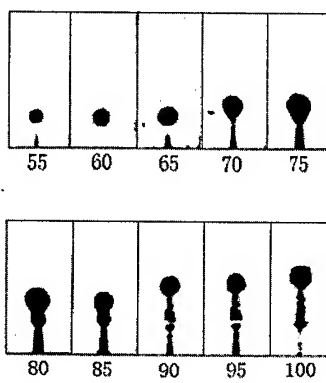


Fig. 3 A series of shadow spot photos of Y4-2 steel (t:μs)

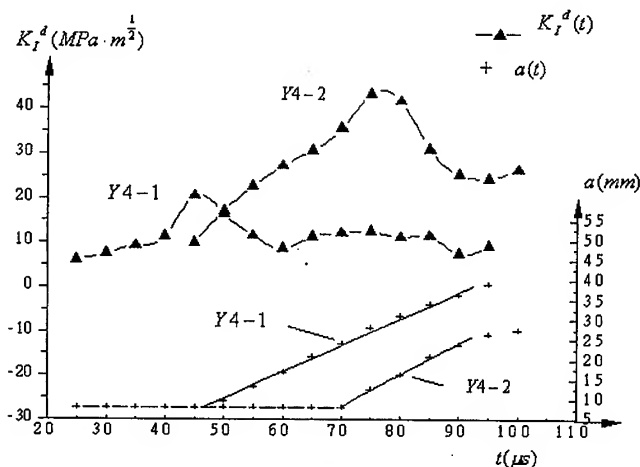


Fig. 4 $K_I^d(t)$ and $a(t)$ curves of Y4 steel

4. RESULTS AND DISCUSSION

If r_p indicates the size of the plastically deformed region, we measure r_p within 0.08~0.20mm for Y4-1 steel and 0.20~0.40mm for Y4-2 steel after fracture process. Consider the time t^* of spending 1μs after the crack onset, i.e. $t^* = \tau + 1$, the variable parameter ξ can be evaluated about 2.65~2.67mm for Y4-1 steel and 2.62~2.96mm for Y4-2 steel. According to the distance z_0 set 700mm, the initial curve will be settled to satisfy the condition as follow

$$2r_p < r_0 < \xi$$

So, the applicability of the shadow spot method for determining dynamic stress intensity factor has been demonstrated, and the experimental results are reliable and valid.

Table 2 The mix designs and dynamic properties of cement blocks

Material Number	Mix Design				Elastic Modulus E_d (GPa)	Poisson's Ratio ν_d	K_{ID} (MPa·m ^{1/2})
	CF(%)	JR(%)	Asbestos(%)	S_{xy} (%)			
1				0.2	19.72	0.196	0.1557
2	1.0			0.5	22.42	0.234	0.3596
3	0.7	15		0.5	10.76	0.207	0.5468
4	0.7	20		0.5	8.17	0.236	0.5208
5	1.0	20		0.5	10.38	0.215	0.5746
6			5	2.5	17.26	0.193	0.5998

Note: CF: carbon fiber; JR: jelly rubber; S_{xy} : scatter.

From Table 1 we can notice that the mechanics properties of these two Y4 steels are quite similar, but the dynamic fracture behaviors have obvious difference. Compare to Y4-2 steel, the time of crack onset for Y4-1 is earlier and dynamic fracture toughness is lower, but the crack velocity is in agreement and all near constant. Otherwise, $K_I^d(t)$ curves indicate that the peak of the curve of Y4-1 steel is occurred at the onset time of crack propagating, but the curve of Y4-2 steel will continue increasing. As a conclusion, the higher temperature of temper during the heat treatment is used, the better dynamic fracture toughness is.

According to the results of Table 2, we find that the cement block reinforced by carbon fiber only can enhance the material intensity more obviously but not the fracture toughness. If the cement block at the same time reinforced by jelly rubber, the dynamic fracture toughness can be improved in company with the volume of jelly rubber increasing. Therefore, 5[#] material has very good mechanics properties. The other mix design is reinforced by asbestos, and the cement block has a good fracture behavior too. Consider the value of carbon fiber is expensive; the better mix design is 6[#] material since asbestos is more cheaply.

ACKNOWLEDGEMENT

The research described here has been supported by the National Nature Science Foundation of China under Grant No. 19872006.

REFERENCE

1. J. F. Kalthoff, S. Winkler, and J. Beinert, Int. J. Frac., **12** (1976) p.317
2. P. S. Theocaris, Eng. Frac. Mech., **14** (1981) p.363
3. P. S. Theocaris and L. Petron, Eng. Frac. Mech., **23** (1986) p. 681
4. L. B. Freund, J. Mech. Phys. Solids, **20** (1972) p. 129
5. A. J. Rosakis and L. B. Freund, J. Eng. Mater. Tech., **104** (1982) p.115
6. K. Ravi-Chander and W. G. Knauss, J. Appl. Mech., **54** (1987) p.72



High Strain-rate Deformation of Composite Materials using a Split Hopkinson Bar Technique

O.S. Lee¹, J.Y. Lee¹, G.H. Kim¹ and J.S. Hwang²

¹ School of Mechanical, Aerospace and Automation Engineering, Inha University,
Inchon 402-751, Korea

² School of Mechanical Engineering, Yeungnam University,
Gyungsan-gun 712-160, Korea

Keywords: Composite Materials, Dynamic Maximum Compressive Stresses, Dynamic Stress-Strain Behavior, High Strain Rate, Pseudo Dynamic Elastic Moduli, Split Hopkinson Pressure Bar SHPB

ABSTRACT

A specific experimental method, the Split Hopkinson Pressure Bar (SHPB) technique has been constructed to determine the dynamic stress-strain relationships for composite materials under the impact compressive loading conditions with strain-rate of the order of $10^3/s$. The dynamic stress-strain behaviors are estimated by using the strain output from the gages attached on the incident and transmitted bars in the SHPB technique. Both the dynamic compressive maximum stresses and pseudo dynamic moduli of the tested composite materials are found to be highly sensitive to the strain rate. Furthermore, a bilinear relationship between the dynamic compressive maximum stresses and the log strain rate is noted.

1. THEORY

1.1 Basic Principle and Assumption

Pochhammer and Chree solved the longitudinal and radial inertia effect [1,2] of a specimen perfectly contacted with the bars in SHPB experiment. An important character of the stress wave in the bar is that its longitudinal wave propagation velocity may be changed by its wavelength [3].

Even though the specimen deforms uniformly, errors by the longitudinal and radial inertia generated by the sudden particle acceleration in high strain rate have to be compensated by following equation [4,5].

$$\sigma(t) = \sigma_m(t) + \rho [L^2/6 - vD^2/8] \frac{d^2 \epsilon(t)}{dt^2} \quad (1)$$

Where, σ_m , ρ , v and d are the measured stress, the specimen density, the Poisson's ratio, the

specimen length and the specimen diameter, respectively. From Eq. (1), L/D ratio of the specimen should be chosen by Eq. (2) to remove inertia effects on the measurable quantities.

$$\frac{L}{D} = \sqrt{\frac{3\nu}{4}} \quad (2)$$

1.2 The Stress-Strain Rate Determination by SHPB

In the conventional SHPB, specimen is located in between the incident and the transmitted bars. When the striker bar of density, ρ_0 , impacts the incident bar with velocity, V , the magnitude of stress wave generated in the incident bar will be about $\rho_0 CV/2$. By signals from strain gages bonded on the both bars and one-dimensional elastic wave propagation theory, time dependent load and strain rate can be determined. Fig. 1 shows a schematic diagram of a specimen and propagation behavior of elastic stress waves for the SHPB test.

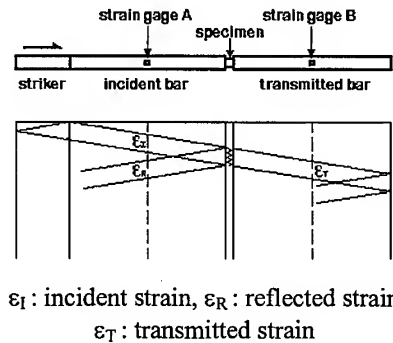


Fig. 1 A schematic diagram of specimen and elastic stress waves for the SHPB test (the subscript I, R, and T refer to the incident, reflected and transmitted pulses, respectively).

The stress pulse is assumed to be a non-dispersive elastic wave comparing the incident and transmitted pulse shapes. The stress and strain in the specimen can be obtained in terms of the recorded strains of the two bars as

$$\sigma_{specimen} = E \left(\frac{A}{A_s} \right) \epsilon_T \quad (3)$$

$$\epsilon_{specimen} = \frac{-2C_0}{L} \int_0^t \epsilon_R dt \quad (4)$$

Where, E , A , and C_0 are the elastic modulus, the cross-sectional area and the longitudinal wave speed of the incident and transmitted bars, respectively. L and A_s are the length and the cross-sectional area of the specimen, respectively.

2. EXPERIMENT

2.1 SHPB Facility

In this study, the incident, transmitted and striker bar are made of SM45C whose yield stress is 490MPa. The length and the diameter of the striker are 300mm and 16mm (same size as the incident and transmitted bars), SHPB apparatus and striker bars are shown in Photo. 1.

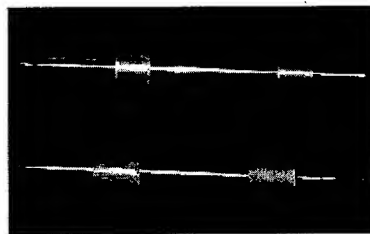
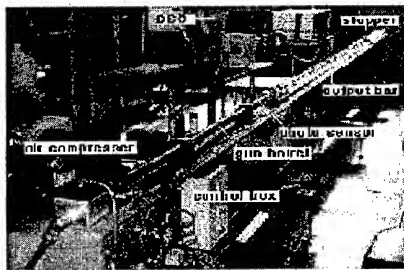


Photo. 1 SHPB facility and Striker bars of length 300mm with 16mm diameter.

2.1.1 Straight-Line Guider and Stopper

One of the most important things of the apparatus is the straight-line guide so that the stress pulse can propagate in one dimension. After fine grinding an I-beam, the bars are setup on the beam by using the fine bearing system.

2.1.2 Velocity and Wave Measurement System

To measure the velocity, three photo sensors are located at the distance of 50mm in the end of the gun barrel. When the striker cuts the light of the photo sensors, an oscilloscope, Nicolet 410, gets electric signals. By the strain gages bonded on the middle of the bars, the stress pulse can be obtained.

2.2 Specimen Material

The specimen numbers 1001, 350 and 325 stand for Vinylester Resin, Isophtharic Resin and ORTHO Resin(G-type), respectively. The static mechanical properties of three Resin material specimens are 110MPa of bending strength and 63MPa of tensile strength at 20°C. The schematics of the specimen used for this study is shown in Fig. 2

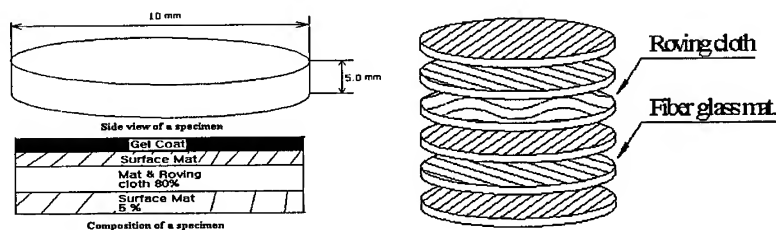


Fig. 2 Specimen geometry (Woven state schematics).

3. EXPERIMENTAL RESULTS

The typical signal outputs from strain gages attached on incident and transmitted bars are shown in Fig. 3. It is noted that the superposition of the reflected and transmitted waves are almost the same as the incident waves.

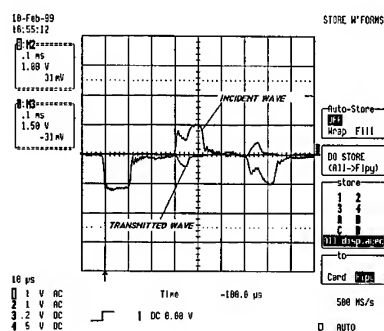


Fig. 3 A typical signal output from incident and transmitted bar in SHPB experiment.

The velocities of the striker bar(300mm) impacting the incident bar are 15, 20 and 25m/s, respectively. The relationships between the strain rates and the maximum compressive stresses are shown in Fig. 4. It is also noted that the maximum stresses of the tested materials are highly dependent on the strain rates.

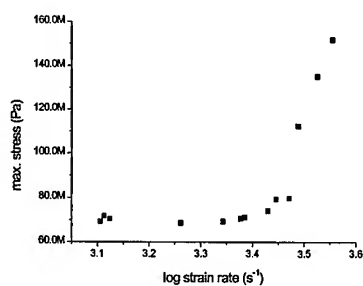


Fig. 4(a) Dynamic compressive maximum stress vs. log-strain rate for 1001P.

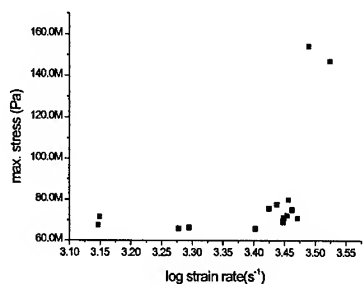


Fig. 4(b) Dynamic compressive maximum stress vs. log-strain rate for 325P.

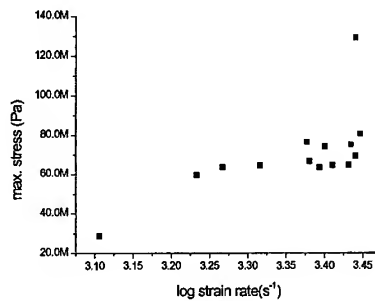


Fig. 4(c) Dynamic compressive maximum stress vs. log-strain rate for 350P.

Fig. 5 shows pseudo dynamic elastic moduli estimated by the initial slope ($d\sigma/d\varepsilon$) of the experimentally determined dynamic stress-strain diagram. As a result, pseudo dynamic elastic moduli are found to be highly sensitive to the strain rate. In the figure, it is noted that 325P(Isophtharic Resin) and 350P(ORTHO Resin) are more sensitive than 1001P (Vinylester Resin).

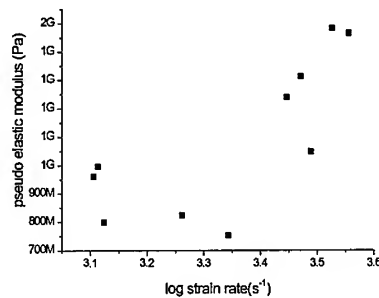


Fig. 5(a) Pseudo dynamic elastic modulus of 1001P under high strain rate loading conditions.

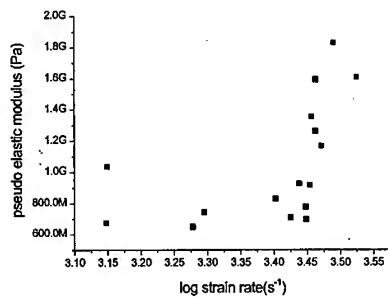


Fig. 5(b) Pseudo dynamic elastic modulus of 325P under high strain rate loading conditions.

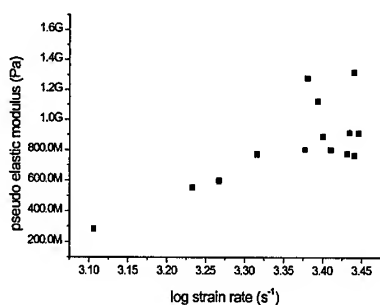


Fig. 5(c) Pseudo dynamic elastic modulus of 350P under high strain rate loading conditions.

4. CONCLUSIONS

The dynamic deformation behaviors of the composite materials are estimated by using SHPB techniques and the results are obtained as follows;

1. The dynamic deformation behaviors of tested composite materials are found to be very sensitive to the dynamic strain rate of the order of $10^3/\text{sec}$. It is noted that a relationship between maximum compressive stresses and the log strain rate is bilinear as commonly appeared for engineering metallic materials.
2. Pseudo dynamic elastic moduli of the tested composite materials are also found to be sensitive to the strain rate of the order of $10^3/\text{sec}$.

Acknowledgment: This study has been supported by Inha University Research Fund in 1999.

REFERENCES

1. L. Pochhammer, On the Propagation Velocities of Small Oscillations in an Unlimited Isotropic Circular Cylinder, *J. Reine Angewandte Math.*, **81**, (1876), pp. 324.
2. C. Chree, "The Equations of an Isotropic Elastic Solid in Polar and Cylindrical Coordinates, Their Solutions and Applications", *Cambridge Phil. Soc. Trans.* **14**, (1889), pp. 250
3. M. A. Meyers, "DYNAMIC BEHAVIOR OF MATERIALS", (1994), pp. 54-55
4. C. K. H. Dharan and F.E.Hauser, "Determination of Stress-Strain Characteristics at Very High Strain Rates," *Experimental Mechanics*, September, (1970), pp. 370-376.
5. D. A. Gorham, "Specimen inertia in high strain-rate compression", IOP Publishing Ltd. (1989), pp. 1888-189

Experimental Studies on Dynamic Fracture Phenomena

T. Nishioka, T. Fujimoto and K. Sakakura

Simulation Engineering Laboratory, Department of Ocean Mechanical Engineering,
Kobe University of Mercantile Marine, 5-1-1 Fukae Minamimachi, Higashinada-ku 658-0022, Japan

Keywords: Dynamic Crack Bifurcation, Dynamic Crack Curving, Dynamic Crack Kinking, Dynamic Crack Propagation, Dynamic Fracture, Dynamic Interfacial Fracture, High-Speed Photography, Impact Fracture, Method of Caustics

ABSTRACT

To investigate and visualize extremely fast transient dynamic fracture phenomena, the authors and coworkers have developed an experimental system together with an ultra-high speed camera system, synchronized laser systems, and various trigger systems. This paper presents the high-speed photography system, and experimental results for (i) mixed-mode impact fracture, (ii) impact interfacial fracture, and (iii) dynamic branching fracture. For each dynamic fracture phenomenon, a series of high-speed photographs, dynamic fracture histories, variations of fracture parameters such as the dynamic J integral and dynamic stress intensity factors are presented. Governing mechanisms of such dynamic fracture phenomena are also presented.

1. INTRODUCTION

Dynamic fracture can broadly be classified into "impact fracture" and "fast fracture". In any case, dynamic fracture phenomena are extremely fast transient. To investigate and visualize such transient phenomena, a high-speed photography system is needed. Understanding of the mechanisms governing various dynamic fracture phenomena is necessary for developing dynamic fracture mechanics aimed at sound design methodology assuring the integrity of structures.

In dynamic fracture experiments, we sometimes observe curved cracks, kinked cracks, and branched cracks. Those types of cracks suggest an important role of mixed-mode state during various dynamic fracture processes. In those phenomena, the dynamic stress intensity factors may become the basic data for the prediction of fracture path. Those data are important for the assessment of structural integrity against the final overall failure of structures. The knowledge on the mechanism of dynamic crack growth may also become useful in the assessments of manufacturing controllability as well as of structural integrity for brittle materials, such as composite materials, ceramics, and rocks.

Among the experimental techniques for the measurement of stress intensity factors, the method of caustics has many advantages, for example, the simplicity of equipment and measurement, and applicability to static and dynamic crack problems. This method can also be applied to opaque materials such as metals. For the above reasons, the method of caustic has been used to measure static and dynamic stress intensity factors in many cases (see, Theocaris [1], and Beinert and Kalthoff [2]). Nishioka and Kittaka [3] have established an exact theory and proposed a new procedure for the determination of mixed-mode dynamic stress intensity factors from the overall dimensions of the caustic pattern.

This paper provides a summary of recent experimental studies on various dynamic fracture phenomena, using the high-speed photography system.

2. HIGH-SPEED PHOTOGRAPHY SYSTEM

In the present experiments, high-speed photographs of the caustic patterns were taken by a laser caustic method which can be quickly synchronized to the onset of brittle fast fracture. A typical optical setup is shown in Fig.1. An Argon laser was used as the light source of the caustics.

Since dynamic fracture and impact fracture are extremely fast transient phenomena, two types of trigger system for the optical system were devised. For brittle dynamic fracture under a static loading, a conductive paint line is placed around the initial crack tip. When the conductive paint line is broken due to the initiation of crack propagation, the trigger signal is sent to the acoustic optical modulator (see Fig.1). Contrary to this, for impact fracture under an impact loading, a trigger laser beam is set just above the site of impact loading. When the trigger beam line is intercepted by the impact rod, the trigger signal is sent to the acoustic optical modulator.

Then, the direction of the laser beam is changed in an extremely short time. The laser beam reaches an ultra-high speed camera, passing through the specimen (see Fig.1). The photograph of ultra-high speed camera is shown in Fig.2. This camera is capable of taking 80 high-speed photographs with the maximum framing rate of two million frames per second.

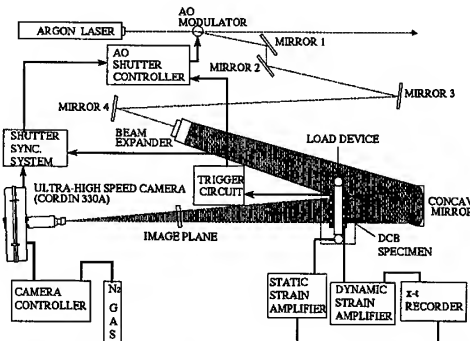


Fig.1 Optical system for transmitted caustics

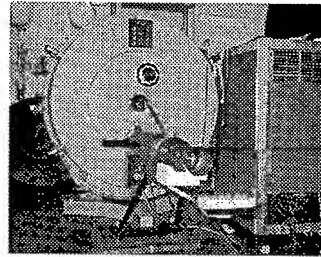


Fig.2 Ultra-high speed camera

3. EXPERIMENTAL EVALUATION OF DYNAMIC FRACTURE PARAMETERS

In order to determine a dynamic fracture parameter such as the dynamic J integral [4] by the caustic patterns, the crack velocity must be evaluated first since the caustic pattern depends on the crack velocity. The crack velocity can be determined by a series of high-speed photographs. Thus we have to determine the crack-tip locations within the dark spots. We have devised an accurate procedure for determining the crack-tip locations within the caustic patterns [3,5].

The crack-tip location measured from the extreme point A (see Fig.3) in the x' direction is denoted by W_x^{\max} . Then this can be related to the maximum diameter D in the y' direction [3], and to the size of D_I in the x' direction ($A'B'$) as follows:

$$W_x^{\max} = k D \quad (1)$$

$$W_x^{\max} = k_I D_I \quad (2)$$

where k and k_I are crack-tip location factors. The values of the crack-tip location factors are listed in Table 1, for the normalized crack velocity by the shear wave velocity C_s . It is seen that the k_I remains almost constant for all range of crack velocity. This is extremely convenient in determining the histories of crack length and crack velocity. For a mixed-mode caustic pattern, the crack tip location factor k slightly depends on the crack velocity, and is independent of the state of mixed-mode [3].

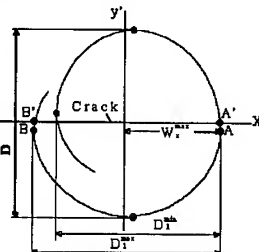


Fig.3 Mixed-mode caustic pattern

Table 1 Crack-tip location factors (mode I)

$\beta = C/C_s$	0.0	0.2	0.4	0.6	0.8
k	0.526	0.525	0.523	0.520	0.515
k_I	0.562	0.562	0.562	0.562	0.563
k_I/k	1.068	1.070	1.075	1.081	1.093

The stress intensity factors can be expressed by the characteristic dimensions, D and D_I^{\max} .

$$K_I = \frac{2\lambda^{-3/2}}{3N} \frac{1}{\sqrt{1+\alpha^2}} \{D / \delta(C)\}^{5/2}, \text{ or } K_I = \frac{2\lambda^{-3/2}}{3N} \frac{1}{\sqrt{1+\alpha^2}} \{D_I^{\max} / \delta_I(C)\}^{5/2}, \text{ and } K_{II} = \alpha K_I \text{ (3.a,b,c)}$$

where $N=C_0 \cdot h \cdot z_0 \cdot (2\pi)^{-0.5}$, λ is the magnification of the optical system, C_0 is the elasto-optical constant, and h is the thickness of the specimen. The parameters α , δ and δ_i in the above equations can be determined by the sizes of caustic pattern D , D_i^{\min} , D_i^{\max} and the crack velocity [3,5]. For the mode I case, $\delta(C)$ and $\delta_i(C)$ can be expressed in a polynomial series:

$$\delta(C) = 3.1702 + 0.0964 \beta - 0.1443 \beta^2 + 1.4994 \beta^3 \text{ and } \delta_i(C) = (k/k_i) \delta(C). \quad (4.a,b)$$

Then the dynamic J integral components with respect to the crack-axis coordinates can be determined for the dynamic crack, as in [4,5]:

$$J_1^0 = (1/2\mu) \{ A_I(C) K_I^2 + A_{II}(C) K_{II}^2 \} \text{ and } J_2^0 = - (1/\mu) A_{IV}(C) K_I K_{II}, \quad (5.a,b)$$

where A_I , A_{II} , and A_{IV} are functions of the crack velocity [4].

4. EXPERIMENTAL RESULTS

Using the ultra-high speed photography system, Nishioka and coworkers have conducted experimental studies on various dynamic fracture phenomena. However, due to the page limitation, the following studies are not included in this paper. These are (a) three-dimensional dynamic fracture [6], (b) fast curving fracture [7,8], and (c) nonlinear (elasto-plastic) impact fracture [9].

4.1 Mixed-Mode Impact Fracture

Three-point bend specimens of PMMA (Polymethyl methacrylate) were used for mixed-mode impact fracture test. The initial crack was placed along the center of the specimen. The impact load by a dropping rod (14.7 Kg) was applied at the off-center point, to induced a mix-mode state at the initial crack tip. The impact velocity of the rod was set as 5m/s. The loading eccentricity is defined as $e=l/(S/2)$ where l is the distance between the loading point and the centerline of the specimen, and S is the span of the supports of the specimen.

The high-speed photographs of dynamically fracturing specimen under the loading eccentricity of $e=0.1$ are shown in Fig.4. In the photographs at $t=123.7\mu s$ to $143.7\mu s$, the caustic patterns of the mode II (in-plane shearing mode) dominated type can be seen. At $t=148.8\mu s$, the crack had already propagated for a short distance. Immediately after the fracture initiation, the caustic pattern rapidly changed to mode I dominated type. Then, the crack propagated toward the impact loading point.

The caustic patterns due to the impact loading are always seen under the impact rod. This

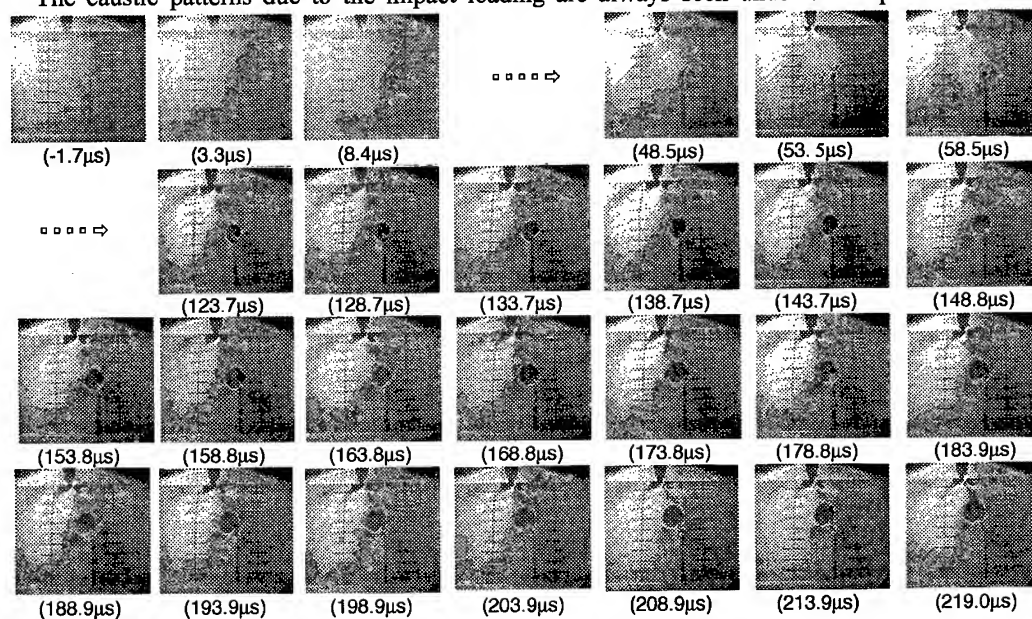


Fig.4 High-speed photographs of mixed-mode impact fracture

implies that the specimen was always pushed after the impact loading. Thus the loading rod was in contact with the specimen throughout the fracture test. Crack propagation histories were measured by the caustics in the high-speed photographs. The maximum crack velocity observed was about 300 m/s.

Figure 5 shows the variations of the stress intensity factors. In this case, the compressive longitudinal wave obliquely impinges to the crack tip at about $30\mu\text{s}$. After that, the K_{II} starts to manifest itself. The impact fracture occurred under shear-dominated condition. After the onset of dynamic fracture, the K_{II} values are almost completely zero.

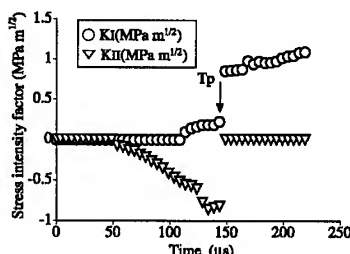


Fig.5 Stress intensity factors of mixed-mode impact fracture

4.2 Impact Interfacial Fracture

Most studies on interfacial fracture mechanics have been done under static conditions. Thus the establishment of dynamic interfacial fracture mechanics is one of the most important issues in the field of fracture mechanics.

Figure 6 shows high-speed photographs for dynamic interfacial fracture in a bimaterial specimen consisting of aluminum and epoxy resin under impact loading. The crack started propagating at $63.3\mu\text{s}$.

In most photographs for the propagating crack, narrow band shapes of caustic pattern are seen. One of these is magnified in Fig.7. We believe that this is the first

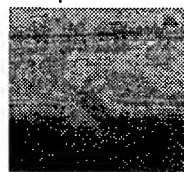


Fig.7 Transonic caustic

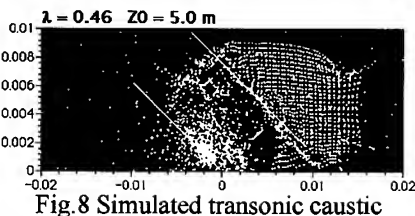


Fig.8 Simulated transonic caustic

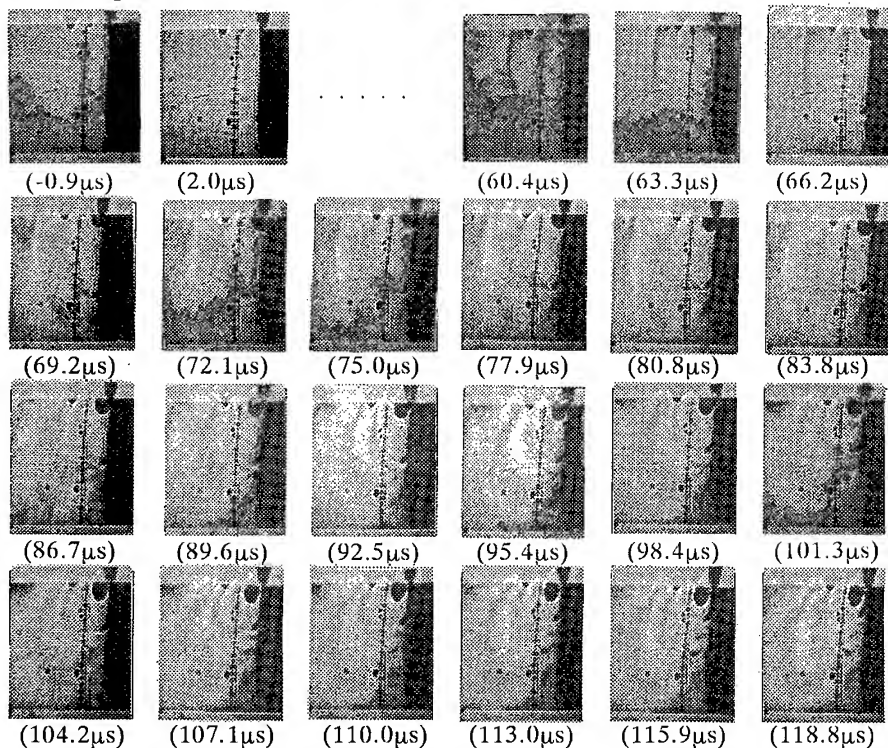


Fig.6 High-speed photographs of dynamic interfacial fracture

observation of caustic pattern for a transonically propagating crack tip. To verify it, the formation of caustic pattern was simulated using a moving finite element method developed for transonic interfacial crack propagation [10,11]. The simulated caustic pattern is shown in Fig.8. The transonically propagating crack emanates the Mach shock wave from its tip, as shown in Fig.9. The angles of Mach shock waves in Figs.7 and 8 agree excellently. Figure 10 shows comparison of crack velocities inversely estimated by the caustic angle, with those estimated by the crack-tip position. From this figure it can be concluded that the crack propagated in transonic regime.

4.3 Dynamic Branching Fracture

Branched cracks are often observed in brittle materials and structures. Many researchers have attempted to clarify the mechanism of crack branching (or crack bifurcation). However, the governing condition of dynamic crack bifurcation had not been fully clarified until our recent experimental studies [12,13]. Thus, dynamic crack bifurcation had remained as one of the most important unsolved problems in dynamic fracture mechanics.

Two sets of loads were applied to a Homalite 911 specimen through two pairs of loading pins. First the lower loading system was applied and held constant. Then the upper loading system was applied until dynamic crack propagation occurs. The lower loading produces a strong tensile stress

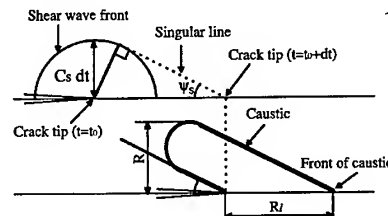


Fig.9 Mach shock wave and caustic

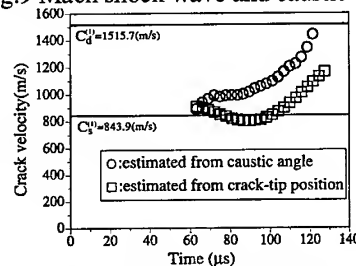


Fig.10 Crack velocity history

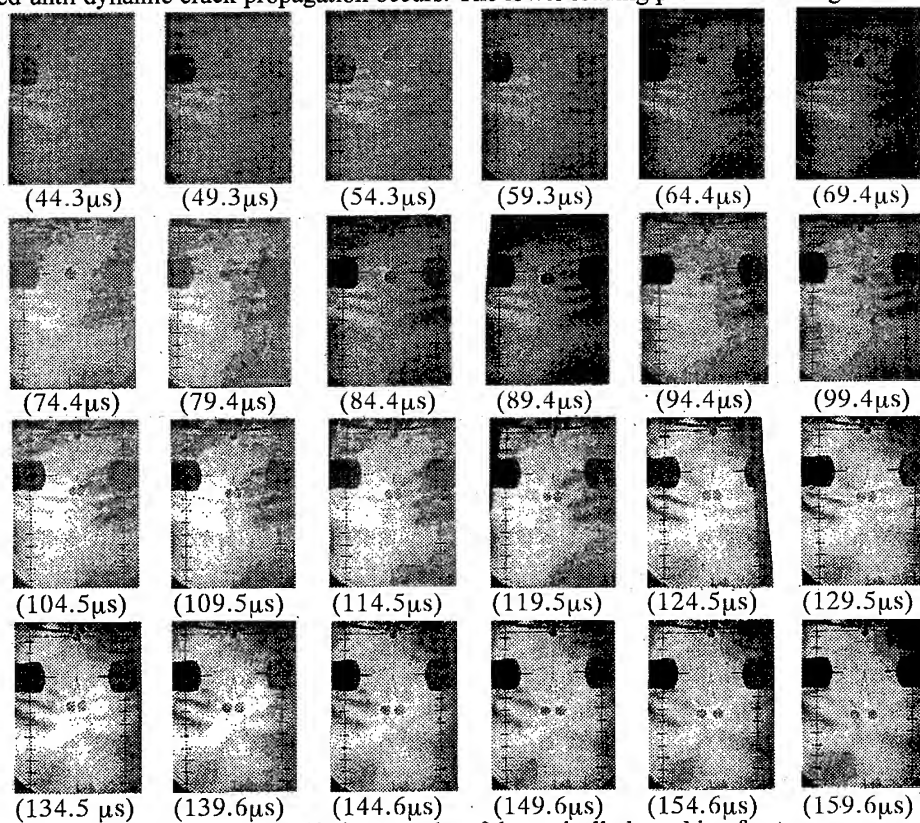


Fig.11 High-speed photographs of dynamically branching fracture

field to accelerate the propagating crack and to supply enough energy into the propagating crack for crack branching.

Figure 11 shows photographs for dynamically branching fracture in the specimen. The crack bifurcated at the line of the lower loading system (see the photograph of 79.4 μ s).

The sizes of caustic patterns in the high-speed photographs were converted to the dynamic J values by using Eqs.(3) and (5). The dynamic J integral values at dynamic crack branching are plotted in Fig.12 against the crack velocity. It is seen that dynamic crack branching does not occur either at a particular value of the dynamic J integral or at a particular crack velocity.

The total energy flux at dynamic crack branching are evaluated by $\Phi_{\text{total}} = J' \cdot C$, and plotted in Fig.13. The total energy flux into the tip of a branching crack is constant for various crack velocities at the instance of dynamic crack branching. Thus, it can be concluded that dynamic bifurcation occurs when the total energy flux Φ_{total} into the process zone or into the tip of a propagating crack reaches a critical material resistance.

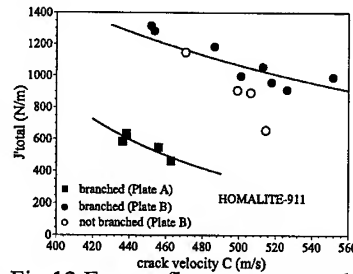


Fig.12 Energy flow rates at crack branching

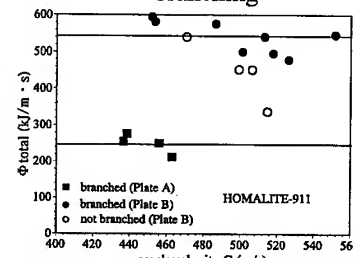


Fig.13 Energy flux at crack branching

5. CONCLUDING REMARKS

Recent experimental studies on various dynamic fracture phenomena were summarized. In all cases presented here, the high-speed photographs for caustic patterns were presented. The experimental results revealed the mechanisms of their processes.

Acknowledgements: Some of the studies presented here were supported by the Grant-in-Aid for Scientific Research (No.08455063) from the Ministry of Education, Science and Culture in Japan. The experiments were carried out with the aids of graduate students, T. Kishimoto, Y. Ono, H. Miyauchi, and M. Takagi.

REFERENCES

1. P.S.Theocaris, Elastic stress intensity factors evaluated by caustics, *Experimental Evaluation of Stress Concentration and Intensity Factors* (G.C.Sih, ed.), Martinus Nijhoff, (1981), 189-252.
2. J.Beinert and J.F.Kalthoff, Experimental determination of dynamic stress intensity factors by shadow patterns, *Experimental Evaluation of Stress Concentration and Intensity Factors* (G.C.Sih, ed.), (1981), 281-330.
3. T.Nishioka and H.Kittaka, A theory of caustics for mixed-mode fast running cracks, *Eng. Fract. Mech.*, **36** (1990), 987-998.
4. T.Nishioka and S.N.Atluri, Path independent integrals, energy release rates and general solutions of near-tip fields in mixed-mode dynamic fracture mechanics, *Eng. Fract. Mech.*, **18** (1983), 1-22.
5. T.Nishioka, et al., Governing criterion of dynamic crack bifurcation, *Proc. 8th Int. Conf. Mech. Behaviour of Mat.*, Volume I, (1999), 255-260.
6. T.Nishioka, et al., Experimental study on three-dimensional dynamic fracture, *Dynamic Fracture, Failure and Deformation*, (T.Nishioka and J.S.Epstein, eds.), ASME Publ., PVP-Vol.300, (1995), 87-97.
7. T.Nishioka, et al., A laser caustic method for the measurement of mixed-mode dynamic stress intensity factors in fast curving fracture tests, *Int. J. Pres. Ves. & Piping*, **44** (1990), 17-33.
8. T.Nishioka, et al., Experimental and numerical studies on fast curving fracture, *Dynamic Failure of Materials*, (H.P.Rossmann and A.J.Rosakis, ed.), (1991), 232-247.
9. T.Nishioka, et al., A method of caustics for the direct experimental measurement of the T^* -integral in nonlinear and dynamic fracture mechanics problems, *Nucl. Eng. Design*, **133**, (1992), 433-446.
10. T.Nishioka and A.Yasin, The dynamic J integral, separated dynamic J integrals and moving finite element simulations, for subsonic, transonic and supersonic interfacial crack propagation, *JSME Int. J.*, **42**(1999), 25-39.
11. A.Yasin and T.Nishioka, Moving finite element simulation of dynamic interfacial crack propagation under shear-dominated loading, *Progress in Exp. & Comp. Mech. in Eng. and Material Behaviour*, (1999), 178-183.
12. T.Nishioka, et al., Basic studies on the governing criterion for dynamic crack branching phenomena, *Trans. of JSME, Ser. A*, **65** (1999), 1123-1131.
13. T.Nishioka, et al., Governing criterion of dynamic crack bifurcation, *Proc. 8th Int. Conf. Mech. Behaviour of Mat.*, Volume I, (1999), 255-260.

The Fracture Problem of Framed Plate under Explosion Loading

Yutang Li, Yaobing Wei and Yunfeng Hou

Department of Mechano-Electronic Engineering,
Gansu University of Technology, Lanzhou 730050, China P.R.

Keywords: Explosion Experiment, Explosion Loading, Fracture, Framed Plate, Separation of Solid, Stress Intensity Factor

ABSTRACT

The regular separate of metallic material is very common in use in engineering. Explosion is a typical shock loading and it can produce a large amount of energy. The principle of fracture design is led into the regular separation of framed plate in this paper. The framed plate is simplified into a shear specimen with double cracks at first. The actual two level finite element method, then, is used to evaluate the dynamic stress intensity factor. And, after that, the experimental research was conducted for the fracture of framed plate under explosion loading.

1. INTRODUCTION

Fracture, corrosion, and wearing are the three inactivation forms in machine parts and engineering structural units. Fracture is a kind of "breakout disaster" and causes usually heavy losses of life and property. The fractures include the brittle failure caused by the destabilizing propagation of macroscopic flaw or crack and the fatigue failure. All engineering structures have inevitably flaw similar to crack, which is either intrinsic in material or produced in the process of manufacturing or caused in the exploitation process. The supporting capacity of the structure would be reduced or even totally lost if the flaws or cracks existed in structure. The purpose of fracture mechanics is just the safety design to prevent it from happening.

The history of exploiting the flaw to achieve the fracture is much more remote than the history of fracture mechanics. In fact, making primitive tools by using the process of fracture are the one of major starting point of human civilization. One can turn the disastrous character of crack into profitable effect and exploit low-stress brittle fracture to separate solid materials. This technique has been applied to blanking of machine work [1-3] and explosive engineering [4] at present.

The gas cutting and other methods are commonly used to separate the solid material at present. These methods are both of low efficiency and with high waste of processed materials. It is an urgent task to explore the effective and economic method for separating solid materials. The principle of fracture design is led into the regular separating of thin plate of metallic materials. The explosive loading for separation of thin metallic plate is investigated experimentally. The fracture problem is simplified to a shearing model with double cracks at first. Then actual two level finite element method is used to evaluate the dynamic stress intensity factor. And, finally, we make an experiment to separate the framed plate by means of explosive loading and analyze the experimental results.

2. ACTUAL TWO LEVEL FINITE ELEMENT METHOD AND IT'S FORMULATION

The infinite series formulas of dynamic plane crack problem can be written as follows [5]:

$$\begin{aligned}
 u_x &= \sum_{j=0}^{\infty} \frac{r^{j/2}}{2\mu} \left\{ C_j^R(t) \left[\left(\kappa + \frac{j}{2} + (-1)^j \right) \cos \frac{j}{2} \theta - \frac{j}{2} \cos \left(\frac{j}{2} - 2 \right) \theta \right] \right. \\
 &\quad \left. + C_j^I(t) \left[\left(\kappa + \frac{j}{2} - (-1)^j \right) \sin \frac{j}{2} \theta - \frac{j}{2} \sin \left(\frac{j}{2} - 2 \right) \theta \right] \right\} \\
 u_y &= \sum_{j=0}^{\infty} \frac{r^{j/2}}{2\mu} \left\{ C_j^R(t) \left[\left(\kappa - \frac{j}{2} - (-1)^j \right) \sin \frac{j}{2} \theta + \frac{j}{2} \sin \left(\frac{j}{2} - 2 \right) \theta \right] \right. \\
 &\quad \left. - C_j^I(t) \left[\left(\kappa - \frac{j}{2} + (-1)^j \right) \cos \frac{j}{2} \theta + \frac{j}{2} \cos \left(\frac{j}{2} - 2 \right) \theta \right] \right\} \quad (1)
 \end{aligned}$$

where $C_j^R(t)$ and $C_j^I(t)$ are coefficients to be determined after loads and other boundary conditions being imposed. It should be noted that the terms of $j=0$ denote the rigid body translations and the terms of $j=1$ in equation (1) contain a factor in itself which accounts for the singular behavior at the crack tip. Therefore, the relationship between dynamic stress intensity factor and coefficients $C_j(t)$ becomes

$$K_I(t) - iK_{II}(t) = \sqrt{2\pi} [C_1^R(t) - iC_1^I(t)] \quad (2)$$

In order to clarify the effect of a crack on the plane elastic problem, an area Ω is taken and divided around the crack tip whose outmost boundary is polygon L_1 and, then, a super element for dealing with the singularity is established as shown in Fig. 1. The thickness ratio of the neighboring layer is $c < 1$.

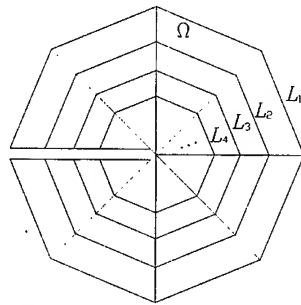


Fig. 1. Similar shape element configuration

Equation (1) can be rewritten as following matrix form

$$\{\mathbf{u}\} = [\mathbf{T}]\{\mathbf{C}\} \quad (3)$$

For the similar shape elements in Fig. 1, we have following equations

$$[\mathbf{K}]_j^e = [\mathbf{K}]_{j+1}^e \quad (4)$$

$$[\mathbf{D}]_j^e = [\mathbf{D}]_{j+1}^e / c^2 \quad (5)$$

$$[\mathbf{M}]_j^e = [\mathbf{M}]_{j+1}^e / c^2 \quad (6)$$

2.1 Transition Formulation of First Layer

Let the nodes on the boundary polygon L_1 be master nodes and those on other inner polygons slave nodes. For solving the problem linking with other elements outside Ω , only the degrees of freedom of slave nodes need to be transformed. The stiffness, damp, and mass matrices of the first layer after being transformed can be written as

$$[\mathbf{K}^f] = \begin{bmatrix} \mathbf{M}_{mm} & \mathbf{M}_{ms} \mathbf{T}^f \\ (\mathbf{T}^f)^T \mathbf{M}_{sm} & (\mathbf{T}^f)^T \mathbf{M}_{ss} \mathbf{T}^f \end{bmatrix} \quad (7)$$

$$[\mathbf{D}^f] = \begin{bmatrix} \mathbf{D}_{mm} & \mathbf{D}_{ms} \mathbf{T}^f \\ (\mathbf{T}^f)^T \mathbf{D}_{sm} & (\mathbf{T}^f)^T \mathbf{D}_{ss} \mathbf{T}^f \end{bmatrix} \quad (8)$$

$$[\mathbf{M}^f] = \begin{bmatrix} \mathbf{M}_{mm} & \mathbf{M}_{ms} \mathbf{T}^f \\ (\mathbf{T}^f)^T \mathbf{M}_{sm} & (\mathbf{T}^f)^T \mathbf{M}_{ss} \mathbf{T}^f \end{bmatrix} \quad (9)$$

where $[\mathbf{T}^f]$ is the transition matrix of the first layer.

2.2 Transition Formulation of Other Layers

All degrees of freedom of the inner nodes need to be transformed. The stiffness, damp, and mass matrices of inner layers after being transformed can be written as

$$K_{ij}^n = c^{(m+k)(n-1)/2} \{\mathbf{T}_i^s\}^T [\mathbf{K}]_1 \{\mathbf{T}_j^s\} \quad (10)$$

$$D_{ij}^n = c^{[(m+k+4)(n-1)/2+2]} \{\mathbf{T}_i^s\}^T [\mathbf{D}]_1 \{\mathbf{T}_j^s\} \quad (11)$$

$$M_{ij}^n = c^{[(m+k+4)(n-1)+2]} \{\mathbf{T}_i^s\}^T [\mathbf{M}]_1 \{\mathbf{T}_j^s\} \quad (12)$$

where

$$k = \begin{cases} (i-1)/2 & \text{for } i = \text{odd} \\ (i-2)/2 & \text{for } i = \text{even} \end{cases} \quad \text{and } i > 0 \quad (13)$$

It can be found from equations (10)-(12) that K_{ij} , C_{ij} and M_{ij} of different inner layers form geometric progressions. Therefore, we have

$$\sum_{n=2}^{\infty} K_{ij}^n = \frac{R_{mk}}{1-R_{mk}} \{\mathbf{T}_i^s\}^T [\mathbf{K}]_1 \{\mathbf{T}_j^s\} \quad (14)$$

$$\sum_{n=2}^{\infty} D_{ij}^n = \frac{S_{mk}}{1-S_{mk}} \{\mathbf{T}_i^s\}^T [\mathbf{D}]_1 \{\mathbf{T}_j^s\} \quad (15)$$

$$\sum_{n=2}^{\infty} M_{ij}^n = \frac{S_{mk}}{1-S_{mk}} \{T_i^s\}^T [M]_i \{T_j^s\} \quad (16)$$

where

$$R_{mk} = c^{(m+k)/2} < 1 \quad m, k \geq 1 \quad (17)$$

$$S_{mk} = c^{(m+k+4)/2+2} < 1 \quad m, k \geq 1 \quad (18)$$

By using equations (7)~(9) and equations (14)~(16), the global stiffness, damp, and mass matrices for domain Ω can be assembled. Adding the global matrices to the stiffness, damp, and mass matrices of other elements, the general stiffness, damp, and mass matrices can be obtained. Solving the equation, the column matrix $\{C\}$ and the dynamic stress intensity factor can be obtained directly.

3. STRESS INTENSITY FACTOR OF SHEARING MODEL WITH DOUBLE CRACKS IN EXPLOSIVE LOADING

For dynamic fracture problem, the normalized dynamic stress intensity factors are defined as [5]

$$K_I = K_I(t) / K_{IS}$$

$$K_{II} = K_{II}(t) / K_{IIS} \quad (19)$$

where K_{IS} and K_{IIS} are static stress intensity factors of mode I and II cracks, respectively. For the pure shearing model shown in Fig. 2, K_{IS} is zero and $K_I(t)$ isn't always zero because the effect of stress wave. Therefore, the first of equation (19) is meaningless. For the convenience of problem analysis, the normalized dynamic stress intensity factors are defined as

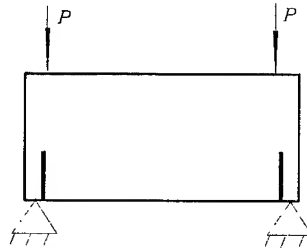


Fig. 2. Shearing model with double

$$K_I = K_I(t) / K_{IIS}$$

$$K_{II} = K_{II}(t) / K_{IIS} \quad (20)$$

The explosive shock loading can be expressed as

$$\begin{aligned}
 F(t) &= tF_{\max} / t_f & t \leq t_f \\
 F(t) &= (t_m - t)F_{\max} / (t_m - t_f) & t > t_f
 \end{aligned}
 \quad (21)$$

where $t_m \approx 4t_f$ and $t_f \approx 100\mu s$. The curves of normalized dynamic stress intensity factors with $a/b = 0.3$ are shown in Fig. 3.

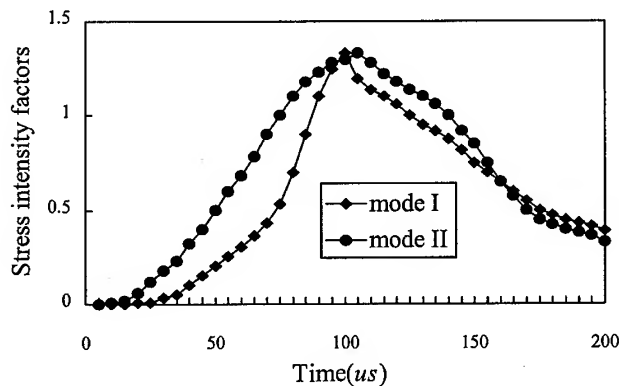


Fig. 3. Curves of normalized dynamic stress intensity factors

4. EXPERIMENT OF FRAMED PLATE UNDER EXPLOSIVE LOADING

A fracture experiment of framed plate is performed under explosive loading. The experimental model was welded one making use of 1008 steel plate with thickness of 8mm. The dimensions of the experimental model are $800 \times 800 \times 800$ mm. A 700×700 mm square V-notch was made on one plate surface of the model. The geometric parameters of the V-notch are: field angle $\alpha = 30^\circ$, notch depth $a = 2$ mm, and tip radius $r = 0.05$ mm. The experimental model and the disposition of dynamite are shown in Fig. 4. For testing and verifying the effect of the external factor on the fracture, two water bags were laid up on two opposite side of the square V-notch. The dynamite TNT is used in the experiment.

Fig.5 is the framed plate after being fractured. The experimental result shows that the fracture faces are regular and neat on the sides without water bags and the fracture effect is good. The fracture faces are irregular and rough on the sides with water bags laid aside. The bad effect is

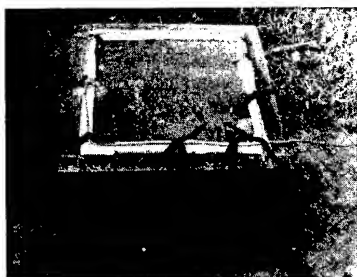


Fig.4. The model and explosive position



Fig. 5. The fractured model

caused by the fact that water bags take the shock of explosive loading and there are forces acting on both two boundaries of notch. Therefore, the force near welding joint is increased greatly and makes the experimental model of framed plate broken due to tension fracture alone welding joint. It is feasible that the dynamite is laid beside the notch in the fracture of framed plate.

5. THE DISCUSSION AND CONCLUSIONS

The framed plate with double cracks can be simplified to mode II crack problem if there are loading near boundary of notches. The propagation of mode II crack under static loading is the typical plastic fracture and the fracture face has clear slip characteristic of plastic metal like 1008 steel. The metallographical photograph of fracture shows that the fracture surface of 1008 steel under explosive loading is that of typical cleavage fracture as shown in Fig. 6. If there are external



Fig. 6. Metallographical photograph of regular fracture face



Fig. 7. Metallographical photograph of irregular fracture face

force interference near the notch, the fracture surface is also cleavage fracture surface as shown in Fig. 7 and quasi-cleavage fracture appear in some places. The above mentioned result shows that multidirectional and instable stress state appear in the process of fracture. The propagation of mode I crack plays a leading role for the framed plate with double cracks under explosive loading. Both the speed effect of explosive loading and the stress wave play an important role in the process of fracture. It is feasible that the principle of fracture design is led into the regular separation of framed plate and the regular separation can be achieved by explosive loading.

REFERENCES

1. Q.T.Wei and F.Y.Lang, J. Gansu Univ. Technology, 8(1982) p.1 (in Chinese)
2. B.J.Zhao, Q.T.Wei and F.Y.Lang, *Advances in Mechanics*, 18(1988) p.343 (in Chinese)
3. Y.T.li, F.Y.Lang, Q.T.Wei, *Chinese J. Mechanical Engineering*, 29(1993) p.17 (in Chinese)
4. Y.G.Du, Z.H.Zhang and T.L.Li, *Explosion & Shock Waves*, 11(1991) p.26
5. C.B.Hu, Y.T.Li and J.Gong, *Key Engineering Materials*, 145-149(1997) p.267
6. T.Y.Fan, *Advance in Mechanics*, 16(1986) p.1
7. J.L.Yu, *Mechanics & Practice*, 14(1992) p.7

Dynamic Mixed Mode Crack Propagation Behavior of Structural Bonded Joints

Ouk Sub Lee¹ and Albert S. Kobayashi²

¹ School of Mechanical, Aerospace and Automation Engineering, Inha University,
Inchon 402-751, Korea

² Department of Mechanical Engineering, University of Washington,
Seattle WA 98195-2600, USA

Keywords: Dynamic Crack Propagating Velocity, Dynamic Interface Crack Stress Field, Dynamic Stress Intensity Factor, Mixed Mode Loading, Rayleigh Wave Velocity

ABSTRACT

The stress field around the dynamically propagating interface crack tip under a mixed mode loading condition has been studied by using a hybrid experimental method. The variation of dynamic stress field around the dynamic interfacial crack tip is photographed by the Cranz-Shardin type camera having 10^6 fps rate. The dynamic interfacial crack propagating velocities and the shapes of isochromatic fringe loop are characterized for varying mixed load conditions in double cantilever beam (DCB) specimen. The dynamic interfacial crack tip complex stress intensity factors, K_1 and K_2 , are extracted by using the overdeterministic least square method. In addition, it is found that the dynamic interface crack propagating velocities under the mixed mode loading conditions are significantly small compared to those obtained under the mode I impact loading conditions by Shukla and Rosakis in the USA.

1. INTRODUCTION

During the last few decades many interesting problems pertaining to dynamic crack propagation and arrest phenomena have been investigated by many researchers throughout the world [1,2,3]. In recent years, there has been considerable interest in the study of dynamic bimaterial interface crack propagation from both theoretical and experimental viewpoints [4]. Even though the majority of these studies have been either analytical or numerical in nature, a few experimental studies on the dynamic interfacial fracture have been appeared in the Technical Journals from 1991. Rosakis group at California Institute of Technology and Shukla group at University of Rhode Island are the representatives among others. This study is motivated by the need to establish procedures and investigate the applicability of dynamic photoelasticity to study interface failure under mixed mode loading condition [5]. Thus, this paper attempts to develop the framework for employing photoelasticity to observe and investigate the phenomena of dynamic interface failure. The initial failure was obtained by subjecting the bimaterial specimen to dynamic mixed mode loading. The dynamic isochromatic fringe patterns surrounding a crack tip propagating along a bimaterial interface are photographed and characterized. A parametric investigation has been carried out to study the influence of varying fracture parameters on these isochromatic fringe patterns. The

primary relevant fracture parameters of interest include the crack tip velocity and the complex stress intensity factors. The complex stress intensity factors for the stress field surrounding the dynamic interface crack tip are extracted by using a hybrid-experimental technique.

2. THEORETICAL

2.1 Stress field and dynamic stress intensity factors at the dynamic interface crack tip

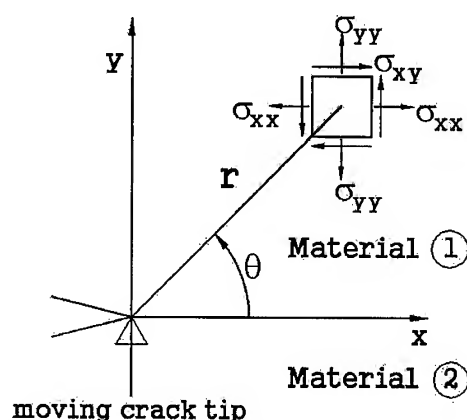


Fig. 1 A coordinate system and stress component for a small element around crack tip

The stress field shown in Fig. 1 at the dynamic interface crack tip developed by Deng [4] are rearranged to fit the photoelastic analysis conducted in this study in polar coordinate system. Combining the stress-optics law, with $\tau_m = Nf_\sigma / 2t$ we can relate the experimental results with the theoretical stress field as the below.

$$\left(\frac{Nf_\sigma}{t}\right)^2 = (2\tau_m)^2 = (\sigma_{xx} - \sigma_{yy})^2 + (2\sigma_{xy})^2 \quad (2.1)$$

where N = the experimental fringe order of the dynamic isochromatic.

f_σ = dynamic fringe constant of the materials (6.7KN/m-fringe for polycarbonate).

t = specimen thickness (4.5mm).

2.2 Characterization of isochromatic fringe loops at the dynamic interface crack tip

The Newton-Raphson method and over-deterministic least square method (OLSM) are used to extract the complex stress intensity factors, K_1 and K_2 implicitly appeared in Eq. (2.1) for the dynamic interface crack tip stress field. To determine the stress intensity factor K_1 and K_2 we should take experimental data at the vicinity of the crack tip to reduce boundary effect. However, it is difficult to distinguish the experimental isochromatics data due to concentrated fringe and local plastic zone at the vicinity of the crack tip. Therefore a multi-functional determination procedure should be used to extract the more precise stress intensity factors.

2.3 Theoretical dynamic isochromatic fringes

Substituting the K_1 and K_2 determined by the above procedure into Eq. (2-1), we can generate theoretical dynamic isochromatic fringe patterns and compare the generated fringes with experimental results. By this final check process, we can confirm the appropriate values of K_1 and K_2 .

3. EXPERIMENTAL

3.1 Multi-spark camera system

The dynamic photoelasticity method consisted of the Cranz-Shardin camera system with a multi-spark camera set, a dynamic photoelastic apparatus, a loading equipment, field lens and controllers is used in this study.

3.2 Specimen and loading

Revealing the dynamic interface crack propagation phenomena and the dynamic stress field surrounding the rapidly propagating interfacial crack tip under the mixed mode loading condition, we manufactured the specimens using polycarbonate(PC) and aluminum(Al). The residual stress along the interface was checked to be negligible by using a photoelastic setup. The specimen configuration is shown in Fig. 2.

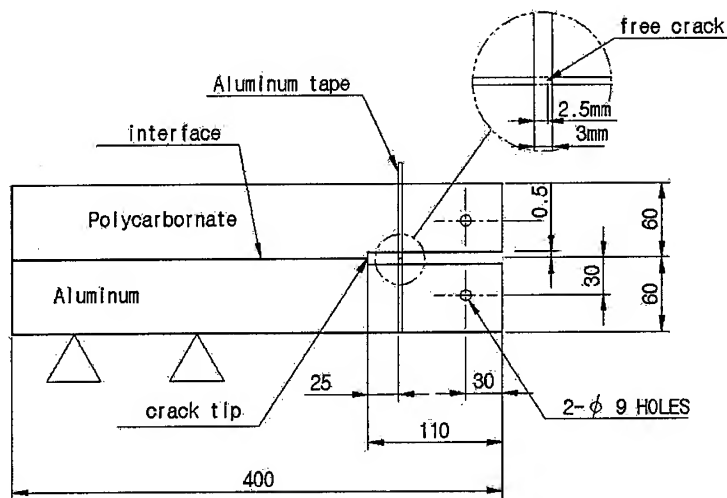


Fig. 2 Configuration of test specimen (thickness : 4.5mm)

The mechanical and physical properties of PC and Al-7075 are listed in table 1.

Table 1 Material and physical properties of Polycarbonate and Aluminum

Property \ Material	Polycarbonate	Aluminum
Poisson's ratio	0.38	0.33
Young's modulus, E(Gpa)	2.72	71.0
Material stress optics fringe value(Mpa-mm/fr)	6.7	-
Shear modulus(Gpa)	0.98	-
Density(g/cm ³)	1.196	2.80
Dilatational wave speed(m/s)	1960	6320
Distortional wave speed(m/s)	910	3100

4. RESULTS AND CONSIDERATION

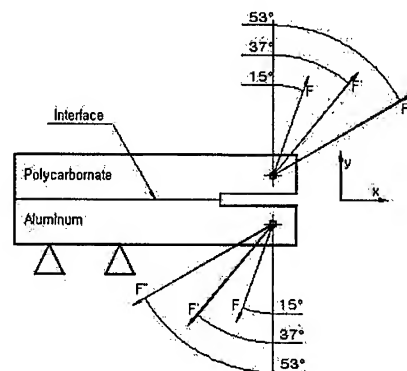


Fig. 3 Various mixtures of applied loads

Figure. 3 shows the varying directions of mixed mode loadings which changes the load mixture ratio of y/x (vertical/horizontal) value. Three different y/x ratios such as $3.7(=F)$, $1.3(=F')$ and $0.75(=F'')$ were applied in the present study.

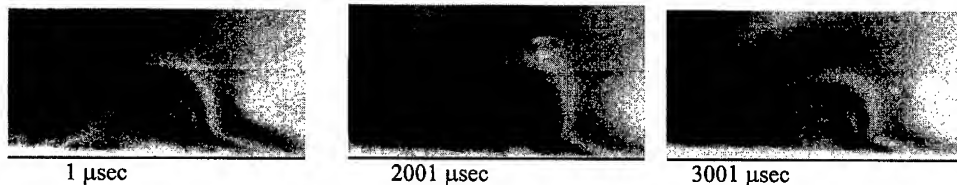


Fig. 4 Dynamic isochromatic fringe patterns in PC for a crack dynamically propagating along the interface by initial load F (crack runs left to right, scale: 4/1)
(μsec = time after break, \longrightarrow : propagating crack tip position)

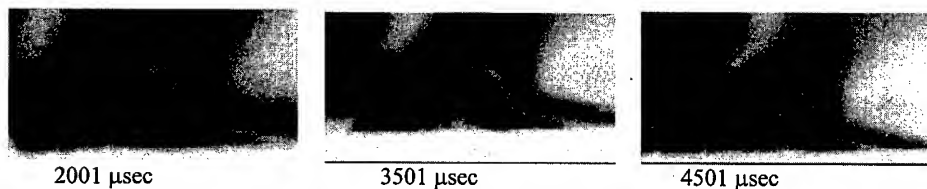


Fig. 5 Dynamic isochromatic fringe patterns in PC for a crack dynamically propagating along the interface by initial load F' (crack runs left to right, scale: 4/1)
(μsec = time after break, \longrightarrow : propagating crack tip position)

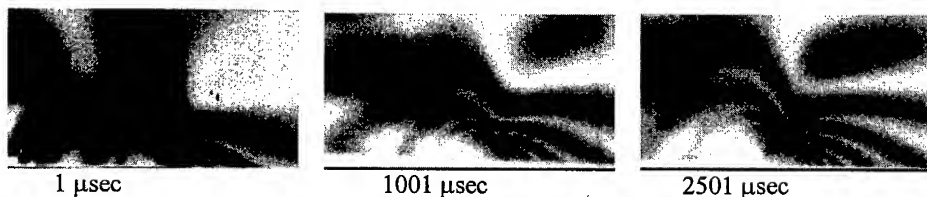


Fig. 6 Dynamic isochromatic fringe patterns in PC for a crack dynamically propagating along the interface by initial load F'' (crack runs left to right, scale: 4/1)
(μsec = time after break, \longrightarrow : propagating crack tip position)

Figures 4, 5 and 6 show the dynamic stress field at the vicinity of the interface crack tip with varying loading condition such as F , F' and F'' , respectively. It is interesting to note that the initially mixed loading condition considerably affects the characteristics of isochromatic loop.

Comparing the crack propagating velocities for three different loads, we found that the crack propagating velocities decreases as y/x values become smaller ranging from 3.7 to 0.75. This means that the maximum crack propagating velocity becomes faster when mode I load increases as we expected from the experimental results for the isotropic materials. The more study about geometrical shape, thickness, the bonding strength of the interface, the direction of mixed load and etc has to be needed. The crack velocities for the dynamic interface cracks are found to be very low comparing to other investigator's experimental results appeared in literatures [3] which was obtained under mode I loading condition.

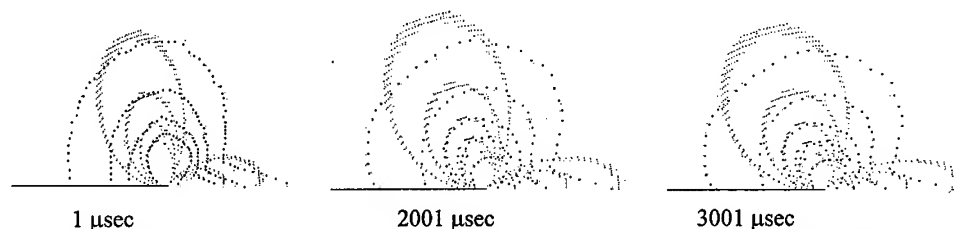


Fig. 7 Theoretical isochromatic fringe patterns for a crack propagating along the interface by initial load F

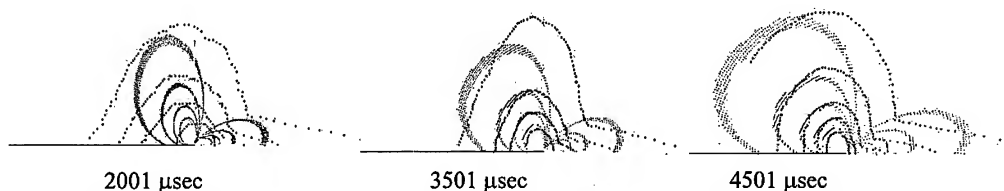


Fig. 8 Theoretical isochromatic fringe patterns for a crack propagating along the interface by initial load F'

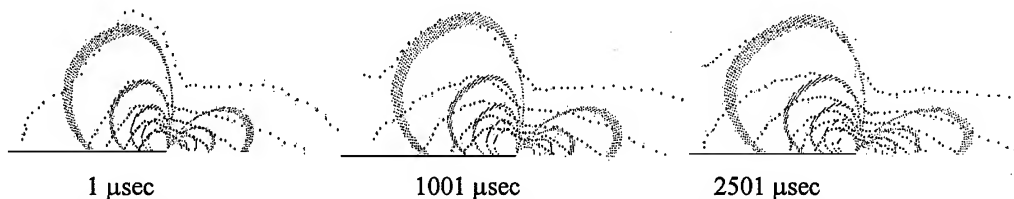


Fig. 9 Theoretical isochromatic fringe patterns for a crack propagating along the interface by initial load F''

Figures 7, 8 and 9 show the comparison between the theoretical isochromatics and the experimental fringes in the quantitative aspect. The fringes are similar around the crack tip. It is found that K_1 and K_2 increase as y/x decreases as shown in Fig. 10. The fringes are similar at vicinity of the crack tip. However, the errors are getting bigger as we take data far from the crack tip where we need to add higher order coefficients.

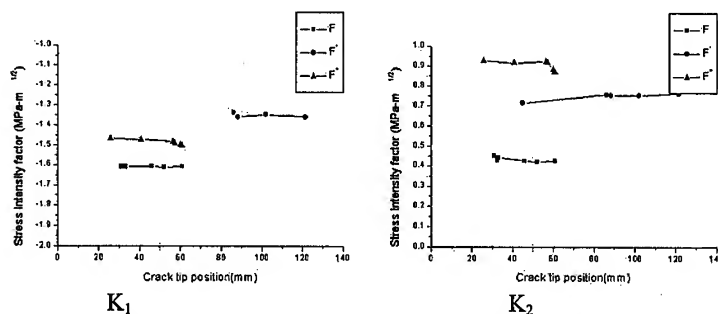


Fig. 10 Stress intensity factor vs. crack tip location by initial load F , F' and F''

5. CONCLUSIONS

In this study, the dynamic mixed mode crack propagation behavior for structural bonded joints(interfaces) are investigated by using the hybrid-experimental methods with the aid of dynamic photoelastic methodology. The results obtained are as follows.

(1) The propagating interface crack velocities in the DCB specimens under initially mixed mode loading condition are found to be about 7% of Rayleigh wave velocity of polycarbonate. These are significantly small compared to those obtained under the mode I impact loading conditions by Shukla [2] and Rosakis [3] in the USA. We need to have more detailed experimental studies about the effect of geometrical shape, interface thickness, the bonding strength of the interface, and the ratio of mixture of the load in structural joints(interfaces) on dynamic interface crack propagation velocities.

(2) We utilize a hybrid experimental-theoretical method to find good agreements between the theoretical dynamic interface stress fields and experimental ones.

Acknowledgment : These authors wish to acknowledge the financial support of Korea Research Foundation made in the program of 1997.

REFERENCES

1. Lee, O.S. and Kim, D.Y., Crack-Arrest Phenomenon of an Aluminum Alloy, *Mechanic Research Communications*, Vol. 26, No. 5 (1999) p. 575-581.
2. Singh, R. P. and Shukla, A., Subsonic and Transonic Crack Growth along a Bimaterial Interface, *International Journal of Fracture*, Vol. 63, (1996a) p. 293-310.
3. Rosakis, A.J., Samudrala, O., Singh, R.P. and Shukla, A : Intersonic Crack Propagation in Bimaterial System, *Journal of Mechanics and Physics of Solids*, Vol. 46, (1998) p. 1789-1813.
4. Deng, X., Complete Complex Series Expansions of Near-Tip Fields for Steadily Growing Interface Cracks in Dissimilar Isotropic Materials, *Engineering Fracture Mechanics*, Vol. 42, No.2, (1992) p. 237-242.
5. Mohammad, M. and Loren, Z., Photoelastic determination of mixed mode stress intensity factors for sharp reentrant corners, *Engineering Fracture Mechanics*, Vol. 52, No. 4, (1995) p. 639-645.

Analysis of a Crack in a Functionally Gradient Interface Layer under Static and Dynamic Loading

Y.S. Wang^{1,2} and D. Gross²

¹ Institute of Engineering Mechanics, Northern Jiaotong University,
Beijing 100044, China P.R.

² Institute of Mechanics, Technical University of Darmstadt,
Hochschulstrasse 1, DE-64289 Darmstadt, Germany

Keywords: Crack, Dynamic Fracture, Functionally Gradient Material, Interface Layer, Stress Intensity Factor

ABSTRACT

An analytical model is developed for a functionally gradient interface layer between two dissimilar elastic solids. The interface layer with material properties varying continuously in an arbitrary manner is modeled as a multi-layered medium with the elastic modulus varying linearly in each sub-layer and continuous on the sub-interfaces. With this new multi-layered model, we analyze the both static and dynamic problems of a crack in the interface layer. The transfer matrix method and Fourier integral transform technique are used to reduce the mixed boundary-value problem to a Cauchy singular integral equation. The stress intensity factors are calculated.

1. INTRODUCTION

Interface plays an important role in composite materials. Usually the discrepancies in mechanical and thermal properties between the component materials cause the strength problems of the interface and therefore influence the strength of the whole material. In an attempt to solve such problem, the Functionally Gradient Materials (FGMs) are used as the interface layer between two component materials. The FGMs are devised in such a manner that material composition is continuously varied spatially in order to smooth the strain discontinuity between different materials. The fracture analysis of the FGM interface layer has received considerable attention in recent years. However, it is noted that all of published works assume that the material properties vary in an exponential manner [1-3] or a power manner [4,5]. This, we argue, is of little use to the design of the FGMs. The analysis should allow the material properties to vary in arbitrary manner. In this paper, we develop an analytical model for the FGM interface layer with continuously varying elastic properties and solve the problem of a crack in the interface layer subjected to a static or harmonic dynamic anti-plane shearing load. The method is based on the fact that an arbitrary curve can be approached by a continuous broken line. Therefore we model the FGM interface layer as a multi-layered medium with the linearly varying elastic modulus which is continuous on the sub-interfaces. The Fourier integral transform technique and singular integral equation method are employed to solve the mixed boundary-value problem. The stress intensity factors are presented.

2. PROBLEM FORMULATION

2.1. A New Multi-Layered Model for a Functionally Gradient Interface Layer

Consider a Griffith crack on the interface between two bonded dissimilar elastic homogeneous half-spaces, with the shear moduli μ, μ^* and mass densities ρ, ρ^* , which are loaded by remote anti-plane shearing traction. Here the interface is not the "mathematical interface" with zero thickness, but an interfacial region with finite thickness h_0 , as shown in Fig. 1a. The crack is located in the interfacial region. This interface layer is made of the FGMs with material constants $\{\mu(y), \rho(y)\}$ continuously varying from $\{\mu, \rho\}$ to $\{\mu^*, \rho^*\}$. Generally, $\mu(y)$ and $\rho(y)$ may be of arbitrary forms. However, considering the fact that an arbitrary curve can be approached by a continuous broken line, we develop a new multi-layered model as shown in Fig. 1b. The interfacial region $(h_0, 0)$ is divided into N sub-layers (h_{j-1}, h_j) , $(j=1, 2, \dots, N; h_N = 0)$. The crack is on the k th sub-interface (k may be any integer number from 0 to N). The shear modulus in each sub-layer varies linearly with the form:

$$\mu(y) \approx \mu_j(y) = \bar{\mu}_j(a_j + b_j y), \quad h_j \leq y \leq h_{j-1}, \quad j=1, 2, \dots, N \quad (1)$$

and is equal to the real values on the sub-interfaces, $y = h_j$. This leads to

$$a_j = \frac{h_{j-1} - h_j \bar{\mu}_{j-1} / \bar{\mu}_j}{h_{j-1} - h_j}, \quad b_j = \frac{\bar{\mu}_{j-1} / \bar{\mu}_j - 1}{h_{j-1} - h_j} \quad (2)$$

with $\bar{\mu}_j = \mu(h_j)$. The mass density in each sub-layer is assumed to have the similar form so that $\mu_j(y)/\rho_j(y)$ is a constant, i.e.

$$\rho(y) \approx \rho_j(y) = \bar{\rho}_j(a_j + b_j y), \quad h_j < y < h_{j-1}, \quad j=1, 2, \dots, N \quad (3)$$

where $\bar{\rho}_j$ is determined by

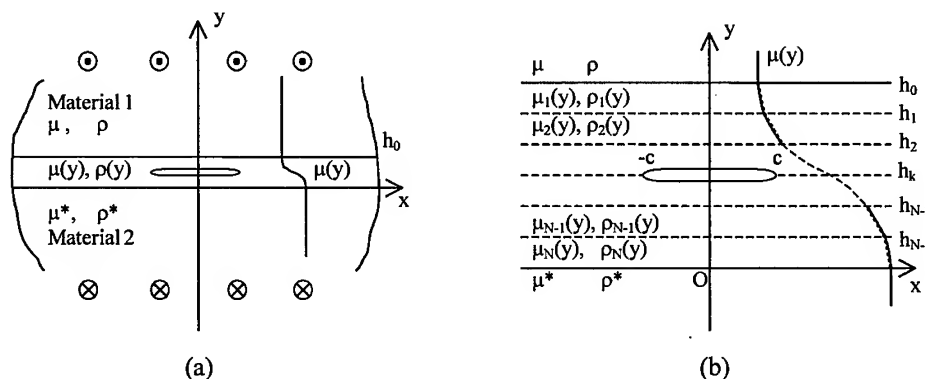


Fig.1 Two dissimilar half-spaces bonded through a FGM interface layer (a); and the new multi-layered model of the FGM interface layer (b)

$$\int_{h_j}^{h_{j+1}} \rho(y) dy = \bar{\rho}_j \int_{h_j}^{h_{j+1}} (a_j + b_j y) dy \quad (4)$$

which ensures that the averaged mass density in each sub-layer remains unchanged. It is noted that the mass density is discontinuous on the sub-interfaces. But it is known that the discontinuity of the mass density causes less influence on the strain discrepancy.

2.2. Transfer Matrix and Dual Integral Equations

We consider the harmonic dynamic loading case. The only non-zero displacement component is $W_j(x, y, t) = w_j(x, y)e^{i\omega t}$ along the z -axis, which satisfies the following wave equation:

$$\mu_j(y) \frac{\partial^2 w_j}{\partial x^2} + \frac{\partial}{\partial y} \left(\mu_j(y) \frac{\partial w_j}{\partial y} \right) = -\omega^2 \rho_j(y) w_j \quad (5)$$

where ω is frequency and $j = 1, 2, \dots, N$. Substituting Eqs.1 and 2 into the above equation and applying Fourier integral transform with respect to x , we obtain

$$\frac{\partial^2 \tilde{w}_j}{\partial y^2} + \frac{b_j}{a_j + b_j y} \frac{\partial \tilde{w}_j}{\partial y} - \beta_j^2 \tilde{w}_j = 0 \quad (6)$$

where “ \sim ” indicates the Fourier transform, and

$$\beta_j = (s^2 - \bar{k}_j^2)^{1/2}, \quad \bar{k}_j = \omega / \bar{c}_j, \quad \bar{c}_j = \sqrt{\bar{\mu}_j / \bar{\rho}_j} \quad (7)$$

with $\text{Re } \beta_j \geq 0, \text{Im } \beta_j \leq 0$. The solution of Eq.6 can be written as

$$\{S_j\} = [T_j(y)] \{A_j\}, \quad j = 1, 2, \dots, N \quad (8)$$

with $\{S_j\} = [\tilde{w}_j, \tilde{\tau}_{y,j}]^T$, $\{A_j\} = [A_{1j}, A_{2j}]^T$, and

$$[T_j(y)] = \begin{bmatrix} K_0(\beta_j \bar{y}_j) & I_0(\beta_j \bar{y}_j) \\ \mu_j(y) \beta_j K'_0(\beta_j \bar{y}_j) & \mu_j(y) \beta_j I'_0(\beta_j \bar{y}_j) \end{bmatrix}$$

where the prime indicates the differentiation; $K_0()$ and $I_0()$ are modified Bessel functions; and $\bar{y}_j = b_j^{-1}(a_j + b_j y)$. The solutions for the homogeneous half-spaces are

$$\{S_0\} = [T_0(y)] \{B\} A_{10}, \quad \{S_{N+1}\} = [T_{N+1}(y)] \{X\} A_{2,N+1} \quad (9)$$

where $\{B\} = \{1, 0\}^T$, $\{X\} = \{0, 1\}^T$, and

$$[T_0(y)] = \begin{bmatrix} e^{-\beta_0 y} & e^{\beta_0 y} \\ -\mu \beta_0 e^{-\beta_0 y} & \mu \beta_0 e^{\beta_0 y} \end{bmatrix}, \quad [T_{N+1}(y)] = \begin{bmatrix} e^{-\beta_{N+1} y} & e^{\beta_{N+1} y} \\ -\mu^* \beta_{N+1} e^{-\beta_{N+1} y} & \mu^* \beta_{N+1} e^{\beta_{N+1} y} \end{bmatrix}$$

The subscripts “0” and “N+1” correspond, respectively, to the upper and lower half-spaces. On the interfaces we have the following relations

$$\{S_j\} - \{S_{j+1}\} = \{\Delta S_k\} \delta_{kj}, \quad y = h_j, \quad j = 0, 1, 2, \dots, N \quad (10)$$

where $\{\Delta S_k\} = \{\Delta \tilde{w}_k, 0\}^T$, and δ_{kj} is Kronecker delta. Eq.10 is a recurrence relation which, on substitution of Eqs.8 and 9, may yields the expression of $\{C_j\}$ in terms of $\{\Delta S_k\}$,

$$\{C_j\} = ([\bar{L}_{jk}] + [\bar{K}_{jk}]H(j-k-1))\{\Delta S_k\}, \quad j = 1, 2, \dots, N \quad (11)$$

where $[\bar{L}_{jk}]$ and $[\bar{K}_{jk}]$ may be easily obtained and will not be given here because of limited space. Substituting Eq.11 into Eq.8 and taking the inverse Fourier transform, we have

$$\{w_j, \tau_{yzj}\}^T = \frac{1}{2\pi} \int_{-\infty}^{\infty} [M_{jk}]\{\Delta S_k\} e^{-isx} ds, \quad j = 1, 2, \dots, N \quad (12)$$

where $[M_{jk}] = [T_j(y)]([\bar{L}_{jk}] + [\bar{K}_{jk}]H(j-k-1))$ is the transfer matrix of the multiple layered medium with an interface cracks. Suppose the stress caused by the remote loading in the medium without crack is $\tau_{yz}^L(x, y)$. Then the free traction condition on the crack faces and the displacement single-valued condition yield a set of dual integral equations:

$$\frac{1}{2\pi} \int_{-\infty}^{\infty} \bar{m}_k(s) \Delta \tilde{w}_k(s) e^{-isx} ds = -\tau_{yz}^L(x, h_k), \quad |x| < c \quad (13)$$

$$\int_{-\infty}^{\infty} \Delta \tilde{w}_k(s) e^{-isx} ds = 0, \quad |x| > c \quad (14)$$

where $\bar{m}_k = \{0, 1\} [M_{jk}|_{y=h_k}] \{1, 0\}^T$ ($j = k$ or $k-1$).

2.3. Cauchy Singular Integral Equation

By introducing the dislocation density function of the crack,

$$\phi_k(x) = \frac{\partial}{\partial x} [\Delta w(x)], \quad |x| < c \quad (15)$$

Eqs.13 and 14 reduce to

$$\frac{i}{2\pi} \int_{-\infty}^{\infty} s^{-1} \bar{m}_k(s) \int_{-c}^c \phi_k(u) e^{is(u-x)} du ds = -\tau_{yz}^L(x, h_k), \quad |x| < c \quad (16)$$

$$\int_{-c}^c \phi_k(u) du = 0 \quad (17)$$

Considering the asymptotic behavior of $K_0()$ and $I_0()$ for large arguments, one may prove

$$\lim_{s \rightarrow \pm i\infty} s^{-1} \bar{m}_k(s) = \pm \bar{\mu}_k / 2 \quad (18)$$

Then Eq.16 can be converted into a Cauchy singular integral equation,

$$\frac{\bar{\mu}_k}{2\pi} \int_{-c}^c \frac{\phi_k(u)}{u-x} du + \int_{-c}^c \phi_k(u) P_k(u, x) du = -\tau_{yz}^L(x, h_k), \quad |x| < c \quad (19)$$

where we have denoted

$$P_k(u, x) = -\frac{1}{\pi} \int_0^\infty \left[s^{-1} \bar{m}_k(s) + \frac{1}{2} \bar{\mu}_k \right] \sin[s(u-x)] ds \quad (20)$$

Eq.19, together with Eq.17, can be solved numerically by the method of Erdogan and Gupta [6]. It should be noticed in evaluating the semi-infinite integral in Eq.20 that the integrand, in some cases, may involve simple poles along the integral path. These poles correspond to the general type of Love-waves. To overcome this difficulty, we use the method developed by Kundu [7] to express the integral as the sum of a Cauchy principal integral and residues of the integrand, see [7] for details.

3. NUMERICAL RESULTS AND DISCUSSION

The above formulas are derived for the harmonic dynamic loading case. The results for static loading case can be obtained by setting the frequency $\omega \rightarrow 0$. Furthermore, if we replace $K_0(z)$ and $I_0(z)$ with, respectively, $\exp(-z)$ and $\exp(z)$, we have the solution for the traditional piecewise multi-layered model. In this section we present some numerical examples. Special attention is devoted to the Stress Intensity Factors (SIFs) which are defined as

$$K_{III}^\pm = \lim_{x \rightarrow \pm c^\pm} \sqrt{2|x \mp c|} \tau_{yz}(x, h_k) \quad (21)$$

Numerical results are given by

$$K_{III}^\pm = (\bar{\mu}_k/2) \sqrt{c} F_k(\pm 1) \quad (22)$$

where $F_k(\eta) = \phi_k(c\eta)(1-\eta^2)^{1/2}$.

We consider two different elastic half-spaces bonded through a FGM interface layer of thickness h_0 . A Griffith crack of length $2c$ is located on the center line ($y = h_0/2$) of the layer. The crack faces are subjected to the uniform anti-plane shearing traction τ_0 . The mass density of the layer is supposed to vary linearly from ρ to ρ^* . Here we take $\rho^*/\rho = 0.8$. The shear modulus $\mu(y)$ is approximated by a two-piece broken line, that is, the interface layer is divided into two sub-layers.

Fig. 2 presents the static SIFs versus h_0/c for some selected values of $\mu:\mu_1:\mu^*$ [where $\mu_1 = \mu(h_0/2)$]. It is shown that the SIFs increase as h_0/c decreases. The solid and dot-dashed lines are for the case with $\mu(y)$ varying linearly in the whole interface layer. It is seen that the larger the value of μ/μ^* is, the higher the SIFs are. For a fixed value of μ/μ^* , a bigger value of μ_1 can also cause the higher SIFs (Compare the dashed, solid and dotted lines which show the results for $\mu/\mu^* = 9$). Fig. 3 shows the dynamic SIFs versus normalized frequency, $k_0 c$, of the load for some selected values of μ_1 with $\mu/\mu^* = 9$ and $h_0/c = 1$. At lower frequencies, the SIFs are higher for larger μ_1 . But it is not the case at higher frequencies. The influences of h_0/c and μ/μ^* on the dynamic SIFs are shown in Figs. 4 and 5 for the case with $\mu(y)$ varying linearly in the whole interface layer. The smaller value of h_0/c and/or the larger value of μ/μ^* may cause higher SIFs at lower frequencies. Here in Fig. 4, we take $\mu/\mu^* = 9$, and in Fig. 5, $h_0/c = 1$.

Generally, for a crack with fixed length, the decrease of interface layer thickness and/or the increase of the difference between shear moduli of the two half-spaces may result in higher SIFs due to rapid change of the modulus in the layer. But the decrease of the value of the modulus on the crack surface may reduce the SIFs.

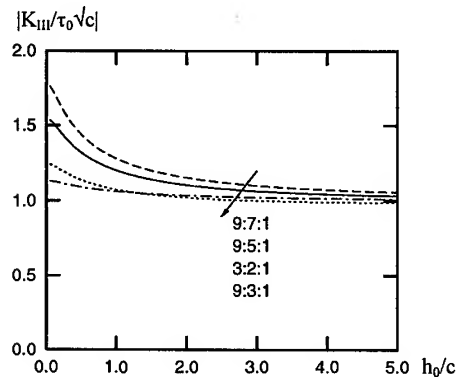


Fig. 2 Static SIF versus h_0/c for selected values of $\mu : \mu_1 : \mu^*$

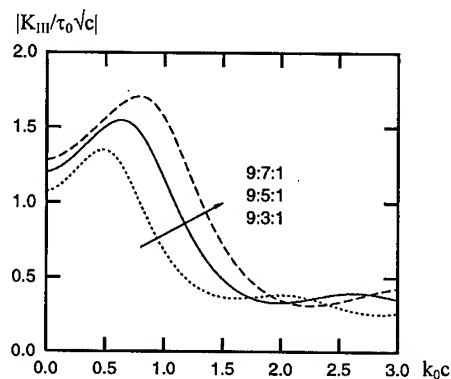


Fig. 3 Dynamic SIF versus k_0c for selected values of μ_1 ($\mu/\mu^* = 9$)

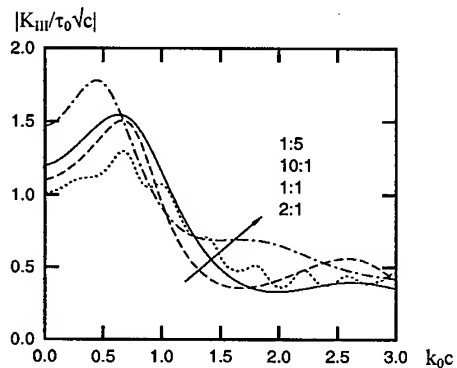


Fig. 4 Dynamic SIF versus k_0c for selected values of h_0/c ($\mu/\mu^* = 9$)

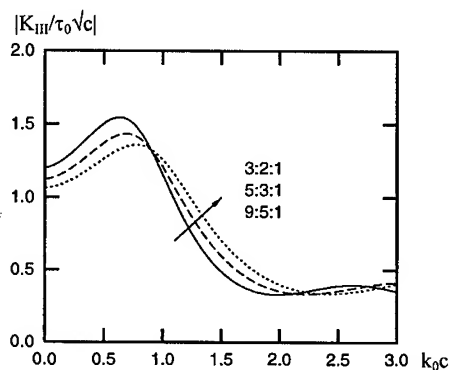


Fig. 5 Dynamic SIF versus k_0c for selected values of μ/μ^* ($h_0/c = 1$)

ACKNOWLEDGEMENTS

The first author gratefully acknowledges the Alexander von Humboldt Foundation for awarding a research fellowship.

REFERENCE

1. F. Delale and F. Erdogan, *J. Appl. Mechanics*, **55** (1988) p. 317
2. P. Gu and R. J. Asaro, *Int. J. Solids and Structures*, **34** (1997) p. 1
3. R. Babaei and S. A. Lukasiewicz, *Z. Angew. Mathematics and Mechanics*, **78** (1998) p. 383
4. X. Y. Wang, Z. Z. Zou and D. Wang, *Int. J. Solids and Structures*, **34** (1997) p. 3911
5. C. Li and Z. Zou, *J. Appl. Mechanics*, **66** (1999) p. 566
6. F. Erdogan and G. D. Gupta, **29** (1972) p. 525
7. T. Kundu, *Wave Motion*, **7** (1985) p. 459

Fundamental Study of Dynamic Stress Wave Using a Dynamic Photoelastic Method

Tsuyoshi Kanemitsu¹ and Yoshiaki Sawa²

¹ Graduate School, Science University of Tokyo, 2641, Yamazaki,
Noda-shi, Chiba-ken 278-8510, Japan

² Department of Mechanical Engineering, Science University of Tokyo,
2641, Yamazaki, Noda-shi, Chiba-ken 278-8510, Japan

Keywords: Crantz-Schardin Type Stroboscopic Camera, Dynamic Photoelasticity, Stress Wave

ABSTRACT

Experiments have been conducted to investigate a fundamental relationship between stress waves and photoelastic fringes under condition of applied impact pulse loads to testing objects. The testing objects are made of DAP plastic plates with 15,30,45,60 and 90 mm of width. Impact stresses were applied to the one side of the plates by air-gun. The stress wave propagation speed was determined by observation of photoelastic fringes in the test pieces. The fringe position was determined by means of image processing technique and the photoelastic data were compared with those obtained by the measured impact pulse wave forming with strain gauges under the same conditions to raise the reliability of photoelastic measurement.

The impact stress wave propagation speed decreased with a distance from the initial loading point, and took a minimum at a distance of about 1.2 times of plate width, then it increased and became constant at a distance of over 2 or 3 times of plate width. For the test piece with smallest width, 15mm, the constant wave speed was approximately equal to the theoretical ones calculated for a thin rod. For the other test pieces, the constant wave speed decreased with increase of the plate width and they were different from any theoretical values for a thin rod and an infinite flat plate.

1. INTRODUCTION

Since the dynamic photoelastic method was introduced into impact problems in the earlier studies on material science, many investigations have been preformed for the dynamic stress conditions including quasi-static conditions. In practice, it is difficult to distinguish the both stresses in stress analysis and the most of loading impact stresses are quasi-static state. However, we have still no sufficient information about details of impact stress behavior in materials and there are many unknown factors to use the dynamic photoelastic method for impact problems.

In the present study, an air-gun was employed to give impact stresses to testing objects and a Crantz-Schardin type stroboscopic camera was used for analysis of stress wave propagation. The testing objects

were made of DAP (diallyphotalate polymer) plastic plates with 15,30,45,60 and 90mm of width. The present study gives a relationship between stress wave and photoelastic fringes and a dynamic stress wave behavior in homogeneous materials as an example of fundamental treatments for impact problems by means of the dynamic photoelastic method.

2. DYNAMIC PHOTOELASTIC EXPERIMENT

2.1. Cranz-Schardin type stroboscopic camera

Fig.1 shows the optical system of a 300 ϕ m/m photoelastic equipment with Cranz-Schardin type stroboscopic and impact equipment. The dynamic photoelastic microflash with 9 built-in flashbulbs is adjusted and the dynamic photoelastic camera with 9 built-in camera lenses is also focussed. It is coming to be sent out by each flashbulb after flash time delay was set up in each flashbulb with the dynamic photoelastic microflash source and the time when a signal from the input device set up in the outside was caught and set up passed. Then flashlight is gathered to camera lenses, placed diagonally, and dynamic fringe pattern is shot on film. The other flashlights are gathered to each diagonal camera lens so that there is never a double exposure of the dynamic fringe pattern.

Shutter speed to record impact stress should be determined in consideration of the propagation speed. In theory, dynamic stress wave propagation speed is determined by the following equations.

The speed of the longitudinal wave in a narrow strip

$$C_n = \sqrt{\frac{E}{\rho}} \quad (2-1)$$

The speed of the longitudinal wave in a plate of infinite width

$$C_e = \sqrt{\frac{E}{\rho(1-\nu^2)}} \quad (2-2)$$

E; Young's modulus ρ ; density ν ; Poisson's ratio

The speed in the test pieces made of DAP used in this experiment is calculated from these equations. The result gives about 1500 to 2000m/s. So the exposure time should be within 1.3 μ s to control the fringe width to 2mm.

2.2. Impact stress load equipment

In the dynamic photoelastic experiment, the occurrence of the impact power itself influences the results of the experiment directly. To apply an impact pulse load, it is necessary to arrange for an object with a small mass and high energy to collide with the test piece. In experimental stress analysis, stress waves are created in many ways, e.g. the drop-weight method, the explosion method, the airgun method, and the electromagnetic repulsion method. We chose the airgun method, because it makes improvement of reenactment easier than the other ways.

2.2.1. Striker

It is known that the material and length of the striker effect the peak and the continuity of the stress waves. In this report, the striker is made of acryl resin, and it is formed accurately to fit the size of the gun barrel. The tip of the striker is also formed into a hemisphere. The striker is 30mm long and weighs

1gram, because a short striker makes the continuity of the stress wave shorter than a long one, but a short striker can also be used for the discharge.

2.2.2. Air pressure at discharge

Air pressure at discharge of the striker effects the impact energy. A low pressure gives a low impact energy, and a high pressure causes the destruction of the test pieces. In this report, the pressure is fixed at $9.807 \times 10^4 \text{ Pa}$ because it gives an impact energy worth examining and little possibility of the destruction of the test pieces.

2.2.3. Distance that striker is pushed into gun barrel

The distance that the striker is pushed into the barrel effects the impact energy. The greater the distance, the higher the impact energy is. With a distance of 100mm, the impact load is worth examining. So the length is fixed at 100mm.

2.3. Test pieces

In this report, test pieces are made of DAP plastic plate, 15(30, 45, 60, and 90) mm-wide. Two strain gauges are set on a 15mm-wide test piece to check the wave and to measure the dynamic Young's modulus. The distance between one gauge and the impact end is 75mm. And the other is 175mm. Fig.2 shows the experimental system to determine stress wave.

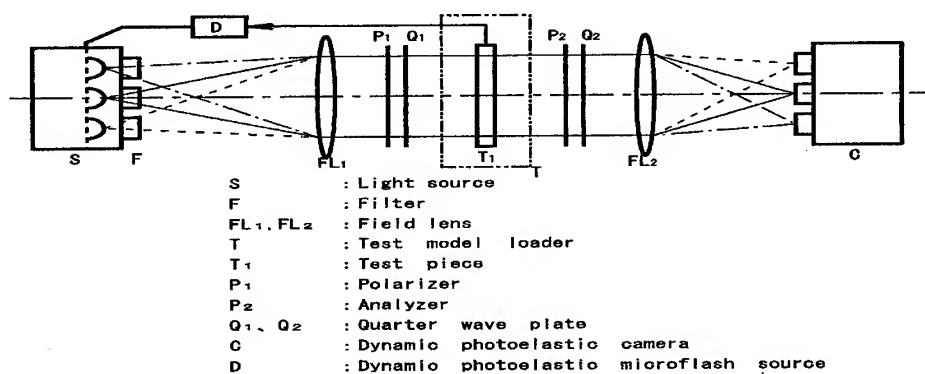


Fig.1 Optical system for the dynamic photoelastic experiment

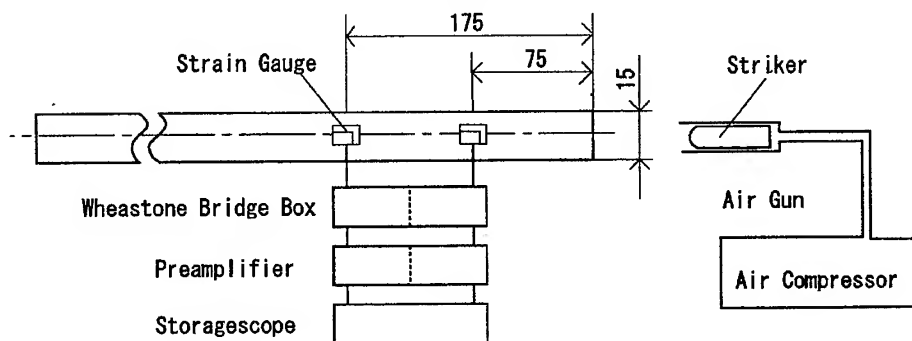


Fig.2 Experimental system to find the stress wave

3. RESULT

In this report, 5 types test pieces (15, 30, 45, 60 and 90mm-wide) are used in the dynamic photoelastic experiment. Fig.3,4,5 show photoelastic fringe patterns of 30mm-wide and 90mm-wide test pieces as an example.

The dynamic Young's modulus is determined as $E=4.461 \times 10^9 \text{GPa}$ by measurement with strain gauges.

4. CONCLUSION

Distribution of dynamic stress wave propagation speed are shown for each test pieces in the series of Fig.6 □ Fig. 10. In the figures, the vertical axis indicates distance from the initial point of dynamic stress wave and the horizontal axis indicates distance from the initial point of applied impact stress. The dynamic stress wave propagation speed decreases and takes a minimum at a distance of about 1.2 times of plate width from the initial point, then it increases and becomes constant at a distance of over 2 or 3 times of plate width as soon from the figures. Also stationary dynamic stress wave speeds are 1839m/s in the 15mm-wide test piece, 1698m/s in the 30mm-wide test piece, 1615m/s in the 45mm-wide test piece, 1550m/s in the 60mm-wide test piece and 1480m/s in the 90mm-wide test piece. The wider test piece is, the slower the dynamic stress wave speed is. In our report of last year, we make the hypothesis that the stationary speed is based on the theory of dynamic stress waves in a narrow strip and that the pre-stationary speed is based on the theory of dynamic stress waves in plates of infinite width. So we compared stationary speeds, changing the test piece width.

As a result, the narrow test piece is closer to the theoretical speed of the stress wave than the wide one. And the speed in the 10mm-wide test piece corresponds to the theoretical speed. The speed of the wide test piece is much slower than the theoretical speed. The precise wave speed could not be obtained at close range of the initial point in the present study. The lowest wave speed indicated about 1.2 times of plate width from the initial point is approximately equal to a theoretical value given by Rayleigh wave. According to the experimental results, it is considered that not only longitudinal wave but also transversal wave and Rayleigh wave give an effect on the dynamic stress wave propagation speed. It is also thought that the stress wave reflects at the impact end of the test piece because the fringe formed change from elliptical to circular, the fringe speed after the deceleration accelerates until constant at a point 2 or 3 times as far from the impact end as the width of the test piece and the shape becomes "<" because the fringe speed spread on the impact end side is fast and the speed spread on the extension line or the impact end is slow.

REFERENCE

- (1) N. NAKAYAMA, M. OHASHI, and H. TAKEISHI, Dynamic Stress Concentration in a Strip Plate with Fillet, JSME International Journal, Series A, Vol 41, No 3, 1998
- (2) K. KAWATA, N. TAKEDA, and S. HASHIMOTO, Photoelastic-coating Analysis of Dynamic Stress Concentration in Composite Strips, Exp. Mech., Vol 12 (1984), p.316-327
- (3) Heywood, R.B., Designing by Photoelasticity, (1952), p.178, Chapman and Hall

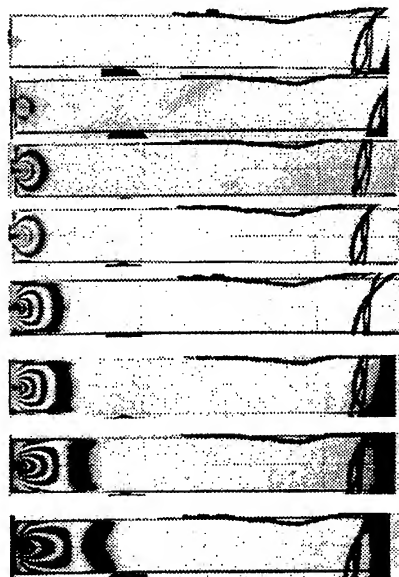


**Fig.3 30mm-wide test piece
(Pre-stationary)**

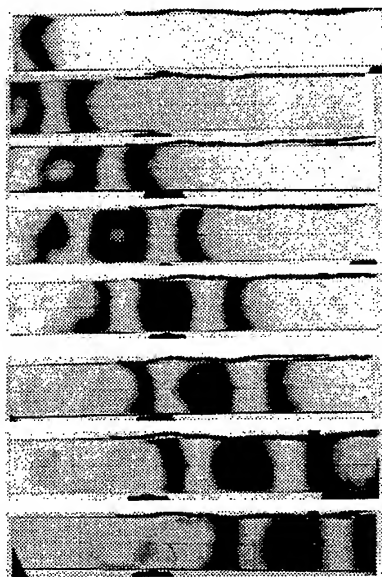


**Fig.4 30mm-wide test piece
(Stationary)**

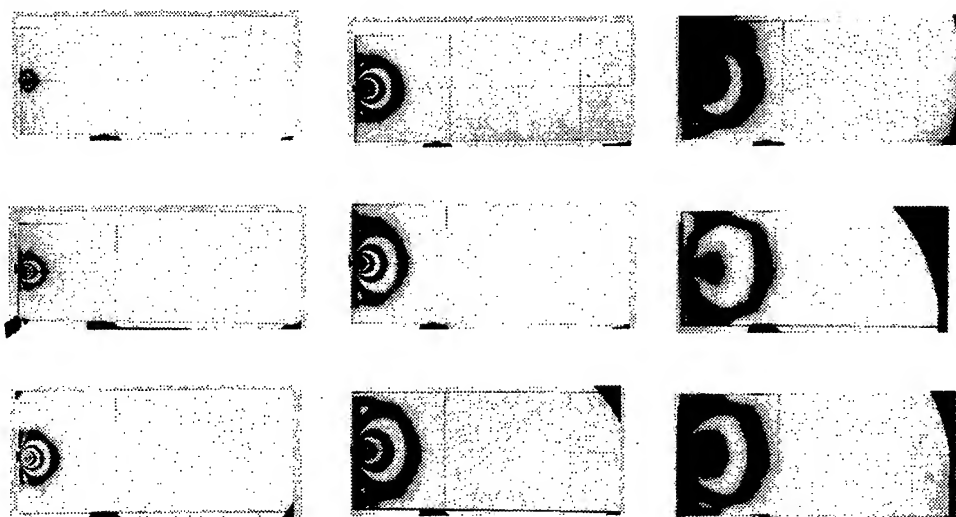


Fig.5 90mm-wide test piece (Pre-stationary)

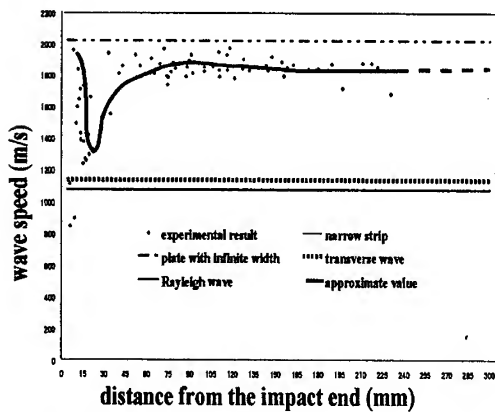


Fig.6 The relationship between wave speed and distance from the impact end of 15mm-wide plate

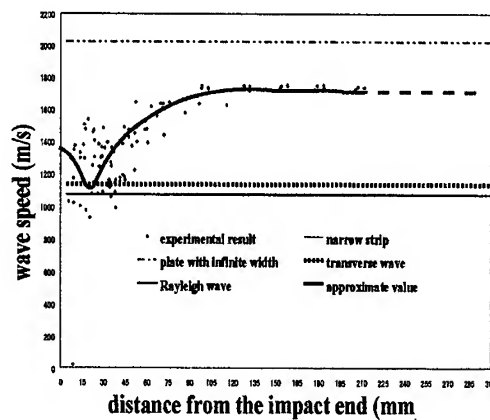


Fig.7 The relationship between wave speed and distance from the impact end of 30mm-wide plate

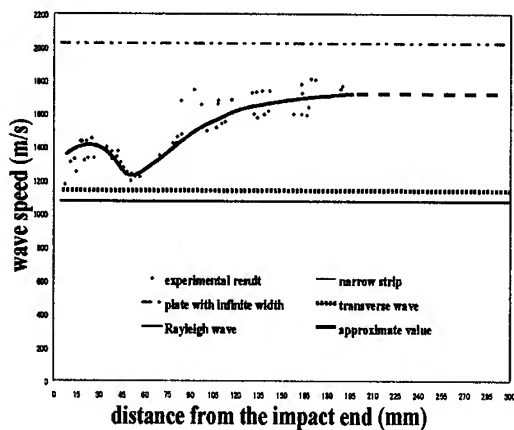


Fig.8 The relationship between wave speed and distance from the impact end of 45mm-wide plate

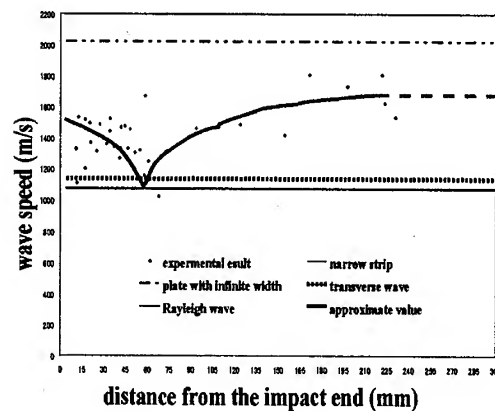


Fig.9 The relationship between wave speed and distance from the impact end of 60mm-wide plate

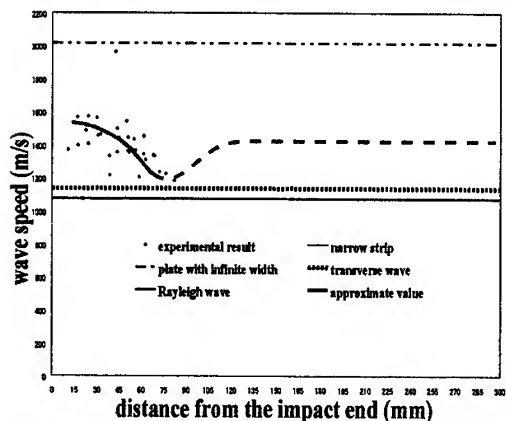


Fig.10 The relationship between wave speed and distance from the impact end of 90mm-wide plate

Using High-Speed Camera to Investigate Failure Waves in K9 Glass

Jianheng Zhao^{1,2}, Chengwei Sun^{1,2}, Zhuping Duan²,
Xianxiang Tan¹, Feng Zhao¹ and Sanggang Wen¹

¹ Institute of Fluid Physics, PO Box 919-113, Mianyang, Sichuan 621900, China P.R.

² Institute of Mechanism, Chinese Academy of Sciences, Zhongguancun,
Haidian, Beijing 100080, China P.R.

Keywords: Detonation, Failure Wave, High-Speed Shadowgraph Technique

ABSTRACT

The high-speed shadowgraph technique was used in visualization of the shock wave moving, damage formation and development in the glass specimen. It is found that failure wave formed at the shocked surface and inner interface, and propagated into specimen following the shock wave. It is concluded that formation of failure wave was connected with the surface of glass-specimen, and it is a moving fractured front. The work finished here will be helpful to understand the mechanism of failure wave.

1. Introduction

When Rasorenov and G.I.Kanel[1] researched the dynamic response of K19 glass specimen under shock loading by detonation in 1991, they found that there exists a small recompression signal in the record of rear free-surface velocity of the specimen using VISAR. They conjectured that there must have been a moving front at the velocity of 1.5-2.5 Km/s following compressive wave to propagate into the specimen, behind which the material is comminuted, and has a lower impedance and no tensile strength. This moving front was called by them as failure wave. Many researchers devoted their much efforts to this subject in recent years. But until now, failure wave was only observed in glass-like brittle materials with higher compressive strength and lower density than metals, and its mechanism is far from clear. Kanel[1], He Hongling[2] and Zhang Guanren[3] speculated on that the mechanism of failure wave connected with the micro-cracks on the surface of specimen. The experiments of different impact surface roughness can be used to test this speculation correct or not. Unfortunately, There are contrary experimental results about this topic from two independent experiments[4,5]. R.J.Clifton[6] presented a phase transformation model,

attempting to explain the mechanism of governing the generation and propagation of failure wave. This model can explain many experimental phenomena, but until now, no experiments can testify the relation between failure wave and phase transformation. Grady[7] put forward a shear failure model, his model also meet disputable points in contrary to explain the experimental observation. In this paper, we attempted to visualized the failure wave formation at the shocked surface and inner-interface of K9 glass specimens, and attempt to understand the mechanism of failure wave formation.

2. Experiment setup

Fig.1 shows the experimental setup. The detonation device of planar wave consist of detonator 10, booster 11 and planar wave lens 12. In the experiment, it takes only $1.42/1.45 \mu\text{s}$ to detonate the detonator 10. It is very important to control the synchronization of the system. The pressure behind the detonation wave is 10.78GPa before detonation wave arrive at the end of the planar wave lens. Copper plate 13 is used to let loading stress in K9 glass specimen smaller than its Hugoniot elastic limits(HEL). Table 1 shows experimental conditions.

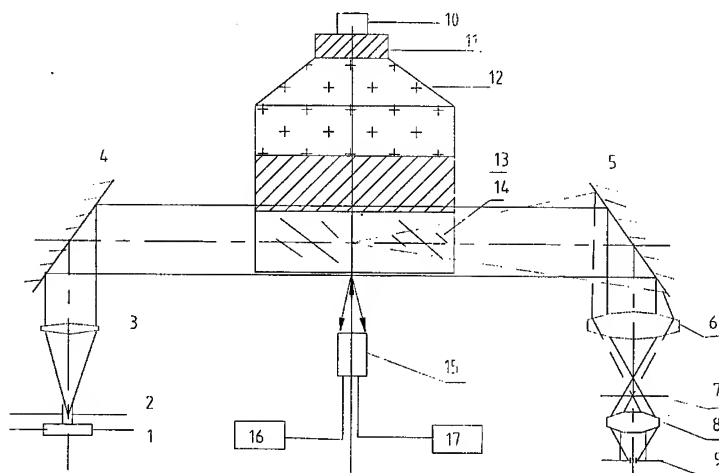


Fig.1 Experimental setup

1. Xenon discharge tube, 2. light aperture, 3. illuminating lens, 4, 5. mirror
6. First object lens 7. graticule, 8. first group of second object lenses. 9. first frame aperture of camera, 10. detonator, 11. Booster, 12 planar wave lens
13. attenuation plate, 14. K9 glass specimen, 15. VISAR probe, 16. laser, 17. VISAR

表2-1 Loading condition

No.	Thickness of copper plate /mm	Loading stress in K9 glass/ GPa	Thickness of K9 specimen /mm
1	Cu 19	8.26	24
2	PMMA(10)+ Cu(18)	5.89	6.5+24

The K9 glass specimen was cut from 24 mm or 6.5 mm thick sheets into 120X120 mm², each surface of specimen was polished. The density of K9 glass is 2.52 g/cm³, Young's modulus $E=47.14$ GPa, HEL is 8.4-9.16 GPa, Poisson rate $\nu=0.209$, and the longitudinal sound velocity is $C_l=6.06$ km/s.

The optical path of shadowgraph 1-9 used in experiment is shown in Fig.1. Xenon discharge tube is located at the focus of illuminating lens 3. When the light from Xenon discharge tube 1 pass through light aperture 2 and lens 3, it will be parallel to illuminate the specimen 14. The specimen 14 is first imaged at the graticule 7 by lens 6. The grating of the graticule can be used to quantificationally analyze. The graticule 7 is imaged on negative by lens 8 and framing lens of high-speed camera. When the refractive index in the specimen under shock loading change, it will induced the light through the specimen deflection, and lead to change of intensity of illumination on the negative. This is the working principle of shadowgraph technique.

The high-speed camera used in the experiments was FJZ 250. Its exposure time for each frame is 100ns, interframe time is 400ns, and forty frames can be recorded. The magnification of the shadowgraph system is 0.28. The field of view of this system is 74x54 mm². Its spatial resolution is about 24 lp/mm. The most of the parameters in this system is better than Bourne's[8].

3. Experimental results and analysis

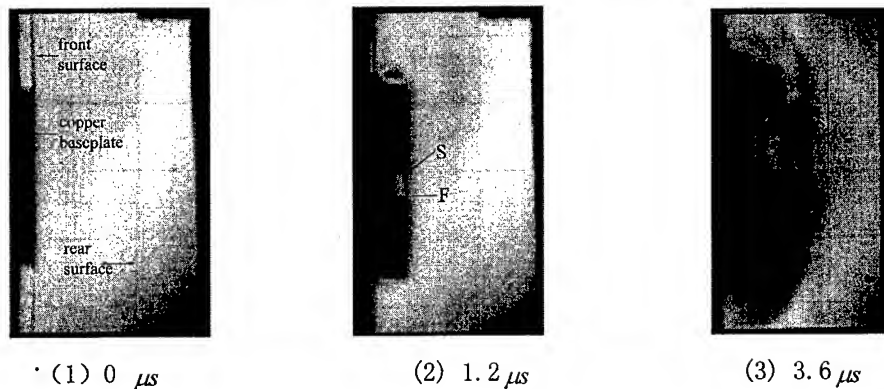


Fig. 2 Framing camera pictures of K9 glass specimen 24mm thick under detonation loading

Fig.2 shows the experimental records of No.1. The figure 2(1) is the frame in which shock wave still not propagate into glass specimen. We can found the surfaces of the specimen. The black area at the left of this frame is one part of copper plate. From Fig2(2) and (3), it is found a black shadow move into the specimen, and divided into two parts. One moves more quickly than another, and the velocity of the faster one is 5.8 ± 0.2 mm/ μ s. Its front is obviously shock wave. The front of the second shadow area is irregular, Bourne[8] speculated the irregular front is caused by cracks. It can deduced its average velocity is about 1.8 ± 0.5 mm/ μ s based its position in each frame and interframe time. Figure 3 shows the relation of velocity of rear free surface of 8.1mm thick K9 glass specimen vs. time under the same loading condition as No.1. It is obviously failure wave formed in K9 glass specimen 8.1 mm thick because there is a small velocity increase on this profile, and its velocity is 1.342 mm/ μ s. This slow moving front of shadow in fig.2 is so called failure wave, because its

velocity is almost same as that failure wave got by VISAR in Fig.3 , It is found there are irregular shadow stripes behind the shock wave front. They appear in the frame, and disappear or change in the next frame. These stripes are caused by the triangle spatial profile of pressure behind shock front. When the pressure behind shock wave changed, and lead to variety of refractive index .

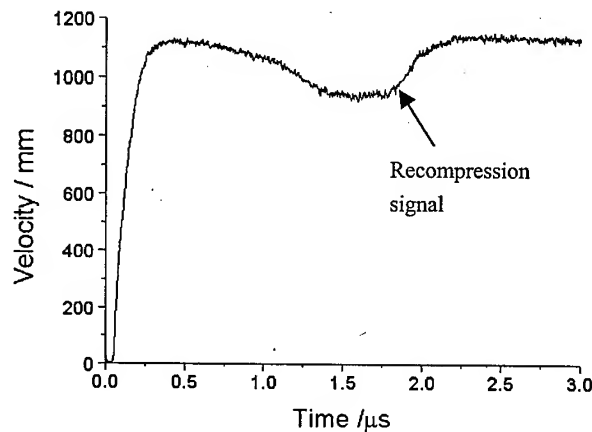
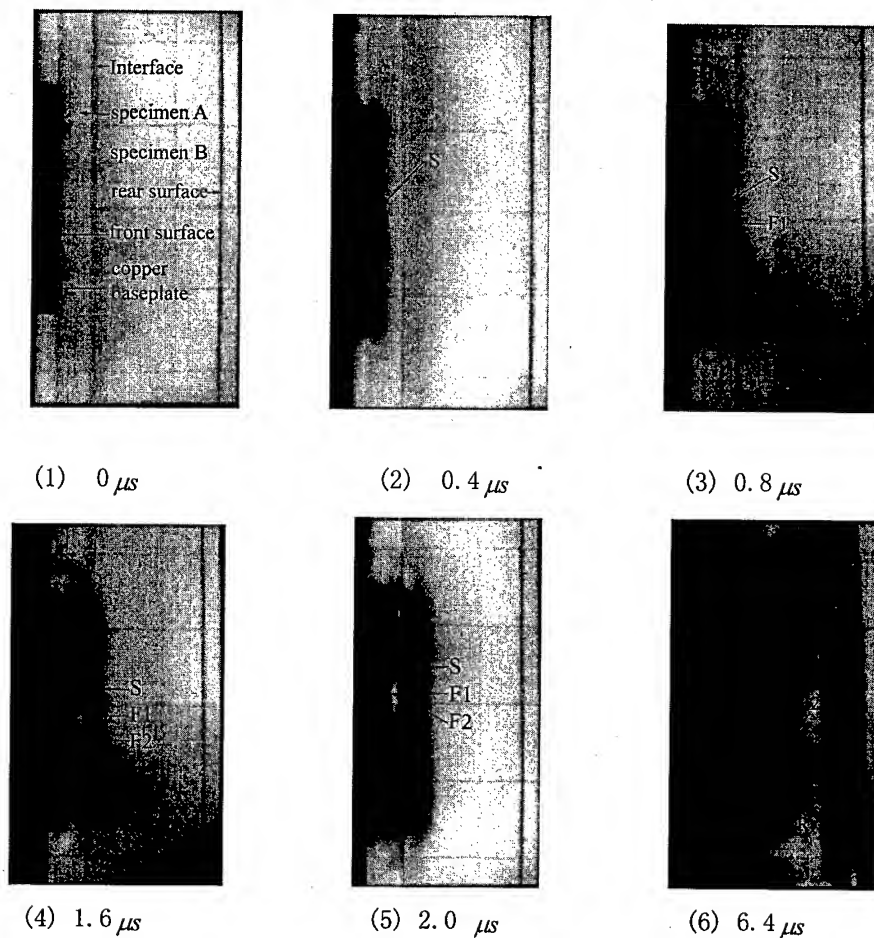


Figure 3 The velocity of rear free-surface of 8.1mm K9 glass specimen vs. time under detonation loading

Figure 4 shows the frames of double glass specimens under detonation loading. Specimen A is 6.5 mm thick, Specimen B is 24 mm. Both of these specimens are clung together. The maximum stress in specimen is 5.89 GPa in No.2 experiment. In fig.4(2), the shadow moved into specimen A from left at 0.4 μ s, and is also divided into two parts in figure4(3) at 0.8 μ s, which is same as that of figure 2. It is of course the first one is shock wave, and the second one is failure wave. In fig.3 (4) we can find another black region form at the inner interface between the two specimen at 16 μ s. This black region developed, and moving with velocity 1.6 ± 0.5 mm/ μ s behind shock front in the next frames, and its front is same as that of the failure wave in specimen A. This indicates the front of this black region is another failure wave, which formed at the interface of two specimens. It is difficult to say the mechanism of failure wave contacted with the micro-cracks on the surface of specimen or phase-transformation on the base of the failure wave formed at the impacted surface. But it can be concluded that failure wave contacted with the surface of glass specimen according to the experimental frame that another failure wave formed at the inner-interface of two glass specimens. Because if failure wave is phase-transformation wave, it ought to propagated into specimen from impacted surface into specimen, how to explain the second phase-transformation wave form at the inner-interface in the front of the first one at the same loading condition for same material. That authors reckon the formation of failure wave is contacted with the special structure of surface of glass specimen are on the base of following reasons. (1) Because the failure wave is formed at surface and inner-interface of specimens under shock wave loading, the failure wave must contacted with the surface of glass specimen. (2) The structure of surface is different from the inner for glass specimen. (3) Each surface of glass specimen has hundreds or thousands of micro-cracks per square centimeter when they were polished, even for the optical surface. The exist

of these micro-cracks lower the strength of surface of glass specimen. These micro-cracks were activated and developed into the specimen when the pressure is higher enough. When they propagated into specimen, their front is the failure wave because dynamic impedance behind of this front is lower than that in front of this front due to material comminuted.



(F1-Failure wave 1, F2-Failure wave 2, S-Shock wave, R-release wave)

Fig.4 Framing camera pictures of double specimens of K9 glass under detonation loading

4 Conclusion

Failure wave is a moving comminuted front. Its formation is connected with special structure of glass specimen and the micro-cracks on the surface.

Reference

- 1.S.V.Rasorenov, G.I.Kanel ,V.E.Fortov and M.M.Abasehov, High Pressure Research, Vol.6. (1991),p.225-232,
2. Zhang Guanren, Chinese Journal of high pressure physics, , 10(1997),p.1

3. He Hongliang, dynamic response and microstructure damage of brittle materials under shock wave loading. A dissertation in partial fulfillment of requirements for the degree of PH.D, Southwest Institute of fluid physics, 1997.
4. Neil Bourne, J. Appl. Phys. Vol 81 (1997), p. 6670-6674,
5. G.F. Raiser, et al. D.E. Grady and D.E. Cox, J. Appl. Phys. 75 (1994), p. 3862-3870
6. R.J. Clifton, Appl. Mech. Rev. 46 (1993), p. 540-546
7. D.E. Grady, NTIS, 1994
8. N.K. Bourne et al., Journal De Physique IV, Vol. 4, Colloque C8, (1994), p. 635-640,

A Study on Dynamic Fracture in Stiffened Cylinder Subjected to a Strong Acoustic Wave

E. Kim¹, H.L. Yin², K.S. Kim¹, C.H. Jo¹, O.S. Lee² and C.W. An³

¹Department of Naval Architecture and Ocean Engineering, Inha University,
253 Yonghyun-dong, Nam-gu, Incheon 402-751, Korea

²Department of Mechanical Engineering, Inha University,
253 Yonghyun-dong, Nam-gu, Incheon 402-751, Korea

³Agency for Defense Development, Korea

Keywords: Caustic Curve, Dynamic Photoelasticity Method, Dynamic Stress Intensity Factor, Fluid-Structure Interaction, Stress Wave Propagation

ABSTRACT

The analysis of dynamic fracture of ships and its response by shock wave caused by the non-contact underwater explosion is very important in the design of reliable marine vessels.

In this study, a dynamic fracture analysis of a ring-stiffened cylinder subjected to a strong acoustic wave is carried out by two steps; the macro analysis and micro analysis. In macro analysis, the dynamic response of the structure is investigated. In micro analysis, the dynamic stress intensity factor of a pre-cracked ring stiffener is determined by the pressure time history of load which is obtained in the macro analysis. Three numerical methods determining the dynamic stress intensity factors are proposed and discussed. To check the validity of numerical analysis, numerically calculated stress intensity factors are compared with the theoretical and experimental results decided by the dynamic photoelasticity method.

1. INTRODUCTION

To improve the structural hardness of marine vessels against the shock, a clear understanding of the modes of failure and their causes is highly required. In the past, the data necessary for failure modes and the physics to failure have been obtained through process of underwater shock tests. However, this process is very costly and extremely limited to certain conditions. Therefore it is strongly recommended to develop an accurate numerical simulation technique. Recently researchers have applied commercial software to perform shock response analysis of structure subject to underwater explosion loads[1, 2]. But the numerical study on the dynamic fracture of the structural members by underwater explosion loads is rarely performed, because of the large numerical model size and lengthy computational time.

To investigate the dynamic fracture of a ring-stiffened cylinder under a strong acoustic wave, the two procedures are applied such as the macro and micro analyses. To confirm the validity of the analyses the stress intensity factor determined by the numerical approaches is compared with the theoretical value[3]. The dynamic stress intensity factors for I-form stiffener with inclined crack are numerically calculated and compared with the dynamic photoelasticity method.

2. THE COMPARISON OF THEORETICAL ANALYSIS

To confirm the validity of numerical calculation of dynamic stress intensity factor, the cracked rectangular plate by the plane step load is selected since the problem has the analytic solutions[3]. To calculate the dynamic stress field of the cracked plate, the MSC/NASTRAN is applied. The mode I dynamic stress intensity factors K_I at the crack tip are calculated using by the numerically simulated caustic method[4], the stress gradient method[5] and the CRAD2D of MSC/NASTRAN.

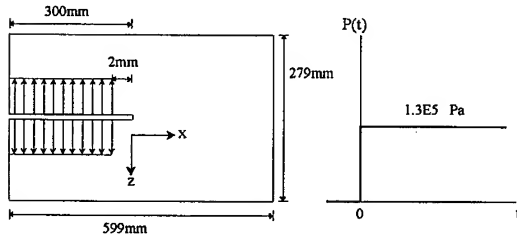


Fig. 1 Model geometry and loading history

Fig. 2 shows numerically simulated caustics. The dynamic stress intensity factors are shown in Fig. 3. The dynamic stress intensity factors calculated by numerical caustic method and stress gradient method agree well with theoretical result. But the K_I -values obtained by CRAC2D are lower than the others.

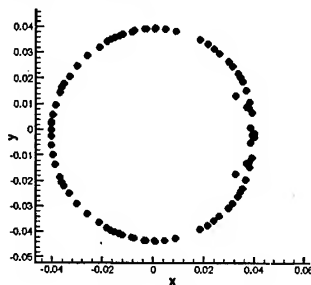


Fig. 2 Simulated caustic curve [110 μ sec]

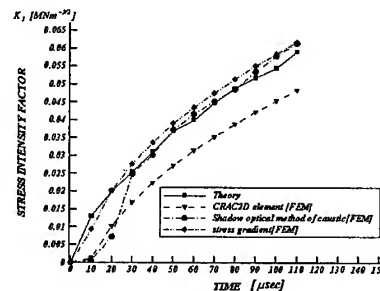


Fig. 3 Comparison of dynamic stress intensity factor

3. COMPARISON OF EXPERIMENT

The dynamic stress intensity factor was calculated by numerical analysis for the inclined crack in I-form stiffener subject to free fall impact loading. The K_I -values are compared with the dynamic photoelastic method.

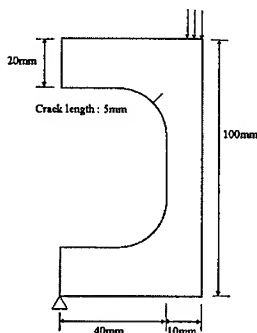


Fig. 4 Experiment model

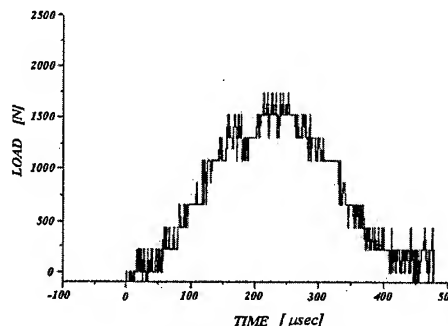


Fig. 5 Free fall loading

The analyzed model geometry and free fall loading are shown in Figs. 4 and 5. The polycarbonate was used as specimen material.

3.1. The dynamic photoelasticity method

The dynamic photoelasticity method is applied which consisted of the Cranz-Shardin camera system with a multi-spark camera set, a dynamic photoelastic apparatus, a loading equipment, field lens and controllers.

Fig. 6 shows a typical stress field at the around of the dynamically loaded crack tip in the specimen shown in Fig. 4.

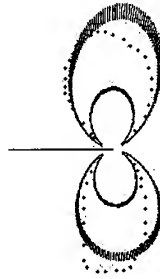


Fig. 6 Dynamic isochromatics Fig. 7 Experimental(dotted) and theoretical isochromatics loops

The Newton-Raphson method and over-deterministic least square method(OLSM) are applied to extract the dynamic stress intensity factors. The isochromatics are generated with the extracted dynamic stress intensity factors as shown in Fig.7.

3.2. Comparison numerical analysis with experiment

The dynamic stress fields of I-form stiffener were numerically analyzed by using MSC/NASTRAN. To compare with the experiment, the identical geometry, material properties, dynamic loading history were adapted. The analyzed stress fields were used to calculate dynamic stress intensity factors. The numerical caustic curve is shown in Fig.8. Because this model has a inclined crack from the free fall load, under the tensile and shear loadings to crack tip the numerical caustic reveals the mixed shape.

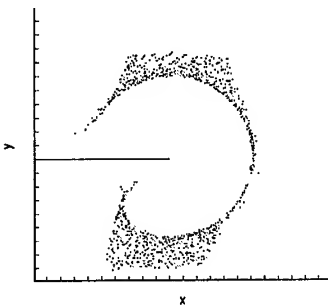


Fig. 8 Numerical caustics curve [91μ sec]

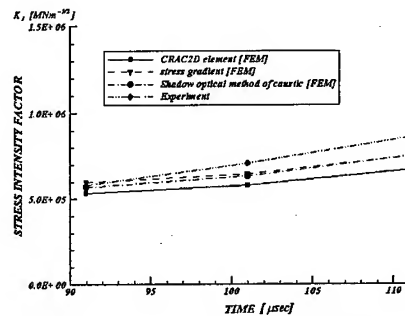


Fig. 9 The comparison of dynamic stress intensity factors

From numerical caustics curve, it is confirmed that loading state is mixed mode condition[6].

Fig. 9 shows comparison of dynamic stress intensity factors. The numerical results are similar to each other except the results by CRAC2D element of MSC/NASTRAN. The experiment is shows somehow larger values than others. It seems that the free fall tup applied to the specimen incorrectly to experiment may cause some error.

4. DYNAMIC FRACTURE ANALYSIS OF STIFFENED CYLINDER

4.1. Macro analysis

In the shock response analysis of ring-stiffened cylinder subject to spherical acoustic wave was carried out by the MSC/DYTRAN. This hydrocode has been also utilized in underwater explosion problems which yields a good agreement with analytic and experimental results[7, 8]. The model geometry and size of the ring-stiffened cylinder are as shown in Fig. 10 and Table 1. The ring-stiffened model is under a side-on explosion of 1kg TNT. And the standoff distance is 7m. The cylinder and the end plate have been modelled with Lagrangian quad shell elements. The ring stiffeners are attached to the beam element by adjusting sectional properties of the beam. Since the general coupling technique is used for fluid-structure interaction, dummy elements have been used for wrapping around the cylinder which is placed inside the Eulerian mesh. Because the charge is located at the middle of the cylinder over the centerline, a quarter symmetry can be used. The model of the macro analysis is introduced in Fig. 11. The material properties of cylinder are $\rho = 7840 \text{ kg/m}^3$, $\nu = 0.32$, and $E = 200 \times 10^9$.

Table 1 Model size

Radius of Cylinder	Length of Cylinder	Thickness of Cylinder	King Frame	Ordinary Frame	Frame space (King/Ordinary)
3 m	15 m	20 mm	500x12/200x30	180x12/90x20	5000mm/500mm

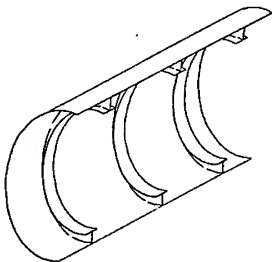


Fig. 10 Model geometry

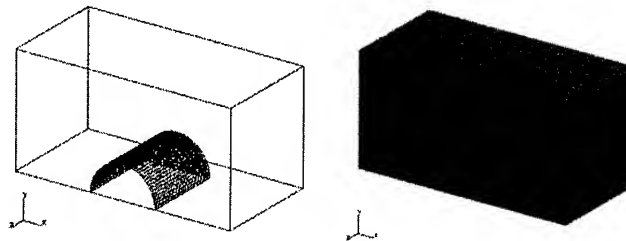


Fig. 11 Stiffened cylinder model

The results of the macro analysis are presented in Fig. 12 and Fig. 13. The shock wave produced by underwater explosion is transmitted through the water medium and attack the cylinder. Fig. 12 is the fringe illustration of the position of the shock wave at 4.2msec. The shock wave impacts the cylinder and it causes local deformation and stress wave at side of the cylinder. Fringe plot of effective stress at 4.2msec is seen from Fig. 12. Fig. 13 shows the propagation of stress wave through the cylinder.



Fig. 12 Computed shock wave at 4.2 [ms]

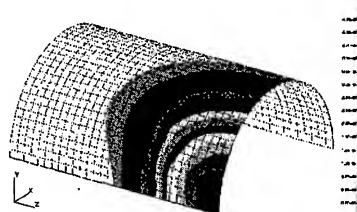


Fig. 13 Effective stress at 4.2 [ms]

4.2. Micro analysis

In the micro analysis, a dynamic stress intensity factor was numerically calculated in a cracked I-form ring stiffener under impact loading obtained from the macro analysis. The model geometry and loading profile were shown in Fig. 14.

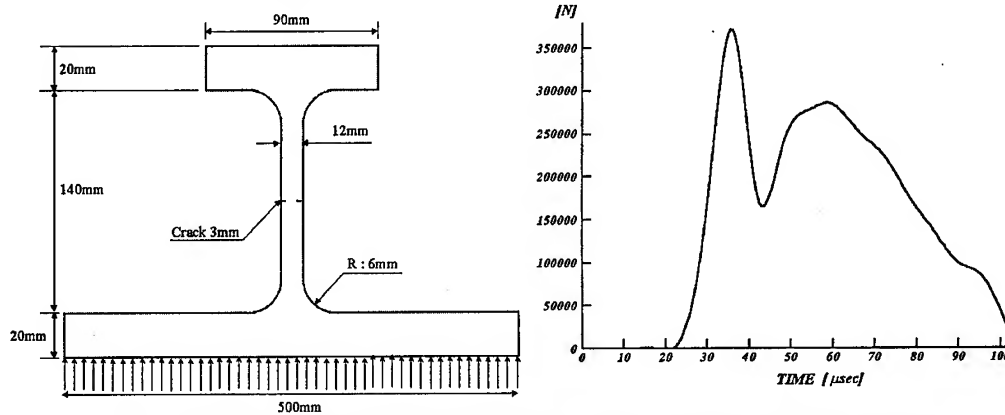


Fig. 14 Cracked I-form stiffener and impact loading as results of macro analysis

As a result, isochromatic fringe plotted of the maximum shear stress and numerically simulated caustics curve is shown in Fig.15. The stress wave is propagated through stiffener and as compressive wave encounters free surface, it reflects back as a tensile wave. The compressive wave and tensile wave are superposed in the time-step shown in Fig. 15

The numerically simulated caustic curve revealed mode I loading condition by tensile wave and the isochromatic fringe showed as the butterfly shape at the crack tip.

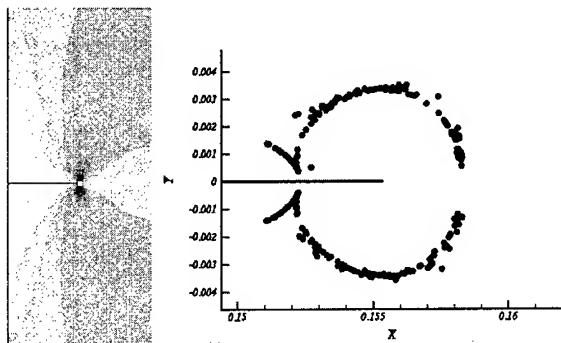


Fig. 15 Isochromatic fringe and numerical caustic curve [160μ sec]

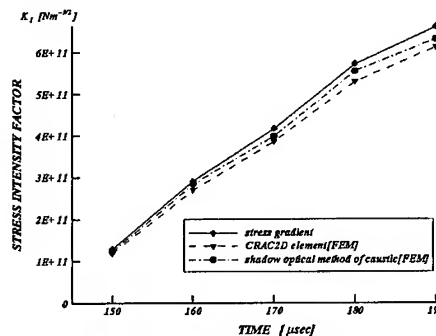


Fig. 16 Comparison of dynamic stress intensity factor

The comparison of dynamic stress intensity factor is shown Fig. 16. The results show a good agreement.

However, the output by CRAC2D of MSC/NASTRAN indicate little lower than others.

6. CONCLUSION

Dynamic fracture analysis of stiffened cylinder subjected to underwater explosion was investigated by two steps ; the macro and micro analyses. In the macro analysis, a shock response analysis of ring-stiffened cylinder subjected to spherical acoustic wave was carried out using MSC/DYTRAN. In the micro analysis, a dynamic stress intensity factor was numerically calculated for the cracked I-form ring stiffener under the impact load. In order to verify of numerical analysis, theoretical and experiment results were compared with those by numerical analysis.

The dynamic stress intensity factor is calculated by the numerical simulated caustics, stress gradient method and CRAC2D element of MSC/NASTRAN. The numerical results were similar to experiment and theoretical results.

It is observed in the study that the simulation from the CRAC2D element of MSC/NASTRAN indicate consistently lower magnitude of the dynamic stress intensity factor than other approaches.

REFERENCES

1. Kwon, Y. W., Fox, P. K., Computers & Structures, Vol. 48, No.4, 1993
2. Marco, J., Proceedings of the 67th Shock & Vibration Symposium, 1989.
3. Kim, K. S., Journal of Applied Mechanics, Vol. 52, 1985, pp.585-592.
4. Kim, K. S., VDI Verlag, Reihe 18, Nr.91, 1991
5. Kim, K. S., Kim, E., Proceedings of the Annual Spring Meeting, the Society of Naval Architects of Korea, 1999.4, pp. 431-434.
6. Kobayashi, A. S., *Handbook on Experimental Mechanics*, PRENTICE-HALL, INC.,1987.
7. Lenseink, H., de Vreis, E., 1994 MSC World Users' Conference, 1994.
8. Chisum, J. E., Shin, Y. S., ASME PVP-Vol. 299, 1995.

Static and Mode Analyses of Composite Plates Using Modified 16-Node Solid Elements, and Prediction of Stiffness Errors Resulting from Reduced Integration

Y.D. Kwon¹, Y.S. Kim¹, T.H. Yun² and M.H. Cho³

¹Department of Mechanical Engineering, Kyungpook National University, Taegu 702-701, Korea

²Department of Mechanical Design, Kumi College, Kumi 730-170, Korea

³Graduate School, Kyungpook National University, Taegu 702-701, Korea

Keywords: Composite Plate, Errors of the Reduced Integration, Gauss Sampling Point, Mode Analysis, Modified 16-Node Solid Element, Static Analysis

ABSTRACT

In this paper, an equation for sampling point modification is derived which can correct the stiffness stiffening phenomena in a composite plate. This stiffening phenomena is corrected by modifying Gauss sampling points in the numerical integration of stiffness matrix. The stiffness is assumed to be a quadratic function, thereby enabling the prediction of the errors caused by reduced integration. This assumption is confirmed through a comparison of the predicted and actual errors.

1. INTRODUCTION

A 16-node solid element exhibits a relative stiffening effect with respect to 20-node element in bending problems. The stiffening effect can be resolved by using modified sampling points in a numerical quadrature. A modified 16-node solid element which uses translated Gauss sampling points is considered. The Gauss sampling points of 16-node element are modified in thickness direction that produces an accuracy very close to that of a 20-node element. To accomplish this object, modification equations of 16-node solid elements for composite plates are derived. Various examples are used to confirm the validity of these modification equations.

2. MODIFICATION OF GAUSS SAMPLING POINTS

To derive the modification equation of 16-node elements modeling a composite laminate, the 2-D bending deformation of 8-node element in x-z plane is considered as in Fig.1. This state is assumed to be in a plane stress condition. Thereafter, the stress-strain relation can be obtained as in Eq.1.

$$\begin{bmatrix} \sigma_x \\ \sigma_z \\ \tau_{xz} \end{bmatrix} = [D] \{\varepsilon\} = \begin{bmatrix} \overline{D}_{11} & \overline{D}_{12} & 0 \\ \overline{D}_{21} & \overline{D}_{22} & 0 \\ 0 & 0 & \overline{D}_{33} \end{bmatrix} \begin{bmatrix} \varepsilon_x \\ \varepsilon_z \\ \gamma_{xz} \end{bmatrix} \quad (1)$$

Where, $[D_{ij}]$ is a material property matrix.

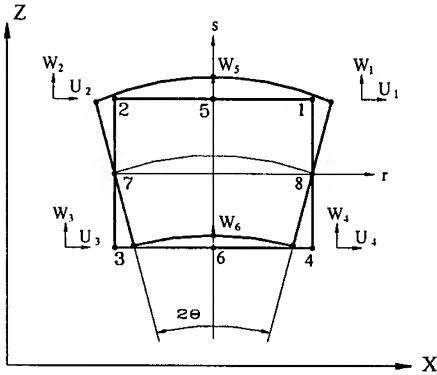


Fig.1 8-node composite plane stress element under pure bending

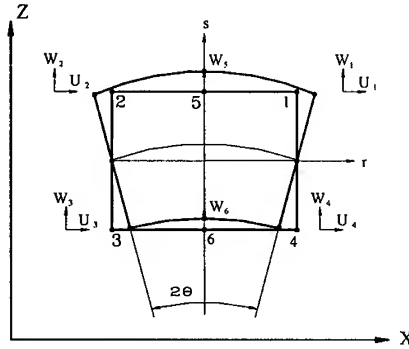


Fig.2 6-node composite plane stress element under pure bending

Equivalent nodal forces of the 8-node element in pure bending deformation are expressed as in Eq.2.

$$\{F_8\}_{x-z} = \sum_{k=1}^{NL} \sum_{i=1}^N \sum_{j=1}^N [B_s]^T [D] [B_s] [U]_s \cdot J W_{ki} W_{kj} h_k b_k / h \quad (2)$$

Where, N = the order of integration, k = the layer number, NL = the number of layers, h_k = the thickness of the k th layer, b_k = the width of the k th layer, W_{ki} or W_{kj} = the weight factor of the Gauss sampling point, $\{U_s\}$ denotes the displacement vector.

By using stress and displacement vector, Eq.2 can be rearranged to Eq.3.

$$\{F_8\}_{x-z} = \sum_{k=1}^{NL} \sum_{j=1}^N \left[A \ B \ -A \ B \ A \ B \ -A \ B \ 0 \ 0 \ 0 \ -2B \ 0 \ 0 \ 0 \ -2B \right]^T t_{kj}^2 J W_{kj} h_k b_k / h$$

$$A = \theta \overline{D}_{11} - 2w \overline{D}_{12}, \quad B = 2\theta \overline{D}_{21} - 4w \overline{D}_{22} \quad (3)$$

Here, t_{kj} is the sampling point of the k th layer, θ = the rotation angle, J is the Jacobian determinant, and w represents the vertical deflection of node 7 or 8. In a case of pure bending, the z -directional nodal forces should be zero. Therefore, the relation, $2\theta \overline{D}_{21} - 4w \overline{D}_{22} = 0$ should be satisfied, so $w = \theta \overline{D}_{21} / (2\overline{D}_{22})$. By inserting this value into Eq.3, one can obtain Eq.4.

$$\{F_8\}_{x-z} = \sum_{k=1}^{NL} \sum_{j=1}^N \left[\theta C \ 0 \ -\theta C \ 0 \ \theta C \ 0 \ -\theta C \ 0 \ 0 \ 0 \ 0 \ 0 \ 0 \ 0 \ 0 \right]^T t_{kj}^2 J W_{kj} h_k b_k / h$$

$$C = D_{11} - D_{12} D_{21} / D_{22} \quad (4)$$

Meanwhile, the equivalent nodal forces of the 6-node element in a pure bending deformation(Fig.2) can be expressed as in Eq.5.

$$\{F_6\}_{x-z} = \sum_{k=1}^{NL} \sum_{i=1}^N \sum_{j=1}^N [B_6]^T [D] [B_6] [U]_6 J W_{ki} W_{kj} h_k b_k / h \quad (5)$$

Eq.5 can be rearranged into Eq.6.

$$\{F_6\}_{x-z} = \sum_{k=1}^{NL} \sum_{j=1}^N \frac{1}{2} [\overline{\theta D_{11}} \quad 0 \quad -\overline{\theta D_{11}} \quad 0 \quad \overline{\theta D_{11}} \quad 0 \quad -\overline{\theta D_{11}} \quad 0 \quad 0 \quad 0 \quad 0 \quad 0]^T t_{kj}^2 J W_{kj} h_k b_k / h \quad (6)$$

For equal deformation energies for the bending of the 6-node and 8-node elements in the x-z plane, the following force equilibrium must be satisfied.

$$\{F_6\}'_{x-z} = \{F_8\}_{x-z} \quad (7)$$

Here, $\{F_6\}'_{x-z}$ is $\{F_6\}_{x-z}$, the dimension of which is expanded to the size of $\{F_8\}_{x-z}$. From the equilibrium in Eq.7, one can obtain the modification of the Gauss sampling points as in Eq.8, where t_{k16j} and t_{k20j} denote the sampling points of the kth layer of a 16-node element and that of 20-node element, respectively.

$$t_{k16j} = t_{k20j} [1 - \overline{D_{12}} \overline{D_{21}} / (\overline{D_{11}} \overline{D_{22}})]^{1/2} \quad (8)$$

To recover the wrong effect on torsional mode, an additional modification equation, Eq.9, is needed along with Eq.8.

$$G_{(16)12k} = G_{(20)12k} / [1 - \overline{D_{12}} \overline{D_{21}} / (\overline{D_{11}} \overline{D_{22}})] \quad (9)$$

Here, $G_{(16)12k}$ denotes the modified shear modulus of the kth layer in the 1-2 plane used in a 16-node element, and $G_{(20)12k}$ denotes the original shear modulus of the kth layer in the 1-2 plane used in a 20-node element.

3. REDUCTION OF THE QUADRATURE IN LAMINATED COMPOSITE PLATES

One of the authors of this paper has already shown^[1] that part of the stiffness $[K_{NL}]$ can be evaluated by an order 1 quadrature in the thickness direction. Accordingly, it is assumed that the remaining part of the stiffness, $[K_L]$ varies quadratically in the thickness direction. When an orthogonally layered composite $(0/90\dots)_s$ is considered, the integrand is assumed to be $F(x) = a E_k X^2$. Then the analytical result can be given as in Eq.10.

$$\int_{-h/2}^{h/2} F(x) dx = \frac{1}{12} W_1 a E_1 h^3 + \frac{1}{12} W_2 a E_2 h^3 \quad (10)$$

Where, W_1, W_2 are weight factor depending upon specific layering scheme, E_1 and E_2 are elastic coefficients of the k th layer. The relative error of reduced integration for $[K_L]$ of a composite laminate can be obtained as follows.

$$\text{error} = \left\{ W_1 (E_1 h^3 / 12) + W_2 (E_2 h^3 / 12) - \sum_{i=1}^{NL} h_k E_k X_k^2 \right\} / \left\{ W_1 (E_1 h^3 / 12) + W_2 (E_2 h^3 / 12) \right\} \quad (11)$$

4. NUMERICAL EXAMPLES AND DISCUSSIONS

4.1. Static Analyses of Pure Bending Isotropic Plate^[2]

The length to thickness ratio of the plate (Fig.3) was 100, and the linear and geometrically nonlinear analyses were performed using 5 elements of a 16-node or 20-node element. The results are plotted in Fig.4. In this case, the Poisson's ratio was 0.2 and the quantity of modification was 2.0%. The results for the conventional element had 4.1% linear errors and 3.8% nonlinear errors. Meanwhile, the results for the modified elements had only 0.13% linear errors and 0.16% nonlinear errors.

4.2. Static Analyses of Four-Layer Composite Plate

The material properties of each lamina are given in Table 1 and the stacking sequences are shown in Table 2. The dimension is 300x50x3.2 (mm), and it is subjected to a tip load. The plate is discretized into 10 elements. In Table 2, the results of the conventional 16-node and modified 16-node element models are compared with those of the 20-node element model.

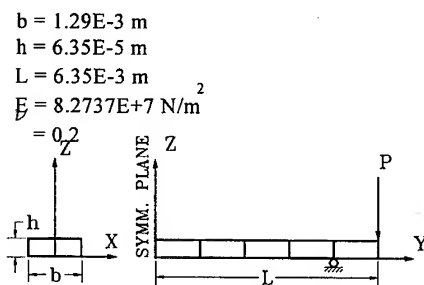


Fig.3 Finite element model of pure bending plate under end load

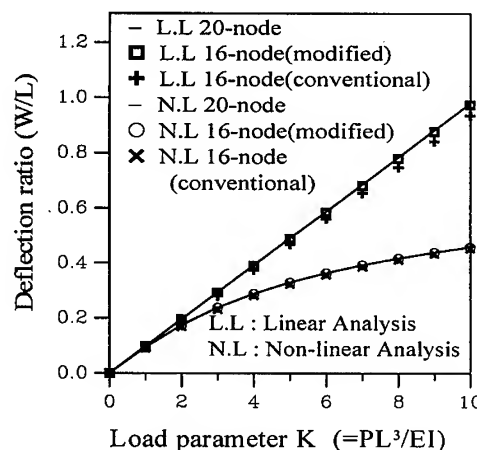


Fig.4 Static linear and nonlinear deflection of cantilever plate under end load ($L/h = 100$)

For the unidirectional lamina, some case $(0/90)_s$ needed almost no modification, whereas others $(90/90)_s$ definitely needed modification, depending on the stacking sequences. For the woven lamina, the orthogonally woven in-plane fibers resulted in quasi-isotropy and small

quantities of modification. Thus, the modification is not necessary, in essence. The case of braided composite is quite similar to isotropic case, and modification is inevitable to produce reasonable results.

Table 1 Material properties of composite laminae in static analysis

Properties		E_{11} (Gpa)	E_{22} (Gpa)	E_{33} (Gpa)	G_{12} (Gpa)	G_{13} (Gpa)	G_{23} (Gpa)	ν_{12}
Lamina								
A	Unidirectional	132.4	10.8	10.8	5.7	5.7	3.6	0.24
B	Woven	132.4	132.4	10.8	55.2	5.7	5.7	0.20
C	Braided	120.0	120.0	120.0	48.0	48.0	48.0	0.25

Table 2 Comparison of the deflections of modified and conventional 16-node models with the result of 20-node models

Type of Layer	Element Layer	Displacements		
		20-Node Model	Conv. 16-Node (Error %)	Mod. 16-Node (Error %)
Unidirectional Lamina	(0/90)s	0.4896	0.4837 (1.2)	0.4879 (.34)
	(90/0)s	2.0959	1.9011 (9.3)	2.1022 (.30)
	(45/-45)s	2.4280	2.2910 (5.6)	2.4590 (1.3)
	(90/90)s	4.4390	3.6220 (18.)	4.4380 (.016)
Woven Lamina	(0/0)s	0.4320	0.4297 (.51)	0.4317 (.042)
	(45/45)s	0.4319	0.4297 (.51)	0.4317 (.042)
	(0/90)s	0.4319	0.4297 (.51)	0.4317 (.042)
Braided Lamina	(0/0)s	2.6620	2.4820 (6.8)	2.6460 (.61)

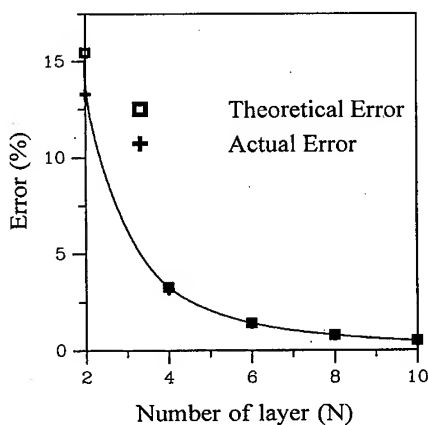


Fig.5 Integration errors(order 1) of isotropic composite plates in mode analysis

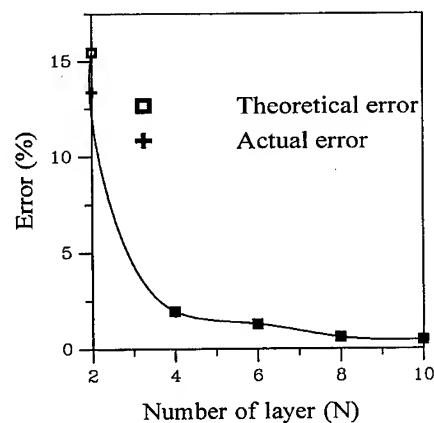


Fig.6 Integration errors (order 1) of orthotropic composite plates in mode analysis

5. REDUCTION OF ORDER OF QUADRATURE IN MULTILAYERED COMPOSITES

The predicted errors based on this assumption were then compared with the actual errors in Fig.5 for isotropic plates, and in Fig.6 for orthotropic composite plates.

The material properties of these laminae were given in Table 1. The actual errors are calculated from the results of an order 1 reduced integration and an order 3 full integration, in the thickness direction. For both the isotropic and orthotropic mode analyses, the predicted errors agreed well with the actual ones.

5.1. Verification of Modification Equations in Mode Analyses

To verify the two modification equations, a 3-layered(90/0/90) model cantilever plate of 300x50x3.2(mm) was discretized into 10 elements and analyzed. The material properties are $E_{11} = 172.7\text{GPa}$, $E_{22} = E_{33} = 7.20\text{GPa}$, $G_{12} = G_{13} = 3.76\text{GPa}$, $\nu_{12} = \nu_{13} = 0.30$, $\nu_{23} = 0.50$, $\rho = 1551 \text{ kg/m}^3$.

Table 3 Comparison of the results of 16-node elements with the results of 20-node element

Mode Number	Element(Error %)			
	20-Node	Conv. 16-Node	Mod. 16-Node Eq.8	Mod. 16-Node Eq.8,9
1st	107.7	116.8(8.5)	107.8(.09)	107.8(.09)
2nd	300.3	325.0(8.2)	291.4(3.0)	300.2(.03)
3rd(torsional)	333.3	333.7(.12)	300.2(9.9)	333.5(.06)
4th	600.0	647.0(7.8)	598.0(.33)	598.1(.34)
5th(torsional)	683.0	686.3(.48)	601.1(12.)	683.4(.06)

In Table 3, the results of conventional 16-node element showed a substantial error in the 1st, 2nd, and 4th mode, and the modified 16-node element(modification of Gauss sampling points only) showed a substantial error in the torsional(2nd mode and 3rd) mode. The results of the 16-node element which applied the modification equation and material properties showed a very close result to that of the 20-node element.

6. CONCLUSIONS

1) The modification equation of the Gauss sampling points was derived for the 3-dimensional 16-node element of a composite plate. The effectiveness was verified by comparing the static and mode analysis results of 20-node element those of the modified and conventional 16-node element.

2) In the static and mode analyses of composite plates, the errors in the stiffness evaluation that resulted from the reduced integration could be predicted as a function of the number of layers.

REFERENCES

1. Y.D. Kwon, J.M. Choi, "Linear and nonlinear analysis of initially stressed elastic solid", J. of KSME Vol.12 (1988) pp. 642-651
2. J.O. Kim, Y.D. Kwon, "On the Modification of Gauss Sampling Points of 6-Node and 16-Node Isoparametric Finite Elements", Computers and Structures, Vol. 63 (1995) pp. 607-623

Shape Optimization of General Structures

S.Y. Han and J.S. Maeng

School of Mechanical Engineering, Hanyang University,
17 Haengdang-Dong, Sungdong-Ku, Seoul 133-791, Korea

Keywords: Distributed Parameter, Growth-Strain Method, PID Control, Shape Optimization, Stress Control, Volume Control

ABSTRACT

Growth-strain method was used for general two and three dimensional shape optimization. It was verified in previous papers that the growth-strain method is very effective for shape optimization of structures with only one free surface to be deformed. However, it could not provide reasonable optimized shape for structures with two or more free surfaces such as structures with holes inside. Problems occurred, as the growth-strain method was applied to structures with two or more free surfaces, were investigated. Accordingly, an improved method was suggested. The effectiveness and practicality of the improved method was verified by some examples.

1. INTRODUCTION

The optimization techniques can be classified into three categories, namely sizing [1,2], shape [3,4] and topology [5,6] according to the characteristics of the design variables and formulation. Most of the optimization techniques which have been reported regarding the shape optimization are based on the mathematical programming method. The optimization techniques perform the optimization by boundary parameterization and design sensitivity analysis. Therefore, many calculations and a large memory for optimization are inevitable.

Recently, the growth-strain method [7,8], which is not based on the mathematical programming method, has been proposed. Hence, the shape of the maximum strength or the maximum stiffness can be designed by the method without boundary parameterization and sensitivity analysis. The growth-strain method has successfully been applied to shape optimization of two or three-dimensional structures without a hole inside or with only one deformable free surface even though there is a hole inside. But when this method is applied to structures with two or more deformable free surfaces, a valid optimal shape, such as the shape obtained by the mathematical programming

method, cannot be obtained.

In this paper, the problems occurred, as the growth-strain method was applied to structures with two or more deformable free surfaces, were examined. Accordingly, an improved method was suggested. The validity and the practicability of the improvement of the method for a structure with two or more deformable free surfaces were also verified.

2. THE GROWTH-STRAIN METHOD

The growth-strain method optimizes a shape by generating the bulk strain to make the distributed parameters uniform. The optimization consists of a two-step iteration. The first step is a standard stress analysis to estimate the distributed parameter under mechanical conditions. The second step is a growth analysis to calculate the growth displacement or the shape modification based on the generation law of the bulk strain under shape constraint conditions. Analysis at each step is performed by the finite element method.

If the distributed parameter is defined as quantity per unit volume or area such as Von Mises stress, the distributed parameter generally has the property of decreasing with the increase in volume in a local infinitesimal volume. Therefore, the bulk strain is generated as a function of the distributed parameter due to the following growth law of equation (1) to modify the shape so that the distributed parameters are uniform. The contracting bulk strain is generated where σ is less than $\bar{\sigma}$, while the expanding bulk strain is generated where σ is greater than $\bar{\sigma}$ in all elements.

$$\varepsilon_{ij}^B = \frac{\sigma - \bar{\sigma}}{\bar{\sigma}} \delta_{ij} h \quad (1)$$

where, ε_{ij}^B is the bulk strain, σ is the distributed parameter (Von Mises stress), $\bar{\sigma}$ is the basic value (for example, the average stress or the maximum stress) of the parameter, δ_{ij} is the Kronecker delta and h is the growth rate, which adjusts the magnitude of the growth deformation

and is an arbitrary coefficient to be $h \ll 1$.

Assuming that a material is a thermal isotropy, the thermal strain generated is a bulk strain without shearing components. Hence, the thermal strain can be defined with the similar eq. (2) to that of the growth analysis.

$$\varepsilon_{ij}^T = \alpha \Delta T \delta_{ij} \quad (2)$$

When a designer establishes the objective volume, eq. (3) modified the growth law of eq. (1) by applying the PID control theory. When a designer establishes the objective stress, eq. (5) is applied. Therefore, volume and stress can be controlled effectively by eqs. (3)-(5), respectively.

$$\varepsilon_{ij}^{B(n)} = \frac{\sigma^{(n-1)} - \bar{\sigma}^{(n-1)}}{\bar{\sigma}^{(n-1)}} \delta_{ij} h - \left\{ K_p \frac{V^{(n-1)} - V_{obj}}{V_{obj}} + K_I \sum_{k=1}^{n-1} \frac{V^{(k)} - V_{obj}}{V_{obj}} + K_D \frac{V^{(n-1)} - V^{(n-2)}}{V_{obj}} \right\} \quad (3)$$

$$\bar{\sigma}^{(n-1)} = \sum_e \frac{\sigma_e v_e}{V^{(n)}} \quad (4)$$

$$\varepsilon_{ij}^{B(n)} = \frac{\sigma^{(n-1)} - \sigma_{obj}}{\sigma_{obj}} \delta_{ij} h + \left\{ K_p \frac{\sigma_{\max}^{(n-1)} - \sigma_{obj}}{\sigma_{obj}} + K_I \sum_{k=1}^{n-1} \frac{\sigma_{\max}^{(k)} - \sigma_{obj}}{\sigma_{obj}} + K_D \frac{\sigma_{\max}^{(n-1)} - \sigma_{\max}^{(n-2)}}{\sigma_{obj}} \right\} \quad (5)$$

where (n) is the number of the n th iteration, K_p , K_I , K_D are proportional constants, v_e is the volume of each element, σ_e is the representative stress of each element, V_{obj} is the objective volume, $V^{(n)}$ means the total volume of the n th iteration, σ_{obj} is the objective stress, and $\sigma_{\max}^{(n)}$ is the maximum stress of the n th iteration.

3. IMPROVEMENT OF THE GROWTH-STRAIN METHOD

The Growth-strain method has successfully been applied for shape optimization of structures without a hole inside or with only one deformable free surface, but cannot obtain a valid optimal shape for the structures with two or more deformable free surfaces by the growth-strain method as it is.

In the case of a structure with two or more free surfaces, the bulk strain occurs by the growth law of equation (1) between the two or more free surfaces. This causes an optimized shape to be far from the initial shape. Therefore, in order to maintain the initial shape it is necessary that an additional constraint should be given, and by doing so, a problem with two or more free surfaces is replaced by that with only one free surface. In this paper, the additional constraint was given by the type of a line connected with the points where the bulk strains are zeros.

For example, consider a two-dimensional bracket with a hole. In the case that both the internal hole and the outer surface are deformable, the optimized shape by the growth-strain method is obtained as shown in Fig. 1. It is a shape far from the initial shape, because the shape has been changed with the growth law by thermal deformation between the hole and the outer surface as mentioned before.

In order to apply the growth-strain method to the problems which occur in the structures with two or more deformable free surfaces, an additional constraint between the two free surfaces should be given, as shown in Fig. 2. The constraint is given by a line connected with the points having the strains of zero, that is, where the bulk strain is not occurred. By doing so, the two deformable free

surfaces are deformed by the growth law based on the given line constraints. Then, this problem has been replaced by a problem with two only one free surface. As a result, the final optimized shape can be obtained a reasonable shape, similar to the shape optimized by the mathematical programming method.

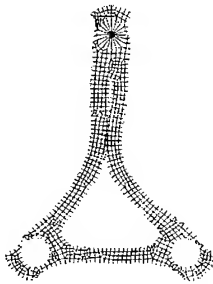


Fig.1. Shape optimized by the growth-strain method for a bracket with a hole

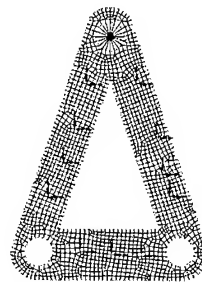


Fig.2. A bracket with an additional boundary condition around a hole

4. APPLICATION EXAMPLES

4.1 A two-dimensional bracket

A shape optimization was accomplished by stress control for a two-dimensional bracket as shown in Fig. 3. The objective volume was established at 50% of initial volume of the bracket. The values of K_p , K_f and K_D were 0.05 and 0.5, 0.1, 0.0, respectively. These values were obtained from a previous study [9]. The changes of the volume (area) to the initial volume and the Von Mises stress to the Maximum Mises stress are shown in Fig. 4. And the optimized shape is shown in Fig. 5. The volume of the optimized shape was converged to the established volume, 50% of the initial volume. And the Maximum Mises stress was converged to 1.1 times the initial Maximum Mises stress.

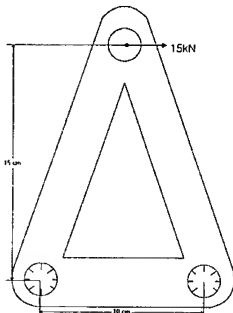


Fig.3. Initial shape of a 2-D bracket

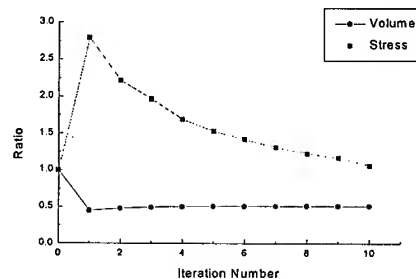


Fig.4. History of iteration by volume control

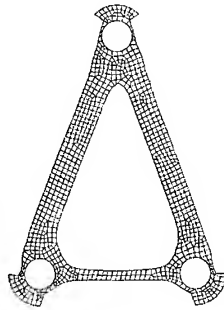


Fig.5. Optimal Shape of a 2-D bracket by volume control

4.2 A three-dimensional bracket

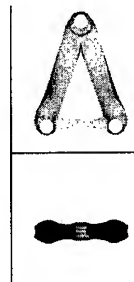
A shape optimization was accomplished by volume control for a three-dimensional bracket as shown in Fig. 6. The objective volume was established at 70% of the initial volume of the bracket. The values of K_p , K_l and K_D were 0.05 and 0.5, 0.1, 0.0, respectively. And the optimized shape is shown in Fig. 7. The final volume was reduced to about 70% of the initial volume. There was no problem to carry out shape optimization for the three-dimensional bracket when the growth-strain method was applied. But the optimal shape is not practical, so that it is better to accomplish shape optimization for making three-dimensional structure two-dimensional structure by imposing some constraints considering producing.



Fig.6. Initial shape of a 3-D bracket



Fig.7. Optimal shape of a 3-D bracket



5. CONCLUSIONS

In this paper, the growth-strain method was improved by giving additional constraints at the points or lines with the strains of zero, which was verified for general two-dimensional structures with two or more deformable free surfaces. There was no problem for general three-dimensional structures in the shape optimization point of view, but it is not practical to produce an obtained

optimal shape. It is better to carry out shape optimization for making three-dimensional structure two-dimensional structure by imposing some constraints considering producing. The shape optimization by the improved growth-strain method could be much more effective than the mathematical programming method for complicated three-dimensional structures.

ACKNOWLEDGEMENT

The authors wish to acknowledge the financial support of Hanyang University, Korea, made in the program year of 1999, and thank H. W. Bai of Daewoo Motor Company for his cooperation.

REFERENCE

1. G. Somayajula and J. Bernard, Finite Elements in Analysis and Design, 5 (1989) P.589
2. M. Matsumoto, J. Abe and K. Yamazaki, Transactions of the JSAE(in Japanese), 39 (1988) p.120
3. J.A. Benett, Int. J. of Vehicle Design, 5 (1984) p.115
4. Y.L. Hsu, Comput. in Industry, 26 (1994) p.3
5. S. Park and S. Youn, KSME Journal, 21 (1997) p.1241
6. D.N. Chu, Y.M. Xie, A. Hira and G.P. Steven, Finite Elements in Analysis and Design, 21 (1996) p.239
7. H. Azegami, SAE 921063 (1992).
8. H. Azegami, T. Ogihara and A. Tagamik, JSME Int. J., Ser. 3, 34 (1991) p.355
9. S.Y. Han and H.W. Bai, J. KSMTE, 8 (1999) p.52
10. I-DEAS Master Series Manual: SDRC Inc. (1994)

Simulation of Crack Growth and Creep Fracture by a Multicrack Growth Model

M. Tanaka

Department of Mechanical Engineering, Akita University,
1-1 Tegatagakuen-cho, Akita 010-8502, Japan

Keywords: Crack Growth, Creep Fracture, Fractal Dimension, Grain Boundary Sliding, Monte Carlo Simulation, Multicrack Growth Model, Percolation

ABSTRACT

Crack growth and creep fracture resulting from the initial defects are studied by a multicrack growth model. The percolated crack patterns and the number of steps to percolation are examined by Monte Carlo simulation on a square lattice. Effects of stress and grain size on creep fracture process are then discussed. The stress and grain size dependence of the number of steps to percolation in the simulation is similar to that of grain-boundary sliding in an austenitic heat-resisting steel, which controls the growth of grain-boundary cracks. The fractal dimension of the percolation crack is also correlated with that of the fracture surface in the steel.

1. INTRODUCTION

The initiation and growth of grain-boundary cracks at high temperatures, which are governed by grain-boundary sliding, lead to the formation of complex grain-boundary fracture patterns. The fractal geometry proposed by B.B. Mandelbrot [1] has been successfully applied to the quantitative description of creep fracture patterns by the fractal dimension [2,3]. The fracture patterns may be affected not only by characteristic microstructures of materials such as grain size but also by creep conditions [4]. However, the relationship between the creep-fracture process and the resulting fracture patterns has not sufficiently been known from the view point of damage mechanics. In this study, a Monte Carlo simulation is made using a multicrack growth model, which is similar to that proposed by Nishimura et al. [5]. The crack growth and creep fracture pattern is examined and is compared with the experimental results of the austenitic 21Cr-4Ni-9Mn steel.

2. SIMULATION METHOD

2.1. Multicrack Growth Model

Growth of grain-boundary cracks with two crack tips from randomly located initial defects is simulated in a personal computer using a multicrack growth model, which is similar to that proposed by Nishimura et al. [5]. In the Monte Carlo simulation using this model, a growth point of a crack may reach an adjacent crack (crack linkage), may reach an edge of the lattice (edge relaxation), may be trapped in its own cluster (self-trap), or may stop to grow (crack arrest) on the square lattice. One step length in the lattice corresponds to one grain-boundary length in the specimens. In this study, simulation was made five times to percolation under the same condition. Percolation in the lattice corresponds to fracture of materials. The fractal dimension of the percolation cluster was determined by the box-counting method [1,6] in the scale length range larger than one

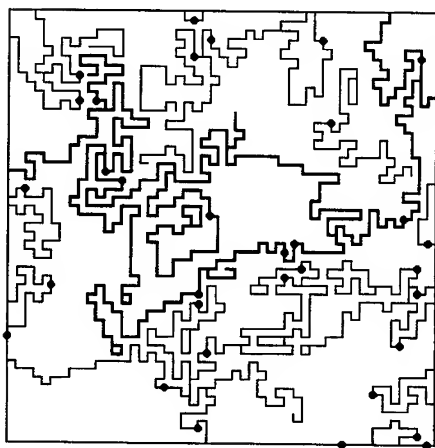


Fig.1. An example of the simulation carried out on square lattices ($N=50$ and $IDD=0.0127$).

2.2. Preliminary Simulation

Figure 2 shows the system size (N) dependence of the number of steps to percolation (NSP). The value of NSP increases as the system size (N) increases and the value is larger at the larger initial defect density. For a lattice with the system size N , the value of NSP divided by $(N+1)^2$ may give a value of NSP per nodal point of the lattice.

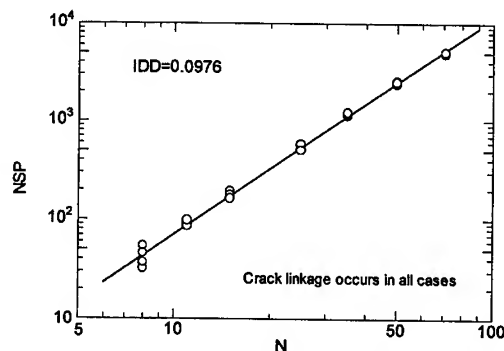


Fig.2. The system size (N) dependence of the number of steps to percolation (NSP).

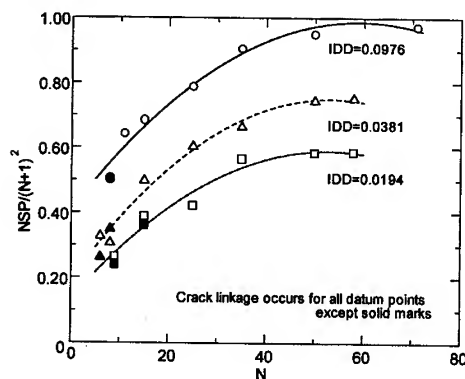


Fig.3. The relationship between the value of $NSP/(N+1)^2$ and the system size (N).

step length of the lattice. Figure 1 shows an example of the simulation carried out on a square lattice with the system size $N=50$ (the initial defect density (IDD) is 0.0127). Solid circles in the lattice show the initial defects. Percolation cluster (percolation crack) is formed in the horizontal and vertical directions (shown in bold line) in this case. The stress direction to the growing cracks is not specified in the simulation, although creep cracks usually tend to grow in the direction normal to the tensile stress. The magnitude of tensile creep stress is indirectly taken into the simulation through the value of IDD. Clusters that are not linked to percolation cluster are considered to be isolated cracks. Clusters are hereafter referred to as "cracks" in this paper.

Figure 3 shows the relationship between the value of $NSP/(N+1)^2$ and the system size (N). The value of $NSP/(N+1)^2$ increases as the system size increases, but becomes almost constant when the system size (N) is equal to or larger than about 50. Thus, there is a kind of "size effect" in the small lattices of the multicrack growth model used in this study. This may indicate that the effect of grain size on the creep fracture should be examined using the lattices with sufficiently large system size (N). In this study, the following simulations are all carried out on the lattices with the

system size $N=50$ and with different values of IDD. The ratios of the system size (n) for the specimens with the grain sizes (d), 8.4, 24, 99, 180, and 310 are 595, 208, 51, 28 and 16, respectively. The value of NSP for the system of the ratio n was calculated using the value of NSP for $N=50$, nsp , by $NSP=(nsp)\{(n+1)/52\}^2$ in this study.

2.3. Determination of Initial Defect Density (IDD)

Creep-rupture experiments were carried out using specimens of the austenitic 21Cr-4Ni-9Mn heat-resisting steel with various grain sizes (d). The details of the chemical composition, the heat treatments and the creep mechanism of the steel are shown in the reference [7]. Figure 4 shows examples of the grain-boundary fracture surface profiles of the 21Cr-4Ni-9Mn steel (973 K, 196 MPa). Grain-boundary microcracks linked to the fracture surface can be observed in these specimens. Table 1 shows the change in the fraction of cracked grain-boundaries linked to the fracture surface, f , with grain size in the ruptured specimens of the 21Cr-4Ni-9Mn steel. The value of f increases as the grain size (d) decreases. Table 2 shows the change in the fraction of the cracked grain-boundaries, f , with creep stress in the specimens (grain size, $d=99 \mu\text{m}$) ruptured at 973 K, 196 MPa. The fraction of the cracked grain boundaries also increases with decreasing creep stress. The initial defect density (IDD) is a two-dimensional quantity, and is assumed to be f^2 in the simulation in this study. The initial defect density may reflect the grain size and stress dependence of the creep fracture process.

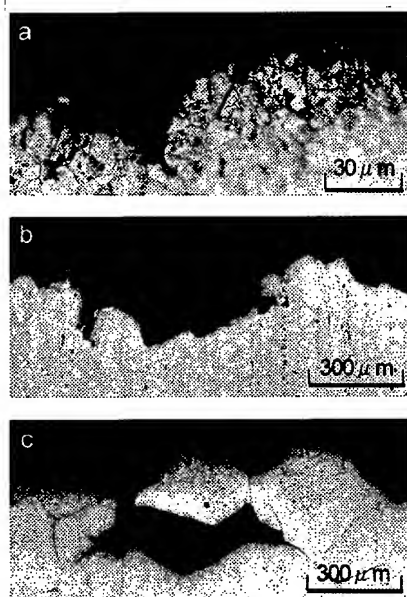


Fig.4. Examples of the grain-boundary fracture surface profiles of the 21Cr-4Ni-9Mn steel (973 K, 196 MPa). a. $d=8.4 \mu\text{m}$ b. $d=99 \mu\text{m}$ c. $d=310 \mu\text{m}$ (d : grain size)

Table 1. The change in the fraction of cracked grain-boundaries linked to the fracture surface, f , with grain size (d) in the ruptured specimens of the 21Cr-4Ni-9Mn steel.

	$d \ (\mu\text{m})$				
	8.4	24	99	180	310
Fraction of cracked grain boundaries, f	0.313	0.273	0.194	0.152	0.118
Initial defect density (IDD), f^2	0.0977	0.0744	0.0375	0.0230	0.0138

Table 2. The change in the fraction of the cracked grain-boundaries, f , with creep stress (σ) in the specimens ($d=99 \mu\text{m}$) ruptured at 973 K, 196 MPa.

	$\sigma \ (\text{MPa})$				
	176	196	245	294	323
Fraction of cracked grain boundaries, f	0.242	0.194	0.161	0.129	0.113
Initial defect density (IDD), f^2	0.0585	0.0375	0.0260	0.0166	0.0127

The initial defects were allotted to arbitrarily chosen nodal points in the lattice in the simulation. The fractal dimension of the fracture surface in the ruptured specimens of the 21Cr-4Ni-9Mn steel, which is estimated in the scale length range larger than one grain-boundary length, is cited from previous study [4].

3. RESULTS AND DISCUSSION

3.1. Effect of Grain Size on Creep Fracture

Figure 5 shows the relationship between the number of steps to percolation (NSP) in the simulation, the rupture life (t_r) of the 21Cr-4Ni-9Mn steel at 973 K, 196 MPa and the grain size (d). The value of IDD listed in Table 1 was used in the simulation. Simulation is carried out using square lattices of the same size ($N=50$), as

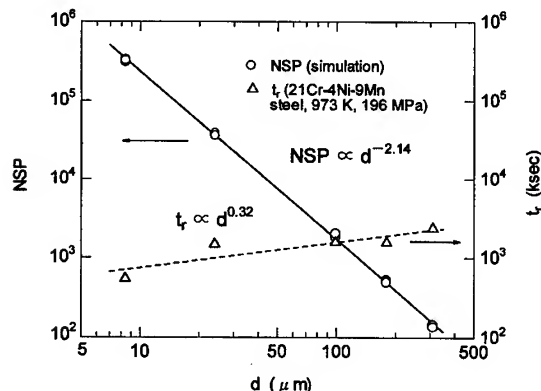


Fig.5. The relationship between the value of NSP in the simulation, the rupture life (t_r) of the 21Cr-4Ni-9Mn steel at 973 K, 196 MPa, and the grain size (d).

growth of a grain-boundary crack, may be proportional to the grain boundary length or the grain size (d), $u \propto d$, although the sliding grain boundaries are not specified in the present model. The total amount of grain-boundary sliding to the percolation crack formation, U , is expressed by the product of NSP and u as $U = (NSP)u \propto d^{-1.14}$. The grain size dependence of the crack growth period (t_c) is not known in this study, but if the value of t_c is proportional to the value of t_r , the strain rate due to grain-boundary sliding, $\dot{\epsilon}$, can be given by

$$\dot{\epsilon} = U/(t_c L) \propto U/(t_r L) \propto d^{-1.46} \quad (1)$$

where L is the side length of the lattice and corresponds to the gauge length of the specimens. The grain size (d) dependence of $\dot{\epsilon}$ in Eq. 1 lies between that of the grain-boundary sliding model proposed by Langdon ($\dot{\epsilon} \propto d^{-1}$) [9] and that of the model proposed by Gifkins ($\dot{\epsilon} \propto d^{-2}$) [10]. In Langdon's model, grain-boundary sliding is accommodated by the opening of grain-boundary cracks and cavities, while the formation of folds accommodate the grain-boundary sliding process in Gifkins' model. The present results may indicate that both mechanisms operate for accommodation of the grain-boundary sliding process. Figure 6 shows the grain size (d) dependence of the fractal dimension of the fracture surface in the 21Cr-4Ni-9Mn steel (973 K, 196 MPa) [4]

described in the section 2.2. The value of NSP is proportional to $d^{-2.14}$. As grain-boundary sliding drives the growth of grain-boundary cracks, the number of steps in the simulation corresponds to grain-boundary sliding in creep fracture. The value of NSP approximately corresponds to the number of grain boundaries on which the amount of grain-boundary sliding reached a critical value for crack growth. The grain size (d) dependence of the rupture life (t_r) at 973 K, 196 MPa is expressed as $t_r \propto d^{0.32}$. As reported by Kobayashi et al. [8], if the crack geometry does not significantly change during crack growth, the increase in the crack length is proportional to the amount of grain-boundary sliding. The critical amount of grain-boundary sliding, u , necessary for

and that of the fractal dimension of the percolation crack in the simulation. Both fractal dimensions increase with decreasing grain size, but the fractal dimension of the fracture surface is smaller than that of the percolation crack at the same grain size. The present simulation was carried out on the square lattice different from actual grain shape, and the effect of stress direction is not taken into account. Further, the length of grain-boundary microcracks linked to the fracture surface seems to decrease with increasing grain size, since the amount of grain-boundary precipitates that is larger in the specimens with the smaller grain sizes [7] may affect the crack growth (Fig. 4). These may lead to the difference in the values of the fractal dimension between the experiment and the simulation. However, the simulation reproduces the principal features of the creep fracture.

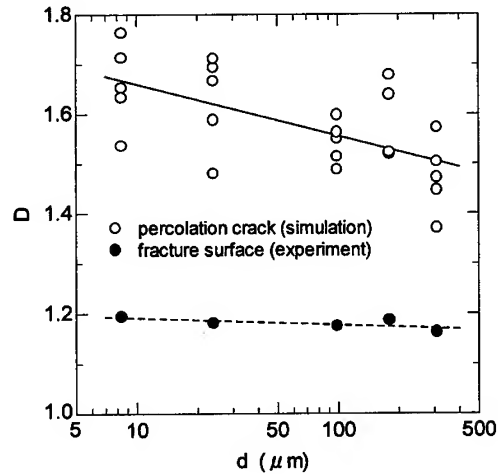


Fig.6. The grain size (d) dependence of the fractal dimension (D) of the fracture surface in the 21Cr-4Ni-9Mn steel (973 K, 196 MPa) [4] and that of the percolation crack in the simulation.

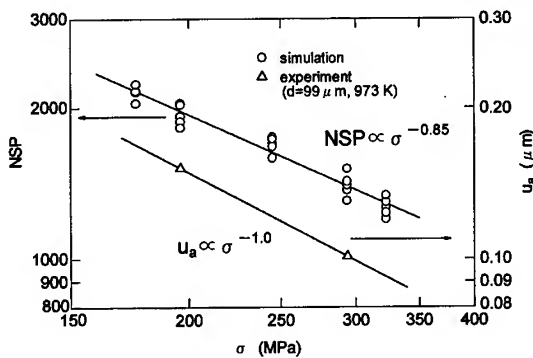


Fig.7. The relationship between the value of NSP in the simulation and the value of u_a in the ruptured specimens at 973 K [11] and the creep stress, σ .

3.2. Effect of Stress on Creep Fracture

The change in the fracture patterns with the creep stress was simulated on the lattices with the system size $N=50$. The value of IDD for the ruptured specimens with the grain size of $99 \mu\text{m}$ was used in the simulation (Table 1). In the previous study [11], the amount of grain-boundary sliding in creep was examined on the ruptured specimens of the 21Cr-4Ni-9Mn steel with the same grain size and the similar microstructures (the specimens with $d=99 \mu\text{m}$ and with straight grain boundaries). The average amount of grain-boundary sliding was examined at different creep stresses, since the amount of grain-boundary sliding

generally depends on the orientation of grain boundaries [11,12]. Figure 7 shows the relationship between the value of NSP in the simulation for $N=50$, the average amount of grain-boundary sliding, u_a , in the ruptured specimens at 973 K and the creep stress, σ . In the simulation, the value of NSP decreases as the creep stress (σ) increases, and is proportional to $\sigma^{-0.85}$. The value of u_a also decreases with increasing creep stress, and is proportional to $\sigma^{-1.0}$ in the specimens. The values of the stress exponent are close to each other (-0.85

and -1.0). Thus, the value of NSP is again correlated to the critical amount of grain-boundary sliding for crack growth. Figure 8 shows the stress dependence (σ) of the fractal dimension of the fracture surface in the ruptured specimens at 973 K [4] and that of the percolation crack in the simulation. The stress dependence of these fractal dimensions is similar, and the feature of the fracture patterns is also reproduced by the present simulation, although the fractal dimension of the fracture surface is a little smaller than that of the percolation crack. As described in the chapters 2 and 4, the simulation is performed on the square lattices and simplifies the creep crack growth process. Those may affect the results of simulation. Nevertheless, the results of the present simulation shows that the stress and grain size dependence of fracture patterns in creep is correlated to the amount of grain-boundary sliding that controls the growth of grain-boundary cracks.

4. CONCLUSIONS

The simulation based on the multicrack growth model reproduced the principal features of the crack growth and creep fracture. The results of simulation explained the stress and grain size dependence of creep-fracture patterns in the 21Cr-4Ni-9Mn steel. The stress and grain size dependence of fracture patterns in creep was correlated by the simulation with the amount of grain-boundary sliding that controls the growth of grain-boundary cracks.

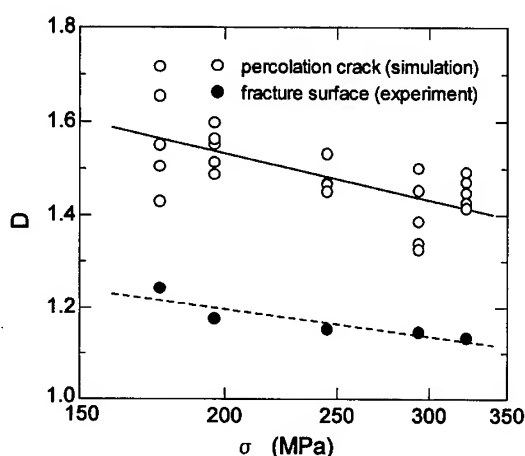


Fig.8. The stress (σ) dependence of the fractal dimension of the fracture surface in the ruptured specimens at 973 K [4] and that of the percolation crack in the simulation.

REFERENCE

1. B. B. Mandelbrot, *The Fractal Geometry of Nature*, translated by H. Hironaka, Nikkei Science, Ltd., Tokyo (1985).
2. M. Tanaka and H. Iizuka, *Z. Metallkd.*, **82** (1991) p. 442.
3. M. Tanaka, *J. Mater. Sci.*, **27** (1992) p. 4717.
4. M. Tanaka, *Z. Metallkd.*, **84** (1993) p. 697.
5. S. Nishimura, Y. Hasegawa and S. Miyazima, *Fractals*, **4** (1996) p. 377.
6. H. Takayasu, *Fractals in the Physical Sciences*, Manchester University Press, Manchester, (1990).
7. M. Tanaka, H. Fujita and D. Fujishiro, *J. Iron and Steel Inst. Japan*, **69** (1983) p.1320.
8. M. Kobayashi, O. Miyagawa and M. Yamamoto, *Int. Conf. on Creep, Japan, Tokyo* (1986) p. 65.
9. T. G. Langdon, *Philosophical Magazine*, **22** (1970) p. 689.
10. R. C. Gifkins, *J. Australian Inst. Metals*, **18** (1973) p.137.
11. M. Tanaka, O. Miyagawa, T. Sakaki, H. Iizuka, F. Ashihara and D. Fujishiro, *J. Mater. Sci.*, **23** (1988) p. 621.
12. F. Garofalo, *Fundamentals of Creep and Creep-Rupture in Metals*, translated by M. Adachi, Maruzen Co. Ltd., Tokyo (1968).

Dual-Phase Functionally Graded Composite Materials: Overall and Discrete Analysis Models

J.R. Cho and D.Y. Ha

School of Mechanical Engineering, Pusan National University,
30 Jangjeon-Dong, Kumjung-Ku, Pusan 609-735, Korea

Keywords: Discrete Micromechanical Model, Finite Element Analysis, Functionally Graded Materials FGM, Overall and Local Responses, Relative Thickness Ratio, Rule of Mixtures, VCFEM, Volume Fraction, Wakashima-Tsukamoto Estimate

ABSTRACT

Functionally graded materials (FGM) includes a dual-phase graded layer in which two different constituents are mixed continuously and functionally according to a given volume fraction. For the analysis of their thermo-mechanical response, conventional overall (averaged, global or homogenized) methods have been widely employed in order to estimate equivalent material properties of the graded layer. However, such overall estimations are insufficient to accurately predict the local behavior. We in this paper intend to compare the thermo-elastic behaviors predicted by several overall material-property estimation techniques with those by discrete analysis models utilizing the finite element method, for various volume fractions and loading conditions.

1. INTRODUCTION

As is well known, classical laminated composites (CLC) exhibit abrupt kinks in thermo-mechanical behavior at layer interfaces owing to the inherent material-property discontinuity at such interfaces. In order to minimize this problem, the NKK Corporation in Japan introduced a functionally graded material (FGM) in 1989 [1]. The basic idea of this new composite is to enforce the material-property continuity at layer interfaces by inserting a dual-phase graded layer in which the volume fractions of two constituents vary continuously from one interface to the other [2].

Besides a remedy of the critical kinks at interfaces, FGMs with the best performance under a given loading condition can be produced by optimally tailoring the volume fraction and the relative thickness of the inserted graded layer [3]. However, since the graded layer is a dual-phase composite, an appropriate estimation of corresponding material properties becomes an important step for the successful analysis and design.

From the beginning of introduction of FGMs, conventional homogenization approaches such as the rules of mixtures [4], the mean-field micromechanics models [5,6], the unit cell model [7] and so on for usual dual-phase composites have been employed. Even though these models provide reasonable overall prediction of thermo-mechanical behavior, these may fail to describe the reliable local behavior owing to the assumptions involved in them.

In reality, the material properties of phase composites are function of shape and size, orientation and dispersion structure of constituents and the loading and boundary conditions. Therefore, in order to predict the reliable local behavior of FGMs, one needs sort of discrete (or local) material-property estimation techniques. Recently, the discrete local analysis approaches utilizing the finite element method have been proposed by several investigators. Grujicic and Zhang [8] presented a numerical technique for predicting the local elastic behavior of FGMs by utilizing the Voronoi Cell Finite Element Method (VCFEM) proposed originally by Ghosh et al. [9]. Dvorak et al. [10] proposed a discrete micromechanical model by replacing each inclusion with a planar hexagonal cell and carried out the comparative numerical experiments for an assessment of the Mori-Tanaka model [5] and the self-consistent method for several dispersion structures.

In this paper, we first describe FGM briefly and make a discussion on the representative overall and discrete methods for the thermo-mechanical properties and behavior. Next, we present the numerical results illustrating the comparison between overall and discrete analysis modes, respectively, for three volume fractions under three loading conditions.

2. FUNCTIONALLY GRADED COMPOSITES

Fig. 1 depicts a two-dimensional ceramic-metal functionally graded composite, where $2d$ and $2d_G$ are the thicknesses of the composite and the graded layer, respectively. The upper layer is 100% ceramic while the lower layer 100% metal. The volume fractions of ceramic and metal constituents in the graded layer vary continuously through the thickness satisfying 100% ceramic at the upper surface and 100% metal at the lower one. For a given loading circumstance, thermo-mechanical behavior of FGMs is strongly influenced by two parameters being defined.

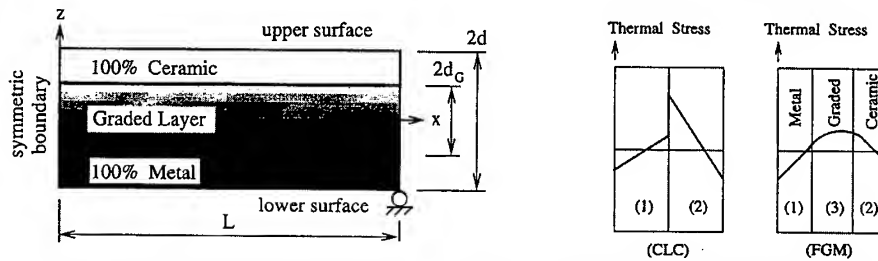


Fig. 1. A functionally graded composite (a) and thermal stress characteristics (b).

Letting $V_m(z)$ and $V_c(z)$ be the volume fractions of metal and ceramic, respectively, we have

$$V_c(z) + V_m(z) = 1 \text{ and } V_c(z), V_m(z) \leq 1, \text{ for } |z| \leq d \quad (1)$$

and

$$\left. \begin{aligned} V_m(z) &= 1, & -d \leq z \leq -d_G \\ V_m(z) &= \left(\frac{d_G - z}{2d_G} \right)^N, & |z| \leq d_G \\ V_m(z) &= 0, & d_G \leq z \leq d \end{aligned} \right\} \quad (2)$$

where N are non-negative real numbers specifying the metal volume fraction. Referring to Fig. 2, the graded layer becomes metal-dominated as N tends to 0 while ceramic-dominated as N approaches $+\infty$. These two limit cases display the behavior of classical laminated composites, thus we denote the former case by the metal-layer-extended CLC (m-CLC) while the other ceramic-layer-dominated CLC (c-CLC), respectively [3].

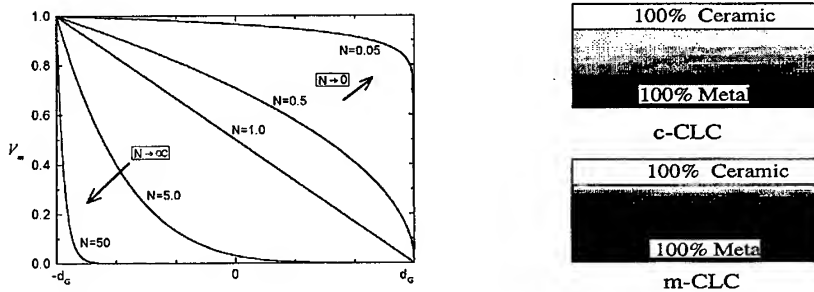


Fig. 2. Metal volume fractions (a) and ceramic- and metal-layer-extended CLCs (b).

The relative thickness ϑ of the graded layer with respect to the composite thickness is defined by

$$\vartheta = d_g / d, \quad 0 \leq \vartheta \leq 1 \quad (3)$$

As ϑ tends to 0, FGMs approach CLCs, while the graded layer extends to the entire composite region as ϑ increases to 1 (fully FGMs).

3. ANALYSIS MODELS FOR THE DUAL-PHASE GRADED LAYER

3.1 Overall Prediction Methods

A large number of papers on the thermo-mechanical response and the estimation of material properties for phase composites have been published, and they can be classified broadly into theoretical and experimental categories. In addition, the theoretical approaches are split into microscopic- and continuum-level (i.e. overall) studies. As is described in [6], the prediction methods of the overall material properties are generally classified into three: (a) direct, (b) variational and (c) approximation approaches.

The direct method seeks closed-form analytic solutions, so a rigorous mathematical treatment becomes troublesome. [11] On the other hand, the variational method such as the Hashin-Shtrikman's bounds [12] does not specify the details in the phase geometry but rather provides the upper and lower bounds for the overall properties. Therefore, one requires some additional approximations to obtain corresponding closed-form estimates.

In the approximation approach, the self-consistent models by Hill [11] and others, the mean-field micromechanics models by Mori and Tanaka [5] and Wakashima and Tsukamoto [6], the linear and modified rules of mixtures by Tamura et al. [4] and the unit cell model by Ravichandran [7] are widely-employed overall estimates. These overall models are simple and convenient to predict the overall thermo-mechanical response and material properties. We here briefly describe three considering models, the Wakashima-Tsukamoto estimates, the linear rule of mixtures and the modified rule of mixtures, together with the remarkable assessment made on them.

As is well known, the linear rule of mixtures is the simplest estimate in which any material property $\varphi(x)$ at the point x in dual-phase composites is approximated by a linear combination of volume fractions and the properties of two composing constituents A and B:

$$\varphi(x) = V_A(x)\varphi_A(x) + V_B(x)\varphi_B(x) \quad (4)$$

Because this estimate does not account for the detailed constituent geometry and dispersion structure, its accuracy is highly questionable.

The Wakashima-Tsukamoto estimate is derived upon the modified Eshelby's equivalent inclusion method by incorporating the Mori-Tanaka concept, wherein the overall macromechanical properties \bar{E} are defined by

$$\langle \sigma \rangle_{\Omega} = \bar{\mathbf{E}} : \langle \varepsilon \rangle_{\Omega}, \quad \langle \cdot \rangle_{\Omega} = \frac{1}{|\Omega|} \int_{\Omega} \langle \cdot \rangle d\Omega \quad (5)$$

where Ω refers to a representative volume element (RVE) and $\langle \cdot \rangle_{\Omega}$ the overall quantities. In the paper [6], they presented the comparative numerical results with the Hashin-Shtrikman's bounds for validating their work, together with the detailed formula. However, the Mori-Tanaka estimates are derived with randomly oriented and uniformly dispersed ellipsoids in an infinite matrix. Therefore, the Wakashima-Tsukamoto estimate leads to generally stiffer mechanical response, and further it becomes increasingly more inaccurate as a macrostructure tends to microstructure size.

In 1976, Tamura et al. [4] proposed the modified rule of mixtures illustrated in Fig. 3(a), for Young's modulus of dual-phase composites, which has been subsequently adopted by other investigators. This estimate treats each sublayer in the graded layer as an isotropic one for which uniaxial stress σ and strain ε are expressed in terms of the average stresses and strains of constituents and the volume fractions

$$\sigma = \sigma_A V_A + \sigma_B V_B, \quad \varepsilon = \varepsilon_A V_A + \varepsilon_B V_B \quad (6)$$

together with

$$q = (\sigma_A - \sigma_B) / (\varepsilon_A - \varepsilon_B) \quad (7)$$

Where, q is defined as the stress-strain transfer ratio determined by experiments. According to numerous experiments, the value q of 4.5GPa has been justified to be appropriate for most dual-phase composites within a wide range of volume fractions and loading conditions.

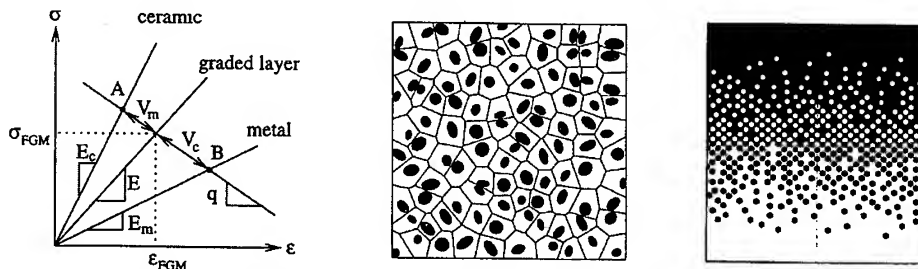


Fig. 3. Schematic representations; the modified rule of mixtures (a), the Voronoi cell finite element method (VCFEM) (b) and the discrete micromechanical model (c).

3.2 Discrete Analysis Models

In order for the more accurate local behavior as well as the assessment of the conventional homogenized methods by taking account for the profound influence of a stochastic dispersion of heterogeneities, recently new numerical techniques utilizing the finite element method are being increasingly studied. Two remarkable techniques are the Voronoi cell finite element method (VCFEM) by Grujicic and Zhang [8] and the discrete micromechanical model by Dvorak et al. [10].

Referring to Fig. 3(b), the former generates a network of Voronoi polygons by Dirichlet tessellation of the composite domain, in which each polygon containing one inclusion at most is treated as a finite element. Then, according to the Pian-Ghosh's assumed stress hybrid FEM [9], the global and local stress and deformation fields as well as the effective material properties are analyzed. This method provides more reliable local response and material properties for randomly dispersed dual-phase composites, but the stresses are overestimated with a coarse mesh. Furthermore, it does not include the macro-micro scale effects that it is limited to composites of rather low volume fractions.

In the latter method, a distribution of inclusions is generated by allocating planar hexagonal cells of equal size according to a specified volume fraction, as shown in Fig. 3(c). Differing from VCFEM, each cell is subdivided into several finite elements, and further usual standard FEM is

directly employed. The dispersion of hexagonal cells is manually preformed so that arbitrary dispersion structure is possible. This numerical technique serves as a reference tool for the assessment of conventional homogenized methods, but it requires fine hexagonal cells and finite elements for accurate approximations that it involves painstaking computational efforts.

4. NUMERICAL EXPERIMENTS

For the numerical experiments, we consider a half of simply supported FGM beam shown in Fig. 1(a) with geometry data: $L=50\text{mm}$, $2d=10\text{mm}$ and $2d_g=8\text{mm}$ (i.e. $\eta=0.8$). Al_2O_3 and Ni are selected for ceramic and metal respectively, and their material properties are: $E=393\text{GPa}$, $\nu=0.25$, $\alpha=7.4\times 10^{-6}/\text{K}$ and $\kappa=30.1\text{W/m}\cdot\text{K}$ for Al_2O_3 , while $E=199.5\text{GPa}$, $\nu=0.3$, $\alpha=15.4\times 10^{-6}/\text{K}$ and $\kappa=90.7\text{W/m}\cdot\text{K}$ for Ni.

In order to generate discrete numerical models, we subdivide the beam into 100×70 uniform rectangular cells (100 in the x-axis and 70 in the z-axis). Four-node rectangular finite elements are then assigned to each cell as similar to the Dvorak's micromechanical model. Here three volume fractions N of 0.5, 1 and 5 are considered, and the resulting numerical models are shown in Fig. 4(a). A specified volume fraction is achieved in a manner that cells in the same row are assigned to Al_2O_3 or Ni in proportion to the volume fractions (black cells for Ni and white cells for Al_2O_3).

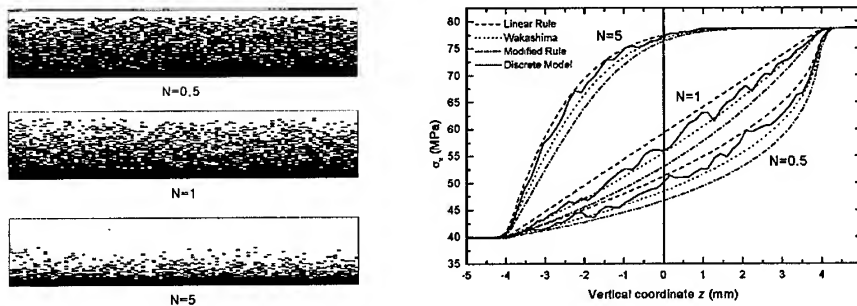


Fig. 4. Micromechanical models with three different volume fractions (a) and thickness-wise axial stress distributions for the loading case I (b).

As loading condition, we consider three cases; (I) uniform axial displacement $u_x=0.02\text{mm}$ along the right-end side, (II) uniform temperature increase ΔT of 200K for the entire beam and (III) non-uniform temperature increase ΔT of 300K at the lower surface and 500K at the upper surface. For two steady thermal loading cases (II and III), the beam is initially at room temperature.

Except for the region in the vicinity of the right end showing the edge effect, the three loading cases produce x-independent thermo-mechanical behavior. However, since micromechanical models exhibit abrupt changes in axial stress across cell interfaces, we average 80 nodal values of cells located within $0 \leq x \leq 40\text{mm}$ in the same row.

The vertical distributions of axial stress for the loading case I are compared in Fig. 4(b). We note here that three material properties for the graded layer except for Young's modulus for the modified rule of mixtures are computed according to the linear rule of mixtures. From the plots, we first observe that the difference between analysis models is considerable at transition zones in the dispersion structure. In addition, for three volume fractions the linear rule of mixtures produces the highest stresses while the modified rule of mixtures the lowest values. For this loading case, the behavior obtained by the discrete micromechanical model is between those by linear rule of mixtures and the Wakashima-Tsukamoto estimate.

Comparative results of axial stress for the thermal loading cases II and III are provided in Fig. 5(a) and (b), respectively. Compared to the loading case I, considerably larger differences between

the homogenized and the discrete models are shown in the transition zones. In addition, such remarkable differences are also observed in two isotropic layers for some volume fractions. This tells us that the overall methods become more inaccurate as the loading condition becomes complex. Also, we notice that the well ordered stress distributions in the loading case I are disarranged. The reason is because the first loading case produces a pure tensile deformation but these two do bending-dominated deformation. For these loading cases, the Wakashima-Tsukamoto estimate provides closer prediction to the discrete model, if we insist on estimating three overall methods.

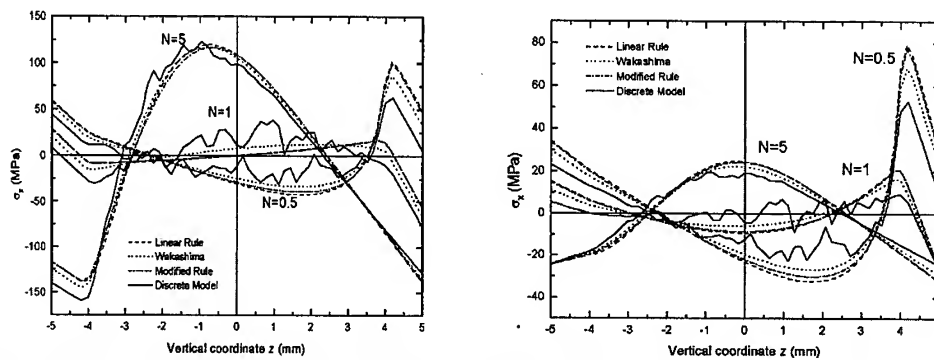


Fig. 5. Thickness-wise axial stress distributions; (a) the loading case II and (b) the loading case III.

5. CONCLUSION

With an introduction of FGM composites, we first presented a brief description on the major conventional overall methods and the newly proposed discrete numerical models for the thermo-mechanical response and the material-property estimation of phase materials. In order to compare and assess three representative overall methods by employing the discrete micromechanical models with uniform rectangular cells, we carried out numerical experiments for three volume fractions and three loading conditions. From the numerical results, we observed that the difference between the overall methods and the discrete models is considerable in the transition zone, and further its magnitude increases when the loading condition is complex. Therefore, one has to carefully choose an appropriate overall estimation method by considering the dispersion structure and loading condition, for the reliable local response of FGMs.

REFERENCE

1. M.Koizumi, *Composites Part B*, **20B** (1997) p. 1
2. A.E.Giannakopoulos, S.Suresh and M.Olsson, *Acta Metallurgica Materialia* **43**(4) (1995) p.1335
3. J.R.Cho and J.T.Oden, *Computer Methods in Applied Mechanics and Engineering*, (in press)
4. Y.Tomota, K.Kuroki and T.Mori and I.Tamura, *Materials Science Engineering*, **24** (1976) p. 85
5. T.Mori and K.Tanaka, *Acta Metallurgica*, **21** (1973) p. 571
6. K.Wakashima and H.Tsukamoto, *Materials Science Engineering, A* **146** (1991) p. 291
7. K.S.Ravichandran, *J. American Ceramic Society*, **77**(5) (1994) p. 1178
8. M.Grujicic and Y.Zhang, *Materials Science Engineering, A* **251** (1998) P. 64
9. S.Ghosh and S.N.Mukhopadhyay, *Computer Methods in Applied Mechanics and Engineering*, **104** (1993) p. 221
10. T.Reiter, G.J.Dvorak and V.Tvergaard, *J. Mechanics and Physics of Solids*, **45** (1997) p. 1281
11. R.Hill, *J. Mechanics and Physics of Solids*, **11** (1963) p. 357
12. Z. Hashin and S. Shtrikman, *J. Mechanics and Physics of Solids*, **11** (1963) p. 127

A Study on Efficiency Improvement of Evolutionary Structural Optimization

S.Y. Han, T.H. Lee and J.K. Lim

School of Mechanical Engineering, Hanyang University,
17 Haengdang-Dong, Sungdong-Gu, Seoul 133-791, Korea

Keywords: Convergence Rate, Element Removal Method, Evolutionary Structural Optimization, Reduction Ratio, Topology Optimization

ABSTRACT

The purpose of this study was to develop a new element removal method for ESO (Evolutionary Structural Optimization), which is one of the topology optimization methods. ESO starts with the maximum allowable design space and the optimal topology emerges by a process of removal of lowly stressed elements. The element removal ratio of ESO is fixed throughout topology optimization at 1 or 2%. In this paper, a new element removal method for ESO was developed for improvement of the convergence rate. Then it was applied to a short cantilever with overall stiffness constraints. From the results, it was verified that the convergence rate was significantly improved and the optimal design structures were obtained very similar to the results of ESO with the fixed element removal ratio of 1%.

1. INTRODUCTION

An important development in topology optimization was made by Bendsoe and Kikuchi [1] who proposed the homogenization method, in which a material with an infinite number of microscale voids is introduced and the optimization problem is defined by seeking the optimal porosity of a porous medium using an optimality criterion. Some of the results of the homogenization method can be found in the references [2-4]. Mlejnek et al. [5] accomplished shape and topology optimization using a simple energy method and a special type of function, that is, Kreisselmeier-Steinhauser function [6] for calculating effective properties.

Recently, a simple method for shape and topology optimization, called ESO (Evolutionary Structural Optimization), has been proposed by Chu [7] and Xie and Steven [8,9] which is based on the concept of gradually removing redundant elements of the low stressed part of the material from

a structure to achieve an optimal design. Since ESO is accomplished by the fixed element removal ratio of 1 or 2%, the convergence rate may become very slow until an optimum is reached. And BESO (bidirectional ESO) was suggested by Querin [10] for generating the optimum shaped structures. The structural domain has regions which are heavily under-stressed and regions which are heavily over-stressed. Elements are removed from the under-stressed regions and added to the over-stressed regions. But since the element removal ratio and the inclusion ratio of BESO are still small, the convergence rate is very slow.

In this study, a new element removal method for ESO is developed to improve the convergence rate and obtain an optimized design. It is an algorithm to determine the removing redundant elements of the low stressed part of a structure, started with the maximum allowable design space. It will be explained in the next section in detail. The validity and efficiency of the improved element removal method (IERM) is verified by comparing the optimized designs for some of the classical optimization problems.

2. THE IMPROVED ELEMENT REMOVAL METHOD (IERM)

The detailed ESO procedure can be found in the work of Xie and Steven [7] and a brief explanation is given in this paper. The strain energy of a structure, which is defined as

$$C = \frac{1}{2} \{P\}^T \{u\} \quad (1)$$

where, $\{p\}$ is the nodal load vector and $\{u\}$ is the global nodal displacement vector. It is commonly used as the inverse measure of the overall stiffness of the structure. It is obvious that maximizing the overall stiffness is equivalent to minimizing the strain energy. The sensitivity number is defined

$$\alpha_i = \frac{1}{2} \{u^i\}^T [K^i] \{u^i\} \quad (i = 1, n) \quad (2)$$

where, $[K]$ is the global stiffness matrix. It indicates the change in the strain energy due to the removal of the i th element. It should be noted that α_i is the element strain energy. It is obviously most effective to remove the element which has the lowest value of α_i so that the increase in C is minimum.

Generally, a structure is not sensitive at the initial stage and becomes sensitive as the number of the removed elements is increased. But, since the removal ratio of ESO is fixed throughout topology optimization at 1 or 2%, it has no flexibility for various types of structures and the convergence rate may not be efficient. In order to improve the convergence rate, it is necessary to increase the element removal ratio at the initial stage and gradually reduce the ratio as the number of the removed elements is increased.

Also, since an optimized design of a structure is highly dependent on the history of element removal, an optimized design is also changed if the removal ratio is changed. But an optimized design should be obtained similarly regardless the element removal ratio.

In order to overcome above two problems, IERM is developed in this study. As mentioned above, when an element is removed the stiffness of a structure reduces and correspondingly the strain energy increases. In the process of ESO, when some elements were removed, the decrease of strain energy often occurred in the next iteration. It means that the removed elements were not properly selected. Thus, before going the next iteration the removed elements from the structure should be determined in order to make the element strain energy increase in the subsequent iteration.

The procedures of IERM are as follows. To start with a piece of material which is large enough to cover the area of the final design of a structure is discretized into a fine mesh of finite elements. Given constraints are applied and a stress analysis is performed. Then the sensitivity numbers are calculated for each element.

In order to determine which elements should be removed from the original structure, the following steps are necessary. First, the numbers of elements with the lowest sensitivity numbers are listed by a flexible element removal ratio of about 7% larger than the 1 or 2% in ESO. Second, the sensitivity numbers are recalculated by another stress analysis for the structure after the listed elements are removed. Third, the numbers of elements having sensitivity numbers which are smaller than the largest sensitivity number of the elements listed at the first step, are listed. Fourth, if the number of the elements listed at the third step is smaller than that at the first step, the elements to be removed from the original structure should be all of the elements listed at the third step and the elements with the lowest sensitivity numbers at the first step. Fig. 1 explains this procedure.

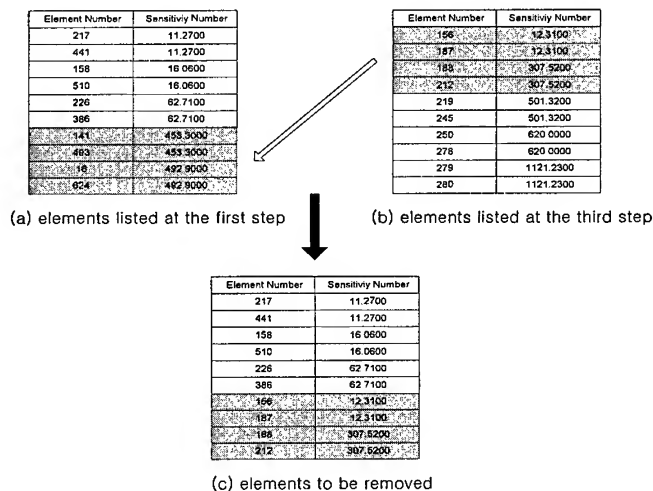


Fig.1. The procedure of the IERM

If the number of the elements listed at the third step, is larger than that at the first step, the removal ratio should be reduced by 1% and return to the original structure whenever this situation occurs. Here, the removal ratio should be at least 2%. In order to satisfy the required mass of the optimal design, the removal ratio can be reduced to 1 or 2% near the last iteration, if necessary.

By using IERM as explained above, a removal ratio of about 7%, which is empirically determined, can be used. Thus, the convergence rate is improved to about 70% and also the optimal designed structures are obtained very similarly to the known optimal design for the examples given in the next section.

3. Application of the IERM

The IERM was applied to the same example problems as those published previously in order to verify the validity and the effectiveness of it.

3.1 A Short Cantilever 1

The IERM is applied to the structures with overall stiffness constraints. It is applied to a short cantilever as shown in Fig. 2. The short cantilever is subject to a concentrated force of 300 kN at the center of free end, and the maximum deflection is limited to 0.75 mm. The rectangular design domain is discretized into 32 x 20 quadrilateral elements and a fixed element removal ratio of 1% is applied. Then, the IERM with a flexible removal ratio of about 7% is applied to the same short cantilever. The results obtained by the two methods are compared to each other.

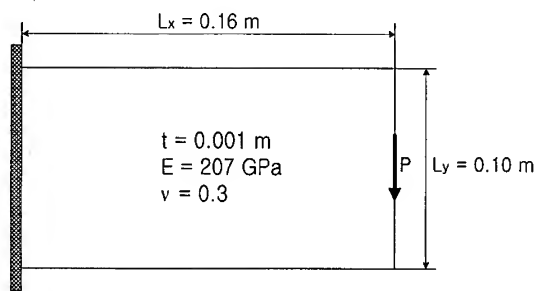


Fig.2. Initial conditions of a short cantilever

The optimal designs by the fixed removal ratio of 1% and by the IERM are shown in Fig. 3(a) and (b), respectively. For the optimal design by the fixed removal ratio of 1%, the call number of finite element analysis is 66, the maximum Mises stress is $8.28\text{E}+5 \text{ MPa}$ and the reduction ratio to the original structure is 62%. For the optimal design by the IERM, the call number of finite element analysis is 20, the maximum Mises stress is $7.89\text{E}+5 \text{ MPa}$ and the reduction ratio to the original structure is 61.6%. Therefore, the convergence rate is improved to 69.6% and a better optimal design is obtained under the conditions of the same displacement limit.

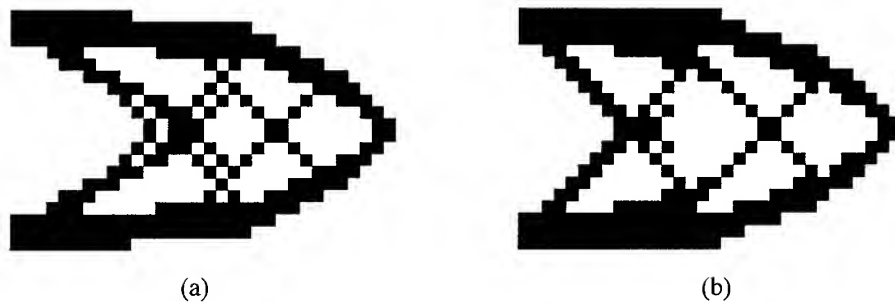


Fig.3. Optimal topology obtained by (a) the fixed element removal ratio of 1% and (b) the IERM

3.2. A Short Cantilever 2

The IERM is applied to the same problem as above. In this case, the short cantilever is subjected to a concentrated force of 3 kN at the bottom of the right free end. The final volume is limited to 24% of the original volume. A fixed element removal ratio of 1% is first applied, and then the IERM with a flexible removal ratio of about 7% is applied to the same short cantilever. The results obtained by the two methods are compared to each other.

The optimal topologies by the fixed removal ratio of 1% and by the IERM are shown in Fig. 4(a) and (b), respectively. For the optimal topology by the fixed removal ratio of 1%, the call number of finite element analysis is 76, and the maximum Mises stress is 1.84 Gpa. The displacement at the load point is 1.16 mm. For the optimal design by the IERM, the call number of finite element analysis is 21, and the maximum Mises stress is the same as the case of the fixed removal ratio of 1%. The displacement is 1.21 mm. The obtained topologies are very similar to each other. Therefore, the convergence rate is improved to 72.3% under the conditions of the same reduction ratio limit of 24% of the original structure.

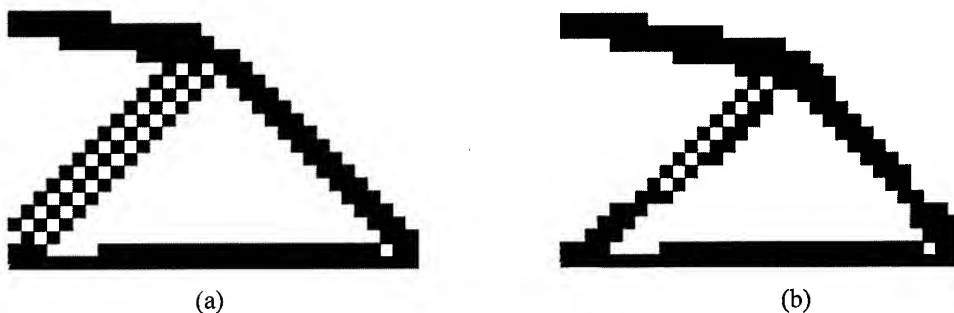


Fig.4. Optimal topology by (a) the fixed element removal ration of 1% and (b) the IERM

4. CONCLUSIONS

In this study, the IERM was developed in order to improve the convergence rate and the optimal shaped structures. By using the developed IERM, a removal ratio of about 7% larger than the fixed element removal ratio of 1 or 2% in ESO can be used. Thus, the convergence rate is improved to about 70% and also similar or better optimal design structures are obtained compared with the results of ESO with the fixed element removal ratio of 1% for some examples in this paper.

ACKNOWLEDGEMENT

The authors wish to acknowledge the financial support of Hanyang University, Korea, made in the program year of 1999, and thank H. W. Bai of Daewoo Motor Company for his cooperation.

REFERENCE

1. M.P. Bendsoe and N. Kikuchi, *Comp. Meth. Appl. Mech. Engng.*, **71** (1988) p.197
2. M.P. Bendsoe, *Struct. Optim.*, **1** (1989) p.193
3. K. Suzuki and N. Kikuchi, *Comput. Meth. Appl. Mech. Engng.*, **93** (1991) p.291
4. S. Park and S. Yoon, *Transaction of KSME*, **21** (1997) p.1241
5. H.P. Mlejnek and R. Schirmacher, *Comp. Meth. Appl. Mech. Engng.*, **106** (1993) p.1
6. G. Kreisselmeier and R. Steinhauser, *IFAC Symp. Computer Aided Design of Control Systems*, Zurich, Switzerland (1979).
7. D.N. Chu, Y.M. Xie, A. Hira and G.P. Steven, *Finite Elements in Analysis and Design*, **21** (1996) p.239
8. Y.M. Xie and G.P. Steven, *Comput. Struc.* **49** (1993) p.885
9. Y.M. Xie and G.P. Steven, *Eng. Computations*, **11** (1994) p.295
10. O.M. Querin, G.P. Steven and Y.M. Xie, *Eng. Computations*, **15** (1998) p.1031
11. S.Y. Han and K.S. Choi, *KSAE, 98 Spring Conference Proceeding*, **2** (1998) p.716

Numerical Simulation of Crack Elongation and Reinforcement Effectiveness of the Isolated Rockmass between Shiplocks of Three Gorges Project

Ping Xu¹ and Xia-Ting Feng²

¹ Huazhong University of Science and Technology, Wuhan 430074, China P.R.

² Institute of Rock and Soil Mechanics, The Chinese Academy of Sciences, Wuhan 430071, China P.R.

Keywords: Crack, Numerical Simulation, Reinforcement, Rock Mass, Three Gorge Project

ABSTRACT

With application of fracture mechanics, propagation rules of cracks with different length and dip on the selected typical cross section of shiplock of Three Gorges Project are numerical simulated. Different reinforcement schemes including designed, constructed in actual, and without any anchor are compared. It indicated clearly that deformation of the isolated mound is mainly due to open of cracks while deformation of rockmass itself is very small. Reinforcement of anchor ropes can restrain effectively open of cracks and their propagation toward deep rockmass. Upper mouth of anchor ropes has better restraining effectiveness on open of cracks and their propagation toward deep rockmass than that of its waist and bottom. When long and short cracks both occurred, long cracks and the cracks close to sidewall of isolated rockmass have bigger open displacement and cracking length than that of cracks at the middle of isolated rockmass. It is necessary to reinforce the long and big cracks which are close to sidewall of isolated rockmass and the cracks parallel to axial of shiplock.

1. INTRODUCTION

Shiplock in Three Gorges Project has five-class double line shiplock room with high and steep slopes in both sidewall and an isolated rockmass with 50-70 m height. It consists of hard jointed rock existing tensile stress zone after excavation of shiplock room. Some results indicate that rockmass has unloaded in three dimensions, some are unloaded in four dimensions after excavation of shiplock room. It is clear that the rockmass experienced tensile state from change of compressive state and that cracks experienced tensile-shear changed from compressive-shear. Therefore, it is possible to have open and elongation of cracks.

The results from the field investigation indicated that concrete constructed on top surface of the isolated rockmass in the second and third shiplock room was getting cracking. The maximum open

displacement is 20 mm. Therefore, it is important to know how cracks are open and elongated toward deep rockmass and effectiveness of rockbolt and anchor ropes to control these open and elongation.

With application of fracture mechanics, several typical cross sections at the second and third shiplock room have been numerically simulated. Several cracks with different length and dip with designed, constructed in actual or without reinforcement have been analyzed. The results are compared. Also, mechanisms of crack open and elongation and their control measured are discussed. These results provide theoretical support for construction.

2. CRACK OPEN STABILITY ANALYSIS

For a plane problem, crack open and elongation have two typical schemes: Type I (for open crack) and II (for shear crack). Open and elongation of cracks in engineering rockmass are not located in these two schemes. It often includes both of them or composite scheme of types I and II. It is clear to see from rockmass near excavation face of slope and top of the isolated mound exists tensile stress zone that crack open and elongation have a composite of type I and II.

From reference [1,2], criteria for open and elongation of crack in little new rockmass at shiplock zone can be described as

$$K_I / K_{IC} + 1.89(K_{II} / K_{IC})^2 = 1 \quad (1)$$

The fracture toughness for this rockmass is $K_{IC} = 1.751 \text{ MPa}\sqrt{\text{m}}$.

The stress intensity K_I and K_{II} for tip of cracks are shown in reference [1,2]. The tensile state is referred to positive, and shear is referred to negative. If K_I is negative and K_{II} exists, then it belongs to composite shear scheme of types I and II. If K_I is positive and K_{II} exists and then it belongs to composite tensile-shear scheme of types I and II. After K_I and K_{II} are computed, the formula (1) can be used to appraise stability of crack open and elongation. The left part at the formula (1) is less than 1, equals to 1 or is greater than 1, corresponding to stable, critical and unstable open of cracks respectively.

Direction of crack elongation can be determined using maximum tensile strain theory. If a crack is elongated a unit length will be added in the direction of elongation of crack and then this analysis will be repeated. And so on, a complete path of crack elongation can be obtained and whether the crack continues to elongate or stops propagating can be estimated. Therefore, the formula can be used to analyze the little new isolated rockmass.

3. COMPUTATIONAL PRINCIPLE

According to elastic fracture mechanics, the structure with cracks loaded, stress and strain at tip of crack has singular point of $r^{1/2}$. For a plane problem, the stress intensity K_I and K_{II} can be calculated by

$$K_I = \lim_{r \rightarrow 0} \left[\frac{\sqrt{2\pi E}}{4(1-\mu)^2} \cdot \frac{U_i}{\sqrt{r_i}} \right] \quad (2)$$

$$K_{II} = \lim_{r \rightarrow 0} \left[\frac{\sqrt{2\pi E}}{4(1-\mu)^2} \cdot \frac{V_i}{\sqrt{r_i}} \right] \quad (3)$$

Where E , μ are elastic modulus and Poisson ratio of rock mass, respectively. U_i , V_i are displacement at the direction of the point i of crack being vertical and parallel to crack plane, respectively. r_i is

distance between the point i and tip of crack. An extrapolation algorithm is used to calculate stress intensity of n points on unit crack. The stress intensity K_I and K_{II} at tip of crack can be obtained by using linear regression method.

4. GEOLOGICAL CONDITION AND SIMPLIFIED CRACK MODEL

Rockmass at shiplock of Three Gorge Project is mainly plagioclase granite with layer of schist capture and small amount of close grained granite dyke, germination dyke, diabase dyke and quartz dyke. It has NNW, NE-NEE, NNE, NW~NWW faults. The top surface of the isolated rockmass mound is 159.75 m high from sea level. There are 2954 cracks on the tope surface and south and north sidewalls of the isolated rockmass mound. According to its strike direction, these cracks can be divided into NNW, NE-NEE, NNE, NW~NWW groups. At one place there is only 1 or 2 ascendant group cracks. At non-weathered rockmass, there is mainly hard and steep dip discontinuous weak plane with a little roughness. Its length is greater than 10 m with 60% at number of total weak planes. The joints with little dip are not so much, with 10% of total amount.

Up to June 1999, the shiplock excavation is almost finished. Four main cracks have been selected for analysis of the typical cross section of the third shiplock room. Their lengths are 6m, 10m, 8m, and 15m respectively. Their dips are 75° , 66° , 60° , 74° . A fault f_5 is also considered during analysis (see Fig.1).

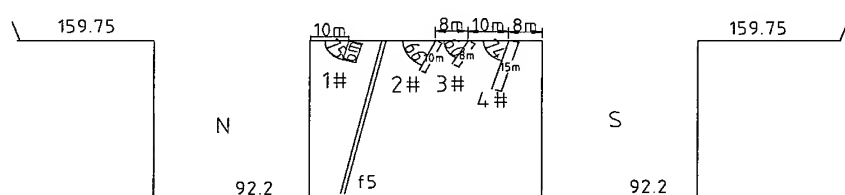


Fig.1. A simplified crack model

5. CONDITION OF CALCULATION

5.1. Mesh Generation and Calculation Parameters

The finite meshes are automatically generated based on geological conditions, excavation process and joint distribution at the selected cross section. Quadrangle with 8 nodes and equal-parameter element with 6 nodes are adopted. There are total 2889 elements with node number of 8240. Physical parameters for full weathered, strong weathered, little weathered, and non-weathered strata are listed in reference [1]. The load comes from initial stress. The different formulas are used to calculate initial stress field for different zone and weathered grade.

5.2. Excavation and Reinforcement Simulation

Actual excavation process is simulated. Only few excavation steps at a height above sea level and time are simplified. Effectiveness of anchor ropes is simulated as concentrated load. The reinforcement force for an anchor rope that both ends are reinforced is designed to be 3MN. Excavation and reinforcement are completed on total 17 steps, which is closed to the actual cases.

5.3. Calculation Schemes

There are three calculation schemes shown in Table 1. The stress intensity K_I and K_{II} are

calculated for without excavation and each excavation step.

Table 1 Calculation schemes

The selected cross section for calculation	Calculation scheme no.	Reinforcement system and (m)
Mouth of the third shiplock room	S1	Without reinforcement
	S2	Anchor rope: $\nabla 151.5, \nabla 138.5, \nabla 136.5, \nabla 133, \nabla 130.5$
	S3	Anchor rope: $\nabla 156.6, \nabla 151.5, \nabla 146, \nabla 138.5, \nabla 136.5, \nabla 133, \nabla 130.5$

6. RESULTS AND DISCUSSIONS

Figs 2 and 3 are comparison of elongation length and open width of each crack under without reinforcement and different reinforcement schemes. Fig.4 shows deformation of slope after finishing excavation under calculation scheme 1.

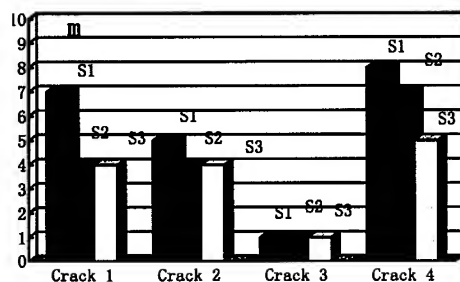


Fig.2. Comparison of elongation length of cracks

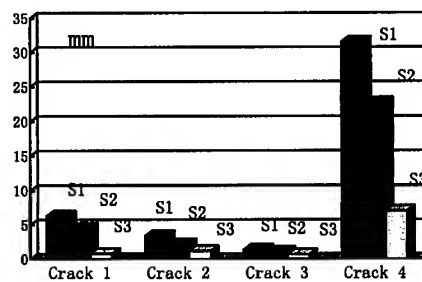


Fig.3. Comparison of open width of cracks

6.1. Deformation and Stress

(1) There is a good agreement on state and value of deformation and stress for the rockmass without crack with the results given by other authors. However, the results in our simulation indicate that there is stress concentration at tip of crack. The maximum tensile stress on tip of the longest crack (crack 4) exceeds 50MPa, while the minimum tensile stress at tip of the shortest crack (crack 1) is less than 4MPa. The maximum tensile stress on tip of the shortest crack (crack 1) on sidewall is still at 30~40MPa. When crack elongates the stress concentration releases. When long cracks occur together with short cracks in the isolated mound, tensile stress of the longer crack and the shorter crack on sidewall exceed that of short crack at middle of the isolated mound.

(2) For the without reinforcement (S1), the maximum open widths of the four cracks on top of the isolated mound after finishing excavation are 6.29mm, 3.38mm, 1.36mm, and 31.55mm. Its total open width is 42.58mm. The displacement of top of the straight wall at south and north sides

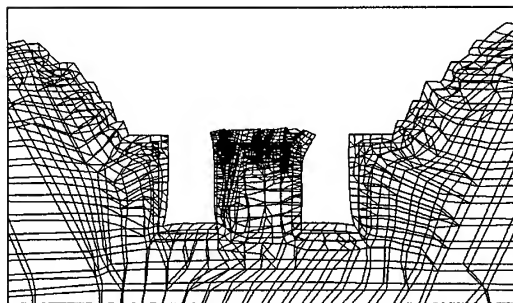


Fig. 4. Deformation of slope after finishing excavation under S1

(toward to shiplock room) are 29.06mm and 14.15mm respectively, with the relative displacement is 43.21mm. Therefore, the deformation of the isolated mound comes from mainly cracking. Open displacement of the longer crack and the shorter crack on sidewall are greater than that short crack at middle of the isolated mound.

(3) Compared to S1(without reinforcement), deformation of four cracks reduces at amount with a type of reinforcement of S2. Deformation of crack 4 reduces by 8.79mm while the relative deformation of top of north and south sidewall reduces by 11.36mm.

(4) Compared to S2, S3 by adding 2 rows of anchor ropes. Open width of four cracks in the isolated mound become smaller, particularly on cracks on sidewalls.

6.2. Crack Elongation Analysis

(1)When without reinforcement is included, lengths of four main cracks after finishing excavation of shiplock are 6.5~7.0 mm, 4.5~5.0mm, <1.0mm, 7.0~8.0mm, respectively. Therefore, when long and middle long cracks occurred in the isolated mound, elongation length of long crack and crack close to side wall is greater than that of cracks occurred in middle of the isolated mound.

(2)When the S2 (with reinforcement) is adopted, lengths of four cracks after finishing excavation of shiplock are 3.5~4.0 mm, 3.5~4.0mm, <1.0mm, 6.0~7.0 mm, respectively, that is smaller than that in the S1.

(3)When the S3 (with reinforcement adding another two row anchor ropes) is adopted, elongation lengths for all four cracks are smaller than that in the S2. Upper mouth reinforcement of anchor ropes takes good effect to control elongation of cracks (particularly cracks occurred in middle wall of the isolated mound).

6.3. Comparison with the Field Monitored Results

(1) Comparison on open width and depth of cracks

At the first of 1997, cracks occurred firstly in north and south top surfaces of the second shiplock room with beginning of excavation of shiplock room. On June 1998, some cracks occurred on top surface of the isolated mound from the second shiplock room to the fourth room. It is more serious on top surface of the isolated mound from the second shiplock room to the third room. Up to February 1999, total 140 cracks occurred in this area. Open width of cracks are measured to be 3.0 ~ 5.0 mm (70% of total cracks). Little is 5 ~ 10 mm. There are four cracks (3% of total cracks) whose open width is greater than 10 mm. The widest open is 23 mm. The crack down to rockmass has normal depth of 10 m, little is 10 ~ 20m, and the maximum value is 20 m.

The results from calculation indicates that open width of cracks 1 and 4 are greater than 5 mm, and their open width are less than 5 mm if without reinforcement. If reinforcement is used this case would be changed at somewhere. For reinforcement scheme 2 close to the actual case, open width of cracks 1, 2 and 3 are greater than 5 mm and 22.76 mm for crack 4. These results are close to measured values.

After shiplock room excavation is finished lengths of four main cracks including initial and elongated lengths are 13m, 15m, 9m, 23m, respectively, for the S1(without reinforcement). If the S2 is adopted, these cases would be improved, i.e., these values would reduce to 10m, 14m, 9m, 22m, respectively. These are greater than the measured values because initial lengths for four cracks are longer than these in actual.

(2) Comparison on rockmass deformation

For the monitoring sections 13-13, 15-15, and 17-17, several monitoring points have been constructed on north and south top surface. Up to May 1999, the north monitoring point on the

section 13-13 had a total deformation of 31.27mm toward to the north and the north monitoring point on the section 13-13 had a total deformation of 5.98mm toward the north. The relative deformation between two points was 37.25mm. The springback deformations in vertical direction for these two points were 9.88 mm and 0.46 mm. For the section 15-15, two monitoring points in south side got deformation toward the north with 17.18mm and 11.76mm respectively. The vertical subsidence for the north monitoring point was 1.82mm. The vertical springback for the south monitoring point was 17.61mm. On the section 17-17, the north and south monitoring points got deformation toward the north of 31.72mm and 30.69mm respectively. The vertical springbacks of 12mm and 21.98mm were for these points respectively.

The calculated resulted for the section 13-13 indicate that the relative deformation between the north and the south top surface of the isolated mound was 43.21mm, while the S2 close to the actual construction got a relative deformation of 31.85mm for these two sides. The later result is agreed with that the measured value. If the S1 is used, the vertical springback deformation for top surface of the north and south straight wall would be 22.62 mm and 17.03 mm respectively. If the S2 is used, the vertical springback deformation for top surface of the north and south straight wall would be 23.78 mm and 19.55 mm respectively. These results are agreed with the measured values for the sections 15-15 and 17-17.

7. CONCLUSIONS

The following conclusions will be drawn out:

(1) During excavation of full shiplock room, there is change between elongation of cracks and stopping cracking. Stress released at some excavation step, tip of crack existing tensile stress elongates toward the deep rockmass. The shorter cracks got stress release on its tip and stopped cracking. The longer cracks got restraining on its elongation after being reinforced. However, the following excavation will result in further elongation of the existed cracks. The length of crack elongation depends on excavation depth, reinforcement and initial length of crack itself, and its location in rockmass.

(2) Because of hard jointed rockmass, deformation of the isolated mound after excavated is mainly due to open of cracks while deformation of rockmass itself is small.

(3) Anchor ropes can restrain open and elongation of cracks. It should be reinforced using anchor ropes at suitable time during construction. Otherwise, open and elongation of cracks could not be controlled well. Anchor ropes constructed at top of the isolated mound have stronger control to open and elongation of cracks than that constructed in middle and bottom. Therefore, reinforcement location of anchor ropes is also important to control deformation of the isolated rockmass.

(4) When long occur together with short cracks, open width and elongation of longer cracks and shorter cracks close to sidewall of the isolated mound are larger than that of cracks occurred in middle of the isolated mound.

Acknowledgment This research was supported by the National Science Foundation of China under grant no. 59679020.

REFERENCE

1. Xu Ping, Xia Xulun, Chinese J. Of Rock Mechanics and Engineering, 1996, 15(1):62-70.
2. Xu Ping, Xia Xulun, J. of Yangtze River Scientific Research Institute, 1995, 12(3):31-36.

Out-Of-Plane ESPI Simulation for the Harmonic Vibration of a Thin Right-Angled Plate

Soon Suck Jarng¹, Je Hyeng Lee², Heung Gu Ahn² and Jae Chull Park²

¹ Department of Electrical Control & Instrumentation, Chosun University,
375 Seosuk-dong, Kwangju 501-759, Korea

² Department of Control & Instrumentation, Graduate School, Chosun University,
375 Seosuk-dong, Kwangju 501-759, Korea

Keywords: Electronic Speckle Pattern Interferometry ESPI, Finite Element Method FEM, Median Filtering, Monte Carlo Method, Phase Shifting, Phase Unwrapping, Simulation, Sobel Edge Enhancement, Vibration

ABSTRACT

A simulating program of the out-of-plane ESPI (Electronic Speckle Pattern Interferometry) method has been developed in order to assist the improvement of the ESPI technique. With this program a new ESPI method is suggested by which the laser speckle noise of the ESPI image could be removed in great amount. The vibrating object for the present application is a thin right-angled STS 304 plate. In the suggested ESPI method, the phase transformation of the reference wave of the ESPI is carried out only one time during harmonic vibration in order to clarify ESPI speckle patterns. Two dimensional vibrational modes are calculated from 3 ESPI patterns; one ESPI pattern before vibration onset and two ESPI patterns during vibrations but with and without the phase transformation. The ESPI modal results with this new phase-controlled method show much more clear modal figures than other previous results. Additionally a new phase unwrapping algorithm has been developed to derive a displacement map from an ESPI phase map.

1. INTRODUCTION

When a structural material is stressed or heated, the object is deformed. If the amount of the deformation is quantitatively measured, the materialistic and structural characteristics of the object could be known. Strain-gauges or piezoelectric sensors are commonly used for measurements of materialistic characteristics of any simple structure. Recently, various non-contacting and non-destructive techniques for such structural measurements using X-ray, ultrasound or laser, are rapidly developed and commercialized. ESPI (Electronic Speckle Pattern Interferometry) technique is one of laser applications for non-contacting measurements. It is reported that the ESPI technique enables in two dimension to measure the deformation of metallic objects caused by heating at more than 500°C [1,2]. The in-plane displacement of a stressed object and the out-of-plane displacement of a vibrating object are both possible to be measured by the ESPI [3]. The ESPI method introduced firstly by Butter and Leendertz [4,5] is an optically measuring device using both the speckle effects of laser and the interferometric phenomena of light. The application of the ESPI technique to industry has been slowly progressive since the earlier ESPI method still has some disadvantages of

measurement in precision and clarification. It is because the ESPI method has to directly use laser speckle noises of random intensities in its technical principle. Therefore differently modified ESPI techniques using subsidiary methods such as phase shifting methods [6] and phase transformation methods have been developed in order to increase the clarification of the ESPI. Also other new statistic or probabilistic algorithms such as least square phase estimation, maximum likelihood estimation and phase unwrapping methods are being developed in order to improve the precision of the ESPI. Those new ESPI techniques completely changed the experimental apparatus of the earlier ESPI techniques. For example, the phase shifting of the laser beam is now precisely controlled by a modified Michelson's interferometry in the realm of one wavelength. While experimental research is carried out on the ESPI development, the necessity of the ESPI simulation development comes into account. The software simulation of the ESPI technique may assist the improvement of the ESPI method. This paper deals with one particular case of the improvement of the ESPI clarification. That is, this paper suggests a new ESPI method for better performance in clarification. In the present paper the out-of-plane ESPI technique had been simulated as a Fortran program. Then, the two dimensional mode of a vibrating thin right-angled plate was calculated by the ESPI simulation.

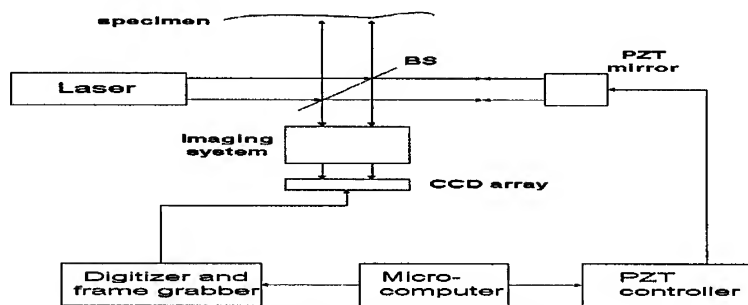


Fig. 1 Out-of-Plane ESPI apparatus

A new ESPI method using the phase shifting is designed for more clarified ESPI patterns than those of previous ESPI methods. The out-of-plane ESPI is mainly composed of a reference laser beam and an objective laser beam (Fig. 1). Both beams are splitted from the same coherent laser source by a beam splitter. The objective beam is expanded and is then crashed onto a plate by a beam expander. Some of scattered objective beam from the plate is reflected to a beam combiner in front of a CCD camera. The reference beam is guided to the same beam combiner but in normal direction so as to be interfered with the reflected objective beam. And the two dimensional image formed on the beam combiner by the two interfered beams is taken by the CCD camera. Since the reflected objective beam is highly random in its phase, the two interfered beams produce a laser speckle pattern. If the plate is vibrating, the laser speckle pattern would contain the information of the structural vibration. The simplest way of getting the vibrational information is pixel by pixel subtracting one laser speckle pattern before vibration with the other laser speckle pattern after vibration. The subtracted pattern image still has random speckle noise, so that the resulting vibrational modal image is difficult to interpret. In this paper, a new phase shifting method is developed for the improved clarification of the vibrational modal analysis. And a new algorithm of phase unwrapping is also presented.

Other results of previous ESPI methods showed poor clarification of vibrational modal patterns where either two laser speckle patterns before and after vibration were simply subtracted each other, or four laser speckle patterns with different phase shifts were arithmetically subtracted one another in order to derive the vibrational mode of the plate. Laser speckle noises were still remained in those figures, and particularly the latter method could only show the phase map of the vibrating plate rather than the displacement map (see results). This paper deals with the vibrational simulation of a thin right-angled STS 304 plate using the ESPI method with a new phase shifting feature. The

finite element method(FEM) is briefly mentioned in order to describe the three dimensional displacement of the thin right-angled plate. The FEM analysis would be helpful to comparatively understand any ESPI measurements.

2. METHODS

2.1. Finite Element Method

The FEM is initially programmed in order to calculate three dimensional displacements of the vibrating thin right-angled plate which are then used for the ESPI simulation. The isoparametric formulation for three dimensional structural elements is well documented by Allik H. et. al and Chung S.C. et. al. If an external force is applied to the plate, the force is distributed throughout whole elements and thereby nodal displacements are generated as a function of frequency as follows in steady state matrix formula:

$$[F] = ([K] - \omega^2[M])[a] \quad (1)$$

where $[F]$ is an applied mechanical force vector, $[K]$ is a elastic stiffness matrix, $[M]$ is a mass matrix, and $[a]$ is an elastic displacement vector. ω is an angular frequency. The thin rectangular right-angled STS 304 plate (L. 150mm x W. 75mm x T. 0.8mm) are rigidly fixed at both end sides and a centre point is vibrated at 10 kHz as an external force drive (Fig. 2). The density of the STS 304 is 8000Kg/m³ and its Young's modulus is 193 GPa and its poisson's ratio is 0.3. The right-angled plate is divided into total 1250 elements (50Lx25Wx1T) (Fig. 3).

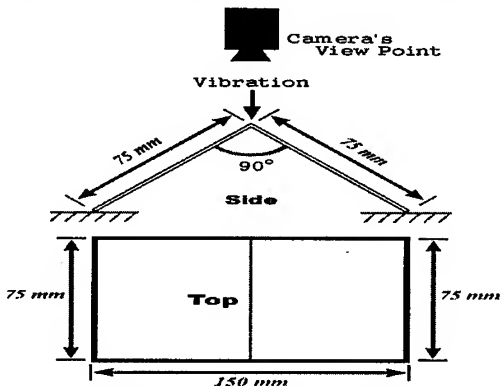


Fig. 2 Vibration applied onto a centre point of a thin rectangular right-angled STS 304 plate.

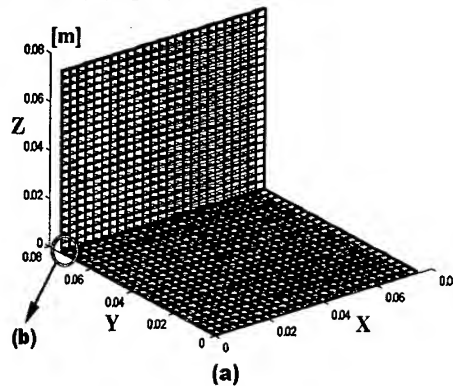


Fig. 3 1250 finite elements of the thin right-angled plate

2.2. Electronic Speckle Pattern Interferometry

The optical apparatus of the out-of-plane ESPI using a He-Ne laser ($\lambda = 632.8$ nm) is well described by Hong J.K. et. al (Fig. 1). The present out-of-plane ESPI has a piezoelectric (PZT) translator in its component in order to enable the phase shift of the reference beam. The PZT translator is calibrated in order to find the most linear realm of the voltage-displacement relationship. Therefore the phase shift is assumed to be controlled precisely. If the intensity of the reference beam, $\zeta_r(x,y)$ is $U_r(x,y)^2$ and that of the objective beam, $\zeta_o(x,y)$, is $U_o(x,y)^2$, and their phases on the interfering point (x,y) of the beam combiner is $\phi_r(x,y)$ and $\phi_o(x,y)$ respectively, then the intensity of the interfered beam is defined.

$$I(x,y) = |\xi_r(x,y) + \xi_o(x,y)|^2 = \alpha(x,y) + \beta(x,y) \cdot \cos\Psi(x,y) \quad (2)$$

Where, $\alpha(x,y) = U_o(x,y)^2 + U_r(x,y)^2$, $\beta(x,y) = 2 \cdot U_o(x,y) \cdot U_r(x,y)$, $\Psi(x,y) = \Psi_o(x,y) - \Psi_r(x,y)$

The displacement amplitude of the vibrating plate is defined as $a(x_1, y_1)$. If the intensity of the

interfered beam is two-dimensionally acquired during vibration by the CCD camera for an interval of $1/30[\text{sec.}]$, then the acquiring time might be much longer than one period of the vibration. The time-averaged (much longer than one period of an input frequency) displacement amplitude of the vibrating plate is derived as the first kind and the 0^{th} order Bessel function, $J_0(4\pi a(x_1, y_1)/\lambda)$. The two-dimensionally acquired intensity values mean a deformed laser speckle pattern caused by the vibration. Let the two-dimensionally acquired intensity values be $I_n(x, y)$. Now three different $I_n(x, y)$ are considered. Firstly Let the acquired intensity pattern before the vibration with no phase shifting be $I_1(x, y)$ and secondly let the acquired intensity pattern during the vibration but with no phase shifting be $I_2(x, y)$. Thirdly let the acquired intensity pattern during the vibration with π phase shifting be $I_3(x, y)$. These intensity patterns of the optical interferometry could be mathematically expressed as following equations;

$$I_1(x, y) = \alpha(x, y) + \beta(x, y) \cdot \cos(\Psi(x, y)) + \varepsilon_1(x, y) \quad (3)$$

$$I_2(x, y) = \alpha(x, y) + \beta(x, y) \cdot \cos \Psi(x, y) \cdot J_0\left(\frac{4\pi a(x_1, y_1)}{\lambda}\right) + \varepsilon_2(x, y)$$

$$I_3(x, y) = \alpha(x, y) + \beta(x, y) \cdot \cos(\Psi(x, y) + \pi) \cdot J_0\left(\frac{4\pi a(x_1, y_1)}{\lambda}\right) + \varepsilon_3(x, y)$$

where $\varepsilon_1(x, y)$, $\varepsilon_2(x, y)$, $\varepsilon_3(x, y)$ are electrical noises of photoelectric sensors inside the CCD camera. From equation (3) J_0 could be derived as

$$J_0\left(\frac{4\pi a(x_1, y_1)}{\lambda}\right) = \frac{I_2(x, y) - I_3(x, y)}{2I_1(x, y) - I_2(x, y) - I_3(x, y)} \quad (4)$$

Then $a(x_1, y_1)$ can be calculated from $J_0(4\pi a(x_1, y_1)/\lambda)$ by the inverse transformation of the Bessel function. Since the Bessel function does not correspond with its variable one by one, a numerical method need to be considered for the inverse transformation. This inverse process is called as phase unwrapping in this paper, and a new practical method will be explained in results.

The computational simulation of the out-of-plane ESPI begins with Monte-Carlo method by which $U_r(x, y)^2$, $U_o(x, y)^2$, $\Psi(x, y)$ and $\varepsilon(x, y)$ are all calculated from their probability density functions (pdf) [16]:

$$P_{I_r}(I_r) = \frac{1}{\sqrt{2\pi\sigma^2 I_r}} \exp\left(-\frac{(I_r - \langle I_r \rangle)^2}{2\sigma^2 I_r}\right) \quad (5)$$

where I_r is the intensity of the reference beam and $\langle I_r \rangle$ is its mean value and σ_{I_r} is a standard deviation. The reference beam has a Gaussian pdf.

$$P_{I_o}(I_o) = \frac{\left(\frac{M}{\langle I_o \rangle}\right)^M I_o^{M-1} \exp\left(-M \frac{I_o}{\langle I_o \rangle}\right)}{\Gamma(M)} \quad (6)$$

where I_o is the intensity of the objective beam and $\langle I_o \rangle$ is its mean value. The pdf of I_o is similar to a gamma function. It happens because the size of the photoelectric sensor is bigger than the size of a laser speckle, so that a small group of laser speckles are acquired in average by a single photoelectric sensor. Because of this effect, it is better to use photoelectric sensors of smaller size. In the other way the size of the laser speckle could be adjusted by a zoom lens in order to make it to have the similar size as the photoelectric cell size. The parameter M of the gamma function depends not only on the distance between the plate surface and the camera lens but also on the size of the iris. Here $M=2$.

$$P_E(\varepsilon) = \frac{1}{\sqrt{2\pi\sigma^2 E}} \exp\left(-\frac{(\varepsilon - \langle \varepsilon \rangle)^2}{2\sigma^2 E}\right) \quad (7)$$

where $\langle \varepsilon \rangle$ and σ_E are a mean and a standard deviation, $\langle \varepsilon \rangle = 0.95$ and $\sigma_E = 1.97$.

$$p_U(u) = \frac{1}{2\pi\sqrt{1-u^2}}, \quad -1 < u < +1 \quad (8)$$

where $u = \cos(\Psi)$

3. RESULTS AND DISCUSSION

A FEM program had been developed in Fortran and was run at a super computer (Cray C90). The simulated three-dimensional displacement of the vibrating thin right-angled STS 304 plate is shown in Fig. 4. The input frequency is 10 kHz. The amplitude of the nodal displacement, $a(x_1, y_1)$, at any point (x_1, y_1) on the plate surface is then calculated by interpolation for which the total plate surface is again divided into $256(L) \times 128(W)$ lattice windows.

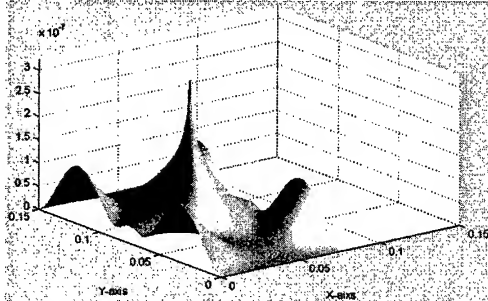


Fig. 4 The amplitude of the three-dimensional displacement is derived from the vibrational magnitude for one cycle

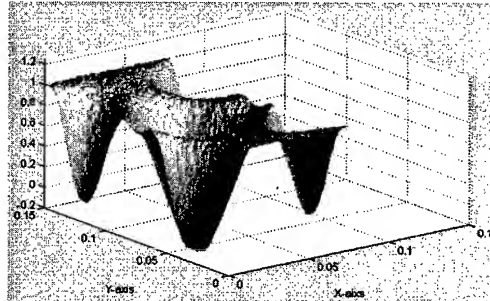


Fig. 5 Laser speckle noise rejection by median filtering

As mentioned in the method, $J_0(4\pi a(x_1, y_1)/\lambda)$ was then calculated from $a(x_1, y_1)$ by the Bessel function. And $\alpha(x, y)$, $\beta(x, y)$, $\varepsilon(x, y)$ and $\Psi(x, y)$ were calculated by equation (2) from intensity patterns with pdfs of equations (5)~(8). And then $I_1(x, y)$, $I_2(x, y)$, $I_3(x, y)$ were calculated by equation (3) from speckle patterns of $\alpha(x, y)$, $\beta(x, y)$, $\varepsilon(x, y)$, $\Psi(x, y)$ and $J_0(4\pi a(x_1, y_1)/\lambda)$. $I_1(x, y)$, $I_2(x, y)$ and $I_3(x, y)$ are the simulated results of the out-of-plane ESPI. From given $I_1(x, y)$, $I_2(x, y)$ and $I_3(x, y)$, $J_0(4\pi a(x_1, y_1)/\lambda)$ is inversely calculated by equation (4). The calculated $J_0(4\pi a(x_1, y_1)/\lambda)$ is often mixed with speckle noise. Median filtering is most effective to remove such speckle noise in $J_0(4\pi a(x_1, y_1)/\lambda)$ (Fig. 5). Fig. 5 shows the simulated ESPI result of the vibrating plate's displacement mode in three dimension. Now, the displacement map $a(x_1, y_1)$ has to be derived from $J_0(4\pi a(x_1, y_1)/\lambda)$ of Fig. 5.

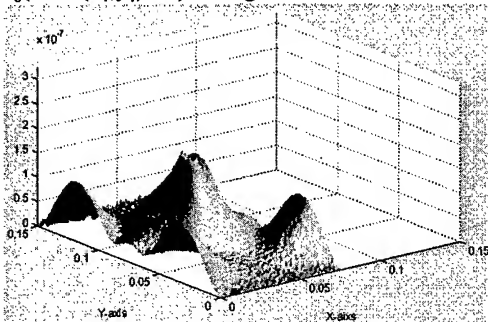


Fig. 6 $4\pi a(x_1, y_1)/\lambda$ are calculated by one by one inverse matching according to Bessel function $J_0(x)$ with $0 \leq x \leq 3.8317$.

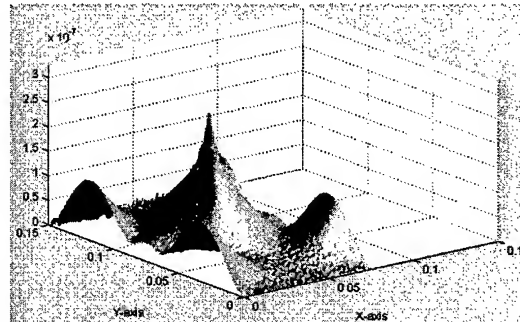


Fig. 7 Vibration displacement amplitude of the STS 304 plate calculated from three laser speckle patterns acquired by the simulated ESPI.

It is called as a phase unwrapping process (inverse transformation of Bessel function). The Bessel function $J_0(x)$ has a maximum value, 1, and a minimum value, -0.4028. The variable x of $J_0(x)$ corresponding to the maximum is 3.8317. Therefore at first, if x is between 0 and 3.8317, $4\pi a(x_i, y_i)/\lambda$ is calculated from the Bessel function by one by one inverse matching (Fig. 6). Some central areas of Fig. 6 are almost close to 3.8317 in their amplitudes. The amplitudes of those corresponding pixels might be in fact bigger than 3.8317 but be decreased by the Bessel function. Therefore a Sobel edge enhancement method can be used to mark the local area of the amplitude more than 3.6. In this method, the two dimensional differentiation of the locally decreased area gives negative values for the local area. If the locally marked area of Fig. 6 are assumed to have bigger displacement amplitudes than 3.8317, since the second maximum value of $J_0(x)$ is 0.3001 at $x=7.0156$, a new increased $4\pi a(x_i, y_i)/\lambda$ could be calculated from the Bessel function by one by one inverse matching between $3.8317 < x < 7.0156$. Fig. 7 shows the displacement amplitude of the vibrating plate, $a(x_i, y_i)$, after removing $4\pi/\lambda$ parameter. Comparing Fig. 7 with Fig. 4, the simulated ESPI displacement results of the vibrating thin right-angled STS 304 plate are very similar to those of FEM results. In case of the FEM, the maximal displacement amplitude in the middle of Fig. 4 is $3.237\text{E-}7$ [m] and the average and the standard deviation of the total nodal displacements are $5.224\text{E-}8$ [m] and $3.594\text{E-}8$ [m] respectively. In the ESPI simulation, the displacement amplitude at the same central location is $2.713\text{E-}7$ [m] and the average and the standard deviation of the total nodal displacements are $5.229\text{E-}8$ [m] and $3.594\text{E-}8$ [m] respectively.

4. CONCLUSION

In this paper the out-of-plane ESPI technique had been simulated. A series of interfered laser speckle patterns of a vibrating thin right-angled STS 304 plate were generated with the phase shifting of the ESPI reference beam. The first laser speckle pattern was acquired before any vibration with no phase shifting. The second laser speckle pattern was acquired during steady-state vibration with no phase shifting. And the third laser speckle pattern was acquired during the vibration with the π phase shifting. Those three laser speckle patterns were all acquired for the estimation of the out-of-plane displacement of the vibrating plate. A FEM program and a phase unwrapping technique had also been developed for the comparative purpose of the structural vibration analysis. Both vibrational modal results of the ESPI and structural displacement results of the FEM are well agreed quantitatively each other.

REFERENCE

1. K.S. Kim, J.H. Kim, J.K. Lee and S.S. Jarng, "Measurement of thermal expansion coefficients by electronic speckle pattern interferometry at high temperature", *J. of Materials Science Letters*, Vol. 16, (1997) p. 1753.
2. D.J.V. Martin, "Laser Speckle Photography Measurement of Movement and Strain in Structure at Temperature of 20-520°C", *Materials Evaluation*, Vol. 36(53), (1987) p. 53.
3. K.S. Kim and S.P. Yang, "A study on the strain analysis of cracked plate by electronic speckle pattern interferometry", *Trans. of the Korean Soc. of Mech. Eng.*, Vol. 19, no. 6, (1995) p. 1382.
4. J.A. Leendertz, "Scientific Instruments", *J. Phys. E.*, Vol. 3, (1970)p. 214.
5. J.M. Burch and J.A. Leendertz, "Scientific Instruments", *J. Phys. E.*, Vol. 4, (1971) p. 1.
6. D. Kerr, F.M. Santoyo and J.R. Tyrer, "Extraction of phase data from electronic speckle pattern interferometric fringes using a single-phase-step method : a novel approach," *Opt. Soc. of Am.*, Vol. 7, (1990) p.820.

Element Modeling for Vibration Analysis of Plate

Y.P. Shi and P. Zeng

Department of Mechanical Engineering, Tsinghua University,
Beijing 100084, China P.R.

Keywords: Composite Element Method, Element Modeling, Plate, Vibration Analysis

ABSTRACT

A new element model for vibration analysis of elastic thin plate is proposed, which couples the versatility of the conventional FEM and the high accuracy of the classical theory through the construction of shape function. Two kinds of approaches are discussed to improve the analytical accuracy of the model: (1) to refine the element mesh, i.e., h-version, (2) to increase the DOF based upon the classical theory, i.e., c-version. A large number of numerical examples show that c-version can lead to a super-convergence. The contents of this paper include: the principle of combining the conventional FEM and the classical theory, the nodal coordinate and the field coordinate, construction of displacement field function, element characteristics, numerical examples.

1. ABOUT COMPOSITE ELEMENT METHOD

From the detailed comparisons between the classical approach and FEM in several aspects: the form of solution function, solving procedure, accuracy, efficiency, versatility and applicable scope, etc., we know that both classical theory and FEM possess individual characteristics when solving differential equation or mechanics problems. In a straightforward manner, it is expected to combine the advantages of these two methods.

According to this philosophy, a new numerical method, Composite Element Method (CEM), is proposed [1]. The first aim of Composite Element method is to utilize the versatility of the FEM wherein the field functions are expressed in the form of nodal values [2,3,4]. The second aim is to embed the analytical solution of classical theory over the domain of the element into the field function of the elements. To this end, the first step is to define the appropriate coordinate system of element, which is used as a fundamental frame to describe the displacement field of element. Then the displacement field is constructed based on the given coordinate system. Meanwhile, the related boundary condition of element must be matched. In fact, the superposition method and singular element method have same concept[5,6], but they have not demand of matching the node boundary condition of element.

We have carried out the following research work.

(1) To develop the theory of Composite Element Method, which can couple the conventional FEM and the classical theory, possesses the versatility to various complex geometric shapes and excellent approximation of solution.

(2) To define two sets of coordinate systems to describe the displacement field of elements: the nodal DOF system (the same as in the ordinary FEM), the field DOF system of element.

(3) To propose the coupling boundary condition of element, which will be as the boundary condition when utilizing the classical theory to obtain the closed solution of the element.

(4) To develop two approaches of CEM, *h*-version and *c*-version, which can help to improve the accuracy of the solution. The latter having an ability to lead up to a super convergence.

For any element, without loss of generality, we choose the following combination of both the polynomials and the analytical functions to describe the displacement field:

$$U = U_{FEM} + U_{CT} = \mathbf{N}\mathbf{q} + \phi c \quad (1)$$

where U_{FEM} is the displacement field function by FEM based on the nodal DOF. \mathbf{N} is the space-dependent shape function of the conventional FEM. U_{CT} is the displacement field function by the classical theory based on the field DOF. ϕ is the analytical function series by classical theory. According to the above expression, obviously, \mathbf{q} is the nodal coordinate of the conventional FEM, also called *nodal DOF*, and c is the field coordinate, also called *c-DOF* or *c-coordinate*. It has to be pointed out that the field coordinate and its corresponding basis function ϕ are not arbitrary. The function ϕ must satisfy some requirements, especially the boundary conditions of element.

2. THIN PLATE ELEMENT OF COMPOSITE ELEMENT METHOD

The compatible rectangular 4-node thin-plate element of CEM is developed as follows. Take the origin of local *x-y* coordination at the corner of beam element, $x \in [0, 2a]$, $y \in [0, 2b]$, where $2a, 2b$ are the length of rectangle's two edge respectively in *x* and *y* direction. Transform the coordination *x, y* into ξ, η , where

$$\xi = \frac{x}{a} - 1, \quad \eta = \frac{y}{b} - 1 \quad \xi, \eta \in [-1, 1] \quad (2)$$

According to the Kirchhoff assumption, the transverse shear strains is considered to be zero. As a result, all of an element's bending properties can be derived from a single variable, the lateral displacement $w(\xi, \eta)$, which is described as

$$w(\xi, \eta) = w_{FEM}(\xi, \eta) + w_{CT}(\xi, \eta) \quad (3)$$

where $w_{FEM}(\xi, \eta)$ is the displacement field function of conventional FEM based on nodal DOF. $w_{CT}(\xi, \eta)$ is the classical solution functions based on field DOF. It can be seen that the conventional FEM and the classical method are combined in the construction of displacement field. The detailed expression of these two parts of $w(\xi, \eta)$ is given below.

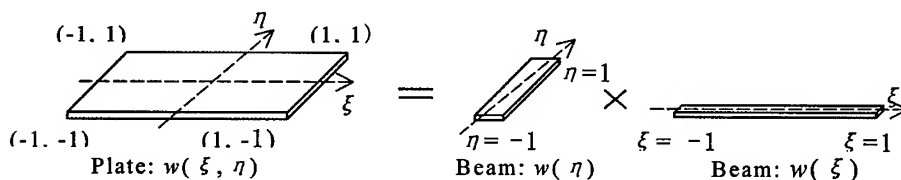


Fig. 1 Expanding the 2D displacement field function as the product of two 1D displacement field functions along the ξ and η directions

A natural and effective approach is considered to construct the rectangle CEM element. As

shown in Fig.1, the 2D displacement field function $w(\xi, \eta)$ is formed by multiplying together the displacement field functions of two beam element respectively in ξ and η directions, i.e.,

$$w(\xi, \eta) = w_{\text{beam}}(\xi)w_{\text{beam}}(\eta) \quad (4)$$

where $w_{\text{beam}}(\xi)$ and $w_{\text{beam}}(\eta)$ take the following form,

$$\begin{aligned} w_{\text{beam}}(\xi) &= \mathbf{N}(\xi)\mathbf{q}_\xi + \Phi(\xi)\mathbf{c}_\xi \\ &= w_{\xi 1}N_{w1}(\xi) + \theta_{\xi 1}N_{\theta 1}(\xi) + w_{\xi 2}N_{w2}(\xi) + \theta_{\xi 2}N_{\theta 2}(\xi) \\ &\quad + c_{\xi 1}F_1(\lambda_1^*, \xi) + c_{\xi 2}F_2(\lambda_2^*, \xi) + \dots + c_{\xi n_\xi}F_{n_\xi}(\lambda_{n_\xi}^*, \xi) \\ w_{\text{beam}}(\eta) &= \mathbf{N}(\eta)\mathbf{q}_\eta + \Phi(\eta)\mathbf{c}_\eta \\ &= w_{\eta 1}N_{w1}(\eta) + \theta_{\eta 1}N_{\theta 1}(\eta) + w_{\eta 2}N_{w2}(\eta) + \theta_{\eta 2}N_{\theta 2}(\eta) \\ &\quad + c_{\eta 1}F_1(\lambda_1^*, \eta) + c_{\eta 2}F_2(\lambda_2^*, \eta) + \dots + c_{\eta n_\eta}F_{n_\eta}(\lambda_{n_\eta}^*, \eta) \end{aligned} \quad (5)$$

Substitution of Eq.(5) in Eq.(4) yields:

$$\begin{aligned} w(\xi, \eta) &= (\mathbf{N}(\xi)\mathbf{q}_\xi + \Phi(\xi)\mathbf{c}_\xi) (\mathbf{N}(\eta)\mathbf{q}_\eta + \Phi(\eta)\mathbf{c}_\eta) \\ &= \mathbf{N}(\xi)\mathbf{q}_\xi \mathbf{N}(\eta)\mathbf{q}_\eta + \Phi(\xi)\mathbf{c}_\xi \Phi(\eta)\mathbf{c}_\eta + \mathbf{N}(\xi)\mathbf{q}_\xi \Phi(\eta)\mathbf{c}_\eta + \mathbf{N}(\eta)\mathbf{q}_\eta \Phi(\xi)\mathbf{c}_\xi \end{aligned} \quad (6)$$

In order to get a more accurate solution, two approaches are available to improve CEM, the h -version and the c -version. The h -version of CEM, just like that of FEM, is to increase the accuracy by refining the element mesh. However, the c -version of CEM is defined as increasing of the c -DOF (i.e., increasing the trial function terms obtaining from the analytical solution of the classical theory), which is different from the p -version of the conventional FEM.

CEM exhibits a super-convergence in the solving of structural dynamical problem. The reason lies in that the trial function used in CEM involves a set of hierarchical analytical bases obtained from the classical theory, instead of the usual polynomial bases. The trial function itself inherently possesses the properties of vibration modes. The c -version is, in some sense, related to the theory of spectral method. Therefore, the use of the c -version of CEM results in achieving an improved approximate solution at less computational expense than the use of mesh refinement.

3. NUMERICAL VERIFICATION

3.1 Free vibration of square plate

A detailed confirmation for the Composite Element Method is given below. Consider the free vibration of a square plate shown in Fig. 2. The boundary conditions are two opposing edges simple supported, one edge clamped and one edge free.

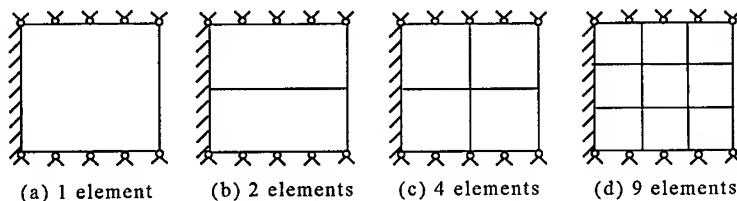


Fig.2 Discretization of square plate

Let

$$\lambda_i^2 = w_i l_x^2 \sqrt{\frac{\rho t}{D}} \quad w_i = 1, 2, 3, \dots \quad (7)$$

where w_i is the natural frequencies. l_x is the length of plate edge along x direction. ρ is the density. t is the plate thickness. D is the flexural rigidity:

$$D = \frac{EI}{1-\nu^2} = \frac{E}{1-\nu^2} \int_{-t/2}^{t/2} z^2 dz = \frac{Et^3}{12(1-\nu^2)} \quad (8)$$

where ν is the Poisson ratio.

One idealizes the plate into 1 element and 4 elements, then applies the Composite Element Method to calculate the natural frequencies. Consider several calculating schemes wherein the number of c -order respectively equals to 0, 1, 2 and 3. Here, "the number of c -order equals to m " means that the order of classical functions in Eq.(5) equals to m , i.e., $n_\xi = n_\eta = m$.

Table 1 Eigenvalue λ_i of various schemes in case of 1 element discretization

	FEM(1e)* c-order: 0 c-DOF ***: 0 Total DOF:4	CEM(1×1c) c-order: 1 c-DOF: 5 Total DOF:9	CEM(1×2c)** c-order: 2 c-DOF: 12 Total DOF:16	CEM(1×3c) c-order: 3 c-DOF: 21 Total DOF:25	ANSYS (1225 elements)	Exact
λ_1	3.7321	3.5633	3.5633	3.5621	3.5622	3.562
λ_2	6.8062	5.7984	5.7550	5.7536	5.7496	5.750
λ_3	7.2664	7.2189	6.4650	6.4605	6.4587	6.457
λ_4	9.1972	8.5264	7.9502	7.9499	7.9373	7.938
λ_5		11.140	8.5446	8.5175	8.5065	8.509
λ_6		11.305	10.252	9.5293	9.5209	9.519
λ_7		12.007	11.140	10.173	10.153	
λ_8		12.828	11.921	10.603	10.577	
λ_9		15.277	13.479	11.493	11.460	
λ_{10}			15.195	12.389	12.353	
λ_{11}			15.758	12.814	12.624	
λ_{12}			16.178	14.711	12.734	
λ_{13}			16.949	15.187	13.430	

* The symbol FEM(1e) denotes using one thin plate element of the conventional FEM.

** The symbol CEM (1×2c) means using one composite element with the c -order of 2.

*** In the count of both c -DOF and Total DOF, the DOF constrained in boundary conditions are excluded.

As shown in Table 1 and Table 2, various order of eigenvalues λ_i resulted from above calculating schemes are compared with the exact classical solutions, as well as the result from ANSYS. In the ANSYS model, the element type is bending-only 4-node shell, and totally 1225 elements is used.

It can be found that in each scheme of CEM, when the orders of the resultant eigenvalues are less than the element number multiplied by the square of the number of c -order, the result will be very close to the exact solution and ANSYS results. Take the scheme of CEM(4×2c) as example, in which the element number $n_e=4$ and the number of c -order $n_c=2$, the resultant eigenvalues from λ_1 to λ_{16} are very close to the exact solution, and the maximum relative error (i.e., that of λ_{16}) is only 0.17%.

Table 2 Eigenvalue λ_i of various schemes in case of 4 element discretization

	FEM(4e)* c-order: 0 c-DOF: 0 Total DOF:16	CEM(4 × 1c)** c-order: 1 c-DOF: 20 Total DOF:36	CEM(4 × 2c) c-order: 2 c-DOF: 48 Total DOF:64	CEM(4 × 3c) c-order: 3 c-DOF: 84 Total DOF:100	ANSYS (1225 elements)	Exact
λ_1	3.5708	3.5622	3.5620	3.5619	3.5622	3.562
λ_2	5.7879	5.7539	5.7507	5.7504	5.7496	5.750
λ_3	6.7803	6.4591	6.4582	6.4578	6.4587	6.457
λ_4	8.1864	7.9451	7.9399	7.9387	7.9373	7.938
λ_5	9.2362	8.5290	8.5104	8.5095	8.5065	8.509
λ_6	10.579	9.6536	9.5242	9.5218	9.5209	9.519
λ_7	10.833	10.191	10.161	10.159	10.153	
λ_8	11.483	10.694	10.585	10.581	10.577	
λ_9	13.407	11.580	11.492	11.468	11.460	
λ_{10}	14.227	12.481	12.370	12.365	12.353	
λ_{11}	14.389	12.869	12.628	12.627	12.624	
λ_{12}	15.133	14.215	12.771	12.748	12.734	
λ_{13}	16.203	14.786	13.442	13.439	13.430	
λ_{14}	16.363	14.843	14.552	14.507	14.493	
λ_{15}	18.032	16.060	14.615	14.592	14.569	
λ_{16}	20.313	16.936	14.900	14.893	14.874	
λ_{17}		17.721	15.592	15.537	15.515	
λ_{18}		17.822	16.087	15.769	15.744	
λ_{19}		18.384	16.721	16.415	16.390	
λ_{20}		18.868	16.828	16.810	16.772	

* The symbol FEM(4e) denotes using four thin plate element of the conventional FEM.

** The symbol CEM (4 × 1c) means using four composite elements with each c-order being to 1.

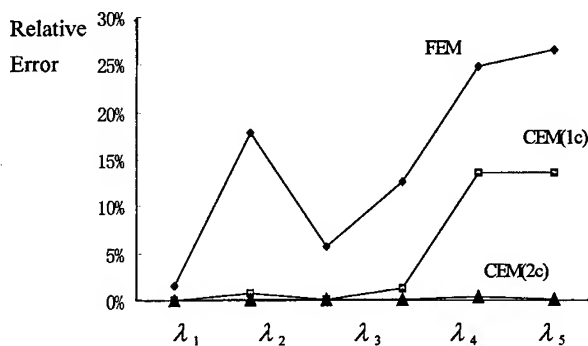


Fig.3 Comparison between the relative errors of FEM and CEM

As shown in Fig.3, the relative errors of FEM and CEM, both of which use 2 elements, is compared. It can be found that under the same number of elements, the accuracy of CEM is much higher than that of FEM. Take the 8th-order eigenvalue as the example, the relative error of FEM is 26.5%, while that of CEM(2 × 1c) is 13.5% and that of CEM(2 × 2c) is 0.156%. With the increase of c-order, the accuracy is effectively improved.

4. REMARKS

The thin plate element of The Composite Element Method, a new numerical approach for structural dynamics, is developed in this paper. The related characteristics and convergence of CEM are summarized as follows.

(1) The Composite Element Method is proposed by combining the conventional FEM and classical theory. Therefore, it inherits the powerful versatility of FEM in dealing with various complex geometric shapes and boundary conditions, as well as the excellent approximation and super-convergence of the classical theory.

(2) The core of CEM is to choose a special combined function as the trial function of a displacement field, which is constructed by the combination of the nodal interpolation polynomials of the FEM and the analytical solutions based on the classical theory

(3) The 2D displacement field function of plate element in CEM can be effectively formed by multiplying together the displacement field functions of two beam element respectively in ξ and η directions.

(4) In order to get a more accurate solution, two approaches are available to improve CEM, the h -version and the c -version. Numerical examples show the c -version of CEM is of paramount significance in obtaining the fine approximate solution in structural dynamics.

(5) CEM exhibits a super-convergence in the solving of structural dynamical problem. The reason lies in that the trial function used in CEM involves a set of hierarchical analytical bases obtained from the classical theory, instead of the usual polynomial bases.

ACKNOWLEDGEMENT

This work is supported by the National Natural Science Foundation of China (Grant No. 59775017), the Aviation Science Foundation of China (Grant No.96G51105) and the FOK YING TUNG Education Foundation. Also thanks to K.Z. Tang and W.W. Liang for their programming work.

REFERENCE

1. P. Zeng, Composite Element Method for Vibration Analysis of Structure, Part I: Principle and C^0 Element(Bar), Part II: C^1 Element(Beam). Journal of Sound and Vibration, **218**(1998),p.619-696
2. Zienkiewicz and B.Morgan, Finite Elements and Approximation, Wiley, New York (1983)
3. Zienkiewicz and R.L. Taylor, The Finite Element Method, Vol.1, Basic Formulation and Linear Problems, McGraw-Hill Book Company, 4th Edition, London(1989)
4. A.G.Peano, Hierarchies of conforming finite elements for plane elasticity and plate bending. Computers and Mathematics with Applications. **2**(1976), p.211
5. G.Yagawa and T.Nishhioka, Finite element analysis of stress intensity factors for plane extension and plate bending problems, Int. J. For Num. Methods. In Eng., **14**(1979), p.727-740
6. T.Nishioka and S.N.Atluri, Numerical modeling of dynamic crack propagation in finite bodies, by moving singular elements – part I formulation, J. App. Mech., **47**(1980), p.570-576

Hierarchical Models for Laminated Composite Structures Based on p-Extensions

J.R. Cho, S.H. Kim and D.Y. Ha

School of Mechanical Engineering, Pusan National University,
30 Jangjeon-Dong, Kumsong-Ku, Pusan 609-735, Korea

Keywords: Finite Element Analysis, Hierarchical Models, Laminated Composites, Model Accuracy, Modeling Error, Numerical Approximation Error, Thickness Polynomials

ABSTRACT

This paper is concerned with the exploration of hierarchical models for the reliable numerical analysis of laminated composite structures. Here, a construction of the hierarchical models and the investigation on their spectral characteristics along the model level and the relative structure thickness are major concerns. By varying the maximum thickness-polynomial orders in the displacement field, we sequentially define the hierarchical models. Through the numerical experiments, we examine the variations of stress and local modeling error distributions and the convergence rates along the two key parameters.

1. INTRODUCTION

In every numerical analysis of real natural problems, at least two error components, the modeling and the numerical approximation errors, are inherently involved in the final numerical results, as illustrated in Fig. 1(a). Therefore, the selection of suitable analysis model becomes a first important step for the results with the desired quality. However, most research efforts so far in computational mechanics have been made for minimizing the numerical approximation error.

Fortunately, a new modeling technology called hierarchical modeling has been introduced early in 1990's by Babuska et al. [1], Oden and Cho [2-3], Szabo et al. [4] and other several investigators. As illustrated in Fig. 1(b), this technology is to adaptively and systematically generate an optimal spatial combination of analysis models u^q with different model levels, called hierarchical models, so as to meet the predefined modeling tolerance.[3-4] Here, the hierarchical models refer to a set of analysis models for a specific physical problem which are sequentially defined by a key parameter defining the model level in the solution field.[1-2,4,7] These models possess sort of spectral model accuracies such that the model accuracy increases in proportion to the model level.

Thin structures such as beam-, arch-, plate- and shell-like bodies are representative engineering problems for the hierarchical modeling. This is because, owing to their geometry feature of small thickness to the reference surface dimension, the displacement and stress fields can be distinguished by the maximum thickness-polynomial order wherein. In these cases, the relative thickness and the maximum polynomial order become two key parameters characterizing the hierarchical models.

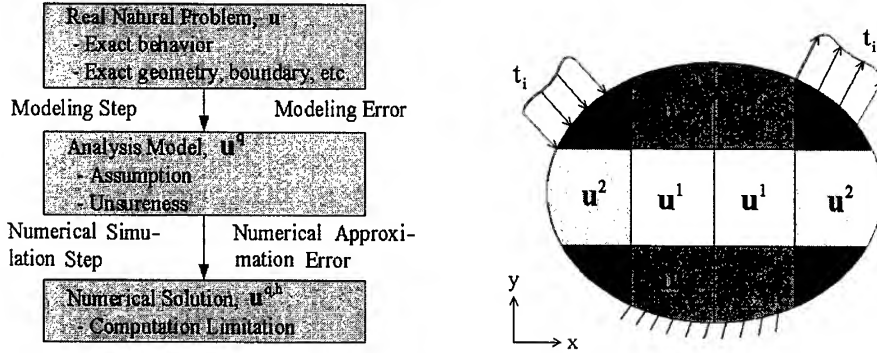


Fig. 1. Illustrations; (a) numerical analysis steps and (b) hierarchical modeling.

For the numerical analysis of laminated composites, traditionally two broad analysis models, equivalent single layer models [5] and layerwise models [6], have been widely used. However, most of conventional models are restricted to lower thickness-polynomials in displacement field, and which may be insufficient at the region where stress field exhibits complex variations through the thickness. One can use higher-order theories for better results, but which is strongly faced with the accuracy-computation cost dilemma. In order to resolve these difficulties, Szabo et al. [4] and Bertoti [7] extended the hierarchical modeling concept to laminated composites. But, their studies are at the preliminary stage.

In this paper, we aim at the intensive exploration of hierarchical models of laminated composites. For this goal, we first construct them and investigate their characteristics. And then, through numerical experiments, we examine the sequential variations in stress and local modeling error distributions and the d-convergence rates along the model level and the relative thickness.

2. HIERARCHICAL MODELS FOR LAMINATED COMPOSITES

2.1. A Model Problem

For a simplicity purpose, we consider a two-dimensional plane-strain laminated composite Ω of uniform thickness $2d$ composed of M orthotropic layers, as shown in Fig. 2(a), where ω indicates the reference line with its end boundary $\partial\omega$. Layerwise constant body force $\mathbf{f} \in [L^2(\Omega)]^2$ and external traction $\mathbf{t} \in [L^2(\partial\Omega_N)]^2$ are applied on the upper and lower surfaces $\partial\Omega_N$. Details on the mathematical definitions in this paper are referred to Adams [8]. Viewing the laminated structure as a two-dimensional linear elasticity, we formulate the elliptic boundary-value-problem:

$$\left. \begin{aligned} \sigma(\mathbf{u})_{\alpha\beta,\beta} + f_\alpha &= 0, & \text{in } \Omega \\ \sigma_{xy} &= \pm t_x \\ \sigma_{yy} &= \pm t_y \\ u_\alpha &= 0, & \text{on } \partial\omega \times [-d, d] \end{aligned} \right\}, \quad (\alpha, \beta = x, y) \quad (1)$$

Referring to Fig. 2(b) presenting k -th laminate, its material coordinates $(x', y')_k$ are aligned such that $y' = y$ and x' is rotated by θ_k with respect to the global coordinates. For such a two-dimensional orthotropic material, the laminar material stiffness matrix $[C]_k$ in the material coordinates constitutes the local plane-strain stress-strain relations:

$$\{\sigma'\}_k = [C]_k \{\epsilon'\}_k : \begin{cases} \sigma_{x'x'} \\ \sigma_{y'y'} \\ \tau_{x'y'} \end{cases}_k = \begin{bmatrix} C_{11} & C_{12} & 0 \\ C_{12} & C_{22} & 0 \\ 0 & 0 & C_{66} \end{bmatrix}_k \begin{cases} \epsilon_{x'x'} \\ \epsilon_{y'y'} \\ \gamma_{x'y'} \end{cases}_k \quad (2)$$

with Cauchy stress and strain tensors $\sigma'_{\alpha\beta}, \epsilon'_{\alpha\beta}$ measured in the material coordinates. In above relations, $C_{\alpha\alpha} = (1 - \nu_{\beta 3} \nu_{3\beta}) E_\alpha / \Delta$, $C_{12} = (\nu_{21} + \nu_{23} \nu_{31}) E_1 / \Delta$ and $C_{66} = G_{12}$ with Δ defined by $(1 - \nu_{12} \nu_{21} - \nu_{23} \nu_{32} - \nu_{31} \nu_{13} - 2\nu_{12} \nu_{23} \nu_{31})$ and reciprocal relations for materials parameters in the material coordinates (no sum: α and β , and 3 refers to the z-axis). By defining a coordinate transformation matrix $[T]_k$ between material and global coordinate systems given by

$$[T]_k = \begin{bmatrix} \cos^2 \theta_k & \sin^2 \theta_k & 0 \\ \sin^2 \theta_k & \cos^2 \theta_k & 0 \\ 0 & 0 & (\cos^2 \theta_k - \sin^2 \theta_k) \end{bmatrix} \quad (3)$$

the local relations (2) are transformed into the stress-strain relations in the global coordinates:

$$\{\sigma\}_k = [E]_k \{\epsilon\}_k : \begin{cases} \sigma_{xx} \\ \sigma_{yy} \\ \tau_{xy} \end{cases}_k = \begin{bmatrix} E_{11} & E_{12} & E_{16} \\ E_{12} & E_{22} & E_{26} \\ E_{16} & E_{26} & C_{66} \end{bmatrix}_k \begin{cases} \epsilon_{xx} \\ \epsilon_{yy} \\ \gamma_{xy} \end{cases}_k, \quad [E]_k = [T]_k^T [C]_k [T]_k \quad (4)$$

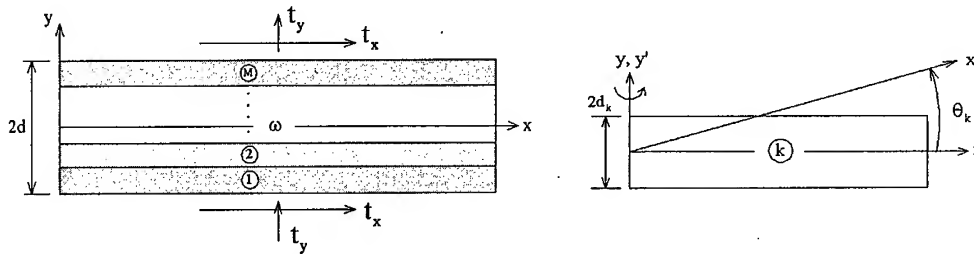


Fig. 2. A plane-stain laminated structure (a) and its k-th layer (b).

2.2. Hierarchical Models

We define the kinematically admissible displacement field space $V(\Omega)$ as $V(\Omega) = \{v: v \in [H^1(\Omega)]^2 \mid v = 0 \text{ on } \partial\Omega_D\}$, where $\partial\Omega_D$ refers to Dirichlet boundary region (i.e. $\partial\omega \times [-d, d]$). Then, according to the usual weighted residual formulation, we have the variational formulation of the problem (1) for the fully two-dimensional linear elasticity solution u : Find $u \in V(\Omega)$ such that

$$a(u, v) = \ell(v), \quad \forall v \in V(\Omega) \quad (5)$$

Here, the internal virtual strain-energy functional $a(u, v)$ and the external virtual-work functional $\ell(v)$ are respectively given by

$$a(u, v) = \int_{\omega} \left\{ \sum_{k=1}^M \int_{y_k^b}^{y_k^t} \{\epsilon(v)\}_k : \{\sigma(u)\}_k \right\} dy \quad (6)$$

$$\ell(v) = \int_{\omega} \left\{ \sum_{k=1}^M \int_{y_k^b}^{y_k^t} v^T f dy \right\} dx + \int_{\partial\Omega_N} v^T t ds \quad (7)$$

where y_k^b and y_k^t indicate y coordinates at the bottom and top surfaces of k-th layer, and $\partial\Omega_N$ Neumann boundary region where external tractions are applied.

Since the hierarchical models are distinguished by the maximum thickness-polynomial order, we define two separated one-dimensional scalar function spaces $X(\omega)$ and $Y[-d, d]$ such that

$$X(\omega) = \{v: v \in H^1(\omega) \mid v = 0 \text{ on } \partial\omega\} \text{ and } Y[-d, d] \in C^0[-d, d] \quad (8)$$

Letting $q = (q_x, q_y)$ be a non-integer set, we define the thickness order-restricted subspace $V^q(\Omega)$ of $V(\Omega)$ by $(\alpha = x, y)$

$$V^q(\Omega) = \left\{ \mathbf{v} : \mathbf{v}_\alpha = \sum_{\ell=0}^{q_\alpha} V'_\alpha(x) \cdot \Theta'_\alpha(y/d) \mid V'_\alpha \in X(\omega) \text{ and } \Theta'_\alpha \in Y[-d, d] \right\} \quad (9)$$

where Θ'_α are ℓ -th order thickness polynomials. Then the previously defined space $V(\Omega)$ is equivalent to $V^\infty(\Omega)$, and furthermore $V^q(\Omega) \Rightarrow V(\Omega)$ as $q \rightarrow +\infty$ from the density argument. [8]

Within the subspaces, the previous problem (5) becomes a dimensionally-reduced problem: Find $\mathbf{u}^q \in V^q(\Omega)$ such that

$$a(\mathbf{u}^q, \mathbf{v}^q) = \ell(\mathbf{v}^q), \quad \forall \mathbf{v}^q \in V^q(\Omega) \quad (10)$$

From Eqs. (5) and (10) together with $V^q(\Omega) \subset V(\Omega)$, it is easy to prove the following orthogonal projection holds: $a(\mathbf{u} - \mathbf{u}^q, \mathbf{v}^q) = 0, \forall \mathbf{v}^q \in V^q(\Omega)$.

By varying the set q sequentially, we can construct a family of infinite solutions \mathbf{u}^q through the formulation (10). We define it as a hierarchical family $\mathfrak{H} = \{\mathbf{u}^q, q=1, 2, \dots, \infty\}$ and each \mathbf{u}^q as a hierarchical model with the model level q (or the q -model). Mathematically, hierarchical models are defined as orthogonal projections of two-dimensional elasticity solution \mathbf{u} of problem (5) onto the subspace $V^q(\Omega)$. [2] In this family, the lowest model \mathbf{u}^1 corresponds the first-order shear deformation theory while the highest mode \mathbf{u}^∞ to fully 2-D elasticity theory. The derivation of the thickness-polynomials is well addressed in [2-3] for isotropic structures and [4,7] for laminates.

The finite element analysis of hierarchical models with the pre-determined thickness-polynomials is to seek the one-dimensional coefficients V'_α in Eq. (9). But, differing from isotropic materials, the analytic integration through the thickness becomes significantly complicated as the model level increases owing to complex thickness polynomials. [4] An easy alternative numerical implementation is to use 2-D tensor-product finite elements:

$$\varphi_k(x, y) = \sum_{m=1}^{p+1} \sum_{n=1}^{q+1} \varphi_m(x) \cdot \varphi_n(y). \quad (11)$$

In other words, by restricting the element order q in the y -direction while increasing p as high as possible (usually $p=8-9$), we can equivalently carry out the finite element approximations, and which holds mathematically according to the order completeness [8] of the thickness-polynomials.

2.3 Characteristics of Hierarchical Models

Every model member \mathbf{u}^q in the hierarchical family \mathfrak{H} possesses common characteristics (or requirements) with respect to the two parameters, the model level and the relative thickness:

- (i) For given external loads and boundary conditions, each $\mathbf{u}^q \in \mathfrak{H}$ should be uniquely defined.
- (ii) The limit requirement should be satisfied: $\lim_{d \rightarrow 0} \|\mathbf{u} - \mathbf{u}^q\|_{E(\Omega)} \rightarrow 0, \forall q$, with $\|\cdot\|_{E(\Omega)} = \sqrt{a(\cdot, \cdot)}$.
- (iii) For applied loading with the regularity s , there exists a constant C such that ($\alpha = \min(q, s)$)

\tilde{d} the relative thickness $2d/L$) [2]

$$\|\mathbf{u} - \mathbf{u}^q\|_{E(\Omega)} \leq C \cdot (\tilde{d})^{(\alpha+1/2)} \quad (12)$$

3. NUMERICAL EXPERIMENTS

Consider a symmetric three-layer plane-strain laminate shown in Fig. 3(a), composed of three orthotropic layers of equal thickness $2d/3$ and subjected to uniform normal load $p_o/2$ on the upper and lower surfaces. The laminate is assumed to be in state of plane strain with respect to the xy -plane, and each layer is of square symmetric unidirectional fibrous composite material possessing: $E_L = 25 \times 10^6$ psi, $E_T = E_L/25$, $G_{LT} = 0.5 \times 10^6$ psi, $G_{TT} = G_{LT}/2.5$ and $\nu_{LT} = \nu_{TT} = 0.25$, where L and T indicate the directions parallel and transverse to the fibers, respectively. In this problem, the L -direction coincides with the x -axis in the outer layers while the T -direction is parallel to the x -axis in the central layer (i.e. 0/90/0 graphite/epoxy composite). Fig. 3(b) shows the uniform finite-element mesh constructed with 2-D tensor-product elements with p of 8.

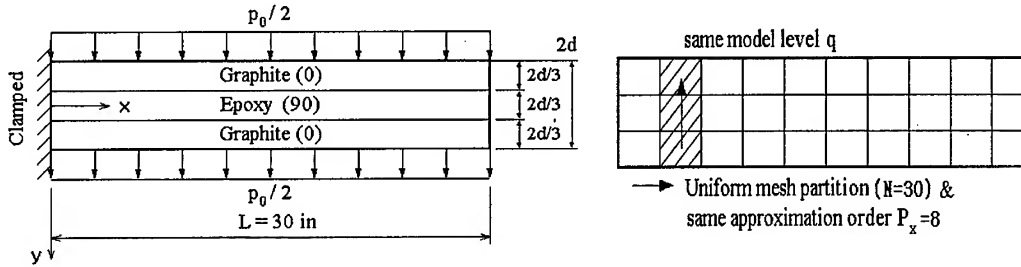


Fig. 3. Symmetric three-layer plane-strain laminate (a) and the uniform finite-element mesh (b).

Fig. 4(a) represents limits of non-dimensional vertical deflection $\tilde{u}_y(L,0)$ at the tip for different hierarchical models \mathbf{u}^q along the relative thickness, where \tilde{u}_y is calibrated by the CLPT solution [6]: $\tilde{u}_y = 18 E_T (2d)^3 u_y / p_0 L^4$. Regardless of the model level, the non-dimensional limits approaches the CLPT solution, and which illustrates the above-described limit requirement. Vertical distributions of the calibrated transverse shear stress $\tilde{\tau}_{xy} = \tau_{xy} / p_0$ at $x=2d/3$ are given in Fig. 4(b), where the model of $q=1$ shows the distribution of FSDT [6]. The refinement in the description of transverse shear stress becomes considerable as the model-level increases, particularly for $q \geq 3$.

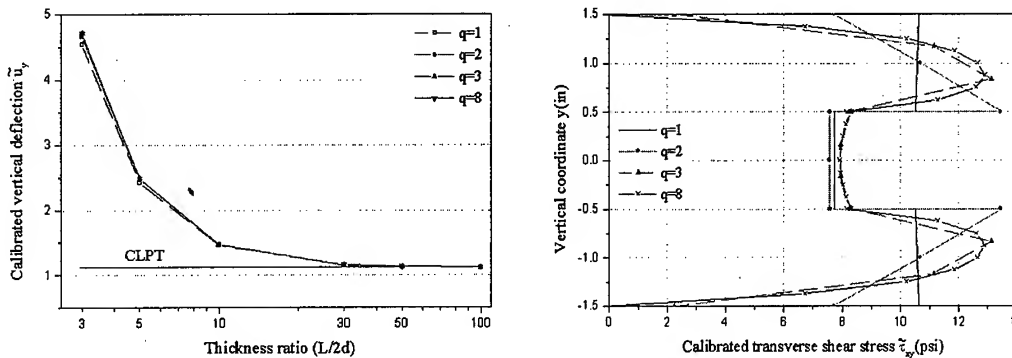


Fig. 4. Limits of the calibrated vertical deflection $\tilde{u}_y(L,0)$ (a) and distributions of the calibrated transverse shear stress $\tilde{\tau}_{xy}(2d/3, y)$ when $(L/2d)$ is 10 (b).

Next Figs. 5(a) and 5(b) respectively represent the variations of total relative modeling errors η_{TOT} (%) to the model level and the d-convergence rates γ_d , which are defined respectively by

$$\eta_{TOT} = \left\{ \sum_{k=1}^N \left(\frac{\| \mathbf{u} - \mathbf{u}^q \|_{E(\Omega_k)}}{\sqrt{U(\mathbf{u})}} \times 100\% \right)^2 \right\}^{1/2} = \left\{ \sum_{k=1}^N (\eta_k^2) \right\}^{1/2}, \quad \gamma_d = \log \left(\frac{\| \mathbf{u} - \mathbf{u}^q \|_{E(\Omega)}}{\log(2d/L)} \right) \quad (13)$$

where $U(\mathbf{u})$ indicates the total strain energy of the laminate while η_k is defined as the local relative modeling error within each finite element Ω_k . For the numerical implementation, 2-D elasticity solution \mathbf{u} is replaced with a higher model \mathbf{u}^8 . As shown in the plots, η_{TOT} decreases as q increases, and this reduction tendency becomes considerable for thicker laminate. Within relatively thin thickness range, γ_d increases together with q up to 2 according to the error bound (12), but it saturates when $q \geq 3$ owing to the regularity limitation.

Distributions of η_k are shown in Figs. 6(a)-(c) when hierarchical models \mathbf{u}^q with the same model level q of 1, 2 and 3, respectively are employed within the entire laminate region. We see that the closer to the fixed end finite elements are the higher η_k are obtained. Even though η_k can be uniformly reduced by increasing the model level, this model enrichment with the same model level leads to expensive computation. Fig. 6(d) shows a conceptual example of hierarchical modeling, for

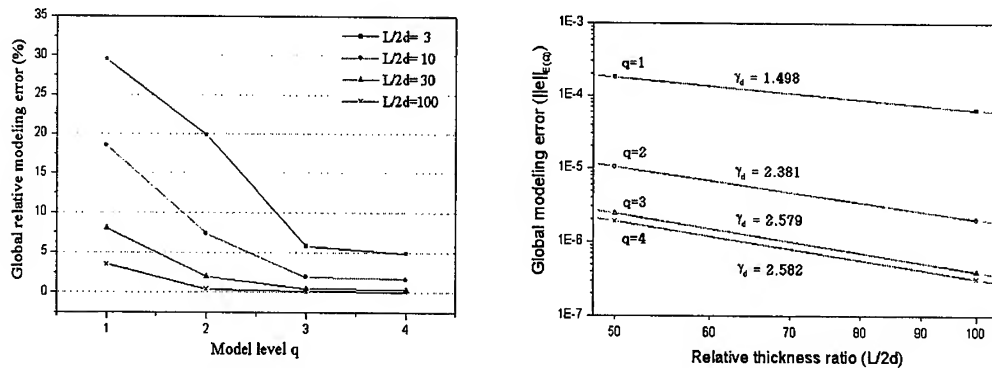


Fig. 5. Total relative modeling errors; (a) along the model level and (b) the d-convergence rates.

which we selectively combine hierarchical models such that u^3 in the left region, u^2 in the middle region and u^1 in the right region. Then, we achieve the low η_{TOT} as the case with a single u^3 (i.e. Fig. 6(c)), but the η_K -distribution is more uniform and the required degrees-of-freedom are smaller.

6.36	5.95	5.47	4.84	4.13	3.39	2.65	1.92	1.24	0.80
0.97	0.19	0.22	0.17	0.13	0.11	0.09	0.09	0.09	0.22
6.36	5.95	5.47	4.84	4.13	3.39	2.65	1.92	1.24	0.80

(a) uniform q of 1 ($\eta_{TOT} = 18.5\%$)

4.35	2.18	1.17	0.77	0.58	0.45	0.33	0.22	0.11	0.34
1.21	0.26	0.05	0.05	0.04	0.03	0.02	0.02	0.02	0.09
4.35	2.18	1.17	0.77	0.58	0.45	0.33	0.22	0.11	0.34

(b) uniform q of 2 ($\eta_{TOT} = 7.39\%$)

1.356	0.137	0.039	0.013	0.006	0.004	0.004	0.006	0.015	0.061
0.134	0.004	8E-04	1E-04	3E-05	4E-05	5E-05	9E-05	5E-04	0.017
1.356	0.137	0.039	0.013	0.006	0.004	0.004	0.006	0.015	0.061

(c) uniform q of 3 ($\eta_{TOT} = 1.94\%$)

0.43	0.38	0.45	0.33	0.22	0.34	0.58
0.02	0.04	0.03	0.02	0.02	0.04	0.02
0.43	0.38	0.45	0.33	0.22	0.34	0.58

■: $q=3$ ■: $q=2$ □: $q=1$

(d) model combination ($\eta_{TOT} = 2.57\%$)

Fig. 6. Distributions of local relative modeling error η_K (%) when $(L/2d)$ is 10.

4. CONCLUSION

According to the orthogonal projection of the fully 2-D elasticity theory onto the subspaces defined by restricting the maximum thickness-polynomial order in displacement field, we constructed hierarchical models for laminated structures. In order to investigate their spectral modeling-error characteristics, we carried out finite element analysis utilizing 2-D tensor-product elements. Through numerical experiments, we presented the model limit, the stress variation, distributions of local modeling errors and the d-convergence rates together with a conceptual example illustrating hierarchical modeling.

REFERENCE

1. I.Babuska, L.Li, Computer Methods in Applied Mechanics and Engineering, **40** (1991) p. 419
2. J.R.Cho and J.T.Oden, Mathematical and Computer Modelling, **23**(10) (1996) p.117
3. J.T.Oden and J.R.Cho, Computer Methods in Applied Mechanics and Engineering, **136** (1996) p. 317
4. I.Babuska, B.A.Szabo and R.L. Actis, J. for Numerical Methods in Engineering, **33** (1992) p. 503
5. A.K.Noor, W.S.Burton and J.M.Peters, Applied Mechanics Review, **42** (1989) p. 1
6. J.N.Reddy, Mechanics of Laminated Composite Plates, CRC Press, New York (1997)
7. E.Bertoti, Computer Methods in Applied Mechanics and Engineering, **123** (1995) p. 327
8. R.A.Adams, Sobolev Spaces, Academic Press, New York (1978)

Nonlinear Displacement Field in the Vicinity of Notch-Tip in Rubber Toughened PMMA

M. Todo, K. Arakawa and K. Takahashi

Research Institute for Applied Mechanics, Kyushu University,
Kasuga-shi, Fukuoka 816-8580, Japan

Keywords: Finite Element Modeling, Fracture Mechanics, Moiré Interferometry, Nonlinear Displacement Field, Rubber Toughened PMMA

ABSTRACT

Displacement field in the vicinity of notch-tip in a rubber toughened PMMA was measured at different levels of load using moiré interferometry. The displacement field obtained was then compared with the analytical fields calculated on the basis of the linear elastic fracture mechanics and obtained from nonlinear finite element analysis that was based on the deformation theory of plasticity. The displacement field experimentally measured at about 90% of the maximum load exhibited nonlinearity. There were both similarity and difference between the measured and the analytical displacement fields. The nonlinearity of the displacement field is also discussed on the basis of the microscopic damage formation in the notch-tip region.

1. INTRODUCTION

Rubber modified polymers have been developed by blending rubbery phases with polymer matrices to improve the fracture toughness and impact resistance of the brittle neat polymers [1]. For example, various types of rubber particles are blended in brittle PMMA to improve its fracture properties [2]. It is known that damage zone is formed and extends in the vicinity of crack-tip as the applied load increases in rubber toughened PMMA (RT-PMMA) [3]. The damage zone consists of microcrazes generated in the surroundings of rubber particles as a result of local stress concentration and/or failure of the rubber particles. This type of microdamage formation is different from yielding in metals and therefore, the macroscopic nonlinear deformation field caused by the damage zone is naturally expected to be different from that of metals. Thus, applicability of elastic-plastic fracture mechanics that has been developed on the basis of metal plasticity to rubber modified polymers has to be carefully inquired.

In this study, mode-I deformation behavior of a rubber toughened PMMA (RT-PMMA) was studied. Displacement field in the vicinity of a notch-tip was measured using moiré interferometry. The experimental result was then compared with an analytical result obtained using nonlinear FEM analysis that is based upon the deformation theory of plasticity. Nonlinear deformation behavior of the toughened PMMA is discussed on the basis of those experimental and analytical results.

2. EXPERIMENTAL

2.1. Material and specimen

The RT-PMMA examined was a press formed material containing 40wt% butyl acrylate-co-styrene rubber. Its microstructure observed using a field emission scanning electron microscope

(FE-SEM) is shown in Fig.1. The diameter of the core-shell rubber particles is approximately 300 nm. A neat PMMA was also examined for comparison. Single edge notched specimens were prepared for mode-I fracture testing. The specimen geometry is shown in Fig.2.

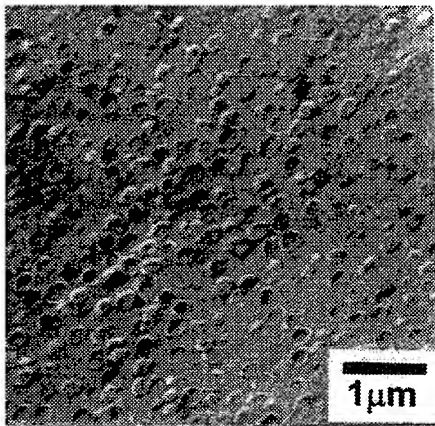


Fig.1 Microstructure of RT-PMMA.

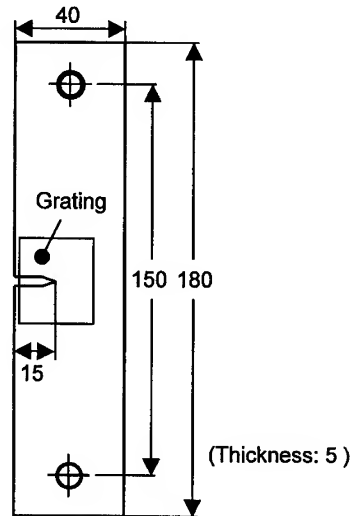


Fig.2 Specimen geometry (in mm).

2.2. Measurement of displacement field

Notch-tip displacement fields in the v -direction in the neat PMMA and the RT-PMMA were measured by using moiré interferometry [4,5]. Specimen gratings of 400 lines mm^{-1} were replicated on the surfaces of the specimens as shown in Fig.2. Moiré fringes associated with v -displacement field were obtained with a two-beam moiré interferometry setup and recorded using a camera at two different load values, $P \approx 0.5P_{\max}$ and $0.9P_{\max}$ where P_{\max} is the maximum value of the applied load. It is noted that no crack growth occurred during the moiré measurements.

Examples of moiré fringe pattern obtained for the neat PMMA and the RT-PMMA are shown in Figs.3. Those patterns were obtained at $P \approx 0.5P_{\max}$. The difference of v -displacement between two fringes is 1.25 μm . It is seen that the fringe pattern observed in the RT-PMMA was denser than that in the neat PMMA, suggesting that larger deformation field existed in the RT-PMMA. The v -displacement as a function of the distance r from the notch-tip and the angle θ is given by:

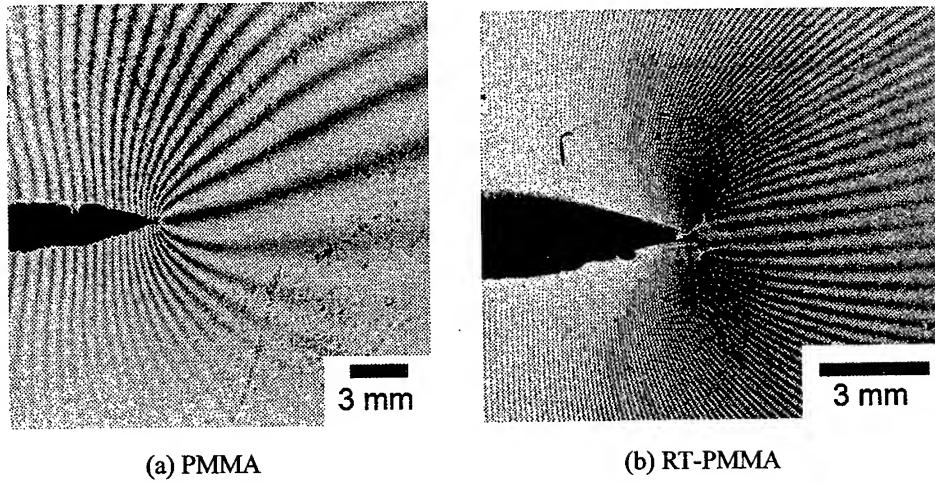
$$v(r, \theta) = N(r, \theta) / 2F \quad (1)$$

where $N(r, \theta)$ is the fringe number at (r, θ) , and F is the frequency of the specimen grating (400 lines mm^{-1} in the present study).

3. FEM ANALYSIS

3.1. Nonlinear theory

Crack-tip HRR singular field derived from the deformation theory of plasticity is the basis of elastic-plastic fracture mechanics [6]. A stress-strain relation deduced from the nonlinear theory is given by:

Fig.3 Moiré fring patterns at $P \approx 0.5P_{max}$.

$$\varepsilon_{ij} = \frac{1+\nu}{E} S_{ij} + \frac{1-2\nu}{3E} \sigma_{kk} \delta_{ij} + \frac{3}{2} \frac{\bar{\varepsilon}^P}{\bar{\sigma}} S_{ij} \quad (2)$$

Where E is the elastic modulus, ν the poisson's ratio and δ_{ij} the Kronecker delta. The deviatoric stresses S_{ij} , equivalent stress $\bar{\sigma}$ and equivalent plastic strain $\bar{\varepsilon}^P$ are given by:

$$S_{ij} = \sigma_{ij} - \frac{1}{3} \sigma_{kk} \delta_{ij} \quad (3)$$

$$\bar{\sigma} = \left(\frac{3}{2} S_{ij} S_{ij} \right)^{1/2} \quad (4)$$

$$\bar{\varepsilon}^P = \left(\frac{2}{3} \varepsilon_{ij}^P \varepsilon_{ij}^P \right)^{1/2} \quad (5)$$

where ε_{ij}^P are plastic strain components. Mises yield criterion is employed here. Using Ramberg-Osgood model, relation between $\bar{\sigma}$ and $\bar{\varepsilon}^P$ is defined by:

$$\bar{\varepsilon}^P = \alpha \varepsilon_y \left(\frac{\bar{\sigma}}{\sigma_y} \right)^n \quad (6)$$

where σ_y and ε_y are yield stress and strain, respectively, and n is the strain hardening exponent and α a dimensionless material constant. From Eqs.2-6, the stress-strain relation becomes:

$$\varepsilon_{ij} = \frac{1+\nu}{E} S_{ij} + \frac{1-2\nu}{3E} \sigma_{kk} \delta_{ij} + \frac{3}{2} \alpha \varepsilon_y \left(\frac{\bar{\sigma}}{\sigma_y} \right)^{n-1} \frac{S_{ij}}{\bar{\sigma}} \quad (7)$$

A nonlinear FEM can be developed using Eq.7.

3.2. FEM model

A FEM model for the specimen used in the present study is shown in Fig.4. Plane stress condition was assumed. Isoparametric 8-node and 6-node elements were used and the numbers of the elements and nodes were 584 and 1805, respectively. Nonlinear FEM analyses with the aid of Eq.7 were performed for the RT-PMMA and the material constants used were $E=1.58\text{GPa}$, $\nu=0.40$, $\sigma_y=18\text{MPa}$, $\alpha=0.01$ and $n=20$. For the neat PMMA, linear elastic FEM analyses were carried out with the material constants, $E=3.03\text{GPa}$ and $\nu=0.35$.

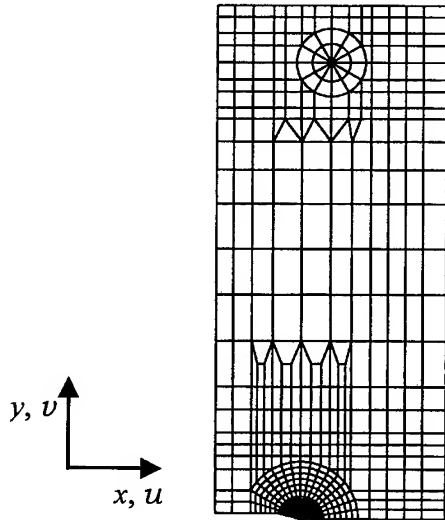


Fig.4 Finite element model.

4. RESULTS AND DISCUSSION

4.1. Unmodified PMMA

Experimental and FEM results of v -displacement field at $P=0.47P_{\max}$ are shown as a function of θ in Fig.5(a). In the figure, v -displacement calculated on the basis of the linear fracture mechanics (LEFM) is also shown. The v -displacement in the vicinity of a crack-tip derived from LEFM is given by:

$$v(r, \theta) = \frac{K_I}{2G} \sqrt{\frac{r}{2\pi}} \sin \frac{\theta}{2} \left(\frac{3-\nu}{1+\nu} + 1 - 2 \cos^2 \frac{\theta}{2} \right) \quad (8)$$

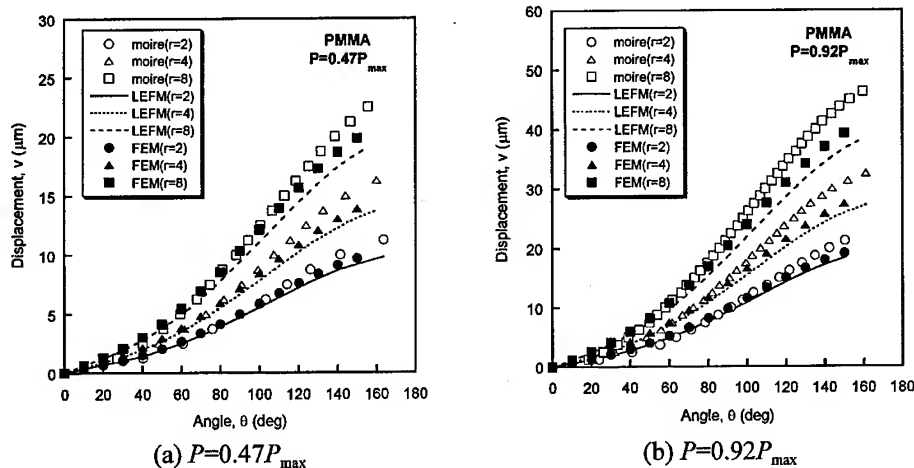


Fig.5 ν -displacement fields as a function of θ for PMMA.

where K_I and G are the stress intensity factor and shear modulus, respectively. For the specimen used, K_I can be calculated using:

$$K_I = \sigma \sqrt{\pi a} F(\xi), \quad \xi = a/W \quad (9)$$

where σ is the applied tensile stress, a the crack length and W the specimen width. The correction factor F is given by:

$$F(\xi) = 0.265(1-\xi)^4 + (0.857 + 0.265\xi)/(1-\xi)^{3/2} \quad (10)$$

It is seen from the figure that those three ν fields, i.e. the moiré, LEFM and FEM, exhibited good agreement at $\theta \leq 90^\circ$, and the difference became larger as θ increased. It is noted that the difference between the moiré and LEFM fields was larger than that between the moiré and FEM fields at $\theta \geq 90^\circ$. This is mainly because of the difference of geometry between the crack-tip and notch-tip.

ν -displacement fields obtained at $P=0.92P_{max}$ are shown in Fig.5(b). The moiré displacement field coincided with the FEM field well, suggesting that the PMMA specimen exhibited linear elastic deformation even at $P=0.92P_{max}$. Figs.5(a) and (b) show that the moiré data was the largest of all three results at $\theta \geq 90^\circ$. It is known that craze formation leads crack growth in neat PMMA. It therefore appears that a crazing in front of the notch-tip enabled the specimen to rotate towards the direction of applied load, as a result, the ν -displacement at $\theta \geq 90^\circ$ in the vicinity of the notch-tip became larger than the FEM result.

4.2. Rubber toughened PMMA

For the RT-PMMA tested, experimental and analytical ν -displacement fields are shown as a function of θ in Figs.6. At $P=0.53P_{max}$, the three results showed a good agreement and it is therefore understood that the deformation was very similar to that of a linear elastic material. On the other

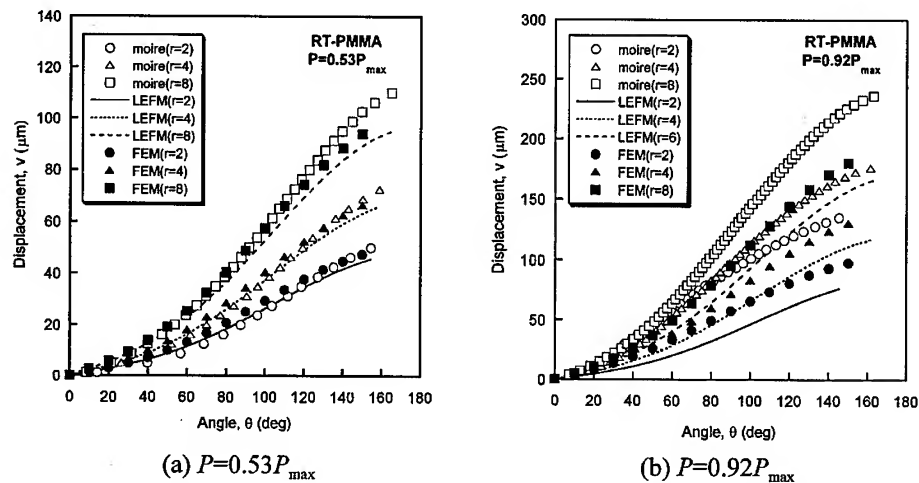


Fig.6 ν -displacement fields as a function of θ for RT-PMMA.

hand, at $P=0.92P_{\max}$, the difference between the experimental and analytical results was significant, implying that extensive nonlinear deformation occurred in the vicinity of the notch-tip. Although the FEM result included the effect of elastic-plastic nonlinear deformation, the ν values obtained were much smaller than the experimental values. This nonlinearity appears to be caused by damage zone formation in the notch-tip region. It has been elucidated that the damage zone is formed as a cloud of microcrazes generated in the surroundings of distributed rubber particles [3]. It is thus considered that the mechanism of nonlinear deformation in RT-PMMA may not exactly be described by the HRR singular field.

5. CONCLUSIONS

Mode I displacement field of a rubber toughened PMMA in the vicinity of a notch-tip was measured using moiré interferometry. The experimental results were then compared with displacement fields obtained by a nonlinear finite element analysis. It was seen that there existed a similarity between the experimental and analytical displacement fields. However, the difference between them became larger as the nonlinearity increased. Thus, a new constitutive law is needed to be developed in order to properly express the nonlinearity observed in the RT-PMMA.

REFERENCE

1. C. B. Bucknall, Toughened Plastics, Applied Science Publishers Ltd., 1977.
2. P. A. Lovell, J. MacDonald, D. E. J. Saunders, M. N. Sherratt and R. J. Young, Toughened Plastics I, Advances in Chemistry Series 233, American Chemical Society, 1993, p.61.
3. M. Todo, K. Takahashi, P.-Y. B. Jar and Ph. Beguelin, JSME Int. Journal, A, 42, 4(1999), p.585.
4. K. Arakawa, M. Ishiguma and K. Takahashi, Int. J. Fracture, 66(1994), p.205.
5. K. Arakawa and K. Takahashi, Int. J. Fracture, 86(1997), p.289.
6. M. F. Kanninen and C. H. Popelar, Advanced Fracture Mechanics, Oxford University Press, New York, 1985.

Optimum Design for Fatigue Strength Improvement of Spot-welded T-type Bus Window Pillar Member

M.H. Kim, D.S. Kim, M.W. Suh and D.H. Bae

Department of Mechanical Engineering, Sungkyunkwan University,
300 Chunchun-dong, Jangan-Gu, Suwon, Kyungki-do 440-746, Korea

Keywords: B-spline, Fatigue Strength, Optimization, Spot-welded, Window Pillar Member

ABSTRACT

The body structure of a bus is generally assembled by using various spot welded box members. Window pillar member is ordinarily built up by T-type member. It has been shown that T-type member has problems such as high stress concentrations, low fatigue strength and low structural rigidity on spot welding nugget. In this study, a new approach to optimize the design of the bus window pillar member concern with stress concentration on spot welding nugget was proposed based on optimization technique, finite element method. To describe the shape of the gusset connecting the vertical and horizontal members of the T-type window pillar member, B-spline was adopted and this curve was optimized to have minimum weight satisfying strength constraints. It was found that the new approach could effectively improve fatigue durability and structural rigidity.

1. Introduction

Recently, interests on conservation of environment and resources have been growing. Automotive manufacturers are concentrating their research activities upon light weight vehicles. Especially, the body structure is received strong interest on the weight issue due to the high weight ratio of 30% of the whole vehicle. However, to build a light weight body is limited due to its functions such as strength, stiffness and crash worthiness. There are many means for light weight body such as design change, adoption of new technology for adhesion and application of lighter materials. Since the replacement of material or change of the adhesion method may increase the cost, reshaping of the design is generally adopted[1]

However, simple reshaping of parts may cause fatigue cracks in an actual structure as shown in Fig.1 because stress concentration around spot welding nugget is intensified. Therefore the design

techniques to obtain minimum weight while conserving or improving the strength is getting more important.

Window pillar member in Fig.1 is the significant structural member connecting upper and lower bodies. In addition, it is the weakest region in the body structure of bus. In this study, load pattern, deformation and stress distribution for the window pillar members including the spot welding nugget is firstly investigated. And then, optimum design technique is proposed to improve structural rigidity and fatigue strength with minimum weight based on the finite element analysis with the previous loading pattern and deformation.

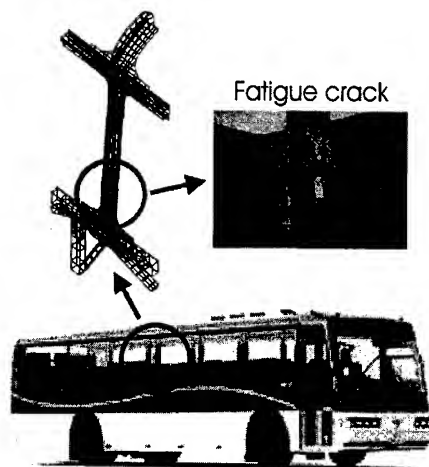


Fig.1 The shape of bus window pillar member and typical fatigue crack

2. Finite element analysis

2.1 Deformation of bus body

Deformation modes of bus body can be classified into bending and torsion.[1] Usually, bending deformation is sufficiently restrained by a ladder type main frame. However, torsional deformation cannot be well support in case of typical bus structure of these days. The severe torsional deformation directly influences the fatigue fracture in the window pillar members due to the warping along longitudinal direction and lateral direction on side panel. Effective manner to cope with the torsional deformation of bus body is to insert diaphragms which are perpendicular to the longitudinal direction. To maximize the inner space of bus for passengers, however, there is no diaphragm except the front and rear wind shield glasses. Moreover, the body structure of the bus must provide wide view for the passengers. This makes the window be wider and wider.[2] Therefore, the numbers and the cross section area of the window pillar member are reducing. The structure may be put in more severe strength and rigidity conditions.

2.2 Analysis model and condition

Finite element analysis is performed to investigate the stress distribution of the window pillar member. Firstly, whole body structure is modeled with beam elements as illustrated in Fig.2 to

obtain the boundary conditions for the window pillar member of Fig.3. Torsional load which is known as the most dominant factor for the strength and stiffness of window pillar member, is applied to the beam model. Two FAC's(front axle center) and one RAC(rear axle center) are fixed and forced displacement at the other RAC is applied in the vertical direction. From this result, loading conditions for the window pillar member depicted in Fig.3 are obtained in the form of displacements. Shell element with 4-node is utilized for the finite element analysis of the window pillar member. To investigate the stress distribution of the spot welding points, solid element with 8-node is utilized for more detail describing of the spot welding points. FEM program for the analysis is EMRC/NISA-II, Version 7.0(1997).[3]

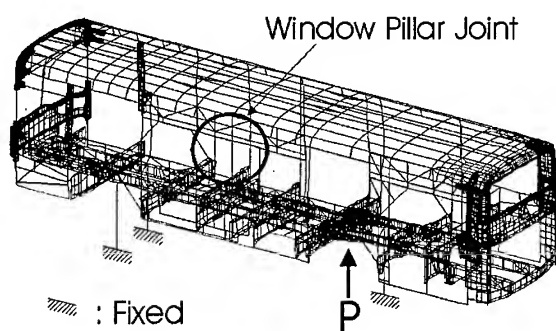


Fig. 2 Beam element model of bus body

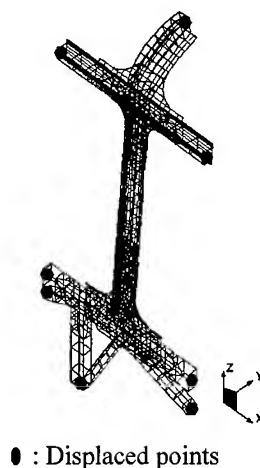


Fig.3 FEA model of window pillar member

2.3 Result of analysis

Stress distribution and deformation of the window pillar member are shown in Fig.4, and Fig.5. And, Figure 6 illustrates the composition of typical window pillar member. Deformation of longitudinal direction and lateral direction in upper structure of the member is observed as shown Fig.5. Maximum stress appears at the spot welding point around the fillet of the outer gusset in Fig.6, which set up in order to prevent stress concentration at the joint region of vertical and horizontal member. It coincides with the region in which fatigue crack appears indicated in Fig.1.

On the other hand, with the same model, analyses subjected to the unit displacement of longitudinal and lateral direction are performed. As the result, maximum stress due to the longitudinal displacement is about four times as large as it due to the lateral displacement. Maximum stress with the former displacement occurs where the fatigue crack of the actual model does. Therefore, it may be concluded that the mechanical main factor, relating with fatigue failure caused by stress concentration at the outer gusset of window pillar member, is the longitudinal deformation. This longitudinal deformation may also be called as in-plane deformation.

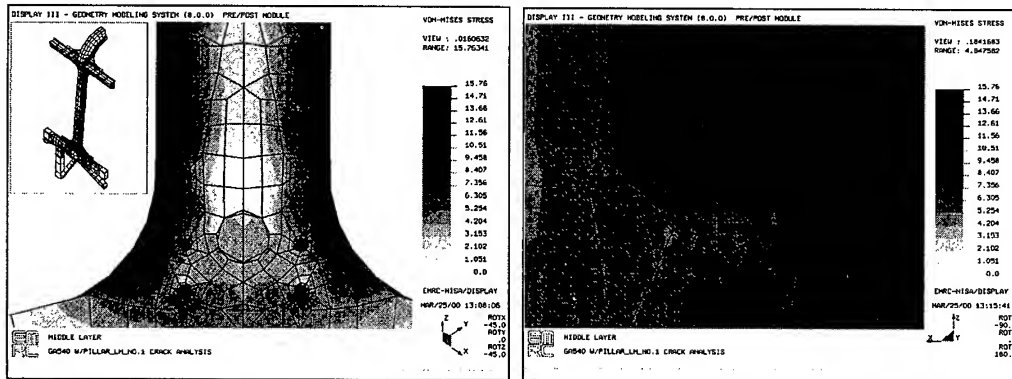


Fig. 4 Stress distribution subject to torsional load

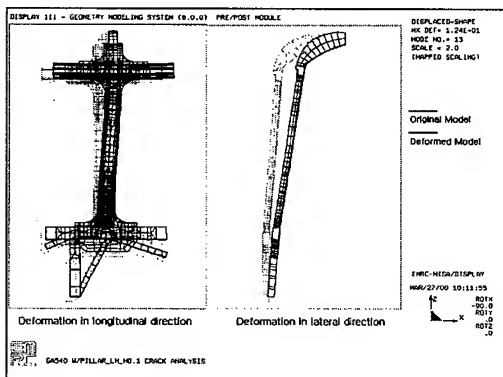


Fig. 5 Deformation subject to torsional load

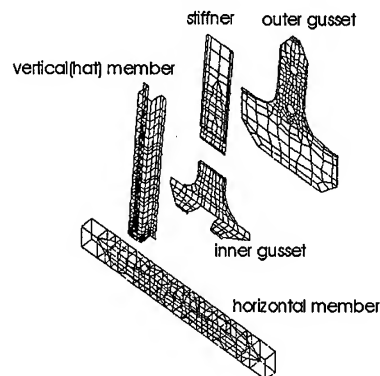


Fig. 6 Composition of typical window pillar joint

4. The optimum shape of the bus window pillar member

As already noted, the main mechanical factor, which causes the stress concentration, is in-plane deformation or force. The maximum stress in window pillar member by that force is located in spot welding point around the fillet of the outer gusset. Because stress distribution and concentration are dramatically changed according to a shape of outline of outer gusset as shown in Table 1, the goal of this study is to decide the shape for the alleviation of the maximum stress. The shape of the outer gusset of the present model is a single circular arc as shown in Fig.7. By increasing the radius, the stress concentration at the spot welding point and the outer gusset can be alleviated. However, to increase only its radius is not an effective counter plan from the viewpoint of the mass and the passenger's view. Therefore, the outline of the outer gusset will be determined in this study by the optimum design technique.

Table 1 The maximum stress according to change of fillet radius

Fillet radius(mm)	Maximum stress(Mpa)
80	151.2
82	143.7
84	136.8

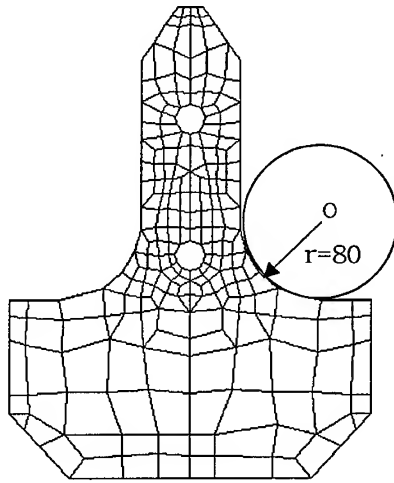


Fig. 7 Shape of outer gusset in present model

4.1 The shape optimization of the outer gusset using B-spline

When an in-plane force acts on the window pillar member, the maximum stress occurs at the connecting area between a circular arc and a vertical tangential line. when this connection has a smooth transition by a proper control of the curve, the stress concentration can be alleviated.[4] As already verified in Table 1, it could be adopted to alleviation of the stress at the spot welding point. In this study, the outline is expressed by B-spline of the 3rd order, which could freely govern the shape of the curve by changing the location of control points. As the B-spline is the versatile curve, which not only sensitively reacts to infinitesimal change of the location of the control points but also does not allow a mathematical discontinuity, it is suitable for representation of free shape and is useful to apply to manufacture easily using the CNC machines.[5] The optimization method is applied to the half model of the outer gusset.

The problem statement is expressed as follows.

$$\begin{aligned}
 & \text{Min : } volume(\vec{x}) \\
 & \text{subject to :} \\
 & G(\vec{x}) = \sigma_j(\vec{x}) - \sigma_a \leq 0 \\
 & x_i' < x_i < x_i'' \quad (i=1, \dots, 12)
 \end{aligned} \tag{1}$$

where \vec{x} is design variable vector; the components of design variable \vec{x} are x,y coordinates of the control points($C_1 \sim C_6$) which determine the shape of B-spline as illustrated in Fig.8; and σ_j represents the stress at the j th node on the outer curve. In this study, the stresses on 26 nodes along the outline of the outer gusset surface are adopted, i.e., $j=26$. The volume of resource is constrained to be less than C which is taken as the weight of the current design in this study. The side constraints are set up to avoid impractical shape. The optimization algorithms in this study [6] are

presented in Table 2.

Table 2 The algorithm using in optimization

Whole routine Algorithm	Augmented Lagrange Multiplier method
Search direction detecting algorithm	Broydon-Fletcher-Goldfarb-Shanno Variable metric method
One-Dimensional Search Algorithm	Golden Section method followed by polynomial interpolation

4.2 The results of the shape optimization

The stress distribution and maximum stress on the spot welding point around the fillet of the outer gusset after the optimization are shown in Fig.9 and Table 3. The figure shows that the maximum stress occurred to spot welding point is reduced by 43% comparing to the initial design. In addition, the rigidity of the member is improved by 28%. The maximum deformation is decreased by that percentage. It is noticeable that the weight of the optimized design in the same as the initial one. By the reduction of the maximum stress and the deformation in the window pillar member, it is expected the fatigue strength and structural rigidity of the whole body structure are improved.

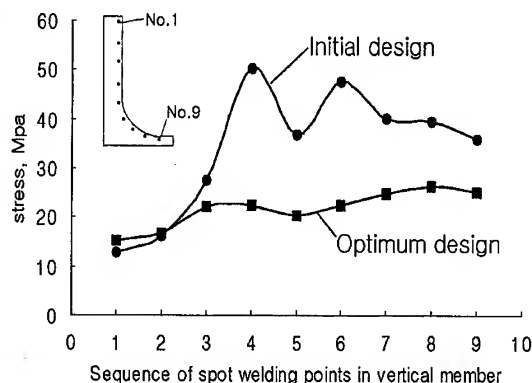
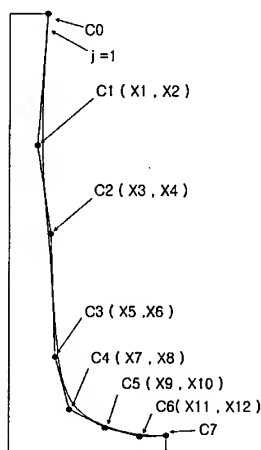


Fig. 8 Design variables and control points for the shape optimization

Fig.9 Stress distribution on the spot welding points

Table 3 Optimization results

		Before optimize	After optimize	Reduction Ratio
In-plane Load (2940N)	Max. stress(MPa)	151.1	85.5	43.8%
	Max. deform.(mm)	0.52	0.37	28.8%
	Weight (kg)	16.5	16.48	0.15%

5. Conclusion

Window pillar member of bus body which greatly influences the body stiffness and strength was

optimized through the following procedures. Firstly, whole body structure is modeled with beam elements to obtain the boundary conditions for the window pillar member. Detailed finite element analysis was performed to investigate the stress distribution of the window pillar member with the boundary conditions.

An approach to optimize the design of the bus window pillar member was performed. To describe the shape of the gusset connecting the vertical and horizontal members of the T-type window pillar member, B-spline was adopted and this curve was optimized to have minimum stress satisfying weight constraint. By changing the shape of the outer gusset, the maximum stress decreased by 43% and the maximum deformation decreased by 28%, with the same weight.

From this study, it is confirmed that the B-spline is highly effective means for shape optimization. The approach in this study is expected to contribute to improve fatigue strength and the structural rigidity of the body structure of bus.

< Acknowledgement >

The authors are grateful for the support provided by a grant from the Korea Science & Engineering Foundation(KOSEF) and safety and Structural Integrity Research Center at the Sungkyunkwan University.

References

- [1] S. Masahiro, K. Yukio, The strength of automobile body, AddTech, Tokyo(1998), pp.93
- [2] S.H.Lim, D.M.Shin, The Design of the Automobile, Hyungseol(1996), Korea, pp. 454
- [3] NISA-II / Version 7.0 User's Manual, EMRC(1997).
- [4] N. Masataka, Stress Concentration, Morikita, Tokyo(1967), pp.112 ~ 126
- [5] Vera B. Anand, Computer graphics and geometric modeling for engineers, John Wiley and sons, Inc.(1996)
- [6] S. Arora, Introduction to optimum design, McGraw-Hill, Singapore(1989)

Dynamic Response Analysis of a Structure under High Over-Load

Li Liu and Xiaoying Lin

School of Mechatronics, Beijing Institute of Technology,
Beijing 100081, China P.R.

Keywords: Dynamic Response, Overload, Structure Analysis

ABSTRACT

In this paper, theoretic and experimental researches were conducted to analyze the mode and damping properties of a structure. Based on the comparison of theoretic and experiment results, a suitable finite element model of a structure was selected. With this model, the dynamic response of the structure under high over-load was analyzed with FEM. The results show that the dynamic stress and displacement of the structure satisfy the design requirements.

1. INTRODUCTION

In some special circumstance, structure may experience high over-load. For example, the over-load of projectile launched by cannon could reach 10000g in 2-3ms, and its dynamic response presents different properties due to different over-loading procedure.

Numerical method is an effective way to analyze the dynamic response of structure. Due to high acceleration of the basement, the structure will undergo high inertial force. Large mass method, large stiffness method, or Lagrange amplify method may be used in obtaining the solution of the enforced motion. In this paper, the dynamic response of a structure is analyzed by the "large mass" method with NASTRAN.

2. ESTABLISHMENT OF MODEL

Fig.1 is the structure, which is made of high molecular material.

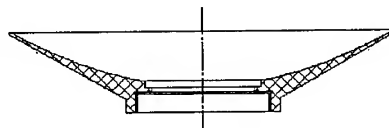


Fig. 1 The structure

2.1. FEM model

Considering the properties of the structure, two FEM models were established:

- ① Model I : solid element (Fig. 2 a).
- ② Model II : solid and plan element (Fig.2 b).

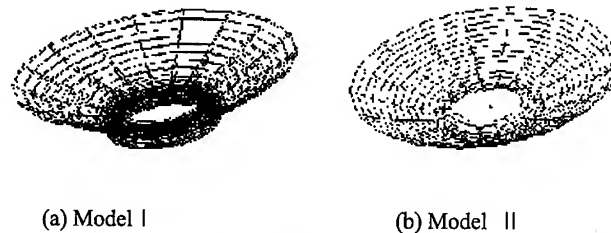


Fig. 2 FEM model

2.2. Acceleration curve

Fig.3 is the acceleration curve in y direction.

2.3. Constraint conditions

Main constraint conditions are:

- ① bolt constraint;
- ② one direction constraint.

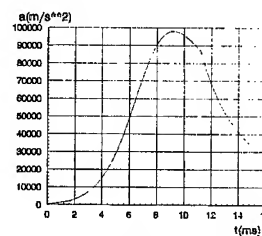


Fig. 3 Acceleration curve

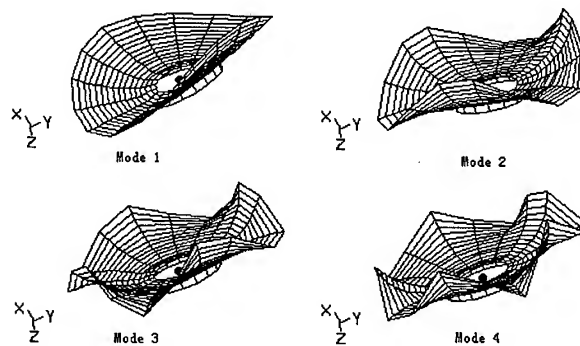
3. THE MODAL AND DAMPING ANALYSIS

3.1. Numerical analysis of mode

The mode of unconstrained structure is analyzed using NASTRAN with two FEM models. The results were shown in Table 1 and Fig.4

Table 1 Mode result of structure with Model I and Model II

Mode	Model I	Model II
1	720.3 Hz	465.5 Hz
2	1148.5 Hz	818.6 Hz
3	1463.1 Hz	1008.4Hz
4	2162.0 Hz	1138.7Hz

Fig.4 the 1st—4th mode shapes of structure

3.2. Experimental study of mode and damping

1) The mode of unconstrained structure

Table.2 Mode result of unconstrained structure

Mode	Frequency(Hz)
1	455.1
2	872.5
3	1269.4
4	1689.9

The 1st—4th mode shapes of the experiment are consistent with that of numerical results.

Comparing the frequency of the numerical and the experimental results, the Model II is more suitable, and is selected in the analysis of the dynamic response.

2) The damping experiment of constrained structure

Table.3 Damping coefficient of constraint structure

mode	Damping coefficient (%)
1	3.83
2	3.68
3	4.46

4. NUMERICAL ANALYSIS OF STRUCTURAL DYNAMIC RESPONSE

When the basement is accelerated, the structure is in a enforced motion. Large mass method is used in yielding the solution with NASTRAN[1]. The dynamic displacements of the structure at four different times are shown in Fig. 5.[2]

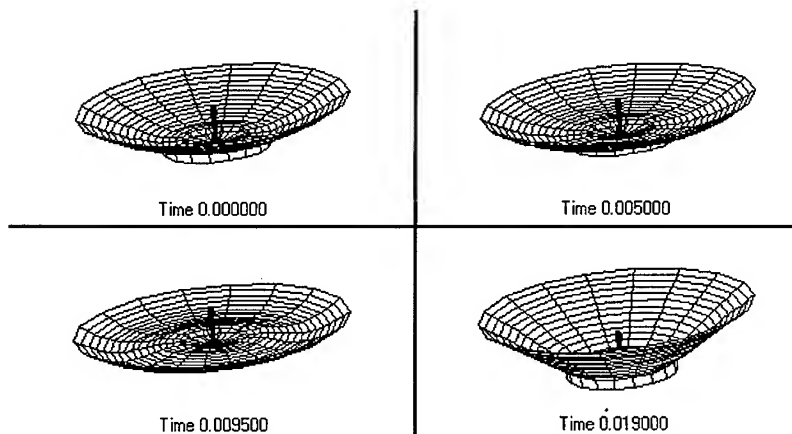


Fig. 5 Dynamic displacement of the structure

The largest vibration of the structure occurred at the edge. Fig. 6 is an illustration of the dynamic displacement of an edge point. Due to the high damping coefficient, the vibration may disappear after 0.03s.

The largest Von Mises stress occurred at the root of the structure. Fig.7 is the dynamic stress curve of a root element. The largest stress is below the strength limit of material.

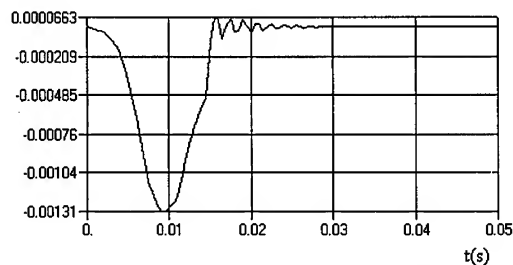


Fig.6 Dynamic displacement curve of a node

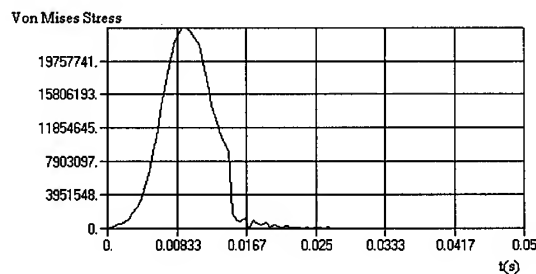


Fig.7 Dynamic stress curve of an element

5. CONCLUSION

- 1) Numerical and experimental researches of mode for a structure are conducted. Based on the comparison of results, a suitable FEM model is selected.
- 2) The damping coefficient of constraint structure is obtained with experimental study.
- 3) Numerical analysis of dynamic response of structure under high over-load is conducted using NASTRAN. The results show that the design of the structure satisfies the requirement.

REFERENCE

1. MSC/NASTRAN User's manual, The MacNeal-Schwendler Corporation 1991
2. Liu Bin, Lin Xiaoying, Liu Li, '98 MSC China User's Conference Proceedings, p49-52

Nonlinear Analysis of Thick Composites with Fiber Waviness under Flexural Loading

H.-J. Chun¹ and S.W. Lee²

¹ School of Electrical and Mechanical Engineering, Yonsei University,
134, Shinchon-dong, Seodaemun-gu, Seoul 120-749, Korea

² Department of Mechanical Engineering, Yonsei University,
134 Shinchon-dong, Seodaemun-gu, Seoul 120-749, Korea

Keywords: Fiber Waviness, Nonlinear Flexural Behavior, Thick Composites

ABSTRACT

A FEA(Finite Element Analysis) model was developed to predict the nonlinear behavior and to study stress and strain distributions in thick composites with fiber waviness under flexural loading. In the analytical model, both material and geometrical nonlinearities were incorporated into the model using energy density, iterative mapping and incremental method. Three types of fiber waviness model were considered in this study: uniform, graded and localized fiber waviness models. A special fabrication technique was developed to produce thick composite specimens with various degrees of uniform fiber waviness. Four-point bending tests were conducted to obtain the nonlinear behavior of thick composites with fiber waviness. It was found that the predictions from the model were in good agreement with the experimental results and the nonlinear behavior as well as local stress and strain distributions of composites were significantly affected by both the type and degree of fiber waviness.

1. INTRODUCTION

Fiber waviness is one of the manufacturing defects frequently encountered in thick composite structures. It results from local buckling of prepreg or wet hoop-wound filament strands under the pressure exerted by the overwrapped layers during the filament winding process or from lamination residual stress built up during curing. Its characteristics can be represented by the through the thickness undulation of fibers within a thick composite laminate.

A number of studies[1-5] have been conducted on the behavior of thick composites with fiber waviness. Chun *et al.*[6] investigated nonlinear flexural behavior of thick composites with fiber waviness by using an analytical model(thin slice model). In this study, the nonlinear flexural behavior of thick composites with fiber waviness is investigated theoretically and experimentally. The effects of material and geometrical nonlinearities are incorporated into the finite element analysis by employing energy density and iterative mapping method.

2. ANALYSIS

2.1. Uniform Fiber Waviness Model

Figure 1 illustrates a representative volume of uniform fiber waviness model. The fibers are assumed to maintain sinusoidal curvature along a spatial coordinate direction (x -axis). The representative volume is then divided into subelements in both x and z directions. Then, each subelement can be treated as an off-axis unidirectional laminate.

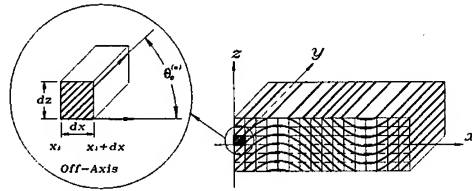


Fig. 1. Schematic drawing of a representative volume for unidirectional composite material with uniform fiber waviness.

The fiber waviness is assumed to be planar sinusoidal in the x - z plane defined by

$$z = a \sin \frac{2\pi x}{\lambda} \quad (1)$$

From Fig. 1, the initial fiber orientation of the n^{th} subelement, $\theta_0^{(n)}$, can be written as

$$\theta_0^{(n)} = \frac{1}{2} \left[\tan^{-1} \left(\frac{dz}{dx} \right)_{x=x_1} + \tan^{-1} \left(\frac{dz}{dx} \right)_{x=x_1+dx} \right] = \frac{1}{2} \left[\tan^{-1} \left(\frac{2\pi a}{\lambda} \cos \frac{2\pi x_1}{\lambda} \right) + \tan^{-1} \left(\frac{2\pi a}{\lambda} \cos \frac{2\pi(x_1+dx)}{\lambda} \right) \right] \quad (2)$$

where a and λ are the amplitude and wavelength of the wavy fiber, respectively.

Energy density (W) is used to incorporate the material nonlinearity in the model. The fourth order expansion of W is considered for nonlinear elastic composite

$$\begin{aligned} W = & \frac{1}{2} C_{11} \epsilon_{11}^2 + \frac{1}{2} C_{22} \epsilon_{22}^2 + \frac{1}{2} C_{33} \epsilon_{33}^2 + \frac{1}{2} C_{44} \gamma_{23}^2 + \frac{1}{2} C_{55} \gamma_{13}^2 + \frac{1}{2} C_{66} \gamma_{12}^2 \\ & + C_{12} \epsilon_{11} \epsilon_{22} + C_{13} \epsilon_{11} \epsilon_{33} + C_{23} \epsilon_{22} \epsilon_{33} + \frac{1}{3} C_{111} \epsilon_{11}^3 + \frac{1}{3} C_{222} \epsilon_{22}^3 + \frac{1}{3} C_{333} \epsilon_{33}^3 \\ & + \frac{1}{4} C_{1111} \epsilon_{11}^4 + \frac{1}{4} C_{2222} \epsilon_{22}^4 + \frac{1}{4} C_{3333} \epsilon_{33}^4 + \frac{1}{4} C_{4444} \gamma_{23}^4 + \frac{1}{4} C_{5555} \gamma_{13}^4 + \frac{1}{4} C_{6666} \gamma_{12}^4 \end{aligned} \quad (3)$$

where ϵ_{ij} , γ_{ij} and C 's are on-axis normal strains, on-axis shear strains and stiffness, respectively. If the nonlinear coupling terms between normal and shear strains are neglected, from energy density, stress-strain relations referred to material coordinates can be expressed in following matrix form

$$[\sigma]_{1,2,3} = [C^*][\varepsilon]_{1,2,3} \quad (4)$$

For the plane problem, the off-axis stiffness matrix can be transformed as

$$[Q^*] = [T^{-1}][Q][T] \quad (5)$$

where $[Q^*]$ and $[T]$ are an off-axis stiffness matrix and a transformation matrix, respectively.

For a particular subelement, the changed fiber orientation due to the deformation is obtained as a function of strains, coordinates of nodes and nodal displacements. Figure 2 illustrates the deformation and associated nodal displacements of a subelement.

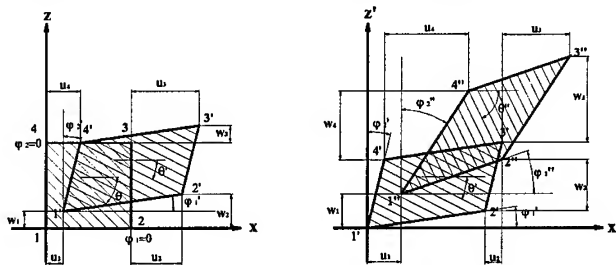


Fig. 2. Schematic drawing showing the deformation of subelement.

From Fig. 2 and Eq. 2, the fiber orientation of deformed subelement, $\theta^{(n)}$, is given as:

$$\theta^{(n)} = \tan^{-1} \left[\Delta\varphi_1 - \Delta\varphi_2 + \frac{1 + \varepsilon_z^{(n)}}{1 + \varepsilon_x^{(n)}} \tan \theta_0^{(n)} \right] \quad (6)$$

where

$$\varphi_1 = \tan^{-1} \frac{z_2 - z_1}{x_2 - x_1}, \quad \varphi_2 = \tan^{-1} \frac{z_3 - z_1}{x_3 - x_1}, \quad \varepsilon_x^{(n)} = \frac{\partial u}{\partial x} = \frac{1}{2} \left(\frac{u_2 - u_1}{x_2 - x_1} + \frac{u_3 - u_4}{x_3 - x_4} \right),$$

$$\varepsilon_z^{(n)} = \frac{\partial w}{\partial z} = \frac{1}{2} \left(\frac{w_4 - w_1}{z_4 - z_1} + \frac{w_3 - w_2}{z_3 - z_2} \right), \quad \gamma_{xz}^{(n)} = \frac{\partial w}{\partial x} + \frac{\partial u}{\partial z} = \frac{1}{2} \left(\frac{w_2 - w_1}{x_2 - x_1} + \frac{w_3 - w_4}{x_3 - x_4} + \frac{u_4 - u_1}{z_4 - z_1} + \frac{u_3 - u_2}{z_3 - z_2} \right)$$

$\varepsilon_x^{(n)}$ and $\varepsilon_z^{(n)}$ are strains in the x and z directions for the n^{th} element, respectively. u_i, w_i, x_i and z_i are displacements and coordinates in the x and z directions for the i^{th} node, respectively.

From the equilibrium equation for finite element analysis, the relation between force vector $[F]$ and displacement vector $[d]$ is expressed as follows

$$[K][d] = [F]$$

$$[K]_ij = \int_{\Omega^e} [B_i]^T [D] [B_j] d\Omega^e = \int_{-1}^1 \int_{-1}^1 [B_i]^T [D] [B_j] |J| d\xi d\eta \quad (7)$$

where $[B]$, $[D]$ and $|J|$ are the strain shape function matrix, elasticity matrix and the determinant of Jacobian matrix, respectively.

Once the stiffness matrix is determined, for given boundary conditions and force vector $[F]$, the corresponding displacement vector $[d]$ is obtained by Newton-Raphson method. The strain vector is determined from the displacement vector and strain-displacement relations. The stress

vector is then derived from stress-strain relations. Iterative mapping is used to recalculate the $[K]$ due to fiber orientation during incremental deformation. An incremental method is adopted to incorporate the nonlinear characteristics into the analysis. These procedures are repeated till the final value of load is reached.

2.2. Graded Fiber Waviness Model

The representative volume of graded fiber waviness model consists of thicknesswise volume fraction (V_{ct}) of graded fiber waviness and volume fraction without fiber waviness. It is assumed that amplitude of fiber waviness decays linearly from a maximum at the middle of the beam to zero at the certain profiles parallel to the outer surfaces.

2.3. Localized Fiber Waviness Model

The representative volume of localized fiber waviness model consists of lengthwise volume fraction ($V_{cl} = L_w / L$) of localized fiber waviness and volume fraction without fiber waviness. L and L_w are length of representative volume and length of volume containing fiber waviness, respectively.

3. EXPERIMENTAL PROCEDURES

The material investigated in this study was DMS 2224 graphite/epoxy composite material (Hexcel Co. Inc.). In order to determine the elastic properties and the nonlinear stress-strain behaviors of this composite material, quasi-static tests with standard specimens were conducted in a MTS servo-hydraulic testing system. A special fabrication technique[5] was developed for producing the thick composite specimens with the controlled fiber waviness. Molds with various sinusoidal waves were used to fabricate the composites with fiber waviness in an autoclave following special two-step curing cycle. Specimens with three waviness ratios (amplitude/wavelength) were fabricated. The fiber waviness ratios were 0.011, 0.034 and 0.059. The specimens were 150 mm long, 10 mm wide and 5.2 mm thick. The test coupons were instrumented with strain gages on both sides. Four point flexural tests were conducted in a servo-hydraulic testing machine while monitoring the deflections, strains and applied loads. The deflections of the composite beam were measured with the home-made deflection meter.

4. RESULTS AND DISCUSSION

Figure 3 (a) shows the comparisons among the predicted and experimentally obtained load-deflection curves under flexural loading for uniform fiber waviness model with various fiber waviness ratios. It is observed from the figure that the predicted deflections for corresponding load by the FEA model are lower than that obtained by the thin slice model[6] and the experiments for all fiber waviness ratios. It is also noted that load-deflection curves show more nonlinearity as the fiber waviness ratio increases. The predicted curves by the FEA model show good agreement with the predictions by thin slice model[6] and the experimental results.

Figure 3 (b) shows the comparison of load-deflection curves for three types of fiber waviness pattern : uniform, graded and localized fiber waviness. It is observed from the figure that the type of fiber waviness significantly affects the nonlinear behavior of thick composites. The load-deflection curve of the uniform fiber waviness model shows the most degradation and nonlinearity among the three models.

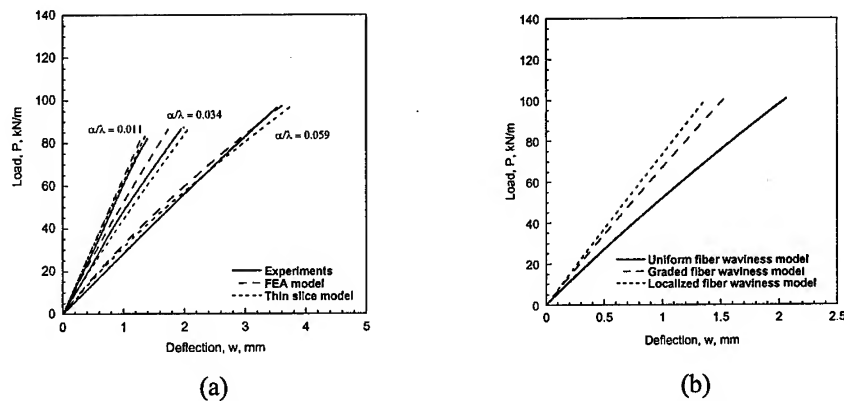


Fig. 3. (a) Predicted and experimentally obtained load-deflection curves for uniform fiber waviness model with various fiber waviness ratios, (b) Predicted load-deflection curves for three types of fiber waviness with fiber waviness ratio (a/λ) of 0.034 ($V_{cf}=1.0$ for graded fiber waviness model, $V_{cf}=1.0$ and $V_{cf}=0.5$ for localized fiber waviness model).

Figures 4-6 show schematic drawings of specimen with fiber waviness and contour plots of effective stress and strain for three types of fiber waviness model. When flexural loading is applied to a composite beam, some portion of the beam is exposed to tensile stress and the remainder to compressive stress. The portion of the beam under tensile stress tends to stretch the wavy fibers while the portion under compressive stress tend to increase the fiber waviness. Thus, the portion under tensile stress stiffens while that under compressive stress softens during the deformation. Those effects are clearly shown in the effective stress and strain distributions. The figures show that relatively high effective stress distribution is observed in the uniform fiber waviness model while relatively low effective stress distribution is observed in the localized fiber waviness model for the same amount of applied load. The uniform fiber waviness model shows the most decrease of effective stress while the localized fiber waviness model shows the least decrease of effective stress toward midplane of the beam. It is believed that these effects are due to stiffening associated with type of fiber waviness as shown in Fig. 3 (b). The effective strain distributions for the three types of fiber waviness model show some influence of fiber waviness whereas the effective stress distributions show a little influence of fiber waviness. This influence is relatively more pronounced in the uniform fiber waviness model and relatively less pronounced for the graded and localized fiber waviness models as the portions containing wavy fibers decrease in the composite specimens.

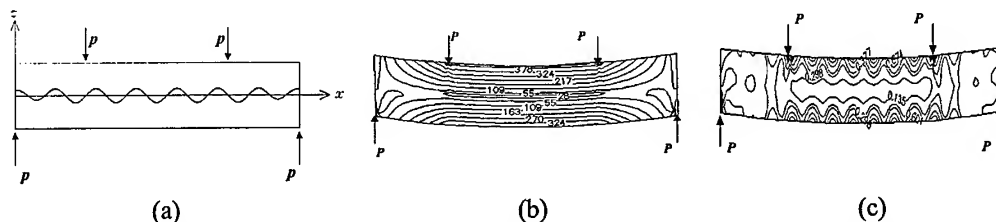


Fig. 4. Stress and strain analyses of composites with uniform fiber waviness (applied load, $P=50$ kN/m and $a/\lambda=0.034$): (a) schematic drawing of specimen with uniform fiber waviness, (b) contour plot of effective stress (σ_{eff} , MPa), (c) contour plot of effective strain (ϵ_{eff} , %).

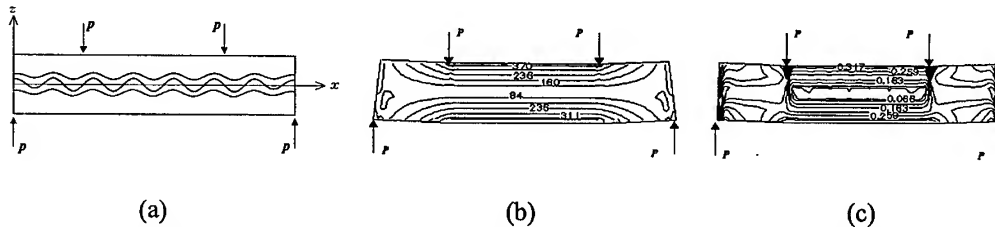


Fig. 5. Stress and strain analyses of composites with graded fiber waviness (applied load, $P=50$ kN/m, $a_0/\lambda = 0.034$ and $V_{cl} = 1.0$) : (a) schematic drawing of specimen with graded fiber waviness, (b) contour plot of effective stress (σ_{eff} , MPa), (c) contour plot of effective strain (ϵ_{eff} , %).

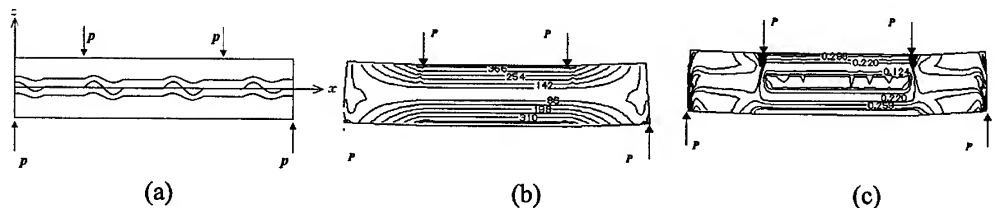


Fig. 6. Stress and strain analyses of composites with localized fiber waviness (applied load, $P=50$ kN/m, $a_0/\lambda = 0.034$, $V_{cl} = 1.0$ and $V_{cl} = 0.5$) : (a) schematic drawing of specimen with localized fiber waviness, (b) contour plot of effective stress (σ_{eff} , MPa), (c) contour plot of effective strain (ϵ_{eff} , %).

5. CONCLUSIONS

A FEA model was proposed to study the nonlinear flexural behavior of thick composites with three types of fiber waviness. It was found that the degree of fiber waviness as well as the type of fiber waviness in composites significantly affected the nonlinear flexural behavior. In addition, stress and strain analyses were also conducted. It was concluded that the type of fiber waviness also affected the stress and strain distributions in composites. The uniform fiber waviness model showed relatively high stress and strain distributions compare to those of other models under the same amount of applied load and showed strong influence of fiber waviness in the strain distributions under flexural loading.

ACKNOWLEDGEMENT

The authors are grateful for the support provided by Brain Korea 21 from Korea Research Foundation (KRF).

REFERENCES

1. M. J. Stuart, AIAA Journal, **27** (1989) pp. 1274-1279.
2. H. K. Telegadas and M. W. Hyer, Journal of Reinforced Plastics and Composites, **11** (1992) pp. 127-145.
3. T. -W. Chou and K. Takahashi, Composites, **19** (1987) pp.25-33.
4. H. M. Hsiao and I. M. Daniel, Journal of Engineering Materials and Technology, **118** (1996) pp. 561-570.
5. H. M. Hsiao, S. C. Wooh and I. M. Daniel, Journal of Advanced Materials, **26** (1996) pp. 19-26.
6. H. -J. Chun, J. -Y. Shin and I. M. Daniel, Materials Science Research International, **5** (1999) pp. 181-188.

Fuzzy Mathematical Method for Evaluation of Rock Mechanical Indexes

Guang Zhang, Tingjie Li and Shiwei Bai

Institute of Rock and Soil Mechanics, The Chinese Academy of Sciences,
Wuhan 430071, China P.R.

Keywords: Fuzzy Method, Mechanical Parameter, Rock Mass

ABSTRACT

A new fuzzy model to assess synthetically the rockmasses quality is established which considers the uniaxial compressive strength R_c , integrity coefficient k_v , joint spacing d_p and rock quality designation RQD as the assessing factors of the rockmass quality. The fuzzy attributions of the assessing factors to the rockmass quality are described with normal subordinative functions and the weights of the factors are determined using the *dualistic contrast method*. The synthetical assessment on rockmass quality is performed using $M(\cdot, +)$ type fuzzy operator. A method to evaluate rockmass shear strength indexes is proposed based on the synthetical fuzzy assessment of the rockmass quality.

1. INTRODUCTION

The *rockmass quality grades method* (RQG method) is often used to evaluate the mechanical parameters of rockmass, in which the mechanical indexes of a specific rockmass is determined indirectly: firstly, establish the corresponding relationship between the mechanical index and the rockmass quality through summarizing and analysing in statistics a mass of engineering experiences based upon the inner link between the mechanical index and the rockmass quality and then evaluate the mechanical parameters of a specific rockmass according to the rockmass quality. Of many RQG methods, those proposed by N. Barton, Z. T. Bieniawski, Gu Dezhen and Liu Fuzheng are widely used [1].

The inadequacy of the aforesaid RQG methods lies in: (1) too clear RQG levels sometimes result in great difference of two rockmasses in mechanical indexes because their RQGs just fall on the two sides of two adjacent levels, in fact, the two rockmasses have no remarkable quality differences; (2) each RQG level has too large index range, resulting in inevitable man-made differentiation in evaluating a parameter value. As a matter of fact, no abrupt change exists between adjoining levels and transition from one to another is a progressive course, in other words, the RQG levels' boundary is unclear or ambiguous. Classical mathematical method fails to describe this characteristic. For this reason, the fuzzy mathematical theory is introduced into the study of rockmass quality grades.

This paper tries to establish a new fuzzy synthetical assessing model for rockmass quality

mainly on the basis of Bieniawski RQG method, in connexion with the experiences of previous researchers and through rescreening assessing factors. Additionally, this paper suggests a new method to estimate the mechanical indexes of a rockmass.

2. MATHEMATICAL MODEL FOR FUZZY ASSESSMENT OF ROCKMASS QUALITY

By *fuzzy synthetical assessing* is meant to deduce the fuzzy subset B established on the discourse universe of remarks, V , from the fuzzy composite operation between the fuzzy subset A that is established on the discourse universe of factors, U , and the fuzzy relationship of R between U and V .

Write fuzzy subsets A and B in terms of vectors as $A = \{a_i\}_{1 \times m}$ and $B = \{b_j\}_{1 \times n}$ where a_i ($0 \leq a_i \leq 1$) is the subordinative degree of u_i on A , measuring how the single factor of u_i plays a role in the overall assessing factor of A ; b_j ($0 \leq b_j \leq 1$) is the subordinative degree of the grade v_j on B that is obtained from synthetical assessment, i.e., the result needed by the synthetical assessment.

Write the fuzzy relationship R between U and V in terms of matrix as $R = \{r_{ij}\}_{m \times n}$ where $r_{ij} = \mu_{v_j}(u_i)$ ($0 \leq r_{ij} \leq 1$) is the subordinative degree to which an object is judged as the grade v_j from the angle of the factor u_i , i.e., r_{ij} is the subordinative degree of the assessment from the factor u_i on the grade v_j .

When A and R are known, the synthetical assessment can be made through fuzzy product of A and R

$$B = A \cdot R \quad (1)$$

Depending upon the operator form in the product, a variety of specific models have been proposed [2], among which $M(\cdot, +)$ model is the one of *weighted mean* type that makes synthetical assessment take into account the effect of various affecting factors and suitable for fuzzy assessment of rockmass quality. In the model, the fuzzy vector is of weight vector meaning, whereas the right side of Eq. (1) becomes the multiplication between common matrixes, i.e.,

$$b_j = \sum_{i=1}^m a_i r_{ij}, \text{ where the weight coefficient of } a_i \text{ meets } \sum_{i=1}^m a_i = 1.$$

3. FUZZY SYNTHETICAL ASSESSING MODEL FOR ROCKMASS QUALITY

3.1. Determination of Factor Set U

There are many and complex factors affecting the rockmass quality. In assessing rockmass quality, the attempt to take all affecting factors into consideration is not only very difficult but also out of value in practice because it is impossible to implement overall investigation of all factors. It is necessary to screen the factors accordingly.

To screen affecting factors should follow as fully as possible the four basic principles: (1) Importance: the assessing factor should be the important or fairly important ones that governs the rockmass quality and at least reflect a special basic aspect of the quality; (2) Independence: they are independent of each other relatively; it should be avoided to employ multiple factors that reflect the same basic aspect, which produces needless duplications; (3) Easy measurement: the index of assessing factors should be obtained easily and convenient for measuring with reliable results; and

(4) Universal in use: The assessing factors should be those that are necessary for general projects and easy to be widely applied to engineering.

By analysing the factors that affect the rockmass quality under the above stated principles and consulting the previous RQG methods, we select such factors as elements of *assessing factor set* for rockmass quality as uniaxial compressive strength (R_c), integrity coefficient (k_v), joint spacing (d_p) and RQD value of rocks. So-comprised assessing factor set has the expression of

$$U = \{u_1, u_2, u_3, u_4\} = \{R_c, k_v, d_p, \text{RQD}\} \quad (2)$$

where $k_v = (V_{pm}/V_{pr})^2$, V_{pm} standing for the longitudinal wave velocity of rockmass and V_{pr} for the same velocity of intact rock blocks.

3.2. Determination of Remark Set V

The current RQG methods with multiple factors divide rockmass quality into four or five grades. For correspondence, our method also has five quality grades, i.e., I - V grades, that comprise remark set:

$$V = \{v_1, v_2, v_3, v_4, v_5\} = \{G1, G2, G3, G4, G5\} \quad (3)$$

3.3. Establishment of Subordinative Functions

The normal function is used to describe the subordinative function $\mu_{v_j}(u_i)$ on the factor u_i [3]:

$$\mu_{v_j}(u_i) = \exp \left[\frac{(u_i - m_{ij})^2}{b_{ij}^2} \right] \quad (4)$$

where m_{ij} and b_{ij} are the character constants describing the $\mu_{v_j}(u_i)$ function's center and amplitude. Eq. (4) is suitable for each factor with respect to the subordinative functions of remarks v_2, v_3 and v_4 , whereas with respect to the subordinative functions of remarks v_1 and v_5 , it may as well rewrite Eq.(4) in increasing seminormal form or in decreasing seminormal form.

Table 1. Relation between rockmass quality grades and affecting factors

grades factors	$v_1(G1)$	$v_2(G2)$	$v_3(G3)$	$v_4(G4)$	$v_5(G5)$
$u_1(R_c(\text{MPa}))$	>250	250 - 100	100 - 50	50 - 25	<25
$u_2(k_v)$	>0.9	0.9 - 0.75	0.75 - 0.45	0.45 - 0.2	<0.2
$u_3(d_p(\text{m}))$	>2	2 - 0.6	0.6 - 0.2	0.2 - 0.06	<0.06
$u_4(\text{RQD}(\%))$	100 - 90	90 - 75	75 - 50	50 - 25	<25

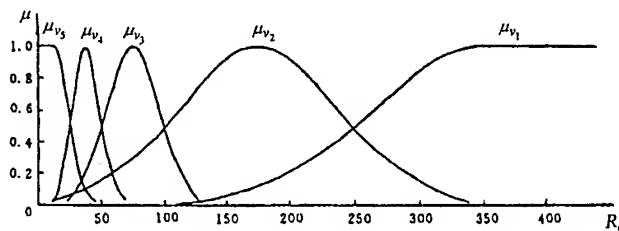
Tabulated in Table 1 are the rough correspondent relations between rockmass quality and affecting factors, which are summarized after studies of Bieniawski [4] and Yang Ziwen et al [1]. Given that the ranges of u_1 and u_3 correspondent to v_1 are 450~250 and 4~2 respectively, then, from Table 1, the characters m_{ij} and b_{ij} of all subordinative functions can be determined as shown in Table 2. When m_{ij} and b_{ij} are determined, the subordinative functions are determined accordingly. Shown in Fig.1 is the subordinative function curve of the assessing factor u_1 (uniaxial compressive strength of rocks, R_c).

Providing a set of index values of $U^\circ = \{u_1^\circ, u_2^\circ, u_3^\circ, u_4^\circ\}$ are given to assessing factors after determination of subordinative functions, we have assessing matrix of $R = \{r_{ij}\}_{4 \times 5}$ where

$$r_{ij} = \mu_{v_j}(u_i^0).$$

Table 2. Character constants (m_{ij}, b_{ij}) of subordinate functions

$m_{11}=350.0$	$m_{12}=175.0$	$m_{13}=75.0$	$m_{14}=37.5$	$m_{15}=12.5$
$b_{11}=120.112$	$b_{12}=90.084$	$b_{13}=30.028$	$b_{14}=15.014$	$b_{15}=15.014$
$m_{21}=0.950$	$m_{22}=0.825$	$m_{23}=0.600$	$m_{24}=0.325$	$m_{25}=0.100$
$b_{21}=0.06$	$b_{22}=0.09$	$b_{23}=0.18$	$b_{24}=0.15$	$b_{25}=0.12$
$m_{31}=3.00$	$m_{32}=1.30$	$m_{33}=0.40$	$m_{34}=0.13$	$m_{35}=0.03$
$b_{31}=1.201$	$b_{32}=0.841$	$b_{33}=0.240$	$b_{34}=0.084$	$b_{35}=0.036$
$m_{41}=95.0$	$m_{42}=82.5$	$m_{43}=62.5$	$m_{44}=37.5$	$m_{45}=12.5$
$b_{41}=6.006$	$b_{42}=9.008$	$b_{43}=15.014$	$b_{44}=15.014$	$b_{45}=15.014$

Fig.1. Subordinative function curve of u_1

3.4. Determination of Weight Vector

As stated previously, the element a_i of vector A is the subordinative degree of the assessing factor of u_i upon A , it is the magnitude to measure how the single factor of u_i functions in the overall assessing factor. This magnitude can be determined using the method of *dualistic relative comparison* [3].

Now, if a group of factors, u_1, u_2, \dots, u_m are to be arranged in sequence according to a specific character, we may make a pairwise comparison on the factors: first to establish a dualistic comparing grade and then turn it into the overall ordering through a certain algorithm. If the extent to which u_j possesses a character is given as $f_{u_i}(u_j)$ when we make dualistic comparison on an arbitrary pair of factors (u_i, u_j) , then u_i 's extent to possess this character should be $f_{u_i}(u_i)$. The weight, a_i , of each factor can be obtained only when a certain algorithm is employed according to $f_{u_i}(u_j)$ and $f_{u_j}(u_i)$ of each pair of factors (u_i, u_j) .

The establishment of *dualistic comparing grade* relies upon experts experiences or fuzzy statistic analysis. As concerns the problem of assessing the rockmass quality, a variety of grade-division methods have been developed, we may draw experiences of experts to establish a dualistic comparing grade.

Bieniawski's method takes into account three factors of R_c, d_p and RQD, a pairwise dualistic comparing grade of those factors can be established according to the marks allocated to each one. However Bieniawski's method does not take k_v into consideration but replaces it with another factor of *discontinuity state* that is similar to k_v ; besides, his method pays more importance to the

discontinuity state than to the joint spacing d_p . Liu Fuzheng's method, however, equally considers the importances of k_v and d_p . Comprehensive analysis on Bieniawski's and Liu's methods shows that k_v is somewhat more important than d_p . A rough dualistic comparing grade between any pairwise elements of all factors can be obtained from the above analyses:

$$\begin{aligned} f_{u_2}(u_1) &= (0.6, 1.0) & f_{u_1}(u_2) &= (1.0, 0.6) & f_{u_1}(u_3) &= (1.0, 0.7) & f_{u_1}(u_4) &= (1.0, 0.6) \\ f_{u_3}(u_1) &= (0.7, 1.0) & f_{u_3}(u_2) &= (1.0, 0.8) & f_{u_2}(u_3) &= (0.8, 1.0) & f_{u_2}(u_4) &= (0.9, 1.0) \\ f_{u_4}(u_1) &= (0.6, 1.0) & f_{u_4}(u_2) &= (1.0, 0.9) & f_{u_4}(u_3) &= (0.9, 1.0) & f_{u_3}(u_4) &= (1.0, 0.9) \end{aligned}$$

By employing the algorithm proposed in the literature of [3], we have the following weight vector A :

$$A = \{0.18 \quad 0.31 \quad 0.24 \quad 0.27\} \quad (5)$$

3.5. Fuzzy Synthetical Assessment on Rockmass Quality

Once the weight vector A and the synthetical assessing matrix R are determined, the fuzzy synthetical assessment can be carried out according to Eq.(3), thus obtaining B . According to the assessing criterion of *maximum subordinative degree*, providing

$$b_k = \bigvee_{j=1}^n b_j \quad (6)$$

the rockmass quality is evaluated as the grade of v_k . In Eq.(8), ' $\bigvee_{j=1}^n$ ' means to maximize.

4. EVALUATION OF ROCKMASS PARAMETER CHARACTER VALUE

Shown in Table 3 [5], as an example, is the correspondent relation between the rockmass peak strengths (f and c) and each quality grade.

Table 3. Values of shearing strength index of each grade of rockmass quality

RQG level	G1	G2	G3	G4	G5
f	>1.6	1.6 - 1.28	1.28 - 1.0	1.0 - 0.58	<0.58
$c(\text{MPa})$	>2.5	2.5 - 1.5	1.5 - 1.0	1.0 - 0.3	<0.3

Consider a parameter written as P and take the mean value of P for the j th grade rockmass as the representative of this grade, written as P_j . The subordinative degree to which the rockmass sample belongs to the j th grade is b_j . Obviously, the higher the b_j value, the greater the possibility that the rockmass sample is classified into the j th grade. It is easy to know, therefore, that evaluation of parameter P is related with each P_j . How important P_j is to P is described by the subordinative degree of b_j . By normalizing b_j , we have b_j' , so-obtained b_j' can be considered as the weight to describe the importance extent of P_j . Thereupon, the evaluated value of parameter P , \hat{P} , is the weighted mean value of all affecting factors, i.e.,

$$\hat{P} = \sum_{j=1}^n b_j' P_j \quad (7)$$

where $b_j' = b_j / \sum_{j=1}^n b_j$

Concretely, given that the upper limit of the rockmass shearing strength indexes are $f_{\max}=2.0$ and $c_{\max}=4.5\text{MPa}$ respectively, we have the typical value of f or c for each grade (Table 4) and the evaluation of f and c can be determined from fuzzy subset B and Eq.(7), written as \hat{f} and \hat{c} respectively.

Table 4. Typical values of f and c for each grade

f	$f_1=1.8$	$f_2=1.44$	$f_3=1.14$	$f_4=0.79$	$f_5=0.29$
$c(\text{MPa})$	$c_1=3.5$	$c_2=2.0$	$c_3=1.25$	$c_4=0.65$	$c_5=0.15$

5. CONCLUSION REMARKS

The fuzzy synthetical assessing model for rockmass quality proposed in the present paper are characterized by the followings:

(1) Having analysed and screened all factors affecting the rockmass quality, the uniaxial compressive strength (R_c), integrity coefficient (k_v), joint spacing (d_p) and rockmass quality designation (RQD) are selected as the basic affecting factors. These factors are independent relatively, each reflecting a specific aspect of the rockmass quality.

(2) The normal functions are employed to describe the subordinative relation between rockmass quality and assessing factors. The character constants (mean value, m , and amplitude width, b) of the normal functions are determined according to previous researchers' results and experts' experiences.

(3) Based upon the results of previous researchers and the experiences of experts, the *dualistic relative analogue method* is used to determine the weight vector of the assessing factor.

In addition, this paper on the basis of fuzzy synthetical assessment on rockmass quality puts forward a method following the principle of *First Order Second Moment Method* in which both mean value and quadratic error of rockmass shearing strength parameters are determined.

REFERENCES

1. Cui Guanying, and Pan Pinzheng (editor in chief), Geological Engineering for Hydraulic Projects, Publishing House of Water and Power, Beijing (1995)
2. Wang Guangyuan, On Essence and Application of Several Mathematical Model for Synthetical Assessment, J. Fuzzy Mathematics, No.4 (1984) p.81~83
3. Wang Peizhuang, Fuzzy Set Theory and Application, Shanghai Press of Science and Technology, Shanghai(1983)
4. Bieniawski Z. T., The Geomechanics Classification in Rock Engineering Application, Proceedings of the 4th Conf. of Int. Soc. Rock Mech. (1979) p.41~48
5. Liu Fuzheng, Basic Qulity of Rockmass and Classification of Engineering Rockmass, J. Yangtze Scientific Research Institute, Sum. No.26 (1991) p.55~63

Topology Optimization of the Inner Reinforcement for an Automobile Hood Using Modal Design Sensitivity Analysis

T.H. Lee, S.Y. Han and J.K. Lim

School of Mechanical Engineering, Hanyang University,
17 Haengdang-dong, Sungdong-ku, Seoul 133-791, Korea

Keywords: Automobile Hood Design, Design of Reinforcement, Modal Design Sensitivity Analysis, Topology Optimization

ABSTRACT

Topology optimization technique to find an optimized path of an inner reinforcement of a shell-typed structure is proposed on the basis of the modal design sensitivity analysis. The strength and mode characteristics of an automobile hood are analyzed and their design sensitivity analyses with respect to the thickness of the shell structure are carried out using MSC/NASTRAN. According to the strength and mode design sensitivity analyses, determination of design variables and response functions for the topology optimization is discussed. Many approaches to improve mode characteristics of the automobile hood from design sensitivity information are suggested. Available methods for direction finding and step size determination of the topology optimization process are suggested and their advantages and disadvantages are discussed. Finally the double-layer method is proposed to optimize the path of stiffener for a shell structure. Using the proposed method, we redesign a new inner reinforcement of the automobile hood and compare the mode responses with the original design. It is confirmed that new design is improved in the view of the natural frequency responses without increasing the weight of the automobile hood.

1. INTRODUCTION

For thin shell structures, inner reinforcement is necessary in order to strengthen the weakness of structures to transverse vibrations or loads. However, responses from static and dynamic analyses cannot effectively provide the design information for the topology of the inner reinforcement. Therefore we introduce the new concepts of optimization techniques such as design sensitivity analysis to achieve the optimum path of inner reinforcement for a thin shell structure. For

topology optimization, materials with microstructure were considered in the optimum material distribution for elastic plates in early 1980s [1]. The homogenization and density methods for topology design have led to the capacity to predict computationally the optimal topologies of continuum structures [2]. However, the homogenization method is difficult to apply in industry applications because a commercial finite element analysis code doesn't provide the design sensitivities with respect to material properties. While topology optimization has been promised as solution to the path design of inner reinforcement, design sensitivity method will benefit from modal design sensitivity of the shell structure supplied by commercial finite element programs and how to increase its natural frequency.

In this research, an optimization technique to obtain the optimum path of an inner reinforcement of an automobile hood shown in Fig. 1 is proposed by using modal design sensitivity analysis performed by using MSC/NASTRAN. Without an appropriated initial shape of the inner reinforcement, the optimum path is found. Then we have seen that the proposed method is effective and reliable comparing with the original design that is suggested by a field designer.

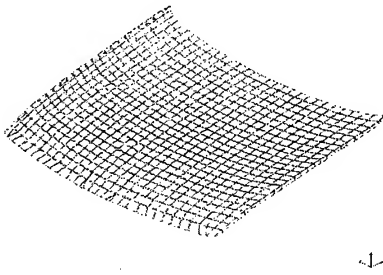


Fig. 1 FE model of the outer panel of an automobile hood.

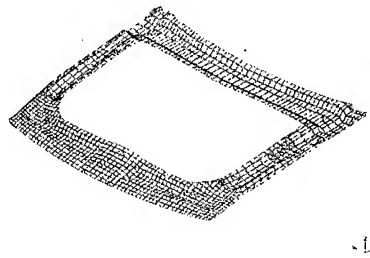


Fig. 2 Sealing region of inner panel.

2. MODAL DESIGN SENSITIVITY ANALYSIS

Modal design sensitivity analysis computes the rate of changes of response-dependent functions, for instance, eigenvalues and eigenvectors with respect to the perturbation of design variables. The definition of modal analysis is given from eigenvalue problem as follows:

$$\mathbf{K}\mathbf{u}_i = \lambda_i \mathbf{M}\mathbf{u}_i \quad (1)$$

where \mathbf{K} and \mathbf{M} represent the stiffness matrix and the mass matrix, respectively. The eigenvalue λ_i and its associated eigenvectors \mathbf{u}_i represent the i -th free vibration frequency squared and corresponding mode shapes, respectively. Then the sensitivity coefficients of the eigenvalues and eigenvectors are defined as the total derivatives of responses with respect to design variable, b , as follows:

$$\frac{d\lambda_i}{db} \text{ and } \frac{du_i}{db} \quad (2)$$

For the complete reviews of modal design sensitivity analysis, work of Lee should be consulted [3].

3. PATH OPTIMIZATION OF INNER REINFORCEMENT

3.1 Definition of Problem

In order to perform the topology optimization of the automobile hood of Fig. 1 by applying modal design sensitivity analysis, its finite element analysis is carried out first. Because the edge of the hood, the so-called sealing region, is required to contact tightly with engine room, we cannot change the path of the edge of the inner reinforcement as shown in Fig. 2. Therefore, the design domain will be the inside of the sealing region of the hood. Geometric and material properties of the hood and inner reinforcement are given in the Table 1.

Table 1 Geometric and material properties of the hood

Panel thickness	Outer panel	1.2 mm
	Inner Panel	1.2 mm
	Reinforced bracket	1.2 mm
Young's modulus		2.07 GPa
Poisson's ratio		0.29
Mass density		$7.83 \times 10^{-6} \text{ kg/mm}^3$

Since the path of the edge of the inner reinforcement must maintain the initial design, the thickness of all shell elements within the inside of the inner panel will be design variables. Therefore, modal design sensitivity analysis of the hood with respect to the defined design variables will be evaluated by using MSC/NASTRAN [4].

In order to determine the objective function for design sensitivity analysis, we examine the design sensitivity analyses of strength at a local point and frequencies of the hood. For strength and durability, torsional deformation due to a concentrated load applied at the corner of the hood must be less than the given limit value to meet the vehicle test standard such as FMVSS. However the design sensitivity analyses of the maximum deformation and stress show that the sensitivity coefficients distribute on the neighborhood of the load point. And design sensitivity of the central transverse loading on the hood also reveals local distribution near loading point. Thus it is important to note that the inner reinforcement of the hood doesn't have an effect on the torsional stiffness or strength of the hood. Maximum deformation or stress that leads local distribution of design sensitivity coefficient in the neighborhood of the load applied cannot be a candidate for objective functions.

Next we consider the modal design sensitivity analysis of the hood and it shows that the modal

sensitivity coefficients are distributed widely on the design domain. Thus it is concluded in the research that the optimal path for the inner reinforcement of the hood can be evaluated by using modal design sensitivity analysis of the hood. Therefore, to prevent the twisting and bending motion of the hood, we define the object functions as the first and second natural frequencies.

3.2 Path Optimization

To generate the path of inner reinforcement from multiple objective functions, i.e., the first and second natural frequencies, we have to determine the design direction and its step size. Modal design sensitivity analysis of multiple objectives can provide the same sign of sensitivity coefficients in some design variables and the different signs in the other design variables. If the sign of sensitivity coefficient is positive for the multiple objectives, we can determine the design direction as the design variable is to be increased to improve the design. For negative sensitivity coefficients, the design variable is to be reduced to improve the design. If the signs of sensitivity coefficients have conflict, it is difficult to determine the design direction. Thus we introduce the root mean squared (RMS) to count the magnitude of the opposite sign of sensitivity coefficients. Based on these observations, we examine four methods of design directions as shown in Table 2. For the method 1, we increase the design variables if the signs of sensitivity coefficients of the multiple objectives are all positives and decrease the design variables if those are all negatives. It can be seen that the method 1 shows fair design improvement and good path generation comparing with other methods. Thus we choose the method 1 for design direction.

Table 2 Methods of design directions using design sensitivity coefficients

Methods		Thickness			
		1	2	3	4
Sign of sensitivity coefficients	+	increase	increase	no change	no change
	-	reduce	reduce	reduce	reduce
	+/-	no change	change-RMS	no change	reduce-RMS
Weight reduction		fair	good	fair	good
Freq. Improvement		fair	good	fair	good
Path Topology		good	bad	fair	bad

Once we determine the design direction, we must determine step size of the design variables for optimization. For step size determination, we can consider many different methods. Here we use the uniform proportional step that change the design variable in proportional to the previous design variable as follows:

$$b_i^{(n)} = b_i^{(n-1)} \times R^{\text{sign}[c_i^{(n)}]} \quad \text{with} \quad \text{sign}[x] = \begin{cases} 1 & \text{if } x > 0 \\ 0 & \text{if } x = 0 \\ -1 & \text{if } x < 0 \end{cases} \quad (3)$$

where the superscript (n) denotes the design step, and $b_i^{(n)}$, $c_i^{(n)}$ and R represent the value of i -th

design variable, the design sensitivity coefficient of $b_i^{(n)}$, and proportional ratio of design variables, respectively.

3.3 Double-layer Method

Whenever the inner reinforcements are employed to strengthen the thin shell structure, the topology of inner reinforcement doesn't affect the shape of outer panel in general. Thus initially we add an identical shell panel (inner panel) to the outer panel and shear the node numbers of the finite element analysis. Then we change the thickness of the inner panel only, i.e., the design variables become the shell thickness of inner panel within the design region. In this way, the path of inner reinforcement becomes natural and clear.

In the finite element model, quadrilateral element of CQUAD4 and triangular element of CTRIA3 elements are used and 1420 elements with 2313 common node points in the design region are employed. Method 1 for design direction and proportional step size are used to generate the topology of reinforcement. Initial thickness of the inner panel is given as 0.5 mm and lower and upper limits of the design variables are 0.001 mm and 1.0 mm, respectively. The free boundary condition is employed to carry out the response analysis and optimization. It is important to note that the convergence is very fast and reliable because the path of the reinforcement appears in one or two design steps as shown in Fig. 3(a). In the Fig. 3(a), the gray region becomes the path of reinforcements and dark region can be eliminated.

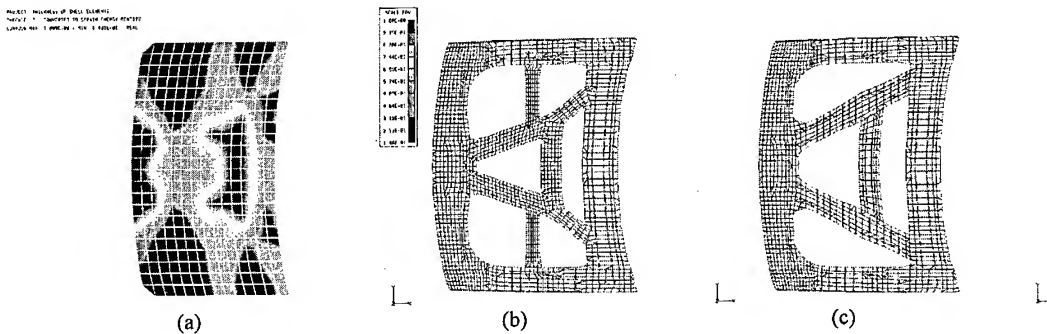


Fig. 3 Optimum design of inner reinforcement of automobile hood: (a) Topology of reinforcement, (b) FE model of optimized design, and (c) FE model of original design

4. RESULTS

The path of inner reinforcement can be designed so that a designer can draw the path along the relative thick region of inner panel of Fig. 3(a). Finally, Fig. 3(b) shows the finite element model of the optimized inner reinforcement. Then the modal analysis of the automobile hood attached

with the inner reinforcement is carried out and its responses are given for both free and fixed boundary conditions in Table 3. The results shows that the first and second natural frequencies of the optimized design are improved for the free and fixed boundary conditions without increasing the weight comparing to the original design shown in Fig. 3(c).

Table 3 Comparison of the modal analyses of the hood

		Original design	Optimized design
Weight		23.3 kg	23.0 kg
Free boundary	Mode 1	12.6 Hz	14.6 Hz
	Mode 2	48.8 Hz	49.5 Hz
Fixed boundary	Mode 1	32.4 Hz	37.8 Hz
	Mode 2	56.2 Hz	58.0 Hz

5. CONCLUDING REMARKS

Topology optimization technique of the inner reinforcement for a thin shell structure is proposed by using modal design sensitivity analysis. The criteria to determine the objective function and design variables are suggested to achieve the optimum path of the inner reinforcement. And the developed double-layer method is so natural and fast that it can show clear pattern of topology because the inner reinforcement doesn't change the shape of the outer panel but is added to it. The optimized design of the automobile hood is considerably improved in the view of vibration characteristics without increasing the weight. The proposed method can be used to design the topology of reinforcement of a thin shell structure in general.

ACKNOWLEDGEMENT

The authors wish to acknowledge the financial support of Hanyang University, Korea, made in the programming year of 1998.

REFERENCES

1. M.P. Bendsoe, Optimization of Structural Topology, Shape, and Material, Springer-Verlag, Berlin Heidelberg (1995).
2. K. Suzuki, N. Kikuchi, Comp. Meth. Appl. Mech. and Eng., Vol. 93 (1991), p. 291.
3. T.H. Lee, KSME International J., Vol. 13 (1999), p. 470.
4. MSC/NASTRAN Design Sensitivity and optimization User's Guide, MSC Co., CA.

Computational Studies on Dynamic Fracture Phenomena

T. Nishioka and T. Fujimoto

Simulation Engineering Laboratory, Department of Ocean Mechanical Engineering, Kobe
University of Mercantile Marine, 5-1-1 Fukae Minamimachi, Higashinada-ku 658-0022, Japan

Keywords: Delaunay Automatic Triangulation, Dynamic Crack Propagation, Dynamic Fracture, Dynamic Fracture Mechanics, Dynamic J Integral, Fracture Path Prediction, Impact Fracture, Moving Element Method, Path Independent Integral, Separated Dynamic J Integral

ABSTRACT

This paper provides a summary of recent computational studies on various dynamic fracture phenomena. First, the dynamic J integral and the separated dynamic J integral are presented. These path independent integrals are very useful for accurately evaluating various fracture parameters. Next, several types of fracture simulation are explained. These are generation-phase simulation, mixed-phase fracture-path prediction mode simulation, mixed-phase crack-growth prediction mode simulation, and application phase simulation. Simulation results are presented for (i) impact kinking and curving fracture, (ii) dynamic interfacial fracture, and (iii) dynamic crack bifurcation.

1. INTRODUCTION

Numerical simulations of dynamic fracture phenomena involve many inherent difficulties. Main reasons of these difficulties may be listed as follows:

- (1) Moving singularities at the tips of dynamically propagating cracks should be treated accurately. The ordinary numerical methods cannot treat the moving singularities.
- (2) When a propagating crack tip passes a material point, the material point instantaneously separates into at least two parts. In the ordinary numerical models with nodal release techniques, this sudden unloading process often produces spurious oscillations.
- (3) Cracks may curve, kink or bifurcate. Automatic mesh generations for these non-self-similar fast fracture phenomena are extremely difficult.
- (4) The crack propagation velocity along a bimaterial interface can become extremely fast and can exceed the shear wave speed of the compliant material.

To overcome such difficulties, the author and coworkers have developed various numerical simulation technologies, such as various moving finite element methods, the path independent dynamic J integral, concept of separated dynamic J integral, and concept of mixed-phase simulation.

Using the developed concepts and technologies, various dynamic fracture phenomena including (i) impact kinking and curving fracture, (iii) dynamic interfacial fracture, and (iv) dynamic crack bifurcation, are successfully simulated. The simulation results for dynamic fracture path prediction, variations of the dynamic J integral and dynamic stress intensity factor during the dynamic fracture processes are presented.

2. PATH INDEPENDENT DYNAMIC J INTEGRAL

To evaluate various fracture mechanics parameters for a crack subject to impact stress wave loading, and for a dynamically kinking as well as dynamically curving crack, the path independent dynamic J integral derived by Nishioka and Atluri [1] is used.

In most numerical analyses, the dynamic J integral (J') can be evaluated by

$$J'_k = \int_{\Gamma + \Gamma_c} [(W+K)n_k - t_i u_{i,k}] dS + \int_{V_r} [(\rho \ddot{u}_i - f_i) u_{i,k} - \rho \dot{u}_i \dot{u}_{i,k}] dV \quad (1)$$

where W and K are the strain and kinetic energy densities, respectively. The integral paths are defined in Fig.1.

The crack-axis components of the dynamic J integral can be evaluated by the coordinate transformation, $J_l^0 = \alpha_{lk}(\theta_0) J'_k$ where α_{lk} is the coordinate transformation tensor. The tangential component of the dynamic J integral J_1^0 corresponds to the rate of change in the potential energy per unit crack extension, namely, the dynamic energy release rate. The dynamic J integral can be related to the instantaneous stress intensity factors for the elastodynamically propagating crack with velocity C , as in [1].

To accurately evaluate the inplane mixed-mode stress intensity factors from the dynamic J integral values, the component separation method [2] has been proposed. The formulae of the component separation method are expressed by

$$K_I = \delta_I \left(\frac{2\mu\beta_2 (J'_1 \cos\theta_0 + J'_2 \sin\theta_0)}{A_I (\delta_I^2 \beta_2 + \delta_{II}^2 \beta_1)} \right)^{1/2}, \quad K_{II} = \delta_{II} \left(\frac{2\mu\beta_1 (J'_1 \cos\theta_0 + J'_2 \sin\theta_0)}{A_{II} (\delta_I^2 \beta_2 + \delta_{II}^2 \beta_1)} \right)^{1/2} \quad (2.a, b)$$

where δ_I and δ_{II} are the mode I and mode II crack opening displacements, and $A_I(C)$, $A_{II}(C)$ are functions of crack velocity and given in [1].

3 SEPARATED DYNAMIC J INTEGRAL FOR AN INTERFACIAL CRACK

Now we consider an interfacial crack (see Fig.2). The interface may be curved or straight. Then the separated dynamic J integral [4] which has the physical meaning of energy-flow rate from the materials 1 or 2, can be defined as

$$J_k^{(m)} = \int_{\Gamma_c^{(m)} + \Gamma_1^{(m)}} [(W+K)n_k - t_i u_{i,k}] dS + \int_{V_r^{(m)}} [(\rho^{(m)} \ddot{u}_i - f_i) u_{i,k} - \rho^{(m)} \dot{u}_i \dot{u}_{i,k}] dV, \quad (m=1,2) \quad (3)$$

where $\Gamma_1^{(m)}$ ($m=1, 2$) are the integral paths along the interface in the sides of the materials 1 and 2, respectively.

The crack-axis components of the separated dynamic J integrals can be obtained by the coordinate transformation: $J_l^{0(m)} = \alpha_{lk}(\theta_0) J_k^{(m)}$, ($m=1,2$). Thus the separated energy-release rates $G^{(m)}$ ($m=1,2$) [4] which are the energy-flow rates from the material m ($m=1,2$) into the propagating interfacial crack tip per unit crack extension can be expressed by

$$G^{(m)} = J_1^{0(m)} = J_1^{(m)} \cos\theta_0 + J_2^{(m)} \sin\theta_0, \quad (m=1,2). \quad (4)$$

4. TYPES OF FRACTURE SIMULATION

For non-self-similar fracture such as curving crack growth, three types of numerical simulation were proposed by Nishioka [5]. First, the generation phase simulation can be conducted, using both experimental data of the crack-propagation and the curved fracture-path histories (see Fig.3(i)).

On the other hand, in the application phase simulation for curving crack growth, two criteria must be postulated or predetermined as shown in Fig.3(ii). One is the crack-propagation criterion

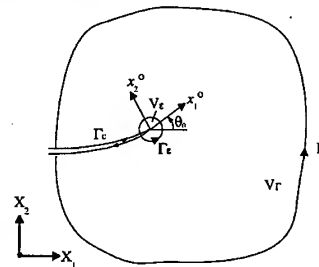


Fig.1 Integral paths

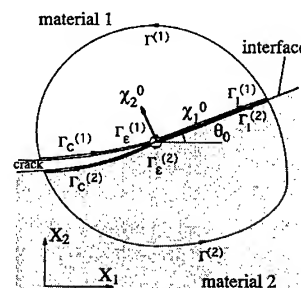


Fig.2 Definition of integral paths for separated dynamic J integral

that governs the rate of crack growth. The other one is a criterion for predicting the direction of crack propagation (propagation-direction criterion). However, the application phase simulations of curving crack growth have not been fully established, due to several critical difficulties in those simulations. For instance, in dynamic brittle fracture, the crack-propagation criterion described by fracture-toughness versus crack-velocity relation itself has several unsolved problems.

To verify only the propagation-direction criterion such as the maximum energy release rate criterion, Nishioka [5] has proposed "mixed-phase simulation" as depicted in Fig.3(iii). In "fracture-path prediction mode" of mixed-phase simulation, the experimental data for the a - t relation is used. Thus, the increment of crack propagation is prescribed for the given time-step sizes in this mode of simulation. Then a propagation-direction criterion predicts the direction of fracture path in each time step. If the simulated final fracture path agrees with the actual one, the postulated propagation-direction criterion is valid.

Another mode of the mixed-phase simulation can be considered as depicted in Fig.3(iii-b), i.e., "crack-growth prediction mode". In this mode, the experimental data for the fracture-path history and the crack-propagation criterion are used simultaneously. In this case, the crack is forced to propagate along the actual fracture path during the numerical simulation. Simulated crack-propagation history should agree with the experimentally obtained actual one if the postulated crack-propagation criterion is valid.

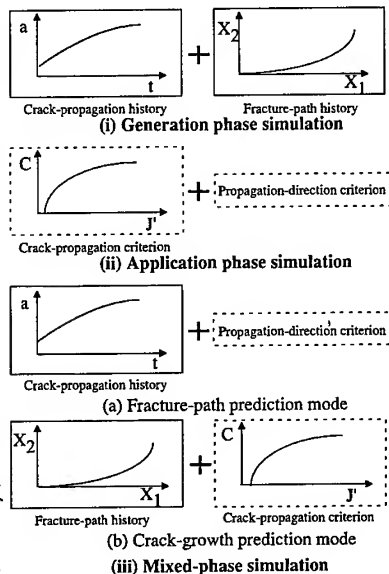


Fig.3 Mixed-phase simulation for non-self-similar dynamic fracture

5. DYNAMIC FRACTURE SIMULATIONS

To simulate dynamic crack propagation, two different concepts of computational modeling can be considered, i.e., (i) the stationary element procedure, and (ii) the moving element procedure, as reviewed by Nishioka and Atluri [6], and Nishioka [2,5]. For self-similar dynamic crack propagation problems, it is well known that the numerical results of the moving element procedure are generally more accurate than those of the fixed element procedure. Nishioka and coworkers developed various moving finite element methods [7-9] for self-similar dynamic fracture problems. However, the moving element procedure was difficult to be applied for non-self-similar dynamic crack propagation problems except for smoothly curving fracture problems (Nishioka et al.[10,11]), because of the difficulties in moving the near-tip elements along curved or kinked path.

5.1 Impact Kinking Fracture

Mixed-mode impact fracture tests were conducted in [12]. The geometry of the impact fracture specimen is shown in Fig.4. The impact load was applied at the off-center point as shown in Fig.4. The loading eccentricity is defined as $e=l/(S/2)$. The initial impact velocity of the hammer was 5 m/s. The history of crack propagation was recorded by using a high-speed camera [12]. The crack started propagating at $t=120 \mu s$ after the initiation of impact ($t=0$). The maximum crack velocity observed was 300 m/s.

Since the local symmetry ($K_{II}=0$) criterion has demonstrated [10,11] the best prediction of smoothly curving fracture paths in DCB specimens, this criterion is also employed in this study. Using the local symmetry criterion together with the experimentally obtained crack-propagation

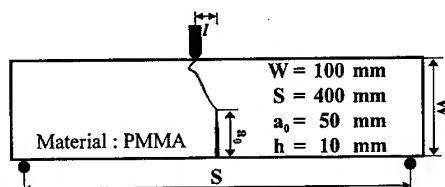


Fig.4 Mixed-mode impact fracture specimen

history, the mixed-phase fracture-path prediction mode simulation was carried out. The time increment $\Delta t = 2 \mu s$ is used. The dynamic J integral values at various instants of time shows excellent path independence.

The deformation of the dynamically fracturing specimen is shown in Fig.5. The deformation is magnified by 30 times. It is seen that the postulated local symmetry criterion predicts the dynamically propagating fracture path toward the point of impact loading. The simulated fracture path excellently agrees with the experimental fracture path (see Fig.4).

Figure 6 shows the variations of the stress intensity factors converted from the average values of the dynamic J integral using Eqs.2(a) and (b). As seen in Fig.6, the impact fracture for the case of $e=0.1$ occurs under almost pure mode II condition. Contrary to that, the mode II stress intensity factors are zero during dynamic crack propagation, since the $K_{II}=0$ criterion is forced in the fracture-path prediction mode simulation.

5.2 Dynamic Interfacial Fracture

Dynamic crack propagation along the interface of a bimaterial plate is considered as shown in Fig.7. The dimensions of the plate are $W=2L=40$ mm. The plate is subject to shear loading τ_0 or tension loading σ_0 at the upper and lower ends of the plate. Then at the time $t=0$, the crack is assumed to propagate with a constant velocity C .

The strain energy density distribution for the transonic crack velocity regime under tension loading is shown in Fig.8. It is seen that the highly dense contours of the strain energy density agree excellently with the theoretical Mach shock wave angle of $\psi_s = 56.4^\circ$ measured from the crack face [4]. These results may be the first computational visualization of distinct shock waves emanated from the transonically propagating interfacial crack tip [4].

Figure 9 shows the energy release rates calculated by the dynamic J integral during the interfacial crack propagation under the shear loading [13]. In this figure, the dynamic J integrals are normalized by the static one for the initial crack. In each case, the dynamic J integral drops immediately after the onset of dynamic crack propagation.

Figure 10 shows the minimum values of the normalized dynamic J integral for all types of calculated models. The crack velocities are normalized by the shear wave velocity of material 1. It is seen that the curves of the tension-dominated models do not depend on the material mismatch ratio and always become zero for transonic interfacial cracks. For the shear-dominated models, it is found that the minimum energy release rate remains finite in transonic interfacial crack propagation. It almost does not change with the variation of crack tip velocity in cases $C=1.0C_s^{(1)}$, $C=1.2C_s^{(1)}$ and $C=1.4C_s^{(1)}$. Thus, once the crack velocity reaches in this range, the crack will accelerate very

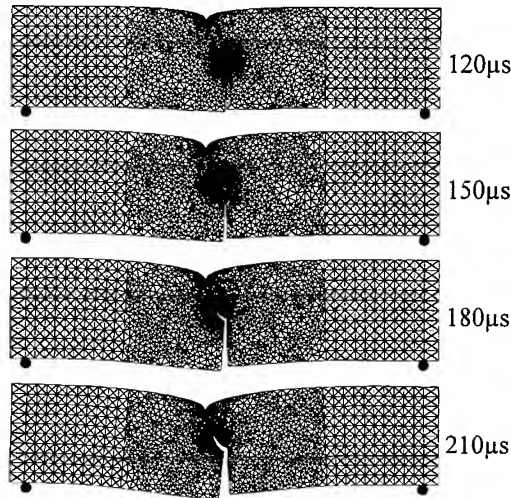


Fig.5 Dynamic fracture path simulated with the local symmetry criterion

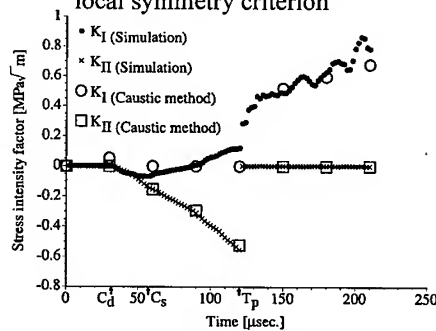


Fig.6 Dynamic stress intensity factors σ_0 or τ_0

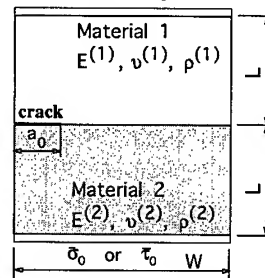


Fig.7 A bimaterial plate

rapidly up to $C=1.4C_s^{(1)}$.

The separated dynamic J integrals showed excellent path independence [4,14] although they are not given here. For subsonically propagating cracks under shear as well as tension loading, it was observed in the present results that the energy flow rate from the compliant material is much larger than that from the stiffer one. Furthermore, for the transonically propagating cracks under shear loading, the energy release rates from both material sides become the same.

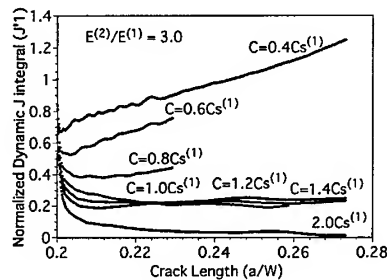


Fig.9 Dynamic J integral under shear loading

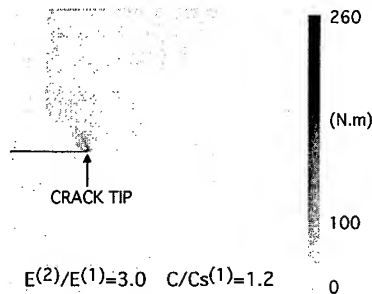


Fig.8 Mach shock wave

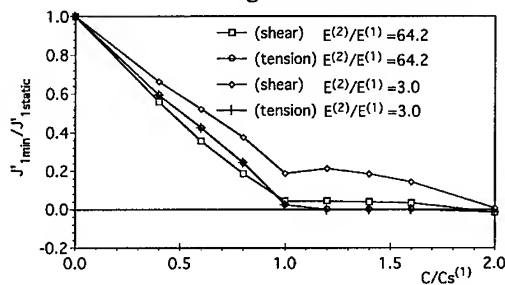


Fig.10 Dynamic J integral vs. Crack tip velocity

5.3 Dynamic Crack Bifurcation

The governing condition of dynamic crack bifurcation phenomena had not been fully clarified until our recent experimental studies [14,15]. We found from the experimental results that the energy flux per a unit time into a propagating crack tip governs the crack bifurcation.

Regarding the numerical simulation of dynamic crack bifurcation, to the authors' knowledge, no simulations have been carried out, due to several unresolved difficulties.

In order to overcome the difficulties, for the analysis of dynamic crack bifurcation, we have developed a moving finite element method based on Delaunay automatic triangulation. Using this moving finite element method, the generation phase simulation was carried out, based on the experimentally recorded fracture histories by an ultra-high speed camera [14,15]. In order to evaluate the dynamic J integral values for dynamically branching cracks, a special form of the dynamic J integral has been derived as follows:

$$J_k = \int_{\Gamma+\Gamma_c} [(W+K)n_k - t_i u_{i,k}] s dS + \int_{V_r} \left[\{ (\rho \ddot{u}_i - f_i) u_{i,k} - \rho \dot{u}_i \dot{u}_{i,k} \} s + \sigma_{ij} u_{i,k} s_{,j} - (W+K) s_{,k} \right] dV \quad (5)$$

where s is a continuous function defined in V_r (see Fig.11). When we evaluate the dynamic J integral components at the crack tip a, we set the s function as $s=1$ for the whole domain except $s=0$

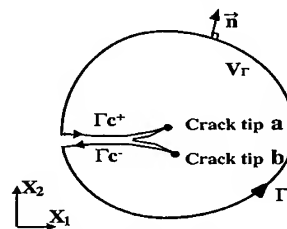


Fig.11 Evaluation of the dynamic J integral for branched cracks

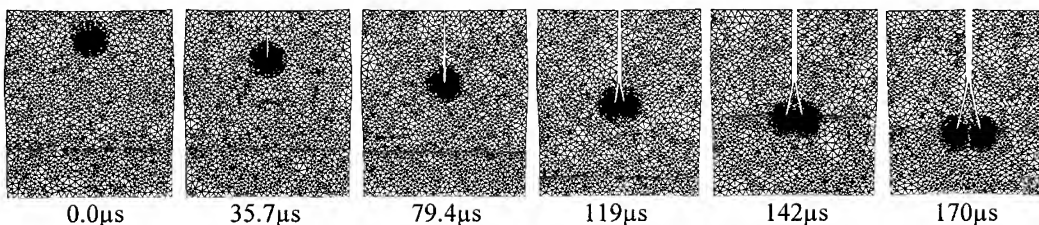


Fig.12 Generation phase simulation of dynamic crack bifurcation

at the tip b, and vice versa. Equation (5) made it possible to evaluate the dynamic J integral components for interacting branched crack tips.

The deformed mesh patterns of dynamically fracturing specimen are shown in Fig.13. In order to visualize the crack profile, the deformation was magnified by 10 times.

Figure 13 shows the variations of the crack-axis components of dynamic J integral. It is seen that the total energy release rate is continuous before and after the crack bifurcation. In other words, the energy release rate for each branched crack becomes a half of the one at the crack bifurcation.

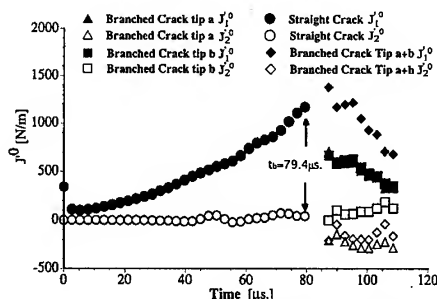


Fig.13 Dynamic J integral components

6. CONCLUDING REMARKS

Recent computational studies on various dynamic fracture phenomena were summarized. In all cases, the moving finite element method and the path independent dynamic J integral demonstrated their excellent applicability for solving dynamic fracture phenomena. The numerical simulations provided valuable results and insights to clarify the mechanisms of various dynamic fracture phenomena.

Acknowledgements: Some of these studies were supported by the Grant-in-Aid for Scientific Research (No.08455063) from the Ministry of Education, Science and Culture in Japan. The numerical simulations were carried out by graduate students, A.Yasin, H.Nishida and J.Furuzuka.

REFERENCES

1. T.Nishioka and S.N.Atluri, Path independent integrals, energy release rates and general solutions of near-tip fields in mixed-mode dynamic fracture mechanics, *Eng. Fract. Mech.*, **18** (1983), 1-22.
2. T.Nishioka, The state of the art in computational dynamic fracture mechanics, *JSME Int. J.*, **37** (1994), 313-333.
3. T.Nishioka, R.Murakami and Y.Takemoto, The use of the dynamic J integral (J') in finite element simulation of mode I and mixed-mode dynamic crack propagation, *Int. J. Press. Ves. & Piping*, **44** (1990), 329-352.
4. T.Nishioka and A.Yasin, The dynamic J integral, separated dynamic J integrals and moving finite element simulations, for subsonic, transonic and supersonic interfacial crack propagation, *JSME Int. J.*, **42** (1999), 25-39.
5. T.Nishioka, Computational dynamic fracture mechanics, *Int. J. Fract.*, **86** (1997), 127-159.
6. T.Nishioka and S.N.Atluri, Computational methods in dynamic fracture, *Computational Methods in the Mechanics of Fracture*, (S.N.Atluri, ed.), Elsevier Sci. Pub. (1986), 336-383.
7. T.Nishioka and S.N.Atluri, Numerical modeling of dynamic crack propagation in finite bodies, by moving singular elements - part I. formulation, *J. Alpp. Mech.*, **47** (1980) 570-576.
8. T.Nishioka, R.B.Stonesifer and S.N.Atluri, An evaluation of several moving singularity finite element models for fast fracture analysis, *Eng. Fract. Mech.*, **15** (1981), 205-218.
9. T.Nishioka and S.N.Atluri, A path-independent integral and moving isoparametric elements for dynamic crack propagation, *AIAA J.*, **22** (1984), 409-414.
10. T.Nishioka, M.Nakatani, S.Okizuka and T.Okada, Numerical simulations of self-similar and non-self-similar dynamic fracture phenomena, *Proc. Asian Pacific Conf. Fract. & Strength*, Kyongju, Korea, (1996), 699-704.
11. T.Nishioka, T.Okada and M.Nakatani, Mixed-phase simulation with fracture-path prediction mode for dynamically curving fracture, *Adv. in Fract. Res.*, Pergamon, **4** (1997), 2063-2070.
12. T.Nishioka, T.Murakami, Y.Takemoto and K.Sakakura, Mixed-mode impact fracture tests and their numerical simulation, *Proc. 6th Int. Conf. Mech. Behaviour of Mat.*, Kyoto, (1991), 457-462.
13. A.Yasin and T.Nishioka, Moving finite element simulation of dynamic interfacial crack propagation under shear-dominated loading, *Progress in Exp. & Comp. Mech. in Eng. and Material Behaviour*, (1999), 178-183.
14. T.Nishioka, T.Kishimoto, Y.Ono and K.Sakakura, Basic studies on the governing criterion for dynamic crack branching phenomena, *Trans. of JSME, Ser. A*, **65** (1999), 1123-1131.
15. T.Nishioka, T.Kishimoto, Y.Ono and K.Sakakura, Governing criterion of dynamic crack bifurcation, *Proc. 8th Int. Conf. Mech. Behaviour of Mat.*, Volume I, (1999), 255-260.

Nonlinear Dynamic Buckling Analysis of a Grid Structure

K.H. Yoon¹, K.N. Song¹ and Y.S. Lee²

¹ Advanced Reactor Development, Korea Atomic Energy Research Institute,
150 Dukjin-dong, Yusung-gu, Taejon 305-600, Korea

² Department of Mechanical Engineering, Chungnam National University,
220 Kung-dong, Yusung-gu, Taejon 305-764, Korea

Keywords: Buckling, Buckling Mode Shape, Dynamic Impact, Elastic-Plastic Behavior, Free Fall Shock, Grid, Initial Velocity, Thin-Walled Plate

ABSTRACT

The spacer grid is one of the main structural components in fuel assembly, which supports the fuel rods, guides cooling water, and protects the fuel assembly from the external impact load such as earthquakes. Therefore, the mechanical and the structural properties of the spacer grid must be extensively examined while designing it. In this paper, a numerical method for reliably predicting the buckling strength of the spacer grid is presented. Numerical analyses on the buckling behavior of the spacer grid are performed for a various array of grid sizes, considering that the spacer grids are an assembled structure of thin-walled plates. The nonlinear dynamic impact analysis is conducted by using the finite element code ABAQUS/Explicit. Buckling tests are also carried out for several kinds of the specimens of the spacer grids in order to compare the results between the test and the simulation. This test is accomplished by a free fall dummy weight onto the specimen. From this test, only the uppermost and lowermost layers of the multi-cell are buckled, which implies the local buckling at the weakest point of the grid structure. Simulation results also similarly predict the local buckling phenomena. It is found to correspond well with the test results. In addition, a correlation that can predict the maximum impact strength is empirically derived from the simulation results in the case of the grids having the larger number of cells.

1. INTRODUCTION

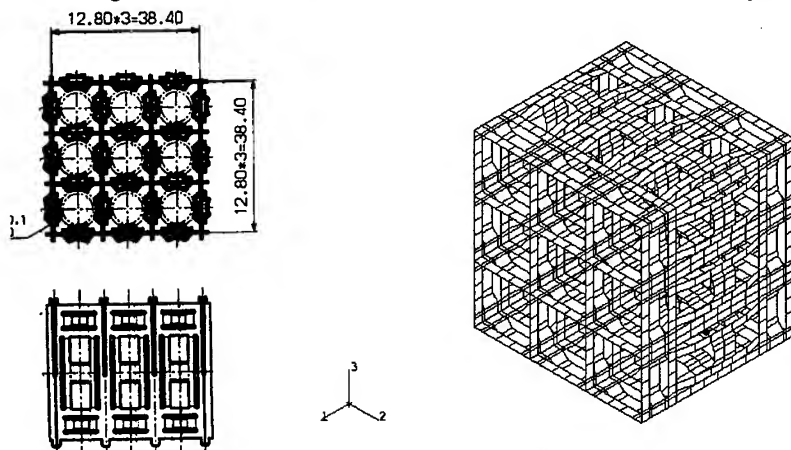
The spacer grid, one of the most important components of nuclear fuel assembly, is composed of straps, which are crossed to form an egg-crate like structure. It constitutes the skeleton of the fuel assembly together with guide thimbles, top and bottom end pieces. The structural grid assemblies provide both lateral and vertical support for the fuel rods. The pitch of the fuel rods in the core is a carefully selected parameter, which has a major effect on the nuclear and thermal/hydraulic performance of the core. The spacer grid is an interconnected array of slotted grid straps welded at

the intersections. The fuel assembly incorporates either seven or eight spacer grids. The spacer grid outer straps constitute contact surfaces that can transmit possible seismic loads between the fuel assemblies. The principal design concern with regard to grid strap buckling is that the fuel rods should maintain the coolable geometry and that the control rods should be inserted. Therefore, thermal/hydraulic testing and analysis are necessary to demonstrate that a deformed grid is coolable and that control rod motion is not impeded. Design practice is to adopt the incipient buckling load as a failure criterion for the grid. The diagonal axis of the grid assembly has the lowest impact strength. Sustained loads applied along the diagonal axis, however, are not credible because slipping between grid assemblies causes diagonal loads to be applied to the grids in normal directions only. Consequently, the limiting loads imposed upon the grid assembly are the result of impacts due to lateral seismic accelerations, lateral LOCA (Loss Of Coolant Accident) blowdown forces, and shipping and handling loads. The ability of the grid to resist lateral loads is characterized in terms of its dynamic and static crush strengths. These quantities and the grid dynamic stiffness are required for fuel assembly seismic and LOCA blowdown analyses to verify that coolable grid geometry is maintained. During calculations, the cutout section is not regarded to affect the buckling strength. The dynamic impact properties (dynamic stiffness and coefficient of restitution) are determined by measuring the impact force and its duration as a function of impact velocity, with suitable assumptions.

2. NONLINEAR DYNAMIC IMPACT ANALYSIS

2.1. FE Model and Boundary Conditions

The nonlinear dynamic impact analysis is simulated by a finite element method. The commercial code ABAQUS/Explicit (version 5.8)[1] is used for the FE analysis. The geometrical data for the FE analysis follow the specimen of the dynamic free fall tests as shown in Fig. 1. Besides the geometry, 186.8 GPa is used for Young's modulus of the grid material, stainless steel. 0.3 is used for the Poisson ratio. Since the characteristic curve shows the nonlinear elastic-plastic behavior, the plastic property of the material is also considered, such as the yield strength (258.6 MPa) and the hardening curve. The stress vs. strain curve of stainless steel for the dynamic analysis



is applied.

(a) geometry

(b) FE model

Fig. 1. Schematic diagram of grid specimen.

4-node shell elements are used for the FE model of the analyses because the thickness of the strap (0.6 mm) is much smaller than the width (12.8 mm). A thin shell element is used when the transverse shear flexibility is negligible and the Kirchhoff constraint must be satisfied accurately. For the boundary conditions of the FE analysis, three translational degrees of freedom at the lower four edges are constrained since the specimen is regarded to have the simply supported condition on the edges of the grid specimen during the dynamic impact test. The number of elements is 2352, and the number of nodes is 3296[2]. The dynamic impact load onto the grid is simulated by imposed initial velocity onto rigid surface, which initially contacts the top of the grid. The boundary conditions are well depicted by Fig. 2[3, 4]. The impact force is obtained from the total reaction force at four lower edges by applying the initial velocity on the rigid surface.

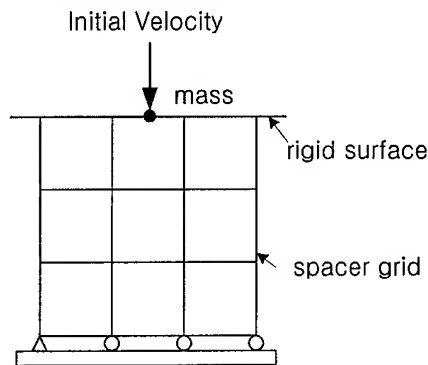


Fig. 2. Boundary condition for the simulation of 3 by 3 cell grid.

2.2. Analysis Results

The FE results for simulating the dynamic impact characterization curves are given in Fig. 3. The impact force increases more and more until the buckling of a grid cell occurs. The local buckling occurs only at the upper and lower cells of the grid. The difference in impact force between the simulation and test is +1.7%. The maximum stress is revealed at the corner leg of the unit cell as shown in Fig. 4(a). The deformed shape is very similar to the test result. The energy input to the entire model is shown in Fig. 4(b).

3. FREE FALL TEST

3.1. Test Setup

A free fall shock machine, as shown in Fig. 6, is used to perform the tests. It is intended to simulate the type of load and impact velocities anticipated under seismic disturbance. The upper part of the structure consists of two guide rods and supporting columns, which are erected from the base. The carriage moves with the guidance of the two guide rods. The carriage is aluminum casting,

the shape of which is determined for obtaining maximum rigidity with minimum mass.

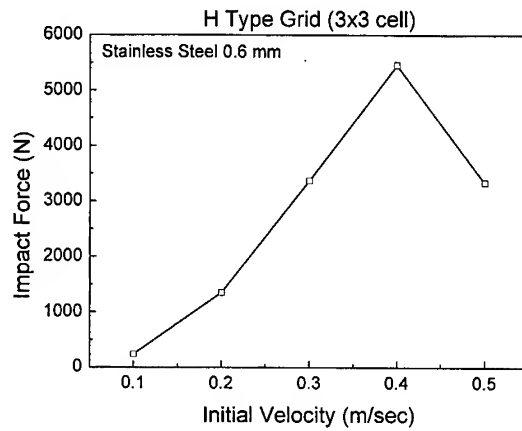


Fig. 3. Initial velocity vs. impact force of 3 by 3 cell grid.

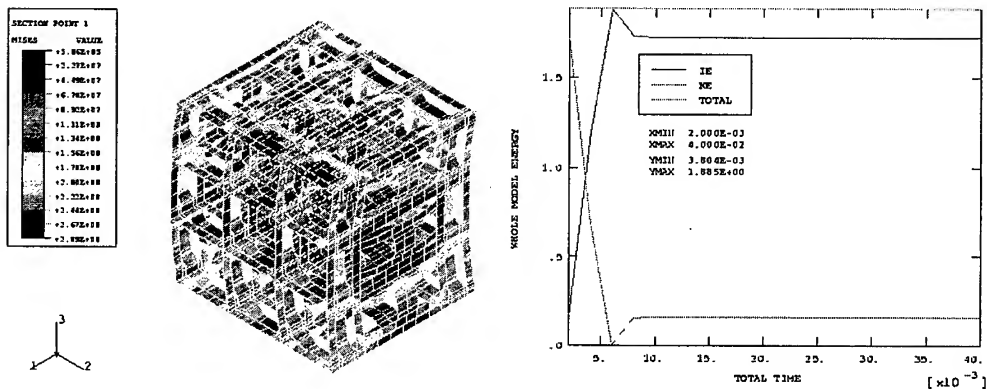


Fig. 4. Analysis results by nonlinear dynamic impact analysis.

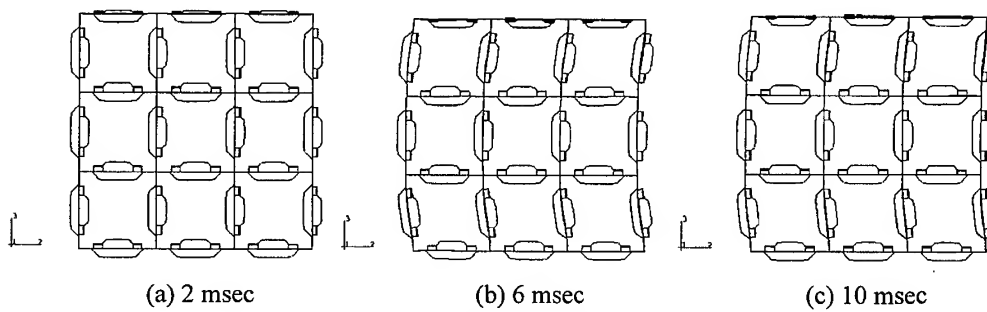
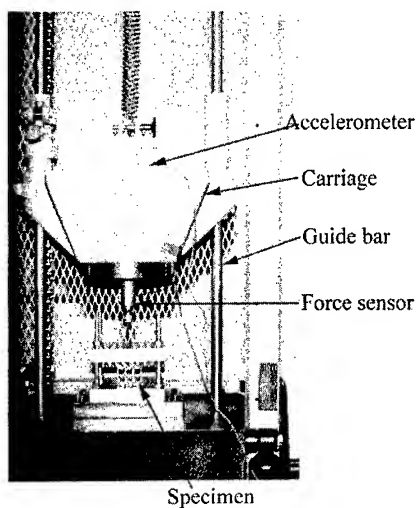


Fig. 5. Deformed shape by dynamic impact analysis.

The general test setup consists of the floor, dummy weight, force transducer, dynamic accelerometer,

and mounting fixtures. A carriage weight of 45 lbs (20.43 kg) for the specimen is selected. The impact force by the tester is found too high to investigate the critical buckling load of a grid. Therefore, an additional spring damper is mounted on the carriage in order to decrease the impact velocity. The static force transducer is mounted on the carriage to measure the impacting forces. One dynamic accelerometer is mounted on the top surface of the carriage. The grids are rigidly clamped to the holding plate that is also placed on the floor. The initial drop height of the impact weight is 7.75 inches (196.85 mm). The impacting tests were performed on the 3×3 array grids. The grids are fixed with holding fixture by 4 screws. The carriage is moved to initial height and then dropped onto the grid. This procedure is repeated, increasing the height by 0.5 inches at each step



until the specimen buckles.

Fig. 6. Test setup for grid impact test.

3.2. Test Results

The impact forces of the test are varied from 4778 N to 6401 N and impact accelerations are from 17.6 g to 25.8 g. The average values of these are 5365 N and 21.5 g. The deformed shape of specimen is shown in Fig. 7.

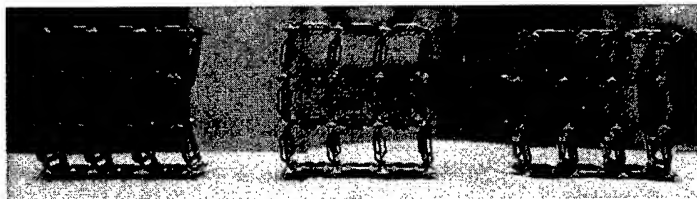
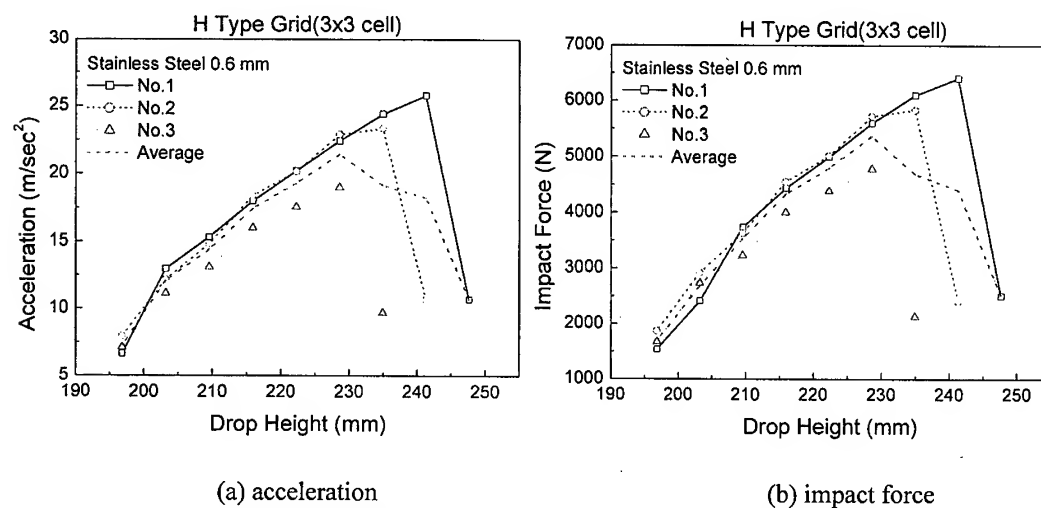


Fig. 7. Deformed shape after grid impact test.

4. CONCLUDING REMARKS

The nonlinear dynamic impact analysis for the spacer grid is conducted and the intrinsic boundary condition of the grid structure is checked. The importance of the boundary condition is apparently verified by using several boundary conditions. It seems that the difference is caused by the geometry, an each specimen. Comparing the analysis results with the test chooses the boundary

conditions finally applied.



(a) acceleration

(b) impact force

Fig. 8. Impact force and acceleration by grid impact test.

The free fall shock test shows the interesting buckling behavior of the grid. The deviation bounds of the impact force and acceleration by test are within 10%. The acceleration and impact force by test are showed in Fig. 8. The average critical drop height is 0.083 m. The buckling of the grid initiate at only the uppermost and lowermost cells, but the middle layer cells retain in the original grid shape. It is the weakest layer of the grid, which initiates buckling in the shear direction by the strain localization phenomenon.

ACKNOWLEDGEMENT

This project has been carried out under the Nuclear R&D Program by MOST.

REFERENCE

1. H. D. Hibbitt, G. I. Karlsson, and E. P. Sorensen, "ABAQUS/Explicit User's Manual (version 5.8)", Vol. I and II, Hibbitt, Karlsson & Sorensen Inc., Pawtucket, R.I., USA (1998).
2. K. H. Choi, K. H. Yoon, et al., "FE Analysis of Nonlinear Buckling Behavior of a Spacer Grid in Fuel Assembly", Structural Mechanics in Reactor Technology, SmiRT-15, Seoul, Korea (1999), Paper No. C02/3.
3. K. H. Yoon, et al., "FE Analysis of Nonlinear Buckling Behavior of a Grid Structures", Proceedings of the KSME 1999 Fall Meeting A, Korea, Paper No. 99F077.
4. K. H. Yoon, et al., "Mechanical Performance Evaluation Test of Spacer Grid Specimen for Integrated Reactor Fuel", KAERI/TR-1147/98, Korea Atomic Energy Research Institute, Korea (1998).

Dynamic Modeling and Numerical Analysis for Large Scale Chime Group

P. Zeng¹, L. He¹ and G.H. Tang²

¹ Department of Mechanical Engineering, Tsinghua University, Beijing 100084, China P.R.

² Beijing Materials Handling Research Institute, 52 Yong He Gong Street,
Beijing 100007, China P.R.

Keywords: Chimes, Dynamic Modeling, Numerical Analysis

ABSTRACT

The large-scale chime group composes of three layer of steel frames and 108 various mass of bells. This set of chimes named "Chinese Peace Chime Group" was put in the "Tai Temple" of Forbidden City of Beijing for the millennium celebration. Since the structure of the chimes is coupled by the frame and various of single-pendulum bells, how to treat the coupling between the single-pendulum and the frame structure and to model the full structure with a large group of single-pendulum bells are the objective of this paper. First of all, one uses a beam element plus a mass block to model the a single pendulum, which is considered as a "eigen" structure, then analyzes the approximation between the "eigen" structure and the origin in the aspect of dynamics, and sets up the relationship among various parameters. Based upon this modeling, one completes the modal analyses of full large-scale chime group on the platform of ANSYS software. The result shows that the first part of modals are the independent swing of various single-pendulum bells, then the following part is the coupled modals, which is very reasonable.

1. INTRODUCTION

Modern large and precise structures (such as building, civil engineering, spaceshuttle, space station, aircraft, train, automobile, robotics, antennas, satellites, manipulator, etc.) raise a demand on the accurate dynamic analysis for both lower eigen frequencies and higher eigen frequencies[1]-[4]. The large-scale chime group is a such structure, which composes of three layer of steel frames and 108 various weight of bells (see Fig.1). Since the acoustic effect of each bell and the free vibration of the frame must be coupled together, the design and analysis of this complex structure is an objective of this paper by using new modeling technique.

2. MODELING OF SINGLE-PENDULUM IN STRUCTURE VIBRATION

In order to do the coupling analysis of this large-scale chime group, one must get an equivalent model to describe the single-pendulum in structural analysis platform. Since a single-pendulum is a system of rigid dynamics (see Fig.2 (a)), its natural circular frequency is characterized by following

formula (1).

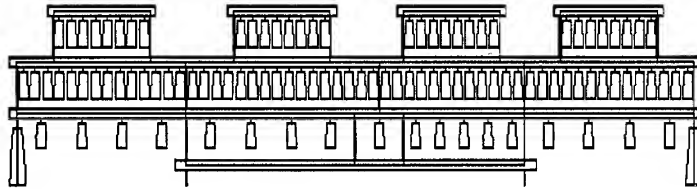


Fig.1. The large-scale chime group composed of three layer of steel frames and 108 various weight of bells

$$\omega = \sqrt{\frac{g}{l}} \quad (1)$$

where l is the length of single-pendulum, g is the gravity acceleration.

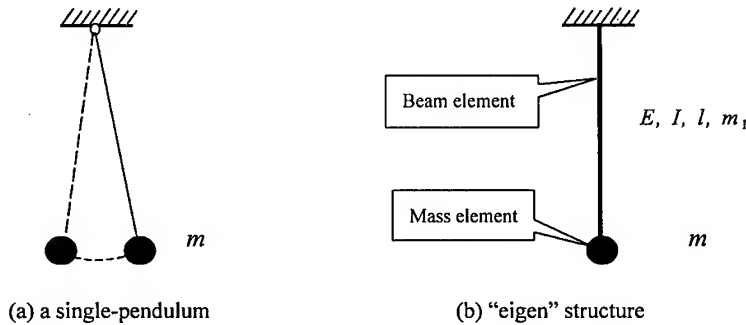


Fig.2. Using an "eigen" structure to model a single-pendulum

We consider a similar structure to model a single pendulum[5], which called "eigen" structure composed of two components: a linking beam and a mass block. Assume E, I, l, m_1 of beam are the elastic modulus, inertial, the length, the mass of the beam element, respectively, the m is the mass of bell. From the vibration analysis of this "eigen" structure, one has its natural circular frequency as following.

$$\omega = \sqrt{\frac{k}{m + \frac{33}{140}m_1}} \quad (2)$$

where k is the stiffness of linking beam, i.e.,

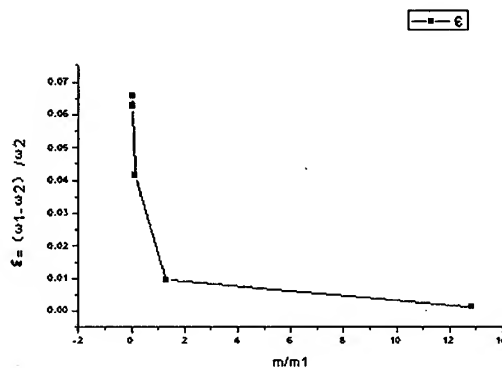
$$k = \frac{3EI}{l^3} \quad (3)$$

From the Eq.(2), one know that the parameters m, m_1 and their combination will play an important role for the natural vibration of "eigen" structure. we study the error of ω corresponding to the combination of the parameters m and m_1 , which are listed in Table 1 and Fig.3.

Table 1. The error of ω vs. the combination of the parameters m and m_1 ¹⁾

$m(\text{kg})$	m/m_1	ω_1	ω_2	$\varepsilon(\%)$
10^2	0.001282	53.29	50.00	6.58
10^3	0.01282	52.04	48.97	6.269
10^4	0.1282	43.00	41.29	4.141
10^5	1.2882	21.06	20.86	0.959
10^6	12.82	7.180	7.172	0.112
10^7	128.2	2.289	2.289	0

¹⁾ ω_1 : the result of Eq.(2); ω_2 : the result of single-pendulum; ε : $(\omega_1 - \omega_2) / \omega_2$

Fig.3 The error of ω vs. m/m_1

Within a scope of error, one considers the approximation between the single-pendulum (see Fig.2(a)) and the "eigen" structure (see Fig.2(b)). Let Eq.(2) approximate to Eq.(1), one has

$$\omega = \sqrt{\frac{k}{m + \frac{33}{140}m_1}} = \sqrt{\frac{g}{l}} \quad (4)$$

Substituting Eq.(3) into Eq.(4) can get

$$3EI = gl^2 \left(m + \frac{33}{140} \rho Al \right) \quad (5)$$

For the sake of convenience, one fixes the parameters: A, l, ρ, I, m unchangeable and only changes the elastic modulus of linking beam: E corresponding to each bell of single-pendulum. To do so, we can completely model the 108 single-pendulum bells using the corresponding "eigen" structure. According to the actual case of chimes, the maximum m/m_1 of upper layer bells is more than 30%, so the analogue error of nature frequency is less than 3%; the maximum m/m_1 of middle and low layer bells is more than 10, so the analogue error of nature frequency is less than 0.1%. Such an accuracy is very good for engineering analysis.

3. COUPLING MODELING FOR PENDULUM AND STRUCTURE

Based upon the "eigen" structure for single-pendulum, one can implement the coupled modeling for both the pendulum and the frame structure in an uniform computing platform. we choose ANSYS 5.5 code to analyze the large-scale chime group. In ANSYS 5.5, BEAM4 is a uniaxial element with tension, compression, torsion, and bending capabilities. The element has six degrees of freedom at each node: translations in the nodal x, y, and z directions and rotations about the nodal x, y and z axes. Stress stiffening and large deflection capabilities are included. MASS21 is a point element having up to six degrees of freedom: translations in the nodal x, y, and z directions and rotations about the nodal x, y, and z axes. A different mass and rotary inertia may be assigned to each coordinate direction. The mass element is defined by a single node, concentrated mass components ($\text{Force} \cdot \text{Time}^2 / \text{Length}$) in the element coordinate directions, and rotary inertias ($\text{Force} \cdot \text{Length} \cdot \text{Time}^2$) about the element coordinate axes. The element coordinate system may be initially parallel to the global Cartesian coordinate system or to the nodal coordinate system (KEYOPT(2)).

4. MODAL ANALYSIS

According to the analysis result by ANSYS 5.5, the first 106 orders of natural frequencies are corresponding to that of each single-pendulum, please see Table 2.

Table 2. Parts of natural frequencies of structural analysis compared with the results of single-pendulum (Hz)

order	By ANSYS	By single-pendulum	Error(%)
1	0.43723	0.41592	0.5829
2	0.43736	0.43749	0.2857
3	0.44661	0.43749	0.6198
4	0.44676	0.44689	0.2842
20	0.62721	0.62757	0.5673
21	0.63158	0.63215	0.8954
22	0.64077	0.6414	0.9853
23	0.64536	0.64591	0.8577
24	0.65003	0.65058	0.8423
25	0.65462	0.65517	0.8456
64	0.75570	0.75708	0.18162
65	0.75570	0.75708	0.18162
90	0.96667	0.96877	0.21667
91	0.97372	0.96877	-0.51106
100	1.0099	1.00474	-0.51357
101	1.0100	1.01259	0.25627
105	1.0296	1.02625	-0.32643
106	1.0366	1.03351	-0.29888

Parts of modal shapes corresponding to the first 106 orders of natural frequencies are shown in

Fig.4.

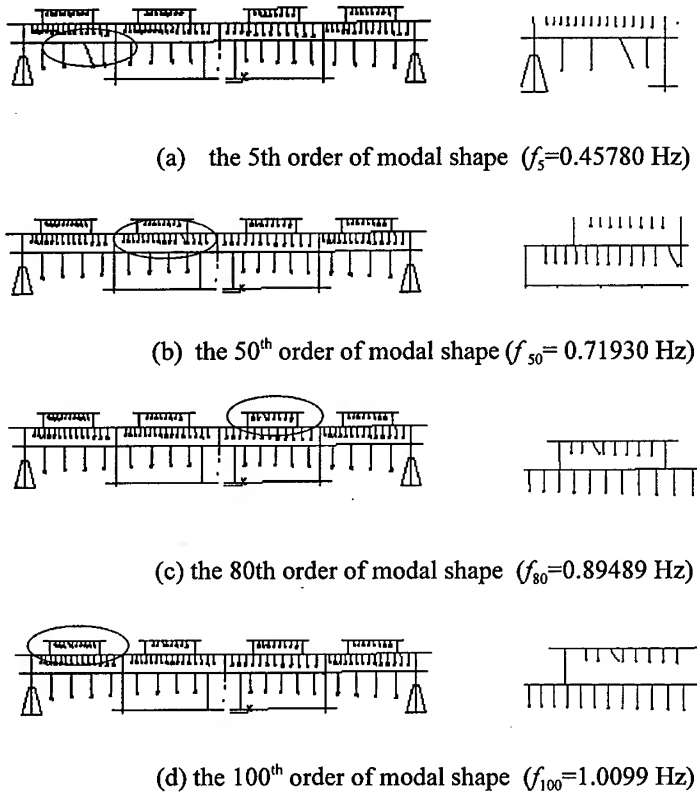


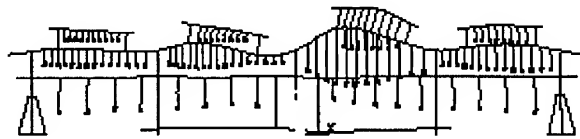
Fig.4 Parts of modal shapes of the first 106 orders of natural vibrations

Parts of the natural vibration frequencies coupling the single-pendulum and the frame structure are listed in Table 3.

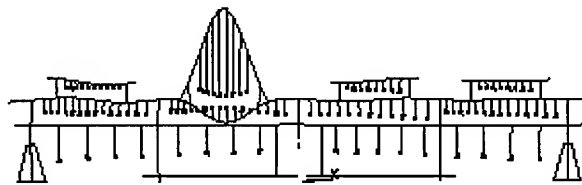
Table 3. Parts of natural frequencies of structural analysis coupling the single-pendulum and the frame structure (Hz)

order	f_i	order	f_i
110	8.1920	120	8.6394
112	8.4196	122	8.7031
113	8.5495		

Parts of modal shapes of natural vibration coupling the single-pendulum and the frame structure are shown in Fig.5.



(a) the modal shape of natural vibration
coupling the single-pendulum and the frame structure ($f=104.60$ Hz)



(b) the modal shape of natural vibration
coupling the single-pendulum and the frame structure ($f=152.30$ Hz)

Fig.5 Parts of modal shapes of natural vibration
coupling the single-pendulum and the frame structure

5. DISCUSSION

How to set up the coupling model on a uniform analysis platform is a main work of this paper. The key to this purpose is to study the equivalent model, e.g., to use a beam element plus a mass block to model the a single pendulum, which is considered as a "eigen" structure. The analysis results should contain two parts: vibration character of each single-pendulum and the coupled vibration of frame and single-pendulum, first part will be as an essential verification to the modeling method. The work of the paper concerns how to treat two kinds of problems (mechanical oscillation and structural vibration) on a uniform FEM platform, which can provide a useful strategy and experience to some complex engineering problem.

ACKNOWLEDGMENT

This research work was supported by National Natural Science Foundation of China (Grant No.59825117 and 59775017)

REFERENCE

1. S.S.Rao, The Finite Element Method in Engineering, Pergamon Press, 2nd edition, England(1989)
2. R.D.Cook, Concepts and Applications of Finite Element Analysis, John Wiley & Sons, 2nd Edition, NY(1981)
3. O.C.Zienkiewicz and R.L.Taylor, The Finite Element Method, Vol.1, Basic Formulation and Linear Problems, McGraw-Hill Book Company, 4th Edition, London(1989)
4. W.D.Pilkey and Wunderlich, Mechanics of Structures: Variational and Computational Methods, CRC Press, Florida(1994)
5. S.S.Rao, Mechanical Vibration, Addison-Wesley, MA(1986)

Plastic Analysis of Square Grillage under A Point Load

S.C. Lee, K.S. Hong and K.S. Kim

Department of Naval Architecture and Ocean Engineering, Inha University,
253 Younghyun-dong, Nam-gu, Incheon 402-751, Korea

Keywords: Condition, Fixed Boundary, Grid, Grillages, Mechanism Method, Plastic Hinge, Virtual Work

ABSTRACT

Grillage is common types of structures in marine and land-based structural system. The plastic collapse modes of those structures are dependent on the loads, which are lateral, in plane or combination of those directions as well as boundaries.

In this paper, a plastic analysis method is applied to grillages or grids under a single concentrated load to find the worst load point. The worst load point would be either at the central intersection or on the point of between intersections.

In the present paper, general formulae for plastic collapse for the square grillages with fixed boundaries are derived.

1. INTRODUCTION

The rational design procedure requires a sound and scientific background in the following key areas.

- (a) Accurate load prediction.
- (b) Definition of safety margins and design criteria.
- (a) Response analysis methods.
- (d) Synthesis and optimization.

In a certain structural system such as grillages in ships and ocean structural system, it is possible to predict the more accurate limiting condition by applying plastic analysis method [1-5].

In grillage design, the central intersection point load may be used as a worst loading condition especially with larger numbers of beams in each direction as long as local collapse is prevented. But, a point load may often move around anywhere on the grid system. In such case, the worst load point would not necessarily be at the central point. In this case, the worst load point is located between intersections.

To find the plastic collapse equations, upper bound theorem or mechanism method is applied to the square grillages with fixed boundaries.

2. BEAM WITH FIXED BOUNDARIES

In the plastic analysis of grillage, virtual work method (i.e. mechanism method) is useful. Virtual work equation could have been derived by writing the work balance for small movement δ of the

load and the hinge rotation at the center of each beam as shown in Fig. 1.

$$\text{Work equation: } P\delta = M_p \frac{16\delta}{L}$$

Collapse load can be expressed as follows.

$$P_c = M_p \frac{16}{L}$$

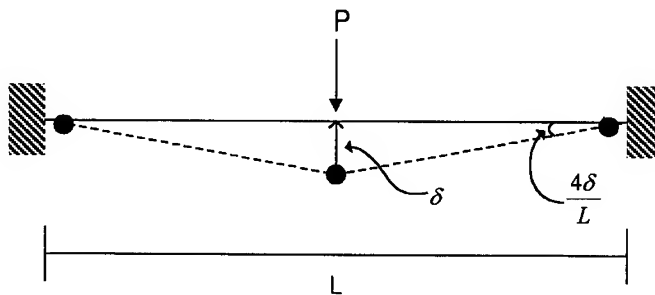


Fig. 1 Work Equation of Fixed Beam

3. SQUARE GRILLAGE UNDER POINT LOAD BETWEEN INTERSECTIONS

In practice, a point load may move around anywhere on the grid system as in the case of wheel load on the deck of ships and heliport deck. So the worst point is not always central intersection.

In the present study, collapse mechanism method is applied to find the worst point load position and collapse load formula for fixed boundaries with the following and assumptions with the grid system.

- (a) A load is applied perpendicular.
- (b) Joints are rigidly connected to transfer forces and moments.
- (c) A local collapse is prevented.
- (d) All the beams are equal sizes in each direction.

If lengths of horizontal and vertical beams are equal, plastic hinges are occurred at the center of a beam, and then the plastic collapse load of each beam can be calculated as usual method. To find collapse load, parameter "z" is used as in Fig.2

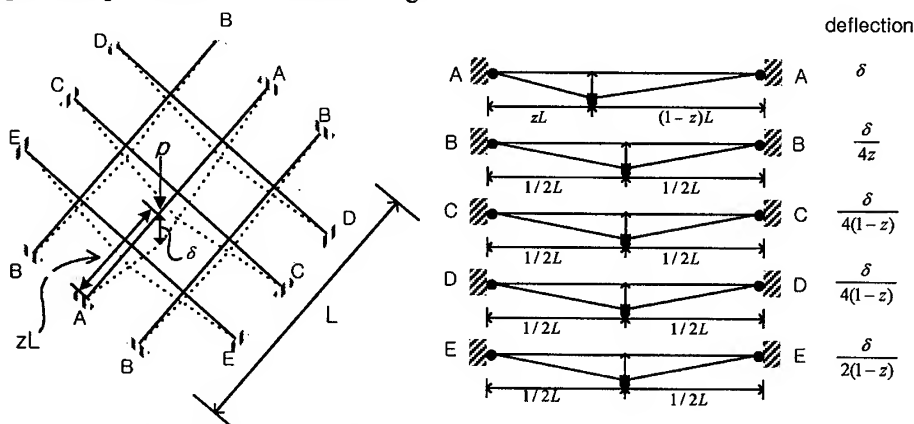


Fig. 2 Plastic Collapse Modes of 3x3 Grillage under off-center Load

The detail analysis process is introduced in the reference[6].

To find collapse load, virtual work method is applied as follows.

External work: $P\delta$

$$\text{Internal work: } \frac{(2+4z)\delta}{z(1-z)L} M_{pl} + \frac{(2+4z)\delta}{z(1-z)L} M_{pt}$$

Therefore work equation becomes as follows.

$$P_c = \frac{2+4z}{z(1-z)L} M_{pl} + \frac{2+4z}{z(1-z)L} M_{pt}$$

When M_{pl} and M_{pt} are equal work equation is as follows.

$$P_c = \frac{(4+8z)\delta}{z(1-z)} M_p \quad (M_p = M_{pl} = M_{pt})$$

Fig. 3 and Fig. 4 show a change of collapse loads for the (3×2) and (3×3) grillages. When the load applied between intersections in the central bay. Parameter z start from the end boundary of central horizontal beam and parameter x is located at between central intersection as shown in Fig. 3 and Fig. 4.

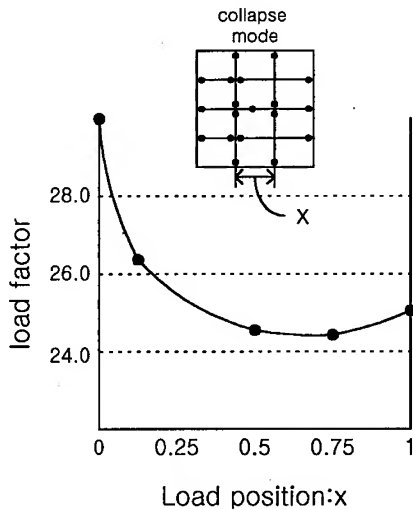


Fig. 3 Collapse Load Factors with Moving Load (3x2 Grillage)

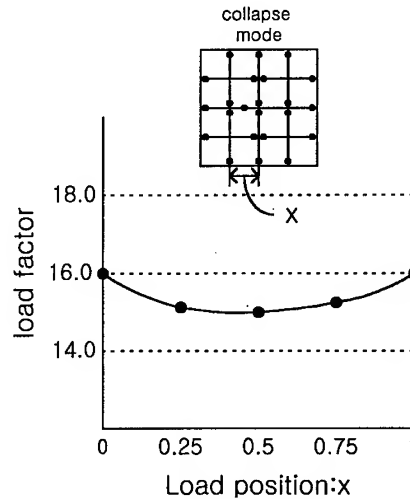


Fig. 4 Collapse Load Factors with Moving Load (3x3 Grillage)

If $M_{pl} = M_{pt}$, collapse loads are found as follows.

The collapse load of (3×2) grillage.

$$P_c = \frac{5-3z}{z(1-z)} M_{pl} + \frac{8}{3z(1-z)} M_{pt}$$

$$P_c = \frac{23-9z}{3Z(1-z)} M_p \quad (M_p = M_{pl} = M_{pt})$$

The collapse load of (3×3) grillage.

$$P_c = \frac{2+4z}{z(1-z)L} M_{pl} + \frac{2+4z}{z(1-z)L} M_{pt}$$

$$P_c = \frac{4-8z}{z(1-z)} M_p \quad (M_p = M_{pl} = M_{pt})$$

In Fig.3, if z is 0.562 ($x=0.6860$), minimum P_c is 24.30 M_p . And in Fig.4, if z is 0.455 ($x=0.464$) minimum P_c is 29.86 M_p . Minimum collapse loads of structures are lower than central intersection point load by about 6%-8%.

Types of grillages are grouped into 3 cases as follows.

(a) Case 1: $(m \times n) = (\text{odd} \times \text{odd})$

(b) Case 2: $(m \times n) = (\text{odd} \times \text{even})$

(c) Case 3: $(m \times n) = (\text{even} \times \text{even})$

Where, m and n represent the numbers of beams in horizontal and vertical directions respectively.

Then the plastic collapse load in each case can be expressed as follows.

$$\text{Case 1: } P_c = \alpha_1 M_{pl} + \beta_1 M_{pt}$$

$$\text{Case 2: } P_c = \alpha_2 M_{pl} + \beta_2 M_{pt}$$

$$\text{Case 3: } P_c = \alpha_3 M_{pl} + \beta_3 M_{pt}$$

Where $\alpha_1, \beta_1, \alpha_2, \beta_2, \alpha_3$ and β_3 are coefficients including variable z , M_{pl} and M_{pt} are plastic moments of horizontal and vertical beams respectively.

The coefficients (α_i, β_j) are calculated by virtual work method, and then the results are shown in the next tables for different numbers of vertical and horizontal beams.

Case 1: In case of $(\text{odd} \times \text{odd})$ grillage, the worst point is clearly located at central beam. Variable z is defined from end of the beam to unknown point. Table 1 and Table 2 show coefficients (α_1, β_1) that are varied by the numbers of horizontal and vertical beams.

Table 1 The Coefficients (α_1) of Horizontal Beam for $(\text{odd} \times \text{odd})$ Grillage

$\frac{n}{m}$	1	3	5	7
1	$\frac{4z}{z(1-z)L}$	$\frac{4z}{z(1-z)L}$	$\frac{4z}{z(1-z)L}$	$\frac{4z}{z(1-z)L}$
3		$\frac{2+4z}{z(1-z)L}$	$\frac{2+4z}{z(1-z)L}$	$\frac{2+4z}{z(1-z)L}$
5			$\frac{4+4z}{z(1-z)L}$	$\frac{4+4z}{z(1-z)L}$
7				$\frac{6+4z}{z(1-z)L}$

Table 2 The Coefficients (β_1) of Vertical Beam for $(\text{odd} \times \text{odd})$ Grillage.

$\frac{n}{m}$	1	3	5	7
1	$\frac{2}{z(1-z)L}$	$\frac{2+4z}{z(1-z)L}$	$\frac{2+8z}{z(1-z)L}$	$\frac{2+12z}{z(1-z)L}$
3		$\frac{2+4z}{z(1-z)L}$	$\frac{2+8z}{z(1-z)L}$	$\frac{2+12z}{z(1-z)L}$
5			$\frac{2+8z}{z(1-z)L}$	$\frac{2+12z}{z(1-z)L}$
7				$\frac{2+12z}{z(1-z)L}$

General formula of coefficients in Table 2 and Table 3 can be simplified as α_1, β_1 . Where m and n are the numbers of horizontal and vertical beams respectively.

$$\alpha_1 = \frac{2(m-1) + 8z}{z(1-z)L} \quad \beta_1 = \frac{2 + 2(n-1)z}{z(1-z)L}$$

Case 2: In case of (odd×even) grillage, the worst point is clearly located at central beams. Table 4 and Table 5 show coefficients (α_2 , β_2) that are varied by the numbers of horizontal and vertical beams.

Table 3 The Coefficients (α_2) of Horizontal Beam for (odd×even) Grillage

$\begin{smallmatrix} n \\ m \end{smallmatrix}$	2	4	6	8
3	$\frac{10-6z}{2z(1-z)L}$	$\frac{16-10z}{3z(1-z)L}$	$\frac{22-14z}{4z(1-z)L}$	$\frac{28-18z}{5z(1-z)L}$
5		$\frac{26-20z}{3z(1-z)L}$	$\frac{36-28z}{4z(1-z)L}$	$\frac{46-32z}{5z(1-z)L}$
7			$\frac{50-42z}{4z(1-z)L}$	$\frac{64-54z}{5z(1-z)L}$
9				$\frac{82-72z}{5z(1-z)L}$

Table 4 The Coefficients (β_2) of Vertical Beam for (odd×even) Grillage

$\begin{smallmatrix} n \\ m \end{smallmatrix}$	2	4	6	8
3	$\frac{8}{3z(1-z)L}$	$\frac{24}{5z(1-z)L}$	$\frac{48}{7z(1-z)L}$	$\frac{80}{9z(1-z)L}$
5		$\frac{24}{5z(1-z)L}$	$\frac{48}{7z(1-z)L}$	$\frac{80}{9z(1-z)L}$
7			$\frac{48}{7z(1-z)L}$	$\frac{80}{9z(1-z)L}$
9				$\frac{80}{9z(1-z)L}$

General formula of coefficients in Table 4 and Table 5 can be simplified as α_2, β_2 .

$$\alpha_2 = \frac{2m(n+1) + 2 - 2(n+1)(m-1)z}{(n+2)z(1-z)L} \quad \beta_2 = \frac{n^2 + 2n}{(n+1)z(1-z)L}$$

Case 3: In case of (even×even) grillage, the worst point is clearly located at off-central beam. Table 6 and Table 7 show coefficients (α_3 , β_3) that are varied by the numbers of horizontal beams.

Table 5 The Coefficients (α_3) of Horizontal Beam for (even×even) Grillage

$\begin{smallmatrix} n \\ m \end{smallmatrix}$	2	4	6	8
2	$\frac{7-3z}{2z(1-z)L}$	$\frac{13-9z}{2z(1-z)L}$	$\frac{19-15z}{2z(1-z)L}$	$\frac{25-21z}{2z(1-z)L}$
4		$\frac{21-15z}{3z(1-z)L}$	$\frac{31-25z}{3z(1-z)L}$	$\frac{41-35z}{3z(1-z)L}$
6			$\frac{43-35z}{4z(1-z)L}$	$\frac{57-49z}{4z(1-z)L}$
8				$\frac{73-63z}{5z(1-z)L}$

Table 6 The Coefficients (β_3) of Vertical Beam for (odd×odd) Grillage

$\begin{smallmatrix} n \\ m \end{smallmatrix}$	2	4	6	8
2	$\frac{49}{3z(1-z)L}$	$\frac{25}{9z(1-z)L}$	$\frac{49}{18z(1-z)L}$	$\frac{81}{30z(1-z)L}$
4		$\frac{75}{15z(1-z)L}$	$\frac{147}{30z(1-z)L}$	$\frac{243}{50z(1-z)L}$
6			$\frac{294}{42z(1-z)L}$	$\frac{486}{70z(1-z)L}$
8				$\frac{810}{90z(1-z)L}$

General formula of coefficient in Table 6 can be simplified as α_3 and β_3 .

$$\alpha_3 = \frac{(m^2 + 2m)(n+1)^2}{(m+1)(n+2n)z(1-z)L} \quad \beta_3 = \frac{2(mn+n+1) + 2(mn-m+n-1)}{(m+2)z(1-z)L}$$

Above tables are expressed to case when the number of vertical beams is more than that of horizontal beams. Other cases also can be found, since the grillage is square.

Therefore the collapse loads are summomised for case as follow.

$$\text{Case 1: } P_c = \frac{(m-1) + 4z}{z(1-z)L} M_{pl} + \frac{2(1+(n-1)z)}{z(1-z)L} M_{pt}$$

$$\text{Case 2: } P_c = \frac{2m(n+1) + 2 - 2(n+1)(m-1)z}{(n+2)z(1-z)L} M_{pl} + \frac{n^2 + 2n}{(n+1)z(1-z)L} M_{pt}$$

$$\text{Case 3: } P_c = \frac{(m^2 + 2m)(n+1)^2}{(m+1)(n+2n)z(1-z)L} M_{pl} + \frac{2(mn+n+1) + 2(mn-m+n-1)}{(m+2)z(1-z)L} M_{pt}$$

Minimum collapse load can be found by simple calculus with the above plastic collapse equations.

4. CONCLUSIONS

By applying upper bound theorem to plastic collapse analysis of square grillages with fixed boundaries collapse equations are obtained. These collapse equations are grouped into 3 cases depending on the numbers of beams in two directions.

These equations can easily be applied to optimization study of grillages under a concentrated load.

ACKNOWLEDGEMENT

The work described in this paper is supported by the fund from Regional Research Center for Transportation of Yellow Sea.

REFERENCES

1. M.R. Horne, Plastic Theory of Structures, Thomas Nelson and Sons(1971).
2. T.P. Boufounos, Plastic Shakedown Behavior of Ship Frame and Panels, Ph.D. Dissertation, MIT(1975).
3. K.S. Kim, Strength Analysis as a Basis for Structural Design and Optimisation, Ph.D Thesis, University of Newcastle upon Tyne, UK(1982).
4. K.S. Kim, Application of Plastic Design Method to Ship Grillages, PRADS'83, Toykyo & Seoul, (1983) pp 539-546.
5. K.S. Kim and Y.H. Park, A Plastic Design Method of Grillages under a Lateral Point Load, J. of Hydrospace Technology, Vol. 1, No. 2, (1995)pp 100-115.
6. S.C. Lee, K.S. Hong and K.S. Kim, Plastic Analysis of Grillage under A Point Load. (To be presented at ISOPE-2000, Seatle, May 28-June 2, 2000)

Finite Element Analyses of Specific Damping Capacity and Undamped/Damped Forced Motion of Composite Plate Using Modified 16-Node Solid Elements

T.H. Yun¹, Y.D. Kwon², C. Kim² and J.G. Park³

¹Department of Mechanical Design, Kumi College, Kumi 730-170, Korea

²Department of Mechanical Engineering, Kyungpook National University, Taegu 702-701, Korea

³Graduate School, Kyungpook National University, Taegu 702-701, Korea

Keywords: Composite Plate, Errors of the Reduced Integration, Forced Motion, Gauss Sampling Point, Modified 16-Node Solid Element, Specific Damping Capacity

ABSTRACT

This paper examines the validity of modification equations of Gauss sampling points in the analysis of specific damping capacity. In the mean time, the damping matrix used in the evaluation of specific damping capacity is symmetrized with the conventional asymmetric damping matrix.

In addition, the validity of a modification equation of Gauss sampling points in the analysis of undamped/damped forced motion of a composite plate is also examined. In this case, the theoretical errors of the undamped/damped forced motion of a composite plate are predicted from the reduction in the order of numerical integration.

1. INTRODUCTION

Modified Gauss sampling points applied to laminated composite plates are found to be effective in the evaluation of specific damping capacity and the analysis of time-dependent motion when comparing the results of conventional and modified 16-node models with those of 20-node models. The damping stiffness matrix is symmetrized, thereby improving the convenience and effectiveness of computation.

In addition, forced dynamic response errors caused by reduced integration are predicted, and compared with actual errors versus the number of layers in a laminate. If the prediction is acceptable, the decision can be made whether to use full integration or reduced integration based on an allowed error bound and the number of layers in the laminated composite plates.

2. ANALYSIS OF SPECIFIC DAMPING CAPACITY

The specific damping capacity of laminated composite plates can be defined as in Eq.1.

$$\phi = \Delta U / U \quad (1)$$

Here, U denotes the maximum strain energy and ΔU represents the dissipated energy during the stress cycle. The strain energy of each layer can be represented as in Eq.2.

$$U_k = \frac{1}{2} \int_{V_k} \{\varepsilon\}^T \{\sigma\} dV_k = \frac{1}{2} \int_{\Omega} \int_{h_{k-1}}^{h_k} \{\varepsilon\}^T [\bar{Q}] \{\varepsilon\} dz d\Omega \quad (2)$$

Where, U_k = the strain energy of the k th layer, V_k = the volume of the k th layer, $[\bar{Q}] = [A]^T [Q] [A]$, Ω = the plane of the plate, and Q_{ij} = the elastic coefficients of the material when the principle axes of the material coincide with the axes of coordinates. Then, total strain energy of the laminated composite plates with NL -layer can be given by Eq.3.

$$U = \sum_{k=1}^{NL} U_k \quad (3)$$

Meanwhile, the dissipated energy of a layer during the stress cycle can be represented by Eq.4^[1,2].

$$\begin{aligned} \Delta U_k &= \frac{1}{2} \int_A \int_{h_{k-1}}^{h_k} \{\varepsilon\}^T [\phi] \{\sigma\} dz dA \\ &= \frac{1}{2} \int_A \int_{h_{k-1}}^{h_k} \{\varepsilon\}^T [A]^T [\phi] [Q] [A] \{\varepsilon\} dz dA \end{aligned} \quad (4)$$

In Eq.4, $[A]$ is the coordinates transformation matrix as presented, and $[A]^T [\phi] [Q] [A]$ is asymmetric matrix.

The matrix in Eq.4 can be symmetrized as in Eq.5. Therefore, advantage can be taken of the symmetricity of the specific damping stiffness matrix represented in Eq.6 instead of the conventional asymmetric one given in Eq.4.

$$\Delta U_k = \frac{1}{2} \int_A \int_{h_{k-1}}^{h_k} \{\varepsilon\}^T [S] \{\varepsilon\} dz dA \quad (5)$$

$$S = [A]^T [T] [A] \quad ; \quad \text{symmetric} \quad (6)$$

Here,

$$[T] = \frac{1}{2} \begin{bmatrix} 2\phi_1 Q_{11} & (\phi_1 + \phi_2) Q_{12} & (\phi_1 + \phi_3) Q_{13} & (\phi_1 + \phi_{12}) Q_{14} & 0 & 0 \\ (\phi_2 + \phi_1) Q_{21} & 2\phi_2 Q_{22} & (\phi_2 + \phi_3) Q_{23} & (\phi_2 + \phi_{12}) Q_{24} & 0 & 0 \\ (\phi_1 + \phi_3) Q_{31} & (\phi_2 + \phi_3) Q_{32} & 2\phi_3 Q_{33} & (\phi_{12} + \phi_3) Q_{34} & 0 & 0 \\ (\phi_1 + \phi_{12}) Q_{41} & (\phi_2 + \phi_{12}) Q_{42} & (\phi_{12} + \phi_3) Q_{43} & 2\phi_{12} Q_{44} & 0 & 0 \\ 0 & 0 & 0 & 0 & 2\phi_{23} Q_{55} & (\phi_{23} + \phi_{31}) Q_{56} \\ 0 & 0 & 0 & 0 & (\phi_{23} + \phi_{31}) Q_{65} & 2\phi_{31} Q_{66} \end{bmatrix} \quad (7)$$

The total dissipated energy during the stress cycle can be given by Eq.8.

$$\Delta U = \sum_{k=1}^{NL} \Delta U_k \quad (8)$$

3. DAMPED TIME-DEPENDENT MOTIONS ANALYSIS

The motion equation for the time-dependent motions of a laminated composite plate can be given by Eq.9.

$$[M]\{\ddot{U}\} + [C]\{\dot{U}\} + [K]\{U\} = R(t) \quad (9)$$

Here, $[C]$ is the damping matrix and $R(t)$ represents the time-dependent external forces. In Eq.9, the displacement vector U represents the same as in Eq.10.

$$[U] = \sum_{i=1}^n X_i(t) \{\Phi_i\} \quad (10)$$

Here, $X_i(t)$ denotes the generalized coordinates, $\{\Phi_i\}$ denotes the modal vectors.

Eq.10 is inserted into Eq.9, and rearranged to produce Eq.11.

$$\ddot{X}_i(t) + 2\omega_i \xi_i \dot{X}_i(t) + \omega_i^2 X_i(t) = \gamma_i(t) \quad (11)$$

Where ξ_i : damping ratio, ω_i : circular frequency, $\{\Phi_i\}^T [M] \{\Phi_i\} = 1$,

$$2\omega_i \xi_i = \{\Phi_i\}^T [C] \{\Phi_i\}, \quad \omega_i^2 = \{\Phi_i\}^T [K] \{\Phi_i\}, \quad \gamma_i(t) = \{\Phi_i\}^T R(t)$$

4. MODIFIED 16-NODE SOLID ELEMENT

4.1. Modification Equations of Gauss Quadrature

The modification equations^[3] of the Gauss quadrature can be given as follows. These are applied to the analyses of undamped/damped time-dependent motion.

$$t_{k16j} = t_{k20j} [1 - \overline{D_{12}} \overline{D_{21}} / (\overline{D_{11}} \overline{D_{22}})]^{1/2} \quad (12)$$

$$G_{(16)12k} = G_{(20)12k} / [1 - \overline{D_{12}} \overline{D_{21}} / (\overline{D_{11}} \overline{D_{22}})] \quad (13)$$

4.2. Reduced Order of Quadrature in Laminated Composite Plates

The relative error^[3] of reduced integration for $[K_L]$ of a composite laminate can be obtained as follows. It is compared with actual errors of undamped/damped time-dependent motion.

$$error = \left\{ W_1 (E_1 h^3 / 12) + W_2 (E_2 h^3 / 12) - \sum_{i=1}^{N_l} h_{(k)} E_k X_k^2 \right\} / \left\{ W_1 (E_1 h^3 / 12) + W_2 (E_2 h^3 / 12) \right\} \quad (14)$$

Where, W_1, W_2 : weight factor depending upon specific layering scheme, E_k = elastic coefficient of k th layer.

5. NUMERICAL EXAMPLES AND DISCUSSION

5.1. Evaluation of Specific Damping Capacity

The material properties of specimen model A are represented in Table 1-A, and the model dimensions are the same as in reference[4]. The material properties of specimen model B are represented in Table 1-B and the model dimensions are the same as in reference[1]. The finite element model A is discretized into 10 elements, whereas model B is discretized into 4×4 elements of equal size. In Table 2, the maximum errors are 0.65% in the case of A, and 2.5% in the case of B.

Table 1 Material properties of composite laminate

TYPE	E_{11} (GPa)	E_{22} (GPa)	E_{33} (GPa)	G_{12} (GPa)	G_{13} (GPa)	ν_{12}	ν_{13}	ν_{23}	ρ (Kg/m ³)
A	112	8.81	8.81	5.45	5.45	.033	0.33	0.50	1575
B	172.7	7.20	7.20	3.76	3.76	0.30	0.30	0.50	1636

Table 2 Comparison of natural frequencies and SDCs

Size(mm)	Model	Natural Frequencies			SDC1 (Error %)	SDC2 (Error %)	SDC3 (Error %)
		1st Mode (Error %)	2nd Mode (Error %)	3rd Mode (Error %)			
A 120× 19.6 × 0.88 (mm)	20-Node	82.80	392.1	526.3	1.05	2.16	1.06
	Ref.[4]	83.04 (.29)	393.5 (.35)	523.2 (.60)	1.04 (1.1)	2.15 (.65)	1.05 (.47)
	Mod.16-Node	83.26 (.56)	393.7 (.40)	524.1 (.42)	1.05 (.00)	2.15 (.65)	1.05 (.47)
B 215× 215 × 1.62 (mm)	20-Node	88.13	233.2	290.7	3.07	0.81	1.71
	Ref.[1]	86.33 (2.0)	224.5 (3.7)	280.4 (3.5)	3.11 (1.3)	0.80 (1.2)	1.70 (.58)
	Mod.16-Node	88.20 (.079)	231.18(.85)	293.6 (1.0)	3.08 (.33)	0.79 (2.5)	1.74 (1.8)

5.2. Analysis of Time-Dependent Motion Using Modified 16-Node Element

The plates were composed of three laminae stacked according to two schemes, (0/90/0) and (0/90/0). The finite element model was discretized into 10 elements, and the specifications are shown in Table 2-A. A load of 0.1N was suddenly applied at the tip of the cantilever plate

(0/90/0). The responses obtained using the conventional 16-node model, modified 16-node model and 20-node model are compared in Fig.1 and Fig.2 for undamped and damped cases, respectively. Similar responses are also plotted in Fig.3 and Fig.4 for the cantilever plate (90/0/90), undamped and damped.

From the results it can be seen that in one case the modification was unnecessary, whereas in another case it was necessary for all situations irrespective of the damping effect. This implies that the modified 16-node element can predict almost the same result as that of a 20-node element, even though it only has a small degree of freedom.

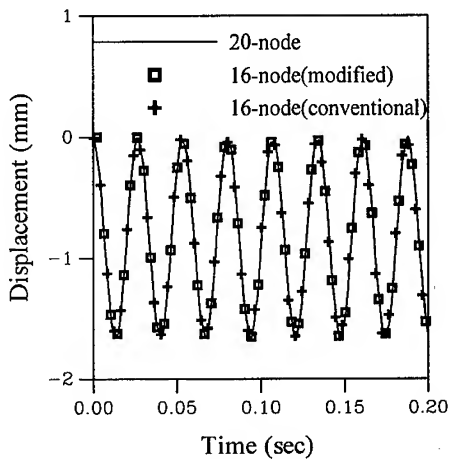


Fig.1 Time dependent motion analysis of laminated composite plate (0/90/0) [no damping]

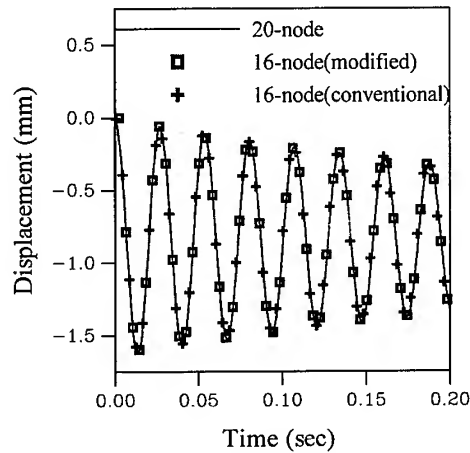


Fig.2 Time dependent motion analysis of laminated composite plate (0/90/0) [damping ratio=0.01]

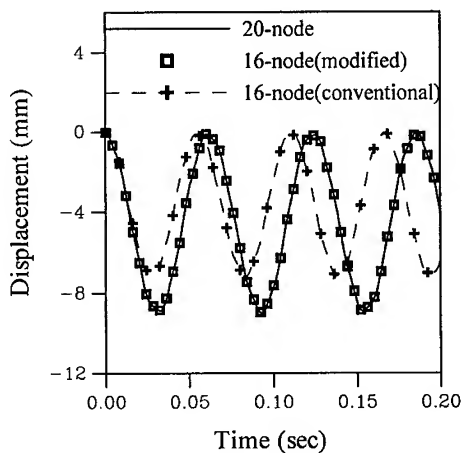


Fig.3 Time dependent motion analysis of laminated composite plate (90/0/90) [no damping]

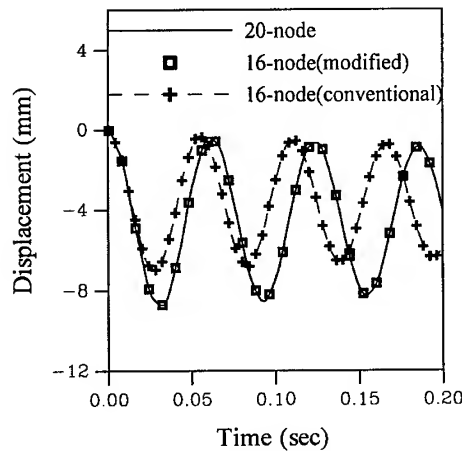


Fig.4 Time dependent motion analysis of laminated composite plate (90/0/90) [damping ratio = 0.01]

5.3. Reduction of Integration Order

The undamped/damped time dependent dynamic responses of the composite plates were computed using both full order quadrature and reduced order quadrature. With these responses, the actual errors resulting from a reduction in the integration order could be obtained. These errors were then compared with the predicted ones and exhibited good agreements for both undamped and damped motions. The errors are decreasing with the increment of the number of layers. Accordingly, it would appear that either full order integration or reduced order integration can be used in evaluating stiffness, in a time-dependent analysis, depending on the allowable error bound and the number of layers.

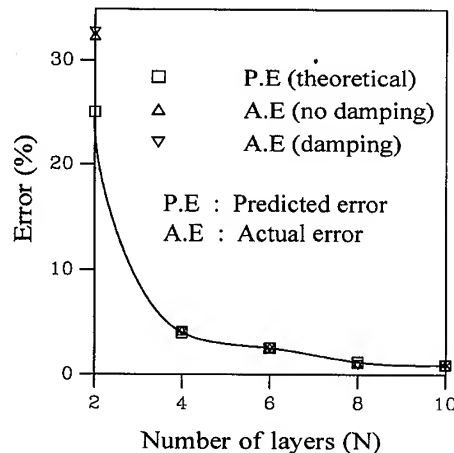


Fig.5 Integration errors(order 1) of laminated composite plates in time dependent motion analysis

6. CONCLUSIONS

- 1) Damping matrix can be symmetrized. Therefore, a much simpler algorithm can be utilized which can achieve a better efficiency in the computation of specific damping capacity.
- 2) The effectiveness of the modification equations of Gauss sampling points was shown based on evaluations of time-dependent undamped/damped motions analyses.
- 3) The errors in undamped/damped time-dependent motions caused by reduced integration can be theoretically predicted by assuming that the stiffness varies quadratically in a thickness direction. As a result, full or reduced integration can be selected for a given number of layers in laminated composite plates, in the evaluation of stiffness satisfying a required error criterion.

REFERENCES

1. D.X. Lin, R.G. Ni and R.D. Adams, "Prediction and Measurement of The Vibration Damping Parameters of Carbon and Glass Fiber-Reinforced Plastics Plates", J. Comp. Mat., Vol. 18 (1984) pp. 135-151.
2. Zabaraas, N. and Pervez, T., "Viscous Damping Approximation of Laminated Anisotropic Composite Plates Using the Finite Element Method," Com. Meth. App. Mech. Eng., Vol. 81, No. 3 (1990) pp. 291-316.
3. Y.D. Kwon, Y.S. Kim, T.H. Yun and M.H. Cho, "Static and Mode Analyses of Composite Plates Using Modified 16-Node Solid Elements, and Prediction of Stiffness Errors Resulting from Reduced Integration", 4th International Conference on Fracture and Strength of Solids (2000)
4. B.N. Kim, K.N. Ku, "A research on the dynamic characteristics of thermoplastic composite material", Proceedings of KSCE (1992) pp. 87-92.

Stress Analysis for New Gasketless Flange and Superseal

N.-A. Noda¹, K.-I. Takeuchi¹, Y. Takase¹ and M. Nagawa²

¹ Department of Mechanical Engineering, Kyushu Institute of Technology,
1-1 Sensui-cho, Tobata, Kitakyushu, Fukuoka 804-8550, Japan

² Daiso Corporation, 4-5-1, Nishihon-machi, Yahatahigashi, Kitakyushu 804-0061, Japan

Keywords: Contact Problems, Coupling, Finite Element Method, Fixing Element, Machine Element, Pipe Flange, Sealing Performance, Stress Analysis

ABSTRACT

This paper deals with a new seal system between two flanges without using gaskets. The system includes a groove and an annular lip that is held by one of the flange with its highest point in contact with the other flange to form a seal line when the flanges are assembled. The condition whether the system leaks or not depends on the shape and dimension of a thinned area with the annular lip deformed during the contact. In this study several gasketless flanges are prepared with varying the fundamental dimensions of the deformed area to investigate the condition through an experiment and FEM analysis. The analysis indicates that the conditions can be expressed in terms of the maximum contact stress and the plastic zone size when the flanges are assembled.

1. INTRODUCTION

Between any pipe flanges it is necessary to choose a suitable gasket depending on the kind of fluids with their pressure and temperature to obtain good seal systems. However, generally the sealing performance of gaskets deteriorates in several years, and, therefore, the maintenance to find a leak and to renew the gasket has been required. In this paper a new seal system between two flanges without using gaskets has been treated. Figure 1 shows the system that includes a groove and an annular lip that is held by one of the flange with its highest point in contact with the other flange to form a seal line when the flanges are assembled. Figure 2 also shows a similar system called "superseal", which is inserted between the flanges currently used. In this study several gasketless flanges and superseals are prepared with varying fundamental dimensions of the deformed area to investigate the sealing mechanism through an experiment and FEM analysis.

2. EXPERIMENTAL METHOD

Figure 2 indicates dimensions of models used in this study. By comparing the results of the model A and model B, we may find how the groove works. From the results of models B and C we may find a suitable dimension of the thickness h . From the results of the models C and D we may find a suitable dimension of the groove depth. The material used is 0.25 percent carbon steel S25C (JIS). The maximum surface roughness at the annular lip is $R_{\max}=4$ (JIS) and the maximum surface roughness of the other flange is $R_{\max}=80$. After the flanges are clamped by bolts of

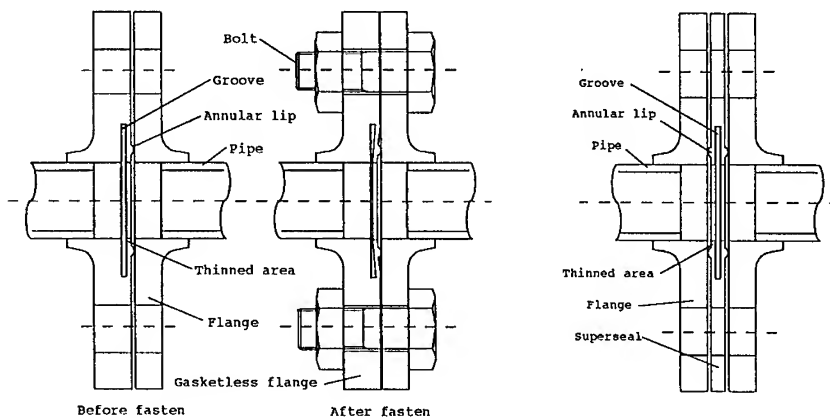


Fig. 1. Gasketless flange and superseal

M16, an internal pressure 4.9MPa is applied to these models by water-hydraulic pump. The results of sealing performance are shown in the right end in Table 1. The symbol \bigcirc means there has been no leak for model B, \triangle means there is no leak in the first trial but leaks in the second trial after released and clamped again for model A, and \bullet means there is leak in the first trial for model C. Through the experiment it is found that the sealing performance depends on the shape and dimension of a thinned area involving the annular lip, which is deformed during the contact.

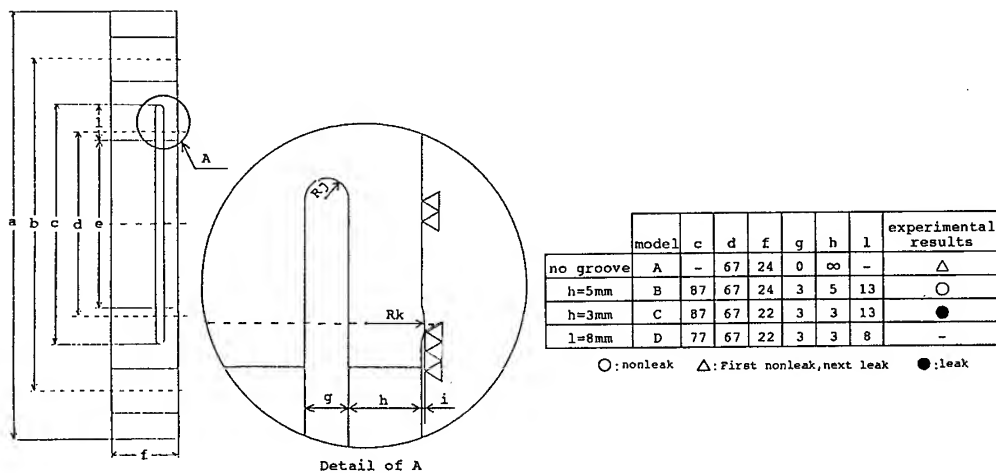


Fig. 2. Dimension of experiment model (mm)

3. ANALYTICAL METHOD

The FEM analysis is applied using 4 node axisymmetric element. The total number of element is 2624~2961 and the total number of node is 2816~3173. The clamping force is estimated about 98kN from the torque applied to the bolts and approximated by axisymmetric uniform distribution. The stress-strain relation is indicated in Fig. 3. Figure 3 shows the stress-strain relation with Young's modules $E=20580\text{MPa}$, Poisson's ratio $\nu=0.3$, the yielding stress is 255MPa.

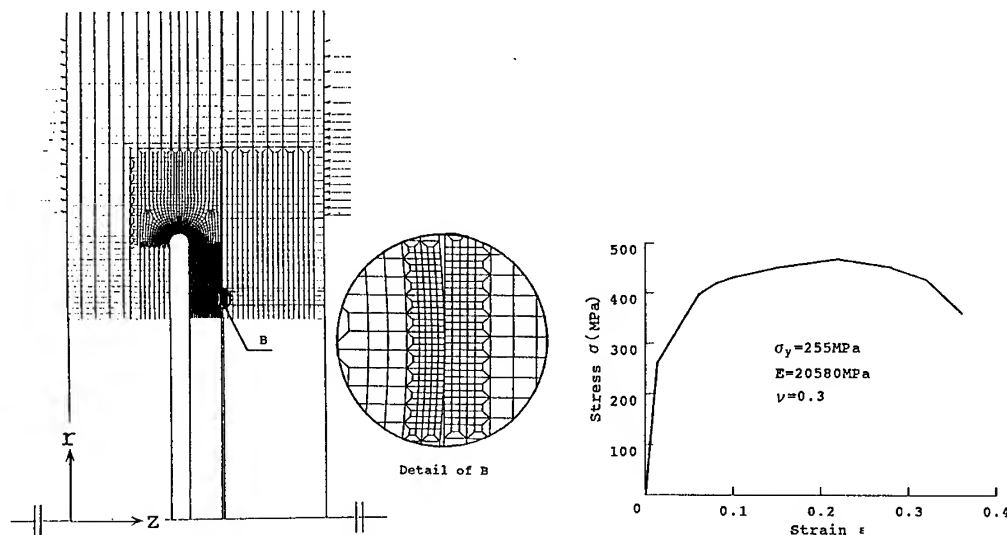


Fig. 3. Finite element mesh and material property

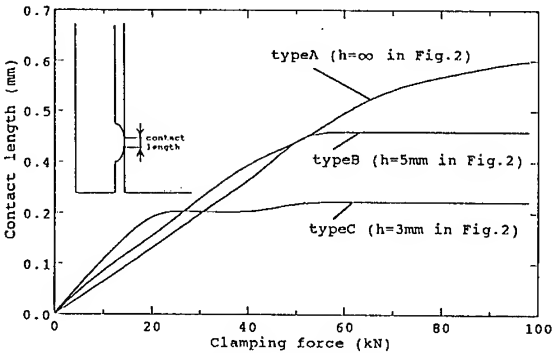
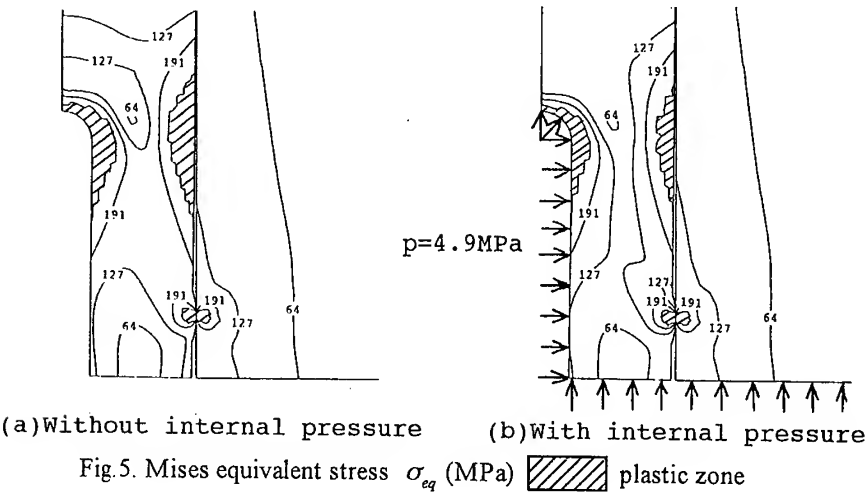
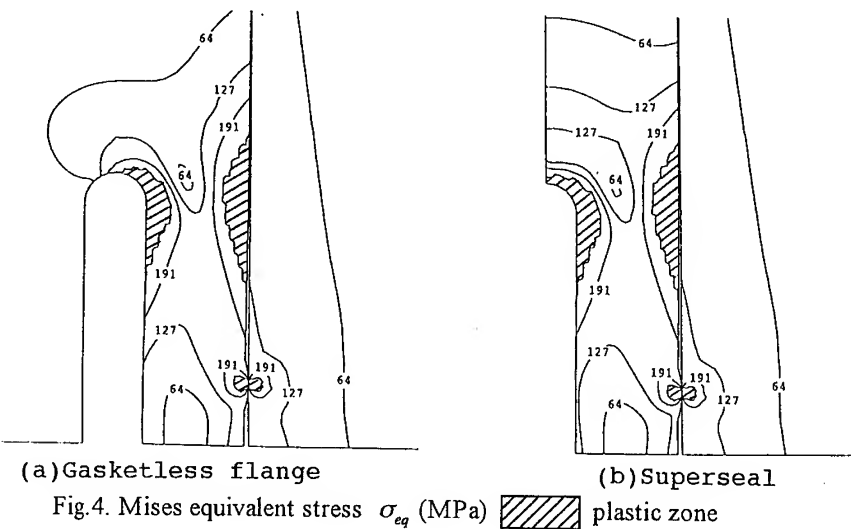
4. RESULTS AND DISCUSSION

Figure 4 shows Mises equivalent stress for (a) gasketless flange and (b) superseal. Since Fig. 4 (a) and Fig. 4 (b) are not very different, the results of superseals can be regarded as the ones of gasketless flanges. Figure 5 indicates the effect of internal pressure 4.9 MPa applied to the model B. The plastic zone size around the root of groove in Fig. 5(b) is smaller than the one in Fig. 5(a). Therefore large internal pressure may be useful for sealing performance because of the small plastic zone size. Figure 6 shows the relation between the clamping force and contact length. For models B and C, if the clamping force is large enough the contact length becomes independent of the force.

Figures 7-9 show Mises equivalent stress. The maximum stresses are almost equal for models A, B, C, that is, $\sigma_{eq \max} \approx 286 \text{ MPa}$. On the other hand, the maximum stresses in the z-direction $\sigma_{z \max} \approx -1200 \text{ MPa}$ for models A and B, but $\sigma_{z \max} \approx -900 \text{ MPa}$ for model C, which is smaller by about 25 percent. It may be concluded that the reason why model C leaks at the small value of $\sigma_{z \max}$. The FEM results also indicate that for model A the plastic zone size around the contact region is larger. Because of this large plastic deformation, model A seems to leak in the second trial after released and clamped again although there is no leak in the first trial. Finally, a suitable groove depth is considered because models A, B, C have a constant groove depth, $l = 13 \text{ mm}$. Figure 10 shows the results for model D, where $l = 8 \text{ mm}$ and $h = 3 \text{ mm}$. By reducing the depth the maximum stresses in the z-direction $\sigma_{z \max} \approx -1300 \text{ MPa}$ with a suitable plastic zone size. However, around the root of the groove the plastic zone prevails all over the section, and therefore, the sealing performance seems worse in the second trial. The FEM analysis indicates that the conditions whether the system has a leak or not can be controlled by the maximum contact stress with the plastic zone size when the flanges are assembled. It may be concluded that the dimensions of model B is suitable because of large contact stress and suitable plastic zone size.

5. CONCLUSION

Generally the sealing performance of gaskets between any pipe flanges deteriorates in several



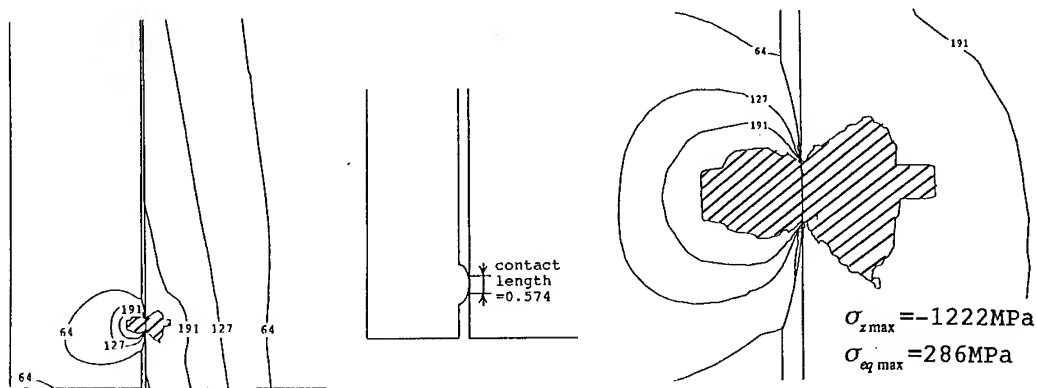



Fig. 7. Equivalent stress σ_{eq} for model A (no groove, $h=\infty$ in Fig.2)  plastic zone

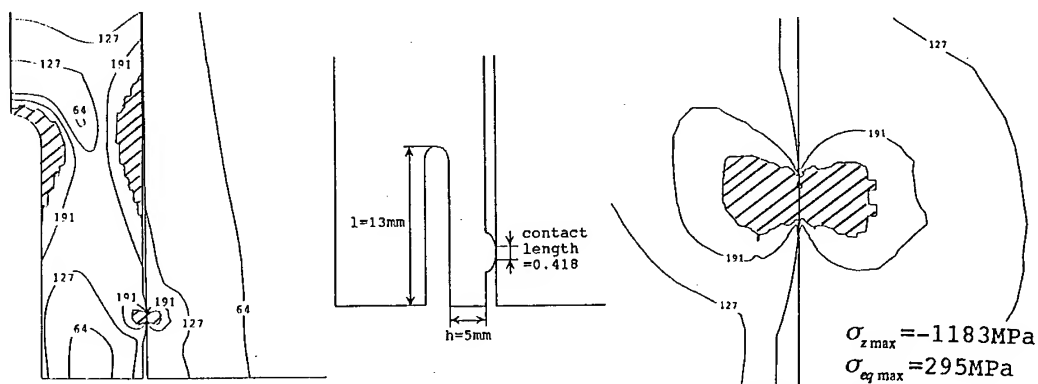



Fig. 8. Equivalent stress σ_{eq} for model B ($h=5\text{mm}$ in Fig.2)  plastic zone

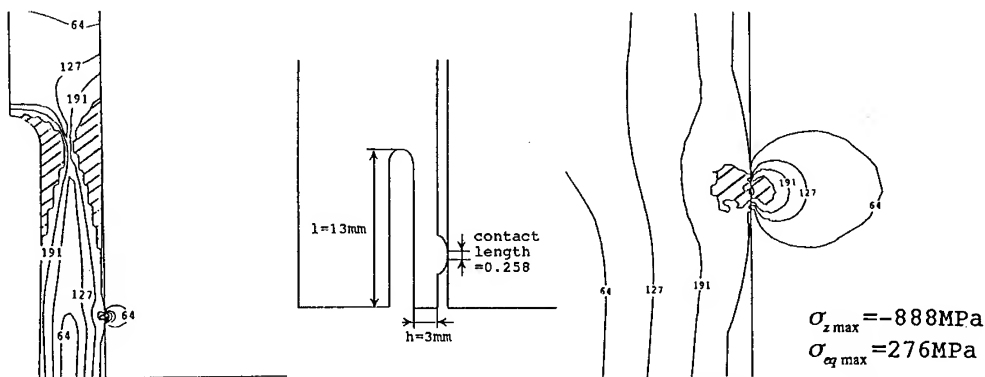



Fig. 9. Equivalent stress σ_{eq} for model C ($h=3\text{mm}$ in Fig.2)  plastic zone

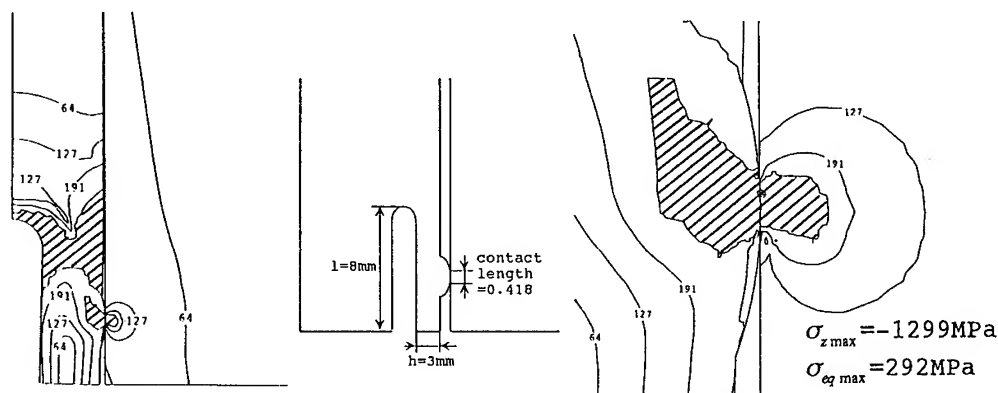



Fig.10. Equivalent stress σ_{eq} for model D ($l=8\text{mm}$ in Fig.2)  plastic zone

years, and, therefore, the maintenance to find a leak and to renew the gasket has been required. In this paper a new seal system without using gaskets has been considered. In this study several gasketless flanges are prepared with varying fundamental dimensions of the deformed area to form a seal line during contact in order to investigate the sealing mechanism. Through an experiment and FEM analysis the following conclusions can be made.

(1) Three experimental models A, B, C are investigated. For model A, which has no groove, there is no leak in the first trial but leaks in the second trial after released and clamped again. There has been no leak for model B, whose thickness of a thinned area $h = 5\text{mm}$. There is a leak from the first trial for model C, where $h=3\text{mm}$. Through the experiment it is found that the sealing performance depends on the shape and dimension of a thinned area involving the annular lip, which is deformed during the contact.

(2) FEM analysis indicates that the maximum stress at the contact zone $\sigma_{z\max} \approx -1200\text{MPa}$ with a suitable plastic zone size is necessary for good sealing performance. For example, model C leaks because of the small value of $\sigma_{z\max} \approx -900\text{MPa}$, and model A leaks in the second trial due to the large plastic deformation at the contact region. It may be concluded that the dimensions of model B is suitable because of large contact stress and suitable plastic zone size.

(3) The experiment and FEM analysis show the internal pressure is useful for sealing performance because it makes a large contact stress and small plastic zone size. This new seal system, therefore, may be effective for high internal pressure, under which current gaskets cannot be used.

ACKNOWLEDGEMENT

The authors wish to express their thanks to Mr. Hiroshi Otsuji and Dr Hiroyuki Tanaka, who gave useful discussion and supported our research.

REFERENCE

1. Jun Akagawa, Seal Technology, (1972), 365-369, Kindaienshusha (in Japanese)
2. Nikkan-Kogyo Newspaper, (Dec. 2. 1998), 37 (in Japanese)
3. Hiroshi Otsuji and Masato Nagawa, Japan patent no. 2849345 (in Japanese)
4. Yoshio Matsuzaki, Ph. D dissertation, Fundamental property of metal gasket, Nagoya Institute of Technology, (1993), 27-88 (in Japanese)
5. JIS B 1083 (1990)

A Study on Stress Wave Propagation in Stiffened Cylinder Subjected to a Strong Acoustic Wave

J.H. Choi¹, K.S. Kim¹, C.H. Jo¹, O.S. Lee² and C.W. An³

¹ Department of Naval Architecture and Ocean Engineering, Inha University,
253 Youghyun-dong, Nam-gu, Incheon 402-751, Korea

² Department of Mechanical Engineering, Inha University,
253 Youghyun-dong, Nam-gu, Incheon 402-751, Korea

³ Agency for Defense Development, Korea

Keywords: Dynamic Photoelastic Methodology, Fluid-Structure Interaction, Stiffened Cylinder, Stress Wave Propagation, Underwater Explosion

ABSTRACT

The shock wave caused by an underwater explosion can damage to the equipment inside vessels and can create a local defect on ship hull. As reaching structure, this shock wave propagates in the form of stress wave which may cause an instant failure at a local point. This stress wave creates reflection, deflection at the free boundary and the corner of structure and forms a complex stress fields.

In this paper, the stress wave propagation of stiffened cylinder subjected to a strong acoustic wave is studied by both experimental and numerical methods. To confirm the validity of the numerical analysis, the dynamic stress fields for a I-form stiffener under a simple impact load history are compared with the dynamic photoelastic methodology. For the application to a more complex structure, the numerical analysis is carried out in two steps such as the macro and micro analyses by MSC/DYTRAN and MSC/NASTRAN. In macro analysis, the dynamic response of the whole structure is investigated. And the pressure history obtained from the analysis is used as the external dynamic load in the micro analysis. The stress wave propagation of the local stiffener is numerically analyzed for the micro method.

1. INTRODUCTION

The marine vessels are to be designed considering the impact caused by underwater explosion to maintain their functions. In the USA navy, it is regulated to conduct the shock test of the marine vessels under the explosion condition in the development phase. But the ship shock test is limited because of very high costs and environmental safety concerns. And analytic solutions are also limited to very simple cases of fluid-structure interaction problems[1]. Therefore, it is strongly recommended to develop an accurate numerical simulation technique.

In the nineties, a number of commercial softwares have been applied to resolve the interaction between fluid and structure, such as MSC/DYTRAN[2], LS/DYNA[3] and DYSMAS/ELC[4]. Recently, these hydrocodes have been also utilized in underwater explosion problems yielding good

agreement with analytic and experimental results[5].

In this study, the stress wave of stiffened cylinder is analysed by two steps such as the macro and micro analyses by MSC/DYTRAN and MSC/NASTRAN. In the macro analysis, fluid-structure interaction of stiffened cylinder subjected to underwater explosion load is investigated. For the validity of the macro analysis, the response of spherical body under simple plane wave and fluid-structure interaction of cylinder under a spherical wave by underwater explosion are analyzed and compared with analytic solution and experimental data.

In the micro analysis, the stress wave propagation of ring stiffener subjected to early shock pressure time history which is calculated in macro analysis is studied. To confirm the validity of the micro analysis, stress patterns of stiffener under simple load history obtained by the dynamic photoelastic methodology and numerical simulation are compared.

The preprocessor which links macro analysis to micro analysis is developed by using PCL(Patran Command Language). Fig. 1 shows the procedure of the study.

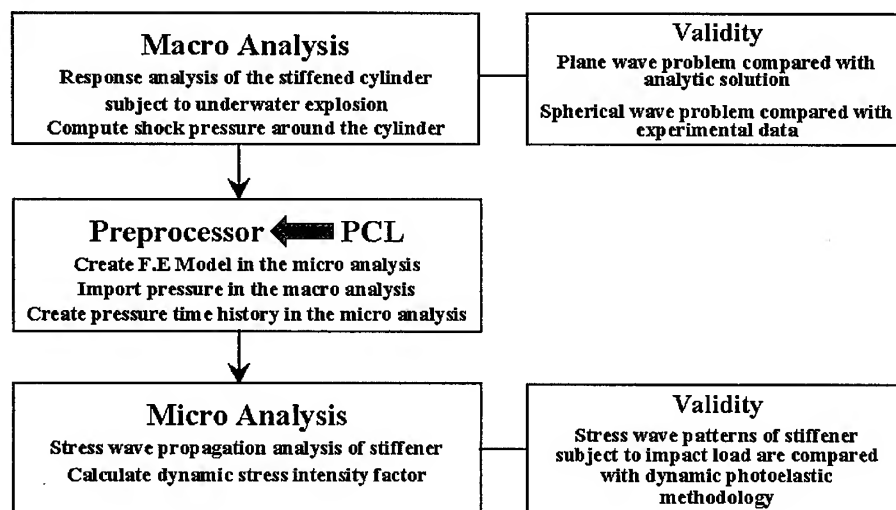


Fig. 1 Procedure diagram

2. MACRO ANALYSIS

2.1. Spherical shell/Plane step wave

To check the validity of macro analysis, an elastic response of a spherical shell subject to a plane step wave was numerically analyzed. Huang has solved this problem analytically, using a direct inverse Laplace transform to a finite number of terms of the infinite series expansion of the equations for the respective shells[6]. The same material properties and dimensionless procedures by Huang in his analysis were used for the numerical investigation.

Figure 2 shows the numerical model for the spherical shell/plane step wave problem. A quarter symmetry model consisting of 150 quadrilateral Lagrangian shell elements was generated. For this problem, the fluid-structure interaction was studied by a general coupling method of MSC/DYTRAN. Since this method requires the coupling surface forming a closed volume, 450 dummy elements were used to generate the surface. The fluid model which consists of 65,536 hexagonal Eulerian elements is a rectangle bounded by the planes $x=0$ and $x=4$, $y=0$ and $y=4$, and $z=4$ and $z=-4$, where the point $(0, 0, 0)$ represents the center of sphere and units are in terms of the radius of the sphere.

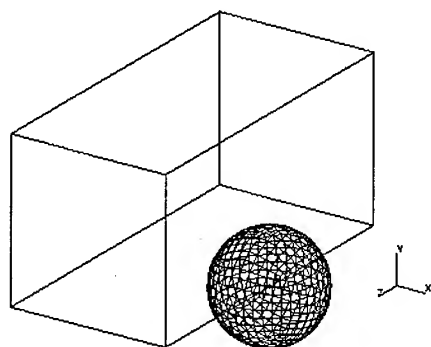


Fig. 2 Analysis model

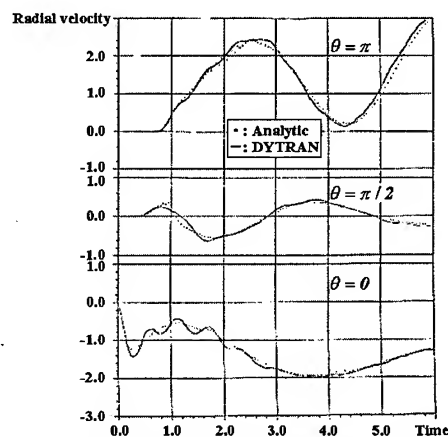


Fig. 3 Dimensionless radial velocity

The resulting transient solution for the radial velocity of the shell at azimuth angles of 0° , 90° , 180° are shown in Fig. 3. Huang's analytic solution for these same points is shown for comparison. Numerical result is in a quite good agreement with analytical solution.

2.2. Cylinder/Spherical shock wave

The response analysis of the cylinder in the infinite water medium subjected to spherical shock wave caused by an underwater explosion in consideration of the fluid-structure interaction was carried out numerically and compared with experimental result by Umemoto[7]. The model consisted of cylinder with diameter of 356mm and thickness of 25.5mm. The material of model was a steel. Also the explosive, Composition B, has mass of 23.8g. The distance from the center of the charge to the nearest point on the cylinder was 500mm for the side-on explosion.

As a fluid domain consists of explosive and water, the multi-material Euler volume elements have been used. The region where the explosive is initially located has been modeled fine to be able to accurately compute the detonation process. The water is modeled by a polynomial equation of state. The pressure depends on the density and explosive is modeled by the Jones-Wilkins-Lee(JWL) equation of state. For the consideration of the fluid-structure interaction, ALE(Arbitrary Lagrange Euler) coupling as well as general coupling was applied. Fig. 4 shows numerical analysis model.

To compare the results of the analysis with the experiment, the pressure time history of point P in Fig. 4 has been plotted in Fig. 5. From the results it is clear that MSC/DYTRAN is well suited to analyze underwater explosion problems.

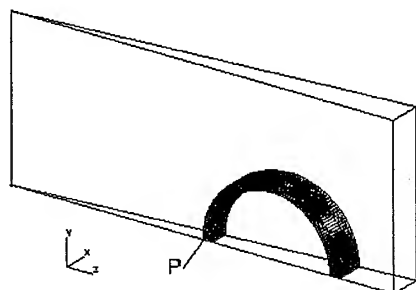


Fig. 4 Analysis model

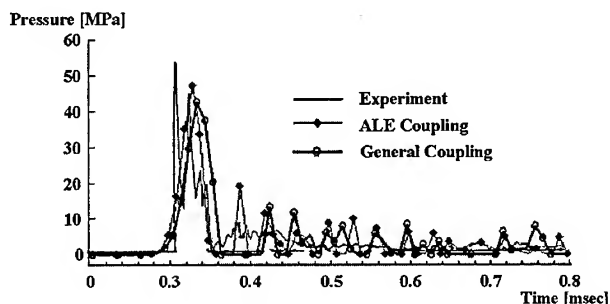


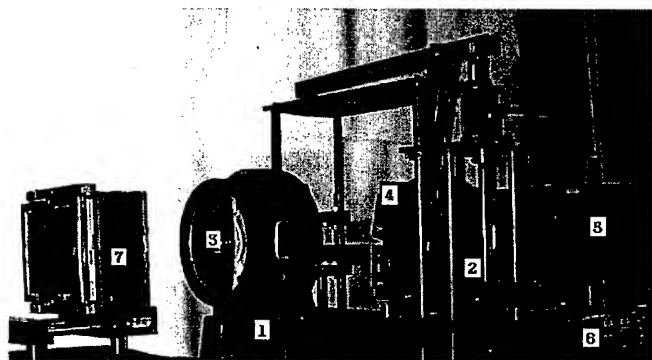
Fig. 5 Pressure time history of point P

3. MICRO ANALYSIS

3.1. Experiment

3.1.1. Multi-spark camera system

The dynamic photoelasticity method consists of the Cranz-Shardin camera system with a multi-spark camera set, a dynamic photoelastic apparatus, a loading equipment, circular polarized set, field lens and controller. A general view of the experimental apparatus is shown in Fig. 6. The spark time delay can be controlled by start delay and horizontal-vertical delay in the range from $1\mu\text{sec}$ to 0.1sec for each frame. The pulse time to high speed camera frame was measured by a optical detector to check the reliability of the framing rate.



1. Polarizer 2. Analyser 3. Field lens 4. Loading apparatus
5. Multi-spark high speed light source 6. Trigger controller 7. Screen

Fig. 6 A general view of dynamic photoelasticity experimental apparatus

3.1.2. Specimen and loading

To reveal the dynamic isochromatics fringe propagation phenomena, a polycarbonate (PC) as specimen material (Table 1) was used. The configuration of the test specimen is shown in Fig. 7. The dynamic impact loading was applied to the specimen by a free-fall tup with the Wheatston bridge circuit attached on it. The load trace is shown in Fig. 8.

Table 1. Material and physical properties of Polycarbonate

Poisson's ratio	0.38
Young's modulus, E(GPa)	2.72
Material stress optics fringe value(MPa-mm/fr)	6.7
Shear modulus(GPa)	0.98
Density (g/cm^3)	1.196
Dilatational wave speed (m/s)	1960
Distortional wave speed (m/s)	910

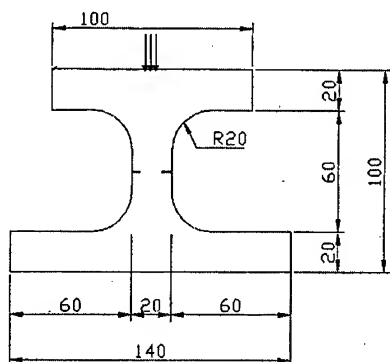


Fig. 7 Configuration of test specimen
(dimension : mm)

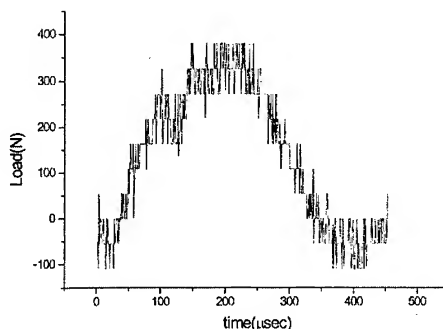


Fig. 8 Load vs. Time

3.2. Comparison numerical analysis with experiment

The stress wave propagation of stiffener is numerically analyzed by MSC/NASTRAN. To compare with experiment, same geometry, material properties and dynamic loading history were implicated. Assuming plane stress problem, stiffener model which consists of 12,800 quadrilateral shell element was used. The crack was modeled by CRAC2D element of MSC/NASTRAN. Also the stiffener was modeled by PCL (Patran Command Language). PCL is a fully functional computer programming language in the pre/post-processor MSC/PATRAN.

As the results, fringe plots of maximum shear stress are shown in Fig. 9. This figure shows the stress wave propagation through the stiffener. First, the compressive wave generated by dynamic impact loading was propagated (Fig 9a). When this compressive wave encounters a free surface, it reflects back as a tensile wave. This tensile wave causes the tensile tearing failure at the crack. The wave reflected at free edge is shown in Fig. 9b. Intensification of stress by tensile wave and 'butterfly shape' of stress fringe pattern at crack tip is as shown in Fig. 9b. It was observed that the stress distribution is similar with experimental results.

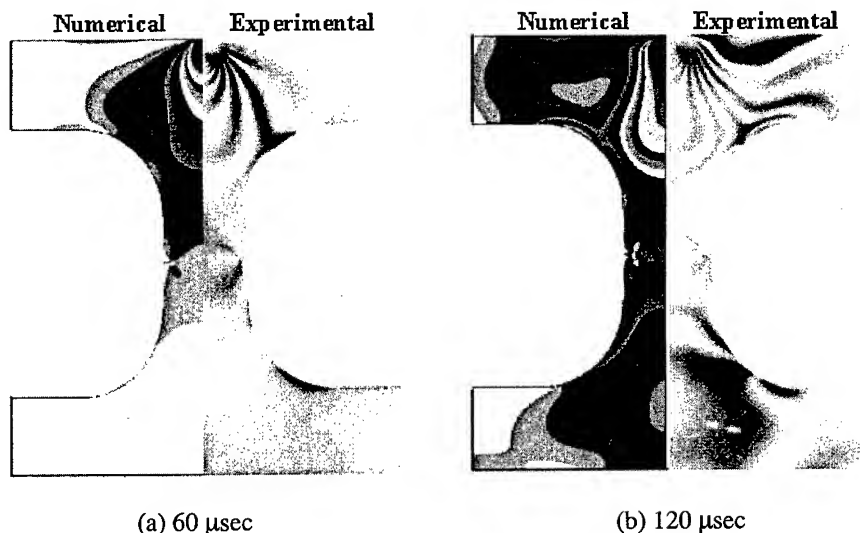


Fig. 9 Dynamic isochromatic fringe

4. CONCLUSION

Stress wave analysis of stiffened cylinder subjected to underwater explosion was investigated by two steps such as the macro and micro analyses. The macro analysis was performed to simulate an underwater explosion in consideration of fluid-structure interaction. The shock wave caused by an explosion was propagated in the water medium. It caused stress wave in the cylinder. Numerical results of macro analysis were in a quite good agreement with analytic solution and experimental result.

In the micro analysis, stress wave analysis of stiffener was investigated through experiment by dynamic photoelastic methodology and thorough numerical analysis with a finite element method. The reflected tensile wave by free edge and stress concentration at crack tip is investigated. Numerical results agree well with experimental results.

As the result of this study, it was confirmed that dynamic fracture analysis of structural members could be numerically performed by macro and micro analyses. Furthermore, it is suggested that the relationship between stress wave and deformation, stress wave-crack interaction and active regulation for relaxation of stress wave should be investigated to complete the study of stress wave interactive phenomena.

REFERENCES

1. H. Huang, J. of Applied Mechanics, 1970, pp. 1091-1099.
2. J. E. Chisum, Y. S. Shin, ASME PVP-Vol. 299, 1995.
3. J. Marco, Proceedings of the 67th Shock & Vibration Symposium, 1996.
4. H. J. Schittke, et al, Proceedings of the 60th Shock & Vibration Symposium, 1989.
5. K. S. Kim, et al, Proceedings of the Annual Autumn Meeting, the Society of Naval Architects of Korea, 1998. 11, pp. 390-394.
6. H. Huang, J. of the Acoustical Society of America, 1968 pp. 661-670.
7. K. Umemoto, et. al, J. of the Society of Naval Architects of Japan, 1998.

Element-Free Galerkin Methods for Fracture of Functionally-graded Materials

Jian Chen, Linzhi Wu and Shanyi Du

Institute of Composite Materials, Harbin Institute of Technology,
Harbin 150001, China P.R.

Keywords: Element-Free Galerkin Method EFGM, Functionally Graded Materials FGM, Moving Least-Squares MLS Method, Stress Intensity Factor

ABSTRACT

Since the material properties of the functionally graded materials (FGMs) vary continuously with the coordinates, it is difficult to analyze their mechanical behavior. The conventional finite element method (FEM) treats the nonhomogeneous materials as numerous homogeneous elements, so a very fine mesh is required to analyze FGMs. The element-free Galerkin method (EFGM) adopts the material properties of the integration point when analyzing the homogeneous or nonhomogeneous materials, so it has a good approximation to the actual material properties and requires fewer nodes. In addition, EFGM has no strict element concept and nodes can be distributed freely according to the need without remeshing. The moving least-squares interpolations can produce the continuous results, which have high derivatives. The numerical results show that EFGM has a higher efficiency, accuracy and flexibility to analyze FGMs.

1. INTRODUCTION

The material properties of the functionally graded materials (FGMs) are the functions of the coordinates, so the mechanical behavior is very complex. The analytical approach can only deal with some problems that the distribution of material properties and loads are simple and particular. Therefore, numerical methods have to be developed for the analyses of many practical problems.

Because the material properties in an element of the conventional FEM is constant, FEM often treats nonhomogeneous materials as numerous homogeneous elements and takes the material properties of some point (such as the center point) in the element as that of the whole element. Although it is convenient to form the element stiffness matrix, a very fine mesh is required to approximate the actual material properties. Li Chunyu and Zou Z.Z [1] recognized that this approach only takes the zero-order for the material property interpolations in the element and it couldn't improve the accuracy even with higher order displacement interpolations. In order to improve the numerical accuracy, they proposed a multi-isoparametric element method, in which the material property interpolations are the same as the displacement interpolations. In fact, adopting the actual material properties at every integration point in FEM is an especial multi-parametric element method, and it will improve the accuracy of FEM.

The element-free Galerkin method (EFGM) [2,3] is very suitable to analyze non-homogeneous materials such as FGMs. Firstly, the distributions of the nodes and the integral elements are very

free and independent. It is convenient for modeling the crack propagation. Secondly, the moving least-squares interpolations, which is not constrained by the element, can produce the local smooth approximation and lead to the continuous results which have high derivatives. Thirdly, EFGM adopts the material properties of the integration point when analyzing either homogeneous or nonhomogeneous materials. This has a good approximation to the actual material properties. The numerical results in the present work show that EFGM has a higher efficiency, accuracy and flexibility to analyze FGMs.

2. ELEMENT-FREE METHOD

Considering an elastic medium Ω bounded by the boundary Γ . The equilibrium equations and boundary conditions are as follows:

$$\sigma_{ij}n_j = \bar{t}_i \quad \text{on } \Gamma_t \quad (1)$$

$$\sigma_{ij,j} + b_i = 0 \quad \text{in } \Omega \quad (2)$$

$$u_i = \bar{u}_i \quad \text{on } \Gamma_u \quad (3)$$

where σ_{ij} is the stress tensor, which corresponds to the displacement field u_i , b_i is the body force vector, n_j is the outward unit normal components to the domain Ω . \bar{t}_i and \bar{u}_i denotes prescribed tractions and displacements on Γ_t and Γ_u , respectively.

In order to approximate the displacement, the interpolation basis function $\mathbf{p}^T(\mathbf{x})$ is defined first. Here, a linear polynomial basis $\mathbf{p}^T(\mathbf{x})$ is used. It is expressed as:

$$\mathbf{p}^T(\mathbf{x}) = (1, x, y) \quad (4)$$

Using the moving least-squares interpolation, the displacement interpolations are obtained as follows

$$u(\mathbf{x}) = \sum_{i=1}^n \phi_i(\mathbf{x}) \hat{u}_i \quad (5)$$

where the shape function $\phi_i(\mathbf{x})$ is defined by

$$\phi_i(\mathbf{x}) = \sum_{j=1}^m p_j(\mathbf{x}) [\mathbf{A}^{-1}(\hat{\mathbf{x}}) \mathbf{B}(\hat{\mathbf{x}})]_{ji} \quad (6)$$

$$\mathbf{A}(\hat{\mathbf{x}}) = \sum_{i=1}^n w(\hat{\mathbf{x}} - \mathbf{x}_i) \mathbf{p}(\mathbf{x}_i) \mathbf{p}^T(\mathbf{x}_i) \quad (7)$$

$$\mathbf{B}(\hat{\mathbf{x}}) = [w(\hat{\mathbf{x}} - \mathbf{x}_1) \mathbf{p}(\mathbf{x}_1), w(\hat{\mathbf{x}} - \mathbf{x}_2) \mathbf{p}(\mathbf{x}_2), \dots, w(\hat{\mathbf{x}} - \mathbf{x}_n) \mathbf{p}(\mathbf{x}_n)] \quad (8)$$

$w(\hat{\mathbf{x}} - \mathbf{x}_i) > 0$ is the nodal weight function. Here, the weight function is taken as

$$w(r_i) = \begin{cases} e^{-7s_i} \cos^k(\frac{\pi}{2} \cdot s_i^2) & (r_i \leq r_m^{\frac{1}{2}}) \\ 0 & (r_i > r_m^{\frac{1}{2}}) \end{cases} \quad (9)$$

in which k is a positive integer (here $k = 2$); $s_i = r_i / r_m^{\frac{1}{2}}$ is a normalized radius; $r_i = \|\hat{\mathbf{x}} - \mathbf{x}_i\|$;

r_m^* is the radius of the compact support domain for \hat{x} .

The partial derivatives of $\phi_i(x)$ can be obtained as follows:

$$\phi_{,k} = \mathbf{p}_{,k}^T \mathbf{A}^{-1} \mathbf{B} + \mathbf{p}^T \mathbf{A}_{,k}^{-1} \mathbf{B} + \mathbf{p}^T \mathbf{A}^{-1} \mathbf{B}_{,k} \quad (10)$$

$$\mathbf{A}_{,k}^{-1} = -\mathbf{A}^{-1} \mathbf{A}_{,k} \mathbf{A}^{-1} \quad (11)$$

Using the variational principle, the total discrete equation can be obtained. In this paper, we adopt the following variational principle

$$\int_{\Omega} \delta \varepsilon_{ij} \sigma_{ij} d\Omega - \int_{\Omega} \delta u_i b_i d\Omega - \int_{\Gamma_t} \delta u_i \bar{t}_i d\Gamma_i + 2\alpha \int_{\Gamma_u} \delta u_i (u_i - \bar{u}_i) d\Gamma_u = 0 \quad (12)$$

in which α is a constant much greater than 1. The final discrete equation can be written as

$$\mathbf{K} \mathbf{u} = \mathbf{f} \quad (13)$$

and \mathbf{K} and \mathbf{f} consist of 2×2 submatrices \mathbf{K}_{IJ} and 2×1 submatrices \mathbf{f}_I , respectively, given by

$$\mathbf{K}_{IJ} = \int_{\Omega} \mathbf{B}_I^T \mathbf{D} \mathbf{B}_J d\Omega + 2\alpha \int_{\Gamma_u} \Phi_I^T \mathbf{S} \Phi_J d\Gamma_u \quad (14)$$

$$\mathbf{f}_I = \int_{\Gamma_t} \Phi_I \bar{t} d\Gamma_t + \int_{\Omega} \Phi_I b d\Omega + 2\alpha \int_{\Gamma_u} \Phi_I^T \mathbf{S} \bar{\mathbf{u}} d\Gamma_u \quad (15)$$

where

$$\mathbf{D}(x, y) = \frac{\bar{E}(x, y)}{1 - \bar{\nu}^2(x, y)} \begin{bmatrix} 1 & \bar{\nu}(x, y) & 0 \\ \bar{\nu}(x, y) & 1 & 0 \\ 0 & 0 & (1 - \bar{\nu}(x, y))/2 \end{bmatrix} \quad (16)$$

$$\mathbf{B}_I = \begin{bmatrix} \phi_{I,x} & 0 \\ 0 & \phi_{I,y} \\ \phi_{I,y} & \phi_{I,x} \end{bmatrix} \quad (17)$$

$$\Phi_I = \begin{bmatrix} \phi_I & 0 \\ 0 & \phi_I \end{bmatrix} \quad (18)$$

$$\mathbf{S} = \begin{bmatrix} s_x & 0 \\ 0 & s_y \end{bmatrix} \quad (19)$$

and

$$s_i = \begin{cases} 1 & \text{if prescribed } u_i \text{ on } \Gamma_u \\ 0 & \text{if no prescribed } u_i \text{ on } \Gamma_u \end{cases} \quad (20)$$

$$\bar{E}(x, y) = \begin{cases} E(x, y) & \text{planestress} \\ \frac{E(x, y)}{1 - \nu^2(x, y)} & \text{planestrain} \end{cases} \quad (21)$$

$$\bar{\nu}(x, y) = \begin{cases} \nu(x, y) & \text{plane stress} \\ \frac{\nu(x, y)}{1 - \nu(x, y)} & \text{plane strain} \end{cases} \quad (22)$$

in which $E(x, y)$ and $\nu(x, y)$ are Young's modulus and Poisson's ratio at the integration point, respectively.

3. NUMERICAL EXAMPLES

Consider a single edge-cracked FGM plate under uniform strain ε or stress σ along the y direction far away from the crack region described in Fig. 1. W and a are the width of the plate and the edge crack, respectively. In this paper, $W = 1$ m, $l = 4$ m, and $a = 0.2$ m \sim 0.6 m. Poisson's ratio is taken as constant and Young's modulus is described by:

$$E(x) = E_0 e^{\beta x} \quad (23)$$

where β is a positive or negative constant.

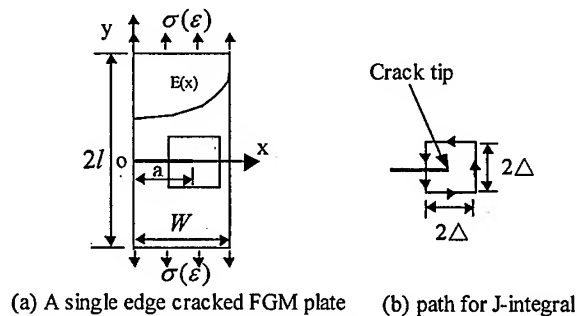


Fig. 1 Problem statement for a single edge cracked FGM plate

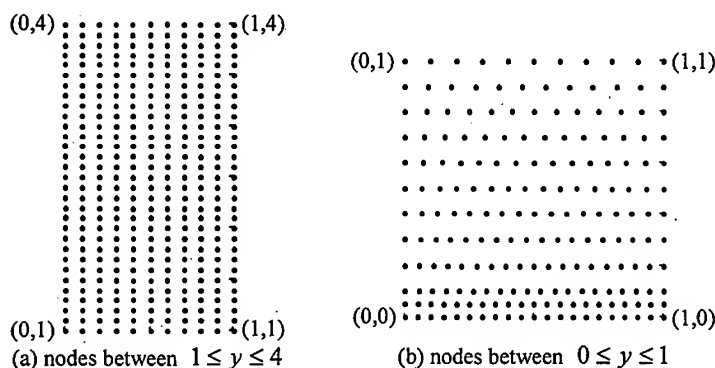


Fig.2 Node distribution for the FGM plate

Because of the symmetry of geometry and load, it is a mode I crack problem, and we will evaluate its stress intensity factor K_I under the plane strain condition. Erdogan [4] has given the analytical values of K_I when $l \rightarrow \infty$. According to the Saint Venant principle, there is little difference between the present model and one investigated by Erdogan [4], and we can use

them to check the accuracy of the results obtained by EFGM.

Symmetry conditions are imposed on the edge of $y = 0$, and the load ε or σ is applied on the upper edge of $y = 4$.

The distribution of 527 nodes is given in Fig. 2: Coarse nodes are distributed uniformly between $1 \leq y \leq 4$; Fine nodes are distributed between $0 \leq y \leq 1$. The domain between $0.5 \leq y \leq 4$ was subdivided into 10×35 square integral subdomain and the domain between $0 \leq y \leq 0.5$ was subdivided into 20×10 square integral subdomains. 5×5 Gauss quadrature is adopted inside every integral subdomain.

During the whole procedure, we remain the same distribution of nodes and integral subdomains. Therefore, we just form the whole stiffness matrix once for a special material parameter β and then modify the whole stiffness matrix according to the position of the crack tip. This greatly reduces the numerical costs.

For the mode I crack problem of homogeneous materials, the J integral is often used to evaluate the SIFs because of its integral path independence and high accuracy. When the J-integral path is very close to the crack tip of FGMs, the influence of the nonhomogeneity could be neglected. When J is obtained, we can get the SIFs from $J = K_I^2 / E$ (for plane stress) or $J = K_I^2 (1 - \nu^2) / E$ (for plane strain). Here, E and ν are Young's modulus and Poisson's ratio at the crack tip, respectively.

The stress intensity factor is normalized as

$$K_I = K_1 / (\sigma_i \sqrt{\pi a}) \quad (24)$$

in which $\sigma_i = \sigma$ for the load σ and $\sigma_i = E\varepsilon / (1 - \nu^2)$ for the load ε .

The numerical results and its corresponding analytical or approximate values are stipulated in Table 1 and 2. In these tables, a is the crack length; K_I corresponds to the numerical results with $l = 4$ obtained by EFGM in this paper; K_I^* are the analytical results obtained with $l \rightarrow \infty$ by Erdogan [4]; and K_I^{**} are the results obtained from the following approximate equation [5].

$$K_I^{**} = \left[1.99 - 0.41\left(\frac{a}{W}\right) + 18.70\left(\frac{a}{W}\right)^2 - 38.48\left(\frac{a}{W}\right)^3 + 53.85\left(\frac{a}{W}\right)^4 \right] / \sqrt{\pi} \quad (25)$$

Table 1. Normalized SIF K_I for an edge crack in a FGM plate under ε

a		0.2	0.3	0.4	0.5	0.6
$\beta = \ln(0.1)$	K_I	1.2961	1.4919	1.7962	2.2594	3.0544
	K_I^*	1.2963	1.5083	1.8246	2.3140	3.1544
$\beta = \ln(0.2)$	K_I	1.3145	1.5283	1.8659	2.3877	3.2910
	K_I^*	1.3058	1.5330	1.8751	2.4031	3.2981
$\beta = \ln(1)$	K_I	1.3951	1.6776	2.1337	2.8626	4.1544
	K_I^{**}	1.3734	1.6627	2.1065	2.8297	4.0301
$\beta = \ln(5)$	K_I	1.5414	1.9499	2.6238	3.7429	5.7936
	K_I^*	1.4946	1.9118	2.5730	3.6573	5.5704
$\beta = \ln(10)$	K_I	1.6296	2.1206	2.9398	4.3272	6.9171
	K_I^*	1.5740	2.0723	2.8736	4.2140	6.6319

Table 2. Normalized SIF K_I for an edge crack in a FGM plate under σ

a		0.2	0.3	0.4	0.5	0.6
$\beta = \ln(0.1)$	K_I	1.3193	1.8642	2.5588	3.5213	5.0726
	K_I^*	1.2965	1.8581	2.5699	3.5701	5.1880
$\beta = \ln(0.2)$	K_I	1.4188	1.8497	2.4486	3.3234	4.7860
	K_I^*	1.3956	1.8395	2.4436	3.3266	4.7614
$\beta = \ln(1)$	K_I	1.3951	1.6776	2.1337	2.8626	4.1544
	K_I^{**}	1.3734	1.6627	2.1065	2.8297	4.0301
$\beta = \ln(5)$	K_I	1.1622	1.3899	1.7746	2.4125	3.5736
	K_I^*	1.1318	1.3697	1.7483	2.3656	3.4454
$\beta = \ln(10)$	K_I	1.0324	1.2499	1.6146	2.2234	3.3371
	K_I^*	1.0019	1.2291	1.5884	2.1762	3.2124

The present numerical results in Table 1 and 2 coincide with the analytical results obtained by Erdogan or the approximate results, and they reveal the relationship between the SIFs and the graduation of the elastic properties. Under the uniform strain ε , the more the latter is, the more the former will increase; under the uniform tension σ , the trend is opposite. The little difference between the numerical results and the analytical or approximate values show that EFGM has high accuracy and flexibility to analyze FGMs and its efficiency is not influenced by the continuous variation of the nonhomogeneous material properties.

4. CONCLUSION

The FGM plate with an edge crack is studied by using EFGM. The accurate results reveal that the efficiency and flexibility of EFGM isn't influenced by the continuous and gradient variation of the material properties with the coordinates. It is convenient and accurate to obtain the relationship between the graduation of the material properties and the stress intensity factor. While using the conventional FEM to analyze FGMs, a great number of nodes and elements are often needed, and it is still difficult to obtain the accurate results. It is expected that EFGM will be more widely used to analyze the mechanical problem of FGMs.

REFERENCES

1. Chunyu Li, Zhenzhu Zou, Int. J. Pressure Vessels and Piping, **75** (1998) p.499
2. Belytschko T, Lu Y Y, Gu L, International Journal for Numerical Methods in Engineering, **37** (1994) p.229
3. Lu Y Y, Belytschko T, Gu L, Computer Methods in Applied Mechanics and Engineering, **113** (1994) p.397
4. F. Erdogan, B.H. Wu, Journal of Applied Mechanics, **64** (1997) p.449
5. Chenkang Shen, Fracture Mechanics, the publishing house of Tongji University, 1996

A Study on the Shape Design and Contact Characteristic of Wheel-Rail for Rolling Stock

K.D. Sung¹, W.H. Yang² and M.R. Cho³

¹ Graduate School of Mechanical Engineering, SungKyunKwan University,
KyungGi-Do, Suwon 440-746, Korea

² School of Mechanical Engineering, SungKyunKwan University,
KyungGi-Do, Suwon 440-746, Korea

³ Department of Mechanical Design, Induk College, Wolgae-Dong, Seoul 139-749, Korea

Keywords: Contact Stress Distribution, Optimum Design, Rolling Stock, Wheel-Rail Contact

ABSTRACT

One of the main causes of severe wear or crack initiation in wheel and rail is the contact stress due to the wheel-rail contact. Firstly, we obtain contact stress due to the rail mounting slope using the finite element method. Secondly, the shape design based on more reasonable contact stress analysis rather than a general Hertzian contact theory is investigated in order to reduce the contact stress. The optimum design is performed using the simple 2-D finite element model and its results are verified by 3-D finite element analysis.

1. INTRODUCTION

The rolling stock is a prominent transportation system characterizing safe, speedy and mass transport. Especially, the safety is necessary to its running. The most important thing of rolling stock, from a safe point of view, is the wheel-rail interaction as the fundamental condition of running.

A significant number of accidents of rolling stock are caused by the failure of wheel and rail. In many cases they are occurred by the severe wear and the crack propagation of wheel and rail. So, many researchers are investigating this subject by fracture mechanics to prevent catastrophic accidents. However, the fundamental way to reduce the severe wear or the crack initiation in wheel and rail is to lower contact stress due to the wheel-rail contact.

Recently, the need to perform this kind of research is growing as the axle loads increase. Now, many researchers have been carrying out a study[1-3] on the shape design. However, the former works were based upon the Hertzian contact theory[4] in order to obtain the contact stress distribution due to the wheel-rail contact. But since the actual geometry of wheel and rail is different from the theoretical one, the contact stress distribution due to the wheel-rail contact is likely to differ from that of the Hertzian contact.

Therefore, in this paper, the contact characteristic between SSW1 wheel and 60kg rail is investigated, and the variation of contact stress due to rail mounting slope used at present is studied in order to reduce contact stress. Also, the shape design based upon more reasonable contact stress distribution rather than a general Hertzian contact theory is investigated. The shape optimization is performed using a simple 2-D finite element model and then its results are verified by 3-D finite element analysis.

2. Finite element analysis (3-D contact stress distribution)

2.1 Analysis model and method

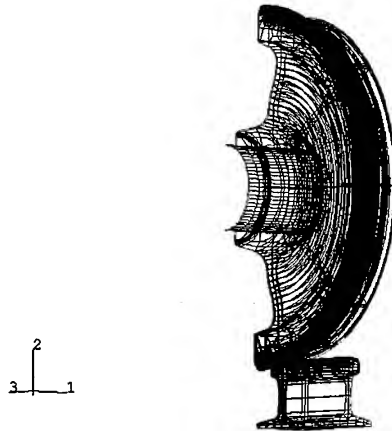


Fig. 1. Finite element mesh for wheel-rail contact

As the material properties of wheel and rail employed in this analysis, Young's modulus(E) is 206 GPa and Poisson's ratio(ν) is 0.3. The finite element model of wheel and rail is shown in the Fig. 1, where it exploits symmetry about the running direction, so the half model is considered

The fixed boundary condition is applied to the bottom of rail, the load is assumed to act on the center of axle and then the displacement control is employed. It is assumed that the wheel as an elastic body and an axle as a rigid body are in contact with each other since the wheel and the axle are assembled by force/shrink fit, so contact surface is able to be kept being in contact. In the contact surface of wheel-rail contact, the coefficient of friction(μ) is 0.25. PATRAN Ver.7.0 has been used for the modelling and the commercial finite element code ABAQUS Ver.5.8 has been used for the finite element analysis.

2.2 Result of finite element analysis (Rail mounting slope=0)

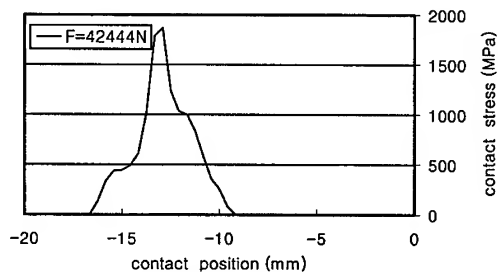


Fig. 2. Contact stress distribution about the lateral direction

The contact stress distribution, when the magnitude of axle load is 42,444N, is given in the Fig. 2 and Fig. 3. Fig. 2 shows the one about the lateral direction of rail and Fig. 3 gives one about longitudinal direction of rail. In all the graphs, the contact position is the distance between the center of rail head as zero and the contact point.

As shown in the Fig. 2 and Fig. 3, the fact that the contact stress distribution about the lateral direction differs from half elliptical one and the contact stress distribution about the longitudinal direction is similar to that of theory is known. The reason why the contact stress distribution about the lateral direction is not half elliptical distribution is thought as fact that the slope of wheel tread exists and the contact position of rail head is eccentric from the central point of radius of curvature.

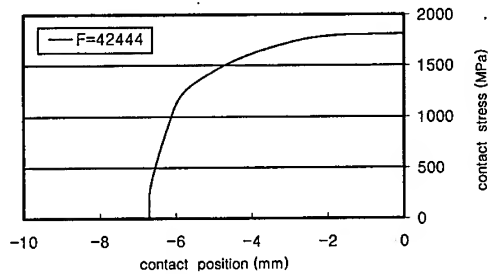


Fig. 3. Contact stress distribution about the longitudinal direction

2.3 Result of contact stress analysis due to the rail mounting slope(γ)

Generally, $1/40$ or $1/20$ slope is used for the rail mounting slope in order to reduce contact stress. Selecting this slope depends on the type of wheel and rail. This is because determination of the mounting slope is related to the wheel tread slope and the radius of curvature of rail head.

In this study, contact stress between the wheel and the rail is analyzed when the mounting slope is $1/40$ and $1/20$, respectively. Analysis method is the same as mentioned in section 2.1.

Fig. 4 and Fig. 5 show contact stress distributions in lateral directions when the mounting slope is $1/40$ and $1/20$, respectively. When the result of $1/40$ is compared with 0 and $1/20$, the contact stress distribution in case of $1/40$ is almost half elliptical one. This is, in case of $1/40$, because the initial contact position is located at the center of rail head and the contact condition is similar to that of the Hertzian contact.

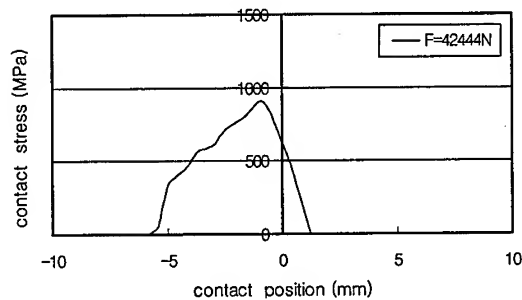


Fig. 4. Contact stress distribution in lateral direction ($\gamma=1/40$)

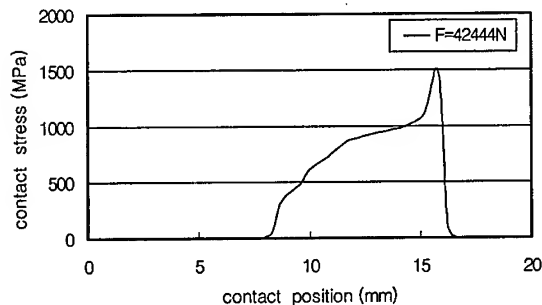


Fig. 5. Contact stress distribution in lateral direction ($\gamma=1/20$)

Comparison of the maximum contact stress due to the rail mounting slopes (0, 1/40, and 1/20) is shown as Table 1. As in Table 1, contact stress of rail with rail mounting slope can be reduced much more than one without rail mounting slope. And, In case of SSWI wheel and 60kg rail, rail mounting slope 1/40 has to be selected in order to reduce contact stress.

Table 1. Comparison of the maximum contact stress due to the rail mounting slope

	Maximum contact stress (Mpa)	Reduction ratio (%)
No rail mounting slope	1810	
Rail mounting slope 1/40	903.3	50.1
Rail mounting slope 1/20	1483	18.1

3. Optimum design

3.1 Introduction to optimization

In this paper, the design variables for the optimum design are the wheel tread slope, the radius of curvature of rail head (R) and rail mounting slope (γ), which greatly affect on the contact stress distribution due to the wheel-rail contact. The objective function is to minimize the maximum contact stress. The constraint for the optimum design is that initial contact position of wheel-rail contacts in $\pm 15\text{mm}$ at rail head center. They constrain the initial contact position and mean the model should be analyzed considering manufacturing process.

Since 3-D analysis is very difficult due to its much time-consuming, analytical invalidity and modeling of design variables, a simple 2-D analytical model is presented to perform the optimization. SUMT (Sequential Unconstrained Minimization Technique) algorithm is used this optimum design.

3.2 Validity of a simple 2-D analysis model

Fig. 6 gives a 2-D finite element model used in the optimum design, in which the rail is modelled as an elastic body and the wheel is modelled as a rigid element having the slope of wheel tread slope in practice. The fixed boundary condition is applied to the bottom of rail and the load acts on the rail head by moving the rigid element.

The advantages of optimum design using this analysis model are to increase the efficiency of optimization time, overcome the problem of the initial contact point caused by the variety of design variables and simplify a finite element model with the variety of design variables.

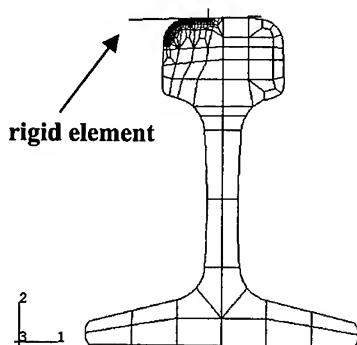
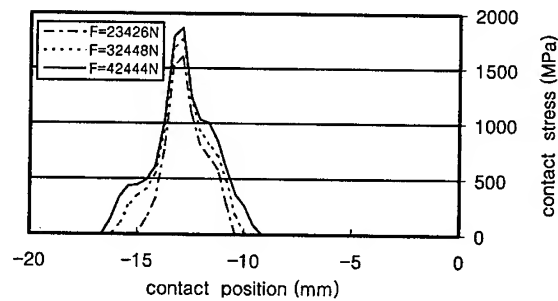
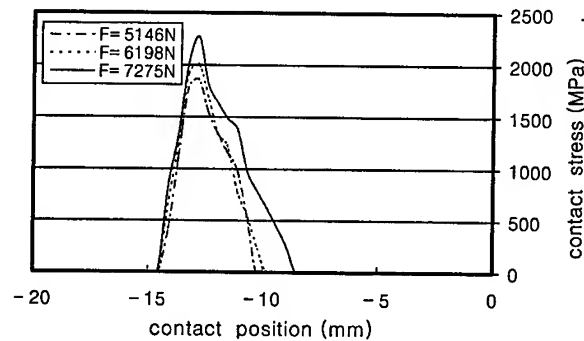


Fig. 6. Finite element mesh for optimization design

Fig. 7 shows the graph which presents the validity of optimum design using a 2-D model. Fig. 7(a) shows the contact stress distribution about the lateral direction of rail using 3-D finite element analysis mentioned above and Fig. 7(b) shows the result using finite element analysis of a 2-D model for optimum design. Of course, although two analyses are not performed under the same loading conditions, the contact stress distribution of two analyses are similar to each other due to the relative variety of load provided that the contact areas are about the same. In addition, the positions of maximum contact stress are similar to each other. This study focuses on the fact that the variety of contact stress distribution resulted using a 2-D analysis will show the same tendency with one resulted using a 3-D analysis according to the relative variety of load. Therefore, in this optimum design, we are going to analyze this model, based upon the fact that the results by a 2-D model give a good agreement with those by a 3-D model.



(a)



(b)

Fig. 7. Contact stress about the contact position
(a) 3-D F. E. analysis (b) 2-D F. E. analysis

3.3 Result of Optimization and Conclusion

During the analysis, the shape ($R=13$) of gage corner in the rail head is kept as it was since this optimization is considered in the straight running condition. As the results of optimum design, conclusions are as follows.

1. The larger is the radius of curvature of the rail head, the lower is contact stress. This result is predictable since the contact area became larger.
2. In the current 60kg rail, the maximum contact stress is greatly reduced by removing the portion of $R=50$ and lengthening the portion of $R=600$ to the gage corner, the portion of $R=13$.
3. In the current 60kg rail, after lengthening the portion of $R=600$ to the gage corner (the portion of $R=13$) with the portion of $R=50$ removed, in case of the rail mounting slope $1/40$ and the wheel tread slope $1/20$, contact stress can be most reduced.

4. 3-D finite element analysis for the results of optimization

In the results of optimum design, 3-D finite element analysis for two cases is performed, respectively. The method to analyze them is the same as one by 3-D finite element analysis mentioned above and their results are shown in Table 2.

Case 1. Rail having $R=600$ lengthening to $R=13$ without rail mounting slope and SSW1 wheel (wheel tread slope $1/40$).

Case 2. Rail having $R=600$ lengthening to $R=13$ with rail mounting slope $1/40$ and wheel with wheel tread slope $1/20$.

Table 2. Comparison of the maximum contact stress

	Maximum contact stress (MPa)	Reduction ratio (%)
SSW1 wheel - 60kg rail	1810	
Case 1	964.8	46.7
Case 2	876.9	51.6

5. Conclusion

3-D finite element method is used in order to obtain the contact stress distribution between the wheel and rail due to the rail mounting slope, and the optimization technique is employed to reduce contact stress. Conclusions are as follows.

1. The contact stress distribution about the lateral direction of rail is not half elliptical one while one about the longitudinal direction is half elliptical one.
2. In case of SSW1 wheel and 60kg rail, $1/40$ is more favorable slope for the rail mounting slope in order to reduce contact stress.
3. A simple 2-D model is introduced to optimize the wheel tread slope, the radius of curvature of rail head and the rail mounting slope that greatly affect on contact stress.
4. In the current 60kg rail profile, the maximum contact stress is greatly reduced by removing the portion of $R=50$ and lengthening the portion of $R=600$ to the gage corner, the portion of $R=13$.
5. The best way to reduce contact stress is to lengthen $R=600$ to the portion of $R=13$ with the rail mounting slope $1/40$ and then to change the wheel tread slope of SSW1 from $1/40$ to $1/20$.
6. This method of optimum design using a simple 2-D model is able to be similarly applied to the different kind of wheel and rail.

ACKNOWLEDGEMENTS

The authors are grateful for the support provided by a grant from the Korea Science & Engineering Foundation (KOSEF) and the Safety & Structural Integrity Research Center at the Sung Kyun Kwan University.

REFERENCES

1. R. Smallwood, An optimization technique to minimize rail contact stresses, *Wear* 144(1991), 373-384
2. John F. Leary, Development of freight car wheel profiles - a case study, *Wear* 144(1991), 353-362
3. Yoshihiko Sato, Design of rail head profiles with full use of grinding, *Wear* 144(1991), 363-372
4. K. L. Johnson, Contact mechanics, Cambridge University press(1985), 84-106
5. L. Ramanan, R. Krishna Kumar, R. Sriraman, Thermo-mechanical finite element analysis of a rail wheel, *International Journal of Mechanical Sciences* 41(1999), 487-505
6. Chung-Kyun Kim, Ki-Hwan Kim, Finite element analysis on the stress distributions in rail-wheel contacts of high speed trains, *Journal of KSTLE* Vol. 13, No.3(1997), 93-101
7. S. Bogdanski, M. Olzak, J. Stupnicki, Numerical modelling of a 3D rail RCF 'squat'-type crack under operating load, *Fatigue & Fracture of Engineering Materials & Structures* 21(1998), 923-935

Stress Analysis of Toroidal Hole in an Infinite Body

T. Matsuo¹ and N.-A. Noda²

¹Department of Mechanical Engineering, Fukushima National College of Technology,
30 Nagao, Kamiarakawa Taira, Iwaki, Fukushima 970-8034, Japan

²Department of Mechanical Engineering, Kyushu Institute of Technology,
1-1 Sensui-cho, Tobata, Kitakyushu, Fukuoka 804-8550, Japan

Keywords: Body Force Method, Elasticity, Numerical Analysis, Singular Integral Equation, Stress Concentration Factor, Toroidal Hole

ABSTRACT

This paper deals with stress analysis of toroidal hole in an infinite body under uniform tension. The problem is formulated as a system of singular integral equation with Cauchy-type singularity, where the densities of body forces distributing in the r - and z - directions are unknown functions. In order to satisfy the boundary conditions along the hole boundary, eight kinds of fundamental density functions are introduced in the similar way of previous papers treating plane stress problems. Then the body force densities are approximated by a linear combination of those fundamental density functions and polynomials. In the analysis, shape of toroidal hole is varied systematically; then, the magnitude and position of the maximum stress are shown in tables. The stress distributions along the boundary are shown in figures. The accuracy of the present analysis is verified by comparing the present results with the results obtained by the conventional method. It is found that this method gives rapid convergence numerical results for the stress distribution along the boundary and stress concentration factors of toroidal hole are close to stress concentration factors of notched round bar and deep notch when $a/d \rightarrow 1$.

1. Introduction

It is known that most engineering materials contain some defects in the form of holes, cavities and inclusions. To evaluate the effect of defects on the strength of structures, it is important to know the stress concentration of defects in a material. Therefore, a lot of useful results of 3-D stress concentration problems have been obtained by applying suitable numerical methods. For example, stress concentration problems of one and two spherical cavities were treated by several researchers [1-3]. However, there is few analyses for more than one ellipsoidal cavity is in a material. Because the degree of stress concentration depends on the shape, size, location of the ellipsoidal cavity, the

loading conditions and other factors.

In preceding paper the authors have considered ellipsoidal cavities using singular integral equations of the body force method [4]. This method can be applied to the analysis of various shapes and spacing of ellipsoidal cavities. In this paper, the method will be applied to a stress concentration problem of toroidal hole. Then, stress concentration factor is calculated when the shape of toroidal hole is varied systematically. The stress concentration factor of toroidal hole is compared with stress concentration factor of notched round bar and deep notch.

2. Numerical Solution for Singular Integral Equations

Consider an infinite body having a toroidal hole under uniform z-direction tension as shown in Fig. 1. The problem is formulated in terms of singular integral equations, that is the stress field at an arbitrary point ($r=d+a \cos \psi, z=b \sin \psi$) when two ring forces act on another points ($\rho=d+a \cos \alpha, \zeta=\pm b \sin \alpha$) in an infinite body [5]. The formation is simply based on the principle of superposition. The integral equation is expressed by eq. (1), where the body force densities distributed along the prospective boundaries in the r-, z-directions are to be unknown functions.

$$\begin{aligned}
 & -(1/2)\{\rho_r^*(\psi) \cos \psi_0 + \rho_z^*(\psi) \sin \psi_0\} + \int_{-\pi/2}^{\pi/2} K_{nn}^{Fr}(\alpha, \psi) \rho_r^*(\alpha) ds \\
 & \quad + \int_{-\pi/2}^{\pi/2} K_{nn}^{Fz}(\alpha, \psi) \rho_z^*(\alpha) ds = -\sigma_z^\infty \sin^2 \psi_0 \\
 & -(1/2)\{-\rho_r^*(\psi) \sin \psi_0 + \rho_z^*(\psi) \cos \psi_0\} + \int_{-\pi/2}^{\pi/2} K_{nt}^{Fr}(\alpha, \psi) \rho_r^*(\alpha) ds \\
 & \quad + \int_{-\pi/2}^{\pi/2} K_{nt}^{Fz}(\alpha, \psi) \rho_z^*(\alpha) ds = -\sigma_z^\infty \sin \psi_0 \cos \psi_0
 \end{aligned} \tag{1}$$

ψ_0 is an angle between the r-axis and the normal direction at the point (r,z). Equation (1) is virtually the boundary conditions at the imaginary boundary. The first terms of eq. (1) represent the stress due to the body force distributed on the \ominus boundary. The \ominus boundary means the imaginary boundary composed of the internal points that are infinitesimally apart from the initial boundary [6, 7].

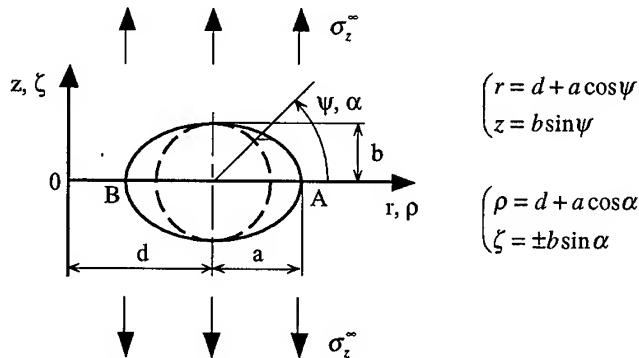


Fig. 1 Toroidal hole in an infinite body.

To solve eq. (1) is to determine the body force densities $\rho_r^*(\alpha), \rho_z^*(\alpha)$ in the region of $-\pi/2 < \alpha < \pi/2$. Here, consider auxiliary functions $\rho_{r1}^*(\phi_k) \sim \rho_{r4}^*(\phi_k)$ and $\rho_{z1}^*(\phi_k) \sim \rho_{z4}^*(\phi_k)$ defined by eqs.

(2), (3) instead of densities $\rho_r^*(\alpha), \rho_z^*(\alpha)$.

$$\rho_{r1}^*(\alpha) = \{\rho_r^*(\alpha) + \rho_r^*(\pi - \alpha) + \rho_r^*(\pi + \alpha) + \rho_r^*(-\alpha)\} / 4 \quad (2.a)$$

$$\rho_{r2}^*(\alpha) = \{\rho_r^*(\alpha) + \rho_r^*(\pi - \alpha) - \rho_r^*(\pi + \alpha) - \rho_r^*(-\alpha)\} / 4 \quad (2.b)$$

$$\rho_{r3}^*(\alpha) = \{\rho_r^*(\alpha) - \rho_r^*(\pi - \alpha) - \rho_r^*(\pi + \alpha) + \rho_r^*(-\alpha)\} / 4 \quad (2.c)$$

$$\rho_{r4}^*(\alpha) = \{\rho_r^*(\alpha) - \rho_r^*(\pi - \alpha) + \rho_r^*(\pi + \alpha) - \rho_r^*(-\alpha)\} / 4 \quad (2.d)$$

$$\rho_{z1}^*(\alpha) = \{\rho_z^*(\alpha) + \rho_z^*(\pi - \alpha) + \rho_z^*(\pi + \alpha) + \rho_z^*(-\alpha)\} / 4 \quad (3.a)$$

$$\rho_{z2}^*(\alpha) = \{\rho_z^*(\alpha) + \rho_z^*(\pi - \alpha) - \rho_z^*(\pi + \alpha) - \rho_z^*(-\alpha)\} / 4 \quad (3.b)$$

$$\rho_{z3}^*(\alpha) = \{\rho_z^*(\alpha) - \rho_z^*(\pi - \alpha) - \rho_z^*(\pi + \alpha) + \rho_z^*(-\alpha)\} / 4 \quad (3.c)$$

$$\rho_{z4}^*(\alpha) = \{\rho_z^*(\alpha) - \rho_z^*(\pi - \alpha) + \rho_z^*(\pi + \alpha) - \rho_z^*(-\alpha)\} / 4 \quad (3.d)$$

These new functions $\rho_{r1}^*(\phi_k) \sim \rho_{r4}^*(\phi_k)$ and $\rho_{z1}^*(\phi_k) \sim \rho_{z4}^*(\phi_k)$ must satisfy eqs. (4), (5) because of the definition (4), (5).

$$\rho_{r1}^*(\alpha) = \rho_{r1}^*(\pi - \alpha) = \rho_{r1}^*(\pi + \alpha) = \rho_{r1}^*(-\alpha) \quad (4.a)$$

$$\rho_{r2}^*(\alpha) = \rho_{r2}^*(\pi - \alpha) = -\rho_{r2}^*(\pi + \alpha) = -\rho_{r2}^*(-\alpha) \quad (4.b)$$

$$\rho_{r3}^*(\alpha) = -\rho_{r3}^*(\pi - \alpha) = -\rho_{r3}^*(\pi + \alpha) = \rho_{r3}^*(-\alpha) \quad (4.c)$$

$$\rho_{r4}^*(\alpha) = -\rho_{r4}^*(\pi - \alpha) = \rho_{r4}^*(\pi + \alpha) = -\rho_{r4}^*(-\alpha) \quad (4.d)$$

$$\rho_{z1}^*(\alpha) = \rho_{z1}^*(\pi - \alpha) = \rho_{z1}^*(\pi + \alpha) = \rho_{z1}^*(-\alpha) \quad (5.a)$$

$$\rho_{z2}^*(\alpha) = \rho_{z2}^*(\pi - \alpha) = -\rho_{z2}^*(\pi + \alpha) = -\rho_{z2}^*(-\alpha) \quad (5.b)$$

$$\rho_{z3}^*(\alpha) = -\rho_{z3}^*(\pi - \alpha) = -\rho_{z3}^*(\pi + \alpha) = \rho_{z3}^*(-\alpha) \quad (5.c)$$

$$\rho_{z4}^*(\alpha) = -\rho_{z4}^*(\pi - \alpha) = \rho_{z4}^*(\pi + \alpha) = -\rho_{z4}^*(-\alpha) \quad (5.d)$$

It should be noted that determining auxiliary functions $\rho_{r1}^*(\phi_k) \sim \rho_{z4}^*(\phi_k)$ in the range $0 < \alpha < \pi/2$ is equivalent to determining original unknown densities $\rho_r^*(\alpha), \rho_z^*(\alpha)$ in the range $-\pi/2 < \alpha < \pi/2$. In other words, if the auxiliary functions $\rho_{r1}^*(\phi_k) \sim \rho_{z4}^*(\phi_k)$ are given in the range $0 < \alpha < \pi/2$, original unknown functions $\rho_r^*(\alpha), \rho_z^*(\alpha)$ are expressed in the range $-\pi/2 < \alpha < \pi/2$ using eqs. (6), (7).

$$\rho_r^*(\alpha) = \rho_{r1}^*(\alpha) + \rho_{r2}^*(\alpha) + \rho_{r3}^*(\alpha) + \rho_{r4}^*(\alpha) \quad (6.a)$$

$$\rho_r^*(\pi - \alpha) = \rho_{r1}^*(\alpha) + \rho_{r2}^*(\alpha) - \rho_{r3}^*(\alpha) - \rho_{r4}^*(\alpha) \quad (6.b)$$

$$\rho_r^*(\pi + \alpha) = \rho_{r1}^*(\alpha) - \rho_{r2}^*(\alpha) - \rho_{r3}^*(\alpha) + \rho_{r4}^*(\alpha) \quad (6.c)$$

$$\rho_r^*(-\alpha) = \rho_{r1}^*(\alpha) - \rho_{r2}^*(\alpha) + \rho_{r3}^*(\alpha) - \rho_{r4}^*(\alpha) \quad (6.d)$$

$$\rho_z^*(\alpha) = \rho_{z1}^*(\alpha) + \rho_{z2}^*(\alpha) + \rho_{z3}^*(\alpha) + \rho_{z4}^*(\alpha) \quad (7.a)$$

$$\rho_z^*(\pi - \alpha) = \rho_{z1}^*(\alpha) + \rho_{z2}^*(\alpha) - \rho_{z3}^*(\alpha) - \rho_{z4}^*(\alpha) \quad (7.b)$$

$$\rho_z^*(\pi + \alpha) = \rho_{z1}^*(\alpha) - \rho_{z2}^*(\alpha) - \rho_{z3}^*(\alpha) + \rho_{z4}^*(\alpha) \quad (7.c)$$

$$\rho_z^*(-\alpha) = \rho_{z1}^*(\alpha) - \rho_{z2}^*(\alpha) + \rho_{z3}^*(\alpha) - \rho_{z4}^*(\alpha) \quad (7.d)$$

The fundamental density functions for the body forces in the r-, and z-directions are defined by following expression:

$$w_{r1}(\alpha) = n_r(\alpha) / \cos \alpha, w_{r2}(\alpha) = n_r(\alpha) \tan \alpha, w_{r3}(\alpha) = n_r(\alpha), w_{r4}(\alpha) = n_r(\alpha) \sin \alpha \quad (8)$$

$$w_{z1}(\alpha) = n_z(\alpha) / \sin \alpha, w_{z2}(\alpha) = n_z(\alpha), w_{z3}(\alpha) = n_z(\alpha) \cot \alpha, w_{z4}(\alpha) = n_z(\alpha) \cos \alpha \quad (9)$$

Using eqs. (8), (9), original body force densities are expressed as shown in eqs. (10), (11).

$$\rho_{rj}^*(\alpha) = \rho_{rj}(\alpha)w_{rj}(\alpha) \quad j=1, 2, 3, 4 \quad (10)$$

$$\rho_{zj}^*(\alpha) = \rho_{zj}(\alpha)w_{zj}(\alpha) \quad j=1, 2, 3, 4 \quad (11)$$

where $\rho_{r1}(\alpha) \sim \rho_{r4}(\alpha)$ and $\rho_{z1}(\alpha) \sim \rho_{z4}(\alpha)$ are unknown functions, which have been called weight functions. Then all $\rho_{r1}(\alpha) \sim \rho_{r4}(\alpha)$ and $\rho_{z1}(\alpha) \sim \rho_{z4}(\alpha)$ must satisfy eq. (12).

$$f(\alpha) = f(\pi - \alpha) = f(\pi + \alpha) = f(-\alpha) = f(\phi_k) : \rho_{r1}(\alpha) \sim \rho_{z4}(\alpha) \quad (12)$$

Finally, original unknown densities $\rho_r^*(\alpha), \rho_z^*(\alpha)$ can be expressed in eq. (13) as linear combination of the fundamental densities and the weight functions.

$$\rho_r^*(\alpha) = \sum_{j=1}^4 \rho_{rj}(\alpha)w_{rj}(\alpha), \rho_z^*(\alpha) = \sum_{j=1}^4 \rho_{zj}(\alpha)w_{zj}(\alpha) \quad (13)$$

By considering the symmetry of the problem, $w_{r1}(\alpha), w_{r3}(\alpha), w_{z2}(\alpha), w_{z4}(\alpha)$ are suitable. Unknown functions $\rho_r^*(\alpha), \rho_z^*(\alpha)$ can be expressed by the following equation.

$$\rho_r^*(\alpha) = \rho_{r1}(\alpha)w_{r1}(\alpha) + \rho_{r3}(\alpha)w_{r3}(\alpha), \rho_z^*(\alpha) = \rho_{z2}(\alpha)w_{z2}(\alpha) + \rho_{z4}(\alpha)w_{z4}(\alpha) \quad (14)$$

Here all unknown weight functions can be approximated as shown in eqs. (15), (16) because all of these must satisfy eq. (13).

$$\rho_{r1}(\alpha) = \sum_{n=1}^{M/2} a_n t_n(\alpha), \rho_{r3}(\alpha) = \sum_{n=1}^{M/2} b_n t_n(\alpha), \rho_{z2}(\alpha) = \sum_{n=1}^{M/2} c_n t_n(\alpha), \rho_{z4}(\alpha) = \sum_{n=1}^{M/2} d_n t_n(\alpha) \quad (15)$$

$$t_n(\alpha) = \cos\{2(n-1)\alpha\} \quad (16)$$

Where M is the number of the collocation points in $0 < \alpha < 2\pi$. Using the approximation method mentioned above, we can obtain the system of linear equations for determining the coefficients a_n, b_n, c_n, d_n . Then, the magnitude and position of the maximum stress are calculated, when the shape of the toroidal hole is changed systematically.

3. Numerical Results and Discussion

Table 1 shows the convergence of the values of stress $\sigma_n, \sigma_v, \tau_{nt}$ along the toroidal hole boundary with increasing the collocation number M when $a/b=1, a/d=2/3, v=0.3, \sigma_z^\infty=1$ in Fig. 1. In the present analysis, the boundary conditions ($\sigma_n=0, \tau_{nt}=0$), which should be zero along the boundary, are less than 10^{-5} even when $M=16$. Therefore, the boundary requirements can be highly satisfied along the entire boundary.

In Table 2 the convergence of the stress concentration factors at point A ($\psi=0^\circ$) and B ($\psi=180^\circ$) is shown to be compared with the conventional body force method using step-function when $a/b=1, a/d=0.9, v=0.3, \sigma_z^\infty=1$ in Fig. 1. In table 2, the symbol ∞ designates the extrapolated value using the results $M=32$ and 48. The present results show rapid convergence than the results using the step-function which need the extrapolation.

In Table 3 the stress concentration factor is shown to be compared with the conventional body force method using step-function when $a/b=1, v=0.3, \sigma_z^\infty=1$ in Fig. 1. The solution of the notched round bar [5, 8] and the deep notch [9] are also shown in Table 3 for reference. The present results

coincide with the results of the conventional body force method in the 4 digits. The stress concentration factors of toroidal hole are close to stress concentration factors of notched round bar and deep notch when $a/d \rightarrow 1$.

Table 1 Stress distribution along the boundary when $a/b=1$, $a/d=2/3$, $\nu=0.3$, $\sigma_z^\infty = 1$ in Fig. 1.

ψ (deg.)	M	σ_t	σ_n	τ_{nt}
0	8	2.69383	1.0×10^{-5}	0
	12	2.69676	2.3×10^{-5}	0
	16	2.69373	9.5×10^{-7}	0
	20	2.69373	-3.9×10^{-7}	0
40	8	1.37277	3.8×10^{-4}	3.9×10^{-4}
	12	1.37306	-1.7×10^{-5}	-2.8×10^{-6}
	16	1.37307	2.0×10^{-7}	-1.2×10^{-8}
	20	1.37307	-3.6×10^{-8}	2.8×10^{-10}
80	8	-0.62466	2.6×10^{-4}	6.9×10^{-5}
	12	-0.62409	-2.9×10^{-5}	6.6×10^{-6}
	16	-0.62408	-1.5×10^{-6}	7.4×10^{-7}
	20	-0.62408	-3.7×10^{-8}	2.1×10^{-9}
100	8	-0.76442	3.5×10^{-4}	-5.0×10^{-6}
	12	-0.76488	-3.3×10^{-5}	1.8×10^{-5}
	16	-0.76478	-1.5×10^{-6}	1.3×10^{-6}
	20	-0.76478	-3.1×10^{-8}	5.4×10^{-8}
140	8	1.65287	1.8×10^{-3}	-1.1×10^{-3}
	12	1.65293	-1.7×10^{-5}	4.3×10^{-5}
	16	1.6528	3.9×10^{-8}	-4.6×10^{-7}
	20	1.65281	1.3×10^{-9}	-9.2×10^{-9}
180	8	4.30702	1.2×10^{-3}	0
	12	4.30589	-3.7×10^{-5}	0
	16	4.30593	-2.1×10^{-6}	0
	20	4.30593	-9.5×10^{-8}	0

Table 2 Convergence of the maximum stress when $a/b=1$, $a/d=0.9$, $\nu=0.3$, $\sigma_z^\infty = 1$ in Fig. 1.

M	Present analysis			Step-function (ρ_{13} , ρ_{22})		
	K_{tA}	K_{tB}	K_t	K_{tA}	K_{tB}	K_t
4	2.7032	8.3236	1.0242	2.6894	8.9249	1.0185
8	2.6529	8.4751	1.0422	2.6446	8.8165	1.0330
12	2.6373	8.3918	1.0470	2.6387	8.5311	1.0403
16	2.6343	8.3802	1.0476	2.6368	8.4558	1.0435
20	2.6338	8.3785	1.0477	2.6353	8.4132	1.0458
24	2.6337	8.3783	1.0477	2.6347	8.3989	1.0465
28	2.6336	8.3783	1.0477	2.6343	8.3884	1.0470
∞				2.633	8.373	1.048

Table 3 Stress Concentration factor for toroidal hole when $a/b=1$, $\nu=0.3$, $\sigma_z^\infty = 1$ in Fig. 1.

$$[K_t = \sigma_{zB} / \sigma_a, \sigma_a = F / \{ \pi(d-a)^2 \}]$$

	Present analysis	Step- function (ρ_{r3}, ρ_{z2})	Notched round bar		Deep notch
a/d	K_t	K_t	K_t [5]	K_t [8]	K_t [9]
0	3.0000	3.0000	3.065	3.065	∞
0.1	2.5484	2.5484	2.601	2.593	3.1845
0.2	2.1836	2.1836	2.196	2.191	2.2272
0.3	1.8803	1.8803	1.869	1.871	1.8052
0.4	1.6309	1.6308	1.610	1.608	1.5571
0.5	1.4321	1.4320	1.412	1.411	1.3908
0.6	1.2820	1.2818	1.270	1.270	1.2705
0.7	1.1762	1.1761	1.172	1.172	1.1790
0.8	1.1036	1.1037	1.103	1.101	1.1069
0.9	1.0477	1.0481	1.048	1.046	1.0484

4. Conclusions

In this paper, the numerical solution of the singular integral equations based on the body force method in toroidal hole problem was investigated. The conclusions were summarized as follows:

- (1) The stress concentration problem of toroidal hole was formulated in terms of singular integral equations of the body force method. The unknown functions were approximated by the product of the fundamental density functions and polynomials.
- (2) The accuracy of the present analysis was verified through examining the boundary conditions and the convergence of the maximum stress. The present results could highly satisfy the boundary conditions and showed rapid convergence than the conventional body force method.
- (3) The stress concentration factors of toroidal hole were close to stress concentration factors of notched round bar and deep notch when $a/d \rightarrow 1$.

REFERENCE

1. C. B. Ling, Quarterly of Applied Mathematics, 10 (1952) p. 149.
2. E. Stenberg and M. A. Sadowsky, Journal of Applied Mechanics, 16 (1952) p. 19.
3. H. Miyamoto, Transaction of the Japan Society of Mechanical Engineers, 23 (1957) p. 431.
4. N.-A. Noda and T. Matsuo, Trans. of the Japan Society of Mech. Engineers, 59 (1993) p. 1964.
5. N.-A. Noda, Doctor's Thesis of Kyushu University, (1984) p. 50.
6. H. Nisitani, Journal of the Japan Society of Mechanical Engineers, 70 (1967) p. 627. [Bulletin Japan Society of Mechanical Engineers, 11 (1968) p. 14.
7. H. Nisitani and D. H. Chen, The body force method (Taiseikiryokuhou), Baifukan, Tokyo (1987).
8. H. Hasegawa, Transaction of the Japan Society of Mechanical Engineers, 46 (1980) p. 805.
9. H. Neuber, Kerbspannungslehre, Springer Verlag, 1st edition (1937), 2nd edition (1958) p. 9.

A Parametric Study on the Fracture Mechanics Analysis of Elbow with Surface Crack

Yoon-Suk Chang, Hyun-Su Kim and Tae-Eun Jin

Power Engineering Research Institute, Korea Power Engineering Company,
360-9 Mabuk-ri, Kusong-myon, Yongin-shi, Kyunggi-do 449-713, Korea

Keywords: Cracked Piping System, Engineering Analysis, Finite Element Analysis, Fracture Ratio, J-Integral, Surface Crack, Tearing Modulus

ABSTRACT

During IPIRG-2 program, various experiments and numerical analyses for surface cracked elbow had been performed, and thereafter the analytical code named IP2ELBOW was developed. However, because of the inherent limitation of this code to predict fracture behavior of cracked elbow, the necessity of further investigation was issued. For this reason, in this paper, engineering analyses and 3-dimensional finite element analyses for cracked elbow with internal pressure and bending load were carried out varying elbow geometry(R_m/t), crack depth(a/t) and crack size($2c/\pi D$). These analysis results were compared each other and with the corresponding experimental data. Finally, additional assessment was also conducted to provide better insight into the effect of dead weight load.

1. INTRODUCTION

Since 1980's, EPFM technology in nuclear piping has been enhanced through several international research programs[1~4]. The emphasis on these programs was the development of experimental data and analytical methods to verify fracture behavior of the cracked piping, and thereafter considerable products were achieved. During the development stage of these programs, several analytical methods and FEM were utilized. However, it was issued that further investigation for the several analytical methods was necessary because some discrepancies with the corresponding experimental data were observed in the previous studies. Therefore, in this paper, numerous engineering analyses and FE analyses were carried out for various elbow and crack geometries to find out the optimum method.

2. ANALYSIS MODELS

In order to produce elbow fracture behavior data, four elbow tests with surface crack were carried out during the previous international piping research program[4]. The tests were performed at representative PWR condition and Fig.1 shows the two types of test facilities used in these tests.

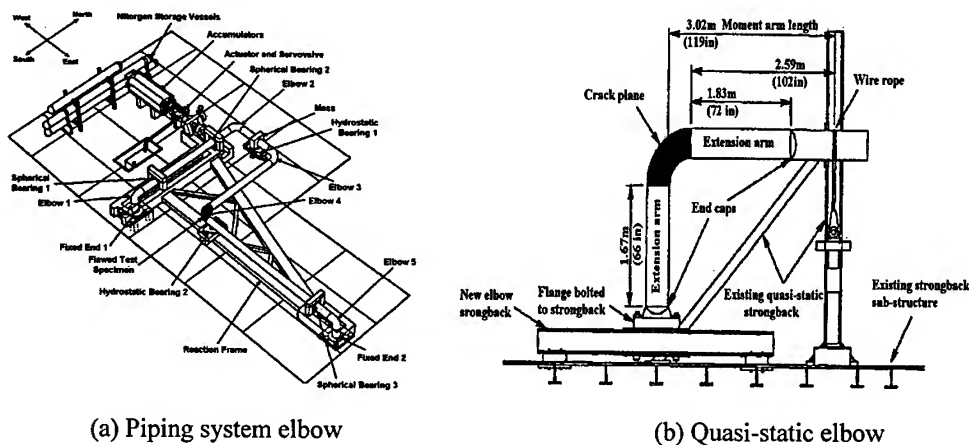


Fig.1 Schematic of elbow test facilities[4]

2.1. Geometry

The test specimens contained an internal circumferential surface crack centered at the extrados of about 406mm(16inch) nominal diameter and 33mm(1.3inch) thickness, long-radius 90° elbow. The nominal planned surface cracked geometry was about 50 percent of the elbow circumference in length and 63~68 percent of the elbow wall thickness in depth.

2.2. Material

Elbow materials used in these tests were A106 Gr.B carbon steel and TP 304L stainless steel. Table 1 shows chemical compositions of the elbow materials.

Table 1. Chemical composition of test materials

Identification	Fe	C	Mn	P	S	Si	Ni	Cr	Mo	V	Co	Cu	Al	Ti	Nb
A106 Gr.B Carbon Steel	-	0.17	0.93	0.017	0.003	0.26	0.02	0.03	0.01	-	0.002	0.01	0.03	0.014	0.03
TP304L Stainless Steel	70.5	0.03	1.90	0.020	0.030	0.32	8.30	18.8	0.19	0.05	0.080	-	0.04	0.006	0.01

2.3. Loading

The piping system test specimens were subjected to an increasing amplitude single frequency displacement-time history forcing function, with a constant internal pressure of 15.5MPa and at a temperature of 288°C. The companion quasi-static test specimens were loaded in bending, with the same condition.

2.4. Summary of analysis models

Table 2 shows the summary for geometry, material, loading and key test results of the cracked elbow which were used as base models of fracture mechanics analyses.

Table 2. Geometry, material, loading and key test results of base models of cracked elbow

Identification	2-1	2-2	2-3	2-4
Test Type	Piping System	Quasi-Static	Piping System	Quasi-Static
Elbow Material	A106 Gr.B CS	A106 Gr.B CS	TP304L SS	TP304L SS
Outer Diameter[mm(inch)]	409 (16.1)	406 (16.0)	409 (16.1)	406 (16.0)
Thickness [mm(inch)]	32.1 (1.263)	32.0 (1.26)	33.2 (1.31)	33.0 (1.30)
R_m/t	5.9	5.8	5.7	5.7
Crack Length/Circumference	0.49	0.50	0.50	0.50
a/t (Average)	0.67	0.68	0.63	0.64
Young's Modulus [GPa(ksi)]	196.5(28,500)	196.5(28,500)	182.7(26,500)	182.7(26,500)
Yield Strength [MPa(ksi)]	209 (30.3)	209 (30.3)	194 (28.1)	194 (28.1)
Tensile Strength[MPa(ksi)]	448 (65.0)	448 (65.0)	410 (59.4)	410 (59.4)
α	3.36	3.36	14.78	14.78
N	4.421	4.421	3.981	3.981
J_{IC} [kN/m(in-lb/in ²)]	361 (2,060)	425 (2,430)	1,359 (7,761)	1,087 (6,206)
M_{ini} [kN-m (in-kips)]	562 (4,970)	593 (5,250)	601 (5,320)	536 (4,745)
M_{max} [kN-m (in-kips)]	580 (5,132)	608 (5,380)	729 (6,448)	548 (4,850)

3. FRACTURE MECHANICS ANALYSES

To verify the validity of the analytical methods developed in the previous studies, a number of engineering analyses and FE analyses were performed for circumferential surface cracked elbows under the combined load.

3.1. Engineering Analyses

Engineering analyses were performed using the SC.ELB[5], NSC[6] and Simplified method[7] for both the base models in which experimental data[8~11] were available and specific models in which R_m/t , a/t , $2c/\pi D$ parameters were varied. In these analyses, to predict the fracture behavior, crack initiation and maximum moments were determined by using the experimental values corresponding to the J_{IC} and $(dJ/da)_{app} = (dJ/da)_{mat}$, respectively.

3.2. FE Analyses

Elastic-plastic finite element analyses were also performed using ABAQUS code for only the base models in same manner with the engineering analyses. Fig. 2 shows the representative 3-dimensional FE model for the circumferential surface cracked elbow and, in which 1/2 of the elbow was modeled because of the geometric symmetry. As the analysis results, crack initiation moment was determined by using the experimental values corresponding to the J_{IC} .

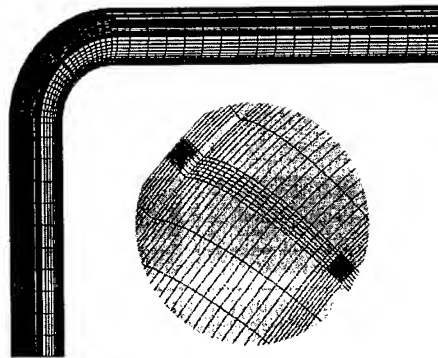


Fig.2 FE model of surface cracked elbow

4. ANALYSIS RESULTS

Fig. 3 shows the fracture ratios obtained by comparison of the engineering and FE analysis results to the experimental ones for 4 base models. As shown in these figures, the predicted moments by the analytical methods were generally conservative, and the differences between experimental and predicted maximum moments were larger than the crack initiation cases. In addition, predicted results obtained by the SC.ELB1, NSC, and FE methods were similar to the corresponding experimental values, while the SC.ELB2 and Simplified methods underpredict the load-carrying capacities.

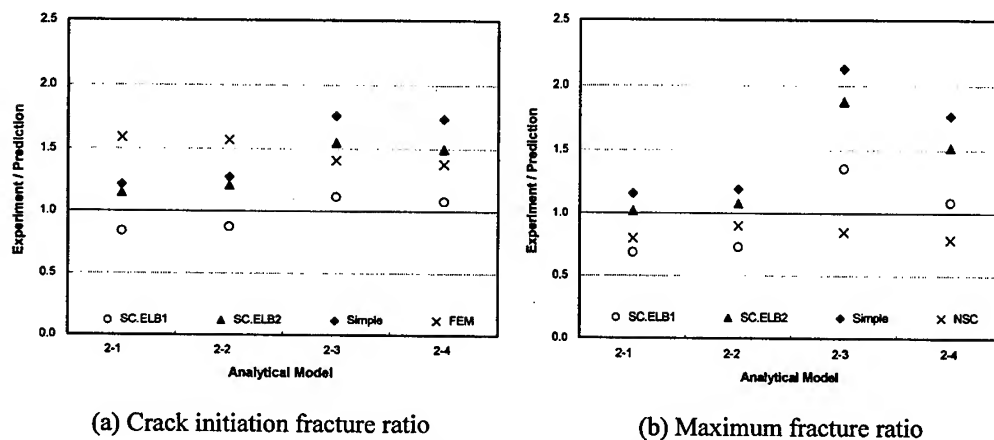


Fig. 3 Analysis results for base model

4.1. Influence of R_m/t

Fig. 4 shows the predicted moments obtained by the SC.ELB1, SC.ELB2 and Simplified methods for the variation of R_m/t . As R_m/t increases from about 5.5 to 6.5, the load-carrying capacities tend to decrease about 15% and these tendencies were similar in spite of the difference of elbow materials and analytical methods.

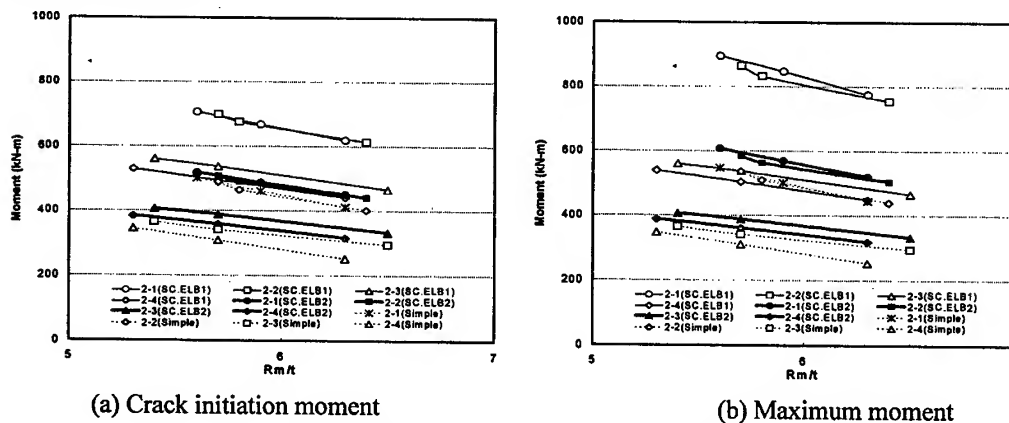


Fig. 4 Analysis results for variation of R_m/t

4.2. Influence of a/t

Fig. 5 shows the predicted moments obtained by the SC.ELB1, SC.ELB2 and Simplified methods for the variation of a/t . As a/t increases from about 0.5 to 0.8, load-carrying capacities tend to decrease about 20% and these tendencies were similar in spite of the difference of elbow materials and analytical methods except for Simplified method.

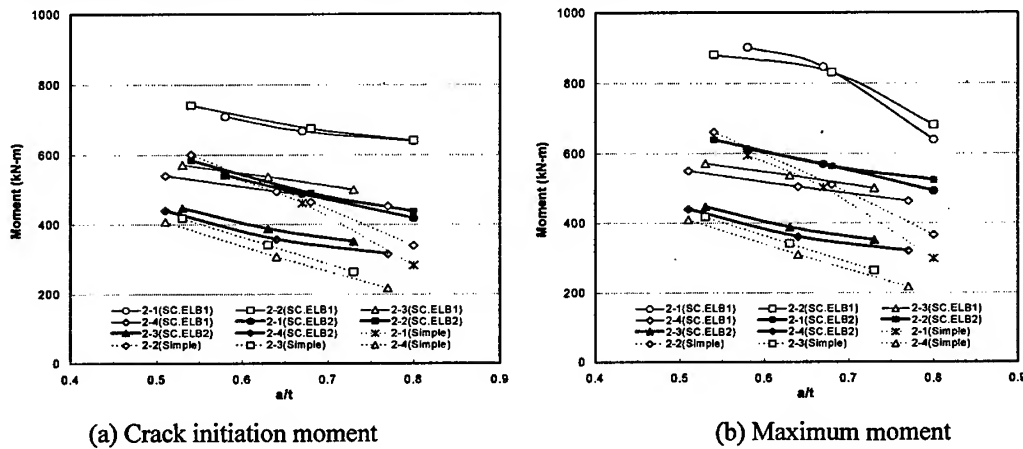


Fig. 5 Analysis results for variation of a/t

4.3. Influence of $2c/\pi D$

Fig. 6 shows the predicted moments obtained by the SC.ELB1, SC.ELB2 and Simplified methods for the variation of $2c/\pi D$. As $2c/\pi D$ increases from 40% to 50%, load-carrying capacities tend to decrease about 10% and these tendencies were similar in spite of the difference of elbow materials and analytical methods.

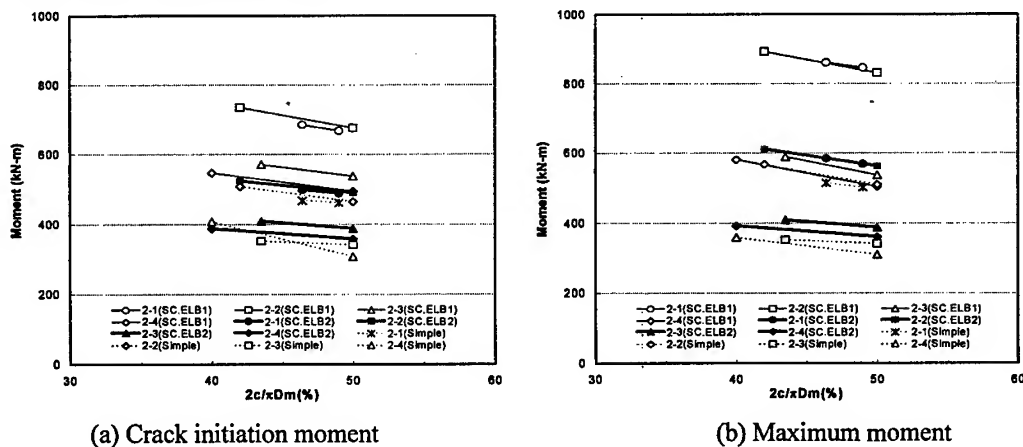


Fig. 6 Analysis results for variation of $2c/\pi D$

4.4. Influence of dead weight load

The load-carrying capacities considering the pipe and water weights were reviewed using moment equilibrium equation. However, contribution of the dead weight loads for fracture was proved to be not significant because the values of less than 2kN were considerably lower than the experimental value of about 200kN at crack initiation.

5. CONCLUSIONS

In this paper, to find out the optimum analytical method for cracked elbow, numerical analyses and synthetic assessment were performed, and the conclusion of this paper was follows:

- (1) In general, the moment prediction results for surface cracked elbow using analytical and FE methods were underpredictive.
- (2) FE method seemed to be appropriate to predict load-carrying capacity for surface cracked elbow.
- (3) As R_m/t , a/t , $2c/\pi D$ increases, load-carrying capacities tend to generally decrease and the effect of a/t was most significant among these parameters.
- (4) Effect of the dead weight load was relatively negligible.
- (5) Further investigation will be necessary for the analytical methods because of some inconsistent predictive trends.

REFERENCES

1. G.M. Wilkowski, et al., Degraded Piping Program-Phase II, NUREG/CR-4082, Vol.1~Vol.8 (1984)
2. G.M. Wilkowski, et al., Short Cracks in Piping and Piping Welds, NUREG/CR-4599, Vol.1 No.1~Vol.4 No.1 (1994)
3. G.M. Wilkowski, et al., International Piping Integrity Research Group Program – Final Report, NUREG/CR-6233 (1991)
4. G.M. Wilkowski, et al., Second International Piping Integrity Research Group(IPIRG-2) Program – Final Report, NUREG/CR-6452 (1996)
5. Battelle, Elbow Surface Crack J-Estimation Scheme Computer Program, IP2ELBOW Ver. 1.0 (1996)
6. M.F. Kanninen, et al., Mechanical Fracture Predictions for Sensitized Stainless Steel Piping with Circumferentially Cracks, EPRI NP-192 (1976)
7. G.M. Wilkowski, et al., Development of Simplified Analysis Procedure for Cracks, 14th SMiRT Conference, pp. 227~234 (1997)
8. Battelle, Data record book entry E-2.2.2.8i.1 for IPIRG-2 Experiment 2-1 (1995)
9. Battelle, Data record book entry E-2.2.2.lic.1 for IPIRG-2 Experiment 2-2 (1996)
10. Battelle, Data record book entry E-2.2.2.8i.2 for IPIRG-2 Experiment 2-3 (1996)
11. Battelle, Data record book entry E-2.2.2.lic.2 for IPIRG-2 Experiment 2-4 (1996)

On the Multiple Isoparametric Finite Element Method and Computation of Stress Intensity Factor for Cracks in FGMs

Z.Z. Zou, S.X. Wu and C.Y. Li

Department of Communication Engineering, Shijiazhuang Railway Institute,
Shijiazhuang 050043, China P.R.

Keywords: Crack, Finite Element Method, Functionally Graded Materials FGM, Stress Intensity Factor

ABSTRACT

In this paper, a multiple isoparametric finite element method is presented, and as an example of application of the method, the stress intensity factor for cracks in functionally graded materials (FGMs) is computed. The results have shown that the multiple isoparametric finite element method is much more efficient in computation of the stress intensity factor for cracks in nonhomogeneous materials.

1. INTRODUCTION

The worldwide interests in FGMs research are growing rapidly in recent years. The reason is that the FGMs have many advantages, such as effectively resisting high temperature and corrosion, significantly reducing the residual and thermal stresses in the materials and so on. However, this kind of material also brings us some new problems. The foremost challenge that we are faced is that the FGMs are nonhomogeneous solids with its material properties varying continuously. From the viewpoints of applied mechanics, the nonhomogeneity of FGMs has a great influence on their mechanical behavior. Due to the mathematical complexity, most of the existing analytical solutions to problems relating to nonhomogeneous solids had to make a lot of simplicity. It was usually assumed that the material is isotropic, the Poisson's ratio is constant and only the Young's (or the shear) modulus is a specially designated continuous function of the space variable. Such idealizations offer a considerable amount of simplification to the analysis of nonhomogeneous materials. Even so, however, the analytical approaches that had been used can only deal with unbounded media and simple distribution of material properties, such as an exponential form [1] or power form [2]. It is difficult to consider the influences of finite size and complex material property distributions on the fracture parameters. Therefore, the numerical methods should be take as

powerful tools in analyzing the behavior of FGMs.

In numerical methods, the most versatile method is the Finite Element Method (FEM) and it has been used to solve many practical problems. However, in conventional isoparametric finite element method, both the displacement and shape of the element are expressed as the functions of the coordinates in one or two order, for the properties of the material, however, only a constant is used to present them throughout the element. It is worked very well for the homogeneous materials, but not the case for the nonhomogeneous materials, since the properties of the materials are varied in the element, and the expansions for the displacements, shape and the properties of the materials in the element are not consistent.

In this paper, we propose a simpler and more versatile finite element formulation. The concept of isoparametric transformation is adopted for simulating the variations of the material properties in individual finite elements. The properties of the materials in the element are also expressed as the functions of the coordinates in one or two order. Because of this consistency of the expansions, much higher efficiency and accuracy of the computation is obtained with a little increasing of the amount of the computation. As an example of application of the method, the stress intensity factor for cracks in a FGMs is computed.

2. MULTIPLE ISOPARAMETRIC ELEMENTS

The finite element stiffness equations can be written as

$$\mathbf{K}^e \mathbf{u}^e = \mathbf{F}^e \quad (1)$$

where

$$\mathbf{K}^e = \int_{\Omega_e} \mathbf{B}^{eT} \mathbf{D}^e \mathbf{B}^e d\Omega_e \quad (2)$$

$$\mathbf{F}^e = \int_{\Omega_e} \mathbf{N}^{eT} \mathbf{b}^e d\Omega_e + \int_{\Gamma_e} \mathbf{N}^{eT} \bar{\mathbf{t}}^e d\Gamma_e + \int_{\Omega_e} \mathbf{B}^{eT} \mathbf{D}^e \boldsymbol{\varepsilon}_T d\Omega_e \quad (3)$$

Where \mathbf{B}^e is the strain shape function, \mathbf{D}^e is the constitutive matrix containing the appropriate material properties, \mathbf{b}^e , $\bar{\mathbf{t}}^e$ and $\boldsymbol{\varepsilon}_T$ are the body force vector, the traction vector and the thermal strain vector respectively; Ω_e is the domain of the element and Γ_e is the boundary on which traction is prescribed.

In above finite element formulation, the constitutive matrix \mathbf{D}^e , the body force vector \mathbf{b}^e and the thermal strain $\boldsymbol{\varepsilon}_T$ have relations with the material properties E (elastic modulus), ν (Poisson's ratio), ρ (density) and α (the coefficient of linear thermal expansion) respectively. For nonhomogeneous materials, these material properties are functions of spatial coordinates. In order to properly describe the variations of material properties in nonhomogeneous media, we introduce

the concept of the well-known isoparametric transformation into the interpolation of material parameters. It is stated below for two-dimensional problem.

Consider a m -node plane element. The global coordinates of a point on the element at (ξ, η) are given by

$$x = \sum_{i=1}^m N_i(\xi, \eta) x_i, \quad y = \sum_{i=1}^m N_i(\xi, \eta) y_i. \quad (4)$$

Where N_i are the shape functions corresponding to the node i , whose coordinates are (x_i, y_i) in the global system and (ξ_i, η_i) in the local system. As an isoparametric element, the displacements within the element are interpolated as follows

$$u = \sum_{i=1}^m N_i(\xi, \eta) u_i, \quad v = \sum_{i=1}^m N_i(\xi, \eta) v_i. \quad (5)$$

Where (u, v) are the nodal displacements in x and y directions respectively. Now, we let the material properties E , ν , ρ and α at the point (ξ, η) be expressed as

$$\begin{aligned} E &= \sum_{i=1}^m N_i(\xi, \eta) E_i, & \nu &= \sum_{i=1}^m N_i(\xi, \eta) \nu_i, \\ \rho &= \sum_{i=1}^m N_i(\xi, \eta) \rho_i, & \alpha &= \sum_{i=1}^m N_i(\xi, \eta) \alpha_i, \end{aligned} \quad (6)$$

Where $(E_i, \nu_i, \rho_i, \alpha_i)$ stand for the material properties at the node i of the element. By using Eq.6, the actual variations of the material properties in a specified element can be approximated by polynomial forms. We can choose the same shape functions to achieve the same simulating accuracy for coordinates, displacements and material properties in an element. We name this kind of elements as multiple isoparametric elements.

Substituting Eq.6 into the element constitutive matrix $\mathbf{D}^e(E, \nu)$, the body force vector $\mathbf{b}^e(\rho)$ and the thermal strain $\mathbf{\epsilon}_T(\alpha)$ in Eq.2 and Eq.3 respectively, we obtain the element stiffness matrix and the load vector in the domain of the reference element. Because the variations of material properties have been simulated properly in the level of element, it insures that the higher accuracy can be obtained with relative coarse mesh for the stress analysis of nonhomogeneous media. Clearly, the finite element formulation presented above is also suitable for homogeneous medium and piecewise homogeneous medium merely by making the value of each material property be the same at all of nodes on an element.

3. NUMERICAL INTEGRATION

The problem that should be paid attention is the numerical integration of the element stiffness matrices and the element load vectors. For a multiple isoparametric element, the order of the

integrand is generally higher than the corresponding isoparametric element, because the matrix \mathbf{D}^e and the vectors \mathbf{b}^e , \mathbf{e}_r are functions of the coordinates ξ and η , as shown in Eq.7 and Eq.8. The elements of the matrix \mathbf{D}^e are usually rational fractions because they are calculated by E and ν . Therefore, the minimum number of integration points required by the matrix \mathbf{K}^e and the vector \mathbf{F}^e could not be determined easily. But by considering the first term of the load vector \mathbf{F}^e , we can say that the errors of the integration formulae may be at least of the order as follows: linear elements, $O(h^3)$; quadratic elements, $O(h^5)$; cubic elements, $O(h^7)$. Thus, the minimum number of Gaussian integration points will be, for example, 3×3 for eight-node two-dimensional elements.

The effect of different integration points on the accuracy of computed results is illustrated in Fig.1 for quadratic quadrilaterals. It can be seen that 3×3 Gaussian points are adequate for quadratic quadrilaterals. The increase of the number of integration points has little effect on the accuracy. It is revealed that little more efforts in integration for multiple isoparametric elements will be made than that for ordinary isoparametric elements.

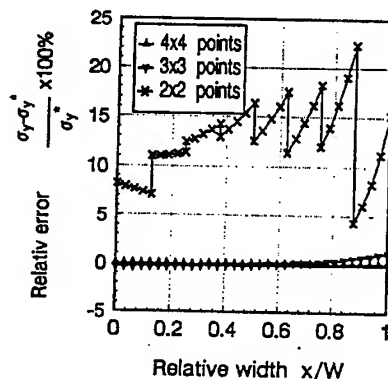


Fig.1. The effect of Gaussian points on the computational accuracy.
(σ_y^* is the result of 10×10 points)

4. APPLICATION TO FRACTURE MECHANICS

In this section, the multiple isoparametric element method is used to analysis of fracture mechanics of functionally graded materials. The studies of the literature [3] have shown that in nonhomogeneous materials with continuously varying properties the nature of the stress singularity at a crack tip would remain to be identical to that in homogeneous solids. It has been confirmed that the result is independent of the form for material properties and the orientation of the crack [4]. Thus, we can now use the crack tip finite element developed for the ordinary square-root singularity to compute the fracture parameters of FGMs. Following we give out the formulations of the SIF by using the triangular crack tip element for FGMs.

From the displacement fields on the crack surfaces, we obtain

$$\begin{aligned}
 K_I(r) &= \sqrt{\frac{2\pi}{L}} \frac{\mu(r)}{\kappa(r)+1} [w(r^+) - w(r^-)] \\
 K_{II}(r) &= \sqrt{\frac{2\pi}{L}} \frac{\mu(r)}{\kappa(r)+1} [u(r^+) - u(r^-)]
 \end{aligned}
 \quad (7)$$

Where $\kappa = (3-4\nu)$ for plane strain and $\kappa = (3-\nu)/(1+\nu)$ for plane stress, $\mu = E/2(1+\nu)$ is the shear modulus. $u(r)$ and $w(r)$ are the displacement components at crack face point r . The values of K_I and K_{II} at the tip o can be obtained by linear extrapolation as following

$$\begin{aligned}
 K_I &= 2K_I(L/4) - K_I(L) \\
 K_{II} &= 2K_{II}(L/4) - K_{II}(L)
 \end{aligned}
 \quad (8)$$

5. NUMERICAL RESULTS AND DISCUSSION

As an example, an FGM plate with an edge crack is computed by the present method. As shown in Fig.2, the plate is assumed under uniform tension. Its Poisson's ratio is constant and its elastic modulus is

$$E(x) = E_0 \exp\left(\frac{x}{W} \ln \frac{E_W}{E_0}\right) \quad (9)$$

Where E_0 and E_W are the elastic moduli at $x=0$ and $x=W$, respectively. The reason we choose this problem as an example is that it has analytical solutions [1] and hence it is convenient to analyze the computational accuracy and efficiency.

As shown in Fig.2, the crack plane is a plane of symmetry and the crack problem is one of Mode I. The finite element division is only needed for the part of $y \geq 0$. In the computation, we

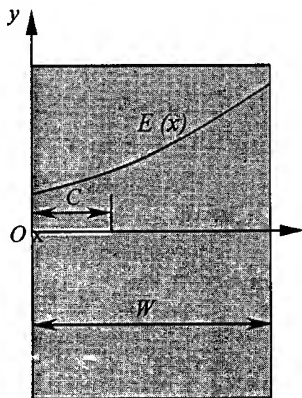


Fig.2. The FGM plate with an edge crack.

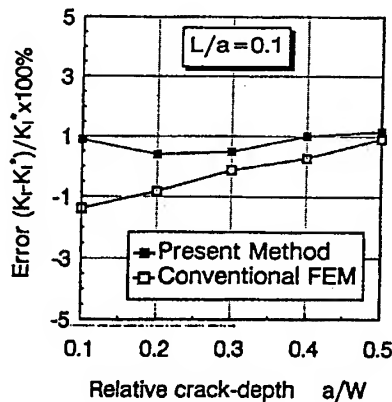


Fig.3. The error analysis of computational results.

(K_I^* is from reference [1])

used total 184 elements and total 599 nodes. The crack tip elements are six-node triangular quarter-point elements. Other elements are eight-node multiple isoparametric elements. The error analyses of the computed results are shown in Fig. 3. As comparison, this problem was also solved by using the conventional FEM. The crack tip elements were also six-node triangular quarter-point elements and other elements were eight-node isoparametric elements. However, to achieve the acceptable accuracy, the total number of elements that was used reached 852 and the number of nodes reached 2229. It is shown that the multiple isoparametric finite element method is much more efficient in computation of the stress intensity factor for cracks in nonhomogeneous materials.

6. CONCLUSION

In this paper, the technique of isoparametric transformation is adopted for simulating the variation of material properties and then a multiple isoparametric finite element method is presented. It makes the description of geometry, displacements and material properties be achieved the same accuracy. Due to this consistency of the expansions, much higher efficiency and accuracy of the computation is obtained with a little increasing of the amount of the computation. Because of the expansion for the properties of the materials, the order of the expressions for the stiffness matrix of the element is higher than that in the conventional one. But it is proved that the minimum number of the points of numerical integration is 3×3 for the linear element, and it is also enough for the element of second order. As an example of application of the present method, the stress intensity factor for an edge-cracked FGM plate is computed. It is shown that the present method provides enormous flexibility in meshing and much more efficiency in computation of the stress intensity factor for cracks in nonhomogeneous materials.

ACKNOWLEDGEMENT

This research was supported by the National Natural Science Fund of China under project No. 19772029.

REFERENCES

1. F. Erdogan and B. H. Wu, ASME Journal of Applied Mechanics, **64** (1997) p. 449
2. C. Li and Z. Zou, ASME Journal of Applied Mechanics, **66** (1999) p. 566
3. Z. H. Jin and N. Noda, ASME Journal of Applied Mechanics, **61** (1994) p. 738
4. P. Gu, and R. J. Asaro, International Journal of Solids and Structures, **34** (1997) p.1

The Effect of a Longitudinal Stiffener on the Elastic Shear Buckling of Orthotropic Web Plate

S.J. Yoon¹, J.H. Jung¹ and S.K. Cho²

¹Department of Civil Engineering, Hongik University, 72-1 Sangsu-dong, Mapo-gu, Seoul 121-791, Korea

²Department of Civil Engineering, Seoul National University of Technology, 172 Kongneong-dong, Nowon-gu, Seoul 139-743, Korea

Keywords: Elastic Shear Buckling, In-plane Shear Forces, Longitudinal Stiffener, Orthotropic Plate, Rayleigh-Ritz Method, Strain Energy

ABSTRACT

This paper presents the effect of a longitudinal stiffener on the elastic buckling of orthotropic web plate under in-plane shear forces. In the study, the edges of web plate are assumed to be simply supported. The stiffener is modeled as a beam element and the torsional rigidity of stiffener is neglected. The minimum value of shear buckling coefficient of longitudinally stiffened orthotropic plate is estimated by the buckling analysis of an infinite long plate with a longitudinal stiffener under in-plane shear forces. The buckling analysis of longitudinally stiffened orthotropic rectangular plate is also performed and the results are presented in the graphical form. For the buckling analysis, the Rayleigh-Ritz method is employed. To verify the results obtained by using the ensuing equation, the orthotropic material properties are replaced with the isotropic ones and the results are compared with published ones.

1. INTRODUCTION

In recent years, pultruded fiber-reinforced plastic (FRP) members have been increasingly used in many engineering fields including civil engineering, due to their favorable mechanical and physical properties such as light weight, corrosion resistance, and electromagnetic transparency. Despite their availability and diversity, analysis method and design tools developed for members of conventional materials can not always be readily applied to FRP shapes because of the complexity of mechanical properties of composite materials. Thus there is an urgent need to understand the behavior of pultruded structural members under various loading and boundary conditions.

Since the structural members are commonly consisted with plate elements, local buckling can be one of the critical failure modes. In order to prevent the local buckling, plate thickness to width

ratio can be increased and/or the stiffener may be located on the plate element. In the case of slender web plate, longitudinal and transverse stiffeners may be located to increase the local buckling strength and each stiffener can be designed under bending and shear stresses, respectively. While, the effect of longitudinal stiffener on the elastic shear buckling needs to be considered in some practical cases such as the shear webs in thin wings and bridge girders.

This paper is focused on theoretical investigation of the effect of a longitudinal stiffener on the elastic shear buckling of orthotropic web plate. The boundary conditions of orthotropic web plate are assumed to be simply supported and the longitudinal stiffener is modeled as a beam element.

2. THEORETICAL DERIVATIONS

In this paper, following assumptions in addition to the basic assumptions for the plate are commonly introduced at the junction of plate and stiffener.

- (1) The deflection of stiffener is equal to the out-of-plane deflection of plate at the common junction of plate and stiffener.
- (2) The torsional rigidity of stiffener is negligibly small.

In order to derive the instability equation, two different conditions are considered and the Rayleigh-Ritz method is employed. For the first case, the plate is modeled as a long plate in order to investigate the minimum value of buckling coefficient. For the second case, which is in general, the web plate bounded by transverse stiffeners is modeled as a simply supported plate.

2.1 Longitudinally stiffened long plate

Fig. 1 shows the orthotropic infinite long plate with a longitudinal stiffener under uniformly distributed shear forces at the longitudinal edges.

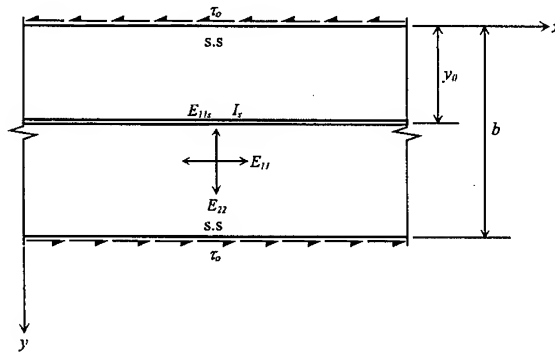


Fig. 1 Orthotropic infinite long plate with a longitudinal stiffener

Using the axes and notation in Fig. 1, the deflection curve for buckled shape is assumed as [1, 2]:

$$w = \sin \frac{\pi x}{\lambda} \sum_{n=1}^{\infty} A_n \sin \frac{n\pi y}{b} + \cos \frac{\pi x}{\lambda} \sum_{n=1}^{\infty} B_n \sin \frac{n\pi y}{b} \quad (1)$$

In Eq. (1) λ is the half wavelength of buckled shape in the x-direction, and A_n , B_n are the amplitude of deflection. The deflection curve of a longitudinal stiffener can be found by replacing y

with y_0 .

Substituting assumed deflection curves into the basic energy equation of orthotropic plate [3], one can find the strain energy of bending of orthotropic plate (U_p), the strain energy of stiffener (U_s), and the work done by the applied shear forces (T). Then the total potential energy ($\Pi = U_p + U_s + T$) can be obtained as a function of in-plane shear buckling coefficient of orthotropic plate k_s , the half wavelength of buckled shape λ , and the flexural rigidity ratio γ .

The in-plane shear buckling coefficient of orthotropic plate k_s is defined as [4]:

$$k_s = \frac{\tau_0 t b^2}{\pi^2 \sqrt{D_{11} D_{22}}} \quad (2)$$

Therefore the in-plane shear buckling stress τ_{cr} can be calculated from the following equation:

$$\tau_{cr} = k_s \frac{\pi^2 \sqrt{D_{11} D_{22}}}{b^2 t} = k_s \frac{\pi^2 \sqrt{E_{11} E_{22}}}{12(1 - \nu_{12} \nu_{21}) \left(\frac{b}{t}\right)^2} \quad (3)$$

According to the principle of stationary potential energy, the coefficients A_n and B_n must be chosen to make the total potential energy being stationary. Using the Rayleigh-Ritz method, the minimization of total potential energy with respect to each A_n and B_n results in two sets of simultaneous homogeneous linear equations represented by following equations:

$$A_n Q_n + \sum_{q=1}^{\infty} A_q N_{nq} + \sum_{q=1}^{\infty} B_q M_{nq} = 0 \quad (4)$$

$$B_n Q_n + \sum_{q=1}^{\infty} B_q N_{nq} + \sum_{q=1}^{\infty} A_q M_{nq} = 0 \quad (5)$$

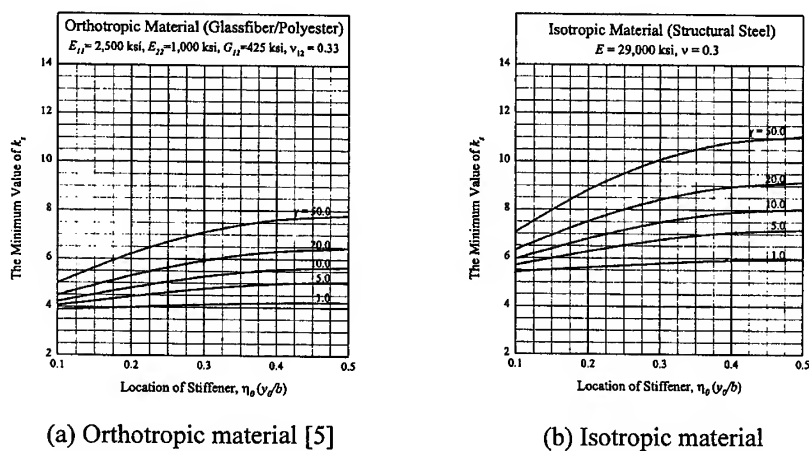
In Eqs. (4) and (5), $n \neq q$ are odd numbers, and Q_n , N_{nq} , and M_{nq} 's are given in Appendix.

Since Eqs. (4) and (5) are homogeneous, the determinant of coefficients of A_n 's and B_n 's must be vanished to get the solution other than the trivial one. In this study, the factored determinant is expanded up to four terms, and it gives good approximation [1].

Using the ensuing equation, the minimum value of k_s of longitudinally stiffened plate is calculated at various locations of stiffener as shown in Fig. 2. In Fig. 2, the minimum value of k_s approaches the maximum value when the stiffener is located at the middle of plate.

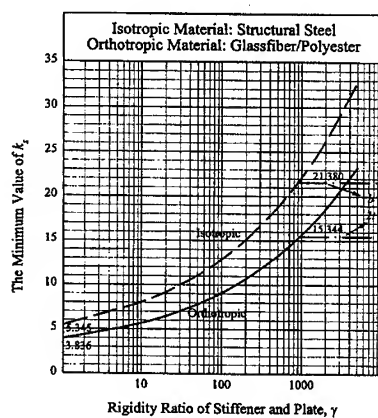
Fig. 3 represents the trend of minimum value of k_s with respect to the flexural rigidity ratio γ when the stiffener is located at the middle of plate. As can be seen in Fig. 3, increasing the stiffener rigidity increases the buckling coefficient of plate, and it indicates that the load needed to buckle the plate increases. The dashed-dot line in Fig. 3 indicates the buckling coefficient of one panel of plate of which boundaries are simply supported and this value can be assumed to be the upper limit of buckling coefficient of an infinite long plate with a longitudinal stiffener.

In order to verify the ensuing equation, the orthotropic material properties are replaced with isotropic ones and the results are plotted with dashed line in Fig. 3. The results obtained coincide with the existing ones (Crate and Lo, 1975).



(a) Orthotropic material [5]

(b) Isotropic material

Fig. 2 Minimum value of k_s at various locations of stiffenerFig. 3 Minimum value of k_s with respect to the rigidity ratio γ of stiffener and plate ($y_0=0.5b$)

2.2 Longitudinally stiffened rectangular plate

Fig. 4 represents the orthotropic rectangular plate with a longitudinal stiffener under in-plane shear forces.

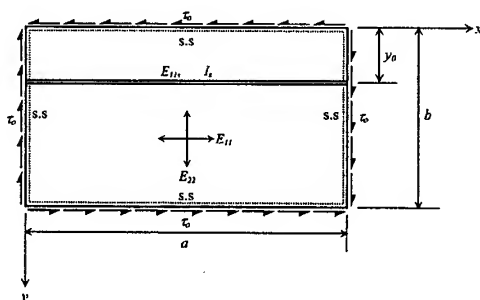


Fig. 4 Orthotropic rectangular plate with a longitudinal stiffener

Since all edges of plate are assumed to be simply supported, the deflection curve for buckled shape can be expressed as a double trigonometric sine series as follow:

$$w = \sum_{m=1}^{\infty} \sum_{n=1}^{\infty} A_{mn} \sin \frac{m\pi x}{a} \sin \frac{n\pi y}{b} \quad (6)$$

In Eq. (6) A_{mn} is the amplitude of deflection, and as mentioned earlier, the deflection curve of a longitudinal stiffener can be found by replacing y with y_0 .

Using the same method for the case already mentioned in the previous section, the total potential energy of the system must be extremized by the amplitude A_{mn} . Employing the Rayleigh-Ritz method, following system of linear homogeneous equations can be derived:

$$A_{mn} \frac{Q_{mn}}{k_\beta} + \frac{2\gamma m^4}{k_\beta} \sin n\pi\eta_0 \sum_{r=1}^{\infty} A_{mr} \sin r\pi\eta_0 - \sum_{p=1}^{\infty} \sum_{q=1}^{\infty} A_{pq} \frac{mnpq}{(p^2 - m^2)(q^2 - n^2)} = 0 \quad (7)$$

where, η_0 is the relative stiffener location ($\eta_0 = y_0/b$) and $m \pm p$ and $n \pm q$ are odd numbers.

Each of the equations represented by Eqs. (7) is associated with a specific pair of values of m and n . Since $m \pm p$ and $n \pm q$ are both odd, $m \pm n$, $m \pm r$, and $p \pm q$ are odd or even at the same time. Each of the homogeneous linear equations can therefore involve only the coefficient A_{ij} for which $i \pm j$ is either even or odd [6, 7].

In this paper, the set of Eqs. (7) is divided into two independent equations, which can be solved separately, one group consisting of equations $i+j$ is odd and the other group consisting equations $i+j$ is even. Each set of equations is expanded up to ten terms and written in matrix form. Since the equations are homogeneous, the determinant of the equations must be vanished to get the solution other than the trivial one. By expanding the determinant one can obtain the characteristic equation which is a function of k_s , flexural rigidity ratio γ , and plate aspect ratio ϕ ($\phi = a/b$).

Using ensuing equation, the shear buckling coefficient of longitudinally stiffened rectangular plate k_s with respect to the plate aspect ratio is calculated for each flexural rigidity ratio as shown in Fig. 5.

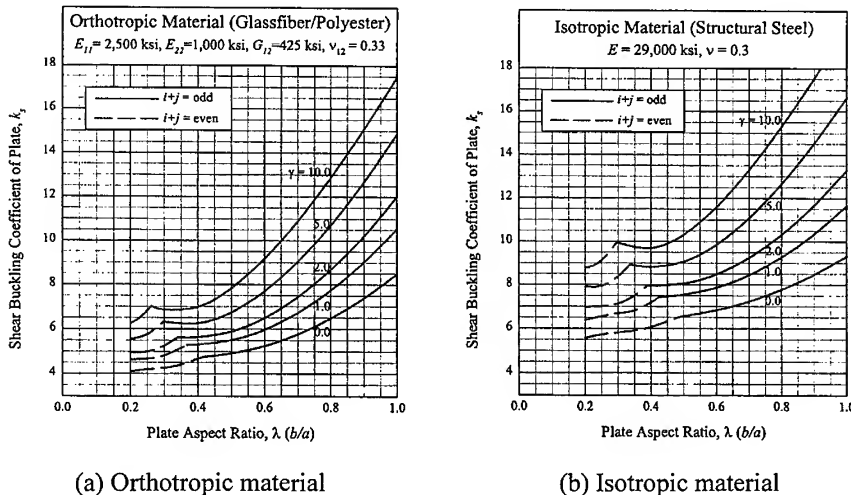


Fig. 5 The buckling coefficient of longitudinally stiffened plate under pure shear

3. DISCUSSION AND CONCLUSION

The effect of a longitudinal stiffener on the elastic shear buckling of orthotropic web plate was investigated. Using the ensuing equation, the graphical forms of results were suggested.

When the stiffener was located at the middle of plate, the largest shear buckling coefficient of plate was obtained. A longitudinal stiffener serves to increase the shear buckling strength of plate and the greater the rigidity of the stiffener the greater will be this increase, until the point where the stiffener remains straight and only the panels deflect. Thus, the upper limit of shear buckling coefficient of longitudinally stiffened plate can be assumed to be the buckling coefficient for one panel of the plate for which boundaries are simply supported (dashed-dot line in Fig.3). This is not strictly true since each panel tends to stiffen the adjacent one, but gives conservative value.

In this paper, we discussed the elastic buckling behavior of orthotropic web plate with a longitudinal stiffener under in-plane shear forces.

In general, the web of flexural member resists shear and bending forces simultaneously. Therefore, it is necessary to investigate the buckling of longitudinally stiffened web plate under shear and bending forces.

REFERENCES

1. H. Crate and H. Lo, National Advisory Committee for Aeronautics, NACA Technical Note **1589** (1975)
2. S.P. Bulson, The Stability of Flat Plates, American Elsevier Publishing Company Inc., New York (1969)
3. S.G. Lekhnitskii, Anisotropic Plates, S.W. Tsai and T. Cheron (Trans.), Gordon and Breach, Second Printing, New York (1984)
4. S.P. Timoshenko and J.M. Gere, Theory of Elastic Stability, Second ed., McGraw-Hill, New York (1961)
5. Strongwell, Extern Design Manual, Strongwell, Bristol, Virginia (1997)
6. S. Way, Presented at the fourth National Applied Mechanics Meeting, Applied Mechanics, ASME, June 11-13 (1936), p. A-131 ~ A-135
7. S.J. Yoon, B.H. Park, and S.K. Jeong, Composite Materials, **Vol. 11, 6** (1998), p. 10 ~ 20

APPENDIX

$$\gamma = \frac{E_{11} I_s}{b \sqrt{D_{11} D_{22}}}, \quad \phi_m = \frac{\lambda}{b}, \quad \eta_0 = \frac{y_0}{b}, \quad Q_n = \sqrt{\frac{E_{11}}{E_{22}}} + 2n^2 \phi_m^2 \nu_{21} \sqrt{\frac{E_{11}}{E_{22}}} + n^4 \phi_m^4 \sqrt{\frac{E_{22}}{E_{11}}} + 4n^2 \phi_m^2 \frac{G_{12}(1 - \nu_{12} \nu_{21})}{\sqrt{E_{11} E_{22}}}$$

$$N_{nq} = 2\gamma \sin n\pi\eta_0 \sin q\pi\eta_0, \quad M_{nq} = \frac{8k_s \phi_m^3}{\pi} \frac{nq}{(n^2 - q^2)} = -M_{qn}$$

$$\phi = \frac{a}{b}, \quad k_\beta = \frac{32\phi^3 k_s}{\pi^2}, \quad Q_{mn} = m^4 \sqrt{\frac{E_{11}}{E_{22}}} + 2m^2 n^2 \phi^2 \nu_{21} \sqrt{\frac{E_{11}}{E_{22}}} + n^4 \phi^4 \sqrt{\frac{E_{22}}{E_{11}}} + 4m^2 n^2 \phi^2 \frac{G_{12}(1 - \nu_{12} \nu_{21})}{\sqrt{E_{11} E_{22}}}$$

Interaction among a Row of N Semi-Elliptical Notches and Edge Cracks

T. Matsuo¹ and N.-A. Noda²

¹Department of Mechanical Engineering, Fukushima National College of Technology,
30 Nagao, Kamiarakawa Taira, Iwaki, Fukushima 970-8034, Japan

²Department of Mechanical Engineering, Kyushu Institute of Technology,
1-1 Sensui-cho, Tobata, Kitakyushu, Fukuoka 804-8550, Japan

Keywords: Body Force Method, Edge Cracks, Elasticity, Interaction Effect, Numerical Analysis, Semi-Elliptical Notch, Stress Concentration Factor, Stress Intensity Factor

ABSTRACT

This paper deals with a row of equally spaced equal elliptical notches and edge cracks in a semi-infinite plate subjected to tension. Based on the concepts of the body force method, the notch and crack problems are formulated as a system of singular integral equations with a Cauchy-type and a hypersingular kernel, respectively, where the densities of body forces distributed in the x- and y-directions of semi-infinite plate are unknown functions. In order to satisfy the boundary conditions along the notches, eight kinds of fundamental density functions introduced in our previous paper are used. Then the body forces densities are approximated by a linear combination of the fundamental density functions and polynomials. In the analysis, the shape and position of notches are varied systematically; then, the magnitude and position of the maximum stress are examined. For any fixed shape and size of notches and cracks, the maximum stress is shown to be linear with the reciprocal of the number of notches.

1. Introduction

A lot of useful results, which have been obtained by applying suitable numerical methods of analysis, are available in 2-D stress concentration. However, several fundamental and important problems are still unsettled because of the difficulty of analysis. As an example, with regard to periodic elliptical holes, the maximum stress for arbitrary number of hole was recently given by Isida and Igawa [1] although the stress at the central hole in an infinite number of holes has been treated in several previous researches [2-4]. In a similar way, the interaction of a row of semi-elliptical notches in a semi-infinite plate under tension has been treated by Nisitani using the body

force method; then the stress at the central notch in an infinite number of notches has been given in tables [4]. However, no one has calculated the maximum stress in an arbitrary number of notches in a semi-infinite plate. In these problems, the interaction effect reduces the magnitude of stress concentration factor (SCF) compared to the single notch. Then, maximum stress appears at slightly outside of the notch-root of the outermost notch. To obtain the maximum stress accurately, therefore, it is necessary to calculate the stress distributions along the boundary.

In this paper, the interaction of an arbitrary number of elliptical notches and edge cracks in a semi-infinite plate is analyzed by using the singular integral equations based on the body force method [5-7]. In the numerical solution, the unknown functions are approximated by fundamental density functions and polynomials. Then, the magnitude and position of the maximum stress are examined, when the shape, position and number of notches are changed systematically. Also, the stress concentration factor of an infinite number of notches or cracks is extrapolated in terms of a linear relationship between the maximum stress and the reciprocal of the number of them.

2. Numerical Solution for a Row of Semi-Elliptical Notches

Consider a semi-infinite plate under uniform tension having a row of semi-elliptical notches as shown in Fig. 1. The problem is formulated in terms of singular integral equations by using a Green's functions, that is the stress field at an arbitrary point (x,y) when a point force act on another point (ξ, η) in a semi-infinite plate [8, 9]. The formation is simply based on the principle of superposition. The integral equation is expressed by (1), where the body force densities distributed along the prospective boundaries in the x-, y-directions are to be unknown functions. Here, ϕ_k is the angle that specifies the points where the body force is distributed.

$$\begin{aligned} -(1/2)(\rho_x^*(\theta_i)\cos\theta_{i0} + \rho_y^*(\theta_i)\sin\theta_{i0}) + \sum_{k=1}^N \int_0^\pi K_{nn}^{Fx}(\phi_k, \theta_i) \rho_x^*(\phi_k) ds \\ + \sum_{k=1}^N \int_0^\pi K_{nn}^{Fy}(\phi_k, \theta_i) \rho_y^*(\phi_k) ds = -\sigma_x^\infty \sin^2 \theta_{i0} \\ -(1/2)(\rho_x^*(\theta_i)\sin\theta_{i0} + \rho_y^*(\theta_i)\cos\theta_{i0}) + \sum_{k=1}^N \int_0^\pi K_{nn}^{Fx}(\phi_k, \theta_i) \rho_x^*(\phi_k) ds \\ + \sum_{k=1}^N \int_0^\pi K_{nn}^{Fy}(\phi_k, \theta_i) \rho_y^*(\phi_k) ds = -\sigma_x^\infty \sin\theta_{i0} \cos\theta_{i0} \end{aligned} \quad (1)$$

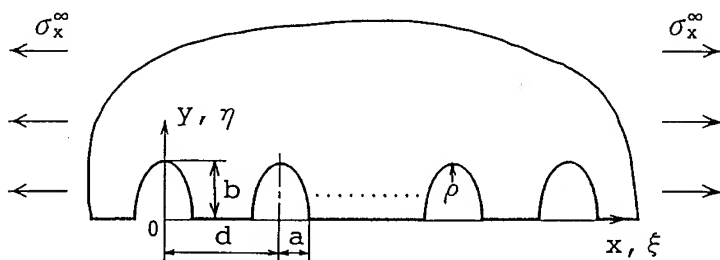


Fig. 1 A row of semi-elliptical notches.

θ_{i0} is an angle between the x-axis and the normal direction at the point (x,y) on the ellipse. The notation means the summation of integrating the body force density on the prospective boundary of the semi-elliptical notches.

Equation (1) are virtually the boundary conditions at the i-th imaginary boundary. The first terms of (1) represent the stress due to the body force distributed on the \ominus boundary. The \ominus boundary means the imaginary boundary composed of the internal points that are infinitesimally apart from the initial boundary [8]. Equations (1) include the singular terms having the singularity of the form $1/\sin\{(\theta_i - \phi_k)/2\}$ when $i=k$ [9]. In the case $\theta_i = \phi_k$ ($i=k$), the integration should be interpreted as the meaning of Cauchy's principle values. The unknown functions in eq. (1) $\rho_x^*(\phi_k)$, $\rho_y^*(\phi_k)$ are defined by the following equations.

$$\rho_x^*(\phi_k) = \frac{dF_\xi}{ds}, \quad \rho_y^*(\phi_k) = \frac{dF_\eta}{ds} \quad (2)$$

where dF_ξ , dF_η are the components of the resultant of the body force in the x-, y-directions, respectively, both acting on the infinitesimal arc length ds .

To solve eq. (1) to determine the body force densities $\rho_x^*(\phi_k)$, $\rho_y^*(\phi_k)$ in the region of $0 < \phi_k < \pi$. Here, consider auxiliary functions $\rho_{x1}^*(\phi_k)$, $\rho_{x2}^*(\phi_k)$, $\rho_{y1}^*(\phi_k)$, $\rho_{y2}^*(\phi_k)$ are defined by eqs. (3), (4) instead of densities $\rho_x^*(\phi_k)$, $\rho_y^*(\phi_k)$.

$$\rho_{x1}^*(\phi_k) = \{\rho_x^*(\phi_k) + \rho_x^*(\pi - \phi_k)\}/2, \quad \rho_{x2}^*(\phi_k) = \{\rho_x^*(\phi_k) - \rho_x^*(\pi - \phi_k)\}/2 \quad (3)$$

$$\rho_{y1}^*(\phi_k) = \{\rho_y^*(\phi_k) + \rho_y^*(\pi - \phi_k)\}/2, \quad \rho_{y2}^*(\phi_k) = \{\rho_y^*(\phi_k) - \rho_y^*(\pi - \phi_k)\}/2 \quad (4)$$

These new functions $\rho_{x1}^*(\phi_k) \sim \rho_{y2}^*(\phi_k)$ must satisfy eqs. (5), (6) because of the definition (3), (4).

$$\rho_{x1}^*(\phi_k) = \rho_{x1}^*(\pi - \phi_k), \quad \rho_{x2}^*(\phi_k) = -\rho_{x2}^*(\pi - \phi_k) \quad (5)$$

$$\rho_{y1}^*(\phi_k) = \rho_{y1}^*(\pi - \phi_k), \quad \rho_{y2}^*(\phi_k) = -\rho_{y2}^*(\pi - \phi_k) \quad (6)$$

It should be noted that determining auxiliary functions $\rho_{x1}^*(\phi_k) \sim \rho_{y2}^*(\phi_k)$ in the region of $0 < \phi_k < \pi/2$ is equivalent to determining original unknown densities $\rho_x^*(\phi_k)$, $\rho_y^*(\phi_k)$ in the region of $0 < \phi_k < \pi$. In other words, if the auxiliary functions $\rho_{x1}^*(\phi_k) \sim \rho_{y2}^*(\phi_k)$ are given in the region of $0 < \phi_k < \pi/2$, original unknown functions $\rho_x^*(\phi_k)$, $\rho_y^*(\phi_k)$ are expressed in the region of $0 < \phi_k < \pi$ using eqs. (7), (8).

$$\rho_x^*(\phi_k) = \rho_{x1}^*(\phi_k) + \rho_{x2}^*(\phi_k), \quad \rho_x^*(\pi - \phi_k) = \rho_{x1}^*(\phi_k) - \rho_{x2}^*(\phi_k) \quad (7)$$

$$\rho_y^*(\phi_k) = \rho_{y1}^*(\phi_k) + \rho_{y2}^*(\phi_k), \quad \rho_y^*(\pi - \phi_k) = \rho_{y1}^*(\phi_k) - \rho_{y2}^*(\phi_k) \quad (8)$$

The fundamental density functions for the body forces in the x-, and y-directions are defined by following expression [5, 6, 10]:

$$w_{x1}(\phi_k) = n_x(\phi_k)/\cos\phi_k, \quad w_{x1}(\phi_k) = n_x(\phi_k) \quad (9)$$

$$w_{y1}(\phi_k) = n_y(\phi_k), \quad w_{y2}(\phi_k) = n_y(\phi_k)\cos\phi_k \quad (10)$$

Using eqs. (9), (10), original body force densities are expressed as shown in eqs. (11), (12).

$$\rho_x^*(\phi_k) = \rho_{x1}(\phi_k)w_{x1}(\phi_k) + \rho_{x2}(\phi_k)w_{x2}(\phi_k) \quad (11)$$

$$\rho_y^*(\phi_k) = \rho_{y1}(\phi_k)w_{y1}(\phi_k) + \rho_{y2}(\phi_k)w_{y2}(\phi_k) \quad (12)$$

where $\rho_{x1}(\phi_k)$, $\rho_{x3}(\phi_k)$, $\rho_{y2}(\phi_k)$, $\rho_{y4}(\phi_k)$ are unknown functions, which have been called weight functions. Then all $\rho_{x1}(\phi_k)$, $\rho_{x3}(\phi_k)$, $\rho_{y2}(\phi_k)$, $\rho_{y4}(\phi_k)$ must satisfy eq. (13).

$$f(\phi_k) = f(\pi - \phi_k) \quad f(\phi_k) : \rho_{x1}(\phi_k), \rho_{x3}(\phi_k), \rho_{y2}(\phi_k), \rho_{y4}(\phi_k) \quad (13)$$

Here all unknown weight functions can be approximated as shown in eqs (14) ~ (16) because all of these must satisfy eq. (13).

$$\rho_{x1}(\phi_k) = \sum_{n=1}^{M/2} a_n t_n(\phi_k), \quad \rho_{x2}(\phi_k) = \sum_{n=1}^{M/2} b_n t_n(\phi_k) \quad (14)$$

$$\rho_{y1}(\phi_k) = \sum_{n=1}^{M/2} c_n t_n(\phi_k), \quad \rho_{y2}(\phi_k) = \sum_{n=1}^{M/2} d_n t_n(\phi_k) \quad (15)$$

$$t_n(\phi_k) = \cos\{2(n-1)\phi_k\} \quad (16)$$

Where M is the number of the collocation points for each semi-elliptical notch in the range $0 < \theta < \pi$. Using the approximation method mentioned above, we obtain the system of linear equations for determining the coefficients a_n , b_n , c_n , d_n . Then, the magnitude and position of the maximum stress are calculated, when the shape, position and number of notches are changed systematically.

Numerical solution for a row of edge cracks when $a/b=0$ in Fig. 1 is omitted. This problem is reduced to the hypersingular integral equation [7].

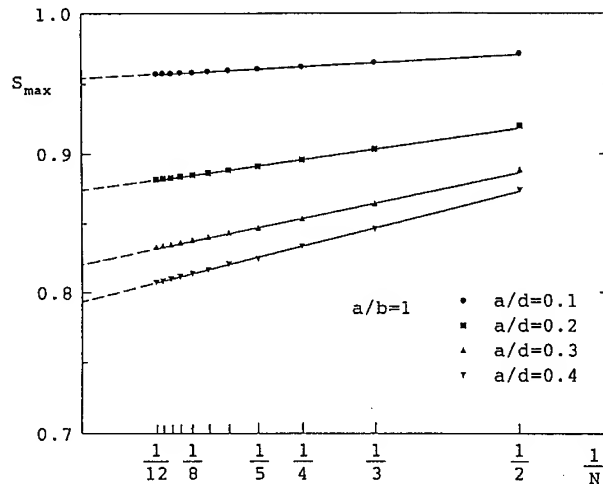


Fig.2 Relationship between S_{\max} and $1/N$ when $a/b=1$ in Fig. 1.

3. Numerical Results and Discussion

Figure 2 shows the relationship between S_{\max} and $1/N$ when $a/b=1$, $\sigma_x^\infty=1$ with $a/d=0.1, 0.2, 0.3, 0.4$, and Fig. 3 shows the one when with $a/b=0$, $\sigma_x^\infty=1$ with $b/d=0.1, 0.2, 0.3, 0.4$. The values of S_{\max} shown in Fig. 2, 3 mean the maximum values of $S_{j\max}$ that occur at the outermost notches and cracks. In Fig. 2, $S_{j\max}=\sigma_{j\max}/\sigma_0$ is the dimensionless factor, $\sigma_{j\max}$ denotes the maximum stress at each notch and σ_0 denotes the maximum stress of a single semi-circular notch. In Fig. 3, $S_{j\max}$ defined by $S_{j\max}=F_I/F_{I|N=1}$, where $F_{I|N=1}$ denotes the stress intensity factor of a single edge crack. For elliptical holes [1] and edge cracks [11], Isida et al. have found the relationship between S_{\max} and $1/N$. The present results for a row of semi-elliptical notches also indicate that the values of S_{\max} are nearly proportional to $1/N$.

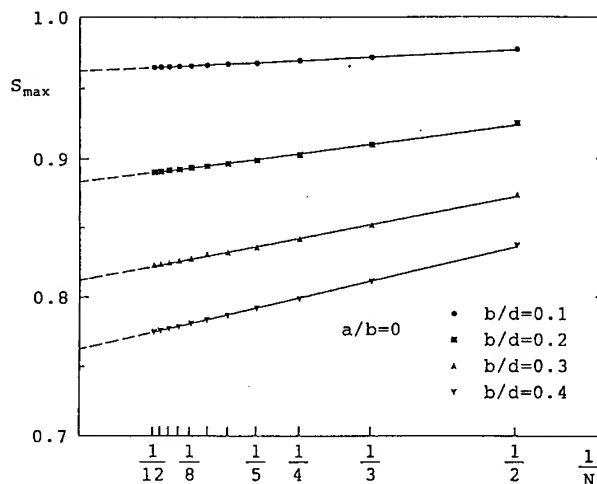


Fig. 3 Relationship between S_{\max} and $1/N$ when $a/b=0$ in Fig. 1.

Table 1 Maximum stress at the outermost notch and crack in a row of semi-elliptical notches or edge cracks shown in Fig. 1. (Number of notch or crack $N=\infty$)

$\rho/b=(a/b)^2$	b/a	$\sigma_0 (*: F_{I N=1})$	$S_{\max} = \sigma_{\max} / \sigma_0, F / F_{I N=1}$					
		$b/d=0.0$	$b/d=0.0$	$b/d=0.1$	$b/d=0.2$	$b/d=0.3$	$b/d=0.4$	$b/d=0.5$
0.00	∞	1.1215*	1.0000	0.9620	0.8841	0.8137	0.7631	0.7283
0.20	≈ 2.24	5.7353	1.0000	0.9596	0.8817	0.8190	0.7775	0.7503
0.25	2.00	5.2202	1.0000	0.9592	0.8823	0.8181	0.7789	0.7525
0.40	≈ 1.58	4.3120	1.0000	0.9579	0.8793	0.8200	0.7825	0.7568
0.60	≈ 1.29	3.6867	1.0000	0.9571	0.8776	0.8201	0.7855	0.7620
0.80	≈ 1.12	3.3166	1.0000	0.9567	0.8762	0.8214	0.7893	0.7667
1.00	1.00	3.0653	1.0000	0.9549	0.8740	0.8229	0.795	0.771

Using relationship mentioned above, Table 1 shows the factor S_{\max} when $N \rightarrow \infty$ at the outermost notches and cracks ($p/b=0$) with varying the geometrical parameters $(a/b)^2 = p/b$ and b/d .

4. Conclusions

In this paper, the interaction for semi-elliptical notches and cracks in a semi-infinite plate is analyzed by using the singular integral equations based on the body force method. The conclusion are summarized as follows:

1. Numerical solutions of the singular integral equations were considered. To satisfy the boundary condition along the notches, new fundamental density functions proposed in our previous paper were applied. Then the unknown functions are approximated by the products of the fundamental density functions and polynomials.
2. In the problems of semi-elliptical notches or edge cracks, the maximum values of stress or stress intensity factor occur at the outermost notches or cracks. Except outermost notches the magnitude of stress at each notch is almost equal and smaller than that of outermost notch. In a row of notches and cracks, the interaction effect is mainly controlled by the distance, almost independent of the shape and the number except for the case of small number of notches or cracks.
3. For a row of semi-elliptical notches, the maximum stress is found to be nearly proportional to the reciprocal of the number of notches. By using those relationships, the extreme values of maximum stress are also estimated and tabulated when the number of notches $N \rightarrow \infty$.

REFERENCE

1. M. Isida, and H. Igawa, Trans. Jpn. Soc. Mech. Engineers, 58 (1992) p. 1642.
2. R. C. J. Howland, Proc. Roy. Soc. London, A, 148 (1935) p. 471.
3. K. J. Schultz, Advances in Applied Mechanics, 1. Academic Press, New York (1948) p. 1940.
4. H. Nisitani, Proc. Int. Conf. on Fracture Mechanics and Technology, (Ed. G. C. Sih and C. L. Chow), (1977) p. 1127.
5. N.-A. Noda and T. Matsuo, Trans. Jpn. Soc. Mech. Engineers, 58 (1992) p. 2179.
6. N.-A. Noda and T. Matsuo, Trans. Jpn. Soc. Mech. Engineers, 59 (1993) p. 785.
7. N.-A. Noda and K. Oda, Int. Jour. Fracture, 58 (1992) p. 285.
8. H. Nisitani, Jour. Jpn Soc. Mech. Engrs, 70 (1967) p. 627. [Bull. Jpn Soc. Mech. Engrs 11 (1968) p. 14.
9. H. Nisitani and D. H. Chen, The body force method (Taiseikiryokuhou in Japanese), Baifukan, Tokyo (1987).
10. N.-A. Noda and T. Matsuo, Fracture Mechanics, 25, ASTM STP 1220, Edited by F. Erdogan, (1995) p. 591.
11. M. Isida, Trans. Jpn. Soc. Mech. Engineers, 45 (1992) p. 306.

A Computational Investigation on Metal/Ceramic Joints under Thermal Cyclic Loadings

M.K. Park and Saemahn Bahk

Department of Mechanical Engineering, College of Engineering, Myongji University,
Kyunggi-Do, Yongin-Shi, Nam-Dong, San 449-728, Korea

Keywords: Finite Element Analysis, Metal/Ceramic Joint, Residual Stress, Thermal Cycle

ABSTRACT

Thermal stresses at ceramic/metal interfaces in ceramic-metal joints are analyzed with emphases on assessing residual stresses produced and retained in the joints during joining processes of ceramics with metals, and evaluating their redistributions under applied thermal cycles. A thermo-elastic plastic finite element method is adopted to compute various physical quantities associated with the thermal processes. The computational results demonstrate that the residual stresses on the ceramic side in the metal-ceramic joints, generally, increase with increasing peak temperatures in the thermal cycles. Also, the higher the peak temperatures are in the thermal cycles, the higher values are obtained for intensities (Q) and coefficients (λ) of stress singularity near the end point along the interface on the ceramic side.

1. INTRODUCTION

Joining of ceramics with metals is usually accomplished at elevated temperatures where one of the two member materials could remain solid. Upon cooling after completion of joining the two materials residual thermal stresses would be inevitably set up in the ceramic-metal joints. This is largely due to mismatches between thermal expansion coefficients of the two member materials. The residual stresses are known to have strong effects on strengths of ceramic-metal joints. Therefore, their distributions and levels are extensively investigated in many cases and relatively well understood. However, the stress levels can not remain the same when the joints are used as parts of such structures as gas turbines and heat exchangers because of repeated thermal cyclic loadings applied to the joints. The applied thermal cycles cause redistributions of the residual stresses, but studies on the redistributions of stresses were scanty and their scope has been very limited.

In this investigation a thermo-elastic-plastic analysis is conducted on $\text{Si}_3\text{N}_4/\text{SUS 304}$ joints with Finite Element Method. Single thermal cycle is applied to $\text{Si}_3\text{N}_4/\text{SUS 304}$ joints with its peak temperature of the cycle varying from 100~500°C. A typical thermal cycle is a thermal path that starts from room temperature, reaching peak temperature and returns back to room temperature. Based on the computational results effects of the thermal cycles and characteristics of the stress redistributions are fully discussed. Also, an elastic-plastic aspect of copper interlayer as well as

temperature dependence of yield strength are taken into account in further analyses.

2. MODELLING AND ANALYSIS

Initial residual stress distributions induced in the joining processes are, first, analyzed in light of a thermo-elastic-plastic theory. In the second step single thermal cycle is applied to the joints which already have residual stresses that are formed in the joining processes. The peak temperatures in the thermal cycle are varied from 125°C, 225°C, 325°C to 425°C.

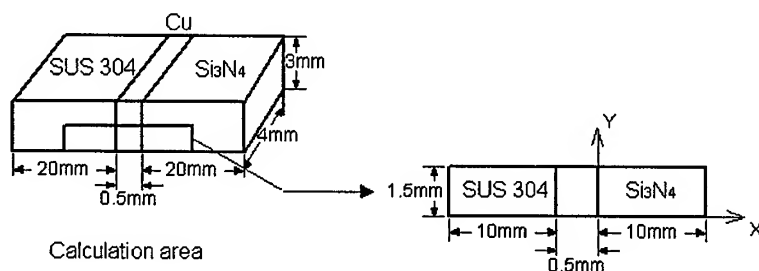


Fig. 1. Configuration of specimen and area for analysis

The dimensions and configurations of specimens for the model are shown in Fig. 1. Basically, the specimen (joint) is made of three parts. A thin copper layer is placed at the center with the ceramic (Si_3N_4) on one side of the layer and the metal (SUS304) on the other side of the layer. The copper layer acts as an interlayer to minimize residual stresses. The marked area in Fig. 1 is selected as the region where computational analyses are applied. In the selection of the area, symmetry of the specimen is considered and an assumption is made that level of the stress is negligible beyond 10 mm from the interface. Fig. 2 shows that fine elements are assigned to the region of stress

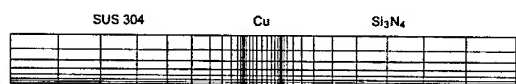


Fig. 2. Finite Element Mesh

concentrations while coarse elements are used for other areas. Table 1 shows material properties at room temperature. The temperature dependences of Young's modulus, thermal expansion coefficients and yield strengths are presented in Table 2. Poisson's

ratios and strain hardening coefficients are taken to be independent of temperature, assumed to have constant values. For copper at the interlayer, both isotropic and kinematic hardenings are considered in the analyses to compare the results from the two hardening mechanisms.

Table 1. Mechanical properties at room temperature

	Si_3N_4	Cu	SUS 304
$E(\text{kgf/mm}^2)$	31.6×10^3	11.2×10^3	19×10^3
ν	0.27	0.33	0.3
α	$3 \times 10^{-6}/^\circ\text{C}$	$17.7 \times 10^{-6}/^\circ\text{C}$	$16.5 \times 10^{-6}/^\circ\text{C}$
$\sigma_y(\text{kgf/mm}^2)$		2	
$H(\text{kgf/mm}^2)$		8.5	

Only single thermal cycles are applied to the ceramic/metal joints to avoid complications that could arise from multiple thermal cycles.

Table 2. Temperature dependence of mechanical properties of materials

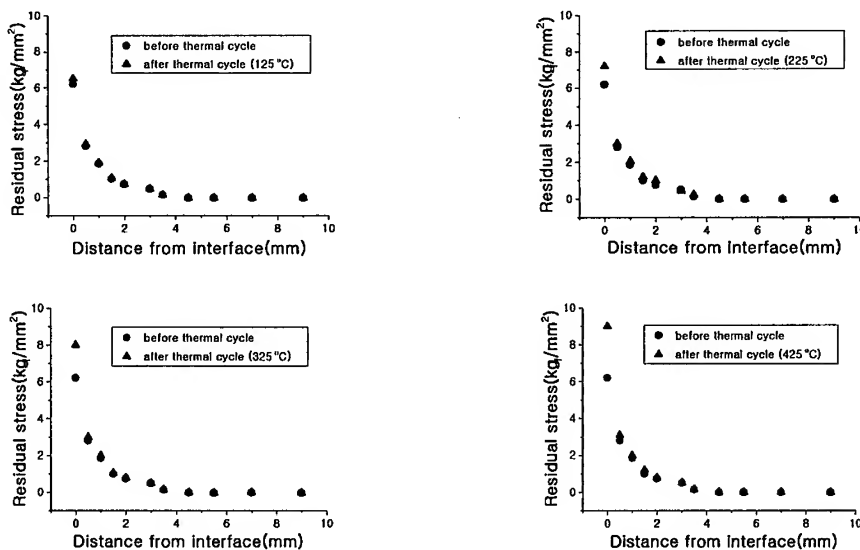
Temp.	Young's modulus(E) (kg/mm ²)			Yield stress(σ_y) (kg/mm ²)			CTE(α) 10 ⁻⁶ /°C		
	25°C	275°C	525°C	25°C	275°C	525°C	25°C	275°C	525°C
Si ₃ N ₄	31.6×10 ³	32.1×10 ³	32.7×10 ³				3.1	3.1	3.1
Cu	11.2×10 ³	10.2×10 ³	9.2×10 ³	2	1.5	0.7	17.5	19	21
SUS 304	19×10 ³	18×10 ³	17×10 ³				16	18	19.5

It is frequently observed that fracture of the joint (Si₃N₄/SUS 304) is usually initiated at the intersecting point where the interface between copper interlayer and Si₃N₄ meets the lower edge of the ceramic (Si₃N₄) part. This point also becomes the origin of the x-y coordinates as shown in Fig. 1. The frequent initiations of the fracture at the origin are believed to be the consequence of concentrations of the residual stresses (σ_x) near the origin in the ceramic part.

3. RESULTS AND DISCUSSIONS

3.1 Effects of single thermal cycle on residual stress

Yield strength of copper is dependent on temperatures, but for simplicity the yield strength is taken at a constant value, 2 kg_f/mm² and also isotropic hardening behavior is initially assumed. Single thermal cycles with peak temperatures at 125°C, 225°C, 325°C, 425°C are applied to the joints(specimens) to determine the stresses σ_x along the edge in the ceramic side. Fig. 3 shows the stress distributions of σ_x both before and after the thermal cyclic loadings. The results in the figure clearly indicate that over-all trend of stress distributions do not deviate noticeably after the thermal loadings, but the residual stresses definitely increase near the interface between the copper interlayer and the ceramic. This aspect of the results is in a qualitative agreement with the experimental results from an X-ray analysis. The maximum residual stresses resulting from the applied thermal cycles are plotted with the peak temperatures in Fig. 4.

Fig. 3. Redistribution of σ_x

Evidently the maximum residual stresses near the interface increase with the increasing peak temperatures of the applied thermal cycles. This can be attributed to the characteristics of elastic-plastic behavior of the copper interlayer as well as the strain hardening effects of copper.

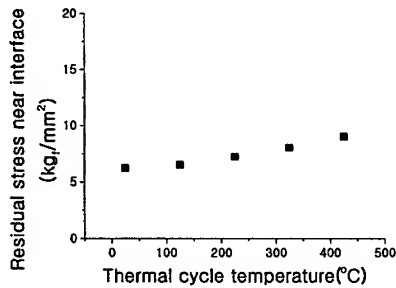


Fig. 4. Residual stresses and peak temperatures of single thermal cycles

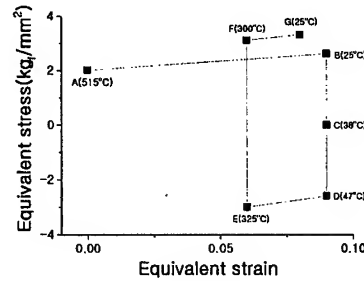


Fig. 5. Equivalent stresses and strains of copper layer with an application of single thermal cycle with peak temperature at 325°C

The Equivalent stresses are plotted against equivalent strains in Fig. 5 for the results from the single thermal cycle loading with its peak temperature at 325°C. During the initial stage of joining process and subsequent cooling, copper recovering its mechanical strength around 525°C, begins to deform elastically, but turns to plastic deformation around 515°C (A) where copper has yield strength of 2kg_f/mm² in tension. With further decrease in temperature plastic deformation develops more until room temperature 25°C (B) is reached. At point B where joining process is completed, the final residual stresses retained in the joints are around 2.8kg_f/mm². As temperature rises from room temperature with the application of single thermal cycle, the level of residual stresses drops rapidly, even reversing its sense in opposite direction near 38°C. Equivalent stresses always take positive values by definition, but in Fig. 5, negative values are taken to indicate the reverse of the direction at points C (38°C), D (47°C) and E (325°C). In this computation isotropic hardening is assumed for copper and thus the negative stress of -2.8kg_f/mm² corresponds to the yield strength of copper in compression. With further increase in temperature, extent of plastic deformation diminishes and during cooling period after the peak temperature (325°C) the equivalent stress reverts again to opposite direction, exceeding the yield strength of copper in tension (3.1kg_f/mm²) around 300°C (F). When the cooling process is completed at the end of the single thermal cycle, the final residual stress becomes 3.3kg_f/mm²(G) which is 15~20% higher than the equivalent stress 2.8kg_f/mm²(B) before the single thermal cycle is applied.

Strains of the copper interlayer (ϵ_p) can be related to temperature differences (ΔT) as following :

$$\epsilon_p = (2/3)^{1/2} (\alpha_s - \alpha_c) \Delta T W / (2t)$$

where ϵ_p : equivalent plastic strain
 α_s : thermal expansion coefficient of SUS 304 (1/K)
 α_c : thermal expansion coefficient of Si₃N₄ (1/K)
 ΔT : temperature difference (K)
 W : width of specimen (mm)
 t : thickness of copper interlayer (mm)

From the above relation residual stresses in the ceramic in the joints are seen to increase in proportion with the increase in peak temperatures of single thermal cycles.

3.2 Elastic-plastic singularity of thermal residual stresses

Residual stresses near the interface between the copper interlayer and the ceramic exhibit stress singularity. The lower end point or the point of intersection (origin of x-y coordinate in Fig. 1) is the point of stress singularity. The stress distribution (σ_x) along the x direction in the ceramic can be expressed as

$$\sigma_x = Q / x^\lambda$$

Where σ_x : residual stress along x direction (kg/mm^2) Q : stress singularity intensity
 x : distance from the origin (mm) λ : stress singularity coefficient

In the case of elastic bodies intensity (Q) and coefficient (λ) of stress singularity depend on elastic constants, Poisson's ratios and thermal expansion coefficients of the two joining materials. Also, when copper at the interlayer yields elastic-plastic behavior of the interlayer should be taken into account. The results for intensity (Q) and coefficient of stress singularity (λ) are listed in Table 3. It is seen that the thermal cycles noticeably increase magnitudes of Q and λ , but in proportion with the peak temperatures of the thermal cycles.

Table 3. Intensity Q and Coefficient λ of stress singularity

Temp(°C)	Q	λ
None	22.8	0.27
125	23.7	0.27
225	24.2	0.28
325	25.2	0.30
425	26	0.31

3.3 Effect of temperature dependent yield strength of copper interlayer

In the analysis up to this point the yield strength of copper at the interlayer is assumed to be constant for simplicity of the model. The actual yield strengths of copper are shown in Table 2 as a function of temperature, and incorporated in the subsequent analysis.

The results show that the residual stresses in the joints at room temperature after the applications of thermal cycles have almost the same values as those at room temperature before the thermal cycles are applied. This seems to indicate that the residual stresses at room temperature are mainly determined by the yield strength at room temperature, but not influenced by the temperature dependence of the yield strengths.

3.4 Effect of hardening mechanisms of copper

In the stress analysis, so far, all the applied thermal cycles are limited only to single thermal cycles, meaning that a predetermined specific thermal cycle is applied just only once, not many times. Also, copper is assumed to follow the isotropic hardening mechanism. From the results with the two assumptions, it may be conceivable that the level of residual stresses could increase continuously with increasing number of thermal cycles (multiple thermal cycle). This seemingly logical, but unrealistic prediction may in fact suggest that the assumed isotropic hardening of copper may not be an adequate mechanism.

In an attempt to provide more realistic prediction in case of multiple thermal loadings, copper is assumed to follow kinematic hardening mechanism for the next computational analysis. Equivalent stresses and strains are computed for the single thermal cycle with its peak temperature at 525°C. The results show that the equivalent stresses and strains of copper, before and after the application of the single thermal cycle are almost identical. The maximum equivalent stress (6.5 kg/mm^2) near the interface after the single thermal cycle is indeed very close to the maximum value before the single thermal (6.6 kg/mm^2) cycle. This may be interpreted as an indication that the level of stresses may not increase continuously even if thermal cycles are applied repeatedly. Consequently the kinematic hardening may be considered to be operative at least, at certain stage of the copper hardening during cooling at the end of joining processes.

4. CONCLUSIONS

A finite element analysis is conducted on $\text{Si}_3\text{N}_4/\text{SUS 304}$ joints with a copper interlayer. The SUS 304 is an austenite stainless steel. Single thermal cycles are applied to joints. Elastic-plastic behavior of copper is incorporated in the analysis.

The analysis includes both estimations of final residual stresses retained at the end of joining processes as well as redistributions of the residual stresses resulting from applied single thermal cycles. The following statements can be drawn from the analysis.

- (1) The over-all trend of distributions of residual stresses after the thermal cycles are not very different from those before the thermal cycles are applied, but residual stresses near the singular point increase with the increasing peak temperatures in the thermal cycles.
- (2) The intensity (Q) and coefficient (λ) of stress singularity increase in proportion with the peak temperatures in the thermal cycles.
- (3) The distributions of residual stresses under the thermal cycles are affected by elastic-plastic characteristics of the copper interlayer, especially by the yield strength of copper at room temperature.
- (4) Kinematic hardening mechanism may be operative for the deformation of copper in the cooling process.

REFERENCE

1. D.B. Bogy, J. Appl. Mech., 42(1975) p.93
2. C.H. Hsueh and A.G. Evans, J. Am. Ceram. Soc., 68(1985) p.120
3. Y. Zhou, F.H. Bao, J.L. Ren, and T.H. North, Mater. Sci. Technol., 7(1991) p.863
4. Y. Yamada, K. Yori and A. Kohno, J. Mater. Sci., 25(1990) p.2188

Progressive Failure Analysis of Composite Laminates Using 3-D Finite Element Method

S.G. Joo and C.S. Hong

Department of Aerospace Engineering, Korea Advanced Institute of Science and Technology,
373-1 Kusong-dong, Yuseong-gu, Taejeon 305-701, Korea

Keywords: Composite Laminates, Failure Mode, Progressive Failure Analysis, Stiffness Reduction Method

ABSTRACT

Progressive failure analysis was conducted in the present study for the cross-ply and quasi-isotropic laminates subjected to axial extension. Stresses and strains are calculated by the 3-d finite element method based on the generalized layerwise plate theory (GLPT) in order to consider the local effect near the free edges. The types and size of damage in composite laminates are predicted in the failure analysis that consist of a set of failure criteria and property degradation models for each mode of failure. In case of matrix cracking, the macroscopic stiffness reduction model based on the shear-lag method is introduced to the finite element method in order to consider nonlinear reduction of stiffness at each strain level. Mesh refinement is conducted both in-plane and through the thickness direction in order to predict the failure load and the damage accumulation accurately. The failure mechanism and ultimate failure loads of the cross-ply and quasi-isotropic laminates for different stacking sequences with the same thickness are investigated.

1. INTRODUCTION

The high strength and stiffness to weight of advanced composite materials often makes these materials attractive candidates for weight sensitive structures, especially aircraft structures. The damage of laminated composite is characterized by matrix cracking, fiber breakage and delamination. The types and extents of damage significantly affect the strength and performance of composite laminates. In order to optimally design and accurately assess the damage tolerance of the composite structures, the information on the internal damage as a function of applied load as critically important as the strength to designers. For investigating the post failure behavior from the initiation of damage to the ultimate failure, progressive failure algorithm is developed in the present study such that the damaged material with many micro cracks is replaced with an equivalent material of degraded properties. Based on this model, a computer code is developed.

Since computing cost is an important factor, most researchers[1-6] used two-dimensional finite element techniques to analyze the progressive failure. However stress singularities may occur at the interface between two layers of different ply orientation on the free edges. High magnitudes of stresses at the free edge of the ply interface are responsible for failure initiation at those locations. Therefore the state of stress near the edge is important and 3-d stresses are required. In the studies of progressive failure analysis of composite laminates using 3-d stress field[7,8], they showed the exact stress field but used the constant or assumed stiffness reduction method in the failure evaluation.

In the present study, stresses and strains are calculated by the 3-d finite element method based on the generalized layerwise plate theory (GLPT) in order to consider the local effect near the free edge. The types and size of damage in composite laminates are predicted in the failure analysis consist of a set of failure criteria and property degradation models for each mode of failure. In case of matrix cracking, the macroscopic stiffness reduction model based on the shear-lag method [5] is introduced to the finite element method in order to consider nonlinear progressive reduction of stiffness at each strain levels. In order to predict the failure load and the damage accumulation accurately the refined finite element model with 3-d finite element method is used. In the present formulation, a linear elastic behavior is assumed and a damaged layer in an element is substituted by a degraded homogeneous layer. The effect of damage accumulation is accounted for by degrading the stiffness properties of failed element layers in the equilibrium iterations.

2. FINITE ELEMENT METHOD

2.1. Finite Element Formulation

In the GLPT a piecewise continuous displacement field through the thickness [9] is assumed and hence has the ability to capture the interlaminar stress fields near the free edges and supports of composites laminates more accurately. Layerwise expansion is used for all three displacement components.

In GLPT the displacement field is expanded as :

$$\begin{aligned} u(x, y, z) &= \sum_{j=1}^N U_j(x, y) \phi^j(z) \\ v(x, y, z) &= \sum_{j=1}^N V_j(x, y) \phi^j(z) \\ w(x, y, z) &= \sum_{j=1}^N W_j(x, y) \phi^j(z) \end{aligned} \quad (1)$$

where u, v, w are displacement component along x, y, z directions, respectively, of a material point initially located at (x, y, z) in the undeformed laminate, and the reference plane of the plate coincides with xy -plane. The laminate thickness dimension is subdivided into a series of N one dimensional finite elements (i.e. thickness subdivisions) whose nodes correspond to plane of constant z in the undeformed laminates. The 1-D finite element mesh contains a total of N nodes distributed through the thickness at function $z_j (j=1, 2, \dots, N)$. The function $\phi^j(z) (j=1, 2, \dots, N)$ are the one dimensional Lagrangian interpolation functions associated with the series of n nodes distributed through the thickness of the laminates. The function U_j, V_j, W_j represent the displacement components of all points located on the j -th plane (defined by $z = z_j$) in the undeformed laminates.

The finite element model corresponding to the displacement field of equation (5) is developed by applying the principle of virtual displacements to a representative finite element of the plate:

$$\int_V (\sigma_{ij} \varepsilon_{ij}) dV = \int_S (T_i \delta u_i) dS \quad (2)$$

In equation (2), σ_{ij} are the components of the stress tensor, ε_{ij} are the components of the strain tensor and T_i are the components of surface traction vector.

The force resultants are given by

$$\begin{aligned}
 N_x^J, N_y^J, N_{xy}^J &\equiv \sum_{k=1}^{N-1} \left[\int_{z_k}^{z_{k+1}} (\sigma_x, \sigma_y, \sigma_{xy}) \phi^J dz \right] \\
 Q_y^J, Q_x^J &\equiv \sum_{k=1}^{N-1} \left[\int_{z_k}^{z_{k+1}} (\sigma_{yz}, \sigma_{xz}) \phi^J dz \right] \\
 \tilde{N}_z^J, \tilde{Q}_y^J, \tilde{Q}_x^J &\equiv \sum_{k=1}^{N-1} \left[\int_{z_k}^{z_{k+1}} (\sigma_z, \sigma_{yz}, \sigma_{xz}) \frac{d\phi^J}{dz} dz \right]
 \end{aligned} \quad (3)$$

Finite element equation can be obtained as

$$\mathbf{K} \mathbf{u} = \mathbf{F} \quad (4)$$

where stiffness matrix \mathbf{K} , displacement vector \mathbf{u} and external force \mathbf{F} are as follows:

$$\mathbf{K} = \int_{\Omega} \begin{bmatrix} \mathbf{H}^T \mathbf{Q}^{1H} & \mathbf{H}^T \mathbf{Q}^{12H} & \mathbf{H}^T \mathbf{Q}^{13H} & \dots & \mathbf{H}^T \mathbf{Q}^{1NH} \\ \mathbf{H}^T \mathbf{Q}^{12H} & \mathbf{H}^T \mathbf{Q}^{22H} & \mathbf{H}^T \mathbf{Q}^{23H} & \dots & \mathbf{H}^T \mathbf{Q}^{2NH} \\ \mathbf{H}^T \mathbf{Q}^{13H} & \mathbf{H}^T \mathbf{Q}^{23H} & \mathbf{H}^T \mathbf{Q}^{33H} & \dots & \mathbf{H}^T \mathbf{Q}^{3NH} \\ \vdots & \vdots & \vdots & \ddots & \vdots \\ \mathbf{H}^T \mathbf{Q}^{1NH} & \mathbf{H}^T \mathbf{Q}^{2NH} & \mathbf{H}^T \mathbf{Q}^{3NH} & \dots & \mathbf{H}^T \mathbf{Q}^{NNH} \end{bmatrix} dA \quad (5)$$

where,

$$\mathbf{Q}^{JK} = \begin{bmatrix} A_{11}^{JK} & A_{12}^{JK} & A_{16}^{JK} & B_{13}^{JK} & 0 & 0 & 0 & 0 \\ A_{12}^{JK} & A_{22}^{JK} & A_{26}^{JK} & B_{23}^{JK} & 0 & 0 & 0 & 0 \\ A_{16}^{JK} & A_{26}^{JK} & A_{66}^{JK} & B_{36}^{JK} & 0 & 0 & 0 & 0 \\ C_{13}^{JK} & C_{23}^{JK} & C_{36}^{JK} & D_{33}^{JK} & 0 & 0 & 0 & 0 \\ 0 & 0 & 0 & 0 & A_{44}^{JK} & A_{45}^{JK} & B_{44}^{JK} & B_{45}^{JK} \\ 0 & 0 & 0 & 0 & A_{45}^{JK} & A_{55}^{JK} & B_{45}^{JK} & B_{55}^{JK} \\ 0 & 0 & 0 & 0 & C_{44}^{JK} & C_{45}^{JK} & D_{44}^{JK} & D_{45}^{JK} \\ 0 & 0 & 0 & 0 & C_{45}^{JK} & C_{55}^{JK} & D_{45}^{JK} & D_{55}^{JK} \end{bmatrix} \quad (6)$$

$$\begin{aligned}
 A_{rs}^{JK} &\equiv \sum_{k=1}^{N-1} \int_{z_k}^{z_{k+1}} [(\bar{C}_{rs})_k \phi^J \phi^K] dz \\
 B_{rs}^{JK} &\equiv \sum_{k=1}^{N-1} \int_{z_k}^{z_{k+1}} [(\bar{C}_{rs})_k \phi^J \frac{d\phi^K}{dz}] dz \\
 C_{rs}^{JK} &\equiv \sum_{k=1}^{N-1} \int_{z_k}^{z_{k+1}} [(\bar{C}_{rs})_k \frac{d\phi^J}{dz} \phi^K] dz \\
 D_{rs}^{JK} &\equiv \sum_{k=1}^{N-1} \int_{z_k}^{z_{k+1}} [(\bar{C}_{rs})_k \frac{d\phi^J}{dz} \frac{d\phi^K}{dz}] dz
 \end{aligned} \quad (7)$$

2.2. Solving Scheme

At n th load step, stresses are expressed in terms of incremental form

$${}^n \sigma = {}^{n-1} \sigma + \Delta \sigma \quad (8)$$

Then, finite element equilibrium equation can be obtained in a similar manner

$$\mathbf{K} \Delta^n \mathbf{u}^{(i)} = \mathbf{F}^n - \mathbf{P}^{(i-1)} \quad (9)$$

where, superscript (i) is the number of iteration, and superscript n is the load step.

3. FAILURE EVALUATION

3.1 Failure Criteria

Failure of composite laminates is evaluated at each lamina in laminates by failure criteria in every load step. In order to distinguish the mode of failure, Hashin's failure criteria is used.

3.2 Stiffness Reduction Models

If the failure occurs at the lamina in the laminates, the stiffness of that lamina are reduced gradually. In present works, the values of stiffness matrix C_{ij} are reduced gradually according to the macroscopic failure models as a function of strain values. Fiber bundle failure theory for fiber failure and shear-lag analysis for matrix cracking is used as macroscopic failure models. It is assumed that the matrix cracks in the shear-lag model are distributed with the uniform spacing 2ℓ as shown in Fig. 1.

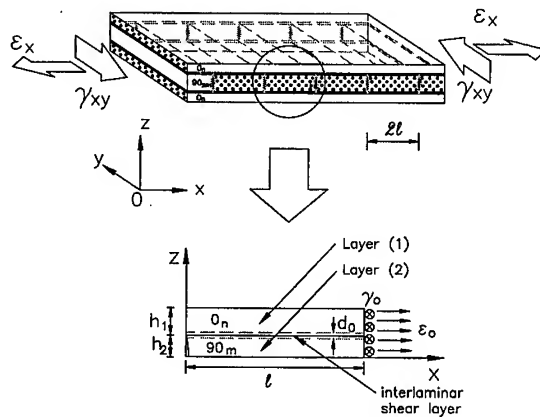


Fig. 1 Shear-lag modeling of matrix cracked laminate subjected to tensile and in-plane shear loading.

4. RESULTS AND DISCUSSION

Progressive failure analysis is conducted for quasi-isotropic laminates for different stacking sequences with the same thickness. The geometry is 100 mm × 20 mm × 0.6 mm. Using symmetry boundary conditions, only quadrant region is modeled. Mesh refinements are conducted both in-plane and through the thickness direction as shown in Fig. 2. The material properties of HFG-CU125NS graphite/epoxy are used as $E_1=130.0$ GPa, $E_2=E_3=10.0$ GPa, $G_{12}=G_{13}=4.85$ GPa, $G_{23}=3.62$ GPa, $\nu_{12}=\nu_{13}=0.31$, $\nu_{23}=0.52$, $X_T=1933$ MPa, $X_C=1051$ MPa, $Y_T=51$ MPa, $Y_C=141$ MPa, $Q=74$ MPa, $R=84$ MPa, $S=61$ MPa. 4 types of the stacking sequences are selected as

$[0_2/90_2/\pm 45_2]_s$, $[0_2/\pm 45_2/90_2]_s$, $[0_2/45_2/90_2/-45_2]_s$ and $[\pm 45_2/0_2/90_2]_s$.

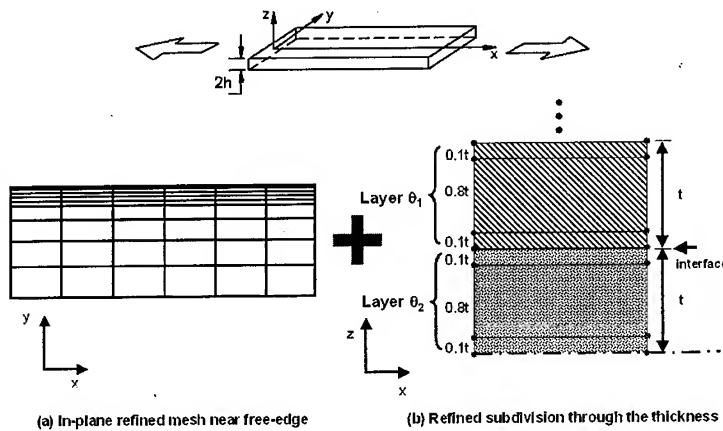


Fig. 2 Mesh refinement both in-plane and through the thickness directions of quasi-isotropic laminates.

The distribution of stress along the width in the quasi-isotropic laminates subjected to 0.1% tensile strain is shown in Figure 3. From Figure 3, quasi-isotropic laminates are classified into two types. In case that the 90 degree layer is located at the mid-plane such as $[0_2/\pm 45_2/90_2]_s$ laminates, the magnitude of σ_z is higher at the free edges compared with that of $[0_2/90_2/\pm 45_2]_s$.

In case of the cross-ply laminates, matrix failure loads in $[0/90_2]_s$ and $[90_2/0]_s$ laminates at the 90 layer show the almost same values because the effect on failure due to interlaminar stresses are negligible. But the failure initiation load of the quasi-isotropic laminates at the free edges is very different according to the stacking sequences. This phenomenon is mainly due to the high magnitude and the different distribution of stress through the thickness. Matrix failure load in $[0_2/\pm 45_2/90_2]_s$ laminate at the free edges is about 89% (100MPa) lower than that of $[0_2/90_2/\pm 45_2]_s$ laminate. In order to consider the free edge effect more effectively, mesh refinement through the thickness direction is conducted in combined with 2-d in-plane direction as shown in Figure 2. In that case, the failure loads of $[0_2/\pm 45_2/90_2]_s$ laminate according to the number of subdivisions are compared in Figure 4. Delamination onset load of the refined 12 subdivisions through the thickness is 23% lower than that of 4 subdivisions through the thickness. And the fiber failure load at the free edges in the refined 12 subdivisions is 15% lower than that of 4 subdivisions through the thickness.

5. CONCLUSION

Failure analysis is conducted for cross-ply and quasi-isotropic laminates. The damages are estimated more progressively when use 3-d stress field and nonlinear stiffness reduction method.

ACKNOWLEDGMENT

The authors would like to thank the **Korea Agency for Defense Development** for the support of this study

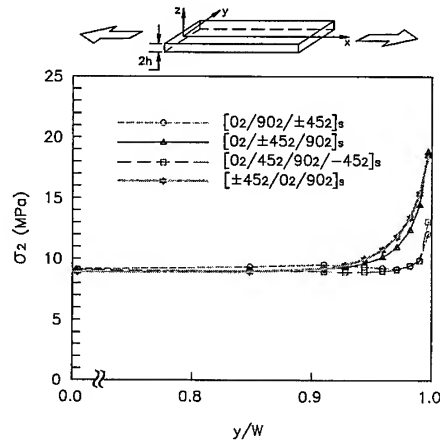


Fig. 3 Distribution of stresses, σ_2 , along the width in quasi-isotropic laminates for various stacking sequences.

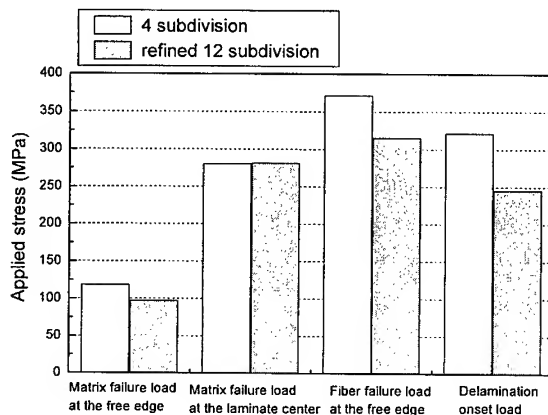


Fig. 4 Failure loads of $[0_2/\pm 45_2/90_2]_s$ laminate according to the number of subdivisions through the thickness.

REFERENCES

1. Lessard, L. B. and Chang, K. Y. and Chang, F. K., *Applied Mech. Rev.*, **43** No. 5, part 2, May (1990) p. 304
2. Chang, K. Y., Liu, S. and Chang, F. K., *JCM*, **25** March (1991) p. 274
3. Tan, S. C., *JCM*, **25** May (1991) p. 556
4. Tolson, S. and Zabaraz, N., *Computer & Structures*, **38** No. 3 (1991) p. 361
5. Kim, Y. W. and Hong, C. S., *J.R.P.C.*, **11** October (1992) p.1078
6. Shahid, I. and Chang, F. K., *JCM*, **29** No. 7 (1995) p. 926
7. Lee, J. D., *Computer & Structures*, **15** No. 3 (1982) p. 335
8. Reddy, Y. S. and Reddy, J. N., *J. Composite Technology & Research*, **15** No. 2 Summer (1993) p. 73
9. Robbins, D. H. and Reddy, J. N., *Int. J. Numerical Method in Engineering*, **36** (1993) p. 655

The Influence of Plastic Deformation on Interface Fracture Behavior

M. Omiya, K. Kishimoto and T. Shibuya

Department of Mechanical and Intelligent Systems Engineering, Tokyo Institute of Technology,
2-12-1 O-okayama, Meguro-ku, Tokyo 152-8552, Japan

Keywords: Cohesive Force Model, Finite Element Method, Fracture Mechanics, Interface Crack, Interface Fracture Toughness, J-Integral, Mixed Mode, Plastic Deformation

ABSTRACT

The purpose of this paper is to investigate the influence of plastic deformation on the mixed mode fracture toughness of an interface crack. Based on the internal variable theory of thermodynamics, a continuum interface constitutive relation between interface traction and interface separation has been developed. To simulate the crack propagation of the interface crack, this cohesive force model is applied to FEM analyses of the interface crack between two elastic-plastic materials. The results show that plastic deformation affects the interface separation ahead of the interface crack tip. This effect yields the enhancement of the mixed mode fracture toughness. Therefore, in bimaterial systems, the fracture toughness varies with the mixed mode condition at the crack tip. The tendency of the fracture toughness curve is roughly consistent with the experimentally measured mixed mode fracture toughness.

1. INTRODUCTION

Recently, bimaterial systems and composite materials are widely used. Typical examples include fiber reinforced materials, adhesive joints, microelectronic devices and so on. The performance of these systems strongly depends on the strength of weak interfaces. Therefore, it is important to evaluate the interface strength precisely. A lot of experimental researches have been performed. Xu and Tippur[1], Ikeda et al.[2] and Liechti and Chai[3] measured the fracture toughness of interface cracks covered wide range of mode mixity. They reported that the fracture toughness increased with the loading phase angle and had strongly dependence of the mode mixity. However, the toughening mechanism of the interface remains unclear.

The analyses on the elastic-plastic interface crack problems shown by Shih and Asaro[4] and Zywicki and Parks[5] gave insight into the possible explanations for the strong mixed mode effect due to plastic deformation. Tvergaard and Hutchinson[6] have shown numerically the effect of plastic deformation on the interface fracture toughness. They introduced a simple traction-separation law to model the fracture process ahead of the crack tip. Swadener and Liechti[7] have

classified the toughening mechanism of the interfaces and the plastic dissipation in adhesive layers can be main contributor to the variation of fracture toughness with mode mixity. However, plastic deformation can be occurred in the adherent materials and this effect can also lead to the enhancement of the fracture toughness.

The intent of this paper is to investigate the influence of the plastic deformation in the substrates on the interface fracture toughness under the mixed mode condition. To simulate a crack propagation on an interface, it is necessary to decide the fracture criterion of the interface. Ma and Kishimoto[8] proposed the interface model based on the internal variable theory of thermodynamics. The continuum constitutive relation between interface traction and interface separation has been developed. This constitutive model is embedded along the crack tip of the interface between elastic-plastic materials. The crack propagation is simulated and the influence of the plastic deformation in the substrates is considered.

2. INTERFACE CONSTITUTIVE MODEL

The mechanical properties of an interface zone are complicated, as shown in Fig.1(a). The interface zone represents the region that includes various microdefects and exhibits inhomogeneity. The mechanical response of interface zone can be equivalently modeled by distributed springs as in Fig.1(b). These springs are assumed to be able to bear loads in any direction. Based on the damage mechanics, Ma and Kishimoto[8] derived the interface constitutive relation between traction force and traction separation. This relation can be expressed as follows,

$$\begin{cases} P_n = K_n^0(1 - \beta_n(\lambda - \lambda_0) + (\lambda^2 - \lambda_0^2))u_n \\ P_t = K_t^0(1 - \beta_t(\lambda - \lambda_0) + (\lambda^2 - \lambda_0^2))u_t \\ P_b = K_b^0(1 - \beta_b(\lambda - \lambda_0) + (\lambda^2 - \lambda_0^2))u_b \end{cases} \quad (1)$$

where K_n^0 , K_t^0 and K_b^0 are the initial values of the interface rigidities and λ is an equivalent interface separation which is defined by,

$$\lambda = \sqrt{3 \left[\frac{c_n u_n^2 + c_t u_t^2 + c_b u_b^2}{c_n + c_t + c_b} \right]^{\frac{1}{2}}}, \quad (2)$$

where c_n , c_t and c_b are introduced to characterize the interface anisotropic state. In this paper, the deformation of the interface is assumed to be isotropic. In this case, c_n , c_t and c_b will be unity and the interface constitutive relation can be simplified as follows,

$$\begin{cases} P_n = K^0(1 - \beta(\lambda - \lambda_0) + (\lambda^2 - \lambda_0^2))u_n \\ P_t = K^0(1 - \beta(\lambda - \lambda_0) + (\lambda^2 - \lambda_0^2))u_t \end{cases} \quad (3)$$

$$\beta = \frac{D_c + \lambda_c^2 - \lambda_0^2}{\lambda_c - \lambda_0}. \quad (4)$$

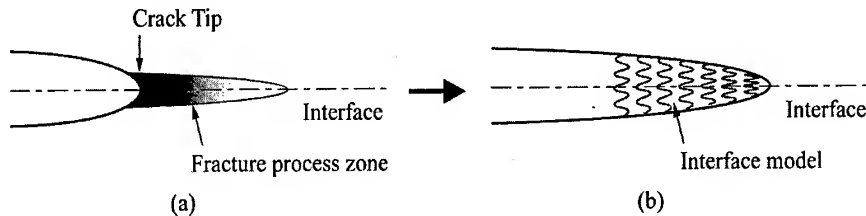


Fig.1. (a) A schematic representation of an interface crack,
(b) the equivalent spring model for the interface crack.

where D_c is the critical interface damage, λ_c is the critical interface separation and λ_0 is the interface damage threshold.

3. NUMERICAL SIMULATION

3.1. Finite Element Method

The crack propagation of an interface crack is simulated by Finite Element Method for several material pairs under various mixed mode loadings. Fig.2 shows the simulation model. Young's modulus of each material is E_1 and E_2 and Poisson's ratio is $\nu_1 = \nu_2 = 0.3$, respectively. We assume that each material obeys the following hardening rule,

$$E\varepsilon = \sigma + \alpha \left(\frac{|\sigma|}{\sigma_0} \right)^{n-1} \sigma \quad (5)$$

where σ_0 is the yield stresses of the adherent materials and material parameters are assumed to be $n = 10, \alpha = 0.1$. In this paper, the yield stresses of the substrates are same, that is $\sigma_0 = \sigma_{01} = \sigma_{02}$.

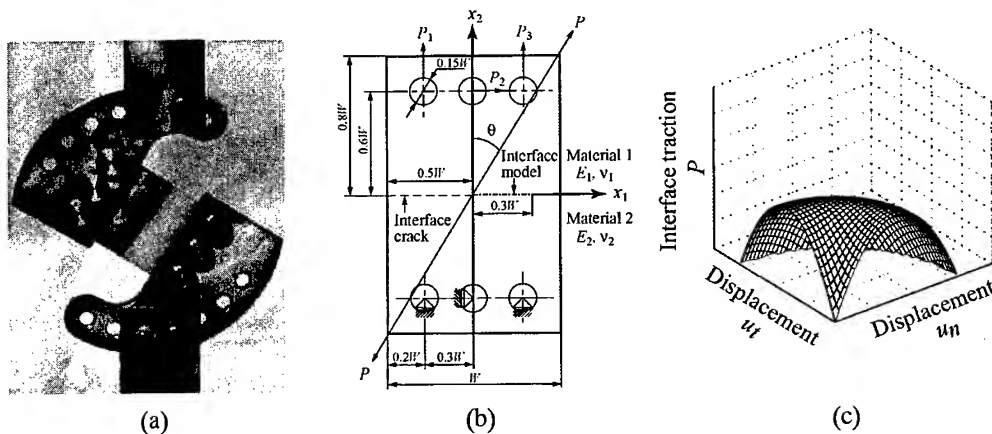


Fig.2. (a) Apparatus for mixed mode fracture test, (b) numerical simulation model,
(c) the property of the interface constitutive model.

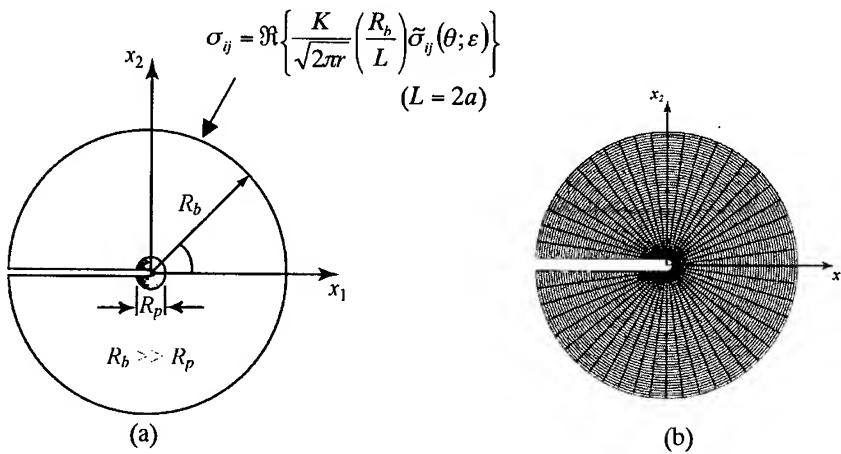


Fig.3. (a) Boundary condition for the analysis of the crack tip region, (b) finite element mesh of the crack tip region.

In this paper, isotropic interface constitutive model is treated. The variation of interface traction with interface separation is depicted in Fig.2(c). This model is embedded along the line extending ahead of the crack tip. The crack growth initiation can be defined by the interface constitutive relation. The ratio of E_1 and E_2 ($\Gamma = E_2/E_1$) and yield stress (σ_0/E_1) are changed variously and the interface fracture toughness is calculated by J -integral.

In order to investigate the influence of plastic deformation on the crack tip in detail, the calculation model in Fig.3 is also used. In specifying the small-scale yielding problem, the asymptotic solution of the interface stress field is imposed. In this analyses, stress intensity factors obtained from the calculation results of the previous model (Fig.2(b)) are used in the boundary condition.

3.2. Results and Discussion

Figure 4 shows the relation between the interface fracture toughness that is characterized by J -integral and the loading angles with various yield stresses. In this case, the ratio of Young's

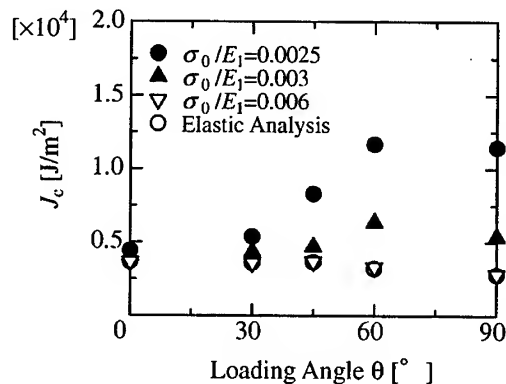


Fig.4. The effect of changing the yield stress on the fracture toughness ($\Gamma=1$).

modulus is $\Gamma = E_2/E_1 = 1$. Elastic analysis is also depicted in this figure. The result of $\sigma_0/E_1 = 0.006$ is almost constant, not depending on the loading angle and is similar with that of elastic analysis. On the contrary, in the case of low yield stresses, the fracture toughness varies with the loading angles. Misses equivalent stress distribution near the crack tip at $\theta = 60^\circ$ is shown in Fig.5. In the case of $\sigma_0/E_1 = 0.0025$, plastic deformation of the substrates is spread around the crack tip. However, in the case of $\sigma_0/E_1 = 0.006$, the plastic deformation is confined only near the crack tip. Interfacial separations inside the crack tip for $\sigma_0/E_1 = 0.0025$ and $\sigma_0/E_1 = 0.006$ are compared in Fig.6. Interfacial separation at $J_c = 0.3 [\text{J/m}^2]$ is shown in Fig.6(a). The effect of plastic deformation can be seen in the region less than $r/R_b = 5 \times 10^{-5}$, R_b is the radius of the outer boundary. Interfacial separation at the crack initiation is shown in Fig.6(b). The slopes of these curves are same and the condition inside the interface model is almost same. Therefore, the enhancement of the fracture toughness in $\sigma_0/E_1 = 0.0025$ can be due to the plastic deformation.

Figure 7 shows the influence of the ratio of Young's modulus on the fracture toughness. In the case of $\sigma_0/E_1 = 0.006$ (Fig.7(a)), the fracture toughness are not influenced by the loading angle. On the contrary, in the case of $\sigma_0/E_1 = 0.0025$ (Fig.7(b)), the fracture toughness depends on the loading angle due to plasticity. The effect of changing the ratio of Young's modulus can be seen as to be increasing the fracture toughness. Especially, in Fig.7(b), the shape of the fracture toughness

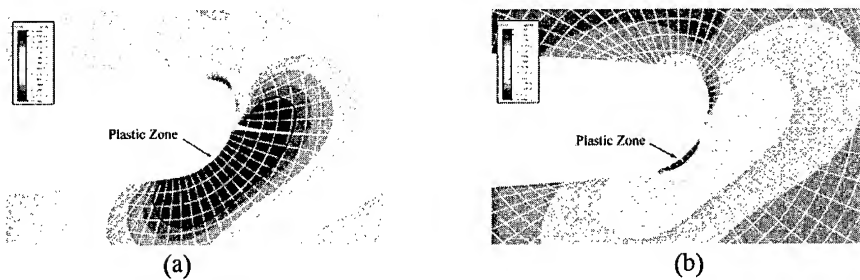


Fig.5. Misses equivalent stress distribution near the crack tip at the crack initiation, (a) $\sigma_0/E_1 = 0.0025$, (b) $\sigma_0/E_1 = 0.006$.

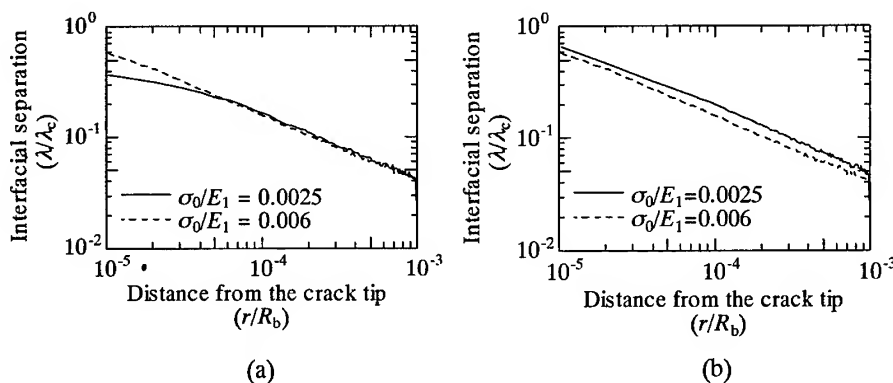


Fig.6. Comparison of the interfacial separation, (a) $J_c = 0.3 [\text{J/m}^2]$, (b) at the crack initiation.

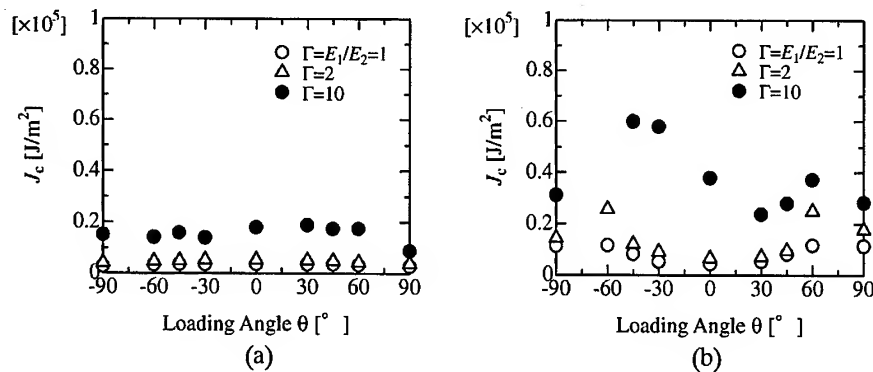


Fig. 7. The effect of changing the ratio of the Young's modulus in bimaterial systems, (a) $\sigma_0/E_1 = 0.006$, (b) $\sigma_0/E_1 = 0.0025$.

curve become asymmetric. That is because the mixed mode condition at the crack tip is not directly corresponding to the loading angle. The tendency of these curves are roughly consistent with the experimentally measured mixed mode toughness curves[3].

4. CONCLUSION

A continuum interface constitutive relation between interface traction and interface separation is applied to FEM analyses for the interface crack between two elastic-plastic materials. The propagation of the interface crack is simulated and the effect of the plastic deformation is investigated. The results are summarized as following:

1. Plastic deformation of the substrates affects the interface separation in the region of the interface model. This effect yields the enhancement of the fracture toughness.
2. In bimaterial systems, due to the plastic deformation, the fracture toughness varies with the mixed mode condition at the crack tip and this trend is roughly consistent with the experimental results.

5. REFERENCES

1. L. Xu and H.V. Tippur, *Int. J. Fract.*, **71** (1995) p.345
2. T. Ikeda, N. Miyazaki and T. Soda, *Eng. Fract. Mech.*, **59** (1998) p.725
3. K.M. Liechti and Y.S. Chai, *J. Appl. Mech.*, **59** (1992) p.295
4. C.F. Shih and R.J. Asaro, *J. Appl. Mech.*, **55** (1988) p.299
5. E. Zywickz and D.M. Parks, *Int. J. Fract.*, **52** (1990) p.129
6. V. Tvergaard and J.W. Hutchinson, *J. Mech. Phys. Solids*, **41** (1993) p.1119
7. J.G. Swadener and K.M. Liechti, *J. Appl. Mech.*, **65** (1998) p.25
8. F. Ma and K. Kishimoto, *JSME Int. J. Series A*, **39** (1996) p.496

An Analysis of Ironing Limit in Sheet Metal Forming

Jaebok Nam¹ and Kyung Seop Han²

¹ Sheet Products and Process Research Group, Technical Research Laboratories,
Pohang Iron and Steel Co., Koe-dong, Nam-gu, Pohang 790-785, Korea

² Department of Mechanical Engineering, Pohang University of Science and Technology,
San 31 Hyoja-dong, Nam-gu, Pohang 790-784, Korea

Keywords: Die Entrance Angle, Finite Element Analysis, Friction Coefficient, Hill's Nonquadratic Yield Function, Limit Ironing Reduction, Steel D&I Can, Stress Analysis, Wall Ironing

ABSTRACT

Ironing is drawing of hollow bodies through an ironing ring, with an inner tool (punch) pressing against the bottom of workpieces such as cups or cans to reduce the wall thickness of deep-drawn cups or cans. This process is currently applied widely in industries requiring more accurate wall thickness tolerance and better surface brightness of final products. In this paper, an analytical equation incorporating Hill's non-quadratic yield function is proposed to analyze stress states in the deformation zone of ironing process, and to compute limit ironing reduction ratios (LIRs) under various ironing conditions. The material considered is a tinplate for the production of steel D&I can. Forming variables include material anisotropy, friction coefficients and entrance angles of ironing die. The computed results are compared with those from both experiments and a finite element analysis.

1. INTRODUCTION

An ironing process is a kind of plastic forming, in which previously deep-drawn workpieces such as cups or cans are pushed by an ironing punch through a stationary ironing die to reduce wall thicknesses of cups or cans and increase their heights. This process has been widely used in manufacturing cartridges, electronic parts and beverage cans. Among these applications, the most important one is for the production of D&I (drawn and ironed) cans. In the D&I canmaking, a coil of thin-gauged sheet metal is first blanked into circular disks and simultaneously deep-drawn into cylindrical cups, which are then transferred to an ironing press to be redrawn and ironed. A punch mounted on the end of ram of the ironing press forces each cup first through the redrawing die and then through the ironing dies (usually 3 dies) having successively smaller inner diameters. The total reduction ratio of 60 to 70% after the 3 ironing steps is generally obtained in commercial canmaking.

From a viewpoint of economy it is desirable to obtain a large reduction ratio in one step ironing because fewer ironing dies would be required. Thus, ironing limits of materials have been a concern for the engineers in the field.

Earlier studies, which were based on elementary plasticity theories, mainly concentrated on computing ironing forces [1,2]. An elastic-plastic finite element analysis attempted by Odell [3] drew much attention although effects of material anisotropy were not considered. Shi et al. [4] obtained a complete plastic solution on ironing using a two-dimensional axisymmetric shell theory incorporated with the Hosford yield criterion, which is generally believed to be suitable to materials of low anisotropy (strain ratio) like aluminum. Studies on the ironing limit in canmaking industries were focused on evaluating effects of materials and tool factors. Rajagopal [5] and Misonoh [6] examined the forming behavior of D&I can under various surface conditions by experimentally determining the friction coefficients on the punch side and the die side of the can.

In this study, a stress analysis on an ironing deformation zone is carried out to determine the limit ironing reduction ratio (LIR) without failures of materials under various forming conditions. Hill's non-quadratic yield function is combined with the equilibrium equation of the ironing zone in order to derive a complete plastic solution for axial stress variations. Material properties entered in the computations are those for a tinplate which is a kind of low carbon steel, and is generally used in the commercial production of steel D&I can. Factors considered are material anisotropy, friction coefficients at the tool-material interfaces and an entrance angle of an ironing die. To compare the results from the analytical solutions derived in this work, both the canmaking experiments and the finite element analysis using a commercial FE code, ABAQUS are also conducted.

2. ANALYSIS OF IRONING

A stress state in an ironing process is shown in Fig. 1. In order to simplify the analysis, the following assumptions are made: 1) a material is homogeneous and stresses in the deformation zone are constant through the thickness of the material. 2) tangential stresses due to friction are proportional to normal pressures. 3) the coefficients of friction do not vary along the length of the tool profile.

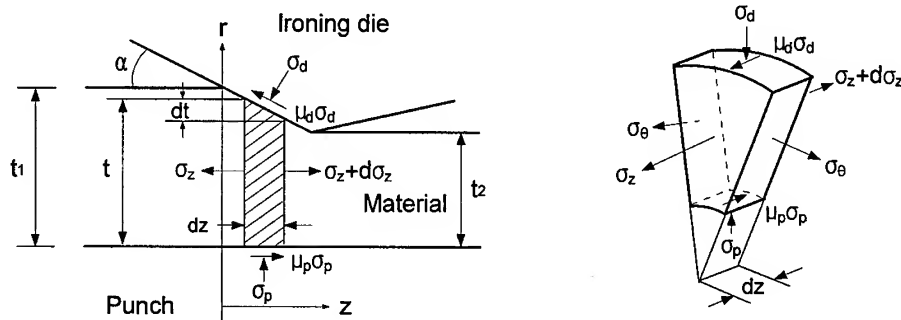


Fig. 1 Stress state in deformation zone of ironing process

After substituting $dt = -dz \tan \alpha$ and neglecting higher order terms while rearranging remaining terms in general equilibrium equations, the governing equations along z and r directions can be written respectively as

$$t \frac{d\sigma_z}{dz} + \sigma_z = -\sigma_d \left(\frac{\mu_d}{\tan \alpha} + 1 \right) + \frac{\mu_p \sigma_p}{\tan \alpha} \quad (1)$$

$$r \{ \sigma_p + \sigma_d (\mu_d \tan \alpha - 1) \} - \sigma_\theta t = 0 \quad (2)$$

A combination of the two equations, (1) and (2), yields the differential equation for the axial stress σ_z as follows:

$$t \frac{d\sigma_z}{dt} + \sigma_z = \left[\frac{\sigma_p - \sigma_\theta(t/r)}{\mu_d \tan \alpha - 1} \right] \left(\frac{\mu_d}{\tan \alpha} + 1 \right) + \frac{\mu_p \sigma_p}{\tan \alpha} \quad (3)$$

The stress σ_z can be obtained by solving equation (3) together with a yield criterion. In this study, the widely used Case IV of the nonquadratic anisotropic yield criterion by Hill [7] is chosen for its generality and proven capability to model a wide spectrum of sheet materials. Assuming in-plane isotropy (normal anisotropy), Hill's criterion becomes

$$h|\sigma_1 - \sigma_2|^M + c|2\sigma_3 - \sigma_1 - \sigma_2|^M = \sigma^M \quad (4)$$

Introducing the relations of $h = (1 + 2R)c$ and $\sigma^M = (c + h)\sigma_Y^M$ into equation (4) and assuming $\sigma_z \gg \sigma_\theta, \sigma_r$, Hill's yield criterion in the ironing process can be expressed as

$$(1 + 2R)|\sigma_z - \sigma_\theta|^M + |2\sigma_r - \sigma_z - \sigma_\theta|^M = 2(1 + R)\sigma_Y^M \quad (5)$$

where R is anisotropy, σ_Y is a yield strength and M is a yield surface shape factor, which is experimentally determined. With the applications of flow rule $d\varepsilon_{ij} = d\lambda(\partial F / \partial \sigma_{ij})$ and plane strain condition along the circumferential direction, the following equation can be obtained.

$$(1 + 2R)^{1/(M-1)} |\sigma_z - \sigma_\theta| = |2\sigma_r - \sigma_z - \sigma_\theta| \quad (6)$$

Substituting equation (6) into equation (5) yields

$$\sigma_\theta = \sigma_z - \left[\frac{2(1 + R)}{(1 + 2R)\{1 + (1 + 2R)^{1/(M-1)}\}} \right]^{1/M} \sigma_Y = \sigma_z - X_1 \quad (7)$$

Upon combining equation (5) and equation (7), it follows that

$$\sigma_r = -\sigma_p = \sigma_z - \frac{X_1}{2} \{ (1 + 2R)^{1/(M-1)} + 1 \} = \sigma_z - X_2 \quad (8)$$

By the substitution of equation (7) and equation (8) into the equilibrium equation (3), the governing differential equation for the axial stress σ_z is found as

$$\frac{d\sigma_z}{dt} + \left(\frac{X_4}{t} + \frac{X_3}{r} \right) \sigma_z = \frac{X_5}{t} + \frac{X_1 X_3}{r} \quad (9)$$

where,

$$\begin{aligned} X_1 &= \left[\frac{2(1 + R)}{(1 + 2R)\{1 + (1 + 2R)^{1/(M-1)}\}} \right]^{1/M} \sigma_Y \\ X_2 &= \frac{X_1}{2} \{ (1 + 2R)^{1/(M-1)} + 1 \} & X_3 &= \frac{\mu_d + \tan \alpha}{\mu_d \tan^2 \alpha - \tan \alpha} \\ X_4 &= X_3 + \frac{\mu_p}{\tan \alpha} + 1 & X_5 &= X_2 \left(X_3 + \frac{\mu_p}{\tan \alpha} \right) \end{aligned} \quad (10)$$

The LIR can be determined by numerically solving the differential equation (9) with $\sigma_z = \sigma_Y$. A 4th order Runge-Kutta method is applied in the computations.

3. FE ANALYSIS AND EXPERIMENT

3.1. Finite element analysis

To compare the analytical solution with the finite element solution, the commercial code ABAQUS [8] has been selected and used to model the ironing process. In the simulation the material is modeled as a homogeneous, temperature independent and strain rate independent elastic-plastic material. According to the experimental data from tensile test, a curve for true stresses and logarithmic strains of a tinplate is fitted with the power function of

$$\sigma = 0.645(0.00286 + \varepsilon_p)^{0.138} \quad (kN/mm^2) \quad (11)$$

The material (tinplate) is divided into quadrilateral elements (the CAX4R) in 3 layers as shown in Fig. 2. Some interface elements (the IRS21A) at the material/tool boundary are used to introduce the frictional conditions at the boundary. The material is considered to be strained enough to the ironing limit when the visible neck or thinning of the material occurs under the conditions of given tool and material.

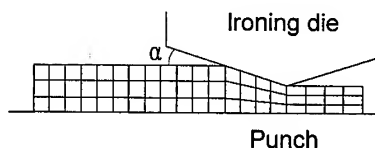


Fig. 2 Tool and mesh layout in FEA

3.2. Ironing experiment

An ironing experiment is performed on an ironing press (CMB5000 model) equipped with an ironing die of the entrance angle (α) of 7° . In the experiment LIR is regarded to be achieved only when all the five tested cans exhibit no fractures in their bodies during one step ironing. Some physical properties of the tested tinplate are as follows; thickness (0.245mm), yield strength (287MPa), anisotropy (1.1).

4. RESULTS AND DISCUSSIONS

Fig. 3 shows the analytical results of the axial stresses for varying degrees of ironing reductions. It is observed that the axial stress σ_z increases continuously with increasing the ironing reduction. According to the analytical solution, the LIR under the conditions given in Fig. 3 almost reaches 57% at which σ_z/σ_y becomes unity. The effect of material anisotropy on the LIR is illustrated in Fig. 4. As anisotropy of a rolled sheet increases, the LIR decreases linearly. Although a somewhat wide range of anisotropy is considered in the analytical solution, it seems that the LIR is not greatly

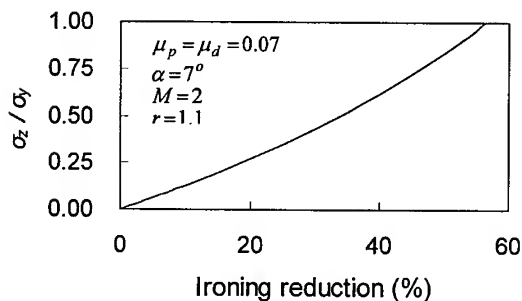


Fig. 3 Variation of axial stress with ironing reduction

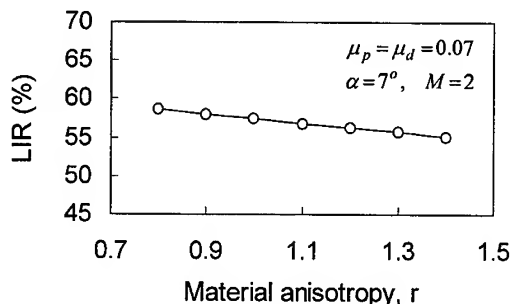


Fig. 4 Effect of anisotropy on limit ironing reduction

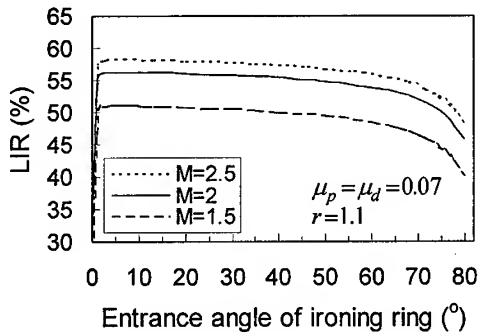


Fig. 5 Effect of entrance angle of ironing ring and shape factor (M) on the LIR

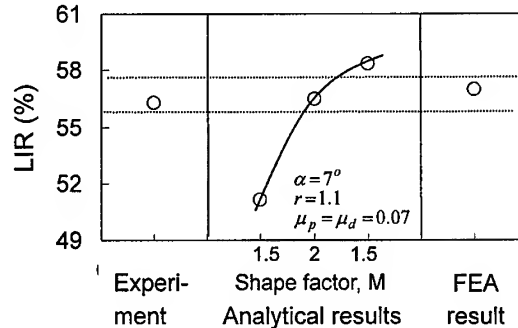


Fig. 6 Comparisons of analytical results with experimental and FEA results

influenced by the material anisotropy.

Fig. 5 represents effects of entrance angles of the ironing die on the LIRs for different yield surface shape factors (M). For all values of M the analytically obtained LIRs show almost the same tendency. That is, LIRs increase rapidly with increasing die angles up to about 3 degrees and then show a slight decreasing trend. For angles larger than 50 degrees, however, the decrease in LIRs becomes more evident. It is observed that the optimum entrance angle of the ironing ring for higher values of the LIR is computed to be in the range of 5 to 12 degrees. Regarding the effect of shape factor, it is easily seen that the larger the M value is, the higher the LIR is. As mentioned earlier, the shape factor should be determined experimentally to reflect the yielding behavior of materials tested.

Fig. 6 shows how to determine the yield surface shape factor (M) in Hill's non-quadratic yield function. The LIRs predicted from the analytical solution of stresses for the different shape factors are compared with those from the experiments and the finite element analysis. It can be safely concluded that the M value of the tinplate is 2 since the analytical result of $M=2$, is well within the range of the results obtained from the experiments and the finite element analysis. For the computations of analytical results, the both friction coefficients on the punch side and on the die side are assumed to be same at 0.07 which is taken from Misonoh's experimental data [6] obtained from actual canmaking tests with the tinplates.

The effect of friction coefficients on the punch side (μ_p) is shown in Fig. 7. It is clear that the LIRs increase progressively with the increasing μ_p . However, on the contrary, Fig. 8 demonstrates that LIRs decrease continuously with the increasing friction coefficients on the die side (μ_d). From these two opposing effects of μ_p and μ_d on the LIRs, it is conceivable that an ideal combination of high μ_p values and low μ_d values could provide even 100% reduction ratio in one step

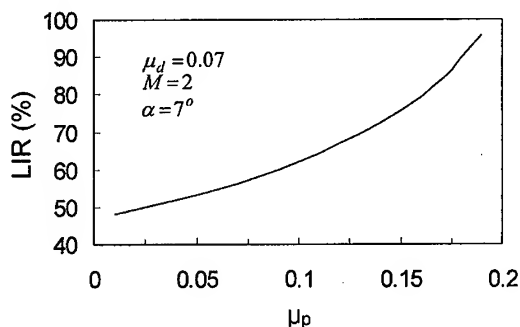


Fig. 7 Effect of friction coefficient on the punch side (μ_p) on the LIR

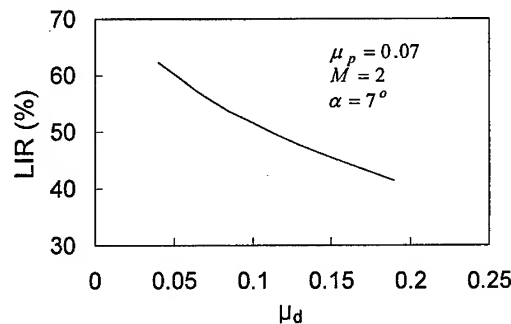


Fig. 8 Effect of friction coefficient on the die side (μ_d) on the LIR

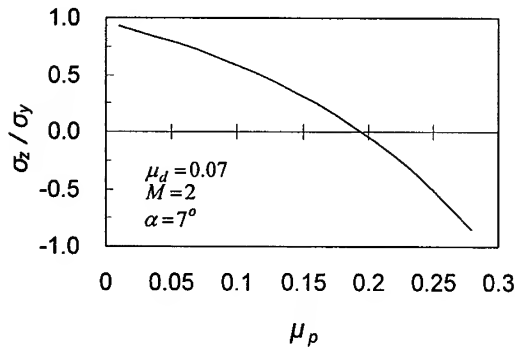


Fig. 9 Variation of axial stress (σ_z) with friction coefficient on punch side (μ_p)

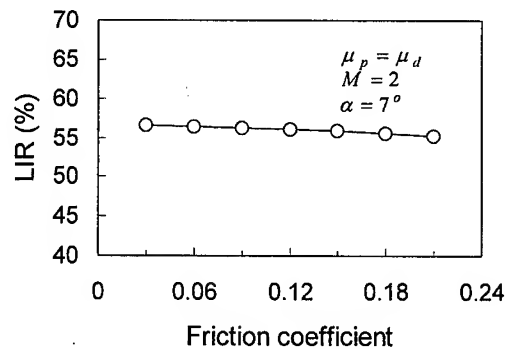


Fig. 10 Effect of friction coefficients of both sides on the LIR

ironing. The ideal combination may be best expressed in terms of difference (Δ) between the values of μ_p and μ_d , $\Delta = \mu_p - \mu_d$, which may be designated as a friction differential. The two opposing effects of μ_p and μ_d can be explained from the state of stresses in Fig. 1. High values of μ_p induce large forces of $\mu_p \sigma_p$ directing toward the die exit, helping the material easily pass the die. On the other hand, low values of μ_d reduce the frictional resistances of $\mu_d \sigma_d$ opposing the movement of the material toward the die exit. Therefore, in general, the large differences between the two values of μ_p and μ_d would effectively lower the ironing loads. Fig. 9 shows that the computed axial stresses (σ_z) decrease with the increasing values of μ_p . Consequently, low ironing loads would result from the low σ_z , thus making greater reductions possible. Fig. 10 shows changes in LIRs that would occur when the friction coefficient of μ_p and μ_d are the same. As expected, the changes in LIRs are very slight, regardless of the values of μ_p and μ_d as long as μ_p and μ_d take same values, confirming the opposing effects of μ_p and μ_d on LIRs.

5. CONCLUSIONS

An analytical equation incorporating Hill's non-quadratic yield function is proposed to analyze the axial stress at the exit of ironing die, and to compute the limit ironing reduction ratio (LIR) under various ironing conditions. Almost 57% of LIR is predicted in the case of ironing a tinplate, a low carbon steel for D&I can production. This is in good agreement with the results from the experiments and a finite element analysis. The optimum entrance angles of the ironing die for high values of LIR is computed to be in the range of 5 to 12 degrees. The LIR seemed not to be greatly influenced by material anisotropy although it decreases slightly as the anisotropy increases. It is found that high friction coefficients at the punch-material interface induce increases in the values of LIR, while high friction coefficients at the die-material interface cause decreases in the values of LIR.

REFERENCE

1. H. Weiss, Dr.-Ing. Thesis, Technische Hochschule, Stuttgart (1964)
2. E.G. Thomsen and S. Kobayashi, Proc. 9th Sagamore Army Metals Conf., Syracuse (1964) p.43
3. E.I. Odell, J. Engineering for Industry, **100** (1978) p.31
4. M.F. Shi and J.C. Gerdeen, J. Mater. Shaping Technol., **7** (1989) p.203
5. S. Rajagopal and S. Misra, Proc. 7th NAMRC (1979), p.89
6. K. Misonoh and A. Nakajima, J. Japanese Soc. Tech. of Plasticity, **27** (1986) p.508
7. R. Hill, Math. Proc. Camb. Phil. Soc., **85** (1979) p.179
8. Hibbitt, Karlsson and Sorensen, Inc., ABAQUS User's Manual Version 5.8 (1998)

The Versatility of the Method of K_I , K_{II} Analysis by FEM Based on the Stress Value at a Crack Tip

H. Nisitani¹, T. Teranishi¹, A. Saimoto² and K. Fukuyama¹

¹ Department of Mechanical Engineering, Kyushu Sangyo University,
2-3-1 Matsukadai, Higashi-ku, Fukuoka 813-8503, Japan

² Department of Mechanical Systems Engineering, Nagasaki University,
1-14 Bunkyo-machi, Nagasaki 852, Japan

Keywords: BFM, Extrapolation Method, FEM, Stress Intensity Factor

ABSTRACT

FEM is useful for the stress analysis and used widely in general. However, it is still not necessarily easy to obtain the highly accurate values of the stress intensity factors by FEM. Therefore, many methods, such as the stress extrapolation method, the displacement extrapolation method, the hybrid extrapolation method and so on have been proposed until now. However, these methods have some weak points.

Recently, a method for calculating the highly accurate values of stress intensity factors is proposed by H. Nisitani, based on the usefulness of the stress values at a crack tip calculated by FEM. Although this value at a crack tip by FEM is finite, it is very effective as a measure of the strength of singularity at the crack tip. This method is called the crack tip stress method.

In this study, first the crack tip stress method and its physical background were explained. Then the weak points of the extrapolation methods in FEM were made clear by using the exact stress distributions near a crack tip obtained by the body force method. Moreover the crack tip stress method was applied to the problems of the crack large compared with the strip width, the interference of two close parallel cracks in a strip and so on. It is difficult to treat these problems through the extrapolation method. Finally the accuracy of the crack tip stress method was discussed based on the exact solution obtained by the body force method.

1. INTRODUCTION

FEM is useful for the stress analysis and used widely in general. However, it is still not necessarily easy to obtain the highly accurate values of the stress intensity factors by FEM. Therefore, many methods, such as the stress extrapolation method [1], the displacement extrapolation method [1], the hybrid extrapolation method [2] and so on [3-8] have been proposed until now. However, these methods have some weak points.

Recently, a method for calculating the highly accurate values of stress intensity factors is proposed by H. Nisitani, based on the usefulness of the stress values at a crack tip calculated by FEM [9]. Although this value at a crack tip by FEM is finite, it is very effective as a measure of the strength of singularity at the crack tip. This method is called **the crack tip stress method**.

In this study, the weak points of the extrapolation method in FEM are made clear by using the

exact stress distributions near a crack tip obtained by the body force method (BFM) [10]. Then the crack tip stress method was applied to the problems of the crack large compared with the strip width, the interference of two close parallel cracks in a strip and so on. It is difficult to treat these problems through the extrapolation method.

2. THE CRACK TIP STRESS METHOD AND ITS PHYSICAL BACKGROUND

Figure 1 shows the element pattern used for checking the effectiveness of the crack tip stress method. The elements near the crack tip are made fine systematically as shown in Fig. 1. The element size near the crack tip is $1/243$ mm. The width of the strip is 20 mm, and the crack length is 2, 4, 6, 8 or 9 mm. Figure 2 shows the stress distributions calculated by FEM under the condition of $K_{I,real} = \text{constant}$ ($= 1 \text{ MPa}\sqrt{\text{mm}}$). The values of $K_{I,real}$ are calculated by BFM [10].

As seen from Fig. 2, when the real values of K_I are the same, the stress distributions are very close to each other. Especially the stress values at the crack tip $\sigma_{y0,FEM}$ are almost the same, independent of crack length. This means that the stress values at a crack tip calculated by FEM is very effective as a measure of the strength of singularity at the crack tip, independent of crack length.

Since the values of $K_{I,real} / \sigma_{y0,FEM}$ are almost constant independent of crack length, Eq.1 is obtained. In this equation, $K_{I,real}$ stands for the real stress intensity factor, $\sigma_{y0,FEM}$ stands for the stress value in the y-direction at the crack tip calculated by FEM and the asterisks * mean the values of the reference problems.

$$\frac{K_{I,real}}{\sigma_{y0,FEM}} = \frac{K_{I,real}^*}{\sigma_{y0,FEM}^*} \quad (1)$$

Therefore, we use the next equation in order to obtain the approximate value $K_{I,appr.}$ of the given problem.

$$\frac{K_{I,appr.}}{\sigma_{y0,FEM}} = \frac{K_{I,real}^*}{\sigma_{y0,FEM}^*} \quad (2)$$

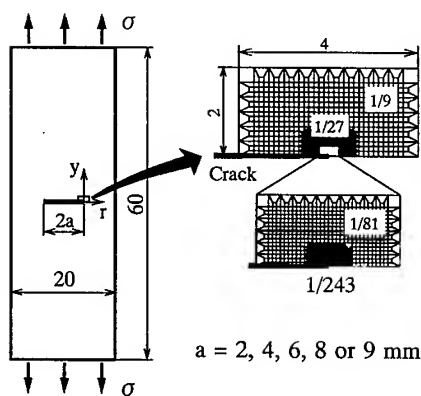


Fig.1. Dimensions of the strip and the elements near the crack tip.

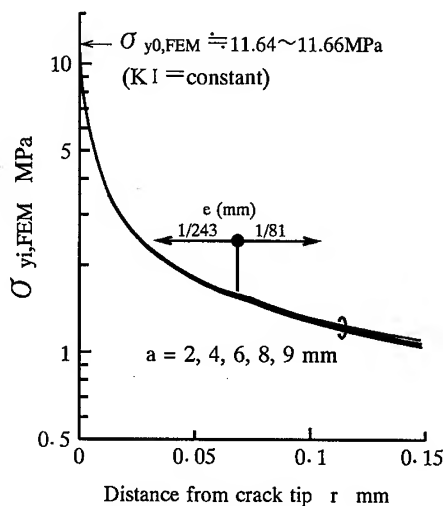


Fig.2. Stress distribution calculated by FEM under the condition of $K_I = \text{constant}$ ($= 1 \text{ MPa}\sqrt{\text{mm}}$).

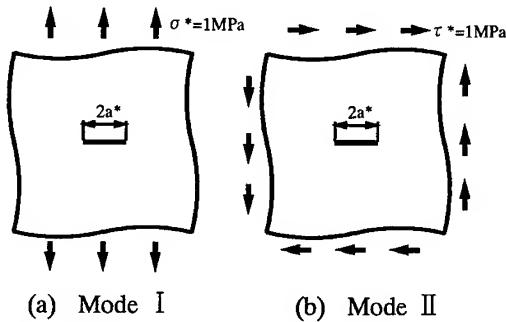


Table 1. Reference values.

σ^* or τ^* (MPa)	a^* (mm)	e^* (mm)	Mode I		Mode II	
			$\sigma_{y0,FEM}^*$ (MPa)	$F_{I,real}^*$	$\tau_{xy0,FEM}^*$ (MPa)	$F_{II,real}^*$
1	0.01	$\frac{1}{48600}$	29.5336	1.00000	16.2991	1.00000

$F_{I,real}^*$ and $F_{II,real}^*$ were obtained by BFM.

Fig.3. Reference problems (Exact solutions).

In using Eq.2, it should be noted that the same mesh patterns near the crack tip have to be used in the calculation of $\sigma_{y0,FEM}$ and $\sigma_{y0,FEM}^*$.

The value of $K_{I,appr}$ can be obtained through the value of $\sigma_{y0,FEM}$ in the given problem, provided that a pair of values $K_{I,real}^*$ and $\sigma_{y0,FEM}^*$ in the reference problem is obtained in advance.

If we use the definition (3), Eq.2 can be transformed into Eq.4.

$$F_I = \frac{K_I}{\sigma \sqrt{\pi a}} \quad (3)$$

$$F_{I,appr} = \sigma_{y0,FEM} \times \frac{F_{I,BFM}^*}{\sigma_{y0,FEM}^*} \times \frac{\sigma^*}{\sigma} \times \sqrt{\frac{a^*}{a}} \quad (4)$$

(a: half crack-length, σ : loading stress for a strip)

When the crack tip stress method is applied to the problems having the various element sizes at the crack tip, Eq.5 should be used, where e means the element size at the crack tip. This is based on the fact that the stress value near the crack tip decreases in proportional to $1/\sqrt{r}$.

$$F_{I,appr} = \sigma_{y0,FEM} \times \frac{F_{I,BFM}^*}{\sigma_{y0,FEM}^*} \times \frac{\sigma^*}{\sigma} \times \sqrt{\frac{a^*}{a}} \times \sqrt{\frac{e}{e^*}} \quad (5)$$

For the mode II, the following similar equation should be used.

$$F_{II,appr} = \tau_{xy0,FEM} \times \frac{F_{II,BFM}^*}{\tau_{xy0,FEM}^*} \times \frac{\tau^*}{\tau} \times \sqrt{\frac{a^*}{a}} \times \sqrt{\frac{e}{e^*}} \quad (6)$$

Figure 3 shows the dimensions of a strip used for obtaining the reference values. Figures. 3 (a) and (b) are the cases of mode I and mode II crack problems, respectively. The half crack-lengths of Figs. 3 (a) and (b) are both 0.01 mm. The elements near the crack tip are made fine systematically as shown in Fig. 1. The element size at the crack tip is $1/48600$ mm. Table 1 shows the results of Fig. 3. These values of the reference problems are used for Eq.5 or Eq.6.

3. WEAK POINT OF THE EXTRAPOLATION METHODS

The several extrapolation methods proposed until now [1,2] can be used to obtain the approximate values of stress intensity factor in FEM analysis. However, these methods have some weak points. Taking as an example of the stress extrapolation method, the weak points of the extrapolation methods will be shown in the following.

Figure 4 (a) shows the dimensions of a strip and the element size near the crack tip of FEM analysis. The ratio a/w is 0.4 (a : half crack-length, w : half-width of the strip). The element size at the crack tip is 1/243, 1/81 or 1/27 mm. Figure 4 (b) shows the relation between $F_I(r)$ and the distance from the crack tip under the conditions of $e=1/243$, 1/81 and 1/27mm. The dotted line stands for the exact values calculated by BFM [10]. Figure 4 (c) shows the relation between the error of $F_{I,FEM}$ and the node number from the crack tip. This error stands for the difference of $F_{I,FEM}$ and $F_{I,BFM}$. This figure is based on the rearranged data of Fig. 4 (b).

As seen from Fig. 4 (c), the errors of $F_{I,FEM}$ are almost the same at each node number, independent of the element size. This is based on the fact that the stress value near the crack tip decreases in proportional to $1/\sqrt{r}$. It can be concluded from Fig. 4 (c) that the high accurate values of the stress intensity factors can not be obtained from the extrapolation methods even in the case of extremely fine mesh pattern.

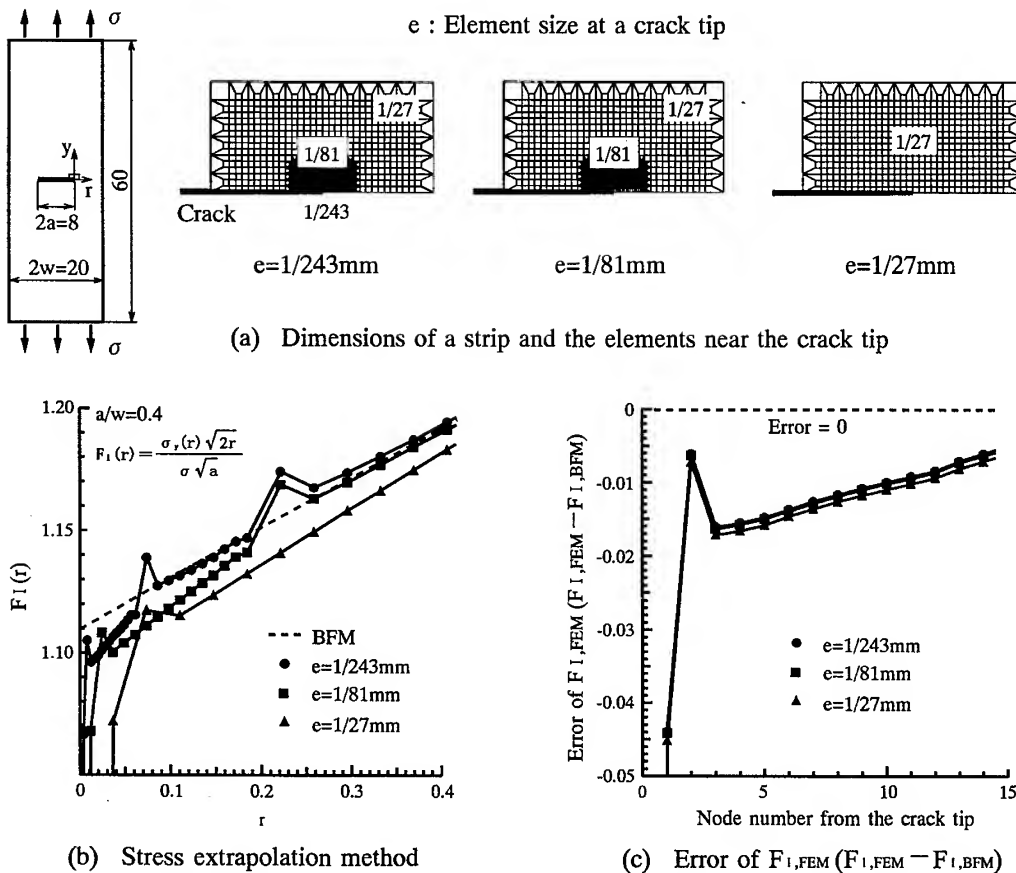


Fig.4. Weak point of the extrapolation methods.

4. APPLICATION OF THE CRACK TIP STRESS METHOD

In the following, the crack tip stress method in FEM is applied to the several problems to which the extrapolation method is difficult to apply. These problems are calculated under the following conditions. The elements near the crack tip are made fine systematically as shown in Fig. 1. The minimum element size at the crack tip is 1/243 mm.

The values of F_I obtained by BFM [10] are shown in Table 2 ~ 4. The reference values used in Eq.5 are shown in Table 1.

4.1. Large Crack Compared with the Strip Width

Table 2 shows the non-dimensional stress intensity factors F_I of strips with a crack under tension. The values of ratio a/w is from 0.1 to 0.99.

The error is 0.58 % at the maximum. Therefore, it can be said that the highly accurate values of stress intensity factors can be obtained by the crack tip stress method even in the case of large crack and short ligament.

4.2. Problems of the Interference Effect between Two Cracks in a Strip

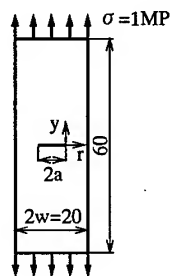
Table 3 shows the non-dimensional stress intensity factors F_I of strips with two close parallel cracks under tension. In this problem, there exists the mode I and mode II stress singularities at the crack tip at the same time. The ratio of p/a is 1/9, 1/3 or 2/3 (p : distance between the cracks, a : half crack-length).

The errors are less than about 0.23 % in all cases. This means that the crack tip stress method is very useful even in the case of the interference effect between two close cracks in a strip.

4.3. General Problems

Table 4 shows the non-dimensional stress intensity factors F_I of the general problems with a crack under tension.

Table 2. Results of a strip with a crack.

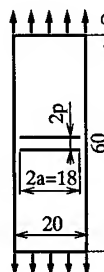


a/w	$\sigma_{yo,FEM}$ (MPa)	$F_{I,appr}$	$F_{I,BFM}^{(10)}$	Error of appr. value (%)
0.10	21.0092	1.0060	1.0060	0.00
0.20	30.2545	1.0244	1.0246	-0.02
0.40	46.3200	1.1090	1.1094	-0.03
0.60	66.6385	1.3027	1.3033	-0.05
0.80	107.157	1.8142	1.8160	-0.10
0.90	161.367	2.5757	2.5798	-0.20
0.95	235.574	3.6599	3.6682	-0.23
0.99	538.138	8.1898	8.2377	-0.58

$$\text{Error} = (F_{I,appr} - F_{I,BFM}) / F_{I,BFM} \times 100 (\%)$$

$$F_I = K_I / (\sigma \sqrt{\pi a})$$

Table 3. Results of a strip with two close parallel cracks.



p/a	Mode I				Mode II			
	$\sigma_{yo,FEM}$ (MPa)	$F_{I,appr}$	$F_{I,BFM}^{(10)}$	Error of appr. value (%)	$\tau_{xyo,FEM}$ (MPa)	$F_{II,appr}$	$F_{II,BFM}^{(10)}$	Error of appr. value (%)
1/9	127.412	2.0337	2.0334	0.02	11.2290	0.3268	0.3215	0.23
1/3	149.626	2.3883	2.3911	-0.12	10.9083	0.3155	0.3122	0.14
2/3	158.521	2.5303	2.5339	-0.14	4.98826	0.1443	0.1430	0.05

$$\text{Error} = (F_{I,appr} - F_{I,BFM}) / \sqrt{F_{I,BFM}^2 + F_{II,BFM}^2} \times 100 (\%)$$

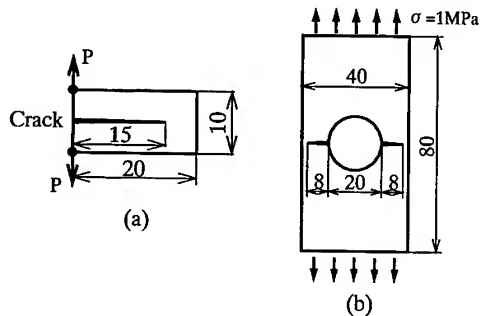


Table 4. Results of general problems.

Problems	$\sigma_{yo, FEM}$ (MPa)	FI_{appr}	$FI_{BFM}^{(10)}$	Error of appr. value (%)
(a)	85.9319	1.0625	1.0637	-0.11
(b)	260.495	4.4102	4.4065	0.08

The errors are less than about 0.11% in these problems. Therefore, it can be said that the highly accurate values of the stress intensity factors are obtained by the crack tip stress method in general.

5. CONCLUSIONS

The weak points of the extrapolation method in FEM were made clear by using the exact stress distributions near a crack tip obtained by the body force method. Then the crack tip stress method was applied to the problems of the crack large compared with the strip width, the interference of two close parallel cracks in a strip and so on. It is difficult to treat these problems through the extrapolation method. The main results are summarized in the following.

- (1) The errors of the non-dimensional stress intensity factor FI obtained from the stress extrapolation method are almost constant, independent of the element size. Therefore, the highly accurate values of the stress intensity factors can not be obtained from the extrapolation methods even in the case of extremely fine mesh pattern.
- (2) It was confirmed that the crack tip stress method in FEM has the sufficient accuracy in the problems to which the extrapolation method is difficult to apply.

REFERENCE

- [1] S. K. Chan, I. S. Tuba, and W. K. Wilson, Eng. Frac. Mech., 2 (1970), p. 1.
- [2] H. Kitagawa, R. Yuuki, H. Kisu, and H. Kawabata, Transactions of the Japan Society of Mechanical Engineers, 50-450, Series A, (1984), p. 129 (in Japanese).
- [3] Y. Yamamoto, and M. Taniguti, Transactions of the Japan Society of Mechanical Engineers, 38-306 (1972), p. 269 (in Japanese).
- [4] P. D. Hilton, and G. C. Sih, Mechanics of fracture, Noordhoff, Vol. 1 (1973), p. 426.
- [5] Y. Murakami, Transactions of the Japan Society of Mechanical Engineers, 42-360 (1976), p. 2305 (in Japanese).
- [6] H. Miyata, S. Shida, and S. Kusumoto, Transactions of the Japan Society of Mechanical Engineers, 43-356 (1977), p. 26 (in Japanese).
- [7] H. Kisu, R. Yuuki, and H. Kitagawa, Transactions of the Japan Society of Mechanical Engineers, 51-463, Series A, (1985), p. 660 (in Japanese).
- [8] W. Fujisaki, and M. H. Aliabadi, Boundary Elements 19, CMP (1997), p. 287 (in Japanese).
- [9] H. Nisitani, T. Kawamura, W. Fujisaki, and T. Fukuda, Transactions of the Japan Society of Mechanical Engineers, 65-629, Series A, (1999), p. 26 (in Japanese).
- [10] H. Nisitani, D. Chen and A. Saimoto, Versatile Program of Two-dimensional Stress Analysis Based on Body Force Method, Baifukan, 1994 (in Japanese).

Detecting Tool Wear in Face Milling with Different Workpiece Materials

D.W. Cho¹, W.C. Choi² and H.Y. Lee³

¹ Department of Mechanical Engineering, Pohang University of Science and Technology,
San 31 Hyoja-dong, Nam-gu, Pohang 790-784, Korea

² Department of Mechanical Engineering, Korea University,
5-1 Anam-dong, Sungbuk-gu, Seoul 136-701, Korea

³ Daewoo Motor Co., 199, Cheongcheon-dong, Pupyong-gu, Incheon 403-714, Korea

Keywords: Face Milling, Neural Network, Tool Wear, Workpiece Material

ABSTRACT

This paper proposes a neural network for the decision-making system for monitoring tool wear while working materials such as Al6061, SB41, SM45C. The raw cutting forces signals are filtered and processed with adaptive AR modeling. The AR parameters and cutting conditions are used as input to the neural network along with the frequency band energy. The experimental results show that each neural network trained for each specified material can recognize tool wear with a more than 85% detection rate. When the normalized tensile strength of each material is used as additional input to the unified neural network, the network still has a success rate higher than 80 %.

1. INTRODUCTION

In the past decade, there have been numerous reports on monitoring milling tool wear. Ko and Cho [1,2] proposed a method that monitors tool wear using time series parameters as input into a neural network. Waldorf et al. [3] extracted the features of tool wear by relating the wear to a static cutting force model determined experimentally. On the other hand, Elbestawi [4] utilized a cutting force component with a particular frequency that varies with tool wear.

In this paper, we also use a time series model to extract the features of milling tool wear and include the normalized frequency band energy in the feature vector. The frequency band energy increases with progressive tool wear and it has been used to monitor tool wear in turning [5]. Constantinides et al. [6] showed that tool wear is closely related to the power spectral energy obtained by frequency analysis of spindle motor power. Ko and Cho [1,2] clarified that the power of the tooth passing frequency component increases with tool wear.

All of this research, however, monitors tool wear when machining a given piece without considering the properties of the material being worked. In practice, different materials are machined, so the magnitudes and frequency components of the cutting forces will also differ. In this regard, this paper estimates the tool wear using the features extracted from measurements of the

cutting forces when machining three different materials with carbide tools. The cutting forces are first modeled with AR models with an adequate order to obtain the AR parameters and the sum of the spectral power at different cutting conditions. Then a neural network is constructed to detect the tool wear for different workpiece materials using the AR parameters, spectral power at a particular frequency band, and cutting conditions as input. Finally, a new neural network is constructed that detects tool wear on-line while machining three different workpiece materials using an additional input feature that represents the characteristic of the workpiece material. The workpiece materials tested were Al6061, SB41, and SM45C, which are all widely used

2. MODELING MILLING PROCESS

Since machining is a typical time varying-process, more weight should be put on recent data than on older data. We achieved this by adopting the Recursive Least Square (RLS) method [1,7], which uses discounted measurement as a forgetting factor. This recursive method updates the model whenever a new sampling is made, and follows the progressive changes well. To model the milling process, experiments were conducted with a vertical machining center (ACE - V30, Daewoo Heavy Industries). The milling cutter was equipped with five inserts. The workpieces were $50 \times 70\text{mm}$ rectangles made of SB41. The feed directional cutting forces were measured with a tool dynamometer (Kistler type 9257B) and recorded on a VHS cassette data recorder while observing on an oscilloscope. Each time, 1,024 data points were sampled through an AD converter.

In a typical case, the cutting conditions used for modeling were spindle speed 720rpm , feedrate 120mm/min , depth of cut 1.0mm , and a worn tool was used to cut the SB41 workpiece. To remove the DC and run-out component, the cutting force signals were bandpass-filtered between 50 and 220Hz . The sampling frequency was set at 440Hz . These cutoff and sampling frequencies were automatically adjusted to adapt the cutting conditions. The order of the AR model was chosen to be 8, referring to Ko and Cho [1]. Fig. 1 shows the converging process of the first three model parameters, and the power spectra [4] obtained from the 8th AR model parameters are shown in Fig. 2. The harmonic components of the tooth passing frequency can clearly be seen.

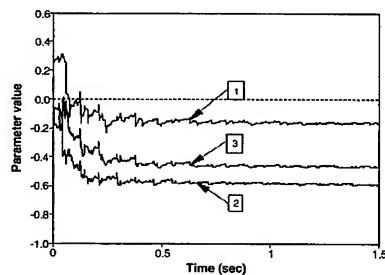


Fig. 1. Convergence of the first three parameters

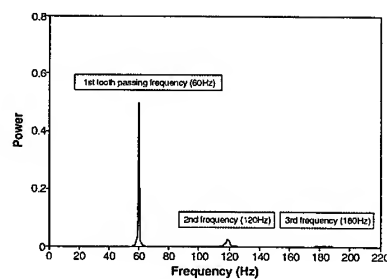


Fig. 2. Power spectral density of the cutting force

3. EXPERIMENTS

3.1. Tool Wear

According to the tool life criterion recommended by ISO, the average flank wear width (VB_{av})

is 0.3mm and the maximum flank wear width (VB_{max}) is 0.6mm. In this paper, the former was chosen as our tool-life criterion. Due to the axial and radial run-out, every insert wears differently. These differences were averaged using Eq. (1).

$$VB_{av} = \frac{1}{n} \sum_{i=1}^n VB_{av}(i) \quad (1)$$

where n is the number of inserts in the cutter. In each and every experiment, the tool life was investigated using a tool microscope.

3.2. Frequency Band Energy

The mean frequency band energy can be written as [7]:

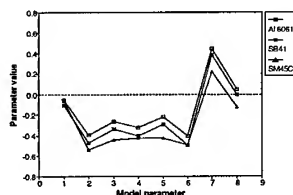
$$E_{x_{BPF}} = \int_{f_L}^{f_H} G_x(f) df \quad (2)$$

where $G_x(f)$ is the one-sided power spectral density function of signal $x(t)$, and f_L and f_H represent the lower and higher cutoff frequencies of the band pass filter, respectively. The variance of signal $x(t)$, $E_{x_{BPF}}$ (mean frequency band energy) can be calculated directly in the time domain, by applying the sampled time series data $\{x_{n_{BPF}}\}$ as:

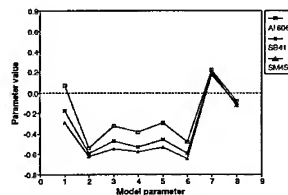
$$E_{x_{BPF}} = \frac{1}{N} \sum_{n=1}^N x_{n_{BPF}}^2 \quad (3)$$

3.3. Tool Wear Experiments and Feature Extraction

Cutting experiments were conducted under a variety of conditions with cutting speeds ranging from 240 to 720 rpm, feed rates from 40 to 160 mm/min, and depths of cut from 0.5 to 1.0 mm. Many combinations of the cutting parameters were tested. The AR parameters estimated from the new and worn tools are shown in Fig. 3. The AR parameters for the worn tool significantly differ from those for the new tool. The parameters also varied with different workpiece materials. On the other hand, Fig. 4 shows the variation in the magnitude and frequency band energy of the feed directional forces for SB41 and SM45C as tool wear progresses. The frequency band energy tends to increase proportionally with the tool wear and with the cutting force. Fig. 5 represents the frequency band energy of the new tool along with that of a worn tool, for different cutting conditions with three different workpiece materials. For the same workpiece material, a worn tool generates greater frequency band energy, while for the same tool state, the band energy increases in the order Al6061, SB41, and SM45C.



(a) AR parameters for new tools



(b) AR parameters for worn tools

Fig. 3. Variation in the AR parameters of three materials
(Cutting speed: 720rpm, Feed rate: 120mm/min, Depth of cut: 1.0mm)

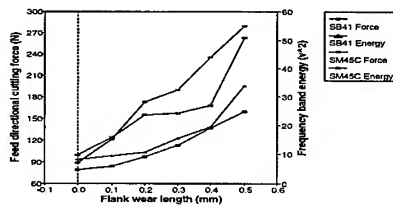


Fig. 4. Cutting force and frequency band energy for SB41 and SM45C

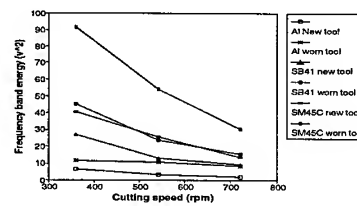


Fig. 5. Frequency band energy for different materials and cutting conditions

4. TOOL WEAR MONITORING USING NEURAL NETWORKS

4.1 Individual Neural Networks for Different Materials

Error back propagation neural networks were used to classify the tool states [8]. The AR model parameters and frequency band energy were fed into the networks as input. Since the experiments were conducted under various cutting conditions, the conditions should also be considered as input. These cutting conditions were normalized with the maximum usable values to prevent difficulties in learning due to early saturation.

The numbers of selected training patterns were 36, 40, and 38 for Al6061, SB41, and SM45C, respectively. The frequency band energy was also normalized between -1 and 1. The first step toward this is to obtain the following function of the cutting conditions that describes band energy:

$$\text{bandenergy} = A(\text{rpm})^B (\text{feedrate})^C (\text{depthof cut})^D \quad (4)$$

Of all the factors affecting the band energy, only the cutting conditions and the tool wear state change when machining the same material with the same tool. Therefore, the frequency band energy can be represented by a function of the cutting conditions for a given tool wear state.

The least squares solutions of the coefficients A, B, C, and D in Eq. (4) can be obtained for new and worn tools with the same cutting data that were used to evaluate the AR parameters. A typical result is as follows and the rest are obtained likewise:

$$\text{Al6061bandenergy}_{\text{newtool}} = 214.30(\text{rpm})^{-1.4621} (\text{feedrate})^{1.0472} (\text{depthof cut})^{1.7791} \quad (5)$$

For input to the network the band energy for a worn tool was normalized using Eq. (6) whereas the normalized band energy for a new tool was taken as -0.5 irrespective of the cutting conditions.

$$E_{\text{worn tool, Normalized}} = -0.5 + \frac{E_{\text{worn tool}} - E_{\text{new tool}}}{E_{\text{worn tool}}} \quad (6)$$

where $E_{\text{new tool}}$ and $E_{\text{worn tool}}$ are the frequency band energy for new and worn tools, respectively. Then any newly calculated band energy can be normalized using $E_{\text{worn tool, Normalized}}$, which is input to the neural network.

4.2 Results of Tool Wear Monitoring for Various Materials

As stated earlier, the input to the network were the AR parameters, frequency band energy and cutting conditions. Three separate neural networks were constructed for the three different materials. Each network has 12 input nodes (8 AR parameters, 1 band energy, and 3 cutting conditions) and one output node. To represent the state of tool wear, the output was trained to be 0.1 for a new tool

and 0.9 for a worn tool. The recognition results are shown in Table 1. For all three materials, the correct recognition rate was higher than 90%. An example of the recognition results is shown for AL6061 in Fig. 6.

Table 1 Performance in tool wear detection

	Structure of hidden layer	New tool	Worn tool
Al6061	14-12	98.3%	100%
SB41	14-8	98.4%	97.2%
SM45C	14-8	94.9%	95.3%

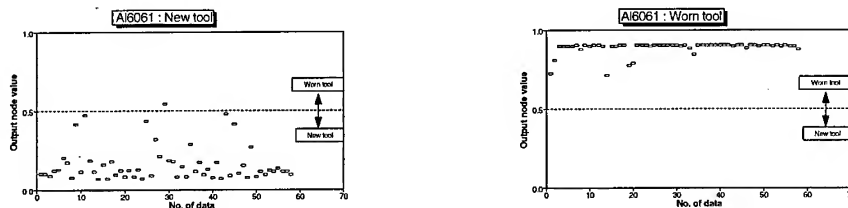


Fig. 6. Tool wear recognition results using separate neural networks

4.3 Construction of a Unified Neural Network That Considers Material Properties

The literature states that the hardness of the workpiece is one of the factors affecting tool life. Since the hardness and tensile strength are related, this paper uses the tensile strength as an additional input to the network.

The following equation can be set up using the same pattern that was used to train the tool state while cutting Al6061, SB41, and SM45C:

$$\text{bandenergy} = A(\text{rpm})^B (\text{feedrate})^C (\text{depthof cut})^D (\text{tensilestrength})^E \quad (7)$$

The least squares solutions for new and worn tools are

$$\text{bandenergy}_{\text{newtool}} = 0.06607(\text{rpm})^{-1.4106} (\text{feedrate})^{0.95731} (\text{depthof cut})^{1.7576} (\text{tensilestrength})^{1.585}$$

$$\text{bandenergy}_{\text{worn tool}} = 4.5668(\text{rpm})^{-1.1983} (\text{feedrate})^{0.35688} (\text{depthof cut})^{1.2138} (\text{tensilestrength})^{1.2294} \quad (8)$$

The tensile strength was normalized with respect to SM45C, which has the largest value. Now the unified neural network has 13 inputs. They are 8 AR parameters, 1 normalized frequency band energy, 1 normalized tensile strength and 3 cutting conditions. Fig. 7 shows the correct recognition rate for Al6061 as an example of the three materials using a 13-20-1 structure. The correct recognition rates for all three materials are compatible with the three separate neural networks, although there is a slight difference (minimum of 83.3% and maximum of 100%).

A new neural network was constructed from the machining data for Al6061 and SM45C, and applied to the SB41 test data. The resulting recognition rate is shown in Table 2. Even a new material that was not considered in the training could well be recognized. That is, Eq.(9) does reflect the property of the material.

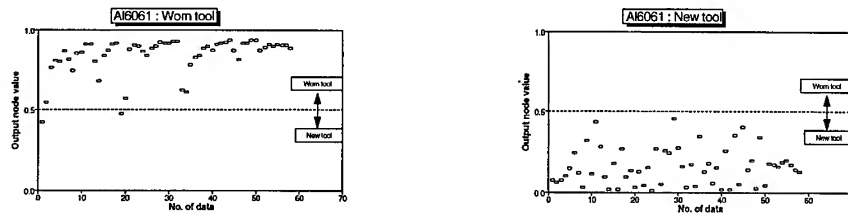


Fig. 7. Results of tool state classification using a sunified neural network

Table 2 Results showing the recognition rate for a new material.

Structure of the hidden layer	material	New tool	Worn tool
14-10	Al6061	100%	100%
	SB41	98.4%	95.8%
	SM45C	93.6%	88.9%

5. CONCLUSIONS

Constructing separate neural networks for each material (Al6061, SB41, and SM45C) identified that the structure and weight values are different for each material. A unified neural network was then constructed to detect tool wear irrespective of the work material by considering the work material property as an additional feature. It has a 13-20-1 structure and 13 input nodes in total. The inputs are 8 AR parameters obtained from cutting force modeling, 1 frequency band energy, 1 tensile strength and 3 cutting conditions. The resulting correct recognition rate ranged between 83 to 100%.

ACKNOWLEDGEMENT

The authors wish to acknowledge the financial support of the Korea Research Foundation made in the program year of 1998 (1998-018-E00150).

REFERENCE

1. T.J.Ko and D.W.Cho, Int. J. Mach. Tools Manufact., **34** (1994) p.659
2. T.J.Ko and D.W.Cho, Int. J. of Advanced Manufacturing Technology, **12** (1996) p.5
3. D.J.Waldorf, S.G.Kapoor and R.E.DeVor, Wear, **157** (1992) p.305
4. M.A.Elbestawi, T.A.Papazafiriou and R.X.Du, Int. J. Mach. Tools Manufact., **31** (1991) p.55
5. C.Y.Jiang, Y.Z.Zhang and H.J.Xu, Annals of the CIRP, **36** (1987) p.45
6. N.Constantinides and S.Bennett, Int. J. Mach. Tools Manufact., **27** (1987) p.225
7. L.Ljung and T.Soderstrom, Theory and Practice of Recursive Identification, MIT Press, Cambridge (1987)
8. Y.H.Pao, Adaptive pattern recognition and neural networks, Addison-Wesley Publishing Company, Inc. (1989) p.113

Three Dimensional Finite Element Analysis for Elastic Plastic Crack Propagation in Thin Metallic Plate

H. Okada¹, Y. Fukui¹, N. Kumazawa¹ and T. Fujisaki²

¹ Department of Mechanical Engineering, Faculty of Engineering, Kagoshima University,
1-21-40 Korimoto, Kagoshima 890-0065, Japan

² Graduate School of Science and Engineering, Kagoshima University,
1-21-40 Korimoto, Kagoshima 890-0065, Japan

Keywords: Crack Propagation, Elastic Plastic Crack Propagation, Eulerian Finite Element Method, Fracture Mechanics

ABSTRACT

In this paper, we present three dimensional solutions for steadily propagating as well as stationary cracks in thin ductile plate. The phenomena of crack propagation in thin metallic plates have certain importance from a view point of structural integrity assessment for many type of structures, as structures such as commercial aircraft fuselage are composed of thin metallic plates. When a crack propagates in thin metallic plate, deformation field at the vicinity of the crack tip (front) is highly three dimensional, as it has been observed in some earlier experimental studies. However, there are very few analytical/numerical studies concerning the three dimensional nature of propagating cracks, due to difficulties in carrying out the analyses. We apply an Eulerian finite element method, and detailed three dimensional solutions for steadily propagating cracks are presented.

1. INTRODUCTION

In recent years, problems related to the structural integrity of aging structures have attracted an attention. Among them, elastic-plastic fracture mechanics to predict the failure of damaged structures is one of the major issues that have been concerned. In the scenario of structural failure, when it is initiated from a fatigue crack, a certain amount of stable crack growth takes place. And, applied load, which drives the stable crack growth, is considered to be the maximum applied load that can be carried by the cracked structure. When the applied load exceeds the structure's maximum load carrying capacity, a catastrophic structural failure would occur. We can find many research outcomes in literature, concerning the stable crack growth problem in thin metallic plate. Most of analytical/numerical studies assume the plane stress condition [1]. However, some experimental studies suggest that the state of deformation at the vicinity of the crack tip is highly three dimensional. Omori et al. [2] pointed out that when a crack propagates in thin aluminum alloy specimen, 100% shear lip failure occurred. Also, Dawicke et al. [3] suggested that the crack tunneling occur when crack propagates in a metallic plate.

In present study, we investigate three dimensional deformation field at the vicinity of growing

crack tip. However computational effort when a three dimensional elastic plastic finite element crack propagation analysis is carried out from the crack propagation initiation through the quasi-steady state (via the transient state), may be prohibitively extensive. Thus, in present study, we use an ordinary elastic plastic finite element method to analyze stationary crack problems and an Eulerian finite element method for steady state crack propagation problems. In Eulerian finite element method, coordinate system is embedded at the advancing crack front and we do not need to carry out the transient analysis. Thus, detailed deformation field at the vicinity of the crack tip can be analyzed at almost the same computational effort as it is required for a stationary crack analysis.

Solutions that have been obtained in present study, reveal that the deformation fields at the vicinity of the crack front are quite different between the cases of stationary and steadily propagating cracks. The distributions of effective plastic strain in the case of propagating crack suggest that the pattern of deformation be analogous to that of diffused necking of thin plate. It corresponds to the 100% shear lip failure at the crack tip. Also, at the center of plate thickness, the magnitude of plastic strain is considerably higher than that at the surface, suggesting the occurrence of ductile fracture. On the other hand, for the stationary crack case, effective plastic strain distribution does not have much variation through the thickness of the plate. Solutions obtained in this study compare favorably with the experimental studies in earlier literature [2, 3].

2. EULERIAN FINITE ELEMENT METHOD FOR CRACK ANALYSIS

2.1 Coordinate Systems

We assume in this study that advancing crack front is straight and perpendicular to the plate and that the crack propagates in X_1 direction in $O-X_1, X_2, X_3$ global coordinate system. The current position of the crack front is $X_1 = a$ and the crack grows at a constant velocity \dot{a} . We consider a moving coordinate system $O-X'_1, X'_2, X'_3$, which is embedded at the crack front, as depicted in Fig. 1. The global and the moving coordinate systems have relationships: $X_1 = X'_1 + a$, $X_2 = X'_2$ and $X_3 = X'_3$.

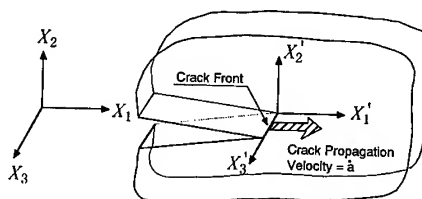


Fig. 1 Propagating crack and $O-X'_1, X'_2, X'_3$ coordinate system which is embedded at the crack front.

We formulate the problem using a finite deformation theory as the material at the vicinity of the crack tip is expected to undergo a large deformation. The coordinate values of a material point before and after large deformation are shown by (X_1, X_2, X_3) and by (x_1, x_2, x_3) , in the $O-X_1, X_2, X_3$ global coordinate system. Also, a material point in original and deformed configurations are written by (X'_1, X'_2, X'_3) and by (x'_1, x'_2, x'_3) , in the $O-X'_1, X'_2, X'_3$ coordinate system.

2.2 Evaluation for Stresses in Eulerian Finite Element Method

We adopt a rate form J2-flow constitutive law. The constitutive law describes the relationship between the Jaumann rate of Kirchhoff stress $\dot{\sigma}_{ij}^J$ and rate of strains $\dot{\epsilon}_{ij}$, which are the symmetric part of the velocity gradients $\partial v_k / \partial x_l$, can be written to be:

$$\dot{\sigma}_{ij}^J = E_{ijkl}^e \left(\dot{\epsilon}_{kl} - \dot{\epsilon}_{kl}^p \right) = E_{ijkl}^e \dot{\epsilon}_{kl} - E_{ijkl}^e \Lambda_{klmn} \dot{\epsilon}_{nm} = E_{ijkl}^e \frac{\partial v_k}{\partial x_l} - E_{ijkl}^e \Lambda_{klmn} \frac{\partial v_m}{\partial x_n} \quad (1)$$

where Λ_{ijkl} represent the plastic strain evolution equation ($\dot{\epsilon}_{ij}^p = \Lambda_{ijkl} \dot{\epsilon}_{kl}$), E_{ijkl}^e are the elastic

constants representing Hooke's law and v_i are velocities at a material point. Both $E_{ijk\ell}^e$ and $\Lambda_{ijk\ell}$ hold the minor symmetries ($E_{ijk\ell}^e = E_{ij\ell k}^e = \dots$ and $\Lambda_{ijk\ell} = \Lambda_{ij\ell k} = \dots$). By assuming that the volume change of material while elastic plastic deformation takes place is negligibly small, we can write the relationship between the rate of Cauchy stresses and the velocity gradients, as:

$$\dot{\sigma}_{ij} = E_{ijk\ell}^e \frac{\partial v_k}{\partial x_\ell} - E_{ijk\ell}^e \Lambda_{klmn} \frac{\partial v_m}{\partial x_n} - \sigma_{ik} \omega_{kj} + \omega_{ik} \sigma_{kj} = E_{ijk\ell}^e \frac{\partial v_k}{\partial x_\ell} - F_{ijk\ell} \frac{\partial v_k}{\partial x_\ell} = D_{ijk\ell} \frac{\partial v_k}{\partial x_\ell} \quad (2)$$

where ω_{ij} are the spin tensor (the anti-symmetric part of the velocity gradients). For steady state, we can show that:

$$\dot{\sigma}_{ij} = -\dot{a} \frac{\partial \sigma_{ij}}{\partial X_1} \quad \text{and} \quad \dot{\sigma}_{ij} = D_{ijk\ell} \frac{\partial v_k}{\partial x_\ell} = D_{ijk\ell} \frac{\partial}{\partial x_\ell} \left(-\dot{a} \frac{\partial u_k}{\partial X_1} \right) = -\dot{a} D_{ijk\ell} \frac{\partial}{\partial X_1} \left(\frac{\partial u_k}{\partial X_m} F_{m\ell}^{-1} \right) \quad (3)$$

where u_i are the displacements and $F_{k\ell}^{-1} = \partial X_k / \partial x_\ell$. Therefore, the stresses can be expressed by:

$$\sigma_{ij}(X_1', X_2', X_3') = \int_{+\infty}^{X_1'} \frac{\partial \sigma_{ij}}{\partial X_1} d\bar{X}_1' = \int_{+\infty}^{X_1'} D_{ijk\ell} \frac{\partial}{\partial X_1'} \left(\frac{\partial u_k}{\partial X_m} F_{m\ell}^{-1} \right) d\bar{X}_1' = E_{ijk\ell}^e \frac{\partial u_k}{\partial x_\ell} - \int_{+\infty}^{X_1'} F_{ijk\ell} \frac{\partial}{\partial X_1'} \left(\frac{\partial u_k}{\partial X_m} F_{m\ell}^{-1} \right) d\bar{X}_1' \quad (4)$$

Eqs. (2-4) are slightly different from the case of infinitesimally small strain analysis of [4]. Here it is noted that the spatial derivatives $\partial/\partial x_i$ and $\partial/\partial x_i'$ are the same.

2.3 Eulerian Finite Element Formulation

Using Eq. (4) to evaluate stresses, one can obtain an Eulerian finite element formulation, as:

$$\int_{\partial\Omega_t} \delta u_i \bar{t}_i d(\partial\Omega_t) + \int_{\Omega} \delta u_i b_i d\Omega + \int_{\Omega} \frac{\partial \delta u_i}{\partial x_i} \left[\int_{+\infty}^{X_1'} F_{ijk\ell} \frac{\partial}{\partial X_1'} \left(\frac{\partial u_k}{\partial X_m} F_{m\ell}^{-1} \right) d\bar{X}_1' \right] d\Omega = \int_{\Omega} \frac{\partial \delta u_i}{\partial x_i} E_{ijk\ell}^e \frac{\partial u_k}{\partial x_\ell} d\Omega \quad (5)$$

where δu_i are the variations of the displacements u_i and \bar{t}_i are the prescribed tractions on $\partial\Omega_t$. By discretizing the above equation by using an appropriate type of finite element, we can construct a system of linear simultaneous equation to solve for the displacements.

The finite element formulation of Eq. (5) is highly nonlinear due to the third term in its left hand side. An iterative algorithm as described in Dean et al. [4] is adopted to obtain the equilibrium.

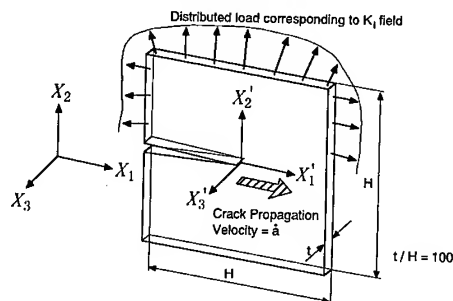


Fig. 2 Problem of cracked plate loaded by K_1 stresses at its edges.

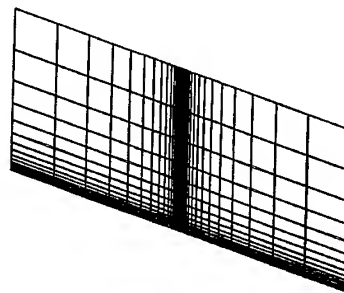


Fig. 3 Finite element model.

3. DEFORMATION AT THE VICINITY OF CRACK TIP

3.1 A Thin Plate Loaded by Edge Stresses Corresponding Elastic Crack Solution

The prescribed tractions corresponding to the elastic K_I stress field are given at the edge of the plate, as shown in Fig. 2. We assume that small scale yielding condition is satisfied and that plastic zone which develops around the crack tip, is well embedded in elastic K_I stress field. The thickness of the cracked plate, which is depicted in Fig. 2, is 1/100 of its total height H . We analyze only one fourth of the plate considering symmetries about $X_1 - X_2$ and $X_1 - X_3$ planes. In Fig. 3, the finite element model is shown. There are 8000 eight node brick elements and 9471 nodes. There are 10 layers of elements in thickness direction. The length of each edge of the elements at the crack front is set to be $H/2000$. Ramberg-Osgood type power law hardening is assumed. For stationary crack case, HRR [5, 6] field should dominate at the vicinity of the crack tip. The power hardening law is:

$$\frac{\varepsilon}{\varepsilon_Y} = \frac{\sigma}{\sigma_Y} + \alpha \left(\frac{\sigma}{\sigma_Y} \right)^n, \quad \varepsilon_Y = \frac{\sigma_Y}{E} \quad (6)$$

where σ_Y and E are yield stress and Young's modulus, respectively. α and n are nondimensional constant and hardening power, respectively. In this study, we let $\alpha=1$ and $n=4,8,12,24$. Ratio between yield stress and Young's modulus $\sigma_Y/E=0.001$ is set to be 0.001, which is within a typical value among metallic materials. Though the material constants are hypothetical, generic solutions, which can be extended to realistic metallic materials, are obtained.

3.2 Deformation Field at the Vicinity of the Crack Tip for Stationary and Propagating Cracks

In this section, the results of the analysis for stationary and propagating crack cases are presented. Though we have investigated cases with various hardening power n , we present solutions only for $n=12$ and can find distinctive differences in three dimensional deformation fields between stationary and propagating cracks.

In Fig. 4, the developments of plastic zone at near the center of the thickness and at the surface of the plate, are depicted for the stationary crack case. In Fig. 5, the developments of active plastic and elastic unloading zones are shown for the propagating crack case (Elastic zone which should not be present, exists in region between the active plastic and elastic unloading zones, due to a problem in drawing the figure. In reality, the elastic unloading zone is immediately behind the active plastic zone.). Obvious difference between the stationary and propagating crack cases is that the plastic unloading zone (wake zone) exists in the propagating crack case. However when we check up the

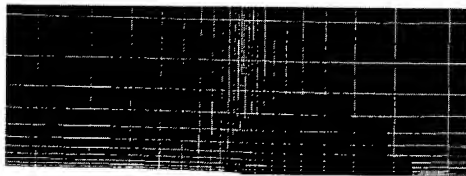


Fig. 4 Development of plastic zone at the center of plate thickness for the stationary crack case. (Black: Plastic zone, Dark gray: Elastic zone)



Fig. 5 Development plastic and elastic unloading zones at the center of plate thickness for the propagating crack case. (Black: Plastic zone, Dark gray: Elastic zone, Light Gray: Elastic unloading zone)

distribution of effective plastic strains for the propagating and stationary crack cases, we find some distinct differences between them. That is, the plastic strain distribution in the cross section of the plate parallel to $X_2 - X_3$ plane at the crack front ($X'_1 = 0$ plane) is somewhat similar to that of diffused necking of thin plate, for the case of propagating crack, as depicted in Fig. 6 (a). In Fig. 6 (b), the plastic strain distribution in $X'_1 = 0$ plane for the stationary crack case, is shown. In this case, less concentration of plastic strain at the center of the plate thickness is observed, in comparison with the propagating crack case. The plastic strain distribution is somewhat more uniform than the propagating crack case. Furthermore, the development of band of plastic strain concentration in about 45 degree from X_2 axis is observed, in propagating crack case. These observations suggest that the development of shear band take place for the propagating crack case. On the other hand, such concentration of plastic strain is not observed in the case of stationary crack, suggesting that three dimensional deformation fields are distinctively different at the vicinity of the crack tip, between the stationary and propagating crack cases.

3.3 T_ϵ^* Integral as Crack Tip Parameter

In this section, we present the results of T_ϵ^* integral evaluation (see Atluri, Nishioka and Nalagaki [7] for its theoretical development and Brust et al. [8], Nishioka et al. [9, 10], Wang et al. [11] for successful applications). Also an extensive investigation on the behavior of T_ϵ^* integral value for two dimensional crack propagation problem was recently presented by Okada and Atluri [12].

For thin plate problem, we extend the two dimensional definition to a quasi-two dimensional plate problem by using an equivalent domain integral (EDI) method (Nikishkov and Atluri [13]). Instead of the integral contour, we consider an integral surface in the quasi-two dimensional case, as depicted in Fig. 7 (a) and then the result of integral is divided by the plate thickness t . Thus, the quasi-two dimensional definition for T_ϵ^* integral in present quasi-static problems, can be written to be:

$$T_\epsilon^* = \frac{1}{t} \int_{A_\epsilon} \left(W n_1 - t_i \frac{\partial u_i}{\partial x_1} \right) dA$$

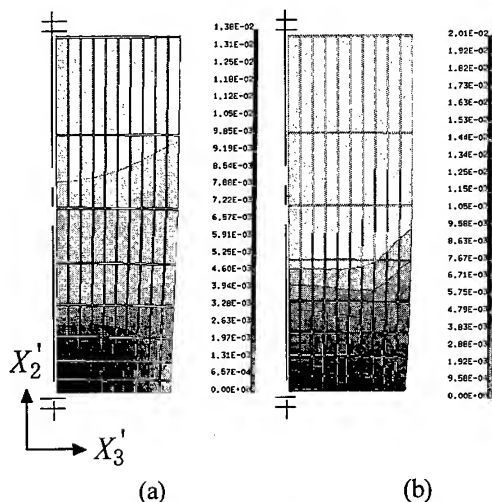


Fig. 6 The distribution of effective plastic strain in X'_1 plane, (a) for the propagating crack case and (b) for stationary crack case.

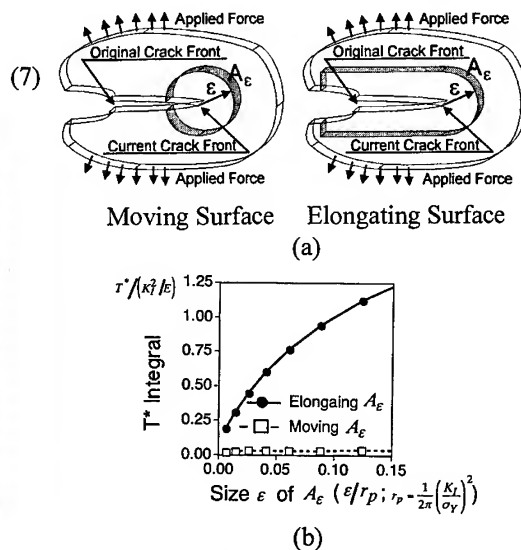


Fig. 7 (a) Moving and elongating integral surfaces, (b) T_ϵ^* integral values on moving and elongating integral surfaces, vs. their size, ϵ for the propagating crack case.

As shown in Fig. 7 (a), elongating and moving integral surfaces are used to evaluate T_ϵ^* integral. The size ϵ of A_ϵ integral surface is varied and its influences on T_ϵ^* value are discussed, for the propagating crack case. In Fig. 7 (b), variation of T_ϵ^* value with respect to the size ϵ of moving A_ϵ integral surface is also shown. It is seen that T_ϵ^* value is small compared with far field J integral value (which corresponds to the applied K_I value [$J = K_I^2/E$]) but takes almost the same value for different ϵ . On the other hand, when T_ϵ^* integral is evaluated on the elongating A_ϵ integral surface, we find that T_ϵ^* integral value strongly depends on the size ϵ of the integral surface. For a large ϵ , T_ϵ^* integral value is also large. This is because, as described by Okada and Atluri [12], T_ϵ^* integral with the elongating integral surface, measures the total sum of the energy dissipated inside the integral surface and the energy spent to open a new crack surface, per unit crack extension. Therefore, for greater volume inside the integral surface, T_ϵ^* integral takes larger value. On the other hand, T_ϵ^* integral with the moving integral surface only measures energy spent to open a new crack surface per unit crack extension. This is why T_ϵ^* integral with the moving integral contour becomes nearly constant.

4. CONCLUDING REMARKS

In this paper, near tip deformation fields for propagating and stationary cracks in thin ductile plate are presented. It has been found that three dimensional deformation fields of the stationary and propagating crack cases are distinctively different. Plastic strain distribution at the vicinity of the crack front shows the eventual development of shear band type deformation, which is similar to the case of thin plate subjected to tension and corresponds to shear lip fracture. Also, the concentration of plastic strain at the center of plate thickness is observed. This may cause crack tunnelling.

Though we presented some new findings on the deformation behavior at the vicinity of propagating and stationary cracks, we must point out that the finite element model was too rough to capture the detailed deformation behavior around the crack tip. We need to refine the finite element model so that more detailed information can be extracted. In order to do so, we need more sophisticated computational strategy, such as parallel computing. We are currently updating our analysis code and computational facility.

REFERENCE

1. X. Deng and A.J. Rosakis, *International Journal of Fracture* **58** (1992), p. 137
2. Y. Omori, H. Okada, L. Ma and A.S. Kobayashi, ASTM STP 1296 (1997).
3. D.S. Dawicke, M.A. Sutton, J.C. Newman and C.A. Bigelow, ASTM STP 1220 (1995), p. 358.
4. R.H. Dean and J.W. Hutchinson, ASTM STP 700 (1980), p. 383.
5. J. R. Rice and G. F. Rosengren, *J. Mech. Phys. Solids* **16** (1968), p. 1.
6. J.W. Hutchinson, *J. Mech. Phys. Solids* **16** (1968), p. 13.
7. S.N. Atluri, T. Nishioka and M. Nakagaki, *Engineering Fracture Mechanics* **20** (1984), p. 209.
8. F.W. Brust, T. Nishioka and S.N. Atluri, *Engineering Fracture Mechanics* **22** (1985), p. 1079.
9. T. Nishioka, T. Fujimoto and S.N. Atluri, *Nuclear Engineering and Design* **111** (1989), p. 109.
10. T. Nishioka, T. Fujimoto and K. Sakakura, ASTM STP 1131 (1992), p. 170.
11. L. Wang, F.W. Brust and S.N. Atluri, *Computational Mechanics* **20** (1997), p. 199.
12. H. Okada and S. N. Atluri, *Computational Mechanics* **23** (1999), p. 339.
13. G.P. Nikishkov and S.N. Atluri, *Engineering Fracture Mechanics* **26** (1987), p. 851.

Study on the Bending Fatigue Damage of the Carbon and the Polypropylene Hybrid Fiber Reinforced Concrete

Y. Hua, H.B. Qi, Z.Q. Jiang, S.Z. Huang and S.B. Zhang

Research Institute of Materials Science and Engineering, Shijiazhuang Railway Institute,
15 Beihuan east road, Shijiazhuang, Hebei 050043, China P.R.

Keywords: Bending Fatigue, Carbon Fiber, Hybrid Fiber Reinforced Concrete, Polypropylene Fiber

ABSTRACT

The bending fatigue damage characteristic of carbon and polypropylene hybrid fiber reinforced concrete (C-P HFRC) was studied in detail. An experiment was designed to obtain the law on the alteration of the C-P HFRC's fatigue life and fatigue strength caused by the fibers. Fatigue equation $S = A - B \lg N$ was obtained through the linear regression. The C-P HFRC's bending fatigue damage characteristic was carried out. The composition and development of the fatigue strain caused by the cyclic load were analyzed on the basis of experimental results, and the bending fatigue strain mode was supposed. The law of the fatigue damage accumulation and evolution under cyclic load was investigated. The fatigue damage model was established.

1. INTRODUCTION

The researches on fatigue damage and fracture properties of concrete absorbed more and more attention of design engineers in recent years. The first reason was that some new type concrete structures appeared which endured serious fatigue loading. The other reason was that some roads, sleepers and bridges were working under serious fatigue and damage environment with the transportation transfer to heavy load and high speed. But the brittle properties of concrete led itself to lower fracture toughness, lower fatigue strength and lower resistance of crack propagation.

The fracture toughness and the resistance to crack propagation of concrete could obviously be improved by using carbon fiber and polypropylene fiber, and so could the fatigue properties. If the high modulus of carbon fiber and high extension of polypropylene fiber are fully utilized at different stress level, the fatigue strength and resistance of fracture of the C-P HFRC would considerably improved.

The entire C-P HFRC specimens, where the volume fraction of carbon fiber and that of polypropylene fiber were 0.5, 1.0, 1.5 and 0.5, 0.7, 0.9, respectively, were subjected to a constant amplitude and high frequency fatigue loading. The law of fatigue residual strain, cyclic strain ranges and total fatigue strain range was analyzed. With the help of fracture mechanics' theory and Weibull's statistic methods, the fatigue life equation of the C-P HFRC were proposed. A fatigue damage model was established, which could easily be used in civil engineering.

2. EXPERIMENTAL PROCEDURE

2.1. Samples

The basic concrete was made up of the ordinary Portland cement, the sand, the crush roast aggregate and the water reducer. C: S: G: W=1:1.81:2.83: 0.53. The C-P HFRC's samples were made of the I -type carbon fibers(CF) and the polypropylene fibers(PF). The volume fraction of the CF and that of the PF were 0.0, 0.5, 1.0, 1.5 and 0.0, 0.5, 0.7, 0.9, respectively. The diameter and aspect ratio of the CF were $6.0\ \mu\text{m}$ and 500, respectively, and those of the PF were $10.0\ \mu\text{m}$ and 800, respectively. The size of the C-P HFRC prism was $100\times 100\times 300\text{mm}$ and the strain gauges were stuck on the surfaces of the concrete prism.

Table 1 shows the relationship between the organizing into groups of the C-P HFRC and the volume percent of the CF and the PF.

Table 1. Relationship between the sample's groups and the volume percent of the hybrid fibers

No.	1	2	3	4	5	6
CF(Vol. %)	0.0	0.5	0.0	0.5	1.0	1.5
PF (Vol. %)	0.0	0.0	0.5	0.5	0.7	0.9

2.2. Experiment Equipment

The bending fatigue experiment was tested on a PLG-100CF high frequency fatigue-testing machine controlled by a computer. The data were collected and recorded by a Y8DL-2 dynamic resistance strainometer fitted with a SC16A photoelectricity oscillograph. The strain gauges stuck points were shown in Fig. 1 (a). Three-point bending method was adopted shown in Fig. 1(b).

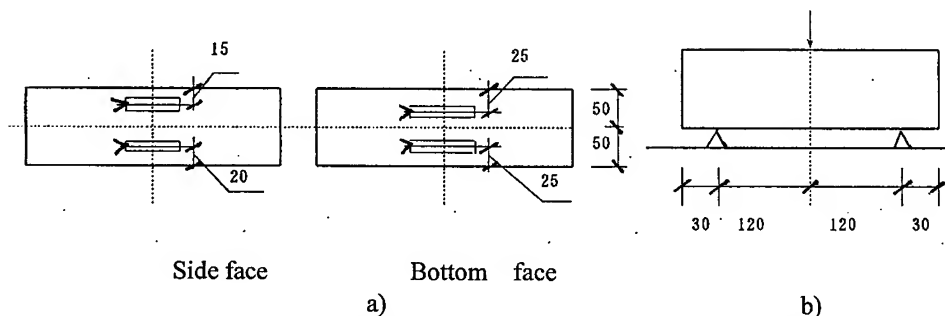


Fig.1. Schematic diagram of a) strain gauges stuck points; b) locations of load head and two of bearing points.

2.3. Experiments

The bending fatigue samples were first bent by a static load, whose maximum value was not over 4kN, and then unloaded. After the preloading test, tests were conducted using a constant range of fatigue loading with a 105Hz sinusoidal waveform.

When the number of cycles reached 2,5,10,20,50,100,150,200,500,1000 and 2000 thousand, the samples were unloaded and the fatigue strain amplitude and the residual strain were measured. After the measurement the samples were reloaded and the fatigue cyclic test continued until the specimens failure occurred.

3. EXPERIMENTAL RESULTS AND DISCUSSION

3.1. Results of Fatigue Life

The fatigue lives of the C-P HFRC were summarized in Table 2.

Table 2. Fatigue lives of the C-P HFRC

No.	S	N	No.	S	N	No.	S	N
1-1	0.50	1843752	3-1	0.50	1897655	5-1	0.55	1251579
1-2	0.55	305947	3-2	0.55	316722	5-2	0.60	328019
1-3	0.60	48982	3-3	0.60	55061	5-3	0.65	75599
1-4	0.65	8197	3-4	0.65	9452	5-4	0.70	18492
1-5	0.70	1419	3-5	0.70	1973	5-5	0.75	4573
2-1	0.50	>2million	4-1	0.55	916737	6-1	0.60	550723
2-2	0.55	638992	4-2	0.60	243620	6-2	0.65	142975
2-3	0.60	185103	4-3	0.65	49819	6-3	0.70	36862
2-4	0.65	31997	4-4	0.70	11499	6-4	0.75	9395
2-5	0.70	7328	4-5	0.75	2713	6-5	0.80	2423

Notes: N is cyclic number to failure.

As the general fatigue life equation of plain concrete and steel fiber reinforced concrete was given by [1,2]

$$S = A - B \lg N \quad (1)$$

in which S is the ratio of maximum stress to minimum stress, N the bending fatigue life, A and B liner regression coefficients, the fatigue life of the C-P HFRC must have the same type of Eq. 1. Inasmuch as A and B had well liner relation with V_{cf} and V_{pf} , the following equation are assumed:

$$A = C + D V_{cf} + E V_{pf} \quad (2)$$

$$B = C' + D' V_{cf} + E' V_{pf} \quad (3)$$

where C , D , E , C' , D' and E' could be derived by the liner regress on analysis fatigue life data, V_{cf} and V_{pf} are the volume fraction of the carbon fiber and that of the polypropylene fiber, respectively.

The data of the C-P HFRC fatigue life, whose survived life percentage exceeded 90%, were first treated by Weibull's statistic methods [3], and then fitted by the liner regression to the S - $\lg N$ type equation. The results were shown in the following:

$$\text{No. 1. } S = 0.901 - 0.064 \lg N \quad \text{No. 2. } S = 0.997 - 0.077 \lg N \quad \text{No. 3. } S = 0.913 - 0.066 \lg N$$

$$\text{No. 4. } S = 1.021 - 0.079 \lg N \quad \text{No. 5. } S = 1.050 - 0.082 \lg N \quad \text{No. 6. } S = 1.088 - 0.085 \lg N$$

Substituting these values of six equations into Eqs. 1 and 2, and using the liner regression, one can obtain the following equations:

$$A = 0.901 + 10.8 V_{cf} + 2.78 V_{pf} \quad (4)$$

$$B = 0.064 + 1.24 V_{cf} + 0.276 V_{pf} \quad (5)$$

The fatigue life equation of the C-P HFRC are finally given by:

$$\begin{cases} S = A - B \lg N \\ A = 0.901 + 10.8 V_{cf} + 2.78 V_{pf} \\ B = 0.064 + 1.24 V_{cf} + 0.276 V_{pf} \end{cases} \quad (6)$$

Table 3 lists in the six groups of the C-P HFRC experimental values and calculated values from Eq. 6 ($S=0, 60$) of fatigue life. From Table 2 and 3, we can find out that the fatigue life of the C-P

HFRC can increase with the increase of fiber volume fraction. When the volume fraction of the carbon fibers exceeds 1.0 and that of the polypropylene fiber exceeds 0.7, the experimental fatigue life does not increase largely.

Table 3. Experimental values and calculated fatigue lives of the C- P HFRC

	1	2	3	4	5	6
Experimental values	48982	185013	55061	243620	328019	550723
Calculated values	50480	204969	59048	264887	359381	542537
Relative error	3.2%	9.7%	6.0%	8.1%	8.7%	2.0%

3.2. Law of Accumulated Residual Strain of the C-P HFRC

When the C-P HFRC was tested by the bending fatigue loading, the amplitude of tensile strain and the compress strain gradually increased with increasing the number of cycles up to the specimen failure. The material failure was mainly due to the tensile strain, which was composed of the cyclic strain and the residual strain.

The bending fatigue residual strain was made up of plastic cyclic strain and creep, which were caused by the average stress. In general, the developing process of residual strain could be divided into three stages: decelerating, steady-state and accelerating stages.

The residual strain rate, $\dot{\varepsilon}_r$, can be describe by the following equation:

$$\dot{\varepsilon}_r = B\sigma_m^n t^\beta \quad (7)$$

in which σ_m is the average stress, t the time variable, n the cyclic number, B and β are parameters which are related to material physical states.

Integrating Eq. 7, one can obtain the value of ε_r :

$$\varepsilon_r = \frac{B\sigma_m^n}{1+\beta} t^{1+\beta} \quad (8)$$

If N_r' is the onset cycles of the fatigue residual strain reach the steadying stage, ε_r' is the corresponding residual strain and t' is time, the following equation similar to Eq. 8 can be obtained:

$$\varepsilon_r' = \frac{B\sigma_m^n}{1+\beta} (t')^{1+\beta} \quad (9)$$

Comparing Eq. 8 with Eq. 9 ($\frac{t}{t'} = \frac{N}{N_r'}$), Eq. 9 is rewritten as:

$$\varepsilon_r = \varepsilon_r' \left(\frac{N}{N_r'} \right)^{1+\beta} \quad (10)$$

Considering decelerating stage ($\beta+1 < 1$), and defining $\lambda = \beta+1$, Eq. (10) can be reduced to:

$$\varepsilon_r = \varepsilon_r' \left(\frac{N}{N_r'} \right)^\lambda \quad (11)$$

in which ε_r is the residual strain of the C-P HFRC.

3.3. Evolution Law of the Cyclic Strain Range

From the analysis on the data of the C-P HFRC bending fatigue life, the evolution of cyclic strain could be divided into two stages: steady-state and increasing stage. Simulating the experimental data as curve, the evolution law of cyclic strain range would be described as

$$\Delta \varepsilon = \begin{cases} \Delta \varepsilon_0 & N \leq N_{cr} \\ \Delta \varepsilon_0 (1 + \alpha \lg N) & N > N_{cr} \end{cases} \quad (12)$$

in which $\Delta \varepsilon$ is the cyclic strain range of the initial stage, N_{cr} is the critical threshold cycles at the opening of initial cyclic strain range evolution, α is the parameter related to the material physical states, which could be determined by experiments.

3.4. Evolution Law of the Total Fatigue Strain Range

The total fatigue strain of the C-P HFRC, which was caused by the fatigue loading, was composed of the residual strain and the cyclic strains. The evolution of total fatigue strain range on the C-P HFRC also has three stages as shown in figure 2.

Therefore, the total fatigue strain range of the C-P HFRC caused by the bending fatigue loading can be described as:

$$\varepsilon = \Delta \varepsilon + \varepsilon_r = \begin{cases} \Delta \varepsilon_0 + \varepsilon_r' \left(\frac{N}{N_r'} \right)^\lambda & N \leq N_{cr} \\ \Delta \varepsilon_0 (1 + \alpha \lg N) + \varepsilon_r' \left(\frac{N}{N_r'} \right)^\lambda & N > N_{cr} \end{cases} \quad (13)$$

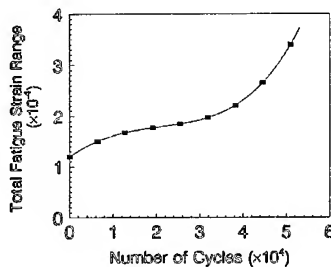


Figure 2. The evolution of the C-P HFRC total fatigue strain range

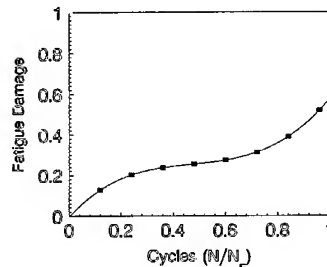


Figure 3. Curve of the fatigue damage evolution with the cyclic numbers

3.5. C-P HFRC Bending Fatigue Damage Model

When the C-P HFRC was tested by the fatigue loading, the damage occurred as the internal crack initiation and crack propagation. The damage was accumulated at each cycle by much nonrecovery minute damage. Obviously, the evolution of damage was related to the cyclic number, the fatigue stress ratio and the fiber percent. Figure 3 gave the curve of the C-P HFRC fatigue damage evolution vs. cycles at a certain stress ratio. Inasmuch as fiber could hinder crack propagation, the C-P HFRC resistance to fatigue deformation and the fatigue damage characteristic were improved by using the carbon fiber and the polypropylene fiber, which exhibited the

prolonged steady-state stage of damage and the decrease of damage developing rate.

By the help of the above analysis, the fatigue damage variable D was defined by a function of cyclic number N , the average stress σ_m and the stress ratio S , namely, $D = f(D, N, S, \sigma_m)$. Based on the experimental data, the following relation can be obtained"

$$\frac{\partial D}{\partial N} = Q(1 - D)^{-\gamma} 10^{\alpha S} \quad (14)$$

in which $D = 1 - \frac{\Delta \varepsilon_r}{\Delta \varepsilon}$, $Q = f(N)$, γ is the parameter related to the material physical states,

which could be determined by experiments, and α the function of cyclic characteristic $R: \alpha = (1 - R)\sigma_f$ (σ_f was the static bending strength of the C-P HFRC, R was the ratio of minimum load to maximum load).

Separating the variables and integrating Eq. 14, the value of D can be expressed as:

$$D = 1 - [1 - (\gamma + 1)10^{\alpha S} \int_1^{N_F} f(N) dN]^{\frac{1}{\gamma+1}} \quad (15)$$

in which N_F is the number of cycles to failure. Since $N_F \equiv N$, $D = D_F$, Eq. 15 is rewritten as:

$$\alpha S = \lg \frac{1 - (1 - D_F)^{\gamma+1}}{\gamma + 1} - \lg \int_1^{N_F} f(N) dN \quad (16)$$

Comparing $S = A - B \lg N_F$ with Eq. 16, one can obtain:

$$D = 1 - [1 - (\gamma + 1)10^{\alpha S} N^{\alpha B}]^{\frac{1}{\gamma+1}} \quad (17)$$

Eq. 17 is the fatigue damage model of the C-P HFRC.

4. CONCLUSIONS

The following conclusions could be drawn from the present study:

(1) The fatigue properties of concrete were improved by using the carbon fiber and the polypropylene fiber at two fields: the initial values of cyclic strain developing raise and the former fatigue residual deformation rise too.

(2) The main reason of the improved fatigue properties on the C-P HFRC was the hybrid fiber that could hinder crack propagation.

(3) The fatigue life of the C-P HFRC precisely predicted using parameter γ , which was determined by experiments. The application of the C-P HFRC to structures needed to use the stress-strain relation, which is still not apparent.

REFERENCE

1. Y. Hua, Z. Q. Jiang and Z. H. Wang, J. Building Materials (in Chinese), 1 (1998) p. 144
2. Y. Hua, S. B. Zhang and Z. Q. Jiang, China Cement and Concrete Products (in Chinese), 4(1997) p.40
3. W. Sun, J. M. Gao and Y. Yan, ACI Material Journal. 1(1996) p. 21

The Effect of Aging Temperatures and Time on Mechanical Properties of CF8M

J.D. Kwon¹, J.C. Park¹, Y.S. Lee¹, W.H. Lee² and Y.W. Park²

¹Department of Mechanical Engineering, Yeungnam University,
214-1 Dae-dong, Kyongsan, Kyongbuk 712-749, Korea

²Korea Institute of Nuclear Safety, Taejon 305-338, Korea

Keywords: CF8M, Degraded Material, Embrittlement, Impact Test, Micro Vickers Hardness Test, Optical Micrograph, Tensile Tests, Virgin Material

ABSTRACT

A stainless steel casting is used in pipes and the valves are subjected to high pressures and temperatures. The primary coolant system of a nuclear power plant is made of stainless steel casting and the operating temperature is in the range of 290~330°C. If the coolant system is exposed to this temperature range for a long period, degradation of the material may occur.

The present investigation is concerned with the degradation characteristics of CF8M (cast duplex stainless steel), exposed to temperatures of 326°C, 430°C and 700°C, respectively. After the CF8M specimens are maintained at the given temperature for the particular thermally degraded specimens, all specimens are water quenched. Each degraded specimen of the thermally degraded materials is classified into four or five classes, depending on holding time at the given temperatures. In order to investigate the characteristics of degradation, microstructure, micro vickers hardness, tensile and impact tests are performed for each class of specimen. From the present investigation the following results are obtained: 1) the difference between the thermally degraded specimens can be understood and distinguished through their microstructures, 2) hardness and tensile strength are increased with degradation, while elongation, and impact energy are decreased by increased degradation.

1. INTROUCTION

When fossil or nuclear power generation or petroleum distillation equipment is exposed to a high temperature environment for a period of time, degradation of the equipment must be considered. This degradation results in variations of microstructure and mechanical properties, including strength, hardness, impact characteristics, fracture toughness and fatigue crack growth. These variations, during normal operational conditions, can cause catastrophic failure of equipment. Thirty-five percent of the total failures of power generation equipment, subjected to high pressure and temperatures in a nuclear power plant, is caused by material degradation[1] while the majority of failures result from poor maintenance. The frequency of failure is increased with the degradation of equipment in the reactor coolant system[2] of nuclear power plants.

Thermal embrittlements can be observed in reactor coolant pump bodies(RCP), reactor coolant pipes and fittings, surge lines, and the spray heads of pressurizers and so on, which belong to the primary pressure boundaries within a nuclear power plant. These materials are made of duplex austenite-ferrite cast stainless steel(CF8M). When a CF8M specimen is exposed to temperatures ranging around 700°C for a long period, it is found that the material degradation is caused by σ -phase[3, 4]. The material degrades through thermal embrittlement when the material is exposed to a long period of temperatures below 500°C. This thermal embrittlement is identified as 475°C degradation[4-8]. Thermal embrittlement is maximum at 475°C. Material degradation can also be observed in pressurized water reactors when the operating temperatures range from 290~330°C [9,10]. Thermal embrittlement is caused by the α' phase which is called the precipitation of a Cr-rich bcc structure[6-8]. It is important to consider the factors associated with material degradation in a nuclear power plant. The degradation is caused by 1) thermal embrittlement in the materials structural integrity and 2) the life prediction of the primary coolant system. In the present paper, the effects of both α' and σ -phase embrittlement on the variations of the mechanical properties are investigated using the aged specimen(CF8M) and varying the aging times.

An accelerated method to degrade the virgin material of CF8M is developed in the present paper. In order to reduce the aging time, the specimens for thermal embrittlement were prepared at 430°C. The specimens for the σ -phase degradation were prepared at around 700°C. The specimens for both thermal embrittlement and σ -phase degradation were divided into five separate classes, depending on the aging time. Four classes of the degraded specimen were at 326°C depending on the aging time. They were compared with the degradation of the mechanical properties of the aged specimen at 430°C and 700°C, respectively.

2. ARTIFICIALLY DEGRADED SPECIMEN PREPARATIONS

The specimens used in the present investigation are ASTM A351 grade CF8M cast stainless steel. This type of steel is used in making many different types of equipment, such as pipes, which are subjected to high temperatures and pressures. The chemical composition of CF8M including the ferrite content which gives major effect on degradation mechanism is given in Table 1. The mechanical properties of virgin CF8M material are shown in Table 2. All specimens used in this investigation were prepared in the laboratory using a method to accelerate the degradation of the material.

Based on this premise[11, 12], the specimens are prepared at a temperature of 430°C and 700°C, respectively, in order to reduce the aging time. They can be escalated rather rapidly to attain the appropriate state of degradation.

Table 1 Chemical composition of CF8M.

Composition, weight %								
C	Mn	P	S	Si	Ni	Cr	Mo	Ferrite Content (%)
0.074	1.21	0.0318	0.0126	1.14	9.59	18.67	2.73	9.6

Table 2 Mechanical properties of CF8M.

0.2% Proof Strength (Mpa)	Tensile Strength (MPa)	Elongation (%)	Reduction Area (%)
318	525	68.6	46.5

The specimens are prepared at 326°C, in order to compare the degradation characteristics between the σ -phase and those specimen at a 475°C degradations temperature. The 326°C degraded specimens are held 2000, 4000, 6000 and 9000hrs at 326°C, respectively. The 430°C degraded specimens are held 100, 300, 900, 1800 and 3600hrs at 430°C, respectively. The specimens associated with the σ -phase degradation are held for 20min, 5, 15, 50 and 150hrs at 700°C, respectively. All of the degraded specimens are quenched in water. It should be noted that virgin material in the investigation is defined as material which has not experienced any degradation.

3. EVALUATION OF DEGRADATION

3.1 Microstructure of the Degraded Material

The degraded material from a piece of equipment that has been used for a long period can be analyzed and understood through observation of the microstructure. The microstructures of the virgin specimen and the degraded specimens that had been subjected to temperatures of 326°C and 430°C, respectively, were compared using an optical microscope. These specimens were prepared by electrolytic etching using 5 volts for 30sec in a solution of oxalic acid. The etched specimens were magnified 400 times through an optical microscope. The microstructure variations in the ferrite phase are shown in Fig. 1 (a, b, c). Fig.1 (b, c) is a specimen that has received maximum degradation. The Cr-rich α' , Ni-rich, Si-rich G phases and $M_{23}C_6$ carbide are major elements that cause thermal embrittlement. They increase in the ferrite phase or in the grain boundary with aging time. These observations are consistent with the results obtained by [5,6]. Therefore, Fig. 1 (b, c) can be considered as an identical thermal embrittlement mechanism. The major elements that cause thermal embrittlement are precipitated in the entire ferrite phase of the aged specimen at 430°C. Those major elements are precipitated in the grain boundary of the austenite-ferrite in the specimen that ha been aged at 326°C

Similarly, the microstructures of the virgin and the five degraded classes of the specimens at various aging times, that were caused by σ -phase degradation, were also compared. In order to find the amount of σ -phase precipitation, an etching reagent which is able to selectively etch σ -phase degradation was prepared. The etching reagent was a solution of HCl(80ml), HNO_3 (5ml), H_2O (20ml) and $CuCl_2$ (1g). The five classes of the specimen degraded by the σ -phase, and the virgin specimen, were etched in the prepared solution for 30 sec, and then the specimens were magnified 400X by an optical microscope. These structures are shown in Fig. 1 (d). Fig.1 (d) is the maximum degraded specimen. The σ -phase precipitation in the etched specimen are also observed in Fig. 1 (d). The amount of σ -phase precipitation increase with aging time is shown in Fig. 1 (d). The σ -phase appears inside the ferrite grains, but the σ -phase does not modify their external shape.

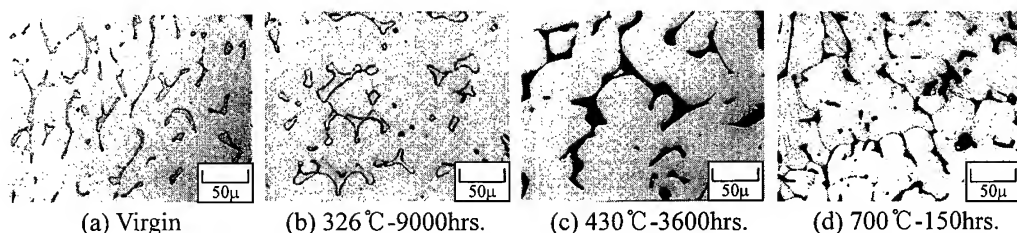


Fig. 1 Optical micrographs of virgin, 326°C, 430°C and 700°C degraded materials.

3.2 Tensile and Hardness Characteristics of Degraded Specimens

The virgin and degraded tensile test specimens, associated with 430°C and 700°C degradation, were prepared based on ASTM E 8M-95a (KS B0801) specimen standards i.e. gage length, 10mm, width, 5mm, distance of parallel portion, 30mm, radius of the corner, 15mm; thickness and 3mm. The elongations, reduction of area and tensile strength of the CF8M (both virgin and degraded specimens) were found from the relationship between load and displacement obtained from the tests.

The tensile strength variations with respect to the aging time of the specimens aged at 326°C, 430°C and 700°C, respectively, are shown in Fig. 2. The strength of the aged specimen at 326°C increases very slowly with aging time and it shows a smaller value than those aged specimens at 430°C and 700°C, respectively. The tensile strength of the aged specimen at 430°C increases rapidly until 300hrs is reached, while it decreases until it arrives at an aging time of 3600hrs. The strength of the aged specimen at 700°C increases rapidly to a maximum strength at 430°C.

The elongation variations of the aged specimen at 326°C decreases slower than those aged specimens at 430°C and 700°C, respectively, as shown in Fig. 3. Those values are larger than those aged specimens at 430°C or 700°C under identical aging times as shown in Fig. 3.

The hardness variations of the precipitated phases, (the ferrite, austenitic matrix and σ -phases) that have been caused by degradation, are measured by a CCD camera that has been attached to the micro vickers hardness tester. The hardness tests, applying a load of 10g, were performed using the etched specimen prepared for microstructural observation. The measurements were repeated twenty(20) times for each degraded specimen.

The average hardness values of the ferrite phase, associated with aging temperatures at 326°C and 430°C, respectively, are shown in Fig. 4. This includes those σ -phase values of the specimen aged at 700°C. The experimental formulas the relationship between the average hardness values and aging times for the specimens aged at 326°C, 430°C and 700°C, respectively, are shown in Fig. 4. The average hardness values of the σ -phase increases rapidly with aging time. Hence, it is difficult to correlate with the aged specimen at 326°C, while the hardness values aged at 430°C can be compared with those aged at 326°C. The average hardness values aged at 326°C can be predicted using those values aged at 430°C.

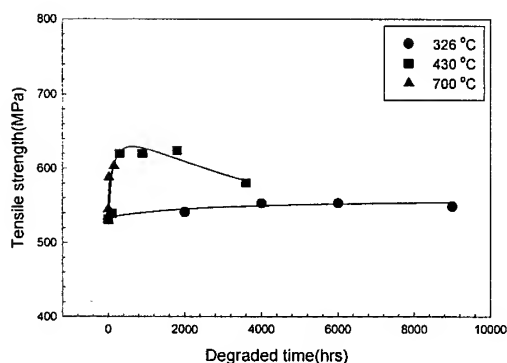


Fig. 2 Tensile strength variations with respect to aging times at various aging temperatures.

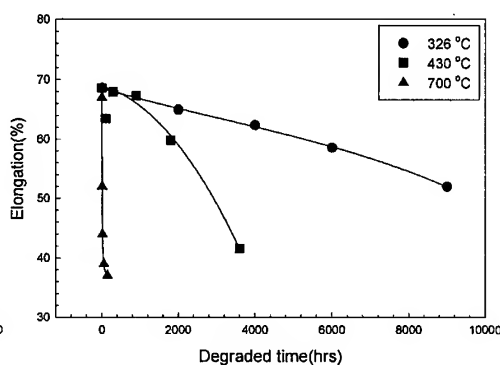


Fig. 3 Elongation variations with respect to aging times at various aging temperatures.

3.3 Degradation and Impact Characteristics

Impact tests were performed to study the mechanical property variations caused by degradation. The specimens were prepared following the specifications given in ASTM E 23-96.

The charpy impact energy variations with respect to aging time and the aging temperatures of 326 °C, 430 °C and 700 °C and room temperature are shown in Fig. 5. The experimental formulas of the relationship between charpy impact energy and aging times for various aging temperatures are shown in Fig. 5. The impact energy of the aged specimen at 700 °C decreases rapidly with the increase of aging time, while the specimen aged at 430 °C can compare with that aged at 326 °C. Upper shelf energy decreases depending on the degradation. The amount of upper shelf energy decrease varies significantly depending on the aging temperature, i.e. 326 °C, 430 °C and 700 °C. It should be noted those results are not shown in the present results.

This phenomenon shows a significant difference from Cr-Mo alloy degradation behavior, where the FATT moves toward higher temperatures, depending on the aging time, and without variation of upper shelf energy values[13].

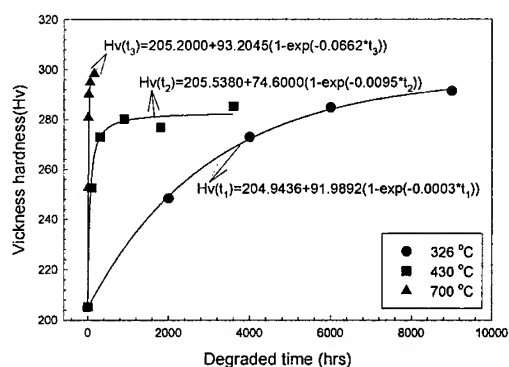


Fig. 4 Vickers hardness variations caused by aging time for various degraded materials depending on aging time.

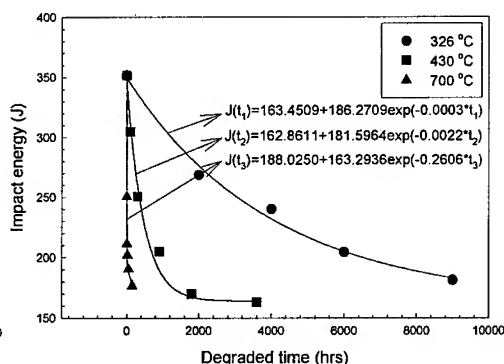


Fig. 5 Charpy impact energy variations with respect to aging times at various aging temperatures (at room temperature).

4. CONCLUSIONS

The degraded CF8M specimen used in reactor coolant systems (RCS) are prepared by an artificially accelerated aging technique. The specimens are aged at 326 °C, 430 °C and 700 °C, respectively, and at various aging times. Microstructure observations, hardness and impact tests are performed using degraded specimens aged at various temperatures and aging times. Through a series of tests the following results are obtained:

1. The degradations at 326 °C, 430 °C and 700 °C can be distinguished by microstructure observations. Mechanisms of degradation at 326 °C and 430 °C are considered on identical degradation mechanism.
2. Hardness and tensile strengths increase with aging time, while elongation decreases.
3. Upper shelf energy values decrease with the increase of aging time and those values are significantly lower depending on degradations than that of the virgin specimen.
4. The experimental formula between the hardness and aging time relationship is obtained. The

mathematical relationship between impact energy and aging time is found. These results can be referred to predict those values that have aged at various temperatures.

5. Degradation at 326°C of the component(CF8M) used in the RCS can be evaluated using the results of 430°C degradation rather than using the degradation results at 700°C.

ACKNOWLEDGEMENTS

The authors are grateful for the support provided by a grant from the Korea Science & Engineering Foundation(KOSEF) and Safety and Structural Integrity Research Center at the Sungkyunkwan University.

REFERENCE

1. International Atomic Energy Agency Advanced Incident Reporting System (1996)
2. Japanese Symposium Regarding "Maintenance and Material Aging of Nuclear Power Plant" sponsored by the Japanese Nuclear Research Committee (in Japanese) (1993)
3. M. Ceylan, V. Kuzucu, M. Aksoy, I. Aksoy, M. Kaplan and M. M. Yildirim, Investigation of the Casting Microstructure of a F-base, Cr-Ni-Mo Duplex Alloy, *Journal of Materials Processing Technology* 69 (1997) p.238-246.
4. Y. Ustinovshokov, M. Shirobokova and B. Pushkarev, A Structural Study of the Fe-Cr System Alloys, *Acta mater.*, Vol. 44, No. 12 (1996) p.5021-5032.
5. T. J. Nichol, A. Datta and G. Aggen, Embrittlement of Ferritic Stainless Steels, *Metallurgical Transactions A*, Vol. 11A (1980) p.573-585.
6. M. Vrinat, R. Cozar and Y. Meyzaud, Precipitated Phase in the Ferrite of Aged Cast Duplex Stainless Steels, *Scripta Metallurgica*, Vol. 20 (1986) p.1101-1106.
7. R. O. Williams, *Trans. TMS-AIME*, Vol. 212 (1958) p.497-502.
8. H. D. Solomon and Lionel M. Levinson, Mössbauer Effect Study of 475°C Embrittlement of Duplex and Ferritic Stainless Steels, *Acta Metallurgica*, Vol. 26 (1978) p.429-442.
9. A. Trautwein and W. Gysel, Influence of Long-time Aging of CF8 and CF8M Cast Steel at Temperatures Between 300 and 500°C on Impact Toughness and Structural Properties, *Stainless Steel Castings*, ASTM STP 756 (1982) p.165-189.
10. O. K. Chopra and H. M. Chung, Aging Degradation of Cast Stainless Steels: Effect on Mechanical Properties, *Environmental Degradation of Materials in Nuclear Power Systems-Water Reactors*, edited by G. J. Theus and J. R. Weeks, The Metallurgical Society, Warrendale, PA (1988) p.737-748.
11. R. J. Eiber, W. A. Maxey, A. R. Duffy, and T. J. Atterbruy, Investigation of the Initiation and Extent of Ductile Pipe Rupture, BMI 1866, July (1969)
12. Jae-do Kwon, Joong-cheul Park, Yong-son Lee, Woo-ho Lee and Youn-won Park, An Investigation of the Degradation Characteristics for Casting Stainless Steel, CF8M, Under High Temperatures, *Nuclear Engineering and Design* (12. 1999 accepted)
13. Hideo Kitagawa, Jae Do Kwon, Yuuji Nakasone, and Tsuyoshi Shimazaki, Fatigue Crack Growth Life Prediction of a Cr-Mo Steel Degraded in Long Service (First Report, Fatigue Crack Growth Properties in a Long-service-degraded Material), *Transactions of the Japan Society of Mechanical Engineers A Tokyo*, Vol. 52, No. 480 (1986) p.1749-1756.

Effect of Temperature on the Damage Behavior of an Adhesively Bonded Butt Joint

A. Fujinami¹, K. Osaka², T. Fukuda² and M. Imanaka³

¹ Graduate School, Osaka City University, Sugimoto 3-3-138, Sumiyoshi, Osaka 558-8585, Japan

² Department of Intelligent Materials Engineering, Osaka City University,
Sugimoto 3-3-138, Sumiyoshi, Osaka 558-8585, Japan

³ Department of Technology Education, Osaka University of Education,
Asahigaoka 4-698-1, Kashiwara, Osaka 582-8582, Japan

Keywords: Adhesively Bonded Butt Joints, Damage, Damage Parameter, Rubber Contents, Rubber Modified Adhesive, Temperature

ABSTRACT

In the present study, in order to evaluate the effects of temperature on the damage behavior of an adhesively bonded joint, the stress-strain relations for two types of specimens have been measured under cyclic loading tests at various testing temperatures. One of the specimens is an adhesively bonded butt joint specimen (joint specimen) and the other is a bulk one. Rubber modified epoxy (RM-epoxy) adhesives with three different rubber contents were used for the specimens. From the results of the experiments, a damage parameter D which is defined as the reduction in the elastic modulus from the initial value was obtained, and the damage behavior of the specimen was evaluated by the values of D . The effects of temperature on the damage behavior of the adhesive layer in the joint specimen and the bulk specimen with different rubber contents were then compared and the damage behavior of the adhesive layer in the joint specimen was investigated.

1. INTRODUCTION

In recent years, rubber modified epoxy (RM-epoxy) adhesives have been widely applied to the structure fields owing to its high toughness. The toughening function in RM-epoxy resin is due to energy dissipation caused by the microdamage formations such as micro crackings and cavitations around the rubber particles. These microdamage formations occur in the vicinity of the crack tip [1,2]. These damages make the materials toughened, but they are the factors of strength reduction. Hence, to apply RM-epoxy adhesives to structural adhesive bondings with high reliability, it is necessary to clarify their damage behavior. However, it has not yet been clarified. Additionally, it is considered that temperature is very important among the parameters affecting the damage behavior of the adhesives. Recently, damage in materials is evaluated by using acoustic emission, variations of the elastic modulus, ultrasonic wave propagation, and so on [3]. When the damage behavior of the adhesive layer of bonded joints is investigated, a damage parameter D designating

the degradation of the elastic modulus is convenient for evaluating damage due to the easiness of their measurement. The stress-strain curves of the bulk adhesives are usually used when the stress analysis of the bonded joints is performed. It is predicted that the damage behavior of the adhesive layer in the bonded joints differs from that of the bulk adhesives, since the deformation of the adhesive layer having a very thin thickness is constrained by the adherends.

In this study, in order to evaluate the effect of temperature on the damage behavior of adhesively bonded joints, the stress-strain curves for two types of the specimens have been measured under uniaxial cyclic loading tests at various testing temperatures. One of the specimens is an adhesively bonded butt joint specimen (joint specimen) and the other is a bulk one. From the results of the experiments, the damage parameter D which is defined as the reduction in the elastic modulus was obtained [3]. The effects of temperature on the damage behavior of the adhesive layer in the joint specimen and the bulk specimen with different rubber contents were then compared, and the damage behavior of the adhesive layer in the joint specimen was investigated.

2. EXPERIMENTAL PROCEDURE

2.1. Materials and Specimens

The adhesives used for the specimens are shown in Table 1. They are unmodified epoxy (UM-epoxy) (Asahi Denka Kogyo: EP4100-E), and three kinds of RM-epoxy (JSR: XER-91) in which the rubber particle weight fractions (R) are 3%, 7%, and 14%. The curing agent used in the experiments is piperidine. The average diameter of the rubber particles is 70nm. The RM-epoxy with $R=3\%$ and 7% were prepared by mixing UM-epoxy resin with the RM-epoxy in which rubber particles of 14% were included. Fig.1 shows the shape and dimensions of the butt joint specimen. The material used for the adherend is JIS S45C steel. The adhesive layer thickness was controlled to be nominally 0.3mm. The adherend surfaces were treated for bonding by dry polishing with 320-grade emery paper and washing with acetone. The bulk specimen has a dog-bone shape and the details are defined in JIS K7113. The bulk and joint specimens were cured in a furnace for 5 hours at 160°C.

Table 1 Adhesives used for the specimens.

Name	Rubber contents (wt%)	Composition of adhesives (gr.)
R14	14	<ul style="list-style-type: none"> • Xer-91 50 • Piperidine 1.6
R7	7	<ul style="list-style-type: none"> • Xer-91 25 • EP-4100 25 • Piperidine 1.6
R3	3	<ul style="list-style-type: none"> • Xer-91 10.7 • EP-4100 39.3 • Piperidine 1.6
UM-epoxy	—	<ul style="list-style-type: none"> • EP-4100 50 • Piperidine 2.5

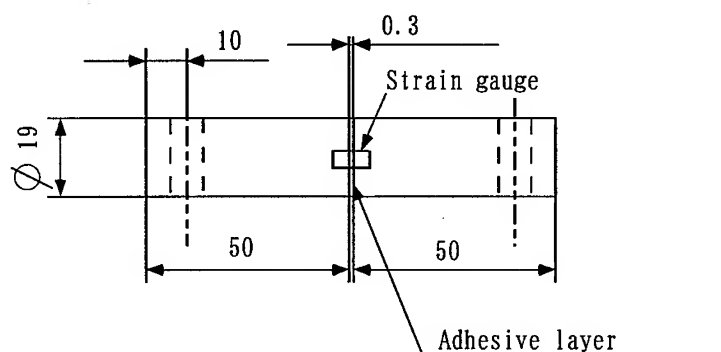


Fig.1. Shape and dimensions of butt joint specimen.

2.2. Measurements of damage behavior

The bulk and joint specimens were tested by a universal material testing machine at testing temperatures (T)=23°C, 40°C and 60°C under uniaxial cyclic loading conditions. The specimens with various rubber contents were loaded at a constant crosshead speed of 0.5mm/min. In the uniaxial cyclic loading tests, the specimens were loaded until showing nonlinear behavior and then were unloaded until the stress-strain curve became straight. The specimens were then reloaded and unloaded repeatedly until they broke, as shown in Fig.2 designating the stress-strain curves in the experiments. The strains of the bulk specimens and those of the joint specimens were measured by a strain measurement system using a CCD camera and the electric resistance wire strain gauges, respectively. Since the measurement area of the strain gauges includes the adherends, as shown in Fig.1, the strains of the adherends are included in the measured values. Therefore, the strains of the adhesive layer were calculated from the measured values of the strain gauges. From the obtained stress-strain curves, the damage parameter D which is defined as the degradation of the elastic modulus was obtained. The damage parameter D can be expressed by the following equation [3]:

$$D = 1 - \frac{E_{eff}}{E} \quad (1)$$

where E and E_{eff} show the initial value of the elastic modulus and the degraded one during reloading, respectively.

3.RESULTS AND DISCUSSION

3.1. Influence of rubber contents

Fig.2 shows the stress-strain curves of the bulk specimens with various rubber contents at $T=23^\circ\text{C}$. The stress-strain curves of R7 and R14 indicate nonlinear behavior. In their cyclic loading tests, the stress-whitening phenomenon was observed after they indicated nonlinear behavior, but it was not observed in the case of the R3 and UM-epoxy specimens. Therefore, the nonlinearity of the stress-strain curves of R7 and R14 are interpreted as a result of the damage. For the purpose of investigating the damage behavior of the bulk specimens, the values D are plotted against the total strain as shown in Fig.3. The values D increase with increasing R . In the

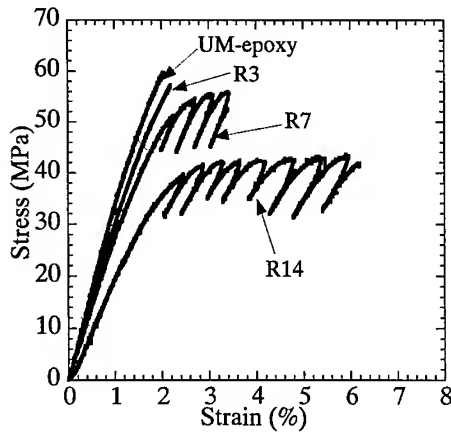


Fig.2 Stress-strain curves of the bulk specimens ($T=23^{\circ}\text{C}$).

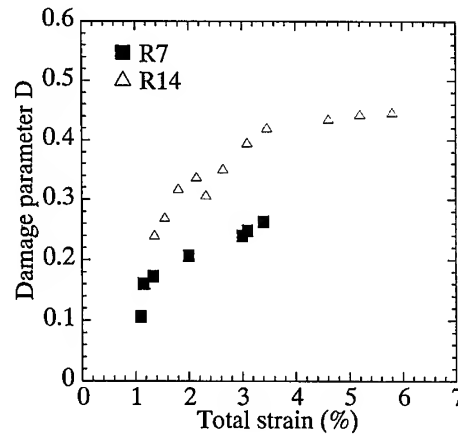


Fig.3 Damage parameters D of the bulk specimens ($T=23^{\circ}\text{C}$).

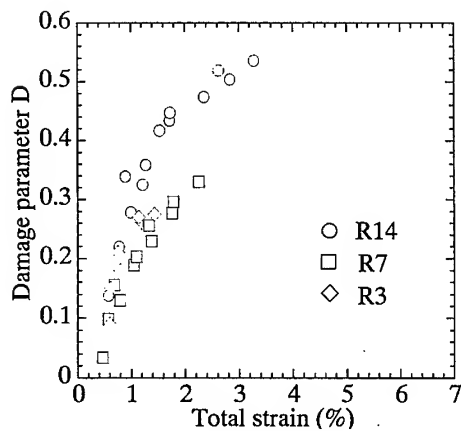


Fig.4 Damage parameters D of the joint specimens ($T=23^{\circ}\text{C}$).

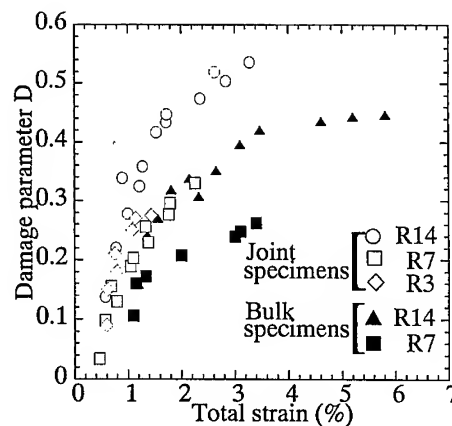


Fig.5 Comparison between the damage parameters D of the bulk and joint specimens ($T=23^{\circ}\text{C}$).

case of R14, the maximum value of D is 0.42. This value is too large, so both void nucleation and micro crackings are expected to cause damage in the bulk specimens. The relation between D and the total strain of the joint specimens is summarized in Fig.4. The values D of R14 are higher than those of R3 and R7 and the damage behaviors of R3 and R7 indicate almost the same. The damage behavior of the bulk and joint specimens are summarized in Fig.5. The value D of the joint specimen starts to increase at a smaller total strain than that of the bulk specimens. Since the deformation of the adhesive layer is constrained by the adherends, the stress state of the joint specimens is triaxial. From the results shown in Fig.5, it can be stated that the values D of the joint specimens are higher than those of the bulk specimen. Additionally, it is known that the stress state changes from the plane strain to the plane stress in the damage zone [4]. The degree of the stress triaxiality in the adhesive layer decreases with increasing damage around the rubber

particles. It can be stated that the values D designating the degradation of the elastic modulus in the joint specimens are attributed to both an increase of void nucleation and micro cracking and a decrease of stress triaxiality. Therefore, it is considered that the values D of the joint specimens show higher values than those of the bulk specimens.

3.2. Influence of testing temperature

Figs.6 (a) and (b) show the stress-strain curves of the bulk specimens with two rubber contents at various testing temperatures (T). The elastic moduli decrease with increasing T for all specimens. The degree of decrease in the elastic moduli of the R7 specimen is more remarkable than that of the R14 specimen. The stress-strain behavior of R14 is affected by the rubber particles more than that of R7, since the rubber particles of R14 are more than that of R7. From the experimental results and the effect of the rubber particles on the stress-strain behavior, it is considered that the rubber particles make the specimen soft at $T=23^{\circ}\text{C}$ and make it hard at $T=60^{\circ}\text{C}$. The effects of the temperature on the damage behavior of the bulk specimens are shown in Fig.7. The values D decrease with increasing T in both specimens. These decreases can be explained by the damage due to micro cracking which tends to decrease with increasing T for the increasing ductility of the matrix. Fig.8 shows the effect of temperatures on the damage behavior of the joint specimens. The values D increase with increasing R , but no significant difference is observed in the damage behavior of the joint specimens. This is a questionable result, because the damage, such as micro cracking in the adhesive layer, is expected to decrease with increasing T for its increasing ductility. Therefore, it is considered that there is another reason why the damage behavior of the joint specimens are not affected by T . One of the expected reasons is the effects of the stress triaxiality on the damage behavior in the joint specimens. To evaluate the effect of temperature on the damage behavior of the joint specimens more exactly, the effects of stress triaxiality in the adhesive layer should be investigated in detail.

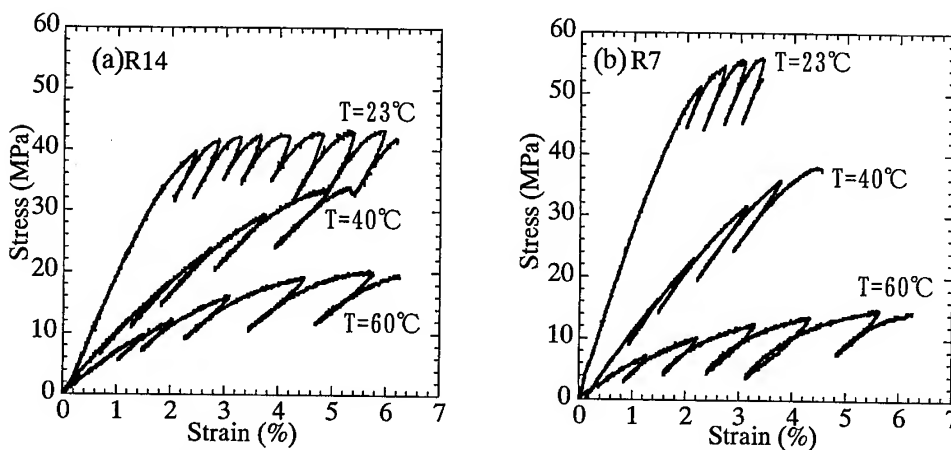


Fig.6 Stress-strain curves of the bulk specimens at various testing temperatures

for the R7 and R14 specimens.

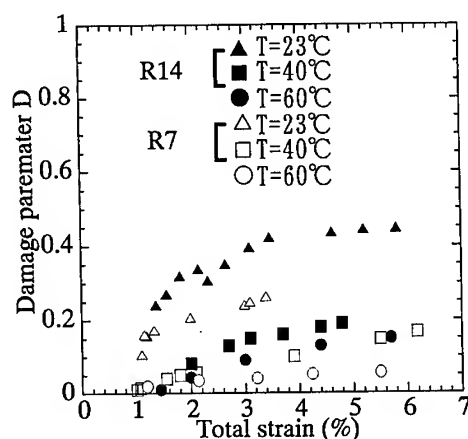


Fig.7 Damage parameters D of the bulk specimens at the various temperatures.

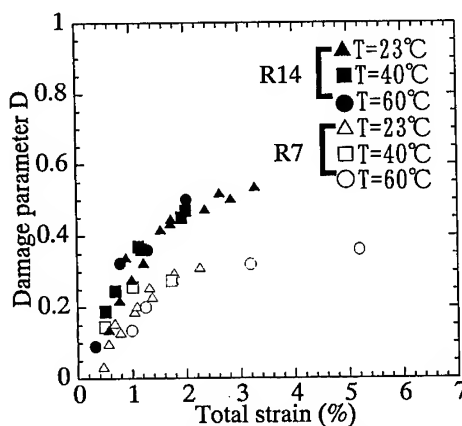


Fig.8 Damage parameters D of the joint specimens at the various temperatures.

CONCLUSIONS

In this study, the effects of temperature and the rubber contents on the damage behavior of the adhesive layer in joint specimens have been investigated. We can give the following conclusions. Due to the reduction in stress triaxiality of the adhesive layer, the damage of the joint specimens evaluated by the elastic modulus is higher than that of the bulk specimens. The values D of the bulk specimens decrease with increasing temperatures, but there is no significant difference in the damage behavior of the joint specimens. In order to make these results clear, further investigation is needed.

REFERENCES

1. M. Tohdoh, S.K.Chaturvedi, R.L.Sierakowski, *Int. J. Fract.*, 75, 4, pp.285-306 (1996).
2. Y. Huang, A. J. Kinloch, *J. Mater. Sci.*, 27, pp.2763-2769 (1992).
3. J.Lemaitre, "A Course on Damage Mechanics", (1992) Springer-Verlag.
4. A.F.Yee, D.Li, X.Li, *J. Mater. Sci.*, 28, pp.6392-6398(1993).

Effect of Yield Strength and Crack Depth on COD-Decrease-Parameter m

Qingfen Li¹, Huocai Ni², Shanglin Yang¹,
Maoyuan Ma¹, Ping Long¹ and Zhaoxia Cui¹

¹ College of Mechanical & Electrical Engineering, Harbin Engineering University,
Harbin 150001, China P.R.

² Zhengzhou Research Institute of Mechanical & Electrical Engineering,
Zhengzhou 450052, China P.R.

Keywords: COD-Decrease-Parameter, Crack Depth/Specimen Width (a/W), Yield Strength

ABSTRACT

A series of tests with three groups of low carbon alloy steel were performed and the influence of yield strength (σ_y), crack depth /specimen width (a/W) on COD-decrease-parameter m is studied. Results show that, m decreases with increasing σ_y and the decreasing rate is getting smaller when σ_y increases further. The curve of m versus σ_y is hyperbolic and the equation may be given as $m = \sigma_y (1.57\sigma_y - 753)$. Results also show that the stretched zone width l which is implicated in the plastic zone R , may affect m values significantly, and that l increases with decreasing a/W and decreasing σ_y . Further analysis is discussed and show that the COD value is more sensitive to a/W than the J-integral value, that is, when a/W decreases further, COD value increases faster than J-integral value. Thus, the lower a/W ratio which has a lower σ_H , yields a lower m value.

1. INTRODUCTION

J-integral and COD, as two important fracture-characterizing parameters in elastic-plastic fracture mechanics are already well developed and used in industrial applications. It is of significance to study the relationship between these two parameters for both theoretical investigation and engineering practice. Theoretical and experimental results suggest that the J-COD relation is normally represented as

$$J = m \sigma_y \delta \quad (1)$$

where σ_y is the yield strength.

From Eg.1, we can see that the value of m is important for learning J-COD relation. Many factors affect the value of m , among them, the parameter σ_y and the ratio of crack depth/specimen width (a/W) are the most important ones.

Some works have previously shown the effect of σ_y and a/W on m [1-5]. However, the equations

about these parameters are not available yet. Some testes were therefore performed and an equation is given in this paper.

2. EXPERIMENTAL PROCEDURE

Three groups of low carbon alloy steel 20Cr2Ni4A, 17Cr2Ni2Mo and 12CrNi3A (represented as A, T, W respectively) are used. The chemical composition are given in Table 1, and Table 2 gives their heat-treatment process.

Table 1 Chemical Composition of Three Steels

	C	Si	Mn	Cr	Ni	Mo	P	S
20Cr2Ni4A (Steel A)	0.17	0.30	0.45	1.42	3.75		0.20	0.023
17Cr2Ni2Mo (Steel T)	0.18	0.32	0.52	1.65	1.55	0.29	0.021	0.028
12CrNi3A (Steel W)	0.13	0.29	0.51	0.81	2.95		0.008	0.022

Table 2 Heat-treatment Process of Specimens

Specimen number	Heat-treatment process
A181,T181 A185,T185	920°C oil quench + 180°C temper
A501,T501 A505,T505	920°C oil quench + 500°C temper
A551,T551	920°C oil quench + 550°C temper
A601,T601 A605,T605	920°C oil quench + 600°C temper
A655,T655	920°C oil quench + 650°C temper
T1-T5 W1-W5	920°C pseudo-carburizing air cold + 650°C temper + 840°C oil quench + 180°C temper

Specimens for tensile test are of $\Phi 8 \times 40$ (mm) and the three-point single-edge notched bend (SENB) specimens are of $12.5 \times 25 \times 120$ (mm). The crack depth /specimen width ratio (a/W) are 0.1, 0.2, 0.3, 0.4 and 0.5 respectively.

The tensile properties and toughness tests were carried out on an Instron 1341 testing machine of 100 KN capacity and a MTS.810 one of 250KN capacity respectively. P-V and P- Δ plots were

recorded simultaneously by two X-Y recorders. After the tests, specimens were marked by heat tinting and then broken at low temperature. The crack length a and crack extension Δa were measured with an optical micrometer with 0.001 mm per division.

All tests were made at room temperature.

3. EXPERIMENTAL RESULTS AND DISCUSSION

The relationship of m and σ_y is shown in Fig.1 and 2. m versus a/W ratio is represented in Fig.3. Figure 4 shows the relation of stretched zone width l and a/W . Figure 5 gives a relation of l versus σ_y and Figure 6 gives m vs l .

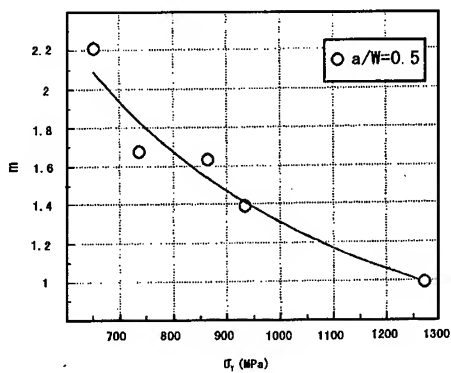


Fig.1 m vs σ_y for steel A

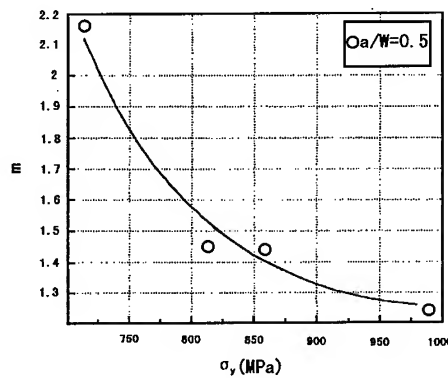


Fig. 2 m vs σ_y for steel T

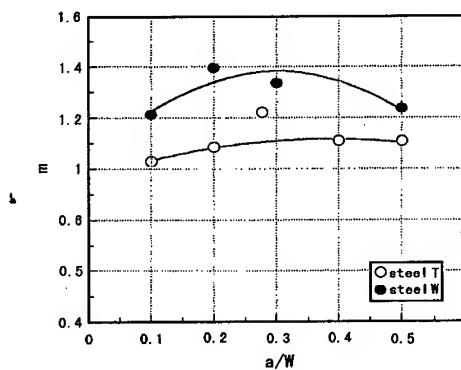


Fig. 3 m vs a/W

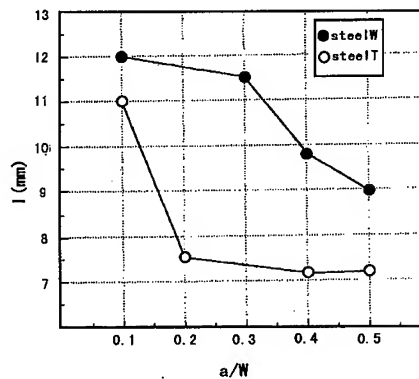
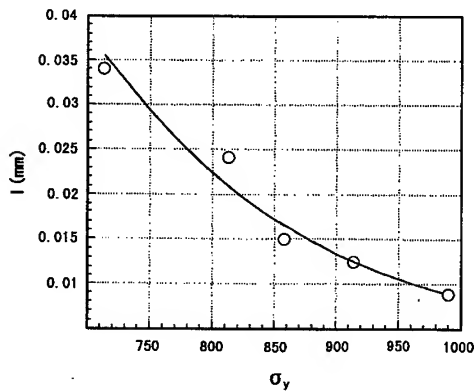
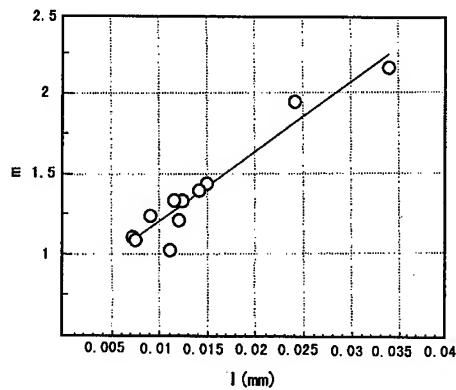


Fig. 4 l vs a/W

Fig.5 l vs σ_y Fig. 6 m vs l

From Figs. 1 and 2, we may see that the curve of m versus σ_y is hyperbolic, and we have the regression equation as follow (for $a/W=0.5$):

$$m = \sigma_y / (1.57\sigma_y - 753) \quad (2)$$

That is, m decreases with increasing σ_y (and the decreasing rate is getting smaller when σ_y increases further).

From Fig. 3, we may see that m is affected by a/W , but not very apparent.

Figs. 4, 5 and 6 shows the effect of stretched zone width l , which is implicated in the plastic zone R . We may see that l increases with decreasing a/W and also with decreasing yield strength σ_y , and that m increases with increasing l apparently.

4. FURTHER ANALYSIS

4.1 The effect of a/W on m :

Shin [6] has shown that

$$m = 0.364 \eta / [(1+n) r_p] \quad (3)$$

Where r_p is the plastic rotational factor, η is the correction factor and

$$\eta = 13.65 (a/W) / (1 + 4.63 a/W) \quad (4)$$

therefore

$$m = 4.97 (a/W) / [(1 + 4.63 a/W) (1+n) r_p] \quad (5)$$

We may see that m is affected by a/W , n and r_p . For ductile low / medium strength steels, r_p is about 0.45, and for the steels used present, we may take $n=0.1$, then Eg.5 may be as follow:

$$m = 4.97 (a/W) / (0.495 + 2.29 a/W) \quad (6)$$

From Eg.6, we may see that m increases with increasing a/W . However, D.Z.Zhang [7] has shown that r_p increases with increasing a/W , which means that m increases more slowly or even decreases when a/W further increases (from Eg.5). Our experimental results are in agreement with it. But we may not conclude any general trend about m vs a/W simply. Since besides r_p , m is also affected by the hardening exponent n . Further study is needed.

4.2. The effect of both l and a/W on m :

Previous work [8,9] have shown that when a/W decreases, the hydrostatic stress σ_H (and also the stress field intensity) decreases. The present work shows that, when a/W decreases, the stretched zone width l , (and also the plastic zone R) increases, therefore, the Δ_p and V_p values which determine the J and COD values, increase accordingly. (Δ_p — the load-point displacement, V_p — the crack mouth displacement).

However, J increases more slowly than COD since J is affected by both the increasing Δ_p and the decreasing σ_H (and also the decreasing stress field intensity), whereas COD is affected mainly by the increasing V_p :

$$\delta = (1-\nu^2)K^2 / 2 \sigma_y E + r_p (W-a) V_p / [(r_p (w-a) + a + z)] \quad (7)$$

We may therefore conclude that the COD value is more sensitive to a/W than the J -integral value. In another words, when a/W decreases further, COD increases faster than J -integral. Thus, the lower a/W ratio which has a lower σ_H , yields a lower m value.

This conclusion may also explain the results of Q.F.Li [10], where J_i values for $a/W=0.17$ are about 1.6 that for $a/W=0.5$, whereas δ_i values are about 2.

4.3. The relation of σ_y and m :

Robinson [11] pointed out that m increases with increasing plastic zone R . In our test (Fig 1, 2 and 5), with increasing temperature, σ_y decreases and l increases rapidly, and the hardening exponent n increases accordingly. It means that lower σ_y (i.e, larger l or R) yields higher m values (when a/W is constant). This is in agreement with Robinson.

From the formula given by Chen Chi [12]:

$$J = m' \sigma_y \delta_e + \left(\frac{1}{1+n} \times \frac{\sigma}{\sigma_y} \right) \sigma_y \delta_p \quad (8)$$

We have

$$J = m' \sigma_y \delta_e + \alpha \sigma_y \delta_p \quad (9)$$

where m' is the elastic factor and α the plastic. Normally $m' \neq \alpha$. Compare Egs.1 and 9, we know that m is interrelated with m' and α . However, for ductile materials, the elastic component is negligible, we therefore have

$$m \approx \alpha = \sigma / [(1+n) \sigma_y] \quad (10)$$

We may easily see that m increase with decreasing σ_y .

We deduced the Eg.2 from the test data by regression analysis. Further tests were made to check their correctness. The error is about 7.6-8.9%, which means that the equation is usable in engineering practice. However, it is on condition that $0.04 < n < 0.10$. For other n values,

correction is necessary.

5. CONCLUSION

- (1) COD-decrease-parameter m decreases with increasing σ_y , and the curve of m versus σ_y is hyperbolic.
- (2) The effect of a/W on m is not very apparent.
- (3) Stretched zone width l may affect m values significantly and m increases with increasing l linearly.
- (4) COD value is more sensitive to a/W than J-integral value.
- (5) The regression equations of m and σ_y in this paper is usable in engineering practice.

REFERENCES

1. J.E.Perez Ipina and H.L.Toloy, Engng Fracture Mech. **24** (1986), p.1.
2. S.A.Paranjpe and S.Baneijee, Engng Fracture Mech. (1979) p.11.
3. Wu Shang-Xian, Int.J.Fracture, **17** (1981) p.63-66.
4. Q.F. Li, et al, Engng Fracture Mech, **42** (1992) p.401.
5. Q.F.Li, et al, Engng Fracture Mech., **53** (1996) p.473.
6. C.F.Shin, J.Mech. Phys. Solids **29** (1981) p.305.
7. D.Z.Zhong, Engng Fracture Mech., **26** (1987) p.247.
8. Q.F.Li, ACTA MECHANICA SOLIDA SINICA, No.3 (1986), P295 .
9. Q.F.Li, et al , Proceedings of ISOPE-91, (1991), p.137.
10. Q.F.Li, Engng Fracture Mech., **22** (1985) p.9.
11. J.N.Robinson, I.J.Fracture **12** (1976), p.723.
12. Chen Chi, J. New Metal Mater. **11-12** (1975), p.57.

A Study on Intergranular Corrosion of Laser Treated Alloy 600 by DL-EPR Method and Microscopic Examination

Y.S. Lim¹, H.P. Kim¹, J.S. Kim¹ and H.S. Kwon²

¹ Steam Generator Materials Project, Korea Atomic Energy Research Institute,
PO Box 105, Yusong, Taejon 305-600, Korea

² Department of Materials Science and Engineering, Korea Advanced Institute of Science and
Technology, 373-1 Kusong-dong, Yusung-gu, Taejon 305-701, Korea

Keywords: Alloy 600, DL-EPR Test, Intergranular Corrosion, Laser Surface Melting, Sensitization

ABSTRACT

Ni-base Alloy 600 has been widely used as a steam generator (S/G) tubing material in nuclear power plants because of its good mechanical and corrosion properties at high temperatures. However, degradations of S/G tubes due to intergranular attack (IGA) and intergranular stress corrosion cracking (IGSCC) during normal operation were frequently reported. In particular, Alloy 600 can be very susceptible to IGA/IGSCC in some sulfur-bearing environments by sensitization. In this paper, the beneficial effects of laser surface melting (LSM) to intergranular corrosion of the sensitized Alloy 600 is presented from the results of the double loop electrochemical potentiokinetic reactivation (DL-EPR) test. The DL-EPR test was performed in de-aerated 0.01 M H₂SO₄ + 20 ppm KSCN at a scan rate of 0.5 mV/sec at room temperature. The degree of sensitization (DOS) of the sensitized Alloy 600 measured from the DL-EPR test was considerably reduced by LSM. The sensitized Alloy 600 after LSM also exhibited a relatively low DOS, comparing with that of the sensitized but not laser treated Alloy 600. From the microscopic observation, it was found that the microstructural changes by the LSM process, especially changes in the precipitation behavior of grain boundary Cr-rich carbides, caused the improvement of resistance to intergranular corrosion of the laser treated Alloy 600. The resistance to IGSCC of the laser treated Alloy 600 in sulfur-bearing environments was also discussed from the results of measured DOS and microstructural examination

1. INTRODUCTION

It is now well recognized that Ni-base Alloy 600 is susceptible to inter-granular attack/intergranular stress corrosion cracking (IGA/IGSCC) under pressurized water reactor operating conditions [1]. In particular, the precipitation of Cr carbides and the resultant creation of Cr depleted zones in the vicinity of the grain boundaries (commonly called 'sensitization') is known to play an important role in determining the alloy's susceptibility to IGA/IGSCC [2]. Once being

sensitized, Alloy 600 can suffer a vital intergranular fracture in the sulfur-bearing environments such as sodium thiosulfate ($\text{Na}_2\text{S}_2\text{O}_3$), and sodium tetrathionate ($\text{Na}_2\text{S}_4\text{O}_6$) solutions even at low temperatures [3].

Laser surface melting (LSM) is one of the laser application techniques to improve the surface properties of materials such as corrosion and wear. LSM can be applied to repair the tubes degraded by IGA/IGSCC during normal operation of the nuclear power plants, since the laser beam can easily be directed to the failed parts through a beam transmission system such as an optical fiber. From the previous studies, it was demonstrated that LSM improved the resistance to IGA/IGSCC of the sensitized Alloy 600 in sulfur-bearing environments [4], mainly due to the metallurgical changes induced by the laser treatment [5]. During the failure by IGSCC, a crack starts at the free surface and propagates through a connected pathway of the susceptible grain boundaries. Therefore, the corrosion resistant surface formed by LSM can provide an effective barrier between the corrosion environment and the underlying sensitized alloy.

The double loop electrochemical potentiokinetic reactivation (DL-EPR) test, originally proposed by Umemura et al. [6], was found to be fast, quantitative, and reproducible in measuring the degree of sensitization (DOS) of alloys. The DL-EPR method has also been used for providing an indication of sulfur compound attack susceptibility to IGSCC by measuring DOS in the alloys.

The present work was aimed to investigate the effects of LSM on the intergranular corrosion of the sensitized Alloy 600 by DL-EPR test. The measured DOS under the given DL-EPR testing condition was analyzed in terms of the microstructural changes caused by the LSM process. Finally, the resistance to IGSCC of the laser treated Alloy 600 in sulfur-bearing environments was evaluated from the experimental results.

2. EXPERIMENTAL PROCEDURES

2.1 Specimen Preparation

Mill annealed Alloy 600 plates 1.6 mm thick were used in this study, and the alloy composition is shown in Table 1. The specimens were sealed in a quartz tube, solution annealed at 1050 °C for 30 minutes, and then water quenched (hereafter, referred to as SA Alloy 600, in short). Some of the SA Alloy 600 were subsequently sensitized at 600°C for 24 hours and then followed by furnace cooling (hereafter, SA+SEN Alloy 600).

Table 1. Chemical composition of the specimen used (wt%)

Ni	Cr	Fe	C	N	S	Si	Mn	Al	Ti	Nb	Mg
Bal.	15.9	7.6	0.04	0.04	0.002	0.15	0.17	0.12	0.21	tr.	0.008

A continuous CO_2 laser beam was used, and the details of the LSM procedure are described elsewhere [5]. Some of the LSM specimens (hereafter, LSM Alloy 600) were also subsequently sensitized under the same conditions as for the SA+SEN Alloy 600 (hereafter, LSM+SEN Alloy 600). The specimens for scanning electron microscopy (SEM) observation were made by etching the polished samples with a solution of 2 % HCl and 98 % methanol at 6 V for about 3 – 5 seconds.

2.2 DL-EPR Test

Cu-wire was spot-welded to one side of each specimen, mounted in epoxy resin, and ground to 2000 grade silicon carbide. To avoid crevice corrosion, the specimen-mount interface was carefully

coated with a thin film of silicone sealant. Approximately 1 cm^2 of the surface was exposed to the test solution. All solutions were prepared from double-distilled water and the chemicals of analytical-grade reagents. Test solution chosen for the evaluation of DOS in Alloy 600 was $0.01 \text{ M H}_2\text{SO}_4$ with addition of 20 ppm KSCN. The test solutions were de-aerated by purging with purified N_2 gas, before and during each DL-EPR test.

The DL-EPR test was performed using a three-electrode cell system consisting of a saturated calomel electrode (SCE) as a reference, a platinum (Pt) electrode as a counter, and a specimen as a working electrode. The sample was kept immersed in the test solution for 0.5 - 1 hour at open-circuit potential. After obtaining the stable corrosion potential (E_{corr}), the potential was raised in the anodic direction, from the value of E_{corr} to a potential in the passive range, at a scan rate of 0.5 mV/sec . After attaining the pre-determined potential ($600 \text{ mV}_{\text{SCE}}$), it was followed by a reactivation scan back to E_{corr} . All the potentials are referred to a saturated calomel electrode (SCE). All the tests were performed at a room temperature of $25^\circ\text{C} - 27^\circ\text{C}$. The DL-EPR test in different solutions was repeated at least twice for each specimen to ensure reproducibility.

3. RESULTS

3.1 Results from DL-EPR Test

Before a DL-EPR test, an immersion test of C-ring specimens was primarily conducted to confirm the effects of sensitization heat treatment on the fracture behavior of Alloy 600 in $0.1 \text{ M Na}_2\text{S}_4\text{O}_6$ solution. After 18 hours of immersion, cracking was found to start on the outer-diameter side, and the maximum-length crack propagated into approximately 80% of the thickness of the C-ring after 86 hours of immersion. The fracture surfaces after C-ring tests revealed a fully intergranular type, as shown in Fig. 6.1(a). From the above results, it can be concluded that the sensitization treatment at 600°C for 24 hours was suitable to exhibit a high susceptibility to IGSCC for Alloy 600 in the sulfur-bearing corrosive environments.

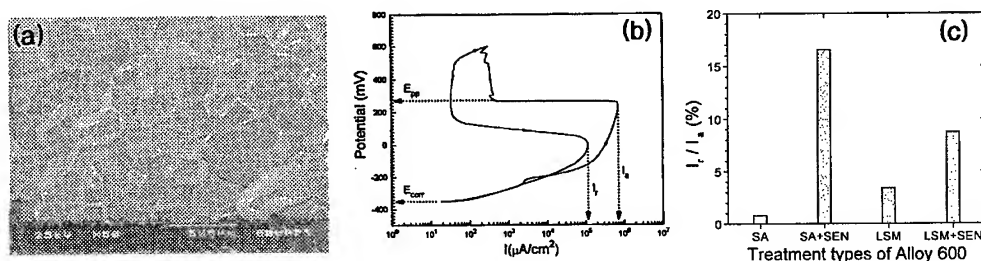


Fig. 1 (a) Fracture surface of the SA+SEN Alloy 600 after C-ring test, (b) a typical DL-EPR curve, and (c) DOS measured from the differently treated Alloy 600. (b) and (c) were obtained in $0.01 \text{ M H}_2\text{SO}_4 + 20 \text{ ppm KSCN}$ solution at a scan rate of 0.5 mV/sec at room temperature.

Fig. 1(b) shows a DL-EPR curve typically obtained from the SA+SEN Alloy 600 under the present DL-EPR testing conditions. DOS is defined, in Fig. 1(b), as the percent ratio of the maximum current density in the reactivation loop (I_r) to that in the anodic loop (I_a), i.e., $I_r / I_a \times 100$. It is evident from Fig. 1(c) that the measured DOS values from the LSM Alloy 600 and LSM+SEN Alloy 600 were considerably reduced by the laser treatment. The average DOS value of the LSM Alloy 600 was measured as 3.42, which was considerably lower than 16.5 of the SA+SEN Alloy 600. The average DOS value of the LSM+SEN Alloy 600 was measured as 8.71, which was still

lower than that from the SA+SEN Alloy 600. From the above results, it can be concluded that the LSM Alloy 600 and the LSM+SEN Alloy 600 are more resistant to intergranular corrosion than the SA+SEN Alloy 600 in the given corrosive environment.

3.2 Microstructural Examination

Fig. 2(a) shows a typical distribution of intergranular Cr-rich carbides in the SA+SEN Alloy 600. By the sensitization treatment, nearly continuous Cr-rich carbides were precipitated on most of the grain boundaries, excluding the special boundaries such as coherent twin boundaries and low-angle grain boundaries, as shown in the Figure. The high DOS values of the SA+SEN Alloy 600 should, therefore, reflect the distribution morphology of Cr-rich carbides and the severe Cr depletion along the grain boundaries in the alloy. The typical microstructures of the LSM Alloy 600 and the LSM+SEN Alloy 600 are shown in Fig. 2(b) and 2(c), respectively.

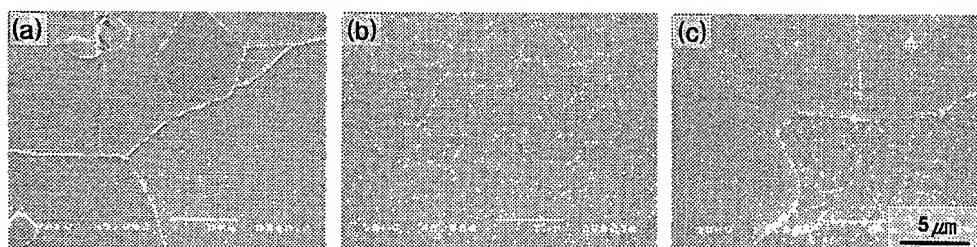


Fig. 2 Typical microstructures of (a) the SA+SEN Alloy 600, (b) the LSM Alloy 600, and (c) LSM+SEN Alloy 600, etched in a solution of 2% HCl and 98% methanol.

Fig. 2(b) shows the particles formed in the laser melted zone (LMZ) during the LSM process. No Cr-rich carbides are seen on the grain boundaries in Fig. 2(b). This result is originated from the fact that pre-existing Cr-rich carbides of the sensitized Alloy 600 had been completely melted/dissolved due to the high energy density of a laser beam. Moreover, Cr-rich carbides were not re-precipitated during cooling due to the high cooling rate during the LSM process [5]. Therefore, low DOS of the LSM Alloy 600 is caused by the de-sensitization (or, disappearance of the Cr depletion zones) due to the LSM process. The tiny particles along the cell boundaries, identified as TiN and MgS, are formed by dissolution and subsequent re-precipitation of the pre-existing coarse TiN and MgS inclusions in the commercial Alloy 600 during the LSM process [7].

The second phases in the LSM+SEN Alloy 600 are shown in Fig. 2(c). There were no noticeable changes in the tiny particles of TiN and MgS, by the sensitization treatment. However, some Cr-rich carbides are seen on some grain boundaries in Fig. 2(c). They were identified as Cr-rich $M_{23}C_6$ and Cr_7C_3 [8], the same is found in the case of the SA+SEN Alloy 600 [5]. The average size of the Cr-rich carbides precipitated on the grain boundaries in the LSM+SEN Alloy 600 was much smaller than that in the SA+SEN Alloy 600. Moreover, they were sparsely distributed on grain boundaries, and were found only on some high angle grain boundaries. The degree of Cr depletion on the grain boundaries was, therefore, not severe. The minimum Cr concentration on the grain boundaries was measured as 12 wt% [8], which was considerably higher than 7.3 wt% of the SA+SEN Alloy 600 [5]. Therefore, it can be concluded that the laser treatment suppressed the precipitation of grain boundary Cr-rich carbides in Alloy 600, and this led to the low DOS value of the LSM+SEN Alloy 600.

3.3 Surface Morphologies after DL-EPR Test

The grain boundary attack in the SA+SEN Alloy 600 after the DL-EPR test is shown in Fig. 3. The grain boundary attack was clearly revealed by the addition of 20 ppm KSCN, without any intergranular and intragranular pitting (Fig. 5(3)). It demonstrates that the DL-EPR testing conditions employed in the present experiment were suitable for measuring the degree of sensitization of the fully sensitized Alloy 600, i.e., grain boundary attack occurred without any noticeable general corrosion and pitting corrosion in the matrix.

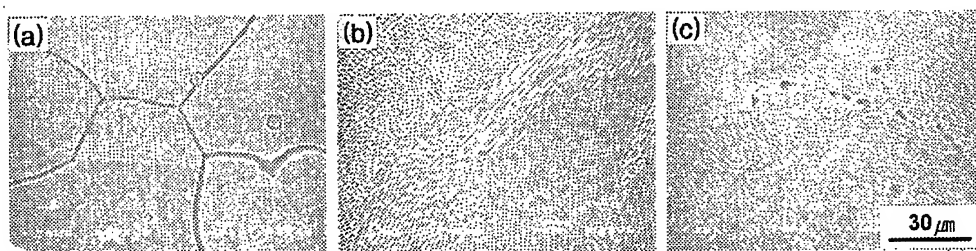


Fig. 3 SEM micrographs showing the surface morphologies after DL-EPT test (a) for the SA+SEN Alloy 600, (b) the LSM Alloy 600, and (c) the LSM+SEN Alloy 600, in 0.01M H_2SO_4 + 20 ppm KSCN solution at a scan rate of 0.5 mV/sec at room temperature.

The grain boundary attacks in the LSM Alloy 600 and the LSM+SEN Alloy 600 after the DL-EPR tests are shown in Fig. 3(b) and 3(c), respectively. The LSM Alloy 600 did not experience any grain boundary attacks, as shown in Fig. 3(b). The white contrast along the cell boundaries in Fig. 3(b) resulted from the different dissolution rates of the elements. Chromium was more enriched along the cell boundaries due to the micro-segregation formed during the laser treatment [5]. The regions around the cell boundaries were, therefore, more corrosion resistant due to the enriched Cr content than those inside the cells in acidic solutions. Fig. 3(c) shows the grain boundary attack in the LSM+SEN Alloy 600. As shown in the Figure, only some grain boundaries were discretely attacked, and the attacked morphology denotes exactly the distribution of grain boundary Cr-rich carbides (Fig. 2(c)).

4. DISCUSSION

Ahn et al. [9] suggested the optimized DL-EPR testing conditions be performed in de-aerated 0.01 M H_2SO_4 + 20 ppm KSCN solution at a scan rate of 0.5 mV/sec at room temperature, to predict the susceptibility to IGSCC in $Na_2S_4O_6$ solutions by the measured DOS. However, the optimized conditions can be varied from test to test due to the different heat treatment procedures resulting in the different extents of grain boundary Cr depletion in the alloys. In the present study, the best results were obtained with the addition of 20 ppm KSCN, i.e., clean grain boundary attacks and suppression of general and pitting corrosion.

The average DOS value was considerably reduced, and grain boundary attack was not observed in the LSM Alloy 600 (Fig. 1(c) and Fig. 3(b)). From the microstructural examination, it was demonstrated that the microstructural changes of the grain boundaries in the sensitized Alloy 600 by the LSM process resulted in the improvement of the resistance to intergranular corrosion of the alloy. Suh et al. [4] found that the fracture mode of the sensitized Alloy 600 was changed by LSM, i.e., from a brittle intergranular fracture of the SA+SEN Alloy 600 to a typical ductile transgranular

failure of the LSM Alloy 600. Moreover, the stress corrosion cracks propagating from the free surface into the center of the sensitized specimen were arrested by the laser-melted track, making the further propagation into the laser treated region impossible [4].

Any continuous grain boundary attack was not observed in the LSM+SEN Alloy 600 with the sufficiently reduced DOS value (Fig. 1(c) and Fig. 3(c)). Was et al. [10] found, from Heuy and Streicher tests, that severe IGA occurred when the measured Cr concentration on the grain boundary was below 9 wt% with a nearly continuous distribution of grain boundary Cr-rich carbides. Therefore, the LSM+SEN Alloy 600 should have a high resistance to IGA in acidic environments. Kai et al. [2] showed that the critical Cr concentration to prevent the IGSCC failure was around 8 wt% from the constant load test with the applied stress of 390 MPa, pH of 3, and the $\text{Na}_2\text{S}_2\text{O}_3$ concentration of 0.001 M to 0.1 M at room temperature. Therefore, it can also be expected that the LSM+SEN Alloy 600 have the high resistance to IGA/IGSCC in sulfur-bearing environments as well.

5. CONCLUSIONS

1. The sensitization treatment of Alloy 600 at 600°C for 24 hours induced a severe brittle intergranular fracture in neutral 0.1 M $\text{Na}_2\text{S}_4\text{O}_6$ solution, due to the precipitation of nearly continuous grain boundary Cr-rich carbides and the severe Cr depletion on the grain boundaries. The present DL-EPR testing conditions revealed the high DOS value in the sensitized Alloy 600 with suppression of other types of corrosion such as general and pitting corrosion.

2. LSM improved the resistance to IGA/IGSCC of the sensitized Alloy 600 by sufficiently reducing the average DOS value. The average DOS value of the LSM+SEN Alloy 600 was also much lower, comparing with that of the SA+SEN Alloy 600. From these results, it can be expected that the LSM Alloy 600 and the LSM+SEN Alloy 600 have a high resistance to IGA/IGSCC in acidic and sulfur-bearing environments. Consequently, the LSM technique was shown to be an attractive method to repair the failed S/G tubes in the nuclear power plants.

ACKNOWLEDGEMENTS

This work has been carried out as a part of the Steam Generator Materials Project under the Nuclear R&D Program by M.O.S.T. in Korea.

REFERENCES

1. T.U. Marston and R.L. Jones, Proc. 5th Int. Symp. on Environmental Degradation of Materials in Nuclear Power Systems - Water Reactors, ANS, La Grange Park, Illinois (1991) p.3
2. J.J. Kai, C.H. Tsai, T.A. Huang and M.N. Liu, Metall. Trans. A, 20A (1989) p.1077.
3. R.C. Newman, R. Roberge and R. Bandy, Corrosion, 39 (1983) p.386.
4. J.H. Suh, J.K. Shin, Y.S. Lim, I.H. Kuk and J.S. Kim, Mater. Sci. Eng. A, A254 (1998) p.67.
5. Y.S. Lim, J.H. Suh, I.H. Kuk and J.S. Kim, Metall. Trans. A, 28A (1997) p.1223.
6. F. Umemura, M. Akashi and T. Kawamoto, Corros. Eng., 29 (1980) p.163.
7. Y.S. Lim, H.D. Cho, and J.S. Kim, Proc. Kor. Nucl. Soc., Vol.2, Kwangju, Korea (1997) p. 80.
8. Y.S. Lim, H.P. Kim, H.D. Cho, I.H. Kuk and J.S. Kim, Trans. 15th Int. Conf. on Structural Mechanics in Reactor Technology (SMiRT-15), Vol. X, Seoul, Korea (1999) p. 231
9. G.S. Was, H.H. Tischner and R.M. Latanision, Metall. Trans. A, 12A (1981) p.1397.
10. M.K. Ahn, H.S. Kwon and J.H. Lee, Corrosion, 51 (6) (1995) p.441.

Damage of FRP Plates Containing Sharp Notches or Blunt Notches

Hiizu Hyakutake and Toshihiro Yamamoto

Department of Mechanical Engineering, Fukuoka University, Fukuoka 814-0180, Japan

Keywords: CCD Camera, Damage, FRP, Luminance, Notch, Polycarbonate, Stress Concentration, Tension

ABSTRACT

Prior to catastrophic fracture for notched FRP plates under static load, the damage appears and grows near the notch root. The validity of the failure criterion based on idea of severity near the notch root for evaluating the damage of notched FRP plate is investigated experimentally in this paper. An experimental method is presented which examines the effect of notch geometry on the initiation and growth of the damage near the notch root of FRP plates subjected to tension. The investigation was accomplished by obtaining experimental data on the tension test of a glass fiber-reinforced polycarbonate plate containing notches for wide range of notch geometries. To evaluate the damage near the notch root, we measured successively the luminance distributions by means of the luminance measurement technique with a CCD camera. The experiment shows that the process of the initiation and growth of damage near the notch root is determined by both the maximum elastic stress and notch-root radius for sharp-notched specimens. On the other hand, for blunt-notched specimens, the process of the initiation and growth of damage is determined by the terms of a combination of the maximum elastic stress, notch-root radius and width of notch section. On the basis of the idea of severity near the notch root mentioned above, the experimental results can be explained.

1. INTRODUCTION

Because of their importance in design applications, the strength and fracture behavior of notched FRP plates have been the subject of much research. In the studies on the fracture behavior of notched FRP plate, it is noted that the intention is mainly to reveal the fracture mechanism near the crack tip. Our goal is to elucidate the fracture behavior of FRP plates containing stress concentrations in various notch geometries and to develop a limiting condition for predicting the load at failure.

Studying stress distributions near the notch root, we have obtained a fracture criterion for notched polycarbonate bars under static loading [1]. The criterion is based on the concept of severity near the notch root. Many experiments have shown that the fracture criterion is applicable to notched FRP plates over a wide range of notch geometries and dimensions of specimens [2].

The aims of the present study are to provide experimental evidence of the validity of the

fracture criterion mentioned above and to develop a limiting condition of the initiation and growth of damaged zone for notched FRP plates under static tension.

To evaluate the damage near the notch root, we measured the luminance distributions by means of the luminance measurement technique with a CCD (charge coupled device) camera [3].

2. SEVERITY NEAR THE NOTCH ROOT

The effects of notch geometry on the stress distributions near the notch root were examined by using the finite element method for a thin, orthotropic, notched plate in tension. The results of an analysis are shown in Fig. 1. The parameter u is the distance from the notch root and σ_{\max} is the maximum tensile stress at the notch root ($u = 0$). The coordinates x and y are principal axes of the lamina. Material constants (Young's modulus E , Poisson's ratio ν and shear modulus G) are represented in Fig. 1.

Figure 1 shows that the relative-elastic-stress distribution near the notch root is independent of the value of b/ρ in the range of $b/\rho > 3$, where b is the half width of notch section. Furthermore, we have shown the relative-elastic-stress distribution is independent of the notch depth a in the range of $a/\rho > 1$ [4]. According to the results mentioned above, it is assumed that the elastic stress distributions near the notch root are the same in all sharp-and-deep-notched plates for which both the maximum elastic stress σ_{\max} and notch-root radius ρ are equal in all cases. Therefore, it is theoretically predicted that the maximum elastic stress at failure of a sharp-and-deep-notched plate is determined by the notch-root radius ρ . The failure criterion for a sharp-and-deep-notched specimen is expressed as [2]:

$$\sigma_{\max} = \sigma_{\max,c}(\rho) \quad (1)$$

where σ_{\max} is the maximum elastic stress at failure and is determined as the product of the nominal stress and the geometrical stress-concentration factor. The parameter $\sigma_{\max,c}$ is the material constant, which is governed by the notch-root radius ρ only, while it is independent of other notch geometries.

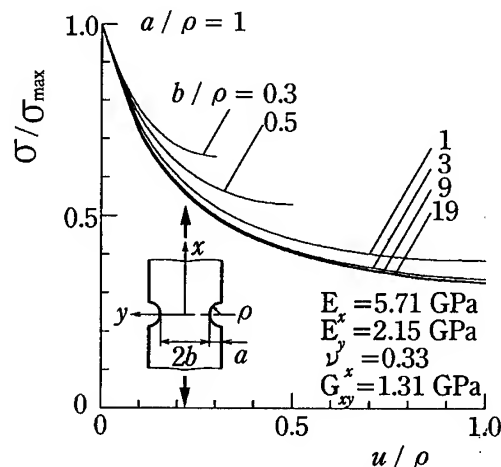


Fig. 1 Relative-elastic-stress distributions near the notch root.

On the other hand, the situation is much more complex for blunt-and-shallow-notched plates. The stress distribution near the notch root depends on the value of b/ρ in the range of $b/\rho \leq 1$ as shown in Fig. 1. It is appropriate to discuss the severity near the notch root for blunt-and-shallow-notched plates in terms of a combination of the maximum elastic stress σ_{\max} , notch-root radius ρ and width of notch section. The failure criterion for blunt-and-shallow-notched plates for which $b/\rho \leq 1$ is expressed as:

$$\sigma_{\max} = \sigma_{\max,c}(\rho, b/\rho) \quad (2)$$

The parameter $\sigma_{\max,c}$ on the right-hand side of Eq. 2 is governed by the notch-root radius ρ and the half width of notch section b .

3. EXPERIMENTAL PROCEDURE

The material used was a glass fiber-reinforced polycarbonate (GF/PC). Idemitsu "Toughlon" PC was applied to the matrix. The plates of GF/PC were molded by injection molding. The dimensions of the plates were 70 mm width, 270 mm long, and 3 mm thick. The plate contains 30 % E-glass fiber (about 0.013 mm in diameter) by weight. The plate is highly anisotropic and the unnotched specimens fail in a brittle manner as shown in Fig. 2.

All specimens were notched in a U-shape on both sides at the midpoint of their length. The notch-root radius ρ were varied from 0.25 mm to 2 mm for sharp-and-deep-notched specimens. On the other hand, the value of ρ ranged from 10 mm to 15 mm for blunt-and-shallow-notched specimens.

Tension tests were performed by an Instron-type testing machine at constant cross-head speed of 0.5 mm/min in a temperature controlled room at 22°C.

To evaluate the damage of notched FRP plates in static tension, we measured successively the luminance distributions near the notch root during test. The luminance-measuring system with a CCD camera is shown in Fig. 3.

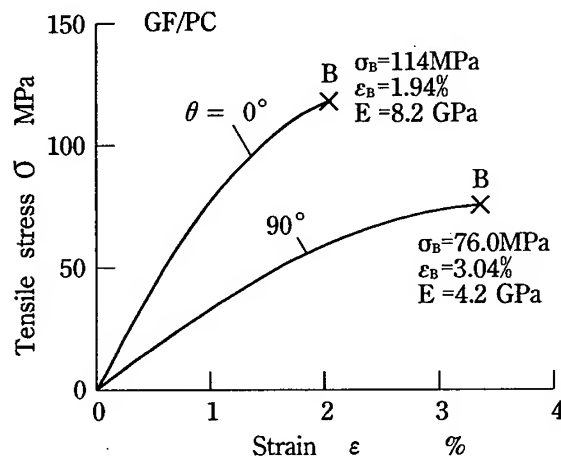


Fig. 2 Tensile stress-strain curves of unnotched specimens

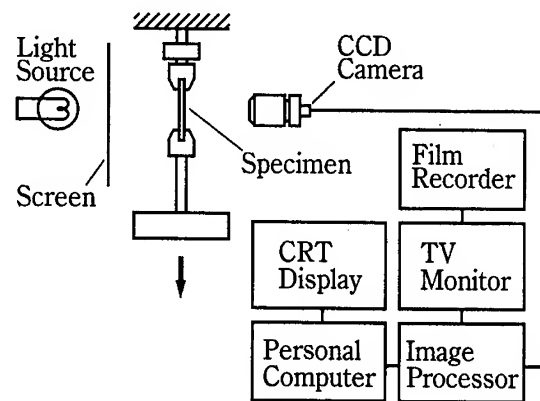


Fig. 3 Luminance-measuring system for tension tests.

4. RESULTS AND DISCUSSION

The experimental results on the fracture tests of notched GF/PC plates for a wide range of notch-root radii have been published previously [5].

Prior to fracture for notched GF/PC plates, the damage zone appears and grows near the notch root. To evaluate the damage, the luminance near the notch root was measured. We observed the decrease of luminance according as the growth of damage. It is evident that the decrease of luminance near the notch root was associated with irreversible damage and microfracture of composites. Applying the luminance measurement technique to evaluate the damage near the notch root, we attempt to develop a limiting condition of damage initiation and growth for notched GF/PC plates under static tension.

Figure 4 shows the luminance distributions at the damaged zone. The patterns with light and shade correspond to the value of luminance that was made at four steps: 90, 85, 80 and 75 %. The value of relative luminance is the ratio of the luminance at a stress to the luminance before testing. The damage is accumulated severely at the region where the value of relative luminance is small.

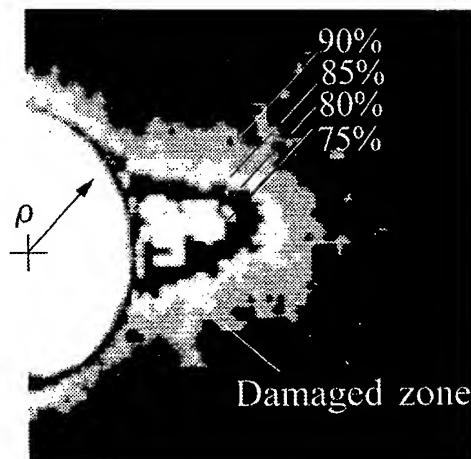
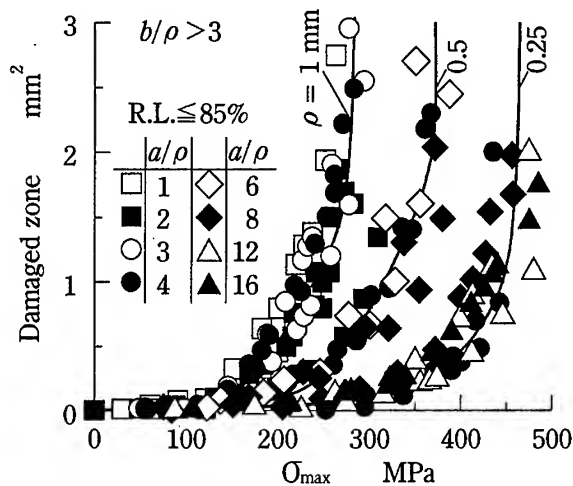
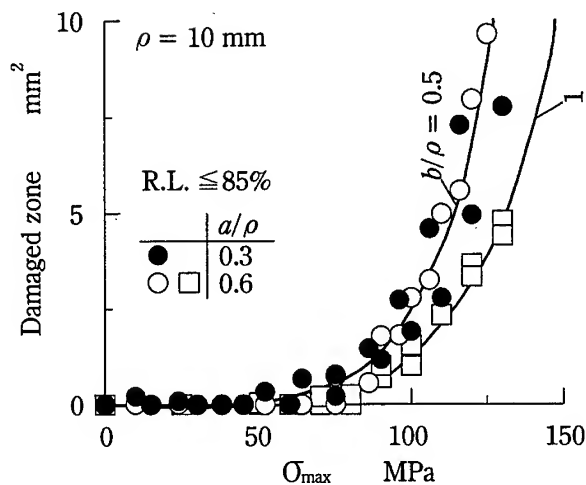


Fig. 4 Luminance distribution at the damaged zone.



(a) Sharp-notched specimens.



(b) Blunt-notched specimens

Fig. 5 Growth of the area of damaged zone.

Luminance measurement revealed the configuration and the area of damaged zone near the notch root. It is evident that the damage depends on the severity near the notch root. As mentioned before, the severity is determined by both the maximum elastic stress at the notch root, σ_{\max} and notch-root radius ρ for sharp-and-deep-notched specimens, and σ_{\max} , ρ and b for blunt-and-shallow-notched specimens. It is conceivable therefore that the damage near the notch root is governed by σ_{\max} , ρ and b , where b is the half width of notch section.

The relation between the area of damaged zone and the maximum elastic stress σ_{\max} is represented in Fig. 5. For sharp-and-deep-notched specimens, as shown in Fig 5(a), three different values are given for the notch-root radius ρ . Notch depth a was varied from 2 to 5 mm for each value of notch-root radius. It can be seen that the area of damaged zone has a one-to-one correspondence with a notch-root radius ρ , and it is independent of notch depth a .

For blunt-and-shallow-notched specimens, the experimental result is shown in Fig. 5(b). There are two different values for b/ρ . The experiment shows that the area of damaged zone has a one-to-one correspondence with the value of b/ρ , and it is independent of notch depth a .

The experimental results mentioned above conform well to the prediction based on the concept of severity near the notch root.

5. CONCLUSIONS

To provide the experimental evidence for the validity of the concept of severity, tension tests on notched GF/PC plates were carried out for a wide range of notch-root radii and notch depths. The initiation and growth of damage near the notch root were investigated by means of the luminance measurement technique using a CCD camera.

The configuration of damaged zone near the notch root is determined by the maximum elastic stress and the notch-root radius for sharp-and-deep-notched specimens. For blunt-and-shallow-notched specimens, the damaged zone is governed by the maximum elastic stress, notch-root radius and width of notch section.

The experimental results mentioned above can be explained by the concept of severity near the notch root, and the limiting condition for predicting the load of failure, Eq. 1 for sharp-and-deep-notched specimens and Eq. 2 for blunt-and-shallow-notched specimens, is applicable to an anisotropic FRP plates.

REFERENCE

1. H. Nisitani and H. Hyakutake, Eng. Fract. Mech., **22**(1985) p. 359.
2. H. Hyakutake, H. Nisitani and T. Hagio, JSME Int. J., **32**(1989), p. 300.
3. H. Hyakutake and T. Yamamoto, Sci. Eng. Compos. Mater., **6**(1997), p. 121.
4. H. Hyakutake and T. Yamamoto, Key Eng. Mater., **137**(1998), p.131.
5. H. Hyakutake, T. Hagio and T. Yamamoto, J. Soc. Mater. Sci., Japan, **47**(1998), p.712.

Radiation Damage of Reactor Pressure Vessel Steels Studied by Nondestructive Methods

D.G. Park¹, T.S. Byun¹, Y.Y. Song¹, J.H. Hong¹ and I.S. Kim²

¹ Reactor Materials Department, Korea Atomic Energy Research Institute,
PO Box 105, Yusong, Taejeon 305-600, Korea

² Department of Nuclear Engineering, Korea Advanced Institute of Science and Technology,
373-1 Kusong-dong, Yusong-gu, Yusong, Taejeon 305-701, Korea

Keywords: Ball Indentation Test, Barkhausen Noise, Dislocation, Domain Walls, Neutron Dose, SA508-3

ABSTRACT

Effects of neutron dose on the mechanical and magnetic properties in SA508-3 nuclear pressure vessel steel using ball indentation test and magnetic Barkhausen noise (BN) measurements were studied. The samples were irradiated in a research reactor up to a dose of 10^{18} n/cm² ($E > 1$ MeV) at 70 °C, and 4.5×10^{19} n/cm² at 290 °C. The change of mechanical properties showed a characteristic trend with neutron dose, especially near the plateau, rapid increase and slow increase. The BN profile in the specimen irradiated at 70 °C decreased markedly, but that in the specimen irradiated at 290 °C was hardly changed. The BN of the specimen irradiated at 70 °C varied in a reverse manner against ball indentation results, a slow decrease up to a neutron dose of 10^{16} n/cm², followed by a rapid decrease up to a dose of 10^{18} n/cm². The change of mechanical properties and magnetic BN can be explained by the pinning effects of moving dislocations and domain walls from the irradiation induced defects.

1. INTRODUCTION

Reactor pressure vessel (RPV) steel degrades due to the irradiation of high energy neutrons. The degradation due to neutron irradiation is characterized by the irradiation embrittlement, resulting in a decrease in the fracture toughness and an increase in the ductile-to-brittle transition temperature. Currently, the degree of degradation is being monitored by an RPV surveillance program with approved models and guidelines [1]. However, the models and surveillance program do not always provide enough information to support decisions for system integrity to the end of its life [2]. Under these circumstances, nondestructive measuring methods are being required to assess the RPV integrity directly or to aid the assessment by giving enough information from the aged RPV steel [3]. There are a variety of non-destructive evaluation (NDE) techniques that have shown some correlation with embrittlement and other types of material degradation, which are ultrasonic attenuation, eddy current techniques, magnetic Barkhausen noise [4] and magnetic acoustic emission, and automated ball indentation (ABI) technique. The ABI test technique is particularly

advantageous for localized testing (e.g. welds and heat-affected zones), for effective use of limited test material, and for providing more test results for statistical analyses [5,6]. On the other hand, magnetic Barkhausen noise (BN), which is due to the discontinuous motion of a magnetic domain wall, is drawing attention as an NDE method in ferromagnetic structural materials. In the present study, the ABI tests and BN measurements have been carried out for the neutron irradiated RPV steel samples irradiated at various neutron doses, and the results were explained as a pinning of dislocations and the magnetic domain wall by irradiation induced defects.

2. EXPERIMENTAL

2.1. Material and Neutron Irradiation

The material tested in the present study is SA508-3 forged steel for nuclear pressure vessels produced by the Korea Heavy Industries and Construction Co (HANJUNG), and the chemical composition is shown in Table 1. The specimens were irradiated in a research reactor at 70 °C and 290 °C, respectively. The accumulated doses for the specimens irradiated at 70 °C were 10^{12} to 10^{18} n/cm², and those for the 290 °C specimens were 4.5×10^{19} n/cm² ($E > 1$ MeV), where an iron wire was employed to determine the neutron dose.

Table 1. Chemical composition and heat treatment history of SA508-3 steel studied.

Element	C	Si	Mn	P	S	Ni	Cr
wt%	0.17	0.004	1.42	0.004	0.003	0.98	0.22
Element	Mo	Al	Cu	V	Co	As	Fe
wt%	0.58	0.003	0.045	0.003	0.006	62ppm	Bal.
* Heat Treatment History 1143 °K/4.5 hr Water Quenching (Quenching, Q) 930 °K/9hr Air Cooling (Tempering, T) 923 °K/24 hr Furnace Cooling, (Simulated post-weld heat treatment (PWHT))							

2.2. ABI Test

The ABI test was conducted with the specimens irradiated at 70 °C using a system of ATC (model: PortaFlow-P1). Details of the ABI test technique are given in references [5,6]. The load versus depth curves (P-h curves) were obtained using a tungsten carbide ball indenter of 0.508 mm diameter. The indentation tests were performed at room temperature with an average strain rate of about 9×10^{-3} s⁻¹. For each specimen three points were tested and the results were averaged.

2.3. Magnetic Property Measurements

Magnetic properties were measured in the same specimen using a specially designed yoke magnet with an amplified sinusoidal wave current of 1 and 5 Hz. The maximum current intensity was set sufficiently high to extend the hysteresis loop beyond the range of approach to saturation. The detected BN signal by the same pick-up coil was amplified and passed through a wide-band filter of flat response between 18 - 19 kHz. The B-H loop and the BN signals including Barkhausen noise energy (BNE) and Barkhausen noise amplitude (BNA), where BNE is defined as the time integration of the squared BN voltage for a magnetizing cycle, were measured as a function of the neutron fluence. The measured data were processed by a computer via a digital storage oscilloscope.

3. RESULTS AND DISCUSSION

3.1. Indentation Data

Fig. 1 shows the indentation load-depth curves of SA508-3 steel samples un-irradiated and neutron irradiated. For a given indentation depth, the applied load increases at a low rate as the neutron fluence increases up to 10^{16} n/cm² and it increases at a higher rate in the fluence range of 10^{16} n/cm² to 10^{17} n/cm². Finally, the load is nearly saturated at a fluence above 10^{17} n/cm².

The true stress-true plastic strain curves in Fig. 2 were calculated from the indentation load-depth curve in Fig. 1. The data points in the flow curves correspond respectively to the unloading points in the load-indentation depth curves. In each flow curve the yield point at a plastic strain of 0.002, the first point, was calculated from the material yield parameter according to the ABI model [6]. The other stress-strain data points in the flow curves are in the plastic strain range of 0.07-0.16. Fig. 3 shows the change of yield strength (YS) with neutron fluence, which were obtained from the load-depth curves in Fig. 1. It is known that the ABI test data agree well with tensile test data with sufficient accuracy [6]. In Fig. 3, YS increases with the neutron dose of 10^{12} n/cm² and it is nearly constant in the dose range of 10^{12} n/cm² to 10^{16} n/cm². However, YS increased rapidly in the dose range of 10^{16} n/cm² to 10^{17} n/cm² and increases slowly above this dose.

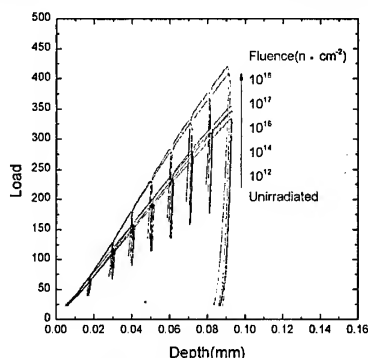


Fig. 1. The indentation load-depth curves of un-irradiated and neutron irradiated SA508-3 steel samples.

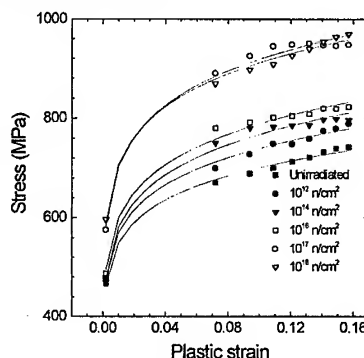


Fig. 2. Stress-strain curves according to the neutron fluences (n/cm², E > 1MeV).

According to the radiation damage model pertinent to the present study, the point defect clusters such as interstitial and vacancy clusters, could provide a major source of RPV steel hardening due to matrix damage, particularly at low irradiation temperatures and high displacement rates, because commonly studied copper-rich precipitates could not be developed at such a low temperature [7]. It is also known that the formation of both interstitial and vacancy clusters lead to significant hardening by acting as obstacles to dislocation motion. The increase of YS with the initiation of neutron irradiation may result from the precipitation of metastable carbides and nitrides at radiation induced nucleation sites [7]. Significant increase in YS does not appear when the neutron dose is less than 10^{16} n/cm². This dose level seems to correspond to the condition where defect clusters

reaches an appreciable fraction [8].

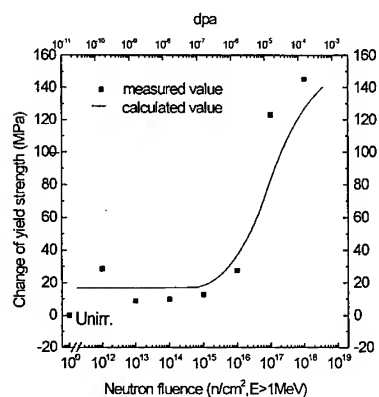


Fig. 3. The change of yield strength as a function of neutron fluence.

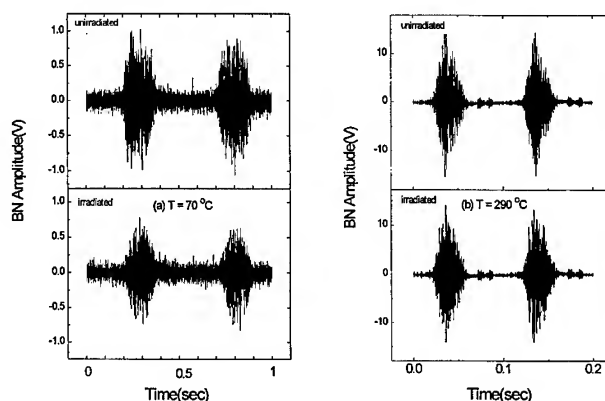


Fig. 4. The BN profiles for as-received and neutron irradiated samples at a temperature of 70 °C and 290 °C.

The significant change of strength occurs between the neutron doses of 10^{16} n/cm² and 10^{17} n/cm². The slow increase of YS at a higher fluence agrees with the model that YS is proportional to the square root of the total neutron fluence [9]. The difference of YS between the specimens unirradiated and 10^{18} n/cm² irradiated was 140 MPa, and it increases with increasing neutron fluence. The difference of YS in the specimen irradiated at 290 °C was 20 MPa, which is similar to the result of the IAEA phase 2 program [9]. This difference, $\Delta\sigma_y = 140$ MPa, is very a large quantity compared with the result of the irradiation test performed at ~ 290 °C and a dose of 4.5×10^{19} n/cm² ($E > 1$ MeV). However, the calculated value of $\Delta\sigma_y$ after irradiation at 60 °C to a dose of 10^{-2} dpa ($\sim 6.7 \times 10^{18}$ n/cm²) is about 600 MPa. It is known that embrittlement decreases with increasing irradiation temperature [10] and SA508-3 steel is fairly insensitive to irradiation at high irradiation temperatures [11]. The present results also imply that degradation is more severe for irradiations at lower temperatures.

The absolute values of strengthening are model-dependent, because the fraction of defects surviving are very sensitive to temperature, dose level, initial sink strength and matrix recombination [12]. The solid line in Fig. 3 is calculated value by Stoller [8] in the condition of 60 °C and 10^{-7} dpa/s. The predicted change of YS after irradiation also showed a characteristic trend with neutron dose, namely near the plateau, rapid increase and slow increase. Considering the absolute values of strengthening are model-dependent [13], the predicted dependence on displacement rate is qualitatively in accordance with our experimental results.

3.2. Change of Barkhausen Noise

The BN profiles during a magnetization cycle for as-received and neutron irradiated samples at a temperature of 70 °C and 290 °C are shown in Fig. 4(a) and (b), respectively. The BN profile in

the 70°C irradiated specimen decreased markedly, but that of the 290°C irradiated one changed hardly. The decrease of BN in the 70°C irradiated specimen is in agreement with the results of Sipahi et al. [14]. The BN is released as a result of the change in the magnetization associated with the domain wall motion. The induced voltage due to the domain wall displacement decreases with the presence of a retarding barrier [15]. The defect clusters induced in the irradiated sample act as a retarding barrier to wall displacement, decreasing the Barkhausen voltage of the specimen irradiated at 70°C [16]. The sizes of defect clusters increase with increasing irradiation temperature [12], and the large size defects are less effective to the domain wall pinning [17]. Therefore, few changes of the BN profile in the specimen irradiated at 290°C are attribute to the sizes of defect clusters.

The changes of BNE and BNA 70°C irradiated specimen are shown in Fig. 5 as a function of neutron dose. The BNE decreased rapidly with the initiation of neutron irradiation, then remains nearly constant up to 10^{16} n/cm², followed by a rapid decrease to 43% of the emission from the as-received sample at a neutron dose of 10^{18} n/cm². The change in BNA also shows a similar trend, but the rate of change is less than that of BNE. The profound effects of irradiation on BN appear above a neutron dose of 10^{16} n/cm² and correspond to the rapid increase of the YS.

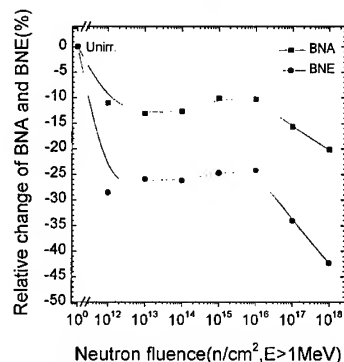


Fig. 5. Relative change of Barkhausen noise amplitude and energy as a function of neutron fluence.

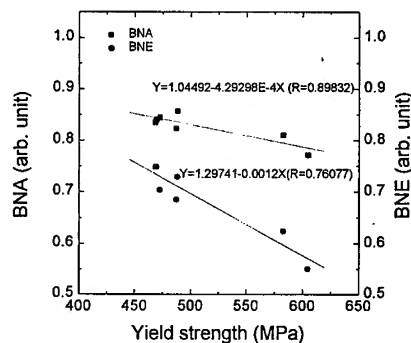


Fig. 6. The linear relation between BNA, BNE and yield strength.

3.3. Correlation Between YS and Barkhausen Noise

The relationship between YS and BN characteristic including the BNE and BNA, is shown in Fig. 6 giving some insight into the relation between mechanical and magnetic properties. The present BNE and BNA show linear relationships with YS in the magnetization region. A similar relationship between Barkhausen parameter and hardness was obtained by the same authors [16]. Radiation strengthening is due to dislocation pinning by small defect clusters, whereas BN is associated with the domain-wall pinning by defect clusters, and consequently a good correlation is found in the parameters. The relation suggests that the radiation embrittlement can be evaluated non-destructively by using the Barkhausen noise parameter. Despite the substantial dimensional difference between the dislocation and domain wall, it is anticipated that the increased density of defect clusters due to irradiation dose causes the increase in YS, resulting in the lower magnetic Barkhausen emissions because the increased number of defect pinning centers impedes both the

movement of magnetic domain walls and dislocations.

4. CONCLUSION

The ABI test technique and magnetic Barkhausen noise measurements were applied in the neutron irradiated pressure vessel steel samples both as-received and irradiated with doses of up to 10^{18} n/cm² ($E > 1\text{MeV}$). The change of YS, the amount of hardening, showed a characteristic trend with neutron dose; namely, near plateau, rapid increase, and slow increase. This result is in qualitative agreement with the prediction by computer simulation performed by Stoller. The BN profile in the 70°C irradiated specimen markedly decreased, but that of the 290°C irradiated one was hardly changed. The difference of BN profiles for the 70°C and 290°C irradiated specimen is attribute to the size of defect clusters. The linear relationship between BN and YS in the 70°C irradiated specimens suggests that the change in mechanical properties, like the YS associated with radiation strengthening, is evaluated nondestructively by using the magnetic techniques of Barkhausen noise measurements.

REFERENCES

1. 10 CFR 50, App. G and H, and ASTM E185
2. M. Blaszkiewicz, Materials Science Forum V. **210-213** (1996) p.9
3. DOE-EPRI R&D plan, V. II (1998) p.3
4. J.F. Stubbins, W.-J Shong, M. Giacobbe, A.M. Ougouag, and J.G. Williams, ASTM STP 1204 (1993) p.5
5. F.M. Haggas, "Field Indentation Microprobe for structural Integrity Evaluation," U.S. Patent 4,852 (1989) p.397
6. T.S. Byun, J.H. Hong, F.M. Haggag, K. Farrell and E.H. Lee, Int. J. Pres. Ves. & Piping **74** (1997) p.231
7. G.P. Seidal, Radiation Effects, V.1 (1969) p.177
8. R.E. Stoller, Proc. 6th Int. Symp. on EDM (1993) p.747
9. S.B. Fisher and J.T. Buswell, Int. J. Pres. Ves. & Piping **27** (1987) p.91
10. C. J. McHargue, Int. Metall. Rev., **27** (1982) p.21
11. G.R. Odette and G.E. Lucas, ASTM STP 909 (1986) p. 206
12. K. Farrell, S.T. Mahmood, R.E. Stoller, L.K. Mansur, J. Nucl. Mat. **210** (1994) p. 268
13. R.E. Stoller, ASTM STP 1175 (1990) p.394
14. L. B. Sipahi, M. R. Govindaraj, D.C. Jiles, P.K. Liaw, and D. S. Drinon, Rev. of Progress in Quantitative Nondestructive Eval. **13** (1994) p.1801
15. D.G. Hwang and H.C. Kim, J. Phys. D: Appl. Phys., **21** (1988) p.1807
16. D.G. Park, J.H. Hong, I.S. Kim and H.C. Kim, J. Mater. Sci. **32** (1997) p.6141
17. D.G. Park, J.H. Hong, I.S. Kim and H.C. Kim, IEEE Trans. **35** (1999) p.3898

Reliability Calculation for Piping Containing Circumferential Crack Based on 3-D Elastic-Plastic SFEM

Lixing Huo, Buolin He and Yufeng Zhang

College of Material Science and Engineering, Tianjin University,
Tianjin 300072, China P.R.

Keywords: Crack, Elastic-Plastic SFEM, Perturbation Method, Reliability, Welded Pipe

ABSTRACT

In this paper, the reliability of welded pipe with circumferential surface crack was calculated by using the 3-D stochastic finite element method. This method has overcome the shortcomings of conservative results in safety assessment with deterministic fracture mechanics method. The calculation of reliability was based on 3-D elastic-plastic perturbation stochastic finite element program which was developed by ourselves. The effects of variables such as fracture toughness δ_c , external load (including bending moment M and inner pressure P) and the depth of the circumferential surface crack A on the structure reliability were also discussed. The calculation results indicate that among the four variables (δ_c, M, P, A), the bending moment M has the greatest effect on the reliability of the welded pipe. The next important influence factor is fracture toughness. The third one is the depth of the circumferential surface crack A . The inner pressure P has lower effect on the reliability of the welded pipe than both δ_c and A . The method has put forward a new way for safety assessment of welded pipe with circumferential surface crack.

1. INTRODUCTION

Safety assessment of welded structure with cracks based on "Fitness for Purpose" principle has widely been studied in China and abroad. Although series of assessment criteria such as IIW/IIS-SST-1157-90, WES-2805, R/H/R6-Ver.3 and PD6493-91 have been set up, all these criteria are based on deterministic fracture mechanics. In engineering structures, there are many uncertain factors such as material properties, structure's geometry and external loading (wind, earthquake etc.). Because the uncertain factors can not be overlooked, the responses of structures became uncertain as well. Recently, calculating the reliability of engineering structures by using stochastic finite element method (SFEM) which combined the FEM with reliability analysis has become an area of extensive investigation for its high efficiency and accuracy^[1-3]. In many situations, cracks are the essential cause that leads to structure failure, however the references about calculation of 3-D elastic-plastic SFEM have seldom been reported.

In this paper, the iteration approach of 3-D elastic-plastic perturbation stochastic initial stress finite element method (PSFEM) has been presented by using incremental method and the perturbation stochastic finite element program has been developed. The reliability index and probability of failure of welded pipe with a circumferential surface crack has been calculated. The program can be used to deal with uncertainties of material properties, geometry and external loading simultaneously. The effects of stochastic variables on the reliability of welded pipe with an circumferential surface crack were also discussed. We hope that this work has put forward a new way for reasonable and accurate safety assessment of welded pipe with circumferential surface cracks.

2. THE ITERATION FORMULAS OF 3-D ELASTIC-PLASTIC INITIAL STRESS FEM

In displacement method of finite element method, the control equations of structure system can be written as:

$$[K]\{U\} = \{F\} \quad (1)$$

where $[K]$ is the global stiffness matrix; $\{U\}$ is the generalized displacement vector; $\{F\}$ is the generalized external force vector. The global stiffness matrix is assembled from the contributions of the standard and enriched elements. For the elastic-plastic problem, here the iteration formulas were given out by using initial stress finite element method based on incremental method:

$$[K]\Delta\{U\}_{i+1} = \Delta\{F\} + \{R\}_i \quad (i = 0, 1, 2, \dots) \quad (2)$$

where $\{R\}_i$ is the initial stress vector. The formula of calculating $\{R\}^e$ can be written as

$$\{R\}^e = - \int [B]^e \Delta\{\sigma_0\} dV \quad (3)$$

in which $[B]^e$ is the matrix determined from the shape function and geometric condition of the element and $\{\sigma_0\}$ is initial stress.

$$\Delta\{\sigma_0\} = -[D]_p \Delta\{\varepsilon\} \quad (4)$$

in which $\Delta\{\varepsilon\}$ is increment of strain and $[D]_p$ is the plastic matrix. Introducing Eq.(4) into Eq.(3), the formula of calculating $\{R\}^e$ can be changed as

$$\{R\}^e = \int [B]^e [D]_p \Delta\{\varepsilon\} dV \quad (5)$$

In formula (2), if we take $\Delta\{U\}_0 = 0, \{R\}_0 = 0, \Delta\{U\}^i = \Delta\{U\}_i - \Delta\{U\}_{i-1} \quad (i = 1, 2, \dots)$, the

whole iteration formulas can be written as

$$\begin{cases} [K]\Delta\{U\}^1 = \Delta\{F\}, \\ \Delta\sigma_i = [D]_e [B]^e \Delta\{U\}_i^e, \\ [K]\Delta\{U\}^{i+1} = \Delta\{R\}^i, \\ \Delta\{R\}^i = \{R\}_i - \{R\}_{i-1}, \\ \Delta\{U\}_i = \Delta\{U\}^i + \Delta\{U\}_{i-1}, \\ \Delta\sigma_i = [D]_{ep} [B]^e \Delta\{U\}_i^e, \end{cases} \quad (6)$$

3.THE ITERATION FORMULAS OF 3-D ELASTIC-PLASTIC INITIAL PSFEM

If there is a small random perturbation in material properties or in geometry in Eq.(1), the global stiffness matrix $[K]$ becomes uncertain. There may also be a small random perturbation in external force vector $\{F\}$, so the generalized displacement vector $\{U\}$ is random .

Supposing Z is a random perturbation factor, the quantity of perturbation can be expressed as a small random variable, that is to say, Z can be expressed as the sum of mean value and the deviation part:

$$Z = Z_0(1 + a) \quad (7)$$

Where Z_0 is the mean value of Z , $a = (a_1, a_2, \dots, a_n)$ is a random field with zero mean value, which indicates the variability of randomness of Z . Z can be expanded in the Taylor series form by truncating the third order:

$$Z = Z_0 + \sum_{l=1}^n Z_l a_l + \frac{1}{2} \sum_{l=1}^n \sum_{k=1}^n Z_{lk} a_l a_k \quad (8)$$

The symbol n stands for the total amount of variables in a vector. Where l , k stand for partial derivatives of a_l , a_k , respectively.

Because every kind of variables can be expressed by using perturbation method, the perturbation stochastic finite element method has widely been used, especially for geometry randomness. The references ^[4] indicate that despite the second order perturbation stochastic finite element method is more accurate than the first order method, the practical use of the former has extremely been restricted for its lower efficiency. In this paper, the perturbation stochastic finite element method recursive equations are obtained by using the first order perturbation method. According to the Eq. (8), all the parameters in Eq. (6) are expanded in the Taylor series form by truncating the second order and are straightened out. The iteration formulas of 3-D elastic-plastic initial stress PSFEM can be written as

$$\begin{cases}
(\Delta\{U\}^1)_i = [K]^{-1}((\Delta\{F\})_i - ([K])_i \Delta\{U\}^1_i) \\
(\Delta\sigma_1)_i = ([D]_e)_i [B]^e \Delta\{U\}^e_i + [D]_e ([B]^e)_i \Delta\{U\}^e_i + [D]_e [B]^e (\Delta\{U\}^1)_i \\
(\Delta\{U\}^i)_i = [K]^{-1}((\Delta\{R\}^i)_i - ([K])_i \Delta\{U\}^{i+1}_i) \\
(\Delta\{R\}^i)_i = (\{R\}^i)_i - (\{R\}^i)_{i-1} \\
(\Delta\{U\}^i)_i = (\Delta\{U\}^i)_i + (\Delta\{U\}^i)_{i-1} \\
(\Delta\sigma_i)_i = ([D]_{ep})_i [B]^e \Delta\{U\}^e_i + [D]_{ep} ([B]^e)_i \Delta\{U\}^e_i + [D]_{ep} [B]^e (\Delta\{U\}^i)_i \\
(\{U\}_m)_i = \sum_{i=1}^m (\Delta\{U\}^i)_i \\
(\sigma_m)_i = \sum_{i=1}^m (\Delta\sigma_i)_i
\end{cases} \quad (9)$$

$$([D]_{ep})_i = ([D]_e)_i - ([D]_p)_i \text{ and } ([D]_p)_i = ([D]_p(\sigma_{k-1} + \sigma_{i-1}))_{(\sigma_{k-1} + \sigma_{i-1})} ((\Delta\sigma_{k-1})_i + (\Delta\sigma_{i-1})_i).$$

Here the $([D]_p(\sigma_{k-1} + \sigma_{i-1}))_{(\sigma_{k-1} + \sigma_{i-1})}$ can be obtained by using difference method.

$$([D]_p(\sigma_{k-1} + \sigma_{i-1}))_{(\sigma_{k-1} + \sigma_{i-1})} \approx \frac{([D]_p(\sigma + \alpha\sigma) - [D]_p(\sigma))}{\alpha\sigma}$$

For 3-D problem, because there are 6 stress components, 6 times difference calculations must be taken. In this paper, high precision results can be obtained when α is taken as 0.001.

4. FAILURE FUNCTION AND THE FORMULAS OF CALCULATING RELIABILITY

In this paper, we aimed at the welded pipe with a circumferential surface crack which was existed inside the weld. The performance function was determined as:

$$g(X) = \delta_c - \delta \quad (10)$$

Where δ_c is the fracture toughness of weld and δ is the crack opening displacement. $X = X_i$ ($i = 1, 2, \dots, n$) are variables which have effect on the performance function $g(X)$. The variables may be correlated and non-normal distribution. In either case, a transformation must be made to change them into uncorrelated variables and normal distribution. Supposing the mean values and variances of X_i and $g(X)$ are $E(X_i)$, $E(g(X))$ and $V(X_i)$, $V(g(X))$, respectively, the formula of calculating the reliability index β can be written as

$$\beta = E(g(X))/V(g(X)) = [E(\delta_c) - E(\delta)]/\sqrt{V(\delta_c) - V(\delta)} \quad (11)$$

Here $E(\delta_c)$ and $V(\delta_c)$ are the mean value and variance of δ_c . $E(\delta)$ and $V(\delta)$ are the mean value and variance of δ . In order to get the reliability index β , $E(\delta_c)$, $V(\delta_c)$, $E(\delta)$ and $V(\delta)$ have to be obtained first. $E(\delta_c)$ and $V(\delta_c)$ can be determined by using experimental method. $E(\delta)$ and $V(\delta)$ have to be obtained by using 3-D elastic-plastic PSFEM. In this paper, in order to

reduce the calculating time of reliability index β , all the factors in equation (9) are expanded in the Taylor series form at the mean value point.

5. THE CALCULATION OF RELIABILITY INDEX OF WELDED PIPE WITH CRACK

5.1. Calculation Model

Considering a circumferential surface crack in the welded pipe, one-fourth of the pipe was considered by taking full advantage of symmetry. In order to account for the stress and strain singularities caused by the crack, 20 nodes singularity element at crack tip was used. 20 nodes isoparametric element was used at non-crack area. The model is divided into 198 elements and the total number of nodes is 1297. The calculation model is shown as Fig.1.

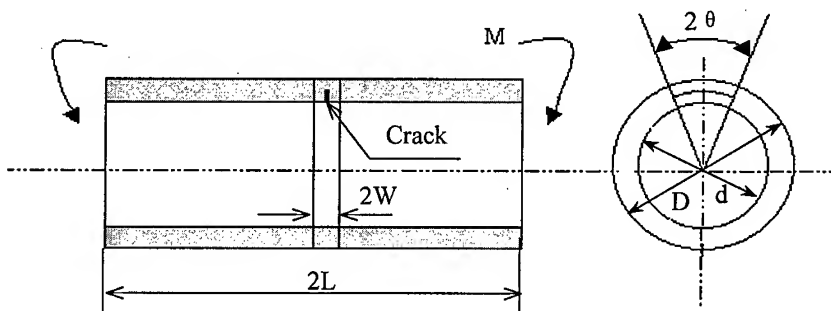


Fig.1. Calculation model and geometry size

5.2. The Chosen Variables

In this paper, the fracture toughness δ_c , external loads (including bending moment M and inner pressure P) and the depth of the circumferential crack A are determined as variables. The Young's modulus E and Poisson ratio γ are described as constants. Here the Young's modulus E is equal to 2.1×10^5 MPa and the Poisson ratio γ is equal to 0.3. The mean values of fracture toughness, bending moment, the inner pressure and the crack depth are equal to 0.21mm, 15000Nm, 1.5MPa and 5mm, respectively. The pipe material is X60 and the welded electrode is E8010-G, which yielded stress σ_s is equal to 470MPa. The coefficients of the four variables are taken as from 0.1 to 0.15, and $D=120$ mm, $d=100$ mm, $2\theta=180^\circ$ in Fig.1.

5.3. Calculation Results and Analysis

The calculation results of 3-D elastic-plastic PSFEM perturbation about the reliability index β and the probability of failure according to the combinations of different coefficient of variations are shown in Table 1. The calculation control tolerance is 0.01.

From Table 1 it can be seen that when all variable coefficients (δ_c, M, P, A) are equal to 0.15, the failure probability of the welded pipe with a circumferential crack ($A=5$ mm, $2\theta=180^\circ$) is still very low (1.9367×10^{-3}). It shows clearly that the welded pipe still has high reliability. Among the

Table 1. Reliability index and failure probability at different combinations of the variations

Combinations	Coefficient of variation(δ_c)	Coefficient of variation (M)	Coefficient of variation(A)	Coefficient of variation(P)	Reliability index β	Probability of failure P_f
1	0.1	0.1	0.1	0.1	4.3494	6.8913×10^{-6}
2	0.1	0.15	0.1	0.1	3.1891	7.1025×10^{-4}
3	0.1	0.1	0.15	0.1	4.1981	1.3836×10^{-5}
4	0.15	0.1	0.1	0.1	3.7954	7.3961×10^{-5}
5	0.1	0.1	0.1	0.15	4.3038	8.5349×10^{-6}
6	0.15	0.15	0.15	0.15	2.8881	1.9367×10^{-3}

four variables, the variation of bending moment has the greatest effect on the reliability. The second effect factor is fracture toughness. The third effect factor is crack depth. The inner pressure has lower effect on the reliability than that of bending moment, fracture toughness and crack depth. As a result, in order to maintain this welded pipe with high reliability, the first thing should be done is to reduce the variation of bending moment M . The second thing should be done is to reduce the variation of fracture toughness δ_c by controlling the metallurgy quality of weld. The third control factor is crack depth A . The last control factor is the inner pressure P .

6. Conclusions

- (1) 3-D elastic-plastic perturbation SFEM is implemented and the program is developed.
- (2) The failure probability of welded pipe with a crack is calculated. the results show that inspite of containing the crack, the pipe still has lower failure probability. This method has overcome the shortcomings which is appeared in safety assessment by deterministic fracture mechanics.
- (3) Among the four variables, the variation of bending moment has the greatest effect on the reliability. The second effect factor is fracture toughness. The third effect factor is the depth of the circumferential surface crack. The inner pressure has the smallest effect on the reliability.

ACKNOWLEDGEMENTS

This project is supported by the National Natural Science Foundation of China, Project No. 59675046.

REFERENCES

1. K.Handa, and K.Anderson, Application of finite element method in statistical analysis of structures. Proc. 3rd Int. Conf. on struct. Safety and Reliability, Norway, Trondheim(1981) p.409
2. T.Hisada, and S.Nakagiri, Role of the stochastic finite element method in struct. Proc. 4rd Int. Conf. on struct. Safety and Reliability, Japan, Kobe(1985) p.213
3. Ghanem R. & Spanos P.D. Spectral stochastic finite element formulation for reliability analysis. J. Engng. Mech., ASCE, **117**(1991) p.2351
4. Yamazaki F., Shinozuka M.&Dasgupta G. Neumann expansion for stochastic finite element analysis. J.Engng., ASCE, **114**(1988) p.1335

Optimum Design of Linear Phased Array Transducer for NDE

Joon-Hyun Lee¹ and Sang-Woo Choi²

¹ School of Mechanical Engineering, Pusan National University,
Pusan 609-735, Korea

² Graduate School of Mechanical Design Engineering, Pusan National University,
Pusan 609-735, Korea

Keywords: Grating Lobe, Nondestructive Evaluation, Phased Array, Piezoelectric Element, Ultrasonic Testing

ABSTRACT

A phased array transducer is a multi-element piezoelectric device which offers a method of dynamic ultrasonic beam focusing, in which the focal length of the ultrasonic beam varies as the pulse propagates through the material. There are various design parameters of the phased array transducer, playing a decisive role in the efficiency of transducer, such as the number of elements, inter-element spacing, frequency specification and element size etc., In this paper, full-field ultrasonic pressure are computed and visualized on the basis of the Huygen's superposition principle to investigate the influence of design parameters for linear phased array. For the simulation, a linear phased array is considered as an array of single elements of finite width and each element is assumed to be made of a large number of simple line source excited at the same time. The wave generated from piezoelectric elements are considered as simplified transient ultrasonic waves which are constructed with the cosine function enveloped with a Hanning window. The effects of inter-element spacing and size of element on beam directivity and ultrasound pressure field are discussed.

1. INTRODUCTION

Ultrasonic testing is one of most common nondestructive evaluation(NDE) technique, which is used to evaluate defects in structure and mechanical properties of materials[1,2]. A phased array is a multi-element piezoelectric device whose elements are individually excited by electric pulses at programmed delay time. Comparing to conventional ultrasonic single-element transducer in NDE application, the phased array transducer provides a method of rapid beam steering and sequential addressing of a large area of interest without requiring mechanical scanning which is particularly important in real time application[3,4].

There are some designing parameters of phased array transducer, playing a decisive role in the efficiency of transducer, such as the number of elements, inter-element spacing, frequency characteristics and element size. However, for their effective use of phased array transducer in NDE, the use of phased arrays must be carefully weighed for each application by understanding the influence of key transducer parameters on the steering directivity and the dynamic focusing. In our

previous study[5-7], the ultrasonic beam profile due to the variation of the number of elements, inter-element spacing and frequency characteristics was studied. However, the piezoelectric elements were considered as point source for this simulation. This is our extended work for the previous study by taking into account the effect of element size. For the simulation, a linear phased array is considered as an array of single elements of finite width and each element is assumed to be made of large number of simple line source excited at the same time. It is also considered for practical situation that each element generates a transient wave that is constructed with the cosine function enveloped with a Hanning window.

2. PRINCIPLE OF PHASED ARRAY TECHNIQUE

The phased array transducer is a multi-element device as shown in Fig. 1. In the phased array technique, piezoelectric elements are excited by each electric pulse that is delayed as much as a calculated delay time in an electronic circuit for the purpose of beam steering and focusing without mechanical movements of transducer. Since there are no mechanical movements that require much time to scan, the phased array technique can scan wide sectors in real-time.

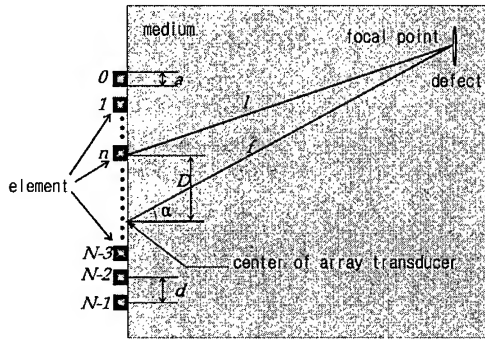


Fig. 1 Phased array transducer

In Fig.1, the width of piezoelectric element is a . The number of elements is N . The focal length from center of transducer is f . The steering angle of ultrasonic beam is α . The distance from $n+1$ th element to the center of transducer is D as shown in Eq. (1), and to the focal point is l as shown in Eq. (2), when the inter-element spacing is d .

$$D = \frac{2n - N + 1}{2} d \quad (1)$$

$$l = \sqrt{f^2 + D^2 - 2fD \sin \alpha} \quad (2)$$

As shown in Eq. (3), the delay time of pulse which excites the piezoelectric element, $T[n]$ is the value of $(f-l)$ divided by the ultrasonic velocity C . The constant t_o is large enough to avoid negative time delays.

$$T[n] = \frac{f - \sqrt{f^2 + D^2 - 2fD \sin \alpha}}{C} + t_o \quad (3)$$

Ultrasonic waves are radiated from each piezoelectric element, by the excitation of each pulse,

which are delayed as much as the delay times calculated with Eq. (3). Then, an ultrasonic beam steered and focused is constructed by the superposition of these waves according to Huygen's principle.

There are various design parameters for a linear phased array transducer, such as frequency, frequency bandwidth, the number of piezoelectric elements, inter-element spacing and the width of the piezoelectric elements. In previous our study, an ultrasonic beam spreads widely and has a low focusing effect, when the number of piezoelectric element is small. On the other hand, when the number of the piezoelectric elements is large, an ultrasonic beam has a high quality focusing effect, but the instrument will be more complex and it is more costly to manufacture it. Instead of increasing the number of element to enhance the focusing effect, the inter-element spacing can be enlarged when the frequency bandwidth is broad. The grating lobes arise when the inter-element spacing is larger than a half wavelength. These grating lobes and side lobes are suppressed in broad frequency bandwidth[5-7].

3. NUMERICAL SIMULATION PRINCIPLE

Hanning window function described in Eq. (4) was used to approach realistic ultrasonic waveform. Wave number is k and frequency is ω . The frequency bandwidth of transient waveform is controlled by variation of Hanning window width, B .

$$\text{win}_-f(r, t) = 0.5 + 0.5 \cos\left(\frac{kr - \omega t}{B}\right) \quad (4)$$

Directivity function of each piezoelectric element is shown in Eq. (5) when the wavelength is λ . This equation was verified with the experiments by previous researcher[8].

$$A(\theta) = A_o \frac{\sin\left(\frac{\pi a \sin \theta}{\lambda}\right)}{\frac{\pi a \sin \theta}{\lambda}} \quad (5)$$

The ultrasonic wave directivity of each piezoelectric element shown in Fig. 2 represents the effect of directivity due to the variation of element size.

$$u(r, t) = A(\theta) \cos(kr - \omega t) \text{win}_-f(r, t) \quad (6)$$

A transient ultrasonic waveform shown in Eq. (6) has directivity represented with Eq. (5).

$$p_n(x, y, n) = \frac{r_o}{r} \frac{p_o}{u_o} u(r, n), \quad r = \sqrt{x^2 + y^2} \quad (7)$$

Ultrasound pressure of one element is represented in Eq. (7). The ultrasound pressure field is represented by the maximum magnitude of summation of the ultrasound pressure that are radiated from each element as shown in Eq.(8).

$$p(x, y) = \text{MAX}\left(\sum_{n=0}^{N-1} p_n(x, y, n)\right) \quad (8)$$

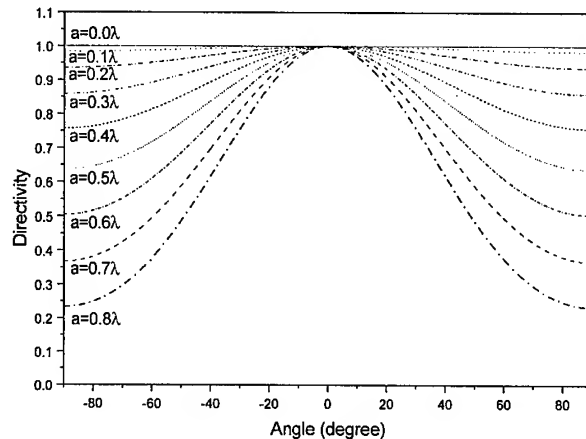


Fig. 2 Ultrasonic wave directivity of each piezoelectric element

4. SIMULATED RESULTS AND DISCUSSION

The ultrasonic beam directivities and the ultrasound pressure fields were calculated when the number of elements, N , was 32 and the focal length was 50mm. The center frequency used in this study is 5 MHz and the shear wave speed in aluminum is 3,200mm/s. The ultrasonic beam directivity and pressure field represents intensities of ultrasound pressure at each azimuth angle and in full field of medium, respectively.

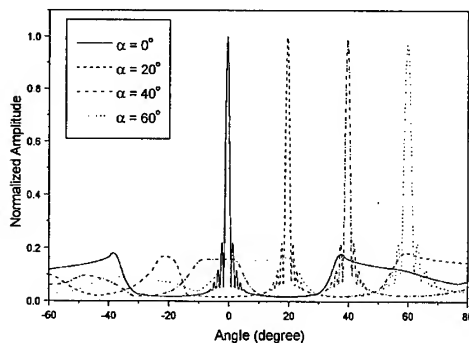


Fig. 3 Ultrasonic beam directivity
($a=0.2\lambda$, $B=10\lambda$, $d=1.5\lambda$)

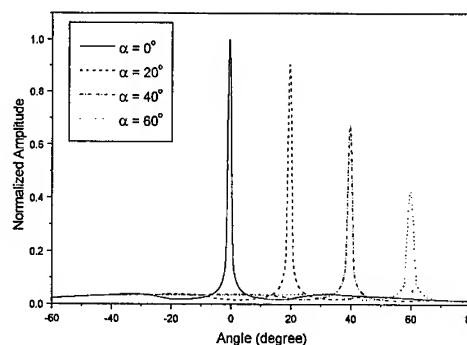


Fig. 4 Ultrasonic beam directivity
($a=0.8\lambda$, $B=2\lambda$, $d=1.5\lambda$)

The characteristics of ultrasonic beam directivity due to change of design parameters were represented in Fig. 3 and Fig. 4 when the inter-element spacing is 1.5 times of wavelength. Figure 3 shows the ultrasonic beam directivity at four different steering angle for the condition of $a=0.2\lambda$, $B=10\lambda$, and $d=1.5\lambda$. Since the inter-element spacing is larger than a half wavelength, there are some deleterious grating lobes at the azimuth angle of -40° , -20° , 0° and 20° respectively, as shown in Fig. 3. Furthermore, some side lobes around main lobes are also observed, which result in spurious

ultrasonic signal and degradation of steering quality. It is also found that the amplitudes and widths of main lobes are same for all steering angles. It is interesting to note that the simulated result at $\alpha=0.2\lambda$ is almost same with the ultrasonic beam directivity presented from the point source, which are already reported in our previous study[6]. However, the grating lobes are eliminated and the side lobes are suppressed for the larger width of element ($\alpha=0.8\lambda$) and broad bandwidth ($B=2\lambda$) as shown in Fig. 4. Comparing this simulated result with that shown in Fig. 3, the amplitude of main lobe is gradually decreased with the increase of steering angle.

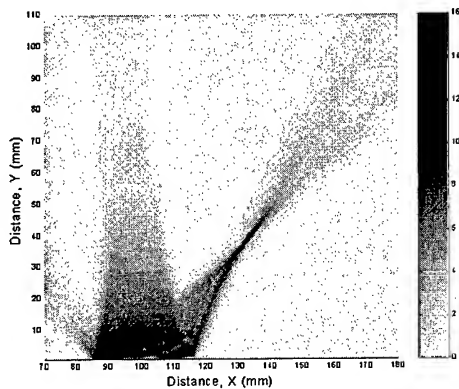


Fig. 5 Ultrasound pressure field
($\alpha=0.8\lambda$, $B=2\lambda$, $d=1.5\lambda$, $\alpha=40^\circ$)

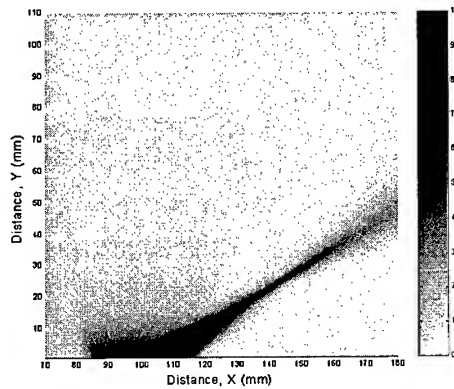


Fig. 6 Ultrasound pressure field
($\alpha=0.8\lambda$, $B=2\lambda$, $d=1.5\lambda$, $\alpha=60^\circ$)

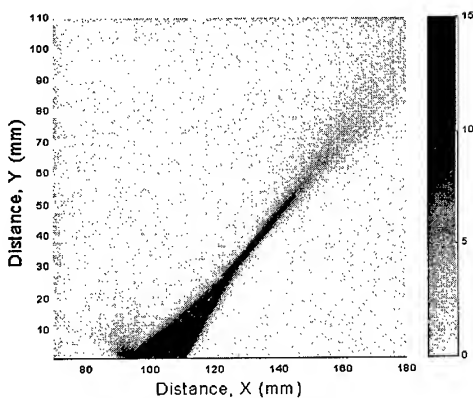


Fig. 7 Ultrasound pressure field
($\alpha=0.8\lambda$, $B=2\lambda$, $d=1.0\lambda$, $\alpha=40^\circ$)

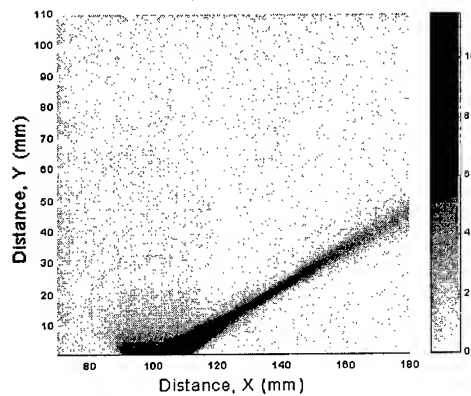


Fig. 8 Ultrasound pressure field
($\alpha=0.8\lambda$, $B=2\lambda$, $d=1.0\lambda$, $\alpha=60^\circ$)

Ultrasound pressure fields for $d=1.5\lambda$ and $d=1.0\lambda$ are represented in Fig. 5, Fig. 6, Fig. 7 and Fig. 8, respectively, where the other parameters are set as $\alpha=0.8\lambda$, $B=2\lambda$ and $\alpha=40^\circ$ or 60° . The main lobe is constructed at steering angle which is 40° and 60° respectively. As shown in Fig. 5 and Fig. 6, the width of main lobe beam at $d=1.5\lambda$ is narrow and ultrasound pressure is high at the focal point, resulting in good focusing effect. However, there is deleterious grating lobe where steering angle is $\alpha=40^\circ$ as shown in Fig. 5. This grating lobe which is influenced from ultrasonic beam

directivity of each element whose width is larger than 0.2λ arises where azimuth angle is 0° and disappeared due to the increase of steering angle as shown in Fig. 6. Since the direction of grating lobe is related with the inter-element spacing, the inter-element spacing must be controlled to eliminate grating lobe where azimuth angle is 0° .

Ultrasound pressure fields shown in Fig. 7 and Fig. 8 for the inter-element spacing $d=1.0\lambda$ demonstrate that there is no grating lobe observed in Fig. 5. Since the inter-element spacing is reduced to 1.0λ , the focusing effect is worse than the ultrasonic beam of Fig. 5 and Fig. 6. However available focusing effect is provided, since width of ultrasonic beam is narrow and ultrasound pressure is high at the focal point. The deleterious grating lobe where azimuth angle is 0° is prevented by the decrease of inter-element spacing which makes the angle between main lobe and grating lobe larger.

5. CONCLUSION

It was found that the ultrasonic beam directivities and the ultrasound pressure fields at the smaller width of element less than 0.2λ showed the almost same results simulated for the point source. The ultrasound pressure field at the larger width of element more than 0.2λ showed that there was the grating lobe that could not be suppressed by broadband frequency when the inter-element spacing was 1.5λ . In order to eliminate this grating lobe, the inter-element spacing needs to decrease less than 1.0λ . As a guideline for optimal design from this study, the inter-element spacing must be one wavelength and the width of element must be 0.8λ to enhance the focusing ability and the intensity of beam without introducing deleterious grating lobes.

REFERENCE

1. J. H. Lee, J. of KSME, **9** (1995) p. 1-7
2. J. L. Rose and J. N. Barshinger, Proc. of 14th WCNDT (1996) p. 157-160
3. M. Zhang, A. Cheng, J. D. Achenbach and W. A. K. Deutsch, Review of Progress in Quantitative Nondestructive Evaluation, **18** (1999) p. 1085-1092
4. L. Azar and S. C. Wooh, Review of Progress in Quantitative Nondestructive Evaluation, **18** (1999) p. 2153-2160
5. S. W. Choi and J. H. Lee, J. of KSNT, **19** (1999) p. 207-216
6. J. H. Lee and S. W. Choi, to appear IEEE Transaction on UFFC, (2000)
7. S. W. Choi and J. H. Lee, CCS-1, Japan, Kyushu (1999) p. 18-19
8. D. K. Lemon and G. J. Posakony, Materials Evaluation, **38** (1980) p. 34-37

A Damage Model for Void Configuration and Failure under Different Constrained Deformation Region in Ductile Matrix

M. Kikuchi¹ and M. Geni²

¹ Science University of Tokyo, Noda, Chiba 278-8510, Japan

² Xinjiang Engineering College, 21 Youhaolu Urumqi, 830008, China P.R.

Keywords: FEM, Gurson Model, MMC, SEM, SiC Particle, Stress-triaxiality, Void Configuration, Void Volume Fraction

ABSTRACT

Metal matrix composites (MMC) achieve high yield stress, high strength and high stiffness by mixing stiff reinforcement SiC particles/whiskers into the aluminum alloy. The density of this composite material decreases with increasing volume of SiC particle/whiskers. For these advantages, this material is attracting attention for potential applications. However, the use of this material is limited by its low fracture toughness and ductility. For its improvement, both experimental and computational studies have been conducted by many authors [1]~[10].

In this study, the constraint effects of SiC particle volume fractions and the specimen geometry are analyzed by conducting tensile tests with changing the SiC particle volume fraction as 0%, 2% and 10% and tensile specimen notch radius as 0.5, 1.0, 2.0, 4.0, 8.0 and 16.0 mm. The smooth specimen was also tested for SiC particle reinforced 2025 aluminum alloy composites. The effect of constraint on the void configuration and coalescence are investigated experimentally using the 3-dimensional SEM fracture surface observations and 3-dimensional image analysis. The average and local void volume fraction at fracture is measured using 3-dimensional image analysis technique and the new modified Gurson model is proposed.

1 TENSILE TEST SPECIMEN AND SEM FRACTURE SURFACE

Fig. 1 shows the tensile test specimen with notch. Two kinds of SiC particulate reinforced aluminum alloys are made by powder metallurgy by changing the volume fraction of SiC particle to 2% and 10%. They are called SiC2% and SiC10% specimen, respectively. A specimen of base matrix aluminum alloy is also tested, which is called SiC0% specimen. The tensile test is conducted by changing the notch radius as 0.5mm, 1.0mm, 2.0mm, 4.0mm, 8.0mm and 16.0mm, respectively. A smooth specimen is also tested. The average diameter of SiC particles is 4 μ m. The tensile test is conducted by MTS machine keeping the cross-head speed at 0.5mm/min.

Geometric constraint due to elastic-plastic deformation gradient in the notch produces inhomogeneous stress-strain states in the notch region when uniaxial load is applied. Stress triaxiality α is quantified by σ_{kk}/σ_e , where σ_{kk} is mean

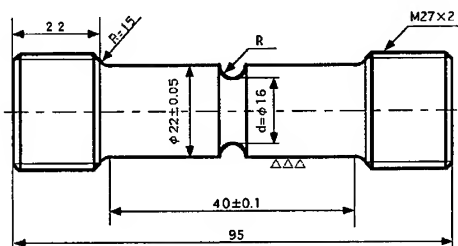


Fig.1 The Tensile Test Specimen with Notch

stress and σ_e is the effective stress. Bridgman's[11] approximate analytical solution for maximum stress triaxiality in the minimum cross section of a notched tensile specimen is given as $\alpha = \sigma_{kk} / \sigma_e = 1/3 + \ln(d/(4R)+1)$, where d is the minimum cross-sectional diameter and R is the notch radius as shown in Fig. 1. The stress triaxiality corresponding to the notch radius is 2.50, 1.94, 1.43, 1.00, 0.75 and 0.56 respectively. For a smooth specimen the stress triaxiality is 0.33.

Figs 2 (a) and (b) show the SEM fracture surface and 3-dimensional image of a SiC2% specimen with notch radius 1mm. It is shown that the whole fracture surface is covered by dimples and the fracture surfaces are made by zigzag pattern. The B-B cross section of the SEM fracture surface (in Fig. 2 (a)) and a 3-dimensional image (in Fig. 2 (b)) are shown in Fig. 2 (c). The void shape at the position A is clearly shown in the B-B cross section. The void aspect ratio A_v is defined as the ratio of the void depth h to the mean void radius $d/2$ in the fracture

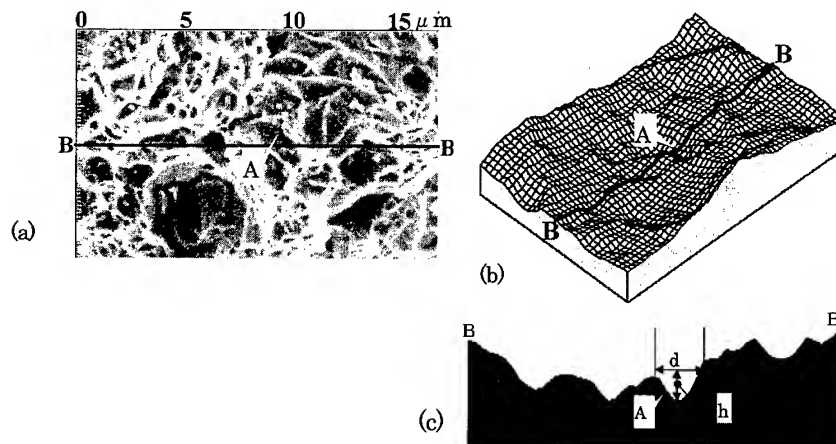


Fig. 2. 3-Dimensional Imaging of SEM Fracture

surface, which is perpendicular to the loading direction. The void volume fraction is obtained by measuring all micro void volume in a local fracture surface, which is calculated using 3-dimensional imaging data from the SEM photos by the following equation.

$$f_F = \frac{\sum_{i=1}^n V_{void}}{Ad_m} \quad (1)$$

where A is the sum of the SEM photos area and d_m is the mean dimple diameter, which is obtained by approximating a void as a sphere. $\sum V_{void}$ is the sum of the micro void volume in measured fracture surface.

2 EXPERIMENTAL OBSERVATION

2.1 The Changes of Void Volume Fraction

Fig. 3 shows the change of the average void volume fraction when void diameter is less or greater than $1.5\mu\text{m}$. The void volume fraction is defined by using equation 1. Only two special specimen results are plotted here. One is SiC0% specimen with $\alpha=0.33$ (very weak SiC particle interaction and low stress-triaxiality), and the other one is SiC10% specimen with $\alpha=2.5$ (very strong SiC particle interaction and higher stress-triaxiality). The real line with square symbol for the SiC10% specimen and

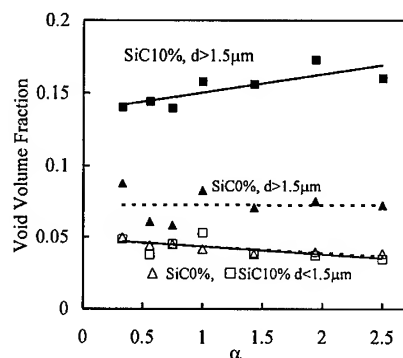


Fig. 3. The Average Void Volume Fraction with Different Stress-triaxiality

dotted line with triangle symbol for the SiC0% specimen. Solid symbol represents void diameter over $1.5\mu\text{m}$ and blank symbol represents the one less than $1.5\mu\text{m}$. When the void diameter less than $1.5\mu\text{m}$, the void volume fraction is nearly equal in all specimens. But when void diameter greater than $1.5\mu\text{m}$, the void volume fraction increases with the increase of stress-triaxiality in SiC10% specimens. Void volume fraction of SiC10% specimens is greater than the SiC0% specimens. It means that there is the same stress state or constraint near the surrounding comparatively smaller voids. This is due to that the largest void nucleated at earlier stages of deformation and it grows various shapes of larger voids. These larger voids make some amount of free surfaces in the matrix simultaneously and global/local constraint is changed. Then at final fracture the largest voids are linked by coalescence of small voids and thus there are nearly same constraint and stress states.

2.2 Relations between the Void Volume and Size

Fig. 4(a) and (b) show the change of the void volume with respect to the void diameter of two special specimens as mentioned above. The solid triangle symbol represents the SiC0% specimen with $\alpha=0.33$ and the blank square symbol represents the SiC10% specimen with $\alpha=2.5$. Real line in this figure is power approximation of plotted data for SiC0% specimen with $\alpha=0.33$, and dotted line for SiC10% specimen with $\alpha=2.5$. The theoretical results for $A_v=0.35$ (blank circle symbol line) and $A_v=1.0$ (solid circle symbol line) are also shown in this figure. It is shown there is no so much difference of these two special specimens plotted data and the approximate curves are very close each others. This also indicates that the approximate void shapes are mainly controlled by void diameter (size). As shown in Fig. 4(b) (enlarged results of Fig. 4(a)), in the area of void diameter less than $1.5\mu\text{m}$, the approximate curve is very close to $A_v=0.35$ curve. In the area of void diameter over $1.5\mu\text{m}$, it is separated from $A_v=0.35$ curve and due to increase of the void diameter it is come near to $A_v=1.0$ curve. It means that the comparatively larger voids deeper than the smaller one. However, as shown in Fig. 4(b), if the voids are too small (in this experimental results the void diameter smaller than $1.5\mu\text{m}$), the shape of voids approximately seems to be a constant.

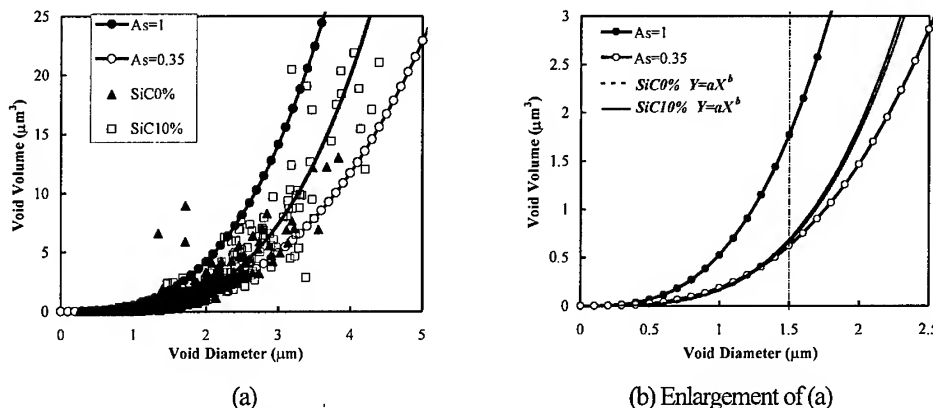


Fig. 4. The Relation between the Void Volume and Void Diameter

2.3 Relations between the Local Void Volume Fraction and a Void Shape

It is difficult to define the void volume fraction of local or single void. The problem is how to define the cell size. Hom & McMeeking[12] cell model results show that the uniaxial straining only occurs in high stress triaxiality condition. In uniaxial tension condition there is no void interaction and in pure shear condition no uniaxial straining. The equivalent plastic strain in high stress triaxiality condition is nearly uniformly distributed on the upper side of cell model. Due to this numerical result it may be roughly assumed that the final fracture occurs by the mutual interaction of neighboring micro void during the uniaxial straining, and the effective plastic straining area, which includes one void, is assumed to be equal to largest diameter of ellipsoidal or oblate void. In

this study as shown in Fig. 5(a) only the final void volume fraction at fracture is considered and it is assumed that the void diameters are equal to cell height and width. Then the local void volume fraction at fracture can be measured from the fracture surfaces. Fig. 5(b) shows the change of the local void volume fraction at fracture with respect to the void aspect ratio of two special specimens as mentioned above. It is shown that the void volume fraction at fracture is increased with increase of the void aspect ratio and gives a linear relation. It means that the voids change verity of shapes and size by the different local constraint during the deformation. Fig. 5(c) shows the distribution of the void aspect ratio of two special specimens as mentioned above. It is shown that the void aspect ratio changed from 0 to 1.0. Though the two special specimens show the different distribution at void aspect ratio 0.3 region, the relation between the aspect ratio and final void volume fraction at fracture show the same linear distribution.

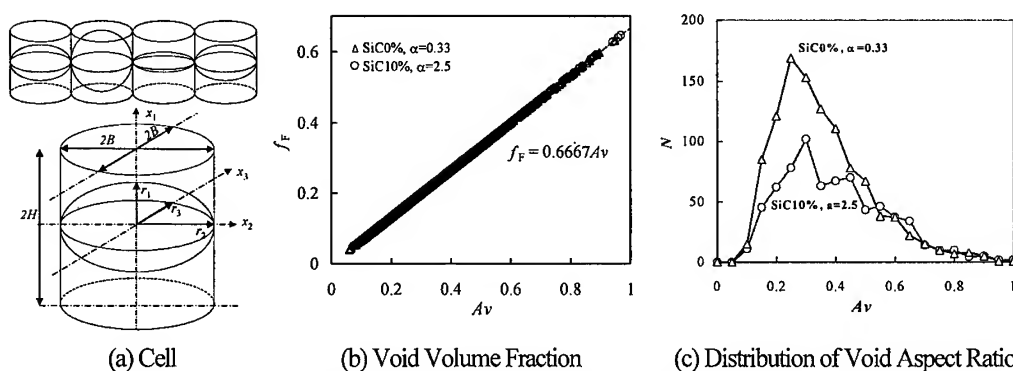


Fig. 5 Final Void Volume Fraction at Fracture

3 NEW MODIFIED GURSON MODEL

Early investigations studied the void evolution in ductile material. McClintock[13] studied the evolution of cylindrical voids and Rice and Tracey[14] considered the spherical voids in infinite rigid perfectly plastic media. Gurson[15] developed an approximate model for ductile metals containing cylindrical and spherical voids. Gurson assumed that the void is distributed randomly in the matrix, so that the global response of the model is isotropic. Then Gurson proposed the yield condition for a spherical void model containing a void volume fraction, f , as follows,

$$\Phi = \frac{\sigma_e^2}{\sigma_m^2} + 2q_1 f \cosh \left\{ \frac{q_2 \sigma_{kk}}{2\sigma_m} \right\} - 1 - (q_1 f)^2 = 0 \quad (4)$$

where σ_e is the equivalent stress, f is the void volume fraction and σ_m is the equivalent stress of the matrix. The constants $q_1=1.5$ and $q_2=1.0$ are introduced by Tvergaard[16]. The change of the value f is modified by Tvergaard and Needleman[17] to model loss of stress carrying capacity of the matrix as follows:

$$f = \begin{cases} f, & f \leq f_c \\ f_c + \frac{1/q_1 - f_c}{f_F - f_c} (f - f_c), & f > f_c \end{cases} \quad (5)$$

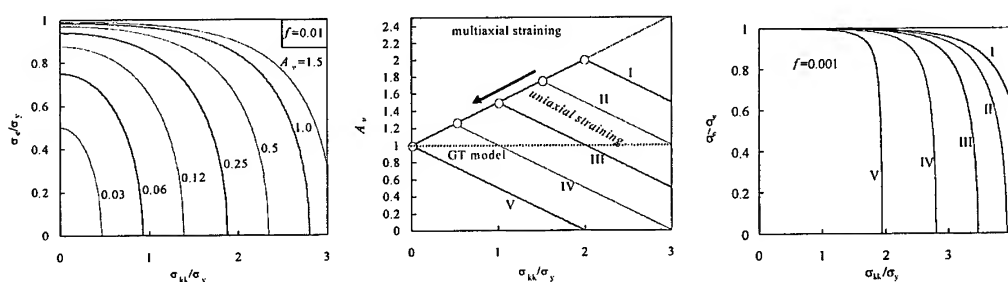
where f_c is the critical void volume fraction, and f_F is the value of f at fracture.

However, the experimental results show: f_F and Av are changed by different stress or deformation state. It means that the void coalescence occur in different condition and with variable shapes. So that the damage parameter f_F and q_1 may change and is not assumed to be constant. As shown in Fig. 7(b) the final void volume fraction at fracture is measured experimentally and the relation with the void shape is $f_{ex}=2Av/3$. As shown in equation (5), Tvergaard introduced that the final void volume fraction (to model loss of stress carrying capacity) is $f=1/q_1$. It is clear that, at final fracture it should be $f_{ex}=f$ and $2Av/3=1/q_1$. So that $q_1=1.5/Av$ and it replaced to equation (4) then obtain following form:

$$\Phi = \frac{\sigma_e^2}{\sigma_m^2} + \frac{3}{Av} f \cosh\left\{\frac{q_2 \sigma_{kk}}{2\sigma_m}\right\} - 1 - \left(\frac{1.5}{Av} f\right)^2 = 0 ; \quad \text{where } Av = \frac{2r_1}{r_2 + r_3} > 0 \quad (6)$$

r_1, r_2 and r_3 are void radius along the 3 principal axis as shown in Fig. 7(a). This equation includes the effect of void shape, which is controlled by stress triaxiality and the deformation constraint.

Fig. 6(a), (b) and (c) show the change of yield surface by changing the void shape. In the usual Gurson model as well as the modified Gurson model, the void aspect ratio is assumed to be constant ($Av=1.0$) and the yield surface is only changed by void volume fraction. So it has difficulty to evaluate the shallow or sharp void using conventional modified Gurson model. In the new model as shown equation (6), the yield surfaces are changed by changing the void aspect ratio as shown Fig. 6(a). It is clear, when $Av=1.0$ the material yield at $\sigma_0/\sigma_y=0.98$ and $\sigma_{kk}/\sigma_y=2.8$, and if $Av=0.03$ it yield at $\sigma_0/\sigma_y=0.5$ and $\sigma_{kk}/\sigma_y=0.45$. This new model also correctly evaluates the multi-axial straining to uniaxial straining during the deformation. Fig. 6(b) shows the change of the void aspect ratio during the multi-axial to uniaxial straining. 5 simple cases, linearly multi-axial straining then linearly uniaxial straining, are shown in Fig. 6(b). The yield surfaces are shown in Fig. 6(c). It is shown that the yield surfaces are largely changed by the different straining rate. In V case, it is shown the material yield at $\sigma_0/\sigma_y=1.0$ and $\sigma_{kk}/\sigma_y=2.0$.



(a) with different Av

(b) change of Av in different straining

(c) with changeable Av

Fig. 6. The Yield Surfaces with Different Void Aspect Ratio

4 CONCLUDING REMARKS

In the present work the damage process under different constraint condition has been qualitatively identified and some reasonable damage phenomena compared with experiments has been observed.

1. The local void size, shape and volume fraction is measured experimentally. The results shown that the final void volume fraction at fracture is increased by increasing the void aspect ratio. The void aspect ratio is increased by increasing the void diameter.
2. The experimental observation shown that the final void volume fraction and void shape are not constant. Stress triaxiality and deformation constraint largely affect the void aspect ratios and the void volume fraction.
3. The effect of void shape is considered and new modified Gurson model is proposed based on the

experimental results and theoretical approach. It is shown the new model gives reasonable results with real structure.

During this study it was clear that the stress triaxiality and constraint largely affect the void aspect ratios and the final void volume fraction at fracture. This effect had been considered by modifying Gurson model using the experimental result. However, it needs comparison with some cell model results by numerical analysis. Then it also needs to find how to define the uniaxial straining point during the deformation and we intend to pursue it in the future.

REFERENCES

1. D. J. Lloyd, *Acta Metall. Mater.* Vol.39, No.1(1991), pp.59-71.
2. D. J. Lloyd, *Int. Materials Reviews*, Vol.39, No.1(1994), pp.1-21.
3. Mamtimin Geni, Masanori Kikuchi and Kazumi Hirano, *Trans. JSME*, Vol.61, No581, A(1995), pp.45 - 51. (In Japanese).
4. J. Llorca, A. Needleman and S. Suresh, *Acta Metall. Mater.* Vol.39, No.10(1991), pp.2317-2335.
5. Tohgo, K., Weng, G.J., *Trans. ASME, J. Engng. Mater. Tech.*, Vol.116, (1994), pp.414-420.
6. M. Geni and M. Kikuchi, *Computational Materials Science.*, To be published. Editorial reference: V31, 1999.
7. J. Llorca, S. Suresh and A. Needleman, *Metallurgical Transactions A*. Vol.23, A(1992), pp.919-934.
8. G. L. Povirk, M. G. Stout, M. Bourke, J.A. Goldstone, A. C. Lawson, M. Lovato, S. R. Macewen, S. R. Nutt and A. Needleman, *Acta Metall. Mater.* Vol.40, No.9(1992), pp.2391-2412.
9. M. Kikuchi, M. Geni and K. Hirano, "Damage analysis of discontinuous SiC reinforced aluminum alloy", in "Computer-Aided Assessment and Control", Localized Damage IV, Edited by H. Nisitani, M.H. Aliabadi, S.-I. Nishida and D. J. Cartwright, Published by Computational Mechanics Publications, 1996, pp.425-432.
10. M. Kikuchi, M. Geni, T. Togo, and K. Hirano, "Strength Evaluation of Whisker Reinforced Aluminum Alloy", in "Mechanisms and Mechanics of Composite Fracture", Edited by R.B. Bhagat, S.G. Fishman and R. J. Arsenault, Published by ASM International, 1993, pp.97-106.
11. P.W. Bridgman: *Studies in Large Plastic Flow and Fracture*, McGraw-Hill, New York, NY, (1952), pp.9-37.
12. Hom and McMeeking, *J. App. Mech.*, Vol.56, (1989), pp.309-316.
13. F. A. McClintock, *ASME Journal of Applied Mechanics*, Vol.35, (1968), pp.363-371.
14. J. R. Rice and D. M. Tracey, *J. Mech. Phys. Solids*, Vol.17, (1969), pp.201-217.
15. Gurson, A. L., *Trans. ASME, J. Eng. Mat. Tech.*, Vol.99, (1977), pp.2-15.
16. V. Tvergaard, *Int. J. Fract.*, Vol.18, No.4 (1982), pp.237-252.
17. V. Tvergaard and A. Needleman, *Acta Metall. Mater.*, Vol.32, (1984), pp.157-169.

Modeling of Mechanical Property Degradation by Short-Term Aging at High Temperatures

J. Kim and W.I. Lee

Department of Mechanical Engineering, Seoul National University,
Shinrim-dong, Kwanak-gu, Seoul 151-742, Korea

Keywords: Flexural Properties, Mathematical Modeling, Mechanical Property Degradation, Numerical Minimization, Thermal Aging, Thermoplastic Polymer

ABSTRACT

A study on the mechanical property degradation by short term aging at high temperatures is performed. Samples are manufactured using a thermoplastic polymer (PEEK) and APC-2, and are aged at different temperatures for different times. The flexural properties of the aged samples are measured by 4-point bending tests. An appropriate form of mathematical equation is proposed to model the degradation data as a function of time and temperature. Numerical techniques are employed to find the optimal values of the parameters using transient temperature profiles. Discussions are made on the physical validity of the results. To illustrate the effectiveness of the derived model, it is applied to a mathematically defined service condition. The model could successfully predict the property loss during service, which could act as a reference in determining the durability and the lifetime of the product.

1. INTRODUCTION

History of exposure to elevated temperatures can affect the mechanical property degradation in a significant manner. Slow and relatively small decay of properties takes place when environmental temperature is below the melting temperature of the polymer [1]. When the aging temperature is higher, rapid degradation occurs resulting in larger property loss. This mode of degradation usually accompanies weight loss of the polymer [2-5]. The main mechanisms involved in the property decrease in this case can be summarized into two categories [5,6]. First one is the structural change within the polymer, which is mainly polymer chain scission. Second one is mass loss, which can also include the effects of voids and cracks. The first mechanism may or may not accompany noticeable weight loss. Therefore, it can be implied that weight loss alone might not act as the sole parameter characterizing property degradation. Thus, in order to predict the mechanical property decrease properly, it is essential to have direct modeling of the data relating various properties directly to the history of thermal aging. In this study, an experimental methodology enabling mathematical modeling of mechanical property degradation by short-term thermal aging at high temperatures is introduced in order to predict the proper mechanical property decrease. PEEK (Polyether-ether-ketone) is chosen as the sample material because it is often used in high

temperatures is introduced in order to predict the proper mechanical property decrease. PEEK (Polyether-ether-ketone) is chosen as the sample material because it is often used in high temperature and, therefore, thermal aging characteristics are very important in lifetime predictions.

2. EXPERIMENTAL PROCEDURES

Samples 1-mm thick are manufactured using PEEK powder. In order to maintain the shape of the sample at temperatures higher than melting temperature, APC-2 (Graphite/PEEK prepreg) are placed on the top and bottom surfaces of the sample. Two thermocouples are embedded within the powder layer at different locations to monitor in-situ temperature history. Hot press is used to mold the sample into a single body. The samples are held in a frame and are heated by radiation from ceramic heating plates. In order to prevent oxidation of the sample during heating, an inert atmosphere of N_2 is employed. The temperatures within the sample are recorded using an A/D converter and a PC. Samples are aged at 21 different time/temperature conditions. The ranges of the temperature and time used are summarized in Table 1.

4-point bending tests are performed to measure the flexural properties of the degraded polymer. Both flexural modulus and strength are measured for each specimen.

Table 1. Aging conditions and number of aging samples and flexural test specimens

Aging Temperature	540~640°C
Time of Exposure	8~60 sec
No. of Aging Samples	21
No. of Flexural Test Specimens	158

3. MATHEMATICAL MODELING

3.1. Temperature Modeling

In order to utilize the unsteady temperature data, the temperature profiles should be fitted into smooth functions of time expressed explicitly in mathematical equations. A typical temperature profile is shown in Fig. 1. This temperature profile is fitted using two different equations, each describing heat up and cool down. The fitted curve is also plotted in Fig. 1 (b), which shows a close resemblance with the actual data.

3.2. Mechanical Property Degradation Model

The kinetic equation describing weight loss of PEEK at high temperatures is as follows [5];

$$\frac{d\alpha}{dt} = k[y_1(1-\alpha) + y_2\alpha(1-\alpha)] \quad (1)$$

where α is a factor representing weight loss. The rate constant k is expressed by the Arrhenius equation. Since the mechanisms of mechanical property degradation by thermal aging can be assumed to be similar with those of weight loss [2,3], it is reasonable to use the same equation form. In order to maintain analogy, α should be replaced with $(1-P/P_0)$ where P and P_0 denote the current and initial value of mechanical property, respectively. Integrating the altered form of Eq. 1, followed by some manipulation, the resulting equation can be written as

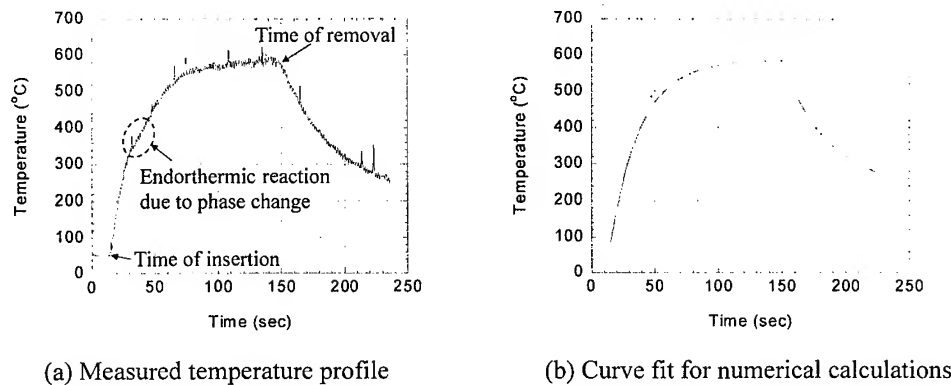


Fig. 1. An example of the temperature profile during sample aging.

$$\frac{P}{P_0} = \frac{1 + y_2/y_1}{\exp(A\tau_n) + y_2/y_1} \quad (2)$$

where

$$\tau_n = \int_{t_{ms}}^{t_{final}} \exp\left(-\frac{E}{T_n(t)}\right) dt \quad (3)$$

$T_n(t)$ denotes the temperature history function for sample n , and A and E are the pre-exponential factor and the activation energy in k , respectively. The simplest numerical integration using trapezoidal method is applied to evaluate τ_n . The parameters A , E and y_2/y_1 in the model Eq. 2-3 are determined as the values yielding best fit to data points. Method of least squares is adapted and the Chi-square indicating deviations between experimental and calculated values is minimized using multi-dimensional *downhill simplex method* proposed by Nelder and Mead [7].

Table 2 summarizes the results of numerical calculations. The standard deviations for both cases are within acceptable range, considering that the large scatter is inevitable in the data due to severe aging conditions. The magnitudes of the ratios of weighting factors y_2/y_1 are very small for both cases, implying that the second order term in Eq. 1 can be ignored for both cases. Thus, the properties can be assumed to decay in a simple exponential manner, and the equations can be rewritten as

$$\text{Modulus: } \frac{d(M/M_0)}{dt} = -3060.61 \exp\left(-\frac{11522.30}{T}\right) \frac{M}{M_0} \quad [s^{-1}] \quad (4)$$

$$\text{Strength: } \frac{d(S/S_0)}{dt} = -23947.66 \exp\left(-\frac{12733.94}{T}\right) \frac{S}{S_0} \quad [s^{-1}] \quad (5)$$

4. DISCUSSIONS

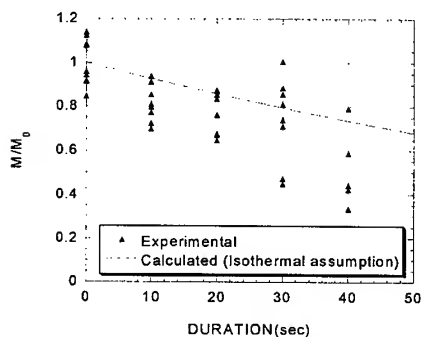
4.1. Illustration of Model Validity

As an example of model verification, the comparisons of experimental data and calculation

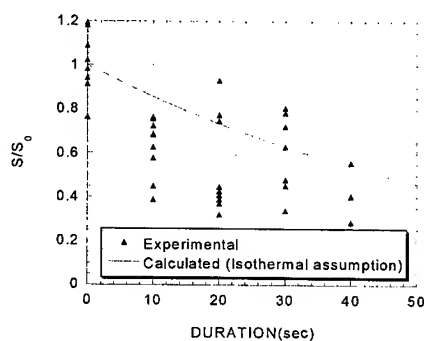
results are shown in Fig. 2. Isothermal assumptions are applied in the calculations using the average steady temperature of the corresponding samples. Results show that the model agrees with the decaying characteristics fairly.

Table 2. Summary of numerical curve-fit results.

Flexural Modulus	$A \text{ (s}^{-1}\text{)}$	3060.612431
	$E \text{ (K)}$	11522.30476
	γ_2/γ_1	$0.31134668 \times 10^{-15}$
	Standard Deviation	0.185044
Flexural Strength	$A \text{ (s}^{-1}\text{)}$	23947.66545
	$E \text{ (K)}$	12733.94401
	γ_2/γ_1	$0.72389448 \times 10^{-12}$
	Standard Deviation	0.216204



(a) Modulus degradation model



(b) Strength degradation model

Fig. 2. Comparison of experimental data with isothermal calculation results (set temperature 620°C)

4.2. Relations Between Mechanical Property Degradation and Weight Loss

The contributions of the two different mechanisms on mechanical property decrease, which are structural change and mass loss, can be compared quantitatively by observing the relations between the property decrease and weight loss. The weight loss factor α is calculated for each temperature history of the samples using the model given by Nam [5]. The experimental and calculated values of the residual flexural strength ratio for each sample are plotted versus α in Fig. 3. Most of the property is lost when weight loss is very small. As weight loss increases, the additional property decrease becomes negligible. Nam suggests that structural changes dominate the early stage of degradation, producing reacting gases from polymer chain scission. Additional weight loss is resulted from the catalytic reactions of the reacting gases. Nam's model equations imply that the chain scission does not accompany large weight loss and the majority of mass is lost by catalytic reactions. Since most of the property decay occur at α 's smaller than 0.2, it can be concluded that the structural changes in the early stage of degradation play a dominant role in the mechanical property decrease. Additional weight loss after deterioration does not have a significant effect because the mass remaining after chain scission possesses poor mechanical properties. Therefore it

can be stated that weight loss alone cannot serve as a sufficient factor describing thermal aging characteristics.

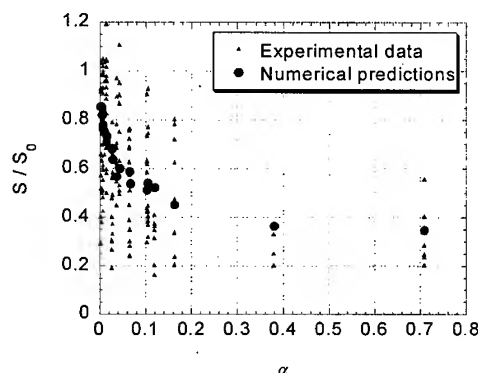


Fig. 3. Relations between mechanical property degradation and weight loss

5. NUMERICAL EXAMPLE (DURABILITY PREDICTION)

Utilizing the ability of predicting property degradation for arbitrary temperature history, the model derived from the experiment can give lifetime predictions when the service condition of a product is well defined. The lifetime of a product is usually determined by defining a lower limit of the mechanical property allowable for service. When the property degrades below the limit, the part is replaced by a new one. The numerical results can serve as a reference in determining the time of replacement.

An example is given here for a product which experiences one thermal spike per week, described as a parabolic function of time. The total duration of the spike is 10 seconds and the peak temperature is changed from 500 °C to 580°C. The thermal conditions and calculated results are illustrated in Figure 4. Assuming the minimum allowable limit of the property to be 90% of its initial value, the lifetime of the product shortens from 37 weeks to 9 weeks when flexural modulus is considered as the dominant property. When the flexural strength is considered, the lifetime changes from 24 weeks to 5 weeks. The 80°C change in the peak temperature results in shortening the lifetime down to a quarter or one-fifth, even though the effective exposure time above critical temperature of degradation (400°C) is only 5 seconds or shorter. This implies that the accumulation of repeated negligible degradation can result in a large difference in the total lifetime of the product.

6. CONCLUSIONS

A method of modeling the mechanical property degradation by short term aging at high temperatures is introduced. PEEK samples are aged at different temperatures for different times. The flexural properties of the aged samples are measured by 4-point bending tests. A mathematical equation is proposed to model the degradation data as a function of time and temperature. Numerical techniques are employed to find the optimal values of the parameters using transient temperature profiles. It could be concluded from the modeling results that the weight loss, which

was previously considered as a factor describing degradation phenomenon, fails to provide sufficient explanations to the mechanical property decrease. Finally, a numerical example is given to illustrate the effectiveness of the derived model.

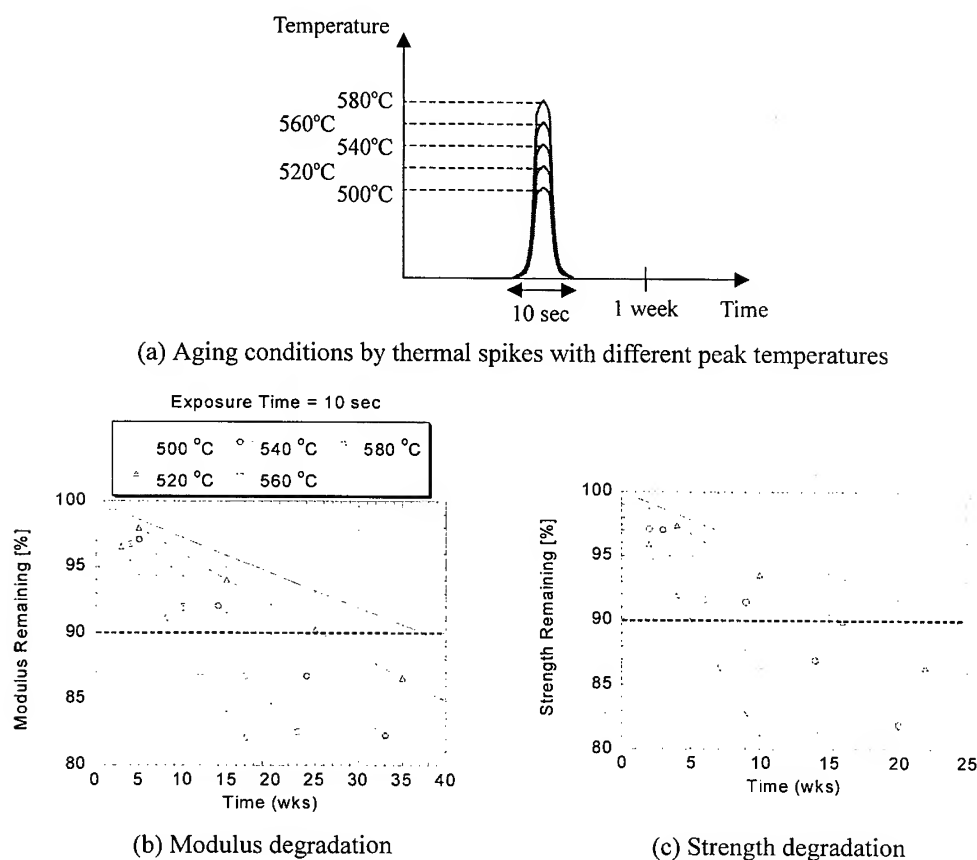


Fig. 4. Durability predictions for thermal spikes with different peak temperatures

REFERENCE

1. M.Buggy and A.Carew, *J. Mat. Sci.*, **29** (1994) p.1925
2. K.L.Reifsnider, D.A.Dillard and A.H.Cardon (Eds), *Progress in Durability Analysis of Composite Systems*, Balkema, Rotterdam (1998) p.193
3. G.A.Pering, P.V.Farrell and G.S.Springer, *J. Comp. Mat.*, **14** (1980) p.54
4. J.Nam and J.C.Seferis, *J. Polym. Sci.: Part B: Polym. Phys.*, **29** (1991) p.601
5. J.Nam and J.C.Seferis, *J. Polym. Sci.: Part B: Polym. Phys.*, **30** (1992) p.455
6. J.Kim and W.I.Lee, *Composites Durability Workshop: CDW '98, Japan, Kanazawa* (1998) p.16.2
7. W.H.Press, S.A.Teukolsky, W.T.Vetterling and B.P.Flannery, *Numerical Recipes in Fortran The Art of Scientific Computing*, 2nd Ed., Cambridge University Press (1992)

On Failure Modes and Strength Characterization of Brittle Disordered Materials under Uniaxial Compression and Tension

C.A. Tang^{1,2}, P. Lin¹, H.Y. Liu¹ and Z.Z. Liang¹

¹ CRISR, Resources and Civil Engineering School, Northeastern University,
Shenyang 110006, China P.R.

² LNM, Institute of Mechanics, Chinese Academy of Sciences,
Beijing 100080, China P.R.

Keywords: Brittle Failure, Heterogeneity, Localization, Nonlinear Behavior, Numerical Simulation, Strength

ABSTRACT

With a newly developed Material Failure Process Analysis code (MFPA^{2D}), influence of heterogeneity on fracture processes and strength characterization of brittle disorder materials such as rock or concrete is numerically studied under uniaxial compression and tension conditions. It is found that, due to the heterogeneity of the disordered material, relatively more diffused micro-fractures appear in the early stage of loading. Different from homogeneous materials such as glass, macro-crack nucleation starts well before the peak stress is reached and the crack propagation and coalescence can be traced, which can be taken as a precursory to predict the macro-fracture of the material. The presence of residual strength in the post-peak region and the resemblance in the stress-strain curves between tension and compression are significant results and are found to be dependent on the heterogeneity of the specimens. Examples showing the tentative applications of MFPA^{2D} in modeling failure of composite materials and rock or civil engineering problem are also given in this paper.

1. INTRODUCTION

The failure behavior of quasi-brittle materials such as rock or concrete is characterized by nonlinear deformation prior to the peak strength is attained, followed by the weakening (or sometimes called softening [1]) and localization of deformation in the post-peak part. Thus, neither linear elastic fracture mechanics nor plasticity models can be adequately used to describe such behavior [2]. Although nonlinear fracture mechanics or nonlocal continuum models can provide a general description, they are incapable of capturing the influence of the heterogeneity at the micro or meso-level [2] and therefore difficult to be used to investigate the micro-fracture induced progressive failure of the disordered materials. Even under uniform loading conditions, the stress distribution in micro or meso scale is not uniform since rock or concrete materials contain numerous small defects that are randomly distributed within the materials. These defects significantly affect the physical properties of the materials and result in local disorder features of the stress distribution if loaded. Consequently, direct simulation of the randomness of disordered material microstructure is useful in arriving at a better understanding of brittle failure and the improved prediction of the mechanical properties.

Based on experimental observations, material behavior models can be constructed. The models can be either analytical or numerical. The analytical models lead to correct answers within the frame

work of axioms underlying the mathematics. However, in most of the cases, analytical models have to be simplified and sometimes this simplification ignores very important factors influencing the material behavior. Heterogeneity is such an example for rock or concrete.

Statistical modeling has emerged as a promising technique for analysis of fracture in heterogeneous materials such as rock or concrete [3]. The combinations of statistical theory with numerical models such as the lattice model [4], the bonded particle model [5-6], or tensile fracture models based on FEM [2,7] are found to be quite appropriate for modeling brittle disordered materials such as rocks

In this paper, uniaxial tensile and compressive tests with specimens of brittle disordered materials were numerically studied by using a Material Failure Process Analysis code (MFPA^{2D}), developed recently by CRISR at Northeastern University [1]. Following a brief description of the numerical model and the loading procedures adopted in this investigation, some characteristic features of the complete stress-strain curves under uniaxial tension and compression and the phenomena observed during progressive fracture of disordered materials will be summarized in terms of heterogeneity, deformation localization, fracture nucleation or coalescence, and micro-fracture induced seismic activities. Finally, some examples showing the tentative applications of MFPA^{2D} in modeling failure of composite materials and rock or civil engineering problems are also given in this paper.

2. BRIEF OUTLINE OF MFPA^{2D}

Numerical simulation is currently the most popular method used for modeling deformation behavior of brittle materials before failure. Even though progress has been made in numerical simulation of failure occurring in these materials, there is a lack of satisfactory models that can simulate the progressive failure in a more visualized way, including simulation of the failure process, failure induced seismic events and failure induced stress redistribution.

The demand for new tools, which may contribute to a better understanding of the failure mechanisms of brittle materials, has initiated the development of MFPA^{2D} (Material Failure Process Analysis code) based on RFPA^{2D}. The code, developed at CRISR, Northeastern University, China, can be used to model failure process of rock by considering the deformation of an elastic material containing a randomly initial distribution of micro-defects. Details of the model are given in [1], so only a few important points will be presented here.

Briefly, the disordered material properties (failure-strength σ_c and elastic module E_c) for elements are randomly distributed throughout the specimen by following a Weibull's distribution. We use a smeared failure approach that a micro-fracturing occurs when the stress of an element satisfies a strength criterion. A Coulomb criterion envelope with a tensile cut-off is used so that the failure of the elements may be either in shear or in tensile.

MFPA^{2D} is a Microsoft Windows application package for material failure analysis of mines/geotechnical structures using finite element technique as a calculator. A user-friendly pre- and post-processor is integrated to generate the model mesh and prepare the data input. The result may be displayed as an "animation" to aid the understanding of the mechanics of collapse.

3. MODEL PREDICTIONS FOR COMPRESSIVE AND DIRECT TENSILE LOADING

3.1. Influence of Heterogeneity on Stress-Strain Response and Strength Characterization

The heterogeneity of disordered materials has an important influence on the shape of stress-strain curves and the strength characterization. Fig.1 shows the simulated stress-strain curves in

compression for specimens with various homogeneity indices, $m=1.5, 2, 3$, and 5 (the smaller the value m , the wider the strength distribution). The specimens have a geometry of 150×100 mm. The load is applied in the vertical direction through displacement control. The simulations show that wider strength distributions yield an earlier onset of non-linear behavior and lower peak stresses, but a more gradual loss of strength after the peak.

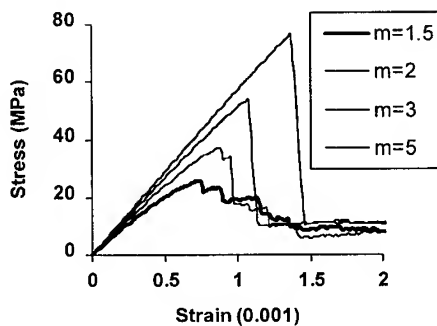


Fig.1 Influence of heterogeneity on stress-strain curves in compression

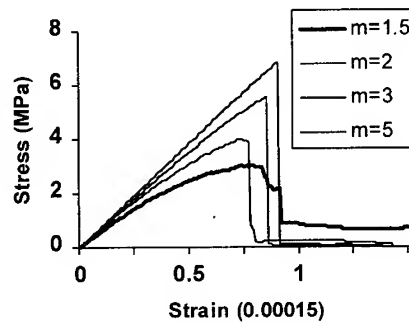


Fig.2 Influence of heterogeneity on stress-strain curves in tension

It is generally considered that the microscopic failure mechanisms in tension and compression are considerably different from each other. In compression, a failed portion does not completely lose its loading bearing capacity because of friction with the surroundings. However, in tension the loading capacity of failed portion decreases more rapidly than in compression. This consideration suggests a relative sharp decrease of loading bearing capacity of a specimen in tension. However, as observed by Okubo and Fukui [8] in their experiments, the shapes of the stress-strain curves do not differ much from each other in tension and compression. This has also been verified with our numerical simulations. Fig.2 shows the simulated stress-strain curves in tension for specimens with the same homogeneity indices as in compression. The resemblance in the stress-strain curves between tension and compression can be easily seen by comparing this Fig.2 with Fig.1. Though exact explanations for this result are difficult, heterogeneity mentioned above at least can be taken as one of the reasons for this resemblance.

Simulations of both compressive and tensile tests reveal that the maximum strength of the specimens is proportional to the homogeneity index.

3.2. Influence of Heterogeneity on Microfracture Behavior

The numerical results also demonstrate that the AE (acoustic emissions) event patterns are influenced greatly by the degree of heterogeneity of the materials. Fig.3 shows that AE count rate as a function of deformation for the four specimens with different homogeneity index. A comparison between Fig.1 and Fig.3 shows a good relationship between the modeled stress-strain curves and the modeled curves of event rate. The results show that the relatively heterogeneous specimen emits more AE events as the precursory of macro-fracture than that of the relatively homogeneous specimen. On the other hand, higher stress drop is observed to be correspondent to the higher event rate in relatively homogeneous specimens. The same conclusion may also be obtained from the simulation of tension tests.

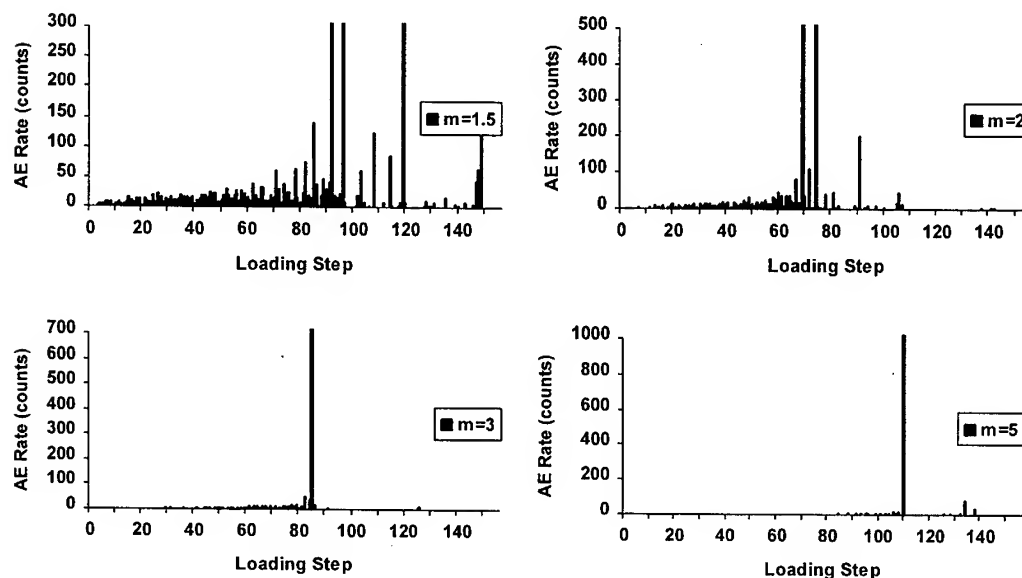


Fig.3 Influence of heterogeneity on AE patterns for specimens under compression

3.3. Influence of Heterogeneity on Failure Modes

One of the most important characteristics of post-peak behavior of brittle material under any loading scheme is the localization of deformation [2]. After reaching the maximum strength of the specimen, the deformation starts to concentrate in the fracture process zone (FPZ), while other parts of the specimen unloaded (the so-called elastic rebound in geophysics). Fig.4 and Fig.5 show that the current numerical model is capable of capturing this phenomenon. Comparing the stress-strain curve shown in Fig.1 or Fig.2 and the failure processes shown in Fig.4 or Fig.5, it is found that, few distributed fractures appear up to approximately 80% of the maximum strength. The number of these fractures increases considerably as the load approaches its ultimate value. Beyond the ultimate load, these fractures begin to concentrate in a certain zone. The maximum strength does not necessarily mean an abrupt failure of the specimen. Although the loading bearing capacity drops dramatically during the post-peak part, this does not indicate the collapse of the specimen. Subsequently, a distinct transition occurs and the loading capacity begins to decrease at a much slower rate until it reaches its residual strength, which is about 10-20% of its maximum strength.

3.4. Influence of Heterogeneity on Residual Strength

In Okubo and Fukui's experimental study, one result of particular interest was obtained in uniaxial tension testing: a large amount of residual strength remains in the post-failure region [8]. Peng conducted uniaxial tension tests and also found considerable large residual strength for tested four rocks [9]. The presence of residual strength in the post-peak region may be attributable to several reasons [9]. Heterogeneity or strength variation in a specimen is considered to be one of the reasons. If local strength variation is large, specimen failure starts in weak portions. Even in the post-peak region, strong portions are still intact and some amount of loading capacity remains whereas a macro-cra-

ck extends from boundary to boundary in a heterogeneous specimen.

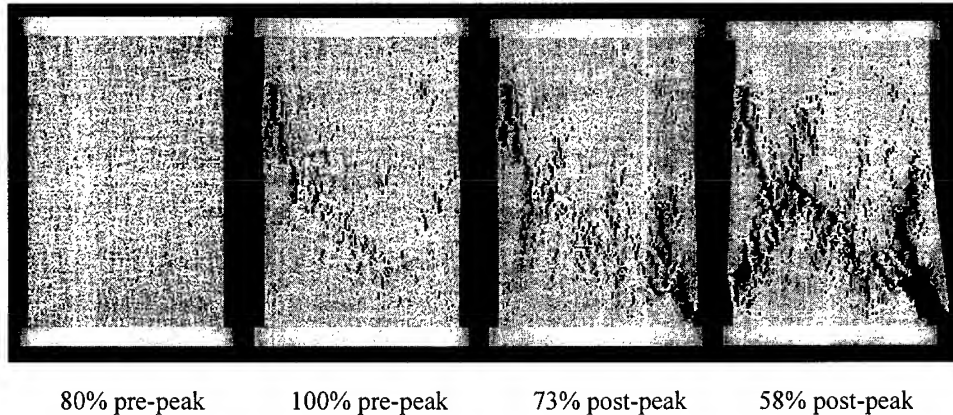


Fig.4 Numerical simulation of failure mode for specimen with $m=1.5$ under compression

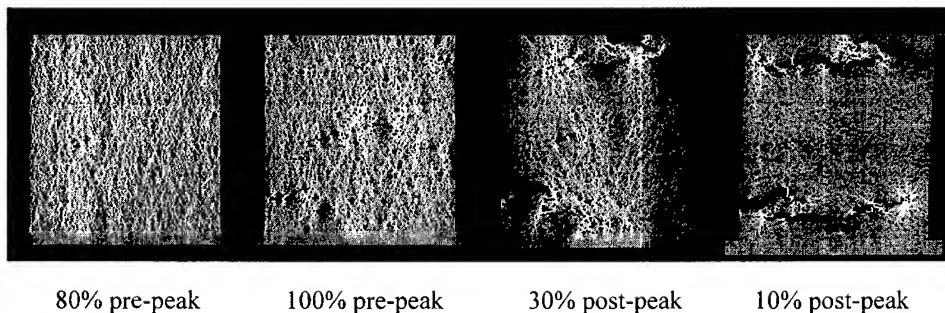


Fig.5 Numerical simulation of failure mode for specimen with $m=1.5$ under tension

The above mentioned reason can be understood well by studying the final failure mode of specimen as shown in Fig.5. Four detailed figures of the development of the crack interface bridging in the specimen in tension are shown in Fig.5. It is seen that at the final loading step, the crack has almost cross the section of the specimen but still showed a non-zero residual stress and further loading (tensile deformation) is very difficult to drive the cracks for a visible propagation. Clearly the cracks are not continuous, but rather overlaps and branches exist. Note that these overlaps are not isolated events in individual specimens, but they have been detected in relatively large quantity [10].

4. CONCLUDING REMARKS

It is important to identify the main failure mechanisms associated with brittle failure under compressive and tensile loading. This identification is crucial for better understanding and interpreting the experimental results and consequently, improves our concepts in material property design or analysis of rock or civil engineering structures. The model predications of brittle failure behavior of disordered materials in this paper capture most of the experimental observed

phenomena, including softening, deformation localization, and crack patterns. Although the simulations are not a quantitative approach and many conclusions presented here may have already been obtained by laboratory tests, the significance of mimicking these phenomena by numerical simulation is obvious. At least, and the most important, the successful reproducing of the experimentally observed failure phenomena with a numerical method implies that our understanding to the mechanisms of material failure has reached a more reasonable level, which in turn will help us to make further progresses in the field of material mechanics and rock or civil engineering. Fig.6 shows three examples of tentative application of MFPA^{2D} in modeling failure of composite materials or rock engineering structures.

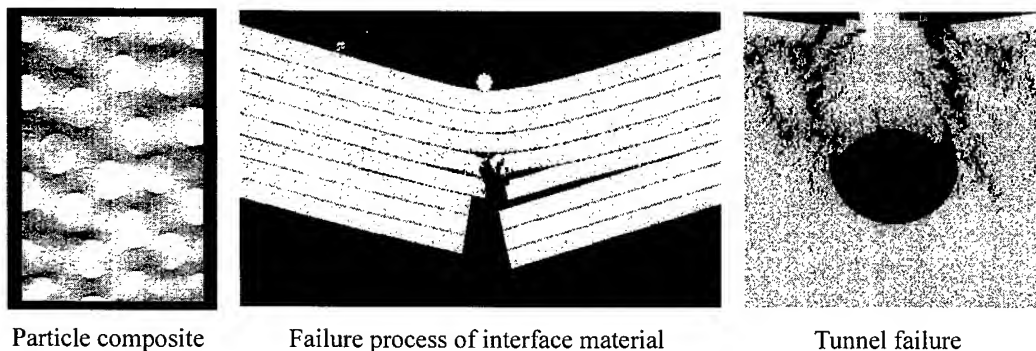


Fig.6 Examples of MFPA^{2D} applications on modeling material failure or construction collapse

ACKNOWLEDGMENT

The authors are grateful for the support of this work from the Chinese National Key Fundamental Research "973 Programme" (No.95-13-07-01) and the National Natural Science Foundation (No. 49974009).

REFERENCE

1. C.A.Tang, *Int. J. Rock Mech. Min. Sci.*, **34** (1997) p.249
2. A.R.Mohamed and W. Hansen, *ACI Materials J.*, **96** (1999) p.196
3. S.C. Blair and N.G.W. Cook, *Int. J. Rock Mech. Min. Sci.*, **35** (1998) p.837
4. J.G.M.Van Mier, *Fracture process of concrete*, CRC Press, New York (1997) p.253
5. P.A.Cundall., *Int. J. Rock Mech. Min. Sci.*, **25** (1998) p.107
6. R.Hart, P.A.Cundall and J.Lemos, *Int. J. Rock Mech. Min. Sci.*, **25** (1988) p.117
7. S.J.D.Cox and L.Paterson, *Deformation Mechanics, Rheology and Tectonics*, Geological Society Special Publication No.54 (1990) p.57
8. S.Okubo and K.Fukui, *J. Rock Mech. Min. Sci.*, **33** (1996) p.549
9. S.S.Peng, *Int. J. Rock Mech. Min. Sci.*, **12** (1975) p.125.
10. Van Mier J.G.M, *Fracture process of concrete*, CRC Press, New York, 1997.

**Influence of Tool Wear on Hole Damage in Small Diameter
Drilling of Printed Wiring Boards**
Investigation based on Estimation of Cutting Forces and Internal Damage

H. Inoue¹, T. Hirogaki², E. Aoyama³ and T. Katayama³

¹ Faculty of Engineering, Aichi University of Technology,
50-2 Manori, Nishihasama-cho, Gamagohri, Aichi 443-0047, Japan

² Faculty of Engineering, University of Shiga Prefecture,
2500 Hassaka-cho, Hikone, Shiga 522-8533, Japan

³ Faculty of Engineering, Doshisha University,
610-0394 Kyotanabe, Kyoto 610-0394, Japan

Keywords: Cutting Forces, Drill's Life, Internal Damaged of Drilled Hole, Printing Wiring Board, Small Diameter Drilling, Tool Wear

ABSTRACT

When drilling a printed wiring board (PWB), internal damage around the drilled hole significantly affects the durability of a PWB. For this reason, we proposed a method for determining the drill's life by studying the relationship between the extent of damaged zone and the number of drilled hole. The validity of this method was proved by observing changes in the cutting force. In addition, the study showed that this method is used for judging the machinability of PWBs made of other materials.

1. INTRODUCTION

Currently, PWBs made of glass fiber reinforced plastic (GFRP) are widely used as circuit boards for electronic devices. With the current trend in downsizing electronic devices, a circuit formed on a PWB is required to have a higher packaging density and reliability. When using a pin-insertion packaging method for integrated circuit (IC) parts on a PWB, the following problems occur: 1. There is a difference of surface roughness on the inner wall of the drilled hole (1-4); 2. A bending of drilled path(5); and 3. The extent of internal damage around the drilled hole (6,7).

Concerning the first problem, it is impossible to make a same surface roughness for the inner wall of a drilled hole because of the glass fiber reinforced composite material used for PWBs. The second problem comes from the installation condition and the rigidity of the drill, the quality of the cutting edge of the drill bit, and the inconsistent wear of cutting edge. Therefore, the problem does not always occur in the same manner. Regarding the third problem, the internal damage around a drilled hole expands as the cutting edge of drill bit wears. The internal damaged zone expands with an increased number of drilled holes. This internal damage around a drilled hole decreases the real hole distance for setting hole distance and also cause of the generation of the ion migration, which possibly causes disconnection when the PWB is used as an electronic circuit. As a result, the internal damage prevents us from increasing the number of holes per area and, furthermore, largely affects the durability, which is the

Reliability, of the product.

At this point, we focused on internal damage around the drilled hole. We examined the drill's life by determining the limit number of drilled hole. This was accomplished by observing the relationship between the extent of the damaged area and the number of drilled hole. The wear condition of the drill bit was observed and defined. Furthermore, a method to judge the influence of the change in materials of PWBs, which affects the wear of drill bit, was established. The relationship between the change in the cutting force and the wear of the drill bit was clarified.

2. SPECIMENS USED FOR THE DRILLING AND THE DRILLING METHOD

Two specimens were used for the drilling. One was a heat-resistant glass-cloth epoxy resin laminate of eight layers, 1.6-mm thick in total, sandwiched between copper films, following the basic structure of PWB materials. The other was a glass cloth-reinforced epoxy resin plate of one ply, 0.2-mm thick, made of the same glass cloth as was used in the first specimen and impregnated into the resin. The latter is for the purpose of observing any internal damage taking place around the drilled hole. For drilling, a numerically controlled (NC) drilling machine (Hitachi Seiko, ND-1H) was used. The two specimens were considered as one set, and when drilling both specimens simultaneously, the number of drillings was counted as one. The drilling was conducted by stacking three sets of specimens sandwiched between an aluminum plate on top and a paper base phenolic laminated sheet on bottom. The drill used was a carbide step drill on the market with a 1-mm diameter by two-step plane grinding. The number of drilled hole was determined to be 30,000 times, which would completely wear out the drill bit. To measure the cutting force, a Kistler dynamometer (Type 9273) was used. And both the spindle speed and the feed rate are changed on drilling the PWBs.

3. OBSERVATION OF THE INTERNAL DAMAGE AROUND THE DRILLED HOLE AND THE WEAR OF DRILL BIT

3.1 Observation of the internal damage around the drilled hole

An example of the internal damage that took place around the drilled hole at various conditions of drilling is shown in Fig. 1. The damaged zone was observed by means of transmitted light placed on the one-ply resin plate, which had been drilled simultaneously. The black portion around the drilled hole in the figure represents the internal damage. The extent of the damaged zone largely depends on the relative

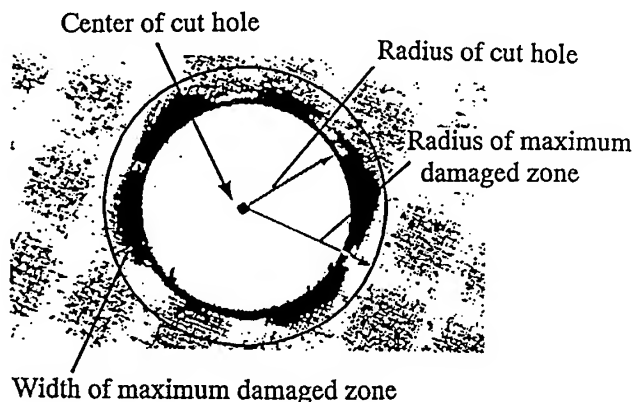


Fig.1 Definition of maximum width for internal damage zone

position of the drill bit against the direction of the glass fiber bundle and is, thus, not same. For this reason, the extent of the internal damage was defined as the maximum width of the internal damaged zone as shown in the figure1. That is, the maximum width of the internal damaged zone (L) is obtained by the difference between the radius of the maximum damaged zone and the radius of the drilled hole.

3.2 Observation of the wear of a drill bit

As the drill used in this study was a carbide step drill of two-step plane grinding, the shape of flank face is a trapezoidal shape. On the other hand, the wear of a drill generally progresses by the abrasive wear when it is used for cutting glass fiber reinforced plastic material(8.9). Therefore, we considered that most of the wear of drill that took place in this study was flank wear. From this, the progress of the drill-bit wear can be estimated by observing the change in shape of the trapezoidal flank face, which is considered to reflect the progress of the flank wear.

4. THE DECISION METHOD OF DRILL'S LIFE

4.1 The relationship between the extent of the internal damage around the drilled hole and the number of drilled hole

An example of the relationship between the maximum width of the internal damaged zone, around the drilled hole and the number of drilled hole is shown in Fig.2. The figure shows their relationship when the spindle speed was 80,000 rpm and the feed rate was $10 \mu\text{m}/\text{rev}$. The figure shows the number of drilled hole at which the maximum width of the internal damaged zone steeply increased. This was observed under other drilling conditions. When drilling PWBs, it is desirable to have as little internal damage around the drilled hole as possible. Therefore, we determined the limit number of drilled hole to be 3,200, occurring just before the maximum width of the internal damaged zone steeply increased, as is shown in this figure.

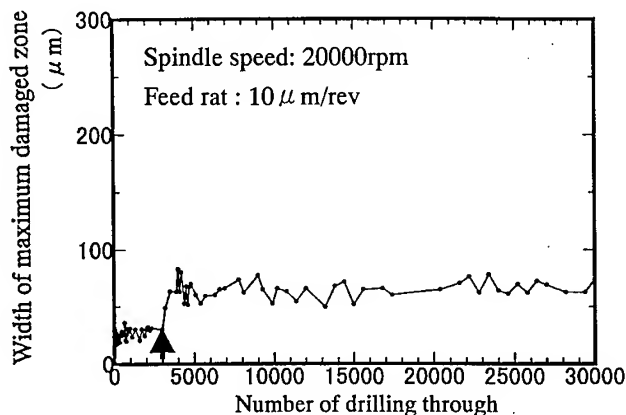


Fig.2 Relation between width of maximum damaged zone and number of drilled hole

The wear of a cutting tool generally taking place in the cutting FRP material is similar to the abrasive wear, and the abrasive wear depends on the cutting length. Therefore, by replacing the change of drilling conditions, such as the feed rate and the number of drilled hole, with the change in the cutting length, which corresponds to the wear on the tip of the drill bit, the cutting length L is obtained by the following equation,

$$L = \pi D N t / f \dots\dots\dots(1),$$

where L is the cutting length (m), D the drill diameter (m), t the thickness of the PWB, f the feed rate of the drill(m), and N the number of drilled hole.

From the above, the cut length which corresponds to the limit number of drilled hole obtained by Eq. (1) is the cutting length (L_c).

4.2 The shape of the worn drill bit at the limit number of drilled hole

Based on the limit number of drilled hole obtained from Fig.2 we drilled the PWBs and observed with scanning microscopy the shape of the drill bit at the limit number of drilled hole as well as before and after. The results are shown in Fig.3. The shape of the flank face of the drill bit at the limit number of drilled hole has been changed with its cutting edge retreating to the cO2 position from the original aO2 position as shown in Fig.3. In other words, if the drill is used until its cutting edge retreats beyond the cO2 position, the width of the internally damaged zone around the drilled hole expands steeply.

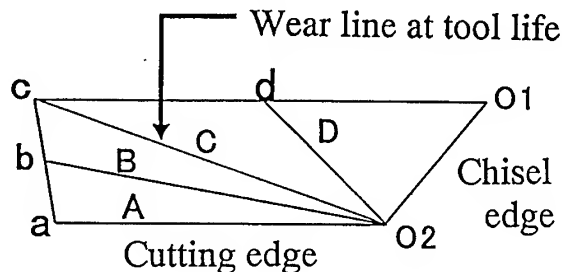


Fig.3 Schematic figure of flank face of worn drill bit

Next, the cutting edge of the drill bit does not retreat parallel to the cutting edge, as does the tool wear in an orthogonal cutting. Instead, it retreats revolving around the chisel edge. Therefore, we decided to use the remaining area of the flank face of the drill bit in order to measure the progress of the wear that occurs at the outer edge of the drill bit. In other words, we defined the amount of wear taking place during the drilling as the worn area of flank face(Φ : %), which reveals how much the cutting edge decreases, as in the following equation:

$$\text{The worn area of flank face} = \{1 - (\text{the remaining area of the flank face}) / (\text{the original area of the flank face})\} \times 100 \dots\dots(2)$$

The worn area of flank face of the drill bit when the drill bit is worn out obtained by Eq. (2) was approximately 60% under the conditions of this study.

5 THE INFLUENCE ON THE RELATION BETWEEN THE CUTTING LENGTH AND THE WORN AREA OF FLANK FACE BROUGHT BY THE CHANGE IN MATERIALS OF PWBS

Figure 4 shows the relationship between the cutting length and the worn area of flank face when various kinds of materials were used for PWBs. The symbols used in the figure show the materials of the PWBs to be as follows: A: Hard resin; B: Soft resin; E: E-glass fiber; and S: S-glass fiber. R indicates the contamination of a crack inhibitor. In the figure, the PWB made of S glass, which has a fiber strength greater than that of E glass, causes the drill bit to wear out sooner, or, in other words, it has poor machinability. On the other hand, the cutting length that can be drilled before wearing out a drill bit with

the hard resin is less than when using soft resin(10). Furthermore, the contamination of the additive changed the characteristics of the PWB because the crack inhibitor was a rubber-like material. Therefore, the cutting length of a drill bit with this changed material containing the additive is nearly the same as with PWBs made of soft resin.

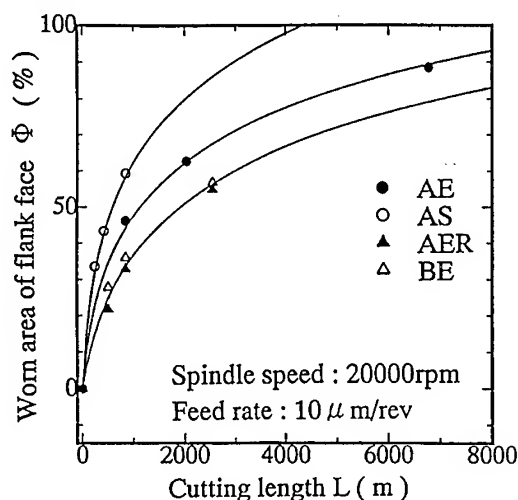


Fig.4 Relation between worn area of flank face and cutting length

6 THE RELATIONSHIP BETWEEN THE WEAR OF DRILL BIT AND THE CUTTING FORCE (THRUST FORCE)

In order to measure the cutting force during the drilling, four drills were prepared with flank faces of drills that were worn in the following conditions: no wear, near the wear line at tool life, and before and after the wear line at tool life, respectively. The relationship between the thrust force and the worn area of flank face when these drills were used is shown in Fig.5. The figure shows that the cutting force increases as the wear of the drill bits progresses, and the increasing rate changed steeply when the worn area of flank face reached the drill's life. On the other hand, the cutting force increases with the increase of the feed rate, and it increases in almost the same manner for the worn area of flank face. In addition, it was observed that the change in materials of PWBs did not largely affect the change in cutting force.

As seen above, the method used in this study to judge the drill's life in relationship to the wear of a drill bit was proved to be appropriate from the measurement results of the cutting force. In addition, it was demonstrated that the machinability of PWBs in various materials could be examined by obtaining a life curve of a drill bit as is shown in Fig. 4.

7. CONCLUSION

In order to judge drill's life used for drilling a PWB, we focused on the extent of internal damage zone that takes place around drilled hole and proposed a method to estimate the drill's life from the relationship between the extent of the internal damage and the number of drilled hole. The results of the study are as follows:

1. The limit number of drilled hole was determined from the relationship between the extent of the internal damaged zone(the maximum width of the internal damaged zone taking place around the drilled hole) and the number of drilled hole.

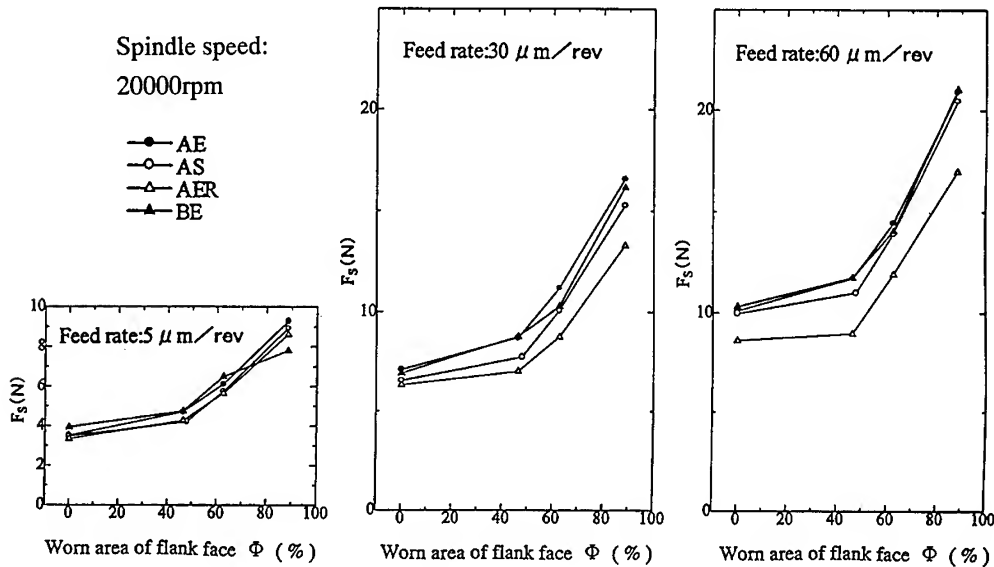


Fig.5 Relation between cutting force and worn area of flank face

2. The drill's life was defined according to the wear of the flank face of the drill bit at the limit number of drilled hole, and the relationship was clarified between cutting length, which corresponds to the number of drilled hole, and the wear of the drill bit.
3. A correlation was found between the change in the cutting force caused by the progress of the drill wear and the extent of the internal damage around the drilled hole
4. It was demonstrated that the influence on the drill's life caused by differences in materials used for PWBs can be easily measured by noting the relationship between the wear of a drill bit and the cutting length when different materials are used in PWBs.

REFERENCES

1. H. Inoue, S. Kondoh, T. Yasuhara, T. Kurashiki, K. Kariya and T. Yamaguchi, J. Textile Machinery Soc. Jpn., 47 (1994) p.T110
2. X. Wang, K. Nakayama and M. Arai, J. Jpn. Soc. for Precision Engineering, 55 (1989) p.709
3. C. W. Wern, M. Ramulu and K. Colligan, J. Mat. Proc. Tech., 37 (1993) p.39
4. H. Ho-Cheng and C. K. Dharan, Trans. ASME, J. Eng. for Industry, 112 (1990) p.236
5. M. Hiranaka, H. Yokouchi, X. Li, K. Kaito and H. Tusaka, J. Jpn. Soc. for Precision Engineering, 59 (1993) p.119
6. E. Aoyama, T. Hirogaki, H. Inoue, S. Gunjima, H. Nobe, Y. Kitahara and T. Katayama, J. Soc. Materials Science Jpn., 45 (1996) p.522
7. H. Inoue, E. Aoyama, T. Hirogaki, K. Ogawa, H. Matsushita, Y. Kitahara and T. Katayama, J. Composite Structures, 39 (1997) p.55
8. S. Tueda, Y. Hasegawa and S. Hanasaki, Trans. Jpn. Soc. Mech. Engr., 34 (1968) p.1813
9. Y. Hasegawa, S. Hanasaki and J. Fujiwara, J. Jpn. Soc. Compos. Mater., 10 (1984) p.29
10. H. Inoue, J. Yamaguchi, K. Mochida and T. Nishino, J. Soc. Materials Science Jpn., 43 (1994) p.45

Damage Tolerance Analysis Software (DATAS) for Crack Growth Life Prediction and Residual Strength Analysis of Aircraft Structures

I.S. Putra

Department of Aerospace Engineering, Institute of Technology Bandung,
Ganesa 10, Bandung 4032, Indonesia

Keywords: CORPUS Model, Crack Closure, Crack Growth Life Prediction, Damage-Tolerance Analysis, Residual Strength Analysis

ABSTRACT

Aircraft structures have to be designed according to the damage tolerance philosophy which requires the damage tolerance evaluation for fatigue critical components. The evaluation includes fatigue crack growth life prediction and residual strength analysis. DATAS (Damage Tolerance Analysis Software) is developed with a special feature to include a crack closure model i.e. the CORPUS model in fatigue crack growth prediction under flight stimulation loading. The CORPUS model is based on crack closure phenomenon which is visualized as humps on the crack faces. Some theoretical background of the CORPUS model will be reviewed, including some characteristic features. Another special feature of DATAS is the use of R curve data for residual strength analysis of thin sheets. Some characteristic features of DATAS are presented and a summary of prediction results is given.

1. INTRODUCTION

Damage tolerance evaluation has to be carried out for fatigue critical components of aircraft structures. The objective of the evaluation is to provide an inspection program for those components such that cracking, initiated by fatigue loading, accidental damage or corrosion, will not propagate to cause catastrophic failure prior to detection [1]. Currently, the majority of aircraft manufacturers use the linear model and the Willenborg model for crack growth life prediction. The linear model, which does not take into account interaction effects, is considered to be too conservative while the Willenborg model does not correctly represent the physical processes of crack growth under variable-amplitude loading. DATAS (Damage Tolerance Analysis Software) [2, 3, 4, 5] is developed to include the CORPUS model for crack growth life prediction. This model is based on the crack closure phenomenon, which can be used to describe quantitatively the interaction effects in fatigue crack growth under variable amplitude loading, which for aircraft structures is the flight simulation loading. The introduction of the CORPUS model is considered as a special feature of DATAS because it has a strong phenomenological base i.e. crack closure. The previous version of DATAS was enhanced with the capability for prediction of part through cracks, the current version includes also multiple-site damage cases.

The current development for DATAS is to employ K_R -curve for residual strength analysis. The use of the K_R -curve is considered to be essential because fracture of thin skin in aircraft structures is always proceeded by slow stable crack extension.

2. DESCRIPTION OF THE CORPUS MODEL

2.1. Crack opening stress and hump mechanism

The CORPUS model was proposed by De Koning [6] for crack growth prediction under flight simulation loading. The model is based on crack closure phenomenon which is visualized to occur due to the formation of humps on the fracture surface. According to the CORPUS model different load level will create different size of plastic zone which will be left on the crack surface as humps of different heights (see Fig. 1).

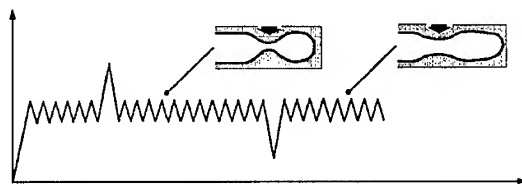


Fig.1. A hump created by an overload, and flattened by an underload

Since humps has height, it causes the crack to open during uploading or to close during downloading. The largest hump will be the last hump which cause the crack faces loosing contact or in other words it will have the highest crack opening stress (S_{op}). Since crack extension only occur when the crack is fully open, then the stress range which cause the crack extension is:

$$\Delta S_{eff} = S_{max} - S_{op} \quad (1)$$

or in terms of stress intensity factor

$$\Delta K_{eff} = K_{max} - K_{op} \quad (2)$$

2.2. Selection of S_{op}

The value of S_{op} of each hump in Eq. 1 of each load level is obtained in a test with constant amplitude loading. The S_{op} is measured usually with the compliance method using extensometer or with direct observations on crack growth rate. Empirical data shows that S_{op} is a function of stress ratio.

$$S_{op} = f(R) \quad (3)$$

For 2024-T3 and 7075-T6 Aluminum alloys the following equations are provided by de Koning [6]:

$$S_{op} = (-0.4R^4 + 0.9R^3 - 0.13R^2 + 0.2R + 0.45)S_{max} \quad (4a)$$

$$S_{op} = (0.1R^2 + 0.2R + 0.45)S_{max} \quad (4b)$$

For thick plates of 7075-T6 Aluminum alloy, experiments by Putra [2] were performed which gives :

$$S_{op} = (0.25 + 0.185R + 0.233R^2 + 0.12R^3)S_{max} \quad (5)$$

The values of S_{op} in Eq. 5 can be considered as representing S_{op} in plane strain condition, while Eq. 4.a and 4.b represents plane stress condition.

The CORPUS model provides an algorithm to select the highest S_{op} from a series of S_{op} resulting from previous load levels or in other words resulting from the opening stress of a series of humps on the crack faces. The algorithm takes into account the following considerations:

1. Interaction between high loads (overload interaction) which cause an increase of S_{op}
2. Influence of high load levels and
3. The influence region of a particular hump

Overload Interaction

A distinguished feature of the CORPUS model is the consideration of overload interaction which increase crack closure. If a series of overloads is applied, S_{op} is increased step by step according to the following equation :

$$S_{op}^n = S_{op} + m^n [S_{max}^n + S_{op}] \quad (6)$$

The value of m^n in Eq. 6 is not constant, it is updated when an overload of level n is applied. In calculating m^n , de Koning [6] introduced some empirical factors, which will not be discussed here. It should be noted that the overload interaction was not applied to 7075 Al-alloy because empirical evidences showed that the interaction of overloads were not significant for this alloy.

Influence of High Load Levels

A high load level will influence the S_{op} level, in the CORPUS model a correction function to take into account this effect was given :

$$h = 1 - 0.2(1 - R^n)^3 \left(\frac{S_{max}}{1.156\sigma_y} \right)^3 \quad (7)$$

Using this correction function S_{op} can be calculated

$$S_{op} = (S_{op})h \quad (8)$$

The Influence Region of A Particular Hump

A very important question concerning the application of an overload is the length of the region where the influence of the overload still exists. In another word, how far the S_{op} value of an overload has to be taken into account. According to the CORPUS model, the extent of the influence of an overload,

is taken as the width of the plastic zone size of the overload. If the crack has grown beyond the plastic zone border, it is assumed that the effect of this hump has vanished and the S_{op} of this hump is zero (see Fig. 2). De Koning used the term "delay switch" to describe this behavior, a delay switch is turned on upon the application of an overload and it is turned off if the crack has grown through the plastic zone. De Koning considered the state of stress in calculating the plastic zone size. Fig. 2 also shows secondary plastic zones which do not extend beyond the existing plastic zone.

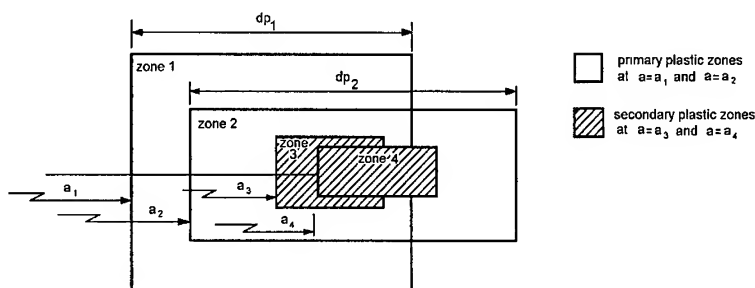


Fig.2. Overlapping plastic zones in the CORPUS model

3. THE USE OF K_R -CURVE FOR RESIDUAL STRENGTH ANALYSIS

For thin sheets the use of plane stress fracture toughness K_c for residual strength analysis always give inconsistent results. The occurrence of slow stable crack extension can be considered as a material property which can be described as a relation between the stress intensity factor K (obtained from a test) and the crack extension Δa . The failure stress can be obtained by superimposing the K_R - a curve with K - a curves for different stresses. Unstable crack extension occur for the stress level where the K - a curve is tangent to K_R - a curve (see Fig. 3).

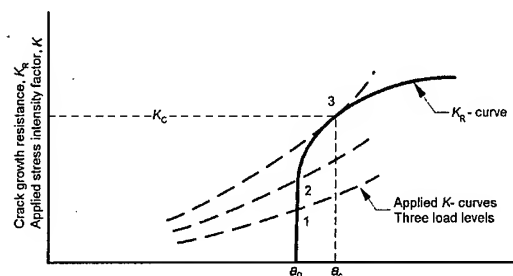


Fig.3. Schematic representation of superposition of K_R - a curve and applied K - a curves to predict instability $\sigma_1 < \sigma_2 < \sigma_3$

4. PREDICTION RESULTS

Some results of crack growth prediction for through cracks using DATAS is given in this section. Fig. 4 shows a comparison of crack growth curve for a sheet specimen with a through crack under flight simulation loading representative for gust loads on wing structures. Prediction results for other type of flight simulation loading is shown in Fig. 5, as the ratio of prediction results to test results. Non-interaction prediction results are also included in Fig. 5, to see the interaction effects predicted by the CORPUS model. From Fig. 4 and Fig. 5 it can be seen that the CORPUS model in DATAS gives a much better prediction compared to the non-interaction prediction, it is not excessively conservative. The accuracy of the CORPUS model is due to its capability to model different phenomena occurring in crack propagation under variable amplitude loading e.g.: multiple overload interactions.

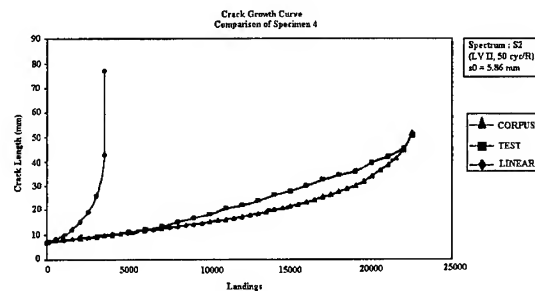


Fig.4. Comparison of crack growth curve under flight simulation loading representative for gust loads on wing structures

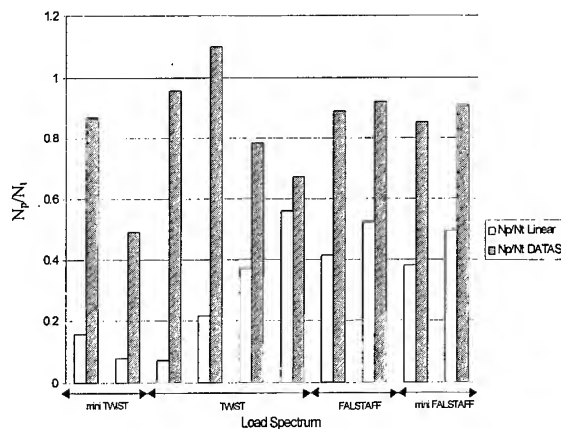


Fig.5. Comparison of ratio N_p/N_t for different flight simulation load spectrum (N_p = predicted results, N_t = test results)

5. CLOSING REMARKS

1. DATAS predictions using the CORPUS model give a much better results (less conservative) compared to non-interaction prediction.
2. The CORPUS model which is based on the crack closure phenomenon, has a number of characteristic features which makes this model suitable for fatigue crack growth life prediction under flight simulation loading.
3. A very important empirical data for the CORPUS model is the crack opening stress level as a function of stress ratio which is not widely available in the literature, thus tests have to be performed to obtain the data.

REFERENCE

1. I.S.Putra, Damage Tolerance Evaluation of Aircraft Structure : The Application of Fracture mechanics, Seminar on Fracture Mechanics ITB – HEDS – JICA, Bandung (1996)
2. I.S.Putra, Further Development of DATAS (DAmage Tolerance Analysis Software) for Crack Growth Life Prediction of Aircraft Structures), Seminar on Fatigue and Fracture Mechanics ITB, Bandung (1998)
3. I.S.Putra, T.Dirgantara, M.T.Dwimunali, and Gunawan, DATAS Theoretical Manual, Technical Note NB-T600-TN-950917, DTT-DT, IPTN, (1995)
4. M.T.Dwimunali, I.S. Putra, DATAS (DAmage Tolerance Analysis Software) Version 1.0 User's Manual, Research Report RR-B3102, DTM-RD, IPTN, Bandung (1997)
5. I.S.Putra, CORPUS Crack Growth Prediction Model Description and Validation Plan for Damage Tolerance Analysis, Research Note RN-B3107, FM-RD, IPTN, Bandung (1997)
6. De Koning, A.U., A Simple Crack Closure Model for Prediction of Fatigue Crack Growth Rates Under Variable-amplitude Loading, " ASTM STP 74,(1981), pp. 63-85

Prediction of Piping Failure Behavior using Wide-Plate Test

N.S. Huh¹, H.J. Cha¹, J.B. Choi¹, Y.J. Kim¹ and C.R. Pyo²

¹ School of Mechanical Engineering, SungKyunKwan University,
300 Ch'onch'on-dong, Changan-gu, Suwon 440-746, Korea

² Department of Mechanical Engineering, Induk Institute of Technology,
San 76 Wolgye-dong, Nowon-gu, Seoul 139-749, Korea

Keywords: Direct Current Potential Drop (DCPD), Full-Scale Pipe, Hardware-in-the-Loop, Leak-Before-Break (LBB), Wide-Plate

ABSTRACT

In order to verify the analytical method predicting the failure behavior of cracked pipes, the full-scale pipe tests are crucial in nuclear power plant pipings. For this reason, series of international test programs have been conducted. However, the full-scale pipe tests require expensive testing equipment and long period of testing time. The objective of this paper is to develop a test system that can economically simulate the full-scale pipe test regarding the integrity evaluation. This system provides the failure behavior of cracked pipe by testing a wide-plate specimen. The system was developed for the integrity evaluation of nuclear pipings based on the methodology of hardware-in-the-loop (HiL) simulation. Using this simulator, the piping integrity evaluation can be performed based on elastic-plastic behavior of full-scale pipe, and the high cost full-scale pipe test may be replaced with this economical system.

1. INTRODUCTION

Recently, the leak-before-break (LBB) concept was accepted as a technically justifiable approach for piping design of new plant and operating plant. In this case, the evaluation method and analysis procedure must be verified. The increasing number of cracks being found in operating plants has raised the necessity for developing more sophisticated analytical and experimental methods for the application of LBB concept.

In order to apply the LBB design concept to nuclear piping system, material properties such as stress-strain curve and fracture resistance curve are required for the elastic-plastic fracture mechanics analysis. The fracture mechanics analysis based on J -integral and tearing modulus has been successfully adopted in the LBB analysis[1,2]. Recently, effects of dynamic strain aging and reverse cyclic loading on LBB application have been raised. In order to resolve these complicated problems, alternative analytical methods with experimental verifications are required. For this purpose, series of international test programs[3,4] have been conducted. However, limited number of full-scale pipe tests was carried out due to the high cost equipment and long period of testing time.

In the present paper, the methodology of hardware-in-the-loop (HiL) simulation has been introduced to replace the full-scale pipe test. This approach utilizes a software algorithm for simulating the full-scale structure behavior, and the resulting output is interfaced to a real hardware component such as a wide-plate specimen which is mounted on a test equipment. The methodology of HiL was originated in the aerospace and the defense industries where it is frequently impossible, impractical, or just too costly to test controllers on actual systems, and popularly used in automobile industries in order to improve the component performance[5-7].

The objective of this paper is to develop a test system which can economically simulate the full-scale pipe test regarding the integrity evaluation based on the methodology of HiL simulation.

2. HiL SIMULATOR FOR PIPE INTEGRITY EVALUATION

The proposed HiL based piping integrity evaluation simulator consists of the software part, the hardware part and the input/output (I/O) part as shown in Fig. 1. The software part is composed of elastic and elastic-plastic finite element analysis module. The hardware part is composed of test machine, wide-plate specimen, sensors, and a display unit. The I/O part consists of A/D and D/A converters for the data transmission between the software and the hardware parts.

2.1. Software Part

- Loading schedule module

The loading schedule module provides information on the variation of loading conditions to the finite element model. The finite element model thus deforms according to the actual loading conditions which corresponds to a real piping. In this paper, only a remote bending condition was considered.

- Finite element analysis module

In this module, series of finite element analyses are conducted on a full-scale pipe to obtain the boundary conditions for a wide-plate specimen which is actually mounted on the testing machine. For the finite element analysis, a commercial finite element analysis program, ABAQUS[8], was used. The resulting boundary conditions for the wide-plate specimen were transferred to the main control PC as shown in Fig. 1.

2.2. Hardware Part

- Specimen and test machine

A full-scale pipe may be subjected to global bending (Fig. 2(a)), but the local loading on a cracked area can be considered as the axial tension condition (Fig. 2(b)). A wide-plate specimen subjected to tension loading, therefore, can simulate the full-scale pipe subjected to remote bending. As shown in Fig. 2, the specimen is cut directly from a section of full-scale pipe. Fig. 3 shows the wide-plate specimen with a through-wall crack which is sharpened with fatigue pre-crack at both sides. Six strain gages were mounted on the surface to produce the equivalent boundary conditions which were obtained from the finite element analysis on the full-scale pipe, as shown in Fig. 3. An Instron test machine (model 8503) was used for applying the loading condition to the wide-plate specimen and was automatically controlled by an electrical motor. Uni-axial tension was applied to the specimen according to the loading schedule produced by the software part.

- Strain measurement system

A specially designed strain measurement system was applied to match the strain field in the wide-plate specimen with the finite element analysis results. In order to minimize the measurement error during the loading process, total of 6 strain gages were attached to the specimen as shown in Fig. 3. A multi-channel strain measurement system covering 16 channels was developed for this purpose. A multi-channel strain measurement system consists of wheatstone bridge, channel control part, filter, amplifier, and A/D converters. The signals from the attached strain gages are transferred into the wheatstone, the filter, the amplifier, the A/D converter, subsequently and finally recorded in the main control PC. The developed low-pass filter has a cut-off frequency of 10Hz and the developed amplifier has gains of 40, 54, 60 and 74dB.

- Crack detection system

The crack growth behavior is monitored by a multi-channel DCPD (Direct Current Potential Drop) system. DCPD is an indirect method of measuring crack size. It provides the amount of crack growth in terms of voltage drop. In this paper, three DCPD channels were used for voltage reading, as shown in Fig. 3. The monitored data are recorded in the main control PC.

In order to determine the crack length from voltage change, the following equation which was analytically developed by Johnson[9] was used.

$$\frac{V}{V_o} = \frac{\cosh^{-1}[\cosh(\pi y / 2W) / \cos(\pi a / 2W)]}{\cosh^{-1}[\cosh(\pi y / 2W) / \cos(\pi a_o / 2W)]} \quad (1)$$

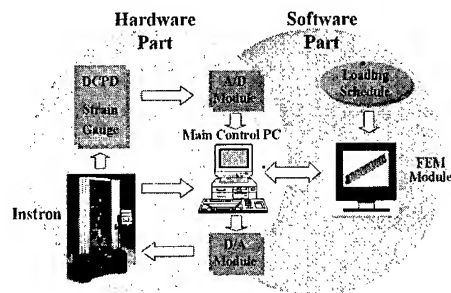
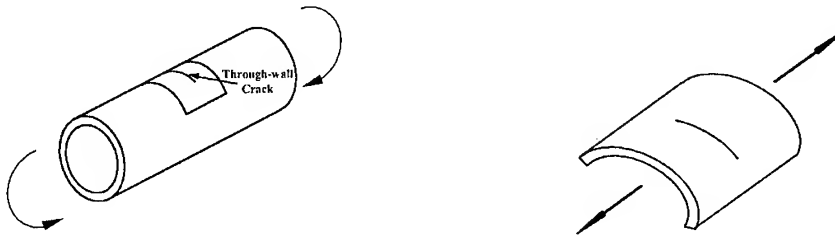


Fig. 1. A schematic illustration of piping integrity evaluation simulator.



(a) The full-scale pipe under remote bending moment (b) The wide-plate specimen under axial tension

Fig. 2. A wide-plate specimen configuration subjected to axial tension.

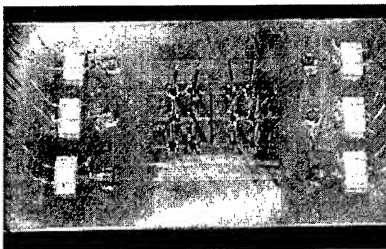


Fig. 3. A wide-plate specimen used in HiL simulation.

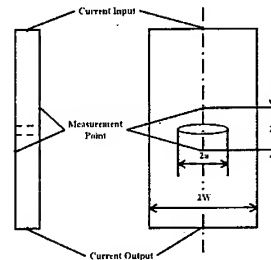


Fig. 4. Electric potential wire placement locations for Johnson's formula.

Equation (1) is valid for all values of a/W . This equation can be rewritten in terms of voltage for calculating crack length as following;

$$a = \frac{2W}{\pi} \cos^{-1} \frac{\cosh(\pi y / 2W)}{\cosh\left\{(V/V_o) \cosh^{-1}[\cosh(\pi y / 2W) / \cos(\pi a_o / 2W)]\right\}} \quad (2)$$

where, a_o and V_o are the initial crack length and the corresponding initial potential, respectively, and a and V are the current crack length and the corresponding potential, respectively. Fig. 4 illustrates the wide-plate specimen geometry and wire placement locations for this solution.

- A/D converters

The analog voltage measurement obtained from the DCPD system is converted to digital signal by passing the A/D converter which was specially designed for the developed DCPD system. The

resulting data are graphically displayed on the main control PC to monitor the crack growth behavior.

- *Main control PC*

Main control PC is in charge of data communication between the hardware part and the software part, the data storage, and the loading schedule control. It also provides the graphical crack growth monitoring display in accordance with the DCPD measurement.

3. PROCEDURES OF HiL SIMULATION

Procedures of HiL simulation for the piping integrity evaluation are explained as follows.

- 1) In the first stage, the finite element analysis is conducted for full-scale pipe model in accordance with pipe loading schedule. As a result, a loading schedule for the wide-plate specimen is produced in terms of strain.
- 2) The wide-plate specimen is mounted on the testing machine with sensors connected. The strain measurement system and the DCPD system are initialized.
- 3) The resulting boundary conditions for the wide-plate specimen are transmitted to the main control PC. The main control PC then initiates the testing machine by controlling loading motor.
- 4) The measured strain values due to the applied loading are transmitted to the main control PC, and are compared with the strain value which was set by the loading schedule. The applied load increases until the measured strain matches with that of loading schedule.
- 5) At the same time, the crack growth behavior is monitored by the DCPD system. The amount of crack growth is recorded as a function of strain which is specified in the loading schedule.
- 6) The above procedure is repeated until the loading schedule is completed.

4. APPLICATION OF HiL SIMULATOR

4.1. Determination of Specimen Size

In order to determine the wide-plate specimen size, a finite element analysis for the full-scale pipe model with the inner diameter of 289 mm and the thickness of 9 mm was performed. Two planes of symmetry were considered in modeling a full-scale pipe, and thus the designed finite element model represents only a quarter of pipe as shown in Fig. 5.

From the finite element analysis result, the size of wide-plate specimen was determined considering the strain field which was not influenced by the local crack tip strain field. In order to simplify the testing geometry, a flat wide-plate was used for the test. Fig. 6 shows the configuration of wide-plate specimen for the HiL simulation. Table 1 shows material properties of wide-plate specimen used for the HiL simulation.

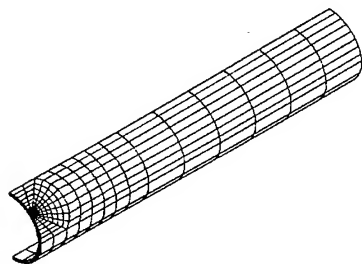


Fig. 5. A three dimensional mesh for the finite element analysis.

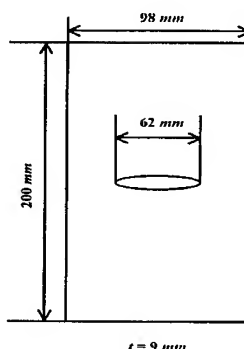


Fig. 6. The configuration of wide-plate specimen.

Table 1. Material properties for the wide-plate specimen

SM45C Carbon Steel	Young's modulus, E (GPa)	207
	Yield strength, σ_y (MPa)	466
	Ultimate strength, σ_u (MPa)	977
	Poisson's ratio, ν	0.3

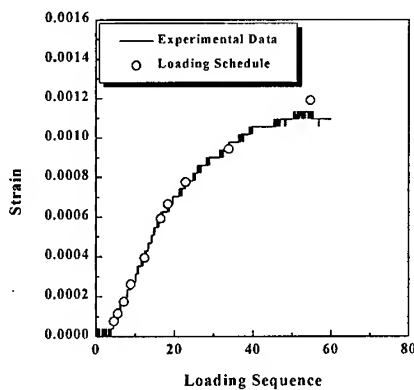
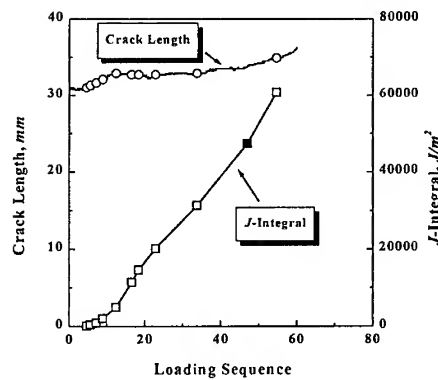


Fig. 7. Comparison of strain values between loading schedule and experimental result.

Fig. 8. Variation of crack length and J -integral during the simulation at each loading step.

4.2. HiL Simulation with Wide-Plate Specimen

For the HiL simulation, a remote bending moment of 200 $kN\cdot m$ to the full-scale pipe was considered. According to the resulting finite element analysis, the loading schedule was set by 15 steps in terms of strain. A wide-plate specimen was tested with an initial crack size ($2a$) of 62 mm. During the simulation, strain values obtained from the strain measurement system were recorded along with the corresponding crack size at each loading step.

Fig. 7 shows the comparison between the strain values from the measurement system and the loading schedule. The strain values at each loading step are indicated by open circle symbols. The measured strain values showed a good agreement with those specified in the loading schedule. This implies that the motor driven loading control system operated well according to the loading schedule, and it can be utilized to correlate the finite element analysis results to the wide-plate specimen.

Fig. 8 shows the measured crack growth during the simulation at each loading step and corresponding J -integral considering the crack growth. The measured crack length at each loading step is indicated by open circle symbols and corresponding J -integral is indicated by open square symbols. By measuring the crack growth simultaneously at each loading step, the crack growth behavior was monitored with the increase in load applied to the full-scale pipe. At the crack initiation point which is indicated by solid square in Fig. 8, corresponding moment and J -integral were 144 $kN\cdot m$ and 47,344 J/m^2 , respectively. However, the J_{IC} obtained from a 1T-CT specimen was 6,438 J/m^2 . This discrepancy seems to be caused by the difference of constraint. It is known that tension loading usually produces lower constraint at the crack tip than bending loading condition. It makes a big difference in case of brittle fracture[10]. Since the tested material, SM45C, is known to be brittle, a big difference was observed between two J -integral values measured at the

crack initiation. The final crack size measured from the DCPD system showed a good agreement with the measurement obtained from the failed specimen with less than 1% of difference, and thus the validity of applied DCPD system was proven to be reliable.

5. CONCLUSION

In this paper, a test system which can economically simulate the full-scale pipe test regarding the piping integrity evaluation was developed. The system was developed for the integrity evaluation of nuclear pipings based on the methodology of hardware-in-the-loop (HiL) simulation. By simulating a full-scale pipe under remote bending, each part of the HiL simulator, such as software part, motor driven loading control system, strain measurement system, and DCPD system was tested. The developed HiL simulator is expected to be utilized to verify the crack initiation load which is currently predicted by engineering J -estimation scheme such as GE/EPRI method etc. And the J -integral calculation considering the crack growth is expected to be performed based on a real pipe behavior. Using this simulator, a more sophisticated piping integrity evaluation is expected to be performed based on an elastic-plastic behavior of the full-scale pipe, and the high cost full-scale pipe test may be replaced with this economical system.

ACKNOWLEDGEMENT

The authors are grateful for the support provided by a grant from the Safety and Structural Integrity Research Center at the Sungkyunkwan University.

REFERENCES

1. Huh, N.S., Kim, Y.J. et al., Journal of the Korean Institute for Industrial Safety, Vol. 14 (1999), pp. 32-41
2. Huh, N.S., Kim, Y.J. et al., Nuclear Engineering and Design, Vol. 191 (1999), pp. 135-145
3. Wilkowski, G.M. et al., NUREG/CR-6233, USNRC (1991)
4. Wilkowski, G.M. et al., NUREG/CR-6452, USNRC (1996)
5. Sailer, U. and Essers, U., SAE Paper 942297, Society of Automotive Engineers Inc., U.S.A. (1994)
6. Suh, M.W., Kim, Y.J. et al., SAE 980244, Society of Automotive Engineers Inc., U.S.A. (1998)
7. Ptak, A. and Foundy, K., Proceedings of 4th Real-Time Technology and Applications (1998), pp. 230-235
8. ABAQUS User's manual, Hibbitt, Karlsson & Sorensen, Inc. (1999)
9. Johnson, H.H., Materials Research and Standards, Vol. 5 (1965), pp. 442-445
10. O'Dowd, N.P. and Shih, C.F., Journal of Mechanics and Physics of Solids, Vol. 39 (1991), pp. 989-1015

Vibration Sensing and Impact Location Detection Using Optical Fiber Vibration Sensor

Y.C. Yang, W. Hwang, H.C. Park and K.S. Han

Department of Mechanical Engineering, Pohang University of Science and Technology
San 31 Hyoja-dong, Nam-gu, Pohang 790-784, Korea

Keywords: Impact Location Detection, Optical Fiber Vibration Sensor, Smart Structure

ABSTRACT

An intensity-based optical fiber vibration sensor is used to monitor the structural vibration and detect the impact location on a plate. The optical fiber vibration sensor is constructed by placing two cleaved fiber ends, one of which is cantilevered in a hollow glass tube. For vibration sensing, optical fiber vibration sensor is mounted on the carbon fiber composite beam and its response to free vibration and forced vibration is investigated. In impact location detection, four optical fiber vibration sensors whose location is predetermined are used and the different arrival times of impact-generated vibration signal are recorded by FFT analyzer. Impact location can be calculated from these time delays. Experimental results show that optical fiber vibration sensor signals coincide with gap sensor in vibration sensing. The precise locations of impact can be detected on an acrylic plate within 3.4% error limit.

1. INTRODUCTION

A smart structure is defined as a structural system whose geometric configuration or inherent structural characteristics can be modified in response to environmental changes. An important component in smart structure is the optical fiber sensor which detects the strain level, temperature and acoustic emission. The data generated by the sensor system can be used to monitor the health of an aircraft structure or to control actuators.

Both low-velocity and high-velocity impacts generate structural vibration and acoustic stress waves in structures. These impacts lead to crack initiation that on progression could lead to severe structural degradation. Hence, it is necessary to detect impacts occurring on the surfaces or edges of a specimen. Many techniques have been proposed to detect the source of origin of acoustic waves. Tobias[1] presented a scheme of locating an acoustic source on a flat plate by employing three piezoelectric sensors. Asty[2] modified Tobias' work by generalizing the theory to calculate the acoustic source location on a sphere. Greene et al.[3] employed extrinsic Fabry-Perot interferometric(EFPI) optical fiber-based sensing system and determined impact locations on an aluminum sample and a composite plate. With fiber Bragg grating(FBG) attached to the surface of a cantilever beam, Davis et al.[4] demonstrated shape determination and vibration mode sensing of the structure.

In the past a few years, considerable effort has been devoted the development of optical fiber

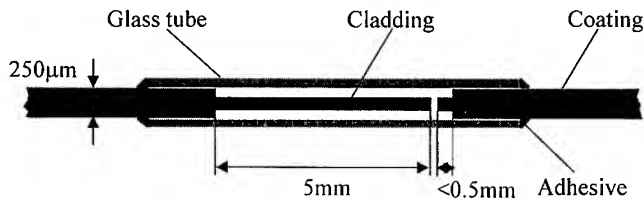


Fig. 1 Schematic illustration of optical fiber vibration sensor

vibration sensors, due to the wide variety of applications where it is necessary to monitor or accurately measure vibrations and this cannot be achieved by the traditional sensors based on piezoelectric or capacitive working principles. Doyle and Fernando[5] described a vibration monitoring system for detecting damage in a material using an intensity-based optical fiber vibration sensor. Several researchers[6,7] applied the optical fiber vibration sensor to a fiber optic accelerometer with attention to the low-frequency range and the low-amplitude measurements.

In this paper, vibration sensing and impact location detection using optical fiber vibration sensor are demonstrated. Design, fabrication and operation of a simple intensity-based optical fiber vibration sensor is described. The sensor is mounted on the composite beam and its response to free and forced vibration is investigated. Experimental results of determination of impact location in an acrylate plate are discussed.

2. OPTICAL FIBER VIBRATION SENSOR

Optical fibers consist of the core, cladding and coating. Since the core has a higher index of refraction than the cladding, the total reflection at core-cladding interface occurs. Fig. 1 shows the configuration of the optical fiber vibration sensor. The sensor consists of two optical fibers, one of which is cantilevered in a glass tube. The movement of the cantilevered section lags behind the rest of the sensor in response to an applied vibration and the amount of light coupled between two fibers is thereby modulated.

Single mode optical fibers(3M Co.) with the coating diameter of 250 μm and the cladding diameter of 125 μm are used in this study. The coating of two optical fiber ends are stripped 5 mm and about 0.5 mm long, respectively. The sensor is assembled by inserting the cleaved end of the fiber into a glass tube with an inner diameter of about 250 μm using special xyz-positioning stage. The fiber is then bonded to the glass tube using an adhesive. Next, the other fiber is inserted into the opposite end of the glass tube and is bonded to the tube. The surface quality of the cleaved fiber ends is critically monitored by a microscope.

The gap separation is maintained 40-50 μm in consideration of output intensity. By inserting the coating part of the optical fiber into the glass tube, simple intensity-based optical fiber vibration sensors can be constructed without additional fiber support tube etc.. The sensor resonance can be tuned over a range of a few thousand hertz, by varying the length of the optical fiber cantilever. Sensors employing shorter cantilevers are able to respond to higher frequencies, but will tend to be less sensitive than longer ones, giving a smaller change in intensity for a given amplitude of vibration.

3. CALCULATION OF IMPACT LOCATION

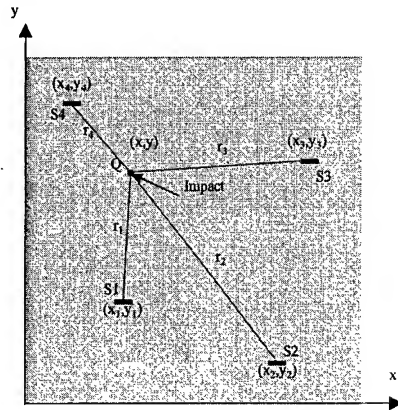


Fig. 2 Coordinate system for impact detection

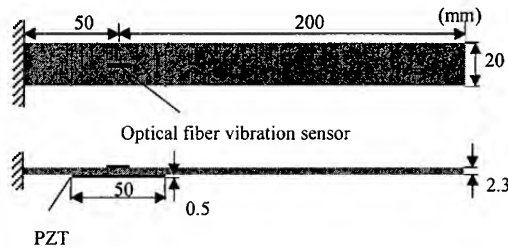


Fig. 3 Configuration of composite beam for vibration test

When an impact is generated, both surface and bulk acoustic waves are excited. If the propagation speed of the wave in the material is exactly known, the use of three sensors should suffice for impact location. Four sensors are needed where the propagation speed is unknown. In this study, the four optical fiber vibration sensors attached to a test plate are used to find the location of impacts. In the coordinate system in Fig. 2, time-velocity relations can be written as

$$v_i t_i = r_i \quad (i = 1, 2, 3, 4) \quad (1)$$

where, v_i is the propagation speed of the wave along the direction from impact point(Q) to each sensor S_i , t_i is the propagation time of the wave from Q to the sensor, and r_i is the distance between Q and the sensor. Assuming that the material is isotropic($v_i = v$, for $i=1,2,3,4$), we obtain,

$$(t_2 - t_1)v = r_2 - r_1 \quad (2)$$

$$(t_3 - t_1)v = r_3 - r_1 \quad (3)$$

$$(t_4 - t_1)v = r_4 - r_1 \quad (4)$$

For example, equation (2) can be rewritten in (x,y) component :

$$(t_2 - t_1)v = \sqrt{(x_2 - x)^2 + (y_2 - y)^2} - \sqrt{(x_1 - x)^2 + (y_1 - y)^2} \quad (5)$$

By eliminating v , equations (2)-(4) can be rewritten as

$$\left(1 - \frac{t_2 - t_1}{t_3 - t_1}\right)r_1 = r_2 - \frac{t_2 - t_1}{t_3 - t_1}r_3 \quad (6)$$

$$\left(1 - \frac{t_2 - t_1}{t_4 - t_1}\right)r_1 = r_2 - \frac{t_2 - t_1}{t_4 - t_1}r_4 \quad (7)$$

Equations (6) and (7) are non-linear system of equations and the coordinates (x,y) of an impact can be determined by using Newton's iteration method.

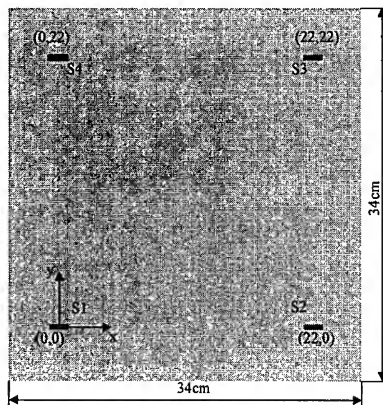


Fig. 4 Configuration of specimen for impact location test

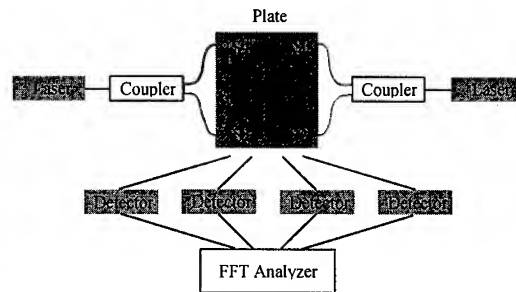


Fig. 5 Schematic diagram of experimental setup for impact location detection

4. EXPERIMENTS

A He-Ne laser whose operating wavelength is 633nm was used as the light source. The laser beam was launched into a Newport 3 dB 2 X 2 bidirectional coupler which splits the optical signals. The fiber optic signals received by photodetectors were transmitted to FFT analyzer. The manufactured optical fiber vibration sensors were adhered to the surface of specimens.

For vibration mode sensing, the optical fiber vibration sensor was mounted on the carbon fiber composite beam and its responses to free vibration and force vibration were investigated. Fig. 3 shows the configuration of composite beam for vibration test. The composite beam was clamped at one end with one optical fiber vibration sensor surface attached at 50mm from the clamped end of the beam. A piezoelectric actuator was attached to the back surface of the beam at the same distance with the optical sensor. The piezoelectric actuator was excited by a function generator for forced vibration test.

An 34x34x0.13cm acrylate plate was used for impact location test. The material is isotropic, hence the propagation speed of the vibration wave is same along the all directions from impact point. Four optical fiber vibration sensors attached to the test plate were used to measure the arrival times of impact generated vibration signal. Fig. 4 shows the configuration of the plate and predetermined optical sensor locations. The fiber optic system is composed of two light sources, two bidirectional couplers, single mode optical fibers, four photodetectors and a FFT analyzer as shown in Fig. 5.

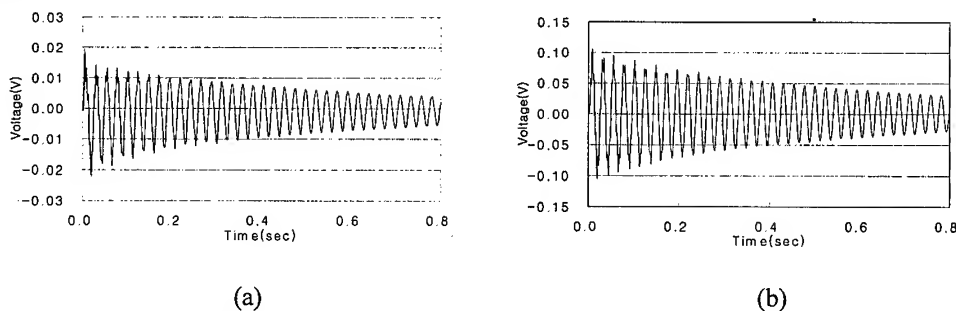


Fig. 6 Time trace curve of (a) optical sensor and (b) gap sensor for composite beam

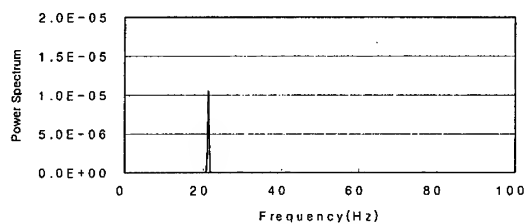


Fig. 7 Impact response measured in frequency domain

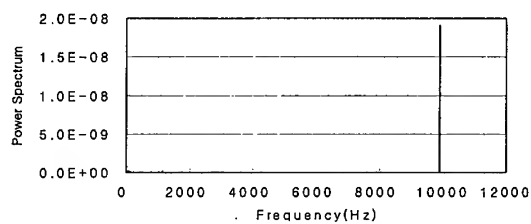


Fig. 8 Power spectrum for forced vibration test (about 10kHz)

5. RESULTS AND DISCUSSIONS

Fig. 6 shows the time trace curve of free vibration for the specimen in Fig. 3. Vibration signals were recorded by optical fiber vibration sensor and a gap sensor simultaneously. The output of the optical fiber vibration sensor is similar to the commercial gap sensor. The first peak point of the optical sensor signals oscillates minutely in high frequencies due to the impact caused by the impact hammer. The natural frequency of the composite beam was measured by the optical fiber vibration sensor as shown in Fig. 7. Fig. 8 shows the power spectrum of forced vibration test for the composite beam. Sinusoidal signal (about 10kHz) from the function generator excited the piezoelectric actuator on the specimen. The signal of the optical sensor was identical with the gap sensor. A typical signal of the optical fiber vibration sensor attached to the acrylate plate during impact is shown in Fig. 9. Overall response of the sensor seems to be mixed with the plate vibration of about 100Hz and vibration of the bare optical fiber of a few thousand hertz. At the early stage of the response, the sensor signal oscillates drastically due to the large amplitude vibration of the internal fiber optic cantilever and this vibration of the optical fiber in the sensor vanishes at near 25msec. Fig. 10 shows output of sensor 2 during impact on the test plate. The magnitude of the sensor noise was about 1.6mV during non-impact. The arrival time of vibration wave to each sensor was identified as the first received data point above the maximum value of the sensor noise signal preceding impact. Marking point in Fig. 10 indicates the arrival time of the wave.

Ten measured and exact impact locations for the acrylate plate are shown in Table 1. The percentage error is defined as

$$Error(\%) = \frac{1}{2} \frac{x_e + y_e}{l} \times 100 \quad (8)$$

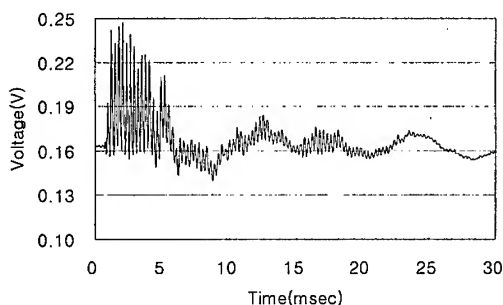


Fig. 9 Typical signal of optical fiber vibration sensor during impact

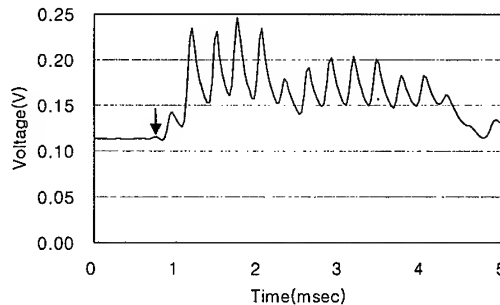


Fig. 10 Voltage output of optical fiber vibration sensor during impact (sensor 2, impact location : (2,14))

Table 1 Measurement of impact location

Impact Location (cm,cm)	Measured Location (cm,cm)	Error (%)
11,11	10.8,11.6	1.2
2,14	1.8,14.0	0.4
18,12	17.5,12.1	1.0
4,2	3.3,1.1	2.4
14,20	13.9,19.5	0.9
12,0	11.3,-0.9	2.3
24,16	24.0,16.3	0.5
-4,8	-5.2,6.9	3.4
20,6	18.3, 5.6	3.2
8,18	7.3,17.8	1.3

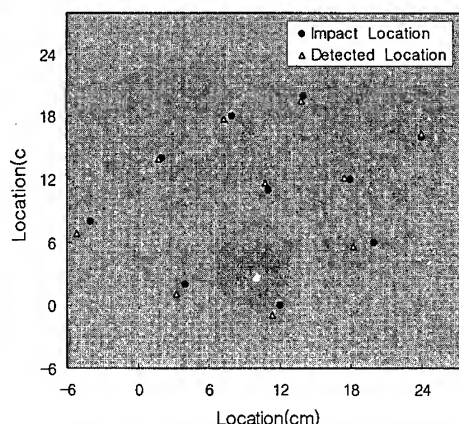


Fig. 11 Comparison of impact location and detected location

where, x_e and y_e are respectively, the errors in measurement of x and y coordinates, and l is the length of one side of the specimen on which the optical fiber vibration sensors are mounted. The error is less than 3.4%. Comparatively precise locations of impact were able to be determined on the acrylate plate. Fig. 11 shows actual and measured impact locations on the plate.

6. CONCLUSIONS

Simple intensity-based optical fiber vibration sensor has been constructed using a bare fiber optic cantilever beam. The optical sensor was mounted on the carbon fiber composite beam and its response to free and force vibration was monitored. The optical fiber vibration sensor detected the vibration signal correctly. In impact location detection, four optical fiber vibration sensors whose location was predetermined were used. The location of impact was determined by using a mathematical model based on the difference in the arrival times of the vibration waves to each sensor. The experimental error in the location of impact was less than 3.4%.

Acknowledgements

The authors wish to thank to Safety and Structural Integrity Research Center for financial assistance.

REFERENCES

1. A. Tobias, Non-Destructive Testing, **9**(1976) pp. 9-12.
2. M. Asty, Non-Destructive Testing, **11**(1978) pp. 223-226.
3. J. A. Greene, T. A. Tran, V. Bhatia, M. F. Gunther, A. Wang, K. A. Murphy and R. O. Claus, Smart Mater. Struct., **4**(1995) pp. 93-99.
4. M. A. Davis, A. D. Kersey, J. Sirkis and E. J. Friebel, Smart Mater. Struct., **5**(1996) pp. 759-765.
5. C. Doyle and G. Fernando, Smart Mater. Struct., **7**(1998) pp. 543-549.
6. J. M. Lopez-Higuera, M. A. Morante and A. Cobo, J. of Lightwave Technology, **15**(1997) pp. 1120-1130.
7. M. Morante, A. Cobo, J. M. Lopez-Higuera and M. Lopez-Amo, Optical Engineering, **35**(1996) pp. 1700-1706.

New Estimates of Effective Moduli of Microcracked Materials

X.Q. Feng

Department of Engineering Mechanics, Tsinghua University, Beijing 100084, China P.R.

Keywords: Constitutive Relation, Heterogeneous Materials, Microcrack Interaction, Microcracks, Overall Elastic Properties

ABSTRACT

The overall elastic moduli of microcracked solids are usually estimated by one of the several established methods based on the concept of effective medium or effective field. The complete formal similarity of these estimation methods is examined in this paper. A one-to-one correspondence relation is found between the effective medium methods and the effective field methods in the sense that they yield identical results. In addition to the conventional estimation techniques, any number of other such approaches may be constructed by appropriately specifying the comparison matrix elastic tensor and the effective stress (or strain) field which a microcrack is subjected to. Several novel and efficient approaches are proposed to take the microcrack interaction effects into account in a simple manner.

1. INTRODUCTION

Several schemes have been established to estimate the effective moduli of microcracked solids. The simplest one is the approximation of non-interacting microcracks, which is sometimes called the Taylor's model or dilute concentration model (DCM) [1]. When considering microcrack interaction, one may estimate the effective moduli with the self-consistent method (SCM) [2], Mori-Tanaka method (MTM) [3], differential method (DM) [4], generalized self-consistent method (GSCM) [5], and other such approaches based on an effective medium or effective field. All these techniques, with few exceptions, neglect the precise locations and orientations of microcracks. Therefore, their applications are limited to solids that are statistically homogeneous and subjected to uniform tractions on or displacements of their surfaces.

In spite of their cumbersome numerical computations or theoretical derivations, however, these techniques do not ensure a satisfactory accuracy of the results. Only in a very few special cases of microcrack arrays can analytical solutions be obtained. In more general cases, the SCM, GSCM and DM offer little attraction. Therefore, it is of interest to develop simpler and more effective approaches to predict the impacts of microcrack interaction on effective elastic properties of solids. To this end, an attempt is made in this work to gain an insight into the formal similarity of the effective medium or effective field methods aforementioned, and to propose some other possibilities of constructing such kind of methods.

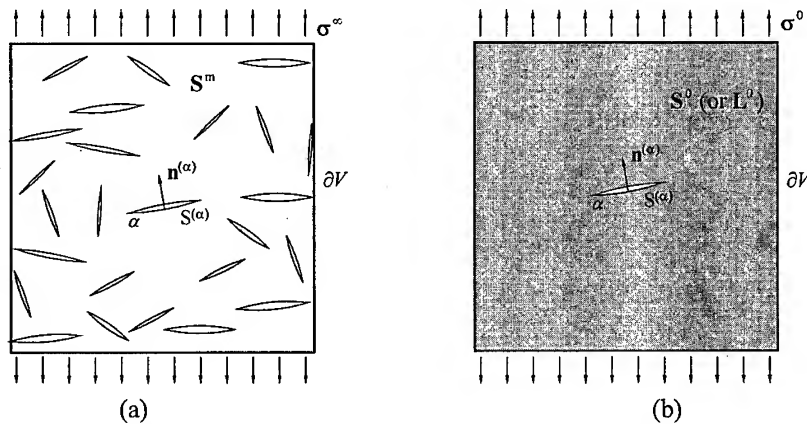


Fig. 1. (a) An RVE, and (b) the calculation model of the crack opening displacement.

2. UNIVERSAL FRAMEWORK FOR ESTIMATING EFFECTIVE MODULI

2.1. Universal framework

Consider a brittle solid containing many distributed microcracks. Choose a *representative volume element* (RVE) V , whose boundary ∂V is subjected to tractions in equilibrium with a uniform overall stress σ^∞ or to displacements compatible to a uniform overall strain ϵ^∞ , as shown in Fig. 1(a). Then, the effective (or overall) compliance tensor \mathbf{S} and stiffness tensor \mathbf{L} are defined by

$$\bar{\epsilon} = \mathbf{S} : \sigma^\infty, \quad \bar{\sigma} = \mathbf{L} : \epsilon^\infty, \quad (1)$$

where $\bar{\epsilon}$ denotes the overall average strain over the RVE in the case of traction boundary conditions, and $\bar{\sigma}$ the overall average stress in the case of displacement boundary conditions. Since the two cases of boundary conditions can be discussed similarly, for conciseness, only that of traction boundary conditions will be considered henceforth. The average strain can be decomposed as

$$\bar{\epsilon} = \bar{\epsilon}^m + \bar{\epsilon}^c, \quad (2)$$

where $\bar{\epsilon}^m$ denotes the matrix strain tensor averaged over the RVE, $\bar{\epsilon}^c$ the increase in the overall average strain due to the presence of microcracks. The constitutive relation of the linear elastic matrix requires that

$$\bar{\epsilon}^m = \mathbf{S}^m : \sigma^\infty, \quad (3)$$

where \mathbf{S}^m is the fourth-order compliance tensor of the pristine matrix.

The microcrack-induced increase of the volume-averaged strain, $\bar{\epsilon}^c$ can be calculated by

$$\bar{\epsilon}^c = \sum_{\alpha=1}^N \bar{\epsilon}^{(\alpha)} = \frac{1}{2V} \sum_{\alpha=1}^N \int_{S^{(\alpha)}} (\mathbf{b}\mathbf{n} + \mathbf{n}\mathbf{b})^{(\alpha)} dS^{(\alpha)}, \quad (4)$$

where the superscript (α) stands for a quantity of the α -th microcrack, $S^{(\alpha)}$, $\mathbf{n}^{(\alpha)}$ and $\mathbf{b}^{(\alpha)}$ denote its surface area, opening displacement discontinuity vector, and unit vector normal to the crack faces, respectively.

Thus, the key problem for the present purpose becomes how to calculate the opening displacement of a microcrack embedded in a solid containing many disordered microcracks. Evidently, it is very difficult if not impossible to determine the exact opening displacements due to the large number of interacting microcracks whose orientations and locations are usually distributed statistically. Therefore, some simplifications are almost exclusively necessary. On one hand, the medium surrounding a microcrack is microcrack-weakened, and then has a stiffness lower than the pristine matrix. On the other hand, the stress field which a microcrack is subjected to is perturbed due to the existence of other microcracks. As a straightforward approximate model, thus, the microcrack is assumed to be surrounded by an effective medium, referred to also as the comparison or reference matrix, with compliance S^0 and subjected to an effective stress σ^0 in the far field, as shown in Fig. 1(b). This approximation, which renders the evaluation of the effective moduli of a microcracked solid possible, is common to all the effective medium methods and the effective field methods, e.g. the DCM, SCM, DM, MTM and GSCM, although the definitions of S^0 and σ^0 in these methods are different, as will be discussed later.

If all microcracks are assumed planar, (4) becomes

$$\bar{\epsilon}^c = \frac{1}{2V} \sum_{\alpha=1}^N S^{(\alpha)} (\bar{\mathbf{b}}\mathbf{n} + \mathbf{n}\bar{\mathbf{b}})^{(\alpha)}, \quad (5)$$

with $\bar{\mathbf{b}}^{(\alpha)}$ denoting the average of $\mathbf{b}^{(\alpha)}$ over the total crack face.

The average opening displacement vector of a microcrack embedded in a linear elastic matrix S^0 and subjected to a far-field stress σ^0 can be expressed as

$$\bar{\mathbf{b}} = \mathbf{B}(S^0, \mathcal{G}, \sigma^0) \cdot \sigma^0 \cdot \mathbf{n}, \quad (6)$$

where the second-rank symmetric tensor \mathbf{B} is referred to as the crack opening displacement tensor [6], and \mathcal{G} signifies the geometry of the microcrack. If all microcracks are assumed to be open or, if closed, to have completely smooth crack surfaces, that is, the friction coefficient between crack faces is zero, then $\bar{\mathbf{b}}$ is a linear function with respect to σ^0 .

Relate σ^0 to σ^∞ by a fourth-order tensor \mathbf{H} defined by

$$\sigma^0 = \mathbf{H} : \sigma^\infty. \quad (7)$$

Assume that the tensor \mathbf{H} is same for all microcracks, as consistent with the inherent assumptions of the effective medium or the effective field methods. This means that \mathbf{H} is unrelated to the orientation and location of the microcrack, and then all microcracks are subjected to the same far field σ^0 in Fig. 1(b).

From (5) and (6), the variations in the overall strain induced by the α -th microcrack can be written as

$$\bar{\epsilon}^{(\alpha)} = \frac{S^{(\alpha)}}{2V} (\mathbf{B} \cdot \sigma^0 \cdot \mathbf{n}\mathbf{n} + \mathbf{n}\mathbf{B} \cdot \sigma^0 \cdot \mathbf{n})^{(\alpha)}. \quad (8)$$

Thus, the components of the overall effective compliance increment due to the α -th single microcrack are expressed from (7) and (8) as

$$S_{ijkl}^{(\alpha)} = \frac{S^{(\alpha)}}{4V} H_{stkl} (n_i B_{js} n_t + n_j B_{is} n_t + n_i B_{jt} n_s + n_j B_{it} n_s)^{(\alpha)}. \quad (9)$$

Thus, the overall compliance tensor \mathbf{S}^0 is arrived at

$$S_{ijkl} = S_{ijkl}^m + \frac{1}{4V} H_{stkl} \sum_{\alpha=1}^N S^{(\alpha)} (n_i B_{js} n_t + n_j B_{is} n_t + n_i B_{jt} n_s + n_j B_{it} n_s)^{(\alpha)}, \quad (10)$$

which evidently possesses the Voigt symmetry, that is, $S_{ijkl} = S_{jikl} = S_{ijlk} = S_{klij}$.

2.2. Estimation methods

Once the shapes and orientations of all microcracks (or their probability density functions) are specified, the overall compliance of the RVE, determined from (10), depends upon the \mathbf{B} tensor and the \mathbf{H} tensor. By definition, \mathbf{H} relates the far field stress σ^0 in the simplified model in Fig. 1(b) to the stress σ^∞ , loaded on the RVE boundary, while \mathbf{B} is a function of the crack shape and the compliance tensor \mathbf{S}^0 of the comparison matrix.

Therefore, the effects of microcrack interaction can be incorporated into the overall effective constitutive relation through an appropriate choice either of the comparison matrix \mathbf{S}^0 or of the far field stress σ^0 . Almost all the estimation techniques available in the literature, based on the concept of effective medium or effective field, can be formulated in the form of (10) and, in other words, have a complete formal similarity. Their differences stem only from the choices of \mathbf{S}^0 and σ^0 , i.e., from the "effective" environment where the microcrack is assumed to be embedded. In the DCM [1], more specifically, each microcrack is placed in the undamaged matrix ($\mathbf{S}^0 = \mathbf{S}^m$) subjected to the unviolated remote stress $\sigma^0 = \sigma^\infty$ (i.e., $\mathbf{H} = \mathbf{I}$ with \mathbf{I} being the fourth-order identity tensor). In the SCM [2], the environment of each microcrack is the unviolated remote stress $\sigma^0 = \sigma^\infty$ and a damaged effective medium having the as-yet-unknown compliance ($\mathbf{S}^0 = \mathbf{S}^{\text{SCM}}$). The SCM generally overestimates the effects of microcrack interaction. Therefore, the GSCM [5] modifies it by assuming that a microcrack is first inserted in an undamaged matrix ($\mathbf{S}^0 = \mathbf{S}^m$) with a certain volume and shape, and then both the microcrack and its surrounding matrix are placed into an effective medium with the as-yet-unknown compliance, \mathbf{S}^{GSCM} . As the simplest version of the effective field method, the MTM [3] puts each inhomogeneity into the undamaged pristine matrix ($\mathbf{S}^0 = \mathbf{S}^m$) loaded by the matrix average stress tensor $\bar{\sigma}^m$. In the DM [4], the opening displacement of the α -th microcrack is calculated by locating it in a damaged effective medium that is subjected to σ^∞ and has the compliance determined from the last step, i.e. the compliance of an RVE containing $(\alpha - 1)$ microcracks, denoted as $\mathbf{S}_{(\alpha-1)}^{\text{DM}}$. In the ESCM [7], the effective moduli of a heterogeneous material are estimated by assuming that each inclusion is embedded in the pristine matrix ($\mathbf{S}^0 = \mathbf{S}^m$) and subjected to an effective stress field ($\sigma^0 = \sigma^E$), which is determined in an interesting manner. Furthermore, the Walpole's bounds on effective compliance, the two-step approximate method in [8, 9] and some other methods can also be implemented into the same framework.

In addition, it can be seen from (10) that an effective field method may be mapped to an effective medium method in the sense that their estimates of effective moduli are identical. Substituting (7) into (6) yields

$$\bar{\mathbf{b}} = [\mathbf{B}(\mathbf{S}^0, \mathcal{G} \sigma^0) \cdot \mathbf{H}] \cdot \sigma^\infty \cdot \mathbf{n}. \quad (11)$$

Therefore, provided that one compliance tensor \mathbf{S}^0 can be found such that

$$\mathbf{B}(\mathbf{S}^0, \mathcal{G} \sigma^\infty) = \mathbf{B}(\mathbf{S}^m, \mathcal{G} \sigma^0) \cdot \mathbf{H}, \quad (12)$$

then the effective medium method defined by $\mathbf{S}^0 = \mathbf{S}^{*0}$ and $\boldsymbol{\sigma}^0 = \boldsymbol{\sigma}^\infty$ will lead to the same results as the effective field method defined by $\mathbf{S}^0 = \mathbf{S}_m$ and $\boldsymbol{\sigma}^0$, that is to say, these two methods are equivalent with each other.

3. NEW ESTIMATES OF EFFECTIVE MODULI

The arguments above indicate that, apart from their heuristic foundations, the conventional estimation methods are developed by only several possible choices of the compliance \mathbf{S}^0 of the comparison matrix material and the far field stress $\boldsymbol{\sigma}^0$ in the simplified calculation model in Fig. 1(b). Clearly, any number of other choices are admissible for estimation of the effective moduli of microcracked solids. Several novel and efficient schemes are presented as follows.

First, choose

$$\boldsymbol{\sigma}^0 = \boldsymbol{\sigma}^\infty, \quad \mathbf{S}^0 = (1 - \xi f^\eta)^{-1} \mathbf{S}^m, \quad (13)$$

where ξ and η are two adjustable parameters, and f is the conventional scalar microcrack density parameter [1, 2].

The effective medium method defined by (13) is first used to consider an isotropic solid containing penny-shaped microcracks whose orientations and locations are uniformly distributed. The normalized effective Young's modulus and shear modulus are easily obtained from (10) and (13) as

$$\frac{E}{E^m} = \left[1 + \frac{16(1 - (\nu^m)^2)(10 - 3\nu^m)f}{45(2 - \nu^m)(1 - \xi f^\eta)} \right]^{-1}, \quad \frac{G}{G^m} = \left[1 + \frac{32(1 - \nu^m)(5 - \nu^m)f}{45(2 - \nu^m)(1 - \xi f^\eta)} \right]^{-1}, \quad (14)$$

where E^m , G^m and ν^m are the Young's modulus, shear modulus and Poisson's ratio of the matrix.

When one takes $\xi = 0$, evidently, the results (14) reduce to those obtained from the DCM. It is also found that when $\xi = 1.778$ and $\eta = 1.0$, the results are in a very good agreement with the SCM estimates. Therefore, the new estimation scheme defined by (13) has the following advantages. First, the derivation of the effective moduli is as straightforward and convenient as the DCM, without numerical iteration being required. Second, the choice of (13) can yield the results in good agreement with DCM, SCM, GSCM, DM when taking appropriate values of ξ and η . For application, the values of the constants ξ and η can be determined by fitting experimental results or other theoretical results of good accuracy. By comparing the effective moduli (14) to the GSCM estimates for the same isotropic case, for example, it is obtained that $\xi = 0.45$ and $\eta = 0.95$. Third, no cut-off point prevails in the present approximate scheme provided that $\xi < 1$.

Second, one may also specify

$$\boldsymbol{\sigma}^0 = \boldsymbol{\sigma}^\infty / (1 - \xi f^\eta), \quad \mathbf{S}^0 = \mathbf{S}^m, \quad (15)$$

which means that the \mathbf{H} tensor is defined as

$$\mathbf{H} = (1 - \xi f^\eta)^{-1} \mathbf{I}. \quad (16)$$

Substituting (15) into (10) yields the results consistent with those obtained from (13). Therefore, the effective field method defined by (15) is equivalent to the effective medium one defined by (13).

Third, we let [8]

$$\sigma^0 = \sigma^\infty, \quad S^0 = S^{\text{DCM}} \quad (17)$$

It is well known that the SCM often overestimates the reduction of effective stiffness, namely, the stress amplifying effects of microcrack interaction. This implies that the effective medium assumed in the SCM is too compliant. Instead, therefore, the effective moduli from the DCM are suggested for the comparison medium. Since the effective stiffnesses from the DCM are higher than those from the SCM, better results may generally be expected from the suggested scheme. Moreover, no numerical iteration procedure is required. Therefore, this scheme combines the advantages of the DCM and SCM, and can account for the interaction effects in a two-step straightforward procedure.

4. CONCLUSIONS

The formal similarity of the intrinsic structures of the conventional estimation schemes is elucidated for microcracked solids. They presents only several possible choices or approximations of the compliance tensor S^0 of the comparison matrix and the far field stress σ^0 which a microcrack is subjected to. A correspondence relation exists between the effective medium methods and the effective stress (or strain) field methods in the sense their results are identical. The approximations in the conventional estimation techniques are by no means better than other possible choices of S^0 and σ^0 . Therefore, several new methods are proposed as examples for estimating the effective moduli of microcracked solids, though any number of other possibilities may be thinkable. In particular, the new effective medium method defined by (13) and its equivalent effective field method defined by (15) can take the effects of microcrack interaction on the effective moduli into consideration in a very simple and efficient manner, and can reduce to some conventional methods when taking appropriate values of ξ and η . The discussion in this paper can be extended to other heterogeneous materials, such as composites containing inclusions and solids with voids.

ACKNOWLEDGEMENT

This work is supported by the National Natural Science Foundation of China (No. 19891100).

REFERENCES

1. J. R. Bristow, *British J. Appl. Phys.*, **11**, (1960) 81-85.
2. B. Budiansky and R. J. O'Connell, *Int. J. Solids Struct.*, **12**, (1976) 81-97.
3. Y. Benveniste, *Mech. Res. Comm.*, **13**, (1986) 193-201.
4. Z. Hashin, *J. Mech. Phys. Solids*, **36**, (1988) 719-734.
5. Y. Huang, K. X. Hu and A. Chandra, *J. Mech. Phys. Solids*, **42**, (1994) 1273-1291.
6. M. Kachanov, *Appl. Mech. Review*, **47**, (1992) 304-335.
7. Q. S. Zheng and D. X. Du, *Key Engng. Mater.*, **145-149**, (1998) 479-486.
8. X. Q. Feng and S. W. Yu, *Mesomechanics 2000*, Tsinghua University Press, Beijing (2000) 341-347.
9. X. Q. Feng and D. Gross, *Acta Mechanica*, **139**, (2000) 143-159.

Realization of Higher-mode Deformation of Beams Using Shape Memory Alloy Wires and Piezoceramics

S.M. Pae, H.J. Lee, H.C. Park and W. Hwang

Department of Mechanical Engineering, Pohang University of Science and Technology
San 31 Hyoja-dong, Nam-gu, Pohang 790-784, Korea

Keywords: Actuator, Higher Mode Deformation, Piezoceramics, Shape Control, Shape Memory Alloy

ABSTRACT

In this study shape memory alloy wires and piezoceramic actuators were employed in order to generate higher modes on the beam deformations without intermediate supporting points. Compressive forces were generated and applied to the beam by the prestrained shape memory alloy wires attached at both ends of the beam. The piezoceramic actuators applied concentrated moments to several locations on the beam. Combinations of the compressive force and concentrated moments were investigated in order to understand the higher-mode deformation of cantilevered and simply supported beams. The first mode shape was obtained by applying heat to the shape memory alloy wires so that the wires generated and applied a compressive force to the beam. First and third mode-shapes of deformation of the cantilever beam have been generated as well as first and second modes of the simply supported beam.

1. INTRODUCTION

For large space structures, due to the high cost of construction and transportation into the space, weight reduction has been an important issue. Unfortunately such weight reduction results in a decrease in structural rigidity, with a possible result in structural instability and inaccuracy in structural shape. Research has been carried out to maintain the design function of the structure by making use of smart materials such as piezoceramic materials (PZT) and shape memory alloys (SMA).[1] The first mode shape in a beam and structure is the fundamental mode in deformation and vibration. However, if higher modes of deformation can be achieved without intermediate supporting points, a new methodology in the shape control of the structure will be provided. The purpose of this research is to build up a design concept of higher-mode deformation on a beam without any intermediate supports. By using SMA wires and piezoceramics as actuators, the weight increase can be minimized and the control method simplified.[2,3]

In this study, Compressive force was generated and applied to the beam by the pre-strained shape memory alloy wires attached at both ends of the beam.[4] The piezoceramic actuators applied concentrated moments to several locations on the beam.[5] Combinations of the compressive force

and concentrated moments were investigated in order to understand the higher-mode deformation of cantilevered and simply supported beams. First and third mode-shapes of deformation of the cantilever beam have been generated as well as first and second modes of the simply supported beam.

2. ANALYSIS

2.1. Piezoceramic(PZT) actuators

The in-plane actuator strain can be derived from the converse piezoelectric equation.[6] The strain developed by the electric field on the actuator layer, ε^A , is given by

$$\varepsilon^A = \mathbf{c}^{-1} \mathbf{e}^T \mathbf{E} \quad (1)$$

where \mathbf{c} is the stiffness coefficients matrix of piezoelectric material, \mathbf{e} is the piezoelectric coefficients matrix and \mathbf{E} is the electric field vector. The equivalent actuator moments by the electric field, M^A , per unit length, can be found by substituting equation (1) and integrating the thickness of the plate, t^A ,

$$M^A = \int_{t^A} \mathbf{c} \varepsilon^A z dz \quad (2)$$

When the control voltage is applied to the actuator in the thickness direction and only d_{31} among the piezoelectric stress components is considered, the equivalent moments, M^a , can be expressed as follows, because the axial components are dominant when applied to the specimen:

$$M^a = c_{11} d_{31} \bar{z} V^A \quad (3)$$

Here, \bar{z} is the z -coordinate of the middle plane of the piezoelectric material.

2.2. Shape memory alloy wires

The constitutive law, with origins in work by Tanaka and recently modified by Brinson, is chosen for use in this study.[7,8] Due to the nature of the transformations, SMA wire is predominantly characterized and utilized in wire (1-D) form. So stress generates compressive force in the axial direction of the wire. Cross sectional area of the SMA wire is relatively small relative to the wire length. If uniform stress occurs in that cross section, compressive force can be calculated by integrating the stress through the cross section area. When deformation of specimen is terminated, this force is balanced by the reaction of the specimen and deformed shape of beam is obtained by using von karman equation, $\varepsilon_b = yw''$. [9] The internal force in the beam balances the generated force in the following equation:

$$F_{SMA} = - \int_{A_b} \sigma dA = - \int_{A_b} E_b \varepsilon_b dA = - E_b I_b w'' \quad (4)$$

where E_b is Young's modulus, A_b the cross sectional area and I_b is the moment of inertia of the beam. So w'' is as follows:

$$w'' = - \frac{A_{SMA}}{E_b I_b} [E_s (\zeta) (\varepsilon - \alpha \zeta_s) + \Theta (T - T_0)] \quad (5)$$

where A_{SMA} is the cross-sectional area of the SMA wire; E_s , stiffness; Θ , thermoelastic constant; T , temperature; and ζ , the volume ratio of the martensitic phase. The "0" subscript indicates initial state of the material at the start of the thermomechanical loading process.

2.3. Deformed shape of the beam

Dividing the beam into n elements, the i th element has nodal points $(i-1)$ and (i) . The shape of the i th element depends on the positions of the two nodal points. By setting X_i and Y_i as the distance between the $(i-1)$ th and the i th nodal points in the x and y direction respectively, shape function of the i th element can be expressed as function of x , X_i , Y_i . The length of the beam is expressed as an integration of the shape function. Generally, all nodal points rotate by angle ϕ with the exception of the clamped nodal point. It should be noted that the shape function also changes because of ϕ , l_x and l_y , which are denoted as the projections for changes in X_i and Y_i respectively, due to rotation. Figure 1 shows the i th element with the concentrated moment actuated in the middle of the element by the piezoceramic actuator.

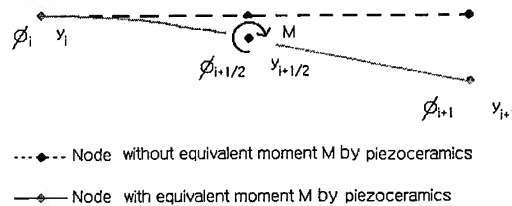


Fig. 1 Effect by the concentrated moment

There are three quantities, l_x , l_y and ϕ , which need to be determined. The $l_{y+1/2}$ and $\phi_{i+1/2}$ in the middle of the i th element are as follows:

$$\phi_{i+1/2} = \frac{M^a L^a l_{x_i}}{2E_b I} + \phi_i \quad l_{y_{i+1/2}} = \frac{M^a L^a l_{x_i}^2}{8E_b I} + \frac{\phi_i l_{x_i}}{2} + l_{y_i} \quad (6)$$

where L^a is the length of the piezoceramic actuator. The rotation ϕ , for the $(i+1)$ th element is the same as $\phi_{i+1/2}$.

$$\phi_{i+1} = \phi_{i+1/2} \quad l_{y_{i+1}} = l_{y_{i+1/2}} + \frac{l_{x_i}}{2} \tan \phi_{i+1/2} \quad (7)$$

Therefore, the deformation of the beam is the combination of deformation due to the compressive force by the SMA wires and the concentrated moment by the PZT actuators.

3. EXPERIMENTS

Cantilevered and simply supported beams were used for shape control experiments. Two different lengths were used for the cantilevered beam. One was $230L \times 20W \times 1.25T$ mm and made of a carbon/epoxy composite material; the other was $350L \times 25W \times 2T$ mm and made of an acrylic material. Acrylic material was used for the simply supported beam and its length was 500 mm. The jigs holding the SMA wires were attached to the ends of the beam so that the wires created and applied an external compressive force to the beam. Positions of the piezoceramics were arranged so that they applied the concentrated moments at one-quarter and three-quarters of the length of the beam, from the clamped side. For the simply supported beam, metallic bars were attached at both ends of the beam. One of the bars was fixed and the other was placed on the roller so that it could move along the beam axis. Figure 3 shows the experimental setup. The specimen was positioned vertically so that the effect of the weight of the specimen was minimized.

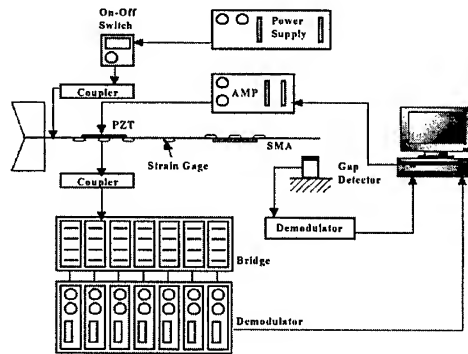


Fig. 3 Experimental setup

4. RESULTS AND DISCUSSION

4.1. Cantilevered beam

Figure 3 shows the deformed shape of the first mode after fine-tuning, using the SMA wires and PZTs. The maximum error was approximately 7% compared with the analysis. Most of the error was attributed to the approximation of stiffness-difference between the beam and the piezoceramics. When the SMA wire had a pre-strain of 5%, the displacement at the free-end was approximately 12 mm, which is nearly ten times more than that compared with PZT actuators alone.

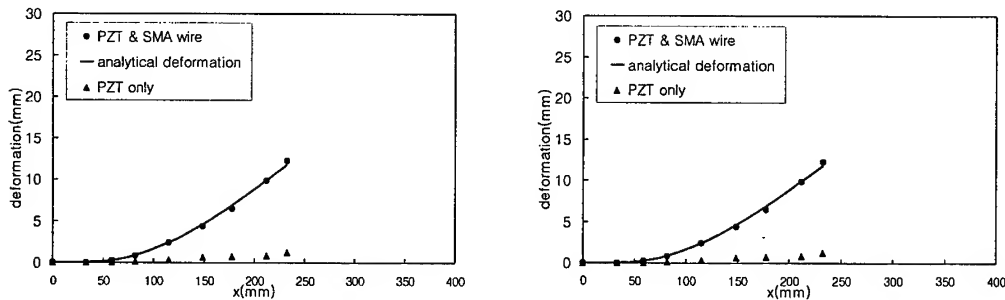


Fig. 3 First mode shape control using SMA wires and piezoceramics

Figure 4 shows the third mode deformation of the beam with an intermediate node. The maximum error was approximately 8%, and the free-end displacement about 8.5 mm.

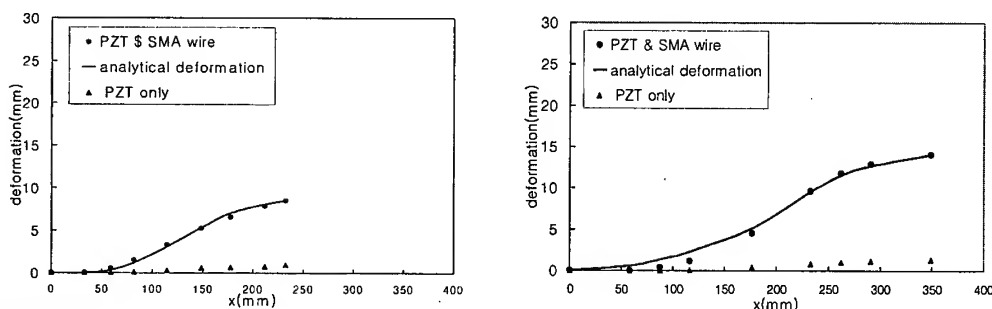


Fig. 4 Third mode shape control using piezoceramics with an intermediate node

Figure 5 shows the third mode deformation of the beam without an intermediate node.

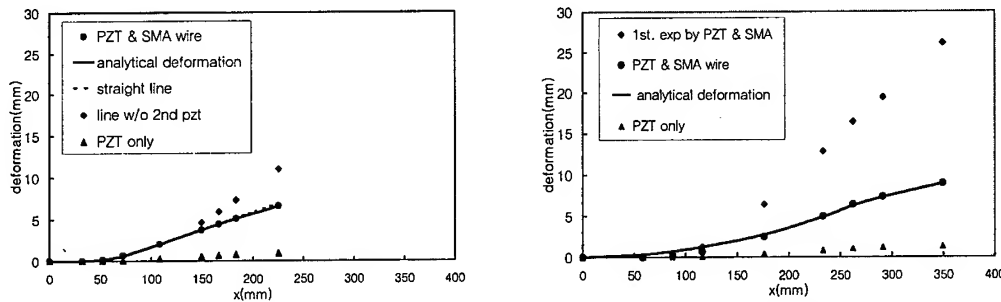


Fig. 5 Third mode shape control using piezoceramics without an intermediate node

The maximum error was approximately 3%. Figure 5 demonstrates that there was no effect on the result obtained when a 230-mm length beam was used. In this case, the line without the second piezoceramics set was the deformed shape, with the piezoceramics set at three-quarters of the beam. In Figure 5, the straight-line tangent to the deformed curve at the inflection point is included in order to show the deformed shape more clearly.

4.2. Simply supported beam

The first and second modes of the deformation for the simply supported beam were carried out. For the first mode-shape generation, the compressive force by the SMA wires was applied first, then the concentrated moments applied in order to fine-tune the shape, as shown in Figure 6.

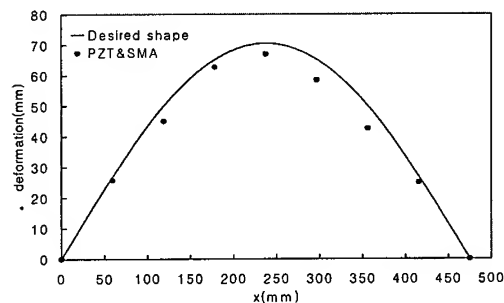


Fig.6 First mode shape control using SMA wires and piezoceramics

For the second mode-shape generation, the concentrated moments were first applied to the beam. Thereafter, the compressive force was applied in order to magnify the deformation. During the application of the compressive force, however, the deformation mode changed to the first mode. These phenomena can happen for the simply supported beam but not the cantilevered beam since both ends of the simply supported beam cannot bear the moments. When concentrated moments were applied to the beam in the beginning, they were localized onto the beam and were not affected by the end conditions. However, when the compressive force was then applied at both ends, it was

affected by the end conditions. When a small amount of imbalance in the moments existed, the intermediate node point moved away from the beam neutral axis. Thus, the deformed shape changed to the fundamental mode of the first mode.

5. CONCLUSIONS

Shape control of cantilevered, simply supported beams was carried out, making use of shape memory alloy wires and piezoceramic actuators. The following conclusions have been drawn:

- (1) Higher-mode deformation shapes can be achieved by employing SMA wire to generate a compressive force, and piezoceramics to generate concentrated moments onto the cantilevered beam.
- (2) For a simply supported beam, it is possible to realize the second mode-shape temporarily. However, if the moment balance in the intermediate node cannot be maintained, the mode-shape changes to the first mode.
- (3) The first mode-shape can be achieved by temperature control of the SMA wire only. The higher mode-shape of the deformation can be achieved by concentrated moments applied to several locations on the beam. However, the magnitude of the deformation is very small.

REFERENCE

1. A. Baz, T. Chen and J. Ro, SPIE, **2190** (1994) p.436
2. Jason B. Ditman, Lawrence A. Bergman and Tsu-Chin Tsao, J. of Intel. Mat. Sys. and Struc., **7** (1996) p.635
3. Minoru Hashimoto, Masanori Takeda, Hirofumi Sagawa, Ichiro Chiba, and Kimiko Sato, J. of Robotic Systems, **2**, **1** (1985) p.3
4. D.E. Hodgson, M.H. Wu and R.J. Biermann, Selected Properties of Niti in Niti smart sheet(sm), Shape Memory Application Inc. (1998)
5. Fuji Ceramics, Piezoelectric Ceramics, Fuji Ceramics Co., Ltd., Tokyo (1994)
6. V.Z. Parton, and B.A. Kudryavtsev, Electromagnetoelasticity Piezoelectrics and Electrically Conductive Solids, Gordon and Beach Science Publishers, Amsterdam (1988)
7. K.Tanaka, Res. Mech., **18** (1986) p. 251
8. L.C. Brinson, M.S. Huang, C.Boller and W.Brund, J. of Intel. Mat. Sys. And Struc., **8** (1997) p.12
9. S.P. Timoshenko, Strength of Materials : Part I, Krieger Publishing, Melbourne FL (1984)

Author Index

A

Adachi, T..... 731
 Ahn, Heung Gu 391
 Akama, M. 1035
 An, C.W. 349, 481
 An, J.Y. 987
 An, W.K. 1087
 Ando, Kotoji 803, 833, 921, 1047
 Aoki, Yoshio 1093
 Aoyama, E..... 643
 Arakawa, K. 265, 409

B

Bae, D.H..... 415, 957, 993, 1345
 Bae, S.I..... 1029, 1267
 Bahk, Saemahn 529
 Bai, C.H. 277
 Bai, Shiwei 433
 Bai, Shu-Lin 761, 839, 987, 1075
 Bai, Yong 1023
 Baik, Y.M..... 31
 Bush, Mark B. 1261
 Byon(Goichi Ben), O.I..... 1093
 Byun, T.S..... 607

C

Cha, H.J..... 655
 Chae, S.H. 1135
 Chang, T..... 181
 Chang, Yoon-Suk..... 505
 Chau, K.T..... 109, 809, 857
 Chen, J.K..... 761, 1075
 Chen, Jian..... 487
 Chen, Junmei..... 1315
 Chen, Z..... 187
 Cheong, YongMoo..... 845
 Cho, D.W. 559
 Cho, J.R..... 373, 403
 Cho, M.H. 355
 Cho, M.R..... 43, 493
 Cho, S.K..... 517
 Cho, S.Y..... 993, 1345
 Cho, Seong-Jae 1249
 Cho, Y.T..... 1219
 Choi, J.B..... 655, 869
 Choi, J.H. 481

Choi, N.S. 247, 1081
 Choi, S.J..... 827
 Choi, Sang-Woo 619
 Choi, W.C. 559
 Choi, Younho..... 1099
 Choo, KeeNam 845
 Chu, M.C. 833, 1047
 Chun, H.-J..... 427, 1069
 Chung, J.H. 1207
 Chung, K.H..... 43
 Clegg, W.J. 1213
 Cotterell, B..... 187
 Cui, Zhaoxia 589, 1303

D

Dai, F.L..... 737
 Ding, C.F. 127
 Du, S.H. 91
 Du, Shanyi 487
 Duan, Zhuping 343

E

Earmme, Y.Y. 1123
 Ebara, R. 939

F

Fang, D.N..... 821
 Fang, F. 175
 Fang, Q.Z. 951
 Feng, W.J. 241
 Feng, X.Q..... 667
 Feng, Xia-Ting..... 385, 713
 Fu, Guoru..... 969
 Fu, Ran..... 695
 Fu, Y.F. 785
 Fujimoto, T. 313, 445
 Fujinami, A. 583
 Fujisaki, T. 565
 Fukuda, T. 583
 Fukui, Y. 565
 Fukuyama, K..... 553

G

Gao, C.Y. 277
 Gao, J.G. 67
 Gao, S.L. 1063

Geni, M.	625
Gladkovsky, S.V.	863
Gladkovsky, V.A.	863
Goo, B.C.	1225
Goto, H.	999
Gross, D.	331
Guo, W.	181, 193
Guo, Yongjin.	1111

H

Ha, D.Y.	373, 403
Ha, J.K.	283
Ham, K.C.	1029, 1267
Han, Jae-Hung.	1201
Han, Kyung Seop.	547, 661, 945, 1011, 1117, 1267, 1297
Han, S.Y.	361, 379, 439
Hattori, N.	169, 963, 1243
Hawong, J.S.	283
Hayashi, K.	1243
He, Buolin.	613
He, L.	457
He, Pengfei.	1213
Herrmann, K.P.	1141
Higashi, K.	851
Hirata, T.	851
Hirogaki, T.	643
Homma, Hiroomi.	893
Hong, C.S.	535, 1189
Hong, J.H.	607
Hong, K.S.	463
Hong, S.I.	1207
Hong, Soon H.	1153, 1183, 1291
Hong, Sun Ig.	1255
Hong, Youshi.	157
Hou, Yunfeng.	319
Hu, X.Z.	1177
Hu, Xiaozhi.	1261
Hua, Y.	571, 881
Huang, Jianlong.	37
Huang, M.L.	785
Huang, S.Z.	571, 881
Huang, Y.	9
Huang, Z.P.	761, 1075
Huh, N.S.	655
Huh, S.C.	1237
Huh, Yong-Hak.	1249
Huo, Lixing.	613, 1315, 1327
Hurtado, Juan A.	1
Hwang, B.S.	791

Hwang, J.S.	307
Hwang, K.C.	9, 821
Hwang, S.S.	707
Hwang, W.	661, 673, 945, 1117
Hyakutake, Hiizu.	601

I

Ibrahim, R.N.	1339
Igawa, H.	25
Ikeda, T.	73
Im, J.W.	1041
Imanaka, M.	583
Inoue, H.	643
Ishigami, H.	921
Ishii, H.	827

J

Jang, P.-S.	1069
Jang, Y.K.	869
Jarng, Soon Suck.	391
Jeong, H.-Y.	1195
Jeong, S.K.	1135
Jiang, H.Y.	79
Jiang, J.G.	67
Jiang, Z.Q.	571, 881
Jin, F.	725, 755
Jin, Tae-Eun.	505, 797
Jing, H.Y.	1327
Jo, C.H.	349, 481
Joo, S.G.	535
Joung, K.K.	1029
Ju, Dong-Ying.	97
Jung, C.K.	1011
Jung, J.H.	517
Jung, S.G.	797
Jung, S.W.	1117, 1297

K

Kanemitsu, M.	1159
Kanemitsu, Tsuyoshi.	337
Kang, Heung-Seok.	743
Kang, K.W.	271
Kang, Tae Jin.	1165
Katayama, T.	643
Kikuchi, M.	625
Kikuchi, Masanori.	875
Kim, B.H.	791
Kim, B.K.	1345
Kim, C.	295, 469
Kim, C.G.	1189

Kim, C.H. 993, 1345
Kim, D.S. 415
Kim, D.Y. 1171
Kim, E. 349
Kim, G.H. 307
Kim, H.G. 1219
Kim, H.P. 595, 707
Kim, H.S. 815, 1207
Kim, Hyoung Seop. 1255
Kim, Hyung-Kyu 743
Kim, Hyun-Su 505
Kim, I.S. 607
Kim, J. 631
Kim, J.B. 767
Kim, J.D. 1309
Kim, J.H. 103, 933, 1029
Kim, J.K. 85, 271, 1063, 1177
Kim, J.S. 595, 707, 1123
Kim, J.Y. 1219
Kim, K.H. 1029, 1147
Kim, K.S. 31, 349, 463, 481
Kim, Kyung-Suk 1
Kim, M.G. 933
Kim, M.H. 415, 1105
Kim, Moon-Saeng 915
Kim, P.W. 1153
Kim, S.H. 403
Kim, S.J. 19
Kim, SungSoo 845
Kim, T.W. 295, 1279
Kim, Y.C. 1153
Kim, Y.H. 1017
Kim, Y.J. 655, 869
Kim, Y.K. 1183
Kim, Y.S. 355, 1309
Kim, YoungSuk 845
Kim, Yun-Jae 133, 1333
Kishimoto, Kikuo 121, 541, 779, 1053
Kobayashi, Albert S. 97, 325
Kobayashi, Y. 999
Kodama, K. 145
Kohzu, M. 851
Komohara, Y. 73
Kong, C.W. 1189
Kook, J.S. 731
Kuboki, T. 289
Kuk, I.H. 707
Kumazawa, N. 565
Kwak, D.S. 1321
Kwon, H.S. 595

Kwon, J.D. 577, 827, 975
Kwon, S.J. 1225
Kwon, SangChul. 845
Kwon, Y.D. 355, 469
Kwon, Y.K. 1321

L

Lang, Fuyuan 55
Lee, C.J. 1321
Lee, C.S. 945
Lee, D.J. 1171, 1219
Lee, Dong Nyung. 679
Lee, H.J. 283, 673
Lee, H.S. 1183
Lee, H.Y. 559
Lee, In. 1201
Lee, J.H. 61, 295, 1297
Lee, J.J. 259, 1147
Lee, J.K. 791
Lee, J.R. 1105, 1183
Lee, J.Y. 307
Lee, Je Hyeng. 391
Lee, Joon-Hyun. 619, 887
Lee, K.R. 767
Lee, K.W. 103
Lee, Kyung Woo. 1165
Lee, Min-Rae 887
Lee, O.S. 283, 349, 481
Lee, Ouk Sub 307, 325
Lee, S.B. 103
Lee, S.C. 463
Lee, S.G. 903
Lee, S.H. 1087
Lee, S.P. 1237
Lee, S.W. 427
Lee, T.H. 379, 439
Lee, W.H. 577
Lee, W.I. 631
Lee, Y.S. 451, 577, 975
Li, C.Y. 511
Li, Ch. 211
Li, Dahong 253
Li, H.B. 67
Li, J.C. 217
Li, Qingfen. 589, 1303
Li, T.J. 67
Li, Tao. 1231
Li, Tingjie 433, 713
Li, Youtang. 37, 319
Li, Z. 181

-
- | | | | |
|-----------------------|----------------|------------------------|---------------------|
| Li, Z.L. | 79, 91 | Nam, Jaebok | 547 |
| Li, Zheng | 301 | Ni, Huocai | 589, 1303 |
| Liang, Wei | 199 | Nie, G.H. | 1005 |
| Liang, Z.Z. | 637 | Nishida, S. | 169, 963, 1243 |
| Liao, Guo-Hong | 1023 | Nishimura, F. | 749, 981, 1017 |
| Lim, B.S. | 1041 | Nishioka, T. | 313, 445 |
| Lim, J.H. | 1123 | Nisitani, H. | 553, 749, 981, 1017 |
| Lim, J.K. | 379, 439 | Noda, N.-A. | 475, 499, 523 |
| Lim, Y.S. | 595, 707 | Noh, H.K. | 1219 |
| Lin, P. | 637, 809, 857 | Notomi, M. | 121 |
| Lin, Xiaoying | 423 | Notomi, Mitsuo | 779 |
| Liu, B. | 821 | | |
| Liu, C.L. | 277 | O | |
| Liu, Chuntu | 151, 163 | Oguchi, T. | 97 |
| Liu, H.Y. | 637 | Oh, T.Y. | 1321 |
| Liu, J.X. | 139 | Okada, H. | 565 |
| Liu, J.Z. | 127 | Omura, M. | 541 |
| Liu, Li | 423 | Osaka, K. | 583 |
| Liu, X.F. | 139 | | |
| Liu, X.L. | 139 | P | |
| Liu, Y.I. | 1327 | Pae, S.M. | 673 |
| Liu, Y.J. | 951 | Paik, K.W. | 1123 |
| Liu, Z.D. | 987, 1075 | Park, D.G. | 607 |
| Liu, Zongde | 839 | Park, H. | 295 |
| Long, Ping | 589 | Park, H.C. | 661, 673, 945 |
| Lyu, M.Y. | 259 | Park, Hoon Cheol | 1099 |
| | | Park, I.S. | 791 |
| M | | Park, J.B. | 1129 |
| Ma, Jun | 1231 | Park, J.C. | 577, 975 |
| Ma, Maoyuan | 589 | Park, J.G. | 469 |
| Machida, Kenji | 49 | Park, Jae Chull | 391 |
| Mada, T. | 265, 289 | Park, K.H. | 1237 |
| Maeng, J.S. | 361 | Park, M.K. | 529 |
| Mai, Y.-W. | 217 | Park, S.B. | 791 |
| Mao, X.P. | 987 | Park, S.J. | 1105 |
| Matsui, K. | 921 | Park, S.K. | 1219 |
| Matsuo, T. | 499, 523 | Park, S.W. | 1279 |
| Miyazaki, N. | 73 | Park, Y.W. | 577, 975 |
| Mizumoto, M. | 719 | Peng, Xianhai | 1303 |
| Morino, K. | 749, 981, 1017 | Putra, I.S. | 649 |
| | | Pyo, C.R. | 655 |
| N | | | |
| Nagawa, M. | 475 | Q | |
| Nakamura, A. | 73 | Qi, H.B. | 571, 881 |
| Nakano, K. | 963, 1243 | Qu, Shaoxing | 1111 |
| Nakayasu, H. | 1159 | | |
| Nakazato, Kohji | 893 | R | |
| Nam, H.W. | 1117, 1297 | Raghukandan, K. | 205, 1273 |
| Nam, J.B. | 1297 | Rew, Keun-Ho | 1201 |
| Nam, J.H. | 115 | Rui, Zhiyuan | 37 |

Ryu, Ho J. 1291

S

Saimoto, A. 553
 Sakakura, K. 313
 Sakamoto, Hidetoshi 719
 Sato, Shigemi 803, 833, 1047
 Sawa, Yoshiaki 337
 Senthilvelan, T. 205, 1273, 1285
 Seo, D.C. 103
 Seto, M. 713
 Shehata, T. 1339
 Shen, Yapeng 199
 Shi, H.J. 277
 Shi, R. 1005
 Shi, Y.P. 397
 Shibuya, T. 541
 Shibuya, Toshikazu 779
 Shih, Shaochiu 253
 Shim, D.J. 869
 Shim, D.S. 85
 Shimamoto, A. 97, 115, 145
 Shimomura, T. 115
 Shin, D.C. 283
 Shin, D.K. 259
 Shin, Hyung-Seop 915
 Shin, I.J. 1171
 Shin, K.C. 1147
 Sohn, I. 957
 Sohn, M.S. 1177
 Sohn, Min-Seok 1255
 Son, S.Y. 963
 Song, D.Y. 1129
 Song, H.S. 791
 Song, J.I. 1029, 1267
 Song, Jiho 1249
 Song, K.N. 451
 Song, Y.Y. 607
 Sonoya, Keiji 909
 Su, B. 211
 Su, Wei 969
 Su, Xianji 301
 Suh, M.W. 61, 415
 Sun, Chengwei 343
 Sun, Hai-Hong 1023
 Sun, Yi 1231
 Sung, K.D. 493
 Susuki, I. 1035
 Syam, Bustami 893

T

Takahashi, Akiyuki 875
 Takahashi, K. 229, 265, 289, 409,
 1017, 1081
 Takao, Y. 815
 Takase, Y. 475
 Takeda, N. 1129
 Takeuchi, K.-I. 475
 Tamasaki, H. 1243
 Tan, Xianxiang 343
 Tanabe, S. 851
 Tanaka, M. 367
 Tanaka, Y. 999
 Tang, C.A. 637, 785, 809, 857
 Tang, G.H. 457
 Teranishi, T. 553
 Tobe, Shogo 909
 Todo, M. 409
 Tong, Pin 695
 Tsuji, Kiichi 803

U

Umezaki, E. 115, 145

V

Venkatraman, A. 205, 1273, 1285

W

Wang, Bintuan 899, 927
 Wang, C.H. 217
 Wang, Dongpo 1315
 Wang, Lili 253
 Wang, Liquan 1303
 Wang, T.J. 725, 755
 Wang, Tiejun 121, 779
 Wang, W.X. 815
 Wang, Y.S. 331
 Wang, Z.K. 725, 755
 Wei, Yaobing 55, 319
 Wen, Sanggang 343
 Won, Y.G. 1153
 Wong, R.C.K. 109
 Wong, Robina H.C. 109, 809, 857
 Woo, S.W. 975
 Wu, Linzhi 487
 Wu, S.X. 511
 Wu, X.R. 127

X

Xing, Y.M. 737

Xu, Ping 385
Xu, Yongjun 151, 163

Y

Yamada, Y. 939
Yamaguchi, T. 719
Yamamoto, H. 169
Yamamoto, Toshihiro 601
Yamamura, H. 939
Yanagida, Y. 1243
Yang, I.Y. 731
Yang, Kun 839, 987
Yang, Qingxiong 899, 927
Yang, Sanglin 1303
Yang, Shanglin 589
Yang, W. 175, 737
Yang, W.H. 43, 493
Yang, Y.C. 661
Yao, F. 833, 1047
Yao, Z.H. 277
Ye, L. 217
Yeh, B.H. 1153
Yin, H.L. 349
Yoon, H.K. 1087, 1237
Yoon, K.H. 451
Yoon, Kwang Joon 1099
Yoon, Kyung-Jin 1249
Yoon, S.J. 517, 1135
You, D.X. 127
Yu, Hualong 157
Yu, J.M. 61
Yu, X.B. 223
Yun, T.H. 355, 469

Z

Zeng, P. 397, 457
Zeng, Xiangguo 1141
Zhan, F.L. 79, 91
Zhang, Guang 433
Zhang, Junqian 1141
Zhang, R.J. 1005
Zhang, S.B. 571, 881
Zhang, S.S. 951
Zhang, Tong-Yi 695, 773
Zhang, X.P. 217
Zhang, Yufeng 613, 1315, 1327
Zhao, Feng 343
Zhao, Hong 1261
Zhao, J. 67
Zhao, Jianheng 343

Zhao, M.H. 951
Zhao, Minghao 199, 695
Zheng, J. 139
Zhong, Z. 223
Zhou, Aixi 55
Zhou, Yu 1231
Zhu, T. 175
Zhuang, Zhuo 1111
Zong, Z. 725
Zou, Z.Z. 241, 511

Keyword Index

2
2-Phase 933

3
30Cr2MoV Steel 987
3D Glass Fabric Reinforced
Composites 1183

8
8 Harness Woven Fabric 1153

A
A Beam Structure 61
Ablative Composites 1153
Abrasive Wear 1267
Acoustic Emission 713, 887, 903
Across-Laminar 1153
Actuator 673
Adaptive Vibration Control 1201
Adhesive 43
Adhesive Shear Stress 43
Adhesively Bonded Butt Joints 583
AE Count 903
AE Energy 903
AE Hit 903
Aero-Engine 969
AFM 827
Aging Treatment 1237
Alloy 600 595, 707
Alloy 690 707
Aluminum Matrix Composite Brake
Disc 1225
Aluminum/GFRP Hybrid Tube 1147
Amorphous Alloys 1255
Anisotropy 679, 1183
Anodic Oxidation 1105
Apparent Strain Hardening Exponent 1273
Apparent Strength Coefficient 1273
APS 909
Artificial Neural Network 957
Atmosphere Corrosion 899, 927
Attenuation-Based Method 887
Austenite 863
Autocorrelation Function 19
Automobile Hood Design 439

Axial Crush 1147

B
Ball Indentation Test 607
Barkhausen Noise 607
Barrier Strengthening 1207
Basal Pole Component (F) 845
Bending Fatigue 571
Bending Strength 803, 833, 1081
BFM 553
Biaxial Load 115
Biaxiality Ratios 115
Blind Hole 749
Body Force Method 499, 523
Boundary Conditions of Displacement 37
Boundary Conditions of Stress 37
Boundary Element Method 91
Boundary-Layer Effect 43
Brazed 1279
Brittle Failure 637
Brittle Polymers 265
B-Spline 415
Buckling 187, 451, 1189
Buckling Mode Shape 451

C
Calendar Fatigue Life 927
Cantilever Beam (CB) Specimen 845
Carbon Fiber 571, 881, 1105, 1129, 1267
Carbon Fiber Composites 1177
Carbon/Epoxy Laminates 945
Carbon/PEEK Composite 1063
Caustic Curve 349
Caustics Method 115, 265
Cavitation 851
Cavity 139, 821
CBA 1123
CCD Camera 601
Cement Block 301
Cement Mortar 253
Center of Dilatation 109
Ceramic Composite 833
Ceramic Materials 1231
Ceramic/Metal Bilayer Composites 1261
Ceramic/Metal System 1279

Ceramics	1213	Coupling	475
CF8M	577, 975	Cr Depletion.....	707
CFGFRP	1129	Crack.....	25, 139, 175, 181, 331, 385, 511, 613, 821
CFRP	1093, 1129	Crack Bridging Model	103
CFRP Laminates	915	Crack Closure	217, 649, 743, 1249, 1345
Chemical Erosion	713	Crack Coalescence.....	809, 981
Chimes	457	Crack Depth/Specimen Width (a/W).....	589
Cluster Structure	1297	Crack Extension.....	779
Coat	839	Crack Growth Life Prediction	649
Coating Crack	211	Crack Growth Rate	31, 367, 993
Co-Curing Method	1087	Crack Healing	803, 833, 1047
COD-Decrease-Parameter.....	589	Crack Identification	61
Coefficient of Friction.....	1273	Crack Initiation	169, 999
Cohesive Force Model	541	Crack Kinking.....	73, 97
Collective Evolution	157	Crack Opening Period.....	743
Collinear Cracks.....	199	Crack Orientation.....	1303
Combined Mechanical and Electrical Loading	695, 773	Crack Propagating Velocity.....	283
Combined Stress	97	Crack Propagation	169, 565, 981, 1017, 1035
Compliance Method.....	993	Crack Surface Displacement.....	103
Compliant Substrate.....	187	Crack System	55
Composite Element Method	397	Crack Technique.....	55
Composite Laminates.....	535	Crack Tip	9, 157, 737
Composite Materials	307, 1111	Crack Velocity.....	247, 265
Composite Plate	355, 469	Cracked Pipe Welds.....	1327
Composite Structures	1201	Cracked Piping System.....	505
Compressive Residual Stress	921	Crack-Healed Zone.....	1047
Compressive Strength	1189	Cracking.....	187, 1261
Compressive Test.....	1183	Crantz-Schardin Type Stroboscopic Camera.....	337
Condition.....	463	Creep Fracture	367
Configuration of Lamina.....	1159	Creep Life	903
Constant ΔK Fatigue Crack Growth Test.....	19	Creep Rupture Strength	903
Constitutive Relation	667	Creep-Fatigue	1041
Constraint Effects.....	193, 869, 875	Critical Impact Energy.....	271
Contact Area	939	Crush Energy Absorption	1099
Contact Damage	1261	Crystallinity	1063, 1171
Contact Failure.....	743	Cumulative Damage	927, 945
Contact Problems	475	Cu-Nb	1207
Contact Stress Distribution	493	Curing Method.....	1087
Contour Induction Heating	921	Cutting Forces.....	643
Controllable Fracture	55	Cyclic Fatigue Crack Growth	1249
Convergence Rate	379	Cyclic Fatigue Strength	803, 1047
Cooling Rate	1063	Cyclic Hardening.....	975
CORPUS Model.....	649	Cyclic Loading.....	1075
Corrosion.....	1285	Cyclic Stress-Strain Curve.....	975
Corrosion Cell.....	993	Cylindrical Interface Crack.....	241
Corrosion Fatigue.....	993, 999, 1023	Cylindrical Specimen.....	749
Coupled Electromechanical Field	725		
Coupled Field.....	139		

D

- Damage 253, 295, 583, 601, 1075
- Damage Detection 1093
- Damage Mechanism 731
- Damage Parameter 583
- Damage Zone 893
- Damage-Tolerance Analysis 649
- Debonding 43
- Defect Assessment Method 1333
- Deformation 121, 679
- Deformation Energy 205
- Defric Coating 939
- Degraded Material 577
- Delamination 187, 731, 1153, 1189, 1201
- Delamination Fracture 247
- Delaunay Automatic Triangulation 445
- Delayed Hydride Cracking DHC 845
- Design of Reinforcement 439
- Detonation 343
- Devitrification 1255
- Die Entrance Angle 547
- Differential Scanning Calorimetry
 - DSC 1171
- Dilatational Phase Transformation 1231
- Dilute Sulfuric Acid 999
- Dimple Fracture 875
- Direct Current Potential Drop DCPD 655
- Directional Stability 55
- Discrete Micromechanical Model 373
- Dislocation 607
- Distributed Parameter 361
- DL-EPR Test 595
- Domain Walls 607
- Double Cracks 37
- Double Shot Peening 921
- Drill's Life 643
- Ductile Polymer 289
- Ductile Fracture 121
- Ductile Iron 933
- Dynamic Crack Bifurcation 313
- Dynamic Crack Curving 313
- Dynamic Crack Kinking 313
- Dynamic Crack Propagation 265, 313, 325, 445
- Dynamic Fracture 259, 313, 331, 445
- Dynamic Fracture Mechanics 445, 1111
- Dynamic Fracture Toughness 229, 301, 893
- Dynamic Impact 451
- Dynamic Interface Crack Stress Field 325
- Dynamic Interfacial Fracture 313
- Dynamic Isochromatics 283
- Dynamic J Integral 445
- Dynamic Loading Device 283
- Dynamic Maximum Compressive
 - Stresses 307
- Dynamic Modeling 457
- Dynamic Photoelastic Experimental
 - Method 283
- Dynamic Photoelastic Hybride
 - Method 283
- Dynamic Photoelasticity 337
- Dynamic Photoelasticity Method 349, 481
- Dynamic Recrystallization 851
- Dynamic Response 423
- Dynamic Stress Component 283
- Dynamic Stress Intensity Factor 241, 301, 325, 349
- Dynamic Stress-Strain Behavior 307
- Dynamic Triaxial Compressive Loads 67
- Dynamical Loading 253

E

- Edge Cracks 79, 523, 743
- Effective Flexural Modulus 247
- Effective Stress Intensity Factor
 - Range (ΔK_{eff}) 1345
- Eigenfunction 163
- Eigenvalue 163
- Elastic Half Plane 109
- Elastic Plastic Crack Propagation 565
- Elastic Restraint 1135
- Elastic Shear Buckling 517
- Elastic Wave Scattering 241
- Elasticity 499, 523
- Elastic-Plastic Behavior 451
- Elastic-Plastic Fracture Mechanics 1327
- Elastic-Plastic SFEM 613
- Electrical Resistance 1129
- Electrodeposition 679
- Electromagnetic Thermoelasticity 139
- Electronic Speckle Pattern
 - Interferometry ESPI 391
- Element Modeling 397
- Element Removal Method 379
- Element-Free Galerkin Method
 - EFGM 487
- Elevated Temperature 1273
- Elliptical Holes 25
- Embrittlement 577, 1255
- Energy Absorption Characteristics 1147

Energy Release Rate	259, 695, 773	Fiber-Metal Laminates.....	1117
Engineering Analysis	505	Filament	1207
Epoxy Fraction	1081	Finite Element.....	1111
Equilibrium Equation.....	157	Finite Element Analysis.....	133, 373, 403, 505, 529, 547, 869, 1099
Equivalent Engineering Modulus	1159	Finite Element Method	61, 97, 391, 475, 511, 541, 767, 1327
Equivalent Stress.....	999	Finite Element Method of Lines	151
Errors of the Reduced Integration.....	355, 469	Finite Element Modelling	409
Eshelby's Method	1219	First and Second Crack Coalescence.....	857
Eulerian Finite Element Method	565	Fixed Boundary	463
Eutectic Silicon Particle	1017	Fixing Element.....	475
Evolutionary Structural Optimization.....	379	Flexural Properties.....	631
Expansion Fracture	277	Flexural Strength	1159
Experimental Measurement	277	Flexural Test	1183
Experimental Study.....	1075	Fluid-Structure Interaction.....	349, 481
Explosion Experiment.....	319	Flux Cored Arc Welding	1339
Explosive Loading	277, 319	Forced Motion	469
Extrapolation Method	553	Formability	1273
F		Fractal Dimension.....	367
Face Milling	559	Fractographic Study.....	1267
Failure	785, 969	Fractography	169, 719, 731
Failure Analysis	1099	Fracture	169, 319, 679, 695, 773, 969
Failure Behavior.....	1129	Fracture Boundary Curve	1053
Failure Criterion.....	1165	Fracture Mechanics.....	91, 97, 115, 145, 193, 409, 541, 565, 1005, 1213
Failure Index	1117	Fracture Origin.....	749
Failure Mode	535	Fracture Path Prediction	445
Failure Pattern.....	809	Fracture Ratio	505
Failure Probability	797	Fracture Strength of Notch	791
Failure Wave.....	343	Fracture Toughness.....	49, 73, 779, 863
Fatigue.....	719, 749, 933, 951, 969, 981, 1321	Fracture Transformation	55
Fatigue Calendar Life	899	Framed Plate	319
Fatigue Crack Growth.....	85, 127, 1303, 1345	Free Fall Shock.....	451
Fatigue Crack Growth Resistance.....	19	Frequency Effects	31
Fatigue Design Criterion.....	957	Fretting.....	743
Fatigue Life	909, 999	Fretting Fatigue.....	915, 939
Fatigue Life Prediction	945, 957, 1011	Fretting Pad Material	915
Fatigue Limit.....	921, 933, 963	Friction Coefficient.....	547, 915
Fatigue Modulus	945, 1011	Friction Temperature	1225
Fatigue Properties	1309	FRP	601, 1135
Fatigue Reliability.....	927	FT-IR	1105
Fatigue Strength	415, 899, 915, 1315	Full-Scale Pipe.....	655
Fatigue Test.....	951, 1029	Functionally Graded Materials	331, 373, 487, 511
FEM	553, 625, 1093, 1219	Fuzzy Method	433
FEM Analysis	875	G	
Ferroelectrics.....	175	Gas Turbine	1029
Fiber	1297	Gauss Sampling Point.....	355, 469
Fiber Bridging.....	247, 1111		
Fiber Orientation.....	815		
Fiber Pull-Out	1153		
Fiber Waviness.....	427, 1069		

Gears	921, 1285
Generalized Energy Function	55
Genetic Algorithm	1117
Glass Fiber	295
Global Displacement Fitting Procedure	79
Grain Boundary	1207
Grain Boundary Characteristic	851
Grain Boundary Sliding	367
Grain Boundary Triple Junction	851
Grain Size.....	707
Graphite/Epoxy Laminates	731
Graphite/Epoxy Square Tubes	1099
Grating Lobe	619
Grid	451, 463
Grillages	463
Growth-Strain Method	361
Gurson's Constitutive Function.....	875
Gurson's Model	625

H

Hardening.....	1255
Hardness.....	987, 1285
Hardware-in-the-Loop	655
HAZ	1303
Healing Condition.....	803, 833
Heat Treatment.....	933
Heterogeneity.....	637, 785
Heterogeneous Materials	667
Hierarchical Models.....	403
High Density Polyethylene	229
High Impact Polystyrene.....	229, 289
High Strain Rate.....	97, 277, 307
High Temperature Fatigue Crack Growth	1041
High Temperature Strength.....	803, 1047
Higher Mode Deformation.....	673
High-Speed Loading	289
High-Speed Photography	289, 313
High-Speed Shadowgraph Technique.....	343
High-Strain-Rate-Superplasticity.....	851
Hill's Nonquadratic Yield Function	547
HIP Treatment.....	1243
Hold Time	31, 1041
Horizontal Crack.....	109
Horizontal Fatigue Tester	993
HREM-Moiré.....	737
Hybrid Composite.....	1297
Hybrid Fiber Reinforced Concrete.....	571, 881
Hybrid Metal Matrix Composite.....	1267

Hysteresis Loop	1249
-----------------------	------

I

Image Processing	145
Impact	731, 1189
Impact Damage.....	271, 1177
Impact Fracture.....	229, 313, 445
Impact Location Detection	661
Impact Test	577
Imperfect Interface.....	223
Inconel	718, 1029
Infinite Plate.....	199
Ingot Material	205
Initial Stress	755
Initial Velocity	451
Injection Moulding	1081
In-Plane Shear Forces.....	517
Insulating and Conducting Cracks....	695, 773
Intensity Factor	139
Interaction Effect	523
Interaction Energy Method	259
Interface	1279
Interface Adhesion.....	1063
Interface Crack.....	49, 73, 541
Interface Fracture Toughness	541
Interface Layer.....	331
Interface of Bi-Material	211
Interfacial Compliance.....	223
Intergranular Carbide.....	707
Intergranular Corrosion	595
Interlaminar Fracture Toughness.....	229, 815, 1063
Interlaminar Shear Strength	1105
Internal Damaged of Drilled Hole	643
Inverse Fracture Problem.....	37
Inverse Problem	61, 1093
Irwin Method	145
ISM Method.....	903
Isochromatics.....	145
Isotropic/Orthotropic Bimaterials	283

J

J-Integral	31, 133, 505, 541, 869, 1327
Joint Strength	1165
J-Q Analysis.....	869
J-Q-Tz Theory	193

K

K-Type Tubular Joints	1005
-----------------------------	------

L		Mesoscopic	785
Laminate	1141	Metal Matrix Composites	1219, 1237
Laminated Composites.....	403, 1165	Metal/Ceramic Joint.....	529
Lamination	1123	Metastable Phases	863
Lamination Theory.....	1159	Method of Caustics	313
Large Strain.....	277, 289	Micro Defects	767
Laser Profilometry	1123	Micro Vickers Hardness Test	577
Laser Surface Melting.....	595	Microcrack Interaction.....	667
Laser Weld	1321	Microcracks	667
Laser Welding.....	1309	Microcrystalline Grain.....	839
Leak Detection.....	887	Micromechanics.....	1, 121, 1219
Leak-Before-Break LBB.....	655	Microscopic Deformation.....	175
Life of Propagation	1005	Microscopic Mechanism.....	127
Life Prediction	1029	Microshrinkage.....	749, 981
Limit Analysis.....	133	Microstructure.....	863, 881, 933
Limit Ironing Reduction	547	Mismatching	1327
LMP Method.....	903	Mixed Mode.....	49, 73, 541
Load Interaction	127	Mixed Mode Fracture	1053
Load-Differential Strain Curve	1249	Mixed Mode Loading	325, 1035
Local Buckling Strength	1135	Mixed-Mode	1141
Local Fracture Criterion.....	1053	Mixture Model.....	1255
Localization.....	637, 785	MMC	625, 1243
Localized Flexibility	1093	Modal Design Sensitivity Analysis	439
Longitudinal Stiffener.....	517	Mode Analysis	355
Love Waves	725, 755	Mode I.....	169, 815
Low Carbon Steel	1315	Mode II	169
Low Cycle Fatigue..	749, 975, 981, 987, 1017	Model Accuracy.....	403
Lower Edge Crack	283	Modeling Error	403
Low-Velocity Impact.....	295, 1177	Modified 16-Node Solid Element.....	355, 469
Luminance.....	601	Modulus Mismatch	1261
M		Moiré Interferometry	409
Machine Element	475	Molded and Machined Notch	791
Magnetoelasticity	199	Monte Carlo Method.....	391
Martensitic Transformation	863	Monte Carlo Simulation	367, 1129
Mathematical Modelling.....	631	Morphology	779
Matrix Cracking	1141	MoSi ₂	909
Matrix Ductility	1063	Moving Element Method.....	445
Maximum Hoop Stress Criterion	1053	Moving Least-Squares MLS Method	487
MCM-D.....	1123	Mullite/SiC Ceramics	803
Mean Friction Coefficient.....	1225	Multi-Axial Loading.....	945
Mechanical Alloying.....	1291	Multi-Crack.....	809
Mechanical Loading.....	863	Multicrack Growth Model.....	367
Mechanical Parameter.....	433	Multidirectional Composites	247
Mechanical Properties.....	1291	Multilayer	1123
Mechanical Property Degradation	631	Multi-Layered Structure	1081
Mechanically Fastened Joints	1011	Multiple Cracks	97
Mechanism Method	463	Multiple Layers CFRP	1159
Mechanistic Model.....	217		
Median Filtering.....	391	N	
		Nanocomposite	1207

Nano-Deformation	737	Path Independent Integral	445
Nano-Fractography	827	PC/ABS	779, 1053
Nanomechanics	1	Peak Strength	809, 857
NaOH	707	Penetration	1231, 1339
Neural Network	559	Percolation	367
Neural Network Modeling	713	Perturbation Method	613
Neutron Dose	607	PET Matrix Composites	1171
Nondestructive Evaluation.....	619, 887, 1069	Phase Shifting	391
Nonlinear Behavior	637	Phase Unwrapping	391
Nonlinear Displacement Field	409	Phase Velocity	725, 755
Nonlinear Evolution.....	713	Phased Array.....	619
Nonlinear Flexural Behavior.....	427	Phenol Resin	1105
Normal Distribution.....	85	Photoelastic Experiment	115
Notch.....	181, 601, 999	Photoelasticity.....	145
Notch Sensitivity Factor	1029	PID Control.....	361
Nucleation Time.....	761	Piezoelectric Actuator.....	1201
Numerical Analysis.....	457, 499, 523	Piezoelectric Ceramics.....	673, 821
Numerical Approximation Error.....	403	Piezoelectric Element	619
Numerical Minimization.....	631	Piezoelectric Layered Structures	725, 755
Numerical Simulation	385, 637, 785	Piezoelectric Materials.....	695, 773
O		Pinned Joint	1165
On-Line Frequency Estimation.....	1201	Pipe Flange	475
On-Line Monitoring.....	887	Pit	939
Optical Extensometer.....	229	Plain-Woven Glass/Epoxy	
Optical Fiber Vibration Sensor	661	Composites	271
Optical Micrograph.....	577	Plane Compressional Wave	223
Optical-Fiber Extensometer.....	289	Plane Problem.....	199
Optimization	415	Plastic Deformation	541
Optimization Technique.....	61	Plastic Hinge.....	463
Optimum Design.....	493, 1117	Plasticity	217
Organic Brake Pad	1225	Plate	397
Orientation Angle.....	1159	PMMA	265
Orthotropic Plate.....	517	Polarization Curve	707
Orthotropic Structural Shapes.....	1135	Polyamide 6	1081
Overall and Local Responses.....	373	Polycarbonate	121, 229, 601
Overall Elastic Properties	667	Polymer.....	121, 1075
Overload.....	423	Polymer Alloy.....	779, 1053
Oxidation.....	833	Polymer Matrix Composites PMC....	229, 295
P		Polynomial Approximation	49
P/M Copper.....	205	Polypropylene Fiber.....	571, 881
Partial Crystallization.....	1255	Porosity.....	963
Partial Interfacial Debonding.....	761	Porous Solid.....	1195
Partial Slip.....	743	Post Welding Heat Treatment.....	1339
Particle	1297	Postbuckling	1189
Particle Dispersed	1219	Powder Metallurgy	1273, 1285
Particulate-Reinforced Composite		Pressure-Sensitivity	1195, 1231
Materials	761	Pressurized Thermal Shock	797
Patched Crack	103	Prestrain	1321
		Printing Wiring Board	643
		Probabilistic Fatigue	927

Probabilistic Fracture Mechanics.....	797
Progressive Collapse.....	1023
Progressive Failure Analysis.....	535, 1165
Pseudo Dynamic Elastic Moduli.....	307
P-S-N Curve.....	951
PTS Screening Criteria.....	797
Punch Shape.....	743

Q

Quasi-Cleavage Fracture.....	737
------------------------------	-----

R

Random Fatigue.....	1005
Random Variable.....	85
Rapid Press Consolidation Technique RPCT.....	1171
Rapid Solidification.....	839
Rate of Test.....	247
Rayleigh Wave Velocity.....	325
Rayleigh-Ritz Method.....	517
Recovery of Strength.....	803, 1047
Recrystallization.....	679
Reduction of Stress Intensity Factor.....	43
Reduction Ratio.....	379
Regular Fracture.....	55
Reinforcement.....	385
Reissner Plate.....	151, 163
Reissner Shell.....	151
Relative Thickness Ratio.....	373
Reliability.....	613, 957
Remaining Life.....	987
Remanent Polarization.....	821
Residual Strength.....	271
Residual Strength Analysis.....	649
Residual Stress.....	73, 529, 1219, 1279, 1339
Resonances.....	969
Response Surface Method.....	1023
Retardation Coefficient.....	85
Rigid Particle.....	1075
Rock Mass.....	385, 433
Rock Material.....	67
Rock Microfracturing Process.....	713
Rolling Contact Fatigue.....	1035
Rolling Stock.....	493
Roughness.....	217
Rubber Contents.....	583
Rubber Modified Adhesive.....	583
Rubber Toughened PMMA.....	409
Rubber-Modified Epoxy.....	1195
Rule of Mixtures.....	373

S

SA508-3.....	607
Scale Effect.....	1
Scattering.....	223
Sealing Performance.....	475
Secondary Curing Method.....	1087
Selected Load Sequence.....	127
SEM.....	625, 749, 981
SEM Observation.....	779
Semi-Elliptical Notch.....	523
SENB Specimen.....	869
Sensitivity Analysis.....	1023
Sensitization.....	595
SENT Specimen.....	869
Separated Dynamic J Integral.....	445
Separation of Solid.....	319
Shadow Spot Method.....	301
Shape Control.....	673
Shape Memory Alloy.....	673, 1309
Shape Memory Effect.....	1219, 1309
Shape Optimization.....	361
Shear.....	37
Shear Fracture.....	1053
Ship Hull Girders.....	1023
Shock Adiabatics.....	253
Short Crack.....	217
Short Fiber Reinforcement.....	1177
Si ₃ N ₄ /SiC Ceramics.....	1047
SiC Particle.....	625
Silica Particulate Filled Epoxide Resin ..	1053
Silicon Carbide Ceramic.....	1249
Silicon Carbide Composite Ceramic	1249
Silicon Nitride.....	833
Simulation.....	391
Single-Asperity-Contact Friction.....	1
Single-Node Quadratic Element.....	91
Singular Integral Equation.....	241, 499
Singular Line Mapping.....	151
SiO ₂	909
Sliding Crack Model.....	67
Slip.....	767
Small Diameter Drilling.....	643
Smart Structure.....	661
S-N Curve.....	1029
SN-DCB Specimen.....	815
Sobel Edge Enhancement.....	391
Soft ferromagnetic Materials.....	199
Softening.....	987
Solid Lubricant Wear.....	1267
Solid State Sintering.....	1291

Solid Wires.....	1339	Stress Interaction Effect.....	767
Solution Treatment.....	1237	Stress Ratio.....	827, 1249
Source Location.....	887	Stress Relaxation.....	1123
Spalling Cracks.....	1213	Stress Shot Peening.....	921
Spatial Random Process.....	19	Stress Triaxiality.....	121, 625, 875
Specific Damping Capacity.....	469	Stress Wave.....	337
Spherical Inhomogeneity.....	223	Stress Wave Propagation.....	349, 481
Spheroidal Graphite Cast Iron.....	749, 981	Stress-Strain Fields.....	193
Split Hopkinson Pressure Bar SHPB.....	307	Striation Height.....	827
Spot-Welded.....	415	Striation Width.....	827
Spot-Welded Joint.....	957	Striation-like Marking.....	719
Spraying.....	839	Structural Steels.....	939
Squeeze Cast Aluminium Alloy.....	1017	Structure Analysis.....	61, 423
Squeeze Casting.....	1237	STS 316L.....	1041
Squeeze Casting Method.....	1267	Substructure Strengthening.....	1207
Stacking Sequence.....	1141	Surface Acoustic Wave Devices.....	725, 755
Stainless Steel 304.....	31	Surface Crack.....	505, 1005, 1327
Staircase.....	951	Surface Roughness.....	915
Static Analysis.....	355	Surface-Roughness Evolution.....	1
Static Fatigue Strength.....	803, 1047	SUS304.....	1011
Statistics.....	951		
Steel D&I Can.....	547	T	
Stiffened Composite Plate.....	1189	Taguchi Method.....	1087
Stiffened Cylinder.....	481	Tailored Welded Blank.....	1321
Stiffness Reduction Method.....	535	Target Strength.....	1231
Stoney's Formula.....	1123	Tearing Modulus.....	505
Strain Constrain.....	1321	TEM Observation.....	779
Strain Control.....	975	Temper Bead Welding.....	1339
Strain Energy.....	517	Temperature.....	583, 815
Strain Energy Density Factor.....	957	Temporal Fractal.....	713
Strain Gauges.....	289	Tensile Properties.....	779
Strain Gradient Plasticity.....	9	Tensile Stiffness.....	25
Strain Hardening Exponent.....	205	Tensile Strength.....	1243
Strength.....	67, 637, 679, 839, 1207	Tensile Tests.....	577
Strength Mismatch.....	1333	Tension.....	25, 601
Strength Recovery.....	833	Texture.....	679, 845
Strengthening Mechanisms.....	1297	The Fourth Compressor Pan.....	969
Stress.....	969	Thermal Aging.....	631, 975
Stress Analysis.....	475, 547	Thermal Barrier Coating.....	909
Stress Concentration.....	25, 601, 767, 969, 1011	Thermal Cycle.....	529
Stress Concentration Factor.....	499, 523, 999	Thermal Shock.....	1213
Stress Control.....	361	Thermomechanical Bow.....	1123
Stress Corrosion Cracking (SCC).....	707	Thermoplastic Polymer.....	631
Stress Cutting.....	55	Thermoplastics.....	121
Stress Double Shot Peening.....	921	Thermotropic Liquid Crystalline	
Stress Intensity Factor.....	25, 31, 37, 49, 79, 109, 115, 145, 151, 163, 211, 259, 265, 319, 331, 487, 511, 523, 553, 743, 993, 1345	Polymers.....	1081
Stress Intensity Factor Range.....	999	Thick Composites.....	427, 791, 1069
		Thickness Effect.....	127, 193, 271
		Thickness Polynomials.....	403
		Thin Film.....	187

Thin-Walled Plate	451	Virgin Material	577
Three Flaws.....	857	Virtual Crack Extension Method	49
Three Gorge Project.....	385	Virtual Work.....	463
Three-Dimensional Cracks	193	Viscoelastic Material	761, 893
Three-Dimensional Fields.....	181	Void	875
Threshold	999	Void Configuration.....	625
Threshold Impact Energy.....	271	Void Growth.....	761
Threshold Stress Intensity Factor		Void Nucleation Model	1195
(K_{IH})	845	Void Volume Fraction	625
Ti-6Al-4V Alloy	1243	Voids.....	157
Ti-Alloy.....	1303	Volume Control	361
Time-of-Flight Base of Method	887	Volume Fraction	373
Time-Variation Reliability		VPS.....	909
Assessment.....	1023		
TiNi Alloy.....	1219	W	
Tool Wear	559, 643	Wakashima-Tsukamoto Estimate	373
Tooling.....	1285	Wall Ironing.....	547
Topology Optimization	379, 439	Wear Rate	1225
Toroidal Hole.....	499	Weibull Distribution	19
Toughness Testing Standards	133	Weight Function Method	103
Trigger Mechanism.....	1147	Welded Joint.....	1315
TTP Method	903	Welded Pipe.....	613
Tungsten Fiber	1243	Welding Process	1303
Tungsten Fiber Content Ratio	963	Welding Residual Stress.....	1345
Tungsten Fiber Reinforced Ti-6Al-4V		Weldment.....	1333
(W/Ti-6Al-4V) Alloy.....	963	Wheel-Rail Contact	493
Tungsten Heavy Alloy	1291	Whisker.....	1237
Two-Dimensional Elasticity	25	White Light Photoelastic Experiment.....	145
Two-Step Sintering	1291	Wide-Plate	655
		Winch.....	719
U		Window Pillar Member	415
Ultrasonic Peening	1315	Wire Rope.....	719
Ultrasonic Testing.....	619	With-Laminar	1153
Ultrasonics	1069	Workpiece Material	559
Underwater Explosion	481	Woven Glass Fabrics	1183
Undulation.....	1153		
Unidirectional Carbon Prepreg	1087	X	
Unified Description.....	181	XPS	1105
Unloading Behavior.....	265		
Unloading Rate	265	Y	
Upper Edge Crack.....	283	Y4 Steel	301
		Yield Strength.....	589
V		Yielding	1261
Vane Components.....	1029		
Vapor Deposition	679	Z	
Variability	85	Zr-2.5%Nb	845
Variable Amplitude Loading	85		
VCFEM.....	373		
Vibration	391		
Vibration Analysis	397		

KEY ENGINEERING MATERIALS

Specializing in Advanced Ceramics and Composites

Recent Volumes:

for complete tables of contents please visit <http://www.ttp.net>

- Electroceramics in Japan III, Eds. N. Murata, K. Shinozaki and T. Kimura
Advances in Engineering Plasticity, Eds. T.X. Yu, Q.P. Sun and J.K. Kim
Engineering Ceramics: Multifunctional Properties, Eds. P. Sajgalik and Z. Lencés
Creep and Fracture of Engineering Materials and Structures, Eds. T. Sakuma, K. Yagi
Electroceramics in Japan II, Eds. N. Mizutani, K. Shinozaki, N. Kamehara, T. Kimura
Damage Assessment of Structures, Eds. M.D. Gilchrist, J.M. Dulieu-Barton, K. Worden
Time Dependent Mechanical Response of Engineering Ceramics, Eds. E. Yasuda, F. Wakai, L.M. Manocha, Y. Tanabe
High Temperature Ceramic Matrix Composites III, Eds. K. Niihara, K. Nakano, T. Sekino, E. Yasuda
The Science of Engineering Ceramics II, Eds. K. Niihara, T. Sekino, E. Yasuda, T. Sasa
Novel Synthesis and Processing of Ceramics, Eds. H. Suzuki, K. Komeya and K. Uematsu
Electroceramics in Japan I, Eds. N. Mizutani, K. Shinozaki, N. Kamehara and T. Kimura
Oxides: Phase Transitions, Non Stoichiometry, Superconductors, Ed. C. Boulesteix
Zirconia Engineering Ceramics: Old Challenges - New Ideas, Ed. E. Kisi
Solidification Processing of Reinforced Metals, by R. Asthana
Sol-Gel Production, Ed. H. Schmidt
Fracture and Strength of Solids, Eds. P. Tong, T.Y. Zhang and J.K. Kim
Experimental Techniques and Design in Composite Materials, Ed. Pierluigi Priolo
Impact Response and Dynamic Failure of Composites and Laminated Materials, Eds. J.K. Kim and T.X. Yu
Advanced Ceramic Tools for Machining Application - III, Ed. I.M. Low
Polymer Blends and Polymer Composites, L. Ye and Y.-W. Mai
Euro Ceramics V, Eds. P. Abelard, J. Baxter, D. Bortzmeyer et al.
Ceramic and Metal Matrix Composites, Eds. M. Fuentes, J.M. Martínez-Esnaola, A.M. Daniel
Electrical Properties of Oxide Materials, J. Nowotny and C.C. Sorrell
Advanced Ceramic Materials, Hamid Mostaghaci
Fracture of Composites, Ed. E.A. Armanios
Metal Matrix Composites, Ed. G.M. Newaz

Key Engineering Materials presents 18 volumes per year, each centering on a special topic of current interest in the fields of advanced ceramics and composites. The yearly subscription rate is 1404.00 CHF.

Please place your trial subscription with complete return rights:

Trans Tech Publications Ltd • Brandrain 6 • CH-8707 Zuerich-Uetikon • Switzerland
Fax: (+41) 1 922 10 33 • E-Mail: ttp@ttp.net • Web Site: <http://www.ttp.net>